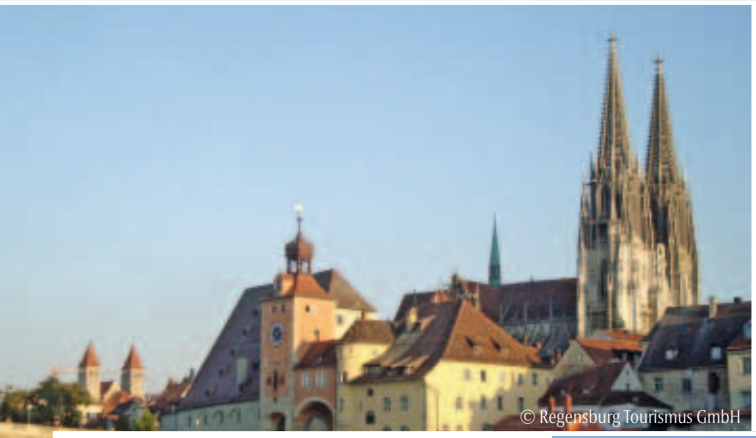

MC 2013 Regensburg

August 25–30, 2013
University of Regensburg
Regensburg/Germany

Universität Regensburg

Organizers

DGE – German Society for Electron Microscopy e. V.

ASEM – Austrian Society for Electron Microscopy

SSOM – Swiss Society for Optics and Microscopy

CMS – Croatian Microscopy Society

CSMS – Czechoslovak Microscopy Society

HSM – Hungarian Society for Microscopy

SDM – Slovene Society for Microscopy

SISM – Italian Society of Microscopical Sciences

SSM – Serbian Society for Microscopy

TEMD – Turkish Society for Electron Microscopy

EMS – European Microscopy Society

Plenary Lectures • Poster Sessions • Workshops • Industrial Exhibition

PROCEEDINGS
INSTRUMENTATION AND METHODS (IM)
MATERIALS SCIENCE (MS)

MC 2013 PROCEEDINGS

Core/shell Nanostructures Embedded in Solid

V. R. Radmilović[1,2]

[1]University of Belgrade, Faculty of Technology and Metallurgy, Nanotechnology and Functional Materials Laboratory, 11120 Belgrade, Serbia.
[2]National Center for Electron Microscopy, Lawrence Berkeley National Laboratory, Berkeley, CA 94720, USA.

VRRadmilovic@tmf.bg.ac.rs; VRRadmilovic@lbl.gov

Keywords: aberration-corrected HRTEM, core/shell nanostructures, light element imaging.

This study illustrates the importance of understanding the fundamental features that underlie the behavior of nanoscale phases with coherent interfaces embedded in a solid and their role in the evolution of microstructure in materials. The fundamental principles established using model systems are employed in the design and testing of new materials such as systems for energy-related applications. Key requirements for advanced alloys are high strength, light weight, coarsening resistance, corrosion resistance, high temperature stability, etc. Unfortunately, these requirements are mutually exclusive in many Al-based alloys. The extraordinary effects on mechanical properties arising from the formation of second-phase particles are well known, and exploited in applications ranging from energy generation to aerospace structures [1].

Al-Li and Al-Sc alloys are of great interest for aerospace and cryogenic applications due to their low density and high strength-to-weight ratio. The excellent mechanical properties of these alloys are based on a fine dispersion of coherent Al_3Li metastable and Al_3Sc stable precipitates. The aim of this report is to show the effect of Li addition on core/shell precipitate formation in the ternary Al-Li-Sc alloys. The atomic structure of these precipitates has been studied by a range of advanced microscopy techniques, such as high resolution TEM with exit wave reconstruction, atomic resolution HAADF imaging, and energy filtered electron energy loss spectroscopy (EELS), combined with the first principle calculation and continuum thermodynamic modeling to uncover the role of Li. We demonstrated that monodisperse Al_3LiSc core/shell ordered precipitates with a Sc and Li-rich core surrounded by a Li-rich shell can be created via a two-stage heat treatment. During the first aging stage at 450°C, Li incorporation into the cores leads to a burst of nucleation followed by rapid depletion of Sc solute. In the second stage, at 190°C, $Al_3(LiSc)$ cores become spherical substrates for solid-state epitaxial growth of Al_3Li, which leads to shell formation through a barrier-less process of solid state wetting [2]. The thickness of the core and shell are anti-correlated, such that the size distribution of the total core-shell particle is narrower than that of either the core or the shell. Li-rich shell shows almost no compositional differences between adjacent columns. By contrast, the core superlattice columns are highly disordered, evidence for random mixing of Li and Sc on these sites. The columns surrounding the superlattice columns are very uniform, showing the amount of solute atoms occupying these sites to be negligible. In fact, no anti phase boundary (APB) defects were observed in any of the investigated $Al_3(LiSc)$ core/shell precipitates. These defects are known to be very energy-costly at room temperature, i.e. 290 mJ/m^2 in Al_3Sc [3] and 118 mJ/m^2 in Al_3Li [4]. The first principle calculation predicts that the core-shell precipitates in the investigated AlLiSc alloy to be thermodynamically stable phases, with no driving force for the diffusion of Li out of the core into the shell. High-resolution phase contrast imaging and geometric phase analysis shown in Figure 1a and b, respectively, reveal that both, the core and the shell are fully ordered in the $L1_2$ structure and fully coherent with the surrounding fcc matrix. With prolonged aging time, for more than 1000h at 190°C, these particles exhibit coarsening, and create an interfacial dislocation at the Al_3Li shell/Al matrix interface, in order to accommodate coherent strain increase due to misfit in their lattice parameters, as shown in Figure 2a and b. Aberration corrected transmission electron microscopy was employed to image Li using exit wave reconstruction [5]. The phase of the exit wave shown in Figure 3 distinguished clearly Al columns from Li columns in the Li rich $L1_2$ shell [6]. Li concentration in the core could be calculated from scanning transmission electron microscopy of $Al_3(LiSc)$ nanoparticles. This procedure uses an analysis technique that normalizes the signal from the $L1_2$ superlattice columns to the immediately adjacent pure Al columns. By knowing that the total amount of Sc and Li is 25 at.%, the composition of each column can be determined individually. This calculation shows appreciable and uniform incorporation of 9.7 ± 2.4 at.% Li in the core of the precipitates. For this ternary AlLiSc alloy we show a way of producing an uniform distribution of coarsening resistant monodispersed $Al_3(LiSc)$ core/shell particles in an Al matrix with unusually narrow size distribution. A detailed analysis of these precipitates has provided important insights into their atomic structure and composition [7].

1. K. Lu, Science 328 (2010) 319.
2. V. Radmilović et al., Nature Materials 10 (2011) 710.
3. K. Fukunaga et al., Materials Science and Engineering A239–240 (1997) 202.
4. S.M. Jeon and J.K. Park, Acta Materialia 44 (1996)1449.
5. Y. Shao-Horn et al., Nature Materials 2 (2003) 464.
6. M. Rossell et al., Physical Review B 80 (2009) 024110.
7. I would like to thank to my former graduate students, post-docs and colleagues at The National Center for Electron Microscopy at Berkeley and at The University of Belgrade, Serbia, for their contributions to this project. This research is supported by the Department of Energy under contract no. DE-AC02-05CH11231. Supports of Nanotechnology and Functional Materials Center, funded by the European FP7 project No. 245916, and from the Ministry of Education and Science of the Republic of Serbia (project No. 172054), are also acknowledged.

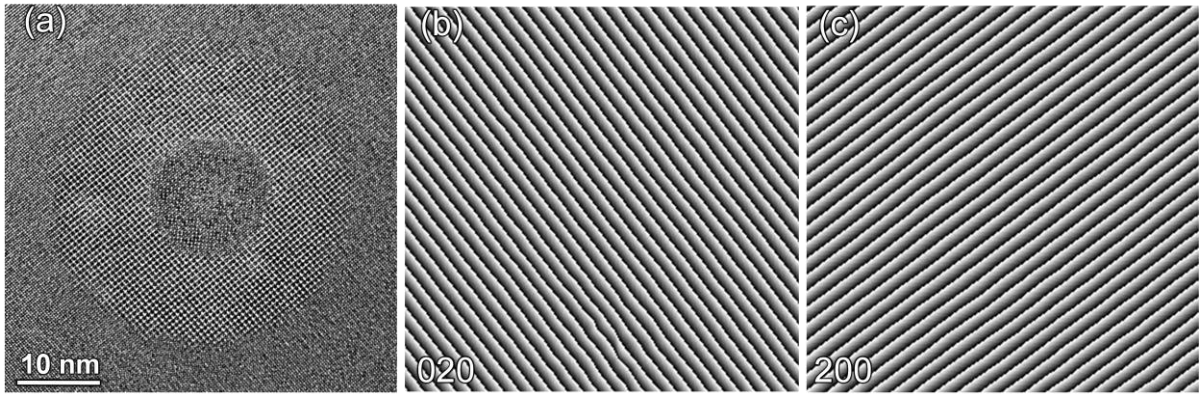

Figure 1. (a) HRTEM micrograph of a single $Al_3(LiSc)$ core-shell precipitate obtained at peak aging, after 4h at 190°C; (b) and c) Moire images created using 020 and 200 reflections in digital diffractogram, respectively, showing perfect alignment of {200} planes in both, Al matrix and core/shell precipitate; no dislocations at Al_3Li shell/Al matrix interface are present.

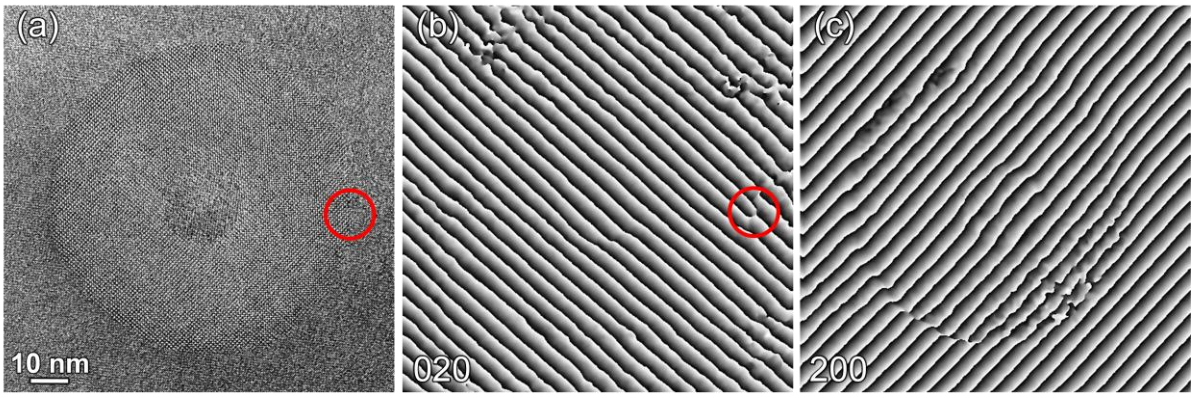

Figure 2. (a) HRTEM micrograph of a single $Al_3(LiSc)$ core-shell precipitate obtained from overaged sample, after 1000h at 190°C; (b) and (c) Moire images created using 020 and 200 reflections in digital diffractogram, respectively, showing significant distortion of {200} planes and the presence of dislocation at the Al_3Li shell/Al matrix interface (in the red circle).

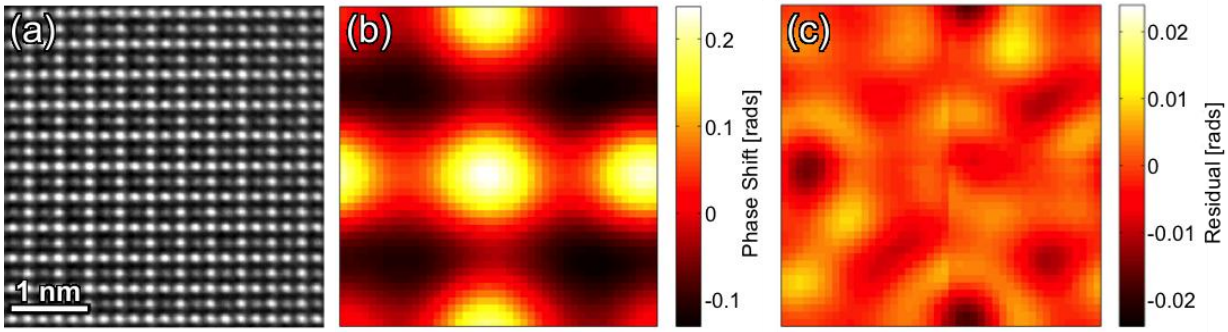

Figure 3. (a) Experimental high resolution exit wave phase image of Al_3Li ordered structure taken close to [001] zone axis; white dots are from Al columns and gray dots are from Li columns; (b) and (c) are 2D representation of the statistics of the experimental data, shown as the average experimental unit cell and the standard deviation image.

Scanning transmission electron microscopy (STEM) and analytical electron microscopy of biological and nano materials

R. D. Leapman[1], J. Zhang [2], J. S. Diamond[2], X. Chen[3], T. S. Reese[3], A. A. Sousa[1]

1. Laboratory of Cellular Imaging & Macromolecular Biophysics, NIBIB, National Institutes of Health, Bethesda, MD 20892, USA
2. Synaptic Physiology Section, NINDS, National Institutes of Health, Bethesda, MD 20892, USA
3. Laboratory of Neurobiology, NINDS, National Institutes of Health, Bethesda, MD 20892, USA

leapmanr@mail.nih.gov
Keywords: STEM, analytical EM, electron tomography

The scanning transmission electron microscope (STEM) offers high collection efficiency for signals generated by interaction of a finely focused, nanometer-sized, electron probe, which makes STEM well suited for analyzing beam-sensitive biological specimens [1]. In particular, elastically scattered electrons collected by the STEM's annular dark-field detector (ADF) yield a signal that is proportional to the mass of a biological structure contained within the volume illuminated by the probe. This mass mapping technique enables molecular weights of large protein assemblies to be determined [2,3]. For example, it is possible to characterize the organization of subunits in filamentous proteins that have indefinite total mass but well defined mass-per-length, such as disease-associated amyloid fibrils [4,5]. The strong ADF elastic scattering signal from heavy atoms can also be applied to visualize heavy atom clusters, which are used to label specific protein assemblies in their cellular context [6].

By collecting the inelastic scattering signal using an electron energy loss spectrometer (EELS), it is possible to quantify the distributions of metal ions and low atomic number atoms contained within macromolecular complexes or subcellular compartments [7,8]. The STEM-EELS spectrum-imaging technique enables weak spectral features to be extracted, e.g., to measure minute concentrations of calcium, an important regulatory element, in specific subcellular compartments of freeze-dried preparations of cells and tissues [9]. It has also been possible to detect the iron cores of individual ferritin molecules distributed in regions of unstained brain, where iron regulates important cellular processes and, when stored as ferritin, gives rise to magnetic resonance imaging contrast [10].

A combination of STEM and EELS has been used in a number of laboratories to analyze the structure and composition of hybrid organic-inorganic bio-nanoparticles developed as diagnostic and therapeutic reagents in applications to nanomedicine [11-13].

Important advantages can be realized when the STEM is employed to perform electron tomography [14-20]. We have demonstrated that STEM tomography enables determination of the three-dimensional ultrastructure of embedded cells sectioned to a thickness of 1 to 2 μm [17-19]. Such specimens are considerably thicker than can be analyzed by conventional TEM tomography, for which resolution is limited by chromatic aberration of the objective lens due to multiply inelastic scattering. We have utilized a probe of small angular convergence (approximately 1 mrad) to give a diffraction-limited probe size of about 1 nm. The small angular convergence also results in a large depth-of-field throughout the specimen thickness since geometrical spreading of the probe is only a few nanometers. Moreover, the use of an on-axis bright-field detector reduces effects of beam broadening, since most electrons that undergo multiple elastic scattering in the lower part of thick specimens do not reach the detector (Fig. 1). Therefore, spatial resolution in bright-field STEM tomograms is improved relative to STEM tomograms acquired with an annular dark-field detector [17].

We have recorded dual-axis bright-field STEM tomograms in an FEI Tecnai TF30 transmission electron microscope equipped with a Shottky field emission gun operating at an acceleration voltage of 300 kV. Specimens were prepared by fixation, dehydration, embedding, ultramicrotomy and post-staining, with or without rapid freezing and freeze-substitution. Gold nanoparticles were deposited on the top and bottom surfaces of the sections to aid in alignment of the tilt series. Images were acquired over an angular range of ±54° after pre-irradiation with a broad beam in TEM mode to stabilize ultrastructure. Tomograms were reconstructed by means of the IMOD program (University of Colorado) [21], and were visualized with the Amira software package.

The STEM tomography approach is ideally suited to visualizing whole neuronal synapses, which have dimensions of order 0.5 to 1 μm, and for making quantitative measurements on the numbers, sizes and shapes of synaptic components. For example, we have applied the technique to study the architecture of two types of retinal ribbon synapses, which are specialized structures at presynaptic active zones encoding a wide dynamic range of sensory signals through continuous vesicle release. We have applied the technique to determine the full 3D architecture of ribbon synapses in mammalian (rat) cone photoreceptor cells and rod bipolar cells as shown in Fig. 2 [22,23].

In another application of STEM tomography, we have reconstructed entire spine postsynaptic densities (PSDs) in cortical regions of mouse brain. It was possible to determine the thickness, shape and area of PSDs for every synapse within defined 60 μm^3 volumes of neuropil [24]. STEM tomography of thick sections provides a useful approach for determining the nanoscale structure of entire synapses in different types of neuronal tissues, which can help to gain insight into specialized synaptic function.

In summary, the STEM offers a variety of quantitative imaging modes for identifying heavy-atom labels, determining molecular mass, measuring elemental content, and elucidating the 3D structure of biological and bio-nanomaterials [25].

1. A.V. Crewe and J.S. Wall, *J. Mol. Biol.* 48 (1970) 375.
2. A. Engel, *Ultramicroscopy* 3 (1978) 273.
3. J.S. Wall and J.F. Hainfeld, *Ann. Rev. Biophys. Biophys. Chem.* 15 (1986) 355.
4. A.T. Petkova, et al., *Proc. Natl. Acad. Sci. USA* 99 (2002) 16742.
5. N. Norlin et al., *J. Struct. Biol.* 180 (2012) 174.
6. J.F. Hainfeld, *Science* 236 (1987) 450.
7. R.D. Leapman et al., *Ultramicroscopy* 49 (1993) 225.
8. R.D. Leapman, *J. Microsc.* 210 (2003) 5.
9. J. Feng, A.V. Somlyo and A.P. Somlyo, *J. Microsc.* 215 (2004) 92.
10. M. Fukunaga et al. *Proc. Natl. Acad. Sci. USA* 107 (2010) 3834.
11. M.M. van Schooneveld et al., *Nature Nanotech.* 5 (2010) 538.
12. R.D. Leapman, *Nature Nanotech.* 5 (2010) 480.
13. A.E. Porter et al., *Nature Nanotech.* 2 (2007) 713.
14. P.A. Midgley et al., *Ultramicroscopy* 96 (2003) 413.
15. I. Arslan, J.R. Tong and P.A. Midgley, *Ultramicroscopy* 106 (2006) 994.
16. A.E. Yakushevska et al., *J. Struct. Biol.* 159 (2007) 381.
17. M.F. Hohmann-Marriott et al., *Nature Methods* 6 (2009) 729.
18. A.A. Sousa et al., *Ultramicroscopy* 109 (2009) 213.
19. A.A. Sousa et al., *J. Struct. Biol.* 174 (2011) 107.
20. N. de Jonge and F.M. Ross, *Nature Nanotech* 6 (2011) 695.
21. J.R. Kremer, D.N. Mastronarde and J.R. McIntosh, *J. Struct. Biol.* 116 (1996) 71.
22. J.S. Diamond, *Nature Neuroscience* 14 (2011) 1097.
23. J. Zhang et al., *Proc. ARVO* (2012) 4318.
24. X. Chen et al., *J Neurosci.* 31 (2011) 6329.
25. This research was supported by the intramural programs of NIBIB and NINDS, NIH.

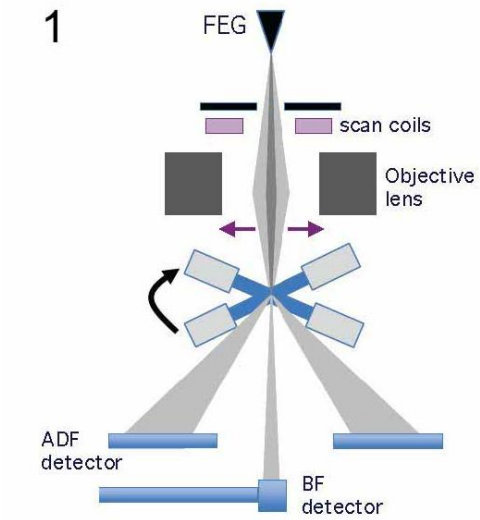

Figure 1. Schematic diagram of STEM tomography acquisition showing field-emission gun (FEG), scan coils, objective lens, and high-angle annular dark-field (ADF) and axial bright-field (BF) detectors.

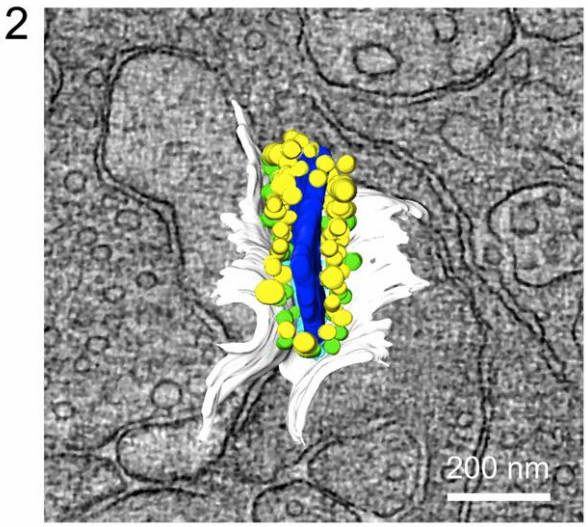

Figure 2. Ortho-slice through portion of dual-axis STEM bright-field tomogram of 1.2-µm thick section of stained rat retina, with superimposed visualization of entire ribbon synapse in cone photoreceptor cell. A central ribbon is evident with a series of docked vesicles (yellow); vesicles that are adjacent to the membrane are shown in green.

Three-dimensional imaging and analysis at the nanoscale by optical sectioning and confocal methods in the transmission electron microscope

P. D. Nellist[1]

[1]Department of Materials, University of Oxford, Parks Road, Oxford, OX1 3PH, UK.

peter.nellist@materials.ox.ac.uk
Keywords: optical sectioning, confocal, 3D

The development of hardware correctors for the spherical aberration of electron lenses has resulted in dramatic improvements in the resolution of electron microscopes (for example [1]). The resolution improvement arises from the increase in numerical aperture allowed by the aberration correction. Increase in numerical aperture results in a reduction in the depth of focus of the microscope, with the depth of focus depending on the inverse square of the numerical aperture. In a state-of-the-art transmission electron microscope (TEM), the depth of focus may be just a few nanometres, which can often be smaller than the thickness of the TEM sample. Although this situation may be regarded as a problem, one could say that the aberration corrector has *improved* the depth resolution to the point where features can be resolved in samples in three-dimensions (3D).

Early work by Van Benthem et al. [2] showed that the height of single impurity atoms in a sample could be determined from their visibility in a focal series of images using annular dark-field imaging in the scanning TEM (ADF-STEM). Each image in such a series can be regarded as representing a lateral section of the sample at the depth set by the focus, hence the term “optical sectioning”. To explore the 3D resolution limits of such an approach, the 3D transfer function can be examined. Figure 1 shows the 3D transfer functions for three different imaging geometries. It can be seen that the incoherent nature of ADF-STEM imaging much improves the 3D transfer compared to conventional high-resolution TEM, but that a large missing cone of transfer persists, which will rapidly worsen the depth resolution for laterally extended objects [3]. Nonetheless, at atomic lateral resolution, ADF-STEM can achieve nanoscale depth resolution. Figure 2 shows how the core of dislocation in GaN, inclined relative to the beam direction, can be seen to translate laterally between frames in a focal series. Optical sectioning in ADF-STEM has also been used to observe the depth dependent displacements that arise from the so-called Eshelby twist effect for dislocations containing a screw component [4]. This approach allows the existence and sign of a screw component to be determined for dislocations viewed end-on, and allows observed dislocation core structures to be associated with specific dislocation types [5].

In light microscopy, optical sectioning is commonly performed in a confocal mode. We have developed the technique of scanning confocal electron microscopy (SCEM), making use of an instrument fitted with both probe and imaging correctors. A theoretical and computational analysis of contrast and resolution limits in SCEM [3] shows that no contrast will be observed for weak-phase objects using elastic scattering, but that the incoherent nature of inelastic scattering will lead to a transfer function that fills the missing cone of information seen in the transfer function of ADF-STEM and provides the most complete transfer of 3D information. Experimental implementation of an energy-filtered SCEM (EF-SCEM) technique confirms that nanoscale depth resolution is maintained for laterally extended objects [6]. It is also found that the effect of the focus spread caused by chromatic aberration does not degrade the depth resolution, but does result in a loss of signal strength. Figure 3 shows the application of the EF-SCEM technique to 3D elemental mapping of a core-shell structure, where the observation of Si in the core material helps elucidate the mechanism of formation of the overall structure [7]. Finally, the development of hardware correctors for chromatic aberration provides a mechanism by which signal strength for EF-SCEM can be improved.

1. P.D. Nellist, M.F. Chisholm, N. Dellby et al., Science 305 (2004) 1741.
2. K. Van Benthem, A.R. Lupini, M. Kim et al., Appl. Phys. Lett. 87 (2005), 034104.
3. E.C. Cosgriff, P.D. Nellist, A.J. D'Alfonso et al. Adv. Imaging and Electron Phys. 162 (2010) 45.
4. J. Lozano, M.P. Guerrero-Lebrero, A. Yasuhara et al., submitted (2013).
5. P.B. Hirsch, J.G. Lozano, S. Rhode et al., Phi. Mag. In press (2013) available online.
6. P. Wang, G. Behan, M. Takeguchi et al., Phys. Rev. Lett. 104 (2010) 200801.
7. P. Wang, A. Hashimoto, M. Takeguchi, Appl. Phys. Lett. 100 (2012) 213117.

8. I am indebted to the former and current members of my research group, and colleagues elsewhere, who have collaborated on this work, including Peng Wang, Gavin Behan, Eireann Cosgriff, Juan Lozano, Prof Sir Peter Hirsch FRS, Angus Kirkland, Les Allen, Adrian D'Alfonso, Scott Findlay, Ayako Hashimoto, Masaki Takeguchi, Kazutaka Mitsuishi, Masayuki Shimojo, Prof Sir Colin Humphreys FRS, Michelle Moram, Sneha Rhode, S. Zhang, Matthew Horton, A. Yasuhara and E. Okunishi.

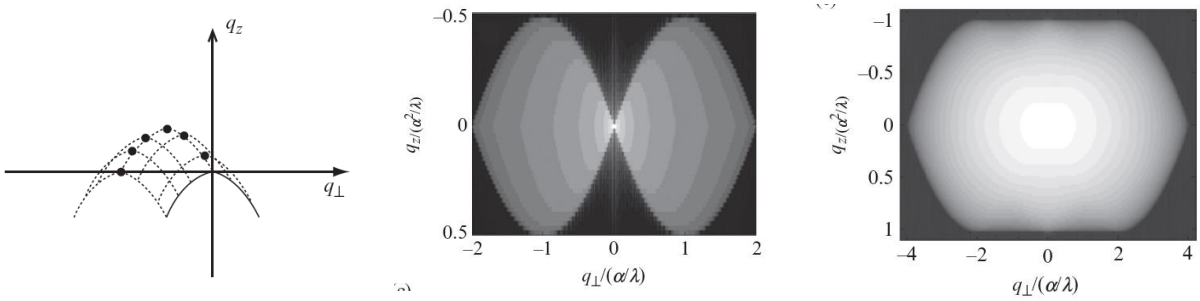

Figure 1. (left) The solid line shows the region of reciprocal space transferred by conventional HRTEM; (middle) incoherent imaging by ADF-STEM gives a larger volume of transfer but with a significant missing cone; (right) EF-SCEM gives the largest volume of transfer with no missing cone ensuring maximum depth resolution over a range of lateral spatial frequencies. For further details on this figure see Ref. [3].

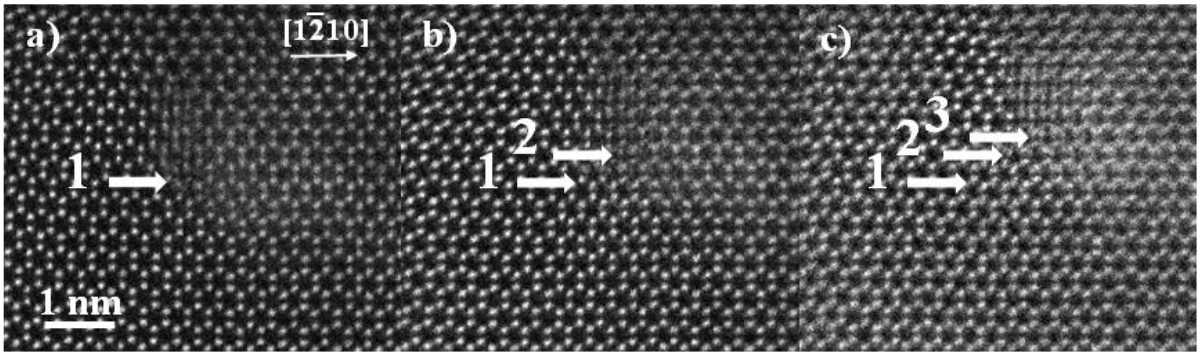

Figure 2. Part of a high resolution STEM-HAADF focal series of micrographs of a mixed dislocation in GaN imaged end-on recorded at three different focus values, showing the shift of the core structure seen below the arrows arising from the inclination of the dislocation. For further details on this figure see Ref. [5]

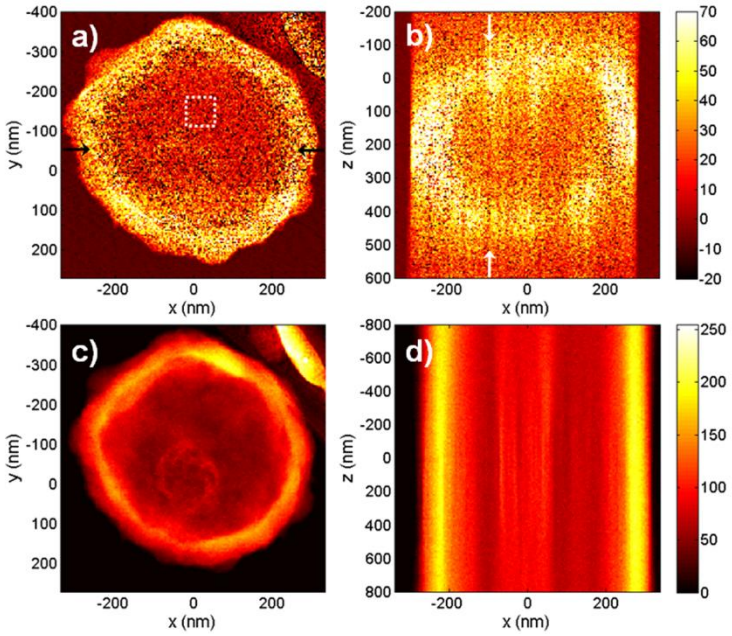

Figure 3 EF-SCEM on a hollow Fe_2O_3@SiO_2 mesoporous sphere. (a) and (b) Si core-loss signals from x-y and x-z scans, respectively, using the "three-window" technique; (c) and (d) HAADF x-y and x-z scans, respectively of the same region. The core can be seen to contain Si. Note the reduction in depth elongation in EF-SCEM compared to ADF-STEM.

High-resolution 3D Structure Determination of Dynamic Macromolecular Complexes by Single Particle cryo-EM

N. Fischer[1], E. Paleskava[1], A. Konevega[1], M. Rodnina[1], H. Stark[1]

[1]Max-Planck-Institute for biophysical Chemistry, 37077 Goettingen, Germany

Using the latest developments in electron microscopic hardware combined with advanced computational image processing it is now possible to determine structures of large and dynamic macromolecular complexes at near atomic resolution. We have determined the structure of a 70S ribosome-SelB complex at 3.8 Å resolution which is sufficient to determine a de novo structure of SelB bound to the ribosome. SelB is the elongation factor specific for the delivery of the selenocysteine-tRNA to the ribosome. This also requires a stop codon in the mRNA being recoded into a signal for selenocysteine incorporation by a SECIS element in the pre-mRNA. Selenocystein incorporation is already a rather inefficient process in vivo making the structure determination of SelB bound to the ribosome an evasive target in structural biology for a long time. Successful structure determination in fact requires extensive optimization of the ribosome-SelB complex preparation and image sorting of a rather heterogeneous population of ribosome complexes. This strategy allows not only the structure determination at very high resolution but also the simultaneous structure determination of numerous functionally distinct states of the ribosome-SelB complex.
As a control we also have determined the structure of the ribosome-EFTu complex at 3.2 Å resolution. EF-Tu is the elongation factor responsible for transport of all canonical aminoacyl-tRNAs to the ribosome. Having both structures available at high resolution we obtained a detailed view of how the ribosome can be hijacked by SelB to allow the recoding of a stop signal into a signal for selenocysteine incorporation.

From form factors to vortex electrons: Following Ariadne's thread

P. Schattschneider

Since the days when spectrometers for the TEM became commercially available, EELS has seen enormous theoretical and experimental progress. Fundamental problems concerning the inelastic interaction of fast probe electrons with matter have occupied the community for decades. It turns out that inelastic scattering can be understood on the basis of the dynamic form factor and its generalisation, the mixed dynamic form factor (MDFF), introduced by Harald Rose more than three decades ago. Amazingly, the experimental verifications of this concept rely on two other well-known contributions of the same researcher: energy filters and correctors.

Like Ariadne’s thread in the Greek myth, the MDFF is a guide throught the maze of so disparate aspects of inelastic interactions as coherence, delocalisation, mapping of orbitals, circular dichroism, and vortex electrons.

Shifting the paradigm in modern light microscopy: Light Sheet-based Fluorescence Microscopy (LSFM, SPIM, DSLM)

E. H. K. Stelzer[1]

[1]Physical Biology (FB 15, CEF-MC, BMLS), Goethe Universität, Frankfurt am Main, Germany

ernst.stelzer@physikalischebiologie.de

Specimens scatter and absorb light. Thus on one hand, the delivery of the probing light and the collection of the signal light (e.g. fluorescence) become inefficient, when relevant almost mm-thick specimens are investigated. On the other hand, not only fluorophores, but many endogenous biochemical compounds absorb light and suffer degradation of some sort (photo-toxicity), which can induce a malfunction of a specimen. In conventional and confocal fluorescence microscopy, whenever a single plane is observed, the entire specimen is illuminated (Verveer 2007). Recording stacks of images along the optical z-axis thus illuminates the entire specimen once for each plane. Hence, cells are illuminated 10-20 and fish embryos 100-300 times more often than they are observed (Keller 2008). This can be avoided by using light sheets, which are fed into the specimen from the side and overlap with the focal plane of a wide-field fluorescence microscope. In contrast to an epi-fluorescence arrangement, an azimuthal arrangement uses at least two independently operated lenses for illumination and detection (Stelzer 1994; Huisken 2004). A SPIM employs a cylindrical lens to generate a light sheet. A collimated laser beam is focused into the plane of the detection lens along one direction while the other direction remains collimated (Engelbrecht & Stelzer, 2006; Greger et al., 2007). Although this approach is relatively simple and straightforward it suffers from the low quality of the cylindrical lens and the inefficiency of the illumination system (Breuninger et al., 2007). The major advantage of a digital scanned laser light sheet-based fluorescence microscope (DSLM; Keller et al., 2008) is that it relies entirely on cylindrically symmetric optics and hence provides a very good optical quality. In addition, a DSLM employs a minimal number of optical components and does not suffer from excessive wavefront aberrations. In general, optical sectioning and no photo-toxic damage or photo-bleaching outside a small volume close to the focal plane are intrinsic properties of light sheet-based fluorescence microscopy (LSFM). It takes advantage of modern camera technologies and can be operated with laser cutters (e.g. Colombelli 2009) as well as in fluorescence correlation spectroscopy (FCS, e.g. Wohland 2010). We have also successfully evaluated the application of structured illumination in a LSFM (SPIM, Breuninger et al., 2007; DSLM, Keller 2010). We also designed and implemented a wide-field frequency domain fluorescence lifetime imaging (FLIM/FRET, Greger 2011) setup. More recently, we applied LSFM for investigations in plant biology (Maizel 2011), three-dimensional cell biology as well as emerging model organisms and developed new scanning schemes based on novel optical arrangements that allow us to take full advantage of very high resolution light microscopy. The development of LSFM draws on many previous developments. In particular, confocal theta fluorescence microscopy played a very important role. About a dozen papers on theta microscopy describe its properties, its relationship to 4Pi microscopy and that of LSFM (single & two-photon, annular/Bessel beams, (a)symmetric arrangements) theoretically as well as practically.

1. http://www.researcherid.com/rid/A-7648-2011

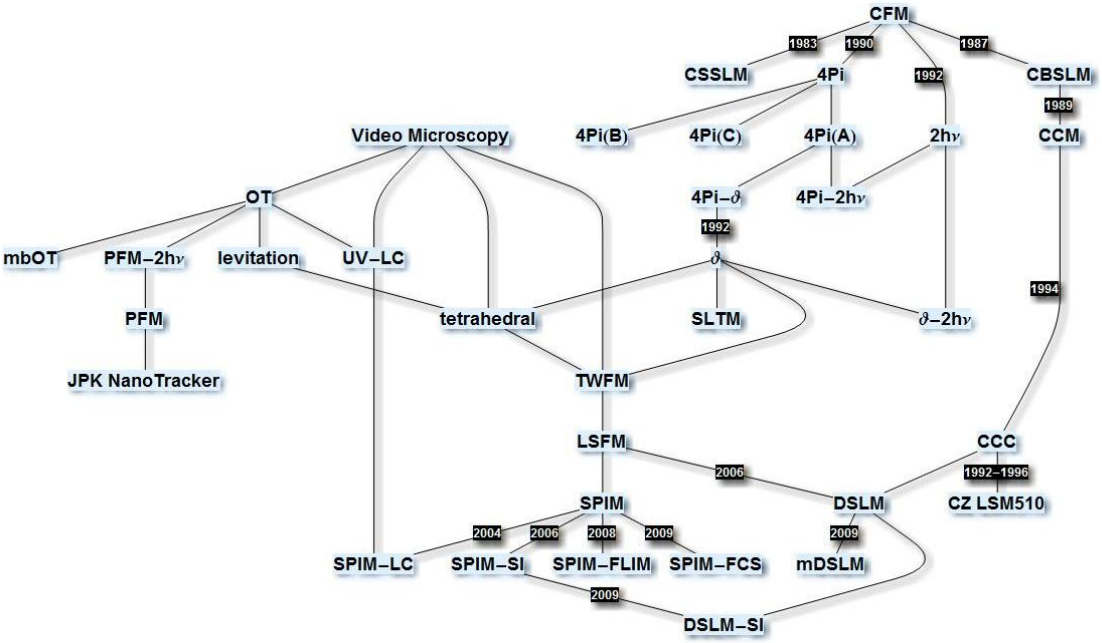
CFM
1983
1990
1987
CSSLM
4Pi
1992
CBSLM
1989
Video Microscopy
4Pi(B)
4Pi(C)
4Pi(A)
2hν
CCM
OT
4Pi–ϑ
4Pi–2hν
1992
mbOT
PFM–2hν
levitation
UV–LC
ϑ
1994
PFM
tetrahedral
SLTM
ϑ–2hν
JPK NanoTracker
TWFM
LSFM
CCC
2006
1992–1996
SPIM
DSLM
CZ LSM510
2004
2006
2008
2009
2009
SPIM–LC
SPIM–SI
SPIM–FLIM
SPIM–FCS
mDSLM
2009
DSLM–SI

Figure 1.

Cryofixation of biological specimens – electron spectroscopic imaging of calcium and phosphorus of osteoblastic cell cultures and an elegant way to produce section ribbons with the help of a newly developed micromanipulator.

D. Studer[1], J. P. Gorski[2], T. Hillmann-Marti[1], A. Klein[1], M.-I. Iacovache[1], H. Gnaegi[3]
B. Zuber[1]

[1]Institute of Anatomy, University of Bern, Bern, Switzerland
[2]Center of Excellence in Mineralized Tissues and Department of Oral Biology, School of Dentistry, University of Missouri Kansas City, Kansas City, USA
[3]Diatome SA, Helmstrasse 1, 2560 Nidau, Switzerland

studer@ana.unibe.ch
Keywords: dry- and cryo-sectioning, oscillating knife, high pressure freezing, electron spectroscopic imaging, bone mineralisation foci, micromanipulation

Transmission electron microscopy has provided most of what is known about the ultrastructural organization of tissues, cells and organelles. Most samples were prepared according to the classical protocol of so called chemical fixation. During fixation with aldehydes, postfixation with heavy metals, dehydration in a solvent and subsequent embedding into a resin samples are preserved in such a way that they are easy processed for electron microscopic evaluation. However chemical fixation cannot preserve the native ultrastructural details in a satisfactory way. Quite some artefacts are introduced by this procedure (precipitations, loss of molecule, swelling, 1,2,3). Furthermore due to the recording of heavy metal staining patterns only an indirect visualization is possible. Subcellular structures of biological samples are preserved close to native state by cryofixation. Bulk specimens (thicker than some micrometre) are only well frozen or vitrified when high pressure freezing is applied. Subsequent cryosectioning and investigation in the cryo-electron microscope (CEMOVIS) leads to a structural preservation which is close to the native state of the sample (4).

A compromise is freezing followed by freeze-substitution. The samples show better structural preservation in comparison to samples chemically fixed (1,2,3). However freezing leading to vitrification is only possible in small samples: experience shows that sample thickness of a biological sample should not exceed a thickness of 200μm. Exceptions are based on the fact that some biological samples contain much more (or less) intrinsic cryoprotectants (eg solutes, sugars etc).

As a recent improvement in elemental analysis of temporally synchronized UMR106-01 osteoblastic cell cultures we discuss calcium and phosphorus distributions which were optimal only when cultures were processed using high pressure freezing (HPF), freeze-substitution and dry ultrathin sectioning with an oscillating knife (5). Three types of culture conditions were analyzed: mineralized, non-mineralized (limiting exogenous phosphate), and inhibited mineralization (treated with protease inhibitor AEBSF). UMR 106-01 cells were grown on fibronectin-coated sapphire discs and processed conventionally or for high pressure freezing (6; EMPact, Leica-microsystems, Vienna). HPF specimen holders containing sapphire discs with frozen cells were transferred to the freeze-substitution apparatus. Specimens were washed in anhydrous acetone and embedded in Epon Araldite resin. Dry 50 nm sections were produced with an oscillating diamond knife (Ultra sonic, Diatome, Nidau, Switzerland). With the help of electron spectroscopic imaging (ESI; Leo 912 with omega filter, Zeiss, Oberkochen, Germany) we could localize calcium and phosphorus in micrographs.

To facilitate the application of cryomethods the improvement and development of tools is necessary. Due to tremendous advances in crystallography and magnetic resonance imaging, almost any protein can now be modeled at atomic resolution. To fully understand the workings of biological “nanomachines” it is necessary to obtain images of intact macromolecular assemblies in situ. Cryofixation by high pressure freezing followed by cryosectioning circumvents many of the artefacts related to staining, dehydration and embedding. The approach immobilizes complex macromolecular assemblies in their native state in situ and the images in some cases reach such a good resolution that macromolecule structure can be fitted into them (7). Sophisticated instruments and software packages are needed, e.g. high voltage electron microscopes equipped with precise goniometers (for high resolution tomograms) that work at low temperature and digital cameras of high sensitivity and pixel number to get this structural information. However first of all good cryosections have to be produced. To get them is quite a challenge. Very steady hands are a prerequisite. To facilitate cryo-sectioning we developed a tool with two micromanipulators. One to guide the ribbon of cryo-sections produced during the sectioning process and the other one to put in place the grid for adsorbing the

ribbon with the help of an ionisation unit developed by Pierson et al. (8, Crion, Leica- microsystems, Vienna, Austria)

1. Hunziker EB, Michel M, Studer D. Microscopy Research and Technique (1997), 37, p.271-284.
2. Vanhecke D, Bellmann R, Baum O, Graber W, Eggli P, Keller H, Studer D. J Microsc. (2008), 230, p. 253-62.
3. Studer D, Hennecke H, Müller M. Planta (1992) 188, p.155-163.
4. Al-Amoudi et al. EMBO J. (2004) 23(18), p. 3583-3588.
5. Studer D, Hillmann-Marti T, Huffman NT, Gorski JP Cells Tissues Organs. (2011) 194(2-4) p. 138-145.
6. Studer, D., W. Graber, A. Al-Amoudi, P. Eggli. J Microsc (2001) 203 p. 285–294.
7. Studer D, Humbel BM, Chiquet M Histochem Cell Biol. (2008) 130(5) p. 877-889
8. Pierson J J Struct Biol. (2010) 169(2) p. 219-25.
9. This study was supported by NIH NIAMS grant AR-052775 (J.P.G.) and a Swiss National Foundation grant (No. 3100AO-118394) (D.S.). The authors wish to thank Barbara Krieger for her excellent photographic services.

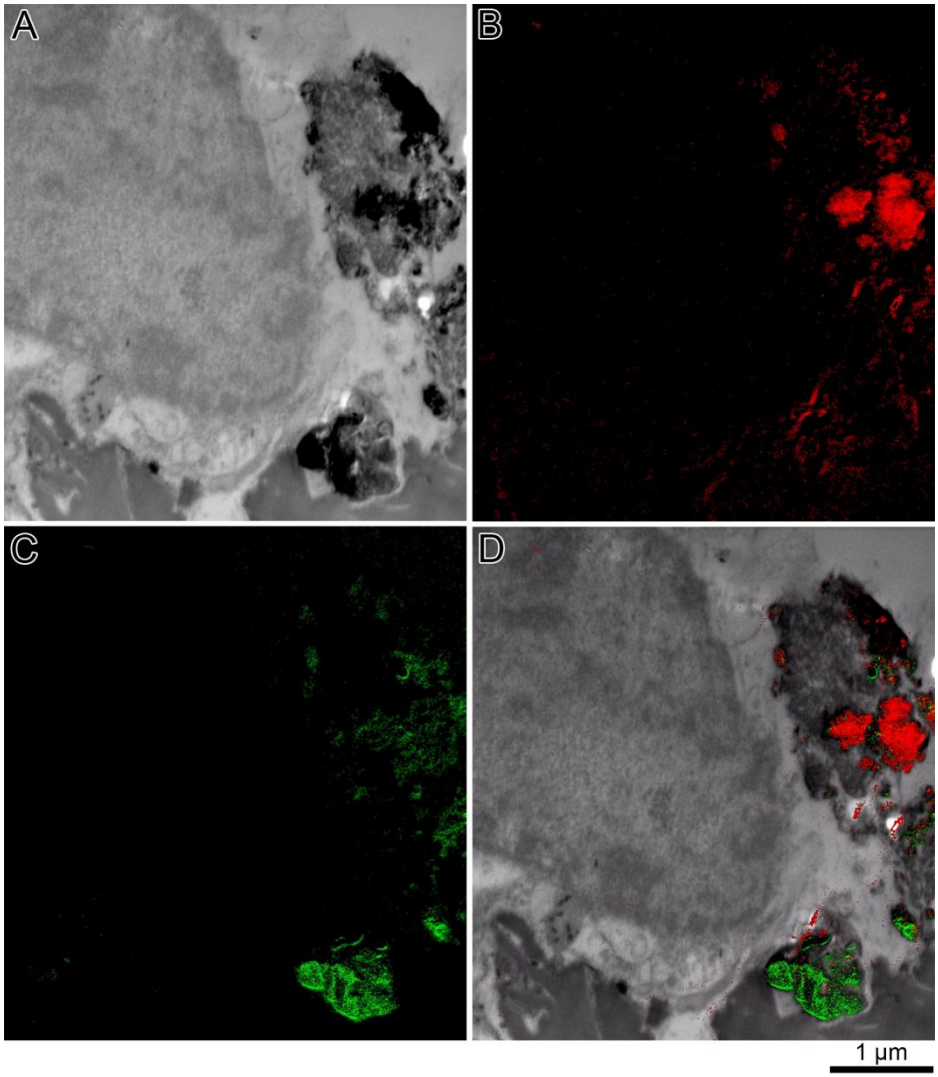

Figure 1. Part of a high pressure frozen osteoblastic cell is shown with portions of closely associated extracellular biomineralization foci containing separated calcium and phosphorus (explanation see above). The sample was freeze-substituted in acetone containing 2% of osmium tetroxide, embedded in Epon and dry ultrathin sectioned with an oscillating knife. In the electron spectroscopic imaging mode we recorded in Fig. 1A the zero loss image (nicely focused sample because no inelastically scattered electrons are present). Fib 1B shows the very same location recorded with inelastic electrons having suffered an energy loss of 346 eV corresponding to calcium (red) and in Fig. 1C inelastic electrons have lost 132 eV corresponding to phosphorus (green). Finally in Fig. 1D all three images are superimposed.

Nanoscale X-ray Tomography of Cells

G. Schneider[1], P. Guttmann[1], S. Werner[1], S. Rehbein[1]

[1]Helmholtz-Zentrum Berlin für Materialien und Energie GmbH, Albert-Einstein-Str. 15, 12489 Berlin

gerd.schneider@helmholtz-berlin.de
Keywords: X-ray microscopy, tomography, cell nucleus, correlative microscopy

X-ray imaging offers a new 3-D view into cells. With its ability to penetrate whole hydrated cells it is ideally suited for pairing fluorescence light microscopy and nanoscale X-ray tomography. Driven by scientific applications in life science, we developed a full-field transmission X-ray microscope (TXM) for automated cryo-tomography and spectroscopy. The system operates at the undulator beamline U41 at the BESSY II electron storage ring which provides a spectral resolution of 104. The spatial resolution of the X-ray microscope is 11 nm (half-pitch).

For high resolution tomography, we adopted a tilt stage originally developed by FEI for electron tomography which supports automated data collection of cryogenic or heated samples. The stage is able to tilt samples in the X-ray microscope up to ± 80°. Such a large tilt of flat sample holders is impossible with soft X-ray microscopes at bending magnet sources because they require a monochromator pinhole to be positioned close to the specimen. Therefore, the HZB full-field TXM overcomes two main limitations of previous concepts. Firstly, it permits spectromicroscopy with high spectral resolution and short exposure times in the range of one second. Secondly, its sample holder geometry is not restricted to glass tubes for 3-D investigations.

Conventional fluorescence images are diffraction-limited to ~200 nm, whereas current X-ray imaging can achieve a ten-fold improvement in resolution. Since fluorescence and X-ray microscopy permit analysis of whole cells, it is possible to investigate the same cell in both microscopes by correlative microscopy. These
correlative studies are ideally suited to X-ray microscopy because of its ability to image cells in 3-D. In the talk, we present the cryo TXM and selected applications. In particular, we will show studies of the internal structure of frozen-hydrated cryogenic mammalian cells and present ways towards 10 nm 3D imaging of cells.

1. G. Schneider, et al., Nature Methods 7 (2010), 985-987

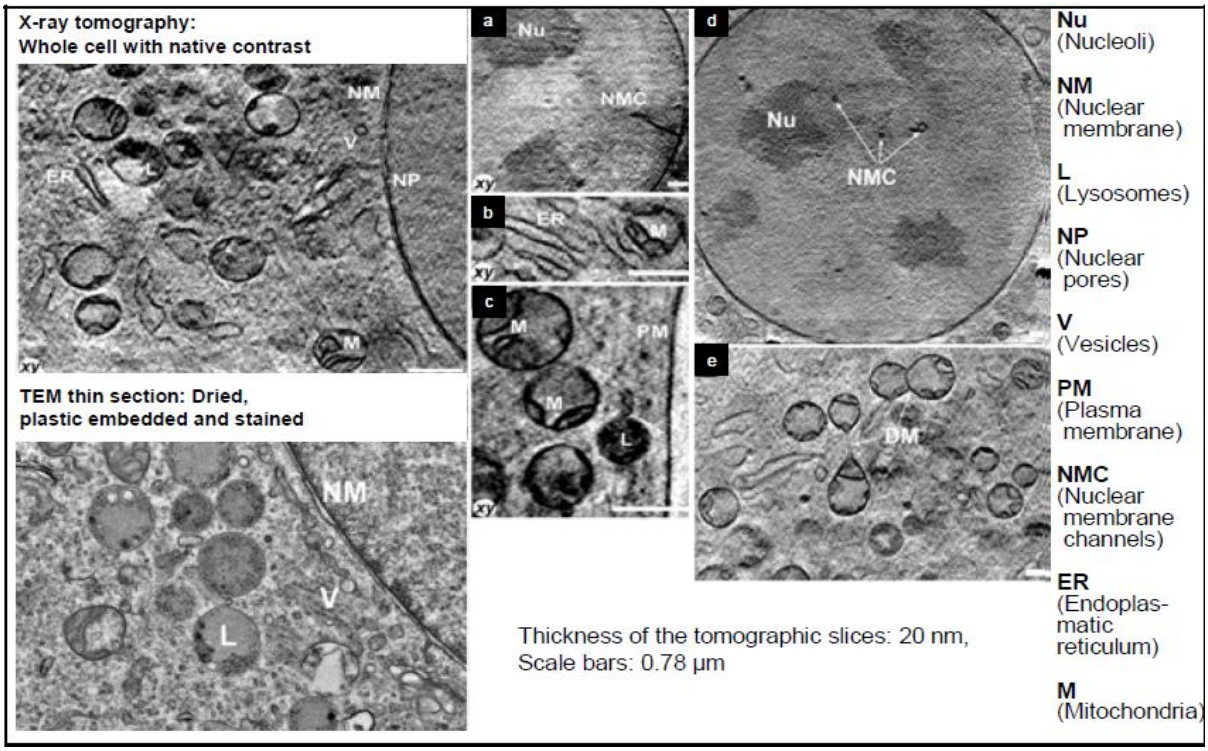

Figure 1. The cyro TXM at HZB allows routinely to visualize the plasma membrane, nuclear membrane, nuclear pores, nucleoli, endoplasmic reticulum, vesicles, lysosomes and mitochondria. It is now also possible to resolve internal organellar structures, such as mitochondrial cristae, the double nuclear membrane and lysosomal inclusions.

Quantitative High-Resolution TEM/STEM and Diffraction

IM.1.001
The influence of detector non-uniformity on STEM imaging

J. M. LeBeau[1] ,S. D. Findaly[2]

[1]North Carolina State University, Department of Materials Science and Engineering, Raleigh, NC 27695, USA
[2]School of Physics, Monash University, Victoria 3800, Australia

jmlebeau@ncsu.edu
Keywords: high angle annular dark-field, annular bright field, STEM

Current trends in atomic-resolution scanning transmission electron microscopy (STEM) investigations involve quantitative comparisons between experimentally recorded and simulated images. While most comparisons between simulation and experiment have been based on relative contrast measures such as peak height ratios and profile shape, direct comparison between experiment and simulation can be achieved by quantitative analysis of the absolute signal [1, 2]. The calibration of the absolute intensity scale requires that any non-uniformity of the detector response be taken into account. Importantly, our prior studies have indicated that the response functions of most annular dark-field detectors are highly non-uniform.

In this talk, we will show that even if the detector response is assumed to be uniform, an uncertainty in the detector inner angle of a few mrad can produce a 10% error in the prediction or interpretation of the peak intensity [3]. Furthermore, we will explore the impact of a typical non-uniform detector response as shown in Fig. 1. We will show that for high angle annular dark-field imaging the intensity can be correctly normalized against simulations that assume a uniform detector response provided that a suitable normalization factor is included. For a typical detector that sits in the lower angle dark-field and/or bright field region, the directional nature of the non-uniformity produces variations in contrast of the order of 5-10% relative to a uniform detector. We will also demonstrate that, for annular bright-field imaging, non-uniformity of the detector response can lead to visible intensity variations in the image, as evident in Fig. 1(f).

As implicit in the simulations to be presented in this talk, accurate theoretical modelling is always possible for a sufficiently-well-characterized detector by including the measured, non-uniform detector response in the simulations. The similarity between the detector responses that have been reported in the literature (Rosenauer et al. [4], Katz-Boon et al. [5], LeBeau and Stemmer [1,2]) indicates that non-uniformity is common (a result of design geometry) and that it is therefore necessary to conduct careful experiments. We will conclude with guidelines for quantifying the absolute intensity to within 10%, especially for an annular detector placed at lower scattering angles.

1. J. M. LeBeau, et al. Phys. Rev. Lett. 100 (2008), 206101.
2. J. M. LeBeau, et al. Nano Letters 10 2010, 4405-4408.
3. S. D. Findlay and J. M. LeBeau. Ultramicroscopy 124 (2013), 52-60
4. A. Rosenauer, et al. Ultramicroscopy 109 (2009), 1171-1182.
5. H. Katz-Boon, et al. Ultramicroscopy 124 (2013), 61-70.
6. S.D.F. acknowledges support by the Australian Research Council and J.M.L. acknowledges support from the State of North Carolina. This work made use of the MRL Central Facilities, supported by the MRSEC Program of the NSF under Award No. DMR 1121053.

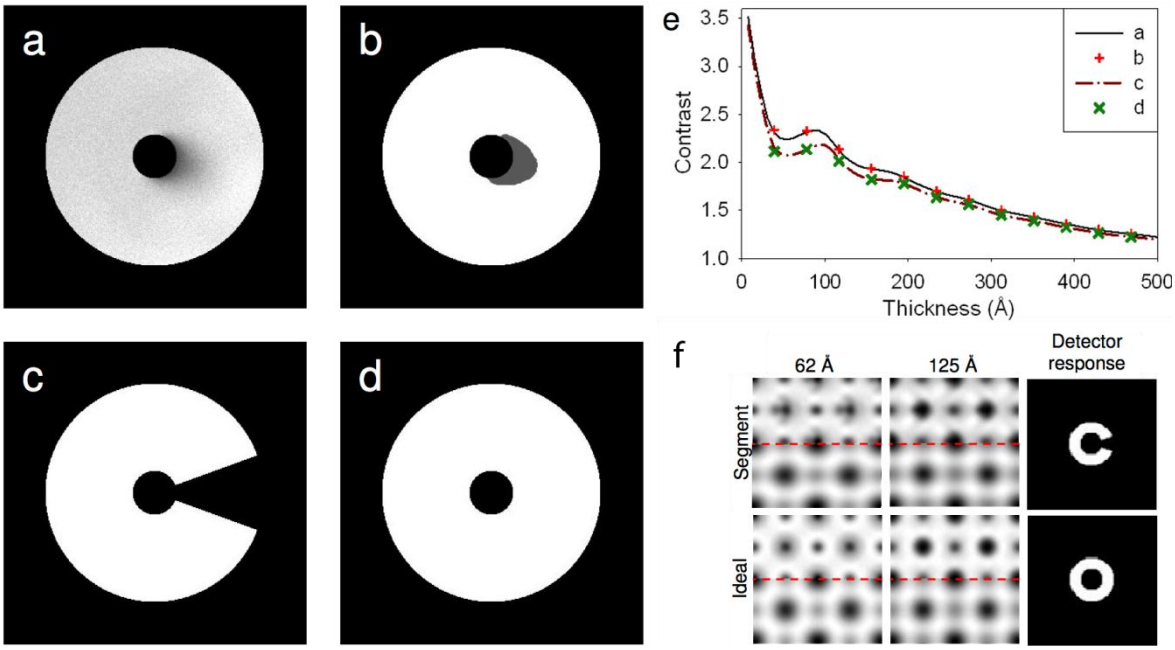

Figure 1. Detector response functions: (a) experimentally measured, (b) two-level approximation to that experimentally measured, (c) uniform with missing segment, and (d) uniform. (e) Contrast as a function of thickness for a $SrTiO_3$ crystal with the four detector response functions spanning the collection range 25-125 mrad. (f) Anisotropic image distortion due to the influence of a segmented detector spanning the collection range 10-20 mrad. Adapted from Ref. [3].

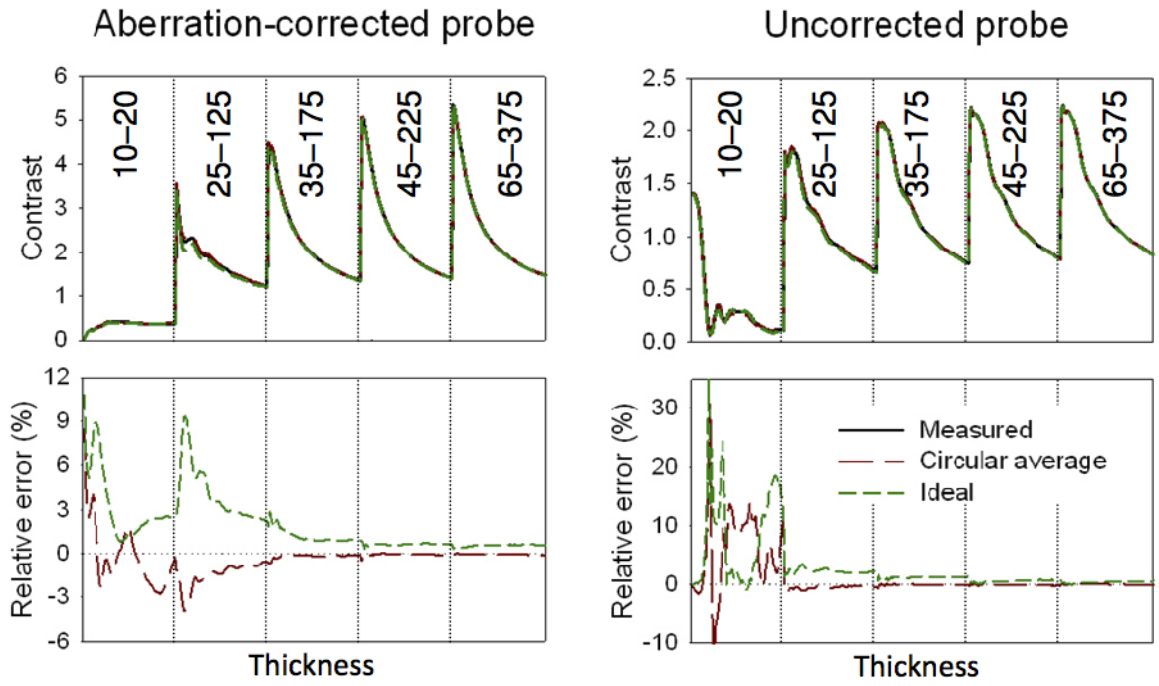

Figure 2. A comparison of the real detector response, the circularly averaged detector response, and the ideal, uniform detector response for both aberration-corrected and uncorrected probes. Spatial incoherence, described by a Gaussian incoherent effective source of half-width-half-maximum 0.5 Å, is included. For each camera length, as denoted by the detector span range labeled in the upper plots in units of mrad, the horizontal axis runs from zero to 500 Å.. Adapted from Ref. [3].

Quantitative High-Resolution TEM/STEM and Diffraction

IM.1.002
Electron holography for characterization of semiconductor structures down to the atomic scale

M. Lehmann[1], F. Genz[1], U. Hömpler[1], F. Kießling[1], T. Niermann[1], J.B. Park[1]

[1]TU Berlin, Institut für Optik und Atomare Physik, Berlin, Germany

Lehmann@physik.tu-berlin.de
Keywords: off-axis electron holography, atomic resolution, semiconductors

Transmission electron microscopy (TEM) is an indispensable method for characterization of semiconductor structures down to the atomic scale. However, solid state physicists and engineers, who grow these increasingly complicated structures on a shrinking scale, do not only have scientific questions, which can be solved just by imaging these structures on the nanometer scale by conventional TEM; there is an increasing demand also for measurements of electric potentials and strain fields, since they mainly determine most macroscopic properties of corresponding devices. Furthermore, structural questions comprising also compositional measurements down to the atomic scale are supposed to be solved by means of HRTEM. Last but not least, error bars for the measured values have to be given. These scientific questions, which are to be answered by TEM, have to be considered within the framework of wave optics. Conventional TEM, however, only records the intensity of the electron wave, whereas the phase information is lost. In particular, this forbids from a single micrograph on the nanometer scale the measurement of electric potentials or on the atomic scale the a-posteriori correction of residual aberrations even necessary for a Cs-corrected TEM, since their accuracy of hardware correction is limited. Off-axis electron holography allows the encoding of amplitude and phase of the electron wave in a single electron hologram. In principle after reconstruction, amplitude and phase of the electron wave is available without transfer gaps down to the information limit of the TEM. Besides the spatial resolution given by the fringe spacing and the information limit of the TEM, the quality of the reconstructed wave in terms of phase resolution is additionally limited by the number of recorded electrons and by the interference fringe contrast. Furthermore, artifacts like Fresnel diffraction at the biprism filament reduce the quality of the reconstructed wave. Careful analysis of all these factors shows that a dedicated instrument like our FEI Titan Berlin Holography Special TEM may overcome these obstacles: Equipped with a high-brightness gun (XFEG), only using a 2-condenser illumination system is simplifying hologram acquisition [1]. Utilizing two biprisms in different planes drastically reduces the Fresnel diffraction over the field of view [2]. Applying exposure times within the stability limits of the instrument of typically 2 .. 8 s for a single micrograph, a special averaging scheme over a series of holograms compensating for specimen drift, defocus drift, biprism drifts as well as hologram contrast variations allows standard deviations in phase and amplitude of 2□/104 and 0.04, respectively, with a lateral resolution better than 0.1 nm [3]. This is the basis for compositional analysis with atomic resolution.

These high-quality electron holograms now permit tackling serious scientific questions, e.g., from solid state physics of semiconductors. One important application field of electron holography is the imaging of potential differences in p-n junctions. Careful analysis of the phase shift of p-n junctions in GaN shows, however, that the measured phase difference is about a factor of ten less than expected. It turns out that the measured potential difference considerably depends on the electron dose rate applied for recording the hologram. This can partially be related to a beam-induced generation of electron-hole pairs [4]. Additionally, the charging character of the sample strongly depends on the modification of its surface [4] demonstrating the need for a full modeling of the specimen under investigation. An even more complicated structure is a multiquantum well comprising of GaN quantum wells (QW) and $Al_{0.48}Ga_{0.52}N$ barriers (figure 1) (5). Because of experimental uncertainties of specimen thickness variation over the field of view, only the potential ratio between QWs and barriers can be given (figure 2). Here, the measured potential ratio is not only given by the different mean inner potential between QW and barrier, but also by strain and resulting piezoelectric field, which only partially compensates the spontaneous polarization of GaN in [0001] growing direction (figure 2). Furthermore, the modulation within barriers may partly be related to interface charges compensating the charge accumulation exhibiting the piezoelectric fields in the QWs.

Such a dedicated experimental setup does not only allow the recording of "conventional" off-axis electron holograms, where normally the object modulated wave is brought to interference with an

unmodulated reference wave, but also the acquisition of dark-field electron holograms, where a strained region of interest is brought to an overlap with an unstrained region as reference utilizing a strain-sensitive reflection by means of the objective aperture [6]. Such an example is a strain analysis of buried AlAs/oxide stressor layers for site-controlled quantum dots (QD) growth important, e.g., for single-photon emitters [7]. In particular, the double biprism setup is beneficial preventing Fresnel diffraction as well as giving extra flexibility in experimental setup in term of spatial resolution and field of view. In summary, recent progress of electron holography and related methods enables now tackling important solid state problems in semiconductor physics.

1. F. Genz et al., this conference.
2. K. Harada et al., Appl. Phys. Lett. 84 (2004) 265.
3. T. Niermann et al., this conference.
4. J.B. Park, this conference.
5. Udo Hömpler, Master thesis, TU Berlin (2013).
6. Hytch et al., Nature 453 (2008) 1086.
7. F. Kießling et al., this conference.

8. We kindly acknowledge financial support from the DFG within the Collaborative Research Center 787 and DFG INST 131/508-1.

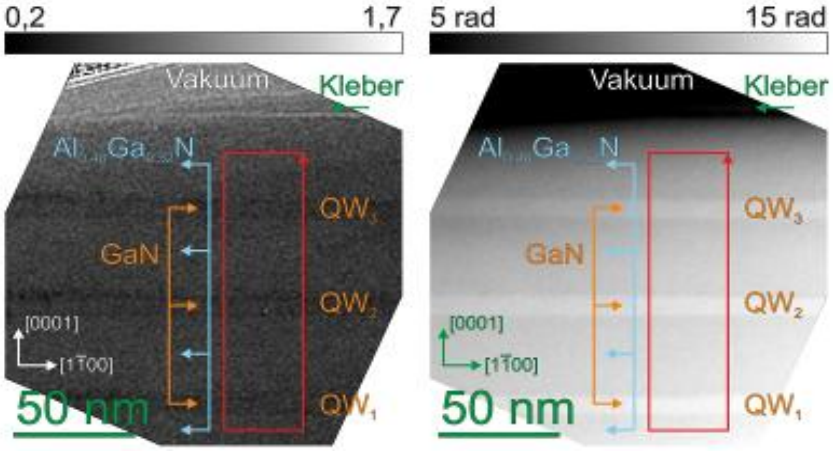

Figure 1. GaN/AlGaN-MQW: Amplitude (left) and phase (right) of the electron wave as reconstructed from the electron hologram. Almost no Fresnel diffraction can be observed over the field of view. The phase image clearly reveals the QWs. However, the sample has a steep thickness gradient preventing a direct interpretation of the phase modulation in term of absolute potential difference between GaN QWs and AlGaN barriers.

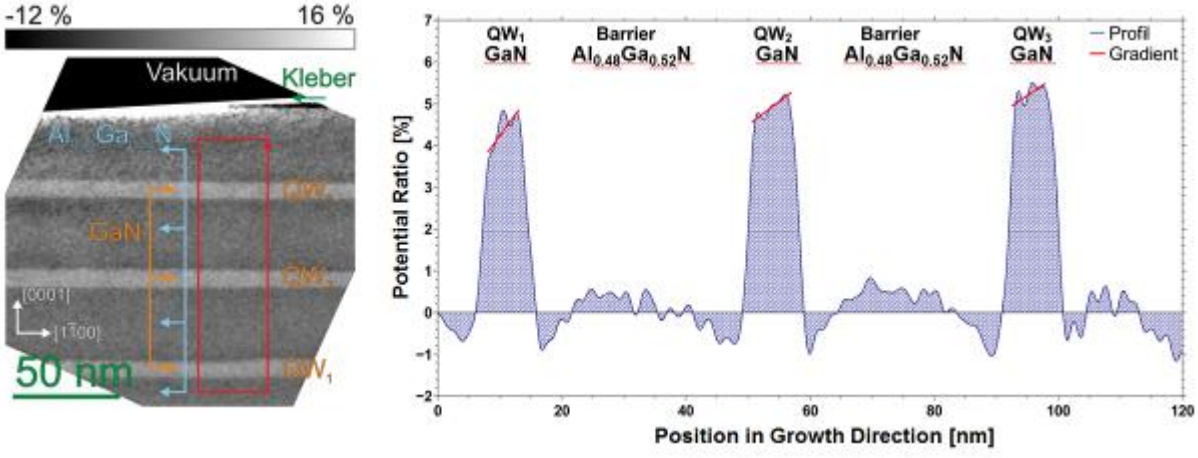

Figure 2. Potential ratio between QWs and barriers of figure 1. The gradient in the QWs can be attributed to piezoelectric fields. Potential modulations in the barriers can have their cause in screening charges compensating interface charges exhibiting the piezoelectric fields in the QWs.

Quantitative High-Resolution TEM/STEM and Diffraction

IM.1.003
From 2D exit wave to 3D atomic structure

D. Van Dyck[1], J.R. Jinschek[2], C. Kisielowski[3], F.-R. Chen[4]

[1]University of Antwerp, Department of Physics, Antwerpen, Belgium
[2]FEI Europe, Eindhoven, Netherlands
[3]NCEM, Berkeley, United States
[4]National Tsing-Hua University Hsin Chu, Taipei, Taiwan

Dirk.vandyck@ua.ac.be
Keywords: exit wave, atomic structure, big bang tomography

The ultimate goal of electron microscopy is not to obtain nice images but to advance materials science. This means that EM has to evolve from describing to understanding materials properties. Understanding means matching observations with ab-initio calculations. And since all the structure-property relations are encoded in the positions of the atoms, they form the ultimate language between theory and experiment. The future EM is then to be considered as a communication channel between object and observer and the images as data planes from which the 3D atom positions can be extracted quantitatively. With the newest generation of Cs corrected EM's the resolution is sufficient to resolve the individual atoms and to refine their position with picometer precision. If the ideal object would be a phase object and the perfect electron microscope would have no aberrations, the HREM image intensity would show no contrast at all. Hence electron microscopic aberrations such as defocus are necessary to create contrast in the images. But on the other hand they scramble the information about the object. The best way to extract this information is by first undoing (deconvolving) the transfer functions of the electron microscope and the recording device. The first step is thus to retrieve the phase of the image wave. This can be done by off-axis electron holography or by focal series reconstruction, which is a kind of in-line holography. The next step is data mining the exit wave so as to retrieve the 3D positions of the object atoms. Since the exit wave is the result of the interaction of the electron wave with the object we need a physical model for this interaction that can be used for fitting. In general a 2D projection does not have sufficient information to retrieve 3D information so that one needs tomographic methods.

We can now consider two different cases: very thin objects and thicker crystalline objects.
In a very thin object we can consider the atom as point object which is the source of a spherical wave (Figure 1). By propagating over a certain distance *d*, the phases of the Fourier components of this wave increase linearly with distance and with the square of the spatial frequency *g*. Thus, by plotting the phase of the Fourier components versus g^2 we obtain a straight line. And from the slope we can then determine the distance *d* between the atom and the plane of observation. This is shown schematically in Figure 1. By analogy with the Hubble plot of cosmology we call this method big bang tomography. The experimental results of bilayer of grapheme are shown in Figure 2.

In case of a crystalline object viewed along a zone axis, the electrons are trapped in the positive potential of the atoms of the column and the propagation (channeling) of electrons is not influenced by the propagation in neighboring columns up to thicknesses of tens on nm, which are typical for HREM. This applies as well for perfect crystalline objects as for defective crystals with a column structure. Thus the exit wave of a crystalline object in a zone axis orientation represents the assembly of the exit waves of the constituting columns. Furthermore the atoms of a column act as weak lenses, which focus the electron wave periodically with depth so that the exit wave of a column is a very sensitive peaked fingerprint of the type of column. The theory of channelling is simple [2] and provides a way to interpret the exit wave, which can be visualized by plotting the complex values of the pixels in complex 2D space. From the exit wave of a column we can deduce the position of the column, the defocus distance (with sub-Angstrom precision), the total mass of the column and the residual aberrations [3].

By combining this information we can then reconstruct the object in 3D including profile of top and bottom surface. Figure 3 shows the Argand plot for a Ge crystal foil in (110) zone orientation. From the Argand plot we can determine the distance of the column to the exit wave and hence also the surface profiles.

1. D. Van Dyck; M. Op de Beeck, Ultramicroscopy 64 (1996), 99-107.
2. A. Wang, F.R. Chen, S. Van Aert,D. Van Dyck, Ultramicroscopy 110 (2010) 527-534.
3. D. Van Dyck, J.R Jinschek, F.R Chen, Nature 486 (2012), 243-246

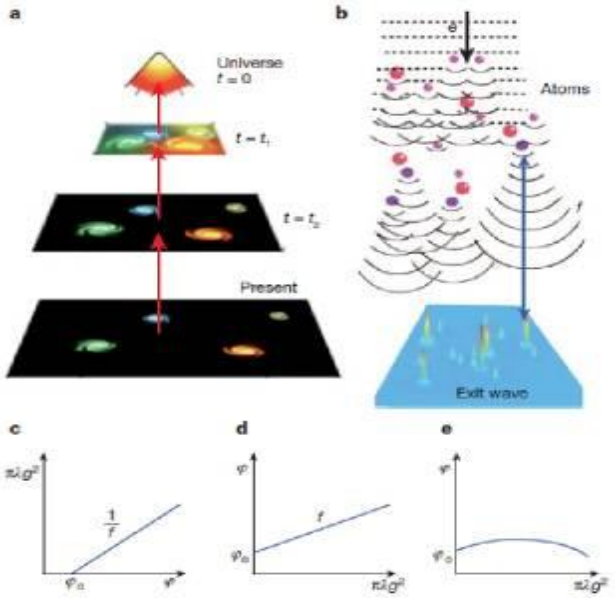

Figure 1. Big Bang analogy. a, b, Comparison between the Big Bang (a) and the point-atom 'big bang' (b). c, Phase speed plotted against phase. The relationship between the two is the same as that expressed in cosmology by Hubble's law, which gives the linear relationship between the distance and the speed of a distant galaxy. Here the slope is the reciprocal focal distance, 1/*f*. Note that at the position of the atom, the phase of the atom wave does not start from zero; instead, it has a value, φ_0, characteristic of the atom. d, Phase plotted against phase speed, which we refer to as the Hubble plot here. The slope gives the focal distance between the emitting atom and the plane of reconstruction of the exit wave. e, Same as in d, but with a minor residual spherical aberration with C_s = 50.3 µm (see text).

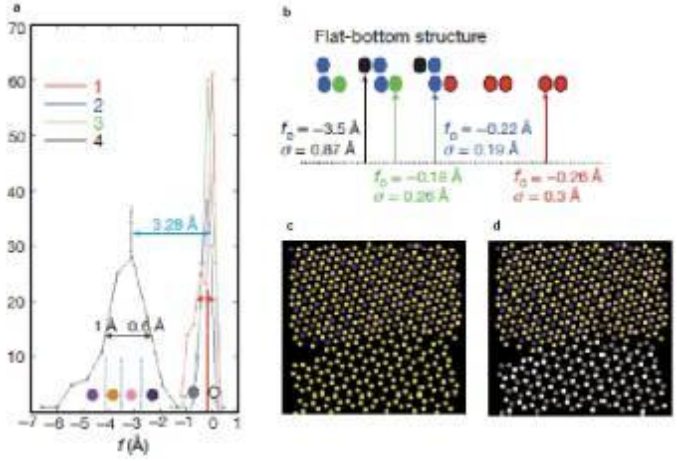

Figure 2. Histogram of the focal distance. **a**, Histogram of *f* for four different types of atom. **b**, the flat-bottom model. f_o, average focal distance, σ, standard deviation. **c**, Subtypes of atoms of type 4. **d**, Subtypes of atoms of type 1.

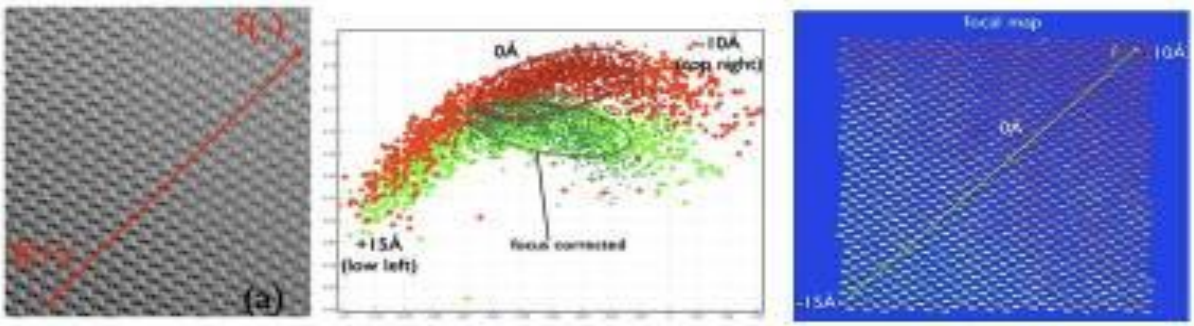

Figure 3. Experimental results for a Ge foil viewed along the (110) zone. Scale bar: 1 nm. From left to right: 1) amplitude of exit wave showing the peaks of the columns. 2) Argand plot showing two branches corresponding with the left (red) and the right (green) columns of the dumbbells. The separation between the two branches corresponds to a mass difference of 1 atom. 3) Defocus corrected phase image.

Quantitative High-Resolution TEM/STEM and Diffraction

IM.1.004
Strain Analysis by Nano-Beam Electron Diffraction (SANBED): Present performance and future prospects

K. Müller[1], H. Ryll[2], I. Ordavo[2], D. Zillmann[1], M. Schowalter[1], J. Zweck[3], H. Soltau[2], S. Ihle[4], L. Strüder[4], K. Volz[5], P. Potapov[6], A. Rosenauer[1]

[1]Universität Bremen, Bremen, Germany
[2]PNSensor GmbH, München, Germany
[3]Universität, Regensburg, Germany
[4]MPI Halbleiterlabor, München, Germany
[5]Philipps Universität, Marburg, Germany
[6]GLOBALFOUNDRIES Dresden Module One, Dresden, Germany

mueller@ifp.uni-bremen.de
Keywords: STEM, CBED, strain, diffraction

Via metal-oxide semiconductor field effect transistors (MOSFET), light emitting or laser diodes, semiconductor nanostructures have developed to a central part of everyday economic and scientific life in industrial countries. Common to nearly all these structures are stoichiometric and strain variations at atomic scale which govern electronic and optical properties. Consequently, large effort on accurate and precise strain measurement in large areas with the high spatial resolution provided by transmission electron microscopy (TEM) is spent by the community since decades.

This study addresses strain analysis from diffraction pattern series acquired in scanning TEM (STEM) mode. In particular, three algorithms [1] have been developed to accurately determine the positions of discs in convergent beam electron diffraction (CBED) patterns originating from a focused STEM probe with a semi-convergence angle of 2.6mrad. From disc positions it is then straight forward to calculate strain via Bragg's equation. In comparison to traditional techniques which use parallel illumination [e.g. 2], we demonstrate that the spatial resolution is improved by a factor of 5 to 0.5nm. On the other hand, CBED disc recognition is more complex than Bragg spot detection because of the rich inner intensity structure as depicted in Figure 1a, which furthermore drastically changes throughout a series of CBED patterns due to variations of specimen thickness and -orientation.

As the most direct approach, we developed the selective edge detection and circle fitting algorithm (SE), in which a Prewitt-type edge detection is applied to raw CBED disc patches, leading to edge pixels shown in Figure 1a, too. Erroneous edges are ruled out by iteratively fitting circles to the edge pixels, whereas edges with the largest distance to a fit are ignored in subsequent iterations. In this way, we finally obtain the fit of the disc border on the right of Figure 1a. For a scan through the 5-fold stack of $In_xGa_{1-x}N_yAs_{1-y}$/GaAs visible in the high-angle annular dark field (HAADF) inset in Figure 1d, we obtain the black strain profile exhibiting an alternating tensile/compressive strain sequence over a distance of 600nm. Whereas SE evaluation takes 15min, a second method called radial gradient maximisation (RG) leads to the same profile as expressed by the blue curve in Figure 1d in 1min. Here, CBED disc position and radius are found by maximising the difference between the sum of rotational averages inside (coloured rings in Figure 1b) and the sum outside (blue rings) the CBED disc. A third method, cross-correlation with masks (CC), again yields equivalent strain as shown by the red profile in Figure 1d, now 75 times faster than SE. As an example, Figure 1c shows two masks which can be used for cross-correlation with the CBED discs. However, the lower one is preferable as it stresses the disc border and suppresses the inner disc structure. In contrast to SE, RG and CC perform best at log-scaled intensities.

While sub-nm resolution over a field of view of more than 500nm with a strain precision of 0.07% is very promising, strain analysis by nano-beam electron diffraction (SANBED) faces several challenges: To enable 2D strain mapping with a sampling of 200x200 scan points, detectors with high quantum efficiency, high signal-to-noise ratio and ultrafast readout are required to record large numbers of CBED patterns in finite time. In pilot works [3], we used a pnCCD [4,5] camera, which is a direct electron, scintillator-free CCD detector, to record CBED patterns with up to 1kHz rate using the same specimen as in Figure 1d. As shown in Figure 2a for a pnCCD frame time of 200ms, the result of Figure 1d (obtained with a conventional scintillator-based Gatan UltraScan2000 CCD with 500ms frame time) is reproduced accurately with respect to strain profile shape and -precision. As the insets in Figure 2a exhibit, this is not self-evident since direct electron detection at 300kV causes split events

an hence significant point spread. However, it has been shown [3] that this mainly causes an isotropic blurring of CBED discs and does not alter the position detection result.
In addition, Figure 2b shows the same strain profile again which has now been obtained from frame times of 1ms. Obviously, precision decreases slighty by a factor of 1.8 but on the other hand acquisition speeds up by a factor of 200, enabling 200x200 2D strain map acquisition in 40s.

Another challenge for SANBED is the compensation of varying crystallographic orientation and specimen thickness for applications where strain is to be mapped at large (15□m²) scale. To this end, electron precession experiments have been conducted via scripting at the COM-interface of an FEI Titan 80/300 machine, to correlate beam tilt and diffraction shift for recording a static CBED pattern while varying the beam tilt. As clearly visible in Figures 2c-d, a semi-opening angle of the precession cone of 1mrad already leads to a nearly homogeneous intensity distribution inside the discs which enhances large-scale SANBED analysis significantly.

Future prospects for SANBED are therefore essentially related to improvements of acquisition hardware as to speed and detection quantum efficiency, development of efficient scripts for automated, dedicated user applications such as a combination of electron precession and STEM, as well as implementing algorithms like CC to in-situ evaluation of CBED disc positions during SANBED scans. Finally, SANBED is very promising in combination with HAADF Z-contrast imaging to allow for simultaneous mapping of strain and composition as the CBED pattern passes the inner detector hole.

1. K. Müller and A. Rosenauer et al., Microsc. Microanal. 18 (2012), p. 995.
2. A. Béché et al., Appl. Phys. Lett. 95 (2009), p. 123114.
3. K. Müller et al., Appl. Phys. Lett. 101 (2012), p. 212110.
4. L. Strüder et al., Rev. Sci. Instrum. 68 (1997), p. 4271.
5. R. Hartmann et al., Nucl. Instrum. Methods Phys. Res. Sect. A 568 (2006), p. 118.
6. I. Ordavo et al. Nucl. Instrum. Methods Phys. Res. Sect. A 654 (2011), p. 250.

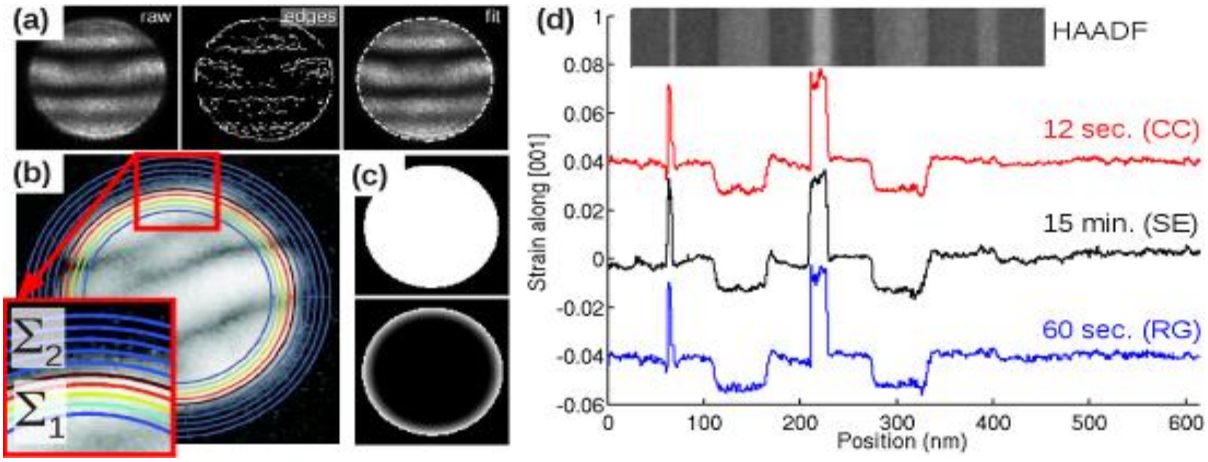

Figure 1. (a-c) Disc position and –radius recognition by **(a)** selective edge detection and circle fitting (SE), **(b)** radial gradient maximisation (RG) and **(c)** cross-correlation with masks (CC). **(d)** SANBED strain profiles for SE,RG,CC.

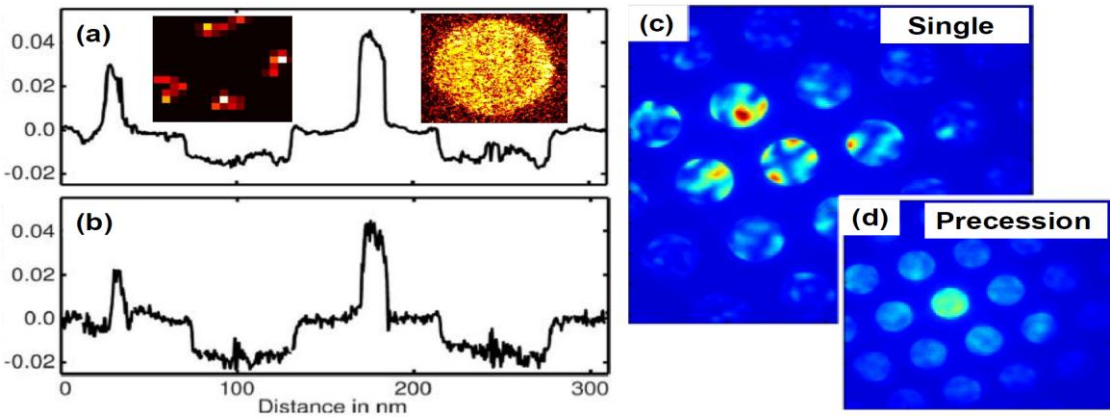

Figure 2.(a,b) Strain profiles as in Figure 1(d) but obtained with the direct electron detector pnCCD for 200 and 1ms frame time, respectively. Single events and a CBED reflection are shown as inset in (a). **(c)** Single CBED pattern. **(d)** CBED pattern obtained by precession and de-scan of the diffraction shift.

Quantitative High-Resolution TEM/STEM and Diffraction

IM.1.005
Towards automated solving of the dynamic inversion problem in electron diffraction for moderately thick crystals

C.T. Koch[1], F. Wang[1]

[1]Ulm University, Institute for Experimental Physics, Ulm, Germany

christoph.koch@uni-ulm.de
Keywords: dynamical electron diffraction, inversion problem, LARBED

In 1984, Herbert Hauptman and Jerome Karle received the Nobel Prize in chemistry for the development of direct methods, a mathematical framework for determining the arrangement of atoms that would give rise to a measured set of kinematic diffraction intensities. Prerequisites for the success of direct methods are that the diffraction intensities are indeed (mostly) kinematic, and that many more reflections than atoms per unit cell have been measured. Both of these conditions are difficult to satisfy in electron diffraction of complex, beam sensitive structures, especially, since, in choosing the electron accelerating voltage, a trade-off between knock-on damage and kinematicity has to be made.

Having dynamical electron diffraction data from multiple angles of incidence, the crystallographic phase problem can be solved, even if neither of the two above-mentioned requirements are fulfilled. This fact is the basis of structure factor refinement by quantitative CBED [1,2]; and also a more recent approach which applies a scattering path expansion [3] to determine the complex structure factors directly from the experimental data without prior knowledge of atom positions [4].

Key to the direct inversion of dynamical scattering described in [4] is a) that the sample is not too thick, and b) the availability of dynamical electron diffraction data for a large range (more than 1°) of incident beam directions. Conventional CBED is limited in the range of incident beam directions it can sample in a single exposure to half the shortest g-vector in the pattern (see, for example, Fig. 1a). However, large-angle rocking-beam electron diffraction (LARBED) [5] overcomes this limitation and easily supplies the necessary data (this can even be done using commercial microscope-controlling software which also makes sure that this data is acquired from a very small area on the sample [6]). The example of an experimental LARBED pattern of an approximately 13 nm thick sample shown in Fig. 1 makes this quite obvious. While the CBED pattern at this specimen thickness shows not much contrast within the discs (Fig. 1a) the LARBED pattern is rich is information, facilitating quantitative determination of structure factor amplitudes and phases.

Fig. 2 shows, that indeed the structure factor phases can be extracted from even just a simple reflection, if the structure factor amplitudes are known, the sample is not too thick, and dynamical diffraction intensities spanning quite a large range (more than 1°) of incident beam directions are available.

We will present our experimental data acquisition technique and report on progress towards automated structure factor phase determination from quantitative LARBED measurements.

1. C. Deininger, G. Necker, J. Mayer, Ultramicroscopy 54 (1994) 15-30
2. J.-M. Zuo, M. Kim, M. O'Keefe, J.C.H. Spence, Nature 401 (1999) 49
3. C.T. Koch and J.C.H. Spence, J. Phys. A: Math. Gen. 36 (2003) 803–816
4. C.T. Koch, arXiv:0810.3811v1
5. C.T. Koch, Ultramicroscopy 111 (2011) 828 – 840
6. The QED plug-in (HREM-Research) for Gatan DigitalMicrograph has been used for the LARBED acquisition.
7. The authors acknowledge the Carl Zeiss Foundation as well as the German Research Foundation (DFG, Grant No. KO 2911/7-1)

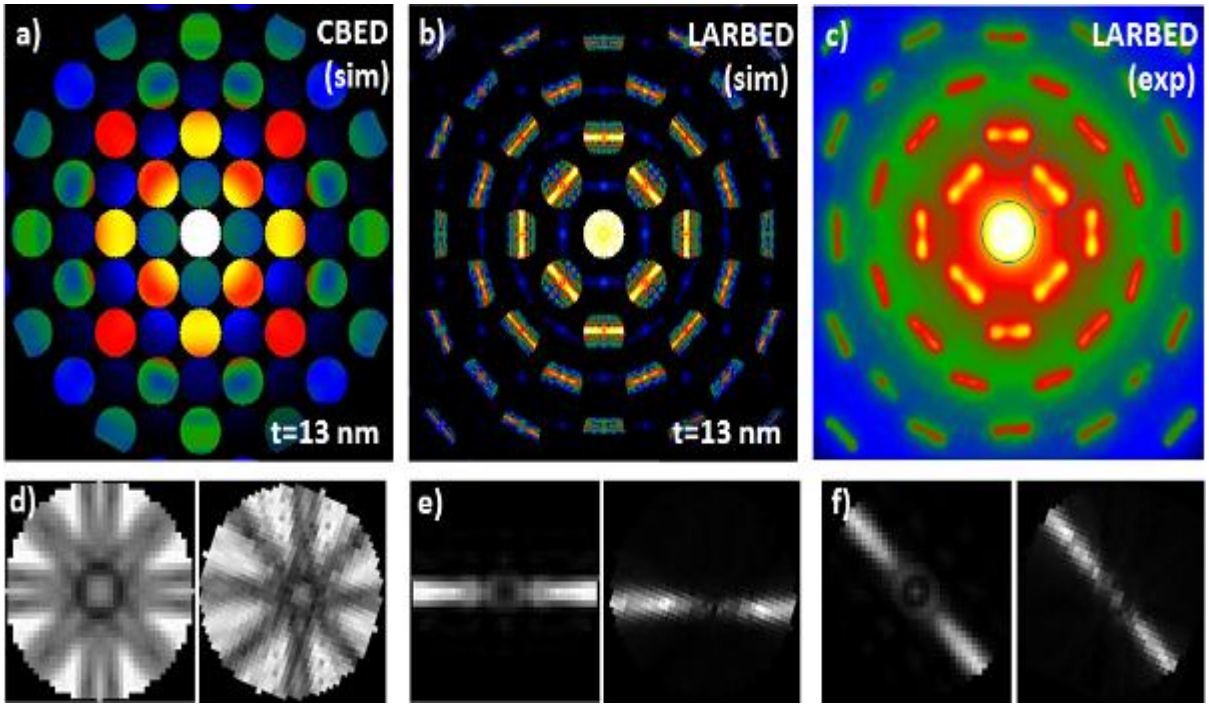

Figure1. a) CBED pattern of $SrTiO_3$ in the [001] orientation. The thickness is only 13 nm, so the CBED discs have almost constant contrast. b) Simulated and c) experimental LARBED pattern for the very same specimen thickness. The size of each disc covers incident beam directions for disc of 70 mrad radius. d) (000), e) (020), and f) (110) background-subtracted LARBED discs extracted from the simulated (left) and experimental (right) LARBED patterns shown in b) and c). The experimental data was acquired on a Zeiss EM912 (120 kV) using the QED plugin (HREM-Research) to Digitalmicrograph (Gatan Inc.), without applying energy filtering. Figures a)-c) are shown on a logarithmic color scale and d) – f) on a linear color scale. All patterns (experimental and simulated) contain 1009 different beam directions (discs with a diameter of 17 pixels).

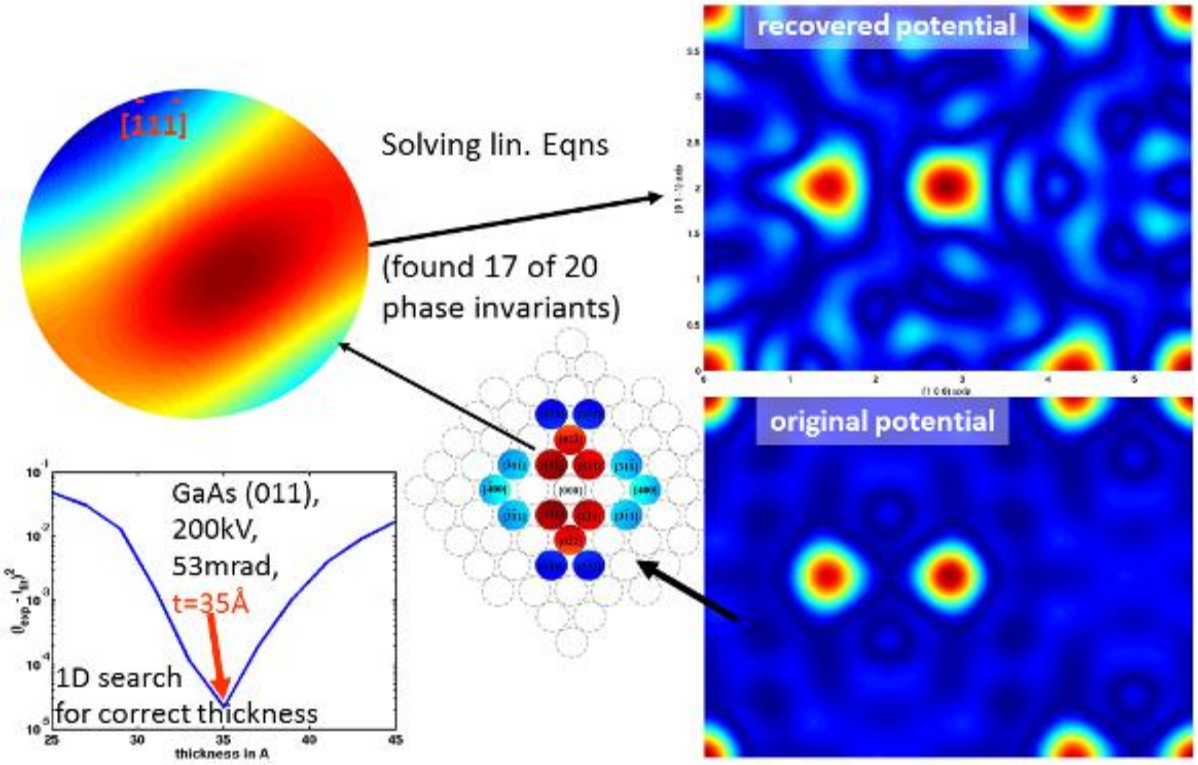

Figure 2: This diagram illustrates the how dynamical scattering can solve the phase problem in crystallography. Starting from the [011]-projected potential of GaAs the (-1,1,-1) LACBED disc for a tilt range of 2° was simulated (see also flat CBED discs in the pattern indicating which beams have been included). The scattering path expansion was used to determine most of the phase triplets involving the reflections shown, so that the potential could be recovered. Note that only the structure factor amplitudes and a single LACBED disc were used to determine the phases directly (not by non-linear fitting).

Quantitative High-Resolution TEM/STEM and Diffraction

IM.1.P006
Structural analysis of ETS-10 with 3D electron diffraction tomography and electron microscopy observations

Y. Ma[1], P. Oleynikov[1], O. Terasaki[1], K.B. Yoon[2]

[1]Stockholm University, Department of Material and Environmental Chemistry, Stockholm, Sweden
[2]Korea Advanced Institute of Science and Technology, Graduate School of EEWS, Daejeon, Korea, Republic of

yanhang.ma@mmk.su.se.
Keywords: 3D electron diffraction tomography; ETS-10; defects

The microporous titanosilicate, ETS-10, composes of tetrahedral SiO_4^{4-} and TiO_6^{8-} units, which form layers of –Ti-O-Ti-O- chains and three dimensional 12-ring pore systems. Previous study suggests that ETS-10 can be constructed on basis of layers parallel to main channels. Each layer contains two sets of mutually orthogonal $[(TiSi_5O_{13})^{2-}]_n$ columns. The packing of layers along *c* direction is achieved by shifting ±1/4*a* and ±1/4*b* with respect to its former layer, which produce various stacking arrangements, as well as two kinds of defects, layer stacking defect and defect in one layer. The high degree of defects existed in ETS-10 introduce the complexity and variety of its crystal structure, which are close related to its perspective catalytic and photoelectric properties. [1-3]

In this work, structural study of ETS-10 was investigated by combination of the recently developed three dimensional electron diffraction tomography (3D EDT) method [4] and electron microscopy (EM) observations. Sweeping reciprocal space is conducted by using electron beam tilt in an available angular range with a designated step. The total tilting angles covered was from –62.7° to +68.9° (~132° in total) with a step size of 0.15°. From the reconstructed 3D reciprocal space, strong diffusion scattering was observed in ED pattern frames due to extensive defects present in crystal. The diffuse streaks appear only in the direction of *c** axis, which is the orientation of layer packing. According to layer shifting rules, stacking defects will affect those reflections which satisfy *h*=2n+1 or *k*=2n+1, which are consistent with (1-10) slice in Figure 2a.

Even in the presence of strong diffuse scattering , the *ab* initio structure can still be solved based on extracted reflections using charge flipping method in Jana2006 (Figure 1b,c). [5] The structure solution gives a rather reasonable model of polymorph B (s.g. *C*2/*c*, *a*=*b*=21Å, *c*=14.5 Å and β=111.12°). Only three O atoms are missing in comparison with the model reported before with *R* factor equal to 38.9%. This structure is consistent with the projection along [1-10] zone axis in HRTEM image (Figure 2d).

Figure 2a, b show SEM images of ETS-10 along different viewpoint, which present a point groups of 4/mmm. The 4-fold symmetry along *z* axis can be explained by the existence of twins in 110 planes, which also show the evidence in ED pattern along [1-10] in Figure 1a. The main stacking sequence of layers is *ABCDABCD*…, consistent with polymorph B structure (Figure 2b). This might be the reason that *ab* initio structure solution gives a model of polymorph B.

Besides, layer stacking defects can be clearly seen in EM image as shown in Figure 2. Stacking sequence was marked by yellow line with the notation of *A* (*B, C* or *D*) layer in Figure 2d. Different packing styles might form other possible polymorph, like polymorph A (s.g. $P4_1$, *a*=*b*=14.8Å, *c*=27.0Å) with *ABAB*… stacking. The other type of defects appears in the same layer, which might form a large pore or block the straight pores along [1-10] direction as shown red square marked areas in Figure 2d.

In conclusion, structure of ETS-10 has been solved using 3D EDT method and EM observations. Defects in the structure have been discussed briefly.

1. M. W. Anderson, O. Terasaki, T. Ohsuna, P. J. O. Malley, A. Philippou, S. P. Mackay, A. Ferrerira, J. Rocha and S. Lidin, Nature 367 (1994), p. 347.
2. N. C. Jeong, M. H. Lee and K. B. Yoon, Angew. Chem. Int. Ed. 46 (2007), p. 5868.
3. P. D. Southon and R. F. Howe, Chem. Mater., 14 (2002), p. 4029.
4. D.L. Zhang, P. Oleynikov, S. Hovmoller and X. D. Zou, Z. Kristallogr. 225 (2010), p. 94.
5. V. Petricek, M. Dusek, and L. Palatinus, "Jana2006. the crystallographic computing system." http://jana/fzu.cz/ Institute of Physics. Praha, Czech Republic (2006).
6. The authors gratefully acknowledge the Swedish Research Council (VR) for the financial support.

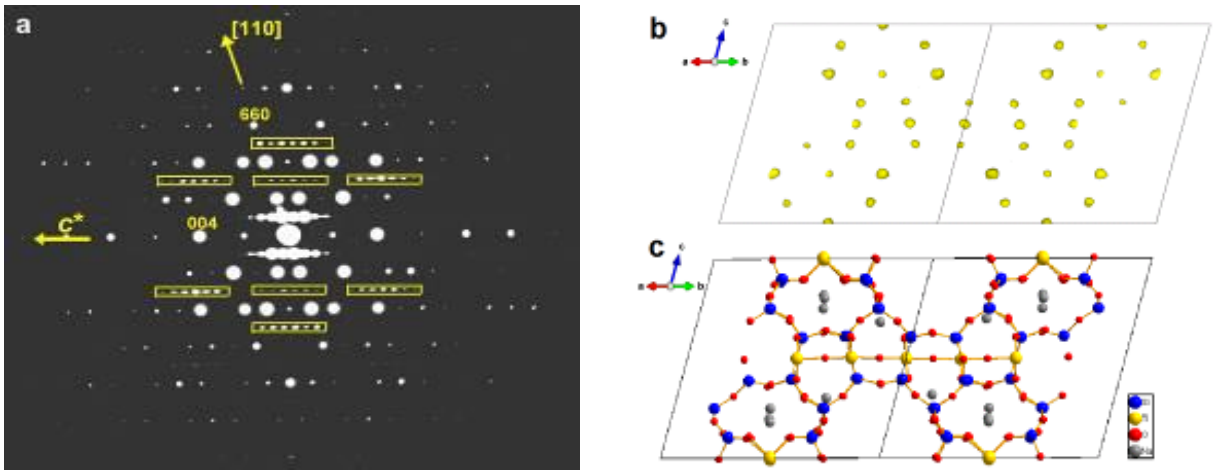

Figure 1. (a) One (1-10) slice of reconstructed 3D reciprocal space from 3D EDT data, (b) electrostatic potential map and structural model obtained using charge flipping method in Jana2006. The yellow rectangle marked diffuse streaks with intensity maxima along *c** axis.

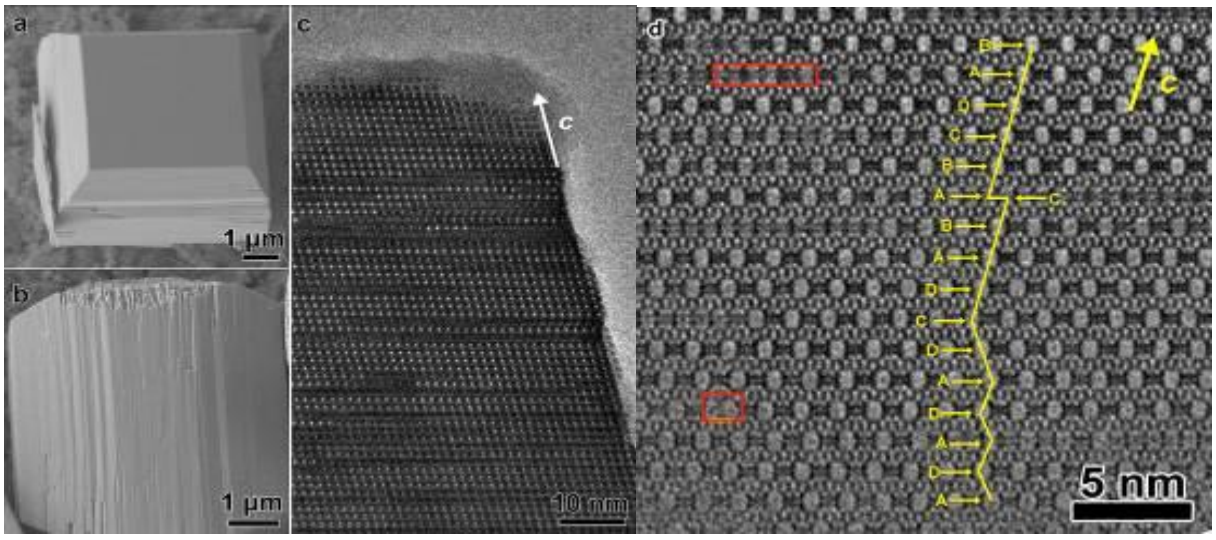

Figure 2. (a), (b) SEM image of ETS-10 viewed along different directions, (c) low-mag HRTEM image and (d) high-mag HRTEM images along [1-10] (or [110]) direction. The yellow line in Figure 2d traced layer stacking sequence along *c* axis, and red rectangle marked defects in one layer introduced by different stacking style in the same layer.

Quantitative High-Resolution TEM/STEM and Diffraction

IM.1.P007
Averaging scheme for the reconstruction of atomic resolution off-axis electron hologram

T. Niermann[1], M. Lehmann[1]

[1]Technische Universität Berlin, Institut für Optik und Atomare Physik, Berlin, Germany

niermann@physik.tu-berlin.de

For quantitative atomic resolution electron microcopy, the access to the amplitude and phase of the object exit wave is indispensable, as object information is distributed into both channels. Furthermore, the inevitable residual aberrations must be numerically corrected for comparison with calculations as the accuracy of hardware-correctors is limited. A numerical correction requires both amplitude and phase of the electron wave, but conventional high-resolution transmission electron microscopy only offers the access to the amplitude of the image wave, which contains somewhat intertwined amplitude and phase information as given by the transfer function of the microscope.

Several routes exist to achieve access to both the amplitude and phase [1]. A very intriguing one is off-axis holography as the recorded information in the hologram as well as the reconstruction scheme are linear, thus allow a rather straight-forward unbiased access to the exit wave.

As with nearly all electron microscopic techniques, the precision of the obtained information is limited by the number of electrons recorded. For non-beam sensitive materials, this limitation can in principle easily be overcome by longer exposure times. However, the limited temporal stability of the instrumentation prohibits extended exposures, as for instance the specimen or biprism start to drift.

This limitation can be overcome in principle by compensating the instrumental instabilities. Such a compensation can be achieved easily by a posteriori off-line processing [2]. We present an electron holographic reconstruction scheme suitable for holograms of atomic resolution. It is based on a series of several holograms (20-30) recorded with exposure times within the stability limits of the instrument (2-8s). The object holograms are recorded using a double biprism setup in order to reduce diffraction artifacts [3, 4] and due to the improved experimental flexibility [5]. The complex wave functions of these holograms are off-line processed in two steps. In a first step, a common region of interest is selected across the series while compensating coarse drift via central band cross-correlation. In the second step the side-bands of these regions are reconstructed and the resultant wave functions are preliminarily averaged, while compensating subpixel specimen drift, defocus drift (corresponds to specimen Z-drift), biprism drifts as-well-as hologram contrast variations. Between the iterations the individual drifts are estimated based on the preliminary average and the averaging/estimations are repeated iteratively until the averaged wave converges (Fig. 1).
Figure 2 show the phase and amplitude exit wave of a GaAs wedge reconstructed from 20 holograms of 2 second exposure time. The wave was corrected for residual aberrations using the edge on the lower right as reference. The stronger phase shifts of the heavier As-columns compared to the Ga-columns can be easily identified in the thicker region at the top of the exit wave.

In the vacuum region the standard deviations of the phase and amplitude are $2\pi/104$ and 0.04. At this precision the uncertainty in the residual aberrations and in residual specimen tilt, as-well-as the changes of the specimen structure (especial of the amorphous surfaces and the enhanced vibration of the edge atoms) are the next obstacles to overcome for true matching of the experimentally obtained exit wave-function with simulated ones.

1. J. Cowley, Ultramicroscopy 41 (1992), p. 335
2. E. Voelkl, D. Tang, Ultramicroscopy 110 (2010), p. 447
3. K. Yamamoto, T. Hirayama, T. Tanji, Ultramicroscopy 101 (2004), p. 265.
4. K. Harada, A. Tonomura, Y. Togawa, T. Akashi, T. Matsuda, Appl. Phys. Lett. 84 (2004), p. 3229
5. F. Genz, T. Niermann, B. Buijsse, B. Freitag, M. Lehmann, “Optimized conditions for high-resolution double-biprism holography ”, EMC 2012
6. We kindly acknowledge support from the DFG within the Collaborative Research Center 787 and DFG INST 131/508-1.

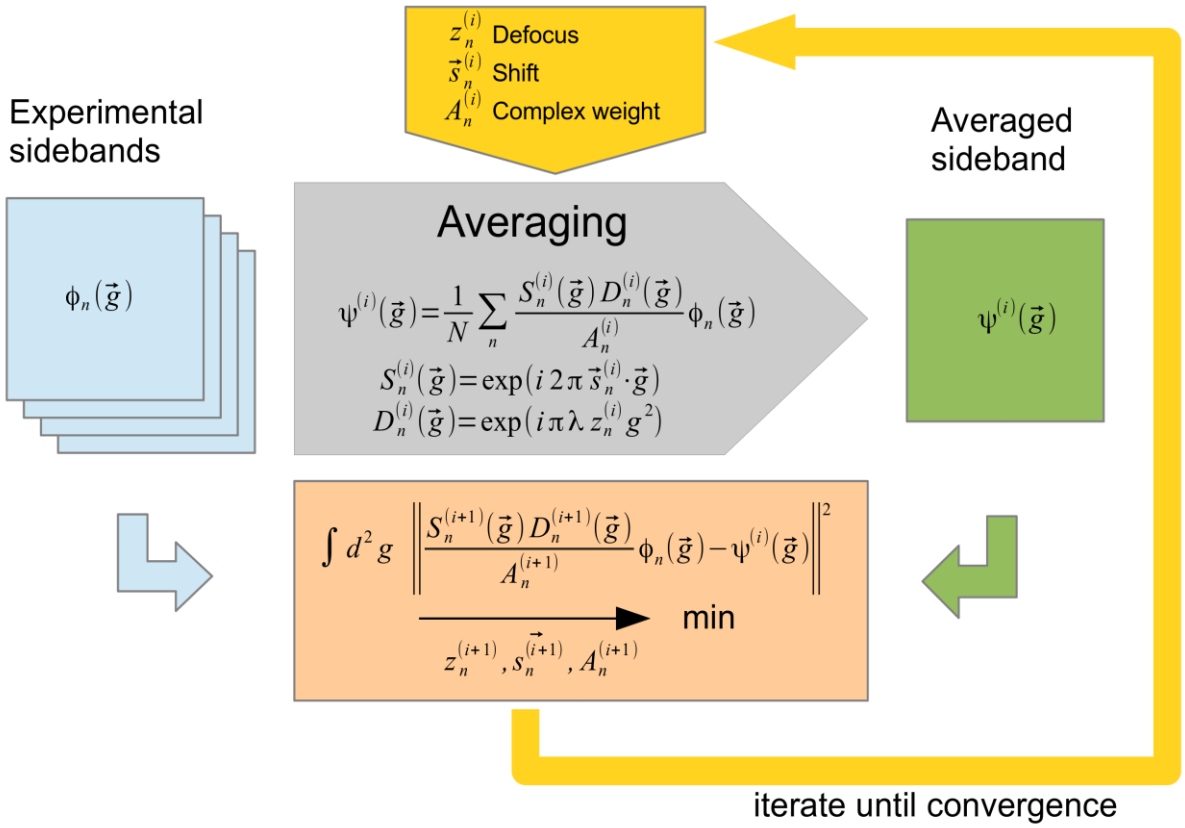

Figure 1. Algorithm for adjustment of the parameters for defocus, shift and global phase and amplitude: For each experimental sideband the parameters are optimized with respect to the distance to the averaged sideband. The averaging and optimization are repeated until convergence.

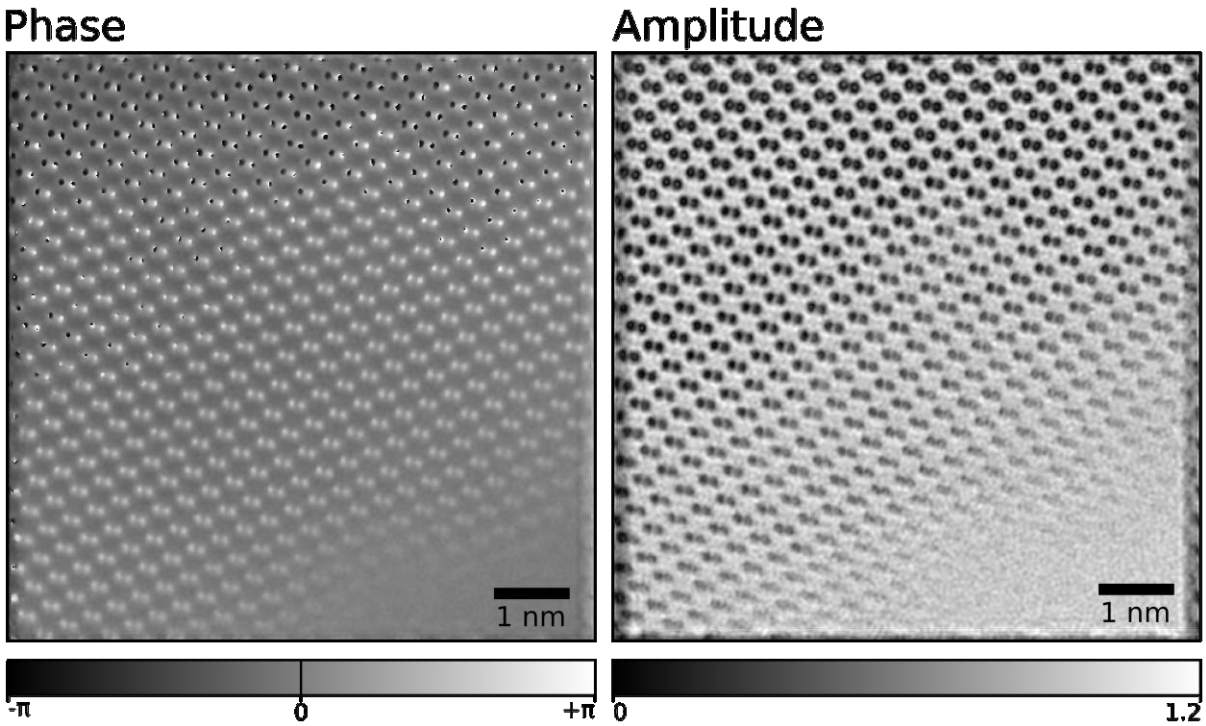

Figure 2. Phase and amplitude of the exit wave of a GaAs wedge after numerical aberration correction. The defocus was corrected for the lower-right edge to the vacuum.

Quantitative High-Resolution TEM/STEM and Diffraction

IM.1.P008
Avoiding surface strain field induced artifacts in 2d chemical mapping of dilute GaNAs quantum wells by HAADF STEM

T. Grieb[1], K. Müller[1], R. Fritz[2], V. Grillo[3], M. Schowalter[1], K. Volz[2], A. Rosenauer[1]

[1]University of Bremen, Institute of Solid State Physics, Bremen, Germany
[2]Philipps University of Marburg, Materials Science Center and Faculty of Physics, Marburg, Germany
[3]CNR, S3-NANO, Modena, Italy

Evaluating high-angle annular dark field (HAADF) intensity in scanning transmission electron microscopy (STEM) by a comparison with simulations is an appropriate method for quantitative chemical analysis [1, 2, 3]. It was recently demonstrated that the HAADF intensity of dilute GaNAs can be accurately simulated using a frozen-lattice multislice approach that takes into account the effect of static atomic displacements (SADs) [4]. The full 2D analysis of nitrogen in GaNAs layers which are pseudomorphically grown on GaAs is hindered by surface strain fields that occur in vicinity of the interfaces. These strain fields decrease the image intensity due to the effect of dechanneling as the lattice planes are slightly bended [5]. This results in dark stripes in the GaAs regions that are running parallel to GaNAs/GaAs interfaces. In this contribution we suggest a method combining two STEM images taken under different camera lengths to render full 2d-mapping of the nitrogen concentration possible. The HAADF STEM image in Figure 1. (a) was taken with detection angles between 36 and 230 mrad (camera length of 196 mm). The intensity close to the quantum well is decreased as explained before but the intensity in the center of the well is not affected by the strain fields due to the symmetry of the lattice plane bending [5]. We confirm by multislice simulations that the scattering intensity in GaAs is decreased in regions affected by surface strain at high scattering angles, whereas the intensity increases in the low-angle regime. Using an inner detector angle of about 14 mrad, the increase at low angles balances the decrease of the intensities at high angles so that no artifacts appear. For this reason the STEM image in Figure 1.(b) was taken with low detection angles between 14 and approximately 87 mrad (camera length of 478 mm) directly after taking the image in Figure 1.(a). The STEM image in Figure 1(b) does not show contrast modifications close to the quantum well and a higher chemical contrast between GaAs and GaNAs.

We suggest an indirect evaluation method by combining information from both STEM images in Figure 1. As Figure 1.(b) shows mainly chemical contrast, we assume that regions that show the same intensity in this image also have the same chemical composition. For the evaluation, the range of intensities found in Figure 1.(b) is subdivided into intervals. For each interval, we search positions (x, y) (atomic column positions as explained in [4]) for which the image intensities in Figure 1.(b) lie in the interval considered. Then, the average intensity is taken from those of the positions (x, y) in Figure 1.(a), which are located in areas not affected by surface strain fields. In this way the intensities in Figure 1.(b) are correlated with intensities in unstrained regions on Figure 1.(a). An image without strained regions is obtained from which the nitrogen concentration can be determined as explained in [4].

Figure 2 (a) shows a concentration profile obtained from the evaluation of the image in Figure 1(a) without and Figure 2.(b) with the suggested method: Artificial negative concentrations do no longer occur in the GaAs regions in Figure 2.(b), whereas the nitrogen concentration in the center of the quantum well is identical to that in the profile depicted in Figure 2 (a).

1. E. Carlino and V. Grillo, Phys. Rev. B 71 (2005), 235303.
2. S. I. Molina, D. L. Sales , P. L. Galindo, D. Fuster,Y. Gonzalez, B. Alen, L. Gonzalez, M. Varela and S. J. Pennycook, Ultramicroscopy 109 (2009), 172.
3. A. Rosenauer, K. Gries, K. Pretorius, M. Schowalter, A. Avramescu, K. Engl and S. Lutgen, Ultramicroscopy 109 (2009), 1171.
4. T. Grieb, K. Müller, R. Fritz, M. Schowalter, N. Neugebohrn, N. Knaub, K. Volz and A. Rosenauer, Ultramicroscopy 117 (2012), 15.
5. V. Grillo, Ultramicroscopy 109 (2009), 1453.
6. This work was supported by the German Research Foundation (DFG) under contract number SCHO 1196/3-1 and RO 2057/8-1-3008074.

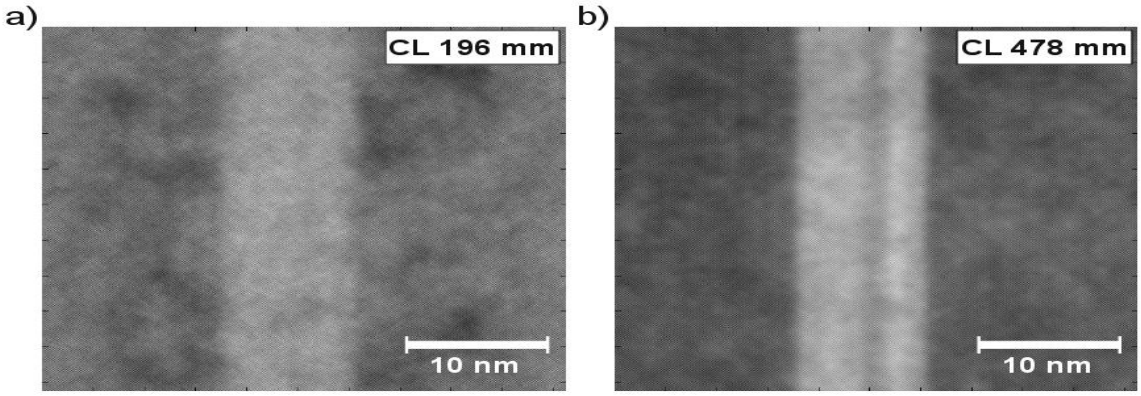

Figure 1. HAADF STEM images taken with a detection range (a) between 36 and 218 mrad and (b) between 14 and 87 mrad. (b) shows a higher chemical contrast compared to (a) and no contrast modifications from surface strain fields.

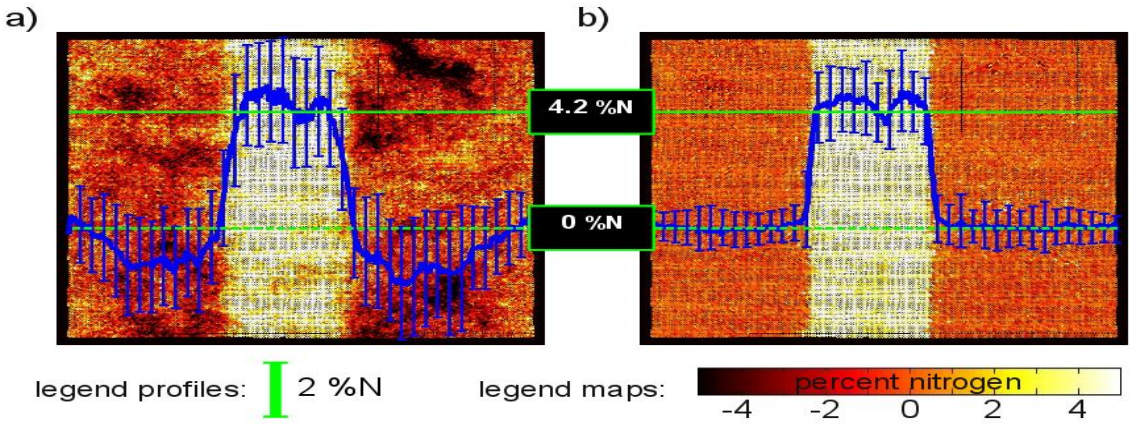

Figure 2. Concentration maps and profiles (a) from the standard method (from the image in Figure 1.(a)) and (b) from the suggested method (information from both images, Figure 1.(a) and (b)).

Quantitative High-Resolution TEM/STEM and Diffraction

IM.1.P009
Study of annular bright-field imaging of light elements in scanning transmission electron microscopy by computer simulation: case study of lithium in $LiFePO_4$

D. Zhou[1], W. Sigle[1], A. Rosenauer [2], P.A. van Aken[1]

[1]Max Planck Institute for Intelligent Systems, Stuttgart Center for Electron Microscopy, Stuttgart, Germany
[2]University of Bremen, Institute of Solid State Physics, Bremen, Germany

danzhou@is.mpg.de
Keywords: ABF, light atom, STEMsim

Light elements, such as lithium, are difficult to detect using high-angle annular dark-field imaging (HAADF) in STEM because of their weak atomic scattering. Recently, a novel imaging mode in aberration-corrected STEM was presented which uses an annular detector spanning an angular range mainly within the illumination cone of the focused electron beam. The scheme of the geometrical set-up is illustrated in Figure 1[1]. It was shown that due to the smaller dependence on atomic number *Z*, approximately $Z^{1/3}$ compared to Z^2 in HAADF, the resultant images enable one to visualize the light element columns[2]. This imaging mode has been called annular bright-field (ABF) imaging. Brief demonstration of ABF imaging and outline of underlying theory were presented previously.

In this work, we studied ABF imaging of light elements, in case of lithium in $LiFePO_4$, in STEM by means of simulation using the STEMsim program[3]. Despite the success of $LiFePO_4$ application in battery materials, the microscopic mechanism of the phase transition from $LiFePO_4$ to $FePO_4$ is still under debate. Previous work briefly demonstrated the possibility to acquire direct images of $LiFePO_4$ and partially delithiated $LiFePO_4$ at atomic resolution[4]. The present work aims at presenting a much more detailed description of the dynamics of ABF imaging of $LiFePO_4$ with a view to its interpretation, explanation and optimization. Thickness, defocus, aberrations, and lithium concentration are taken into account to explain the image contrast. And in particular, the probe and detector configurations in our new installed probe aberration-corrected JEM-ARM 200F are taken into consideration. Figure 2 presents a comparison of the visualization of lithium in $LiFePO_4$ with ABF and ADF by simulation using the STEMsim program.

1. Okunishi, E.; Ishikawa, I.; Sawada, H.; Hosokawa, F.; Hori, M.; Kondo, Y. *Microsc Microanal* 2009, 15, 164-165.
2. Findlay, S. D.; Shibata, N.; Sawada, H.; Okunishi, E.; Kondo, Y.; Ikuhara, Y. *Ultramicroscopy* 2010, 110, (7), 903-923.
3. Rosenauer, A.; Schowalter, M. *Springer Proc Phys* 2008, 120, 169-172.
4. Gu, L.; Zhu, C. B.; Li, H.; Yu, Y.; Li, C. L.; Tsukimoto, S.; Maier, J.; Ikuhara, Y. *J Am Chem Soc* 2011, 133, (13), 4661-4663.
5. The research leading to these results has received funding from the European Union SeventhFramework Programme [FP7/2007-2013] under grant agreement n°312483 (ESTEEM2).

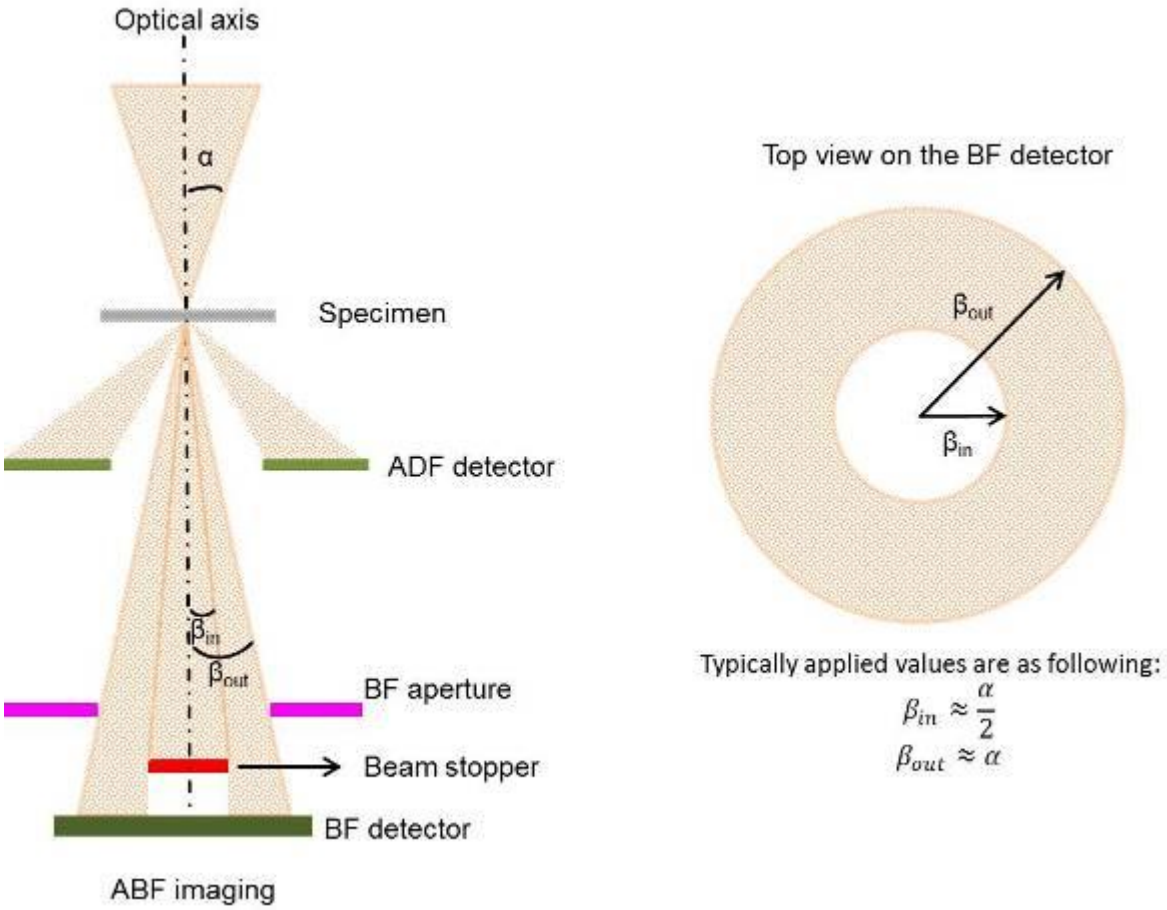

Figure 1. Schematic of the geometry of ABF imaging

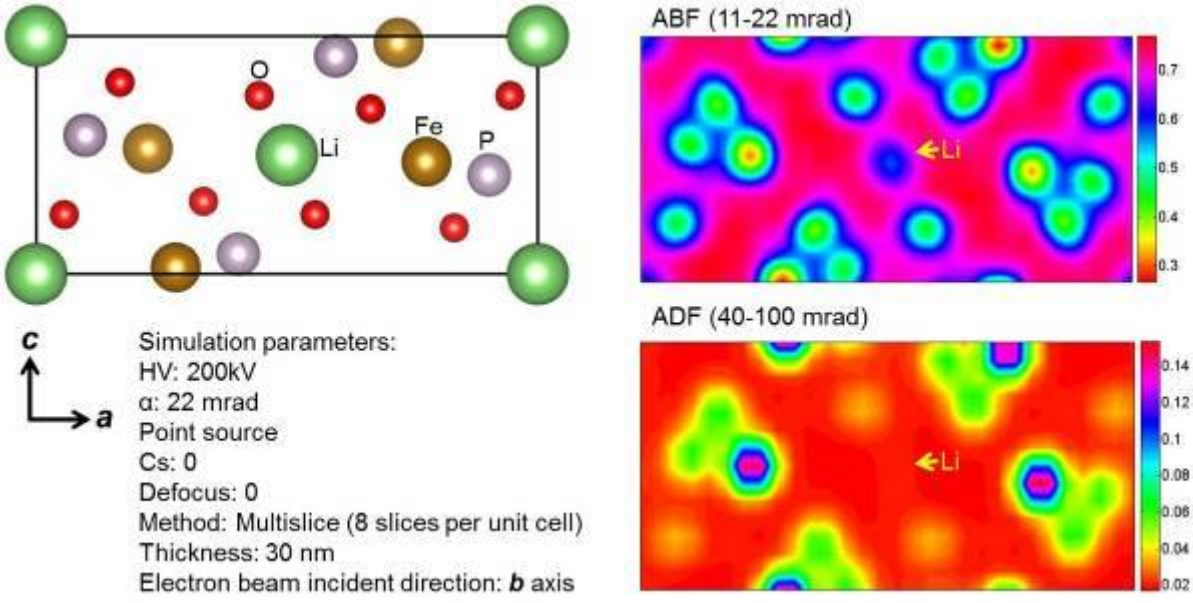

Figure 2. Visualization of lithium in $LiFePO_4$ with ABF and ADF imaging

Quantitative High-Resolution TEM/STEM and Diffraction

IM.1.P010
Atomic number estimation from STEM images: what are the limits?

J. Gonnissen[1], A.J. den Dekker[2], A. De Backer[1], J. Sijbers[3], S. Van Aert[1]

[1]Electron Microscopy for Materials Science (EMAT), University of Antwerp, Antwerp, Belgium
[2]Delft Center for Systems and Control, Delft University of Technology, Delft, Netherlands
[3]Vision Lab, University of Antwerp, Wilrijk, Belgium

Julie.Gonnissen@ua.ac.be
Keywords: Design of experiment, STEM

Statistical parameter estimation theory is a quantitative method to measure unknown structure parameters from electron microscopy images. Such images can be considered as data planes from which structure parameters can be determined. A parametric statistical model of the observations is needed in order to perform computer simulations of the images. This model needs to describe the electron-sample interaction, microscope transfer and image detection. The unknown parameters are then estimated by fitting the model to the experimental images using a criterion of goodness of fit [1]. Since the precision with which the parameters can be estimated is limited by noise, the goal of experiment design is to investigate which microscope settings are expected to yield the highest precision with which the structure parameters can be estimated. Statistical parameter estimation theory can be used for this purpose. Previous work has shown the Cramér-Rao Lower Bound (CRLB) to be a very efficient tool to compute the optimal experiment design that provides maximum precision [2-4]. The CRLB is a lower bound on the variance of unbiased estimators of the unknown parameters and can be computed from the parameterized probability (density) function of the observations. However, it is only defined when the probability (density) function is continuously differentiable with respect to the parameters. An alternative approach using the principles of detection theory [5] is therefore investigated for problems concerning the estimation of so-called restricted (or, discrete) parameters.

This alternative approach is needed for instance when considering the problem of identifying the atomic number Z from a Scanning Transmission Electron Microscopy (STEM) image. Note that chemical theory restricts the atomic number to be a positive integer, which makes it is a restricted parameter. A priori knowledge about the atom types that may be present in a sample and their concentration ratios is usually available. In such cases, the question reduces to distinguishing between a finite plausible set of values for the atomic numbers, given the experimental STEM observations. Here we restrict to the problem of deciding between two hypotheses, where each hypothesis corresponds to the assumption of a specific Z value: H_0: $Z=Z_0$ and H_1: $Z=Z_1$. H_0 is referred to as the null hypothesis and H_1 as the alternative hypothesis. Following the so-called Bayesian approach, prior probabilities $P(H_0)$ and $P(H_1)$ are assumed known. In this way, we express a prior belief in the likelihood of the hypotheses. If the presence of an atom of type Z_0 or Z_1 is equally likely, then it is reasonable to assign equal probabilities of 1/2. An expression for the probability of error P_e can now be defined as the sum of the probabilities of deciding H_i if H_j is true, where the two possible errors are weighted appropriately to yield an overall error measure. For the computation of P_e a simplified discrete parametric model of an isolated atom is derived, assuming Poisson noise statistics. Decision rules are now defined such that P_e is minimized. For this purpose, it is shown in [5] that for equal prior probabilities, we should then decide H_1 if the conditional joint probability function given Z_1 evaluated at the available observations, is greater than that given Z_0. This corresponds to choosing the hypothesis for which the log likelihood function is maximal. The difference between the log likelihood function for Z_1 and this for Z_0 is defined as the log likelihood ratio. Using repetitive simulations, P_e can be computed for different experimental settings, in order to compute which experimental settings minimise the probability to assign an incorrect hypothesis.

A tightly connected performance measure that is investigated as a possible alternative to optimize the experiment design, is based on the Kullback-Leibler divergence [7,8]. This measure quantifies the difference between two probability distributions, circumventing the need for excessive image simulations. The sum of Kullback-Leibler divergences corresponds to the difference of the expected or mean log-likelihood ratio under H_1 and the corresponding value when assuming H_0 to be true.

An experimental case study is presented to show the practical use of these proposed measures for the optimisation of the experiment design. More precisely the optimal inner detector radius of an annular detector is derived when deciding between the presences of an Al or Ti atom in STEM

images, such as in the experimental study in [6]. Simulations are performed under both hypotheses H_0: $Z=Z_0=13$ (Al) and H_1: $Z=Z_1=22$ (Ti). For every simulation experiment the log likelihood ratio is calculated and so Figures 1-3 are obtained for three different inner detector radii (0.7 $Å^{-1}$, 1.1 $Å^{-1}$ and 2.5 $Å^{-1}$). It is found that the sum of Kullback-Leibler divergences and the probability of error provide consistent results. Indeed, the probability to assign the wrong hypothesis decreases when the distributions of the log-likelihood ratio under the considered hypotheses are better separated, and thus when the sum of Kullback-Leibler divergences increases. It is seen in Figure 4 that a minimum for the probability of error is found for the inner detector radius maximising the sum of Kullback-Leibler divergences, namely for 1.1 $Å^{-1}$. We see in Figures 1-3 that for this inner detector radius the log-likelihood functions under H_0 and H_1 are separated the most. This proves the Kullback-Leibler divergence to be an efficient alternative performance measure to optimize the experiment design.

1. A.J. den Dekker, S. Van Aert, D. Van Dyck and A. van den Bos, Ultramicroscopy 104(2) (2005), p. 83–106.
2. D. Van Dyck, S. Van Aert, A.J. den Dekker and A. van den Bos, Ultramicroscopy 98(1) (2003), p. 27–42.
3. A.J. den Dekker, J. Sijbers, and D. Van Dyck, Journal of Microscopy 194 (1999), p. 95–104.
4. S.M. Kay. “Fundamentals of Statistical Signal Processing. Volume II Detection Theory”, (Prentice-Hall, New Jersey) (2009).
5. M. Huijben et al., A. Brinkman, and H. Hilgenkamp, Nature materials 5 (2006), p. 556−560.
6. S. Kullback and R.A. Leibler, Annals of Mathematical Statistics 22 (1951), p. 79–86.
7. S. Kullback. “Information theory and statistics”, John Wiley and Sons (1959).

8. The authors acknowledge financial support from the Research Foundation Flanders (FWO, Belgium) through project fundings (G.0393.11, G.0064.10 and G.0374.13).

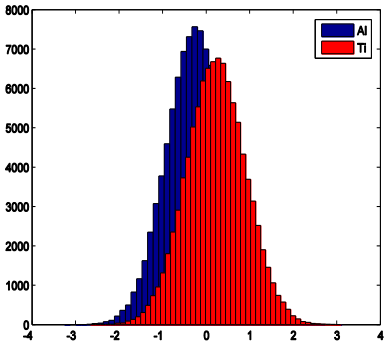

Figure 1. Log likelihood ratio for inner detector radius 0.7 $Å^{-1}$ for Al (blue) and Ti (red)

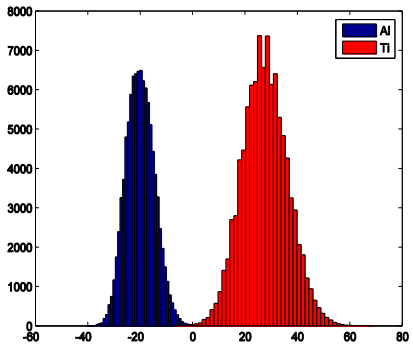

Figure 2. Log likelihood ratio for inner detector radius 1.1 $Å^{-1}$ for Al (blue) and Ti (red)

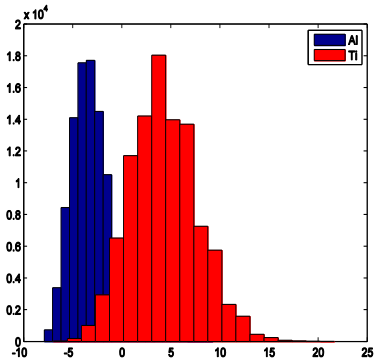

Figure 3. Log likelihood ratio for inner detector radius 2.5 $Å^{-1}$ for Al (blue) and Ti (red)

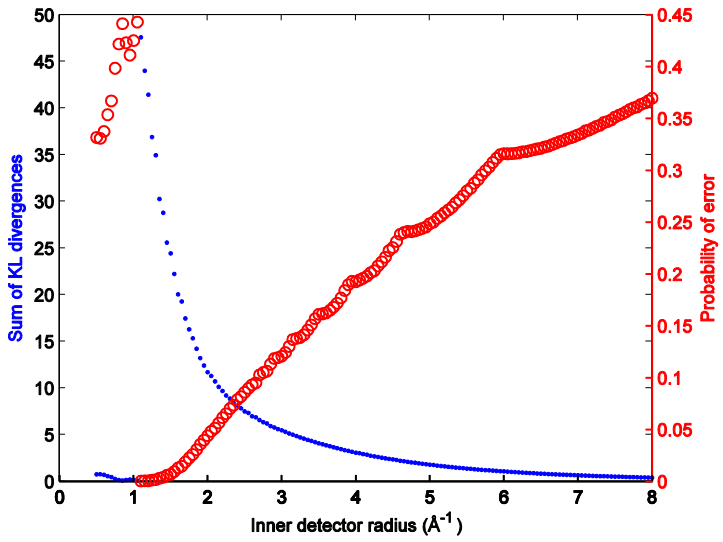

Figure 4. Probability of error (red) and sum of KL divergences (blue) for Al and Ti as a function of the inner detector radius ($Å^{-1}$).

Quantitative High-Resolution TEM/STEM and Diffraction

IM.1.P011
Electron irradiation damage in dependence of the acceleration voltage studied by C_C/C_S corrected HRTEM on the example of functionalized carbon nanotubes

J. Biskupek[1], T. Zoberbier[1], U. Kaiser[1], T.W. Chamberlain[2], A.N. Khlobystov[2], P. Hartel[3], M. Linck[3]

[1]University of Ulm, Central Facility of Electron Microscopy, Ulm, Germany
[2]University of Nottingham, School of Chemistry, Nottingham, United Kingdom
[3]Ceos GmbH, Heidelberg, Germany

Johannes.Biskupek@uni-ulm.de
Keywords: carbon nanotubes, irradiation damage, aberration correction

Aberration corrected high resolution transmission electron microscopy (AC-HRTEM) at conventional accelerating voltages of 200 or 300 kV allows atomic structural investigations at sub-Ångstrøm point resolution. Samples made of light atoms like carbon nanostructures or Li-based materials are easily subjected to knock-on damage at 200 keV and higher energies. The nowadays state-of-the-art is to operate the C_S-corrected microscopes at 80 kV to lower the damage of carbon nanostructures like graphene and carbon nanotubes. But even 80 keV energies are sufficient to damage delicate objected like C_{60} molecules and other organic molecules that are supported by free-standing graphene sheets of filled into nanotubes (nanotubes and graphene act as sample/object holder). Operating a TEM considerably below 80 kV e.g. 40 kV or less requires the correction not only of the spherical aberration but also of higher order geometric aberrations up to the 5^{th} order. Moreover, the correction of chromatic aberrations is necessary to archive atomic resolution at high contrast [1].

We are going to study by TEM single-walled and double-walled carbon nanotubes that are filled and functionalized with molecules like C_{60}, tetrathiafulvalene (TTF, sulphur rich molecule) [2] or metal carbonyls [3]. The effect of the electron beam on the behaviour of nanotubes and their fillings is investigated as function of electron energy (80, 40, 20 keV), total electron dose, and electron dose rate. A dedicated aberration corrector is used to archive atomic resolution at lower voltages especially at 20 and 40 kV. Geometric axial aberrations are corrected up to the 5^{th} order except for C_5 that was designed to be 4 mm to obtain an optimized phase contrast transfer function. Off-axial aberrations are corrected up to the 2^{nd} order for larger fields of view as well as chromatic aberrations for increased contrast.

Figure 1 shows as example HRTEM images of C_{60} molecules at different stages of electron irradiation. At 80 kV already a relatively small accumulated dose of $5x10^{-7}$ e^-/nm^2 is sufficient to form first dimers of C_{60} (this dose corresponds to just about 4 or 5 HRTEM acquisitions at conventional dose rates in the order of some 10^6 $e^-/nm^2/s$). However, no visible changes of the structure of C_{60} molecules are visible at 40 kV after irradiation with the same accumulated electron dose. A coalescence of the C_{60} molecules is clearly visible at a electron dose of $2x10^{-8}$ e^-/nm^2 and 80 kV irradiation. It requires almost two magnitudes of order higher dose (40 times) to get small hints of coalescence of the C_{60} molecules at 40 kV. Unfortunately, at 40 kV increased dynamics such as the typical vibrations of free-standing carbon nanotubes and longitudinal motion of C_{60} molecules lowered the image contrast and resolution. Part of the reduced contrast at 40kV might also arise from an image spread within the corrector. An image spread is almost equivalent to a Debye-Waller factor and hence cannot be distinguished from vibrations of the tube.

1. Z.Lee, J.C.Meyer, H.Rose and U.Kaiser, Ultramicroscopy 112 (2012) 39-46
2. A. Chuvilin, E. Bichoutskaia, M. C. Gimenez-Lopez, T. W. Chamberlain, G. A. Rance, N. Kuganathan, J. Biskupek, U. Kaiser and A. N. Khlobystov, Nature Materials 10 (2011) 687-692
3. T. W. Chamberlain, J. Biskupek, G. A. Rance, A. Chuvilin, T. J. Alexander, E. Bichoutskaia, U. Kaiser, A. N. Khlobystovm ACS Nano 6, (2012) 3943-3953.

4. This work was supported by the DFG (German Research Foundation) and Ministry of Science, Research and the Arts (MWK) of Baden-Württemberg in the frame of the SALVE (Sub-Angstroem Low-Voltage Electron Microscopy) project

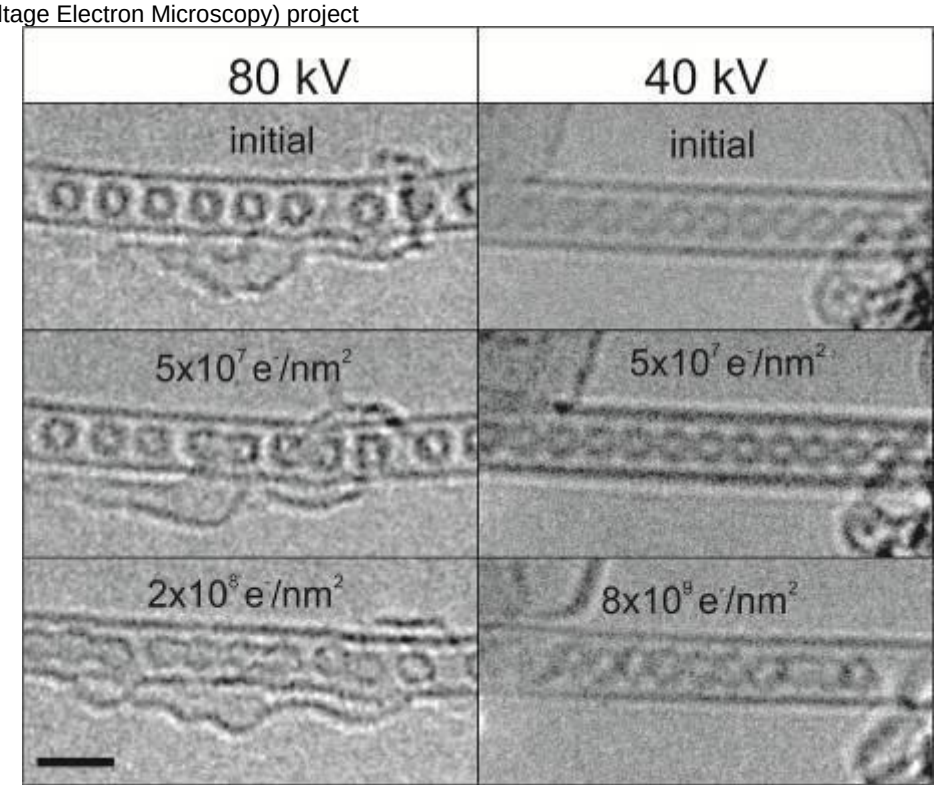

Figure 1. Aberration corrected HRTEM images of C_{60} molecules in carbon nanotubes. (left) C_{60} in a double-walled carbon nanotube imaged at 80 kV. (right) C_{60} in a single-walled carbon nanotube imaged at 40 kV. Dimers (two connected C_{60} molecules) occurs at a dose ca. $5x10^{-7}$ e^-/nm^2 at 80 kV at 40 kV no changes are visible. A coalescence of the C_{60} molecules is clearly visible at a dose of $2x10^{-8}$ e^-/nm^2 and 80 kV irradiation. At 40kV it requires almost two times magnitude of order higher dose (40 times) to get first indications of coalescence and rupturing of the C_{60} molecules. (size of scalebar is 1 nm).

Quantitative High-Resolution TEM/STEM and Diffraction

IM.1.P012
GPU-accelerated Bloch wave calculation for quantitative structure factor determination

F. Wang[1], R. Pennington[1], C. Koch[1]

[1]Universität Ulm, Institut für Experimentelle Physik, Ulm, Germany

feng.wang@uni-ulm.de
Keywords: dynamical electron diffraction, Bloch waves, matrix exponential, GPU, LARBED, image simulation

Multiple scattering solves the crystallographic phase problem. This allows for structure-factor refinement by quantitative convergent-beam electron diffraction (QCBED) [1,2]. In QCBED, iterative refinement from dynamical electron diffraction data from multiple beam directions yields structure-factor amplitudes and phases, but QCBED only works for small unit cells and requires a good initial guess of the structure factors. In contrast, by using quantitative large-angle rocking-beam electron diffraction (QLARBED) [3] data from thin crystals (see, for example Fig 1b,c), even unknown crystal structures may be determined, even for large unit cells. This is possible because, for moderately thick crystals, the Bloch wave formalism for dynamical scattering can be expanded using a scattering path expansion [4] to find an initial guess for the structure factors [5]. This initial guess can then be refined using the classical QCBED approach. Fortunately, the initial guess for QLARBED need not be as precise as for QCBED, since, for thinner crystals, there are fewer local minima than for thick crystals.
While QCBED must be applied only to crystals with small unit cells with only a few reflections, QLARBED is targeted at arbitrarily large structures and must therefore be able to handle many simultaneously excited beams. Therefore, QLARBED requires a very fast and scalable algorithm for computing dynamical diffraction intensities. In QCBED, this computation is mostly done with the Bloch wave method. For QLARBED, we also chose the Bloch wave method, because, compared to the multislice method, the Bloch wave method allows for beam tilt, Ewald-sphere curvature, and specimen surface orientation to be included in a very direct manner *i.e.* without having to deal with non-periodic boundary conditions or insufficiently thin slices [6].

In this work, we compare the numerical efficiency of multiple implementations of computing dynamical diffraction intensities. We discuss how using state-of-the-art graphics processing unit (GPU) hardware acceleration has helped to speed up the calculation by more than two orders of magnitude (see Fig. 2). For an optimal accuracy-time trade-off, a hybrid method using Taylor expansion and the scaling/squaring method has been employed to compute the matrix exponential [7, 8, 9].

1. C. Deininger, G. Necker and J. Mayer, Ultramicroscopy 54 (1994) pp. 15-30.
2. J.-M. Zuo, M. Kim, M. O'Keefe, and J.C.H. Spence, Nature 401 (1999) p. 49.
3. C.T. Koch, Ultramicroscopy 111 (2011) pp. 828-840.
4. C.T. Koch and J.C.H. Spence, J. Phys. A: Math. Gen. 36 (2003) pp. 803-816.
5. C.T. Koch, arXiv:0810.3811v1.
6. J.C.H. Spence and J.-M. Zuo, *Electron Microdiffraction*, (Plenum, New York) (1992).

7. C. B. Moler and C. F. Van Loan, SIAM Review 20 (1978) pp. 801-836.
8. C. B. Moler and C. F. Van Loan, SIAM Review 45 (2003) pp. 3-49.
9. M.L. Liou, Proc. Inst. Elect. Electron. Engrs. 54 (1966) pp. 20-23.
10. E. Jones, T. Oliphant, P. Peterson et al. SciPy: Open source scientific tools for Python. http://www.scipy.org.
11. J. R. Humphrey, D. K. Price, K. E. Spagnoli, A. L. Paolini, and E. J. Kelmelis, SPIE Defense and Security Symposium (DSS), 2010.
12. The authors acknowledge the Carl Zeiss Foundation as well as the German Research Foundation (DFG, Grant No. KO 2911/7-1).

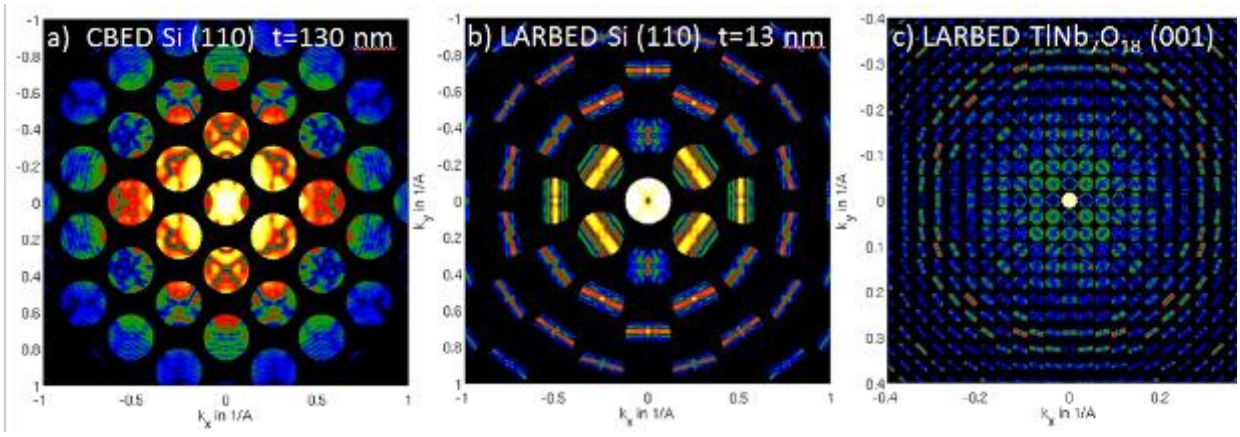

Figure 1. CBED and LARBED patterns computed using the GPU-based diffraction code. The patterns are displayed on a logarithmic scale. The simulation conditions were a) thickness = 130 nm, convergence-semi-angle α_{max} = 4.2 mrad, scan compensation = 0 (descan turned off); b) thickness = 13 nm, α_{max} = 70 mrad, scan compensation = 88%; c) thickness = 10 nm, α_{max} = 70 mrad, scan compensation = 99.2%. These patterns have been computed without using the Bethe approximation for any reflections.

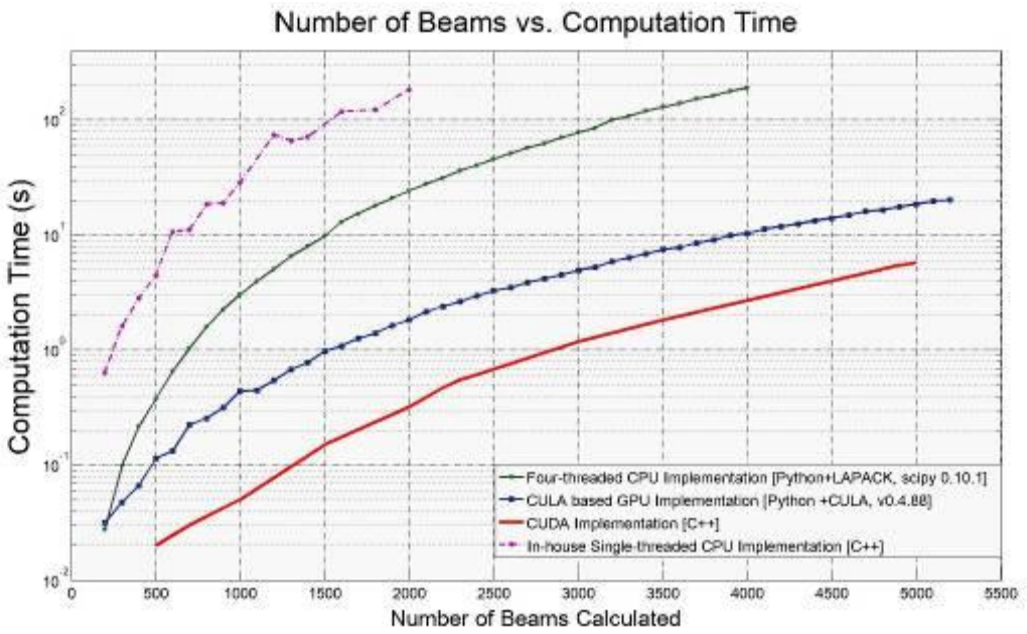

Figure 2. Matrix exponential implementation benchmark: The GPU-based CUDA code (running on an Nvidia Tesla K20) is 2 orders of magnitude faster than the parallelized CPU code (running on an Intel Xeon W3550). The purple and the green curves show the performance on the CPU: the purple one is a single-threaded native C++ implementation, while the green one is a LAPACK/BLAS-based implementation, using 4 CPU threads and the SciPy Python package [10]. The blue and the red curves show the performance on the GPU: the blue one is based on CULA [11] and written in Python, while the red one is a native CUDA C++ implementation. The algorithm corresponding to the purple, green and blue curves uses the Padé approximation (purple: order 14, green and blue: order 7). The algorithm corresponding to the red curve uses the scaling and squaring method with a 9th-order Taylor expansion.

Quantitative High-Resolution TEM/STEM and Diffraction

IM.1.P013
The power spectrum of an EFTEM image recorded with low intensity levels

C. Kreyenschulte[1,2], H. Kohl[1,2]

[1] Physikalisches Institut, University of Münster, Münster, Germany
[2] Interdisziplinäres Centrum für Elektronenmikroskopie und Mikroanalyse, Münster, Germany

carsten.kreyenschulte@uni-muenster.de
Keywords: EFTEM, power spectrum, CCD camera

The power spectrum of electron micrographs can be used to evaluate the structure of the specimen quite accurately by determining its structure factor. By use of energy filtered transmission electron microscopy (EFTEM) it is even possible to determine the partial two particle structure factors by using elemental maps. We have done so for disordered structures [1]. Another use of the power spectrum can be the separation of detection noise from the specimen signal, allowing for a better distinction between signal and noise [2].

In order to get useful data the composition of the power spectrum needs to be understood. Considering a specimen signal , with **u** being the spatial frequency vector, the influence of the scattering process, the microscope and the detector, e.g. a CCD-camera, needs to be determined.

In Fourier space, the camera is usually characterized by the modulation transfer function , with being the modulus of , which is the Fourier transformed point spread function. It is either supplied by the camera manufacturer or can be determined by one of the methods described in [2].

In EFTEM the scattering process cannot be separated from the imaging process. Together, they are described by the inelastic transfer function which can be calculated theoretically [3,4]. and are shown in figure 1. These functions are cause a signal broadening in real space.

The noise of the detection system needs also to be taken into account. The noise power spectrum is a characterization of the statistical nature of the detection process [5]. It is also called noise transfer function or noise based modulation transfer function. In EFTEM or other low intensity applications it can be necessary to add the noise power spectrum from the dark current correction , which stems from the thermal fluctuation in the camera and is dependent on the recording time.

Combining all these functions the power spectrum of the recorded image can expressed as

When the flatfield image used to calculate is in the same intensity regime as the micrograph and the exposure time is sufficiently low, one can usually neglect .

Special care has to be taken when recording and evaluating elemental maps. In this case the difference in recording intensities and times can yield unexpected results. To avoid specimen drift, the overall exposure time for one image can be split into several shorter exposures which are summed up after drift correction [6]. Using the same dark current correction image for each of these shorter exposures will result in a recognizable increase of the noise power spectrum by a constant value over all spatial frequencies (figure 2).

Another problem can arise when the same illumination parameters are used for recording the flatfield images for the calculation of the noise power spectrum after recording a series of energy filtered images at higher energy losses. When using a full frame CCD camera, the recorded image is shifted line by line to the readout lane. If there is an afterglow due to high illumination intensities, the recorded images will show a signal broadening in readout direction showing the exponential decay of the scintillator. In Fourier space this will show as a symmetry breaking function for the noise power spectrum with being the spatial frequency in readout direction of the detector, the decay constant and the pixel size

.

This effect is more pronounced when using the binning function of the camera because of the much faster readout process. In figure 3 we show a fit of the above function to the quotient of an affected noise power spectrum by an unaffected one.

1. C. Kreyenschulte and H. Kohl, Eur. Phys. J. Appl. Phys. 54 (2011), 33506.
2. C.B. Boothroyd, T. Kasama and R.E. Dunin-Borkowski, Ultramicroscopy 129 (2013),p 18.
3. H. Kohl and H. Rose, Adv. Electron El. Phys. 65 (1985), p. 173.
4. R. Knippelmeyer and H. Kohl, J. Microscopy 194 (1999), p. 30.
5. T. Niermann, A. Lubk and F. Röder, Ultramicroscopy 115 (2012), p. 68.
6. T. Heil and H. Kohl, Ultramicroscopy 110 (2010), p. 745.
7. The authors gratefully acknowledge funding from the Deutsche Forschungsgemeinschaft (DFG) under grant number Ko885/8-1.

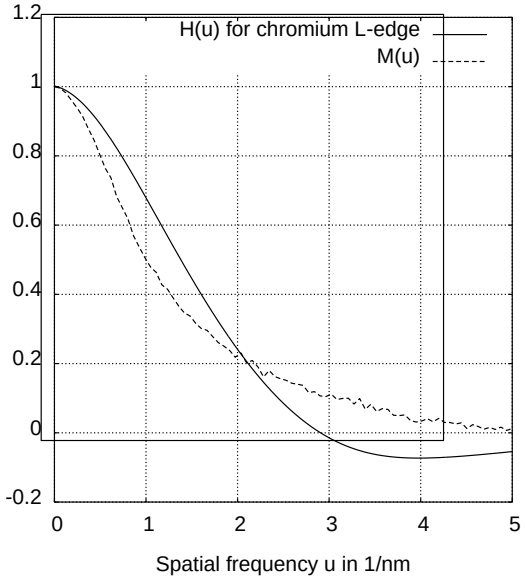

Figure 1. for the case of a CCD camera with a pixel size of and a magnification of 150k, calculated for an acceptance half angle of at an energy loss of , corresponding to an energy window on the chromium L-edge.

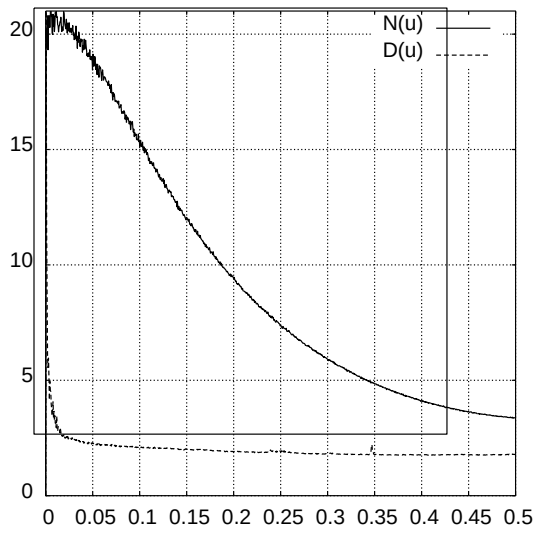

Figure 2. Noise power spectrum and dark noise for our CCD-camera, with a recording time of , at a low illumination intensity for the bright flat images.

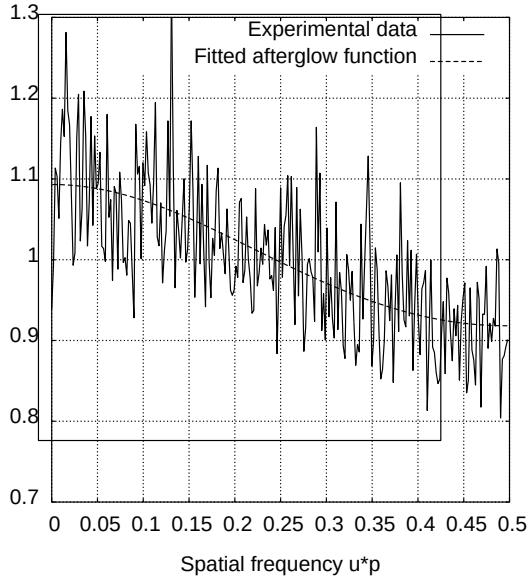

Figure 3. Afterglow function determined by dividing the noise power spectrum of a flat image recorded with high illumination intensity by the noise power spectrum of a flat image recorded by low illumination intensity. The decay parameter was found to be

.

Quantitative High-Resolution TEM/STEM and Diffraction

IM.1.P014
High-resolution TEM investigation of an epitaxially strained $LaNiO_3/LaMO_3$ superlattice

H. Qi[1], M.K. Kinyanjui[1], J. Biskupek[1], D. Geiger[1], H.-U. Habermeier[2], B. Keimer[2], L. Jin[3], C. Jia[3], R.E. Dunin-Borkowsk[3], U. Kaiser[1]

[1]Central Facility of Electron Microscopy, Electron Microscopy Group of Materials Science, University Ulm, Ulm, Germany
[2]Max Planck Institute for Solid State Research, Sttutgart, Germany
[3]Ernst Ruska-Centre for Microscopy and Spectroscopy with Electrons and Peter Grünberg Institute, Forschungszentrum Jülich, Jülich, Germany

haoyuan.qi@uni-ulm.de
Keywords: high-resolution transmission electron microscopy, negative C_S imaging, oxygen imaging

It has been reported that epitaxially strained $LaNiO_3/LaMO_3$ (M = a trivalent cation Al, Ga…) superlattice structures may provide favorable conditions for high-T_c superconductivity [1]. Depending on the choice of substrate, either tensile or compressive strain may be introduced at the interface due to the lattice mismatch. In $LaNiO_3/LaMO_3$ heterostructures, epitaxial strain can be accommodated in the form of a distortion of the NiO_6 octahedra, resulting in elongation or compression along the growth direction (depending on the sense of the strain), as well as in their rotation. The resulting rearrangement of the NiO_6 structure may lead to drastic changes in the electronic and magnetic properties of the heterostructures. It may therefore be possible to tailor the electronic structure of the system by controlling the atomic structure, in order to achieve favorable charge states for high-T_c superconductivity.

Here, we present initial results from an aberration corrected high-resolutuion transmission electron microscopy (HRTEM) study of an epitaxially strained $LaNiO_3/LaGaO_3$ (LNO/LGO) superlattice grown on (001) $SrTiO_3$ (STO). The atomic structure model is shown in Figure 1. Since the most direct indicator of the structural change is the distortion and rotation of the oxygen octahedra, our work is focused on high-resolution imaging of the oxygen columns.

In order to enhance the contrast of the oxygen columns, we have applied negative C_s imaging (NCSI) [2]. We have used optimum imaging conditions, as described by Lentzen [3]. A C_s-corrected FEI Titan 80-300 microscope with the accelerating voltage of 300 kV was used. Figure 2 shows an experimental HRTEM image of an LNO/LGO superlattice grown on STO acquired using a value for C_S of ~ -15 µm. Each atomic column can be resolved clearly. A simulated image is shown on the right side of Fig. 2. A detailed comparison between the experimental image and such simulations suggests that the specimen thickness is ~ 10 nm and that the defocus is ~ +5 nm (i.e., overfocus). An atomic structure model is overlaid on the simulated image.

When using the chosen imaging conditions, the oxygen columns have the highest intensity and contrast in the image. The simulations confirm that the intensity of the oxygen columns does not result from channeling effects associated with the neighboring heavier atomic columns. The clearly resolved atomic columns allow the distortion and rotation of the oxygen octahedra, as well as the atomic structure of the interface, to be investigated directly.

1. J. Chaloupka and G. Khaliullin, Phys. Rev. Lett. 100 (2008), p. 016404.
2. C. Jia, M. Lentzen and K. Urban, Microsc. Microanal. 10 (2004), p. 174.
3. M. Lentzen, Microsc. Microanal. 14 (2008), p. 16.

4 .We are grateful to S. Grözinger for assistance with TEM specimen preparation and the German Research Foundation (DFG) for financial support (project DFG: KA 1295/17-1).

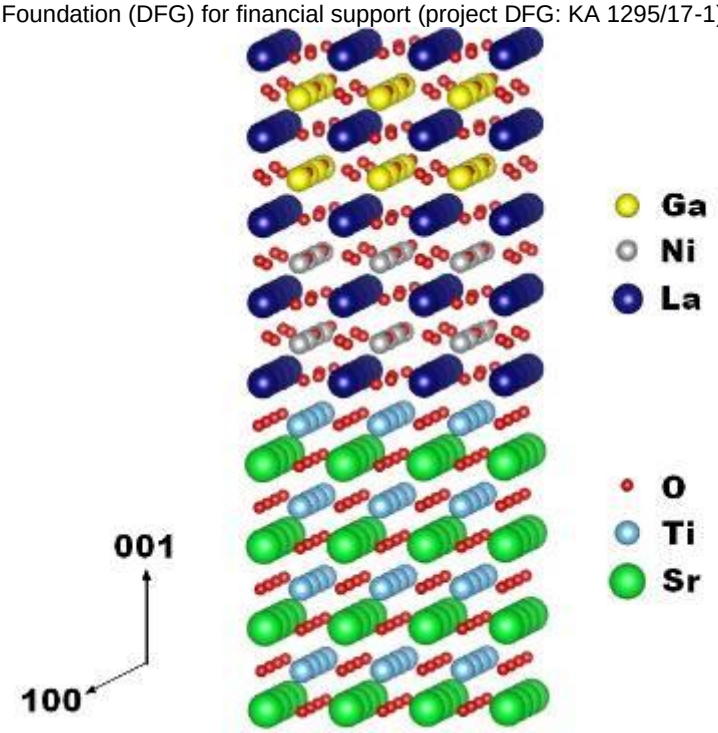

Figure 1. Atomic structure model of an $LaNiO_3/LaGaO_3$ (LNO/LGO) superlattice grown on (001) $SrTiO_3$ (STO) substrate.

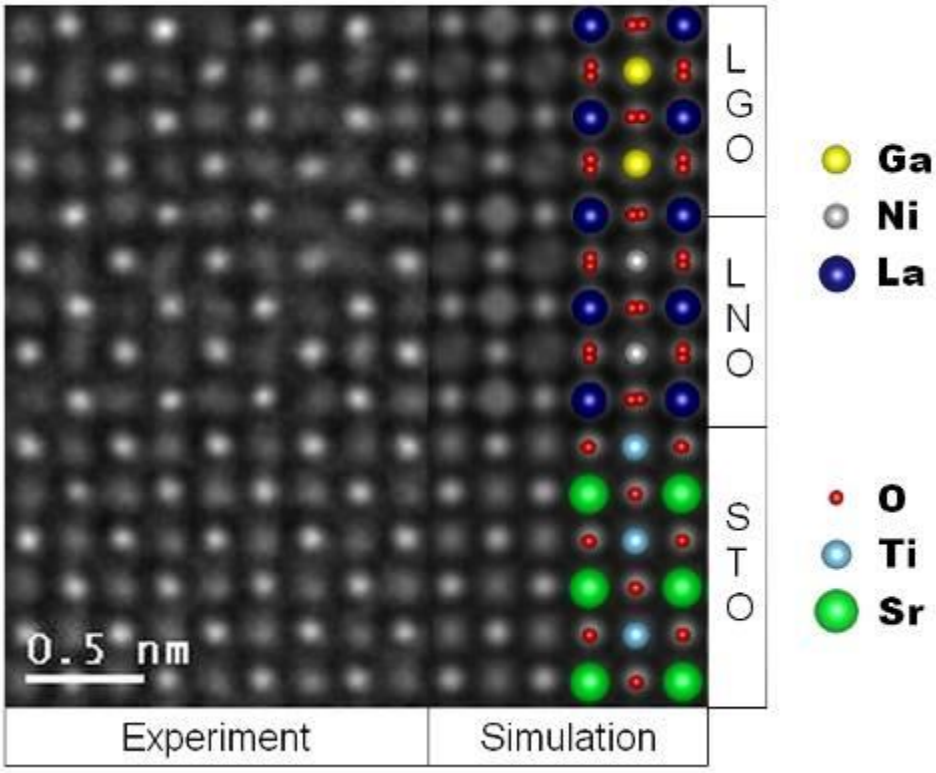

Figure 2. High-resolution TEM image of an LNO/LGO superlattice grown on STO. The image was acquired in [100] projection using negative C_S imaging conditions (C_S ~ -15 µm, defocus ~ +5 nm). A corresponding simulated image is shown on the right. The identities of the atomic columns are indicated on the simulation.

Quantitative High-Resolution TEM/STEM and Diffraction

IM.1.P015
Quantitative HR-TEM studies on BaNaNbO Crystal with aberration corrected focus series reconstruction

D. Sudfeld[1], E. Yücelen[2], B. Freitag[1]

[1]FEI Electron Optics B. V., BU Materials Science, Eindhoven, Netherlands
[2]FEI Company, SS EU Nanoport TEM, Eindhoven, Netherlands

daniela.sudfeld@fei.com
Keywords: atomic imaging, exit wave reconstruction, focus series

Today, HRTEM imaging provides vital information about the atomic structure of crystals, interfaces, grain boundaries and nanoparticles to improve their properties in material science. Delocalization effects caused by the spherical aberration (Cs) of the objective lens obscure the real crystal structure image or the shape of particles in non spherical aberration corrected HRTEM.
Focus series reconstruction (FSR) [1, 2] overcomes this problem by giving access to the complex exit wave and not only to the intensity distribution of the phase and amplitude of the object. With reconstructing the complex wave all aberrations, including the most dominant spherical aberration, can be compensated by this FSR method after the acquisition. Even using a Cs image corrector (hardware) does not make focus series reconstruction obsolete since residual aberrations have to be compensated still, if images of deep sub-Ångstrom resolution at high acceleration voltages or Ångstrom resolution at low acceleration voltages like 80 kV have to be interpreted in a quantitative manner. Moreover the focus series reconstruction is the only method to obtain the complex exit wave besides holography for quantitative HRTEM image information.

While applications with deep sub-Ångstrom resolution are required for a precise determination of atomic position for metrology, atomic low voltage imaging is required for carbon based materials like graphene, because the knock-on damage by the electron irradiation is reduced. The residual aberrations typically mask the imaging data results and are very difficult to be removed using empirical methods which require a good understanding, a skilled user and customized, manual correction in hardware and software.

In general the interpretation of the results is also highly influenced by the achievable ultimate performance in Cs-corrected HR-TEM imaging and dependent on the quality of the specimen, the defocus settings and other higher order residual aberrations introduced by the imaging system. To overcome the residual aberration problem and give easy access to the complex exit wave, FEI has an automatic solution: The TrueImage™ Atlas [3, 4] package with its ultra precise aberration measurement. That is pushing the limits to a better, more reproducible, objective and quantitative understanding of Cs-corrected HR-TEM experiments, especially a more accurate interpretation of atomic structures. The TrueImage Atlas supports distinguishing in the image contrast between the atomic information of the material and the optical contribution of the electron microscope and correction of imperfect optical alignments of the electron column, like coma or astigmatism, to ensure the highest quality resolution. Consequently, on the Cs image corrected Titan™ systems from FEI Company the acquisition is automated: Before the focus series acquisition the optical parameters of the imaging system are properly measured using a Zemlin tableau and the Atlas software algorithms, see Figure 1 b). The measured residual aberrations are automatically stored with the focus series and are applied to the exit wave after reconstruction. This enables a precise and reproducible way of minimizing imaging artifacts.

An example is given for a single crystal with complex unit cell which crystal structure cannot be revealed without TrueImage Atlas. The different reconstruction results are presented for the BaNaNbO crystal in Figure 1. In Figure 1 a) the BaNaNbO crystal structure was acquired by manual correcting the low-order aberrations with the Cs image corrector (hardware) alone and after the best possible corrector tuning the representative image is not uniquely interpretable due to the existing residual aberrations. Compared to the method of manual correcting the hardware (Figure 1a), the software automated aberration correction reduces the residual aberrations without needed interaction by the user so that the exit wave reconstruction phase image is improved with the optimized astigmatism and focus correction. The influence of the degree of higher order aberration correction is also obvious in the comparison of the two cases, images without (Figure 1 d) and with correction of the residual aberrations (Figure 1 e). The matching microstructure of simulations (Figure 1 c) is overlaid into the

final phase contrast image. In conclusion, the exit wave reconstruction with TrueImage Atlas enables both, visualizing light elements easy and determine the final location as in the case of the [001] BaNaNbO crystal atoms where the oxygen can be clearly identified.

1. W.M.J. Coene, A. Thust, M. Op de Beck, D. Van Dyck, Ultramicroscopy 64, 1996, 109-135; “Maximum-likelihood method for focus-variation image reconstruction in high resolution transmission electron microscopy”.
2. C. Kübel, A. Thust, “TrueImage: Introduction to Focal-Series Reconstruction” in Nato Science Series E, edited by T.E. Weirich, J.L. Labar, and X. Zou, page 373-391, Springer, Dordrecht, 2005.
3. Juri Barthel, “Ultra-precise measurement of optical aberrations for sub-Angström transmission electron microscopy“, PhD thesis, Jülich: Forschungszentrum, Zentralbibliothek, 2008.
4. FEI Company, Product Data sheet for TrueImage Atlas.

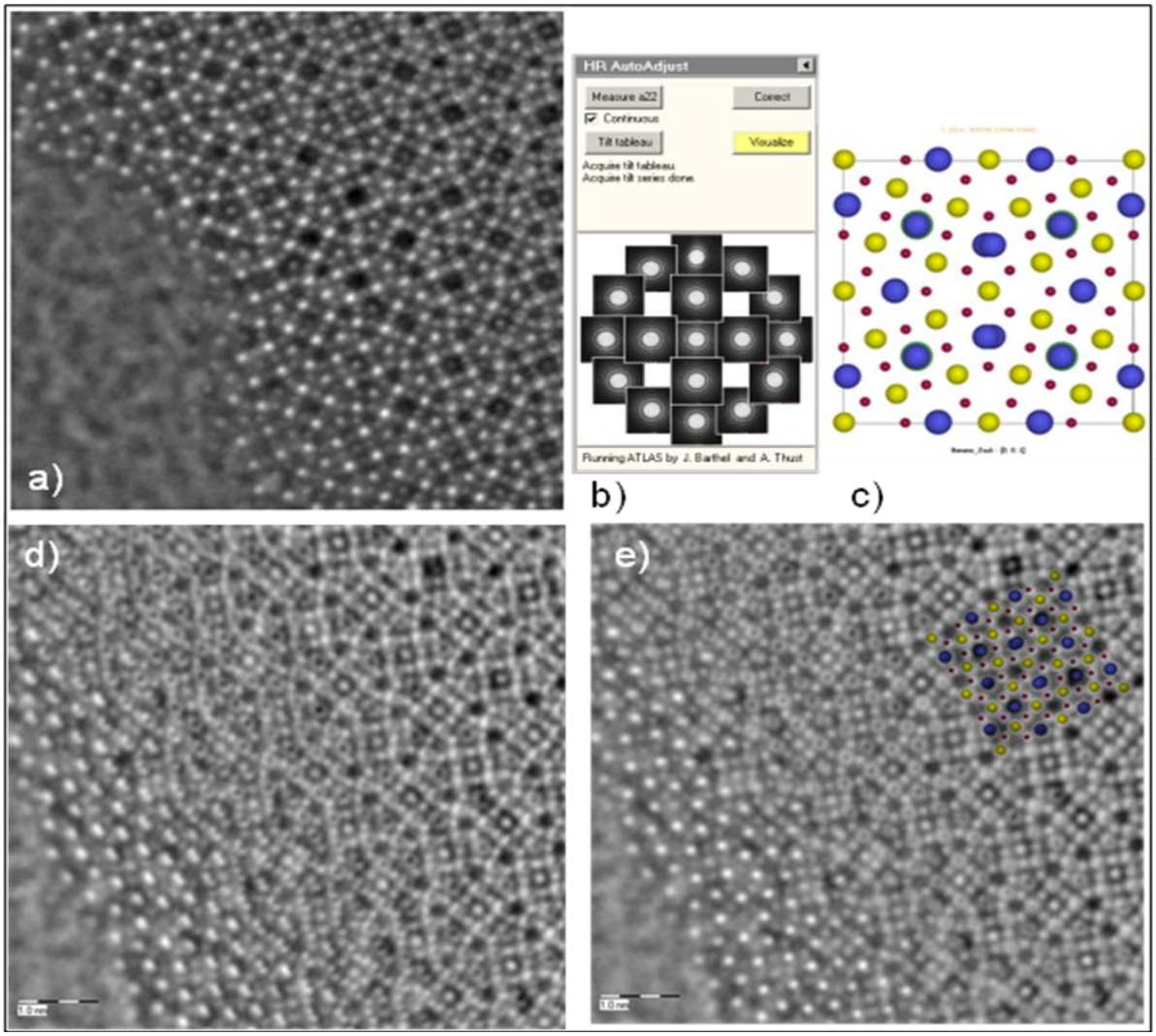

Figure 1. The measurements in Figure 1 of the [001] BaNaNbO crystal on quantifoil were performed at the TU Delft, Kavli Institute of NanoScience in Delft, the Netherlands on a Titan3™ 80-300 with image corrector (Figure 1 a) and on a Titan3™ G2 60-300 with a Cs image corrector and a Gatan US 1000 camera (sampling: 0.0017nm) in the FEI Nanoport, Eindhoven, the Netherlands (Figure 1 d), e)). a) The given BaNaNbO crystal structure was acquired by manual (low-order) aberration correction with Cs image corrector after the best possible corrector tuning and aberration correction. b) The residual aberration analysis is based on the measured Zemlin tableau data as shown in the new graphical user interface of the TrueImage Altas for the acquisition of the residual aberrations on Titan which enables to perform automated and calibrated focus series reconstruction. c) Unit cell of the BaNaNbO crystal structure with red dots: oxygen, yellow dots: niobium, blue dots: barium and green dots: natrium. The difference without (d) and with residual aberration correction (e) is shown on the BaNaNbO crystal structure in [001] projection. In the HR-TEM image (e) the improvement in quality and interpretability of the image is clearly visible; the matching unit cell is overlaid. The images are acquired at a magnification of Mh 460 kx and 1 second exposure time on a Cs image corrected Titan3™ G2 60-300.

Quantitative High-Resolution TEM/STEM and Diffraction

IM.1.P016
Influence of the delocalization of inner-shell excitations on atomic-resolution elemental maps

M.Y. Park[1], S. Majert[1], H. Kohl[1]

[1]Physikalisches Institut und Interdisziplinäres Centrum für Elektronenmikroskopie und Mikroanalyse (ICEM), Westfälische Wilhelms-Universität Münster, Münster, Germany

parkmi@uni-muenster.de
Keywords: STEM, EDX

Using energy dispersive x-ray spectroscopy (EDX) in a scanning transmission electron microscope (STEM) it is possible to obtain elemental maps with atomic resolution.

For a better interpretation of the experimental results it is necessary to compare them with simulations. The theory can show which factors influence the intensity distribution. In particular we investigate the influence of the delocalized excitation of inner-shell electrons on elemental maps using the multislice method [1].

The multislice method treats the behaviour of electrons passing through a thick specimen. For the simulation the specimen is divided into thin slices which are treated as a thin phase object. The transmission and the propagation of the electron wave function are calculated successively through and between the slices.

In a first approximation the intensity of characteristic x-ray quanta during an EDX experiment is proportional to the electron beam intensity at the respective specimen atoms. In this case the atoms can be approximated as being point-shaped. To improve this localized approximation we consider the atom excitation probabilities and replace the point-shaped description of atoms by a delocalized excitation function [2].

We want to compare the results of both approximations with each other and with experimental results to estimate the influence of the atoms' excitation probabilities on elemental maps.

For the simulation we assume a strontium titanate crystal ($SrTiO_3$). Figure 1 shows the structure of strontium titanate in different orientations. Figure 2 shows the simulation with the point approximation for the atom excitation probabilities of Sr-L and Ti-K signals in an elemental map of $SrTiO_3$ assuming an aberration corrected STEM using an acceleration voltage of 300kV, a spherical aberration coefficient of 0 mm, an aperture semiangle of 9.7 mrad, and a defocus of 0 Å. The size of the simulated image is 128x128 pixels [3].

These results are compared with experimental data. The major difference between both results is that the radius of the atomic columns is smaller in the simulation. This can be due to the point approximation for the atom excitation probabilities [3]. We want to investigate how the radius of atomic columns in the simulation changes considering a delocalized atom excitation function.

1. Earl J. Kirkland "Advanced Computing in Electron Microscopy", (Plenum Press, New York, 1998) p. 157
2. D. Von Hugo, H. Kohl, and H. Rose, Optik **79** (1988) 19
3. S. Majert "Simulation atomar aufgelöster Elementverteilungsbilder mit der Multislice Methode, (Bachelorarbeit, Westfälische Wilhelms-Universität Münster, 2012) p.22

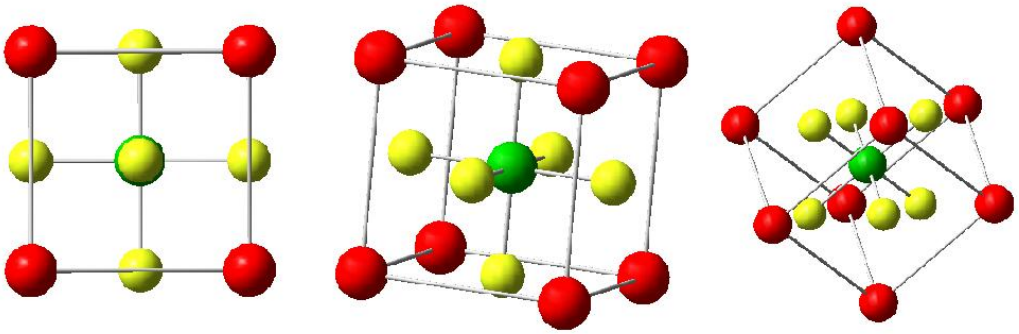

(a) (b) (c)

Figure 1. Structure of strontium titanate (red: strontium, green: titanium, yellow: oxygen); Simulations in the following figures conducted with a strontium titanate specimen in [001]-orientation (a).

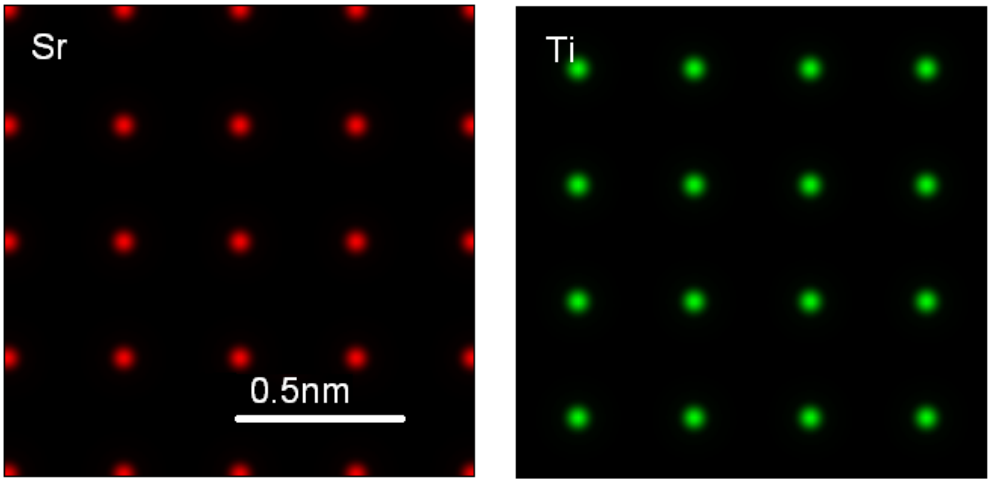

Figure 2. Simulation of Sr-L and Ti-K signals in elemental maps of $SrTiO_3$ assuming an aberration corrected STEM. The size of the simulated image is 128x128 pixels [3].

Quantitative High-Resolution TEM/STEM and Diffraction

IM.1.P017
HRTEM investigation of grain boundaries starting from orientation maps

A. K. Kiss[1], E. Rauch[2], S. Nicolopoulos[3], J. Lábár[1]

[1]MTA TTK FA, Thin Film Physics Department, Budapest, Hungary
[2]SIMAP laboratory, GPM2 team, Saint Martin d'Hères Cedex, France
[3]NanoMEGAS, Brussels, Belgium

labar.janos@ttk.mta.hu
Keywords: grain boundary, HRTEM, method, software

Many properties of polycrystalline materials are influenced by the geometry of the interfaces between the grains (e.g. mechanical or electrical properties, corrosion, segregation, etc.). This is why it is important to be able to characterize the geometry of grain boundaries (GB) by using both conventional TEM and high resolution TEM (HRTEM) effectively.

The optimum condition for HRTEM is that the sample must be oriented along a low index zone axis to visualize differently oriented crystallographic planes simultaneously, i.e. make use of the point resolution of the TEM. If the limited tilting range of the goniometer prevents us from orienting along a zone axis, we need to put up with the line resolution and a single set of planes are only imaged for a given grain. Investigation of GBs needs to fulfill similar conditions for both neighboring grains simultaneously.

In the case of grains with random orientation distribution in a polycrystalline material, the chance is low that there exist parallel pointing low index zones for two neighboring grains and it is even lower chance that we can reach them within the limited tilting range of the goniometer in a HRTEM (if they exist at all). There is larger chance that if we project one grain along a zone axis, its neighbor can only be imaged along a single plane only. The highest chance is that we can find an orientation where both grains can be imaged with lattice resolution (showing only one set of planes for either of them). However, it is very difficult to find and set any of such orientations manually. We have to be lucky to reach the proper orientation if we are not helped by a computer.

Development of a computer program is reported here that facilitates identifying and setting such orientation-pairs. Our software starts with recording an orientation map, using the commercial ASTAR software. Then our own software identifies the net of GBs found in the orientation map by assigning an average orientation to each grain and locating lines where this orientation changes above a threshold. The program highlights those parts of the GBs for which it is predicted that they can be investigated by HRTEM, because lattice resolution can be reached for both neighbors simultaneously within the tilting ranges of the given TEM. The program also gives advice, which tilt angles to set to reach that condition. Using this process increases the efficiency of the investigation of GBs. By scanning an area with several grains, we obtain information about the orientations of many boundaries in a short time. We have a good chance to find a few GBs among the many, which can be investigated by high resolution techniques under the given experimental conditions.

As an example, results are presented here on a polycrystalline TiN thin film. The investigations were carried out in a JEOL 3010 HRTEM with 1.7 Å point resolution. We used a GATAN double-tilt holder with the tilting ranges of ±20° and ±10° for the two orthogonal axes. An orientation map was recorded b the ASTAR precession system of NanoMegas, installed on the microscope.

The example on the TiN shows that using our method, it was easy to locate a low angle grain boundary in the orientation map, whose lattice imaging conditions were predicted within the possibilities of the TEM. The selected orientation is close to the <100> zone. After tilting the sample to the predicted orientation one set of {200} planes are seen in one of the grains, while the other set of {200} planes are seen in the other grain (due to the orientation difference between the two grains). Even though none of the grains were in perfect zone axis orientation, we were able to record an image from the row of dislocations that induced the orientation difference between the two neighboring grains (Figure 1.). The perfect dislocations in this fcc material have an <110> character, with the length of the Burgers-vector b=3 Á. The distance of the dislocations in the row (two of them are indicated by arrows in Fig. 1) is measured from the images to be 17 Á, resulting in 10° orientation difference, in agreement with the approximate value read from the orientation map. The orientation difference measured from the orientation map suggested that the orientations of the two grains differ by 12° (Fig.2). However,

simulated orientations are calculated at 1° steps for determining the orientation maps, so the accuracy of orientation is 1° for either grains. Consequently we can not anticipate prediction of the orientation difference between the two grains better than ±1-2° from the orientation map. Measurement form the HRTEM refined the value of the disorientation from 12° to 10°.

Additionally, the program can also give advice if pre-selected orientation of any selected grain is within reach. Obviously, the number of appropriate orientations increases with improving point resolution of the TEM and a wider pool of defects and boundaries offers themselves for examination if we can orient the sample into orientations from where they can be seen. Consequently, the program can be even more useful for new Cs-corrected TEMs, because it can predict how to set the sample if a special boundary is to be imaged. Very similarly settings for imaging special defects within a selected grain of a polycrystalline sample can also be predicted by the program. Altogether, atomic resolution imaging of defects and grain boundaries should benefit from the usage of that computer program.

This research has been supported by the project of TÁMOP-4.2.2/B-10/1-2010-0025.

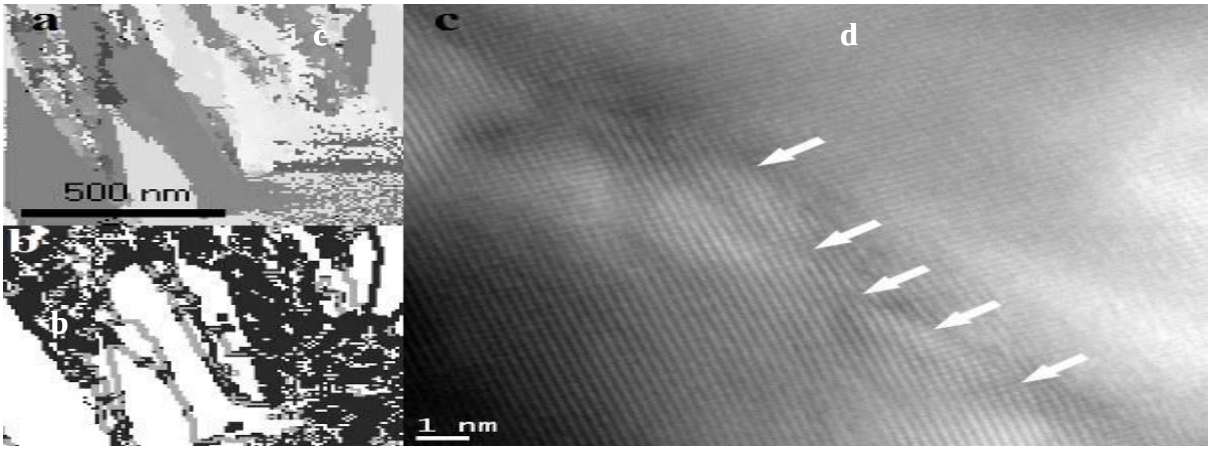

Figure 1. TiN sample: a) orientation map; b) part of GBs (red) to be investigated; c)high resolution image taken on the boundary denoted by arrow; (200) set of planes are shown in both neighboring grains; d) dislocations are present in the enlarged area at places denoted by arrows. The row of dislocations builds up the low angle boundary in the image.

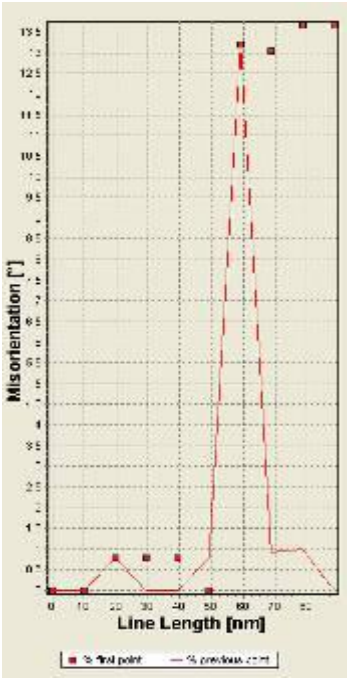

Figure 2. Orientation difference measured along a line crossing the selected grain boundary.

Quantitative High-Resolution TEM/STEM and Diffraction

IM.1.P018
Imaging with a STEM detector, experiments vs. simulation

F. Mika[1], P. Novotny[1], I. Konvalina[1]

[1]ISI ASCR, v.v.i., Electron Microscopy, Brno, Czech Republic

filip.mika@isibrno.cz
Keywords: STEM, image contrast, Monte Carlo simulations, transmitted electrons

Scanning transmission electron microscopy (STEM) is a combination of transmission electron microscopy and scanning electron microscopy (SEM). The electron microscope in STEM scans a focused beam of electrons across the sample in a raster pattern. Interactions between the beam electrons and the atoms on the sample generate transmitted electrons (TE) that are detected by a STEM detector below the sample [1]. The aim of this study is to find out the angular and energy distribution of the TEs that are very important for the understanding of image formation in STEM. The study was done by both an experiment and a simulation.

The experimental part was performed on the ultra-high resolution SEM, Magellan 400 [2], equipped by a multi-annular semiconductor STEM detector. The schematic drawing of the detector is in Figure 1a. The detector is divided into six concentric annuli and imaged in bright field (BF), four dark field (DF1-4) and high angle annular dark field (HAADF) modes. The last HAADF annulus is subdivided into six angular segments, but for our case we used it as one segment.

During the experimental study we imaged light and heavy element foils of 100nm thickness. The foils were made from carbon, silicon, chromium, tungsten and gold. The primary energy range was between 15 keV - 30 keV and we collected the image from each of six annuli and measured the average brightness of a defined image area to determine the signal intensity. The example of images of the chromium foil is in Figure 2. The images were taken under the same settings of the brightness, the contrast, the scan speed, the primary energy and the primary current.

The comparative simulations based on a Monte Carlo (MC) simulations are commonly used for theoretical studies of angular and energy distributions. In this work the Casino [3] and the SEM [4] (based on Geant4 [5]) software were used for carrying out the simulation of electron propagation through thin foils. In both of them, elastic collisions, that are responsible for an angular distribution, are calculated using tabulated Mott cross-sections. Implementations of inelastic collisions which are responsible for electron energy losses, are different in these programs, and lead to different energy distributions of TEs. Figure 1b shows the results of MC simulations of signal intensity for chromium. It was simulated for each annulus of the detector. One can see the same trend of experimental and simulated curves but the measured signal intensity is significantly lower than that of the simulations. This difference is because the MC simulations did not include the influence of the electromagnetic fields.

In order to study the image contrast it is necessary to simulate a realistic arrangement of the specimen chamber including the magnetic field of the objective lens and the electrostatic field between the specimen stage and the STEM detector. Trajectories of TEs with the angular and energy distributions given by the MC simulations were traced in SIMION [6] and EOD [7] that allow simulating trajectories of electrons in electromagnetic fields. An example of a TE tracing is shown in Figure 3.

1. Pennycook S.J., Nellist P.D. in ”Scanning Transmission Electron Microscopy – Imaging and Analysis”, Springer (2011).
2. http://www.fei.com/
3. Demers H. et al, Scanning 33 (2011), p. 135.
4. Kieft E., Bosch E., Journal of Physics D: Applied Physics 41(2008), p. 1.
5. Agostinelli S. et al., Nucl. Instr. and Meth. A 506 (2003), p. 250
6. Dahl D. A., Int. J. Mass Spectrom. 200 (2000), p. 3.
7. Zlámal J., Lencová B., Nucl. Instr. and Meth. A. 645 (2011), p. 278.
8. The work is supported by the Technology Agency of the Czech Republic under grant no. TE01020118 and by European Commission and Ministry of Education, Youth, and Sports of the Czech Republic (project No. CZ.1.05/2.1.00/01.0017).

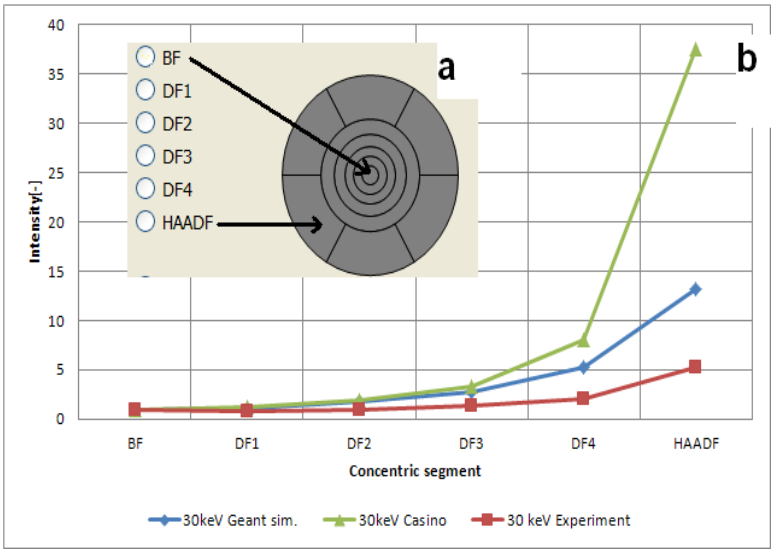

Figure 1a. Schematic drawing of six concentric annuli of the STEM detector.
Figure 1b. Experimental and simulated data of TE signal intensities plotted for each segment of the STEM detector shown in Figure 1a. The experimental chromium data was measured from part of the Figure 2 data.

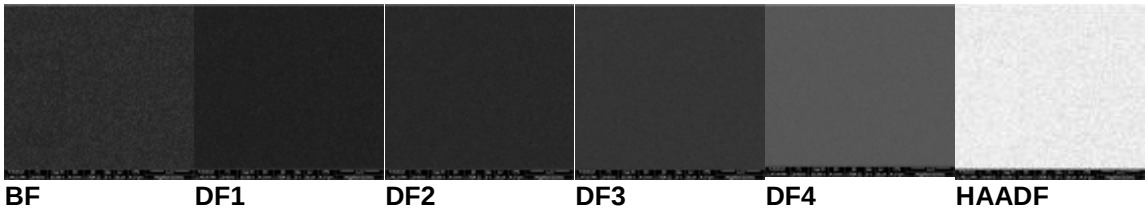

Figure 2. Comparison of grey levels from different annular detector parts taken on a chromium thin foil at 30 keV.

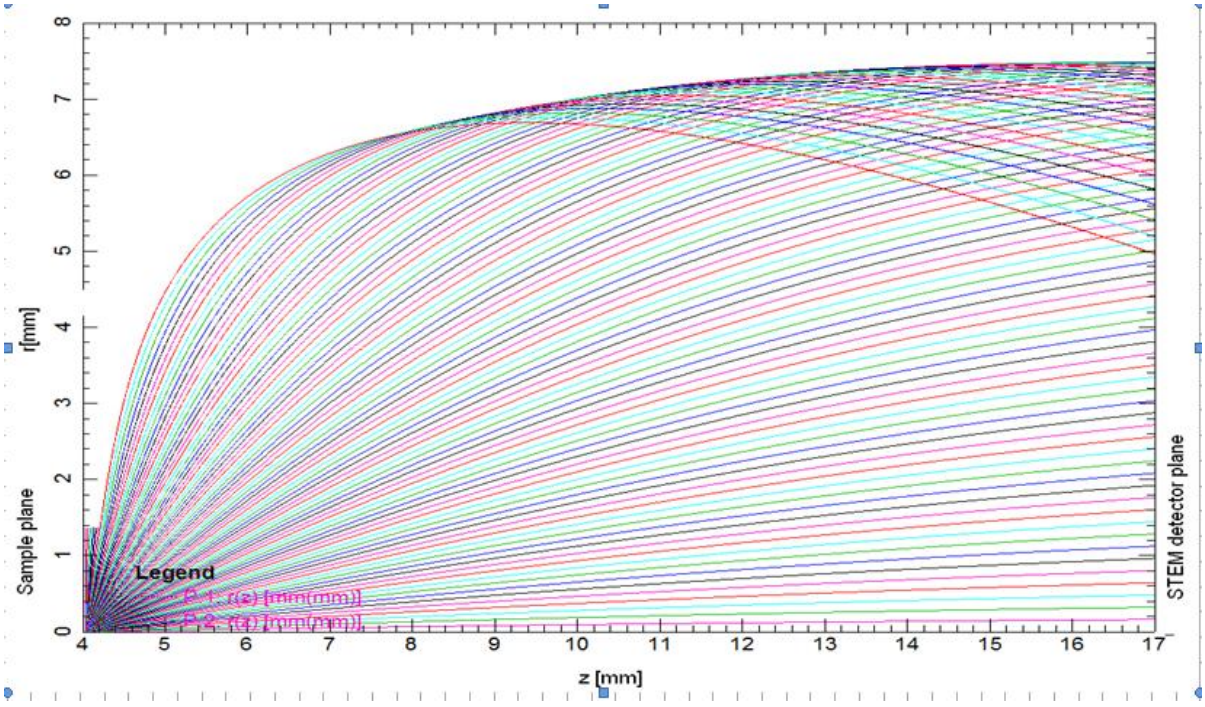

Figure 3. Simulated trajectories of TE between the sample plane (z = 4 mm) and the STEM detector plane (z = 17 mm) of a real experimental arrangement. The TE energy was 30 keV and the range of the polar angle was 0° – 90 ° with 1° step.

Quantitative High-Resolution TEM/STEM and Diffraction

IM.1.P019
Towards an experimental realization of inverse dynamical electron scattering

W. Van den Broek[1], C.T. Koch[1]

[1]Ulm University, Institute of Experimental Physics, Ulm, Germany

wouter.vandenbroek@uni-ulm.de
Keywords: inverse dynamical electron scattering, artificial neural network, atomic resolution tomography

In [1] it is shown that dynamical scattering of fast electrons can be inverted by recasting the multislice algorithm as an artificial neural network [2], enabling the iterative retrieval of the three-dimensional object potential. This allows a non-heuristic treatment of the modulation transfer function of the CCD, partial spatial and temporal coherence and inelastic scattering through an absorptive potential. Furthermore, prior knowledge about the atomic potential shape and the sparseness and positivity of the object can be used. The method is dubbed IDES, inverse dynamical electron scattering.

The backpropagation algorithm [2] calculates the derivative of the error function *E*—the sum of square differences between model and measurements—with respect to the object potential very efficiently in just one extra pass through the network. These derivatives are then used in a type of steepest descent optimization that finds the object in typically ~1000 iterations.

In Ref. [1], IDES was demonstrated on simulated high resolution transmission electron microscope images. The potential of a cuboctahedral Au nanoparticle with 309 atoms arranged in an fcc lattice was reconstructed from 25 noisy images required at a double tilt of −10°, −5°, 0°, 5° and 10° around the two axes. The reconstruction of the potential was faithful; all atoms were reconstructed on the correct positions.

However, in practice the microscope parameters are only known approximately. It is therefore necessary to estimate them simultaneously with the object. In Ref. [3], for example, it is shown that ptychographic reconstructions improve dramatically if the shape and position of the illuminating probe is estimated along with the exit wave. By invoking the chain rule for complex analysis, the error can be derived with respect to the focus value and this derivative can be plugged in the steepest descent optimization. To give priority to the object reconstruction during the first iterations, the derivative is multiplied with $1 - 2^{-n/128}$, with n the iteration number.

In this abstract, a simulation with the same test object as in [1] is performed; see Figure 1. and Table 1. In Figure 2. it is shown that if the initial guess for the focus value of each image is off by a random amount between -5 nm and 5 nm all atom positions can be retrieved if the foci are estimated along with the object. In the other case, a non-physical solution was found. After optimization, the average difference with the real focus values is 0.27 nm (see Figure 3.) and although this value is larger than the slice thickness, no vertical translation of the object is observed.

This work, see [4] as well, paves the way towards an experimental realization of IDES. Apart from focus, also the other microscope parameters, like tilt or residual astigmatism, could be optimized along with the object, as long as sufficiently good starting values are known. [5]

1. W. Van den Broek and C.T. Koch, Phys. Rev. Lett. 109 (2012), p. 245502.
2. R. Rojas in “Neural Networks—A Systematic Introduction”, (Springer-Verlag, Berlin, New-York) (1996).
3. A. Maiden, M. Humphry, M. Sarahan, B. Kraus and J. Rodenburg, Ultramicroscopy 120 (2012), p. 64.
4. W. Van den Broek and C.T. Koch, Phys. Rev. B. submitted, Feb. 2013.
5. The authors acknowledge the Carl Zeiss Foundation as well as the German Research Foundation (DFG, Grant No. KO 2911/7-1)

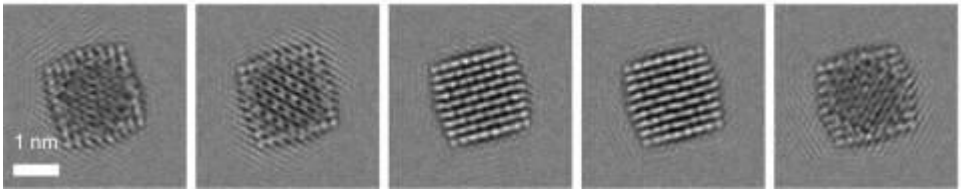

Figure1. Five typical images. From left to right, the tilt is −10°, −5°, 0°, +5° and +10°.

U	C_1	C_3	α	Δf	Δ_{xy}	Δ_z	a	c	d
40 kV	-10 nm	14 µm	0.1 mrad	1 nm	0.025 nm	0.21 nm	0.58	2.7 pix	3.9 pix

Table 1. The simulation parameters. U is the acceleration voltage, C_1 the focus value, C_3 the spherical aberration, α the illumination semi-angle, Δf the focal spread, Δ_{xy} the size of the horizontal dimensions of the voxels, Δ_z the slice thickness, and a, c and d characterize the modulation transfer function [1].

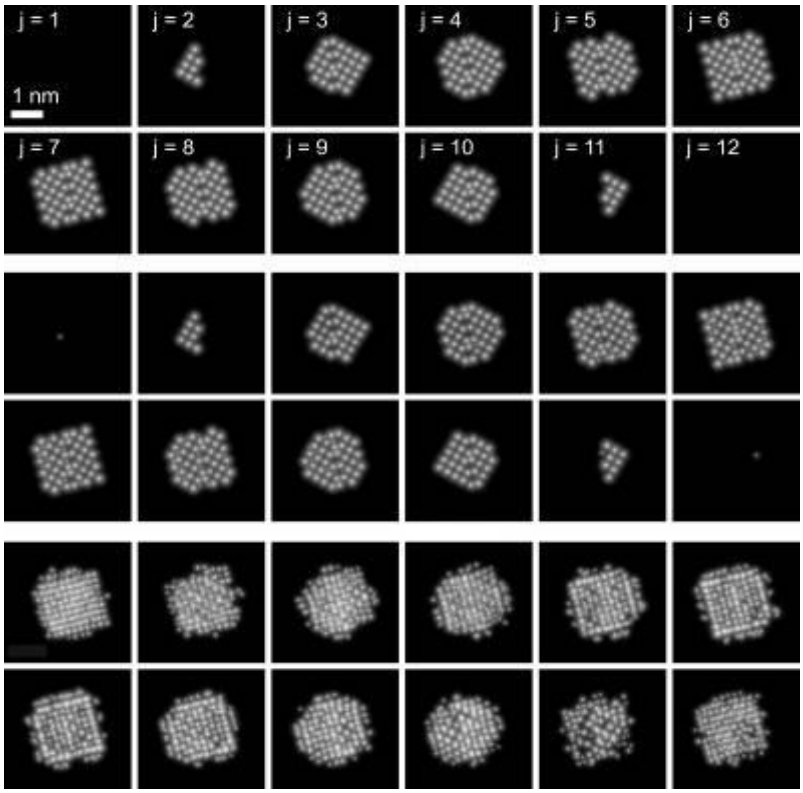

Figure 2. *Upper two rows*: The sliced potential of the test object, on a logarithmic gray scale. *Middle two rows*: Reconstruction with simultaneous defocus estimation. *Lower two rows*: Without defocus estimation.

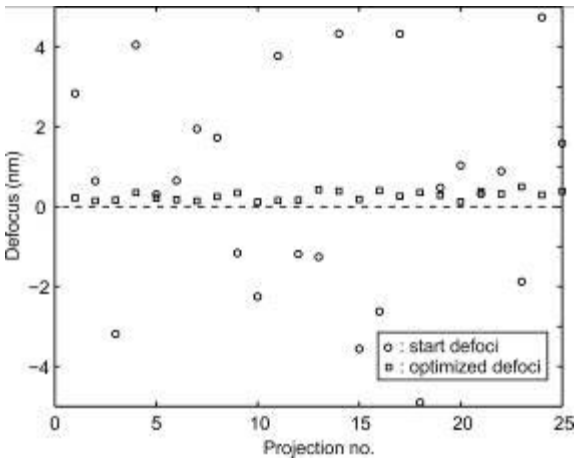

Figure 3. Defoci at the start (*cirlces*) and at the end (*squares*) of the reconstruction.

Quantitative High-Resolution TEM/STEM and Diffraction

IM.1.P020
Sample thickness determination by low-energy scanning transmission electron microscopy

T. Volkenandt[1], E. Müller[1], M. Pfaff[1], D. Gerthsen[1]

[1]Karlsruher Institut für Technologie, Laboratorium für Elektronenmikroskopie, Karlsruhe, Germany

tobias.volkenandt@kit.edu
Keywords: STEM, low electron energy, thickness determination

In this work we present a method to determine the local sample thickness which is an important parameter for any quantitative electron microscopy work. This is accomplished by measuring the image intensity using scanning transmission electron microscopy (STEM) at electron energies below 30 keV.

For low-energy STEM a scanning electron microscope is used in transmission mode [1]. A ring-like segmented semiconductor detector located underneath the thin sample detects transmitted electrons scattered into a hollow cone with a defined angular range. The high-angle annular dark-field (HAADF) segment collects electrons scattered into angles between 190 mrad and 680 mrad. Electrons scattered into these high angles show strong material contrast, which is pronounced due to the use of primary electron energies below 30 keV. Another advantage of the low electron energy is that knock-on damage is negligible, facilitating the investigation of beam-sensitive samples.

The presented method for sample thickness quantification relies on the comparison of measured image intensities with simulated intensities. Measured HAADF intensities are referred to the intensity of the incident beam, which is determined by imaging the corresponding detector ring without any sample. The amplification settings (brightness, contrast) are adjusted for using the complete high dynamic range of the 16 bit detection system. These settings remain unchanged when imaging the sample to keep comparable conditions. The intensity offset (black level) and the intensity of the incident beam (white level) are used for normalization of measured image intensities.

For given microscope parameters (primary energy, collection angle, beam current) the normalized measured HAADF intensity depends only on the sample thickness and composition. If the composition is known the sample thickness can be determined by comparison with calculated intensity values.

Calculated HAADF STEM intensities are derived by Monte Carlo simulations which is an established method for quantitative description of low-energy electron scattering [2]. It is reasonably fast and flexible regarding the sample geometry and the use of different scattering cross-sections. For the presented results the simulation package NISTMonte [3] was used, operating with analytical screened Rutherford and tabulated Mott scattering cross-sections for elastic scattering. The energy loss is described by the continuous slowing down approximation in the modified version by Joy and Luo [4]. The resulting scattering angle histogram of simulated electrons is integrated over the angular range which corresponds to the HAADF segment. Additional corrections have to be applied to account for physical processes within the detector [2]. The corrected integrated intensity is normalized with respect to the incident intensity of the simulation.

The normalized measured intensity is directly compared with the normalized simulated intensity and allows the quantification of the local sample thickness if the sample composition is known.

For verification, this method was applied to different samples of known thickness. To assure a broad usability of the presented method the samples were chosen to cover a wide range of atomic number which comprise light materials like polymer films ($Z<6$), materials with intermediate atomic number (e.g. GaN with $Z=19$) and heavy materials (tungsten with $Z=74$). It was found that light elements require simulations based on screened Rutherford cross-sections while heavier elements are better described by simulations based on Mott cross-sections.

Figure 1a shows a HAADF STEM image of a fluorenyl hexa-peri-hexabenzocoronene (FHBC) film taken at 15 keV. The thickness of the film was previously measured with a Dektak profilometer. Due to the folding of the film several intensity measurements at different well determined sample thicknesses were possible as marked in Figure 1a. The measured intensities of this and thicker films are shown in Figure 1b (solid squares) in dependence of the nominal thickness. Empty symbols denote results from intensity measurements at positions with multiple film thickness due to folding. The dashed line illustrates simulated intensities based on screened Rutherford cross-sections which show best

agreement with the measured intensities. Only one film (solid and empty circles) shows a deviation which can be explained by the uncertainty of the Dektak profilometer thickness measurement.

In Figure 2a a wedge-shaped sample of tungsten prepared by focused ion-beam milling is shown. The HAADF STEM image was recorded at 25 keV. The thickness increases continuously from right to left. The image intensity was measured along the marked line. Using the known geometry of the sample the thickness of each point of the linescan can be determined. Figure 2b shows a comparison of the measured intensity in dependence of the local sample thickness with simulations. The geometric sample parameters (wedge angle, thickness offset at the wedge edge) resulting from the fit with the Mott simulated intensities (solid line) could be confirmed by top-view imaging with secondary electrons.

1. T. Klein in „Advances in Imaging and Electron Physics“, ed. P. Hawkes, (Elsevier) (2012), p. 297.
2. T. Volkenandt et al., Microscopy and Microanalysis 16 (2010), p. 604.
3. N. Ritchie, Surface and Interface Analysis 37 (2005), p. 1006.
4. D. Joy and S. Luo, Scanning 11 (1989), p. 176.

5. This project is funded by the German Research Foundation (Deutsche Forschungsgesellschaft).

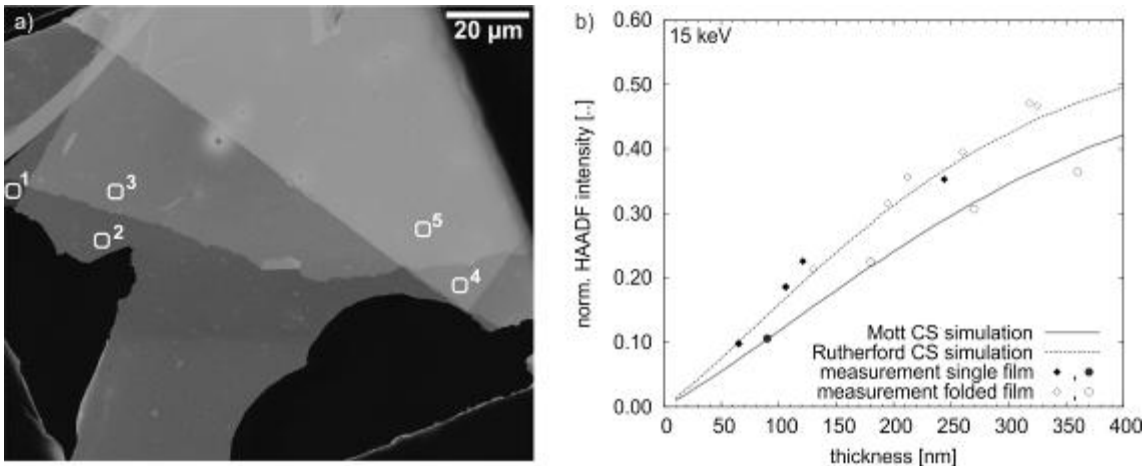

Figure 1. a) HAADF STEM image of a FHBC film taken at 15 keV with marked positions of intensity measurements**. b)** Comparison of measured intensities (solid symbols for films with different thicknesses, empty symbols for folded films as shown in **a)**) with Monte Carlo simulations using screened Rutherford (gray dashed line) and Mott cross-sections (gray solid line).

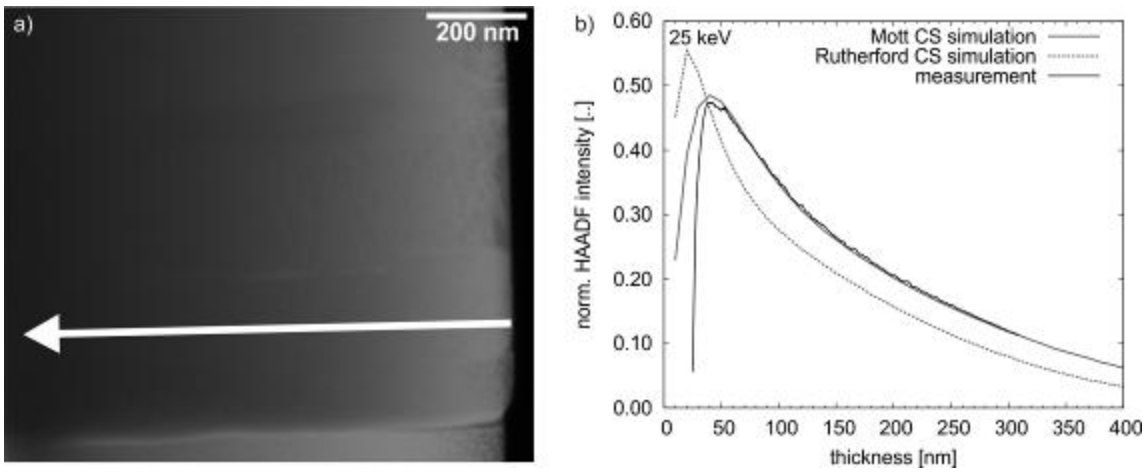

Figure 2. a) HAADF STEM image of a tungsten wedge sample taken at 25 keV with marked position of intensity linescan**. b)** Comparison of measured profile (black solid line) with Monte Carlo simulations using screened Rutherford (gray dashed line) and Mott cross-sections (gray solid line).

Quantitative High-Resolution TEM/STEM and Diffraction

IM.1.P022
Comparison of intensity and absolute contrast of simulated and experimental high-resolution transmission electron microscopy images for differerent multislice simulation methods

F.F. Krause[1], K. Müller[1], D. Zillmann[1], J. Jansen[2], M. Schowalter[1], A. Rosenauer[1]

[1]Universität Bremen, Institut für Festkörperphysik, Bremen, Germany
[2]Delft University of Technology, Delft, Netherlands

f.krause@ifp.uni-bremen.de
Keywords: Stobbs factor, HRTEM, MTF, Frozen lattice simulation, Incoherent Summation

In high resolution transmission electron microscopy (HRTEM) a disagreement of absolute contrast between experimental and simulated images has frequently been reported [1-5]. Intensity discrepancies result in a lower value of the dimensionless quantity of image contrast, defined as the standard deviation of image intensity divided by the mean intensity. Simulated contrast values deviated by a factor of more than 3 from experimental ones [1]. This discrepancy, known as the Stobbs factor problem has prevented the evaluation of absolute HRTEM contrast by comparison with simulated data as has been successfully done with high angle annular dark field scanning transmission electron microscopy (HAADF-STEM) [6].

It has been shown that a crucial part of this mismatch is due to not properly considering the influence of the camera used for acquisition expressed by the modulation-transfer function (MTF) [7]. Furthermore, it has been proposed that additional overestimation of contrast in simulations could be attributed to both the usage of absorptive potentials for thermal diffuse scattering (TDS) resulting in a loss of diffuse intensity and to the treatment of spatial incoherence using the coherent envelope approach damping intensity scattered to high angles [8]. A frozen lattice (FL) approximation [9] combined with incoherent summation of intensities simulated for different incident angles that are Gaussian distributed with the semi-convergence angle accounting for spatial incoherence is a more adequate model [9].

The influence of each of these simulation methods on the contrast of HRTEM micrographs was examined by studies of simulated defocus series for different objective apertures. As can be seen in Figure 1 that shows the results for the simulation of 15 nm thick gold viewed along [100] zone axis, the proper use of the MTF yields the largest contrast reduction by a factor of 2.4. The consideration of TDS by the FL model instead of absorptive potentials only yields a small contrast decrease of maximal 1.1. Incoherent summation of different incident angles for the treatment of spatial incoherence contributes another reduction of about 1.2. For larger objective apertures, the use of the coherent envelope approach instead of the more accurate transmission cross coefficients (TCC) also causes overestimation of image contrast, as damping of high-angle scattered intensity has more impact here.

The mismatch of experimental micrographs and simulations, conducted with the FL method, incoherent summation and properly considered MTF, was investigated. For that purpose, the MTF was measured and used in the simulations. Defocus series of a gold foil oriented in [100] zone axis were acquired with a C_S-corrected microscope. Specimen thickness and orientation were determined by parallel beam electron diffraction refinements and the FL simulations were conducted for these parameters and the measured residual spherical aberration.

With a small objective aperture of 7 nm^{-1} radius, a very good agreement is achieved between simulation and experiment qualitatively for the images and quantitatively for the intensities measured in units of incident intensity. The image contrast also coincides, which is shown in Figure 2. The ratio of simulated and measured contrast is 0.98±0.07.

For larger objective apertures a contrast discrepancy of 1.2 is found and a good agreement of intensities is observed. Without any aperture the difference of contrast amounts to a factor of 1.4; this is still smaller than previously reported values of more than 3.

The contrast mismatch between HRTEM simulations and experiments is definitely reduced by proper consideration of the camera MTF and FL simulations with incoherent summation but still remains observable especially with larger or no apertures applied in the imaging process.

1. M.J. Hÿtch, W.M. Stobbs, Quantitative comparison of high resolution TEM images with image simulations, Ultramicroscopy 53 (1994) 191
2. C.B. Boothroyd, Why don't high-resolution simulations and images match?, J. Microscop. 190 (1998) 99-108.
3. C.B. Boothroyd, Quanti_cation of high-resolution electron microscope images of amorphous carbon, Ultramicroscopy 83 (2000)591-68.16
4. A. Howie, Hunting the Stobbs factor, Ultramicroscopy 98 (2004) 73-79
5. K. Du, K.v. Hochmeister, F. Phillipp, Quantitative comparison of image contrast and pattern between experimental and simulated highresolution transmission electron micrographs, Ultramicroscopy 107 (2007) 281-292
6. J.M. LeBeau, S.D. Findlay, L.J. Allen, S. Stemmer, Quantitative atomic resolution scanning trasnmissiom electron microscopy, Phys.Rev. Lett. 110 (2008) 206101-1 -206101-4
7. A. Thust, High resolution transmission elctron mircoscopy on an absolute contrast scale, Phys. Rev. Lett. 102 (2009) 22080-1-22080-4
8. D. Van Dyck, Persistent misconceptions about incoherence in electron microscopy, Ultramicroscopy 111 (2011) 894-900
9. B.D. Forbes, A.J. Alfonso, S.D. Findlay, D. Van Dyck, J.M. LeBeau, S Stemmer, L.J. Allen, Themal diffuse scattering in transmission electron microscopy, Ultramicroscopy 111 (2011) 1670-1680

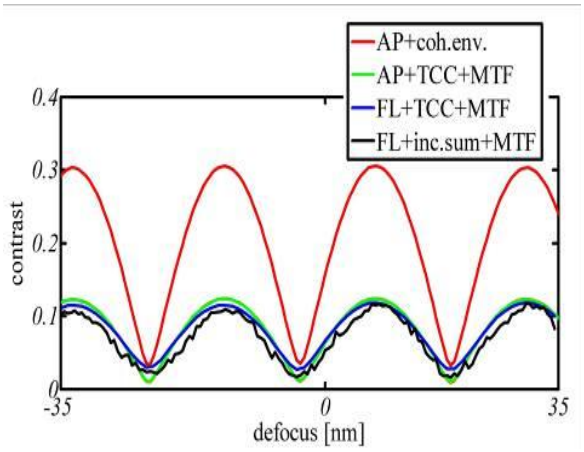

Figure 1: Contrast of images of a defocus series simulated for 15 nm gold in [100] direction with different techniques with an objective aperture of radius 7 nm^{-1}: The red curve is the result of conventional MS calculations and incoherence treated by the coherent envelope approach, the application of the MTF yields the green curve that. For the blue was simulated with incoherent summation.

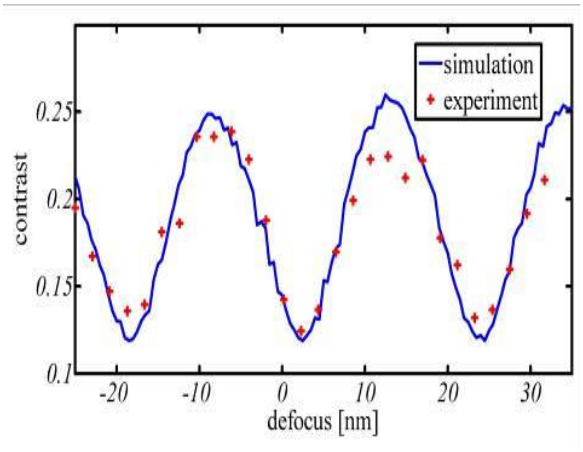

Figure 2: Comparison of experimental and simulated contrast of a defocus series of [100] oriented gold of 12 nm thickness and an objective aperture of 7 nm^{-1} radius. Both the values and the periodicity agree wellof absorptive potentials. For the black curve additionally FL simulations were used instead onein addition to that incoherence was also calculated with TCC instead

Quantitative High-Resolution TEM/STEM and Diffraction

IM.1.P023
Parameter optimization of the Bloch wave method in the frozen lattice approximation

T. Yamazaki[1], T. Soeda[1], Y. Kotaka[1]

[1]Fujitsu Laboratories Ltd., Devices & Materials Laboratories, Atsugi, Japan

There has been some recent progress in the quantitative analysis in scanning transmission electron microscopy imaging owing to the work of LeBeau et al. [1]. They suggested that the good agreement between experimental and calculated images was a consequence of including the effects of thermal diffuse scattering (TDS) in the multislice method and the frozen phonon (FP) approximation. On the other hand, the Bloch wave method has produced many valuable results from dynamical calculations of transmission electron microscopy techniques. However, the Bloch wave method based on the FP or frozen lattice (FL) approximation is considered to be difficult even with current computational resources and algorithms since it repeatedly executes eigenvalue operations for many different atomic configurations. In this study we present an extended Bloch wave method to calculate the effects of TDS in the FL approximation. We optimize the accuracy of the approximations of the extended method by performing a multi-objective optimization over several simulation parameters.

Figure 1 shows brief outlines of the conventional and extended methods for calculating the FL approximation, with the schematic diagram for the FL approximation on the left. In this model, the computational results are obtained by averaging diffraction patterns simulated by different FL configurations. If this approximation is executed by the conventional method, it is necessary to numerically repeat the eigenvalue operation at each slice for each of the different atomic displacements caused by thermal vibrations (see the centre of Fig. 1). To overcome this difficulty, we extended the conventional method by combining it with the classical scattering matrix method. By separating the crystal potential into two parts, one associated with the thermal equilibrium positions and the other with the deviations from thermal equilibrium, the wave functions in each slab are described by the equations given to the right side of Fig. 1. In this formula, the superscript 'e' denotes eigenvalues and eigenvectors obtained from the potential for the thermal equilibrium. The residual crystal potential ($\mathbf{\Delta A}^{(j)}$) is expressed as a matrix exponential. Hence, because eigenvalues and eigenvectors are independent of the atomic vibration in the FL approximation, only one eigenvalue operation is required per incident partial wave. The convergent beam electron diffraction (CBED) patterns simulated by each method are displayed in Fig. 1. The two methods are in good agreement.

The extended method is implemented to decrease the computing time. However, because new approximations are added, the number of simulation parameters increases. The main simulation parameters used in the extended method are the order of the Taylor expansion of the matrix exponential, the number of atomic and separate FL configurations, and the number of slices dividing each unit cell. Since these parameters affect the results in a complicated way, it is difficult to find an optimized combination of these parameters. For this reason, we use multi-objective optimization. The brief flowchart of the optimization is shown in Fig. 2. The object functions of the optimization were chosen as the indices estimated through comparing the results simulated by conventional and extended methods. We estimated the residual of the absolute intensity comparison as well as the residual of the comparison of the scaled intensity obtained by changing a gamma curve. In addition, to guide the optimization to minimize the computing time, we choose to search first those simulation parameters that quickly reject bad parameters. The 24 conditions for the input parameters were carefully arranged in the input variable space as an initial generation, which was then evolved to 20 generations by the Multi-Objective Generic Algorithm (MOGA).

The optimized results are shown in Figs. 3(a) and 3(b). These results show that although 'the number of slices in a unit cell' and 'the order of the Taylor expansion' both need to set to be >1, it is not necessary to increase them indefinitely. Furthermore, the optimized simulation parameters were led by a multivariate analysis. The detailed CBED pattern simulated by the optimized simulation parameters is shown in Fig. 3(c). It is clear that the dynamical simulation based on the Bloch wave method can be extended to simulate the effect of TDS by the FL approximation. We also see that the optimized calculation does not waste computing time and that accuracy is guaranteed.

1. L.M. LeBeau, S.D. Findlay, L.J. Allen and S. Stemmer, Phys. Rev. Lett. 100 (2008) 206101.

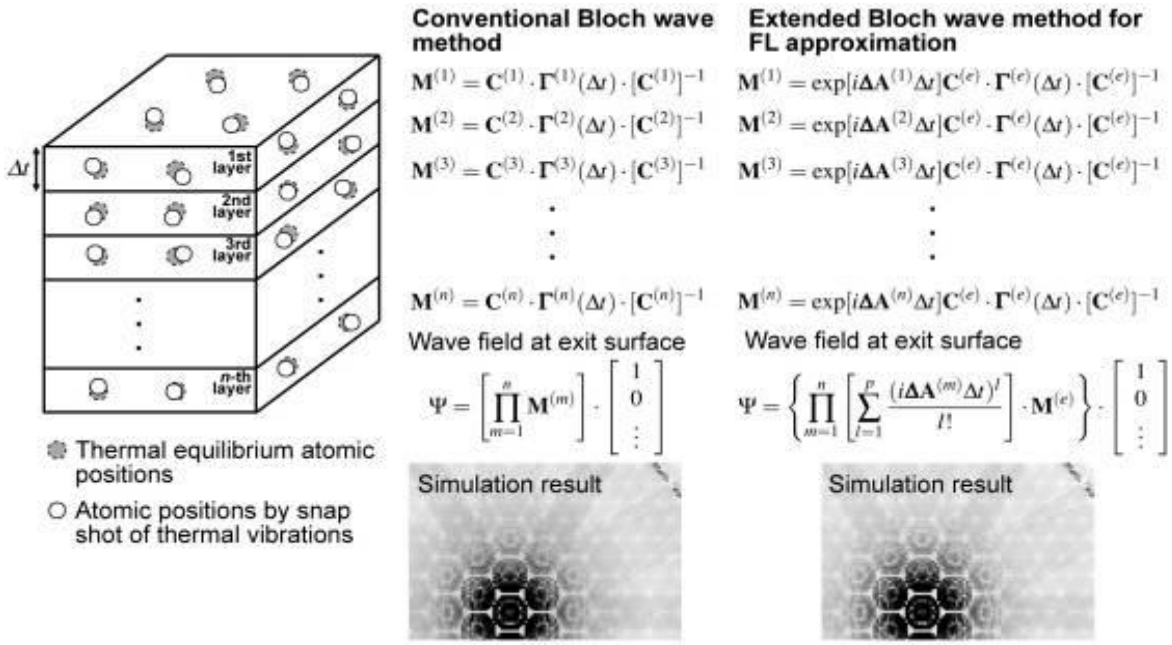

Figure 1. Schematic diagram of the dynamical simulation method for the FL approximation. Although a conventional Bloch wave method is performed by solving eigenvalue operation at each slice, the extended Bloch wave method requires that the eigenvalue operation is executed only once for each partial incident wave using the atomic positions of the thermal equilibrium configuration. Simulated CBED patterns are Si(111) of 150 nm thick. Accelerating voltage is 200 kV.

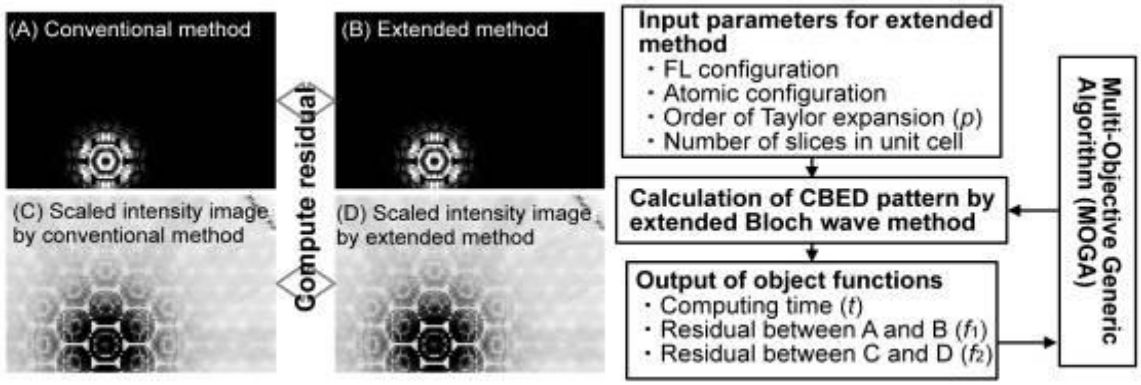

Figure 2. Schematic diagram of the parameter optimization. The optimum input parameters which lead all object functions to the minimum values were searched by MOGA.

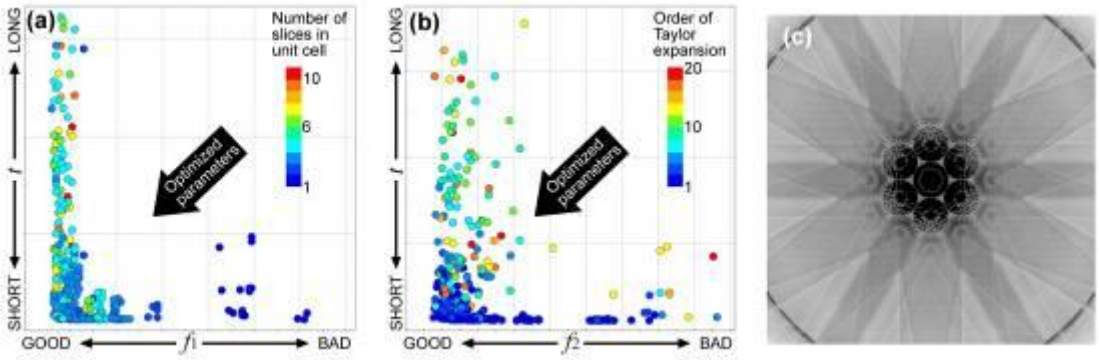

Figure 3. Results of the parameter optimization. (a) displays the relationship between f_1 and t, and (b) displays the relationship between f_2 and t. The colors of each figure denote 'the number of slices in a unit cell' and 'the order of the Taylor expansion.' The CBED pattern simulated by the searched optimized condition and considering many forbidden reflections is displayed in (c).

Quantitative High-Resolution TEM/STEM and Diffraction

IM.1.P024
Determination of In and N concentration in (InGa)(NAs) quantum wells using HAADF STEM and investigation of annealing effects

T. Grieb[1], K. Müller[1], E. Cadel[2], R. Fritz[3], E. Talbot[2], M. Schowalter[1], K. Volz[3], A. Rosenauer[1]

[1]University of Bremen, Institute of Solid State Physics, Bremen, Germany
[2]University of Rouen, Groupe de Physique des Matériaux, Saint Etienne du Rouvray, France
[3]Philipps University of Marburg, Materials Science Center and Faculty of Physics, Marburg, Germany

grieb@ifp.uni-bremen.de

The zincblende crystal $In_xGa_{1-x}N_yAs_{1-y}$ is of technological interest as both, In and N lower the semiconductor's band gap, allowing to emit or to absorb in the infra-red, so that InGaNAs can either be used for laser diodes in telecommunication at wavelengths of 1.3 and 1.55 □m - here glas fibres show optimum transmission - or as part of multi-junction solar cells. It is known that thermal annealing of InGaNAs in order to achieve an increase of the emission intensity typically also causes an unwanted blue shift of the emitted wavelength. In this contribution we present a method to simultaneously determine both, the In and the N concentration, from high-angle annular dark field (HAADF) micrographs recorded in high-resolution (HR) scanning transmission electron microscopy (STEM). For this, two sources of information are extracted on atomic scale: on the one hand the distances of atomic columns are measured which allows for a strain state analysis, on the other hand the characteristic HAADF intensity is evaluated by a comparison to simulated intensities. HAADF-intensity evaluation was already shown for (e.g.) InGaN [1] and GaNAs [2]

For the simulations a frozen-lattice multislice approach is used in the STEMsim software [3]. Besides thermal diffuse scattering (TDS), Huang-scattering at static atomic displacements (SADs) is taken into account [4]. SADs are distortions of the atomic lattice due different covalent radii of In and Ga as well as As and N. We compute these static displacements by relaxing the supercells with the LAMMPS [5] package using Keating's valence force field model [6]. Figure 1. shows the ratio of the simulated HAADF intensity of InGaNAs and GaAs as a function of specimen thickness for different compositions (see Figure 1.). The high concentration dependent contrast allows for an accurate determination of the chemical composition. An MOVPE grown InGaNAs/GaAs quantum well sample (*as-grown*) is characterized in [100] zone axis by the suggested method. Figure 2.(a) shows the concentration maps for In and for N, Figure 2(b) the concentration profile from averaging along [010]-direction (red: In, green: N). The mean concentration is determined to be 32 % of In and 2 % of N. These values are in good agreement with the results from high-resolution X-ray diffraction measurements (HRXRD). Atom-probe tomography (APT) was applied to the sample. The corresponding In profile is also shown in Figure 2(b). Both, profile shape and mean concentration, is in good agreement with the results from the HAADF image.

The evaluations (HAADF-STEM analysis, HRXRD and APT) were also applied to a sample of the same growth series which was annealed under As-stabilized conditions. We found that the composition profiles did not change, but photoluminescence showed a blue shift of approximately 60 meV. This blue shift can be explained by a local redistribution of N atoms from Ga-rich to In-rich sites [7, 8].

1. A. Rosenauer, T. Mehrtens, K. Müller, K. Gries, M. Schowalter, P. V. Satyam, S. Bley, C. Tessarek, D. Hommel, K. Sebald, M. Seyfried, J. Gutowski, A. Avramescu, K. Engl, S. Lutgen, Ultramicroscopy 111 (2011) 1316.
2. T. Grieb, K. Müller, R. Fritz, M. Schowalter, N. Neugebohrn, N. Knaub, K. Volz and A. Rosenauer, Ultramicroscopy 117 (2012), 15.
3. A. Rosenauer and M. Schowalter, Springer Proceedings in Physics 120 (2007), 169.
4. V. Grillo, E. Carlino and F. Glas, Phys. Rev. B 77 (2008), 054103.
5. S. Plimpton, J. Comput. Phys. 117 (1995), 1.
6. P. N. Keating, Phys. Rev. 145 (1966), 637.
7. P. J. Klar, H. Grüning, J. Koch, S. Schäfer, K. Volz, W. Stolz, W. Heimbrodt, A. M. K. Saadi, A. Lindsay, E. P. O'Reilly, Phys. Rev. B 64 (2001) 121203.
8. S. Kurtz, J. Webb, L. Gedvilas, D. Friedmann, J. Geisz, J. Olson, R. King, D. Joslin, N. Karam, Appl. Phys. Lett. 78 (2001) 748.
9. This work was supported by the German Research Foundation (DFG) under contract number SCHO 1196/3-1 and RO 2057/8-1-3008074.

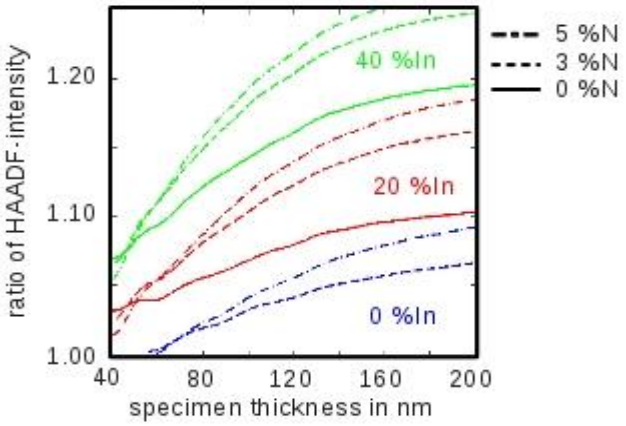

Figure 1. Ratio of the simulated HAADF intensity for InGaNAs and GaAs (contrast) as a function of specimen thickness. Each curve displays a different indium concentration (color) and nitrogen concentration (line style).

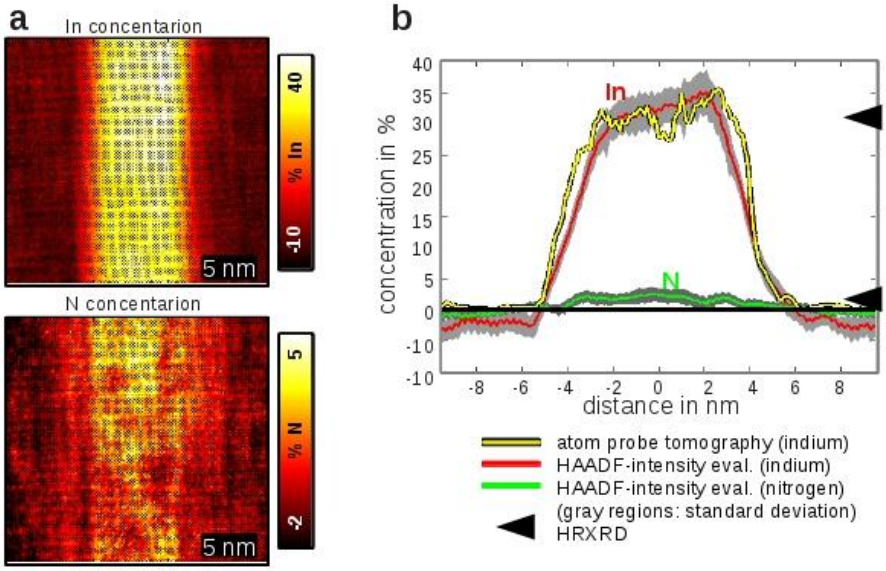

Figure 2. (a) Concentration maps from HAADF-intensity evaluation for indium and nitrogen. (b) Profiles from averaging the maps in (a) and from atom probe tomography. Concentrations derived from HRXRD are marked by arrows.

Quantitative High-Resolution TEM/STEM and Diffraction

IM.1.P025
A modified Bloch-wave approach for dynamical scattering to limited order for structurally complex specimens

R.S. Pennington[1], C.T. Koch[1]

[1]Ulm University, Institute for Experimental Physics, Ulm, Germany

robert.pennington@uni-ulm.de
Keywords: image simulation, Bloch-wave, dynamical scattering, silicon

Transmission electron micrographs are often complicated by dynamical diffraction, requiring image simulation using an algorithm like multislice or Bloch-wave. In the Bloch wave formulation, simulating all scattering orders in a single scattering matrix requires performing a matrix exponential, which can be computationally intensive, especially for structurally complex specimens – those with large unit cells and many allowed beam directions (e.g. proteins) [1]. In this work, we explore an approximation to the Bloch-wave algorithm designed to account for dynamical scattering to limited order in each scattering matrix. The matrix exponential is approximated to include only kinematical and first-order dynamical scattering [2], neglecting higher-order scattering. Higher-order scattering is included for thick specimens by computing one approximate matrix exponential for a thin sub-slice, and then propagating the wave function by repeated multiplication of this transfer matrix with the wave function. Figure 1 shows this, and compares it to a single-matrix limited-order approach. In addition, if the full specimen is thin enough (or consists of mostly light atoms, such as organic crystals) then only one column of the matrix is necessary, providing a useful simplification for image simulation of structurally complex specimens. The incident beam can also be tilted as exactly as in the Bloch wave formalism, and both bright- and dark-field images can be calculated. The approximation compares favorably to exact calculations [3] under some conditions. Using silicon as a benchmark, the exit-wave amplitudes and phases are very close to those generated from full (all-order) Bloch-wave calculations using matrix exponentials with zero absorption (Figure 2). When basic electron absorption is included, the approximated exit-wave phases compare favorably to the full calculation, but the approximated exit-wave amplitudes have systematic discrepancies stemming from beam attenuation. In summary, we explored a modified Bloch wave algorithm designed to calculate dynamical scattering to limited order i.e. only kinematical and first-order dynamical scattering, which requires sectioning thick specimens into stacks of thin slices. The resulting approximate exit wave amplitudes and phases were shown to be in good agreement with a full all-order Bloch-wave calculation, except for electron beam attenuation.

1. D.B. Williams and C.B. Carter. “Transmission Electron Microscopy” (Springer, New York) (2009), Ch. 14.
2. C.T. Koch and J.C.H. Spence. J. Phys. A: Math. Gen. 36 (2003) p. 803-816.
3. P. Stadelmann. Ultramicroscopy 21 (1987) p. 131-145.
4. The authors acknowledge the Carl Zeiss Foundation as well as the German Research Foundation (DFG, Grant No. KO 2911/7-1)

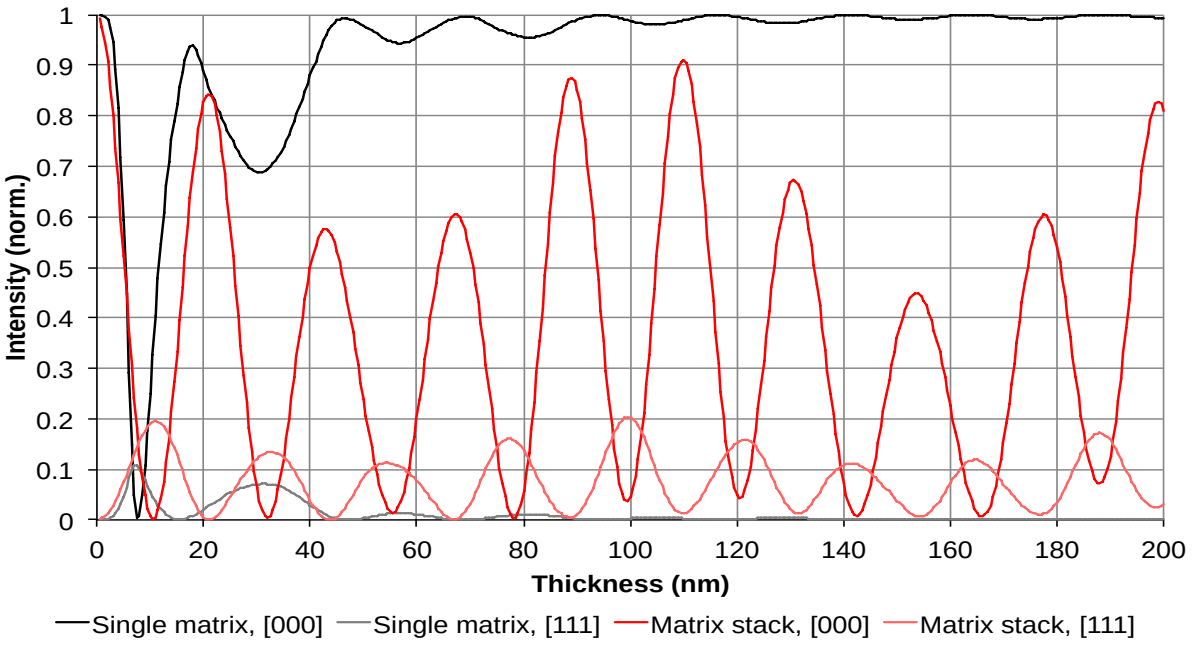

Figure 1. Beam intensity for [000] and [111] beam for the limited-order approximation [2] with a single matrix (black/grey) and a stack of 1Å matrices (red/pink) for a Si [110] zone axis at 80keV primary energy. The single-matrix data models only kinematical and first-order dynamical scattering (and hence is unphysical at higher thicknesses). However, the matrix-stack approach models higher-order dynamical scattering by sub-slicing the specimen every 1Å and sequentially multiplying the beam with the resulting limited-order 1Å matrices to propagate the electron beam slice-by-slice.

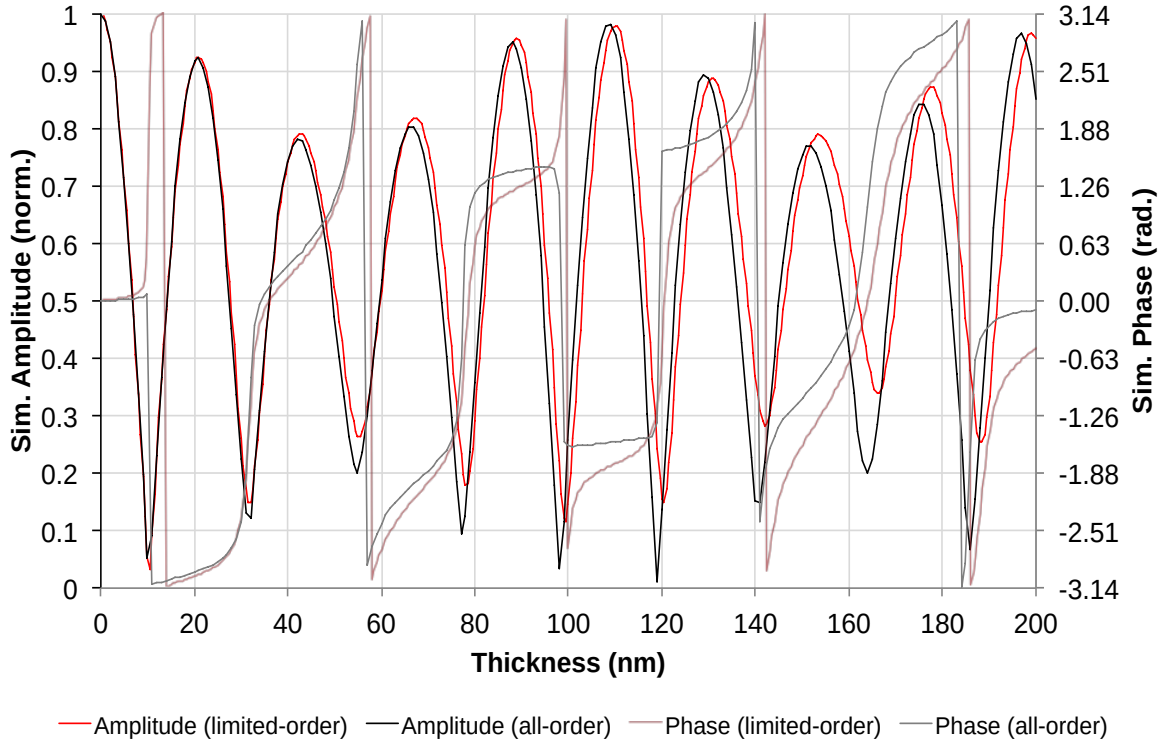

Figure 2. Bloch-wave amplitude (dark) and phase (light) for limited-order approximation (red) and JEMS all-order [3] (black) for a Si [110] zone axis at 80keV primary energy. The limited-order approximation is sliced every 1Å to include the effects of higher-order scattering.

Quantitative High-Resolution TEM/STEM and Diffraction

IM.1.P026
Quantitative HAADF-studies of GaP/Si-heterostructures

A. Beyer[1], K. Werner[1], B. Haas[1], K.I. Gries[1], K. Volz[1]

[1]Philipps Universität, Material sciences centre and faculty of physics, Marburg, Germany

andreas.beyer@physik.uni-marburg.de

The growth of III/V-material on silicon (Si) opens the possibility of new devices like high efficient solar cells, high mobility channel layers [1] or a laser on Si substrate [2]. Nevertheless, the growth of the polar III/V-material on the non polar Si holds several challenges, as anti-phase domains (APDs) may occur at monoatomic steps on the substrate. Moreover, the structure of the interface is not trivial because it is not necessarily charge neutral. We investigate galliumphosphide (GaP) grown on Si as a model system for the heteroepitaxy of polar material on nonpolar substrate because GaP is nearly lattice matched to Si.

GaP-layers were grown via metal organic vapour phase epitaxy on Si substrates with a small intentional offcut of 0.1 ° into one of the <110> directions in an Aixtron 200 GFR reactor. Special growth conditions were applied which result in optimum layer quality and minimum amount of residual APDs [3] as well as modified conditions to intentionally change the interface configuration. Electron transparent foils were prepared using conventional mechanical thinning followed by final argon ion-milling. For the investigation of the GaP/Si-interface high angle annular dark field (HAADF)-measurements were carried out in a JEOL JEM2200 FS, operating at 200 kV. It is equipped with a corrector for spherical aberration of the condensor lens system providing probe sizes below one Angstroem. For the quantification of the chemical composition at the GaP/Si-interface HAADF-intensities were simulated using a FFT-multislice [4] algorithm in an absorptive potential approximation [5]. Additionally, electron energy loss spectroscopy (EELS) was used to determine local thickness of the TEM foil.

Thickness dependent simulations and low resolution HAADF-measurements of wedge shaped samples show that the intensity ratio of Si and GaP is a function of TEM specimen thickness and microscope parameters as convergence angle and detection angle. Therefore, for known microscope parameters the thickness of an investigated sample region can be determined by this ratio.

Figure 1 depicts a representative HAADF-image of the GaP/Si-interface. The comparison to simulated intensities leads to a thickness of 30 nm. This value is in good agreement with the thickness derived from EELS measurements. Moreover, also the absolute HAADF-intensity of GaP and Si, which can be gained by normalizing the measured intensity with the intensity of the impinging beam [6] fits very well to this value. Further simulations at fixed thicknesses allow the investigation of the influence of chemical composition on the HAADF-intensity. With this knowledge it is possible to map the amount of Si on each atomic column. The map derived from the HAADF-image in Figure 1 is shown in Figure 2. It is observable, that the interface is not atomically smooth but an intermixing of 7 monolayers. The same intermixing behavior can be found for a wide range of different samples, irrespective of the Si-orientation and GaP-polarity. In contrast to that, increasing the growth temperature significantly results in different interface configurations.

In this contribution we will show how high resolution HAADF-measurements in conjunction with adequate simulation can be used to determine the thickness of TEM-sample very accurate. At known thicknesses the intermixing behavior of GaP and Si can be quantified on an atomic scale and correlated to the applied growth conditions.

1. L. Desplanque, S. El Kazzi, C. Coinon, S. Ziegler, B. Kunert, A. Beyer, K. Volz, W. Stolz, Y. Wang, P. Ruterana, and X. Wallart, Applied Physics Letters, vol. 101, no. 14 (2012), p. 142111.
2. S. Liebich, M. Zimprich, A. Beyer, C. Lange, D. J. Franzbach, S. Chatterjee, N. Hossain, S. J. Sweeney, K. Volz, B. Kunert, and W. Stolz, Applied Physics Letters, vol. 99, no. 7(2011), p. 071109.
3. K. Volz, A. Beyer, W. Witte, J. Ohlmann, I. Németh, B. Kunert, and W. Stolz, Journal of Crystal Growth, vol. 315, no. 1 (2011), pp. 37–47.
4. K. Ishizuka, Ultramicroscopy, vol. 90, no. 2–3 (2002), pp. 71–83.
5. C. R. Hall and P. B. Hirsch, Proceedings of the Royal Society A: Mathematical, Physical and Engineering Sciences, vol. 286, no. 1405 (1965), pp. 158–177.
6. J. M. Lebeau and S. Stemmer, Ultramicroscopy, vol. 108, no. 12 (2008), pp. 1653–8.
7. This work is supported by the German Science Foundation (DFG) (project numbers VO805/4 and VO805/5).

Figure 1. Representative HAADF-image of the GaP/Si-interface (The width of the scalebar is 1 nm).

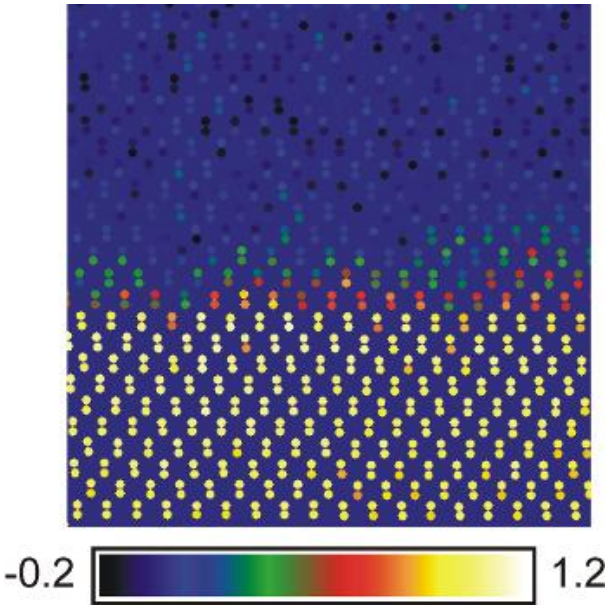

Figure 2. Atomically resolved Si-map, derived from the sample region depicted in Figure 1.

Quantitative High-Resolution TEM/STEM and Diffraction

IM.1.P027
Statistical parameter estimation theory as a tool for quantitative HAADF STEM

G.T. Martinez[1], A. De Backer[1], H. Shi[1], D. Schryvers[1], A. Rosenauer[2], J. Verbeeck[1], S. Van Aert[1]

[1]University of Antwerp, EMAT- Physics Department, Antwerp, Belgium
[2]Universitaet Bremen, Instituet fuer Festkoerperphysik, Bremen, Germany

gerardo.martinez@student.ua.ac.be

The use of statistical parameter estimation theory as a tool for quantitative high angle annular dark field scanning transmission electron microscopy (HAADF-STEM) has shown to be a reliable methodology to extract structural and chemical information of the material under study [1,2,3]. This approach allows one to quantify unknown structure parameters such as atom positions, number of atoms and atom types with high accuracy and precision. The methodology relies on optimizing parameters of an empirical incoherent imaging model using a criterion of goodness of fit that describes the correspondence between the images and the model [2]. Relative quantification of HAADF STEM images can be carried out without a priori knowledge of the structure [2,3]. Towards an absolute quantification, it is common practice to compare experimental data with detailed image simulations [4,5], which consider experimental settings, such as detector sensitivity [6], sample structure information and electron-sample interactions to be known as accurately as possible. In this work, the combination of statistical parameter estimation theory with image simulations to quantify experimental images will be discussed. This methodology can be used to count the number of atoms in the sample [1,3]. As an example, the number of atoms in a Au nanorod can be quantified with trustworthy single atom sensitivity [3]. Detailed frozen phonon simulations including accurate measurements of the experimental microscope settings indeed confirm the counting results. Figure 1 shows the mean intensity variation for an increasing number of atoms from an experiment and simulated images. The importance of knowing the microscope settings as accurately as possible and the use of the detector sensitivity for the image simulations will be discussed. For chemical composition analysis at the atomic level, statistical parameter estimation theory allows one to relatively distinguish between atom column types with a difference in mean atomic number of only 3 [2]. Figure 2 shows another example, where the chemical composition is quantified in a relative way [7]. For this material, the goal is to locate the doping atoms of Nb in the Ni-Ti lattice. It will be shown that by estimating atomic scattering cross sections of the non-doped Ni-Ti matrix, the Ni and Ti sites can be distinguished, whereas this is impossible for the Nb doped case. From this, it can be concluded that the Nb atoms have to be replaced at the Ti site, since the scattering cross section of an atomic column scales with the mean atomic number Z [8]. Towards an absolute quantification, the chemical composition of single atomic columns in a complex perovskite type structure of $Pb_{1.2}Sr_{0.8}Fe_2O_5$ has been determined. In this case, the composition of the mixed Sr/Pb atomic columns are quantified by combining statistical parameter estimation theory and frozen lattice simulations. The assumption of a linear superposition of the atomic column signals has been tested and verified. This allows one to quantify the atomic columns of interest by subtracting the signals of the atomic columns that are not of interest. Figure 3 shows the image process to be followed in order to obtain the chemical composition of the Sr/Pb columns. The validity up to which extent these assumptions hold will also be discussed.

1. S. Van Aert, K.J. Batenburg, M.D. Rossell, R. Erni, and G. Van Tendeloo, Nature 470 (2011), p.374.
2. S. Van Aert, J. Verbeeck, R. Erni, S. Bals, M. Luysberg, D. Van Dyck and G. Van Tendeloo, Ultramicroscopy 109 (2009) p.1236.
3. S. Van Aert, A. De Backer, G.T. Martinez, B. Goris, S. Bals and G. Van Tendeloo, Physical Review B 87, (2013), p.064107
4. J. M. LeBeau and S. Stemmer, Ultramicroscopy 108 (2008), p.1653.
5. A. Rosenauer, K. Gries, K. Mueller, A. Pretorious, M. Schowalter, A. Avramescu, K. Engl and S. Lutgen, Ultramicroscopy 109 (2009) p.1171.
6. T. Grieb, K. Mueller, R. Fritz, M. Schowalter, N. Neugebohrn, N. Knaub, K. Volz, and A. Rosenauer, Ultramicroscopy 117 (2012), p.15.
7. D. Schryvers, H. Shi, G.T. Martinez, S. Van Aert, J. Frenzel and J. Van Humbeeck, Materials Science Forum 738-739 (2013) p.65.
8. S.J. Pennycook and D.E. Jesson, Ultramicroscopy 37 (1991) p.14
9. The authors acknowledge financial support from the Research Foundation Flanders (FWO, Belgium) through project fundings (G.0393.11, G.0064.10 and G.0374.13).

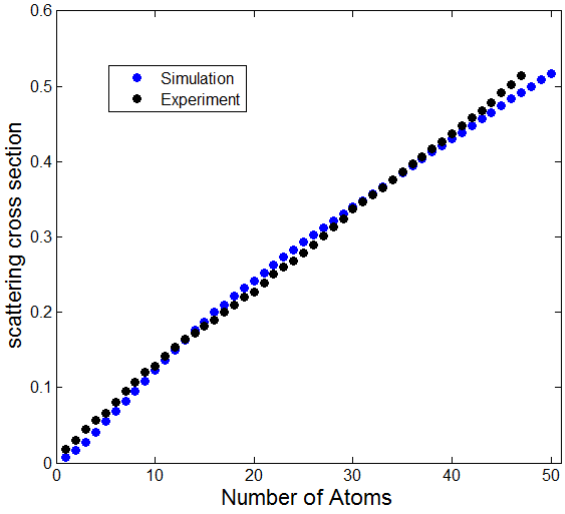

Figure 1. Mean intensity variation for increasing number of Au atoms from experimental and simulated images.

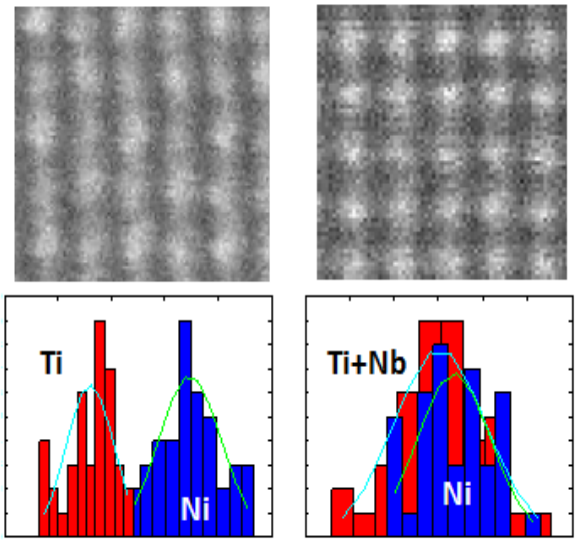

Figure 2. Scattering cross section distributions of Ni-Ti lattice without (left) and with (right) Nb.

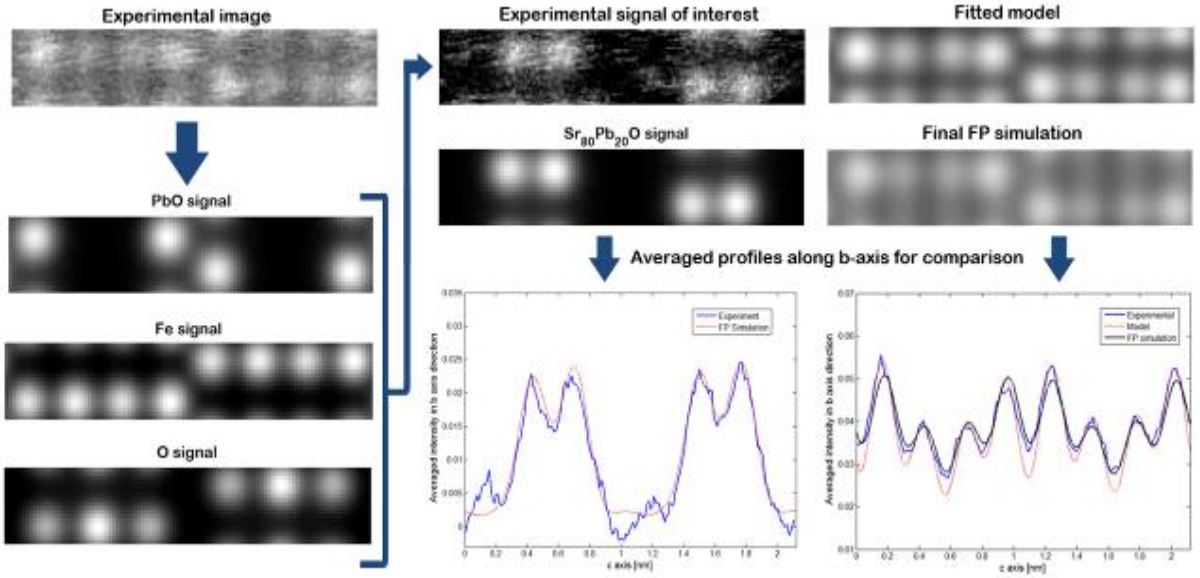

Figure 3. Image process to quantify the chemical composition. Experimental data must be normalized with respect to the incoming beam [4,5]. Firstly, the sample thickness is determined by comparing the scattering cross sections of a known composition atomic column (PbO signal in this example) from an experiment with those resulting from simulations. Secondly, the signals that are not of interest are subtracted to isolate only the signal of the atomic column with mixed composition (SrPbO). The experimental composition is computed by comparison with simulations. Finally, a full crystal simulation with the estimated composition is carried out for confirmation.

Quantitative High-Resolution TEM/STEM and Diffraction

IM.1.P028
Composition determination using HAADF-STEM in AlGaN/GaN heterostructures revisited

M. Schowalter[1], I. Stoffers[1], F. Krause[1], T. Mehrtens[1], K. Müller[1], M. Fandrich[1], T. Aschenbrenner[1]
D. Hommel[1], A. Rosenauer[1]

[1]Institut für Festkörperphysik, Bremen, Germany

schowalter@ifp.uni-bremen.de
Keywords: Composition determination by Z-contrast imaging, AlGaN, static atomic displacements

In recent years methods for quantification of composition from high-angle annular dark field (HAADF) images have been developed and applied to various semiconductor heterostructures by several groups (e.g. [1,2,3]). Usually the HAADF intensity averaged for each atom column is normalized with respect to a region, where the composition is known. The composition is then determined by comparing the measured intensity ratio with reference measurements or image simulations. Principally the normalization is done to minimize the thickness dependence of the evaluation. However, Rosenauer et al. [3,4] showed that the specimen thickness can be directly determined from the HAADF intensity by normalizing the HAADF intensity to the intensity of the incoming electron beam, that is determined by scanning the electron beam over the detector and taking into account the non-uniform sensitivity of the HAADF detector in the image simulations. For the simulations all kinds of disorder in the crystal need to be taken into account, as disorder strongly influences the HAADF intensity. In a pure and perfect crystal disorder is caused only by thermal vibration of the atoms giving rise to thermal diffuse scattering (TDS). In mixed crystals, where e.g. an atomic species is replaced statistically by another one, the different covalent radii cause static atomic displacements (SADs) around a substitutional atom [1]. Due to the similar covalent radii of Al (0.121(4) nm) and Ga (0.122(3) nm) [5] the lattice parameter of Al(group V) and Ga(group V) binary compounds are similar. Therefore, SADs have been neglected in the publication of Rosenauer et al. [3] on quantification of Al concentration in AlGaN. However, despite the similar covalent radii of Al and Ga the lattice parameter mismatch between AlN and GaN is 2.8%. In this contribution we study the effect of SADs on the composition quantification in AlGaN/GaN heterostructures. Typically SADs are taken into account by relaxing the atom positions of the simulation cell using empirical potentials such as the Stillinger-Weber potential [6]. We parametrized the Stillinger-Weber potential (SWP) to describe lattice parameters, elastic constants as well as the binding energies of AlN and GaN. We performed a test of the applicability of our parametrization to SADs: a series of supercells containing 64 atoms and different Al concentrations were set up and relaxed within density functional theory (DFT) approach as implemented in the VASP code [7]. The same supercells were afterwards relaxed using our parameterization and final positions were compared. Maximum SADs were observed to be in the order of 5-6 pm, whereas the maximum shifts between the final positions from DFT and from the SWP were approximately 1-2 pm, which is very close to the maximum reachable accuracy for the potential. The parametrization was then used for the relaxation of atom positions in the supercells for the image simulations. In this way a reference dataset of the average image intensity as a function of the specimen thickness and the Al concentration was obtained. A second dataset, where SADs have been neglected, still was available from the investigation in Ref. [3]. For the comparison a sample consisting of 6 layers with varying Al concentration was used. The Al concentration of each layer was evaluated as described in Ref. [3] using the two different datasets, respectively. In addition the Al concentrations within each layer were determined from strain state analysis (SSA) of the same images. Fig. 1 shows the measured concentrations as a function of the nominal concentrations as points and stars as a function of the nominal concentration determined from calibration samples using X-ray diffraction. The nominal Al concentration and its error region are displayed as the black line and the grey shaded region, respectively. For concentrations below about 50 % the comparison shows that the neglect of SADs in the image simulations is in agreement with the reference measurements. A discrepancy of the measured Al concentration and the nominal one was found for the datapoint at 58 % Al. For this datapoint a nominal concentration of larger than 58 % was given, because the concentration was determined by an extrapolation of the fluxes. However, taking into account the SADs for the image evaluation improves the accuracy of the measurement.

1. V. Grillo, E. Carlino and F. Glas, Phys. Rev. B 77 (2008), p. 054103.
2. S. I. Molina, D. L. Sales, P. L. Galindo, D. Fuster, Y. Gonzáles, B. Alén, L. Gonzáles, M. Varela and S. J. Pennycook, Ultramicroscopy 109 (2009), p. 172.
3. A. Rosenauer, T. Mehrtens, K. Müller, K. Gries, M. Schowalter, P.V. Satyam, S. Bley, C. Tessarek, D. Hommel, K. Sebald, M. Seyfried, J. Gutowski, A. Avramescu, K. Engl and S. Lutgen, Ultramicroscopy 111 (2011), p. 1316.
4. J. LeBeau and S. Stemmer, Ultramicroscopy 108 (2008), p. 1653
5. B. Cordero, V. Gomez, A. E. Platero-Prats, M. Reves, J. Echeverria, E. Cremades, F. Barragan and S. Alvarez, Dalton Transactions (2008), p. 2832.
6. F. H. Stillinger and T. A. Weber, Phys.Rev. B 31 (1985), p. 5262.
7. G. Kresse and J. Furthmüller, Phys. Rev B 54 (1996), p. 11169.
8. We kindly acknowledge financial support by the Deutsche Forschungsgemeinschaft (DFG) under contract number RO2057-8/1.

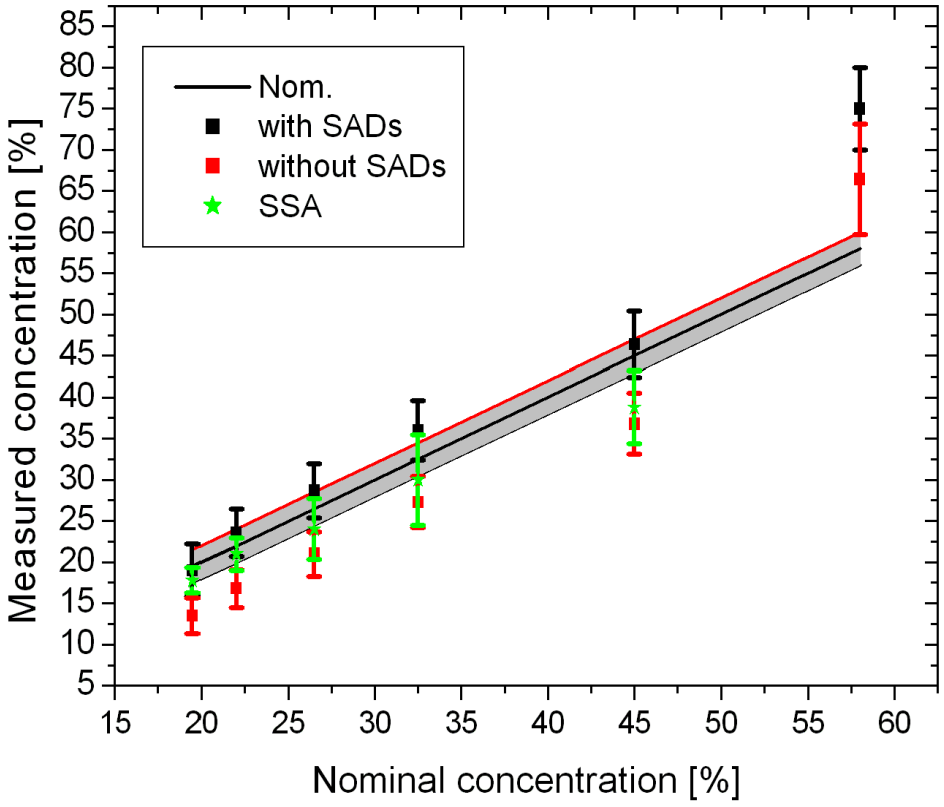

Figure 1. Al concentrations measured from HAADF-STEM image evaluation taking into account SADs (black squares) and neglecting SADs (red squares), nominal concentrations (black line) and concentrations measured from strain state analysis (green stars) as a function of nominal concentration as determined from X-ray diffraction of respective calibration samples.

Quantitative High-Resolution TEM/STEM and Diffraction

IM.1.P029
A new direct electron imaging camera for transmission electron microscopy based on an ultrafast pnCCD

H. Ryll[1], K. Müller[2], S. Ihle[1], H. Soltau[1], I. Ordavo[3], A. Liebel[1], R. Hartmann[1], A. Rosenauer[2], L. Strüder[1]

[1]PNSensor GmbH, München, Germany
[2]University of Bremen, Bremen, Germany
[3]PNDetector GmbH, München, Germany

henning.ryll@pnsensor.de

Since their introduction to transmission electron microscopy (TEM), digital imagers have greatly improved the workflow and enhanced experimental techniques, for example quick successive image acquisition at cryo-tomography. Still, most digital imagers are based on the principle of indirect detection of electrons, with a phosphorous layer where the electrons are converted into photons. These photons are then guided via optical fibers onto a CCD or CMOS imager. Certain disadvantageous effects result from this design, mainly non-perfect conversion efficiency, scattering of photons, reflections at optical interfaces and absorption losses. However, the indirect approach was justified by the low radiation hardness of the imagers to direct exposition with electrons, which would deteriorate the detector performance. The disadvantages of indirect detection can be removed with devices that are radiation hard to electrons in the energy range of 20-300 keV and can therefore directly detect electrons. The pnCCD is inherently radiation hard because of the avoidance of active MOS structures [1]. The structured front side is additionally protected by the 450µm thick bulk volume of the detector in conjunction with backside illumination. While other groups have reported on mostly CMOS based direct imagers [2,3], we present a new TEM camera based on a pnCCD [3], along with first results and simulations. The type of pnCCD used in this camera has a pixel size of 48x48 µm² with 264x264 pixels. Up to 1000 full frames per second can be read out continuously due to the multiparallel readout scheme of the pnCCD. This ultrafast imaging enables the observation of dynamic processes and temporal changes of samples. Aided by adjustable amplification levels, the sensitivity is such that each primary electron can easily be distinguished from noise providing single electron detection capability, independent of the energy of the primary electron between 20 and 300 keV. This is advantageous for low and ultra-low dose imaging of radiation sensitive samples. The individual detection of single primary electrons in a low dose experiment with 100-1000 incident electrons per frame enables further analysis and processing of these electron events.

Final images can be obtained in two ways. In the first way, called intensity mode, multiple frames and their intensities are simply summed up, resulting in an image which is similar to a conventional intensity image. In the second way, called event imaging mode, individual electron events are analysed and processed. The full characteristic properties of each detected primary electron are determined from each frame. The point of entry for each event can be reconstructed with a subpixel precision much finer than the device pixel size. An advanced center of gravity method is used here. The image is then formed by binning and counting each event in a grid with subpixel dimensions.

Evaluation of the imaging capabilities of the pnCCD TEM camera was done at a FEI Titan80/300 at electron energies of 80, 120, 200 and 300 keV. The slanted knife edge method was applied to measure the modulation transfer function (Figure 2.). The contrast increased with lowering the electron energies. In intensity mode, the contrast was 10% at 0.58 and 0.34 Nyquist at 200 and 300 keV respectively. The lower electron energies of 80 and 120 keV showed better contrast with 24% and 11% at full Nyquist in intensity mode. Applying the event processing and a 5x5 subpixel grid, the contrast increased to 72% and 39% for 80 and 120 keV respectively, which in the case of 80 keV is close to the theoretical maximum of 84% at full Nyquist frequency.

Additionally to the camera performance values, a first application [5] will be presented, where single Bragg discs of diffraction patterns are imaged on a millisecond timescale (Figure 3.).

1. R. Hartmann, A. Ziegler, et al., Microscopy and Microanalysis 13 (2007), p.436-437.
2. A.-C. Milazzo, G. Moldovan, et al., Ultramicroscopy 110 (2010), p. 741-744.
3. B. Krieger, D. Contarato, et al., IEEE (2011), p. 1946-1949.
4. L. Strüder, U. Briel, et al., Astronomy & Astrophysics 365 (2001), p.18-26.
5. K. Müller, H.Ryll et al., Appl. Phys. Lett. 101 (2012), p. 2121101-2121104.

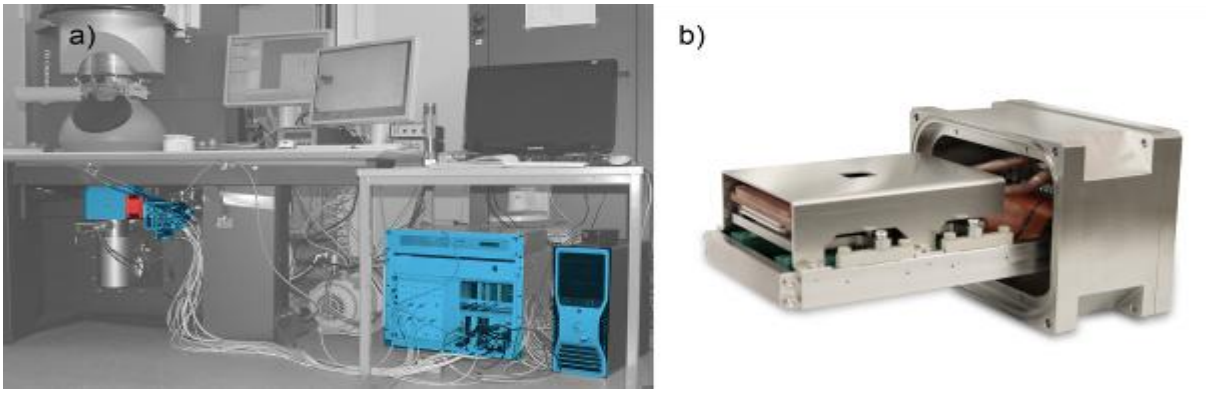

Figure 1. a) Setup of the pnCCD TEM camera at an FEI Titan80/300. The system is highlighted and consisted (from the right): PC, data acquisition and power supplies electronics and the camera mounted at an already installed Gatan Ultrascan camera housing. The compact camera head is highlighted in red and shown in **b)**.

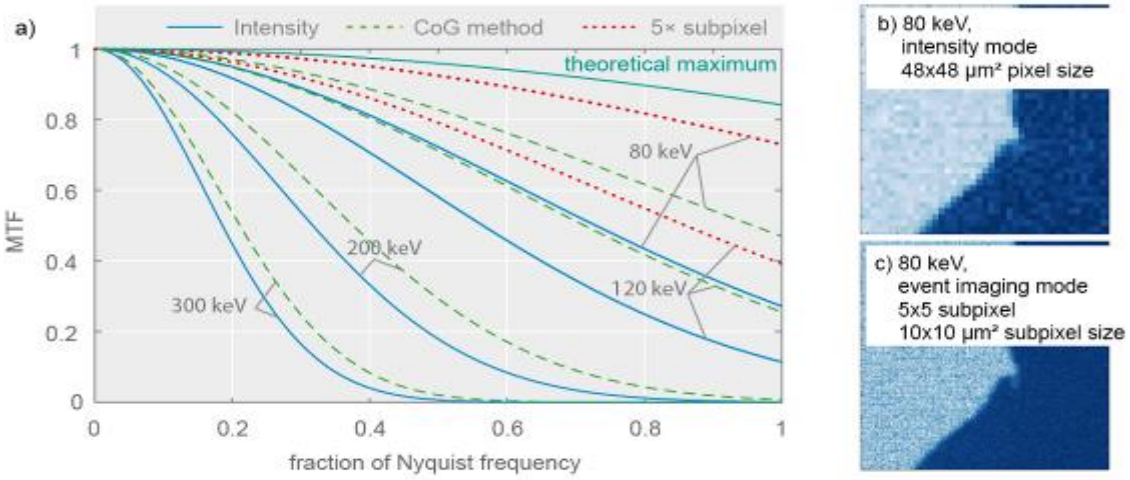

Figure 2. MTFs in **a)** measured with the pnCCD camera at a Titan 80/300 and analyzed with the slanted knife edge method for different imaging modes at primary electron energies of 80, 120, 200 and 300 keV. The solid blue lines correspond to images which were formed with integrated intensity images (Intensity). The dashed green lines correspond to images formed by processing primary electron events and applying the center of gravity method (CoG method) with no subpixel resolution. The dotted red lines for 80 and 120 keV correspond to the CoG method with a 5x5 subpixel resolution. The uppermost curve is the theoretical maximum given by sin(x)/x. An image at a primary electron energy of 80 keV is shown in **b)** formed in the intensity mode and in **c)** formed with event processing and 5x5 subpixels.

Figure 3. Single frame with 1 ms exposure time at a primary electron energy of 300 keV showing a Bragg disc of a diffraction pattern. The signal outside the disc is not noise but originates from primary electrons which are scattered at the sample, while the structure inside the disc is due to dynamical scattering.

Quantitative High-Resolution TEM/STEM and Diffraction

IM.1.P030
Stucture determination with novel ultra-fast automated TEM 3D precession electron diffraction tomography technique

M. Gemmi[1], A. Galanis[2], S. Nikolopoulos[2]

[1]Center for Nanotechnology Innovation@NEST, Instituto Italiano di Tecnologia, Pisa, Italy
[2]NanoMEGAS SPRL, Brussels, Belgium

mauro.gemmi@iit.it
Keywords: structure determination, Ultra-fast automated precession electron diffraction tomography

TEM based 3D precession electron diffraction (PED) tomography technique [1] is a very useful technique for structure determination of nanocrystals that cannot be crystallized big enough to be studied with X-Ray diffraction. Using this technique, a series of ED patterns are collected in a TEM every 1° while the sample is tilted around the goniometer axis but a drawback of the technique is that is time consuming mainly due to the time needed for crystal position tracking after every tilt and CCD slow speed data collection. An automated procedure of 3D diffraction tomography is reported for some TEM platforms, where crystal tracking is performed in STEM mode and the diffraction is collected in nanobeam mode [1, 2]. Although the latter automatic procedure reduces data collection time compared to the conventional PED data collection techniques, acquisition time remains between 1-2 hours and this can be harmful especially for beam sensitive materials (zeolite, hybrid mesoporous crystals, organic crystals, etc).

Herein, an ultra-fast automated precession assisted 3D electron diffraction tomography method is presented, where PED data can be collected about 10-20 times faster compared to hitherto 3D diffraction tomography procedure. We observed that by tilting the TEM holder using 3D tomography, the sample is moving along a definite direction for a specific (quite large) tilt range and consequently, that such crystal movement could be tracked by shifting the beam (instead of tracking the crystal) along the same direction. During the simultaneous beam movement and crystal tilt the patter could be recorded by the CCD bottom mounted camera. The procedure is made possible by the ASTAR control unit for TEM [3,4], which allows to scan a rectangular area with a certain scan step (from 1 to several 100 nm) and collect a PED pattern at each point. As a proof of concept we performed an entire PED 3D tomography experiment on a $MgMoO_4$ crystal by recording a total of 99 patterns on a Zeiss Libra 120 using a 16 bit CCD camera 2k x 2k bottom mounted, using 1° precession angle. Sequential PED collection (with angular resolution 0.9°) was performed during the time required for TEM goniometer to cover the 92° tilt angle (tilt range from -54 to +38° performed in a continuous way) and lasted only 5 min 20 sec. To track crystal movement during TEM stage tilt, a linear area of 3.15 nm was scanned with ASTAR using 0.3 nm step size.

Collected PED data were processed with the ADT3D [2] and PETS [5] software to obtain unit cell parameters. Diffraction intensities measurement and hkl file extraction was carried out by ADT3D software. 3D reciprocal cell reconstruction for $MgMoO_4$ (fig.1) confirmed monoclinic unit cell with space group C2/m and cell parameters have been obtained with an error of less than 1% compared to the reference structure [6], (in parenthesis are reference structure parameters) a=10.211 Å (10.273), b=9.229 Å (9.288), c=7.080 Å (7.020), □=90.194° (90°), □=107.79° (106.950°), □=90.10° (90°). Structure solution was carried out using SIR2011 software using 714 independent reflections and allowed the complete structure to be solved (9 atoms into the asymmetric unit) with final R factor value of 31.96 %, which is a reasonable value for solved structures with ED data. Atomic positions are found very close to the X-Ray refined ideal positions (table 1). It is interesting to note that a similar conditions collection without using PED did not lead to any structure solution

This novel ultra-fast automatic 3D PED diffraction tomography approach can be considered as a breakthrough technique in electron crystallography as it is the first genuine full automated tomography method that could be performed for every commercial available TEM, provided that crystal shift during a specific tilt range is stable and reproducible. The technique help to hugely reduce 3d tomography ED data collection time and most importantly, may allow the application of TEM based 3D tomography to beam sensitive materials.

1. E. Mugnaioli, T. Gorelik and U. Kolb, Ultramicroscopy 109 (2009) p. 758.
2. U. Kolb, T. Gorelik, C. Kübel, M. T. Otten and D. Hubert, Ultramicroscopy 107 (2007) p. 507.
3. NanoMEGAS www.nanomegas.com.
4. E.F. Rauch, J. Portillo, S. Nicolopoulos, D. Bultreys, S. Rouvimov and P.Moeck, Zeitschrift für Kristallographie 225 (2010) p. 103.
5. L.Palatinus, D.Jacob, P.Cuvillier, M. Klementová, W.Sinkler, L.D.Marks, Acta Cryst. (2013) A69, p. 171.
6. Bakakin V. V., Klevtsova R. F. and Gaponenko L. A., Kristallografiya (1982) 27 p. 38

		Reference Structure			Ultra-fast PEDT		
		x	y	z	x	y	z
Mo	Mo1	0.5000	0.2510	0.5000	0.5000	0.2545	0.5000
Mo	Mo2	0.7291	0.5000	0.0957	0.7289	0.5000	0.0915
Mg	Mg1	0.5000	0.1784	0.0000	0.5000	0.1838	0.0000
Mg	Mg2	0.7996	0.5000	0.6431	0.8050	0.5000	0.6534
O	O1	0.5415	0.1533	0.3040	0.5418	0.1668	0.3065
O	O2	0.3587	0.3561	0.3912	0.3481	0.3529	0.3783
O	O3	0.8587	0.5000	0.0391	0.8536	0.5000	0.0413
O	O4	0.6337	0.3448	0.0283	0.6339	0.3410	0.0256
O	O5	0.2983	0.0000	0.3551	0.3244	0.0000	0.3802

Table 1. Atomic position of the reference structure & the Ultra-Fast PEDT crystal structure determination

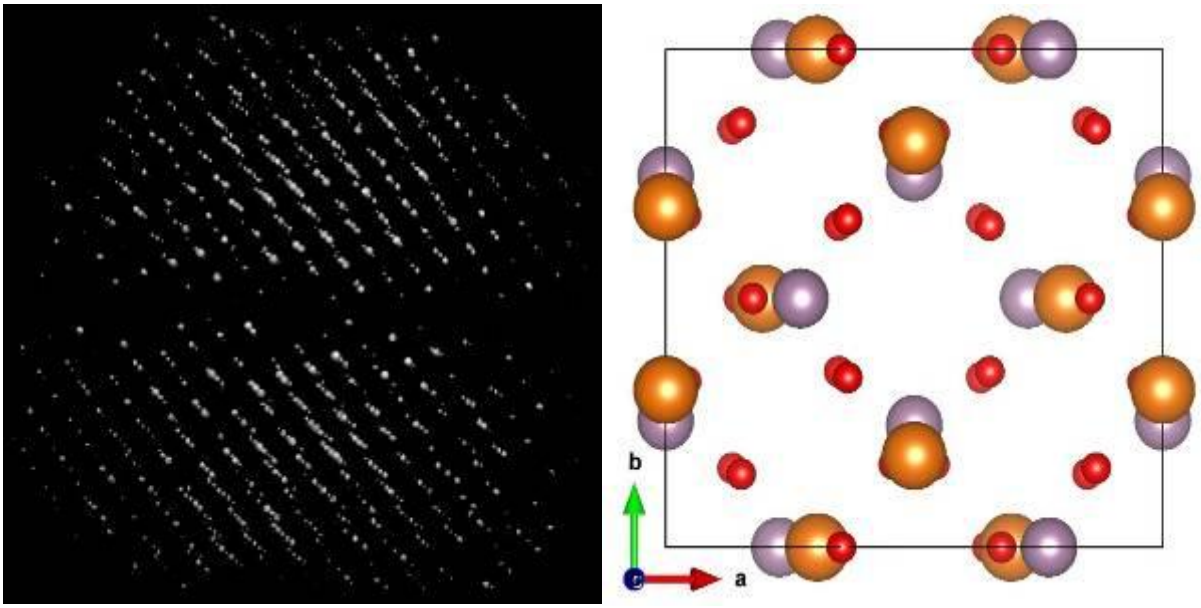

Figure 1. Reconstruction of 3D reciprocal space and structure model of $MgMoO_4$ using the ultra-fast automated 3d PED tomography data acquisition. Labels: Brown Mo , Grey Mg , Red O

Quantitative High-Resolution TEM/STEM and Diffraction

IM.1.P031
Surface-near lattice relaxation in single crystalline Au nanoparticles

D. Pohl[1], L. Schultz[1,2], B. Rellinghaus[1]

[1]IFW Dresden, Dresden, Germany
[2]TU Dresden, Institute for Solid State Physics, Dresden, Germany

d.pohl@ifw-dresden.de

Whereas bulk gold is one of the most noble metals, nanoparticles of Au show high catalytic activities and are presently of large interest for applications in fields such as biomedicine, heterogeneous catalysis, and plasmonics, to name a few. These modified properties of Au at small sizes originate from both an enhanced surface-to-volume ratio and the fact that its physico-chemical properties critically depend on the different local atomic environments of Au atoms on different facets. Consequently, the properties of Au particles depend strongly on the type of faceting and thus on the nanoparticles' shape.

In this report we used aberration-corrected transmission electron microscopy to study directly the lattice structure of single crystalline Au nanoparticles. Due to the delocalization-free imaging a direct measurement of atom position and lattice constants even at the surface layers is possible. It was recently reported that decahedral Au particles exhibit an expansion of the lattice along the (111) direction close to the particle surface [1]. In nanoparticles of binary metallic alloys similar surface-near lattice expansions were attributed to segregation phenomena [2, 3, 4].

Au nanoparticles with a mean diameter of 6.9 nm and a narrow size distribution are prepared by inert gas condensation. The particles nucleate and growth from a supersaturated vapour provided by DC magnetron sputtering from an Au target at a continuous flow of Argon at a pressure of 1.5 mbar. The particles are subsequently ejected into high vacuum through differential pumping and deposited on carbon-coated copper grids in the deposition chamber. Ar with a purity of 99.999% Ar is further purified by means of an oxygen getter prior to feeding it to the sputter gun. Whereas this process produces predominantly icosahedral particles, single crystalline Au nanoparticles were obtained upon modifying the surface (free) energies of Au by adding 5 vol.% oxygen to the process gas [5].

The atomic structure of the likewise prepared Au nanoparticles is investigated by means of aberration-corrected HRTEM using a FEI Titan^3 80-300 microscope. Fig 1a. shows an exemplary HRTEM image of a single crystalline Au nanoparticle as seen along the [011] zone axis. In Fig 1b, the resulting profile of the lattice parameter along the <100> direction is shown after averaging over 52 surfaces, pointing to a significant decrease of the lattice spacing upon approaching the surface. This surface-near lattice compression on (100) facets is due to the so-called smoothing effect at surfaces [6]. In order to properly account for artefacts in the measured lattice relaxation due to lens aberrations, HRTEM contrast simulations of model particles are performed. The simulations show that the effect of aberrations is small compared to errors imposed by the amorphous carbon support. In addition to the experimental investigations, molecular dynamic (MD) simulations are conducted to investigate the lattice relaxation in Au model nanoparticles (s. Fig. 2b).

Since the elastic constants of Au are well known, the effective surface stress can be estimated from the experimentally determined lattice relaxation using a simple thin film model which is also applicable to nanoparticles [7]. The resulting surface stress of the (100) and (111) surfaces will be presented and discussed in comparison with results from MD-simulations.

1. M. J. Walsh et al., Nanoletters 12 (2012), p. 2027.
2. D. Pohl, unpublished.
3. B. Bieneck, D. Pohl, L. Schultz and B. Rellinghaus, J. of Nanoparticle Res. 13 (2011), p. 5935.
4. R. M. Wang et al., Phys. Rev. Lett. 100 (2008), 017205.
5. D. Pohl, A. Surrey, L. Schultz and B. Rellinghaus, APL 101 (2012), p. 263105.
6. R. Smoluchowski, Phys. Rev. 60 (1941), p. 661.
7. R.C. Cammarata and K. Sieradzki, Annu. Rev. Mat. Sci. 24 (1994), p. 215.

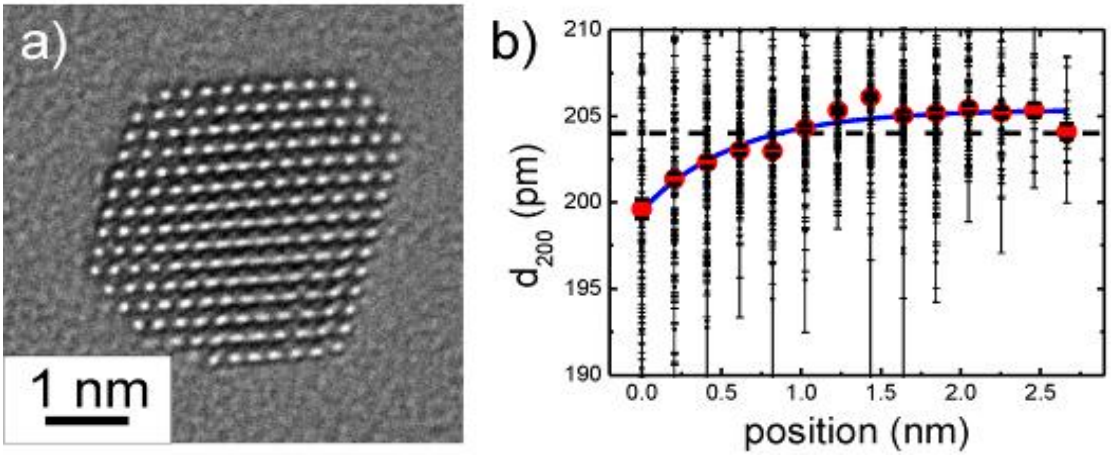

Figure 1. a) Exemplary HRTEM image of a single crystalline Au nanoparticle as seen along a [011] zone axis. b) Measured lattice relaxation along the <100> direction after averaging over 52 surfaces.

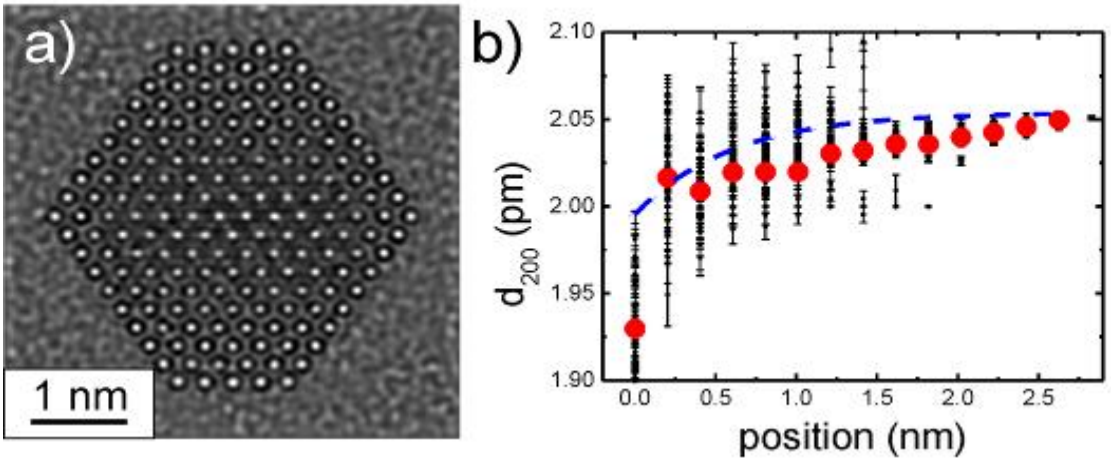

Figure 2. a) Simulated HRTEM image of a single crystalline Au nanoparticle as seen along a [011] zone axis. b) Measured lattice relaxation for model Au particles after structural relaxation by means of MD simulations. The blue line represents experimental lattice relaxation shown in Fig. 1b.

Quantitative High-Resolution TEM/STEM and Diffraction

IM.1.P032
Charge density within a unit cell of GaN imaged withsub-Ångstrøm resolution by differential phase contrast microscopy

J. Zweck[1], S. Lazar[2], B. Freitag[2], M.C.S. Vogel[1], C.K.A. Mewes[3], M. Lohr[1], B. Bauer[1], J. Thalmair[1]
A. Pritschet[1]

[1]Universität Regensburg, Physik, Regensburg, Germany
[2]FEI Company, Eindhoven, Netherlands
[3]University of Alabama, Tuscaloosa, United States

josef.zweck@ur.de
Keywords: differential phase contrast, GaN, spontaneous polarization

Gallium nitride (GaN) is a highly interesting material for optoelectronics (high power LEDs and laser diodes) and actuators. The possibility to form ternary and quaternary alloys with InN and/or AlN allows a modification of the band gap and to tune the emission wavelength continuously from infrared to ultraviolet light. GaN also posesses a spontaneous polarization which causes local fields up to 250 MV/m between the intrinsic sheet charge densities. When strained, a piezoelectric polarization builds up in addition, which causes a tilt of the band structure across quantum wells. This tilt is believed to be responsible at least in part for a reduced performance due to the quantum confined Stark effect (QCSE) for laser diodes emitting in the green spectral range. For a direct measurement of local electric fields, we use the differential phase contrast (DPC) technique (see below) to monitor in STEM mode the minute deflections of the central diffraction disk when the beam passes through a region with a static field. To achieve the resolution needed we used a FEI Titan cubed 60-300kV, equipped with a high brightness gun, monochromator, an image C_s corrector and DCOR probe corrector with a convergence semi angle of about 21 mrad and a probe size of about 0.8Å. The detector used was a dedicated four quadrants solid state detector. The differential phase contrast technique was originally suggested by Rose [1] and later used in large extent to investigate micromagnetic structures in a STEM [2-7]. Recently, its capability to image electrostatic fields has been demonstrated, first on a mesoscopic (nm) scale [8], shortly followed on a microscopic (sub-nm) scale [9]. The specimen is scanned with a finely focused electron beam, and the beam's deflection vector due to local electrostatic fields is measured. This allows us to reconstruct an electric field vector map with a resolution defined by the microscope's probe size of 80 pm, which is sufficient to resolve details even within a single unit cell of GaN. However, although the high brightness gun already yields images with excellent S/N, the noise is still problematic for further data processing. Therefore, we use a cross-correlation averaging technique to add identical patches of the crystal's image to further reduce the S/N ratio. This procedure is repeated for every one of the four segments of the DPC detector, and by taking the difference signal between adjacent sectors we obtain a noise-free directional signal which in effect is a projection of the local electric field vector within the specimen on an orthogonal coordinate system defined by the detector. This allows the reconstruction of an electric field vector map of local fields within the GaN unit cell and subsequently the reconstruction of a 2D charge density map from the crystal by using . Fig.1 shows the DF image, giving the atomic locations (left), the reconstructed vector field map (center) and the reconstructed charge density map (right, some atomic positions are indicated by circles). Obviously, the N atoms are much more clearly visible in the charge reconstruction compared to the pure atomic (DF) image. From a detailed evaluation of the experimental charge density image as well as from a DFT calculation one can conclude that there is a charge transfer from Ga towards N which is in agreement with the highly polar covalent type of bonding known to exist in GaN. In Fig. 2, normalized line scans are shown along the line indicated in the inset, showing the DF signal (green, cross-hatched), the charge density signal (blue), the vertical (red, hatched) and horizontal (green) beam deflection as determined by DPC. Clearly, the charge density is peaked at both the Ga and N atomic sites. Please note that the charge density is shifted by a small amount (ca. 9 pm) with respect to the DF signal, which indicates the location of the nucleus. The vertical deflection of the beam is asymmetric around the Ga site which is due to local electrostatic fields. In conclusion we are able to reconstruct charge density distributions within a single unit cell of GaN.

1. H. Rose, Ultramicroscopy 2 251-267 (1977).
2. J.N. Chapman, P.E. Batson, E.M. Waddell, R.P. Ferrier, Ultramicroscopy 3 203-214 (1978).
3. C. W. Sandweg et al.,J. Appl. Phys. 103 093906 (2008).
4. C. Brownlie, S. McVitie, C. D. W. Wilkinson, J. N. Chapman, J. Appl. Phys. 100 033902 (2006).
5. T. Sannomiya, Y. Haga, Y. Nakamura, Y. Takahashi, O. Nittono, J. Appl. Phys. 95(1) 214-218 (2004).
6. T. Uhlig et al., Phys. Rev. Lett. 95(23) 237205/1-4 (2005).
7. T. Uhlig, J. Zweck, Phys. Rev. Lett. 93(4) 047203 (2004).
8. M. Lohr et al., Ultramicroscopy 117 7 - 14 (2012).
9. N. Shibata et al., Nat. Phys. 8 611-615 (2012).
10. We gratefully acknowledge the funding this project (DFG Grant ‘‘Focused Researcher’s Group: PolarCoN FOR(957)’’ (Polarization Control in Nitrides).

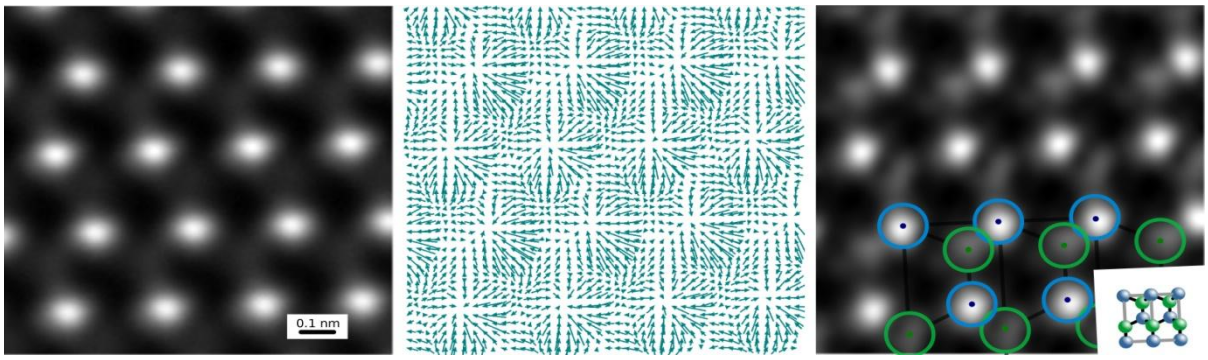

Figure 1. DF image showing atomic locations (Ga atoms. left). Center: reconstructed electric field map of same area as left and (right) reconstructed charge density map with indicators of atomic locations (Ga: blue, N: green).

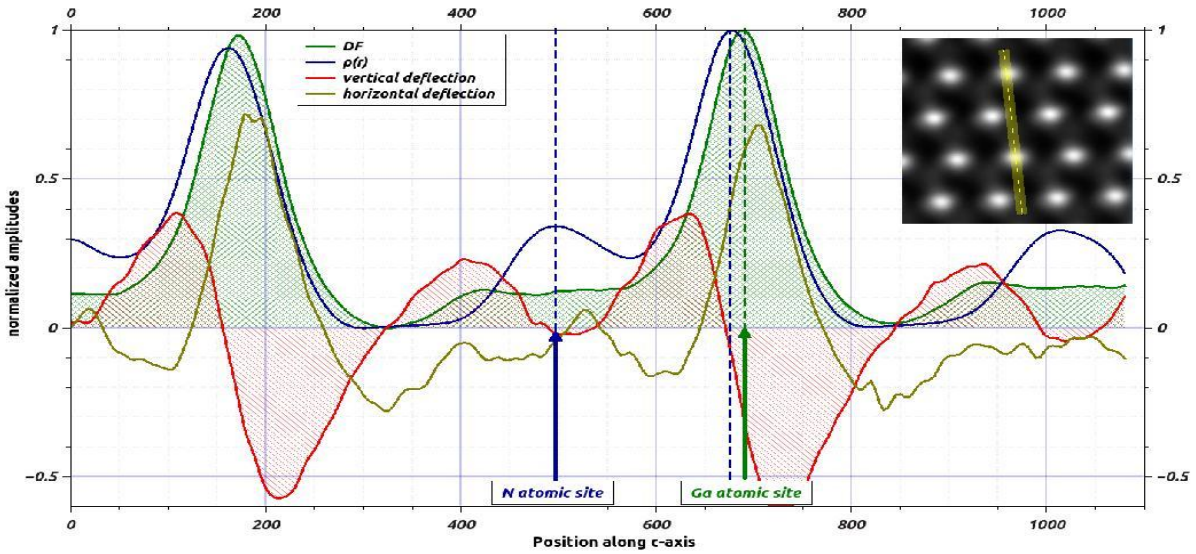

Figure 2. Line scans along the line indicated in the inset image. The DF signal (green) indicates the location of the atomic nuclei, the blue graph shows the reconstructed charge density distribution. Red and yellow curves show the vertical and horizontal beam deflection due to inner electrostatic fields, respectively.

Quantitative High-Resolution TEM/STEM and Diffraction

IM.1.P033
Mapping strain fields in semiconductor nanodevices by dark-field off-axis electron holography and nano-beam diffraction

J. Sickmann[1], H. Geisler[2], A. Würfel[2], H.-J. Engelmann[2], H. Lichte[1]

[1]Technische Universität Dresden, Triebenberg Laboratory, Dresden, Germany
[2]GLOBALFOUNDRIES, Center for Complex Analysis, Dresden, Germany

jan.sickmann@triebenberg.de
Keywords: dark-field holography, nano-beam diffraction, strain mapping

Strained silicon has already become a standard technology in advanced semiconductor device engineering to boost performance and efficiency in modern transistor devices [1]. Therefore, the determination of the exact two-dimensional strain distribution at nanometre scale is of major interest in semiconductor device characterization [2]. For instance, GLOBALFOUNDRIES demands an accuracy better than $\Delta\varepsilon$=0.1% for the strain $\varepsilon\pm\Delta\varepsilon$ measured in the transistor channel. Lateral resolution should at least reach 5 nm.

Dark-field off-axis electron holography (DFH) and nano-beam diffraction (NBD) are TEM-based techniques that are able to match these requirements. In DFH, diffracted waves from adjacent sample areas are interfered using the dark-field off-axis holography configuration [3]. The superposition of one part of the diffracted wave emanating from strained Si and the other part emanating from adjacent strain-free Si substrate forms a dark-field hologram, from which differences in amplitude and phase of the diffracted wave can be reconstructed. The gradient of the phase parallel to the diffraction vector yields the lattice strain in this direction [4]. In NBD, a series of diffraction patterns is acquired along a line profile of interest and compared to a reference diffraction pattern from an unstrained region in the Si substrate. A line profile of the local strain is then calculated from the relative displacement of the diffraction spots in the nanodiffraction patterns [5,6].

Figure 1 illustrates a successful strain measurement in a state-of-the-art transistor structure manufactured by GLOBALFOUNDRIES Dresden. Recessed SiGe at source and drain induces compressive strain in the transistor channel. Our experiments allow reconstruction of a (110) lattice strain map at 800 nm and 200 nm field of view, and lateral resolution of 10 nm and 4 nm, respectively. A statistical evaluation of multiple line profiles from a series of holograms leads to a sensitivity of $\Delta\varepsilon$=0.1% at 10 nm resolution and $\Delta\varepsilon$=0.2% at 4 nm resolution, were noise poses the most severe problem. However, since the strain values are retrieved by means of the derivative of the reconstructed (220) phase along the [110] direction, strain profiles along the channel are more affected by noise than perpendicular profiles.

For the purpose of comparison, NBD patterns have been recorded along the channel of transistor B and C; a parallel NBD scan inside the substrate is needed to receive the reference spot positions. Peak fitting software is used to determine the positions of the <-440> and <440> diffraction spots; their relative displacement to the reference position then yields (110) lattice strain profiles. The FWHM of the diffraction peaks coincides with the scanning probe, and hence can be used to define the resolution in our NBD experiments to around 6 nm. From a statistical evaluation of the NBD reference scans in the substrate, the accuracy in the strain measurement estimates as $\Delta\varepsilon$=0.1%.

A comparison of the line profiles at transistor B and C illustrates that DFH and NBD yield consistent results in the transistor channel. NBD measures ε_{xx}=-(0.7±0.1)% compressive strain in the centre of channel B and C, while DFH experiments yield ε_{xx}=-(0.6±0.1)% or ε_{xx}=-(0.6±0.2)%.

Our results demonstrate that DFH and NBD are two complementary, well suited techniques for strain metrology in state of the art transistor devices at nm-scale resolution. Whereas NBD is a quite simple technique easy to perform, DFH needs more sophisticated equipment and evaluation. However, DFH provides the two-dimensional strain distribution within one single acquisition. Although sensitivity of both techniques is comparable, we will provide further examples of sole DFH experiments on other devices proving a sensitivity better than $\Delta\varepsilon$=0.1%.

1. M. Chu, Y. Sun, U. Aghoram and S. E. Thompson, Annu. Rev. Mater. Res. 39 (2009), p. 203.
2. ITRS, International Technology Roadmap for Semiconductors, 2007 edition, https://itrs.net/reports.html.
3. K.-J. Hanzen, J. Phys. D: Appl. Phys. 19 (1986), p. 373.
4. M. J. Hytch, F. Houdellier, F. Hüe and E. Snoeck, Nature 453 (2008), p. 1086.
5. K. Usada, T. Numata, S. Takagie, Mater. Sci. Semicond. Process. 8 (2005), p.155.
6. H. J. Engelmann, S. Heinemann, E. Zschech, Proceedings 16th International Microscopy Congress IMC 16 (2006), p. 990.
7. This work was financially supported by the European Union and the Free State of Saxony in the framework of R&D project 13579/2323. We also kindly acknowledge financial support from the European Union under the Seventh Framework Programme under a contract for an Integrated Infrastructure Initiative. Reference 312483 - ESTEEM2.

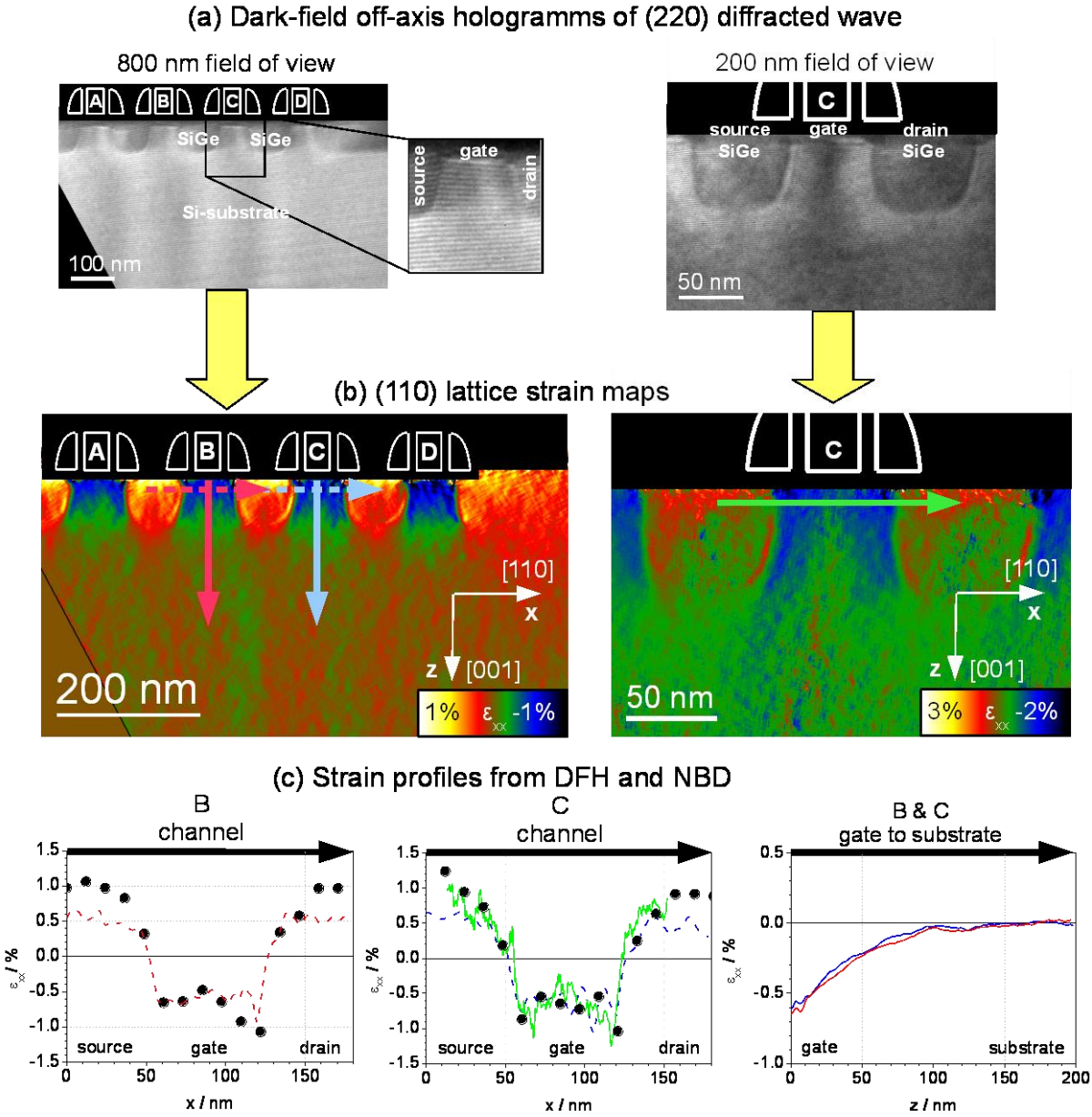

Figure 1. (a) Dark-field off-axis holograms of the (220) diffracted wave: 800 nm field of view is sufficient to cover the 4 MOS transistors (A, B, C, D) with recessed SiGe at source and drain. The bending of the interference fringes indicates strong lattice strain in the transistor channel. 200 nm field of view can cover only transistor C (b) Maps of the (110) lattice strain reconstructed from the holograms: The left strain map provides 10 nm, the right strain map even provides 4 nm lateral resolution. (c) The strain profiles taken from the maps (solid and dashed lines) are compared to the NBD scans (dots). Within the wide error bars, DFH and NBD yield consistent results. Regardless of the method used, compressive strain in the center of the transistor channel can be estimated to ε_{xx}=0.6%.

Quantitative High-Resolution TEM/STEM and Diffraction

IM.1.P034
Investigating nanostructure heterojunctions using nanobeam electron diffraction

J.M. Persson[1,2], J.B. Wagner[2]

[1]RWTH Aachen, Gemeinschaftslabor für Elektronenmikroskopie, Aachen, Germany
[2]Technical University of Denmark, Center for electron Nanoscopy, Copenhagen, Denmark

persson@gfe.rwth-aachen.de
Keywords: TEM, NBED, strain analysis

The microstructure and nanostructure of materials are well known to be decisive for many macroscopic properties[1-3]. Materials can be characterized on the nanometer scale for composition and atomic structure using the transmission electron microscope (TEM). However, TEM normally has many restrictions. Good sample preparation is an integral part of the process, and different analysis modes often have to be combined. High-resolution transmission electron microscopy (HRTEM) usually need the samples to be less than 20 nm [4, 5] to get reliable results for atomic positions. However, useful and unique information is obtainable in thicker samples [6]. Here, nanodiffraction and spatially resolved spectroscopy are presented as means to extend the information available from TEM of heterojunctions and grain boundaries, especially for determining relative atom positions and strain.

Nanostructures such as the epitaxially grown semiconductor nanowire depicted in figure 1a) were analysed for local strain information using nanobeam electron diffraction (NBED) and compared to chemical information from energy dispersive X-ray spectroscopy (EDX) acquired in a TEM. NBED was performed by illuminating as small an area on the sample as possible, with an electron beam parallel enough to get a reliable and interpretable diffraction pattern [7, 8]. Using a three condenser lens microscope the probe size at the sample can be made in the order of a few nanometers. In conventional electron diffraction in the TEM the area selected is limited by the size of the aperture and machine properties to about 200 nm [6]. The resulting diffraction patterns will be easy to analyse as per the schematics in figure 1b). Some results can be seen in figure 2a) and 2b) where energy dispersive X-ray spectroscopy (EDX) has been compared with NBED data of a visually identical wire. The EDX data show the heterojunction transition to be 50 nm shorter compared to the NBED data.

NBED is a useful tool for analysing small grains and heterojunctions. The local strain in heterojunctions can clearly be seen in the diffraction patterns, and this will be a valuable complement to chemical data from spectroscopy. The measurements have been performed on a wide variety of samples[9].

1. N Sköld, et al., Nano Letters, 6 (2006), p. 2743.
2. J.M. Bao, et al., Nano Letters, 8 (2008), p. 836.
3. D Jacobsson, et al., Nanotechnology, 24 (2012), p. 245601
4. M.W. Larsson, et al., Nanotechnology, 18 (2007), p. 015504.
5. A.I. Kirkland, J. Sloan, and S. Haigh, Ultramicroscopy, 107 (2007), p. 501-6.
6. D.B.C. Williams and B. Carter, Transmission Electron Microscopy, 2nd ed. (2009) Springer.
7. , et al, Applied Physics Letters, 95 (2009), p. 123114.
8. P. Favia, et al, Journal of The Electrochemical Society, 158 (2011), p. H438.
9. The authors wish to acknowledge economic support from the EC FP7 project AMON-RA (214814). The nanostructures were provided from Lund University and special thanks goes to M Borgström, D. Jakobsson and J. Wallentin.

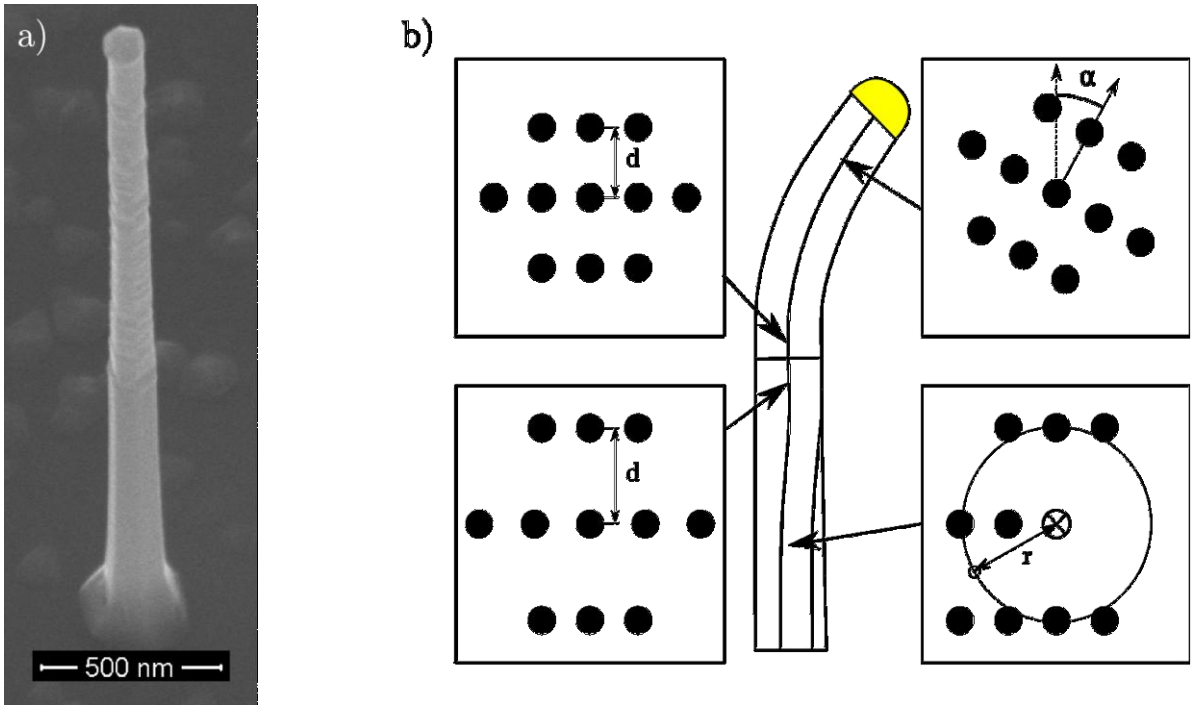

Figure 1. a) An SEM micrograph of a typical nanostructure as examined using NBED. A heterojunction can be seen from the point of morphological change. b) A schematic drawing of the same nanostructure, with schematic examples of NBED patterns as used for seeing a change in lattice constant (to the left) and tilts and twists (to the right)

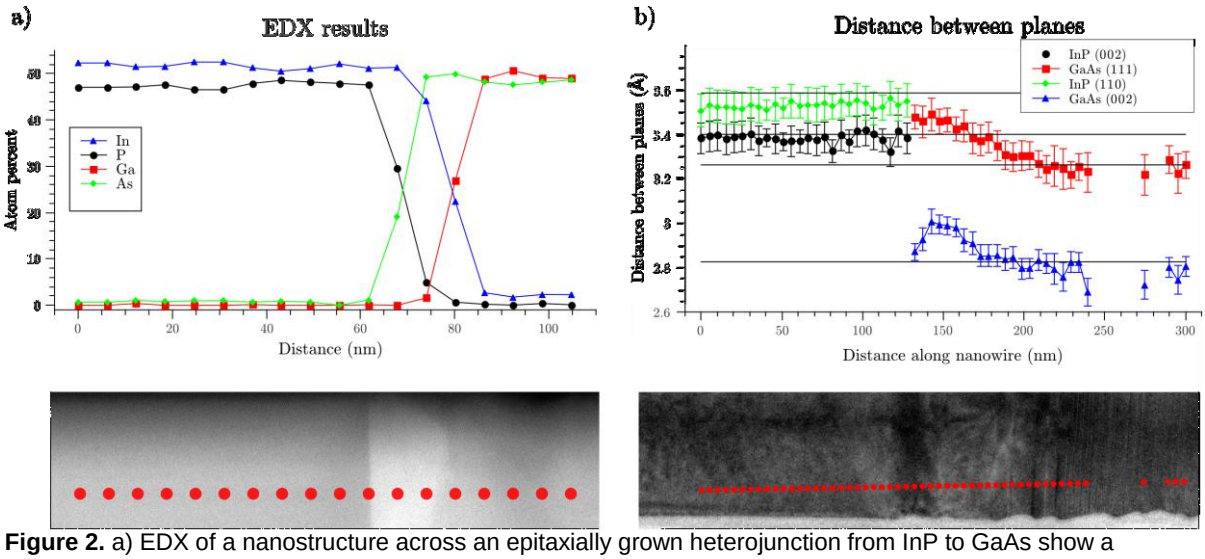

Figure 2. a) EDX of a nanostructure across an epitaxially grown heterojunction from InP to GaAs show a transition length of ca 30 nm with intermediate InAsP and InGaAs states. The red dots in the STEM image correspond to the measurement points above. b) NBED was used to determine the local lattice distance at the position of each of the red dots in the HRTEM image. The resulting slope shows a transition that is ca. 80 nm long and hence much longer than in a). The HRTEM image was acquired prior to the NBED measurement and has been included for comparison. The dark lines in the graph in b) correspond to a literature value of the lattice constant of (top to bottom) InP(110), InP(002), GaAs(111) and GaAs(002).

Quantitative High-Resolution TEM/STEM and Diffraction

IM.1.P035
High-Resolution incoherent imaging in a Cs corrected electron microscope: A new tool for High -Resolution Electron Tomography in life science

D. Van Dyck[1], I. Lobato Hoyos[1], U. Lücken[2], H. Stark[2]

[1]University of Antwerp, Department of Physics, Antwerpen, Belgium
[2]MPI for biomedical engineering, Goettingen, Germany

dirk.vandyck@ua.ac.be
Keywords: high-resolution incoherent imaging, high-resolution electron tomography

In the world of single particle cryo-EM, biological objects are considered as phase objects that can only be studied using phase contrast microscopy. The usual way to get phase contrast in EM is by compensating the spherical aberration Cs with negative defocus (Scherzer focus) so as to create a passband of spatial frequencies for which the phase shift is close to 90°. However, in such a passband the phase transfer at the low spatial frequencies is very poor and is a problem for biological objects as information about their shape is in this range. A possible solution is to develop a phase plate that is able to shift the phase of the central beam over 90° with respect to the diffracted beams but thus far, no workable electrostatic phase plate has been demonstrated. A more practical way to obtain phase contrast in the low spatial frequency range is by using a very large defocus and by compensating for the missing gaps in the transfer function by combining several defocus values. However, at large defocus, the spatial incoherence of the microscope effectively limits resolution to about 0.4nm. Therefore, it is generally believed that the use of a Cs corrector, in this specific case is of limited value at for single-particle Cryo-EM ("Cs is our friend not our enemy"). However preliminary experiments of Cryo-EM with a Cs corrector seem to indicate that one can get better contrast with less defocus as shown in figure 1 for an HppS protein of 125 kDa because its small size is difficult to image under the usual native cryo-EM conditions. Our recent work on incoherence in EM [1] suggested that this dark contrast could be due to thermal diffuse scattered (TDS) electrons scattering into the background. And, contrary to the common belief, the contribution of TDS electrons can be relatively large in soft matter because it is not only a function of the atomic number of the atoms but also of their mean square displacement and it can reach levels of the order of 10 to 40% of the total scattered intensity [1].

This had then inspired us to develop an alternative HREM imaging technique for biological objects that exploits the properties of TDS electrons. TDS scattering is incoherent and thus does not interfere with the central beam so that it generates amplitude contrast. It is maximal at a spatial frequency, which is inversely related to the mean square displacement of the atom, which in soft matter is about $1.0Å^{-1}$. At this spatial frequency, the phase transfer function can be made flat by combining a very low Cs with a small underfocus so as to get the highest resolution. Furthermore it is linear in the "mass-thickness" and easy to interpret and so that is it very suited for tomography. In this abstract we will outline the basic principles and support this by simulations. The details will be published in a forthcoming paper [3].

In a real object, the atoms vibrate around an average position. This is usually described by a Debye Waller factor, which reduces the scattering at large angles with only a minor influence on the image contrast. However. as shown in [1], this is a misconception. Every electron sees a still atom with a sharply peaked electrostatic potential at the nucleus, which scatters at very large angles. Because of the phase oscillations of the transfer function at large spatial frequencies, this information is usually delocalized in the image - but using a low Cs and defocus this delocalization can be minimized by shifting the passband of the transfer function to the spatial frequency of the TDS signal. In addition, the averaging over the vibrating atom positions has to be done at the level of the detection of the image. If we assume that the atom motions are uncorrelated (Einstein model) the TDS contribution of each atom is incoherently (independently) added to the final image [3] which simplifies the interpretation of the high resolution images and it is very suitable for tomographic reconstruction algorithms. It is also possible to correct for slight differences in defocus of the atoms in the 3D object [3]. However the simulation of such imaging conditions requires the averaging of images calculated for

different atom positions so that the computational requirements are comparable to the tedious frozen phonon calculations in HAADF STEM.

It is possible to select only the TDS signal by using an annular dark field aperture [2], which matches the TDS contribution and by optimizing Cs and defocus so that the phase is approximately constant over this window. In a sense the method is then comparable to HAADF STEM but with all the advantages of HREM. Figure 2 shows the simulations of rotationally averaged power spectra of diffraction pattern and HREM image and figure 3 a simulation of the dark field images of the HbpS protein that proves that the incoherent imaging mode yields both high contrast and atomic resolution.

1. D. Van Dyck, Ultramicroscopy 111 (2011), 894-900.
2. S. Bals, R. Kilaas, C. Kisielowski, Ultramicroscopy 104 (2005), 281-289.
3. Dirk Van Dyck, Ivan Lobato Hoyos, Uwe Lücken, Holger Stark[2] to be published

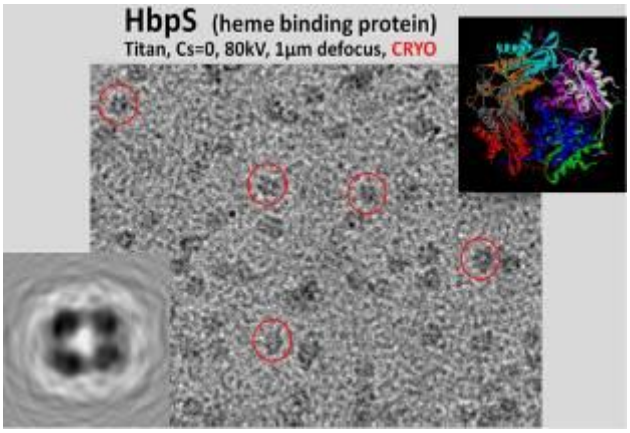

Figure 1. Cs corrected cryo-EM image of HbpS proteins with remarkably high contrast for small particles.

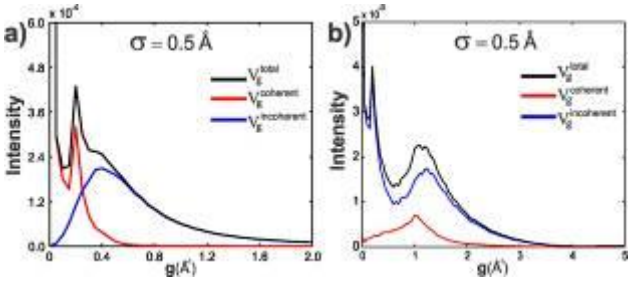

Figure 2. Rotationally averaged power spectra of a frozen atom image calculation of an **HbpS** protein at 300KeV. a) Diffraction and b) Diffractogram for an electron microscope parameters (Δ = 3.2nm, α = 0.2 mrad, C_s = 0.04mm, Δf = 10.9nm) with annular dark-field aperture (g_{min} = 0.5Å^{-1}, g_{max}=2.0^{-1}). Total (black curve), coherent and incoherent RAPS for RMS= 0.5Å.

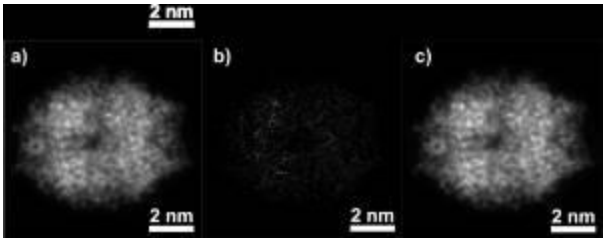

Figure 3. Frozen atom HREM image calculation of an **HbpS** protein with annular dark-field aperture (g_{min}=0.5Å^{-1}, g_{max} = 2.0Å^{-1}). Electron microscope parameters: acceleration voltage (E_0 = 300KeV, Δ = 3.2nm, α = 0.2 mrad, C_s = 0.04mm, Δf = 10.9nm). **a)** Total intensity, **b)** Coherent intensity contribution and **c)** Incoherent intensity contribution.

Quantitative High-Resolution TEM/STEM and Diffraction

IM.1.P036
3D Automated Electron Diffraction Tomography for nanomaterials

P. Oleynikov[1], A. Mayence[1], J. Navarro[1], Y. Ma[1], L. Bergström[1], O. Terasaki[1,2]

[1]Stockholm University, Materials and Environmental Chemistry, Stockholm, Korea, Republic of
[2]KAIST, Graduate School of EEWS, Daejeong, Korea, Republic of

peter.oleynikov@mmk.su.se
Keywords: automated electron diffraction tomography, nanoparticles, electron crystallography

Automated Electron Diffraction Tomography (EDT) is a fast and efficient technique that has been recently developed by us [1]. It can be used for fast three-dimensional (3D) reciprocal space scanning with a given fine step (0.01°-0.1°). We demonstrate how this method can be utilized for characterization of materials that exhibit periodic crystal structure at nano-scale.

In this work two types of nano-crystals were investigated: (i) an individual cubic nano-particle composed of manganese ferrite ($MnFe_2O_4$, cube sizes 14 nm and 20 nm, Figure 1; s.g. *Fd*-3*m*, a = 8.4983Å) and (ii) gadolinium orthophosphate cylindrical nano-rod ($GdPO_4$, diameter ~ 7nm; s.g. $P3_121$, a = 6.9Å, c = 6.35Å).

The crystal structures of the individual nanocube and nano-rod were determined from the EDT data collected in conventional selected area electron diffraction (SAED) mode using EDT-COLLECT software package [2] on JEOL JEM-2100 LaB_6 CTEM equipped with a single ultra-high tilt holder. Two sets of ~600 ($MnFe_2O_4$, exposure 2 sec/frame) and ~700 ($GdPO_4$, exposure 1 sec/frame) unique electron diffraction patterns were recorded from individual single nanocrystals using 3D EDT. Reciprocal space coverage was ~100° for the nano-cube and ~113° for the nano-rod. The recorded frames were processed using the EDT-PROCESS software package [2] and assembled into a corresponding 3D volumetric representation of reciprocal space (Figure 2).

The crystal structures were successfully determined using direct methods from the integrated intensities extracted by EDT-PROCESS program. In case of gadolinium orthophosphate the crystal structure of the hexagonal phase has been determined for the first time (until now it has only been described by an X-ray powder profile [3]).

It is possible to study dynamical scattering effects quantitatively using several 3D EDT frames from each dataset due to relatively small thickness values of the investigated nano-particles. In both cases the *R*-merge values for Friedel pairs were very low (5.7% for $GdPO_4$ and 10.2% for $MnFe_2O_4$). In case of the investigated gadolinium orthophosphate cylindrical nano-rod it was possible to utilize the Bloch wave formalism for the partial dynamical structure refinement using several individual electron diffraction frames.

In this work we show that 3D EDT as a very powerful technique which offers a facile and systematic way to study a wide ranges of materials at different scale levels. Simultaneously EDT studies performed on nano-crystals with almost perfect shape can be utilized for further quantification taking dynamical scattering into account.

1. D.L. Zhang, P. Oleynikov, S. Hovmöller and X.D. Zou, Z. Krist. 225 (2010), p. 94.
2. M. Gemmi and P. Oleynikov, Z. Krist. 228 (2013), p. 51.
3. B. Scheetz in JCPDS (ICDD), file no. 39-0232.
4. We kindly acknowledge Swedish Research Council (VR, 1486801) and Knut and Alice Wallenberg Foundation (3DEM-NATUR).

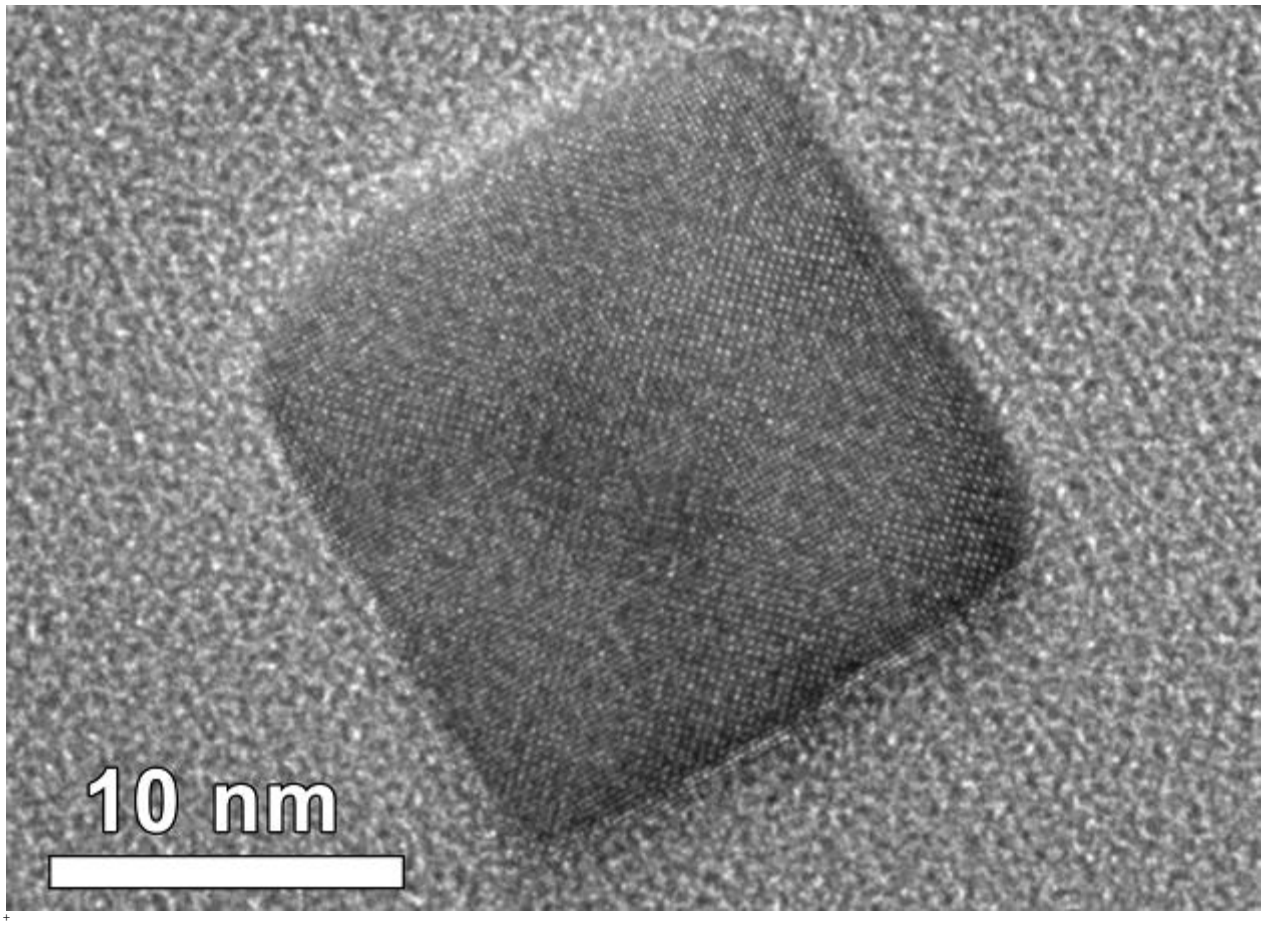

Figure 1. 20 nm cubic nanoparticle of $MnFe_2O_4$.

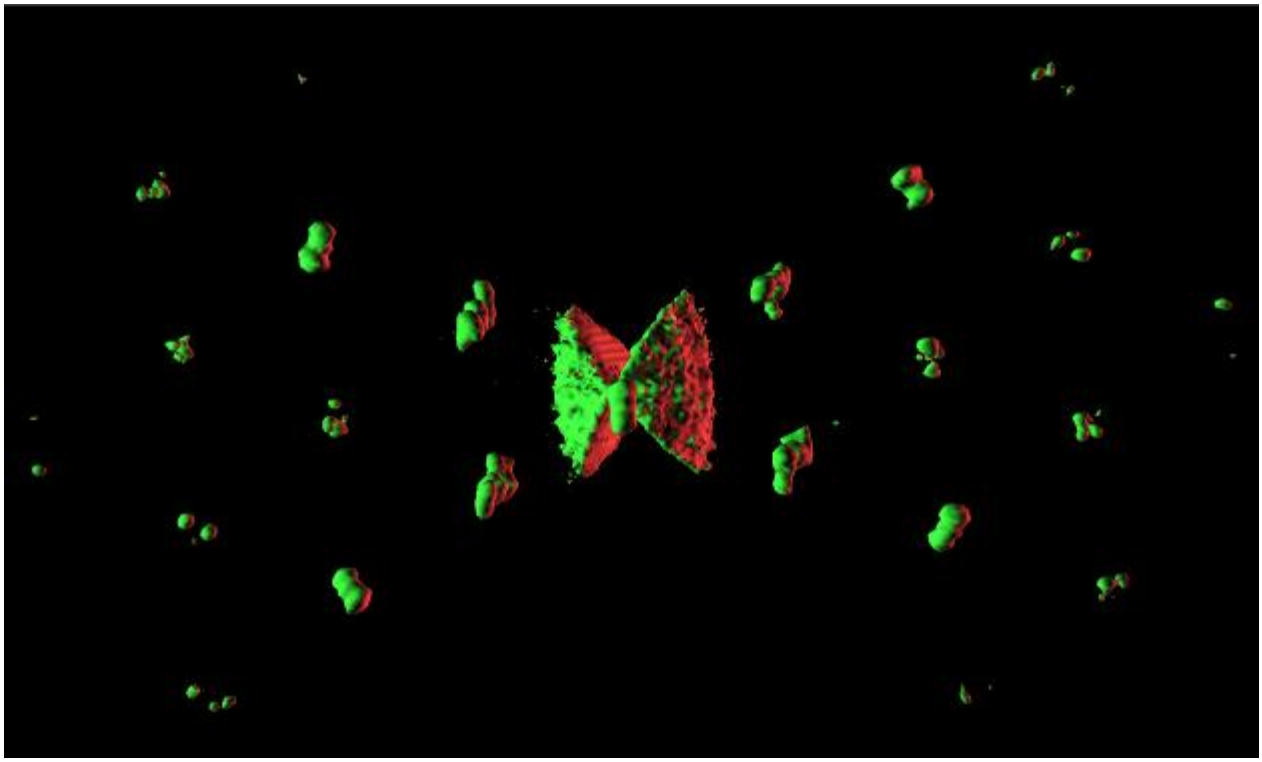

Figure 2. Reconstructed 3D volume of reciprocal space (113° coverage) using 700 unique electron diffraction frames recorded from the individual $GdPO_4$ nano-rod (view along c* axis).

Quantitative High-Resolution TEM/STEM and Diffraction

IM.1.P037
Atomic structure from low-dose exposures via maximum likelihood reconstructions - A new route to circumvent radiation damage

J. Meyer[1], J. Kotakoski[1], C. Mangler[1]

[1]University of Vienna, Faculty of Physics, Vienna, Austria

jannik.meyer@univie.ac.at
Keywords: radiation damage, maximum-likelihood reconstruction, transmission electron microscopy

The recent years have seen remarkable developments in electron microscopy, such that essentially all atomic distances can be resolved by the latest generation of instruments. In particular, the correction of lens aberrations [1,2] has not only pushed spatial resolution well below atomic distances, but also reduced delocalization effects which simplifies the analysis on the level of single atoms. However, increased resolution inevitably requires higher doses on the sample. Radiation damage is a key limitation to the applicability of TEM-based methods, and becomes increasingly relevant also in the study of materials. Atomically resolved images with a reasonable signal-to-noise ratio in a TEM or STEM require on the order of 10^5 high-energy electrons to be passed through every square angstrom of the sample, and only a tiny fraction of known substances survive these extreme conditions undisturbed [3]. When knock-on damage dominates the radiation damage, low-voltage imaging is a viable solution [4,5]. However, lower voltages also increase the electron-electron scattering cross section, which leads to increased ionization damage. While reduced electron energies have enabled the atomically resolved imaging of low-dimensional materials made of light elements [6-8], significant beam-driven dynamics are clearly still present in these studies. An alternative route to circumvent radiation damage is to distribute the dose over many identical copies of the same object. This approach has been under active development for decades for the study of biological molecules [9-11] but it has never before been explored in the context of materials science. Here, we show that it is possible to exploit the multiplicity of identical configurations also in the study of non-periodic atomic configurations (e.g., defects) in materials by statistical means. The big advance of this algorithm is that it does not require the location, classification or alignment of the individual entities in the noisy data set. This new approach has the potential to overcome the limitations set by radiation damage, by reducing the dose on the sample by many orders of magnitude. It can be applied to any case where a discrete set of deviations from a regular lattice can be expected to occur repeatedly across a larger sample area. Examples of such situations encompass point defects in a material or 2D material (shown here), as well as functional groups and small molecules on the surface of a thin membrane. The presented method can be considered as a generalization of the approach in Ref. [10], with the addition of unknown object positions. The data is collected by imaging a larger area of the sample with a very low dose, where the signal-to-noise ratio in the images may be well below what is needed to recognize individual objects (defects). Then, by automatically constructing candidate structures, which evolve to maximize the probability of obtaining the observed data via low-dose exposures, the underlying configurations are revealed without a need for image alignment. An example is shown in Fig. 1. Panel a shows a noise-free case (infinite dose) of a simulated STEM image of graphene with a mixture of three different di-vacancy defects randomly distributed across the sample. Fig. 1b shows a similar simulation, but with Poisson noise corresponding to a dose of only 500 $e^-/Å^2$ on the sample. Simulated noisy data corresponding to an area of 3.2 μm^2 was generated, and split into frames of ca. 1.2nm × 1.2nm. We started with model exposures of a defect free lattice with some added noise (to ensure that different initial structures were not numerically identical). Next, the likelihood value of the model set given the low-dose data was calculated as given by Eq. 1, where the product is over all frames (index i), and the summation runs over all models m and spatial offsets xo, yo. $p(I|M)$ is the probability of recording the image data (I) frame i, given model structure M_m with a position offset xo,yo. w_m is a weight associated with each model structure. The model images and their weights are next modified step by step on a single-pixel level, and every change that increases the likelihood value is kept. Remarkably, this procedure leads to exactly the same configurations that were incorporated in the model structure. No *a priori* knowledge about the defect structures is required. We have successfully tested this method with simulated TEM and STEM data both for defects in graphene and small molecules adsorbed on a graphene sheet. For the next step, i.e., experimental realization, a low dose acquisition approach is needed, with a precision sufficient for atomic resolution.

We point out that the limiting dose and defect density, for which this approach still works, depend on the computing power available for the reconstruction, rather than the to-be expected experimental limitations. Hence, further improvements (dose reduction below values demonstrated here) appear feasible with improved algorithms or the use of larger computing resources.

Equation 1:
$$L=\prod_i \sum_m \sum_{xo,yo} p(I_i|M_m) w_m \quad (1)$$

1. M. Haider et al., *Nature* 392 (1998), p. 768.
2. O. Krivanek, *Ultramicroscopy* 78 (1999), p. 1.
3. R. F. Egerton, *Microscopy research and technique* 75 (2012), p. 1550.
4. R. F. Egerton et al., *Ultramicroscopy* 110 (2010), p. 991.
5. J. Meyer et al., *Physical Review Letters* 108 (2012), 196102.
6. K. Suenaga, *Nature nanotechnology* 6 (2007), p. 358.
7. J. C. Meyer et al., *Nano letters* 8 (2008), 3582.
8. O. Krivanek et al., *Ultramicroscopy* 110 (2010), p. 935.
9. J. Frank, "Three-dimensional electron microscopy of macromolecular assemblies: visualization of biological molecules in their native state". Oxford University Press, 2006, p. 410.
10. P. Schwander, D. Giannakis, and A. Ourmazd, *Optics Express* 20 (2012), p. 12827.
11. N.-T. D. Loh and V. Elser, *Physical Review E* 80, (2009), 026705.
12. C. T. Koch, Determination of core structure periodicity and point defect density along dislocations. Dissertation, Arizona State University 2002, p. 32.

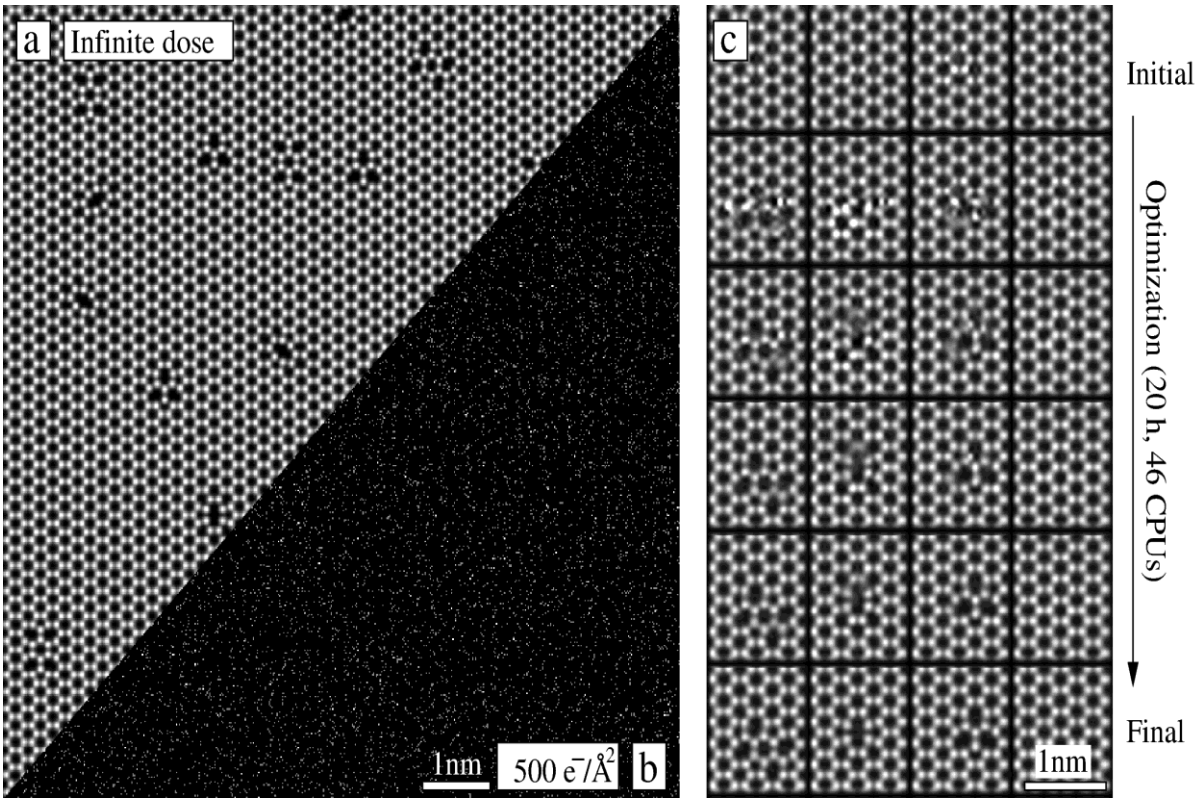

Figure 1. (a) Simulated STEM image (MAADF conditions [8], using QSTEM software [12]) of graphene with di-vacancy defecs (mixture of three different types with all possible orientations at random locations). **(b)** The same simulation for a dose of only 500 $e^-/Å^2$: Most pixels are empty (black) or show a single electron arriving at the ADF detector (gray). A total area of 3.2 μm^2 was simulated. **(c)** Maximum-likelihood reconstructions from the data set, showing 4 out of 20 model images used in the calculation (the others arrived at rotated versions of the defects or empty lattice). All defect configurations were recovered without any *a priori* knowledge, with the low-dose images being the only required input

Quantitative High-Resolution TEM/STEM and Diffraction

IM.1.P038
Calibration of HRTEM for lattice parameter measurements in nanocrystals

G. Sáfrán[1]

[1]Institute for Technical Physics and Materials Science, Research Centre for Natural Sciences, Hungarian Academy of Sciences, Thin Films Physics, Budapest, Hungary

safran.gyorgy@ttk.mta.hu
Keywords: HRTEM calibration, reference layer, composition measurement

Lattice parameter changes in nano-crystalline systems are, in most cases, indicative of altered physical, compositional and catalyst properties. High Resolution Transmission Electron Microscopy (HRTEM) is a very effective technique for the structural and morphological study of nano-crystals. Reliable interlattice spacings measurements, however, are usually problematic due to imprecise magnification of the microscope. In this work, we propose an in situ calibration technique for HRTEM: the nano-crystals of the sample are placed on the face side of a thin amorphous carbon foil, while reference (Au) nanocrystals are deposited on the back side either by evaporation or drop drying from sol. This arrangement enables, that the lattice fringes of sample and reference crystals are HRTEM-recorded simultaneously. This provides extremely precise calibration and, therefore, measurement of the interlattice spacings of the sample, as well, localization of any lattice distortions. Since sample and reference are separated by a substrate no artefacts may occur due to the physical or chemical interactions of sample and reference. The systematic calibration error caused by a typical displacement (~25nm) between sample and reference was found to be negligible (~0.001%) by simple optical model calculations. The advantages of this technique was shown by measuring decreasing lattice spacings in Au nanoparticles as a function of decreasing particles size (finite size effect). Lattice parameter changes in Au/Pd core/shell catalyst nanoparticles or in bimetallic alloy nanoparticles could be also detected. It is to mention that the measured data has to be averaged. The recorded interlattice spacings of- even- the Au reference particles shows a remarkable dispersion due to imaging conditions of particles with random misalignements to exact zone axis [1]. The buildup of a typical sample together with the reference layer is depicted by the cross sectional scheem shown in Figure 1. Figure 2. shows a high resolution TEM micrograph for to measure the finite size effect in small particles. Both the sample (2~4nm in size) and the reference (10~20nm) particles show lattice fringes simultaneously that allows precise comparison of lattice parameters. In this case we suggest that the particles of the sample (small) undergo, while that of the reference does not undergo a lattice distortion due to finite size effect, compared to bulk value.

1. J-O Malm, M.A. O'Kiefe Ultramicroscopy 68 (1997) 13-23
2. This work was supported by the Hungarian National Research Found OTKA, under the project K 101897.
3. The author acknowledge the contribution of E. Fülöp for supplying colloids of reference Au nanoparticles and of O. Geszti for lattice measurements in HRTEM micrographs

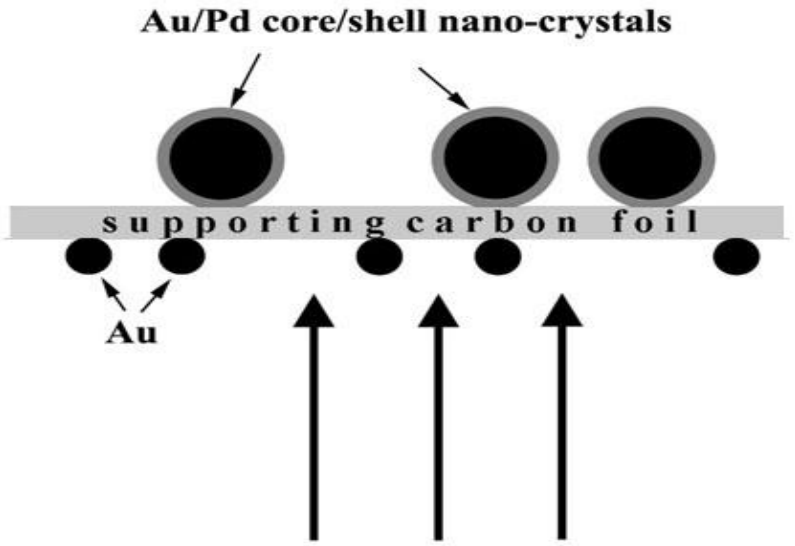

Figure 1. Set-up of a Au/Pd specimen for an in situ HRTEM calibration and measurement of fine lattice distortions. The particles of the sample are on top, while that of the reference are deposited on the bottom of a thin carbon foil.

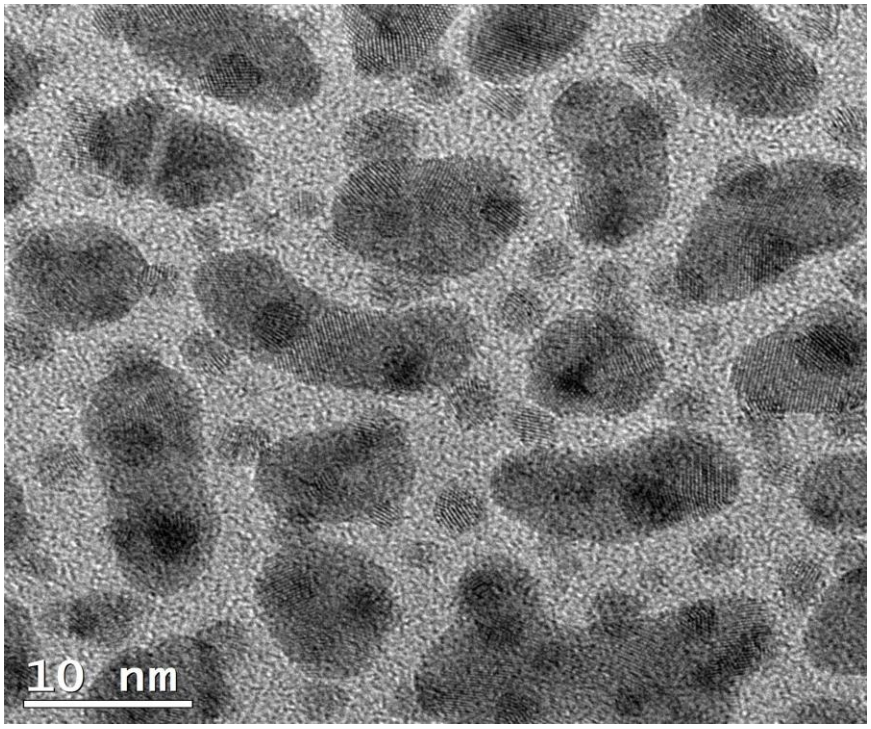

Figure 2. HRTEM micrograph that simultaneously reveal lattice fringes of both sample and reference Au nano-crystals for in situ calibration and measurements. Sample (particles 2~4 nm in size) and reference (particles 10~20nm in size) are deposited on the opposite faces of the carbon substrate.

Advances in Light and Electron Optics

IM.2.039
Advances in monochromators and aberration correctors

O. Krivanek[1], T. Lovejoy[1], N. Bacon[1], G. Corbin[1], M. Murfitt[1], N. Dellby[1]

[1]Nion, Kirkland, United States

lovejoy@nion.com
Keywords: electron optics, monochromators, spectrometers, aberration correctors, STEM

Electron-optical instrumentation and its applications have advanced rapidly in the last few years. Particularly noteworthy progress has taken place in the areas of low kV imaging and analysis, spearheaded by the SALVE project [1], the CREST triple-C project [2] and work by Nion, in rapid elemental mapping using either electron energy-loss spectroscopy (EELS) or energy-dispersive X-ray spectroscopy (EDXS) signals, in improved performance environmental microscopy, and in ultra-fast imaging and analysis. In this paper, the Nion contribution to the general progress is reviewed.

The scanning transmission electron microscope (STEM) which we recently introduced combines a bright, stable and mono-energetic cold field emission electron gun (CFEG) with an ultra-stable probe-forming column corrected to 5^{th} order and a high-stability sample stage operating in an ultra-high vacuum [3,4]. It has allowed experiments to be carried out that seemed unthinkable only a few years ago. Examples include the determination of the position and type of every atom in a monolayer material [5], detecting single atoms by X-ray spectroscopy [6], and even exploring the atomic environment of single atoms, based on their near-edge EELS fine structures [7,8].

More recently still, we have developed a High Energy Resolution Monochromated EELS-STEM (HERMES) system that uses several new design principles [9-11]. The monochromation is carried out at the ground potential (i.e., at the full primary energy) rather than inside the electron gun, with an all-magnetic monochromator (MC) consisting of a main energy-dispersing prism, spectrum-magnifying quadrupoles, auxiliary prisms that bend the beam into an alpha-type trajectory, an energy-selecting slit equipped with current sensing, and aberration-correcting sextupoles and octupoles. The MC uses dispersing-undispersing optics such that the energy dispersion of the beam is precisely cancelled at its exit. The MC's main prism winding is connected in series with the prism of an all-magnetic EEL spectrometer, which means that the energy spectra formed at the slit and at the EELS detector track each other, and small instabilities in the prism supply current do not change the position of the spectrum on the final detector. The high tension (HT) of the microscope is stabilized by sensing the electron current falling on the two halves of the MC's slit in a feedback scheme that adjusts the HT such that the energy-dispersed beam remains precisely centered on the slit opening.

The above approach is roughly equivalent to two parallel EELS systems running back-to-back and thus more complicated than other MC designs. However, it provides several key advantages. First, because the beam traverses the MC at the full energy and the beam intensity is reduced by a pre-MC beam-defining aperture, statistical Coulomb interactions between the beam electrons are greatly reduced, allowing good energy resolution to be reached without broadening the beam unduly. Second, connecting the MC and EELS prisms in series, which is possible precisely because the MC operates on the full-energy beam, results in very good short- and especially long-term energy stability. Third, full energy electrons are less sensitive to effects such as charging at the slit edges, and this allows the system to achieve very good spatial resolution while monochromating.

HERMES has been able to reach 12 meV full-width at half-maximum (FWHM) of the EELS zero loss peak (ZLP) in a short-exposure spectrum at a primary energy of 60 keV (Fig. 1), and 20 meV FWHM in spectra acquired for several seconds. Fig 2. shows a low-loss spectrum of an SiO_2 layer in a MOSFET device acquired at about 40 meV energy resolution at 60 keV. Fig. 3 shows Si L-edges in elemental Si and in SiO_2. Further improvements in energy resolution should become possible once the detector part of the column and the EELS are brought up to the ultra-stable design standards used in the probe-forming part of the column, and we are now working in this direction.

When the energy-selecting slit is opened to admit an electron beam about 100 meV wide at 60 keV primary energy, the spatial resolution of the system is improved compared to running with the MC turned off (and the beam going straight through it), or the MC on and the energy-selecting slit withdrawn from the beam [10]. This is because at primary energies <100 keV, the size of the unmonochromated probe in the Nion STEM is mainly limited by chromatic aberration (C_c), and decreasing the beam energy spread reduces C_c's influence. Bypassing the chromatic resolution

barrier shifts the attention back to geometric aberrations. We are presently working on incorporating extra sextupoles in the Nion C3/C5 quadrupole-octupole probe corrector [12] for more flexible control of parasitic aberrations. The sextupoles work together with other multipoles of the corrector and produce a rich set of combination aberrations, which allows all the important parasitic aberrations up to fifth order to be adjusted via a small subset of controls that addresses each aberration in turn [13]. This should allow HERMES to form aberration-corrected electron probes with semi-angles of up to about 50 mrad, and to reach probe sizes of about 0.8 Å at 60 keV and about 1.2 Å at 30 keV.

1. www.salve-project.de/home.html
2. H. Sawada et al., Advances in Imaging and Elect. Phys. 168 (2011) 298.
3. O.L. Krivanek et al., Ultramicroscopy 108 (2008) 179.
4. N. Dellby et al., Europ. Phys. J. Appl. Phys. 54 (2011) 33505.
5. O.L. Krivanek et al., Nature 464 (2010) 571.
6. T.C. Lovejoy et al., Appl. Phys. Lett. 100 (2012) 154101.
7. W. Zhou et al., Phys. Rev. Lett. 109 (2012) 206803.
8. Q.M. Ramasse et al., Nano Lett. (2012) DOI: 10.1021/nl304187e.
9. O.L. Krivanek et al., Phil. Trans. Roy. Soc. A36 (2009) 3683.
10. O.L. Krivanek et al., Microscopy 62 (2013) 3.
11. O.L. Krivanek and N. Dellby, (2013) US patent #8373137.
12. N. Dellby et al., Physics Procedia 1 (2008) 179.
13. N. Dellby et al., submitted to Ultramicroscopy.

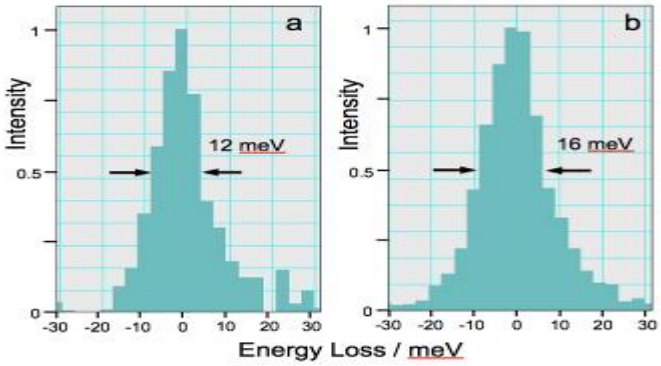

Figure 1. Zero Loss Peaks (ZLPs) acquired in a) 2 ms and b) 55 ms at 60 keV. Nion HERMES, Gatan Enfinium EELS.

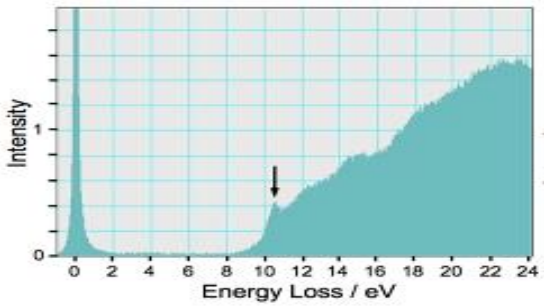

Figure 2. Low loss spectrum of SiO_2 acquired in 0.2 s at 60 keV. The ZLP maximum intensity is 302. Band edge exciton is marked by an arrow.

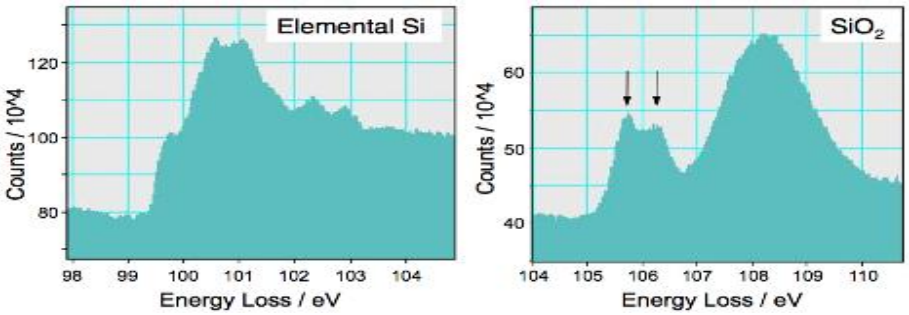

Figure 3. Si $L_{2,3}$ electron energy loss spectra in crystalline Si and in SiO_2. Nion HERMES, Gatan Enfinium EELS, 100 keV. L_3/L_2 splitting of 0.6 eV is marked by arrows in the SiO_2 spectrum.

Advances in Light and Electron Optics

IM.2.040
Monochromatizing without filtering using dynamic fields without bunching: A new concept for d-TEM illumination

R. Janzen[1], C. Koch[2], G. Schönhense[3], A. Parvizi[2]

[1]Laboratorium für Elektronenmikroskopie / KIT, Karlsruhe, Germany
[2]Institut für Experimentelle Physik, Universität Ulm, Ulm, Germany
[3]Institut für Physik, Johannes Gutenberg Universität Mainz, Mainz, Germany

roland.janzen@kit.edu
Keywords: monochromators, dynamic fields, d-TEM, plasmonic field emitters

Commonly used monochromators are energy filters. The majority of the particles with undesired energies is removed. Thus the output current diminishes with increasing degree of monochromatization.

Monochromators in the original meaning of the word that would affect the energy of the particles by an energy selective acceleration can only be realized by use of dynamic fields.

Dynamic field applications without exception involve a condition between the phase of the dynamic field and the entrance point of time of the particle into the field. If this condition is fulfilled, the dynamic field application works exactly. Unfortunately the width of the time interval where the condition is fulfilled is mathematically zero. Thus up to now dynamic field applications in charged particle optics limit themselves to a small time interval around the periodically recurring point of optimum phase where the condition is fulfilled to a good approximation. For that purpose bunches are formed around the optimum phase point. Unfortunately bunch forming suffers from Liouville's theorem: The product of the bunch length and the energy spread within it is a constant.

In this work a concept is presented that circumvents this dilemma. A circularly polarized standing wave deflects the charged particle beam to a rotating orbital feeding the particles into a propagating wave that rotates within a toroidal wave guide (see figure 1.). The circular deflection supplies a time coding. The entrance point of time of any particle is locked to its azimuthal position. Provided that the deflecting field and the rotating propagating wave (denoted by working field in the following) are synchronized correctly the optimum phase condition is fulfilled exactly and constantly. Time uncertainty vanishes within the limits of technical & practical implementing of the concept. The working field may be cascaded. It can be used for a large variety of applications such as monochromatizing, accelerating, pulse forming, spread amplification, spread inversion, time focusing and aberration correction (only examples for monochromatizing and time focusing applications will be given in this contribution). In the end the spiral orbital may be focused to an inverse circular deflector that undoes the action of the first circular deflector and thus leads the particles back to the original axis (see figure 2.).

Computer simulations assuming theoretically ideal TE10 mode microwaves as dynamic fields showed that the dispersion of circular deflection can arbitrarily be chosen. Furthermore a monochromator based on circular deflection was demonstrated to work by computer simulation. The energy spread vanishes within the limits of technical & practical implementing of the concept without any loss of current.

Finally, a vision of a dynamic TEM illumination column based on circular deflection yielding equidistant monochromatic single-electron pulses will be presented. The latter concept makes use of plasmonic field emitters synchronized to the deflection and working fields.

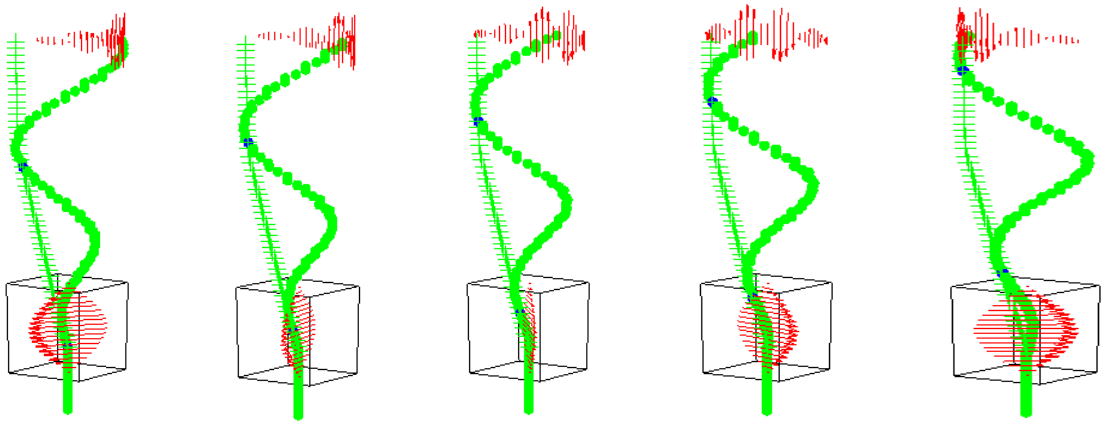

5 snapshots of animation showing circular deflection; Roland Janzen

Figure 1. Five snapshots of an animated schematic drawing illustrating the principle of a typical circular deflection application. The circular deflector wave is a circularly polarized standing wave within a cubic resonator. The electric field vector (shown by the lower group of red arrows) rotates, always pointing perpendicularly to the direction of motion (which is in this figure assumed to point upwards) of the electrons (green). The working field is represented by the upper group of red arrows. It is a propagating wave that is rotating within a toroidal resonator (not shown). If both waves are synchronized properly all electrons arrive at the working field at optimum phase. The electron marked in blue and the corresponding trajectory marked by crosses show that the deflected electrons do not have any azimuthal velocity though their orbital performs a spiral rotation.

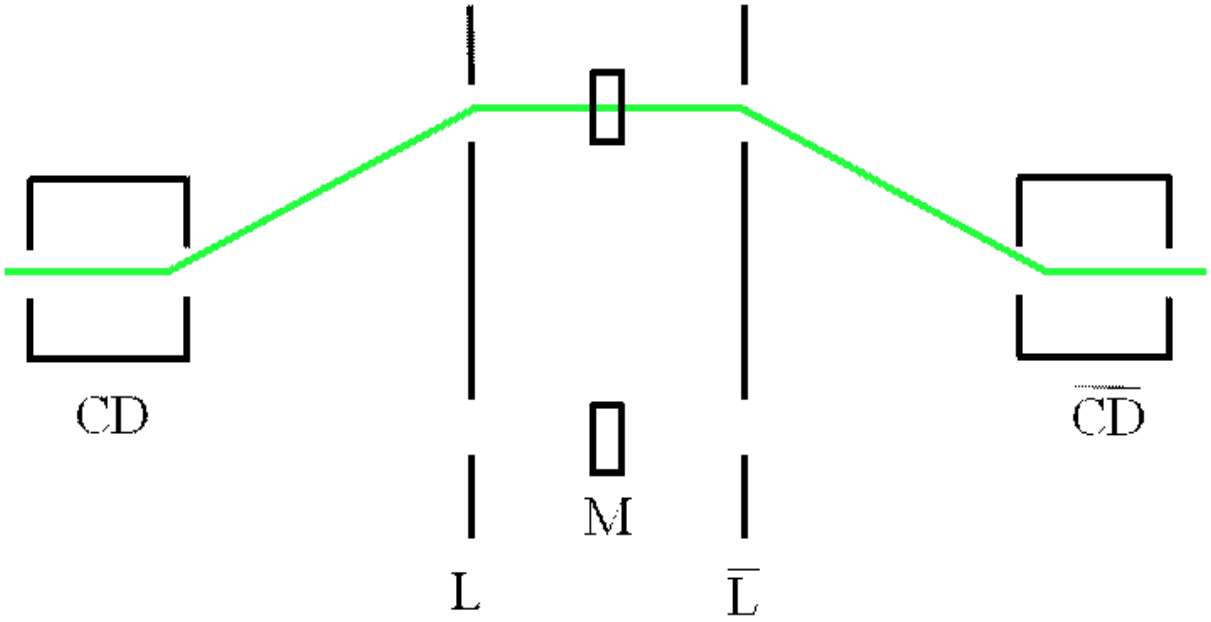

Scheme of circular deflection based monochromator, Roland Janzen

Figure 2. Schematic drawing (cross sectional view) of a simplified monochromator design based on circular deflection. Note that in difference to figure 1 the electrons are assumed to move from left to right. They are deflected by the circular deflector CD, focused by some lens like element L, monochromatized by the working field inside the toroidal resonator M, focused again and deflected by an 'undoing' circular deflector in the end. In order to emphasize the symmetry of the design we used the complex conjugate notation for the names of the elements at the right hand side of the monochromating wave

Advances in Light and Electron Optics

IM.2.041
Electrostatic Zach phase plates for transmission electron microscopy

S. Hettler[1], J. Wagner[1], M. Dries[1], N. Frindt[2], R.R. Schröder[2], D. Gerthsen[1]

[1]Karlsruher Institut für Technologie, Laboratorium für Elektronenmikroskopie, Karlsruhe, Germany
[2]Universität Heidelberg, CellNetworks, BioQuant, Heidelberg, Germany

simon.hettler@kit.edu
Keywords: phase plate, phase contrast, transmission electron microscopy

Physical phase plates (PP) for transmission electron microscopy (TEM) enhance the phase contrast by inducing an additional relative phase shift between the scattered and unscattered electrons. The phase shift can be achieved by the mean inner potential of a thin-film PP [1] or by electrostatic PPs which produce a localized electrostatic potential in the back focal plane of the objective lens [2]. While thin-film PPs induce a fixed phase shift determined by the film thickness, electrostatic PPs provide adjustable phase shifts which are determined by the applied voltage. Some groups have already shown contrast enhancement using a Boersch PP in TEM [3,4]. However, the contrast shown in these publications is dominated by the effects of complete obstruction of electrons at low spatial frequencies by the central ring electrode and the three supporting bars. The obstruction is significantly reduced by the Zach PP [5] (Figure 1a), a PP design consisting of a microcoaxial cable with an open end. The Zach PP comprises an inner electrode which is surrounded by an insulating and a shielding metal layer. The tip width and thus the obstruction of electrons are minimized by an improved fabrication process. The localization of the electrostatic potential is improved by a small open electrode area of 300nm x 60 nm (Insert of Figure 1a). The implementation of a micro-structured heating device yields significantly reduced contamination and electrostatic charging [6].

The inhomogeneous electrostatic field created by the Zach-PP decays rapidly with increasing spatial frequencies as shown in Figure 1b. However, a non-zero phase shift is imposed on electrons passing the PP-tip at low spatial frequencies. Within this “soft” cut-on frequency range, the relative phase shift decreases. Hence, the achievable phase contrast is reduced for low spatial frequencies, which limits phase contrast formation to objects with sizes below 10 nm. Nevertheless, this is an advantage compared to the total obstruction of low spatial frequencies by Boersch PPs.

We present results obtained with a Zeiss Leo 912 Ω equipped with a LaB_6 cathode and a Zach PP. Figure 2 shows images of small CdSe nanoparticles (6-8 nm) deposited on an amorphous carbon film for different applied voltages. The film and the particles exhibit astigmatism-like contrast in the image without applied voltage (Figure 2b) arising from the obstruction of electrons by the Zach-PP bar and the abrupt phase shift change at the PP-tip. If a voltage is applied, positive and negative phase contrast is achieved as demonstrated by Figure 2a and Figure 2c.

Figures 3a-c show three power spectra and small sections of the corresponding PP-TEM images of ~2 nm Au nanoparticles deposited on an amorphous carbon film. The power spectra reveal good imaging conditions without obvious effects of contamination and charging. The phase shift is clearly recognizable by the shift of Thon-rings.

PP-assisted object wave reconstruction is possible with an inline holography method using three PP-TEM images taken at different phase shifts [7]. This method is not restricted to weak-phase objects as the phase shift is only imposed on the zero-order beam and nonlinear image contributions are eliminated in the calculation of difference images. Figure 4 shows the reconstructed amplitude and phase of the Au nanoparticles shown in the inserts of Figure 3.

1. R. Danev, K. Nagayama, Ultramicroscopy 88 (2010), p. 243-252.
2. K. Schultheiß et al., Rev. Sci. Instrum. 77 (2006), 033701.
3. E. Majorovits et al., Ultramicroscopy 107 (2007), p. 213-226.
4. D. Alloyeau et al., Ultramicroscopy 110 (2009), p. 563-570.
5. K. Schultheiß et al., Microsc. Microanal. 16 (2010), p. 785-794.
6. S. Hettler et al., Microsc. Microanal. 18 (2012), p. 1010-1015.
7. B. Gamm et al., Ultramicroscopy 110 (2010), p. 807-814.
8. This work is funded by the German Research Foundation (DFG) under contract Ge 841/16 and Sch 424/11.

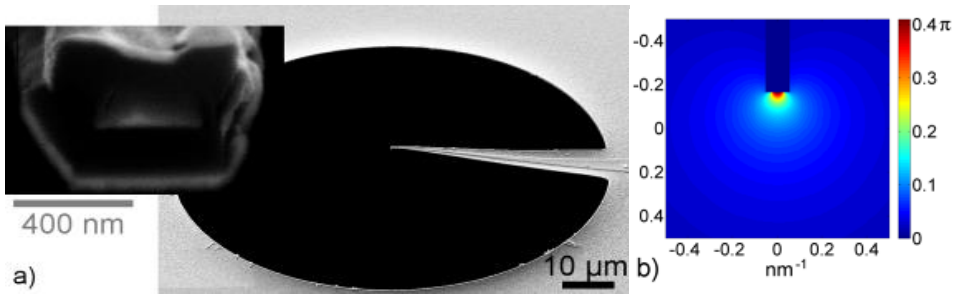

Figure 1. a) Scanning electron microscopy image of a Zach PP. The insert shows the open end of the Zach PP revealing the inner Au electrode, the surrounding insulator (dark contrast) and shielding Au layer. The aperture size is about 80 µm, the tip width is 800 nm. b) Phase shift of a Zach PP simulated for 1 V applied voltage, an electron energy of 120 keV, and 3.6 mm focal length of the objective lens. The phase shift has its maximum at the PP tip and decays rapidly towards increasing spatial frequencies.

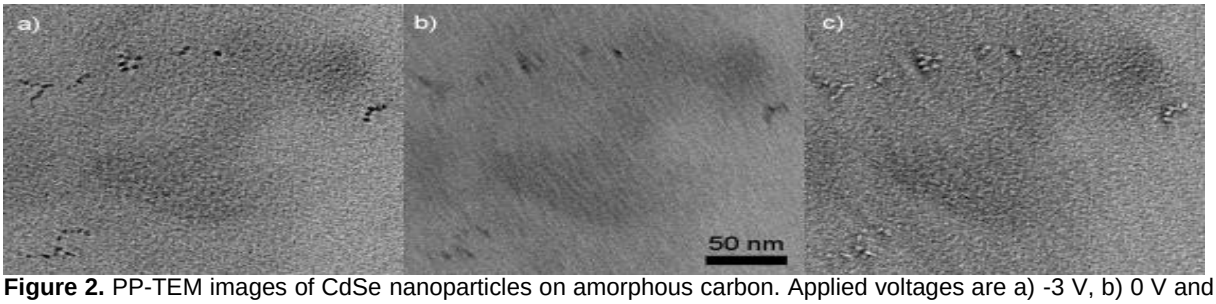

Figure 2. PP-TEM images of CdSe nanoparticles on amorphous carbon. Applied voltages are a) -3 V, b) 0 V and c) + 3 V. The astigmatism-like contrast visible in b) arises from obstruction of electrons by the PP bar. Phase contrast inversion is obtained by inverting the applied voltage.

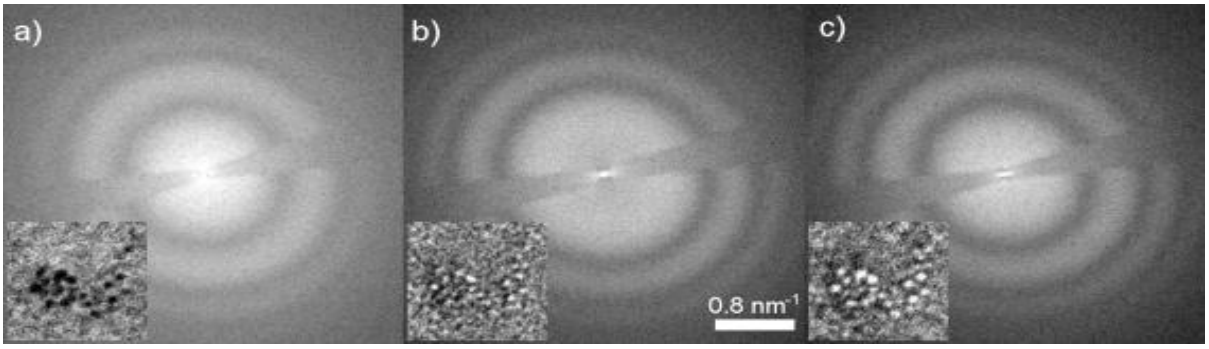

Figure 3. Power spectra of PP-TEM images of Au nanoparticles deposited on an amorphous carbon film. Inlays show 26 nm x 26 nm of the corresponding images. Applied voltages are a) -2 V, b) 0 V and c) + 1 V resulting in a shift of Thon-rings. No contamination and charging artifacts are visible. The defocus value is about -380 nm.

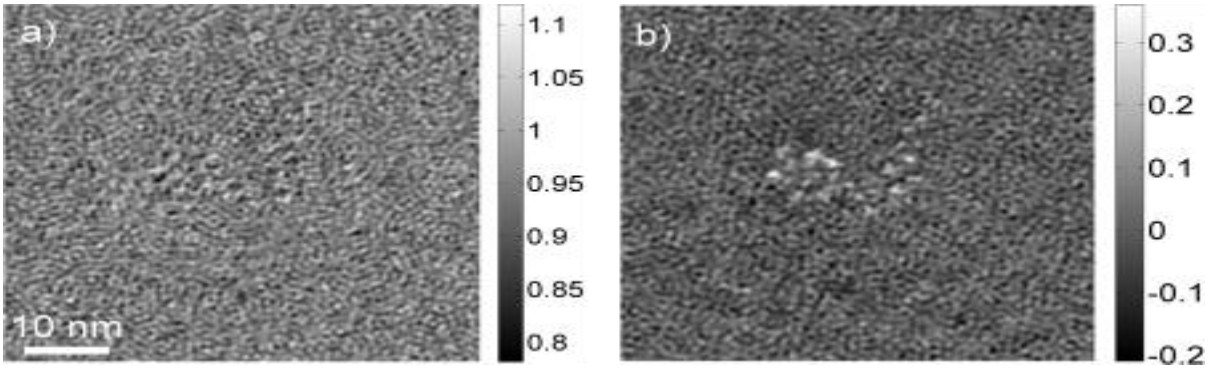

Figure 4. Reconstructed a) Amplitude and b) Phase of Au nanoparticles shown in the PP-TEM images inserted in the PP-TEM images inserted in Figure 3.

Advances in Light and Electron Optics

IM.2.042
On the reconstruction of ultra low-energy electron holograms and diffraction patterns

T. Latychevskaia[1], J.-N. Longchamp[1], C. Escher[1], H.-W. Fink[1]

[1]University of Zurich, Physics, Zurich, Switzerland

tatiana@physik.uzh.ch
Keywords: low-energy electrons, holography, coherent diffraction imaging, phase retrieval

Low-energy electrons (50-250 eV) have been proven to be the best known radiation for imaging individual biological molecules at high resolution, as they have a sufficiently short wavelength (0.7-1.7 Å) and inflict the least radiation damage [1]. Two dedicated low-energy electron microscopes for imaging individual biomolecules are operated in our group: performing either holographic or coherent diffractive imaging (CDI). In both microscopes, a coherent divergent spherical electron wave is generated by field emission from a sharp tungsten tip. In the holographic microscope, part of the divergent wave is scattered by a sample, and the scattered and unscattered wave form an interference pattern – the hologram [2]. In the CDI microscope, the divergent electron wave is collimated by a microlens [3] and the parallel plane wave impinges onto the sample. The far-field diffraction pattern is recorded at a distant detector. Holograms and diffraction patterns are then subject to numerical reconstruction.

We will present holograms of individual biomolecules such as DNA [4-5], bacteriophage [6] and functionalized nanotubes [7] and discuss the key issues concerning their reconstruction. This includes: Problems associated with the elimination of the twin image [8] intrinsic to Gabor's type holography [9-10], and implementing low-energy electron wave scattering properties into classical light optics wave propagation integrals. Numerical solutions and artifact-free reconstructions of experimental holograms will be presented, see an example in Figure 1. We recently showed how holography and CDI can be merged into one superior technique: holographic coherent diffraction imaging (HCDI) [11]. In HCDI, two records of the same sample, a hologram and a diffraction pattern, are used. In the reconstruction, HCDI employs an iterative phase retrieval algorithm where the initial phase distribution is not random as in conventional methods, but directly obtained from the hologram. Such well-defined initial phase distribution provides a stable convergence of the iterative procedure towards a unique solution. Thus, reconstructions obtained by HCDI combine the highest possible resolution and uniqueness of the solution. Reconstructions of experimental low-energy electron diffraction patterns of carbon nanotubes and of free-standing graphene at 2.13 Å resolution will also be presented.

1. M. Germann *et al.*, Phys. Rev. Lett. 104, 095501 (2010).
2. H.-W. Fink, W. Stocker, and H. Schmid, Phys. Rev. Lett. 65, 1204-1206 (1990).
3. E. Steinwand, J.-N. Longchamp, and H.-W. Fink, Ultramicroscopy 110, 1148-1153 (2010).
4. H.-W. Fink *et al.*, J. Opt. Soc. Am. A 14, 2168-2172 (1997).
5. T. Latychevskaia *et al.*, in *Present and Future Methods for Biomolecular Crystallography* (Springer, 2013).
6. G. B. Stevens *et al.*, Eur. Biophys. J. 40, 1197-1201 (2011).
7. J.-N. Longchamp *et al.*, Appl. Phys. Lett. 101, 093701 (2012).
8. T. Latychevskaia, and H.-W. Fink, Phys. Rev. Lett. 98, 233901 (2007).
9. D. Gabor, Nature 161, 777-778 (1948).
10. D. Gabor, Proc. R. Soc. A 197, 454-487 (1949).
11. T. Latychevskaia, J.-N. Longchamp, and H.-W. Fink, Opt. Express 20, 28871-28892 (2012).

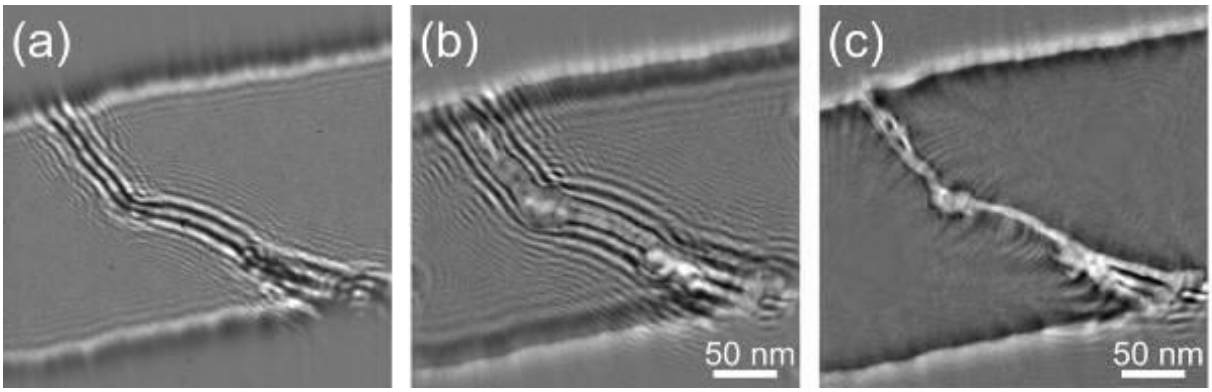

Figure 1. (a) 100 eV low-energy electron hologram of a bundle of nanotubes. (b) Conventional reconstruction of the hologram. (c) Optimized reconstruction of the hologram.

Advances in Light and Electron Optics

IM.2.043
Single molecule imaging and quantification in the cell nucleus by reflected light sheet microscopy

J. C. M. Gebhardt[1,4], D. M. Suter[1,5], R. Roy[1,6], Z. W. Zhao[1,2], A. R. Chapman[1,2], S. Basu[1,3,7], T. Maniatis[3] , X. S. Xie[1]

[1]. Department of Chemistry and Chemical Biology, Harvard University, Cambridge, MA, USA
[2]. Graduate Program in Biophysics, Harvard University, Cambridge, MA, USA
[3]. Department of Biochemistry and Molecular Biophysics, Columbia University Medical Center, New York, NY, USA
[4]. current address: Institute of Biophysics, Universität Ulm, Ulm, Germany
[5]. current address: Institute of Bioengineering, Ecole Polytechnique Fédérale de Lausanne, Lausanne, Switzerland
[6]. current address: Department of Chemical Engineering, Indian Institute of Science, Bangalore, India
[7]. current address: University of Cambridge, Department of Biochemistry, Cambridge, UK

Single fluorescent molecule imaging in the mammalian nucleus is challenged by out-of-focus fluorescent background in common microscopy schemes. We report a novel illumination method, reflected light sheet microscopy (RLSM), that enables selective plane illumination throughout the nucleus of living mammalian cells [1]. Generation of a thin light sheet parallel to the imaging plane and close to the sample surface is achieved by reflecting an elliptical laser beam incident from the top by 90° with a small mirror (Figure 1). The thin light sheet allows for an increased signal-to-background ratio superior to previous illumination schemes and enables imaging of single fluorescent proteins with up to 100 Hz time resolution. With the new microscope we measured the DNA-bound fractions and residence times of the transcription factor glucocorticoid receptor (GR) and distinguished different modes of binding to DNA, including indirect binding via protein-protein interactions. Analogous experiments on estrogen receptor (ER) yielded similar results. Moreover, we demonstrated two-color single molecule imaging by observing the spatio-temporal co-localization of interacting protein pairs [1]. In a second set of experiments, we combined RLSM with superresolving stochastic optical reconstruction microscopy (STORM) imaging and molecular counting, and quantitatively mapped the positions and the abundance of RNA polymerase II throughout the nucleus. We found a homogenous distribution, inconsistent with the model of transcription factories.

1. J.C.M. Gebhardt*, D.M. Suter*, R. Roy, Z.W. Zhao, A.R. Chapman, S. Basu, T. Maniatis, and X.S. Xie, Nature Methods 10 (2013), p421-426

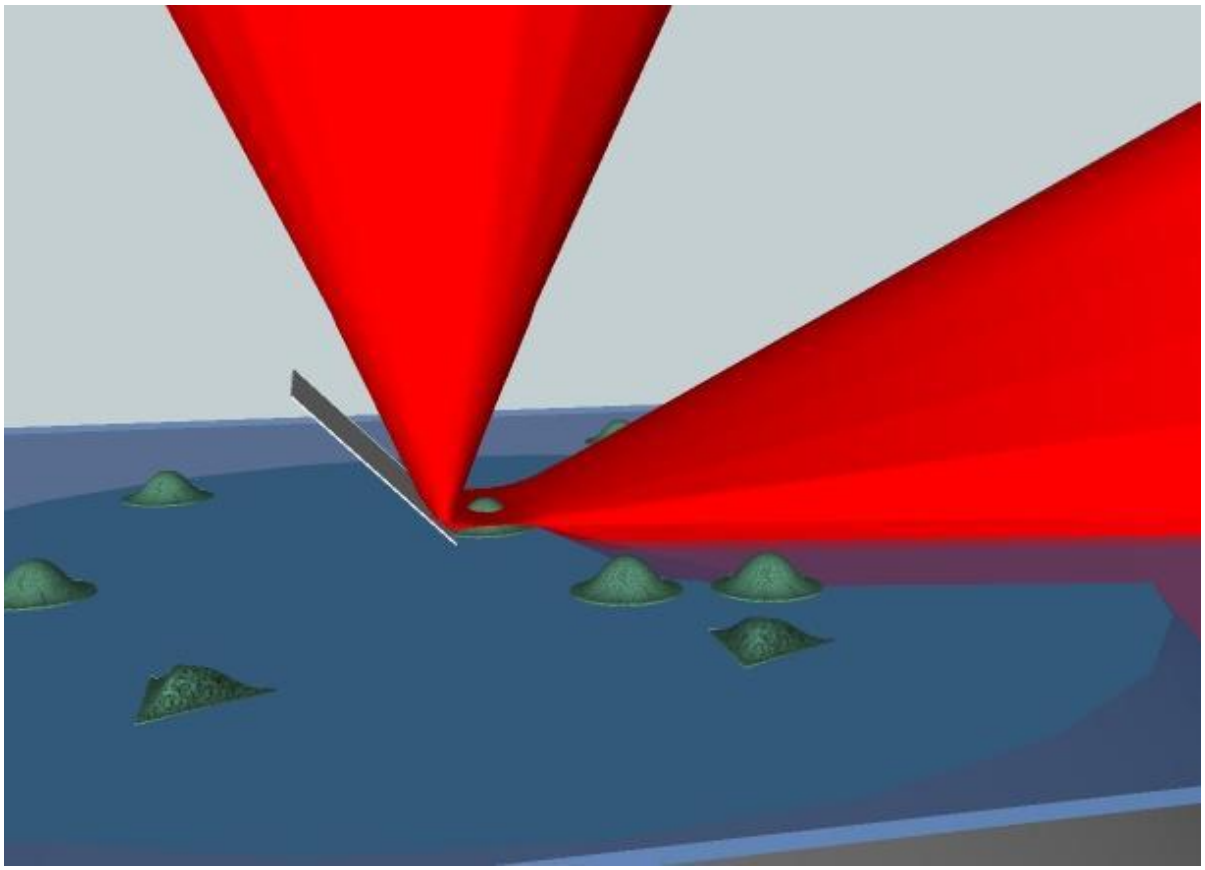

Figure. Scheme of the principle of reflected light sheet microscopy

Advances in Light and Electron Optics

IM.2.044
Direct exploring the electron transfer of Cytochrome *c* by electrochemically modulated multichannel microscopy

Y.-T. Li[1], H. Zhou[1], L.-L. Qu[1], D.-W. Li[1], Y.-T. Long[1]

[1]East China University of Science and Technology, Shanghai, China

ytlong@ecust.edu.cn

The understanding of life process increasingly depends on our ability to monitoring and visualizing the electron transfer process with high spatial and temporal resolution [1]. However, the investigation of electron transfer at the biomolecule-metal interface remains a fundamental challenge. The first profound difficult is *in situ* monitoring electron transfer process on the interfaces. The second major barrier to progress is that the information obtained by spectroscopic methods is restricted to ensemble averages [2].

The combination of *in situ* analytical techniques with spectral microscopy enables the bridging of this gap. The advent of dark-field microscopy (DFM) helped to real-time probe redox reactions at single nanoparticles with high sensitivity. While spatial confinement of electrons in gold nanoparticles (GNPs) will lead to scattering and absorption resonances, whose energies are altered by electron density changes [3]. Therefore, monitoring the localized surface plasmon resonance (LSPR) spectral shifts permits *in situ* spectroscopically observed the electron transfer process precisely under electrochemical modulation. In addition, surface enhanced Raman scattering (SERS) is possible to selectively probe the vibrational spectra of immobilized biological molecules without structural destruction [4].

Herein, we established an attractive electrochemically modulated multichannel microscopy (EMMM) device by coupling a DFM to a charge coupled device (CCD) camera, CCD spectrograph, Raman laser, and an electrochemical workstation (Figure 1). This set-up enables us to simultaneously measure the potential-dependent LSPR spectra and SERS spectra of biomolecules with the corresponding dark-field images at the single-nanoparticle level. As a proof-of-principle experiment, the redox reaction of Cytochrome *c* (Cyt-*c*) at single GNP was monitored *in situ* based on plasmon resonance energy transfer (PRET) of single Cyt-*c* functionalized GNP (CGNP) [5]. The LSPR band shifts and the changes of plasmon quenching dips illustrate that the electron transfer process is reversible between single GNP and Cyt-*c* when potential is cyclically applied. Moreover, the intensity changes of *in situ* SERS spectra of single CGNP imply the transformation changes of Cyt-*c* through electron transfer reaction. The development of the EMMM set-up promises a broad range of potential applications in real-time monitoring of electron transfer and other chemical reaction processes, down to the single-nanoparticle level.

1. C. Novo, A.M. Funston and P. Mulvaney, Nat. Nanotechnol. 3 (2008), p. 598-602.
2. F.M. Boldt, et al. Anal. Chem. 76 (2004), p. 3473-3481.
3. L. Zhang, et al. Angew. Chem. Int. Ed. 123 (2011), p. 6921-6924.
4. S.M. Nie and S.R. Emory. Science 275 (1997), p. 1102-1106.
5. G.L. Liu, et al. Nat. Methods. 4 (2007), p. 1015-1017.
6. We kindly acknowledge the help of the organizers of MC 2013 with the online submission procedure.

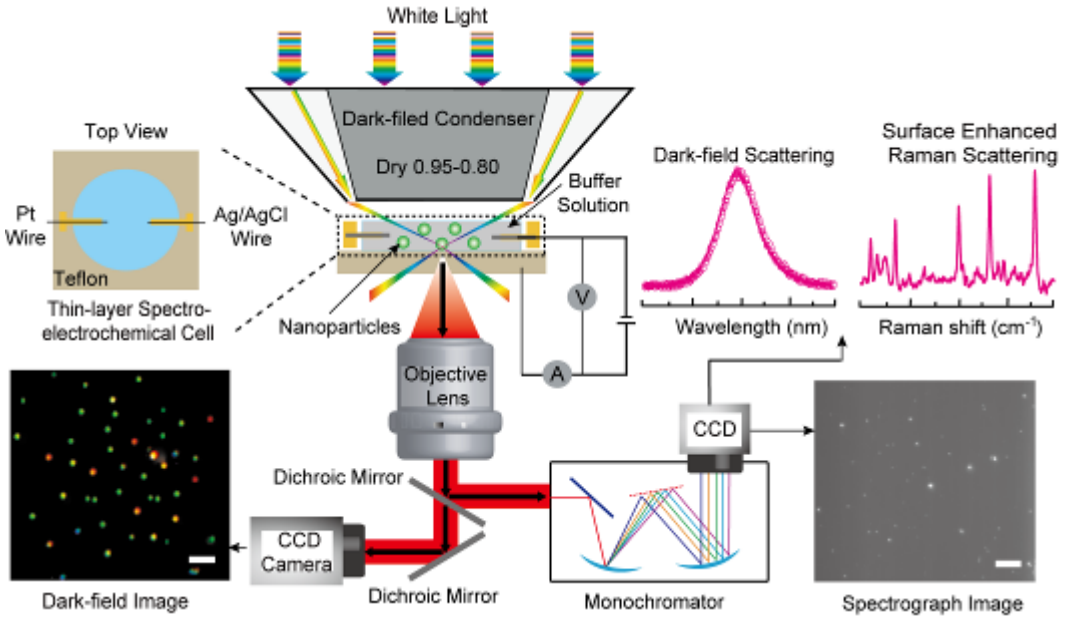

Figure 1. Schematic diagram of the electrochemical modulated multichannel microscopy (EMMM). Representative LSPR spectrum, Raman spectrum, and the corresponding image signatures were obtained on EMMM. The potential-dependent spectroscopic properties were performed in a thin-layer spectroelectrochemical cell. The images and corresponding spectra signatures are drawn based on representative data. The scale bar is 5 μm.

Advances in Light and Electron Optics

IM.2.P045
Low voltage STEM observation in the latest FE-SEM

M. Sasajima[1], K. Koyama[1], N. Sakamoto[1], S. Takeuchi[1], H. Sato[1]

[1]Hitachi High-Technologies Corp., Hitachinaka, Ibaraki, Japan

sasajima-masahiro@naka.hitachi-hitec.com
Keywords: Low voltage STEM, FE-SEM

Ultra high resolution FE-SEM has been broadly utilized for semiconductors and nano materials as an advanced analytical tool. High efficiency signal detection capability and high resolution, high contrast imaging are most effective for research on compositional materials in the field of material science and engineering.

In this study, newly developed STEM holder for FE-SEM low accelerating voltage observation having capabilities of both Bright Field STEM (BF-STEM) and Dark Field STEM (DF-STEM) is used. It is well known that low voltage STEM observation on FE-SEM provides high contrast imaging of low Z compositional materials compared with that of STEM observation on TEM. The newly developed specimen holder with DF-STEM detection system can also be simultaneously used when BF-STEM signal is detected[1,2].

Figure 1 shows the schematic of the BF/DF-STEM detection system for FE-SEM. The detection angle of BF signal is controlled by the STEM aperture and inner crystal information on specimen would be obtained through BF signals generally, while newly developed DF-STEM detection system would have the movable detection element which can be vertically traversed to change the detection angle of DF-STEM signals, so that we can clearly obtain an optimal Z-contrast image.

Figure 2 shows the BF-STEM (a) and DF-STEM (b) imaging of carbon nano tube (CNT) containing iron particles. Both images are of the same field of view at accelerating voltage of 30kV. In the BF-STEM Image (a), not only iron and CNT contrasts but also diffraction contrast reflecting the crystal structure of CNT wall can be clearly observed. In the DF-STEM Image (b), high Z-contrast image is clearly observed by using of the movable detection element which enables us to obtain the optimized position. On top of that, highly precision EDS analysis utilizing the Z-contrast image on the DF-STEM is also available.

1. S. Watanabe et al, J. Electron Microsc. 59(Suppl1) (2003) p.196
2. S. Takeuchi et al, IMC16, Sapporo Conference Proceedings (2006) p.660.CD.

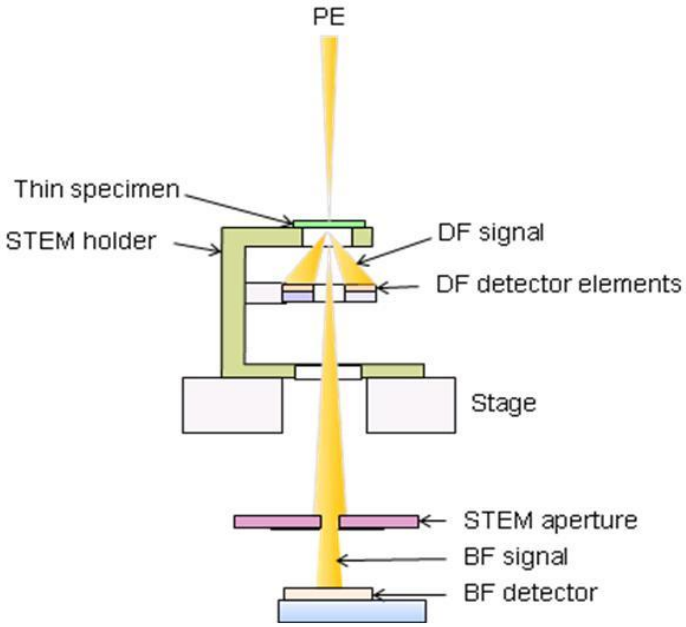

Figure 1. BF/DF-STEM detection system

Figure 1.

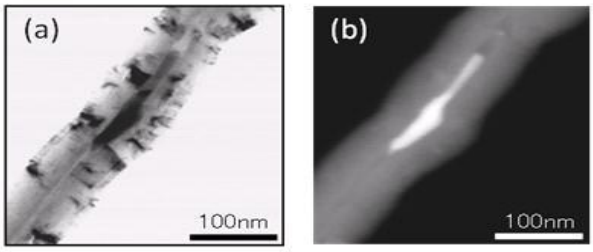

Figure 2. Low voltage STEM observation of CNT
(a) BF-STEM (b) DF-STEM

Figure 2.

Advances in Light and Electron Optics

IM.2.P046
Comparison of 2- and 3-Condenser Illumination in Off-axis Electron Holography

F. Genz[1], T. Niermann[1], M. Lehmann[1]

[1]Technische Universität Berlin, Institut für Optik und Atomare Physik, Berlin, Germany

florian.genz@physik.tu-berlin.de
Keywords: 3-condenser illumination, electron holography

Off-axis electron holography gives the possibility to obtain additional information about an investigated object by retrieving the image phase [1]. In different holography setups the quality of the reconstructed phase may vary. To determine whether two phase values can be clearly separated from each other at a given signal-to-noise ratio, the variance of the phase $\delta\Phi$ can be estimated with the fringe contrast V and the number of electrons N, that were used for imaging [2]. Since these parameters change with different illumination conditions, a comparison of a 2-condenser and a 3-condenser illumination system was done. In the 2-condenser system the second condenser lens is used to illuminate the desired specimen region and to form a divergent or convergent beam. A parallel illumination is possible with only one certain lens excitation and thereby normally not available. In the 3-condenser system the last two lenses both are used for changes in the illumination. In general, both lens excitations are modified to ensure parallel illumination conditions, independent of the size of the illuminated area. For the comparison of both illumination systems mechanical instabilities were neglected. If the contrast reduction by the camera's modulation transfer function is corrected, the fringe contrast is damped by the spatial coherence μ_{SC} only. This simplified system was described as a gaussian beam [3]. In gaussian optics focal points have a finite widening ω, the waist size, which determines the effective angular width of the source φ and hence the conditions for spatial coherence in the system. The number of electrons is set by the extent of the hologram in comparison with the spread of the gaussian beam at the same plane (fig.1). For the calculations the hologram was described as aperture with radius a (fig.1). For a given waist size ω_0, which depends on the source size and the focal length of the first condenser lens, the optimum focal length of the second condenser lens (C2) can be found. The simplified 2-condenser system shows a minimum at a spatial coherence damping of about 0.62 (fig. 2(a)), what is in good comparison to other considerations, where an exact value of $e^{-0.5} \approx 0.61$ was found [4]. In the 3-condenser system the same distances and starting waist size were chosen. The second condenser was kept at a fixed value and the third condenser lens (C3) varied. Equal results in spatial coherence damping and number of electrons were found in both systems.

However, some differences in the two illumination systems exist: The minimum of $\delta\Phi$ is slightly flatter in the 2-condenser system (fig. 2) and tolerates a greater variation of the focal length. Additionally, the optimum focal length in the 3-condenser system does not produce parallel illumination anymore. On the contrary, the divergence angle is in general smaller in the 2-condenser system (in the presented example about 2.5 times smaller). Due to this, the original purpose of the 3-condenser system, the parallel illumination of the desired specimen region, is no longer ensured.

In conclusion, the 3-condenser system with its parallel illumination does not provide an advantage in electron holography, since the focal lengths of the condensing lenses have to be changed for best phase resolution. If these changes are done, the same hologram properties as in the 2-condenser system are possible, but the divergence angle is in general larger. This was confirmed by experiment.

1. M. Lehmann, H. Lichte, Microscopy and Microanalysis 8 (2002), p. 447-466.
2. F. Lenz, Optik 79 (1988), p.13-14.
3. H. Kogelnik, Applied Optics 4 (1965), p. 1562-1569.
4. H. Lichte, Ultramicroscopy 108 (2008), p. 256-262.

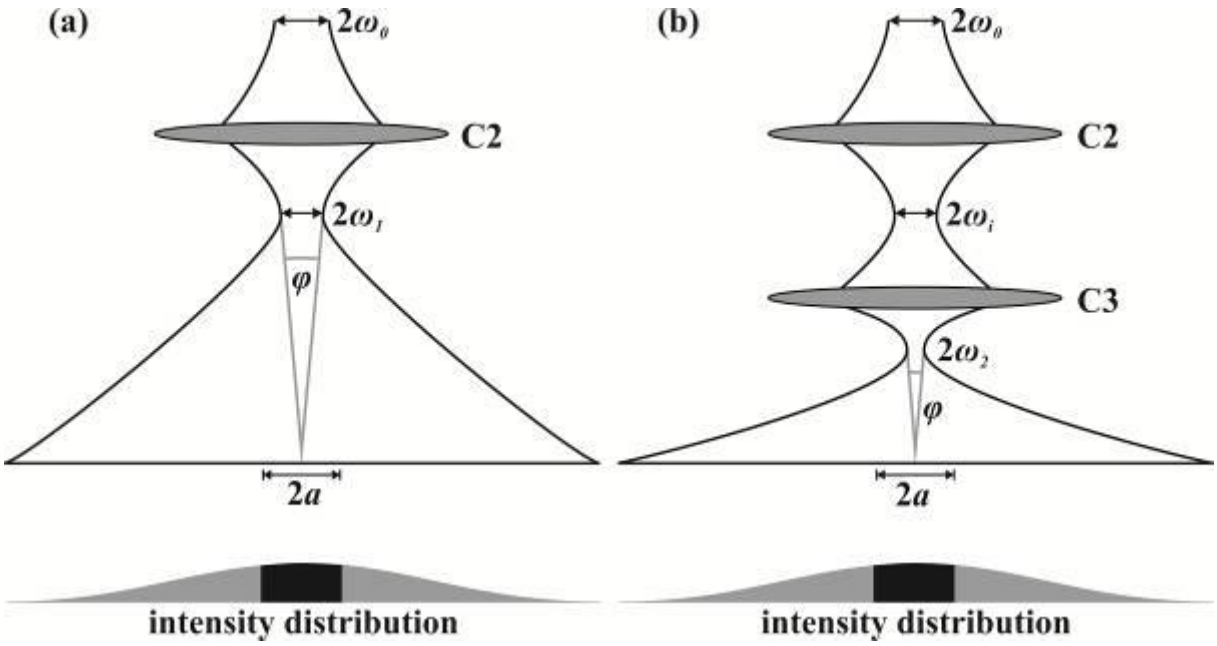

Figure 1. (a) Schematic sketch of the simplified 2-condenser setup. The effective angular source distribution and the intensity in the hologram are determined by the waist size. (b) Schematic sketch of the simplified 3-condenser setup. The same effective angular source distribution and the same intensity in the hologram can be achieved.

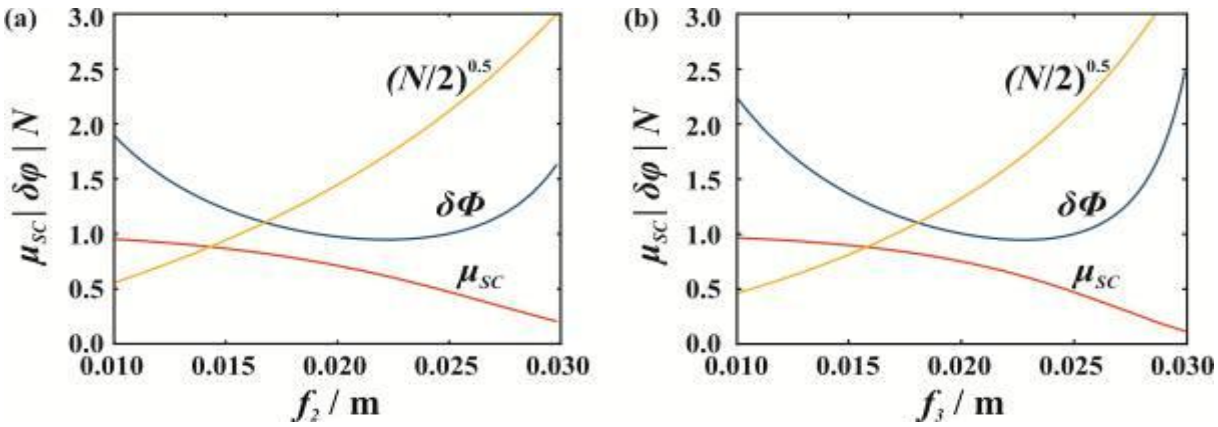

Figure 2. Calculation of phase variance in dependence on electron number and spatial coherence in a 2-condenser (a) and 3-condenser (b) system for an exemplary setup. The minima lie in both cases at a spatial coherence of about 0.62.

Advances in Light and Electron Optics

IM.2.P047
The SPANOCH method: A key to establish aberration correction in miniaturized (multi)column systems?

R. Janzen[1], S. Burkhardt[1], P. Fehlner[1], T. Späth[1],M. Haider[2]

[1]Laboratorium für Elektronenmikroskopie / KIT, Karlsruhe, Germany
[2]CEOS GmbH, Heidelberg, Germany

info@dr-janzen.de
Keywords: miniaturized columns, multicolumn systems, Cs-correction, SPANOCH

Charged particle optics is a continuously developing and expanding technology with a meanwhile broad area of applications.
Unfortunately charged particle optics applications are usually limited by aberrations, especially by the spherical aberration. In the highly sophisticated field of electron microscopy correctors are meanwhile commonly used. Hexapole correctors are state of the art and are continuously advanced by CEOS Company, Germany.

Nowadays charged particle optics finds its way into miniaturized applications. Whereas miniaturized columns including mini lenses exist, the commonly used correctors are too complex for a use in miniaturized single or multicolumn systems. Nevertheless the general principle of multipole based correctors may be transferred to such systems.

The key is the fact that a hole with n-fold shape within an aperture separating two electric fields with different strengths produces a superposition of a round lens field and a 2n-pole field (plus more or less higher order terms depending on the shape). In simple terms all that has to be done in order to use such multipole fields for reduction / correction of aberrations, is to pile up apertures with n-fold shaped holes on adequate voltages in a sophisticated way. The formula how to use which fields may carefully be transferred from working corrector designs.

The method doing so will be denoted by SPANOCH (**S**ophisticated **P**ile of **A**pertures with **no**n **c**ircular **H**oles) in the following, indicating that it uses apertures with non circular holes in order to produce multipole fields (for correction purposes). Using SPANOCH one faces native difficulties:

- The coupling of the round lens- and the multipole fields,
- as well as the coupling of the field strengths with distances and voltages of the apertures and therefore velocity changes.

In 2008 an electrostatic analogue of the commonly used hexapole Cs-corrector was used in order to design a Cs-corrected extraction optics. This was used as a test setting within a ray tracing based computer simulation to demonstrate the SPANOCH concept and its proof of principle. The design did not claim to be of practical interest because of its strong contribution to chromatic aberration and the lack of facilities to adjust it.

Meanwhile the design of a SPANOCH type hexapole corrector is on the run. The design is still in a preliminary state of a generic prototype. It overcomes the disadvantages of the proof of principle design:

- The hexapole strengths and the round lenses can be adjusted independently.
- The entire design shows the well-tried double symmetric structure (see figure (1)) that avoids contributions to second order aberrations.

This is achieved by simultaneously varying five voltages. One controls the strengths of the hexapoles whereas the other four prevent the zeros of the fundamental rays from shifting. The generic design (s. figure (1)) has four parameters: the distances denoted by ‘a’ to ‘d’ in figure (1). Note that the distances denoted by ‘e’ and ‘f’ don’t affect the course of the fundamental rays in the vicinity of the hexapoles and hence don’t influence the correction power of the assembly. Thus we face a four dimensional parameter space for optimization. During the optimization we used two evaluation criteria:

- The continuous and close variability of the correction power under the constraint of reasonable maximum field strength and
- the maximum achievable correction power.

Because of computing time reasons we did the optimization calculations within the SCOFF approximation under the regime of the Gaussian Dioptrics, describing the apertures as thin lenses and the gaps in between as homogeneous fields. Thus the assembly could be described by the transfer matrix method.

As measure of the correction power we used the negative contribution of the assembly to Cs which is related to the Hexapole strengths. Due to the fact that hexapoles can not be described within the used approximations we had to fit analytic functions to simulation results of representative apertures (with 3-fold shaped holes) with the aperture's voltage, the neighboring fields and the aperture's geometry as parameters.

The optimization showed a tremendous optimization potential. For instance decreasing the distance 'a' to one third of its initial value resulted in an increase of the correction power by several orders of magnitude. The results still have to be regarded with some suspicion because the remaining contributions to aberrations of third and higher order have not yet been taken into account.

1. Acknowledgments: We express our special thanks to CEOS GmbH Heidelberg and ICT GmbH, Heimstetten for financial support,

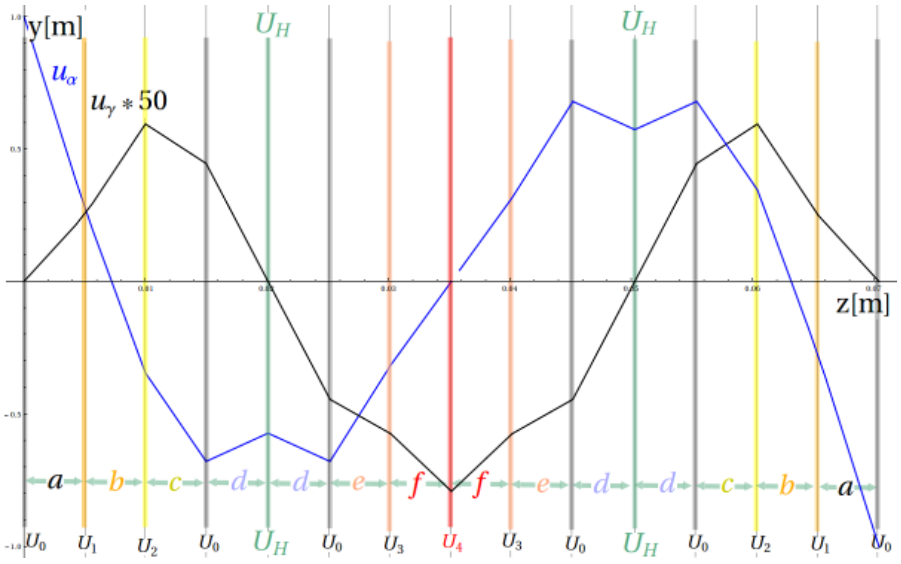

Figure 1. Sketch of the generic design prototype of a SPANOCH-type hexapole corrector together with the course of the fundamental rays. The z-direction is the direction of flight of the electrons. All apertures are represented by colored lines. The two apertures generating the hexapole fields by 3-fold shaped holes are marked in green. All other apertures are conventional ones having round holes. The distances 'a' to 'f' are generic parameters of the design.

Advances in Light and Electron Optics

IM.2.P048
New high-resolution low-voltage scanning electron microscope

J. Jiruše[1], M. Havelka[1], J. Polster[1], F. Lopour[1]

[1]TESCAN, a.s., Brno, Czech Republic

jaroslav.jiruse@tescan.cz
Keywords: scanning electron microscopy, low voltage, high resolution

Scanning electron microscopy (SEM) is a widely used and irreplaceable technique in many branches of science. To achieve resolution of about 1 nm, microscopes with conventional double-pole objective lens use high electron accelerating voltage (30 kV) because they lose resolution at low voltages considerably, typically three or more times at about 1 kV. However, the energetic electrons can worsen charging effects, penetrate deep through the upper layers of the sample, break down bonds between molecules of biological tissues and polymers, and damage sensitive samples. Thus there is an increasing demand for low-voltage observation while keeping high requirements on resolution.

A new analytical microscope MAIA3 with ultra-high resolution of 1 nm at 15 kV and 1.6 nm at 1 kV has been developed (see Figure 1.). This instrument uses a three-lens column equipped with a Schottky field-emission gun. The objective lens is of a single-pole immersion type [1], dramatically decreasing optical aberrations compared to a conventional lens. An additional intermediate lens can operate simultaneously with, or instead of, the objective lens. Therefore, multiple display modes are possible (e.g. for the best resolution, the largest field of view or the highest depth of focus), including a field-free mode.

MAIA3 instrument also benefits from the TESCAN's beam deceleration technology, which allows automatic control of the electron landing energy down to 50 eV (in manual regime down to 0 eV) by applying negative voltage on the sample. This regime also helps to reach a charge-free imaging. The new module provides a sample discharge-and-touch protection, and it also switches between normal and deceleration regimes automatically without the necessity of any manual operation. Very accurate computation of working distance, magnification and all optical parameters together with continuous control of the beam spot size and beam current is ensured by In-Flight Beam Tracing™ technology.

Detection system for secondary electrons (SE), backscattered electrons (BE) or transmitted electrons (TE) consists of several detectors. The set includes innovative In-Beam SE, In-Beam BE and SE in beam deceleration mode, all of which are in-lens (in column) type and provide variety of signals in addition to standard SE, BE or TE detectors in the chamber. Optimized detection system together with ultra-high resolution at low voltages is advantageous for imaging of nanostructures as shown in Figure 2.

The maximum probe current is up to 200 nA, which is suitable for analytical methods such as EDX, WDX, EBSD, CL, etc. All of these detectors are optimized to work at a short analytical working distance of 5 mm.

E-beam lithography benefits from TESCAN's specialized DrawBeam software which provides a familiar CAD-like GUI for drawing of all shapes together with ultra-fast scanning (pixel dwell times down to 20 ns). Fast and efficient microscope control with many automatic functions (focusing, brightness, centring, spot optimization, auto-diagnostics, and many more) and software extensions (image processing, 3D scanning, correlating position with photograph or light optical image etc.) enables a real user-friendly operation [2].

1. Z. Shao, PSD Lin, Rev. Sci. Instrum. 60(11) (1989), p. 3434.
2. We kindly acknowledge funding from Technology Agency of Czech Republic under grant FRTI2/736, project MOREMIT.

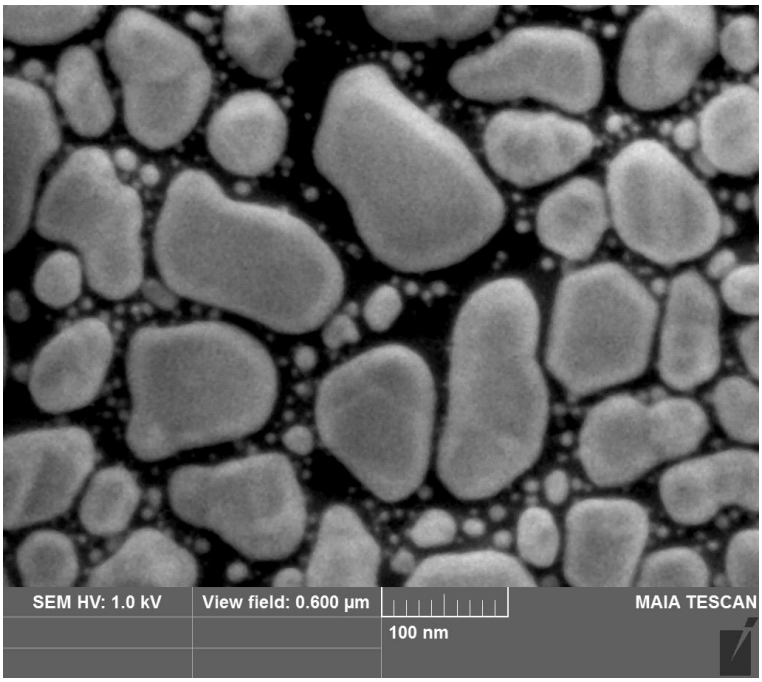

Figure 1. A resolution test sample of gold on carbon at 1 kV.

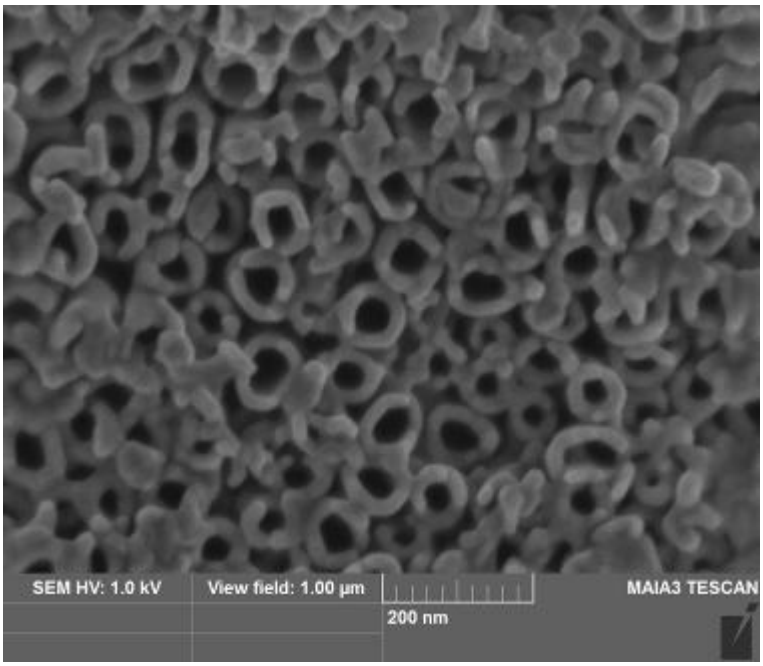

Figure 2. Gold particles (40nm) in sol gel in silicon substrate (left) and TiO2 nanotube array.

Advances in Light and Electron Optics

IM.2.P049
A new design for solid state backscattered electron detectors providing improved image contrast and detection speed

A. Liebel[1], R. Eckhardt[1], A. Niculae[1], H. Soltau[2]

[1]PNDetector, Munich, Germany
[2]PNSensor, Munich, Germany

andreas.liebel@pndetector.de

The typical operation conditions in Scanning Electron Microscopy have changed a lot during the last two decades. Imaging of insulating layers or biological samples demand for the use of low electron energies and currents. These conditions are not only challenging for the microscope itself but also for their detection systems. Many currently used Backscattered Electron (BSE) detectors show a highly reduced quantum efficiency for electron energies smaller 5 keV. This decreases the image contrast and signal to noise ratio and the necessary high gain of the readout electronics limits the detection speed. However, improved collection efficiency and readout concepts can help to expand the operating range of BSE Detectors.

The quality of a BSE image is not only characterized by the spatial resolution but also by the image contrast and signal to noise ratio. The latter is mainly determined by the current of backscattered electrons and the integration time per pixel. Therefore, higher contrast and signal to noise ratio, especially at low primary electron energies, is routinely achieved by using slower scan speeds or higher beam currents. This however may harm sensitive samples or decrease the spatial resolution.

Another solution for increasing image contrast and signal to noise ratio without changing the imaging conditions of the microscope is to enlarge the detector collection efficiency. Advanced entrance windows minimize the detector dead layer and therefore increase the quantum efficiency. Higher collection efficiency can also be achieved by using optimized detector geometries. Figure 1(a) shows the calculated geometric collection efficiency for detectors with different size and geometry. A smaller central hole of the chip through which the primary electron beam is guided increases the detector solid angle. It also helps to more efficiently collect electrons which are preferentially backscattered at high take angles. In figure 1(b) the measured signal to noise ratio with two different detector geometries is plotted versus the pixel dwell time. The profit in signal to noise ratio due to the higher collection efficiency is obvious. Figure 2 shows two sample BSE images taken at 3 keV with identical microscope conditions and readout. The right image is from a detector with optimized geometry and shows a highly improved contrast. We will present further images and measurements which demonstrate the benefit in image quality.

The fact that the signal currents can be enlarged without significantly increasing the active area of the detector can be also advantageous with regard to detection speed. Higher signals can be obtained while keeping the signal capacitance of the chip at a low level of a few pF. With the preamplifier electronics positioned close to the detector, as shown in figure 3, TV-Speed imaging with pixel dwell times smaller 100 nsec can be achieved for moderate to low beam currents. We will present rise time measurements and sample images showing this advantage.

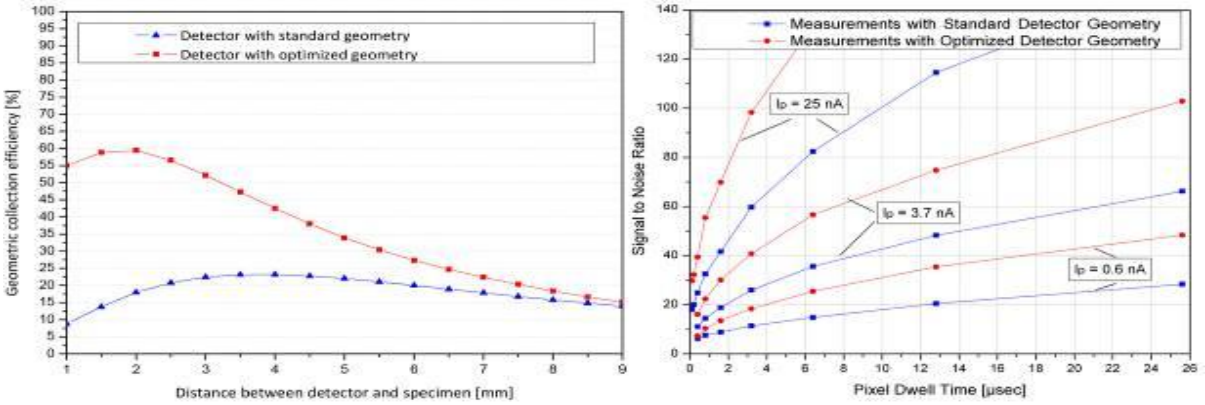

Figure1. a) Calculated geometric collection efficiency for different detector geometries. 100 % correspond to a solid angle of 2π. b) Measured Signal to noise ratio as a function of pixel dwell time for three different primary beam currents. The new detector with optimized geometry shows a large increase of the SNR.

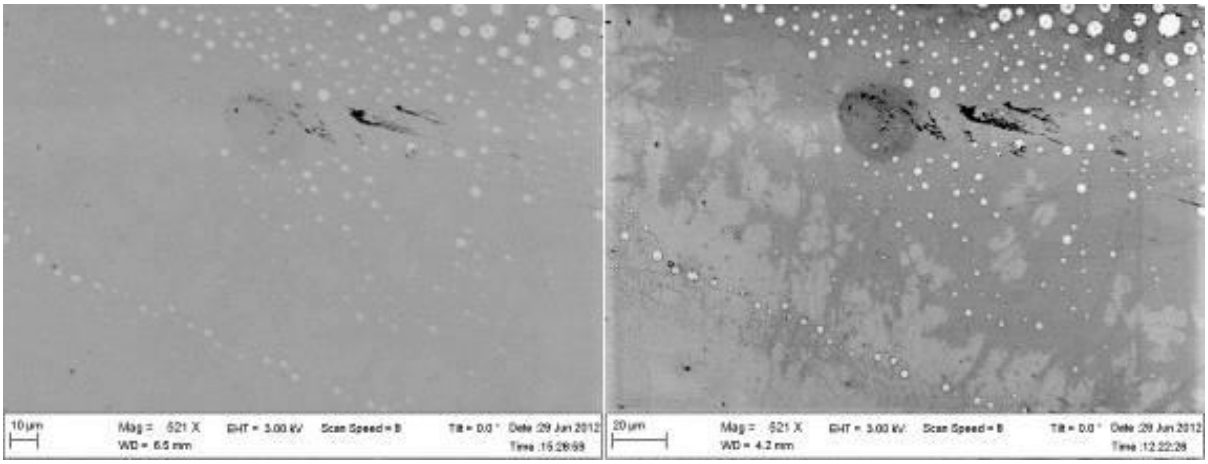

Figure 2. Two BSE images taken at 3 keV primary beam energy and identical microscope and readout conditions. The left image was taken with a standard geometry detector while the right image is from a detector with optimized entrance window and geometry and shows a highly improved contrast.

Figure 3. BSE Detector with optimized geometry (1.0 mm central hole diameter and 40 mm² active area). The Chip is directly connected to the preamplifier electronics which reduces the total signal capacitance and enables TV speed imaging (pixel dwell times < 100 ns) at low primary beam currents and energies.

Advances in Light and Electron Optics

IM.2.P050
New detection methods for fast analysis of nano-particles

L. Roussel[1], S. Sluyterman[1], E. Bosch[1], I. Gestmann[1]

[1]FEI, Eindhoven, Netherlands

seyno.sluyterman@fei.com
Keywords: nano-particles, detection, SEM

In the last years, the sub nanometre spatial resolution at low beam landing voltage of the extreme high resolution scanning electron microscope (XHR SEM) [1] has enabled a routine characterization of particles no bigger than a few nanometres, without any specimen preparation [2]. To access even more precise information and work on a larger variety of materials, it is critical to efficiently collect the signal composed of secondary (SE) and back-scattered (BSE) electrons, and pick from the signal the fraction that delivers the most relevant contrast from the particles and their environment.

Development of the energy dispersive detection infrastructure for the XHR SEM

The newly developed infrastructure in the XHR SEM optimises the signal collection and the contrast thanks to specific optical elements and three detectors built inside the electron column. The immersion lens of the column not only focuses the electron beam on the sample, it also filters the BSE. The closer the BSE energy from the primary beam, the better these BSE are focused and the closer their trajectory is to the optical axis.

Near no-(energy)loss BSE are collected by a first detector called ICD, located higher up in the column (figure 1). Just below, a second detector called MD gathers the low-loss BSE. The remaining higher loss-BSE are directed toward the third detector (TLD), in the lower part of the final lens. To ensure clean BSE imaging, SE are blocked from entering the lens. Both the ICD and MD consist of a solid-state diode with boron layer technology that allows detecting electron energies as low as 200 eV. With this new detection setup, it is possible to work at short working distance to further optimize the signal collection. All three detectors can be used simultaneously: all BSE are detected at once, and their respective annular and energy filtering provides complementary materials information.

An additional optical element, Beam Deceleration (BD) [3], whereby a negative potential is applied on the surface of the sample, is added to the setup for the characterization of particles using very low landing energies (from a few 100 eV to 20 eV). In this case, all SE and BSE are reaccelerated towards the ICD and very high resolution, surface sensitive information is obtained.

Fast characterization of nano-particles and contrast optimization

Several types of nano-particles were characterized using this detection, using a Verios XHR SEM. In figure 2, high-loss, low-loss and no-loss BSE images of catalyst particles on top of nano-tubes are presented. The catalyst particles are coming out clearly when imaging with lower-loss BSE. Signal mixing can be used to further stress the part of the information that is of specific interest. Other particles, such as pyrite crystals in a shale sample or catalyst particles in a fuel cell electrode have been imaged clearly and at high resolution, using the same method. High resolution details of the carbon contamination on the surface of gold particles, using very low landing energies and the ICD, are shown in figure 3.

The collection of the complete SE/BSE signal and the possibility to filter it more accurately are key to better contrast tuning and understanding of its mechanisms. Using the energy dispersive detection in the XHR SEM, the fast characterization of various types of particles with very high resolution, high contrast and no beam damage has been demonstrated.

1. R. Young et al, Proc. SPIE7378, Scanning Microscopy 2009, 737803
2. T. Hachisu et al, Journal of Magnetism and Magnetic Materials 324 (2012) 303-308
3. D. Phifer et al, Microscopy Today (2009) 40-45

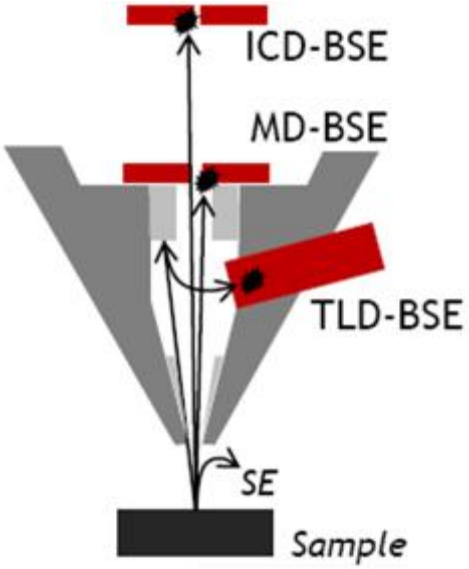

Figure 1. Energy dispersive detection setup in the XHR SEM, BSE mode.

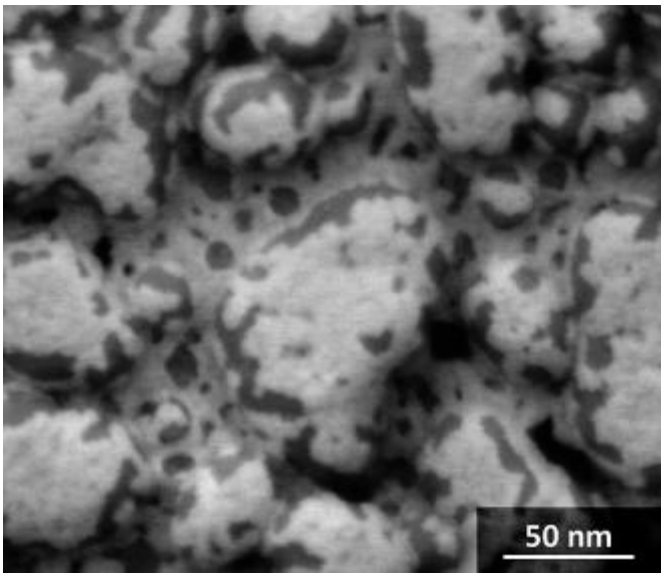

Figure 3. Gold particles on a Carbon substrate, imaged at a landing energy of 50 eV and with a beam current of 6 pA.

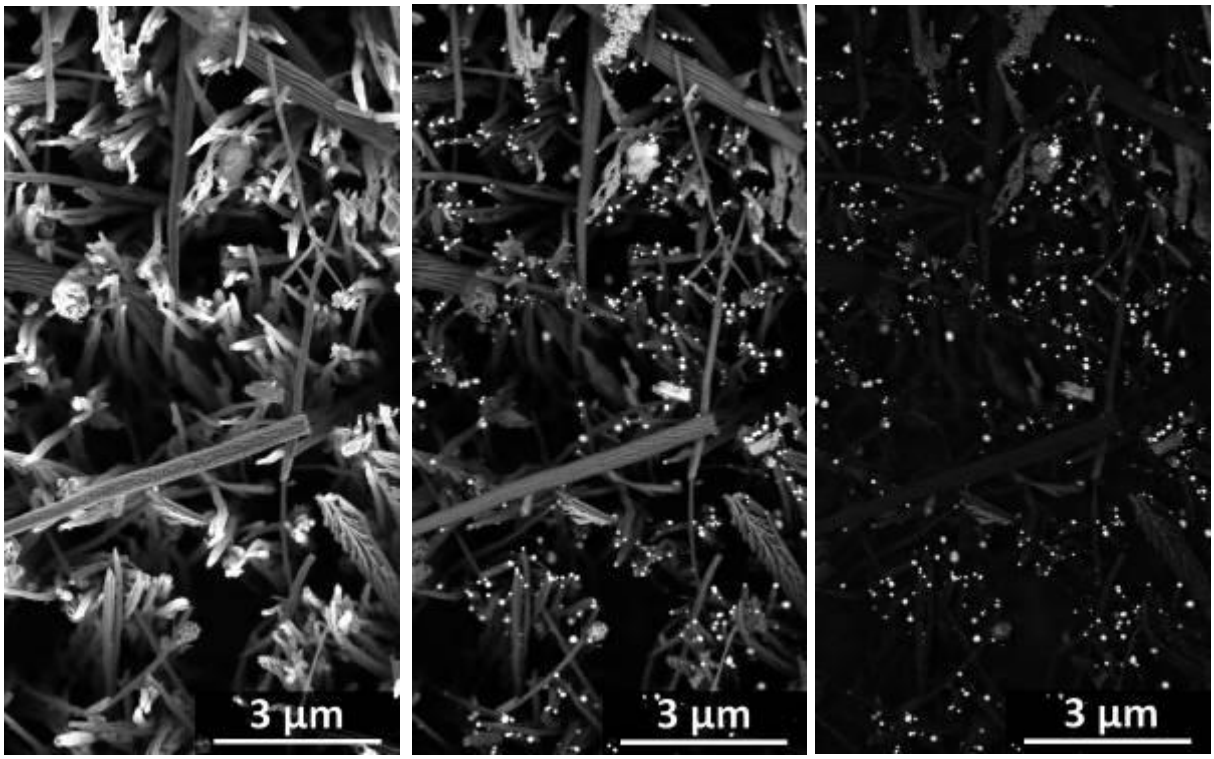

Figure 2. Nanotubes with catalyst particles on top, imaged at a landing energy of 2 keV simultaneously with the TLD (left), MD (middle) and ICD (right) detectors.

Advances in Light and Electron Optics

IM.2.P051
Expanding the boundaries of FIB-SEM technology: Developments for best application results

I. Schulmeyer[1], M. Kienle[1]

[1]Carl Zeiss Microscopy GmbH, Oberkochen, Germany

Ingo.schulmeyer@zeiss.com
Keywords: FIB, high throughput, high current FIB, Analytics, In-Situ experiments

Increasing demands in 3D-imaging, -analytics and Nanofabrication require FIB-SEM Instruments with superior properties, quality and flexibility. The latest developments in Carl Zeiss FIB-SEM technology address this demands and form an instrument that is well prepared for numerous today and future applications. FIB-tomography allows the volumetric reconstruction at a sub-10nm resolution. The trend in Material and Life Sciences is to aquire increasingly large volumes at higher voxel resolution. This leads to a better understanding of compound materials, brain tissues, semiconductors and other samples. Achieving large images at high resolution requires a special design of the electron optics. A non-uniform magnetic field on the sample surface limits the field of view due to distortions in the outer regions. Latest developments of the Carl ZEISS SEM column leads to a minimum magnetic field and thereby to minimum distortions, allowing large field of view imaging without stage movement and stitching. A limitation in large volume FIB-tomography is the time needed to acquire this huge datasets. To reduce the acquisition time it is necessary to perform milling of the slices and imaging at the same time. The acquisition of up to 4 detector signals at the same time leads to maximum information in the least time. Intelligent software algorithms and complete workflow support of ATLAS3D allow to collect only the relevant information and to improve z-resolution.

Throughput for various applications can also be achieved by faster FIB-milling. This requires higher FIB currents. Though, FIB resolution and low kV Performance shall be maintained. The latest column design offers currents up to 100 nA with superior spot profiles while achieving best-in-class resolution at lower currents and excellent low kV performance. Modern FIB-SEM systems cover not only the typical application range but are also able to host and integrate numerous instruments and components for advanced experiments. The Zeiss FIB-SEM allows integration of many 3rd party systems like heating, cooling and tensile stages, SIMS, EBIC and CL, several manipulators, e.g. for probing and liftout, a Laser option for massive ablation and many more. A modern API interface that is open to the user allows the seamlessly integration into the FIB-SEM.

The new SEM lens design offers the optimum conditions for high resolution imaging and high current analytics in one tool. The performance at high current conditions were improved leading to a significant reduction of time for analytics. Changing imaging modes and optical parameters like probe current, acceleration voltage or working distance can be done in a fast and easy way never seen before on a FIB-SEM.

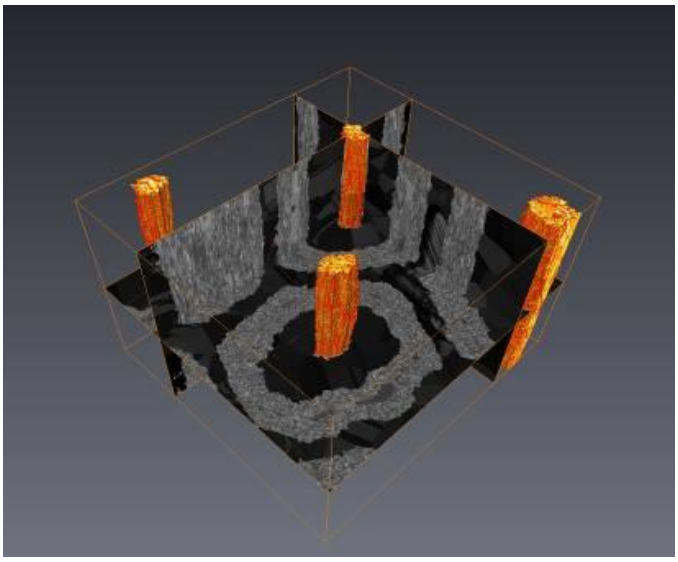

Figure 1. Nb3Sn multi-filament superconducting cable acquired with ATLAS3D. The volume of 25x23x17 µm comprises 1700 slices. The images were acquired using simultaneous milling and imaging with the EsB detector. The 3D reconstruction shows the complex fine grained microstructure. Materials contrast as well as grain orientation contrast can be observed in the superconductor phase as well as in the Cu matrix. (Sample Courtesy of Dr. Marco Cantoni, EPFL, Switzerland)

Advances in Light and Electron Optics

IM.2.P052
The latest innovation on FE-SEM and its applications

H. Sato[1], S. Takeuchi[1], O. Takagi[1], R. Schmidt[2]

[1]Hitachi High-Technologies Corp., 882, Ichige, Hitachinaka, Ibaraki 312-8504, Japan, Japan
[2]Hitachi High-Technologies Europe GmbH., Europark, Fichtenhain A12, 47807, Krefeld, Germany, Germany

sato-hirofumi@naka.hitachi-hitec.com
Keywords: potential contrast, compositional contrast, Low accelerating voltage analysis

Nano materials to be used for batteries and semiconductor devices are being made as composite materials in order to improve its functionality and durability. The latest FE-SEM has been developed to meet these demands by continuous improvements not only on fundamental technologies but also addressing imaging capabilities.

In order to obtain optimized contrast on potential contrast, compositional contrast at high magnification for the above demands, 1) Spreading energy width with emitter, 2) Energy separation of a signal would be key terms for the innovators.

As a field proven technology of Hitachi Cold Field Emission Gun maintains high brightness and high stability with 0.2 to 0.3eV energy spreading while implementing newly innovative evacuation system, the latest FE-SEM would achieve further advanced performance to maintain reliable image observation and analysis for all scientific segments.

And newly developed energy filtering function can control charge-up phenomena and improve detection capabilities on SE/BSE signals. For example, the potential contrast from SE signal is very useful for observation on advanced materials such as battery electrode and effective information from compositional contrast would also be available from BSE signal which would be of use for material differentiation of semiconductor devices. The filter function would be effectively utilized to select any signals for observation and specimen selection. Overall imaging capabilities such as topography, composite, crystal, and potential contrast would be utilized to obtain any useful information for advanced material research.

In this study the latest Hitachi FE-SEM and EDS system are utilized for the evaluations. Figure 1 shows the observation and analysis on anode electrode of rechargeable lithium-ion batteries, and physical characteristics from potential differences on specimen surface at the ultra low landing voltage of 300 V are available from the information both bright contrast of carbon material (a) and dark contrast of resin component (b)[1]. EDS mapping results are shown as (c) C-Kα, (d) O-Kα, (e) F-Kα, and (f) Ni-Lα at accelerating voltage of 2,000 V. Low accelerating voltage analysis enables us to analyze less beam damage even on resin specimens and high spatial resolution on fine surface structure. Therefore the latest innovation on FE-SEM and EDS system provides multiple evaluation results on rechargeable lithium-ion batteries.

1. S. Takeuchi et al, Microsc. Microanal. Vol.16(Suppl S2) (2010) p.p.616-617.

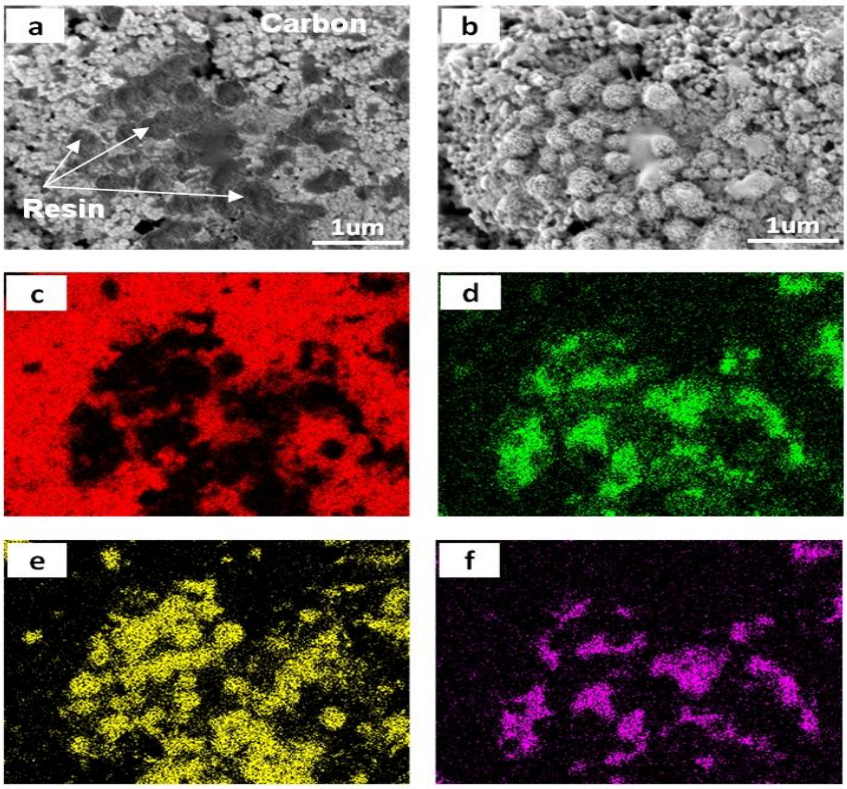

Figure 1. Evaluation results of anode electrode for rechargeable lithium-ion batteries at same field of view. Potential contrast (a) and topographic contrast (b) imaging under the ultra low landing of voltage 300 V. Bruker XFlash Flat QUAD 5060F EDS mapping results (c) C-Kα, (d) O-Kα, (e) F-Kα and (f) Ni-Lα at accelerating voltage 2 kV.

Advances in Light and Electron Optics

IM.2.P053
Density matrix reconstruction by off-axis electron holography

F. Röder[1], H. Lichte[1]

[1]Institute for Structure Physics / TU Dresden, Triebenberg Laboratory, Dresden-Zaschendorf, Germany

falk.roeder@triebenberg.de
Keywords: Off-axis electron holography, density matrix, coherence, inelastic scattering

The phase problem in transmission electron microscopy emerges through the conventional way of detecting intensities. Consequently, it is not possible to deduce the expected intensity at an arbitrary electron optical plane below the object from the measured intensity at the detector. In case of an elastically scattered electron, additional access to its phase suffices to construct a wave in the sense of a pure state, which can be propagated numerically between different electron optical planes. The case of inelastic scattering complicates the situation much more, because both scattering and detection process lead inevitably to decoherence (see e.g. [1]). Since a wave is fully coherent per definition, it is insufficient to describe the inelastically scattered electron by a wave. Here, the beam electron transfers from a pure state into a mixed state, which has to be described e.g. by a reduced density matrix. If this density matrix is known at the detector plane, it is known for all other planes (below the object). The diagonal elements of this matrix directly correspond to the measured intensity and are accessible by means of conventional TEM. The off-diagonal elements describe the coherence of the scattered electron hence require an interferometric approach for their experimental determination. Finally, the significance of the off-diagonal elements of the density matrix for inelastically scattered electrons is comparable to that of the phases for the case of pure elastic scattering.

Off-axis electron holography in combination with energy filtering [2, 3] realizes experimental access to the off-diagonal elements by superposition of different partial beams in dependence on their spatial separation (shear d, see Figures 1a and 1b) [4]. The contrast of the resulting fringe pattern depends on the coherence between the interfering beams. This coherence is determined by the scattering process with the object [5, 6], but also depends on the partial coherence of the beam electron ensemble [7]. Fresnel diffraction at the biprism rim [8] as well as aberrations of the objective lens have a share in the formation of the detected fringe pattern. Thus in general, a direct interpretation in terms of reduced density matrix is complicated. To identify special interpretable cases, we derive and analyze a transfer theory for this holographic measurement setup based on a generalization of the transmission cross coefficient. It turns out that for samples homogeneous perpendicular to the biprism and for small scattering angles, the effect of diffraction at the biprism and partial coherence of the electron beam ensemble can be separated from object influences. That allows a direct and model-independent procedure to determine the density matrix of a scattered electron (Figures 1c and 1d). Limitations are given by the finite biprism diameter providing lower bounds for the shear and, if applicable, by aberrations of the energy filter. We apply this method for the investigation of the influence of surface plasmons on the coherence of the scattered beams [9].

1. M. Schlosshauer, Rev. Mod. Phys. 76 (2004) p. 1267.
2. A. Harscher, H. Lichte and J. Mayer, Ultramicroscopy 69 (1997) p. 201.
3. H. Lichte and B. Freitag, Ultramicroscopy 81 (2000) p. 177.
4. P. Schattschneider and H. Lichte, Phys. Rev. B 71 (2005) p. 045130.
5. H. Kohl and H. Rose, Adv. Electron. Electron Phys. 65 (1985) p. 173.
6. P. Schattschneider, M. Nelhiebel and B. Jouffrey,, Phys. Rev. B 59 (1999) p. 10959.
7. H. Lichte and M. Lehmann, Rep. Prog. Phys. 71 (2008) 016102.
8. J. Verbeeck and G. Bertoni, Ultramicroscopy 108 (2008) p. 74.
9. The research leading to these results has received funding from the European Union 7th Framework Program under Grant Agreement 312483 - ESTEEM2 (Integrated Infrastructure Initiative - I3)
10. P. Potapov, H. Lichte, J. Verbeeck and D. van Dyck, Ultramicroscopy 106 (2006) p. 1012.
11. P. Sonnentag and F. Hasselbach, Phys. Rev. Lett. 98 (2007) p. 200402.

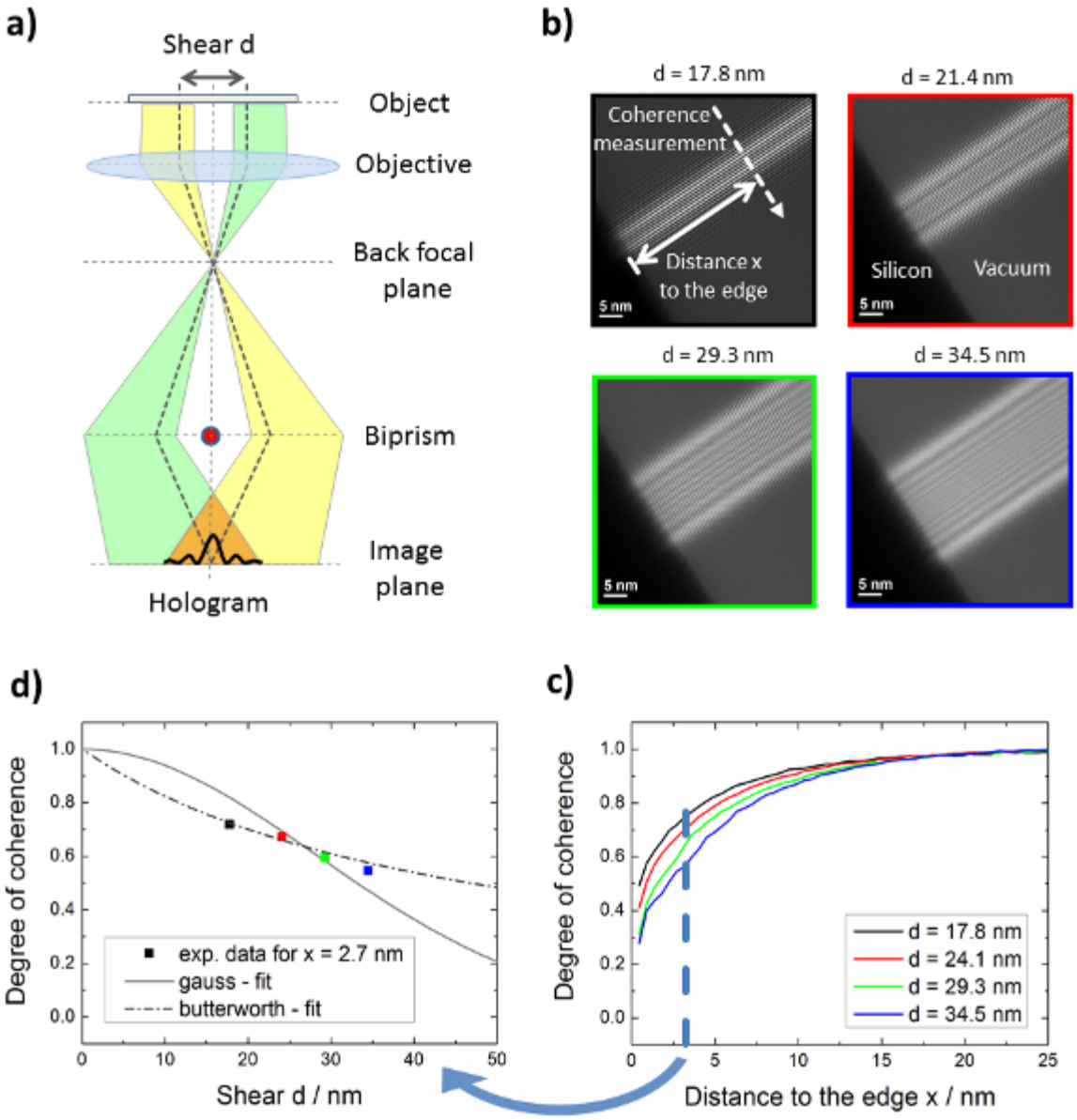

Figure 1. a) Setup for off-axis electron holography (here without energy filter). Voltage applied to Moellenstedt biprism controls the shear between the interfering beams (dashed thick lines). b) Set of fringe patterns for different shears. Biprism oriented perpendicular to a silicon surface. Fringes observed in vacuum region. c) Degree of coherence for different shears (colors) and various distances (x) to the silicon edge. Results are similar to findings in [10, 11]. d) Degree of coherence in dependence on shear for x = 2.7 nm extrapolated by different model functions

Advances in Light and Electron Optics

IM.2.P054
Mechanism of electron-photon conversion in YAG: Ce scintillator for SEM electron detectors

J. Bok[1], P. Schauer[1]

[1]Institute of Scientific Instruments of the ASCR, Electron Microscopy, Brno, Czech Republic

bok@isibrno.cz
Keywords: Everhart-Thornley scintillation detector, cathodoluminescence, image quality

The Everhart-Thornley imaging detector is commonly used one in SEM. In such a detector, the signal electrons are accelerated towards a conductively coated scintillator where they are converted to the visible photons within the cathodoluminescence (CL). The emitted photons are guided out of a vacuum chamber and detected by a photon detector. The scintillator is still a bottleneck of the signal electron detector, because its CL properties can highly affect the scanned image quality. For example, low CL efficiency of the scintillator can result in poor signal-to-noise ratio of the detector [1]. Also long CL decay time can decrease the image contrast during the fast scanning [2]. These problems highly motivate to clearly understand how the energy of the signal electron is converted in the scintillator. This knowledge is essential for modification of the scintillator properties in order to improve the SEM image quality.

One of the most frequently used scintillators in the SEM is the cerium-activated yttrium aluminium garnet (YAG:Ce) single-crystal. It is popular because of its relatively good CL efficiency and short decay time together with good mechanical properties and low price. Electro-optical properties of the YAG:Ce were studied by many researchers since the YAG:Ce first report in 1967 [3]. The CL behavior was explained by a couple of presented models. However, these models are either inaccurate or very complicated to use. We present a more simple CL model of the YAG:Ce which describes only essential electro-optical processes. In spite of the negligence of some luminescence processes, the model is still accurate and corresponds with the experiment.

The YAG crystal is insulating material with the band gap of 6.4 eV. The signal electron, accelerated to the energies typically between 5 and 15 keV, scatters in the YAG crystal and its inelastic diffusion generates hundreds of electronic excitations (charge carriers, free electrons and holes, coupled electron-hole pairs). The major percentage of the electronic excitations is dissipated as a non-visible ionizing radiation such as X-ray, VUV, UV. However, some of the ionizing energy is returned back since this radiation creates other electronic excitations. The duration of this process is in order of femtoseconds.

The electronic excitations can migrate across the YAG crystal lattice until they reach a Ce^{3+} activator or an oxygen vacancy. The activator captures the free electrons from the conduction band, since its $5d_2$ energy level slightly overlap the bottom of the conduction band (see Fig. 1). The capture of the free hole from the valence band is energetically unlikely, thus the hole in the ground state of the activator must be created by activator ionization. When the electron is captured, it is returned back to the conduction band, or more likely thermalized to the $5d_1$ state by a very fast process taking units of picoseconds. The electron in the $5d_1$ state recombines with the hole situated in the twofold 4f state by emitting the characteristic yellow-greenish light (500 – 680 nm). This is the desired CL radiation of the YAG:Ce scintillator. The $5d_1 \rightarrow 4f$ transition takes 70 ns on average, which gives the relatively short decay time.

The oxygen vacancy in the YAG is a crystal defect (called F-center) behaving as a hydrogen-like atom. [4] The electron at the boundary of the vacancy can be in the ground state 1s, or in one of the four excited states 3s, $3p_z$, $3p_y$, or $3p_x$. The energy of the $3p_x$ state lies very close to the bottom of the conduction band and therefore it behaves as an electron trap for the free electrons.

The captured electrons can act according to two scenarios. (1) The electron relaxes to one of the lower excited states from which it recombines with the hole in the ground state. This transition emits the near UV light with the wavelengths between 250 and 350 nm. The transition is slower than the characteristic emission of the activator; it takes approx. 1 μs on average. The part of this emission is absorbed by the activator which excites the electron from the 4f ground state to the $5d_2$ state, and then it relaxes back to the ground state followed by the characteristic emission. As a consequence, the fast activator decay is slow down, however this delayed emission contributes only approx. 1% to the the intensity of the characteristic emission. (2) The electron can be released from the oxygen vacancy by

the thermal vibration of the YAG crystal. This process takes approx. 20 μs on average at the room temperature, and the time decreases with the increasing crystal temperature. The released electrons can be consequently recaptured which prolongs the electron life-time.

The presented model can explain the influence of the scintillator on the image quality in the SEM. One of the problems is the image blurring during the fast scan. The reason lies in the long CL decay of the scintillator caused by the presence of the oxygen vacancy traps. When the "delayed" electrons from the traps reach the activator, they can significantly slow down the characteristic decay. In other words, only the non-trapped electrons are wanted. Luckily, the ratio between the trapped and non-trapped electrons can be reasonably decreased by increasing the activator concentration or decreasing the vacancy concentration. Although the increase of the activator concentration is technologically demanding, the vacancy concentration can be decreased by the annealing of the YAG:Ce in the oxygen atmosphere. This treatment decreases the CL afterglow and increases the contrast of the SEM images. In order to use the YAG:Ce for very fast scanning, the decay time of 70 ns should be shortened. However, this is not possible, because the $5d_1 \rightarrow 4f$ transition time is given by the YAG crystal field. Only the replacement of the YAG crystal by more convenient one could decrease the decay time reasonably.

1. P. Schauer, Nuclear Instruments and Methods in Physics Research Section B 269 (2011), p. 2572-2577.
2. J. Bok and P. Schauer in "Proceedings of 13th International Seminar on Recent Trends in Charged Particle Optics and Surface Physics Instrumentation" (Brno, 2012), pp. 9-10.
3. G. Blasse and A. Bril, Applied Physics Letters 11 (1967), p. 53-54.
4. N. I. Konstantinov, L. G. Karaseva and V. V. Gromov, Doklady Akademii Nauk SSSR 253 (1980), p. 909-912.

5. The research was supported by the European Commission and the Ministry of Education, Youth, and Sports of the Czech Republic (CZ.1.07/2.3.00/20.0103) and by the Technology Agency of the Czech Republic (TE01020118).

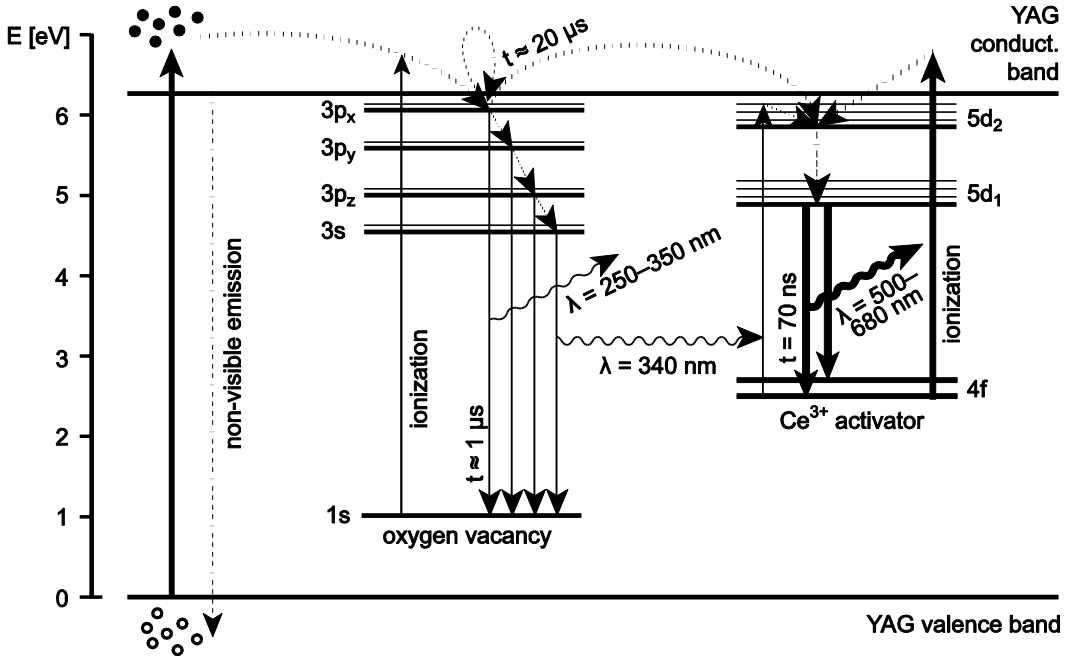

Figure 1. The diagram of the simplified YAG:Ce cathodoluminescence model. The radiative and non-radiative transitions are drawn by the solid and the dotted lines, respectively. The thickness of the lines represents the probability of the transition; the tick line is likely transition and vice versa.

Advances in Light and Electron Optics

IM.2.P055
High contrast Imaging of surface morphology and composition by using Energy-Filtered BSE.

Y. Hashimoto[1], T. Matsuzaki[1], H. Ito[1], M. Konno[1], S. Takeuchi[2]

[1]Hitachi High-Technologies Corporation, Global Application Center, Hitachinaka, Japan
[2]Hitachi High-Tecnologies Corporation, Advanced Microscope Systems Design Department, Hitachinaka, Japan

ito-hiroyuki-2@naka.hitachi-hitec.com

BSE imaging is a useful method to obtain compositional information, and also to reduce charging effect. Demands for compositional characterization at specimen surface are increasing in the field of material science and engineering. In order to characterize compositional structure at specimen surface, Low Loss BSE (LLE) imaging is suitable because of the reduction of the information generated by multiple inelastic scattered electrons [1]. BSE imaging using Ultra Low Voltage (ULV) condition may also suitable because of the reduction of the penetration depth of incident electron beam. However, it is difficult to obtain high contrast BSE image by conventional methods. To address this challenge, we developed a method of filtering signal to the top detector of the newest Hitachi FE-SEM. It is necessary to study imaging parameters to obtain high quality, high contrast BSE image under ULV condition because the signal behavior at ULV condition does not follow the conventional theory used over 1 kV [2]. Here we report the result of fundamental experiments using a test specimen and some applications of this technology for advanced material.

To control the signal detected by the top detector, an energy filter is used. Figure 1 shows a schematic of the energy filter with the top detector in FE-SEM. The filter allows only electrons with higher energy than the filtering voltage to be detected. High angle BSE (HA-BSE) signal is detected by the top detector without filtering voltage, and LLE signal is detected by the top detector with an appropriate filtering voltage. When decelerating field condition is used and an appropriate filtering voltage is applied, BSE signal is detected by the top detector.

A fundamental test of the effect of energy filtering on BSE imaging using ULV was carried out using a basic test specimen. The test specimen consists of four pieces of Si wafer, and 50 nm thick films of three types of materials with different atomic weights (C, Cr, Pt) are deposited on three pieces (Figure 2). Figure 3 shows the BSE images of the test specimen at 300 V. In the conventional BSE image detected by upper detector (a), the contrast between Si, Cr, and Pt is not clear. However, the contrast between each material is clearly observed in top detector image with energy filtering (b). The contrast does not follow the conventional theory used over 1 kV. For example, Pt has the highest Z number but it has the darkest tone in the filtered image. This tendency partially conforms to a previous study [2].

Figure 4 shows the top detector images of the carbon nanotube (CNT)/ polytetrafluoroethylene (PTFE) composite film at 300 V, with no energy filtering (a), with energy filtering (b). In image (a), CNT and PTFE are identified by their voltage contrast but the contrast between the materials is not obvious. In image (b), the contrast between CNT and PTFE is clearly observed. By using ULV in combination with energy filtering, each material can be identified.

1. Oliver C. Wells et al., *Appl. Phys. Lett.* 19, 232 (1971)
2. Ilona Müllerová, *Scanning*, 23, 379 (2001)
3. The CNT / PTFE composite film specimen was kindly supplied by Prof. Yoshiyuki SHOW of the
4. Department of Electrical and Electronic Engineering, School of Engineering, Tokai University

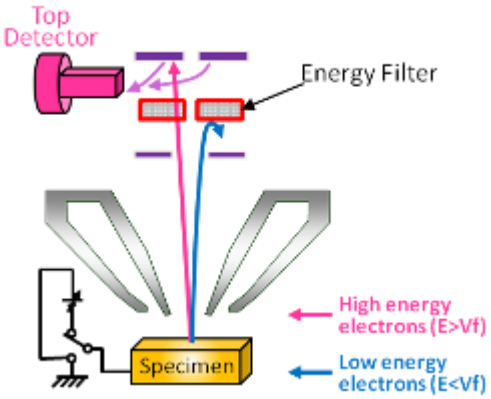

Figure 1. Signal detection system of Top detector with energy filter.

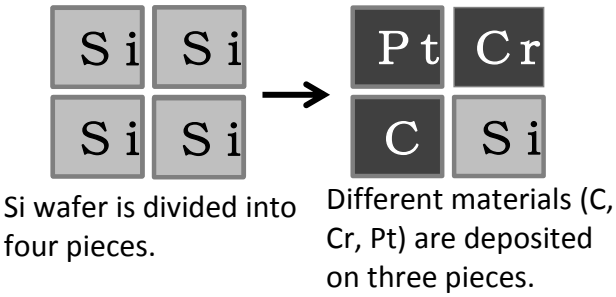

Figure 2. The method of making the test specimen

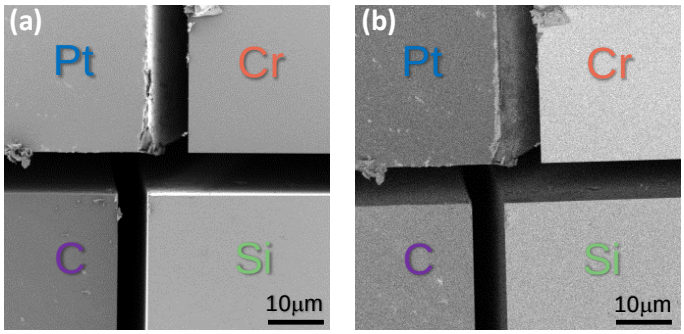

Figure 3. BSE images of test specimen at 300 V.
(a)Conventional BSE image detected by upper detector,
(b)Top detector image with energy filtering

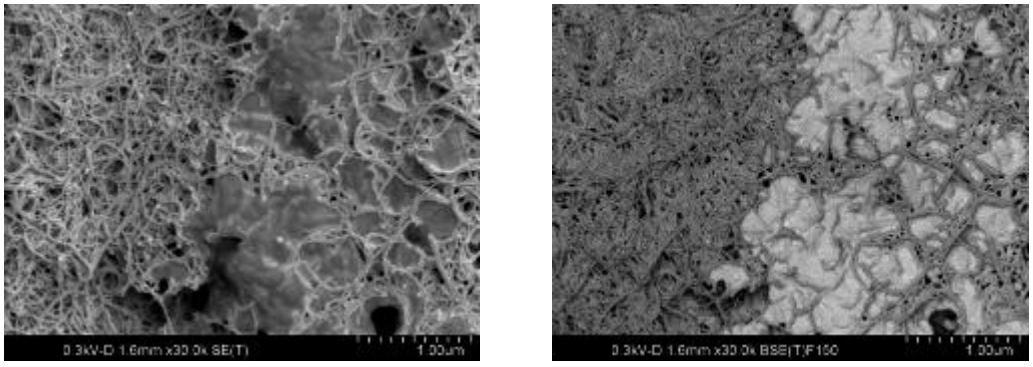

Figure 4. Top detector images of the CNT / PTFE composite film at 300 V, with no energy filtering (a), with energy filtering (b).

Environmental and In Situ SEM/TEM

IM.3.056
Environmental TEM study of manganite perovskite electro-catalysts for oxygen evolution

C. Jooss[1], S. Raabe[1], D. Mierwaldt[1], J. Ciston[2], S. Yazdi[3], T. Kasama[3], M. Beleggia[3], J.B. Wagner[3], T.W. Hansen[3], Y. Zhu[4], P. Blöchl[5]

[1]University of Goettingen, Institute of Materials Physics, Goettingen, Germany
[2]Lawrence Berkeley National Laboratory , National Center for Electron Microscopy, Berkeley, California, United States
[3]Technical University of Denmark, Center for Electron Nanoscopy, Lyngby, Denmark
[4]Brookhaven National Laboratory, Department of Condensed Matter Physics, Upton, NY, United States
[5]Technical University of Clausthal, Institute of Theoretical Physics,, Clausthal, Germany

jooss@ump.gwdg.de
Keywords: Environmental TEM, Catalysis, Beam effects

In-situ studies of catalysts are of high interest since they offer the opportunity to study their atomic and electronic structure in the active state. We present an environmental transmission electron microscopy (ETEM) study of O_2 evolution catalysis during H_2O splitting based on Pr-doped $CaMnO_3$ (PCMO) perovskite electro-catalysts. These systems offer the opportunity for fundamental studies of the role of variable Mn valence state, surface structure and defect chemistry for multi-step charge transfer.

ETEM studies of electro-catalytic water splitting are a challenge, since electro-catalytic activity must be separated from beam effects. In addition, gas phase reactions of H_2O and intermediates at the catalyst surface are difficult to be observed. Here, we show that PCMO fundamentally changes surface morphology and atomic surface structure in contact with water vapor. Oxygen evolution induced by electron beam stimulation can be monitored by mass spectrometry. In addition, oxygen evolution can be visualized by oxidation of silane which reacts with oxygen and thus forms solid SiO_{2-x} at catalytically active surfaces [1]. In order to develop an understanding of the beam induced effects in the catalyst in the presence of gas, we performed a serious of control experiments: ETEM studies of catalytic activity in water vapor are combined with in-situ X-ray absorption spectroscopy (XANES) and ex-situ cyclic voltammetry studies. Electron energy-loss spectroscopy (EELS) as well as the in-situ XANES reveal that the Mn valence is decreased in the active state. Our assumption that oxygen evolution is driven by a positive potential which is induced in the catalyst by inelastic scattering of high energy electrons and subsequent secondary electron emission is supported by off-axis electron holography. First steps in electro-chemical control of the catalyst are performed using a Nanofactroy STM-TEM holder and applying an electric bias to the TEM sample. Careful TEM analysis of samples measured by ex-situ cyclic voltammetry and in-situ bias-controlled ETEM experiments allow us to distinguish between self-formation of the active state during oxygen evolution and corrosion processes at the $Pr_{1-x}Ca_xMnO_3$-H_2O interface. Based on results from density functional theory (DFT) calculations, we can correlate trends in O_2 evolution activity and defect chemistry in the active state to doping induced changes of the electronic band structure in A-site doped manganites.

1. S. Raabe, D. Mierwaldt, J. Ciston, M. Uijttewaal, H. Stein, J. Hoffmann, Y. Zhu, P. Blöchl, and Ch. Jooss, In-situ electrochemical electron microscopy study of oxygen evolution activity of doped manganite perovskites, Adv. Funct. Mater. 22 (2012) 3378–3388, DOI: 10.1002/adfm.201103173

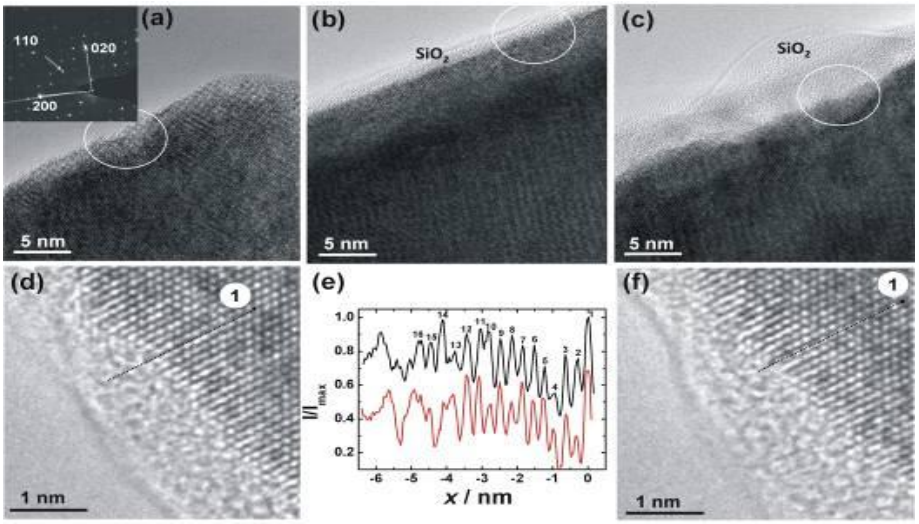

Figure 1. ETEM study of crystalline PCMO with x=0.32 during electron and water exposure. (a) High-resolution TEM image acquired in high vacuum showing the pristine state of a grain at [001] zone axis. The same section as in (a) is shown during an ETEM experiment in water vapor (p_{H2O} = 0.04 mbar), where the growth of an amorphous SiO_{2-x} layer indicates oxygen evolution activity of the edge (b) 20 s and (c) 70 s after start of the electron beam stimulation. The circle is a marker for a specific edge location. (d) and (f) High-resolution TEM images of a grain at [201] zone axis after 300 s and 310 s of electron beam exposure in water vapor and resulting SiO_x coverage. (e) Intensity modulation along the same line depicted in (d) and (f). The first atomic column of this line is labeled as “1”.

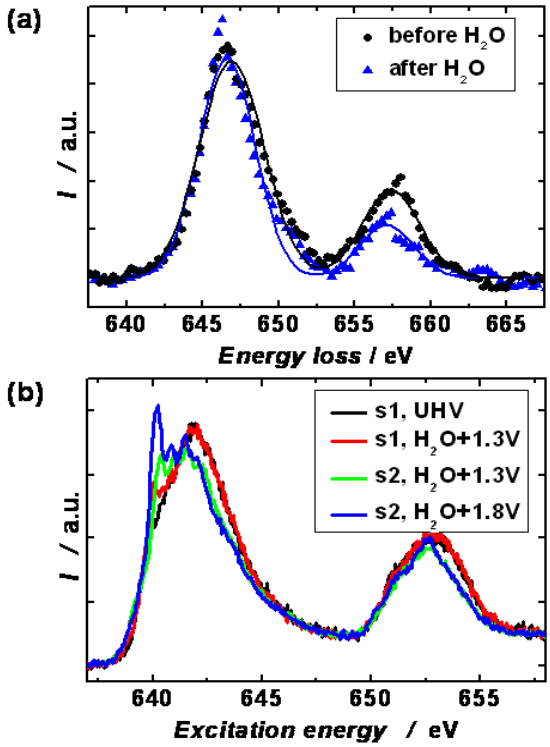

Figure 2: Change of the Mn L-edges in the active state of PCMO with x=0.32 revealed by ETEM (a) and in-situ XANES (b) experiments. (a) Core loss electron energy-loss spectra after Hartee-Slater background subtraction before and after electrocatalytic O_2 evolution. Both spectra are acquired in high vacuum mode before switching to and after switching back from ETEM operation mode and stimulating the sample in 0.013 mbar H_2O vapor with 10^4 e/Å^{2}s. The L_3/L_2 ratio increases from 2.5 to 4.8. (b) In-situ XANES study of two PCMO films s1 and s2 with x = 0.32 in UHV and in contact with H_2O vapor at different positive bias. The increase of intensity at the L_3 edges at about 640.3 eV indicates an increasing fraction of Mn^{2+}.

Environmental and In Situ SEM/TEM

IM.3.057
Nanoscale Dynamics in Liquids visualized with TEM

U. Mirsaidov[1], D. Bhattacharya[1], P. Matsudaira[1]

[1]National University of Singapore, MechanoBiology Institute, Singapore, Singapore

mbiumm@nus.edu.sg
Keywords: in situ TEM, interfacial water, nanofluidics, electron beam tweezers

Nanoscale imaging of frozen aqueous specimens and solid materials with transmission electron microscopes (TEM) has revolutionized our understanding in biological and material sciences. However, there is an ample number of important problems in life and physical sciences that occur only in liquid environments. Therefore, there is an incredible advantage of being able to image nanoscale processes directly in liquids. Recently we have developed a platform for imaging soft materials and biological samples in liquids using TEM (Fig. 1) [1-4]. This platform is also suitable to study liquid properties at nanoscale. Here we show that the properties of fluids at nanoscale dominated by interfacial interactions with the solid substrate surface and drastically differ from the expected bulk behavior. We found that diffusion of nanoparticles in of water is eight orders of magnitudes lower than in bulk. Also flow of water at nanoscale happens in stick-slip manner and not smooth as generally observed for bulk water.

In addition, we will also describe our new all-graphene nanofluidic device that enables high contrast imaging of nanoscale dynamic processes in liquids (Fig. 2). Using these graphene nanochannels we have for the first time to visualize the interface between water and graphene using TEM.

Lastly, we will introduce the concept of electron beam tweezers and demonstrate that by using tightly focused electron beam we can manipulate nanometer sized particles inside the nanochannels and move them over large distances (Fig. 1) [5].

These developments aimed towards imaging dynamics in liquids at nanoscale hold potential to transform how TEM's are used in future and can aide in unlocking properties of liquids and soft materials at atomic scale [1].

1. H. Zheng*, U. Mirsaidov*, L.-W. Wang, P. Matsudaira, "Electron beam manipulation of nanoparticles." *Nanoletters*, 12(11), 5644-5648 (2012).
2. U. Mirsaidov, H. Zheng, D. Bhattacharya, Y. Casana, P. Matsudaira, "Direct observation of the stick-slip movement of nanometer-size water droplets induced by electron beam" *Proc. Natl. Acad. Sci. U.S.A.* 109(19), 7187-7190 (2012).
3. U. Mirsaidov, C. D. Ohl, P. Matsudaira, "A direct observation of nanovoid formation in ultrathin water film" *Soft Matter* 8(27), 3108-3111 (2012).
4. U. Mirsaidov*, H. Zheng*, Y. Casana, P. Matsudaira, "Imaging protein structure in water at 2.7 nm resolution by TEM" *Biophysical Journal* 102(4), p.L15-17 (2012).
5. U Mirsaidov, V.R.S.S Mokapati, D. Bhattacharya, H. Anderson, B. Ozyilmaz, P. Matsudaira, "Scrolling graphene into nanofluidic channel." (submitted)

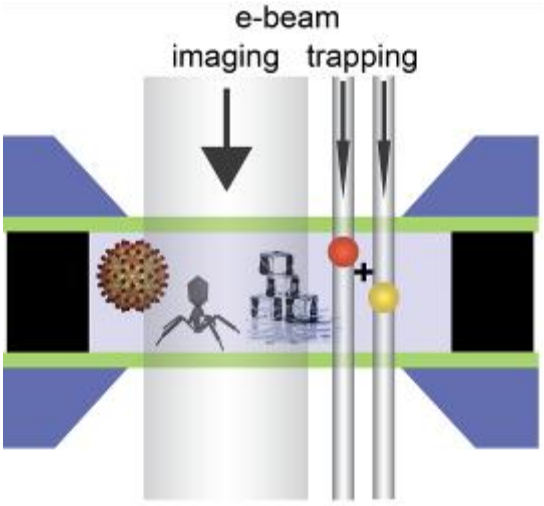

Figure 1. Schematic of the liquid cell encapsulates thin liquid sample between two ultrathin Si_3N_4 membranes (shown in green). Next liquid cell is loaded into TEM. Using this liquid cell we can image samples in native liquid environment. Electron beam is also use to manipulate nanoscale objects inside the liquid cell

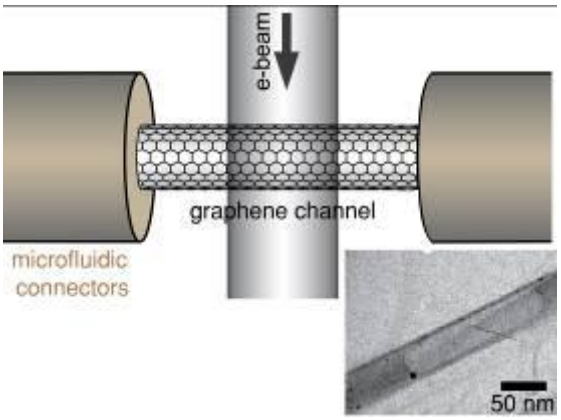

Figure 2. Schematics of graphene naofluidic device that enables high contrast imagin of liquid specimens with TEM.

Environmental and In Situ SEM/TEM

IM.3.058
Static and dynamic behavior of freestanding Cu micron lines observed by *in situ* EBSD

A. Wimmer[1,2,3], A. Leitner[1], T. Detzel[4], W. Robl[5], W. Heinz[3], R. Pippan[1], G. Dehm[2]

[1]Erich Schmid Institute, Leoben, Austria
[2]Max Planck Institute for Iron Research, Düsseldorf, Germany
[3]Kompetenzzentrum Automobil- und Industrie-Elektronik GmbH, Villach, Austria
[4]Infineon Technologies Austria AG, Villach, Germany
[5]Infineon Technologies Germany AG, Regensburg, Germany

alexander.wimmer@k-ai.at
Keywords: *in situ* EBSD, crystal plasticity, dynamic loading

Cu is a widely used metallization material in microelectronic devices. Up to now, micromechanical experiments were performed *in situ* and SEM images were taken during deformation. EBSD images were recorded before and after tensile loading. To investigate the deformation mechanisms and to provide a comparison with crystal plasticity simulations a tilted straining set-up was installed which allows now in addition to *in situ* SEM observations also *in situ* EBSD studies. Through surface polishing of the samples it was possible to reduce exposure time by a factor of 10 to 2 ms. This is the first time for in situ EBSD mapping of an entire sample during static tensile test (Fig. 1a) and dynamic tensile-tensile testing, making it possible to observe the deformation behavior of each single grain during deformation.

The experiment reveals that with increasing grain size the grain rotation and plastic deformation is concentrated in a decreasing number of grains (Fig. 1b and 1c). In large grains rotation, twinning and finally narrowing was observed, but not in small grains. Furthermore in this study it has been shown, that grain rotation is initiated when the yield stress is exceeded and plastic deformation starts (Fig. 1c). All observed grain rotations were non-reversible (Fig. 1d) and have been observed during static loading, whereas no change in microstructure except narrowing was found during dynamic tensile-tensile loading.

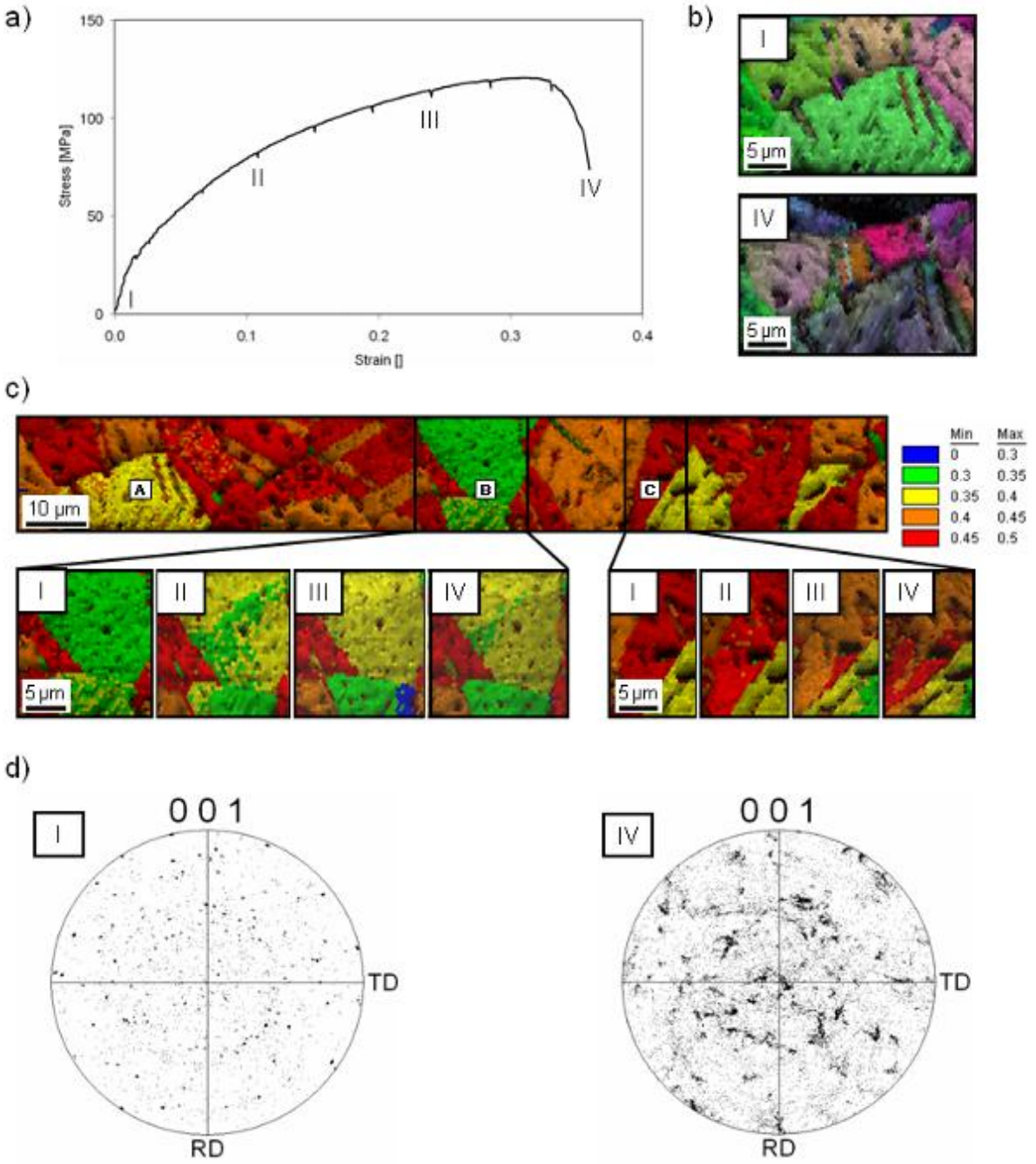

Figure 1. Observations from an *in situ* EBSD experiment (a) Stress-strain curve (b) Grain A showing a uniform grain orientation in tensile direction before the experiment (I) and a strong spread in grain orientation after fracture (IV) (c) Schmid plot of a sample, Grain B showing hardening followed by softening (left) and Grain C showing softening followed by hardening (right) during the experiment and (d) grain orientation plot before (I) and after the experiment (IV), showing a massive spread of orientations after the experiment.

Environmental and In Situ SEM/TEM

IM.3.059
Development of *in situ* nanoindentation inside a transmission electron microscope to characterize the mechanical behavior of ceramic nanoparticles

E. Calvie[1], J. Réthoré[2], L. Joly-Pottuz[1], V. Garnier[1], Y. Jorand[1], I. Issa[1], A. Malchere[1], J. Chevalier[1], K. Masenelli-Varlot[1]

[1]INSA Lyon, MATEIS, Villeurbanne, France
[2]INSA Lyon, LAMCOS, Villeurbanne, France

lucile.joly-pottuz@insa-lyon.fr
Keywords : *in situ*, nanoindentation, nanoparticles, digital correlation imaging, Finite Element Method

In situ compression experiments inside a transmission electron microscopy (TEM) were developed to better understand the mechanical behavior of ceramic nanoparticles. Regarding ceramic materials, knowing the mechanical behavior of materials at the nanoscale is of much interest to optimize the elaboration process of nanostructured materials.The TEM *in situ* nanoindentation technique is well adapted since it is possible to follow the evolution of the particles at the nanometer scale during solicitation. It can, thus, be envisaged to analyze the behavior of ceramics at a scale never analyzed before or to study phases which only exist at nanometer scale. The important point of this new technique lies in the possibility to combine *in situ* imaging and load-displacement measurements. Data processing has also to be optimized. From the in situ experiments results (images and load-displacement curves), a method coupling digital image correlation (DIC) and finite elements (FE) method was developed in order to obtain constitutive law and its parameters.

A commercial transition alumina powder (diameter size from 30 nm until 120 nm) was tested and unexpected results were obtained. Experiments indeed highlight a plastic behavior of the nanoparticles under compression, especially when their size was below a certain critical size [1]. Figure 1 presents the force-displacement curve obtained during an experiment with images at key points of the curve. From the images, the plastic behaviour can be observed. To go further on the data processing, DIC was used to determine the real displacement of the substrate during the experiment and FE method was used to obtain constitutive law and its parameters (red curve on Figure 1 fitting the experimental curve). Results were also compared with results obtained by classical analytical method (blue curve on Figure 1). Values of Young modulus and yield strength of this alumina, not available for such crystallographic form (transition alumina) and for such nanoscale, were obtained. To go further, it is also possible to superimpose the experimental image (deformation 39 %) with a map of the total equivalent plastic strain, calculated by FE simulations using the previously determined constitutive law (Figure 2). It is, thus, possible to better analyze the images obtained like, for example, the observed Bragg fringes which can be attributed to plastic deformation.

To complete these results, a thin section of a real compact pressed from the above alumina powder at high pressure (5 GPa) was prepared by Focused Ion Beam (FIB) and observed using conventional TEM. A plastic deformation of the smallest nanoparticles was observed. This confirms that this plastic deformation really occurs for the ceramic nanoparticles and is not induced by the electron beam. Furthermore it proves the interest of this technique to characterize ceramic nanopowder and its impact on the understanding of important steps of the ceramics processing (compaction process, for example) [2].

1. E. Calvie, L. Joly-Pottuz, C. Esnouf, P. Clément, V. Garnier, J. Chevalier, Y. Jorand, A. Malchère, T. Epicier, K. Masenelli-Varlot, J. Eur. Ceram. Soc. 32 (2012), p. 2067–2071.
2. The authors acknowledge the CLYM (Centre Lyonnais de Microscopie) for the access to the 2010F microscope, the région Rhône-Alpes and the Institut Universitaire de France for financial support.

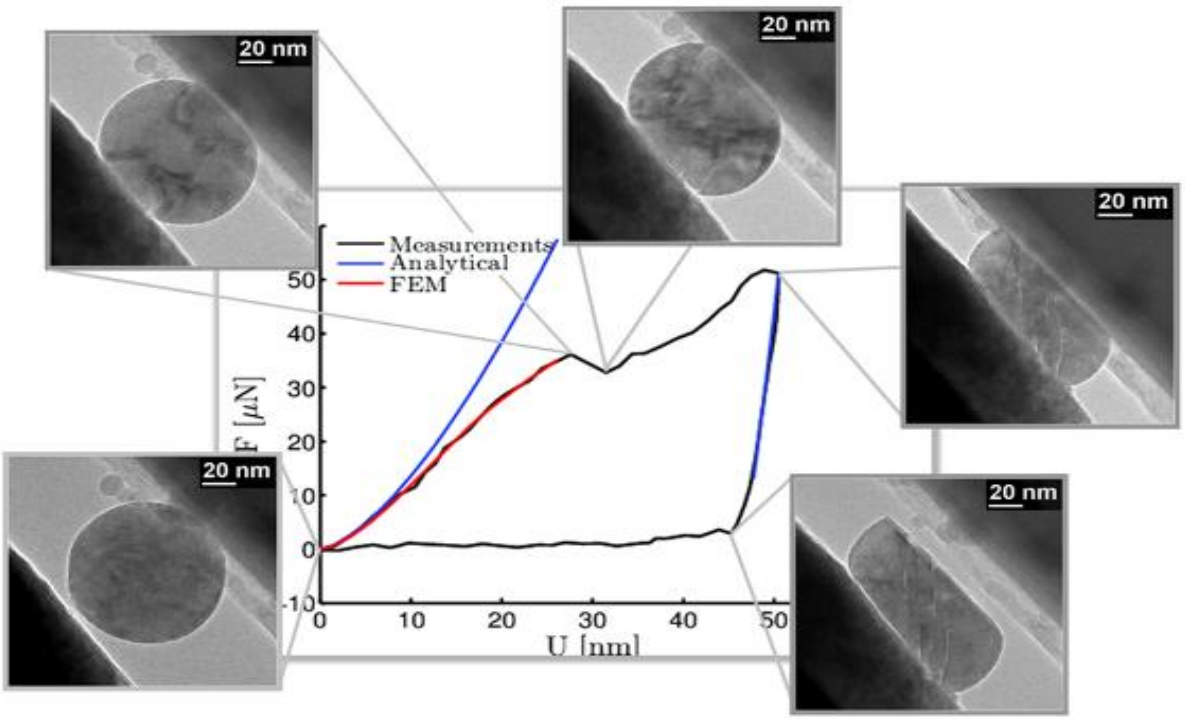

Figure 1. TEM *in situ* nanoindentation force-displacement curve with images obtained at key points of the force-displacement curve. The simulations using DIC-FE (red curve) or the analytical method (blue curves) are also displayed on the curve for comparison. Good agreements are observed especially for the DIC-FE method which takes into account the plastic regime, while the analytical method is valid only in the elastic domain.

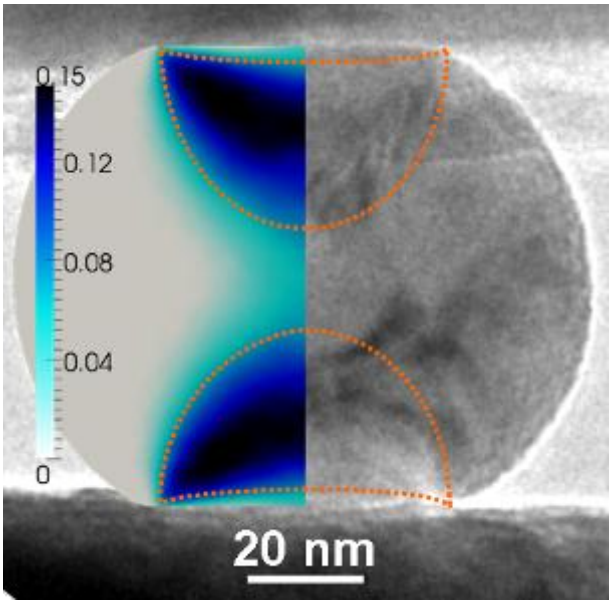

Figure 2. Superposition of an experimental image with the corresponding map of the total equivalent plastic strain calculated by DIC-FE. A good agreement between the experimental image and the calculated map is observed (The contours of the maximum equivalent plastic strain are highlighted with dotted lines). It indicates that the observed Bragg fringes are caused by plastic deformation.

Environmental and In Situ SEM/TEM

IM.3.060
TEM holder for *in situ* transfer

C.D. Damsgaard[1,2], H.W. Zandbergen[3], T.W. Hansen[1], J.B. Wagner[1]

[1]Technical University of Denmark, Center for Electron Nanoscopy, kgs. lyngby, Denmark
[2]Technical University of Denmark, CINF, Department of Physics, kgs. lyngby, Denmark
[3]Delft University of Technology, Kavli Institute of Nanoscience, Delft, Netherlands

christian.damsgaard@cen.dtu.dk
Keywords: ETEM, Catalyst, TEM Holders

The conditions under which samples are studied using *in situ* techniques are in general not the real operando conditions, because these conditions are too harsh. Instead a set of conditions compatible with the instrumentation for characterization are used, like sample geometry, temperature, gas environment etc.

Environmental transmission electron microscopy (ETEM) studies are usually performed using conventional sample holders in a dedicated ETEM [1] or in a traditional TEM by use of a dedicated high-pressure cell sample holder [2]. In both cases, the setup defines the conditions regarding gas, pressure and temperature, which usually are far from the operando conditions of e.g. heterogeneous catalysis. Our efforts focus on bridging these gaps by establishing *in situ* sample transfer between complementary measurement techniques.

ETEM depends on complementary experiments and characterization techniques. Normally, this is done in parallel with experiments separated in time and space [3] or mimicking a reactor bed by changing the feed gas composition according to reactivity and conversion measured in dedicated catalyst set-ups [4]. Furthermore, dedicated transfer holders have been used to transfer catalyst samples between reactor set-ups and TEM at room temperature in inert atmosphere [5]. To take the full advantage of complementary *in situ* techniques, transfer under reactions conditions is essential.

This study introduces the *in situ* transfer concept by use of a dedicated TEM transfer holder that is able to enclose the sample in a gaseous environment at temperatures up to approx. 900°C. By oxidation and reduction experiments of Cu nanoparticles (NP's) it is shown possible to keep reaction conditions outside the microscope.

Figure 1 (A) and (B) shows CAD drawings of the TEM holder tip in open and closed configuration, respectively. The combined MEMS sample grid and micro heater [6] is mounted inside an aluminium compartment. The MEMS based heater ensures fast response and reach of temperature equilibrium. Figure 1 (C) shows a high resolution TEM (HRTEM) micrograph acquired at 150°C in 1.2 mbar H_2 of a 4 nm Cu particle. Figure 2 shows electron energy loss spectrum (EELS), TEM micrograph, and electron diffraction pattern (ED) of Cu nanoparticles (NPs) reduced in 1.2 mbar H_2 at 280°C. The acquisition was performed at 150°C in 1.2 mbar H_2. EELS and ED confirms the metallic state of the Cu NP.

A significant difference is observed between a reduced sample exposed to 150°C in a closed holder configuration with 1.2 mbar H_2 for 15 minutes (Fig. 3) outside the microscope and a reduced sample exposed to 150°C in an open holder configuration i.e. ambient condition for 15 minutes (Fig. 4). The *in situ* transfer sample kept at 150°C in 1.2 mbar H_2 during the simulated transfer shows same EELS, TEM, and ED behaviour as the reduced sample shown in Fig. 2, whereas the sample that experienced 150°C at ambient conditions shows significant changes. EELS shows characteristic "white lines" in the Cu signal that indicates an increased oxidation state of Cu. The TEM micrograph shows clear morphology changes and core-shell structures. This implies that the sample is not fully oxidized and correlates well with ED showing rings that resembles both Cu and Cu_2O.

The study shows that it is possible to keep reaction conditions outside the microscope and thereby opens up for the possibility to do complimentary *in situ* experiments of the exact same sample without changing the sample condition during transfer.

1 T. W. Hansen et al, Science 294 (2001) 1508
2 J. Creemer et al., Ultramicroscopy 108 (2008) 993
3 P.L. Hansen et al., Science 295 (2002) 2053
4 S. Chenna et al., ChemCatChem 3 (2011) 1051
5. P.J. Kooyman et al., Catalysis letters 74 (2001) 49
6. M.A. van Huis et al. Adv. Mater. 21 (2009) 4992
7. We kindly acknowledge the support from the Danish Ministry of Science and Innovation through the Catalysis for Sustainable Energy Initiative (CASE) at DTU and by The Danish National Research Foundation through CINF DTU. Furthermore, the A. P. Møller and Chastine Mc-Kinney Møller Foundation is gratefully acknowledged for its contribution towards the establishment of DTU Cen.

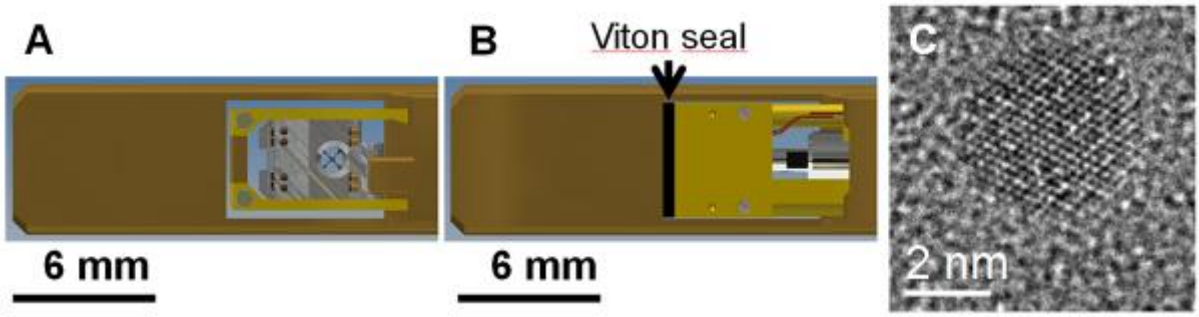

Figure 1. Tip of TEM *In situ* transfer holder in open (A) and closed (B) configuration. HRTEM image acquired at 150°C in 1.2 mbar H_2 of a 4 nm Cu particle.

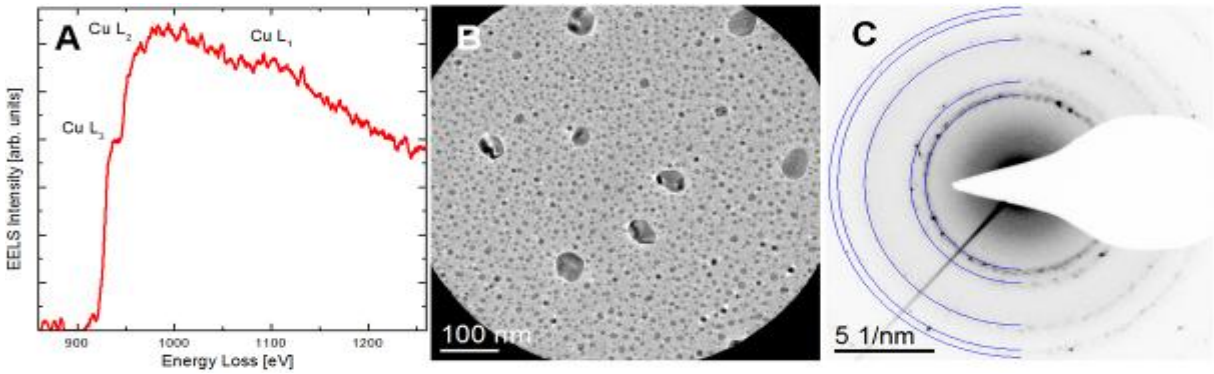

Figure 2. EELS spectrum (A), TEM image (B), and ED (C) acquired at 150°C in 1.2 mbar H_2. The sample was reduced in 1.2 mbar H_2 at 280°C prior to acquisition. The blue rings in (C) represent the theoretical reflections from metallic Cu.

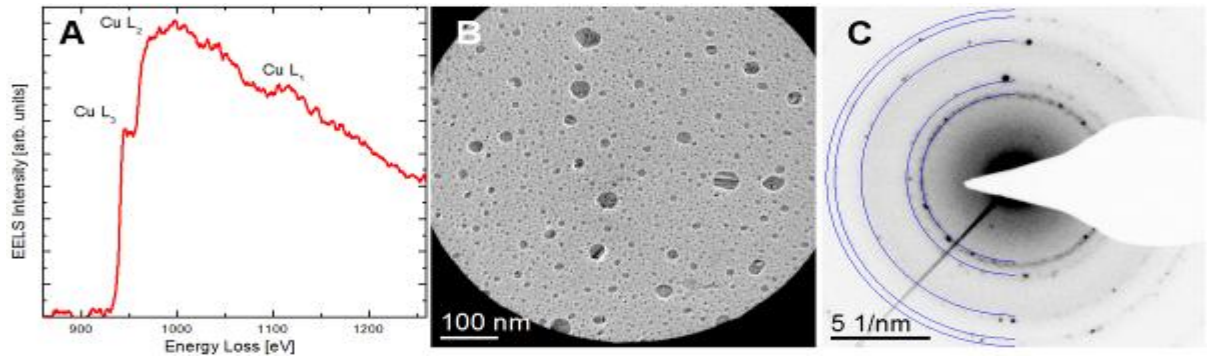

Figure 3. EELS spectrum (A), TEM image (B), and ED (C) acquired at 150°C in 1.2 mbar H_2. The sample was kept at 150°C in ambient conditions with holder in closed configuration. The transfer compartment was closed inside the ETEM in 1.2 mbar H_2. The blue rings in (C) represent the theoretical reflections from metallic Cu.

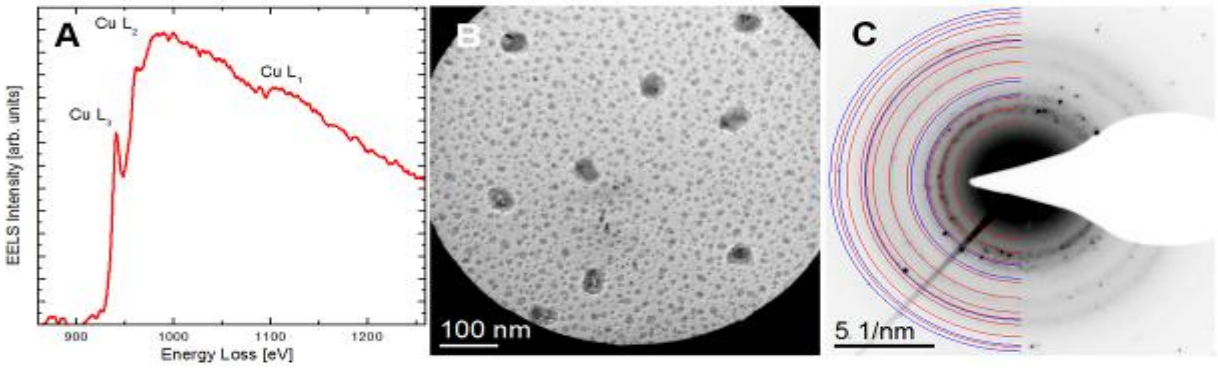

Figure 4. EELS spectrum (A), TEM image (B), and ED (C) acquired at 10^{-5} mbar. The sample was kept at 150°C in ambient conditions with holder in open configuration. The blue and red rings in (C) represent the theoretical reflections from metallic Cu and oxide Cu_2O, respectively.

Environmental and In Situ SEM/TEM

IM.3.061
In situ characterization of Ag-TCNQ nanowires

K. Ran[1], B. Rösner[2], R. Fink[2], E. Spiecker[1]

[1]University of Erlangen-Nürnberg, Center for Nanoanalysis and Electron Microscopy, Erlangen, Germany
[2]University of Erlangen-Nürnberg, Physical Chemistry II, Erlangen, Germany

ke.ran@ww.uni-erlangen.de

Unique properties, such as reversible field-induced electric switching behavior and high densities of charge carriers are found in one-dimensional nanostructures of metal-tetracyanoquinodimethane (M-TCNQ). Consequently, increasing research interests has been generated for their potential application in functional nano-scaled electric devices [1,2,3]. In spite of the very promising performance and inexpensive and convenient synthesis procedure [4], studies about M-TCNQ nanowires, especially for the individual one, like its electric states during phase transition and field emission property have rarely been reported.

In the case of Ag-TCNQ, reversible phase transition was induced by an electric field along the TCNQ π stacking direction. The switching took place within around tens of nanoseconds, and the on-off ratio was reported to be as high as 10^4 [5]. An assumption for the mechanism points out that, a partial neutral species of Ag and TCNQ form during the transition, provide additional conduction channels and increase the material conductivity substantially [6]. However, no direct evidence for the existence of neutral Ag or TCNQ in the nanowires after the phase transition has been reported yet. Moreover, for the probability as a field emitter, investigations in the literatures mainly focus on film or arrays of the Ag-TCNQ nanowires. Typical parameters extracted from these reports, such as onset voltage, field enhancement factor and work function, are quite different among these work [7,8].

We have investigated the structures and electric properties of individual Ag-TCNQ nanowires by (in situ) TEM. Procedure for sample preparation in our study follows the previous report in the literature [1]. Figure 1a-b show typical TEM images of the nanowires at different magnifications. The diffraction pattern in Figure 1c is obtained from a bundle of Ag-TCNQ nanowires. All the spots fit well with the orthorhombic Ag-TCNQ phase II structure [9], and a consistent growth along [100] direction can be determined for these nanowires.

In situ electric measurements were performed using an STM-TEM holder from Nanofactory Instruments AB in combination with the aberration-corrected Titan^3 80-300 microscope at the University of Erlangen-Nürnberg. Figure 2a shows the experiment setup. TEM copper grid (with nanowires grown directly onto it) and W tip (commercially available from Bruker) serve as the two electrodes. Contacts are made when an Ag-TCNQ nanowire suspends in between. During the measurement, we are able to stimulate the phase transition of individual nanowires with an external electric field along the tube axis, and track simultaneously any accompanied changes in the sample structure and electric state. Also, effects of electron beam irradiation on sample are taken into consideration. Figure 2b shows the I-V behavior of an individual nanowire with beam centered and shifted away. Significant increase in conductivity is noticed, as the incident electrons helping overcome the Schottky barriers formed at the electrode/nanowire interfaces.
Both experimental and theoretical results will be discussed in this presentation.[10]

1. Z. Fan, X. Mo, C. Lou, Y. Yao, D. Wang, G. Chen and J. G. Lu, IEEE Transactions on Nanotechnology 4 (2005), p. 238.
2. K. Xiao, J. Tao, A. A. Puretzky, I. N. Ivanov, S. T. Retterer, S. J. Pennycook and D. B. Geohegan, Advanced Functional Materials 18 (2008), p. 3043.
3. L. Ren, L. Fu, Y. Liu, S. Chen and Z. Liu, Advanced Materials 21 (2009), p. 4742.
4. A. P. O'Mullane, N. Fay, A. Nafady and A. M. Bond, Journal of the American Chemical Society 129 (2007), p. 2006.
5. R. S. Potember, T. O. Poehler and D. O. Cowan, Applied Physics Letters 34 (1979), p. 405.
6. J. B. Torrance, Accounts of Chemical Research 12 (1979), p. 79.
7. H. Liu, Q. Zhao, Y. Li, Y. Liu, F. Lu, J. Zhuang, S. Wang, L. Jiang, D. Zhu, D. Yu and L. Chi, Journal of the American Chemical Society 127 (2005), p. 1120.
8. C. Ye, K. Zheng, W. You and G. Chen, Nanoscale Research Letters 5 (2010), p. 1307.
9. L. Shields, Journal of the Chemical Society, Faraday Transactions 81 (1985), p. 1.
10. This work was supported by the German Research Foundation (DFG) via the Cluster of Excellence EXC 315 "Engineering of Advanced Materials" and the Collaborative Research Center SFB 953 "Synthetic Carbon Allotropes".

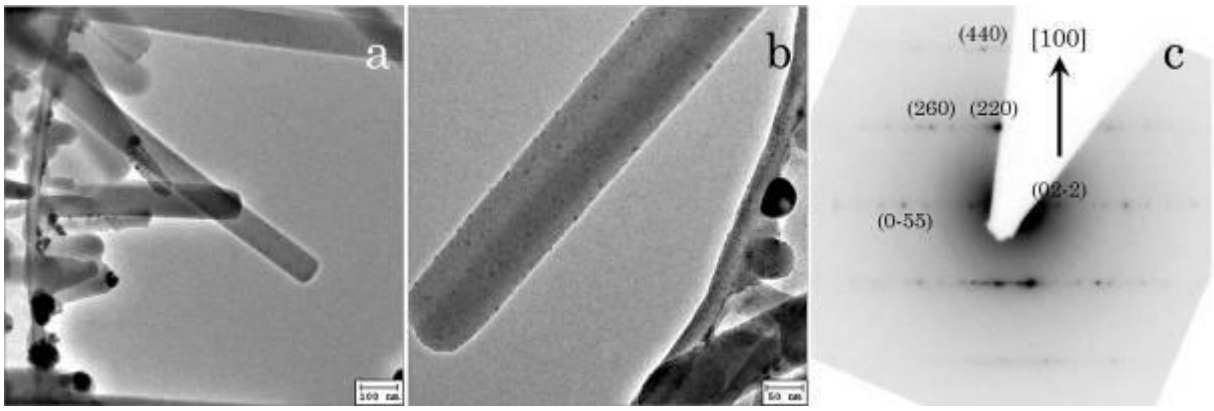

Figure 1. (a-b) TEM images of Ag-TCNQ samples at different magnifications. (c) Diffraction pattern from a bundle of Ag-TCNQ nanowires, reflecting a consistent growth along [100] direction, and indexed by the Ag-TCNQ phase II structure.

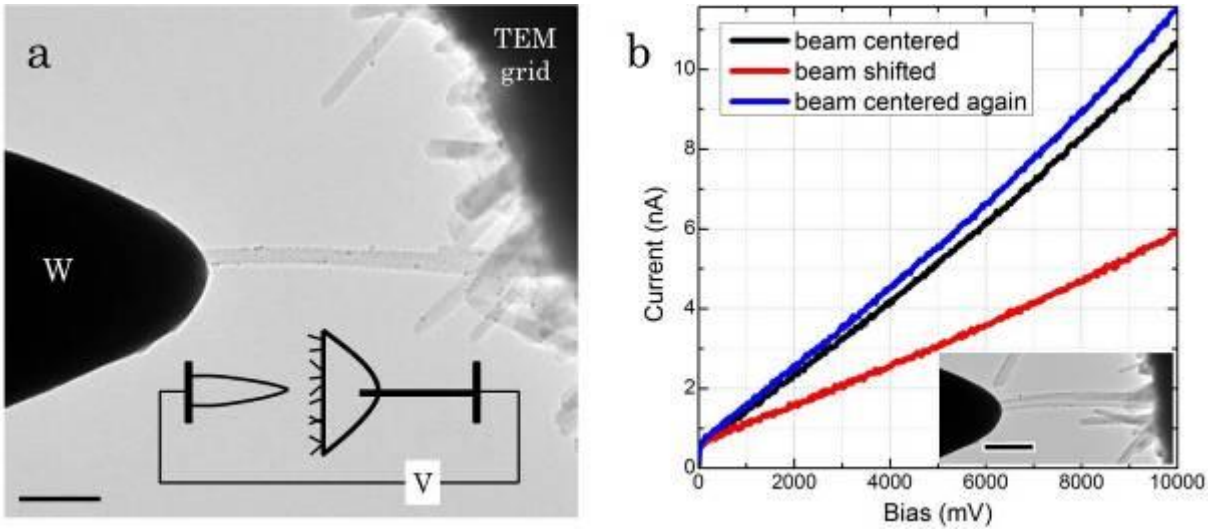

Figure 2. (a) TEM image showing the experiment setup for in-situ measurement, left W electrode, right Ag-TCNQ nanowires protruding from the TEM grid, and one of them contacting the W electrode. Inset is a schematic diagram of the experiment setup. (b) I-V measurements from a single Ag-TCNQ nanowire with electron beam centered and shifted away. Scale bars are 500 nm.

Environmental and In Situ SEM/TEM

IM.3.062
Using hot stage scanning electron microscope for in-situ observations of the crystallization in silicate glass-ceramics

C. Bocker[1], C. Rüssel[1]

[1]University Jena, Otto-Schott-Institut, Jena, Germany

christian.bocker@uni-jena.de
Keywords: glass-ceramics, in-situ SEM, beam damage

In-situ observations using a scanning electron microscope (SEM) are very valuable when studying the crystallization process. The formation of the crystal phase can be monitored continuously. This is achieved by a hot stage which can heat up the sample to the desired crystallization temperature.

However only the surface can be studied in the SEM which leads to the requirement of a system where predominantly surface crystallization occurs.

Barium zinc silicate glasses with the mol% composition 30ZnO, 10Na_2O, 10BaO, 50SiO_2 show a pronounced crystallization at the surface. The formed glass-ceramics are promising novel materials for photonic applications. This system enables in-situ experiments within an acceptable time range due to the rapid formation of the crystal phase. Another system under investigation was a fresnoite glass system with the composition 2BaO, TiO_2, 2.75SiO_2. This system is suitable for oriented crystallization and piezo-ceramics. The third system studied in the hot stage is cordierite (2Al_2O_3, 2MgO, 5SiO_2), a long time known and well described system which still shows surprising crystallization behaviour in the in-situ experiment under vacuum condition.

The electron microscope JEOL JSM-7001F was equipped with a GATAN heating stage H1004. The hot stage can be heated up to 1250 °C. The module is cooled by water and a shield-shutter mechanism protects the objective pole-piece and the electron detector. The sample was placed in a crucible which is positioned within a ceramic furnace which is electrically heated by tantalum wires.

The micrographs were recorded every 30 s to 1 min for a duration up to 2 h. The evaluation of the micrograph series enables the determination of crystal growth kinetics. The experiments showed time-dependent crystal growth velocities in the case of barium zinc silicate and fresnoite glass-ceramics.

This leads to the conclusion that the residual glassy phase changes the composition during crystallization which is characteristic for non-isochemical systems.

A secondary effect could be observed during recording the micrographs: The electron beam irradiation directly affects the nucleation and crystal growth. This leads to a dilemma of applying high magnification and the influence on the experiment

Environmental and In Situ SEM/TEM

IM.3.P063
Tensile / Compression Module in the SEM LEO 982

C. Fahrenson[1], B. Camin[2], P. Schüler[2], C. Hartz[3], D. Berger[1]

[1]Technische Universität Berlin, Zentraleinrichtung Elektronenmikroskopie (ZELMI), Berlin, Germany
[2]Technische Universität Berlin, Institut für Werkstoffwissenschaften und -technologien, Berlin, Germany
[3]Technische Universität Berlin, Institut für Bauingenieurwesen, Berlin, Germany

fahrenson@tu-berlin.de
Keywords: Tensile Module, Compression Module, LEO 982

Tensile / Compression Modules in combination with a microscope are the standard measurement tool in material testing to determine structure-property-relationships. Through the combination the influence of localized changes of material properties (e. g. cracks, pores, grain size or grain orientation) on the strain-stress curves are analysed. If a visible light microscope is used the resolution is limited to about 1 µm. For a higher resolution or to use the extended detection possibilities of the scanning electron microscopic (SEM) it is necessary to apply the Tensile / Compression Module in the vacuum chamber of the SEM. In this poster technical prerequisites of the adaptation of the module and first results are presented.

We used the SEM LEO 982 with Gemini optic from the company Carl-Zeiss and a Tensile / Compression Module from Kammrath & Weiss in the „Narrow version“ allowing Electron Backscatter Diffraction (EBSD) -applications. The module is especially adapted to the available space in the LEO 982. The maximum strength of the module is 5 kN being both applicable in tension and in compression mode. Here the compression mode is demonstrated on a metal foam. The tensile mode is introduced on a Teflon stripe.

The solid construction of the Tensile / Compression Module guarantees the stable and reproducible use even at high loads. Therefore the loading capacity of the sample stage has to fit the weight of the module, i.e. the stage should not produce mechanical vibrations and instabilities like creeping at this load even for high resolution images. Furthermore suitable flanges for the feedthrough of signals for the control of the module are required. If it is planed to perform SEM analysis at tilted samples (as it is necessary for EBSD-measurements in combination with in situ stresses) there has to be enough space close to the pole piece to tilt the stage without touching any detectors while the working distance is kept reasonable small. In our case the maximum tilt of the module is 50° (see figure 1), requiring the use of pretilted samples to fulfil a 70° incident angle of the electron beam with respect to the surface of the sample. On one hand it is not possible to tilt the module more than 50°. On the other hand it is not desirable to tilt the module less than 50° since the modules support will cover the EBSD-detector for this case.

On mounting the module it should be considered additionally that the module does not cover the SEM-detectors (SE, BSE, EDX, etc.) for all operation conditions. The standard requirements for specimens in the SEM are the vacuum suitability and the conductivity. For tensile / compression tests more requirements need to be considered. The size and shape of the sample have to fit to the fixation mechanisms of the module.

The procedure for in situ experiments is determined by the material properties of the specimen and the question to be examined. The important material characteristics to notice are the geometric (homogeneous or heterogeneous structure) and deformation properties (fast, slow or no relaxation after load), e. g. for samples without relaxation it is possible to interrupt the load and to image the area of interest at a static specimen and not during movement. Therefore a higher image quality and series of images at different sample position and different magnifications but with identical conditions are possible. As an example figure 2 shows two image series with two different magnifications during the stepwise compression of a aluminium metal foam. Furthermore an insignificant relaxation is a necessary prerequisite also for long time measurements, such as EDX-Mappings.

Future work will focus on the EBSD analysis of grain size and grain orientation measurements with in situ tensile and compression. For this purpose the SEM is equipped with an EBSD system by EDAX. This system uses a high speed CCD camera (Hikari) to keep the measurement time within reasonable values and to avoid misinterpretation through creeping and relaxation of the sample during the measurements. The reduced spatial resolution of the fast Hikari camera is expected to be no limitation for the EBSD-recognition since it is aimed to analyse orientation but not a detailed phase analysis.

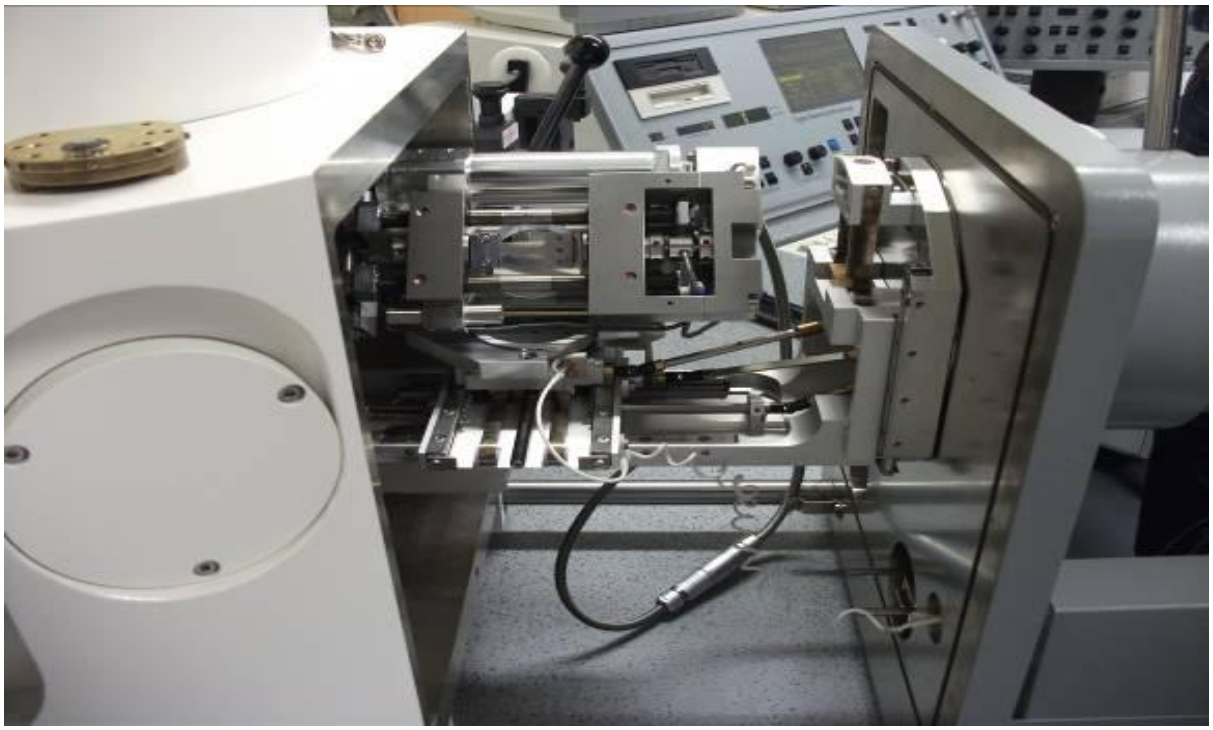

Figure 1. Tilted Tensile / Compression Module for EBSD tests

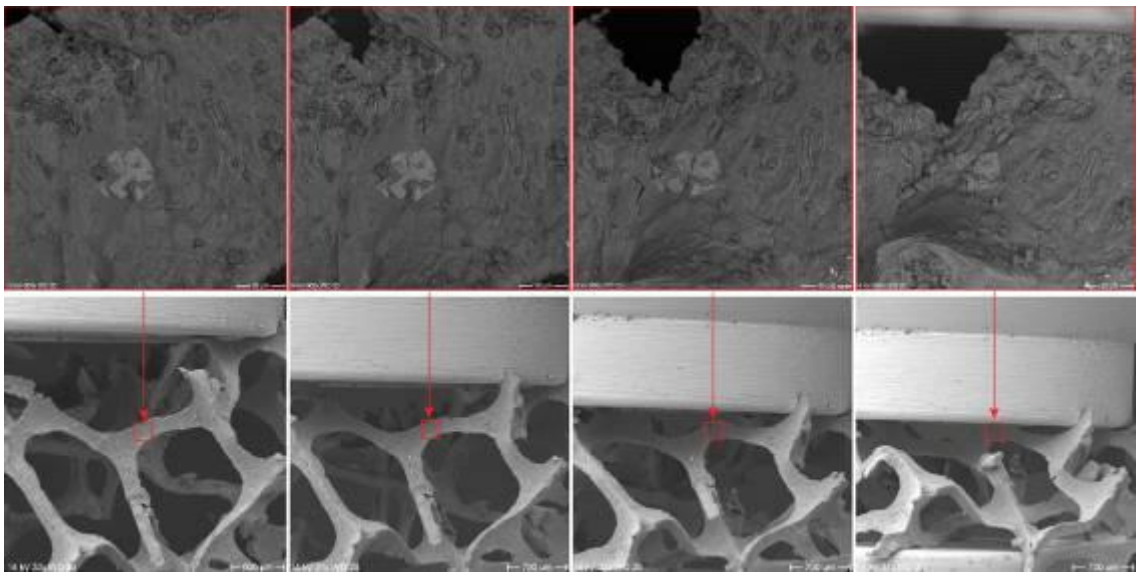

Figure 2. Compression of a metal foam. The first line shows the growing of a rip. The second line shows an

Environmental and In Situ SEM/TEM

IM.3.P064
In situ characterization of microfiltration membranes in the ESEM - Results and limitations

H. Reingruber[1,2], A. Zankel[1,2], P. Poelt[1,2]

[1]Graz University of Technology, Institute of Electron Microscopy and Nanoanalysis, Graz, Austria
[2]Austrian Centre for Electron Microscopy and Nanoanalysis, Graz, Austria

peter.poelt@felmi-zfe.at
Keywords: ESEM, *in situ*, membrane

Polymeric microfiltration membranes consist generally of several different layers and are used in a great variety of applications such as waste water treatment or filtration of colloids and particles in the beverage industry. The structures of such membranes are of microscopic size, but up to now most methods used for the characterization of such membranes yield only macroscopic parameters [1]. But *in situ* experiments in the environmental scanning electron microscope (ESEM) enable the simultaneous measurement of both microscopic and macroscopic parameters and their correlation may provide maximum insight into the system [2]. And with such experiments not only the investigation of the structure of layered membranes, but also the interaction of their pore walls with water is possible.

The investigation of wetting and drying of cooled membranes in the ESEM gives on the one hand results about the number of dry surface pores and of their mean diameter as a function of time (microscopic parameters). On the other hand simultaneously the change of the temperature at both membrane surfaces can be measured (macroscopic parameter). The former provides information about the membrane structure at the surface, the latter information about the wetting and drying process in the interior of the membrane and also about its inner structure. The crucial point is the extremely poor heat conductivity of the membrane. Therefore the temperature of the individual layers is mainly dependent on their water content.

But accurate temperature measurements at the membrane surfaces are a great challenge. The membranes have a thickness of around 150 µm (see Figure 1.), therefore the head of the thermo-couple should be as small as possible. Two types of thermocouples were tested; a T type (copper, constantan) and a K type (chromel, alumel). Their diameter was around 60 µm. Both are suitable for the respective temperature range. Fixing them with a thermally conductive adhesive to the membrane surface did not prove to be successful, because the adhesive penetrated too deep into the membrane. Therefore, thermal contact was realized by only pressing the micro thermocouples against the membrane surface by use of their own flexible contact wires (see Figure 2.).

Figure 3. shows temperature characteristics recorded with both types of thermocouples. It is immediately obvious that all measurements show the same temperature profile, but the absolute values measured differ for the two types. The reason is the different heat conductivity of the contact wires of the two types of micro thermocouple. The values measured with the T type are higher due to the excellent heat conductivity of copper, which causes a heat flux from the much warmer surrounding via the contact wires to the thermocouple head. This could also be confirmed by finite element simulations [3]. Therefore, the heat conductivity of contact wires should be as low as possible. Damage of the membrane material caused by the electron irradiation of the membrane poses another problem. The size of smallest pores that can be imaged is not limited by the resolution of the microscope, but by irradiation damage. Irradiation damage is much stronger in the presence of water, because the free radicals that are generated attack the material. Additionally also contamination of the specimen surface caused by irradiation can influence the wetting and drying process, because it changes the surface properties and thus the interaction of the surface with water.

Thus, the accuracy of the results gained by *in situ* experiments in the ESEM is not only limited by microscope parameters like the resolution, but to a much higher degree by the buildup of the experiment itself and also the type of material investigated.

1. M. Mulders “Basic Principles of Membrane Technology”, Kluwer Academic publishers, 2nd edition, Dordrecht (2003), p. 157.
2. H. Reingruber, A. Zankel, C. Mayrhofer, P. Poelt, J.Membr.Sci. 399-400 (2012), p. 86.
3. H. Reingruber, thesis, Graz University of Technology (2012), p. 48.

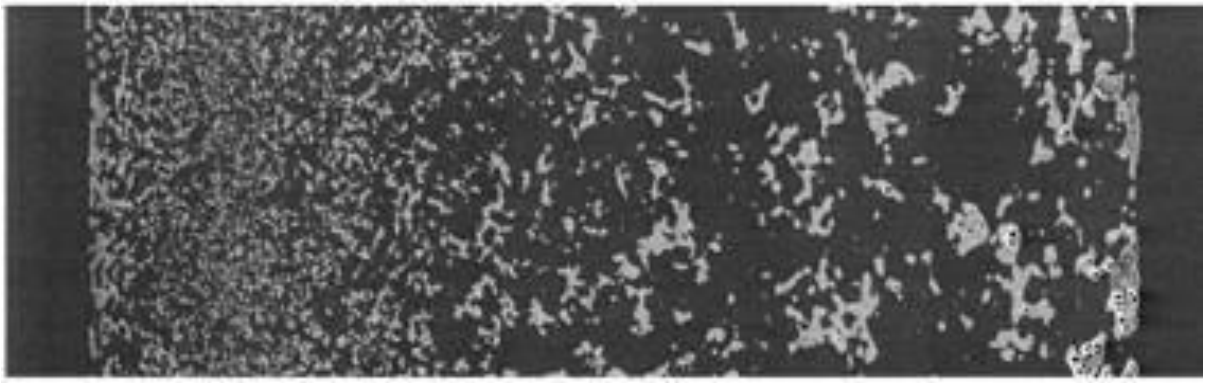

Figure 1. Cross-section of the membrane DuraPES®600 (image width: 174 µm).

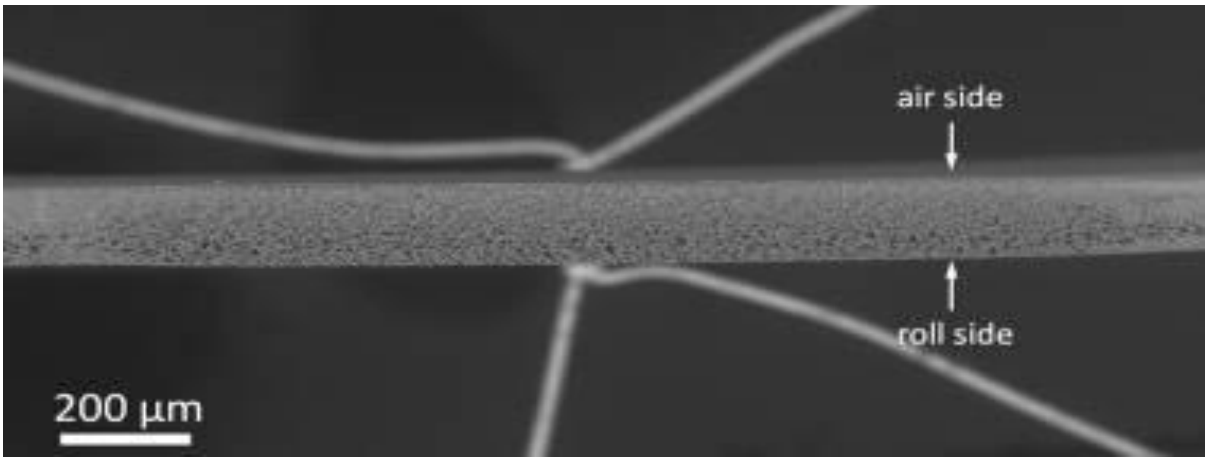

Figure 2. Cross-section of the membrane DuraPES®600 (image width: 174 µm); b: cross-section of the DuraPES®450 membrane with two micro thermocouples (CHAL 0005) contacting the membrane at both surfaces.

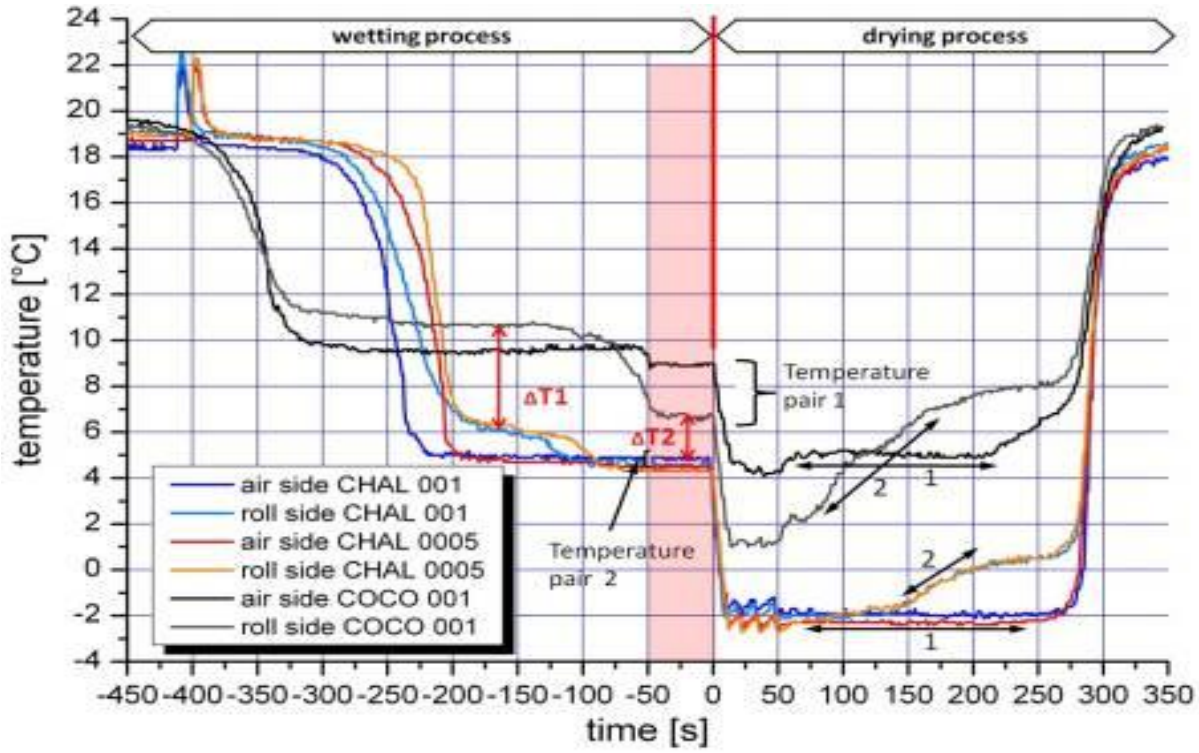

Figure 3. Temperature profiles recorded during the wetting and drying of the DuraPES®200 membrane in the ESEM using K type (CHAL 001, CHAL 005)) and T type (COCO 001) thermocouples.

Environmental and In Situ SEM/TEM

IM.3.P065
Multi-detector system for 3D imaging in the variable pressure and environmental conditions

W. Slówko[1], M. Krysztof[1]

[1]Wroclaw University of Technology , Faculty of Microsystem Electronics and Photonics, Wroclaw, Poland

witold.slowko@pwr.wroc.pl
Keywords: Variable Pressure/Environmental SEM, 3D imaging, quadrant ionisation detector

The authors developed a system enabling environmental techniques and three dimensional imaging (3D) even in a classic high vacuum scanning electron microscope (SEM) as it may be combined with a differential pumping unit capable to keep water vapour or another gas at pressure exceeding 10 mbar in the sample chamber. The system schematically shown in Fig. 1, is designed as a detachable equipment which does not implies changes in an original structure of the instrument. The 3D reconstruction of the sample surface is performed with use of the multi-detector method [1] which can be applied for smooth and weakly modulated surfaces in contrast to popular stereoscopic methods. This advantage may be very attractive particularly for biomedical applications.

A version of the 3D imaging method [2] developed by the authors assumes the Lambert's distribution of backscattered electrons (BSE) generated on the specimen surface and sampling this distribution in strictly defined azimuthal (Θ) and vertical angles (α or β) with a four folded BSE detector system. The detector system is combined with the intermediate chamber of a differential vacuum unit necessary to separate the sample chamber filled with gas from the electron optical column where high vacuum is maintained. In Fig. 2 these components are called the detector-vacuum head (3) and the whole 3D equipment contains digital signal acquisition unit (1) and five-channel signal amplifier (2) additionally. Signals from four BSE detectors amplified and converted into a digital form are finally processed by a computer to obtain the 3D surface visualisation.

The combined directional electron detector system [3] which fulfils mentioned demands is shown in Fig. 3. In general, it comprises two quadruple BSE detectors (a PIN diode for high take off angle BSE_1 accompanied by the ionisation type for low take off BSE_2) and a secondary electron (SE) one. The combined detector has an intermediate chamber (16) situated on the path of the electron beam (EB) to the sample stage (2). It is filled with gas with an intermediate pressure (P_2) lower than the working gas pressure (P_1) in the sample chamber where the place of emission of the electrons subject to detection is located. The detector is equipped with a lower aperture (1) throttling the flow of the gas to the intermediate chamber and in the space between the intermediate chamber and the sample stage it has four anodes (3) in the form of four electrodes identical in shape, arranged in pairs symmetrically around the electron beam axis, equipped with separate electrical leads and positively biased relative to the wall of the intermediate chamber. In the space between the anodes and the sample stage there is an external screening cathode (6) with a hole, delimiting from the sample stage side the maximal backscattered electron BSE_2 detection angle (β_2) at which the electrons enter the electric discharge area around the anodes. This arrangement creates an ionisation detector of low take off angle BSE_2 which can be multiplied thanks to secondary emission from the emission layer (17) covering cathode walls and the ionising avalanche in gas filing the sample chamber.

Inside the intermediate chamber there is a quadrant semiconductor BSE_1 detector (13) with four identical sectors active for electrons, arranged symmetrically relative to the electron beam axis, with their active surfaces facing the lower throttling aperture. This part of the combined detector can capture high take off angle BSE_1 coming into the intermediate chamber through the lower throttling aperture. To prevent limiting a maximal vertical BSE_1 detection angle (α_2) by the aperture its distance to the sample must be lower than the aperture diameter (lower than 1 mm). This limitation prevents investigations of semiliquid samples with semiconductor detector because it could suck such sample into the intermediate chamber. The ionisation BSE_2 detector can work at much higher distances (a few mm) and do not create such limitations for the sample nature (Fig. 4)

1. L. Reimer, R. Bongeler, V. Desai, Scanning Microscopy **1(3)**, 1987, p. 963.
2. J. Paluszyński, W. Słówko, J. Microsc. **233/1**, 2009, p. 10.
3. W. Słówko, Patent application nr PL399438, 06.06.2012.
4. This work was supported with the budged resources for science in 2010/13 as a research project.

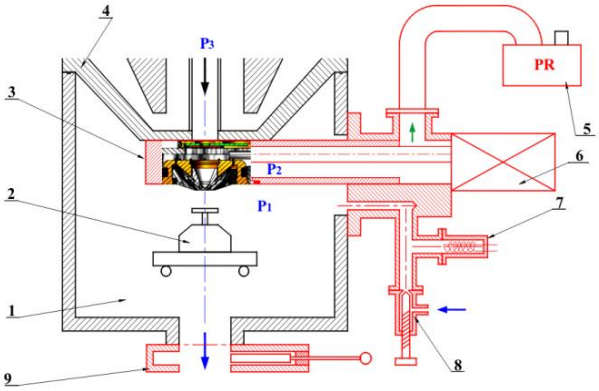

Figure 1. Scheme of the vacuum and detection system for 3D environmental techniques in a standard SEM:
1 - sample chamber; 2 - sample holder; 3 - intermediate vacuum and detection head; 4 - objective lens; 5 - rotary pump; 6 - five-channel amplifier, 7 - vacuum meter gauge; 8 - dosing valve; 9 - gate valve; P_1, P_2, P_3 gas pressures in particular zones.

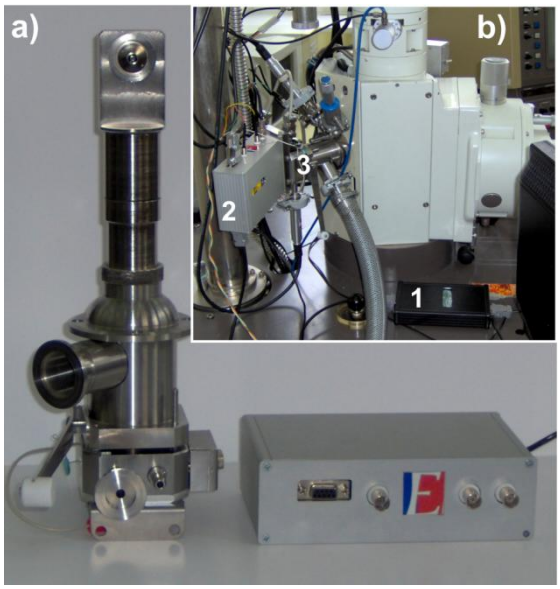

Figure 2. Detector-vacuum system for 3D imaging: a) detector-vacuum head and the five-channel signal amplifier, b) detector-vacuum equipment mounted to the JSM-840 microscope (1 - digital signal acquisition unit, 2 - five-channel signal amplifier, 3 - detector-vacuum head with the vacuum equipment, i.e. two vacuum meter gauges, dosing valve, vacuum line, etc.).

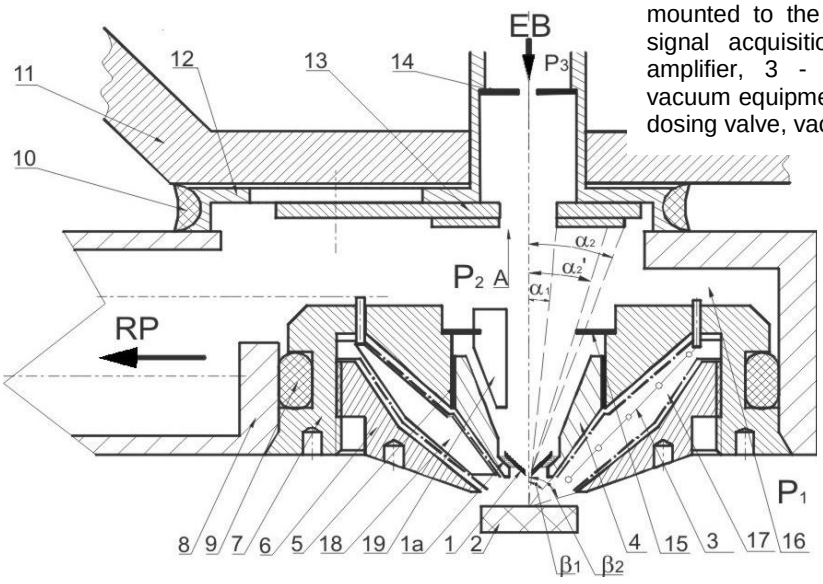

Figure 3. Combined directional electron detector: 1 – lower throttling aperture, 2 – sample stage, 3 – anode, 6 – external screening cathode, 11 – objective lens, 13 – quadrant semiconductor BSE_1 detector, 14 – upper throttling aperture, 16 – intermediate chamber,17 – emission layer, α_1, α_2 – minimal & maximal vertical BSE_1 detection angle, β_1, β_2 - minimal & maximal vertical BSE_2 detection angle, P_1, P_2, P_3 – gas pressures in particular zones, EB – electron beam, RP – vacuum system.

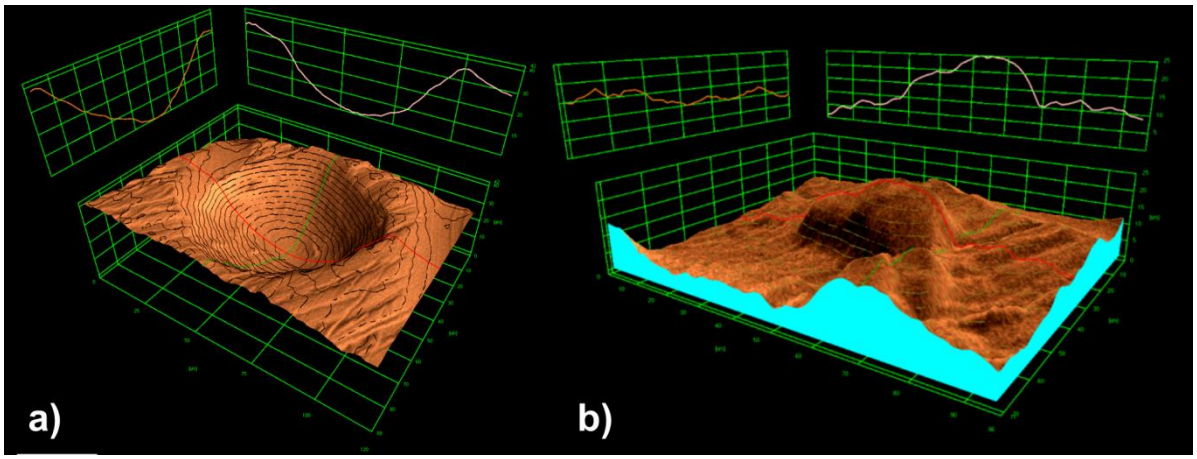

Figure 4. Images obtained from the ionisation BSE_2 detector: a) trace of a needle in polystyrene, b) impurities on the polystyrene surface (texture from a difference of BSE images, air 2 mbar, 20°C, horizontal view-fields: 120 and 95 µm respectively)

Environmental and In Situ SEM/TEM

IM.3.P066
Three dimensional imaging with combined electron detector in the Variable Pressure / Environmental SEM

W. Slówko[1], M. Krysztof[1]

[1]Wroclaw University of Technology , Faculty of Microsystem Electronics and Photonics, Wroclaw, Poland

witold.slowko@pwr.wroc.pl
Keywords: Variable Pressure/Environmental SEM, 3D imaging, quadrant semiconductor detector.

The three-dimensional imaging system has been developed in the form of an attachment to SEM, which consists of a combined directional electron detector, a frame-grabber and a PC-based processing unit. The detector head is integrated with the intermediate vacuum system to separate the sample chamber allowing gas pressure over 10 mbar and the electron optical column where high vacuum must be maintained. Quantitative information about the surface topography is obtained by digital processing of four input images acquired from four electron detectors [1]. This approach is often called a multi-detector method [2]. The multi-detector system developed by authors (Fig. 1) comprises two quadruple (4Q) backscattered electron (BSE) detectors (a PIN diode for high take off angle BSE_1 and the ionisation type for low take off BSE_2) and a secondary electron (SE) one. The multi-detector method is based on Lambert's angular distribution of backscattered (BSE) or secondary electrons (SE). A system of four detectors, placed symmetrically around the specimen (Fig. 2), allows to extract information about local topography and composition. The signal of a particular detector can be written as:

(1)

where: θ_p, φ_p - local surface topography in polar coordinates, δ_0 - secondary emission coefficient (depends on the material composition), d, c, θ_A - detector geometry coefficients, I_{PE} - electron beam current.

The local surface inclination may be obtained by dividing the difference by sum of the opposite detector signals. This provides a specimen topography profile if integrated along a scan line in the x direction. The second pair of detectors gives the initial profile in the y direction:

$$z(x,y_i) = a_x \int_{x_0}^{x_k} \left[\frac{I_A - I_B}{I_A + I_B} \right]_{y=y_i} dx + a_y \int_{y_{i=1}}^{y_i} \left[\frac{I_C - I_D}{I_C + I_D} \right]_{x=x_0} dy \qquad (2)$$

The 3D reconstruction procedure is as following. Four quadrants (4Q) of the chosen BSE detector produce four signals stored in the form of four input images as in Fig. 3b. They are processed to obtain a 3D pattern of the surface shape as a bit-map which can be visualized in any desired form. For instance, it may be a perspective view (Fig. 4a) with surface profiles shown on side grids as in Fig. 4b. This shape may be deprived of subtle details (mainly by the integration process occurring in the algorithm) usually present on every surface as a so called texture. The source of a surface texture overlaying the shape may be a combination of the input BSE images or advantageously an additional SE image shown in Fig. 3a. An impressive form of the surface shape presentation may be an anaglyph. Features of the semiconductor and ionisation 4Q BSE detectors are different. The latter can work at higher pressures and working distances of a few mm. Besides it gives a strong topographic contrast. As the result this detector can give a quantitative 3D image of the subtle meniscus of the semiliquid agar gel in Fig. 4b. Such features are particularly desired for biomedical applications. The semiconductor one captures electrons through the small throttling aperture so the sample distance must be much smaller than its diameter to prevent the detector from shadowing. This feature and its low topographic contrast (but high compositional one) make the detector destined for investigations of solid dielectric samples with strongly modulated surfaces as that in Fig. 3c. On the other hand, this detector can also work in high vacuum so the detector head is retractable to let it operate without the aperture limitations. The system has been mounted to a JSM840 microscope and additionally equipped with an environmental sample holder [3] which enables transfer of wet biological samples through the sample transfer chamber and facilitates keeping them in a natural state during investigations in the sample chamber.

1. J. Paluszyński, W. Słówko, J. Microsc. **233/1**, 2009, p. 10.
2. L. Reimer, R. Bongeler, V. Desai, Scanning Microscopy **1(3)**, 1987, p. 963.
3. W. Słówko, Patent application nr PL403014, 06.03.2013.
4. This work was supported with the budged resources for science in 2010/13 as a research project.

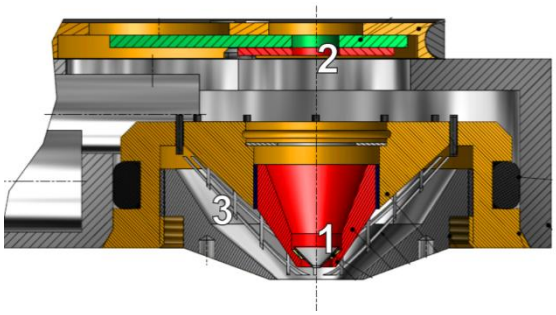

Figure 1. Cross-section of the combined electron detector:
1 - throttling aperture as the SE detector;
2 - semiconductor 4Q BSE detector;

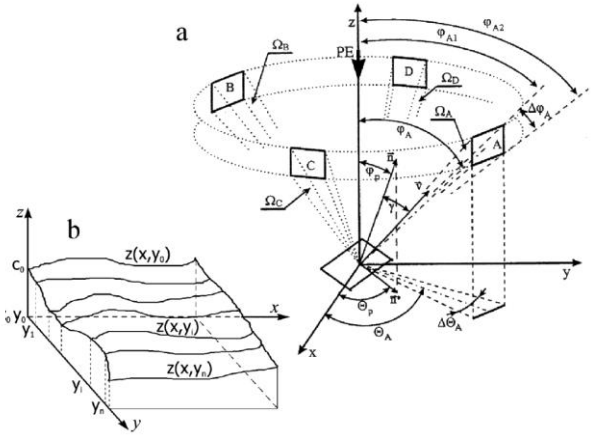

Figure 2. Illustrations to the 3D reconstruction method: a) four detector system in polar coordinates, b) surface shape reconstruction according to Eq. (2).

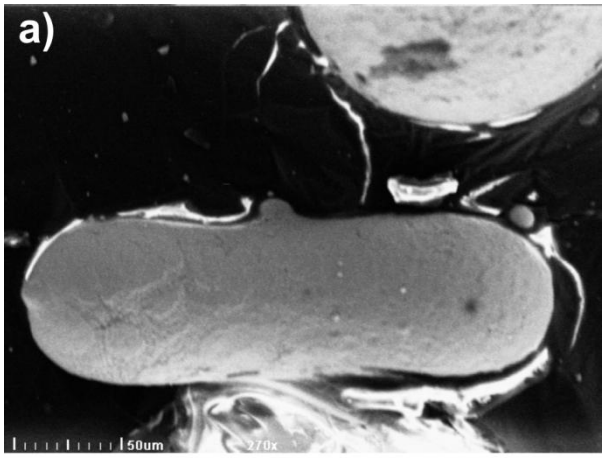

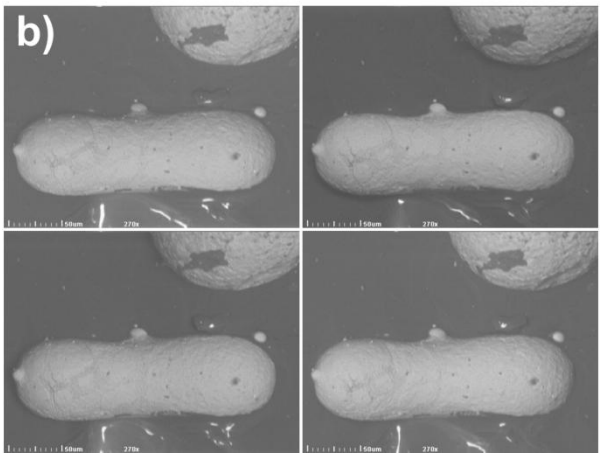

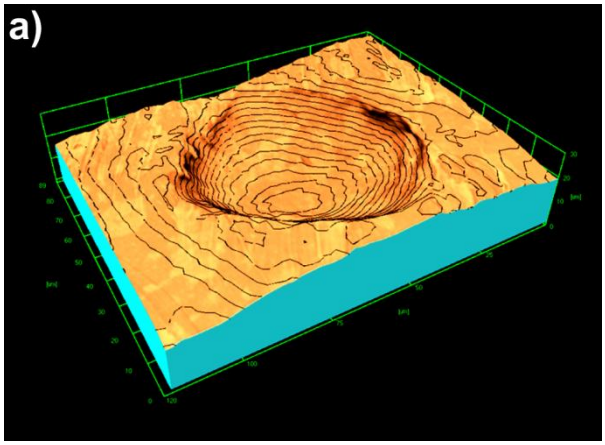

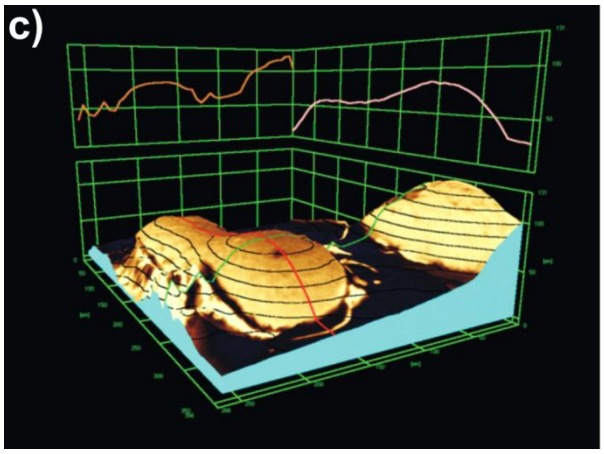

Figure 3.
Ceramic seeds on adhesive (air 2mbar, 20°C):
a) SE image used for the surface texture,
b) Four input BSE images taken from the semiconductor 4Q PIN detector for the 3D reconstruction,
c) axonometric view with level lines and surface texture taken from the SE image in a halftone color

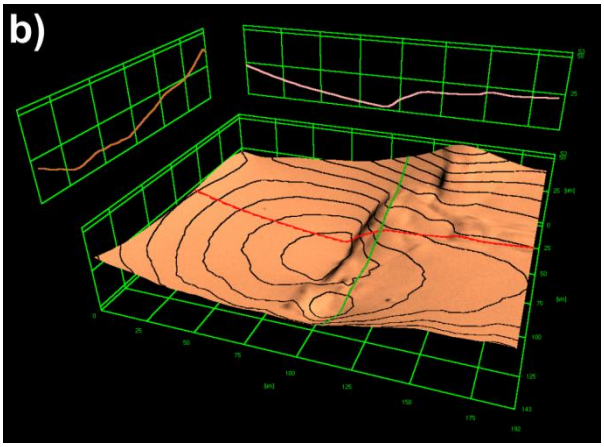

Figure 4. Images taken from the ionisation 4Q BSE detector: a) trace of needle in polystyrene (air 2 mbar, 20°C, a SE image as the texture), b) surface of agar gel with the wave caused by a submerged paper fiber (water 6 mbar, 1°C, texture from difference of BSE images).

Environmental and In Situ SEM/TEM

IM.3.P067
X-ray microanalysis in the environmental or variable pressure scanning electron microscope

J. Rattenberger[1], H. Schroettner[1,2], J. Wagner[1], F. Hofer[1,2]

[1]Centre for Electron Microscopy, Graz, Austria
[2]Graz University of Technology, Institute of Electron Microscopy and Nanoanalysis, Graz, Austria

johannes.rattenberger@felmi-zfe.at
Keywords: ESEM, EDXS quantification, scattering

Environmental or variable pressure scanning electron microscopy enables the opportunity to investigate uncoated insulators, organic, biological or even wet samples in their original state. The drawback of this technique is the scattering of primary beam electrons inside the gaseous environment of the specimen chamber, which degrades the signal to noise ratio and complicates X-ray spectrometry.

The trajectories of the scattered primary beam electrons are deflected and characteristic X-rays which originate from the surrounding but not interesting area are detected. In order to demonstrate this effect a segregation area in a steel sample was investigated under low vacuum and high vacuum conditions (see figure 1). The beam was focused on a segregation area in steel and the spectra were compared. The iron signal is strongly reduced in comparison with the high vacuum spectrum. Therefore, additional correction procedures are necessary for an accurate quantification of such spectra.

There are two basic different correction procedures, the beam stop procedure and the pressure variation procedure. The beam stop procedure is unfunctional because a micromanipulator needle made of a well-known element is needed [1].

The pressure variation method needs no additional equipment and is therefore much more practically orientated [2,3]. To use this procedure the X-ray intensities must be measured for two different chamber pressure conditions. By calculating the fraction of unscattered electrons for both pressures the unaffected intensity at 0 Pascal chamber pressure can be calculated.

The major challenge using this correction method is calculating the fraction of unscattered electrons. Therefore, the total scattering cross section of the imaging gas as well as detailed knowledge of the interaction distance between primary beam electrons and the imaging gas is necessary.

Usually the beam transfer characteristic of the microscope is neglected, which leads to an inaccuracy in measurement because the working distance (distance between pole piece and specimen) is used as interaction distance and not the stagnation gas thickness (□) which considers the static gas flow from the specimen chamber upwards the electron column and the position of the pressure limiting aperture [4]. This distance is depending on the microscope, pressure difference and gas type (see figure 2 and figure 3). Approximations and simplifications in calculating the total scattering cross section lead to additional measurement inaccuracies.

An optimised method and more precise results are presented by considering the beam transfer characteristic and using experimentally measured total scattering cross sections.

1. J.F. Mannsfield, Microchim Acta 132, (2000), p. 137
2. R. Gauvin, Scanning 21, (1999), p. 388
3. E. Doehne, Scanning 19, (1997), p. 75
4. G. Danilatos, J. Rattenberger, V. Dracopoulos, Journal of Microscopy, (2010), DOI: 10.1111/j.1365-2818.2010.03455.x
5. J. Rattenberger, J. Wagner, H. Schröttner, S. Mitsche, A. Zankel, Scanning 31, (2009), p. 107

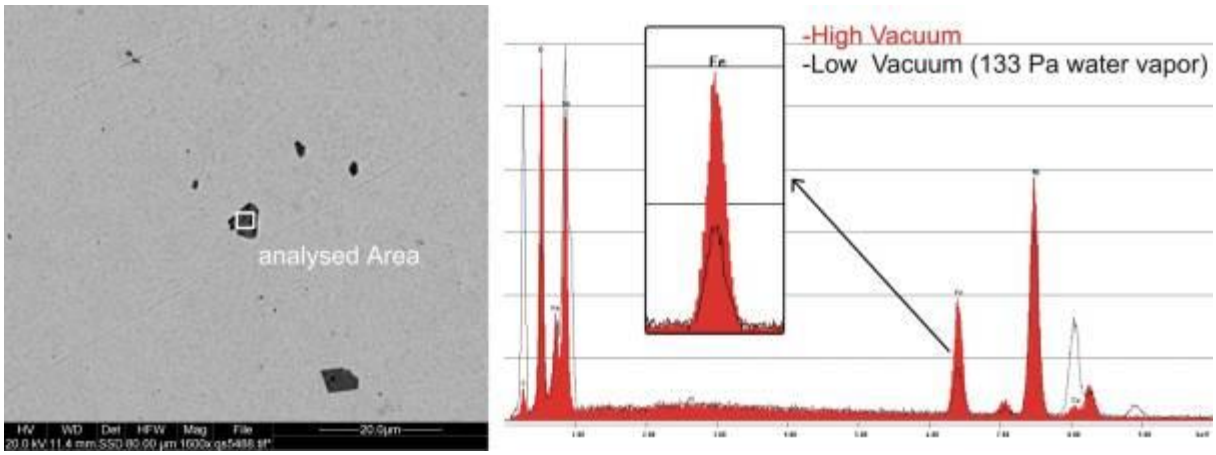

Figure 1. Analyzed area (left); Comparison of EDX spectra (low vacuum and high vacuum) (right)

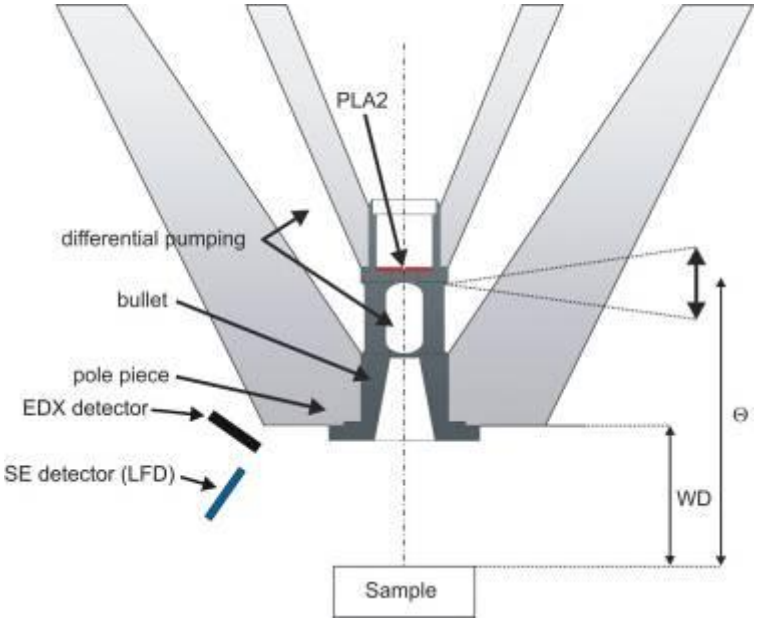

Figure 2. Schematic drawing of the FEI ESEM Quanta 600

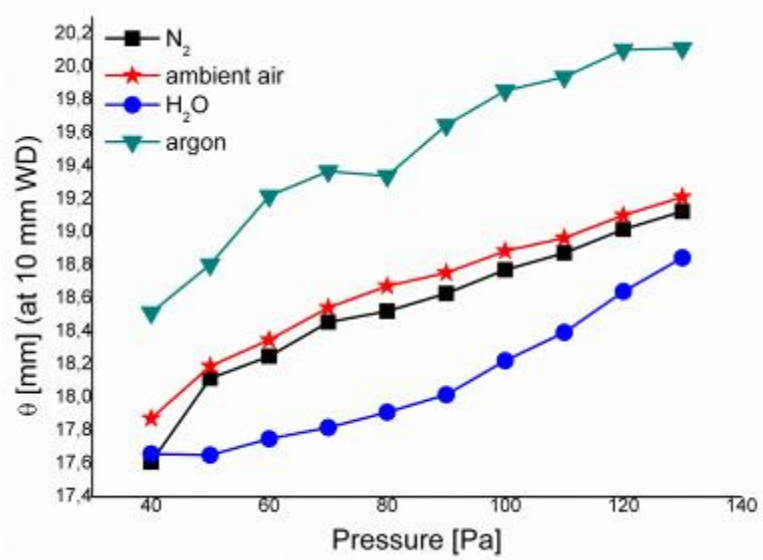

Figure 3. Stagnation gas thickness (□) [mm] as a function of the chamber pressure [Pa]

Environmental and In Situ SEM/TEM

IM.3.P068
Observation of the transformation behavior of CdSe-Cr_2Se_3 nanoparticle composites by in-situ TEM techniques

M. Deng[1], V. Hrkac[1], K. Gerwien[2], B. Hesseler[2], F. Beiroth[2], V. Duppel[3], W. Bensch[2], L. Kienle[1]

[1]University of Kiel, Technical Faculty , Kiel, Germany
[2]Uinversity of Kiel, Institute of Inorganic Chemistry, Kiel, Germany
[3]Max Planck Institute for Solid State Research, Stuttgart, Germany

mden@tf.uni-kiel.de
Keywords: in-situ TEM, CdSe, Cr_2Se_3, HRTEM, 0-3 composite

The synthesis of multinary nanomaterials is generally a complicated process due to occurrence of separation phenomena, e. g. the formation of mixtures containing binary compounds instead of ternary nanoparticles. Such limitation particularly applies when using soft chemical approaches for the syntheses, since low temperatures favor formation of metastable and inhomogeneous products. A few years ago we reported about a well-defined phase separation occurring during attempts to prepare ternary nanoparticles with composition $CdCr_2Se_4$ namely the formation of homogenously dispersed CdSe nanoparticles in an amorphous Cr_2Se_3 matrix [1]. Here we focus on the transformation behavior of CdSe-Cr_2Se_3 0-3 nanocomposites by external stimuli. Two pathways are selected for in-situ transmission electron microscopy (TEM) observations: i) High dose electron beam irradiation and ii) In-situ heating.i). Before an exposure with a high dose of electrons, the nanocomposite exhibited clearly a 0-3 microstructure, cf. the high resolution (HR)TEM micrograph in Figure 1a, top. The associated selected area electron diffraction (SAED) pattern in Figure 1a (bottom) shows strong Bragg reflections located on concentric rings besides diffuse rings of intensity. The diameter of these rings corresponds to the characteristic d-spacings of Cr_2Se_3 (diffuse rings) and CdSe (Bragg intensities) as labeled in the SAED pattern. After electron beam irradiation, the rings originating from the CdSe particles disappeared (Fig. 1b, bottom), and the remaining faint and diffuse intensities on concentric circles can be addressed to the unchanged Cr_2Se_3 matrix. At the previous positions of CdSe nanoparticles newly formed holes are clearly visible in the HRTEM micrograph (Figure 1b, top). Additionally, EDX spectra measured in the same region confirm the selective removal of the CdSe component. This finding was unexpected as the electron beam dose applied in the well known electron beam evaporation method [2] (used for synthesis of CdSe) is 10^{12} times higher than the dose selected for the TEM experiment.

ii) In the second in-situ experiment the dose of electrons was kept low, while the 0-3 nanocomposite was sequentially heated to 800 °C on a heating stage. Concerning CdSe a disappearance of the characteristic reflections in SAED was observed after reaching 550 °C. This result was confirmed by chemical investigations as no Cd could be detected after the heating procedure indicating an evaporation of the CdSe nanoparticles. The thermal evaporation temperature of CdSe in TEM significantly dropped in contrast to that of the conventional thermal physical vapor deposition. [3] Unlike the in-situ irradiation experiment and in contradiction to the phase diagram of bulk Cr_2Se_3 [4] the formation of poorly crystalline Cr after heating was detected. Figure 2(a) depicts a SAED pattern recorded on a region of the composite at 800 °C. The d-spacings of two broad diffuse rings in the SAED pattern can be assigned to (011), (112) planes of chromium (space group: Im-3m, bcc type). Moreover, structural studies performed at room temperature after heating showed also the presence of large crystalline Cr nanoparticles with an hexagonal symmetry (space group: $P6_3/mmc$, hcp type), as demonstrated in Figure 2b. This finding is in agreement with the commonly known phase diagram of Cr, featuring that the hcp type Cr is stable at room temperature, whereas temperatures above 100 °C favor the formation of bcc-Cr [5].

Another feature of the heating studies was the detected increase of the crystallinity of Cr_2Se_3 nanoparticles in comparison to the in-situ irradiation experiment. The d-spacings of the strong Bragg reflections arising in the SAED pattern of Figure 2a matches with literature values (space group: R-3) [6]. High resolution imaging supports these findings as presented in in the HRTEM micrograph and the FFT pattern of Figure 2c.

1. L. Kienle, A. Lotnyk, V. Duppel et al., MC2009 M2.P727, Graz, (2009), p.133-134.
2. N.S. Kissinger, M. Jayachandran, K. Perumal et al., Bulletin of Materials Science 30 (2008), p. 547-551.
3. K. Sharma, K. Barua, Journal of Physics D: Applied Physics 12 (1979), p. 1729-1735.
4. B. Predel in ‘‘Phase Equilibria, Crystallographic and Thermodynamic Data of Binary Alloys’’, 5d, (Springer, Berlin Heidelberg) (1994), p. 1-5.
5. Y. Miura, S. Yokota, Y. Fukai et al., Materials Transactions 46 (2005), p. 963.
6. F. Wehmeier, E. Keve, S. Abrahams, Inorganic Chemistry 9 (1970), p. 2125-2131.

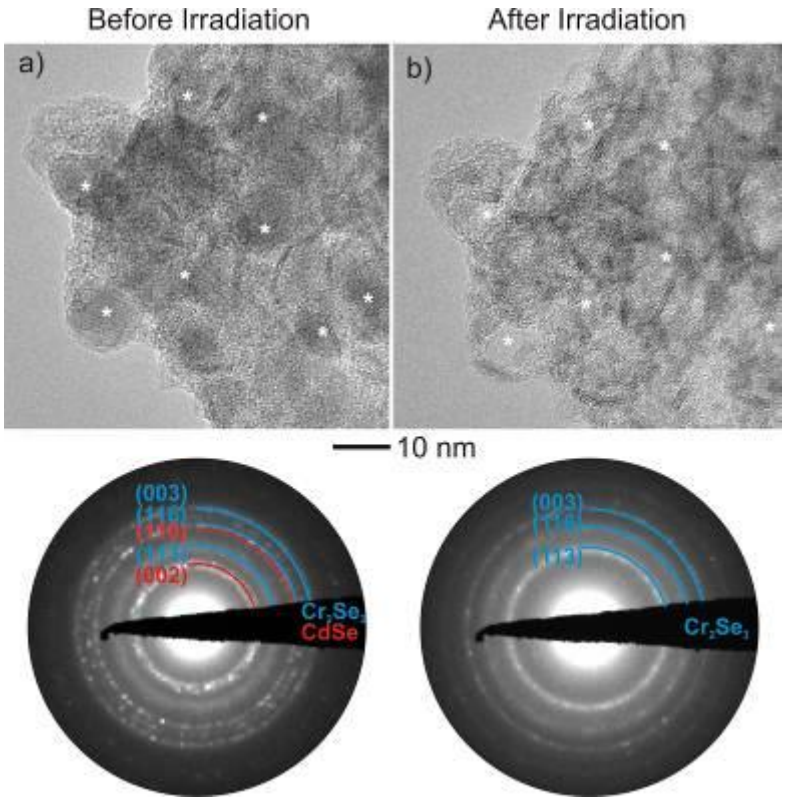

Figure 1. Comparison of HRTEM micrographs and SAED patterns recorded before (a) and after (b) in-situ transformation by exposure with a high dose of electrons evidence the removal of CdSe nanoparticles from the nanocomposite. The asterisks mark the positions of the CdSe nanoparticles present in the pristine material before the in-situ transformation.

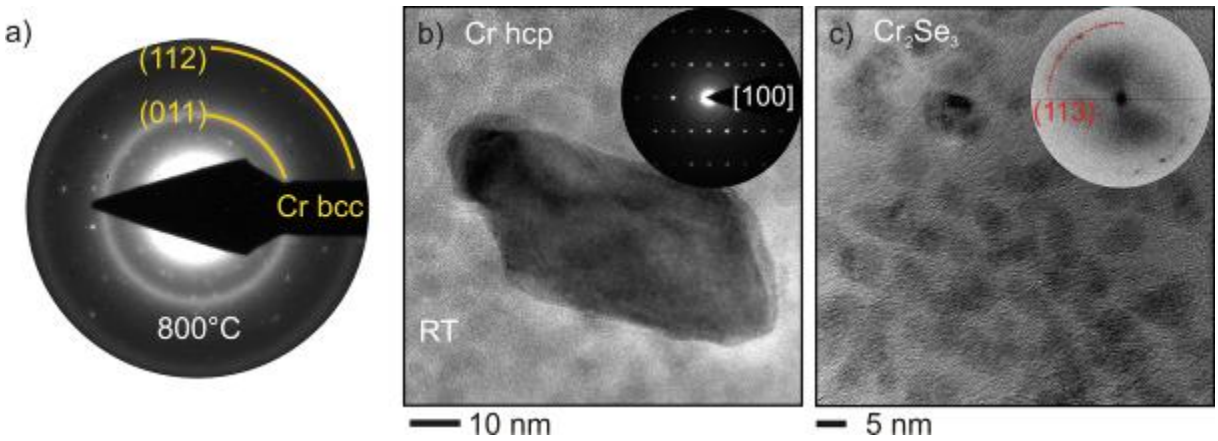

Figure 2. (a) SAED pattern after in-situ heating. (b) HRTEM micrograph of a Cr nanocrystal formed after heating with a corresponding SAED pattern as the inset. (c) HRTEM micrograph of Cr_2Se_3 particles after heating. Inset reveals the corresponding FFT.

Environmental and In Situ SEM/TEM

IM.3.P069
Local temperature measurement by introducing a piezodriven constantan-chromel nanothermocouple in TEM

N. Kawamoto[1], D. Tang[1], T. Mori[1], M. Mitome[1], Y. Bando[1], D. Golberg[1]

[1]National Institute for Materials Science (NIMS), International Center for Materials Nanoarchitectonics (MANA) , Tsukuba, Japan

Kawamoto.Naoyuki@nims.go.jp
Keywords: thermocouple, temperature measurement, transmission electron microscopy

In the last decade, much attention has been given to simultaneous analysis of a micro- and/or nanostructure and the measurements of its physical properties, such as electrical, mechanical, and magnetic ones by using probing techniques in a transmission electron microscope (TEM). For instance, in-situ TEM observation using a scanning tunneling microscopy (STM)–TEM holder equipped with a piezo-driven movable probe inside TEM has revealed electrical properties of individual carbon nanotubes (CNTs) [1], graphenes [2], BN nanoribons [3], and inorganic nanowires [4]. Also, using the same holder in-situ TEM study of an electric field-induced phenomenon, such as the lithiation process of a Li ion battery was accomplished [5]. Moreover, a force measurement on individual nanoscale materials could be performed by using an atomic force microscopy (AFM)-TEM holder [6]. On the other hand, there is a strong demand to elucidate thermal properties of advanced nanoscale materials in addition to the simultaneous study of their microstructure, electrical and mechanical characteristics in TEM [7]. Especially, it becomes quite important to measure thermal conductivity of nanoscale thermoelectric devices, and to reveal portions exhibiting high thermal resistance in a thermoconductive composite. It is thus essential to develop a measurement setup for thermal conductivity analysis across thin films which the nanodevices are made of. To do so, it is required to develop a movable thermometer in TEM possessing high sensitivity, accuracy, and a wide working temperature range. In this study, we assembled a constantan-chromel thermocouple inside TEM using a nanoscale junction by using a twin-probe STM-TEM holder, which is equipped with the two independently driven probes. By using the assembled nanothermocouple, we then performed a local temperature measurement on a thinned composite specimen consisted of highly thermal-conductive Al_2O_3 fillers and a low thermoconductive epoxy resin matrix. Non-magnetic constantan (Cu-Ni) and chromel (Cr-Ni) alloys are suitable materials for a thermocouple introduced into a high magnetic field (up to 2 T) at the specimen position in TEM. In order to make constantan [8] and chromel tips, Figure 1(a), constantan and chromel wires, whose diameters were 200 □m, were sharpened by electrochemical etching using 17 vol. % H_2SO_4 [9] and 88 vol. % H_3PO_4 solutions, respectively. As shown in a bright field TEM image of Figure 1(b), the diameter of a chromel tip could be controlled to be below 10 nm. The constantan and chromel tips were attached and screwed onto two Cu hats, which were placed on the two sapphire balls physically connected with 3 piezoelements for the precise movements in X, Y, and Z directions, Figure 1(c). Those tips can be three-dimensionally and independently moved with a subnanometer scale precision in TEM. As shown in Figure 2(a), in order to perform the measurements a thinned TEM specimen was prepared by using a focused ion beam (FIB) using a JEM-9320FIB instrument. As a sample, a thinned epoxy-Al_2O_3 composite on a flattened W tip was used, as shown in a schematic illustration of Figure 2(b). The thickness of the thinned portion was controlled to be below 100 nm. As shown in Figure 3(b), thermoelectromotive force V_T = 1500 □V could be measured by the assembled nanothermocouple during electron beam irradiation with intensity of ~500 pA/cm^2 on the top of the constantan tip near the thermocouple junction in Figure 3(a). From a calculation using the Seebeck coefficient of S = 61 □VK^{-1} for the present thermocouple, a voltage change can be converted to a temperature change of 25 K. In addition we also performed a local temperature measurement on a thinned composite TEM specimen under electron beam irradiation, as shown in Figure 3(c). The results of the local temperature measurement on this specimen will thoroughly be discussed in the presentation. N. K. and T. M. are also affiliated with the “TIA Nanogreen” Project.

1. Z. L. Wang, P. Poncharal, and W.A. de Heer, J. Phys. Chem. Sol. 61, (2000), p. 1025.
2. A. K. Schaper, H. Hou, M. S. Wang, Y. Bando, and D. Golberg, Carbon 49, (2011), p. 1821.
3. H. Zeng, C. Y. Zhi, Z. H. Zhang, X. L. Wei, X. B. Wang, W. L. Guo, Bando Y, and Golberg D, Nano Lett. 10, (2010), p. 5049.
4. Z. Xu, Y. Bando, W. L. Wang, X. D. Bai, and D. Golberg, ACS Nano 4 (2010), p. 2515.
5. X. Wang, D. M. Tang, H. L, W. Yi, T. Zhai, Y. Bando Y, and D. Golberg, Chem. Commun. 48 (2012) p. 4812.
6. D. M. Tang, C. L. Ren, M. S. Wang, X. L. Wei, N. Kawamoto, C. Liu, Y. Bando, M. Mitome, N. Fukata, and D. Golberg, Nano Lett. 12 (2012), p. 1898.
7. N. Kawamoto, D. M. Tang, X. Wei, X. Wang, M. Mitome, Y. Bando, and D. Golberg, Microscopy 62 (2013), p. 157.
8. N. Kawamoto, M. S. Wang, X. Wei, D. M. Tang, Y. Murakami, D. Shindo, M. Mitome, and D. Golberg, Nanotechnology 22 (2011), p. 485707.
9. R. Kasshing, and E. Oesterschulze, Proceedings of the NATO Advanced Study Institute (Sesimbra, Portugal), (1996), p. 35.

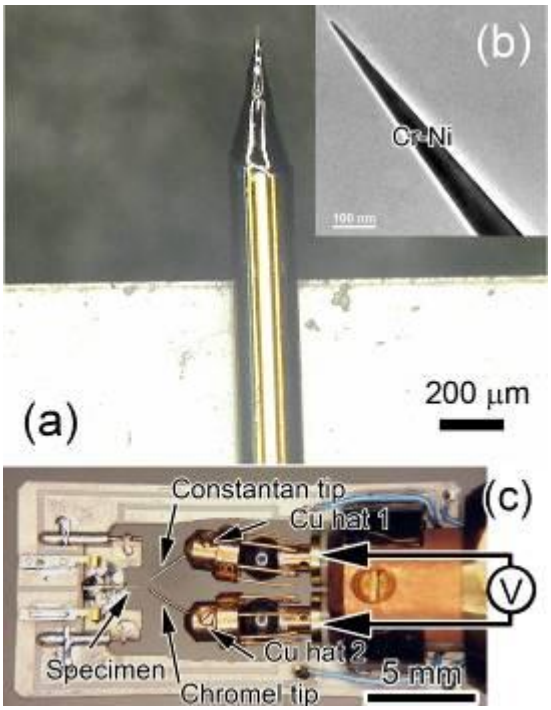

Figure 1. (a) Optical micrograph and (b) TEM image of a Cr-Ni (Chromel) tip prepared by using electrochemical etching. (c) Top part of twin-probe STM-TEM holder.

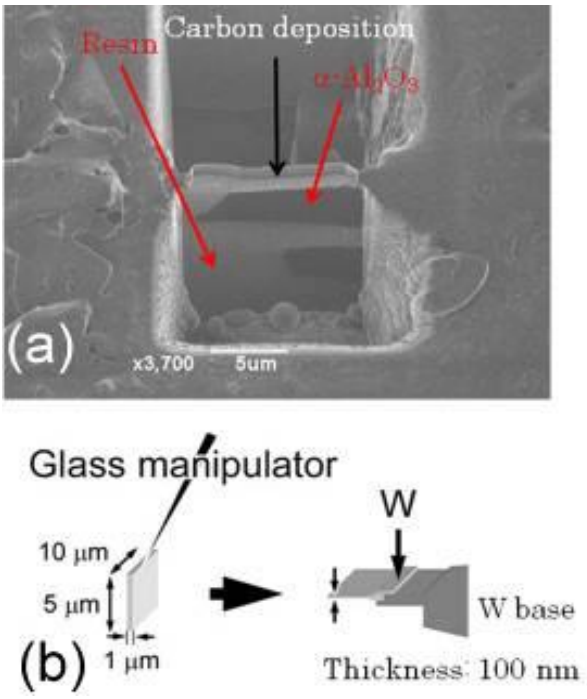

Figure 2. (a) Scanning ion microscopy (SIM) image of a thinned portion of an Al_2O_3-epoxy composite milled by FIB. (b) A schematic illustration of making a thinned portion supported on the W base by using a glass manipulator.

Environmental and In Situ SEM/TEM

IM.3.P070
In situ heating and tomography of gold nanoparticles on carbon structures

M. Fay[1], A. La Torre[1,2], M. Gimenez-Lopez[3], C. Herreros Lucas[3], A. Khlobystov[1,3], P. Brown[1,4]

[1]University of Nottingham, Nottingham Nanotechnology and Nanoscience Centre, Nottingham, United Kingdom
[2]Institut de Physique et Chimie des Materiaux de Strasbourg, Strasbourg, France
[3]University of Nottingham, School of Chemistry, Nottingham, United Kingdom
[4]University of Nottingham, Faculty of Engineering, Nottingham, United Kingdom

michael.fay@nottingham.ac.uk

Supported gold nanoparticles may be used for a wide range of applications, including low temperature catalysis and light absorption [1]. As the functional properties of gold nanoparticles are strongly affected by their size and shape, it is necessary to obtain a full understanding of the thermal stability of supported gold nanoparticles and how it is affected by the material support.
A series of thermally mediated dynamic (in situ) experiments in the transmission electron microscope (TEM) have been performed, in order to obtain improved understanding and control of the ripening and migration processes of gold nanoparticles on multi-wall nanotubes (MWNTs). In particular, post-heating tomography was used to appraise the resultant dispersion of the nanoparticles within these three-dimensional (3D) composite structures.
Arc-discharge produced MWNTs (AD-MWNTs, MER corporation) were treated with nitric acid (16 M for 24 h) at the reflux point and the resulting mixture was then diluted with deionised water (200 mL). This was filtered using a 0.45 μm pore size PTFE membrane filter, washed thoroughly with water until neutral pH and ethanol (50 mL), and dried under vacuum to yield a black solid (192 mg). 1 mg of Gold nanoparticles were suspended in hexane and mixed, *via* sonification, with 1 mg of AD-MWNTs [2]. The resultant composite material was again filtered through PTFE and washed with ethanol and acetone. The composite was dispersed in ethanol and spotted onto graphene oxide TEM support films (Graphene Supermarket). The commercial availability of graphene oxide films is advantageous for work of this nature. This substrate has benefits for both the heating and tomographic analysis of these composite materials. Firstly, the substrate provides better heat conductivity than traditional amorphous carbon films, allowing the temperature at the sample to be more reliably calculated from knowledge of the heating holder crucible temperature. Secondly, the low contrast background of the graphene oxide film assists greatly in tomographic reconstruction, producing minimal background to the sample even at high tilt angles.
Imaging for *in situ* heating and tomographic analysis has been performed largely in scanning TEM mode. This rastering mode of imaging reduces beam heating effects [3], ensuring that the ripening of the nanoparticles during *in situ* heating is predominantly an effect of thermal heating from the support stage, with no observable further ripening occurring during post-heating tomographic analysis. High angle annular dark field (HAADF) imaging is particularly suitable for analysing metal nanoparticles on 3D carbon supports as the atomic number sensitivity makes few-nm sized metallic nanoparticles visible against the background for a significantly greater volume of graphitic material. As the orientation of the crystalline nanoparticles does not strongly affect the intensity of the HAADF image, this mode produces an image series that is particularly suitable for tomographic reconstruction.
TEM investigations were performed using a Jeol 2100F equipped with digital STEM. *In situ* heating was performed using a Gatan 652 double tilt heating holder. Post-annealing tilt series were acquired using a Gatan 916 room temperature tomography holder. The relationship between the temperature of the nanoparticles on a graphene oxide film to the recorded temperature of the heating holder crucible was calibrated prior to this work using the evaporation temperature of Ag nanoparticles dispersed onto graphene oxide film, as a reference point [4, 5].

1. T. Turba, M. Grant Norton, I. Niraula, D. N. McIlroy, *J. Nanopart. Res.*, 2009, 11, 2137-2143.
2. M. Brust, M. Walker, D. Bethell, D. J. Schiffrin, R. Whyman, J. Chem. Soc., Chem. Commun., 1994, 801 804.
3. La Torre, M. C. Giménez-López, M. W. Fay, G. A. Rance, W. A. Solomonsz, T. W. Chamberlain, P. D. Brown, A. N. Khlobystov, *ACS Nano*, 2012, 6, 2000-2007.
4. S. Y. Kang, K. Kim, *Langmuir*, 1998, 14, 226-230
5. T. Yonezawaa, S. Arai, H. Takeuchi, T. Kamino, K. Kuroda, *Chem. Phys. Rev.*,2012, 537, 65-68.

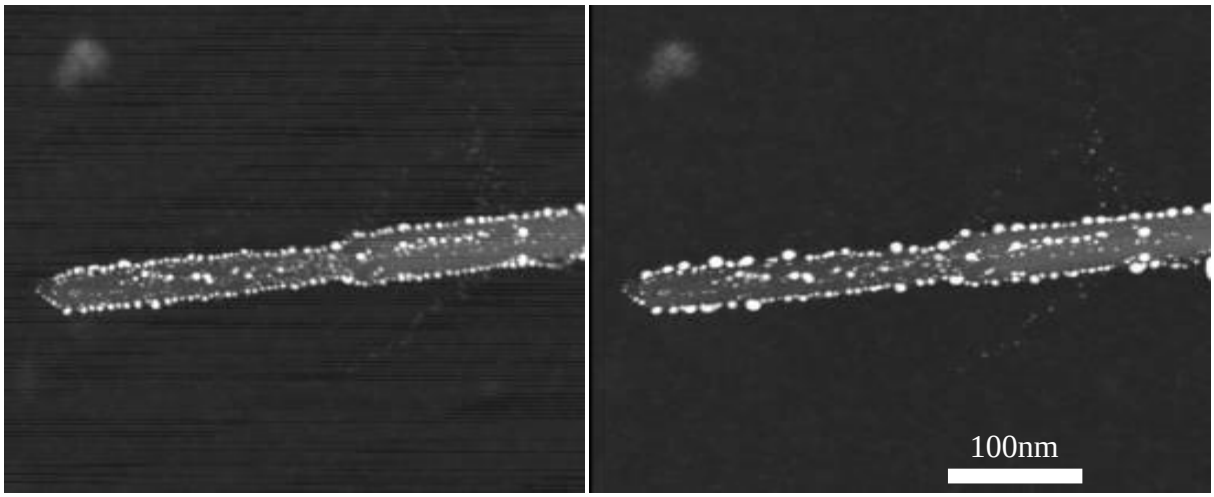

Figure 1. HAADF images of Au nanoparticles on acid treated MWNT, annealed *in situ* at 500 °C for 135 minutes, illustrating the ripening of the nanoparticles. Left: t=0 min, right t=135min.

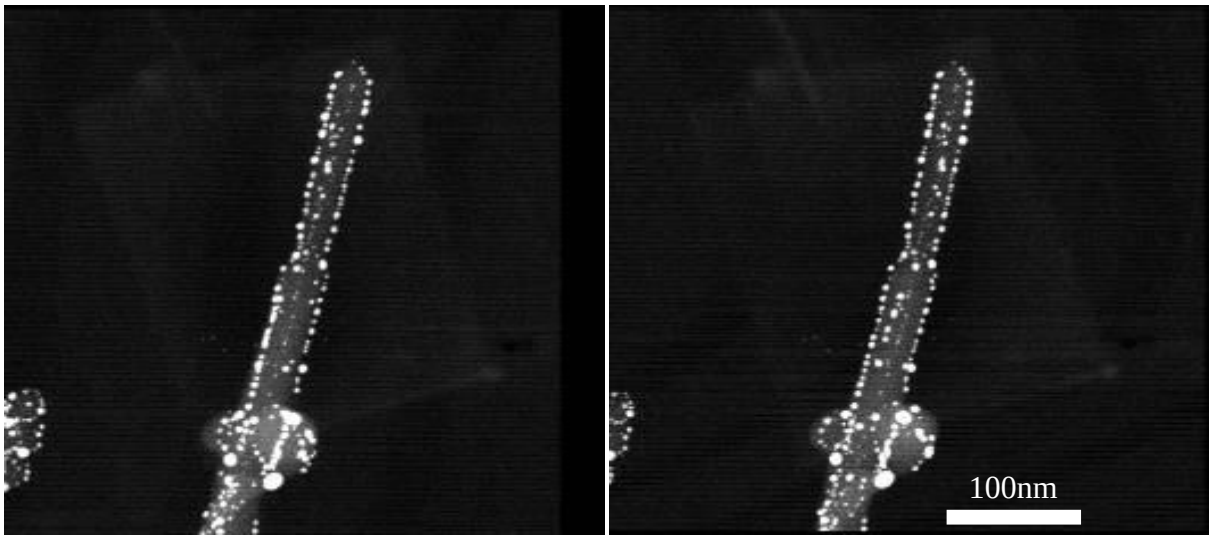

Figure 2. HAADF stereogram images of gold nanoparticles on multi-walled carbon nanotubes after *in situ* annealing. From tilt-series analysis, it can be seen that particles on the exterior of the nanotube exhibit more significant ripening than those encapsulated within the tube, and are located in a linear orientation on the exterior of the nanotubes

Environmental and In Situ SEM/TEM

IM.3.P071
Multifunctional tool FIB-SEM-SPM and its application for electron and ion beam lithography

J. Jiruse[1], B. Lencova[1], M. Rudolf[1], M. Bartosik[2,3], Z. Liskova[2,3], J. Neuman[2,3], T. Sikola[2,3]

[1]TESCAN a.s., Brno, Czech Republic
[2]Brno University of Technology, IPE FME, Brno, Czech Republic
[3]Brno University of Technology, CEITEC, Brno, Czech Republic

bohumila.lencova@tescan.cz
Keywords: FIB-SEM, SPM, electron beam lithography, ion beam lithography

A combined FIB-SEM-SPM tool has been introduced recently by TESCAN as the first commercial system of its kind [1]. The FIB-SEM instrument LYRA GM was integrated with a scanning probe microscope Curlew™ SPM from SPECS so that it allows in-situ investigation by SPM without affecting the FIB-SEM operation. The tool can be equipped with a large number of detectors, e.g. EBSD and energy dispersive X-ray spectrometer, as well as with gas injection system and nanomanipulators [1]. For the compositional analysis the time-of-flight mass spectrometer of TOFWERK AG can be optionally installed [2, 3].
Electron and/or ion beam lithography (EBL, IBL) is yet another technique possible with this tool. Surface patterns to be exposed by electron or ion beams are generated using TESCAN DrawBeam software that enables sketching of arbitrary geometrical shapes, arrays or bitmap pictures. Thus it is possible to manufacture the nanostructures and consequently to investigate and optimize the exposed ones in-situ.
The combined FIB-SEM-SPM was used to create a nanostructure of squares, circles and dots with 0.4 to 1 µm spacing on the surface of oxidized silicon substrate. The use of a focused ion beam (FIB) is a straightforward method to sputter a shallow (less than 10 nm) motive defined in DrawBeam. An example is shown in Figure 1; the structures are created within frames of 40x40 μm^2 made by FIB. It is possible to control and optimize the shapes and the depths of the resulting structures by both the high-resolution scanning electron microscope and the scanning probe microscope (SEM, SPM). Such structures are used for selective growth of metallic (Co, Au) or semiconductor (GaN) islands deposited ex-situ, e.g. by an effusion cell in UHV. Final patterns are again localized by SEM and imaged by SPM.
The investigation of electrical properties of graphene is another topical research subject. Exfoliated graphene flakes are recognized only by optical microscopy on some 280 nm silicon dioxide on silicon. The oxidized silicon substrate contains large area contacts and orientation markers made beforehand by EBL to identify position of suitable graphene flakes in the optical microscope. Then the surface is covered with a 170 nm thick positive resist. The optical image of selected areas is loaded into DrawBeam software as a bitmap and correlated with the SEM image. The resist is exposed by electrons so that the required 60 nm thick gold contacts to the graphene are made. The exposure of the graphene by electrons should be minimized in order to preserve the electrical properties of graphene for the subsequent measurement of its transport properties.
The in-situ imaging with a SPM extends significantly the imaging possibilities of the FIB-SEM system. The depth resolution of SPM in the nm range is used to characterize the efficiency of FIB-SEM for patterning or sputtering on various substrates (for more examples see [2] or the TESCAN web pages). The DrawBeam software defines the area on the sample to be exposed by electrons or ions, thus EBL or IBL becomes available even to smaller university laboratories.

1. J. Jiruše et al, Microsc. Microanal. 18 – suppl. S3 (2012), p. 638-639.
2. M. Zadražil et al, Proc. 3M—NANO 2012, Xi´an, China. ISBN: 978-1-4673-4589-7, p. 175-179.
3. J. Whitby et al, Adv. Mater. Sci. Eng. 2012, 180437.
4. Supported by the European Union FP7 Programme (Contract No. 280566, project UnivSEM).

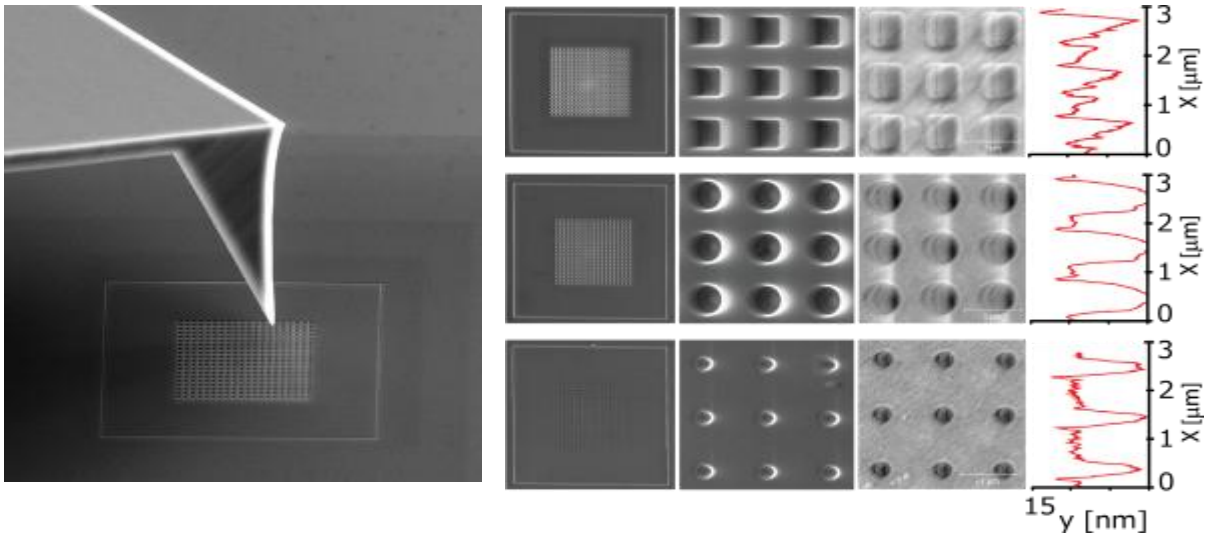

Figure 1. Left figure shows SEM image of a patterned sample with the Akiyama SPM probe. The frames made by FIB are 40x40 μm^2; they are used for SEM navigation and serve as a playground for the arrays made by IBL and optimized using both SEM and SPM. The right figure shows SEM image of the frame and pattern (column 1 from left) and SEM and SPM detailed images of the same patterns with the square, circle and dot elementary motive (column 2 and 3, respectively). The rightmost column, SPM linescans through the centers of the pattern, give the depths and distances of the structures made by IBL.

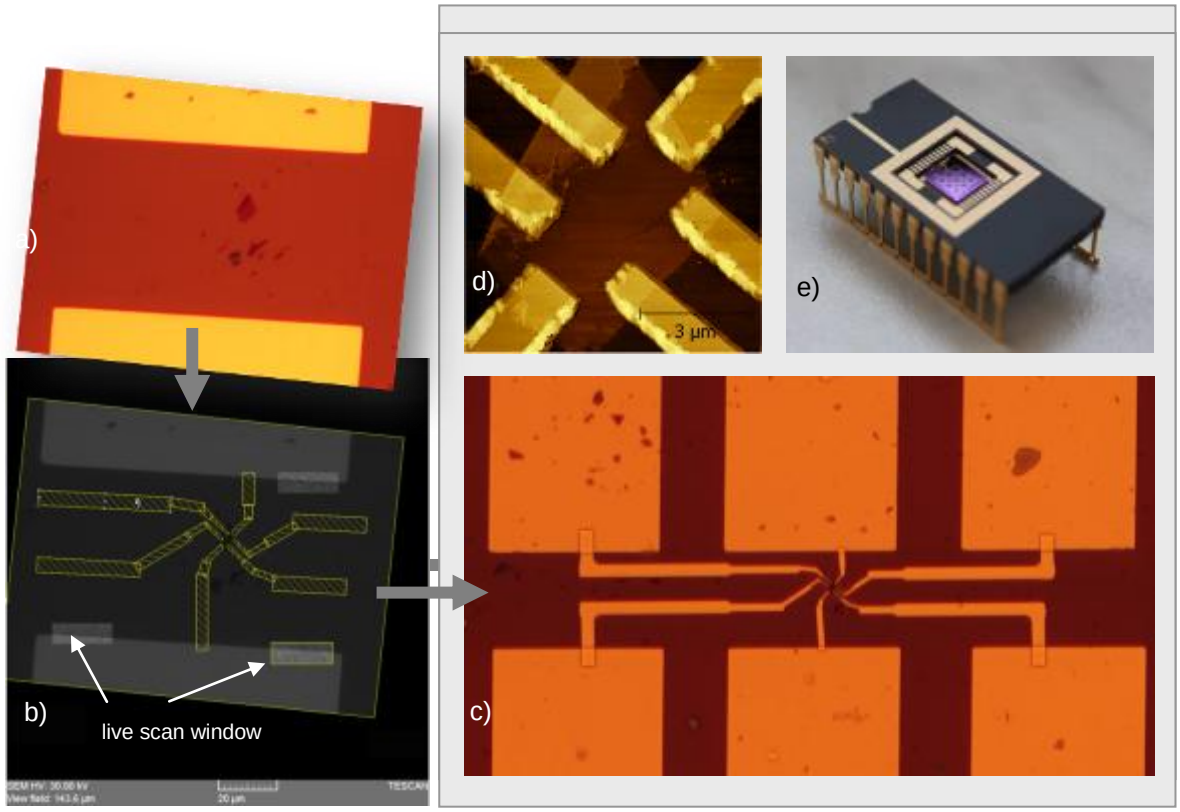

Figure 2. Fabrication of contacts to the graphene flakes. An optical image of the flake is loaded into the DrawBeam software module as a bitmap and correlated with the live secondary electron image. The desired patterns are drawn into the resist by electron beam to the required positions (a, b) without exposing the graphene. Finally we show the optical image (c) and atomic force microscope detailed scan (d) of the contacted graphene, and the sample (e) ready for the measurement of transport properties.

Environmental and In Situ SEM/TEM

IM.3.P072
Atomic-scale Observation of Catalysts in their Functional State using aberration-corrected Environmental Transmission Electron Microscopy (ETEM)

D. Sudfeld[1], J.R. Jinschek[1]

[1]FEI Company, Materials Science BU, Eindhoven, Netherlands

Today's strong focus on efficient energy conversion and environment protection technologies relies on the advancement of (new) functional nanomaterials, such as heterogeneous catalysts. Characterization of the state and properties of such a nanocatalyst as well as of its activity, selectivity and stability demands detailed dynamic atomic-scale insights. High-resolution transmission electron microscopy (HRTEM) has become an indispensable tool for characterizing nanomaterials and provides the unique ability to image size, shape, as well as surface and interface structures at the atomic scale. With more recent advances in electron optics, aberration-corrected HRTEM is now able to detect the atomic structure ultimately with a resolution below 0.1 nm and with single atom sensitivity.

Standard TEM experiments are performed with the sample kept under high vacuum conditions inside the microscope column. But, such conditions might be inadequate to investigate the active functional state of a catalyst whose properties depend on varying reaction conditions. In those cases, studies should preferably be performed *in situ* under the exposure to a gas environment, matching the conditions encountered during the technical use of the nanosystem. Dynamic, atomic-scale visualization of structural evolutions *in situ* under reactive gas environments directly addresses the environment-dependent structure and dynamics of functional states of a nanocatalyst. This is a crucial step in R&D, because generally there is no evidence that the dynamic state of the structure can be derived from postmortem (high vacuum) examinations of the materials alone. State-of-the-art HRTEM imaging and spectroscopy capabilities can now also be applied for *in situ* studies of structure and dynamics of nanocatalysts induced by reactive gas environments. Differentially pumped environmental TEMs (ETEMs) [1,2] are uniquely designed to permit gas in the microscopes specimen area while preserving the atomic-scale performance of an aberration-corrected microscope (Titan ETEM G2) [3,4]. Application of ETEM shows to be an essential complement to theoretical approaches as well as to the arsenal of established spectroscopic techniques (e.g. applied at synchrotron facilities) that average information over length scales considerably larger than the dimensions of the nanostructures. It has been assumed that the added gas environment may affect the ultimate HRTEM image resolution and sensitivity. However, the 0.10 nm (= 1Å) resolution threshold can be maintained up to at least 10 mbar gas pressure inside the specimen area [4]. The optimal imaging conditions for atomic-scale *in situ* studies are determined by a careful selection of electron beam energy and dose-rate as well as image signal-to-noise (S/N) ratio (see Fig. 1) [4]. As an example a catalyst composed of gold (Au) nanoparticles (NP) supported on cerium oxide (CeO_2) has been examined [5]. Au nanoparticles supported on metal oxides such as CeO_2 become active for the oxidation of carbon monoxide (CO), even below room temperature (RT). In situ HRTEM experiments, shown in Fig. 2, depict that adsorbed CO molecules cause the {100} crystal facets of Au NP to reconstruct to Au{100}-hex during CO oxidation at RT. The stable Au{111} surface is considered to be oblivious to the presence of CO gas. The CO molecules adsorbed at the on-top sites of Au atoms in the reconstructed Au{100}-hex surface, and the energetic favorability of this reconstructed structure has been confirmed by *ab initio* calculations and image simulations (Fig. 2) [5]. The experimental data indicates that the active sites of the Au nanocatalysts are located at the particle-support periphery where gas species such as O_2 or -OH probably react with CO. The methodology demonstrated in this study has opened an experimental route toward the elucidation of Au nanoparticles catalytic mechanisms by direct observation of metal atoms and gas species at the particle-support periphery using aberration-corrected ETEM [5].

1. The growing number of application examples proves that a differentially pumped ETEM is a powerful tool for applied research and development on functional nanostructures (such as catalysts, batteries, fuel cells, etc.) that requires exposure to an operational/reactive gas environment. State-of-the-art ETEM techniques provide exclusive data from these dynamic *in situ* processes at the atomic scale.
2. E.D. Boyes; P.L. Gai, Ultramicroscopy 67 (1997) 219.
3. P.L. Hansen, J.B. Wagner; S. Helveg; J.R. Rostrup-Nielsen; B.S. Clausen, H. Topsoe, Science 295 (2002) 2053.
4. http://www.fei.com/ETEM
5. J.R. Jinschek, S. Helveg, Micron 43 (2012) 1156.
6. H. Yoshida, Y. Kuwauchi, J.R. Jinschek, K. Sun, S. Tanaka, M. Kohyama, S. Shimada, M. Haruta, S. Takeda, Science 335 (2012) 317.
7. The authors wish to thank the ETEM community for all the education, the encouragement and for the fruitful discussions. For the work presented here J.R. Jinschek gratefully acknowledges Stig Helveg (Haldor Topsøe A/S) and Seiji Takeda (Osaka University) for their collaboration and continuous support. Also, the authors thank FEI's ETEM team and FEI's Materials Science Business Unit (FEI.com/ETEM).

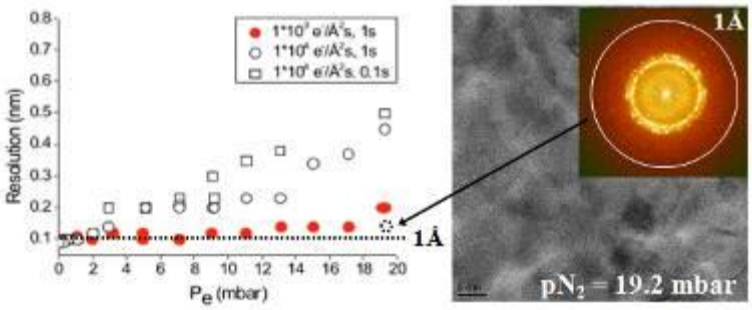

Figure 1. left side: HRTEM image resolution vs N_2 pressure in ETEM. **right side:** HRTEM micrograph taken under the lower dose-rate condition [4].

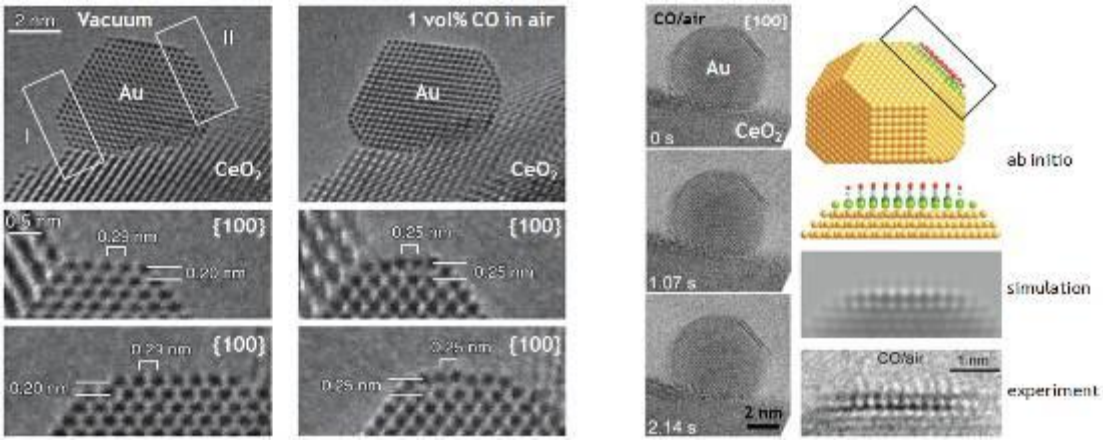

Figure 2. left side: Au/CeO_2 in vacuum and in reaction environment for CO oxidation. Under catalytic conditions Au NP exhibit Au{100}-hex reconstructed surface structures. (see {100} facets in the rectangular regions indicated by I and II). right side: Au/CeO_2 observed in reaction environment. An image feature appeared on the upper-right part of the Au NP & Au NP model with a Au{100}-hex reconstructed surface and adsorbed CO molecules. Comparison between corresponding calculated TEM image and the experimentally observed image confirms the presence of Au{100}-hex reconstructed surface with adsorbed CO [5].

Environmental and In Situ SEM/TEM

IM.3.P073
In situ tensile tests of single crystal metal nanowires inside the SEM and TEM

T. Erichsen[1], B. Roos[1], B. Kapelle[1], G. Richter[2], C.A. Volkert[1]

[1]University of Göttingen, Institute for Materials Physics, Göttingen, Germany
[2]Max Planck Institute for Intelligent Systems, Stuttgart, Germany

terichsen@ump.gwdg.de

It is well known that the mechanical properties of nanoscale metals differ from those of macroscale samples, in particular the strength increases with decreasing sample size. A number of studies on sub-micron sized metals have been performed which attempt to reveal the mechanisms controlling deformation at small length scales. Machine compliance and complex stress states are often major problems in nanomechanical experiments that make the interpretation of the results challenging.

Here we present a combination of two complementary in situ electron microscopy studies: qualitative TEM tensile tests, which allow direct observation of the defect evolution, and quantitative testing inside the SEM, where the stress-strain behavior of the wires is determined. The use of the two methods makes the realization of very stiff set-ups possible and tests on metal whiskers show highly reproducible results both in TEM and SEM.

To test the wires in the TEM a standard straining holder is used. Wires are transferred with the aid of a micromanipulator and electron beam assisted Pt deposition onto a CuBe frame leaving the wires undeformed (see Figure 1). The homogeneous deformation of the gauge length of the frame allows the realization of deformation steps <1nm. During deformation, movies as well as high resolution TEM images are recorded to monitor the defect evolution and investigate the fundamental mechanisms of deformation.

The tensile stage for the SEM consists of two piezoelectric positioners (x- and y-direction) on the one side, with a TEM-grid mounted on top. On the opposite side, a MEMS based force-sensor is mounted on top of a third positioner (z-direction). Nanowires from the same batch are transferred in an analogous manner to stretch from the grid to the tip of the force-sensor (see Figure 2). Strains are obtained by digital image correlation of SEM images taken during testing and stresses are calculated from the measured force and the wire area as measured by a FIB cross-section. Post-mortem TEM investigations of the failed wire segments allow the deformation morphologies of the SEM and TEM tested wires to be compared.

Investigations show that single crystal Au nanowires with diameters ranging from 40 to 250 nm deform at stresses in excess of 1 GPa by homogeneous nucleation of partial dislocations creating stacking faults on {111} planes. The stacking faults thicken into nanotwins through the sequential activation of partial dislocations on neighboring {111} planes. Post-deformation TEM studies show that fracture occurs within the nanotwins.

A quantitative model based on classical nucleation theory will be presented which explains the observed difference in deformation mode. Implications for different materials and loading geometries will be discussed. In addition, preliminary studies of the effect of surface structure and gas ambient on the deformation behavior of the nanowires will be introduced.

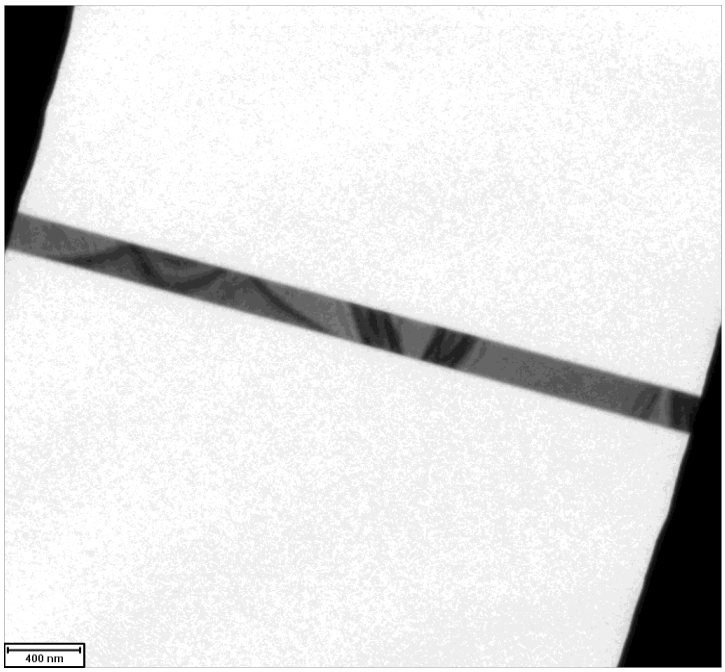

Figure 1. Bright field image of a transferred single crystal Au wire. Only bending contrast is visible indicating that the transfer process leaves the wire undeformed.

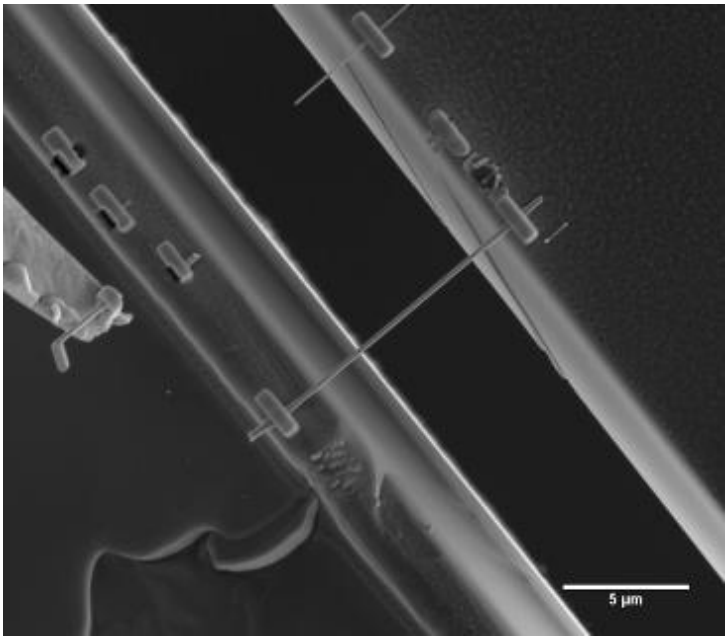

Figure 2. SEM image of a wire glued with aid of a micromanipulator and electron beam assisted Pt deposition to a TEM-grid (lower left corner) and the tip of the force sensor (upper right corner).

Environmental and In Situ SEM/TEM

IM.3.P074
Preventing charging of liquid cell silicon nitride windows for phase contrast *in situ* TEM

G. Tamura[1], U. Mirsaidov[2,1], P. Matsudaira[2,1]

[1]National University of Singapore (NUS), MechanoBiology Institute (MBI), Singapore, Singapore
[2]National University of Singapore (NUS), Centre of Bio-Imaging Sciences (CBIS), Singapore, Singapore

goshu@nus.edu.sg
Keywords: liquid cell, environmental cell, wet cell, phase contrast, TEM, in-situ,

Liquid cells with thin silicon nitride (SiN) membrane windows (Figure 1) that enclose liquid samples are essential for *in-situ* transmission electron microscope (TEM) both for material and life sciences. [1-4]. However, for biological samples the image contrast is substantially reduced due to the low difference of the density between specimen and liquid. Image contrast can be improved by Zernike-type carbon phase plates inserted in back focal plane of TEM [5] and by image capture with fast and sensitive direct electron detection C-MOS camera [6]. This combination allows capture of dynamic processes with high contrast and relatively low doses.

A current drawback of the liquid cells charging of the windows when exposed to electron beam [2] which leads to unintentional beam focusing as shown in Figure 2.

We demonstrate that distortion of the beam focusing is eliminated by carbon coating of SiN membranes in liquid cells as illustrated in Figure 3. By solving the charging problem, we can demonstrate the possibility of imaging biological samples at room temperature and in liquid water by phase contrast in our liquid cell.

1. H. Zheng, U. Mirsaidov, L.-W. Wang, P. Matsudaira, “Electron beam manipulation of nanoparticles.” Nanoletters, 12(11), 5644-5648 (2012).
2. U. Mirsaidov, H. Zheng, D. Bhattacharya, Y. Casana, P. Matsudaira, “Direct observation of the stick-slip movement of nanometer-size water droplets induced by electron beam” Proc. Natl. Acad. Sci. U.S.A. 109(19), 7187-7190 (2012).
3. U. Mirsaidov, C. D. Ohl, P. Matsudaira, “A direct observation of nanovoid formation in ultrathin water film” Soft Matter 8(27), 3108-3111 (2012).
4. U. Mirsaidov*, H. Zheng*, Y. Casana, P. Matsudaira, “Imaging protein structure in water at 2.7 nm resolution by TEM” Biophysical Journal 102(4), L15-17 (2012).
5. R. Danev, K. Nagayama. “Transmission electron microscopy with Zernike phase plate” Ultramicroscopy 88, 243-252 (2001).
6. A. C. Milazzo, G. Molodovan, J. Lanman, L. Jin, J. C. Bouwer, S. Klienfelder, S. T. Peltier, M. H. Ellisman, A. I. Kirkland, N. H. Xuomg. “Characterization of a direct detection device imaging camera for transmission electron microscopy” Ultramicroscopy 110 (7), 744-7 (2010).
7. Acknowledgement: We want to thank to JEOL for using and testing of 2200 FS TEM with the phase plate system.

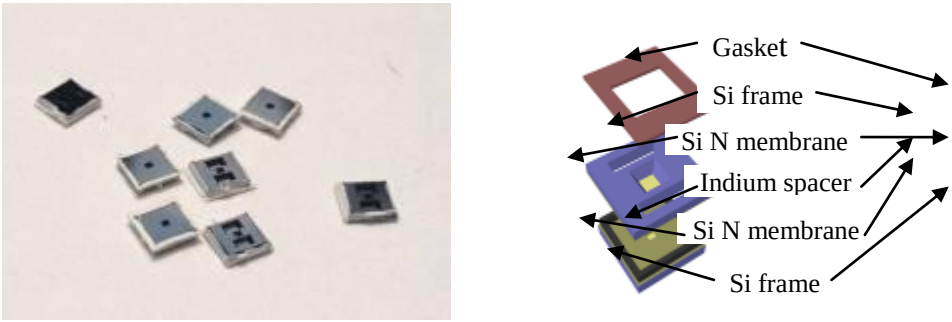

Figure 1. Photo and schematics of liquid cell. The size of the liquid cell is 2.8 mm squared. The window size is 3 by 50 micrometers.

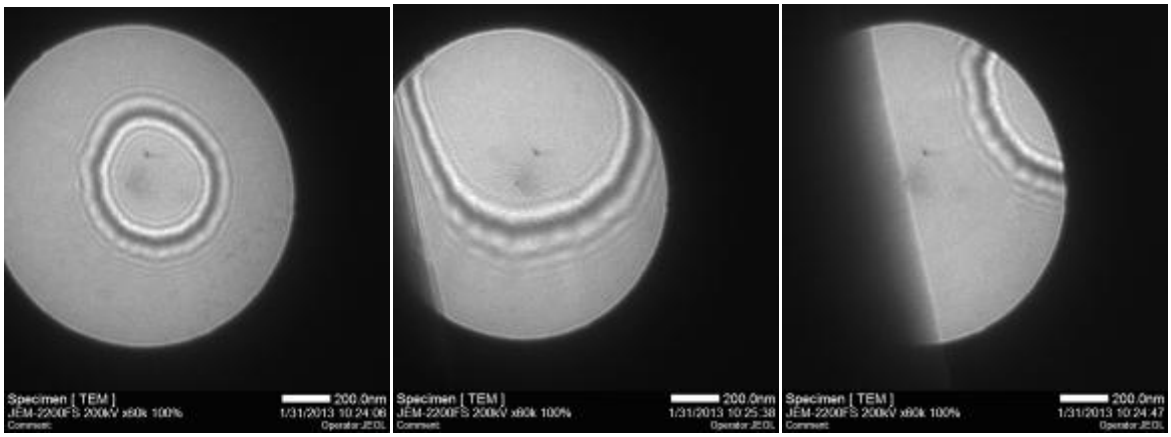

Figure 2. Images of deformed central holes of the phase plate. The window of the liquid cell is not isotropic shape with high aspect ratio, the potential is much varied according locations. Thus the appeared hole size and position of the hole were always changed and moving especially near the edge of the window. Left: image of an anisotropic and focused shape of the phase plate's central hole. Center and right: images of an anisotropic shape of the phase plate central hole near the edge of the window, which is deformed and enlarged by the edge of the liquid cell (edge effect).

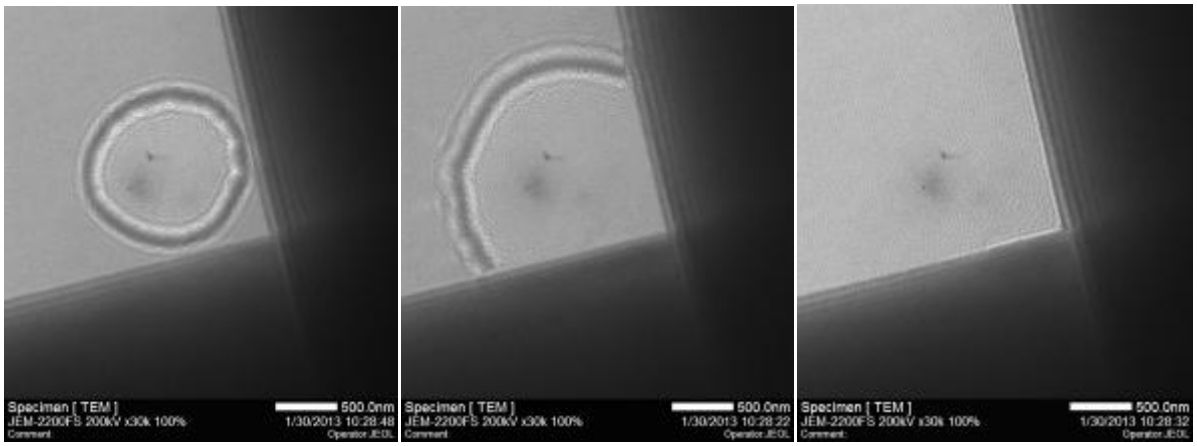

Figure 3. Images of un-deformed central hole of phase plate after carbon coating. Left and center: Hole shape is isotropic and is not deformed or enlarged by the edge effect even at the corner of two edges of the liquid cell. We can enlarge the hole size using the brightness dial as above images. Right: Finally, we can make an ideal condition of parallel beam and achieve effective phase contrast.

Spectroscopy in STEM/TEM

IM.4.075
Probing materials one atom at a time with low-voltage scanning transmission electron microscopy

Q.M. Ramasse[1], D.M. Kepaptsoglou[1], C.R. Seabourne[2], R. Zan[3], B. Schaffer[1], U. Bangert[3]
A.J. Scott[2], F. Azough[3] and R. Freer[3]

[1]SuperSTEM Laboratory, STFC Daresbury Campus, Daresbury WA4 4AD, U.K.
[2]Institute for Materials Research, SPEME, University of Leeds, U.K.
[3]School of Materials, University of Manchester, Manchester, U.K.

QMRamasse@superstem.org
Keywords: STEM, EELS, graphene, oxides defects

An essential corollary to the exciting instrumentation developments electron microscopy has witnessed over the last decade is the significant increase in detection limits and signal-to-noise ratios achieved on the new generation aberration-corrected microscopes, which provide improved data collection ability and greater flexibility. The development of so-called 'gentle', dose-controlled STEM techniques, for instance, has been particularly beneficial for the field of two-dimensional materials [1]. By reducing the acceleration voltage to overcome knock-on damage limitations, many of these structures can be imaged directly at atomic resolution with annular dark field (ADF) detectors, revealing for instance unique structure reconstructions at the edge of MoS_2 nano-catalysts [2] or the propensity of graphene to spontaneously 'heal' itself when perforated (Fig. 1a) [3]. Having shown what atomic species are present and where single atom impurities or defects are located using spectroscopy [4], some fundamental questions remain: how exactly are these atoms bonded to one another and how do structural differences affect their electronic configuration? Answers to these questions can be provided one atom at a time by EELS fine structure analysis, which can distinguish unambiguously between bonding configurations (Fig. 1b) [5]. This truly marks the start of single-atom physical chemistry.

In addition, the wealth of complementary analytical signals available from a single experiment provide unprecedented insights into the properties of materials. Minute changes in the composition of complex oxides can dramatically alter the local atomic configuration and thus transform their physical properties. For instance, the dielectric response of microwave ceramic $Ba_{6-3x}Nd_{8+2x}Ti_{18}O_{54}$ can be fine-tuned by adjusting the Ba and Nd content [6], while the spontaneous polarization of magneto-electric oxide gallium ferrite $Ga_{1-x}Fe_xO_3$ is dependent on the distortions caused by the structural asymmetry of the cation sites [7]. When combining Z-contrast imaging, bright field STEM imaging and true routine 2D EELS chemical mapping with advanced statistical image analysis [8] it is possible to determine statistically variations of only a few atoms in the chemical distribution of the different sites in these structures across a range of compositions, and to relate those to accurately measured small local atomic displacements generated by these compositional changes (Fig. 2).

1. O.L. Krivanek et al., in "Low Voltage Electron Microscopy", D. Bell and N. Erdman Eds., Wiley, London, 2013.
2. L.P. Hansen et al., Angew. Chem. Int. Ed. 50 (2011), p. 10153.
3. R. Zan et al., Nano Lett. 12 (2012), p. 3936.
4. T.C. Lovejoy et al., Appl. Phys. Lett. 100 (2012), 154101.
5. Q..M. Ramasse et al., Nano Lett. Art. ASAP (2013) doi:10.1021/nl304187e.
6. N. Rejab et al., Journal of Mater. Sci. 22 (2011), p. 167.
7. A. Roy et al., J. Phys.: Condens. Matter 23 (2011), p. 325902.
8. M.C. Sarahan et al., Ultramicroscopy 111 (2011), p. 251.
9. The SuperSTEM Laboratory is the U.K. National Facility for Aberration-Corrected STEM, supported by the Engineering and Physical Sciences Research Council (EPSRC).

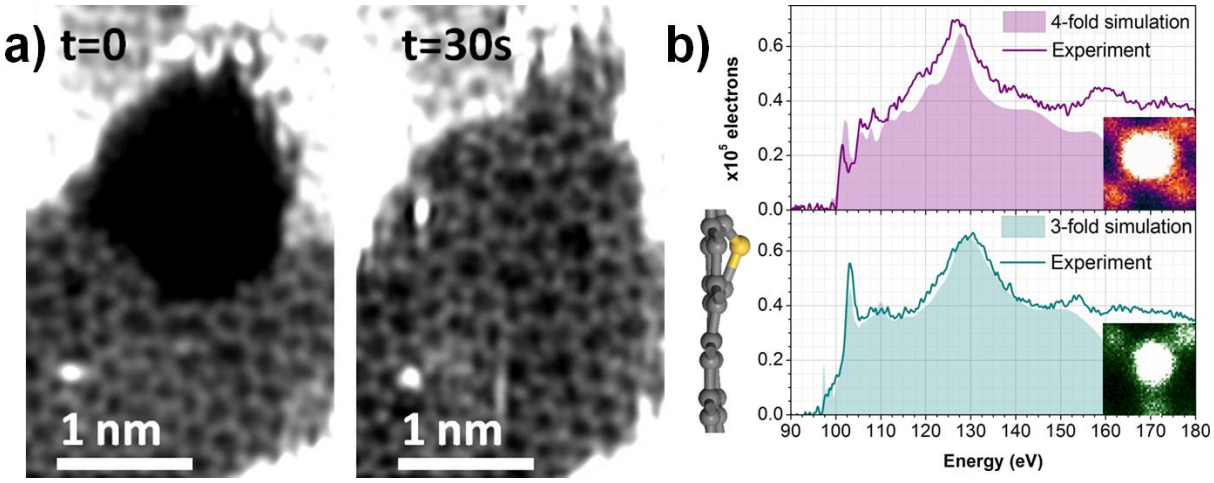

Figure 1. (a) Hole in single-layer graphene heals spontaneously by filling itself with loose carbon atoms to form a 2D amorphous patch. [3]. **(b)** Experimental and simulated EEL spectra acquired from a single Si atom in graphene in two different bonding configurations: trivalently bonded to the graphene lattice (top, inset) or tetravalently bonded to the graphene lattice (bottom, inset). [5]

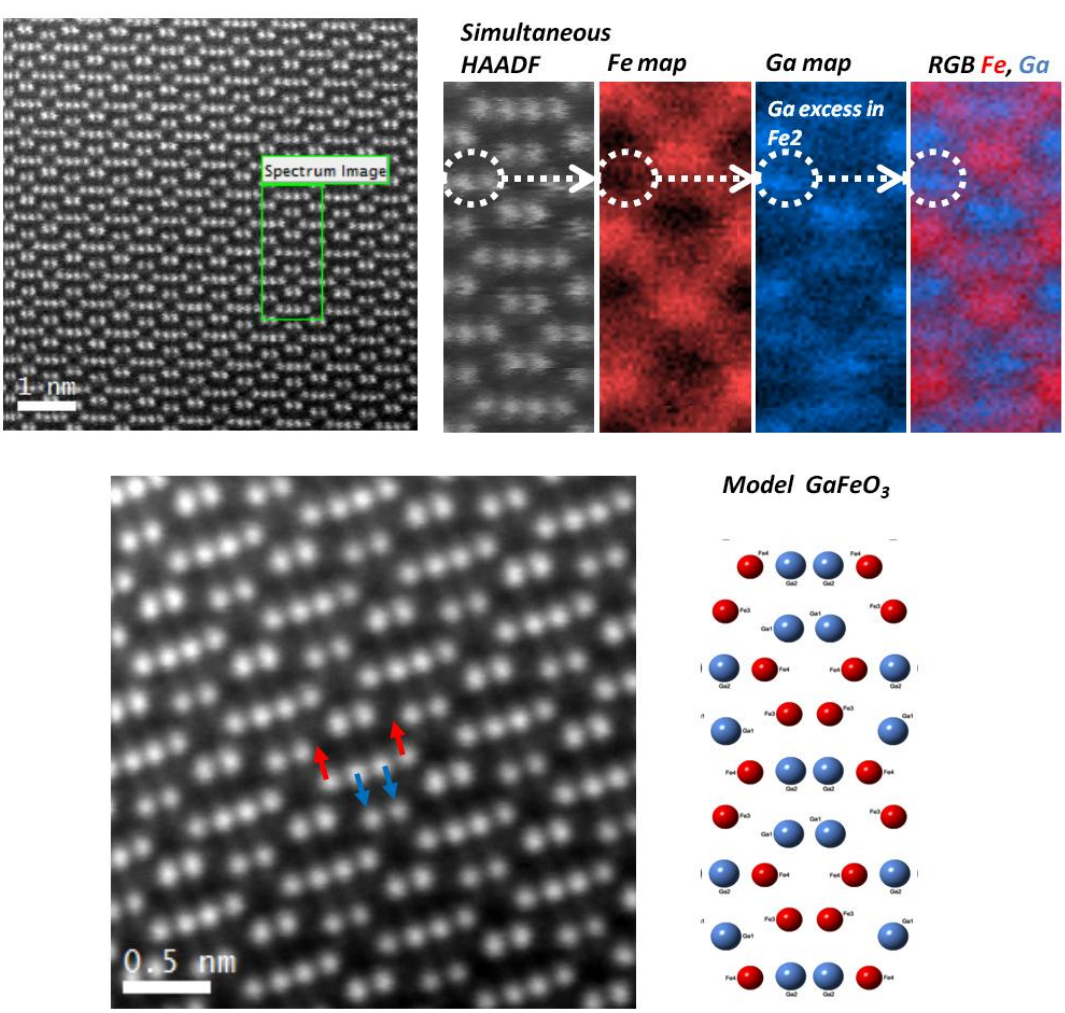

Figure 2. HAADF survey image and atomically-resolved EELS maps of a $Ga_{1-x}Fe_xO_3$ complex oxide revealing excess Ga located at the so-called Fe2 lattice sites. Quantitative analysis of bright field/HAADF images through template matching algorithms suggests these chemical variations are linked small atomic displacements of the Ga sites.

Spectroscopy in STEM/TEM

IM.4.076
FTEM at atomic resolution in the chromatic-aberration corrected transmission electron microscope

K. Urban[1], J. Mayer[2], L. Allen[3]

[1]Forschungszentrum Jülich, PGI 5, Jülich, Germany
[2]RWTH Aachen, GFE, Aachen, Germany
[3]University of Melbourne, School of Physics, Melbourne, Australia

k.urban@fz-juelich.de
Keywords: energy-filtered electron microscopy, aberration correction

Energy-filtered transmission electron microscopy (EFTEM) is a technique that images a specimen using inelastically scattered electrons that have undergone a specific range of energy losses within the specimen□1-4□. By selecting energy windows that cover a range of energies pertinent to inner-shell ionization of elements present in the sample, it is possible to obtain chemical maps and bonding information of different atomic species. However, up to now it was not possible to realize atomic resolution in EFTEM. Chromatic aberration degrades the image formed, as electrons that have lost different amounts of energy within an energy window will be focused in different image planes. This effect can be reduced by decreasing the width of the energy window. However this also leads to a reduction of the signal to noise ratio. Due to these competing effects, the resolution of energy-filtered images has been limited to about 4 Å □5,6□. Recently chromatic aberration (C_C) correction has been implemented □7□. We have used the FEI Titan 60-300 'PICO' instrument to demonstrate that C_C correction allows wide energy windows to be used and atomic resolution to be realized □8□.

Experimental EFTEM images of silicon were obtained using signal from the $L_{2,3}$ ionization edge (threshold energy for ionization ~100 eV). The microscope was operated at 300 keV with a semi-convergence angle for the incident beam of 1.7 mrad. The specimen, a wedge whose thickness varied between 10 and 40 nm, was imaged along the [110] zone axis. The three-window technique □3,4□ was used with the pre-edge images centred at energy losses of 55 eV [Fig. 1(a)] and 75 eV [Fig. 1(b)] to do a background subtraction on the raw post-edge data, for the energy window centred at 120 eV [Fig. 1(c)], thus obtaining the Si elemental map shown in Fig. 1(d). Energy slit widths of 40 eV were used, which was only possible using the achromatic objective lens (C_C = 0). Overlapping windows were chosen in the pre-edge region in order to avoid positioning the first pre-edge window in the strongly oscillating plasmon-loss region. The atomic 'dumbbell' structure of Si in [110] projection is resolved, where the centres of the two atoms in each dumbbell pair are separated by 1.35 Å.

To understand the complex physics and electron optics underpinning the formation of the elemental map in Fig. 1(d) it is necessary to model the elastic and inelastic scattering of the incident electrons in the specimen. To do this we supplement the approach in Ref. □9□ with the use of the quantum excitation of phonons (QEP) model □10□, which calculates the underlying elastic and thermal diffuse scattering (TDS) of the incident electrons and provides the basis for modelling the ionization of the silicon atoms by both elastically and thermally scattered electrons. The transition potential approach allows to understand why the contrast of the 'inelastic' images is similar to that of the ordinary 'elastic' images ('preservation of elastic contrast'). For high-energy incident electrons causing ionization, the transition potentials become the more extended ('delocalized') the lower the energy loss. As a consequence features of the elastic and thermal scattering prior to and after the ionization event contribute directly and significantly to the energy-filtered image.

Our work has demonstrated experimentally that by using spherically and chromatically corrected electron optics the resolution of EFTEM can be improved to atomic. This allows unambiguous identification of the chemical nature of individual atom columns in the transmission electron microscope on the basis of images produced by electrons that have experienced a characteristic inner-shell excitation energy loss. However, the theoretical work clearly shows that carrying out atomic-resolution EFTEM can only be considered a technique satisfying modern standards of quantitative and quantum-mechanically sound image interpretation if the experimental work is accompanied by state-of-the-art image calculations including a proper treatment of the inelastic scattering. This confirms earlier objections against the intuitive interpretation of EFTEM results as (quasikinematical) maps of elements in samples imaged under spectroscopic conditions □11□

1. R. F. Egerton, Electron Energy Loss Spectroscopy in the Electron Microscope (Plenum Press, New York, 1996).
2. C. C. Ahn (ed.), Transmission Electron Energy Loss Spectrometry in Materials and the EELS Atlas (2nd edition; Wiley-VCH, Weinheim, 2004).
3. W. Jäger and J. Mayer, Ultramicroscopy 59, 33 (1995).
4. F. Hofer and P. Warbichler, in [2], p. 159.
5. W. Mader and B. Freitag, J. Microscopy 194, 42 (1999).
6. T. Walter, Ultramicroscopy 96, 401 (2003).
7. B. Kabius, P. Hartel, M. Haider, H. Müller, S. Uhlemann, U. Loebau, J. Zach, and H. Rose, J. Electron Miscrosc. 58, 147 (2009).
8. K. W. Urban, J. Mayer, J. R. Jinschek, M. J. Neish, N. R. Lugg, and L. J. Allen, Phys. Rev. Lett., in press
9. N. R. Lugg, B. Freitag, S.D. Findlay, and L. J. Allen, Ultramicroscopy 110, 981 (2010).
10. B. D. Forbes, A. V. Martin, S. D. Findlay, A. J. D'Alfonso, and L. J. Allen, Phys. Rev. B 82, 104103 (2010).
11. P. Stallknecht and H. Kohl, Ultramicroscopy 66, 261 (1996).
12. R. Kilaas, J. Microscopy 190, 45 (1998).
13. C. L. Jia, M. Lentzen, and K. Urban, Science 299, 870 (2003)
14. K. W. Urban, C. L. Jia, L. Houben, M. Lentzen, S. B. Mi, and K. Tillmann, Phil. Trans. Royal Society A 367, 3735 (2009).

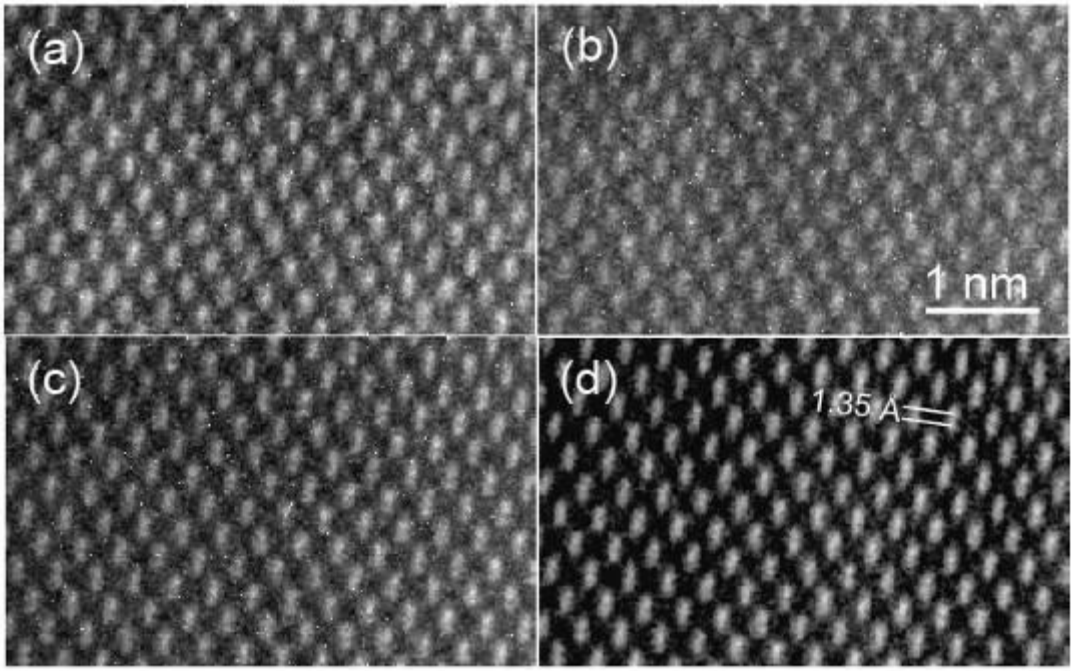

Figure 1. EFTEM images used to construct the Si $L_{2,3}$ elemental map by means of the three-window technique in the chromatic- and spherical-aberration corrected electron microscope. All images were taken using a 40 eV wide energy window. (a) Pre-edge image centred at an energy loss of 55 eV. (b) Pre-edge image cantered at 75 eV. (c) Post-edge image cantered at 120 eV. (d) Resulting atomic-resolution elemental map; a standard 'average background subtraction filter' □12□ was applied. Standard conditions for the negative-spherical aberration imaging mode □13,14□ were applied in all images, i.e. a C_s of -8.27 μm and a defocus of +40 Å

Spectroscopy in STEM/TEM

IM.4.077
Atomic scale investigation of a $PbTiO_3/SrRuO_3/DyScO_3$ heterostructure

R. Egoavil[1], H. Tan[1,2], J. Verbeeck[1], S. Bals[1], B. Smith[3], B. Kuiper[3], G. Rijnders[3], G. Koster[3], G. Van Tendeloo[1]

[1]EMAT/Univeristy of Antwerp, Physics, Antwerp, Belgium
[2]CEMES-CNRS, Univ. de Toulouse, nMat group, Toulouse, France
[3]Faculty of Science and Technology and MESA+ Institute for Nanotechnology/ University of Twente, Twente, Netherlands

ricardo.egoavil@ua.ac.be
Keywords: Ferroelectric, STEM-EELS, Oxides

Ferroelectric thin films have recently received a lot of attention because of the outstanding properties making them highly useful for applications in ferroelectric devices [1,2]. An essential component to create a contact to ferroelectric thin films is a metallic conductive $SrRuO_3$ oxide layer. Structural, physical properties and applications of $SrRuO_3$ have recently been extensively reviewed by Koster et.al. [3]. Particularly interesting is the self-organized formation of epitaxial $SrRuO_3$ ribbon-like structures on $SrTiO_3$ substrate steps. $SrRuO_3$ nanostructures are reported to nucleate on substrate steps followed by a 3D island growth [4]. Recent work reported on self-assembled $SrRuO_3$ nanowires, grow preferentially only on one type of $DyScO_3$ surface termination. A diffusion model was proposed where a difference in surface diffusion between DyO and ScO_2 was responsible for the formation of the $SrRuO_3$ nanowires [5]. Here we provide a thorough structural and chemical characterization at the atomic scale, leading to a comprehensive understanding of the detailed growth of $SrRuO_3$ in heterostructures. An epitaxial $PbTiO_3$ thin film grown on self-organized crystalline $SrRuO_3$ nanowires deposited on a $DyScO_3$ substrate with ordered DyO and ScO_2 chemical terminations is investigated by transmission electron microscopy. In this $PbTiO_3/SrRuO_3/DyScO_3$ heterostructure the $SrRuO_3$ nanowires are assumed to grow on only one type of substrate termination. Here we report on the structure, morphology and chemical composition analysis of this heterostructure. Electron energy loss spectroscopy reveals the exact termination sequence in this complex structure. The energy loss near edge structure (ELNES) of the Ti-$L_{2,3}$, Sc-$L_{2,3}$ and O K edges show intrinsic interfacial electronic reconstruction. Furthermore, $PbTiO_3$ domain walls are observed to start at the end of the nanowires resulting in atomic steps on the film surface [6].

1. J. F. Scott and C. A. Araujo, Science 246 (1989), 1400-1405.
2. J. F. Scott and C. A. Araujo, Science 315 (2007), 954-959.
3. G. Koster et al., Review of Modern Physics 84(1) (2012), 253-298.
4. F. Sánchez, G. Herranz, I.C. Infante, C. Ferrater, M.V. García-Cuenca, M. Varela, J. Fontcuberta, Progress in Solid State Chemistry 34 (2006), 213−221.
5. B. Kuiper, J.L. Blok, H.J.W. Zandvliet, D.H.A. Blank, G. Rijnders, and G. Koster, MRS Communications 1 (2011), 1721.
6. R. Egoavil et al., (submitted to APL)
7. R.E. gratefully acknowledges funding from the European Union Council under the 7th Framework Program (FP7) grant number 246102 IFOX. J.V. acknowledges funding from the European Research Council under the 7th Framework Program (FP7), ERC starting grant number 278510 VORTEX. J.V. and G.V.T acknowledge funding from the European Research Council under the 7th Framework Program (FP7), ERC grant number 246791 COUNTATOMS. The titan microscope was partly funded by the Hercules fund from the Flemish Government. The authors acknowledge financial support from the European Union under the Seventh Framework Program under a contract for an Integrated Infrastructure Initiative. Reference No. 312483-ESTEEM2.

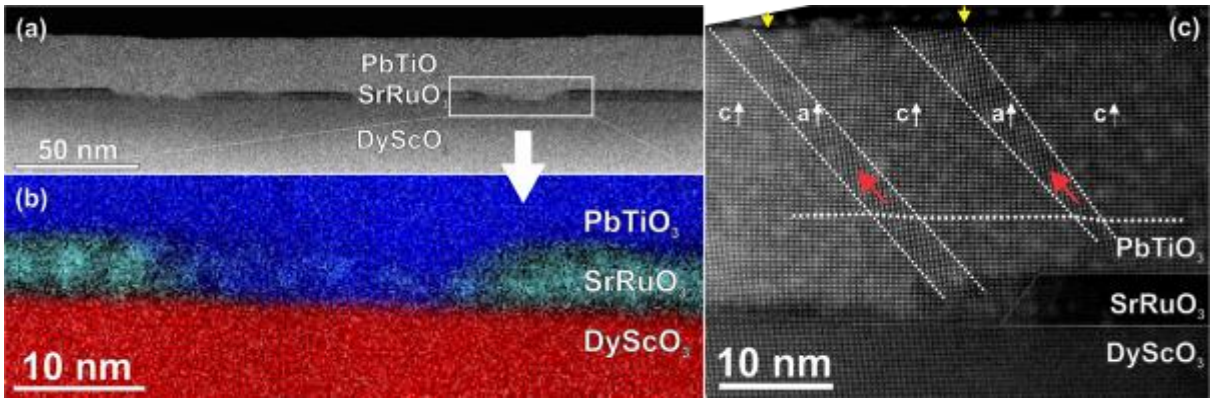

Figure 1. (a) HAADF-STEM overview image of the sample. The surface structure of the $PbTiO_3$ film and the $SrRuO_3$ nanowires of ~5x120nm size are distinct. (b) Colored elemental map with Ti (blue), Ru (light-blue) and Sc (red). (c) Magnified image of a nanowire ending showing the a and c domains. Domain walls in the film (white dashed-lines) occur (mostly) at the end of the nanowires.

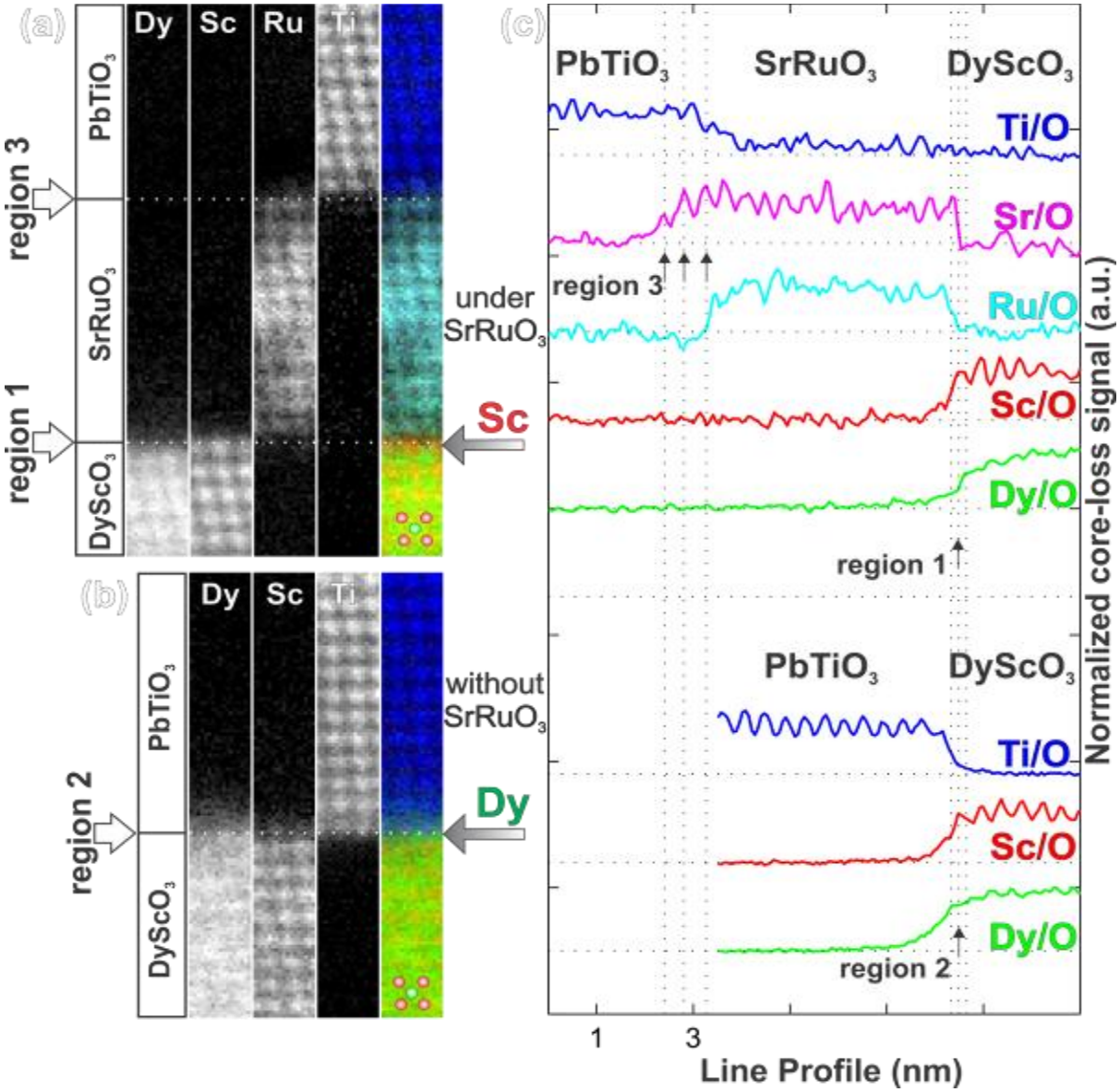

Figure 2. (a,b-left) EELS elemental maps of Dy-$L_{2,3}$, Sc-$L_{2,3}$, Ru-$M_{4,5}$, Ti-$L_{2,3}$ and O K edges (gray scaled) together with the corresponding color map with Dy (green), Sc (red), Ru (light-blue) and Ti (blue). (c) EELS elemental line profiles with Dy (green), Sc (red), Ru (light-blue), Ti (blue), Sr (pink) and O (black).

Spectroscopy in STEM/TEM

IM.4.078
Contribution of thermally scattered electrons to atomic resolution elemental maps

B. Forbes[1], A. D'Alfonso[1], R. Williams[2], S. Rajagopalan[3], H. Fraser[2], D. McComb[2], B. Freitag[4]
D. Klenov[4], L. Allen[1]

[1]University of Melbourne, Physics, Melbourne, Australia
[2]The Ohio State University, Department of Materials Science and Engineering, Columbus, United States
[3]ExxonMobil Research & Engineering Company, Annandale, United States
[4]FEI Company, Eindhoven, Netherlands

bdforbes@unimelb.edu.au
Keywords: transmission electron microscopy; thermal scattering; energy dispersive x-ray analysis

Electron energy loss spectroscopy (EELS) and energy dispersive x-ray (EDX) analysis in scanning transmission electron microscopy (STEM) have the ability to produce elemental maps of a specimen at atomic resolution. Quantitative interpretation of these elemental maps is in general confounded by multiple elastic and thermal scattering. Detailed modelling and simulation of the electron scattering dynamics, including the effects of thermal scattering, leads to an improved understanding of the relative intensities seen in these maps. We present a recently developed, fully quantum mechanical model for thermal scattering, referred to here as the quantum excitation of phonons (QEP) model, which is based on an approximation akin to the Born-Oppenheimer approximation used in molecular systems. Our model agrees with the scattered intensity predicted by the frozen phonon model [2], but does not require the semi-classical justifications contained therein. The QEP model is additionally capable of calculating separately the contributions to the scattered intensity from elastically and thermally scattered electrons. This is illustrated in Figure 1 which shows the contributions to a convergent beam electron diffraction pattern of <001> strontium titanate from both elastically and thermally scattered electrons.

The QEP model is used here to investigate the contribution made by thermally scattering to EELS and EDX maps of strontium titanate (STO) [3]. Figure 2(a) shows a simulated EDX map of the O-K edge in a 700 Å thick specimen of STO. The QEP model is used to separate this EDX map into contributions from elastically scattered electrons [Figure 2(b)] and thermally scattered electrons [Figure 2(c)]. The elastic contribution shows a higher O-K signal on the pure oxygen columns as compared with the titanium-oxygen columns; this is due to the titanium atoms thermally scattering electrons away from the column, resulting in a decreased source for ionisation. However, when the positive contribution of the thermally scattered electrons is included, a higher signal is observed on the titanium-oxygen columns. We also investigate the effects of probe channelling on the EDX map, and investigate the contributions to the O-K signal at a given probe position from oxygen atoms in neighbouring columns, finding that the EDX map for O-K in STO is partially delocalised.

We conclude from our investigation that a quantitative interpretation of experimental EDX elemental maps is aided by thorough studies of the electron scattering dynamics using theory and simulation.

1. B. D. Forbes, A. V. Martin, S. D. Findlay, A. J. D'Alfonso and L. J. Allen, Physical Review B 82 (2010), ac. 104103.
2. R. F. Loane, P. Xu and J. Silcox, Acta Crystallographica A47 (1991), p. 267.
3. B. D. Forbes, A. J. D'Alfonso, R. E. A. Williams, R. Srinivasan, H. L. Fraser, D. W. McComb, B. Freitag, D. O. Klenov and L. J. Allen, Physical Review B 86 (2012), ac. 024108.

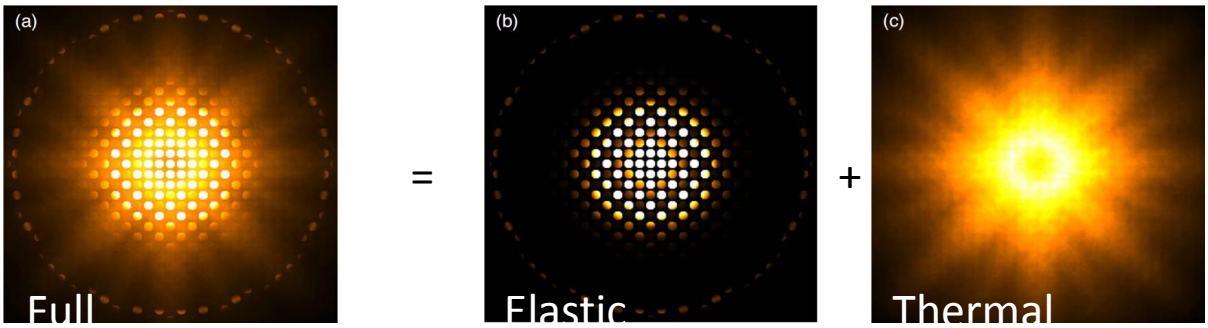

Figure 1. QEP-simulated convergent-beam electron diffraction patterns for a 60 Å thick specimen of <001> strontium titanate, using a 300 keV convergent electron probe having a convergence semi-angle of 2.2 mrad. The QEP model is used to calculate separately the contribution from (a) all electrons, (b) elastically scattered electrons and (c) those electrons which have first been thermally scattered.

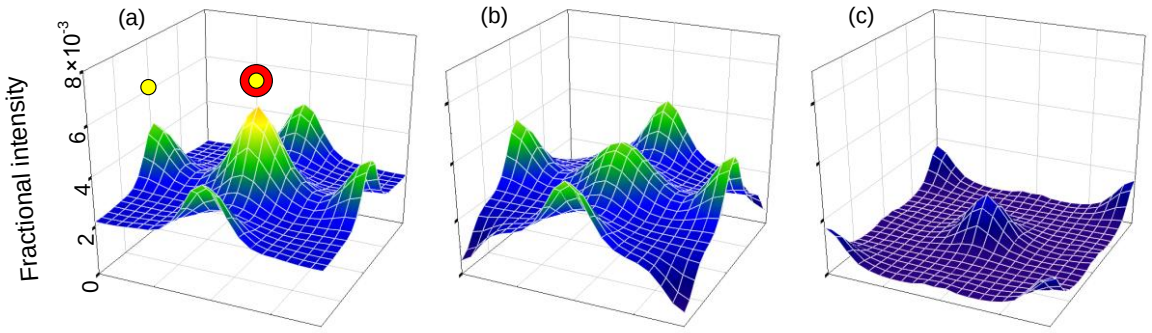

Figure 2. QEP-simulated EDX maps of the signal in the oxygen K edge in <001> strontium titanate across a unit cell, for a 200 keV aberration-corrected probe having a probe-forming convergence semi-angle of 23 mrad, with a specimen thickness of 700 Å. (a) The contribution from all electrons. (b) The contribution from elastically scattered electrons. (c) The contribution from thermally scattered electrons which go on to ionise an oxygen atom. The oxygen-containing columns in the specimen structure are indicated in (a) using small (yellow) circles for oxygen columns and large (red) circles with inset small (yellow) circles for titanium-oxygen columns.

Spectroscopy in STEM/TEM

IM.4.079
Optimization of experimental parameters for minimizing the inelastic delocalization in low loss EELS experiments utilizing Low-Voltage EELS

M. Stöger-Pollach[1]

[1]Vienna University of Technology, USTEM, Vienna, Austria

stoeger@ustem.tuwien.ac.at
Keywords: inelastic delocalization, Low-Voltage EELS, optical properties

The development of transmission electron microscopes (TEMs) has now an eighty year long tradition. In the beginning one strived to increase the beam energy in order to have better spatial resolution. With this advantage sample damage caused by the highly energetic electrons was also increased. In the last few years the development points towards lower beam energies, because lens aberrations can be corrected. This leads to excellent spatial resolution with an additional reduction of beam damage based on the knock-on mechanism. For electron energy loss spectrometry (EELS) the history of beam energies had an opposite effect: with increasing beam energies the spatial resolution was reduced because of the long range Coulomb interaction between the swift probe electron and the specimen. The actual development towards lower beam energies is therefore also advantageous for the spatial resolution of EELS experiments. Beside the spatial resolution also the inelastic cross section is increasing leading to a "stronger" EELS signal. In the present work we discuss the optimization for experimental parameters for performing EELS low loss spectrometry. The parameters which can be adjusted in order to achieve the best possible spatial resolution are (i) beam energy, (ii) convergence and (iii) collection semi-angles. Finally we present an optimized low loss experiment using a 60 keV electron beam for the determination of band gaps and optical properties of $In_{0.12}Ga_{0.88}N$ (InGaN) quantum wells (QWs) embedded in a GaN matrix.

Because the refractive index of InGaN is 2.62, the theoretical Cerenkov limit [1] is 41.843 keV. The experimental Cerenkov limit is a little bit higher, because the intensity in the relativistic losses is below the noise level as long as the normalized probability for Cerenkov photon excitation is below 0.2 - 0.4 photons per inelastic mean free path length per unit charge [1]. For the investigated materials this means that we are restricted to beam energies below 60 keV. The second aspect for the best choice of the applied beam energy is the spatial resolution in the inelastic (low loss) signal. Due to the fact that the QW thickness is 5.3 nm, the spatial resolution must be at least as good. As soon as we can avoid Cerenkov losses the lowest possible energy loss would represent the lower conduction band energy, which is 2.8 eV for InGaN [2]. In the GaN matrix the band gap is 3.24 eV. This means that the lowest observable feature in the VEELS spectrum is the 2.8 eV on-set within the InGaN QW. We therefore have to focus on the spatial resolution of the inelastic image recorded at 2.8 eV energy loss. Because the experiments are performed in scanning TEM (STEM) mode, the minimum achievable beam diameter at the respective beam energy must also be considered. Figure 1 shows the beam diameter of a FEG-STEM probe formed by a condenser lens with a spherical aberration coefficient C_S of 1.2 mm, as it is available in our TECNAI TEMs. The optimum beam diameter requires an aperture angle of 18 mrad. Then it would be equal to the inelastic delocalization of 3.8 nm, which is still below the QW width. The difference in spot size and delocalization between a 60 keV and a 40 keV electron beam is negligible. Hence only the possible appearance of Cerenkov losses determines the choice of the most appropriate beam energy. The best spatial resolution of 0.68 nm can be achieved in the 60 keV HAADF image when the convergence angle is 6 mrad. In the presented experiments we chose a convergence angle of 9 mrad, this leading to a spatial resolution of 0.8 nm. The inelastic delocalization of 5.3 nm is equal to the width of a single QW. The rectangular scan area was 22 nm x 70 nm. The effective pixel size of the STEM-EELS experiment was 4 nm^2. Figure 2b shows the HAADF image recorded simultaneously to the STEM-EELS data cube. When using the EELS data cube a ZLP filtered STEM bright filed image can be extracted (see Figure 2c). The advantage of recording a whole data cube is that single spectra can be extracted from an exactly defined region of the specimen. In Figure 2d we present two spectra, one of the GaN matrix and one of a center of a QW. It can be easily recognized that the QW shows the smaller band gap. Furthermore a plasmon shift is also visible. Finally the refractive index can be calculated for each pixel of the scan. Figure 3a

shows the mean refractive index over five measurements from a QW center compared with the one from the GaN matrix. From the experimentally obtained data set a refractive index map can be generated (Figure 3b).

The main benefit of low beam energies in EELS is definitively in the energy range of optical transitions, which is the VEELS region. This is because the VEELS signal can be altered by relativistic losses and the spatial resolution suffers from the Coulomb interaction. By reducing the beam energy relativistic losses can be avoided and the spatial resolution is intrinsically improved.

1. M. Stöger-Pollach, Micron 39 (2008), pp. 1092–1110
2. A. Rosenauer, T. Mehrtens, K. Müller, K. Gries, M. Schowalter, P. V. Satyama, S. Bley, C. Tessarek, D. Hommel, K. Sebald, Ultramicroscopy 111 (2011), pp. 1316–1321.

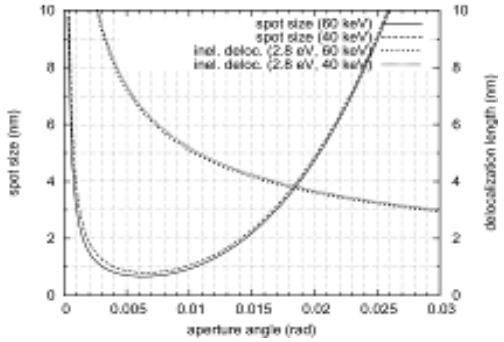

Figure1. STEM probe size as a function the convergence (aperture) angle for 60 keV and 40 keV electron probes in comparison with the inelastic delocalization for a 2.8 eV energy loss as a function of the collection aperture angle.

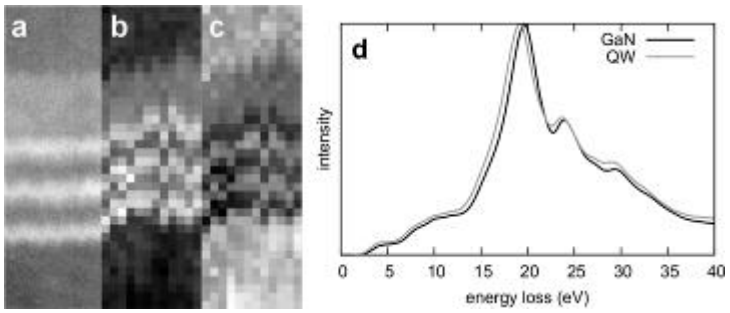

Figure 2. (a) Separately recorded 60 keV HAADF STEM image of the QWs using a short dwell time; (b) 60 keV HAADF STEM image recorded simultaneously with the STEM-EELS experiment. The pixel size of the raster scan is 4 nm^2. The scan area is 22 nm x 70 nm; (c) ZLP filtered STEM bright filed image of the respective area extracted from the STEM-EELS data cube; (d) ZLP subtracted VEELS spectra recorded in the GaN matrix and in the center of a QW. The plasmon peak shift and the smaller band gap of the QW are clearly visible.

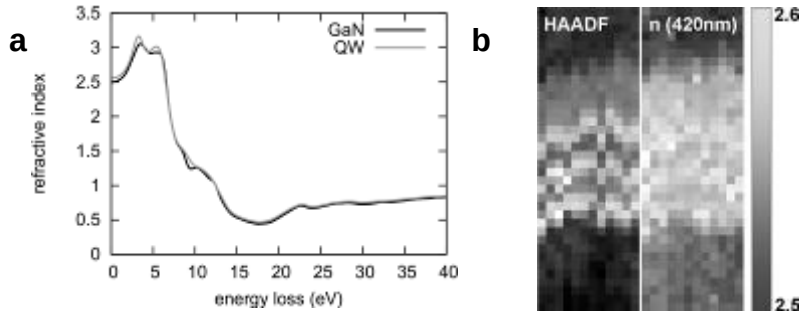

Figure 3. (a) Mean refractive indices of five GaN measurements and five measurements taken from the center of a QW; (b) Experimentally obtained HAADF image and refractive index map for an energy loss of 2.95 eV (420 nm).

Spectroscopy in STEM/TEM

IM.4.080
Momentum-resolved electron energy-loss spectroscopy of free-standing single- and multi-layered graphene

P. Wachsmuth[1], R. Hambach[1], M. Kinyanjui[1], G. Benner[2], U. Kaiser[1]

[1]Ulm University, Electron Microscopy Group of Materials Science , Ulm, Germany
[2]Carl Zeiss Microscopy, Oberkochen, Germany

philipp.wachsmuth@uni-ulm.de
Keywords: momentum resolved, eels, graphene, layered electron gas

Graphene with its unique structural and electronic properties has caused a lot of excitement in last couple of years. Recently the nature of 2D plasmons in graphene has also been in the focus of attention [1,2]. These plasmons are collective excitations of electrons, which are confined on a plane and interact via Coulomb forces. They can be characterized based on their dispersion relation, i.e. the dependence of the plasmon energy on wavelength. Insights into the properties of these 2D plasmons in graphene are not only important for the fundamental understanding of the electronic structure and collective behaviour in graphene, but also for potential applications in nano-plasmonics [3].

Here, we are concerned with the dispersion of high-energy plasmons (>3eV), known as π- and $\pi+\sigma$-plasmon, in free-standing single- and multi-layer graphene. We have applied momentum-resolved electron energy-loss spectroscopy in a Libra200-based low-voltage transmission electron microscope (ZEISS) equipped with a monochromator and in-column Omega-filter to measure the momentum-dependent energy-loss function for two non-equivalent in-plane directions, i.e. ΓM and ΓK.

In figure 1 we have plotted experimental spectra of free-standing single-layer graphene covering momentum transfers along both symmetry direction over the entire 1st Brillouin zone. At small q-values, we find two plasmons peaks located at 4.9eV and 15.3eV and in good agreement to previous findings [4]. The measured loss function for both symmetry directions are identical up to an intermediate momentum transfer of about 0.5 1/Å, with significant differences appearing at larger q-values. In ΓM -direction, above a value of 0.8 1/Å, the π-plasmon splits into a double peak, with a shoulder at around 5eV, similar to observations in carbon nanotubes [1]. For ΓK, no splitting is observed. These experimental results are then compared to ab-inito calculations in the framework of time-dependent density functional theory (TDDFT).

In addition we will present measurements, illustrating the changes of the loss-function with increasing number of layers (up to 6) (figure 2) and a careful study of out-of-plane excitations in single- and multi-layered graphene. These observations are than discussed in terms of a simple layered electron gas model.

1. C. Kramberger, R. Hambach, C. Giorgetti, M. Rümmeli, M. Knupfer, J. Fink, B. Büchner, Lucia Reining, E. Einarsson, S. Maruyama, F. Sottile, K. Hannewald, V. Olevano, A. Marinopoulos, and T. Pichler, Physical Review Letters 100, (2008).
2. E. H. Hwang and S. Das Sarma, Physical Review B 75, (2007).A. H. Castro Neto et al, Reviews of Modern Physics 81 (2009), p. 109-162
3. T. Eberlein, U. Bangert, RR Nair, R. Jones, M. Gass, AL Bleloch, KS Novoselov, A. Geim, and PR Briddon, Physical Review B 77, 233406 (2008).
4. This work was supported by the DFG (German Research Foundation) and the Ministry of Science, Research and the Arts (MWK) of Baden-Wuerttemberg in the frame of the SALVE (Sub Angstrom Low-Voltage Electron microscopy and spectroscopy project.

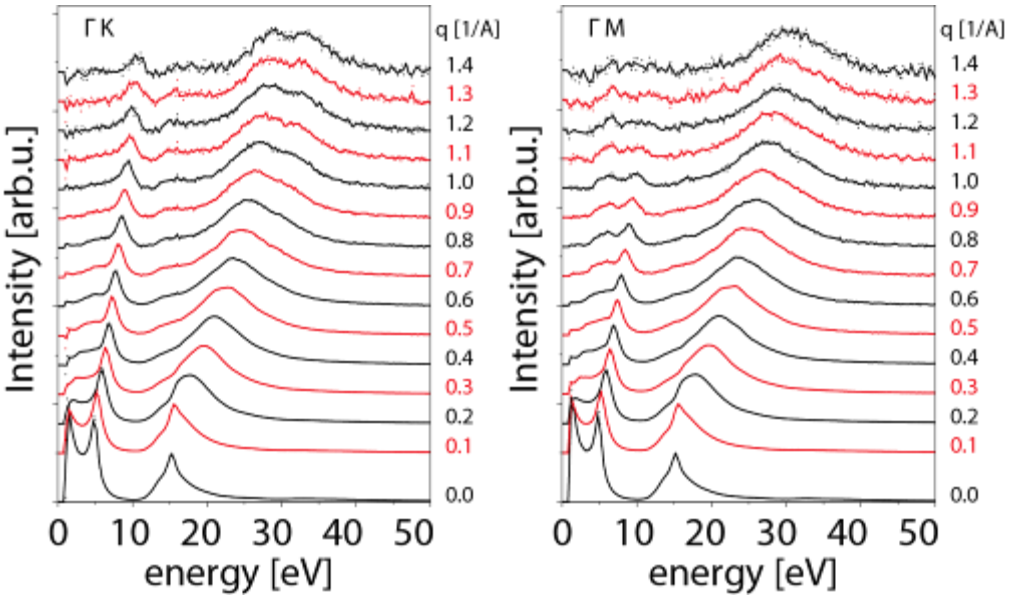

Figure 1. Experimental in-plane energy-loss of free-standing, single-layer. Shown are spectra for momentum transfers along ΓK (left) and ΓM (right). Energy resolution is ΔE = 0.2eV and momentum resolution Δq =+/-0.1 1/Å. Spectra have been shifted vertically and scaled for better visualization

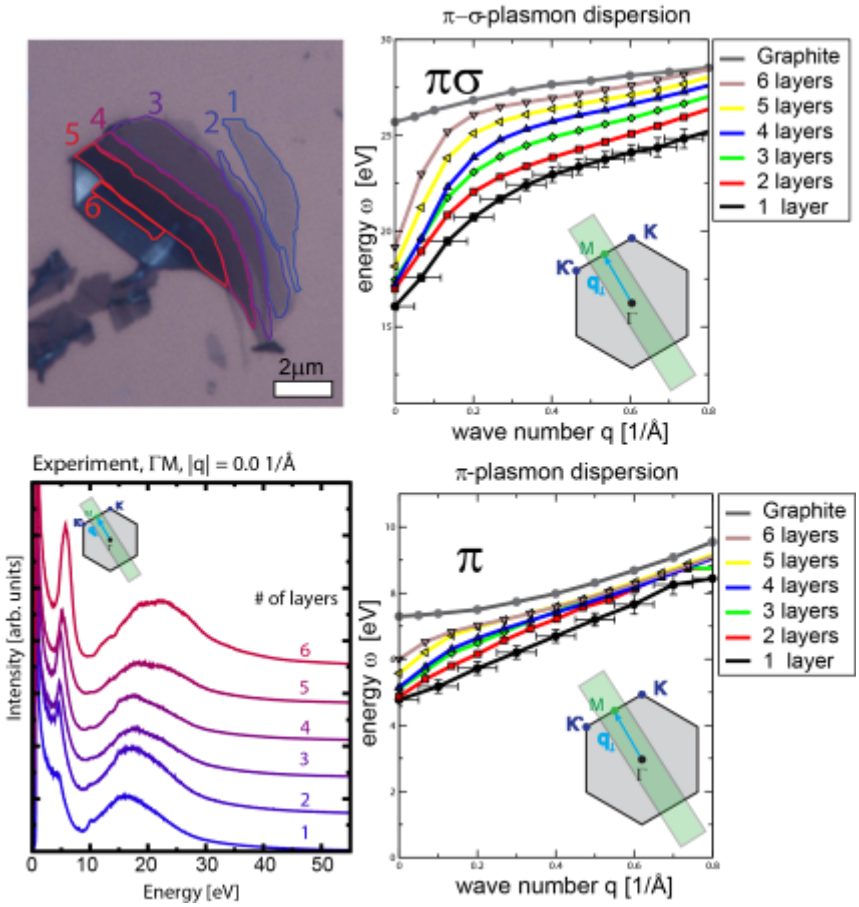

Figure 2. Measured energy-momentum dependence of both the π− and π+σ−plasmon in free-standing graphene. Shown are dispersion curves for in-plane momentum transfers along ΓM (left) and ΓK (middle). For ΓM the plasmon dispersion of graphite was added as reference (gray). Peak positions were extracted from spectra of up to six layers of AB-stacked graphene sheets. Different colours indicate different number of layers. Incident electron energy was 40keV. Energy resolution is ΔE=0.2eV and momentum resolution is Δq=+/-0.1 1/Å. (right) Light optical images showing the probed graphene sample.

Spectroscopy in STEM/TEM

IM.4.081
Accessing low-energy cavity modes in rectangular slits in a thin Au film by STEM-EELS in combination with the Richardson-Lucy algorithm

R. Walther[1], E. Müller[1], R. Schneider[1], D. Gerthsen[1]

[1]Karlsruhe Institute of Technology, Laboratory for Electron Microscopy, Karlsruhe, Germany

roman.walther@kit.edu
Keywords: low-loss STEM-EELS, plasmonics, improved energy resolution

Scanning transmission electron microscopy in combination with electron energy loss spectroscopy (STEM-EELS) is becoming more and more important in the characterization of nanostructures due to its sub-nanometer spatial resolution which renders it far superior compared to optical methods. Even state-of-the-art optical methods like apertureless scanning near-field microscopy (SNOM) are limited to a resolution of 10 nm. Owing to sophisticated energy loss spectrometers or imaging energy filters in combination with electron monochromators and optimized acquisition techniques, an energy resolution better than 50 meV [1] is achievable. However, due to the tail of the zero-loss peak (ZLP), the accessible energy range is limited towards low energy losses which makes STEM-EELS disadvantageous compared to optical methods. The Richardson-Lucy (RL) algorithm [2, 3] was shown to improve the energy resolution of recorded spectra [4] by deconvolving the point-spread function of the detector system. In combination with electron monochromators, the RL algorithm offers the possibility to further improve the energy resolution and the accessible range of energy losses towards low-energy signals.

Recently, standing cavity-like modes hybridized with surface plasmon polaritions (SPP) were reported in rectangular slits in a thin Au film [5]. Additionally, strong enhancements of the cavity modes upon introduction of neighboring slits was demonstrated [6]. Due to this enhancement and the tunability of the cavity-mode energies by variation of the slit length, double slits are superb objects to evaluate the performance of STEM-EELS in the energy-loss range below 1.5 eV.

In this work slits were milled in a 200 nm-thin Au film using an FEI Strata 400S focused ion beam system. The experiments were performed in an FEI Titan³ 80-300 equipped with an electron monochromator (Wien-filter type) and a Gatan imaging energy filter (GIF) Tridiem model 865 HR. Under monochromatized conditions a probe size of about 5 Å is realized. The optimized acquisition procedure proposed by Bosman and Keast [7], binned gain averaging, was implemented to acquire high-quality EEL spectra. 50 spectra with exposure times of 1 ms were summed after energy drift correction and normalized with respect to the ZLP intensity. The RL algorithm was implemented with a self-written script in Digital Micrograph (Gatan). A reference spectrum recorded with the specimen retracted was applied as point-spread function for the deconvolution procedure.

Figure 1 shows spectra recorded within one slit with a size of 900 nm x 180 nm in an array of two slits separated by a metal bar with 100 nm width. A series of EEL spectra were acquired along the center of one slit (cf. arrow in the inset of Figure 1). The spectra are shifted vertically for better visibility. As the central bar separating the two slits is approached, two low-energy peaks are resolved at energy losses ΔE of 0.5 eV and 1.47 eV in addition to the surface plasmon peak at 2.3 eV. These are the fundamental mode and the 3rd harmonic of a cavity standing wave [5] along the long slit direction. Spectra taken close to the opposite slit wall (e.g. the black spectrum in Figure 1) also show these signals as very faint shoulders. The determination of the exact energy loss of these weak signals is difficult. Figure 2 shows how the application of the RL algorithm yields a significant improvement of energy resolution and visibility of these faint signals (for a spectrum recorded at 10 nm distance to the outer wall). With increasing number of iterations, the shoulder at ΔE = 0.5 eV is clearly resolved as a peak. The most significant effect of the RL algorithm is observed close to the ZLP which is strongly sharpened (inset in Figure 2). To check the effect of the RL algorithm, the same procedure was applied to a spectrum recorded at 10 nm distance to the central bar and compared to a spectrum which was only processed by subtraction of the reference spectrum. The results are depicted in Figure 3 which shows the raw spectrum, the reference spectrum, the spectrum obtained after 7 iterations with the RL algorithm, and the spectrum after reference subtraction. It is evident that the application of 7 iterations is, within the error limit, identical to the subtraction of a reference for $\Delta E \geq$ 0.5 eV. A power-

law background fit to the spectrum after application of the RL algorithm can be used to evaluate the 0.5 eV peak.

Figure 4 shows spectra of three double slits with varying lengths, i.e. 900 nm, 1300 nm, and 2340 nm. Each spectrum was treated with 7 iterations prior to a bi-exponential background fit to the right side of the ZLP to recover the signals. As the slit length is increased, the energy of the fundamental cavity mode shifts to lower energies from 0.49 to 0.24 eV (cf. arrow). The small intensity to the left of the fundamental peaks is due to the background-fitting procedure. We also observe more excited high harmonics with increasing slit length. The shortest slit supports only excitation of the fundamental mode and 3rd harmonic, whereas even the 9th harmonic is excited for the longest slit. The ability to resolve a peak with an energy loss as low as 0.24 eV shows the viability of the RL algorithm for the evaluation of very low-energy signals with STEM-EELS.

1. E. Essers *et al.*, Ultramicroscopy 110 (2010), p. 971.
2. W. H. Richardson, J. Opt. Soc. Am. 62 (1972), p. 55.
3. L. B. Lucy, Astron. J. 79 (1974), p. 745.
4. A. Gloter *et al.*, Ultramicroscopy 96 (2003), p. 385.
5. I. Carmeli *et al.*, Phys Rev B 85 (2012).
6. I. Carmeli *et al.*, arXiv:1212.1987 [physics.optics] (2013).
7. M. Bosman, and V. J. Keast, Ultramicroscopy 108 (2008), p. 837.

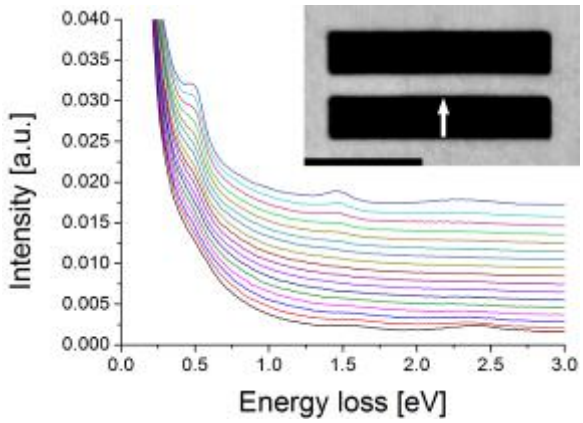

Figure 1. Series of EEL spectra acquired across one slit of double slit array. Inset: HAADF-STEM image. The arrow depicts the position (acquisition direction) of the spectra.

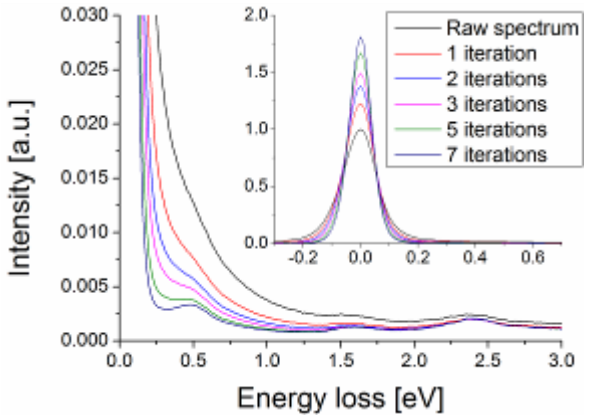

Figure 2. Effect of the RL algorithm on the bottom-most (black) spectrum in Figure 1. The faint signal at ΔE = 0.5 eV is clearly resolved with increasing number of iterations. Inset: Effect on the ZLP.

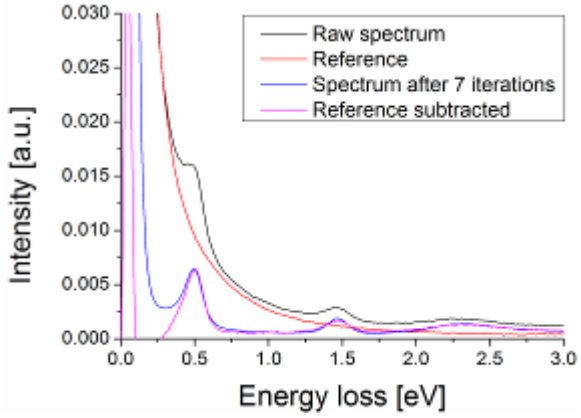

Figure 3. Comparison of the effect of the RL algorithm and reference subtraction to the top-most spectrum in Figure 1. Both methods show nearly identical results for ΔE exceeding 0.5 eV.

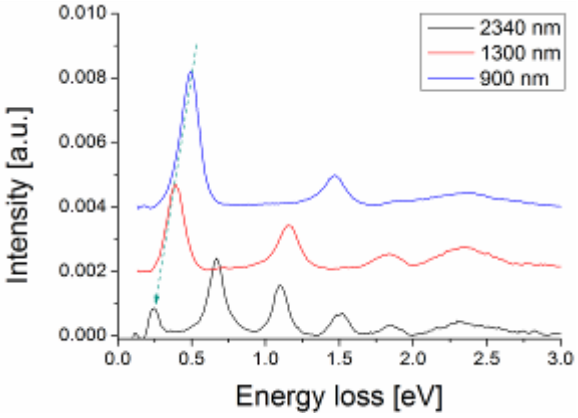

Figure 4. Spectra (after 7 iterations and a power-law background subtraction) acquired near the metal bar in double slit arrays of slits with varying slit lengths. Additionally to the red-shift of the fundamental energy, more high harmonics are excited with increasing slit length.

Spectroscopy in STEM/TEM

IM.4.P082
Peak mapping in EFTEM

W. Sigle[1], C.T. Koch[2], B. Ögüt[1], N. Talebi[1], P.A. van Aken[1]

[1]MPI for Intelligent Systems, Center for Electron Microscopy, Stuttgart, Germany
[2]Ulm University, Institute for Experimental Physics, Ulm, Germany

sigle@is.mpg.de
Keywords: Energy-filtering TEM, low-loss EELS, plasmons.

Energy-filtering transmission electron microscopy (EFTEM) is widely used to identify the elemental distribution in a material. The intensity of absorption edges is measured after subtracting background using typically two pre-edge windows [1]. Alternatively, image series across the absorption edge can be used [2]. This approach allows detection of fine structures and a more reliable background fit, however at the expense of lower signal-to-noise ratio (SNR).

Recently, EFTEM series were also applied for the detection of surface plasmon resonances in metallic nanosystems [3, 4]. These resonances typically occur in the energy-loss range up to 5 eV. Unlike absorption edges, the resonances appear as Lorentzian-shaped peaks with a full width at half maximum between 0.3 and 1 eV. The image series are acquired using a 0.1- or 0.2-eV slit and energy steps in the similar range. EFTEM image series are usually analyzed by displaying intensities in false-colour images. This method allows identification of strong spectral peaks. However, if a small peak is located close to a strong peak, the tails of the strong peak mask the small peak making this peak invisible in an EFTEM intensity map. This problem can be resolved by mapping peak positions instead of intensities.

Peak extraction was done using a Digital Micrograph script [5]. Energy-loss spectra of each image pixel $\{x_i, y_i\}$ are extracted. If the intensity at an energy loss E_j is higher than the neighbouring energy channels E_{j+1} and E_{j-1}, the voxel $\{x_i, y_i, E_j\}$ is given intensity 1. All other voxels belonging to pixel $\{x_i, y_i\}$ are set to zero. This results in a binary data cube containing information solely of peak positions. Energy slices of this data cube are called “peak maps” [6].

Unfortunately, the SNR of EFTEM images recorded with a monochromated electron beam and very narrow energy-selecting slit is poor. Therefore many voxels are erroneously identified as peaks and peak maps suffer from considerable noise (Figure 1a). This problem can be alleviated by the application of multivariate statistical methods like PCA to reduce noise prior to the application of the peak-finding algorithm. After PCA, using 14 out of 35 components, most artificial peaks are absent (Figure 1b).

An example is displayed in Figure 2 showing the plasmonic response of 7 holes in a thin silver film arranged in a circular geometry. An EFTEM intensity map (a), a peak map from the raw data (b), a peak map after PCA noise reduction (c), and simulations using finite-difference time-domain calculations (d) are shown at an energy loss of 3.7 eV corresponding to the resonance energy of a toroidal plasmonic eigenmode [7]. It is clear that the mode cannot be identified from only the EFTEM intensity (a). On the other hand, the peak maps show close correspondence to the calculated data.[8]

1. L. Reimer, Energy-filtering Transmission Electron Microscopy, Springer (1995).
2. J. Mayer and J. Plitzko, J. Microsc. 183 (1996) p. 2.
3. J. Nelayah, L. Gu, W. Sigle, C. T. Koch, L. Pastoria-Santos, L. M. Liz-Marzán and P. A. van Aken, Optics Letters 34 (2009) p. 1003.
4. B. Schaffer, U. Hohenester, A. Trügler and F. Hofer, Phys. Rev. B 79 (2009) p. 041401.
5. The script is freely available from http://portal.tugraz.at/portal/page/portal/felmi/DM-Script
6. N. Talebi, W. Sigle, R. Vogelgesang, C. T. Koch, C. Fernández-López, L. M. Liz-Marzán, B. Ögüt, M. Rohm and P. A. van Aken, Langmuir 28 (2012) p. 8867.
7. B. Ögüt, N. Talebi, R. Vogelgesang, W. Sigle and P. A. van Aken, Nano Letters 12 (2012) p. 5239.
8. The research leading to these results has received funding from the European Union Seventh Framework Programme [FP7/2007- 2013] under grant agreement n°312483 (ESTEEM2).

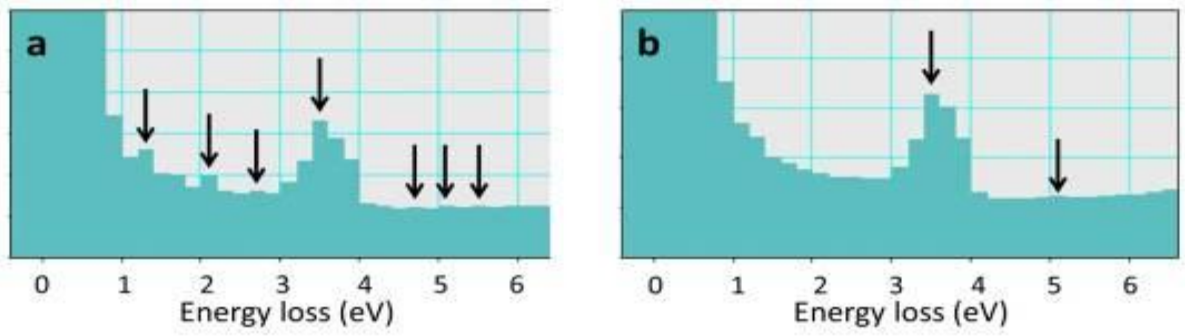

Figure 1. EELS spectra extracted from a single pixel of an EFTEM data cube (a) before PCA and (b) after PCA noise reduction using 14 out of 35 components. Detected peaks are marked by arrows.

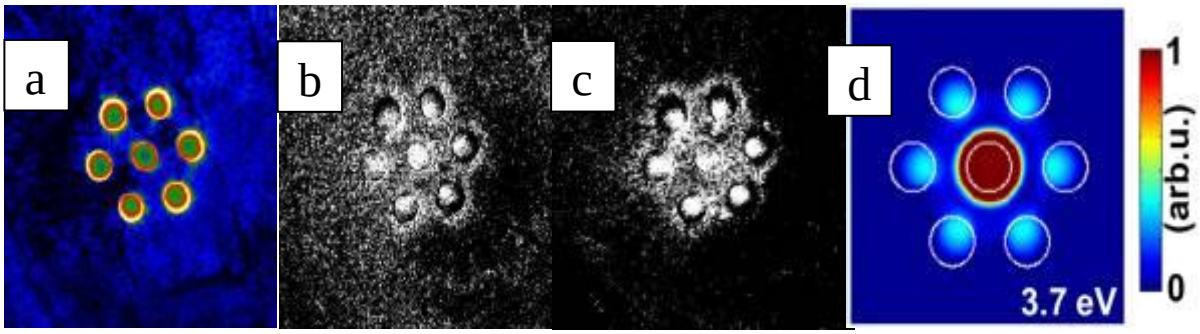

Figure 2. Plasmonic response of an oligomer system consisting of 7 holes drilled into a thin silver film. (a) EFTEM intensity map, (b) peak map from the raw data, (c) peak map after PCA noise reduction, and (d) finite-difference time-domain calculations.

Spectroscopy in STEM/TEM

IM.4.P083
Density measurement in thin layers by electron energy loss spectroscopy (EELS)

J. Thomas[1], T. Gemming[1], J. Ramm[1]

[1]IFW Dresden, 31, Dresden, Liechtenstein

j.thomas@ifw-dresden.de
Keywords: EELS, thin layers, density

Mechanical, optical, and electrical properties of thin films depend strongly on their density. In view of commercial applications the companies have a major interest in methods for measurement of the density even in ultrathin layers. A density measurement method with high lateral resolution could help to optimize the parameters of deposition processes and to tailor the thin film properties for specific applications.

Our method is based on the acquisition of energy filtered images in the low loss region as well as of an element distribution map using core loss edges. We demonstrate the method at thin tetrahedral amorphous carbon layers prepared with an intentional density gradient in an Oerlikon Balzers PVD production system on polished tungsten carbide substrate.

The “normal“ mass thickness contrast in TEM depends on the product of specimen density ρ and thickness t. It is the basic idea of the method to uncouple these two parameters using EELS techniques. Getting high lateral resolution we use an imaging filter for the measurements (Energy Filtered TEM technique). The thickness can be measured as multiples of the mean free path λ for inelastic scattering by comparison of the portions of elastically and inelastically scattered electrons resulting in a thickness map $I_{ThickMap}(x,y)$. The relation between λ and ρ is given by Iakoubovski et al. [1] (see equation (1) on second page).

For the uncoupling of thickness and density we need additional information. This is given by the relation between the element-specific EELS signal (here carbon K-edge) I_C and thickness as well as density (cp. equation (2)). Unfortunately, the proportionality of I_C and thickness t is only valid up to about $\lambda/3$ because of inelastic multiple scattering. We correct this influence by an additional term (polynomial with purely mathematical background and dependence on the experimental setup) and obtain formula (3) for the spatial-resolved density distribution.

Figures 1 and 2 demonstrate the color-encoded results obtained at a cross section of a ca. 1 µm thick carbon layer as mentioned above. Figure 1a shows an example of the thickness map measured on a FIB prepared cross-section of the carbon layer. Figure 1b illustrates the carbon map already corrected regarding the multiple inelastic scattering. Figure 2 shows the two-dimensional result of the density calculation pixel by pixel. For a better understanding two intensity profiles are shown along the line parallel to the substrate surface (white arrow) as well as perpendicular to it (blue arrow). There is a significant difference between them: The line of best fit for the profile parallel to the surface has the slope zero, i.e. there is no systematic change of the density in this direction. The fluctuations at the beginning are believed to be a result of the substrate roughness.

On the other hand, the profile perpendicular to the substrate surface indicates a significant dependence of the carbon layer density on the distance from the substrate which can be approximated by polynomial of 2nd degree as labeled in Figure 2.

The confirmation of the deposition induced expected density gradient in the cross section of the thin carbon layer shows that the method is suitable for the measurement of density fluctuations with a lateral resolution typical for transmission electron microscopy.

1. K. Iakoubovskii, K. Mitsuishi, Y. Nakayama, and K. Furuya, Microsc. Research Techn. **71** (2008), p. 626
2. The authors thank Dina Lohse (IFW Dresden) for the careful electron microscopic specimen preparation and Beno Widrig (OC Oerlikon Balzers AG) for the preparation of the ta-C samples.

Equations.

$$I_{ThickMap}(x,y) \propto \frac{t(x,y)}{\lambda(x,y)} \propto \left[\rho(x,y)\right]^{0.3} \cdot t(x,y) \tag{1}$$

$$I_C(x,y) \propto \rho(x,y) \cdot t(x,y) \tag{2}$$

$$\rho(x,y) \propto \sqrt[0.7]{\frac{I_C}{I_{ThickMap}\left[1+0.42\cdot t/\lambda - 1.34\left(t/\lambda\right)^2 + 0.45\left(t/\lambda\right)^3\right]}} \tag{3}$$

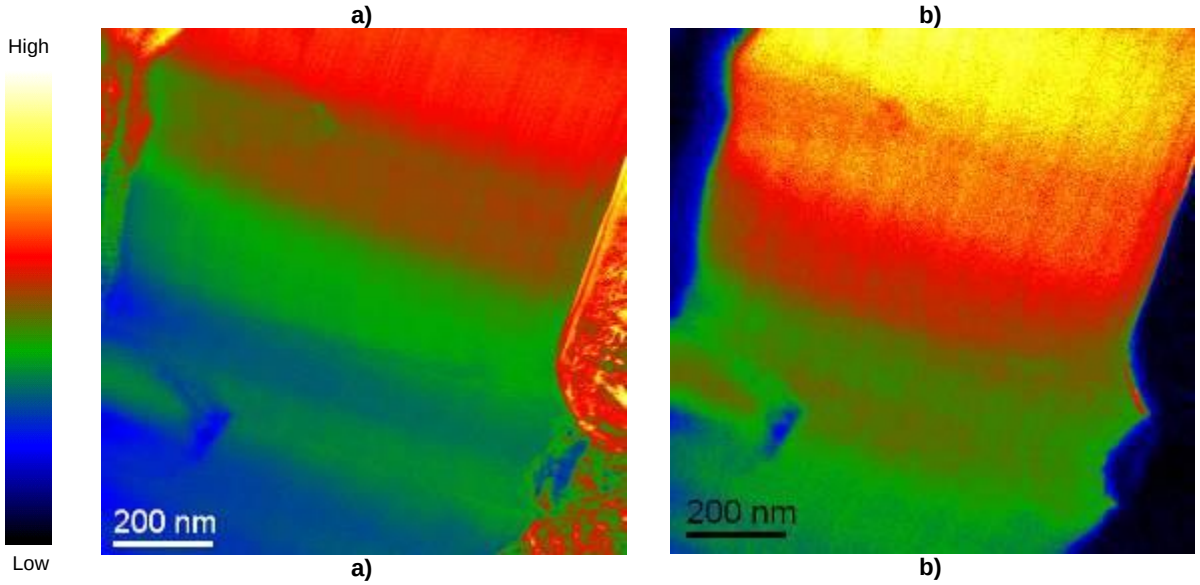

Figure 1. EFTEM results obtained on a cross-section of the carbon layer. a) Thickness distribution *t/λ*. b) Carbon distribution (net intensity of the C K-edge).

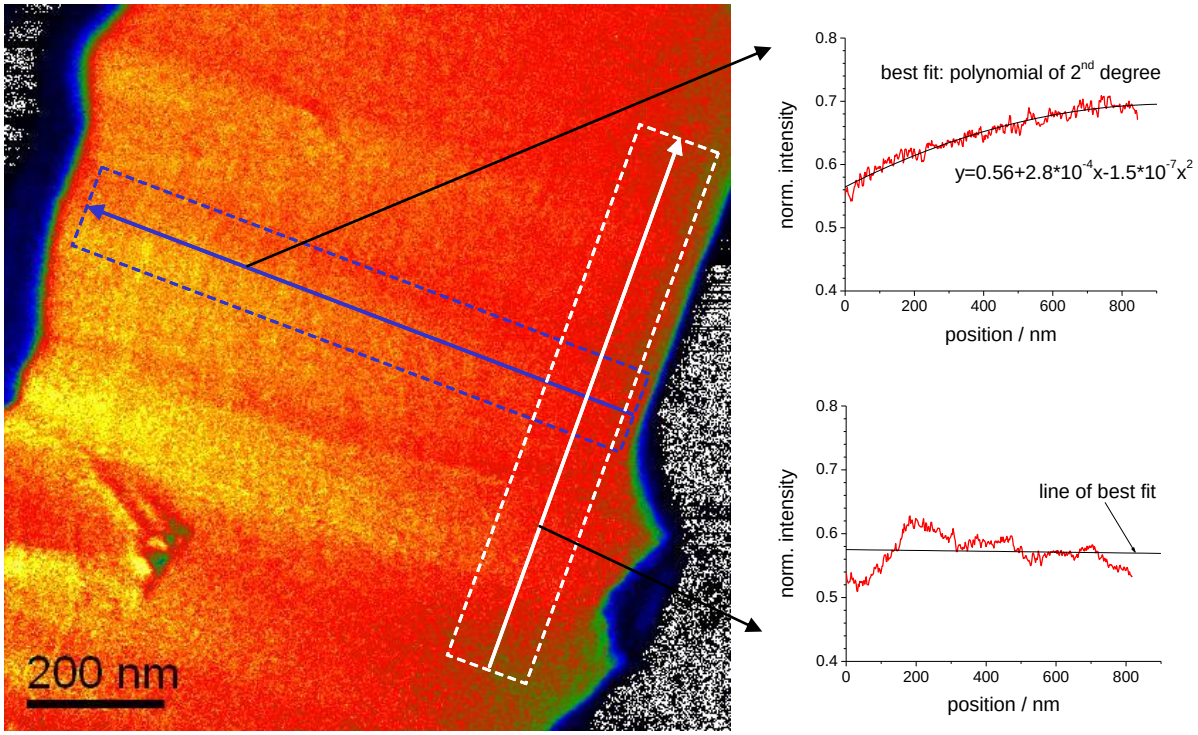

Figure 2. Density distribution derived from the EFTEM results shown in Fig. 1

Spectroscopy in STEM/TEM

IM.4.P084
Coordination fingerprinting using EELS and XANES: experiments and *ab initio* multiplet calculations

C. Patzig[1], H. Ikeno[2], Y. Hu[3], I. Tanaka[4], T. Höche[1]

[1]Fraunhofer Institute for Mechanics of Materials IWM, Center for Applied Microstructure Diagnostics CAM, Halle(Saale), Germany
[2]Kyoto University, Fukui Institute for Fundamental Chemistry, Kyoto, Japan
[3]University of Saskatchewan, Canadian Light Source Inc., Saskatoon, Canada
[4]Kyoto University, Department of Materials Science and Engineering, Kyoto, Japan

christian.patzig@iwmh.fraunhofer.de
Keywords: EELS, XANES, *ab initio* calculation

Both x-ray absorption near edge structure (XANES) and electron energy-loss near edge structure (ELNES) spectroscopy can be applied to determine coordination and valence state of the targeted ion in a specific compound [1]. Especially for transition-metal ions, crystal field splitting of the unoccupied 3d states probed by excitation of core-level electrons by either x-rays (XANES) or electrons (ELNES) can lead to drastic changes of spectral features [2].

While XANES, usually accomplished at synchrotron sources, possessing the benefit of a very good energy resolution (below 100 meV), is rather an integrating method, gaining information from typical sample volumes of some 10.000 µm³), ELNES can offer unsurpassed spatial resolution (just depending on the probe size of the electron beam in the Transmission Electron Microscope) with an energetic resolution on the range of typically 0,8 eV.

We show that *ab initio* charge-transfer multiplet calculations that take into account electronic configuration interactions [3] can be used to efficiently predict the spectral shape of transition-metal ions in different valencies and coordination states.

The variation of the Zr $L_{2,3}$ spectra for tetravalent Zr ions in different coordination states (six-, seven-, and eightfold coordinated), exemplified by different ZrO_2 polymorphs (monoclinic, cubic and tetragonal) and $SrZrO_3$, is proven both experimentally and by calculation. Moreover, it will be shown that all zirconia polymorphs and in particular also cubic and tetragonal ZrO_2, that both have eightfold coordination, can be differentiated using Zr $L_{2,3}$ edge XANES. It is shown that even ELNES at high energy electron losses (above 2,2 keV for the Zr $L_{2,3}$ edge) can be applied for a successful spectrum fingerprinting, in combination with the multiplet calculation thereof [4].

Concerning the interpretation of transition-metal white lines, three fresnoite-type vanadates ($Ba_2VSi_2O_8$ [BVS], $K_2VV_2O_8$ [KVV], and $Rb_2VV_2O_8$ [RVV]) were studied by XANES as model compounds. It is shown that not only the interaction of the target (V) ion with the anions of the first coordination sphere, but also with the cations of the second coordination sphere have to be taken into account in order to gain a good resemblance of the calculated V $L_{2,3}$ edge spectra with the experimental ones [5]. The importance of the latter finding is that simple experimental fingerprinting, i.e., the comparison with spectra obtained from known reference compounds used to interpret spectral features for decades, can result in misleading interpretations when interactions with second-nearest neighbouring cations are not taken into account.

1. R. Brydson, H. Sauer, W. Engel, J.M. Thomas, E. Zeitler, N. Kosugi, and H. Kuroda, Journal of Physics: Condensed Matter 1 (1989), 797-812
2. Th. Höche, M. Mäder, S. Bhattacharyya, G.S. Henderson, Th. Gemming, R. Wurth, C. Rüssel, and I. Avramov, CrystEngComm 13 (2011), 2550-2556.
3. H. Ikeno, F.M.F. de Groot, E. Stavitski and I. Tanaka, Journal of Physics: Condensed Matter 21 (2009), 104208
4. H. Ikeno, M. Krause, T. Höche, C. Patzig, Y. Hu, A. Gawronski, I. Tanaka, and C. Rüssel, Journal of Physics: Condensed Matter 25 (2013), accepted for publication.
5. T. Höche, H. Ikeno, M. Mäder, G.S. Henderson, R.I.R. Blyth, B.C. Sales, and I. Tanaka, American Mineralogist 98 (2013), in print.

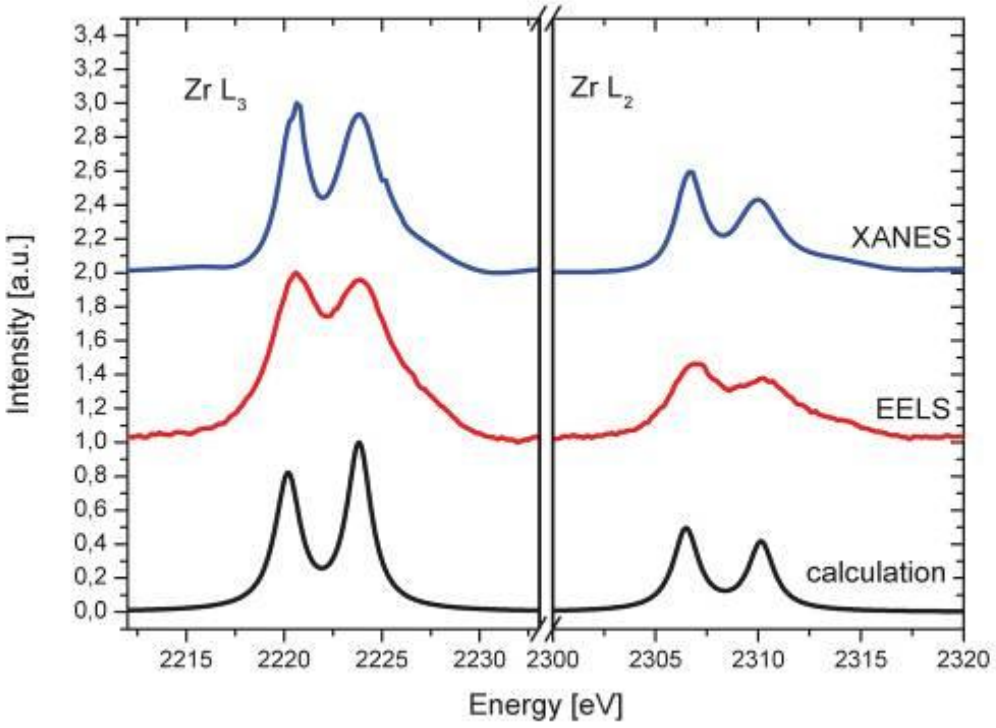

Figure 1. Zr $L_{2,3}$ edge of $SrZrO_3$: XANES, EELS and multiplet calculation.

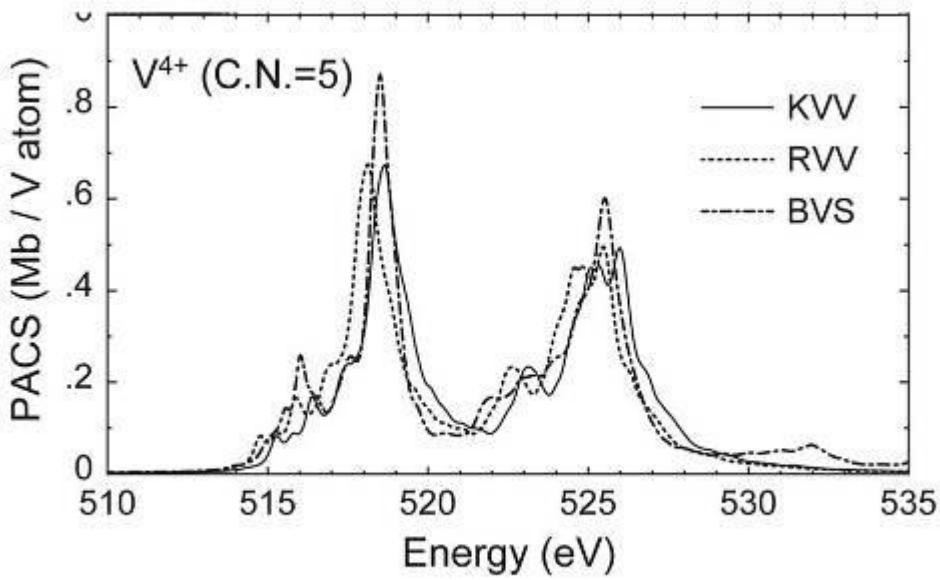

Figure 2. Juxtaposition of V^{4+} contributions to the theoretical V-$L_{2,3}$ XANES in the three compounds BVS, KVV, and RVV.

Spectroscopy in STEM/TEM

IM.4.P085
Calculations of elastic and inelastic scattering processes of relativistic electrons in oriented crystals

D. Hinderks[1], H. Kohl[1]

[1]Physikalisches Institut und Interdisziplinäres Centrum für Elektronenmikroskopie und Mikroanalyse (ICEM), Universität Münster, Münster, Germany

dieter.hinderks@uni-muenster.de
Keywords: relativistic scattering, Dirac equation, Bloch waves

Since modern electron microscopes operate at acceleration voltages up to several hundred kV, a relativistic treatment for simulations is necessary. The focus of this work lies on relativistic scattering processes in crystalline materials (Figure 1).

Beginning from the non-relativistic case we want to build up the necessary theory. Non-relativistic scattering processes in crystalline materials using Bloch waves for the incident electrons have been calculated frequently. Before entering the crystal the incident electrons are expressed as simple plane waves. Inside the crystal the electrons are described using Bloch waves, because of the periodic nature of the periodic potential. After leaving the crystal the electrons are described by a superposition of plane waves to fulfill the boundary conditions. In order to obtain an accurate expression for the wave function of the incident electrons many excited Bloch waves have to be considered. Therefore the calculation of the resulting wave function becomes computationally intensive. The appearance of inelastic scattering processes inside the crystal is considered by using corresponding matrix elements [1].

This work focusses on a fully relativistic description of such scattering processes generalizing the non-relativistic theory outlined above. For high electron energy, the speed of the electrons approaches the speed of light, which makes a relativistic treatment necessary (Figure 2). For a relativistic description the calculation of the matrix elements has to be done considering the Dirac equation

Using the relativistic propagator theory, the scattering matrix can be written as

This notation allows to easily separate the electric and magnetic part in the matrix element. Here and are the wave functions of the excited electrons in the initial and the final state as a function of space-time coordinates, respectively. Moreover, and are scalar and vector potentials depending on space-time coordinates, which are generated by the incident electrons, is one of the Dirac matrices, and is a vector with three components in which every constituent is given by a four dimensional matrix [3].

The excited electron is under influence of the electric and magnetic fields, which are induced by the charge

and the current

which depend on space-time coordinates. The corresponding potentials and are calculated using a Greens formalism. Using this theory with simple plane waves to describe the incident electrons one obtains the differential cross section [2].

As already pointed out, the fast incident electrons have to be described using Bloch waves to consider their movement in the periodic potential. To ensure a fully relativistic treatment the Bloch waves have to be replaced by relativistic Bloch waves [3]

The relativistic character is assembled in four component spinors , is a reciprocal lattice vector, and is the transverse momentum of the incident electrons.

The fourier coefficients of one single Bloch wave depend on the crystal structure and can be determined analoguously to the non-relativistic case. One single Bloch wave leads to a sum over reciprocal space. The full solution for the wave function leads to a sum over different Bloch waves which are excitated at the same time and therefore are weighted with excitation coefficients .

The obtained matrix elements using Bloch waves differ from the matrix elements using simple plane waves [2] basically in additional sums in the matrix elements to consider the Bloch waves.

1. A. Weickenmeier and H. Kohl, Phil. Mag. B60 (1989) 467.
2. R. Knippelmeyer et al., Ultramicroscopy 68 (1997) 25-41.
3. P. Strange in „Relativistic Quantum Mechanics“, (Cambridge University Press, 1998).

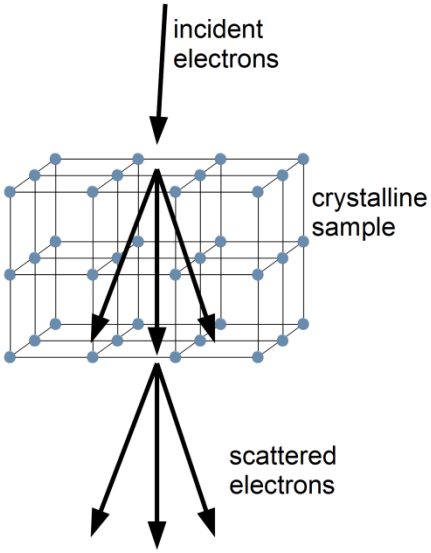

Figure 1. Schematic sketch of the scattering problem. Before entering the crystal the electrons are described as plane waves. Inside the crystalline material the electrons are given as Bloch waves. After leaving the crystal the electrons are described as a superposition of plane waves to satisfy the boundary conditions.

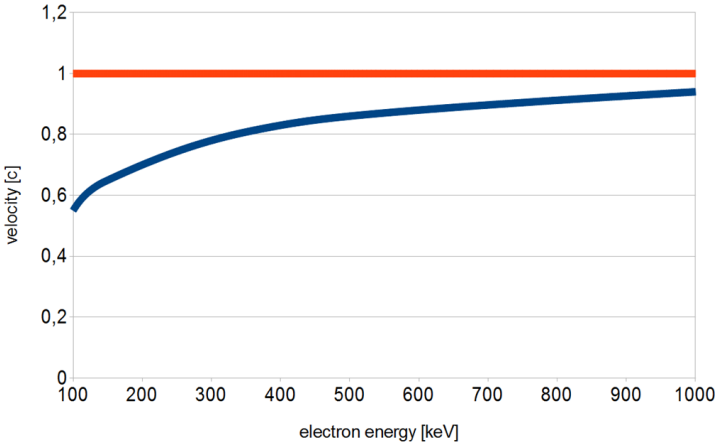

Figure 2. Velocity of the primary electrons in terms of speed of light as a function of their energy.

Spectroscopy in STEM/TEM

IM.4.P086
Towards real-space mapping of valence states using core-loss EFTEM imaging

R. Hambach[1], J. Biskupek[1], S. Löffler[2], V. Motsch[3], P. Schattschneider[2,3], U. Kaiser[1]

[1]Electron Microscopy Group of Materials Science, Ulm University, Ulm, Germany
[2]University Service Center for Transmission Electron Microscopy, Vienna University of Technology, Vienna, Austria
[3]Institute of Solid State Physics, Vienna University of Technology, Vienna, Austria

ralf.hambach@uni-ulm.de
Keywords: EFTEM, valence states, Rutile

Thanks to the improvements in aberration-correction for electron microscopes, it is now possible to determine the position and species of individual atom columns with high accuracy. In particular cases, one can even resolve details at a sub-atomic level, like effects of the electron redistribution in the vicinity of a defect due to chemical bonding [1]. On the other hand, electron energy-loss spectroscopy (EELS) is a powerful method to investigate electronic excitations like plasmons (valence-loss) and interband transitions (core-loss region). In particular, near-edge spectra contain valuable information on conduction states and chemical (anti)binding.

This raises the question, if it is possible to map individual atomic orbitals in real space by combining the spatial resolution of transmission electron microscopes (TEM) with the analytical power of electron energy-loss spectroscopy. At the atomic level, a detailed understanding of the imaging process is only possible in the framework of quantum mechanics and, in order to extract information from the recorded images, a detailed comparison with image simulations is mandatory. Indeed, previous calculations including elastic and inelastic scattering [2] predict the possibility to map the orientation of selected anti-binding states in real-space using EFTEM imaging (energy-filtered transmission electron microscopy) at high energy loss.

In order to evaluate the feasibility of corresponding experiments, we have performed EFTEM imaging for two different samples, Silicon and Rutile (TiO_2). We show that lattice planes can be resolved in core-loss EFTEM and we assess the importance of image aberrations, signal-to-noise, and other limiting factors for orbital mapping. Due to the small scattering cross section for high energy-loss the image intensity is very low. Single recorded images have no apparent structure and the periodicity of the crystal is only clearly visible in the FFT (see Figure 1). We propose an averaging method to improve the S/N ratio of the high-resolution images by making use of the translational symmetry of the crystal summing over many neighbouring unit-cells.

1. J.C. Meyer *et.al.*, Nature Materials, 10 (2011), p. 209.
2. S. Löffler, V. Motsch and P. Schattschneider, submitted to Ultramicroscopy.
3. The authors acknowledge financial support by the Austria Science Fund (FWF) under grant number I543-N20, the DFG (German Research Foundation) and the Ministry of Science, Research and the Arts (MWK) of Baden-Württemberg.

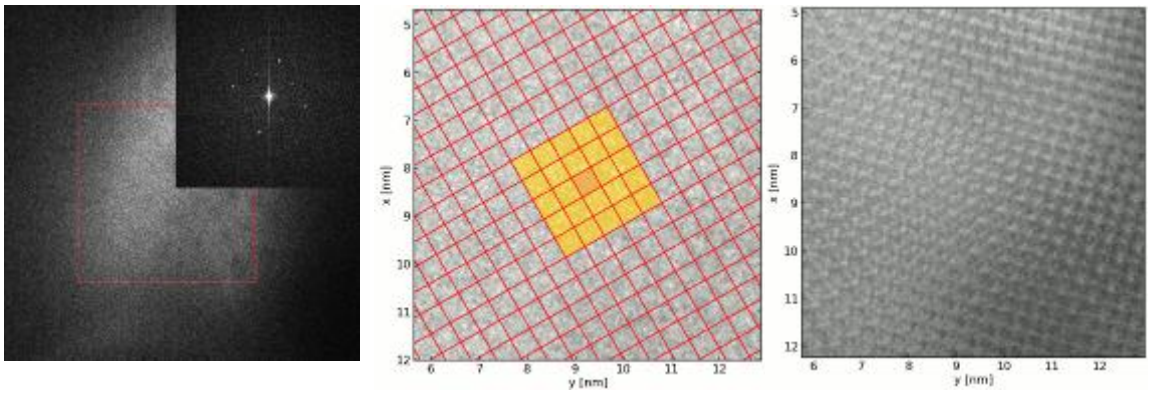

(a) (b) (c)

Figure 1. a) Energy-loss filtered HRTEM image of Rutile at the Ti-L edge (E=463eV, dE=2eV). The inset shows the modulus of the FFT of the highlighted region. The inhomogeneous illumination is due to the strong convergence of the beam. b) Superposition of crystal periodicity and the central part of the HRTEM image (red lines). c) The summed image resulting from a running average over 5x5 unit cells (indicated in yellow) shows atom contrast.

Spectroscopy in STEM/TEM

IM.4.P087
Spatially resolved EELS of FeCr layers - an example for processing TEM images with ImageJ

M. Entrup[1], H. Kohl[1]

[1]WWU Münster , Physikalisches Institut, Münster, Germany

michael.entrup@uni-muenster.de
Keywords: EFTEM, SR-EELS, Elemental-Mapping, ImageJ, EFTEMj

Electron energy loss spectroscopy (EELS) is used to obtain chemical information in the transmission electron microscope. From a selected area a single EEL spectrum is acquired. When using spatially resolved EELS (SR-EELS), a part of the spatial information is preserved. Several EEL spectra are recorded in parallel as a function of one spatial coordinate, perpendicular to the energy dispersive direction. This method is useful for investigating specimens like interfaces and layer systems. In this work we apply SR-EELS in a TEM with in-column Omega filter to a FeCr layer system. Some of the remaining aberrations of this filter can be corrected by processing the recorded SR-EELS images. We will show how the open source software ImageJ [1] can be used to perform this task.

A TEM equipped with an energy filter allows us to create a three-dimensional data cube (Fig. 1). In single measurements we can only cut two-dimensional slices out of this data cube. With SR-EELS we can record images that contain both, spatial information and energy loss information. SR-EELS was first described by Reimer et al. [2]. The energy filter determines how to set up the TEM. The in-column Omega filter of the Zeiss Libra 200FE uses hexapole elements to suppress axial aberrations and the resulting caustic [3]. Therefore SR-EELS data can be recorded directly in the EEL spectrum mode. It is the same data that is used to create an EEL spectrum by summing all pixels of each energy channel. As shown in Fig. 2a, the spatial extension decreases with increasing energy loss. This distortion results from a geometrical aberration and can be corrected by processing the recorded data. Another experimental aspect has to be considered. A round aperture at the filter entrance plane results in a change of intensity along the spatial axis. By using a well aligned slit aperture the uniformity of the intensity is ensured. The narrow slit that is installed in our microscope results in a low overall intensity and therefore long acquisition times are necessary. We therefore decided to use a round aperture to gain as much intensity as possible, to observe the core loss energies of chromium and iron.

ImageJ is used to perform the processing of the recorded data. The advantages of this open source software are the support for a wide range of file formats, the easy to learn macro language and the possibility to write complex plugins with Java. To correct the distortion of the SR-EELS data a plugin has been implemented. At first a partially manual method can be used to apply a linear fit to the inclined border. Applying a linear model to describe the distortion leads to a small error. Therefore the plugin provides an alternative, automatic method that measures the spatial extension of each energy channel separately. This results in a slightly curved fit. The second step is to scale each energy channel to the same spatial extension (Fig. 2b), while preserving the over all intensity of each channel. Intensity variations due to the use of a round aperture can be corrected at the same step.

In combination with EFTEMj [5] - an ImageJ plugin for elemental mapping - it is possible to further analyse the corrected SR-EELS data. At core loss energies we can subtract the background signal to extract the elemental signal. EFTEMj can handle an arbitrary number of pre- and post-edge images, being the ideal tool to analyse the SR-EELS data. But it requires a stack of ESI images (see Fig. 1a). To fulfil this requirement the SR-EELS data are converted to a stack of line traces (see Fig. 1c. One line trace is highlighted by a darker colour). Fig. 2c shows a montage of such a stack. The resulting elemental signal of iron is shown in Fig. 2d.

Further studies have to show if SR-EELS can compete with normal EFTEM analysis of the same specimen. A higher energy resolution will be the main advantage of SR-EELS. Compared to elemental maps of EFTEM images data acquisition times are shorter with the disadvantages of a higher experimental effort - orienting the specimen - and more sophisticated processing of the data. If the spatial resolution is high enough and image processing does not add artefacts to the data, SR-EELS can become a helpful tool to analyse interfaces and layer systems.

1. C. A. Schneider et al., Nature Methods 9 (2012), 671-675.
2. L. Reimer et al., Ultramicroscopy 24 (1988) 339-354.
3. S. Lanio, PhD thesis (1986), TH Darmstadt.
4. https://github.com/EFTEMj/EFTEMj (11.04.2013)
5. The authors gratefully acknowledge funding from the Deutsche Forschungsgemeinschaft (DFG) under grant number Ko885/8-1.

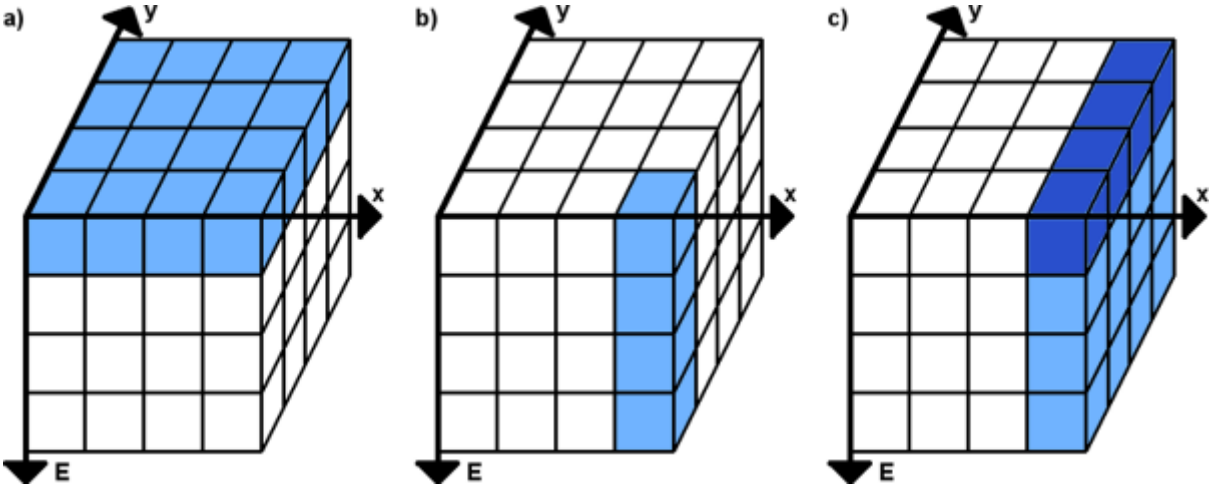

Figure 1. Data cubes for an energy filtering TEM. The highlighted area shows the data that can be acquired with a single measurement by **(a)** electron spectroscopic imaging (ESI), **(b)** EELS and **(c)** SR-EELS

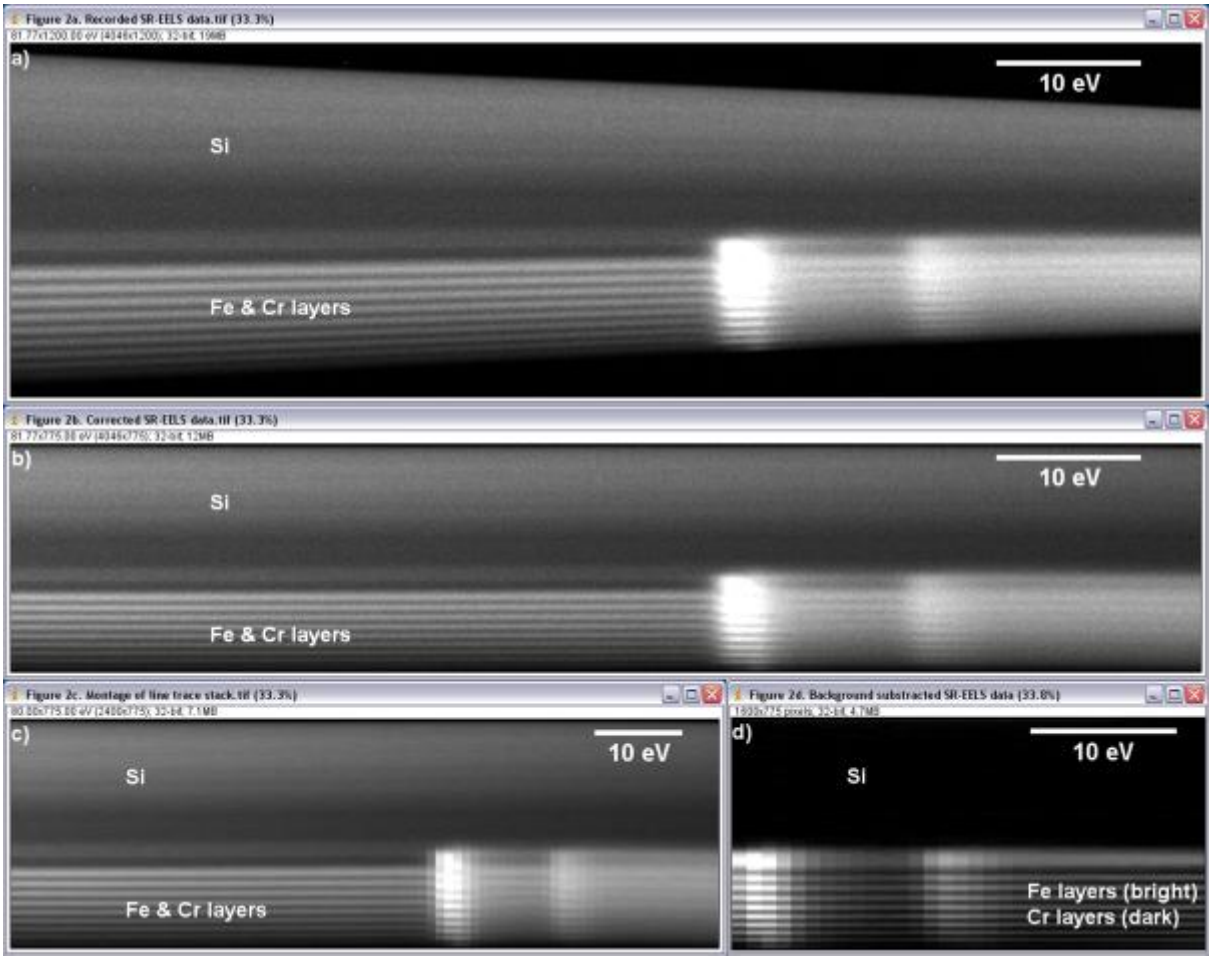

Figure 2. ImageJ workflow for SR-EELS data processing. Fig. 2a - Fig. 2c show an energy interval between 660eV and 740eV. The heights of Fig. 2b - Fig. 2d are 350nm. This results in 0.45nm per pixel. (a) The recorded SR-EELS data. Energy loss as a function of one spatial coordinate, perpendicular to the energy dispersive direction. (b) Corrected SR-EELS data. Each energy channel has been scaled separately. (c) Montage of a line trace stack. The stack has been created by sectioning Fig. 2b into 80 intervals of 1eV width. From each interval a line trace (an image with 1px width and 775px height) has been created by summing all energy channels of the given interval. (d) Montage of the background corrected line trace stack (708eV to 740eV). The stack shown in Fig. 2c has been processed by the ImageJ plugin EFTEMj. All 48 line traces below 708eV contributed to the background calculation. The estimated background has been subtracted from the 32 line traces above 708eV.

Spectroscopy in STEM/TEM

IM.4.P088
Characterization of cubic GaN/AlN multi-quantum wells using state-of-the-art analytical STEM

J. Lindner[1], R.M. Kemper[1], D.J. As[1], D. Meertens[2], A. Kovács[2], M. Luysberg[2], K. Tillmann[2]

[1]University of Paderborn, Dept. of Physics, Paderborn, Germany
[2]Forschungszentrum Jülich, Ernst-Ruska-Centre, Jülich, Germany

lindner@physik.upb.de
Keywords: analytical STEM, EELS, EDS

Analytical transmission electron microscopy provides superior access to structural, chemical and electronic properties of quantum structures grown on locally nanopatterned semiconductor surfaces. Other thin film characterization techniques frequently fail to adequately reveal the properties of nanostructures, if these can be grown only locally, as is the case e.g. if electron beam lithography is used for substrate patterning, because of the small patterned substrate areas on which growth needs to be characterized. With the advent of C_s-probe corrected STEMs, improved electron sources and advanced detectors for both, EELS and EDS, the analytical performance of off-the-shelf electron microscopes has recently significantly improved and facilitates the characterization of such quantum structures. The aim of this contribution is to spread light on the performance and limits of an actual advanced electron microscope in the characterization of an electronic quantum structure.

To this end a multi-quantum well (MQW) structure consisting of a 20 layer stack of cubic AlN (2 nm) and cubic GaN layers (4 nm) were grown by plasma enhanced molecular beam epitaxy on a sub-µm patterned 3C-SiC(001) surface. Patterning of the SiC surface was achieved by electron beam lithography followed by reactive ion etching (RIE), resulting in square-shaped SiC posts of about 550 nm width and 700 nm height. Cross-sectional TEM-samples were fabricated from several posts using focused ion beam preparation and subsequent low-energy ion polishing to remove FIB-induced surface damage. A JEOL ARM200 (S)TEM equipped with a cold field emission gun, C_s-probe corrector, ultra-high-resolution pole piece, GIF Quantum imaging energy filter and a Centurion EDX silicon drift detector was used to characterize the sample. Mostly the STEM mode was employed at 200 kV acceleration voltage in order to benefit from the high lateral resolution available with both, the annular bright-field (ABF) and the high-angle annular dark-field (HAADF) detector. STEM-ABF images as in Fig. 1 (a) indicate that the MQW-structure has grown conformally around the mesas fabricated by RIE. The MQWs exhibit an undulating shape owing to the presence of (111) stacking faults, as can be clearly seen in atomic resolution ABF- (Fig. 1 b) and HAADF-STEM images (Fig. 1c-d). Low-loss EEL spectra were recorded in a spot mode from individual layers of the MQW structure in a region with almost perfectly planar layer sequence, displayed in the ADF-STEM image in Fig. 1 (e). The 0.3 eV energy resolution of the microscope allows to observe the band edges of the two wide band gap semiconductors as well as characteristic surface and bulk plasmon features of the two different MQW materials (Fig. 1 f). The depth profiles of the chemical elements C, N, O, Al, Si, and Ga were recorded in parallel using core-loss EELS and EDS line scans with an electron beam of < 0.2 nm diameter at a step size of 0.1 nm. Even though the overall agreement of depth profiles is impressive for most elements at first glance, some systematic deviations are observed between EDS and EELS profiles e.g. for nitrogen and gallium. The origin of these differences is analyzed and discussed.

1. The authors are grateful to JEOL Tokyo for the accomplishment of STEM studies.

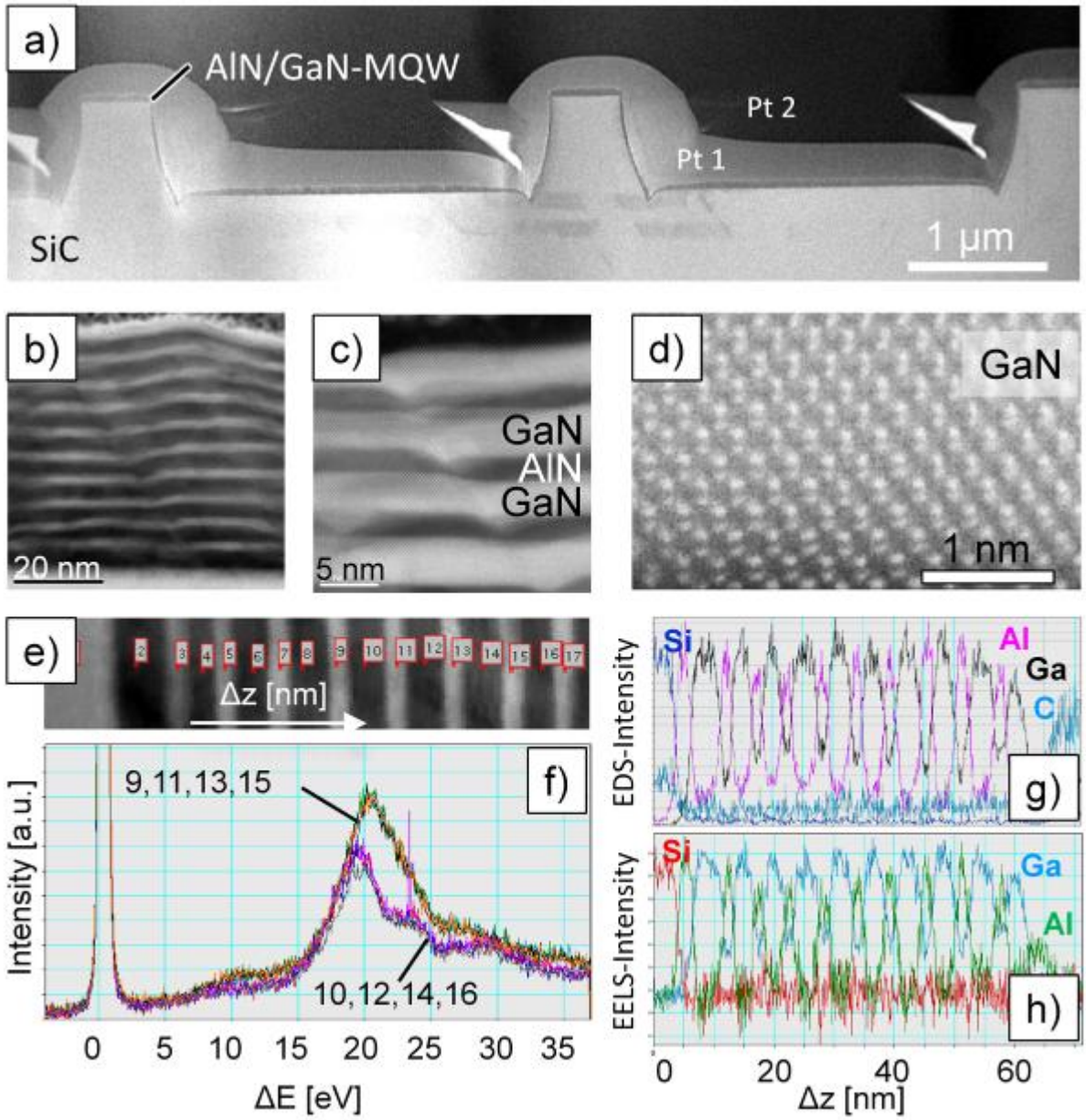

Figure 1. Analytical scanning transmission electron microscopy characterization of a cubic AlN/GaN multilayer quantum well structure (MQW) grown on a nanopatterned 3C-SiC(001) substrate. For details see text.

Spectroscopy in STEM/TEM

IM.4.P089
Electron beam induced reduction of cerium in pure, mixed and doped ceria

A.H. Tavabi[1], S. Arai[2], M. Duchamp[1], S. Muto[3], T. Tanji[2], R.E. Dunin-Borkowski[1]

[1]Forschungszentrum Jülich, Ernst Ruska-Centre, Jülich, Germany
[2]Nagoya University, EcoTopia Science Institute, Nagoya, Japan
[3]Nagoya University, Department of Materials, Physics and Energy Engineering, Graduate School of Engineering, Nagoya, Japan

a.tavabi@fz-juelich.de
Keywords: EELS, ceria, valence change

Cerium and cerium-based oxides are used in a variety of energy-related applications, for example as supports for noble metal catalysts and as electrolyte materials in solid oxide fuel cells [1]. Their redox properties have been described in numerous studies performed using electron diffraction, high-resolution transmission electron microscopy (HRTEM) and electron energy-loss spectroscopy (EELS) [2, 3].

The reduction of cerium from its tetra-valent to its tri-valent state has been observed in the reducing atmosphere of a TEM column, especially in the presence of extensive electron beam illumination. This behaviour can result in the incorrect interpretation of TEM results acquired from materials that have been worked *ex situ*, such as operated electrolytes. Here, we report on a study of the valance change of cerium in three types of ceria due to electron beam induced reduction.

Commercially pure ceria (CeO_2) powders were dispersed on conventional TEM grids and used as a reference material. Two cerium-based oxides that have practical applications, ceria-zirconia solid solution $Ce_2Zr_2O_8$ (CZO) powders [4] and gadolinia-doped ceria $Gd_{0.2}Ce_{0.8}O_{2-\square}$ (GDC) thin films, were also investigated. The GDC thin films were deposited using pulsed laser deposition (PLD) on Si (100). Electron-transparent TEM specimens were prepared using a focused ion beam (FIB) micro-sampling technique. The oxides were studied using EELS on a JEM2100 TEM operating at 200kV. EELS was used to follow the reduction of ceria in the three oxides, by following the evolution of several different Ce edges and the O K edge.

The valence state of cerium in each oxide was determined from core shell Ce N edge spectra, whose shape is well defined for tri- and tetra-valent cerium. Although all three oxides were finally reduced in the TEM column, their reduction rates were very different under constant electron beam irradiation. Whereas the CZO powders were reduced rapidly, both the pure ceria powders and especially the GDC thin films were more stable. In pure ceria, a transformation in the crystal structure took place during the reduction reaction, whereas there was no change in the CZO or GDC microstructures. The GDC film has a large number of oxygen vacancies in its microstructure, primarily as a result of the substitution of tri-valent Gd cations by tetra-valent Ce cations. This substitution may have an influence on the reduction rate of Ce in GDC.

Low-loss EELS measurements showed differences between all of the oxides in both their reduced and their unreduced states. The CZO and GDC low-loss spectra are influenced by the presence of the second cations (Zr^{4+} and Gd^{3+}, respectively). Comparisons with reference spectra acquired from pure zirconia and pure gadolinia suggest that the spectra measured from the reduced oxides show features that are associated with the second cations (e.g., Zr^{4+} in Fig. 1). Similar effects were observed for reduced GDC.

Inner shell Ce N edge spectra were consistent between all of the unreduced oxides. However, different features were observed from the different oxides after reduction. A clear reversal in the intensity ratio of the N_5 and N_4 white lines was observed between reduced and unreduced pure ceria. This effect was weaker for GDC (see Fig. 2) and almost absent for CZO. However, a distinct pre-edge fine structure developed when Ce^{4+} was reduced to Ce^{3+}.

O K edge spectra recorded from the different oxides were similar to each other, containing features similar to those recorded from CeO_2 and Ce_2O_3 for the unreduced and reduced oxides, respectively.

1. P.A. Crozier, R. Wang, R. Sharma, Ultramicroscopy, 108 (2008), p. 1432.
2. S. Arai, S. Muto, J. Murai, T. Sasaki, Y. Ukyo, K. Kuroda, H. Saka, Mater. Trans., 45 (2004), p. 2951.
3. R. Wang, P.A. Crozier, R. Sharma, J. Phys. Chem., 113 (2009), p. 5700.
4. S. Arai, S. Muto, T. Sasaki, Y. Ukyo, K. Kuroda, H. Saka, Electrochem. Solid-State Lett. 9 (2006), p. E1.

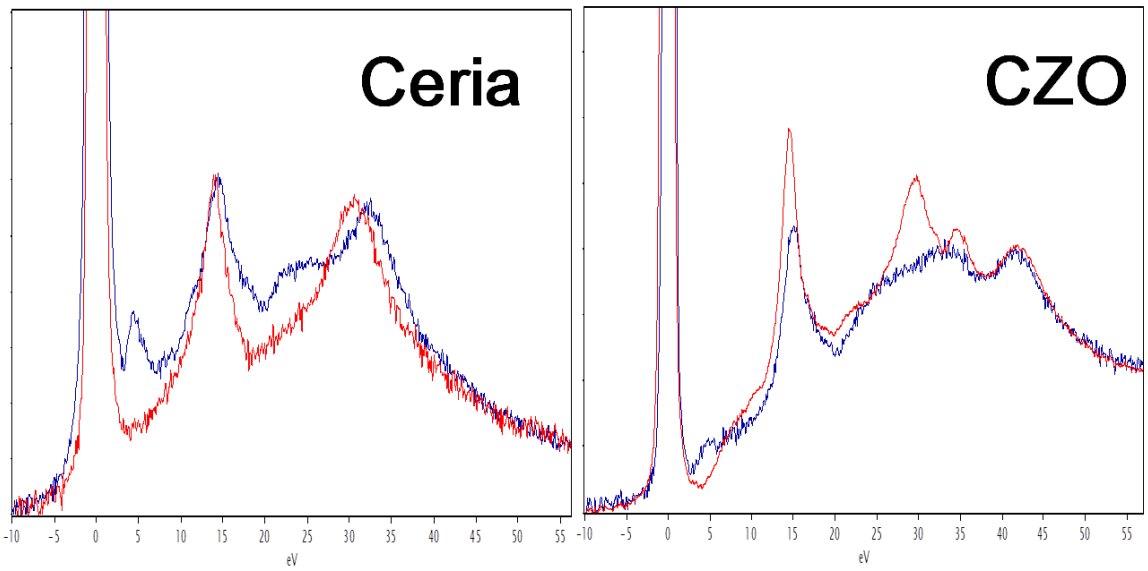

Figure 1. Low-loss electron energy-loss spectra acquired from pure ceria (left) and from a ceria-zirconia solid solution (right) for tetra-valent Ce cations (blue) and for tri-valent Ce cations (red).

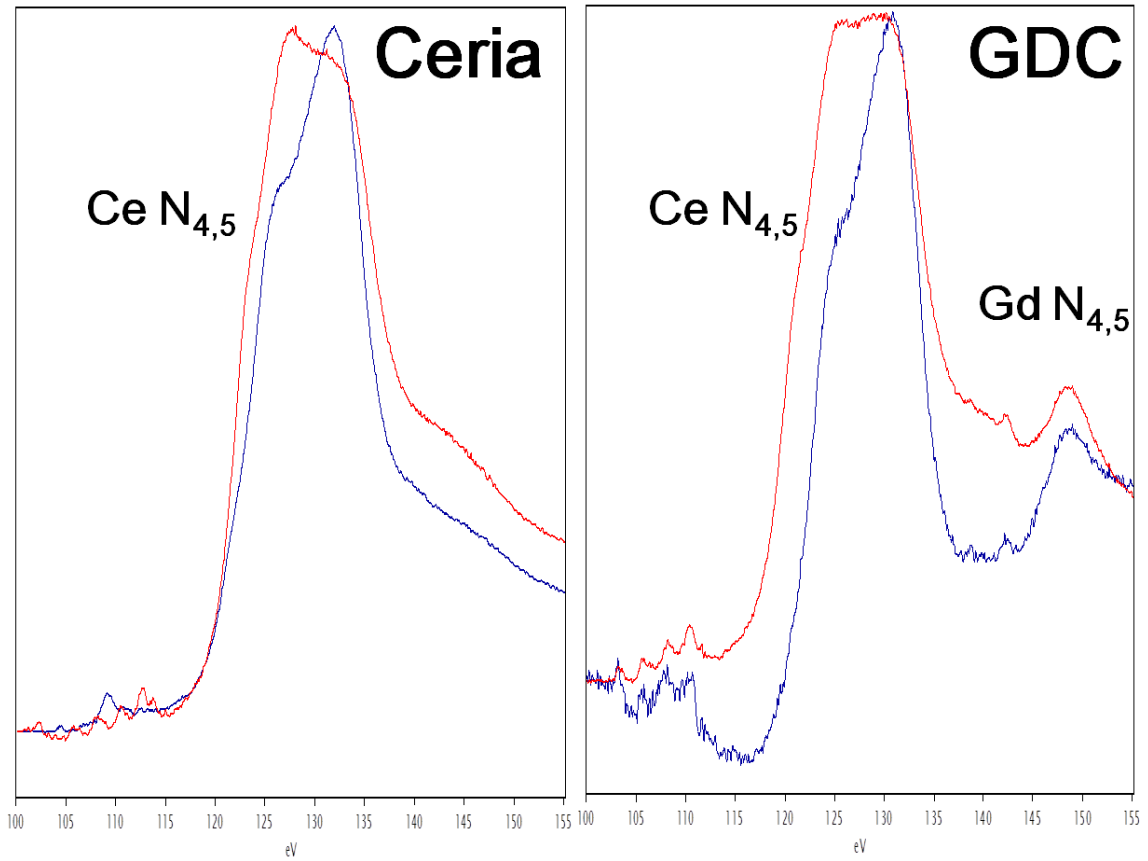

Figure 2. Inner-shell electron energy-loss spectra recorded from pure ceria (left) and from gadolina-doped ceria (right) for tetra-valent Ce cations (blue) and for tri-valent Ce cations (red). The Gd N edge, which is visible in the GDC spectra, shows little difference between the reduced and unreduced oxides.

Spectroscopy in STEM/TEM

IM.4.P090
Composition profiles across the metal-Nb_2O_5-metal stacks for resistive switching as studied by EDX and EELS

F. Hanzig[1], J. Veselý[1], M. Motylenko[1], A. Leuteritz[1], H. Mähne[2], T. Mikolajick[2], D. Rafaja[1]

[1]TU Bergakademie Freiberg, Institute of Materials Science, Freiberg, Czech Republic
[2]NaMLab gGmbH, Dresden, Germany

florian.hanzig@ww.tu-freiberg.de

Resistive switching in MIM (metal-insulator-metal) stacks is an effect that allows a promising technology which is able to overcome the size limitations of conventional non-volatile memories [1]. The resistive switching effect was already demonstrated for several transition metal oxides (TiO_2, NiO, HfO_2) [2]. The models of the switching mechanisms [3] suggest the important role of oxygen vacancies [4].

In this work Nb_2O_5 was used as switching insulator. An amorphous Nb_2O_5 layer was deposited on Pt bottom electrode by reactive dc magnetron sputtering from a metallic niobium target in an argon-oxygen atmosphere at room temperature [5]. In order to describe the effect of the oxygen vacancies on the switching mechanism, materials with different affinity to oxygen like Pt, Al and Ti were used for the top electrode. Cross sections for the transmission electron microscope (TEM) (figure 1) were prepared by focused ion beam (FIB).

Whereas a composition variation at the Nb_2O_5|Ti and Nb_2O_5|Al interfaces due to the oxidation of the electrodes (Ti, Al) could be determined both by energy dispersive X-ray spectroscopy (EDS) (figure 2) and by electron energy loss spectroscopy (EELS) (figure 3) in the scanning transmission electron microscope (STEM) the Nb_2O_5|Pt interface showed no changes in composition applying both methods. This behavior corresponds to electrical measurements indicating resistive switching for MIM stacks with Ti and Al top electrodes (figure 1).

Applying two different argon-oxygen ratios during the Nb_2O_5 deposition process [5] we are able to establish an intrinsic oxygen gradient in the niobium oxide layer between symmetric Pt electrodes. Using this approach we demonstrated resistive switching for Pt top electrodes, respectively. While the quantification of this intrinsic oxygen gradient by EDS failed, the complementary EELS solved this problem and shows a gradient in the oxygen K-edge intensity.

Using their different electron energy loss near edge structure (ELNES) different niobium oxides as well as titanium and aluminum oxides could be distinguished. Therefore a combination of experiment and FEFF simulation [6] is used to correlate switching mechanism and deviations in oxygen stoichiometry [7].

1. T. Mikolajick et al., Advanced Engineering Materials 11 (2009) 235.
2. A. Sawa, Materials Today 11 (2008) 28.
3. L. Chen et al., Current Applied Physics 11 (2011) 849.
4. B. Magyari-Köpe et al., J Mater Sci 47 (2012) 7498.
5. H. Mähne et al., Solid-State Electronics 72 (2012) 73.
6. http://leonardo.phys.washington.edu/feff/.
7. P Calka et al., Nanotechnology, 24(8):085706, 2013.
8. This work was financially supported by the German Research Foundation (DFG) in frame of the research projects RA 1050/13-1 and MI 1247/3-1. TEM JEM 2200 FS was purchased from the funds of the Cluster of Excellence Structure Design of Novel High-Performance Materials via Atomic Design and Defect Engineering (ADDE), which is founded by the European Union (European regional development fund) and by the Ministry of Science and Art of Saxony.

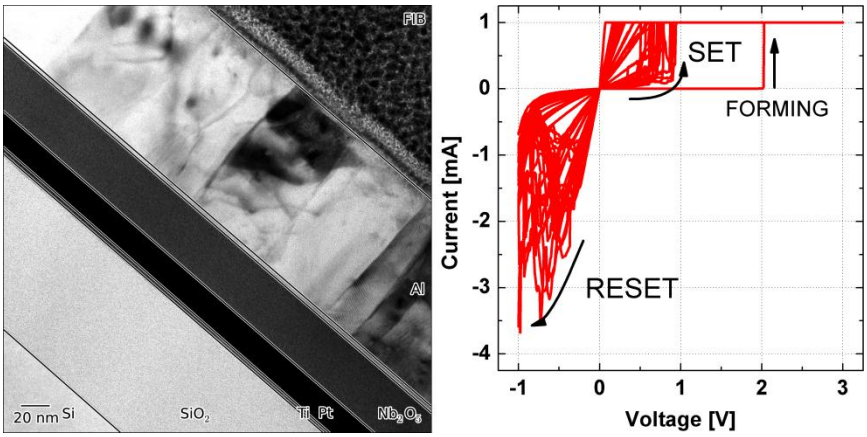

Figure 1. Bright field TEM micrograph of a Nb_2O_5 sample with Al top electrode (left). Current voltage characteristic of a similar stack design shows successful resistive switching (right).

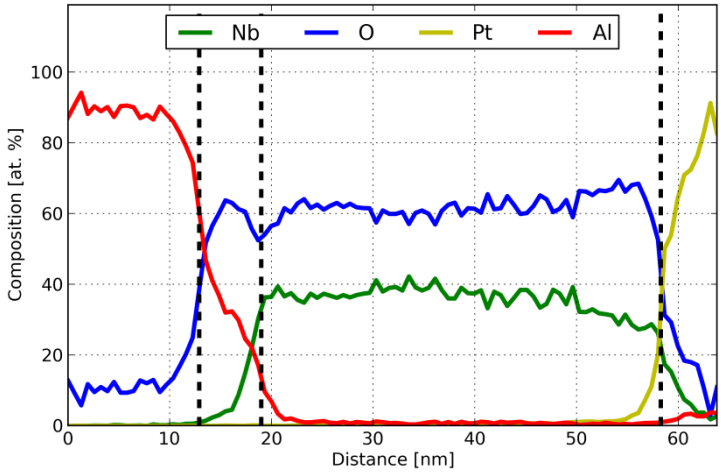

Figure 2. Development of the elementary composition across the MIM stack with Al top electrode obtained by EDS showing on one hand the aluminum oxide at the Nb_2O_5|Al interface and on the other hand the oxygen depletion in the Nb_2O_5 layer starting at this interface.

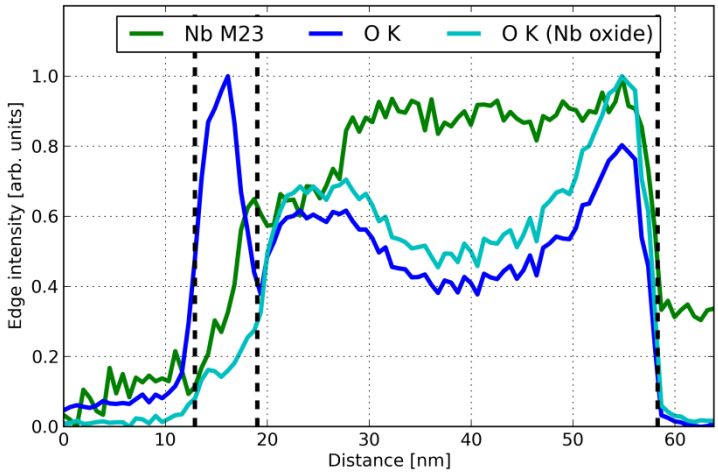

Figure 3. EELS line scan recorded parallel to EDS focusing on the Nb $M_{2,3}$ and the O K edges. Due to differences in edge shape as well as onset aluminum and niobium oxide are plotted separately. The total O K signal including both oxides shows a maximum value corresponding to the aluminum oxide whereas the O K intensity of niobium oxide drops within the Al oxide. Nb and O signal exhibit a similar value next to the Nb_2O_5|Al interface whereas away from this interface the Nb is constant while O content changes across the layer

Spectroscopy in STEM/TEM

IM.4.P091
Detection and quantitative measurement of the number of Yb-dopants in a YAG crystal at the atomic level by high resolution STEM-EELS

T. Epicier[1], M. Bugnet[2], G. Botton[2]

[1]INSA-CNRS, MATEIS, umr CNRS 5510, Vulleurbanne, France
[2]McMaster University, CCEM & Department of Materials Science and Engineering, Hamilton, Canada

thierry.epicier@insa-lyon.fr
Keywords: YAG, Yb dopant, optical ceramic, HAADF, atomic STEM-EELS

Studying quantitatively the bulk distribution of dopants within materials by means of atomically-resolved STEM-HAADF imaging has become possible and efficient using modern microscopes. Because the STEM detector collects incoherent electrons scattered at large angles, the ADF intensity varies as Z^{α} [1], where Z is the atomic number of the probed atom and $\alpha \approx 1.6\text{-}2$. ADF-STEM is then in its principle, and since its origin, suitable to the detection of heavy atoms on a substrate [2], or later on, of dopants embedded in a matrix (for example Sb atoms in silicon [3]). More recently, aberration corrected microscopes were used to identify single dopants and/or impurities in various materials (oxide materials, semi-conductors, ceramic interfaces or catalysts), where the added specie generally substitutes to one specific site, leading, in projection, to one specific type of atomic columns concerned by the doping (see for instance references cited in [4]). However, adding direct chemical information obtained with a spectroscopic method, such as EELS (Electron Energy-Loss Spectroscopy) may bring an unambiguous confirmation that HAADF intensity variations attributed to dopants are not artefact, or produced by any other unexpected impurity. A combined STEM-EELS study of dopants is then possible, as was demonstrated in the case of oxide materials |5].

Good candidates for such studies are luminescent garnet-based structures, such as RE-doped YAG, where RE designates a rare earth element, and YAG, the Yttrium-Aluminium-Garnet $Y_3Al_5O_{12}$, a cubic phase with space group Ia-3d [6] and a = 1.20062 nm. In these compounds, two different sites and types of atomic columns in the <100> projection are concerned by RE^{3+} dopants, see figure 1. We focus here on Yb^{3+}-doped YAG polycrystalline ceramics. This system has great potentialities for replacing single crystals for optical applications, such as in lasers and scintillators. It is then important to check that the dopant distribution is homogeneous, since any kind of heterogeneity (second phases, grain-boundary segregation, clustering) drastically affects the optical properties (e.g. see [7]). Previous HAADF obtained with an uncorrected FEI-TITAN, 300 kV microscope images of Yb^{3+} doped YAG crystals were already reported [8]. We present here the STEM-EELS study of a 1.4 Yb^{3+} at. % doped YAG sample (substitution ratio [Yb]/[Y] = 10 %; details on the elaboration, optical and microstructural characterization can be found in [7]). Results were produced at 200 kV on a double-corrected FEI TITAN-cubed equipped with a Gatan 866 spectrometer. Figure 1 shows that the distribution of Yb^{3+} ions can be revealed in STEM-HAADF micrographs, owing to the contrast enhancement caused by the difference in atomic weights (Z_{Yb} = 70 and Z_Y = 39).STEM-EELS analysis was performed on slightly thicker areas compared to figure 1, because of very rapid irradiation effects in thin regions. Results (such as shown in figure 2) will be discussed quantitatively in terms of statistics (including prediction from the binomial law and thickness estimation), EELS quantification and measurement of the HAADF intensity of atomic columns [9].

1. E.J. Kirkland, R.F. Loane, J. Silcox, *Ultramicroscopy*, 23, (1987), 77.
2. A.V. Crewe, J. Wall, J. Langmore, *Science*, 168,(1970), 1338.
3. P.M. Voyles, D.A. Muller, J.L. Grazul, P.H. Citrin, H.J.L. Gossman, *Nature London* 416, (2002), 826.
4. A. Mittal and K.A. Mkhoyan, *Ultramicroscopy*, 111, 8, (2011), 1101.
5. M. Varela, S.D. Findlay, A.R. Lupini, H.M. Christen, A.Y. Borisevich, N. Dellby, O.L. Krivanek, P.D. Nellist, M.P. Oxley, L.J. Allen, S.J. Pennycook, *Phys. Rev. Letters*, 92, 9, (2004), 095502.
6. A. Nakatsuka, A. Yoshiasa, and T. Yamanaka, *Acta Cryst. B*, 55, (1999), 266.
7. L. Esposito, T. Epicier, M. Serantoni, A. Piancastelli, D. Alderighi, A. Pirri, G. Toci, M. Vannini, S. Anghel, G. Boulon, *J. Eur. Cer. Soc.,* 32 (2012), 2273.
8. T. Epicier, T.J. Konno, K. Sato, G. Boulon, p.127 in Proceed. EMC2012 (15th Electron Microscopy Congress), vol.1, ed. D.J. Stokes, M. Rainforth, RMS, (2012).
9. We thank N. Gauquelin (CCEM, McMaster Univ., Hamilton - Canada), K. Sato and T.J. Konno (IMR, Tohoku Univ., Sendai - Japan) and G. Boulon (ILM, University Lyon I – France) for fruitful discussions.

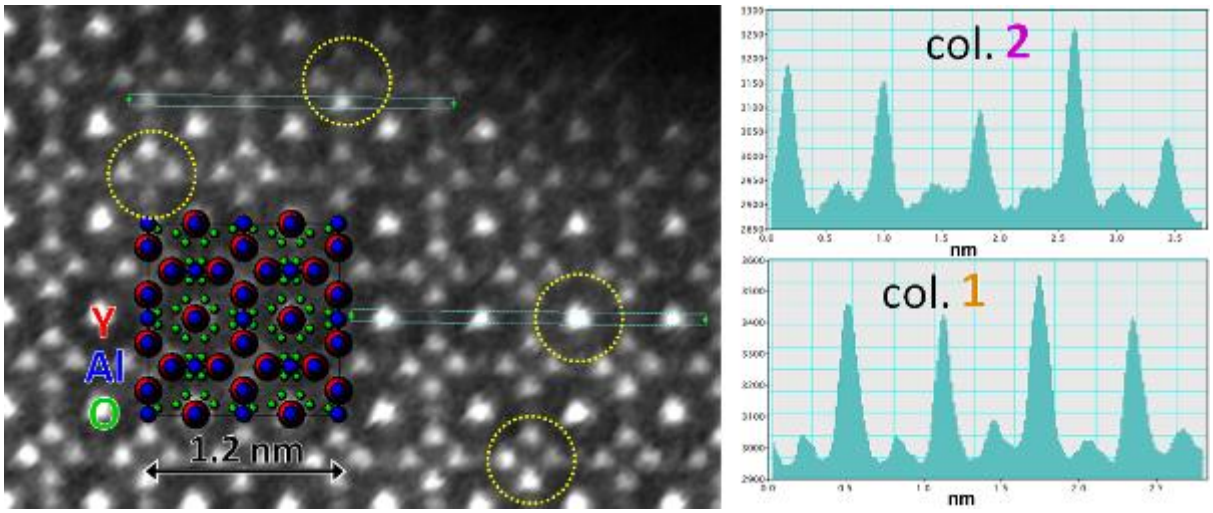

Figure 1. [001] HAADF image of a Yb-doped YAG crystal: note intensity reinforcements (circles) at two types of atomic positions (labelled 'col. 1' and 'col. 2' respectively – col. 1 has twice the atomic density of col. 2, and thus leads to brigther dots –) where Yb is known to substitute to Y. The projection of the cubic cell is shown (Al atoms in blue, Y in red, O in green).

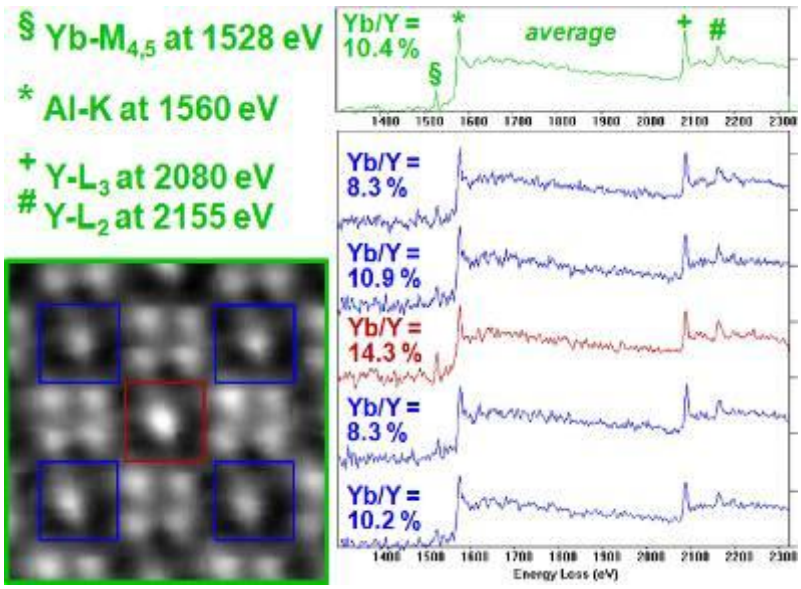

Figure 2. 2x2 nm STEM image during SI acquisition (16x16 pixels with 0.2 s/pixel) and corresponding EELS spectra showing an evident correlation between the 'column 1' HAADF intensity and the Yb content, maximal at the central column (red frame).

Spectroscopy in STEM/TEM

IM.4.P092
Microstructure instability of the $Ba_{0.5}Sr_{0.5}Co_{0.8}Fe_{0.2}O_{3-\delta}$ dense ceramic membranes.

B. Rutkowski[1], J. Malzbender[2], T. Beck[2], A. Czyrska-Filemonowicz[1]

[1]AGH University of Science and Technology, International Centre of Electron Microscopy for Materials Science and Faculty of Metals Engineering and Industrial Computer Science, Al. A. Mickiewicza 30, 30-059 Krakow, Poland, Poland
[2]Forschungszentrum Jülich GmbH, IEK-2, 52425 Jülich, Germany, Germany

rutkowsk@agh.edu.pl
Keywords: BSCF 5582, dense ceramic membranes, oxygen separation, OTM

Electricity demand in highly developed countries is continuously increasing. Fossil fuel power plants are still the major sources of the energy, however they are considered as the main contributors to the global warming due to high amount of CO_2 released to the atmosphere. In order to avoid the CO_2 pollution, an OXYFUEL process can be exploited, in which an advantage of fuel combustion in oxygen atmosphere is utilized. Due to lack of nitrogen, CO_2 content in the flue gas is increased, which significantly assist carbon capture and storage process (CCS), avoiding the CO_2 emission to the atmosphere. Oxygen can be extracted from air with air separation units (ASU), based on the perovskite-structured $Ba_{0.5}Sr_{0.5}Co_{0.8}Fe_{0.2}O_{3-\delta}$ (BSCF 5582) dense ceramic membranes characterized by high level of oxygen permeation [1]. However, operating temperature of this material should be higher than 850 ℃. Below this temperature, a significant degradation of oxygen permeation with operation time was noticed [2], originating in the microstructural instability of the BSCF 5582 material [3].

In order to investigate the instability of the BSCF 5582 membranes, some of the as-received specimens, developed by Fraunhofer Institute for Ceramic Technologies and Systems, IKTS in Hermsdorf, Germany, were annealed in air for two weeks at the temperatures from the range of 750-950 ℃ (with 50 ℃ intervals) and further investigated by light (LM), scanning (SEM) and transmission electron microscopy (TEM). In order to perform LM and SEM investigations, annealed specimens were ceramographically prepared. Analytical TEM analyses of focused ion beam (FIB) lamellas were performed using a probe Cs-corrected Titan^3 G2 60-300 equipped with a ChemiSTEM system and a Tecnai G20 TWIN microscopes of the FEI.

Microstructures of annealed specimens were compared to the one of the as-received BSCF 5582, containing small amount of the hexagonal phase precipitates (Figure 1), located at the grain boundaries due to slow cooling (2 K/min) from the sintering temperature of 1130 ℃. The annealing temperature had an influence on the microstructure stability of BSCF 5582. The increased amount of hexagonal phase precipitates was observed in the material annealed below 850 ℃, however the highest concentration occurred in the specimen heat treated at 750 ℃ (Figure 2), where three phases were found. The precipitates have different chemical composition than the matrix (Ba/Sr and Co/Fe ratios are changing). Precipitation of the hexagonal phase influences the chemical composition of the matrix. Its changes in comparison to the as-received material explain the fact that material is not optimal anymore to obtain high oxygen fluxes at the temperature range of 750 - 800 ℃. The changes mentioned above are responsible of the permeation drop reported by Shao et al. [2].

1. S. Baumann et al., Journal of Membrane Science 377 (2011), p. 198.
2. Z. Shao et al., Journal of Membrane Science 172 (2000), p. 177.
3. C. Niedrig et al., Solid State Ionics 197 (2011), p. 25.
4. This work was supported by the Initiative and Networking Fund of the Helmholtz Association, contract HA-104 (“MEM-BRAIN”). The authors thank Dr R. Kriegel, IKTS for providing the BSCF specimens. The support from the AGH-UST statutory project (nr 11.11.110.148) to microstructure investigation is kindly acknowledged.

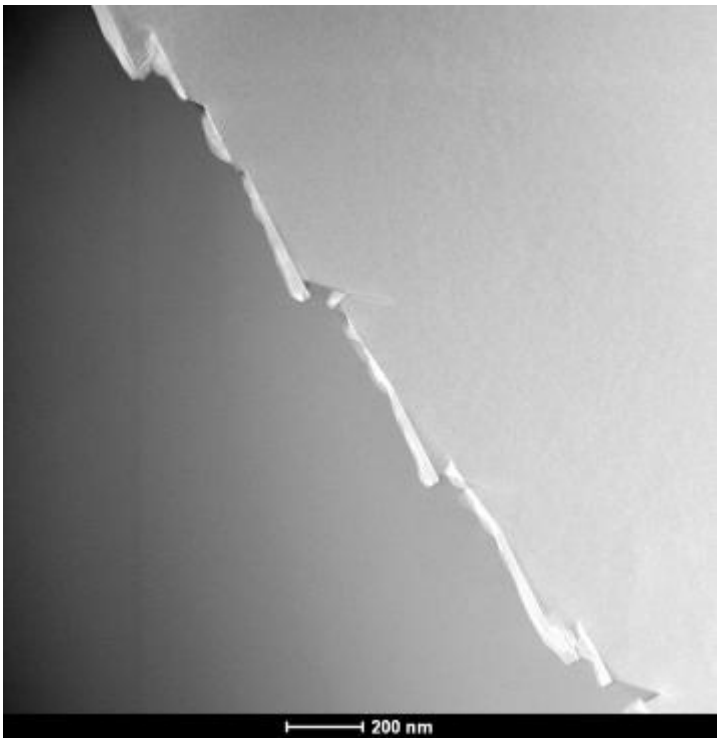

Figure 4. STEM-HAADF image of the BSCF 5582's microstructure in as-received (the hexagonal phase precipitates are visible at the grain boundary).

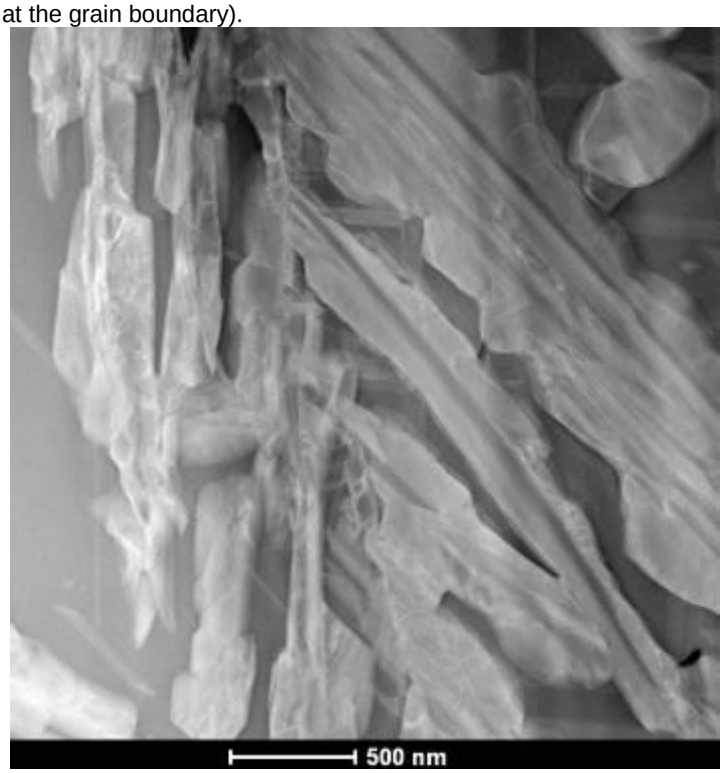

Figure 5. STEM-HAADF image of the BSCF 5582's microstructure after annealing in air for 336h at 750 °C.

Spectroscopy in STEM/TEM

IM.4.P093
Towards mapping atomic orbitals in the TEM

S. Löffler[1], V. Motsch[2], W. Hetaba[1,3], R. Hambach[4], G. Biddau[5], L. Pardini[5], C. Draxl[5], U. Kaiser[4]
P. Schattschneider[1,2]

[1]Vienna University of Technology, USTEM, Wien, Austria
[2]Vienna University of Technology, Institute of Solid State Physics, Vienna, Austria
[3]Bielefeld University, Thin Films and Physics of Nanostructures, Bielefeld, Austria
[4]University of Ulm, Central Facility for Electron Microscopy, Ulm, Germany
[5]Humboldt University Berlin, Department of Physics, Berlin, Germany

stefan.loeffler@tuwien.ac.at
Keywords: EFTEM, orbitals, MDFF

Directly imaging orbitals is possible using a scanning tunneling microscope (STM) [1]. However, this is an intrinsically surface-sensitive technique. As such, it is used mainly for investigating adsorbents or surfaces but cannot be used for studying, e.g., defects in the bulk, grain boundaries, interfaces, etc.

In this work, we propose a way to visualize atomic orbitals — or rather the transition probabilities between an occupied and an unoccupied (antibonding) state — by means of transmission electron microscopy (TEM), electron energy loss spectrometry (EELS), and particularly energy-filtered TEM (EFTEM). With modern TEMs, chemical analyses using EFTEM can readily achieve atomic resolution [2]. Thus, the logical next step is to investigate the possibilities of boosting the resolution to sub-atomic distances in last-generation aberration corrected instruments.

To that end, we performed simulations of EFTEM images, including both elastic and inelastic scattering effects. The central quantity for these simulations is the mixed dynamic form factor (MDFF)[3-4]. It can be used to describe inelastic scattering in a density matrix formalism, which has the advantage of not only modeling single wave functions, but also the correlations between different states and the entanglement between probe and target states.

To simplify the MDFF, we show how it can be interpreted as a quadratic form, regardless of the transition orders investigated. Consequently, the whole theory of quadratic forms can be applied to the MDFF. In particular, a principal axis transformation can be used to diagonalize it. This corresponds to a description in a symmetry-adapted basis which is chosen such that all correlation effects between different states vanish. This facilitates the numerical simulations, but also greatly helps in the physical interpretation of both the underlying physics and the resulting images. Figure. 1 shows an example of transitions that are correlated in a spherical harmonics basis, but clearly show p character in the symmetry-adapted new basis system.

The theoretical framework of diagonalizing the MDFF is applied to a number of systems. Examples include energy-loss magnetic chiral dichroism (EMCD) or the imaging of defects in graphene. Of particular interest is rutile TiO_2 which exhibits a tetragonal distortion giving rise to an e_g–t_{2g} splitting. These are perfect conditions to image transitions between orbitals. Figure. 2 shows a simulated EFTEM image under typical illumination conditions for two different energies. The two images show a 90° rotation consistent with the excitation of p_x and p_y type transitions expected in those energy regions.

Another interesting application is the mapping of asymmetries due to the presence of defects in the crystal structure. As an example, we calculated the electronic properties for graphene with two vacancies and then simulated an EFTEM map of the C K-edge. As expected, we find that the effect of the vacancy is to induce an asymmetry in the p_y orbital of the nearest neigbour carbon atoms, leaving those atoms in an environment similar to pure graphene essentially unaffected.

From these simulations, it is clear that mapping transitions between orbitals can be achieved in the near future. This will give rise to many exciting new possibilities, including the direct imaging of the electronic properties of grain boundaries, defects, or interfaces.

1. J. Repp, G. Meyer, et al., PRL 94 (2005), p. 026803.
2. R. F. Egerton, Rep Prog Phys 72 (2009), p. 016502.
3. H. Kohl and H. Rose, Adv El El Phys 65 (1985), p. 173.
4. S. Löffler, V. Motsch and P. Schattschneider, submitted to Ultramicroscopy.
5. The authors acknowledge financial support by the Austria Science Fund (FWF) under grant number I543-N20.

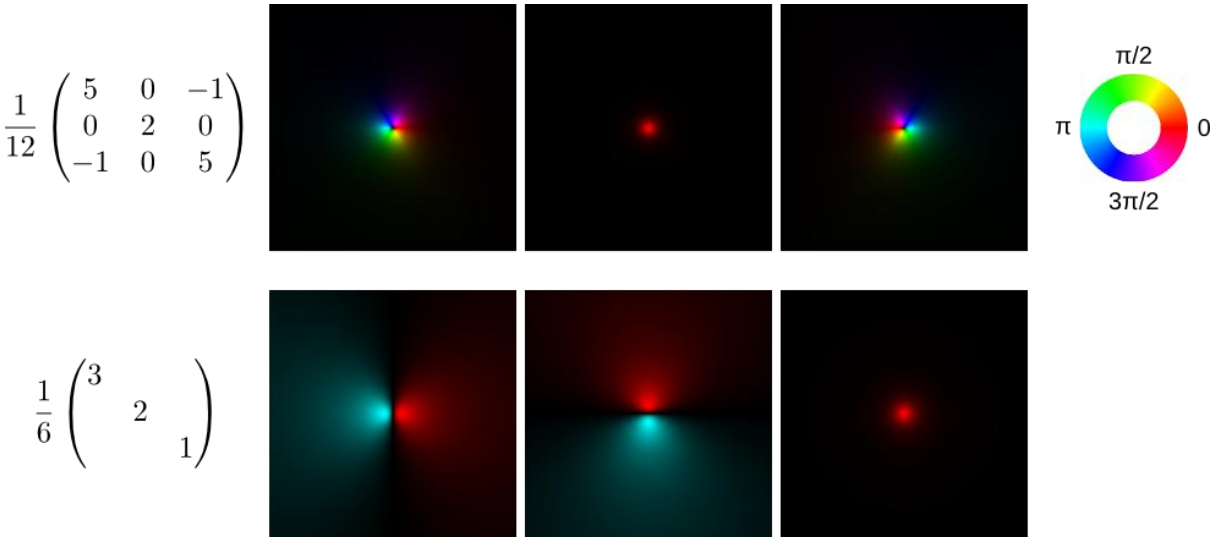

Figure 1. Example of dipole-allowed transitions that are correlated in a spherical harmonics basis (top), but become independent in the symmetry-adapted new basis (bottom). The matrices show the relevant subset of the MDFF matrix while the images show the real space wavefunctions of the basis states. The amplitude is given by the brightness, while the phase is color-coded according to the color wheel on the right.

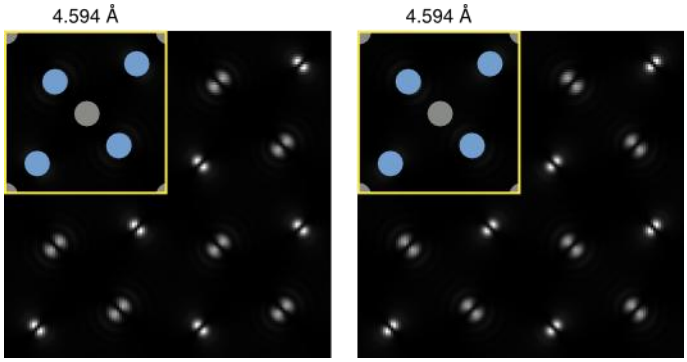

Figure 2. Simulated high-resolution EFTEM images for the O K-edge in a one unitcell thick rutile sample oriented along the [001] zone axis under ideal imaging conditions. The left image shows the situation 4 eV above the edge onset, the right image shows the situation 7 eV above the edge onset. The inset shows the projected unit cell with oxygen atoms in blue and titanium atoms in gray.

Spectroscopy in STEM/TEM

IM.4.P094
Site-specific ionisation edge fine-structure in the electron microscope

W. Hetaba[1,2], M.-G. Willinger[3], M.E. Schuster[3], S. Löffler[1], R. Schlögl[3], P. Schattschneider[1,4]

[1]Vienna University of Technology, USTEM, Wien, Austria
[2]Bielefeld University, Department of Physics, Bielefeld, Austria
[3]Fritz-Haber Institut der Max-Planck-Gesellschaft, Anorganische Chemie, Berlin, Germany
[4]Vienna University of Technology, Institute of Solid State Physics, Wien, Austria

walid.hetaba@tuwien.ac.at
Keywords: EELS, channelling, ELCE

Channelling for site-selective X-ray analysis was first implemented in 1982 by Spence and Taftø [1]. As a versatile method for chemical analysis, it was rapidly extended to electron energy loss spectrometry (EELS) in the transmission electron microscope (TEM). This technique was called energy loss by channelled electrons (ELCE) [2]. The local chemistry and electronic structure of particular crystallographic sites can be determined by this method. It was, however, rarely used because of instrumental and theoretical shortcomings. For ELCE, not only the incoming but also the outgoing electron wave as well as elastic and inelastic scattering processes have to be considered. As the spectrometer is usually placed off axis, long acquisition times are necessary. Therefore, stability and a high beam intensity are crucial. Only because of recent advances in both numerical simulations and instrumentation, the situation has improved dramatically.

In this work, we present recent results of our measurements and calculations for rutile (TiO_2). The combination of two simulation software packages for treating the elastic and the inelastic scattering is applied. The first package [3] is based on the Bloch wave formalism for treating the elastic scattering, while it uses the mixed dynamic form factor (MDFF) [4] for the description of the inelastic scattering of the fast probe electrons. The second simulation package [5] is used to calculate the cross-density of states and wave functions by means of density functional theory. The obtained data is then used for the calculation of the MDFF mentioned above. The energy loss near edge structure (ELNES) under ELCE conditions depends sensitively on the sample thickness, the specimen tilt [3] and the direction of the momentum transfer vector. Thus, detailed simulations are needed to interpret the experimental spectra.

Figure 1. (left) shows the calculated partial density of states (DOS) of p-character for oxygen, whose superposition gives rise to the fine-structure in the energy loss spectrum. In Figure 1. (right) the unit cell of rutile is shown. The arrows denote the directions of the different p_x-, p_y- and p_z-orbitals. The experimental work was performed on an FEI TECNAI G2 TF20 TEM, operated at 200 kV primary acceleration voltage and an FEI TITAN TEM operated at 300 kV. The acquired O K-edge ELNES at different channelling conditions is shown in Figure 2. (left). Figure 2. (right) depicts the calculated O K-edge ELNES under the same channelling conditions. It is obvious that the experimentally obtained spectra are in excellent agreement with theoretical predictions.

Owing to powerful instrumentation and simulation software, ELCE is transforming from a rather exotic application to a promising method for orbital mapping and site-specific chemistry in crystallography.

1. J. Taftø and J.C.H. Spence, Science 218 (1982), p. 49.
2. O.L. Krivanek et al., Ultramicroscopy 9 (1982), p. 249.
3. S. Löffler and P. Schattschneider, Ultramicroscopy 110 (2010), p. 831.
4. H. Kohl and H. Rose, Advances in Electronics and Electron Physics 65 (1985), p. 173.
5. P. Blaha et al., “WIEN2k, an augmented plane wave + local orbitals program for calculating crystal properties”, TU Wien, Austria (2001).
6. The Austrian Science Fund (FWF), grant number I543-N20, is acknowledged.

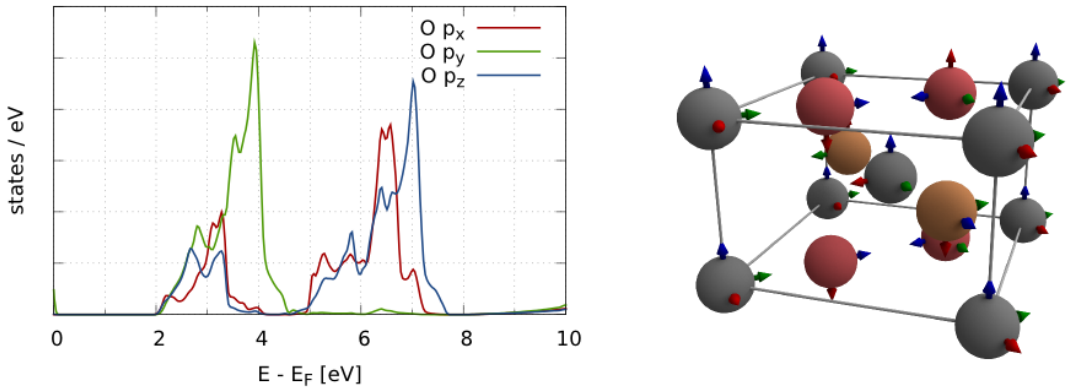

Figure 1. Left: calculated partial DOS of p-character for oxygen. Right: unit cell of rutile (grey: titanium, red/brown: oxygen). The arrows show the directions of the corresponding p_x-, p_y- and p_z-orbitals.

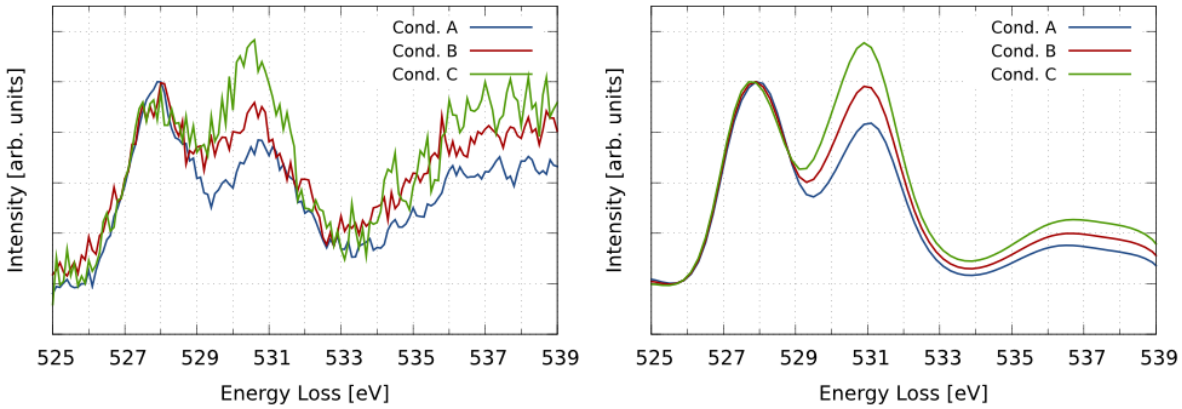

Figure 2. Left: acquired O K-edge ELNES under three different channelling conditions. Right: corresponding calculated spectra. All spectra were normalised to the first peak to facilitate comparison.

Spectroscopy in STEM/TEM

IM.4.P095
Next generation of SDD detectors for ultra-fast, high-resolution EDS in microanalysis

A. Niculae[1], M. Bornschlegl[1], R. Eckhardt[1], J. Herrmann[1], S. Jeschke[1], G. Krenz[2], A. Liebel[2], G. Lutz[2], H. Soltau[1], L. Strüder[2]

[1]PNDetctor GmbH, Munich, Germany
[2]PNSensor GmbH, Munich, Germany

adrian.niculae@pndetector.de

The Silicon Drift Detector (SDD) has become nowadays the standard detector choice for Energy Dispersive X-ray Spectroscopy (EDS) in SEM or TEMs. Recent advances in electron microscopy instrumentation with respect to electron beam brightness and spot size have continuously pushed for higher energy resolution and faster X-ray detectors. SDDs manufactured by PNDetector and PNSensor in Munich with their unique feature of monolithically integrating the first amplifying transistor onto the sensor have established themselves as state-of-the-art detectors for X-ray microanalysis and are distributed worldwide. High-accuracy, ultra-fast elemental analysis requires detectors with extremely low input capacitance, insuring optimum detector operation at very short shaping times. In the recent years a significant development work has been done in this direction at PNDetector by remodeling the geometry of the anode and of the integrated FET with the goal of further reducing all the parasitic capacitances related to the detector anode. This led to a new generation of SDDs – the so-called SDD^{plus} series. The low capacitance anode/ FET can be adopted for all SDD types and sizes (from 5 mm^2 up to 100 mm^2 or multichannel devices). Whereas energy resolution values of down to 126 eV are achieved with the round-shape SDD^{plus} devices (see Fig 1b), when applied to the droplet-shaped SD3 devices, the low capacitance FET drives the energy resolution below 122 eV at shaping times as short as 1 µs (see Fig 1a). With the detector operated at 0.25 µs shaping time (maximum input count rate of 800 kcps) the energy resolution is still below 127eV. Further measurements with SDD^{plus} devices of various sizes will follow. When analyzing thin samples or biological probes with a low photon yield, the measurement time is directly related to the detector collection angle. A very special detector configuration designed for maximum collection angle in SEM or STEM is the annular SDD configuration Rococo2. The detector consists of four kidney-shaped cells with a total active area of 60mm2 arranged around a central hole, therefore allowing the positioning of the detector underneath the pole-shoe in the microscope with the primary electron beam travelling through the detector hole (see Fig 2a). Fig. 2b shows the solid angle coverage of the Rococo2 detector configuration for two different geometries. Representative measurements with a Rococo2 detector system in an SEM will be presented. For applications where boosting the x-ray photon intensity is of primary interest, but no compromises in terms of energy resolution are accepted, multi-channel SDD devices become the first choice. A 7-channel SDD with a total area of 70 mm^2, mounted in a very compact package and capable of dealing with huge count rates up to 7 Mcps will be introduced. Selected measurements with this multi-channel SDD device will be shown.

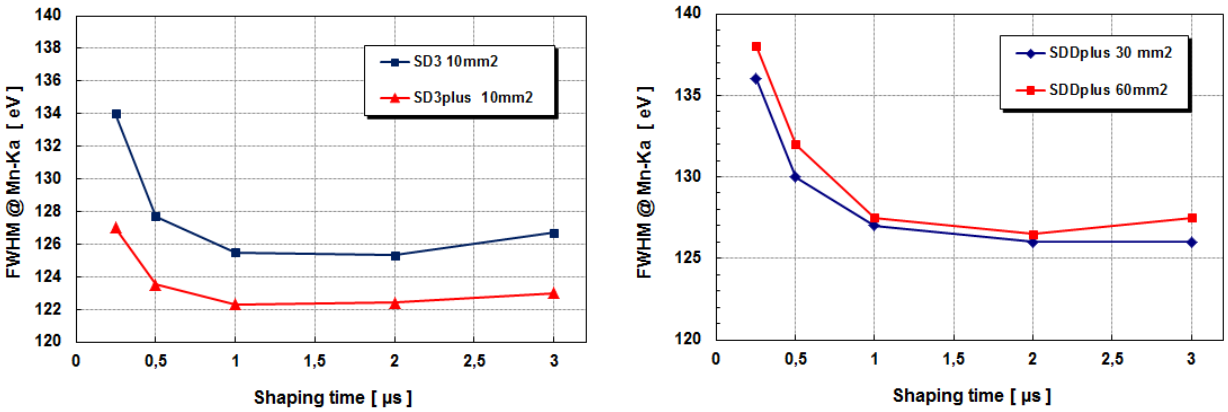

(a) (b)

Figure 1. High-accuracy, ultra-fast elemental analysis requires x-ray detectors with very good energy resolution at short signal processing times: (a) shows spectroscopic results measured with 10 mm^2 SD3^{plus}/SD3 detectors and (b) similar results measured with 30 and 60 mm^2 SDD^{plus} detectors

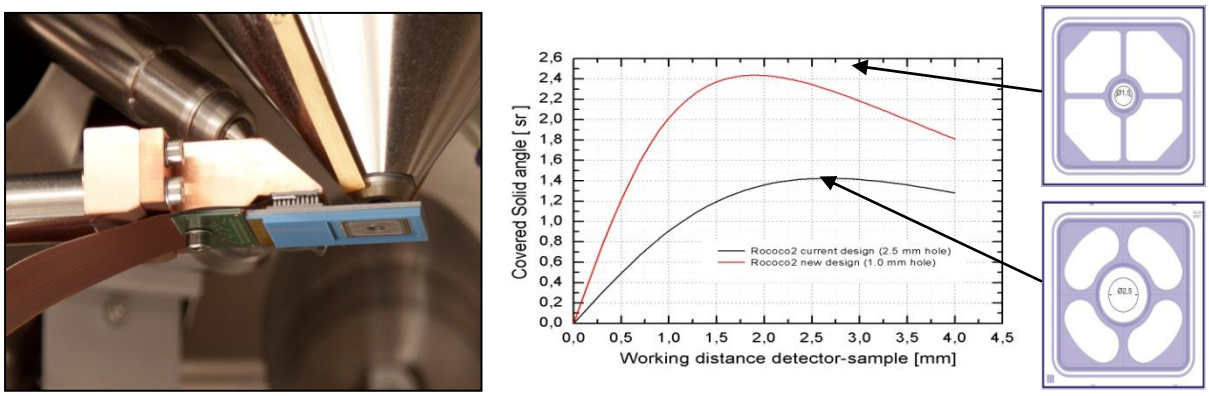

(a) (b)

Figure 2. a) Rocccoc2 detector mounted below the pole-shoe of an SEM; b) Solid angle coverage of the Rococo2 detector as a function of the distance to the sample.

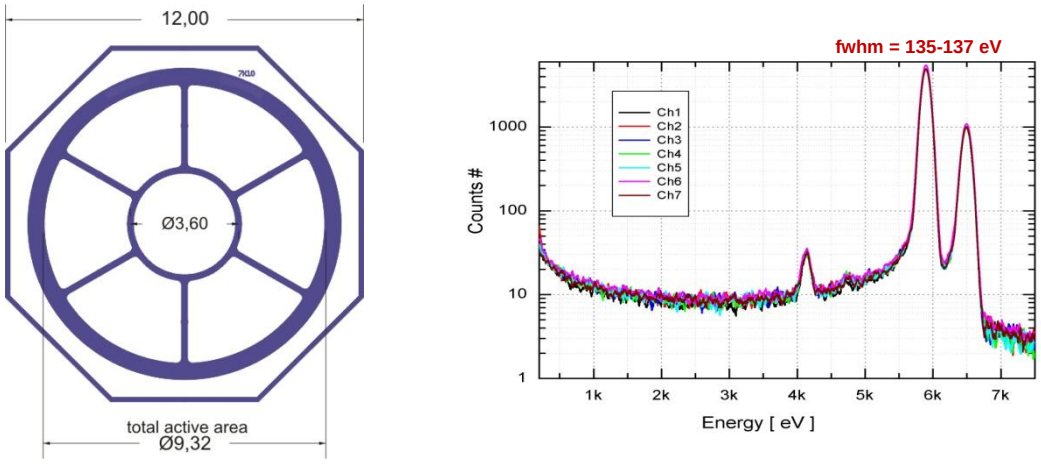

Figure 3. Layout and spectral performance of a 7-channel 7x10 mm^2 SDD capable of total input count rates of 7·10^6 cps. The Fe55 spectra were measured without detector collimator.

Spectroscopy in STEM/TEM

IM.4.P096
Characterization of nanostructured materials by structural and spectroscopic imaging in Cs-corrected TEM/STEM

H. Schmid[1], P. Longo[2], W. Mader[3]

[1]INM - Leibniz-Insitut für Neue Materialien, Saarbrücken, Germany
[2]Gatan Inc., Pleasanton, United States
[3]Universität Bonn, Inst. Anorg. Chemie, Bonn, Germany

herbert.schmid@inm-gmbh.de
Keywords: probe corrected STEM, HAADF, ABF, ESI/SIX, ZnO, inversion domain boundary

Zinc oxide (ZnO) is a highly versatile material used in a multitude of technological applications due to unique combinations of properties, such as piezo-electricity, ferro-magnetism, and wide band gap semiconductivity. These properties can be tailored by doping ZnO with transition metals such as Ti, Mn, Fe, Co, or In, Sn, Ga and Sb. In ZnO crystallizing in the non-centrosymmetric wurtzite structure the formation of characteristic inversion domain boundaries (IDB) is triggered by the addition of trivalent ion species [1]. Analytical Scanning Transmission Electron Microscopy (STEM) is the method of choice for a comprehensive characterization of hetero-structures down to atomic levels. In the present study high-resolution structural and spectroscopic imaging was performed in an advanced TEM/STEM system (JEOL JEM-ARM 200CF) equipped with cold field-emission gun (C-FEG), probe Cs-corrector, X-ray (JED 2300) and electron spectrometer (GATAN GIF Quantum ER) attachments. The present setup provides sub-Å resolution capability in high-angle annular dark-field (HAADF) STEM imaging, whereas bright-field (BF) and particularly annular bright-field (ABF) with increased sensitivity for light elements enable the elucidation of true atomic structures by imaging both cation and anion sites [2,3]. With a probe size of 140 pm, providing a probe current of 320 pA for EELS spectroscopic imaging (ESI) as well as spectroscopic imaging by X-ray (SIX), good counting statistics within reasonable acquisition times were achieved.

The distribution of dopants and evolving domain structures were investigated in a variety of ZnO materials with additions of Fe^{3+}, In^{3+}, Ga^{3+}, Sn^{4+}, and Sb^{5+} transition metal ions. As grown and inverted ZnO domains are separated by two types of inversion domain boundaries: (i) basal b-IDBs on (0001) planes, and (ii) pyramidal p-IDBs parallel to {2□ı□.ı5} lattice planes (tail-to-tail. In HAADF-STEM imaging, utilizing the atomic number sensitive Z contrast, it is clearly revealed that dopants are essentially located within the IDBs as shown for example in Sn doped ZnO nanorods (Fig.1), and in sintered In_2O_3-$(ZnO)_5$ material (Fig.2). The heavier elements such as In and Sn give rise to bright contrasts in comparison with the ZnO matrix. For quantitative assessments of local dopant concentrations both EELS-ESI (electron spectroscopic imaging), and EDS-SIX (spectroscopic imaging by X-ray) were applied in STEM (Figs.1b; 2b). Ex-situ evaluation of acquired data cubes enables detailed evaluations of element maps (Figs.1b; 2b) or line profiling (Figs.1c; 2c,d) in selected regions of interest (ROI).

Under the assumption that metal dopant ions (M) are essentially localized within the IDBs, the ratio of basal cation layers M:Zn (given by the lateral spacings of b-IDBs) can be expected to be proportional to the local dopant concentration. Since the ratio of M:Zn layers within a given ROI can precisely be counted in atomically resolved STEM images (e.g. Fig.2a), corresponding quantitative EDS and/or EELS analyses of these well defined areas containing given numbers of IDBs serve as valuable cross checks on the quantity of dopants contained within the IDBs, as well as local chemical composition and possible solid solution of dopants within the ZnO domains.

In summary, it is concluded that the methods available in advanced analytical TEM/STEM, i.e. high-resolution HAADF-, BF-, ABF-STEM imaging in combination with EELS/ESI and EDS/SIX spectroscopic imaging and quantitative analysis enable a comprehensive characterization of nanostructured materials systems in terms of atomic structure, defect structures, crystallography and chemistry down to atomic scales.

1. Ü. Özgür, Y.I. Alivov, C. Liu et al., Appl. Phys. Rev., J. Appl. Phys. 98 (2005) 041301, 1-103
2. E. Okunishi, H. Sawada and Y. Kondo, Micron 43 (2012) 538-544
3. H. Schmid, E. Okunishi and W. Mader, Ultramicroscopy 127 (2013) 76-84
4. The authors thank E. Arzt for continuous support through INM.

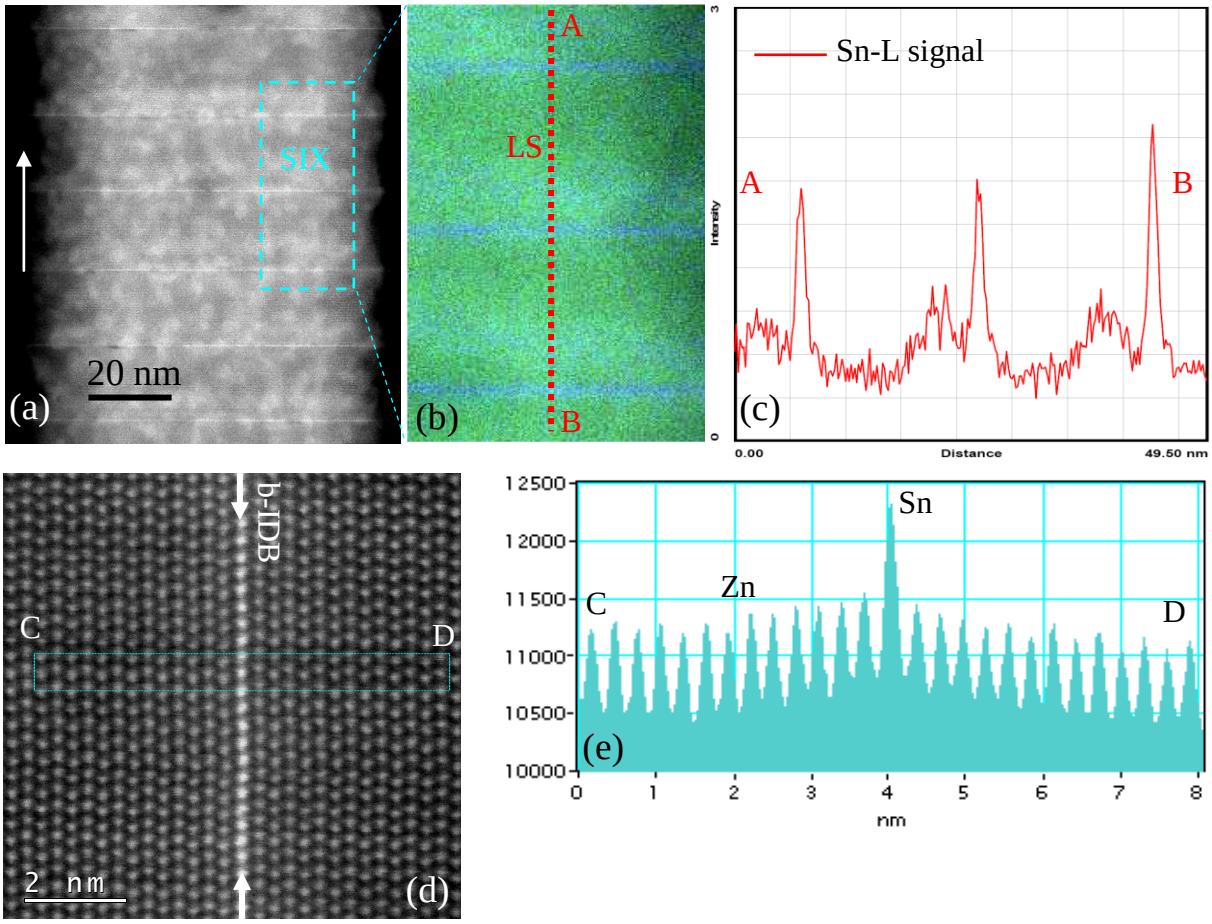

Figure 1.. Inversion domain structure in Sn doped ZnO nanorods:
(a) HAADF-STEM image showing basal inversion domain boundaries (b-IDBs) in edge-on orientation, zone axis [□□□ growth direction (*c* axis) indicated by arrow. (b) X-ray spectrum image (SIX) of boxed area. (c) Line scan (LS) showing Sn-L signal measured along A→B. (d) Atomic resolution HAADF image showing positions of cation columns; Sn ions in b-IDB give rise to bright Z contrast. (e) Profile C→D of HAADF signal across b-IDB (vertically integrated over 50 px).

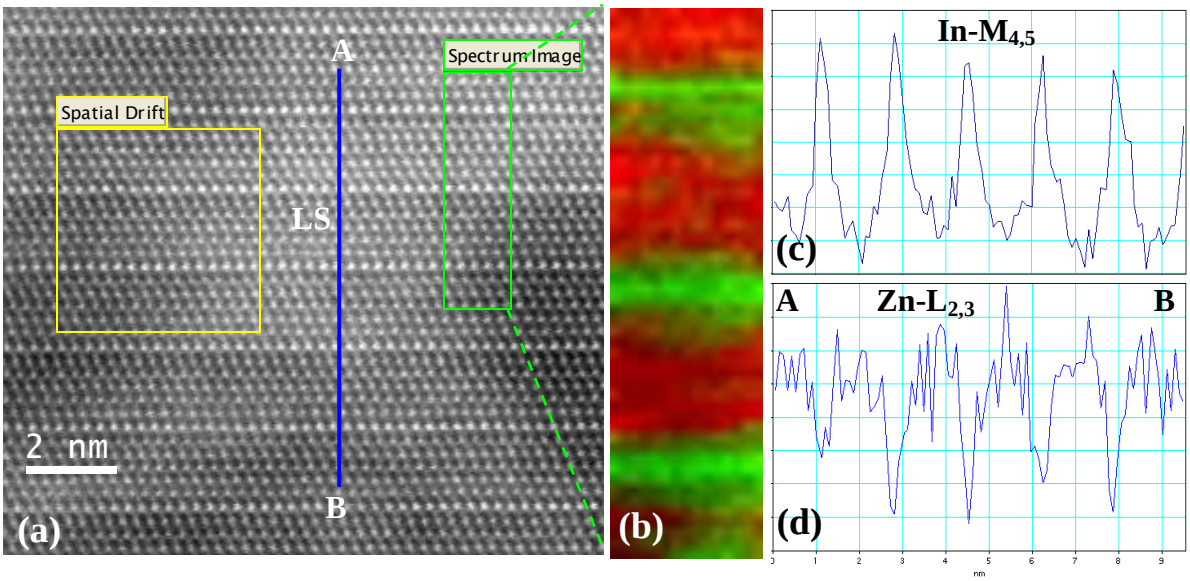

Figure 2. Inversion domain structure in sintered In_2O_3-$(ZnO)_5$: (a) HAADF-STEM image revealing positions of In and Zn columns; (b) EEL spectroscopic image of boxed area (overlay In: green, Zn: red); (c,d) EELS line scan A→B showing In-$M_{4,5}$ and complementary Zn-$L_{2,3}$ signals clearly delineating positions of In and Zn layers.

Spectroscopy in STEM/TEM

IM.4.P097
Plasmon to carbon ratio imaging (PCR): *In situ* determination and imaging of physical properties of organic materials by TEM.

N. Matsko[1], F. Schmidt[2], I. Letofsky-Papst[2], M. Albu[1], A. Rudenko[3], V. Mittal[4]

[1]Graz Centre for Electron Microscopy, Graz, Austria
[2]Institute for Electron Microscopy and Nanoanalysis, Graz University of Technology, Graz, Austria
[3]J. R. Macdonald Laboratory, Department of Physics, Kansas State University, Manhattan, United States
[4]Chemical Engineering Department, the Petroleum Institute, Abu Dhabi, United Arab Emirates

nadejda.matsko@felmi-zfe.at
Keywords: EFTEM, PCR, VEELS.

Measuring material properties such as elasticity, hardness, valence electron density and cohesive energy at the nanoscale is critical to understanding the behavior of nanostructured materials [1]. A novel PCR imaging approach [2] described here represents a powerful asset towards a substantiated structural characterization of multifaceted organic and organic-inorganic materials having complex mechanical properties (interconnected domain organization, local elastic variation etc.), and large range of thickness variations (from 10 to 300 nm). The technique is based on the fact that the bulk plasmon peak (e.g. enrgy-filtered TEM (EFTEM) image from the corresponding energy region) is a sensitive function of the physical properties and thickness of the sample. Although plasmons were initially introduced for simple metals as a consequence of collective inter-electronic Coulomb interaction, they occur in all materials due to the excitation of bonding electrons into the conduction band, where they undergo collective oscillation [3]. Furthermore, Oleshko and Howe [1] have demonstrated that strong scaling correlations exist between the valence electron density, cohesive energy, mechanical properties of materials and volume plasmon energy, Ep. In accordance with the universal binding energy relationship (UBER), the Ep-material property scaling relationships are universal in their applicability to materials with metallic, covalent and partially ionic bonding, and this covers a vast majority of materials. The thickness-related effects, which substantially mask a material contrast in the EFTEM plasmon image, for the carbon-based samples can be adequately removed by normalizing the bulk plasmon image on the carbon elemental map. Normalization by the specimen thickness (t/λ map) which is used in absolute quantification algorithm, in this particular case cannot eliminate thickness (t) variation effects properly because the relative thickness map, in addition to sample thickness variation, also reflects variation in Z (atomic number), and depends on the accuracy of inelastic mean free path (λ) determination [3]. The carbon map reflects mainly the intensity distribution of the signal obtained from the inner shells of carbon atoms within the sample volume, and for thin organic samples can be considered as a more accurate representative of the sample thickness. The resulting PCR image contains enhanced signal from metal atoms which replicates the sample surface and consequently change it hardness/valence electron density (for the metal shadowed/negatively stained organic materials), and from mechanical properties of the sample (for the non modified carbon based systems) [2]. These structural characteristics are in good agreement with the topographical and phase variation obtained by AFM (Figure 1). The ultimate resolution of the PCR method depends on the sample thickness as well as on the energy window position and width (see Figure 2) for the bulk plasmon image, and might be optimized for each particular sample composition. The possibility to obtain both, volume projected and surface-related information in TEM provides a comprehensive description of the sample ultrastructure in terms of bulk morphology and surface characteristics.

1. J. Howe and V. Oleshko V. J. Electron. Microsc. (2004), 53(4), p.339.
2. N. Matsko, I. Letofsky-Papst, M. Albu, V. Mittal. Micros. Microanal. (2013), (doi:10.1017/S1431927613000366)
3. R. Egerton. Electron Energy-loss Spectroscopy in the Electron Microscope, (Springer, New York) (2011).
4. We are very grateful to Ferdinand Hofer for fruitful discussions.

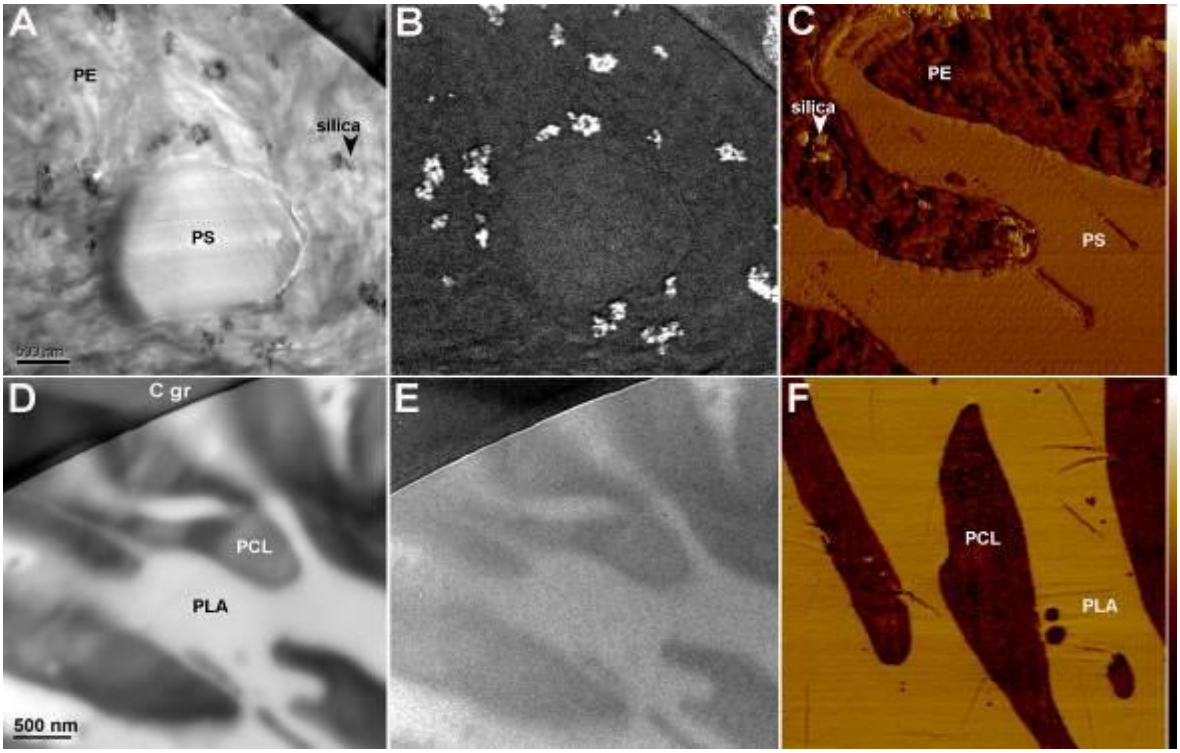

Figure 1. TEM, EFTEM and AFM images of organic(-inorganic) samples. (A, D) elastic filtered TEM images; (B, E) PCR images; (C, F) AFM phase images of the block face of the same samples

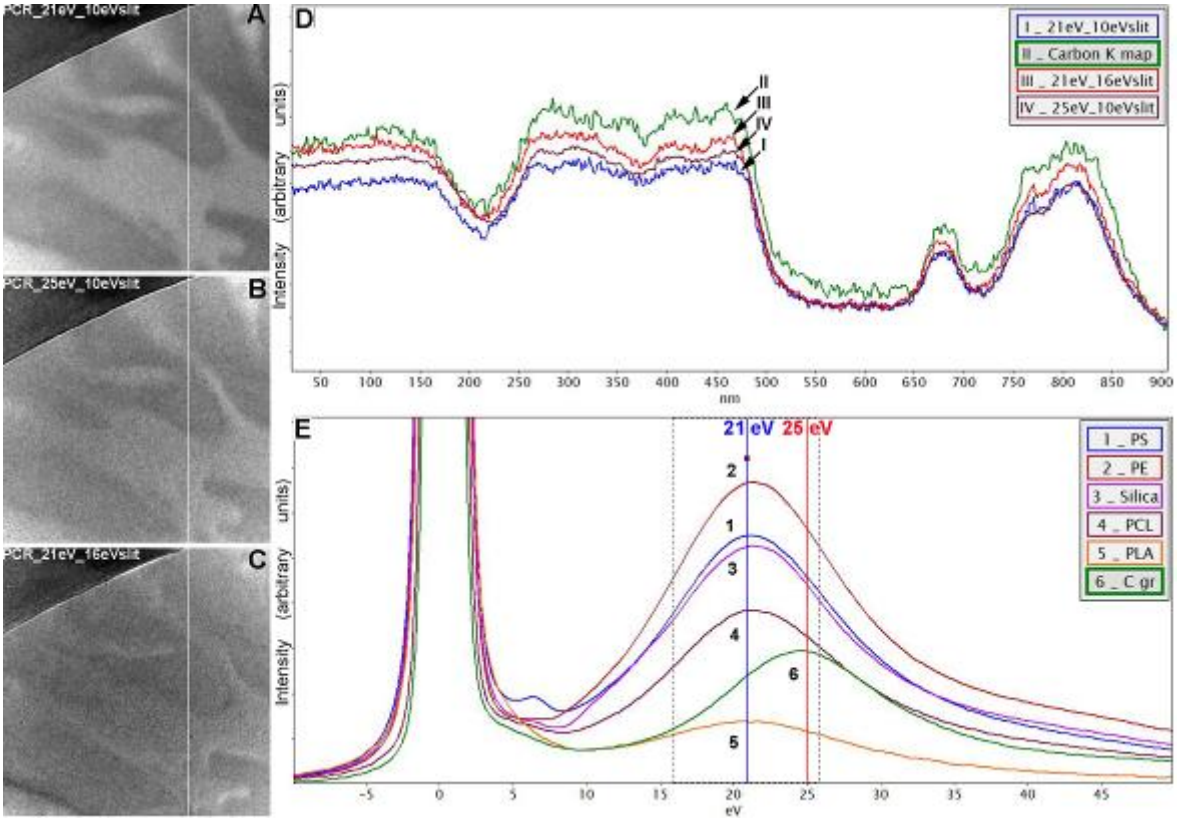

Figure 2. PCR images (A,B,C) which were calculated using different energy window position and width for the bulk plasmon images. (D) Intensity line profiles of corresponding carbon map (II) and bulk plasmon images (I, II, IV), which were used for PCR calculations. The profiles were taken with a 5-pixel integration window across the white lines from the same sample area. (E) EELS spectra of bulk plasmon energy region obtained from the each component of presented organic-inorganic samples. PE - polyethylene, PS - polystyrene, PCL - Poly[oxy(1-oxohexane-1,6-diyl), PLA - Polylactid, C gr - holey carbon grid.

Spectroscopy in STEM/TEM

IM.4.P098
Multivariate Statistical Analysis applied to EFTEM spectrum images of helium bubbles in implanted steel

G. Lucas[1], C. Vieh[1], C. Hébert[1]

[1]EPFL, CIME, Lausanne, Switzerland

guillaume.lucas@epfl.ch
Keywords: Electron Energy Loss Spectroscopy (EELS), Multivariate Statistical Analysis (MSA)

Energy filtered TEM (EFTEM) and electron energy loss spectroscopy (EELS) are useful techniques to investigate the chemistry of materials at the nanometer scale. However long acquisition time and weak signal can be strong limitations. In particular at high-energy losses, the signal-to-noise ratio becomes low. Quantification is somehow a challenging task not only because of possibly noisy data, but also of the nature itself of the signal. Indeed the appearance of fine structures emerging on the edges, the presence of plasmon losses at low energy, multiple scattering in thick specimens, and possible overlapping of edges from different elements, make the deconvolution of signals tedious for accurate quantification.

This work focused on the application of multivariate statistical analysis (MSA) for the improvement of the data in electron energy loss spectroscopy and its analysis. Essentially the usage of principal component analysis and factor analysis will be discussed. Application of MSA for noise removal, elemental mapping and signal extraction will be presented in this work in the particular case of helium bubbles in implanted steels.

Ferritic/martensitic (FM) steels and austenitic steel 316L type (SS316L) are candidate structural materials for a wide range of applications in advanced nuclear fission and fusion facilities such as the first wall blankets of the future fusion reactors, the beam window for the liquid metal spallation target Mega Watt Pilot Experiment (MEGAPIE) and the core structure of the future accelerator driven system (ADS) devices. In the first wall of a fusion reactor, 14 MeV neutrons produce helium at a rate of about 10 appm per dpa (displacement per atom) in steels. In a spallation target, the helium production is even higher, up to about 100 appm per dpa. One of the key issues is to understand the synergistic effects of radiation induced defects and transmutation products, particularly helium (He), on the mechanical properties of these materials. Due to the fact that helium is practically insoluble in structural materials, it has the natural tendency to precipitate and to form bubbles, which may contribute to irradiation hardening and embrittlement effects on structural materials.

In order to understand the behavior and the evolution of the wall material in such reactor, steel samples have been implanted with helium. The helium density and pressure from nanometric bubbles in He-implanted SS 316L steels have been measured using EELS. STEM-EELS spectra and EFTEM spectrum images have been used to extract the 1s to 2p transition peak of helium lying above the iron plasmon by applying deconvolution and MSA techniques.

1. S. Fréchard et al., Journal of Nuclear Materials 393 (2009) p. 102–107.
2 C. A. Walsh et al., Philosophical Magazine A (2000) p. 1507-1543.
3 D. Taverna et al., Physical Review Letters 100 (2008) p. 035301.

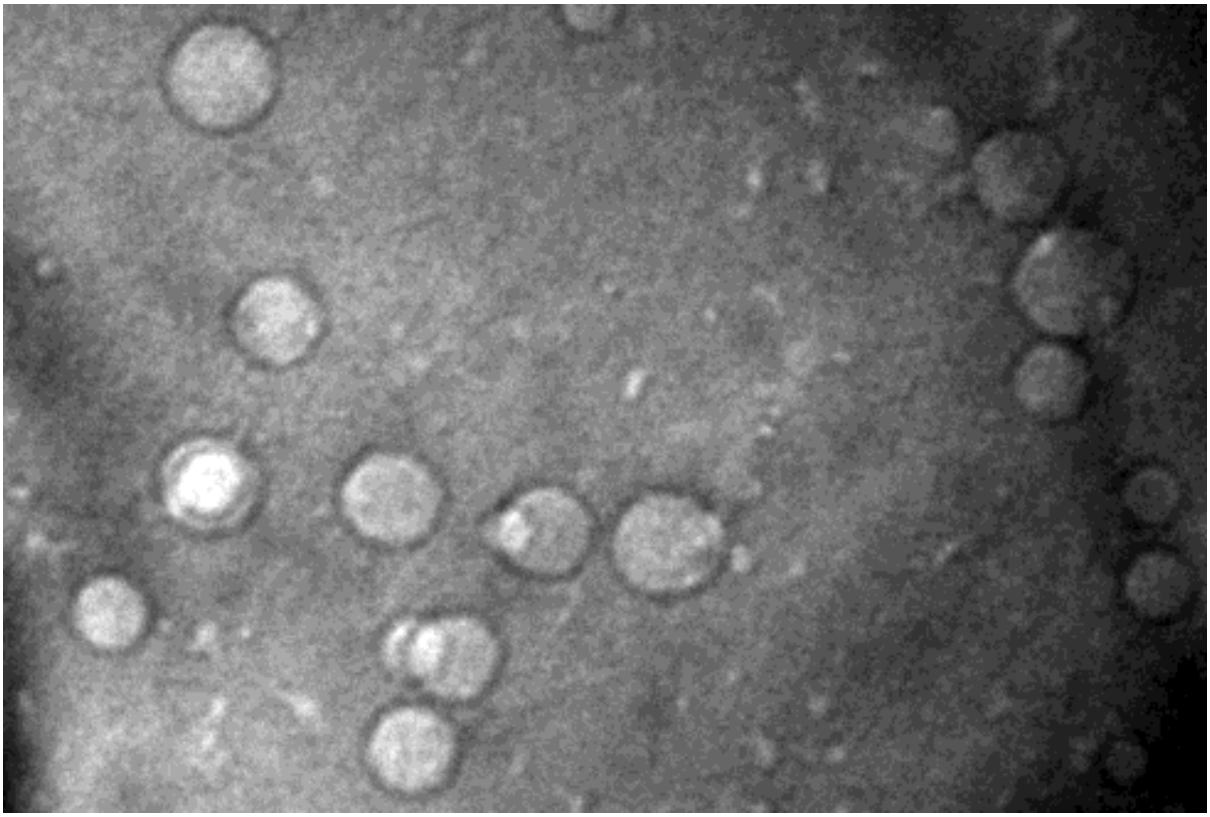

Figure 1. TEM image filtered around the zero-loss peak of typical helium bubbles obtained in implanted bcc iron.

Spectroscopy in STEM/TEM

IM.4.P099
Energy-filtered transmission electron microscopy: a tool to characterize side-wall damage in the low-k inter-metal dielectric

P. Singh[1], S. Zimmermann[1], T. Waechtler[1], S. Schulze[1], S. Schulz[1], M. Hietschold[1]

[1]Technical University Chemnitz, Chemnitz, Germany

pradeep.singh@etit.tu-chemnitz.de

Over last several decades, the characteristic trend of semiconductor industries has been the continuous miniaturization of microelectronic devices following commonly known relationship of Moore's law. As CMOS transistors were scaled, interconnects to link them are also shrunk to reduce the line pitches. The shrinkage in device dimensions to less than 0.25 µm feature size, increases propagation delay, cross-talk noise and power dissipation due to resistance-capacitance (RC) coupling between metal lines on the same level [1]. Insulators with the dielectric constant lower than that of SiO_2 known as low-k dielectrics were introduced to reduce the interconnect parasitic capacitance. Depending on the source gas and plasma conditions used to pattern the dielectric layer for metallization, plasma treatments can modify the surface chemistry (e.g., depletion of carbon), densify the underlying film, and/or roughen the surface. Plasma patterning can degrade low-k dielectrics by depleting methyl groups which increases the effective dielectric constant of a low-k material [2, 3]. In order to understand the modification at sidewalls, energy-filtered transmission electron microscopy (EFTEM) has been used to perform the elemental mapping. The resulting maps suggest damage profiles in Gaussian like shape (Fig. 2 (B)). We made a robust program to handle hundreds of energy-filtered images at a time to characterize the side-wall damage. Carbon and oxygen profiles deduced from the EFTEM mapping suggest that side-wall damage extends around 40 nm in the low-k dielectric layer. Damaged regions are depleted in carbon which increases the density of material and converted it in more SiO_2 like character. The map showing thickness over mean free path in Fig. 2 (D) also indicates a small variation across the low-k layer. Assuming uniform thickness across the low-k layer due to FIB sample preparation technique used, the variation could be explained by the change in mean free path of electrons interacting with the sample. The mean free path seems to be lower towards side-walls as compared to middle of the low-k layer. The oxygen K-edge map shown in Fig. 2 (C) suggests an increase in oxygen concentration towards side-walls as compared with that in middle of the low-k layer. The most probable explanation of increase in oxygen concentration would be the SiO_2 like character formed close to side-walls.

1. S. P. Jeng, M. C. Chang, and R. H. Havemann, "Process integration and manufacturing issues for high performance interconnect", MRS Symp. Proc. Adv. Metallization for Devices and Circuits, (1994), p. 25.
2. M. Chaudhari, J. Du, S. Bahera, S. Manandhar, S. Gaddam and J. Kelber, "Fundamental mechanisms of oxygen plasma-induced damage of ultralow-k organosilicate materials: The role of thermal ^3P atomic oxygen", App. Phy. Letter, 94, (2009), p. 2041021.
3. M. Shimada, Y. Otsuka, T. Harada, A. Tsutsumida, K. Inukai, H. Hashimota and S. Ogawa, "2-Dimensional Distribution of Dielectric Constants in Patterned Low-k Structures by a nm-probe STEM / Valence EELS (V-EELS) Technique", Proceeding of IEEE 2005: Interconnect Technology Conference, (2005), p. 88.

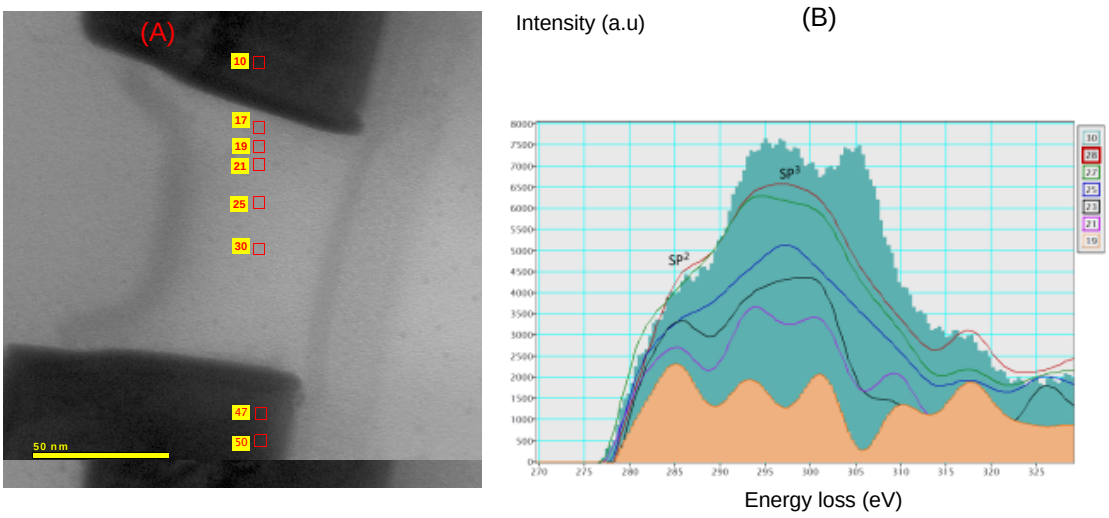

Figure 1.a.) Structure of the sample and **b.)** carbon-1s profile at various positions numbered in the image.

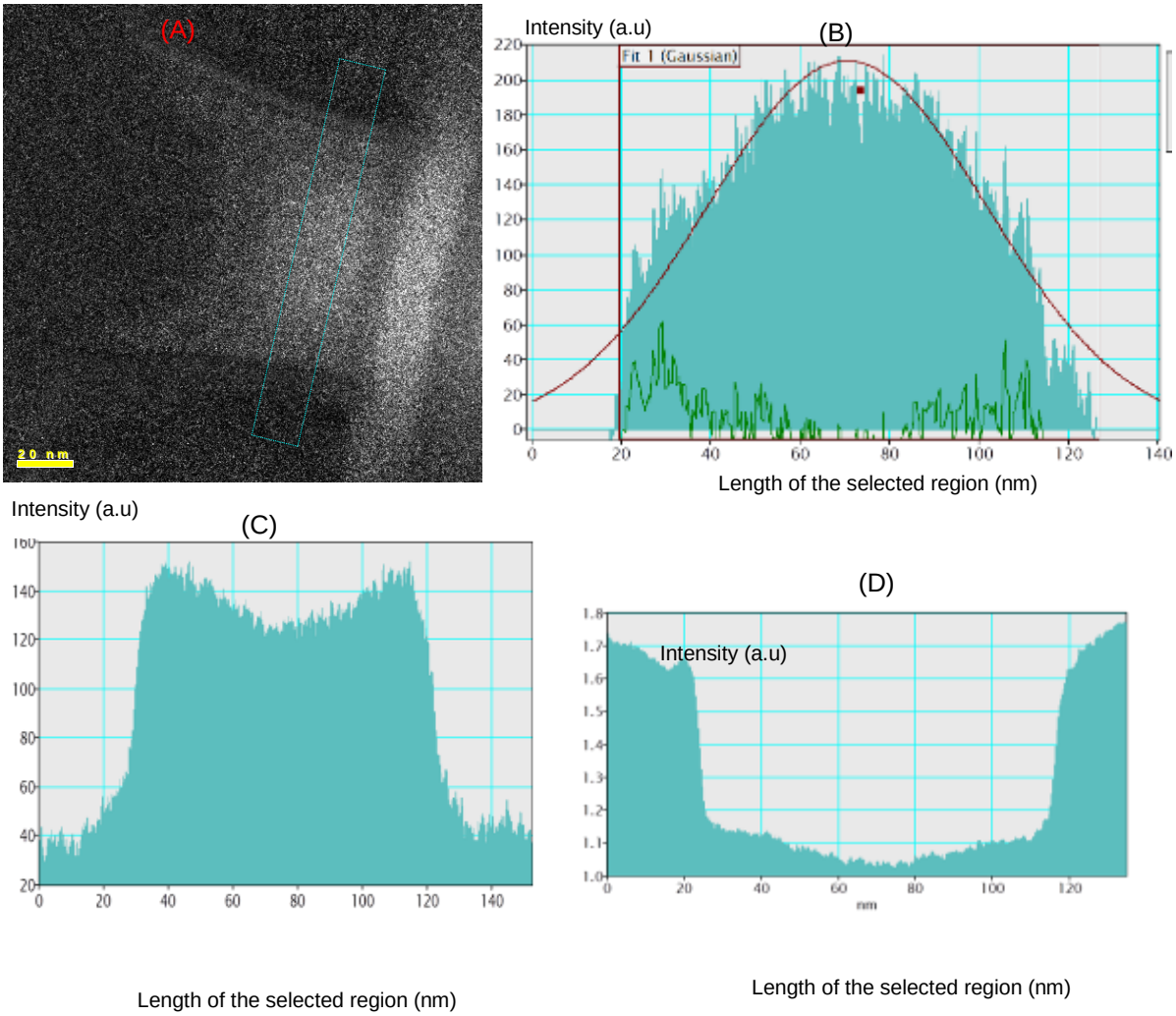

Figure 2. a.) The rectangular block in image used for the mapping **b.)** carbon mapping **c.)** oxygen mapping and **d.)** thickness over mean free path mapping inside the rectangular block.

Spectroscopy in STEM/TEM

IM.4.P100
Influence of inelastic scattering on EFTEM images - exemplified on graphene and silicon at 20kV

Z. Lee[1], H. Rose[1], R. Hambach[1], P. Wachsmuth[1], U. Kaiser[1]

[1]Universität Ulm, Materialwissenschaftliche Elektronenmikroskopie , Ulm, Germany

zhongbo.lee@uni-ulm.de
Keywords: EFTEM, inelastic scattering, mutual coherence, low voltage, zero-loss, plasmon-loss

When the accelerating voltage is decreased to as low as 20kV, all objects are strong scatterers [1]. In this case, the standard calculation and interpretation of TEM images, which are based on elastic scattering theory, is not sufficient anymore and inelastic scattering must be taken into account especially for low-Z objects. In the case of inelastic scattering the incident electron excites the object from the initial state to any allowed state, accompanied by a change of the wave function of the incident electron.

Inelastic scattering is incorporated into the image calculations by means of the Mixed Dynamic Form Factor (MDFF), introduced by Rose [2, 3]. The MDFF accounts for the interference of different scattered partial electron waves. The elastically scattered partial waves can interfere with each other, whereas the partial waves of the inelastically scattered electron can only interfere with each other if they are associated with the same excited object state. The calculation of the MDFF involves the propagation of two coupled waves. Therefore the image calculation involves 4D Fourier transforms, which is too time-consuming. In order to simplify the 4D FT as combinations of 2D Fourier transforms, we have derived an approximation based on independent atom model up to a resolution limit of 1Å. Our approximation is easy to calculate and can be optimized for different imaging conditions.

We calculated EFTEM images for the SALVE II machine, based on the experimental EELS spectra obtained at the SALVE I machine. Based on our calculations at 20kV, even for an one-atom thin structure like graphene, although only less than 1% of the electrons are inelastically scattered, the strong interference of these inelastically scattered waves results in dramatic decrease of the zero-loss filtered image intensity to 72%, compared with pure elastic case. For the thicker structure Silicon<110> (17nm thick), as much as 57% of the electrons are inelastically scattered, however the zero-loss filtered image intensity drops only to 60% compared with the pure elastic case. The examples show that especially for low-Z materials such as carbon-based structures, the interference between the inelastically scattered waves dominates the image intensity. Our two examples show that in general the influence of inelastic scattering cannot be neglected at 20kV. The analysis on the zero-loss and plasmon-loss filtered images shows that the total intensity is conserved.

We may speculate now and further investigate in due course that absorption caused by the interference between inelastically scattered waves is another factor contributing to the Stobbs factor [4] also at higher voltages. We will report further EFTEM experiments for graphene and silicon as soon as the SALVE II microscope is fully operable and functional.

1. Z. Lee, J.C. Meyer, H. Rose and U. Kaiser, Ultramicroscopy 112(2012)39-46.
2. H.Rose, Optik 45(1976)139-158.
3. H.Rose, Ultramicroscopy 15(1984)173-191.
4. A.Howie, Ultramicroscopy 98(2004)73-79.

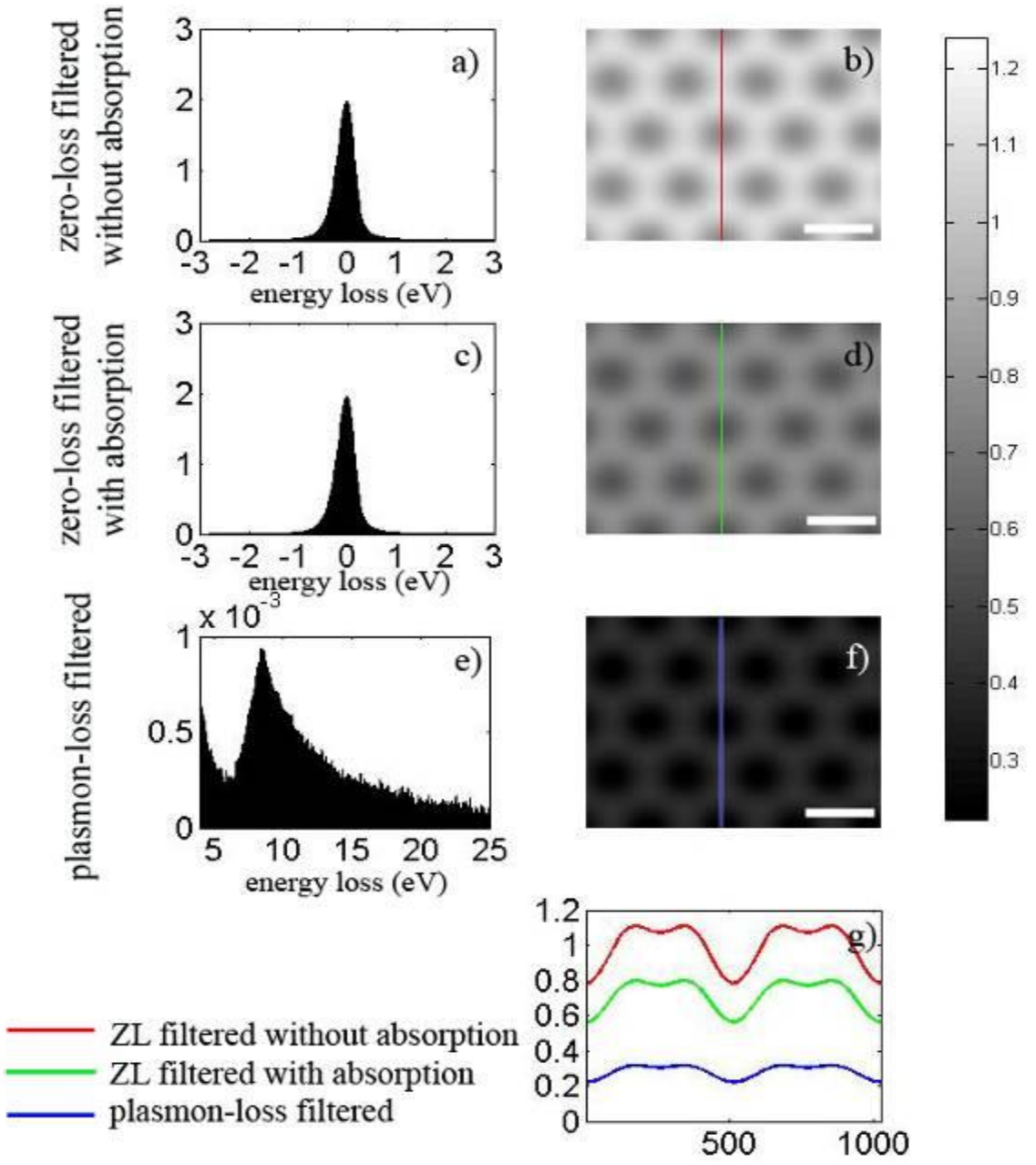

Figure 1. Calculated EFTEM images for graphene at 20kV for the SALVE II microscope (2nd column) based on the experimental EELS spectra (1st column)(Atoms in the images are white). a) The normalized zero-loss peak; b) The zero-loss filtered image without absorption; c) The zero-loss peak extracted from the normalized EELS spectra; d) The zero-loss filtered image with absorption; e) The plasmon peak; f) The plasmon-loss filtered image; g) The line profiles marked in the image b),d) and f). The y-axis shows the intensity and the x-axis shows distance in pixels. Aberration parameters: C_c=0, C_s=-2µm and Δf=42Å. scale bar: 2Å

Spectroscopy in STEM/TEM

IM.4.P101
Characterization of Ancient and Modern Ceramics using EDS with Silicon Drift Detectors on SEM and TEM

T. Salge[1], S. Turan[2], A. Kara[2], H. Yurdakul[3], O. Tunckan[4], L. Klimek[5], D. Pritzel[6], I. Häusler[7], I. Nemeth[1], M. Falke[1]

[1]Bruker Nano GmbH, Berlin, Germany
[2]Anadolu University, Department of Materials Science and Engineering, Eskişehir, Turkey
[3]Dumlupinar University, Department of Materials Science and Engineering, Kutahya, Turkey
[4]Anadolu University, Civil Aviation School, Eskişehir, Turkey
[5]University of Technology, Institute of Materials Engineering, Lodz, Poland
[6]Charité, Universitätsmedizin, Freie Universität, Berlin, Germany
[7]Humboldt Universtät, Institute for Physics, Berlin, Germany

Tobias.Salge@bruker-nano.de
Keywords: EDS, ceramics, SiAlON, hard coatings, dentistry, cultural heritage

Introduction: The element analysis of small structures in ceramic material is relevant for both cultural heritage and advanced technology. The composition of thin electron transparent samples can be analysed in the nm-range using transmission electron microscopes (TEM) or, specific sample holders provided, in the field emission scanning electron microscope (FE-SEM). Nevertheless both methods often require complex sample preparation. An alternative method is to analyse bulk samples with a FE-SEM. In order to decrease the excitation volume for generated X-rays, low accelerating voltages (HV<10) are required. Consequently, only low to intermediate energy X-ray lines can be evaluated and many peak overlaps have to be deconvoluted since the high energy range is not available. Specific examples of both approaches will be discussed for SiAlON ceramic, dental metal-ceramic alloy, titanium based hard coatings on steel and medieval ottoman pottery.

Methods: A BRUKER Quantax EDS system with an XFlash® Silicon Drift Detector was used on a FE-SEM ZEISS Supra 55 VP, a HITACHI SU 6600 and on a JEOL JEM 2200FS STEM. EDS spectra were saved as individual point spectra and in spectrum images. To separate overlapping peaks, an extended atomic database [1] was used. For bulk samples, quantification was carried out using a truly standardless quantification routine without internal references.

Results: (A) Secondary triple junctions at SiAlON ceramic reveal that ytterbium was always found together with aluminium (Figure 1). It documents that EDS can be used to separate the overlapping Yb-M and Al-K lines in addition to other analytical TEM techniques, e.g. EFTEM-3 window and STEM-SI-EELS mapping [2]. The composition of the aluminium-rich triple junction phases effect the high temperature properties of SiAlON materials to be used as cutting tools.

(B) In a dental metal ceramic complex [3], the following elements were detected: O, Zn, Na, Al, Si, W, Y, Zr, Mo, K, Ca, Ba, Ti, Ce, Cr, Fe, Co, Ni. The depletion of chromium in the Cr-Co-alloy toward the opaque layer is associated with the formation of a chromium oxide layer ~0.15-1.5 µm in size (Figure 2). The opaque layer contains different minerals e.g. cerium oxide (Ce_2O_3), zirconium oxide (ZrO_2) and titanite ($CaTiSiO_5$). The controlled crystallisation of alumosilicates has relevance on the mechanical stability.

(C) Five titanium based hard coating samples (see Figure 3 as an example) reveal different compositions (Table 1). It indicates the presence of Ti_2C at sample 1, TiC at sample 5 and three different titanium carbonitride compositions at samples 2-4. The characterisation provides information on the tribological properties e.g. corrosion and diffusion barriers on steels.

(D) Lead glazed Anatolian pottery of the 14th to 15th century contains an interaction zone (Figure 4) between the body and the glaze. The formation of uniaxial potassium lead feldspar $Mg_{0.03}Ca_{0.04}Fe_{0.12}K_{0.35}Na_{0.17}Pb_{0.43}Al_{1.30}Si_{2.56}O_8$ and equiaxial copper ferrites $Cu_{0.46}Al_{0.26}Mg_{0.58}Fe_{1.71}O_4$ is indicated.

The results demonstrate that SDD-based EDS analysis in SEM and TEM contributes essential information on the microstructure of the investigated ceramics which helps to understand their macroscopic behaviour.

1. A. Aßmann and M. Wendt, Spectrochimica Acta Part B 58, p. 711-716.
2. H. Yurdakul and S. Turan, Anadolu University Journal of Science and Technology10-1, p. 67-78.
3. D. Pritzel, PhD thesis. Freie Universität Berlin, p. 118.

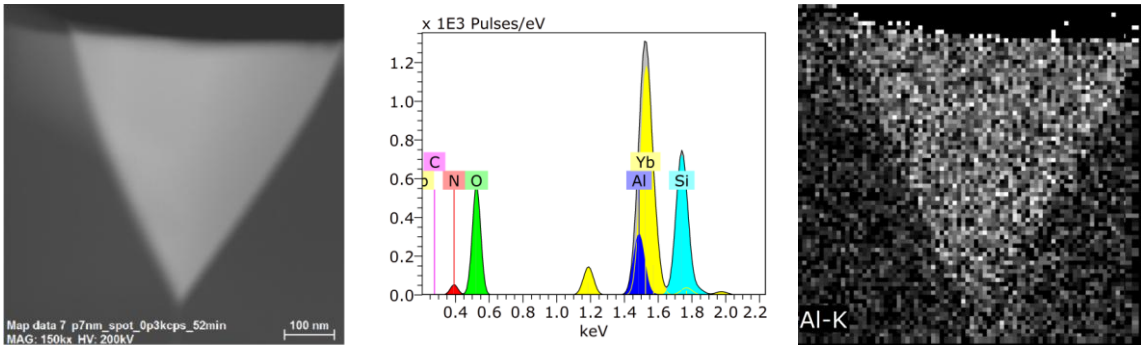

Figure 1. HAADF micrograph (left) showing a secondary triple junction in SiAlON ceramic. It contains aluminium and ytterbium as indicated by the deconvolution result (middle) and the net intensity map (right). 200 kV, 3 kcps.

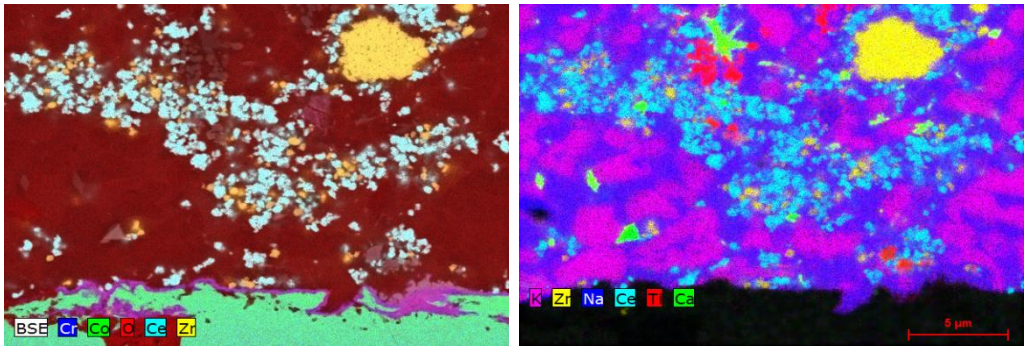

Figure 2. Composite intensity element map of a dental metal ceramic complex overlaid with a BSE micrograph (left) and without (right). 10 kV, ~25 kcps, 60 min, 42 nm pixel size.

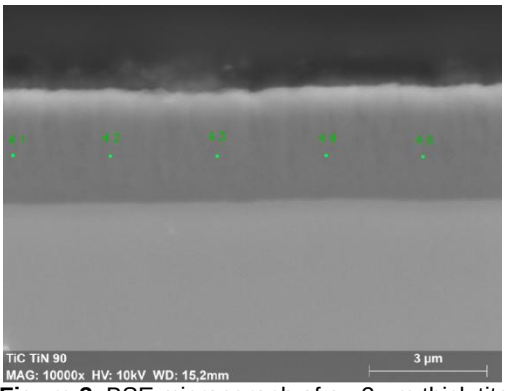

Figure 3. BSE micropgraph of a ~3 µm thick titanium carbonitride hardcoating with the locations where the point spectra were acquired.

Sample	C	N	Ti
1	32.9 ± 0.44	n.d.	67.1 ± 0.44
2	30.4 ± 0.83	13.0 ± 0.51	56.6 ± 0.41
3	17.1 ± 0.78	27.3 ± 0.52	55.6 ± 1.07
4	9.9 ± 0.19	37.3 ± 0.53	52.8 ± 0.44
5	(0.46 ± 0.52)	48.4 ± 0.44	51.2 ± 0.50

Table 1. Mean results (at.%, n=5) of titanium nitride, titanium carbide and titanium carbonitride. A carbon coating calibration function was applied in order to compensate the carbon intensity by coating and contamination. 10 kV, ~4.6 kcps, 20 s. n.d.: not detected.

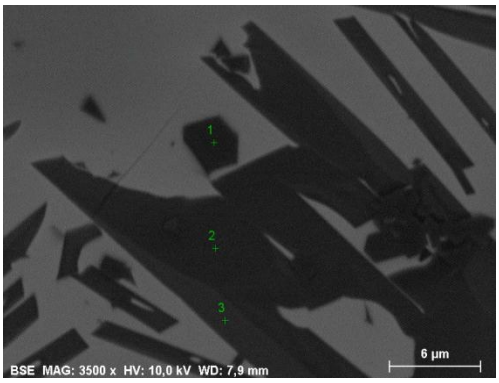

Figure 4. BSE micrograph of lead glazed pottery (10 kV, ~13 kcps, 700-900 s) with the locations where the point spectra were acquired.

Element	Series	Point 1	Point 2+3
SiO_2	K	44.0	n.d.
Al_2O_3	K	18.9	6.3
Fe_2O_3	K	2.7	64.9
MgO	K	0.4	11.2
CaO	K	0.6	n.d.
PbO	M	27.2	n.d.
CuO	L	n.d.	17.6
Na_2O	K	1.5	n.d.
K_2O	K	4.8	n.d.
Total		100.0	100.0

Table 2. Quantification results (mass.%) of the uniaxial potassium lead feldspar (point 1) and equiaxial copper ferrites (mean of point 2 and3) in lead glazed pottery. 10 kV, ~13 kcps, 700-900 s)

Spectroscopy in STEM/TEM

IM.4.P102
Element analysis of nanostructures using EDS

M. Falke[1], I. Nemeth[1]

[1]Bruker Nano GmbH, Application / Product Management, Berlin, Germany

meiken.falke@bruker-nano.de

Modern silicon drift detector (SDD) based energy dispersive X-ray analysis (EDS) became a convenient powerful and more and more accepted tool for chemical analysis reaching the atomic level. Low dimensional and other nanoscale structures and compounds including just a few atomic percent of a particular element or even single atoms on graphene [1-2] can be analyzed using electron microscopy combined with energy dispersive X-ray spectroscopy (EDS). The use of multiple SDD-EDS detectors increases analysis speed [3] and improves analysis geometry avoiding shadowing effects in complicated structures. Thus, SDD-based EDS combined with conventional and aberration corrected scanning transmission electron microscopy (STEM) can help to solve challenging problems of nanoscale characterization in a reasonable amount of time, if proper sample preparation is provided and optimized illumination conditions ensure sample stability at sufficient X-ray yield.

Various examples of nanostructure analysis demonstrate what kind of results can be achieved with particular detector-microscope combinations. Investigated materials include, Pd/Pt core-shell catalysts (Figure 1), ALD coated carbon nanotubes for flexible interconnects in flip chip assemblies and nanorods, such as InAs/InP containing nm-layers rich in Phosphorus used for single-electron transistors development (Figure 2).

Furthermore, we show options for qualitative and quantitative analysis of element distributions which are used in the design of 2D- and other nanoscale (opto)electronic devices. The quantification of light element compounds such as BN, LaB6 and Si3N4 and the routine quantification of e.g. 2 at% of Pt alloyed NiSi thin films or nanostructures serve as examples to demonstrate, what level of characterization is currently accessible.

Data suggest, that the outcome of EDS experiments can be largely improved by Cs-correction, a high brightness electron source, suitable choice of accelerating voltage, EDS-adapted sample holders and not only a high solid angle for X-ray collection but also a high take-off angle of the EDS detector, which ensures a high peak to background ratio in the acquired spectra. Flexible and transparent analysis software is essential to provide complete data mining.

1. T. C. Lovejoy et al., Appl. Phys. Lett.100, 154101 (2012)
2. M. W. Chu et al., Phys. Rev. Lett. 104, 196101 (2010)].
3. S. von Harrach et al., Microsc Microanal 15 (Suppl. 2)(2009) 208 and Schlossmacher et al., Microscopy Today 18(4) (2010) 14-20.

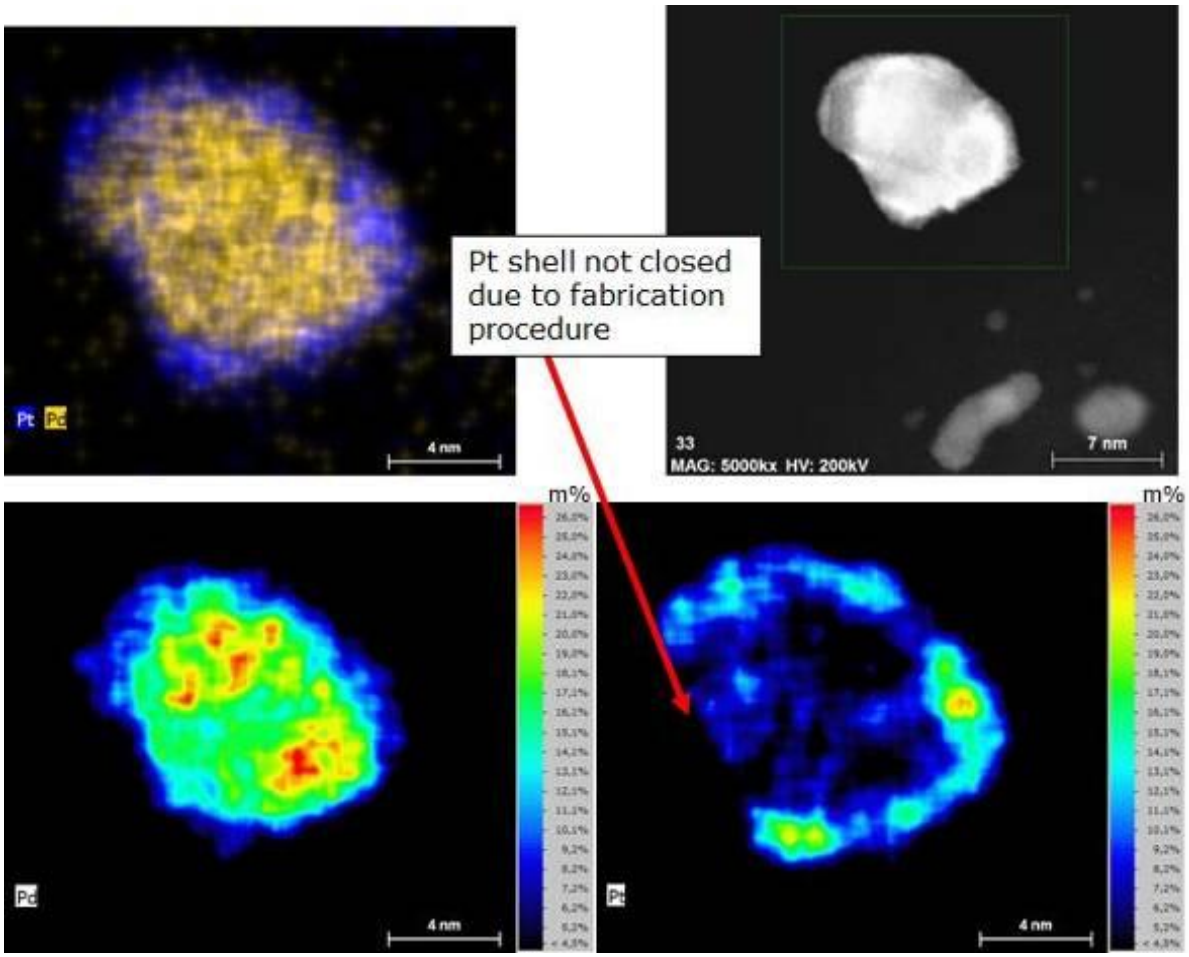

Figure 1. Pd-core / Pt-shell catalyst analysed at a solid angle of 0.12sr and a take-off angle of 22° using a Cs-corrected Schottky-FEG STEM. The open shell structure is due to the manufacturing process.
Data courtesy: D. Ozkaya, Johnson Matthey Technology Center, UK

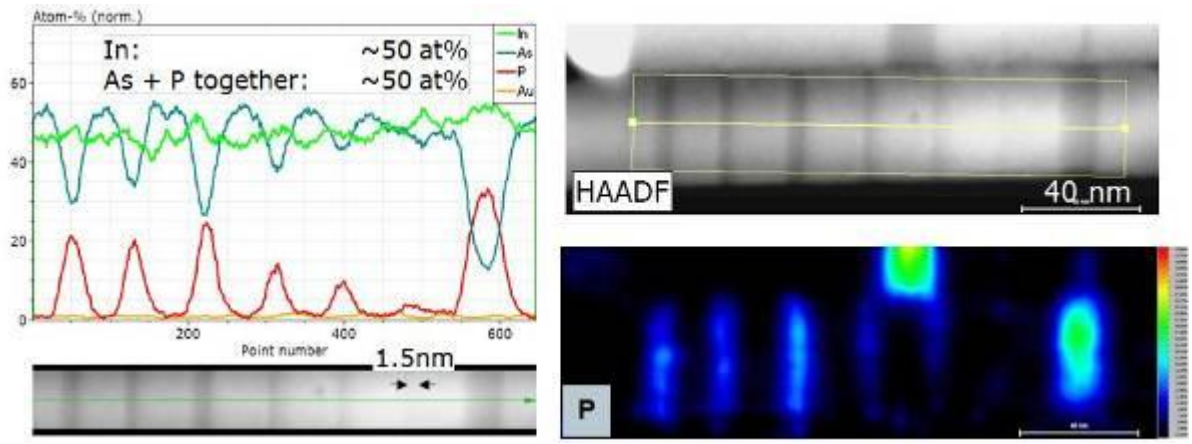

Figure 2. Phosphorus rich regions in InAs/InP nanorods, analysed at a solid angle of 0.12sr and a take-off angle of 22° using a conventional STEM.The line scan shows the quantitative data from the lower left false colour map.

Static and Dynamic Electric and Magnetic Imaging

IM.5.103
Field Mapping by Off-Axis Electron Holography: From Devices to the Detection of single Dopant Atoms.

D.Cooper[1], J-L. Rouviere[2], R.E. Dunin-Borkowski[3]

[1]CEA-LETI, Minatec, 17 rue des Martyrs, 38054 Grenoble Cedex9, France.
[2]CEA-LETI, Minatec, 17 rue des Martyrs, 38054 Grenoble Cedex9, France.
[3]Ernst-Ruska Center for Microscopy and Spectroscopy with Electrons, Research Centre Julich, D-52425 Julich, Germany.

david.cooper@cea.fr
Keywords: electron holography, dopant potentials, strain mapping, semiconductors, graphene

Off-axis electron holography is a unique technique that allows the electrostatic and magnetic fields in and around a specimen to be measured with nm-scale resolution. This makes it an extremely powerful technique for the characterisation for traditional semiconductor devices as well as for new innovative devices that are composed of nanowires and 2D films such as graphene.

The continuous reduction in the size of semiconductor devices means that information about the distribution of strain fields and active dopants at a nanometre scale are more important in order to understand how these properties affect their electrical performance. Indeed, the reduction in the size of these devices is beneficial for electron holography which now contain higher dopant concentrations that are less affected by artefacts from specimen charging and preparation. However, as these devices are miniaturised further, what was once known as a very high dopant concentration will be only a few atoms and that the positions of these individual atoms will affect the properties of the device. Therefore it is important that we develop methods to detect these single dopant atoms.

In this presentation we will show how electron holography can be used to measure the strain and electrostatic potentials in a range of semiconductor devices from 80-nm-gate transistors to graphene sheets. By using a FEI Titan operated at 200kV and combined with back-side focused ion beam milling at low energies, it is now possible to perform routine systematic studies on semiconductor devices during development. Figure 1 shows a series of potential maps for individual electrically tested pMOS devices that have been processed using different gate architectures and dopant implantations. The potential maps have been compared to simulations and electrical tests to provide a comprehensive understanding of the how the dopants affect the device properties. The strain applied using a SiN film was also measured using dark field electron holography [1].

Figure 2(a) shows a potential map that has been acquired of a silicon specimen containing boron-doped delta layers with a spacing of 3.5 and 6 nm. The map has been acquired using Lorentz mode with a spatial resolution of 5 nm and the potential profile shows that the active dopants from the different layers are not resolved. However, the step in potential between the undoped substrate and the layers can be measured. Figure 2(c) shows a potential map of the layers acquired using objective mode holography with a spatial resolution of 1 nm and the individual layers can be clearly resolved. Figure 2(d) shows the potential profiles of the layers compared to a HAADF intensity profile showing that the position of the layers have been accurately measured. Quantitiative analysis of the substitutional dopant concentration from strain mapping has been used to determine the expected step in potential measured across these layers which was in agreement with the measured phase [1].

Graphene has been used to test the sensitivity of electron holography for dopant profiling at atomic resolution. Figure 3(a) shows a potential map of triple graphene that has been acquired using the FEI Titan Ultimate operated at 80 kV. Here the acquisition of electron holograms with a fringe spacing of 0.4 Angstoms has been achieved which in principal can provide a spatial resolution of 1.2 Angstroms in the reconstructed potential map. However the instability of the specimen and microscope during the acquisition means that the spatial resolution is much less than this. Therefore methods of summing series of holograms that are acquired with extremely short acquisition times are required in order to achieve ultimate spatial resolution. Despite these problems, Figure 3(b) shows a potential map of bilayer graphene and a single impurity atom has been detected. We will conclude the talk with a discussion of the ultimate sensitivity of electron holography for the detection of single dopant atoms.

1. DC thanks the European Research Council for funding this work with the Starting Grant "Holoview".
2. D. Cooper et al. Nanoletters 11 4585-4590 (2011)

3. D. Cooper et al. Microscopy (2013) doi: 10.1093/jmicro/dft014
4. D. Cooper et al. Submitted Nanoletters (2013)

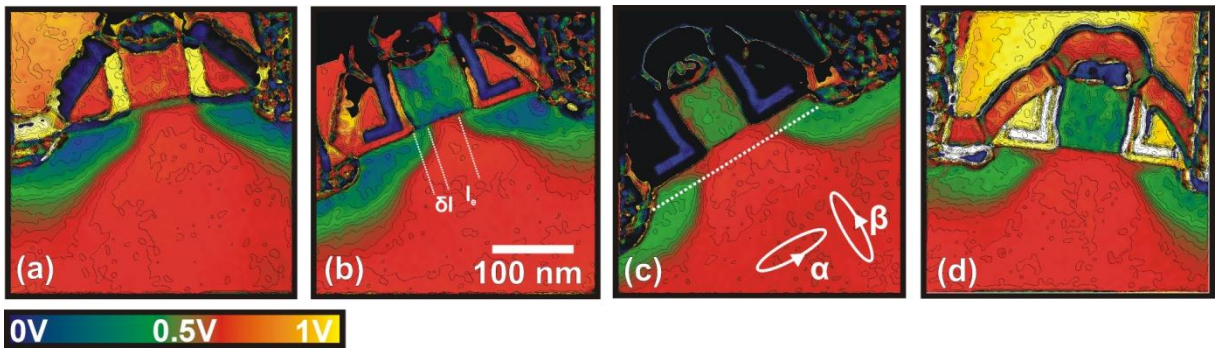

Figure 1. Maps showing the electrostatic potentials in pMOS devices with different gate architectures and dopant implants. The maps have a spatial resolution of 5 nm.

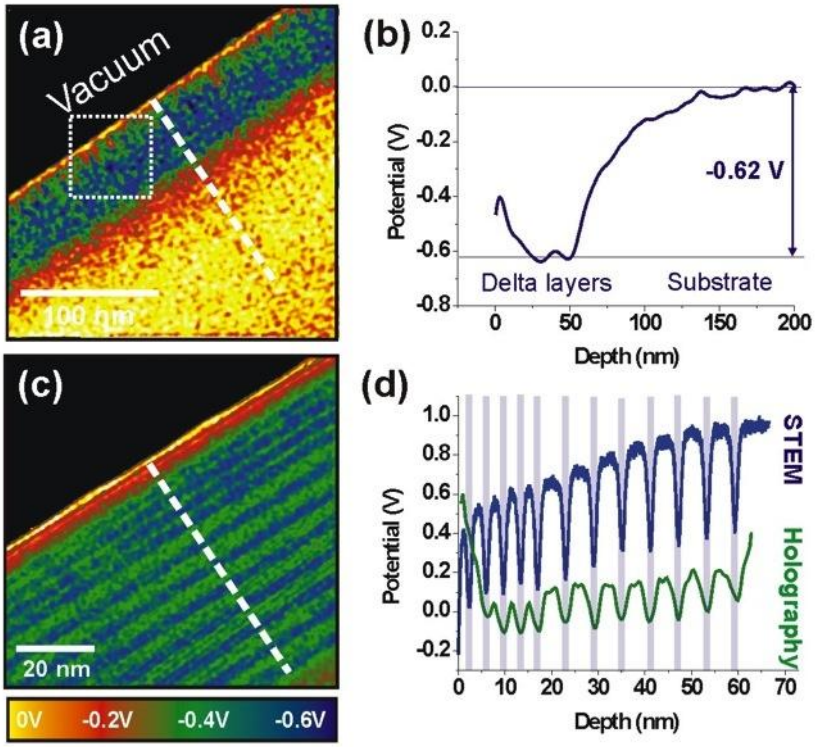

Figure 2. (a) Potential map of a silicon specimen containing 3.5 and 6 nm spaced boron delta doped layers acquired using Lorentz mode. (b) A potential profile of the doped region. (c) Potential map of the same sample except acquired using Objective mode with a spatial resolution of 1 nm. (d) Potential profiles compared to a STEM intensity profiles showing that the position of the delta layers have been accurately resolved.

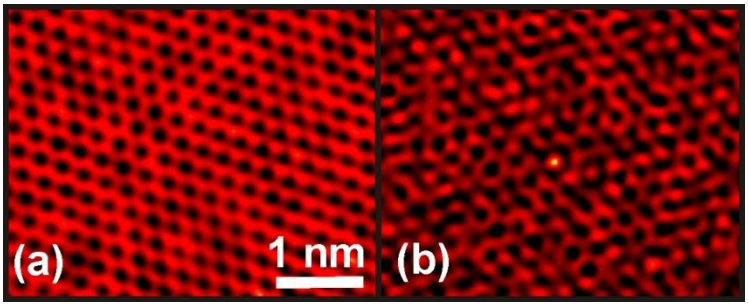

Figure 3. (a) Electrostatic potential of triple layer graphene (b) Electrostatic potential of bi-layer graphene with a single impurity atom present.

Static and Dynamic Electric and Magnetic Imaging

IM.5.104
Voltage Contrast in SEM for revealing charge transport through silver nanowire transparent electrodes

S. Spallek[1], J. Krantz[2], P. Kubis[2], J. Holzmair[3], B. Butz[1], S. Christiansen[3], C.J. Brabec[2], E. Spiecker[1]

[1]University of Erlangen-Nuremberg, Department of Materials Science and Engineering, Center for Electron Microscopy and Analysis (CENEM), Erlangen, Germany
[2]University of Erlangen-Nuremberg, Department of Materials Science and Engineering, Institute Materials for Electronics and Energy Technology (I-MEET), Erlangen, Germany
[3]Max Planck Institute for the Science of Light (MPL), Technology Development and Service Units 1 - Micro- and Nanostructuring, Erlangen, Germany

Stefanie.Spallek@ww.uni-erlangen.de
Keywords: Silver Nanowire, Transparent Electrode, Voltage Contrast dependent SEM

The next generation of optoelectronic devices requires transparent conductive electrodes to be lightweight, flexible, cheap, and compatible with large-scale manufacturing methods [1]. Two dimensional networks of silver nanowires (Ag NWs) synthesized by reduction of $AgNO_3$ with ethylene glycol and poly(vinylpyrrolidone) (PVP) as a surfactant [2, 3] are considered a highly promising candidate as a replacement for sputtered indium tin oxide (ITO) in organic thin-film solar cells [4]. Such Ag NW transparent electrodes have a high transparency and conductivity at low material consumption. In contrast to ITO transparent electrodes Ag NW electrodes can be processed also on flexible substrates and show good performance even after strong bending of the substrate [5]. Moreover, the fabrication by printing processes allows for up-scaling. Because of these advantages there is great interest in understanding charge transport through such NW networks [6]. However, the microscopic mechanism and the role of NW junctions are not yet well understood. In the present study we performed voltage contrast dependent scanning electron microscopy (VC-SEM) to investigate ultrasparse Ag NW networks near the electrical percolation threshold.

The Ag NWs are dispersed on Si covered with 200 nm SiO_2. Figure 1shows secondary electron (SE) SEM images of an ultrasparse Ag NW network at different values of the electrical potential (Figure 1a-c). The contrast profile of one Ag NW is shown in Figure 1d. At U = 0 V the contrast is mainly determined by material and orientation contrast, and the NWs appear bright. With increased positive potential the darker contrast points to a reduced SE yield on the Ag NW and in the vicinity of the Ag NW which can be explained with the help of the schematic shown in Figure 1e. If the Ag NWs are positively charged the SEs coming from the Ag NWs and also the SEs coming from the nearby substrate are attracted by the Ag NWs due to the attractive potential of the Ag NWs' surfaces. Therefore the low energetic SEs cannot reach the detector, so that a dark corona is formed. The extension of this corona depends on the applied potential. The higher the potential, the higher the threshold energy below which SEs are captured by the positively charged Ag NW and cannot reach the detector.

Because of this strong contrast formation VC-SEM can be used to investigate conduction channels within an ultrasparse Ag NW network. Figure 2 shows a Ag NW network electrically isolated by a LASER-cut. Four different positive potentials were applied. At U = 10 V only the upper area of the network appears dark indicating that the upper and the lower area are not electrically connected. At U = 11 V also the lower area shows dark contrast implying charge transport to this area. Interestingly, the newly connected area shows less contrast indicating a lower potential. Contrast profile analysis can lead to a quantitative statement concerning the potential difference of the two areas. Moreover, a detailed analysis shows that the charge transport is reversible pointing to a resistive-switching phenomenon.

Further investigations are underway to evaluate the microscopic processes that initiate charge transport across nanowire junctions and control the resistive-switching behavior [7].

1. A. Kumar and C. Zhou, ACS Nano 4 (2010), p. 11.
2. Y. Sun et al., Chem. Mater. 14 (2002) p. 4736.
3. Y. Sun et al., Nano Lett. 2 (2002). P. 165.
4. J. Krantz et al., Adv. Funct. Mater. 21 (2011) p. 4784.
5. L. Hu et al.,ACS Nano 4 (2010), p. 2955.
6. P. N. Nirmalraj et al., Nano Lett. (2012) published online.
7. The authors thank the Cambrios Technologies Corporation for the supply of the ClearOhm™ silver nanowire ink which was specially made for this study. They gratefully acknowledge financial support by the German Research Foundation (DFG) via the Cluster of Excellence EXC315 "Engineering of Advanced Materials" and the Research Training Group 1161/2 "Disperse Systems for Electronic Applications". They especially thank Dr. J. Jobst from the group of Prof. H. Weber for help with the electron beam lithography and for valuable discussions.

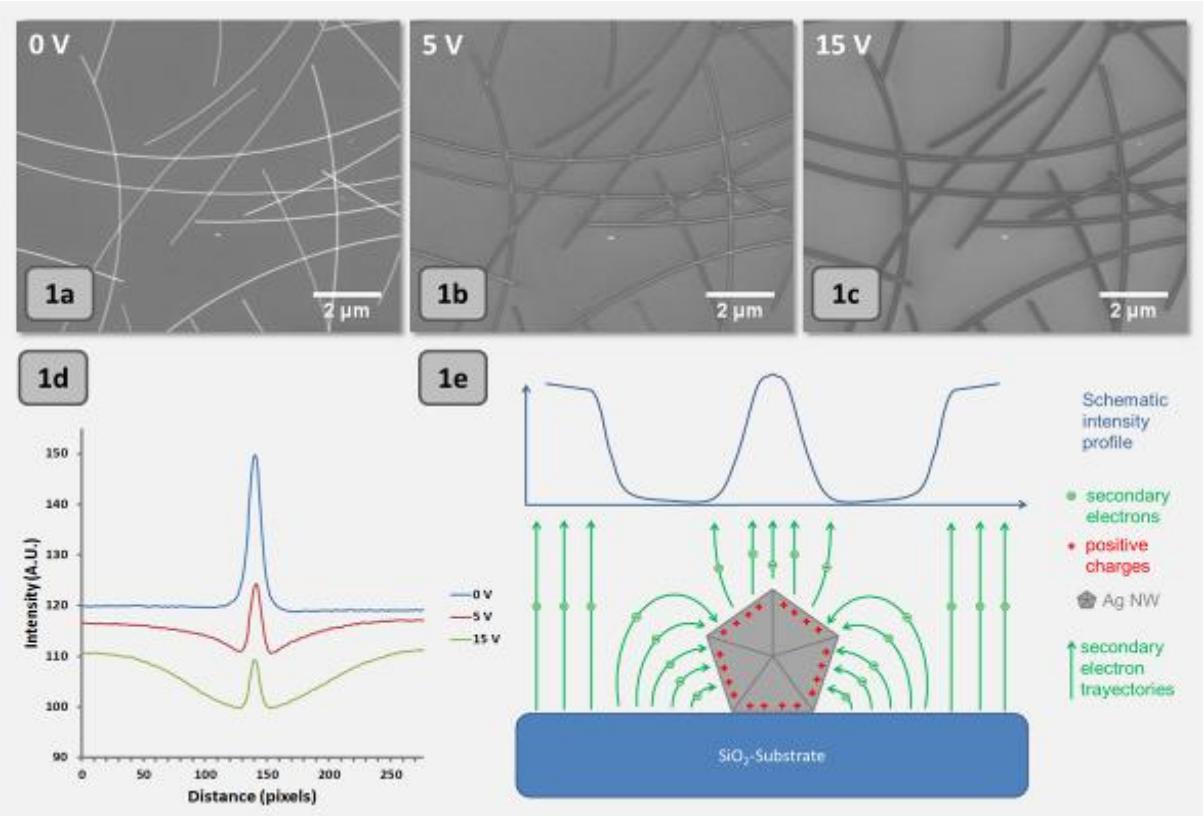

Figure 1.a-c. Voltage contrast series of an ultrasparse Ag NW network on Si with 200 nm SiO_2. **1d.** Contrast profiles of an exemplary Ag NW for each image of 1a-c**. 1e.** Model on the formation of the contrast profile in the positive-potential state.

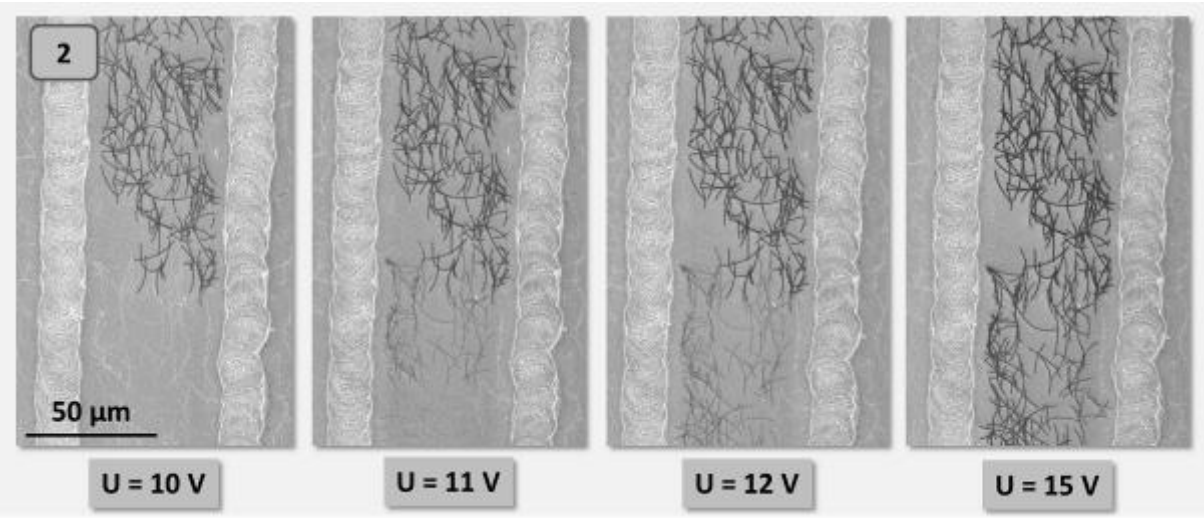

Figure 2. Voltage contrast series of an ultrasparse Ag NW network electrically isolated by a LASER-cut, showing different conductive cells which connect through at U = 11 V. The cells show different contrast profiles, because they are not at the same potential.

Static and Dynamic Electric and Magnetic Imaging

IM.5.105
Charging process simulation of PMMA film on Si substrate irradiated by electron beam

M. Kotera[1], M. Otani[1], S. Hosoi[1], K. Kumagai[1]

[1]Osaka Institute of Technology, Osaka, Japan

kotera@elc.oit.ac.jp
Keywords: Monte Carlo simulation of electron trajectories, PMMA film, charging process simulation

Electron beam (EB) has been used in microscopy and lithography, etc. and it is indispensable in recent nano-technologies. However, if the electric conductivity of the materials to be observed or processed is low, they charge-up during the EB irradiation. In order not only to avoid the charging, but also to make use of the characteristics in the application, quantitative knowledge of the charging process is important. We develop a simulation to calculate individual electron trajectory in and above the specimen, and try to find the charging mechanism during EB irradiation. In the present study, a simulation model is introduced to express a time-dependent charging process of PMMA film on Si substrate under EB irradiation.

Spatial distributions of the electron deposition and the energy deposition in PMMA are obtained by a Monte Carlo simulation of electron trajectories.[1,2] The potential distribution in and above the PMMA layer is obtained by solving the Poisson equation. The electron trajectory bending due to the electric field is calculated. The electron beam induced conduction (EBIC) is calculated based on the energy deposited. The thickness of PMMA is 300 nm, and the acceleration voltage (Vacc) of EB varies from 0.8 to 20 kV and the beam current is 50 pA. The electron density distribution of EB is assumed to be a Gaussian, where the radius at 1/e of its maximum is 100nm. Figure 1 shows the calculation flow. Since the trajectories of electrons less than several eV cannot be treated by the Monte Carlo simulation, electron diffusion by drift is considered by the transport equation. The local electric conductivity is given by the energy deposited by the beam, and the charge drift is calculated by the equation of continuity, and the final charge distribution is obtained in a time step. A typical time step is 1 ns, and after numerous loops of the calculation, the time dependent surface potential is obtained.

Surface potential averaged within the radius of irradiated EB is obtained for various Vacc's, and the potential variation as a function of EB exposure time is plotted in Figure 2. If Vacc is low, like 0.8-1.0 kV, or Vacc is large, like 3-10 kV, the saturated potential is positive. However, if Vacc is between 1.3 kV and around 3 kV, the surface potential saturates toward a negative value. This tendency agrees quite well with our experiment for 300-nm thick FEP film on 70nm-thick Cr on a glass substrate.[2] The reason of a positive value for low Vacc is that the secondary electron (SE) yield is above unity. The positive value for high Vacc is that almost all primary electrons transmit to the substrate and almost no charge is accumulated in the film, and only a small amount of SE emission at the surface makes the surface slightly positive. It is known that the tail of the depth distribution of energy density distribution almost reaches the bottom of the PMMA layer at Vacc=2.7 kV by the simulation. Because of the EBIC, it is expected that if Vacc is above 2.7 kV, electron charge stored in the PMMA will be leaked to the substrate. On the other hand, if primary electrons stop at a relatively shallow region and build a negative potential at e.g. Vacc=1.3 kV no conducting mechanism is present in the film around the deposited charge, unless the electric field becomes strong enough to release the charge toward the surface by EBIC in the film. Then, the saturated potential is negative at those Vacc's. The time constant of the saturation may depend on the size of the volume and the amount of stored charge, or the velocity of carriers in the specimen, etc.

The saturated surface potential as a function of Vacc's shown in Figure 3 is quite similar to the one obtained by our experiment.[3] However, the absolute value of the potential is different. For example, in the experiment the maximum negative potential is about -40V at the Vacc=1.5 kV. Here, the electric field is 40V/300nm=1.3MV/cm, and it is almost at the electric breakdown field. If only intrinsic resistivity ( ) and resistivity due to EBIC ( ), which is given above, are taken into account, [2] the maximum negative potential reaches more than -150V. This potential cannot be reached, because it is more than the break-down voltage of the material. Then, we introduce a consideration of the space charge limited current (SCC) process in the material to the simulation. Space charge limited current is considered by the following equation:

– — – —,

where the is determined tentatively by —.

Overall current regarding intrinsic, EBIC and SCC processes is written by the following equation.

By introducing the SCC, as shown in Figure 4, if the potential is less than 15 V, the attained potential does not change so much, but if the absolute potential increases more than 40 V, the resultant negative value saturates. If the Vacc is 1.8 kV, the maximum negative value attained is about -50V, which is almost comparable to the experimental results.

1. M. Kotera, K. Yamaguchi and H. Suga, Jpn. J. Appl. Phys. 38, 7176 (1999).
2. M. Kotera, J. Vac. Sci. And Tech., B19(6), 2516-22519 (2001).
3. M. Kotera and A. Osada, M. Otani and Y. Ohara, J. Vac. Sci. and Tech., B29(6), 06F316-1 (2011).

4. This work was supported by KAKENHI (C) 22560026.

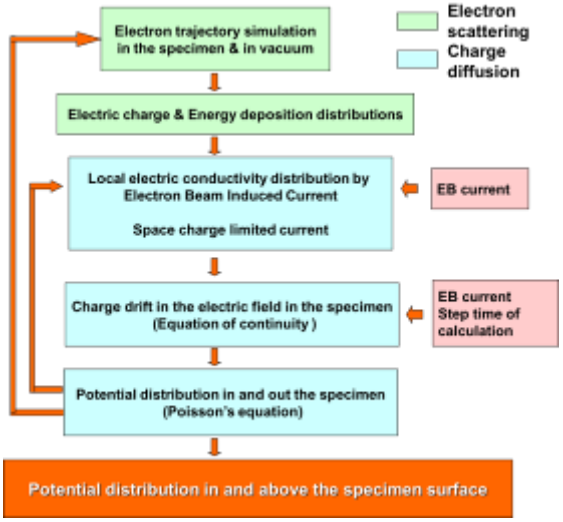

Figure 1. Simulation flow of the present.

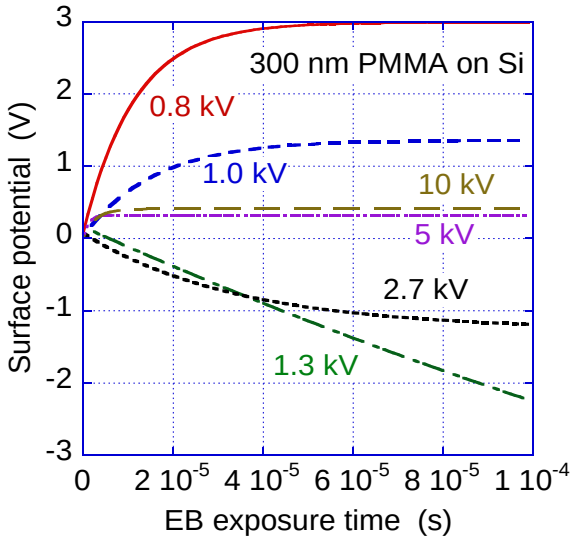

Figure 2. Surface potential variations with time of EB irradiation for various Vacc's

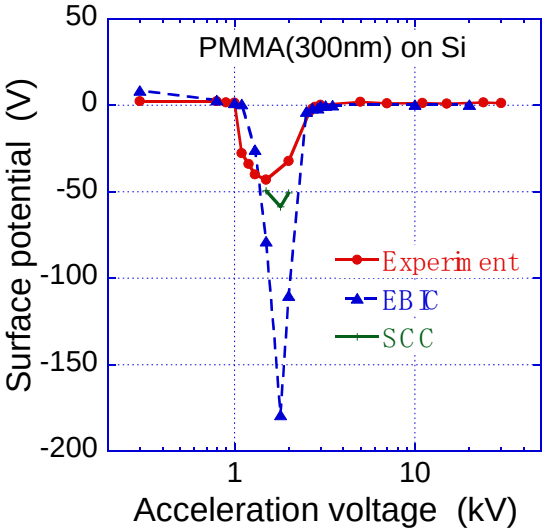

Figure 3. Saturated surface potential obtained as a function of Vacc by the calculation is comparing to the experimental results obtained by our recently developed measurement system.

.

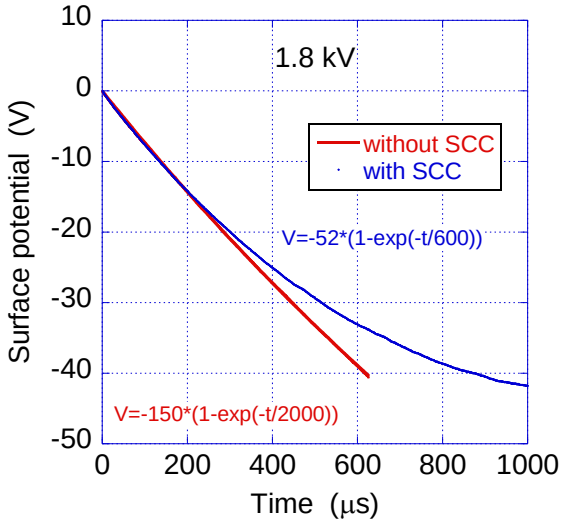

Figure 4. Surface potential variation with time. The initial variation is the same, but after the electric field is increased, difference becomes obvious between results of with and without SCC is considered

Static and Dynamic Electric and Magnetic Imaging

IM.5.106
Dipolar magnetism in nanoparticle assemblies revealed by electron holography

M. Beleggia[1], M. Varon[2,3], T. Kasama[1], R.E. Dunin-Borkowski[1,4], V. Puntes[2], R.J. Harrison[5], C. Frandsen[3]

[1]DTU Cen, Kgs Lyngby, Germany
[2]Institut Catala' de Nanotecnologia, Barcelona, Spain
[3]DTU Physics, Kgs Lyngby, Denmark
[4]Forschungszentrum Juelich, Juelich, Germany
[5]University of Cambridge, Cambridge, United Kingdom

marco.beleggia@cen.dtu.dk
Keywords: electron holography, dipolar interactions, nanoparticle magnets

Nanoparticle magnets are a novel class of materials, in which a lattice of magnetic ions is replaced by a meta-lattice of magnetic nanoparticles. Inter-particle exchange interactions are absent, while dipolar interactions dominate. As a result, nanoparticle magnets behave differently from conventional magnets and their properties may be controlled and tuned by selecting the spacing and compositions of the constituent nanoparticles. We have studied dipolar interactions in self-assembled Cobalt nanoparticle magnets using off-axis electron holography in the transmission electron microscope (TEM). The technique enables the orientation and magnitude of the magnetic moment of each nanoparticle in an array to be determined and correlated with the structural properties of the meta-lattice, including the degree of order of the particles and their size distribution. Our study reveals that dipolar interactions are sufficiently strong to support long-range ferromagnetic order, even when the lattice of nanoparticles is highly disordered. This observation supports the possibility of creating amorphous dipolar magnets, in contrast to the expectation that a disordered dipolar system necessarily implies spin-glass behavior [1].

Chain-like assemblies of 15 nm □-Co particles were prepared with an oleic acid coating on a carbon substrate (with no external magnetic field applied). Figure 1a shows TEM bright-field images of representative particle assemblies. For chains that are wider than 1 particle across, the particles are typically assembled into triangular (close-packed) lattices, although square lattice arrangements are also occasionally seen. We used off-axis electron holography to map the projected magnetic fields of several elongated nanoparticle assemblies non-invasively with a nominal spatial resolution of 6.3 nm (the holographic interference fringe spacing was 2.1 nm). Figure 1b shows color-coded (according to the color wheel shown in the inset) magnetic induction maps acquired at remanence using off-axis electron holography after applying an off-plane field of 2 T to the specimen. The maps reveal the magnetic moment topography of each chain directly.

In order to quantify dipolar ferromagnetic order, we estimated the magnitude and orientation of the magnetic moment of each individual particle, as shown in Fig. 2a for chain IV (note that the color wheel is slightly different than in Fig. 1). The measurements were correlated with the geometrical arrangements of the particles. For each pair of particles, we measured the spatial separation r between their centers and the angular difference □□ between their moments. Figure 2b shows the distribution (r,□□) for chain IV in Fig. 1, from which magnetic and lattice order parameters were determined. Our results show that short-range magnetic order with small domains dominates the initial states, with the local magnetic order (ferromagnetic or antiferromagnetic) often depending on the particle lattice (triangular or square, respectively). In contrast, at remanence after saturation, overall dipolar ferromagnetic order is extremely persistent even in case of a non-triangular lattice. We interpret our results as supporting the existence of amorphous dipolar ferromagnets: i.e., dipolar ferromagnetism in elongated nanoparticle assemblies even in the absence of underlying crystallinity [2].

1. M Varon et al., Sci. Rep. 3 (2013), p. 1234.
2. MV thanks the Spanish MICINN for financial support through scholarship BES-2007-17164. CF thanks the Danish Research Council for Independent Research for funding (Steno stipend).

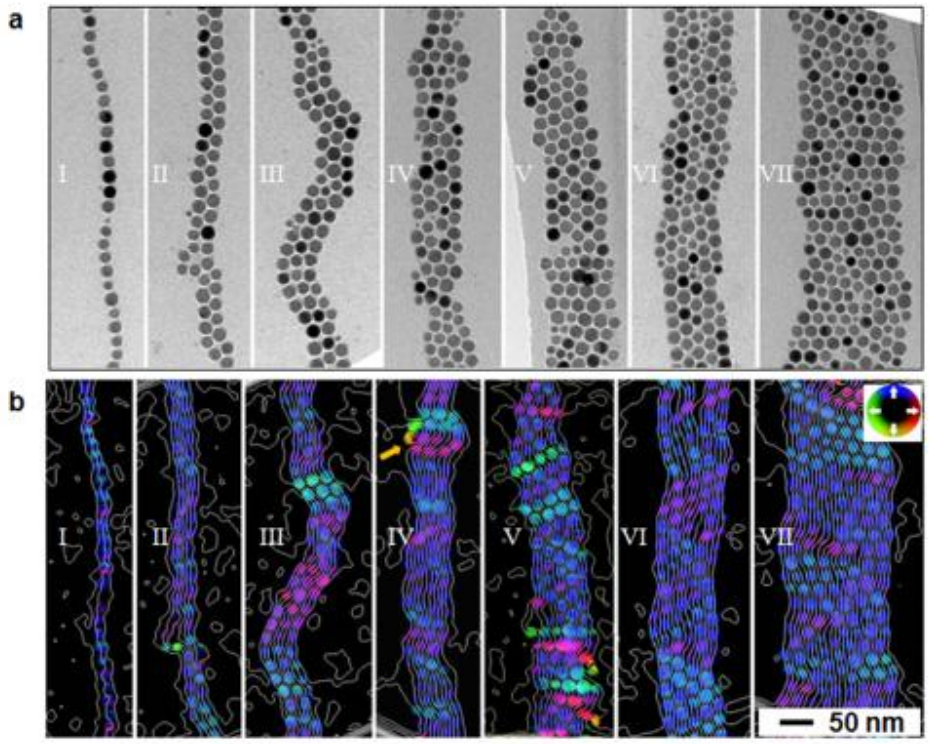

Figure 1. (a) Bright-field TEM images and (b) electron holographic magnetic induction maps obtained from chains of 15 nm Co nanoparticles of increasing width recorded at remanence after magnetic saturation. The white contours and colors in (b) provide a measure of the magnitude and direction of the projected magnetic field in the plane of the particles with a nominal spatial resolution of 6 nm. A magnetic phase variation of □/64, corresponding to 1/64 of a flux quantum $\square_0$=2.07 10^{-15} T m^2, is enclosed between any two adjacent contours

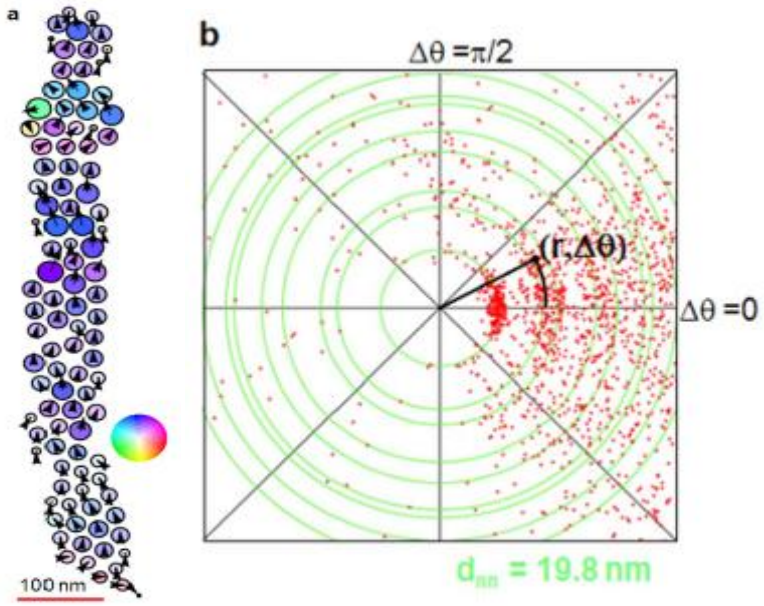

Figure 2. Results obtained from chain IV in Fig. 1. (a) Estimated magnetic moment distribution. (b) radial-angular (*r*,□□) distribution function, where *r* is the distance between two magnetic moments (particle centers) and □□ is the angular difference between their moment orientations, measured for all pairs of moments in the chain shown in (a). The thin green circular lines superimposed on (b) indicate the expected locations of the first few neighbouring peaks of a two-dimensional close-packed lattice with a nearest neighbour distance d_{nn} of 19.8 nm.

Static and Dynamic Electric and Magnetic Imaging

IM.5.107
Electron holography on ripple-shaped magnetic permalloy thin films

F. Röder[1], D. Wolf[1], M. Körner[2,3], M. Fritzsche[2,3], K. Lenz[2], J. Lindner[2], J. Fassbender[2,3], H. Lichte[1]

[1]Institute for Structure Physics / TU Dresden, Triebenberg Laboratory, Dresden-Zaschendorf, Germany
[2]Helmholtz-Zentrum Dresden-Rossendorf e.V., Institute of Ion Beam Physics and Materials Research, Dresden-Rossendorf, Germany
[3]Institute for Physics of Solids / TU Dresden, Dresden, Germany

falk.roeder@triebenberg.de
Keywords: electron holography, signal resolution, phase noise, magnetic thin film, dipolar stray fields

By means of off-axis electron holography (see e.g. refs. [1-3]), we study the distribution of the magnetic induction within and around a poly-crystalline permalloy ($Ni_{81}Fe_{19}$) thin film. Its deposition on a silicon substrate with a given periodic surface morphology emerging through concerted Xe^+ ion beam erosion introduces a ripple shape to the permalloy thin film [4]. The created ripple morphology is expected to pronounce magnetization within the permalloy and to induce dipolar stray fields [5]. Micro-magnetic simulations estimate those stray fields in the order of only 10 mT. Consequently, their experimental determination by electron holography at nanometer spatial resolution is highly demanding and requires advanced acquisition and reconstruction techniques [6].

To ensure the desired spatial resolution under a magnetic field-free object plane, the holographic imaging is conducted using a FEI TECNAI F20 transmission electron microscope with an aberration corrected pseudo-Lorentz lens provided by CEOS company [7]. To separate electric and magnetic contributions of the phase shift we reversed the magnetic field in-situ by using the objective lens [8].For the resulting two opposite magnetization directions, we acquire series of 20 object and corresponding empty holograms, respectively. The subsequent reconstruction of the hologram stacks is performed with the Triebenberg holography software package [9]. The spatial resolution in the reconstructed phase images reaches 5 nm and the mean phase noise level reduces to 2□/250 rad by wave averaging. Instabilities during hologram series acquisition and hysteresis effects after saturation and magnetization reversal mainly induce drift of the object position, defocus, and image distortions. Consequently, the improvement of signal resolution by averaging and the separation of electric and magnetic phase shifts require the reliable removal of such systematic deviations, e.g. by incorporating non-linear fitting routines.

The resulting electric phase images indicate the material contrast due to different mean inner potentials and the object thickness distribution (Figure 1). The magnetic phase image shows a magnetized thin film (Figure 2), in which the magnetization direction follows the given morphology. Furthermore, a closer look to the permalloy/carbon interface reveals systematic magnetic phase signatures at the ripple flanks (Figure 3). The estimated strength of the magnetic stray fields at the detection limit of the method is in the order of 10 mT and agrees well with micro-magnetic simulations [10].

1. H. Lichte and M. Lehmann, Rep. Prog. Phys. 71, 016102 (2008).
2. M. R. McCartney and D. J. Smith, Annu. Rev. Mater. Res. 37, 729 (2007).
3. A. Tonomura, Advances in Physics, 41, 59 (1992)
4. W. L. Chan and E. Chason, J. Appl. Phys. 101, 121301 (2007).
5. R. Arias and D. L. Mills, Phys. Rev. B 59, 11871 (1999).
6. F. Röder, A. Lubk, D. Geiger, H. Lichte, Proceedings of the MC 2009 Graz, Vol. 1, 19-20.
7. F. R, D. W. and H. L highly appreciate technical support by CEOS Company, Heidelberg.
8. R. E. Dunin-Borkowski, M. R. McCartney, David J. Smith and S. S. P. Parkin, Ultramicroscopy 74, 61 (1998).
9. D. Wolf, Triebenberg Software Package for Electron Holography.
10. The research leading to these results has received funding from the European Union 7th Framework Program under Grant Agreement 312483 - ESTEEM2 (Integrated Infrastructure Initiative - I3)

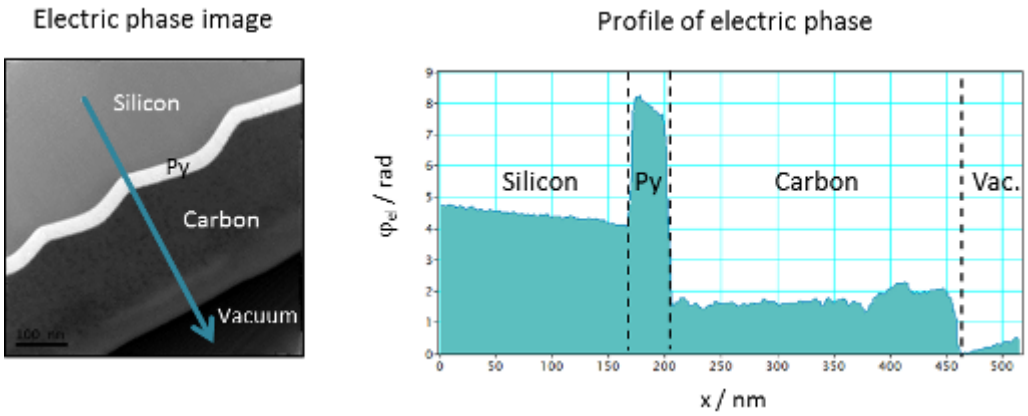

Figure 1 Electric phase image showing the morphology of the ripple-shaped permalloy (Py) thin film. Different mean inner potentials and the sample thickness distribution determine the contrast. From the known mean inner potential of silicon (12 V) the object thickness within the permalloy region (40-45 nm) and its mean inner potential (24.8 V) can be derived.

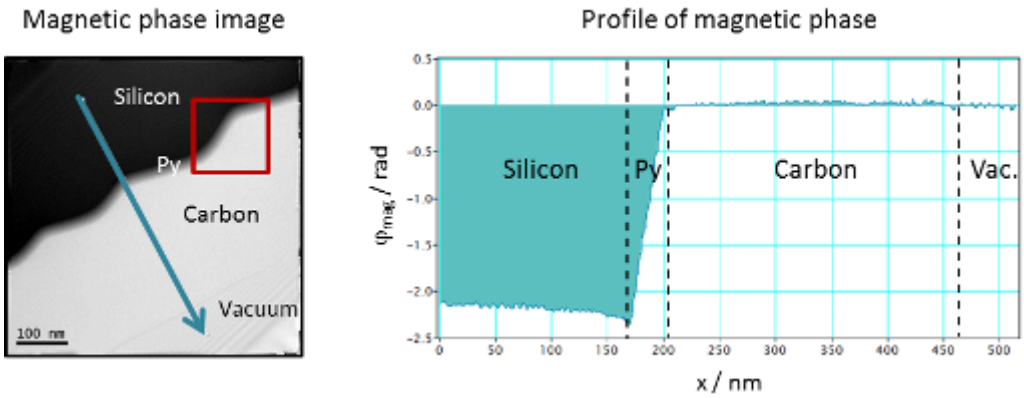

Figure 2 Magnetic phase image exhibiting a strong phase gradient across the permalloy thin film of about 0.07 rad/nm. With the results of Figure 1 a, the magnetic induction of B = 1.1 T can be determined.

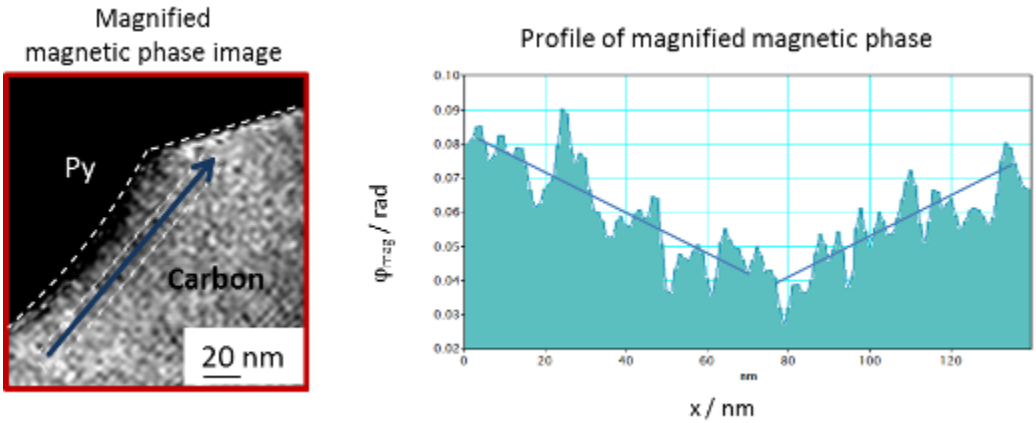

Figure 3 Magnified inset of the magnetic phase shift in Figure 2. The interface is depicted as a dashed white line. The image indicates phase signatures in the carbon film due to magnetic stray fields appearing as a dark convexity at the short ripple flank. The profile shows weak phase gradients of about 0.6 mrad/nm corresponding to field strengths of approximately 10 mT.

Static and Dynamic Electric and Magnetic Imaging

IM.5.108
Electron vortex propagation in the magnetic lens field

T. Schachinger[1], S. Löffler[2], M. Stöger-Pollach[2], A. Steiger-Thirsfeld[2], P. Schattschneider[1,2]

[1]TU Vienna, Solid State Physics, Vienna, Austria
[2]TU Vienna, USTEM, Vienna, Austria

thomas.schachinger@student.tuwien.ac.at
Keywords: electron vortex beams, magnetic field, Lamor rotation

Since it became possible to create electron vortex beams in transmission electron microscopes (TEM) [1, 2], it is very important to understand their motion, in particular in the magnetic lens fields in a TEM. These doughnut shaped beams carry quantized orbital angular momentum (OAM) of $L_z = m\hbar$ as well as a quantized magnetic moment of $M = \mu_B m$ per electron, which opens up the road for applications like particle manipulation [3] and mapping magnetic moments on atomic scales [4].

Standard electron imaging theory predicts that all objects traversing the magnetic lens fields in a TEM rotate with the same speed [5]. Recently, Bliokh et al. theoretically predicted peculiar rotations of electron vortex beams in uniform magnetic fields parallel to the beam axis [6]. They proposed that electron beams consisting of a coherent superposition of vortices with different orbital angular momentum show different rotation speeds in the presence of a vector potential as created, e.g., by the objective lens in a TEM. In particular, depending on the sign of the scalar product $B \cdot M$ where B is the z-component of the lens field and M is the net magnetic moment of the vortex, cyclotron (double-Larmor) rotation or no rotation is expected. Vortices with $M = 0$ should show Larmor rotation.

In this work, we present a series of experiments to investigate these peculiar rotations. To be able to experimentally observe these azimuthal rotations, one has to break the radial symmetry of the vortex beams [7]. We used a sharp edge made by breaking a Si crystal, which was then shifted in z-direction (see Figure 1.). As the blocking edge is moving through the lens field, different rotation angles of the cut vortices were observed (see Figure 2.). The acquired rotation angle over the z-shift distance then gives the azimuthal rotation speed of the vortex electrons. To avoid contributions from the superimposed Gouy rotation, we used the C_2 lens to defocus the electron beams to a point far outside the Rayleigh range [7, 8]. By that, we observed a variety of different rotation speeds, strongly depending on the C_2 defocus, as well as the vortex order m (see Figure 3.).

To better understand this complex behavior, we performed numerical ray tracing calculations using the classical Lorentz force and realistic parameters for the objective lens field. The simulation results are in good agreement with the experimental data as is shown in Figure 2. The remaining discrepancies between theory and experiment are attributed to the inhomogeneous lens field and the imperfect blocking edge.

We found an extended set of peculiar rotations of electron vortex beams in TEM, including zero, Larmor and cylclotron frequency at a certain C_2 defocus value and vortex order m. These findings put the general theorem of Larmor rotation in a TEM in question and necessitate the reevaluation of the applicability of the established theory of imaging in a TEM.

1. M. Uchida and A. Tonomura, Nature 464 (2010), 08904.
2. J. Verbeeck, H. Tian and P. Schattschneider, Nature 467 (2010), 09366.
3. J. Verbeeck, H. Tian and G. Van Tendeloo, Adv. Mat. 25 (2013), 1114.
4. P. Schattschneider, J. Verbeeck and V. Mauchamp, Phys. Rev. B 82 (2010), 144418.
5. W. Glaser, Grundlagen der Elektronenoptik, Springer-Verlag Wien,1952.
6. K. Y. Bliokh, P. Schattschneider and J. Verbeeck, Phys. Rev. X 2 (2012), 014011.
7. G. Guzzinatti, P. Schattschneider and K. Y. Bliokh, PRL 110 (2013), 093601.
8. S. M. Baumann, D. M. Kalb and L. H. MacMillan, Opt. Expr. 17 (2009), 9818.
9. TS, SL and PS acknowledge financial support by the Austrian Science Fund (FWF) under grant number I543-N20.

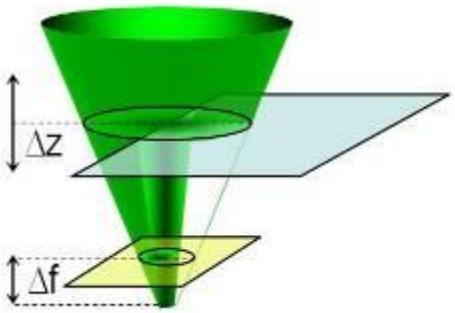

Figure 1. Sketch of the experimental setup (not to scale). Half of the incoming convergent electron beam (green) is blocked by a sharp Si knife edge (blue). The knife edge is then z-shifted from -375 µm to +375 µm in order to see the variation of the azimuthal cutting angle in the observation plane (yellow). Δf is chosen in way that contributions from the Gouy rotation are minimized.

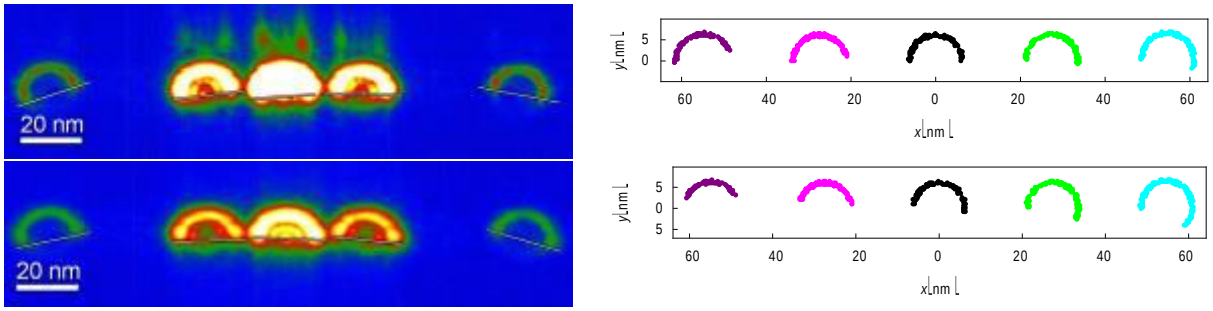

Figure 2. Left: Measurements of cut vortices, where the azimuthal rotation angle of vortices with topological charge m = 0, ±1, ±3 can be seen. The observation plane Δf was 5.7 µm beneath the focused row of vortices and the z-shift value Δz of the blocking edge was 100 µm under the observation plane for the upper row and 300 µm for the lower one. Right: Simulated electron distribution for the experimental parameters on the left side using the Lorentz force and realistic parameters for the objective lens field. The electrons' vorticities were added by assigning transverse velocity components according to $L_z = m_e \cdot (r_e \times v_e) = m\hbar$, where m_e, r_e, v_e are the electron's rest mass, radial distance to the optical axis and transverse velocity, respectively.

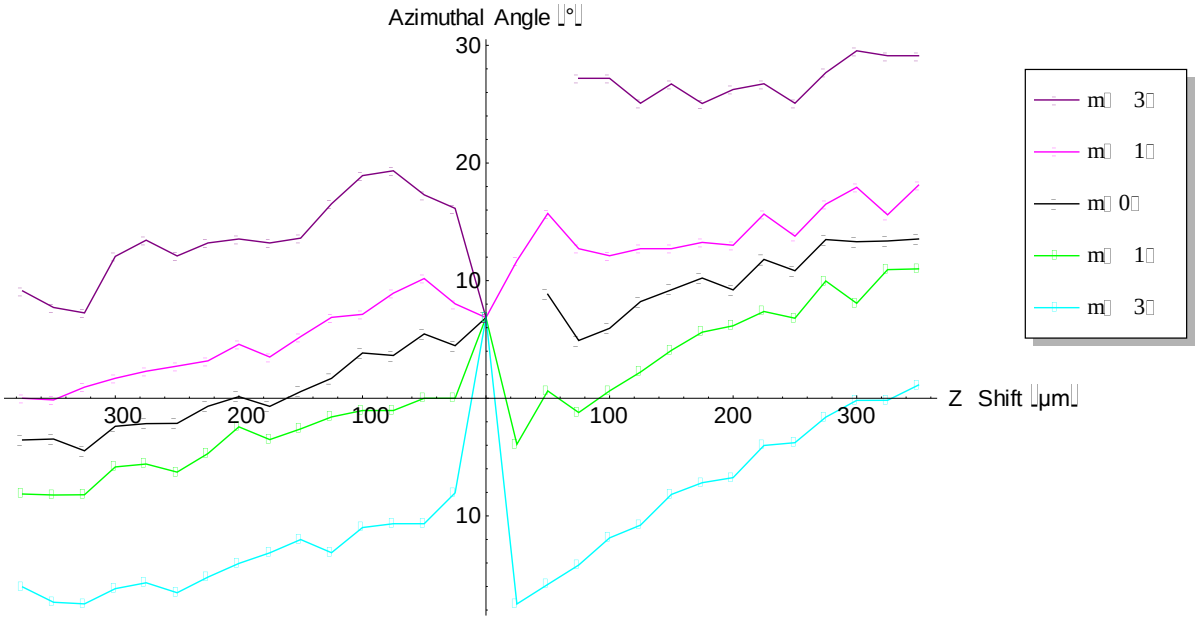

Figure 3. Diagram showing the experimentally observed azimuthal rotation angles over the knife edge's z-shift position for electron beams carrying topological charges m = 0, ±1, ±3 and for Δf = 5.7 µm. The different rotation speeds can be discriminated by the increment of the azimuthal angle.

Static and Dynamic Electric and Magnetic Imaging

IM.5.P109
Phase shift of single-domain ferroelectric nanoparticles

B. Baekke[1], M. Beleggia[1]

[1]DTU Cen, Kgs Lyngby, Denmark

marco.beleggia@cen.dtu.dk
Keywords: electron holography, ferroelectric nanoparticles, depolarization field

Capturing with electron phase sensitive techniques the vacuum electric field that is expected to surround polarized particles has proven to be extremely challenging. On one hand, considering the very large spontaneous polarization of typical ferroelectric materials, and based on a formal analogy with ferromagnetic nanoparticles, one may intuitively expect the phase shift to be very large and the experiments straightforward. On the other hand, in spite of numerous attempts in various electron microscopy facilities worldwide, only hints of a ferroelectric signal from nanoparticles (NPs) are present in the literature (see in particular the recent article [1] reporting on 15 nm Barium Titanate nanocubes studied by electron holography), highlighting the extreme complexity of the matter.

The fundamental reason behind the difficulties in detecting ferroelectric signals from NPs is that P is suppressed by the depolarizing field, so that a NP made of a material which is ferroelectric in bulk form, loses its P and is forced into a paralectric phase. Single-domain ferroelectric NPs, therefore, cannot exist unless depolarization field are compensated. Screening charges from either surface states (generally with metallic character) or nearby conductive elements such as a metallic support, contacts, or electrodes, or, possibly, a surrounding matrix if the NPs are embedded, may provide a relief of the electrostatic energy that suppresses P, so that some degree of polarization survives. Furthermore, differently from ferromagnetic materials, the ferroelectric domain size has no lower bound other than the unit cell, so that the natural anti-ferroelectric nature of dipolar interactions, i.e. the tendency to form domains of opposite polarization in order to lower the energy, is not countered by balancing driving forces (for example: the wall energy cost associated with the formation of 180° domains along the polar direction is very small) and further decreases the net P of NPs [2].

We present here an estimate of the electron-holographic signal (phase shift) we may expect from a spherical particle made of a material that is ferroelectric in bulk form. We use barium titanate (BTO) as reference material since its bulk ferroelectricity is well described by a set of known coefficients for the free energy. The polarization-related free energy density term describing a crystal that undergoes a paraelectric-ferroelectric transition [3] is $F=-(A/2)P^2+(B/4)P^4+(C/6)P^6$, with (A,B,C) known temperature-dependent coefficents [4]. By minimizing the free energy, we find that as long as $A>0$ a spontaneous polarization appears with a value determined exclusively by the three coefficients. For BTO, this value at room temperature equals $P_s=0.26$ C/m^2, its bulk polarization. As soon as a particle is made out of bulk BTO, however, an extra term has to be added to its free energy: the electrostatic energy of the polarization charge density established at the surface of the object. If the object is carved out in the form of a sphere, or a solid with an equivalent symmetry (cube, etc.), then the depolarization field energy density equals $P^2/(6\varepsilon_0)$: the coefficient of the P^2 term in F then changes from A to A-A'=A-$1/(3\varepsilon_0)$. Since $1/(3\varepsilon_0)$ is about two orders of magnitude larger than A, the immediate result is that the energy minimum that gave us P_s disappears: the particle cannot sustain any finite value of P_s, and is forced back to an unpolarized (paralectric) state. The only way to restore a finite value of P_s is to provide means to relieve this huge extra energy preventing ions from displacing inside the unit cell in the way they would do if surfaces and surface charges were not present. We examine here only the effect of embedding the particle in a dielectric matrix of relative constant ε_r. In such situation, the energy density is $P^2/[2\varepsilon_0(1+2\varepsilon_r)]$, so that, if ε_r is sufficiently large, A-A' might remain positive, and the energy minimum that allows a finite P_s is preserved. The $P_s(\varepsilon_r)$ curve shown in Figure 1 illustrates that the polarization onset occurs at ε_r=214, and that the residual polarization approaches the bulk value with a $P_s(1-a/\varepsilon_r)$ dependence (a~73). The curve also highlights the needs for a high-k dielectric as embedding matrix: anything less effective will kill the polarization.

There is another complication. Lorentz deflection of electrons is proportional to the electric field E, not to P. Hence, the signal is large when E, i.e. the depolarization field is large. But when the depolarization field is large, P is suppressed, so E vanishes. On the other hand, when the surrounding dielectric provides compensation of the depolarization field, it allows P to be large, but keeps E small. In the end, the signal is then going to be small either way. Figure 2 shows the effect of the surrounding

dielectric matrix on the phase shift of a polarized spherical (radius=20 nm) BTO nanoparticle: the plot of the maximal phase shift (two times the phase value at *r*=*R*) illustrates that in absence of sufficient dielectric screening, the signal vanishes; it then raises in the interval (214<ε_r<300), and finally drops again because the depolarization field is compensated. The largest possible phase shift we may expect from a single-domain BTO NP embedded in a dielectric matrix is about 400*R[nm]^2 rad when ε_r=300, which is 0.16 rad (or ~π/20) for a 20 nm radius NP. For comparison, if the same BTO NP was polarized with the bulk value, and dielectric screening was not needed to maintain a finite *P*, the expected phase shift would be around 50 rad, more than 300 times larger. Figure 2 confirms that, indeed, detecting ferroelectric signals from NPs is extremely challenging, and that there is a very narrow margin for finding suitable experimental conditions.

1. M.J. Polking et al., Nat Mater 11 (2012) p. 700.
2. W.Y. Shih,
W-H. Shih and I.A. Aksay, Phys Rev B 50 (1994), p. 15575.
3. C. Kittel, Introduction to Solid State Physics, John Wiley & Sons, 8th ed. (2005), p. 474.
4. N.A. Pertsev, A.G. Zembilgotov and A.K. Tagantsev, Phys Rev Lett 80 (1998), p. 1988.

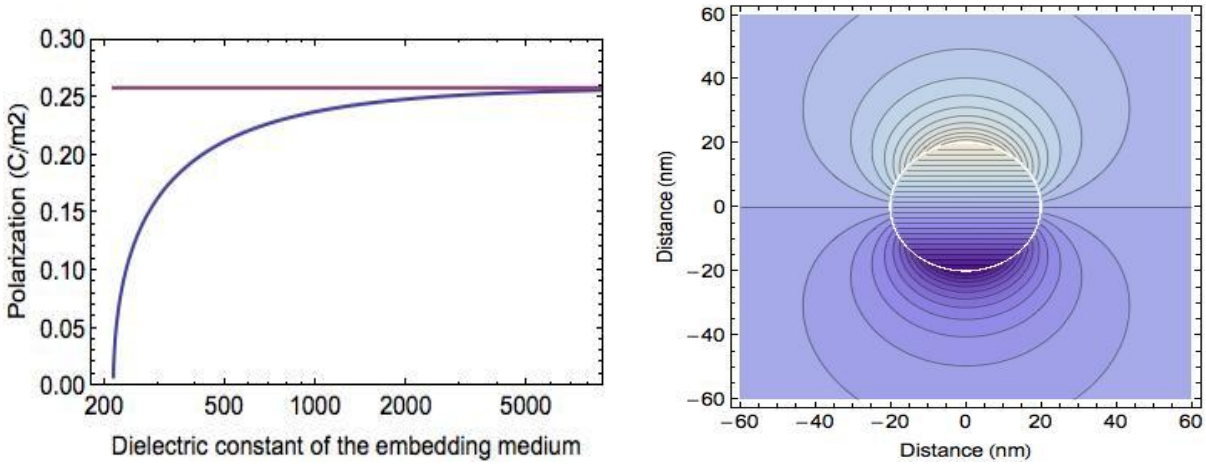

Figure 1. Left: polarization of a hypothetical single-domain BTO nanoparticle as a function of the dielectric constant of the embedding medium; the polarization vanishes below a critical value of ε_r=214. Right: contour plot of the cross-sectional electrostatic potential within an around a polarized BTO NP embedded in a dielectric matrix with ε_r=300; equipotentials are at 50 mV.

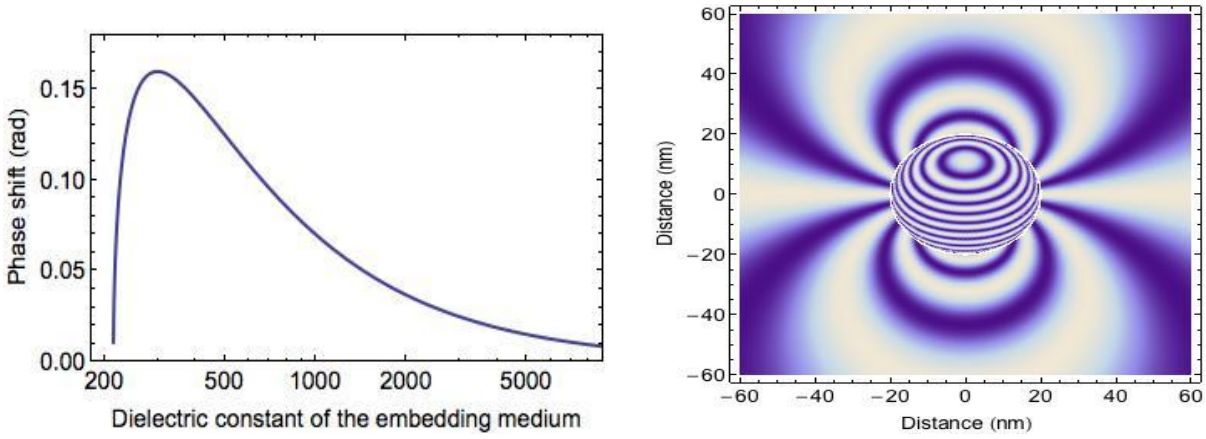

Figure 2. Left: phase shift of a hypothetical single-domain BTO nanoparticle with 20 nm radius as a function of the dielectric constant of the embedding medium; the phase shift vanishes when ε_r<214, reaches a maximum at ε_r=300, and decreases for higher values of ε_r due to the compensation of surface charges (the physical source of phase shift). Right: cosine-map (256x amplified) representation of the phase shift for a BTO NP when ε_r=300 with the effect of the mean-inner-potential (MIP) added to that of the polarization; the particle radius is 20 nm, the accelerating voltage 300 kV, and the MIP 1 V.

Static and Dynamic Electric and Magnetic Imaging

IM.5.P110
Electron holography at low voltages exemplified by graphene

F. Börrnert[1], A. Lubk[1], F. Röder[1], D. Wolf[1], H. Lichte[1]

[1]TU Dresden, Institut für Strukturphysik, Dresden, Germany

Low-voltage transmission electron microscopy (TEM) has re-emerged in the last decade with the advent of the hardware aberration correctors. While the early electron microscopes were operated at accelerating voltages regarded as low nowadays, the voltage was increased over the time in order to achieve the maximum possible resolving power essentially limited by the aberrations of the objective lens. However, the achievement of image resolution allowing characterization of crystal structures had to be paid with increased beam damage induced by the high energy of the imaging electrons. This restricts the investigation of whole classes of the materials containing light elements. The introduction of aberration correctors enables the investigation also of these materials at sufficient resolution with accelerating voltages of 80 kV and even down to 20 kV [1].

Transmission electron microscopy has several drawbacks resulting from the fact that it only records the squared amplitude of the image wave while losing most of the phase information. In particular, because of the phase contrast transfer function, one loses the information about extended structures, *i.e.*, the exact projected electrostatic and magnetic field values encoded in the electron wave. Fortunately, the full wave information can be retrieved by means of off-axis electron holography [2].

Besides the fact that graphene is a material vividly investigated [3] it constitutes a perfect test specimen for TEM and electron holography because of its thickness of exactly one atom. In particular, this allows neglecting all multiple and dynamic scattering phenomena and identifying the projected potential of the object directly from the object exit wave. Moreover, graphene consists of carbon that is very light and thus approximates a pure phase object very well. On the other hand, graphene is susceptible to knock-on damage at normal TEM operation voltages, and hence the use of low acceleration voltages is mandatory [4].

In this contribution, using a FEI Tecnai F20 Cs-corr, we present an investigation about the benefits from using low acceleration voltages in off-axis electron holography. In electron holography the figure of merit of a hologram is the information content concatenating the maximum field of view, lateral resolution, and signal resolution [5]. The information content figure depends on the acceleration voltage directly and indirectly in several parameters like the improved sampling due to a larger maximum magnification, a stronger signal due to a larger interaction cross section and therefore shorter exposure times, a better stability of the biprism at lower filament voltages, and finally the superior characteristics (modulation transfer function and detection quantum efficiency) of the camera at 80 kV [6].

Finally, we present the measurement of the electron phase shift by graphene and discuss the mean inner potential of graphene [7].

1. U. Kaiser *et al.*, Ultramicroscopy 111 (2011) p. 1239.
2. H. Lichte *et al.*, Annual Review of Materials Research 37 (2007) p. 539.
3. M. H. Rümmeli *et al.*, Advanced Materials 23 (2011) p. 4471.
4. J. C. Meyer *et al.*, Physical Review Letters 108 (2012) p. 196102.
5. H. Lichte, Ultramicroscopy 108 (2008) p. 256.
6. F. Börrnert *et al.*, Journal of Microscopy 249 (2013) p. 87.
7. The research leading to these results has received funding from the European Union Seventh Framework Programme under Grant Agreement 312483 - ESTEEM2 (Integrated Infrastructure Initiative - I3). We thank P. Hartel and M. Haider for the alignment of the aberration corrector for 80 kV operation, and S. Melkhanova for providing a graphene sample.

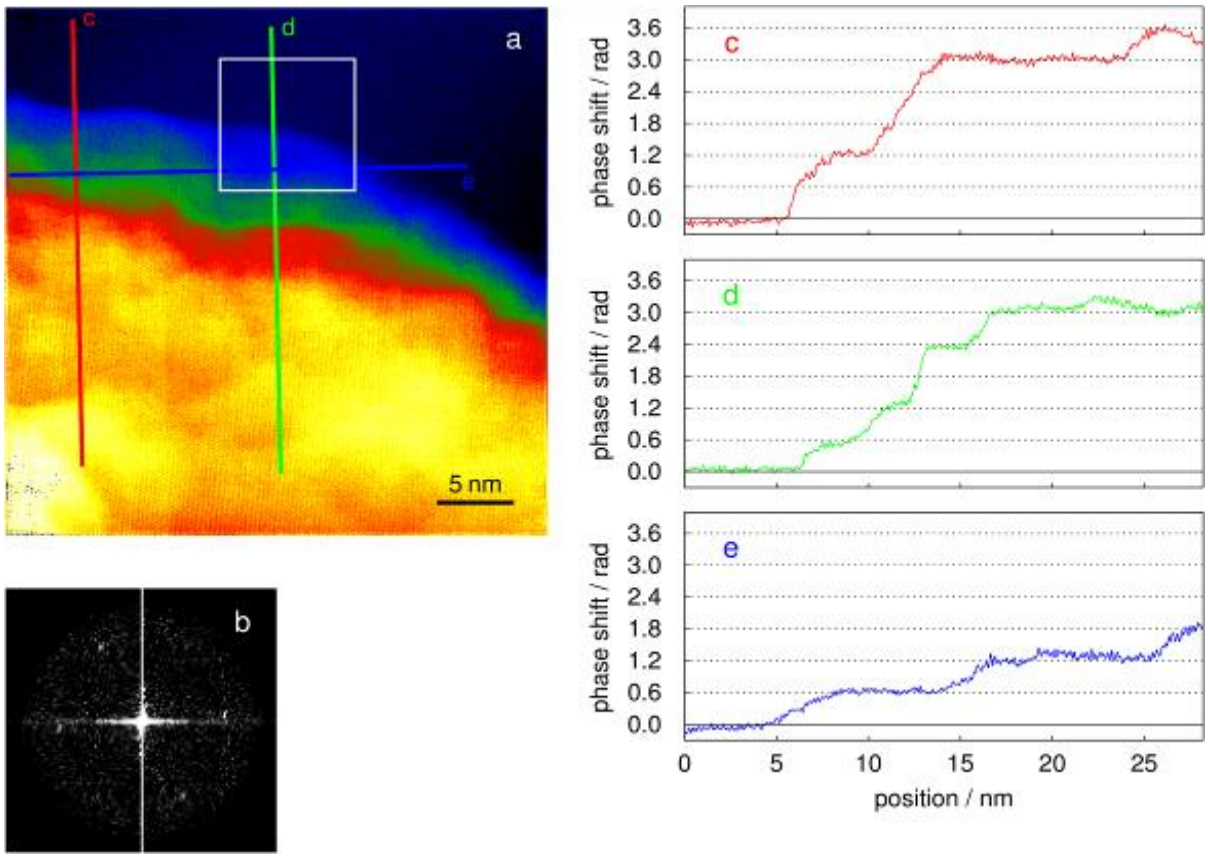

Figure 1. Electron holographic phase image of few-layer graphene. a) false color phase image showing the stacking of graphene layers; b) Fourier transform of the area indicated by the white box reveals corresponding diffraction spots; c), d, e) line profiles as indicated in a), revealing phase steps of 0.6 rad from single graphene layers.

Static and Dynamic Electric and Magnetic Imaging

IM.5.P111
Measurement and simulation of fogging electrons in a scanning electron microscope

S. Hosoi[1], M. Otani[1], K. KUmagai[1], M. Kotera[1]

[1]Osaka Institute Technology, Oosaka, Japan

m1m13318@st.oit.ac.jp
Keywords: fogging electrons, scanning electron microscope, electrostatic force microscope

In recent development of nano-technologies, electron beam (EB) is indispensable in processes, analyses, microscopy, evaluation, observation and measurement, etc. However, if a specimen is an insulator, electrons may be accumulated in the specimen and it is charged negatively or positively depending on materials or irradiation conditions. It has been understood that this charging mainly occurred locally in the specimen around the EB incident point, but in reality, backscattered electrons (BSEs) from the specimen hit a pole-piece plate of the objective lens (POL), which is located in front of the specimen surface, and re-backscattered electrons expose the specimen in a large area. In the present study electrons, produced by multiple scattering events between POL and the specimen, are called the fogging electrons (FGEs).[1] Although the energy of FGEs is low in general, but if they stay on the specimen surface, the charge produces a surface potential distribution. This potential may influence the performance of specific EB applications. We have studied the charging mechanisms of the specimen, and we found that the contribution of FGEs is not negligible. In order to understand the influence of the FGEs, first, it is necessary to find the spatial distribution of the FGEs. In the present study, we measured the distribution in a specimen chamber of an ordinary scanning electron microscope (SEM) (JSM-6490LA). Then, three-dimensional trajectory simulation of FGEs in a simplified configuration of the SEM is done to quantify the distribution, and the results are compared with experiment.

Figure 1 shows a concept of measuring the FGE current in the specimen chamber of the SEM. The EB current is measured using the Faraday cup set on the central electrode. Five concentric annular electrodes (2.5-4, 5-6.5, 7.5-9, 10-11.5 and 12.5-14 mm from the EB irradiation point) are made at a commercially available printed circuit board (PCB) to measure the radial FGE current distribution. The current at every electrode is measured by an electrometer. By changing the working distance (WD) of the electrode from the POL, the radial distribution is verified. On the other hand, electron trajectory simulation in and out the specimen surface considering the existence of the POL is performed. The FGE current density distribution as a function of WD is shown in figure 2, and good agreement between the experiment and the simulation is obtained.

In order to study the FGE distribution in a range of □m, we construct the surface potential measurement system based on the electrostatic force microscope in the SEM specimen chamber.[2] Figure 3 shows an illustration of the system to measure a surface potential distribution, built by FGE irradiation to the insulating specimen. The specimen is 300 nm-thick FEP film on a conductive substrate. Electrically grounded Au wire of 25 □m□ is set just above the cantilever of 50 □m wide to measure the surface potential. EB is irradiated at the centre of the top surface of the Au wire. As illustrated in the figure, only FGEs irradiate the specimen surface. After charging the specimen, we measure the surface potential distribution.

Figure 4 shows a potential distribution obtained experimentally, when Vacc=3 kV with a beam current 1 nA for EB to irradiate the Au wire. In this configuration, if EB of Vacc is between 1 and 3 kV, electrons are accumulated in the FEP layer and the potential shows a negative value on the specimen.[2] FGE trajectories are calculated by a Monte Carlo simulation in the specimen, and straight trajectory in vacuum as shown in Figure 5, the FGE number distribution is obtained at the specimen surface as shown in Figure 6. Because of the Au wire, there is a dip in the centre of the distribution as the shade. In this case the typical FGE energy is between below 3 keV, and they will stop in the FEP layer and the surface potential should be negative. Considering the number distribution and the potential vs. Vacc, the lateral distribution of surface potential can be obtained. The calculated potential distribution is compared with experiment in Figure 4, and fairly good agreement is obtained. However, the WD adopted in the calculation is as small as 300nm, and quantitative comparison cannot be done.

In reality, if WD is large as 20 mm, the probability of FGEs to collide the Au wire is very small, and the dip in the lateral distribution of figure 4 becomes small.

1. M. Kotera, T. Maekawa, Jpn. J. Appl. Phys. 48, 06FB05 (2009).
2. M. Kotera and A. Osada, M. Otani and Y. Ohara, J. Vac. Sci. and Tech., B29(6), 06F316-1 (2011).

3. This work was supported by KAKENHI (C) 22560026

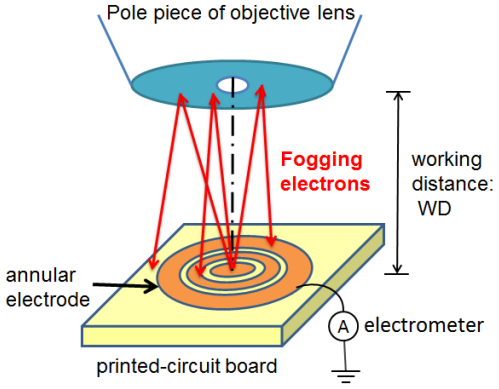

Figure 1. Schematic of the measurement system of the FGE current on the specimen.

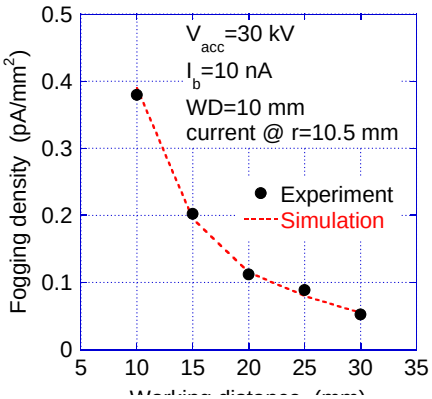

Figure 2. FGE current density variations for one annular electrode for different WD's.

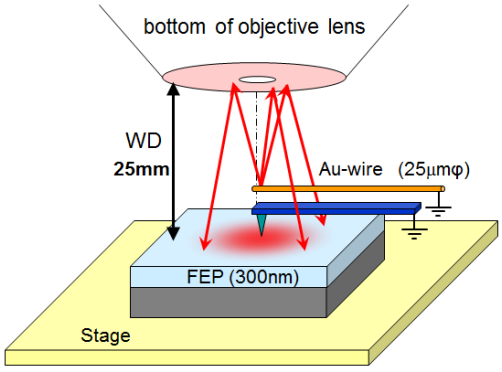

Figure 3. Schematic of charging and measuring the surface potential produced by FGEs.

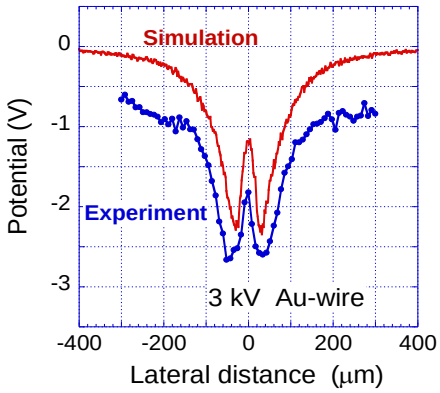

Figure 4. Surface potential distribution obtained by experiment is compared to the simulation, where contributions of FGEs are taken into account with the shade of the Au wire.

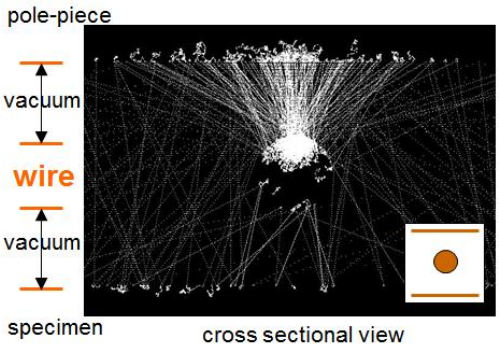

Figure 5. Trajectory of FGEs simulated in (POL)-(Au wire)-(specimen) system in an SEM specimen chamber.

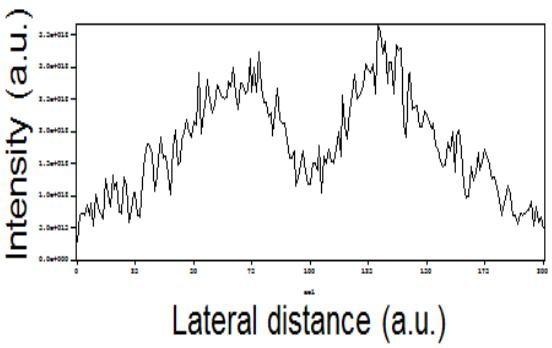

Figure 6. Number distribution of FGEs arrived at the specimen surface.

Static and Dynamic Electric and Magnetic Imaging

IM.5.P112
Measurements of surface potential distribution at FEP resist film on a conductive substrate irradiated by electron beam

K. Kumagai[1], M. Otani[1], S. Hosoi[1], M. Kotera[1]

[1]Osaka Institute of Technology, Osaka, Japan

m1m13309@st.elc.oit.ac.jp
Keywords: electrostatic force microscopy, charging of insulators, surface potential distribution

It is well known that insulating resist film charges up during electron beam (EB) irradiation, and even several volts of the potential gives a severe influence on the position accuracy of 10 nm scale in the EB lithography in an area of several hundreds of mm^2.[1] In order to avoid such a problem in a future instrumentation, we have been trying to quantify the surface potential at a certain EB irradiation condition.

The measurement system is based on the electrostatic force microscope (EFM).[2] Figure 1 shows the schematic diagram of the EFM system under development in the scanning electron microscope (SEM) specimen chamber. Since the conductive probe is electrically grounded, as it approaches a charged surface, charge of the opposite sign is induced at the probe, and attractive force is appeared between the specimen surface and the probe. When the surface potential is +Vs, the force shows its minimum when the applied voltage to the specimen holder is –Vs. Using this null-balance method, the surface potential of a specimen is obtained in our SEM (JSM-6490LA) specimen chamber. We measured the surface potential of 300nm-thick electron resist (FEP171) on 70 nm-thick Cr on a bulk glass substrate with 30 mm on one side.

Figure 2 shows an illustration of the configuration of EB irradiation and the subsequent measurement of the surface potential distribution by the EFM probe. EB irradiation is done by raster scan, and the area is a square with 100 □m on a side. By scanning the position of the probe, the spatial potential distribution is obtained. During the EB irradiation, EFM probe is kept more than several millimetres away from the irradiating area, and after the irradiation the probe comes back to the central field and the SEM stage is scanned to measure the potential along the line from -600 □m to 600 □m. In order to eliminate an influence of residual charge in every measurement, the surface potential, which is measured before the EB irradiation, is subtracted from the potential after EB irradiation.

Figure 3 shows the lateral surface potential distribution, as the EB accelerating voltage (Vacc) is 30 kV, the EB current is 1 nA, and the irradiation period is 60 s. In a region where EB is irradiated the potential is kept constant around +2.6 V, and a large negative potential around -1.6 V is obtained at around 130 □m outside the edge of the irradiated region.

The positive potential at the EB irradiated area can be understood by the following explanation: [2] EB at Vacc of 30 kV can penetrate through the FEP layer and almost all electrons are just transmitted, but there are a small number of scattered electrons under the irradiated area. Nevertheless, those scattered electrons are evacuated toward the conductive substrate by electron beam conduction (EBIC). In addition to the mechanism, secondary electron (SE) emission from the FEP surface may result in a positive potential at the surface.

The negative potential outside the irradiated region can be explained by the following mechanisms: Electrons scattered laterally in the FEP layer or backscattered electrons from the substrate may be stopped and accumulated, because they are far from the irradiated region, and they will not be evacuated by the EBIC. The electron range of electrons of Vacc=30 kV in FEP or backscattered electron range from the substrate is around 10 □m and the maximum negative potential may be found around +/-60 mm in the lateral distance. In addition, since the width of the cantilever is 50 □m, the lateral resolution of the present measurement system is about 50 □m, and this negative potential might be explained. On the other hand, there is a possibility that the negative potential might be attributed to re-backscattered electrons from the pole-piece of the objective lens of the SEM. As a matter of fact, it is known that contribution of “SE3” electrons, which are generated in the wall or optical components are not negligible in the SEM image. We call these electrons generated in the specimen chamber by the multiple backscattering are the “fogging electrons”. Since the lateral distance is larger than the electron range of EB, the possibility of fogging electrons may be the cause of the negative potential.

Figure 4 shows a two-dimensional surface potential distribution at the same experimental condition of figure 3. Since the measurement takes several hours, because of the charge decay the original distribution is deformed. Taking into account the Laplace equation in the field of the measurement, the reconstructed distribution is obtained. Regarding its high symmetric property, it is clear that our EFM system has high stability and high repeatability.

1. N. Nakayamada et al., Proc. of SPIE Vol.8081 (2011).
2. M. Kotera and A. Osada, M. Otani and Y. Ohara, J. Vac. Sci. and Tech., B29(6), 06F316-1 (2011).

3. This work was supported by KAKENHI (C) 22560026.

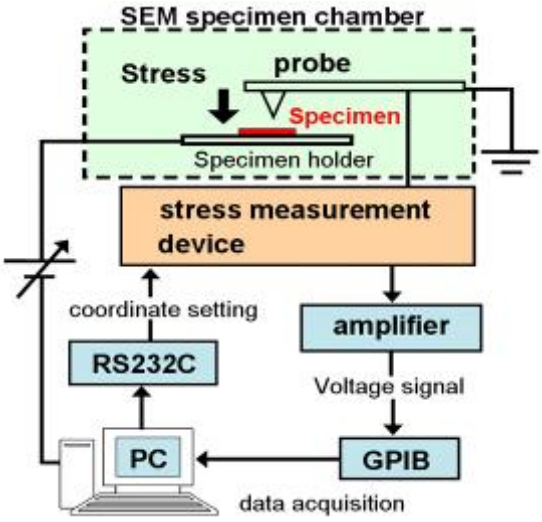

Figure 1. Schematic diagram of the measurement system based on the EFM.

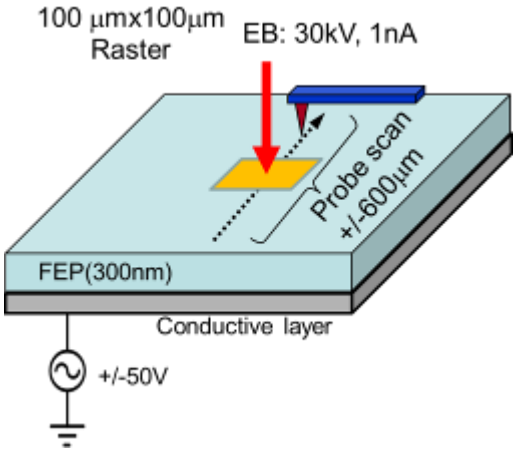

Figure 2. Procedure of the surface potential distribution measurement after EB irradiation at various Vacc's

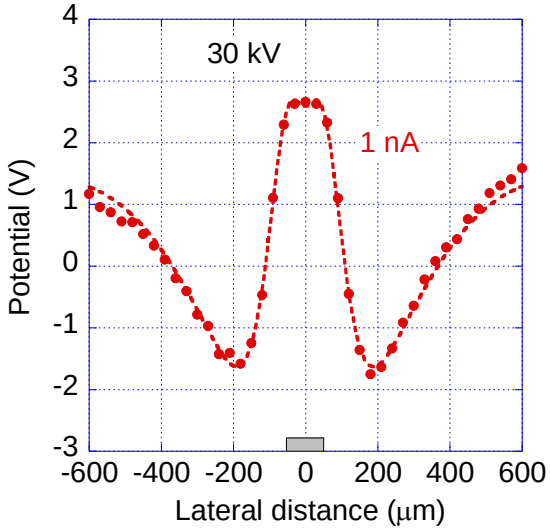

Figure 3. Lateral potential distribution of an EB irradiated surface of the specimen.

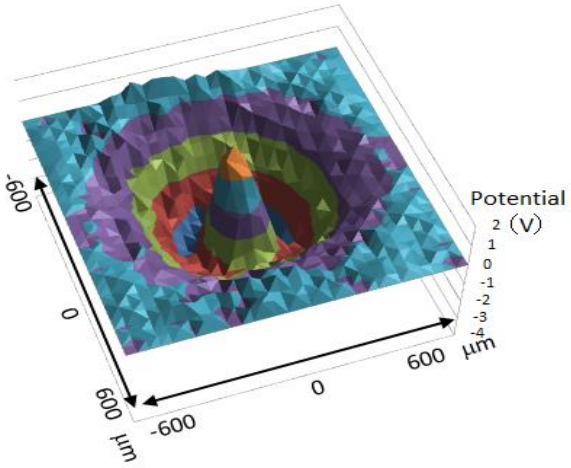

Figure 4. Two-dimensional potential distribution of an EB irradiated surface of the specimen

Static and Dynamic Electric and Magnetic Imaging

IM.5.P113
Holographic Tomography of Fermi Level Pinning at Focussed Ion Beam Milled Surfaces

S. Sturm[1], D. Wolf[1], A. Lubk[1], A. Lenk[1], H. Lichte[1]

[1]TU Dresden, ISP, Triebenberg Laboratory, Dresden, Germany

Sebastian.Sturm@triebenberg.de
Keywords: holography, tomography, electrostatic potential, electronic devices

Tailoring the distribution of dopants in semiconducting materials allows engineering their electronic band structure, which is the basis for modern electronic devices such as diodes, transistors, varistors and many others. It is furthermore well understood that surface states at semiconductor-metal/ insulator/vacuum interfaces have a large impact on the band structure hence influence the electric properties of the devices. Therefore, large efforts have been put in engineering surface states in order to either suppress or enhance the pinning effect.

Since the early works of e.g. Rau et al. [1], electron holography (EH) was prospected to become a key technique for measuring dopant profiles in semiconductor devices via a two-step procedure: (i) reconstruction of a 2D map of the projected electrostatic potential from the phase through

$$\varphi = C_E \int V(x, y, z)\,\mathrm{d}z$$

and (ii) computation of the dopant distribution within an appropriate model relating potential and dopant concentration (e.g. drift-diffusion model). While it has been demonstrated that quantitative potential maps of diffusion potentials can be obtained at nm resolution (e.g. [2]), computed dopant concentrations frequently were significantly lower than SIMS reference data especially at lower dopant concentrations [3]. As part of large efforts invested into resolving that issue, several explanations have been put forward for the observed discrepancy. Among those, it was pointed out that the potential is not constant along projection direction because TEM sample preparation modifies the surfaces. In particular, the most frequent Focussed Ion Beam (FIB) preparation amorphizes the surface layer to a certain depth and dopes the adjacent crystalline layer by introducing Ga. To consider this effect, models of so-called “dead” or “electrically inactive” surface layers followed by a transition layer with increasing electrical activity have been introduced (e.g. [4]).

However, detailed investigations of the surface effect were hampered by the loss of resolution along electron beam direction during projection. Several groups tackled this projection problem by performing electron holographic tomography (EHT) [5,6]. Nevertheless, quality and focus of these investigations did not allow surface potential reconstructions so far. Here, we fill this gap by providing direct evidence for Fermi Level Pinning and thus band bending at FIB-prepared surfaces by employing EHT. We present the most crucial steps in the holographic (optimal filter, phase unwrapping) and tomographic reconstruction (reconstruction algorithm, regularization), facilitating an unambiguous band bending detection. This allows analyzing the characteristic parameters of the bending, i.e. built-in voltage and depletion layer width; and correlate the findings with dopant concentrations. For our investigations we use the two test materials Si and Ge containing differently doped pn-junctions. The needle structures suited for tomographic investigations have been prepared by standard FIB (30 kV Ga^+-ions) milling.

As an example, a reconstructed potential slice of a Si pnp structure is depicted in Fig. 1. One clearly observes opposite band bendings within p and n regions toward the surfaces. This indicates that the Fermi Level has been pinned by the surface states in the band gap most probably introduced by FIB induced damages. The widths of the corresponding depletion regions correlate with the dopant concentration. A similar behaviour is observed with the Ge structures (see second example in Fig. 2). In Ge, however, the surface states are close to the valence band (e.g. [7]), leading to a strong bending only within the n-doped regions.

1. Rau et al., Physical Review Letters 82, 1999, 2614-2617.
2. Li et al., Ultramicroscopy 94, 2003, 149-161.
3. Formanek P. et al., J. Phys.: Condens. Matter 16, 2004, 193-200
4. Lenk, A. et al, Springer Proceedings in Physics, Volume 107, 2005, 205-208, ISBN: 978-3-540-31914-6
5. Twitchett-Harrison et al. Nano Letters 7, 2007, 2020-2023
6. D Wolf et al., Ultramicroscopy 110, 2010, 390
7. Robertson, J. & Lin, L. Conf. Proceedings IEDM 2009 IEEE International, 2009, 1-4.
8. This work is funded by the European Union (ERDF) and the Free State of Saxony via the ESF project 100087859 ENano. We also acknowledge financial support from the European Union under the Seventh Framework Programme under a contract for an Integrated Infrastructure Initiative. Reference 312483 - ESTEEM2

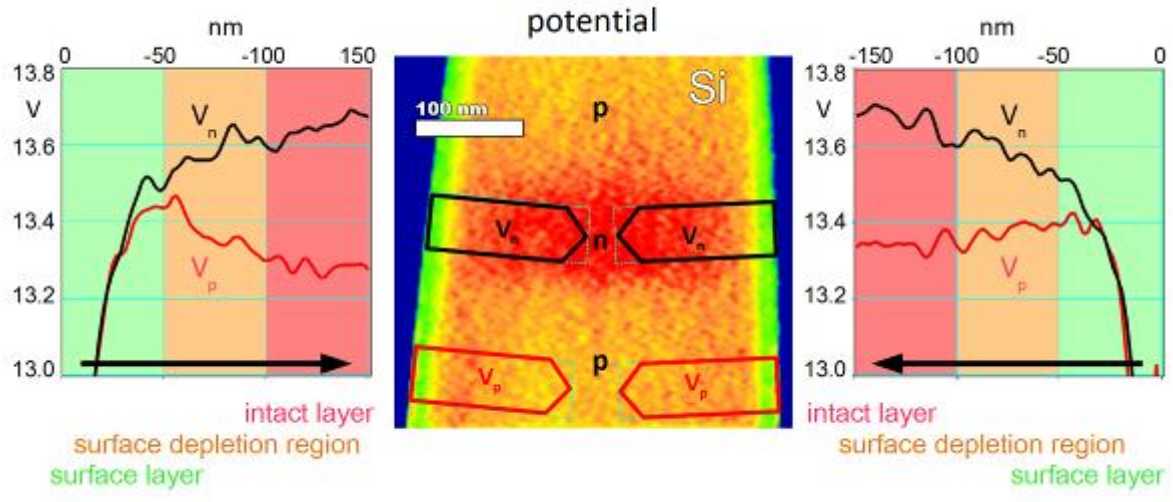

Figure 1. Slice through 3D potential of a Si-Needle with pnp-structure, arrows indicating the direction of the profiles. Adjacent profiles show the potential distribution from the FIB-affected surface, which pins the Fermi-level to the intact region in the n-doped area (black) and in the p-doped area (red), respectively.

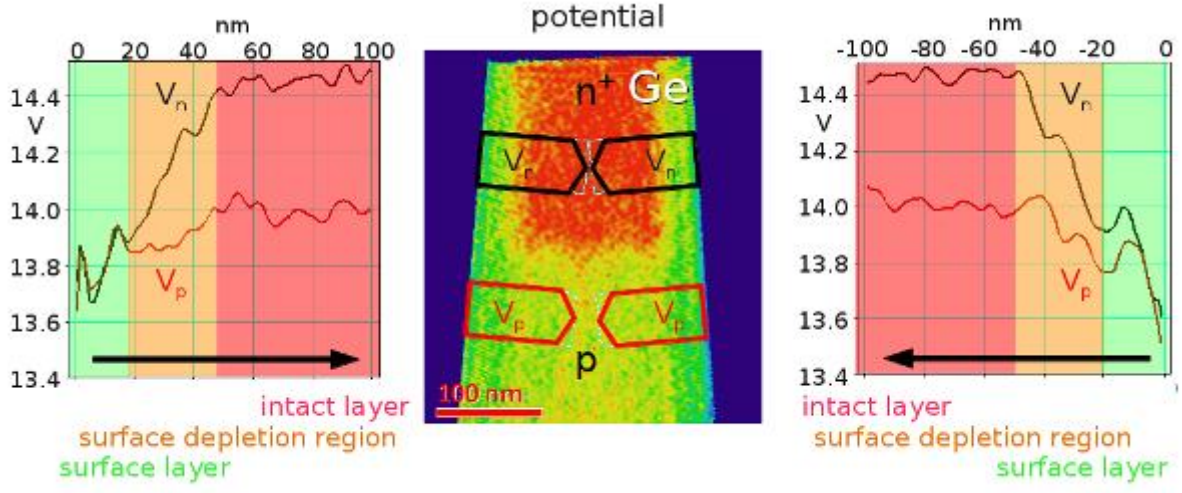

Figure 2. Slice through 3D potential of a Ge-Needle with pn-junction, arrows indicating the direction of the profiles. Adjacent profiles show the potential distribution from the FIB-affected surface, which pins the Fermi-level to the intact region in the n-doped area (black) and in the p-doped area (red), respectively.

Static and Dynamic Electric and Magnetic Imaging

IM.5.P114
Measurement of the electrostatic potential distribution in an in-situ biased p-type silicon field effect transistor using the combination of a Nanofactory-TEM-holder and Electron Holography

A. Lenk[1], F. Börrnert[1], S. Sturm[1], D. Wolf[1], F. Röder[1], A. Lubk[1], H. Lichte[1]

[1]TU Dresden, Triebenberglabor, Dresden, Germany

Andreas.Lenk@Triebenberg.de
Keywords: In-situ Biasing, Dopant Profiling, Electron Holography

Electron holography is an established analysis method for both qualitative and quantitative measurements of diffusion potentials, which appear due to locally varying dopant concentrations in the matrix of a semiconductor [1,2]. The phase $\varphi(x,y)$ of a transmitted electron wave is modulated by variations of the electrostatic potential perpendicular to the electron beam, whereas variations in z-direction parallel to the electron beam are averaged in the projection process:

$$\varphi(x,y) = \sigma \cdot \int_{-\infty}^{\infty} V(x,y,z)\, dz = \sigma \cdot V_{proj}(x,y)$$

with σ the interaction constant depending solely on the accelerating voltage of the microscope.

Electrical biasing changes the potential distribution within such samples; in particular total potential differences across pn-junctions are either de- or increased. The ultimate goal of such experiments is to estimate the true concentration of electrically active dopants, as one often finds a difference between theoretically expected and measured potential drop over a pn-junction. This applies especially for FIB-prepared samples, where a significant number of dopants is obviously deactivated by the Ga^+-sputter process. Holographic in-situ biasing experiments at pn-junctions have been performed in the past [2,3]. Here, electrical biasing is applied directly on a FIB-prepared p-FET structure.

First step of a FIB-preparation is covering the area of interest with a relatively stable material, in this case platinum. The resulting platinum bar covers source, drain and gate of the p-FET and works as an electrical contact for the biasing of the sample. The tungsten probe of a Nanofactory TEM-holder connects the platinum with the voltage source (Figure 1). The bulk silicon of the sample is grounded, because it is mounted on a copper half disc that is electrically connected to the holder shaft. By applying voltages in the range between –8 V and +8 V, the potential distribution in the silicon beneath drain and source changes significantly (Figure 2).

For every biasing voltage, series of 50 holograms were recorded at an exposure time of 10 s each, which is limited by the stability of the used Philips CM 200 Lorentz TEM. All holograms with a fringe contrast larger than 2.5 % were reconstructed using Fourier Reconstruction methods. Subsequently, the resulting object waves were aligned using a semi-automated cross-correlation procedure [4]; their phases were adjusted in offset and tilt using a certain reference area. Finally, the phases were averaged to increase the signal-noise ratio as much as possible.

Unfortunately, electrical stray fields from the tungsten probe strongly influence the whole region around the p-FET, which renders the usual global phase correction impossible. Adding offset and phase wedge works here very localized as correction for only a small part of the image. Therefore, the interpretation of the phase images was performed for three different parts of the image using three different corrective phase wedges. The green dotted rectangles in Figure 2a, 2b and 2c frame the regions for which the corrective phase wedge was added in each image. The phase profiles illustrate the phase curvature under the different biasing voltages, whereas the images show the phase distribution only for the biasing voltage of –8 V. Further investigations of the results, for example calculating the Laplacian of the potential distribution, eventually intend to reveal evidence of an opening and, respectively, closing of the channel beneath the gate oxide.

1. W.-D. Rau, P. Schwander, F. H. Baumann, W. Höppner, and A. Ourmazd, PRL 82 (1999), p 2614
2. A. C. Twitchett, R. E. Dunin-Borkowski and P. A. Midgley, PRL 88 (2002), p 238302
3. H. Myung-Geun, D. J. Smith and M. R. McCartney, APL 92 (2008), p143502
4. D. Wolf, Triebenberg Software Package for Electron Holography
5. We gratefully acknowledge funding of the European Projects NanoHiTEC and ESTEEM2 (funded by the European Commission within the 7th Framework Programme under References 263306 and 312483, respectively) and ENano (funded by the European Union (ERDF) and the Free State of Saxony via the ESF project 100087859) !

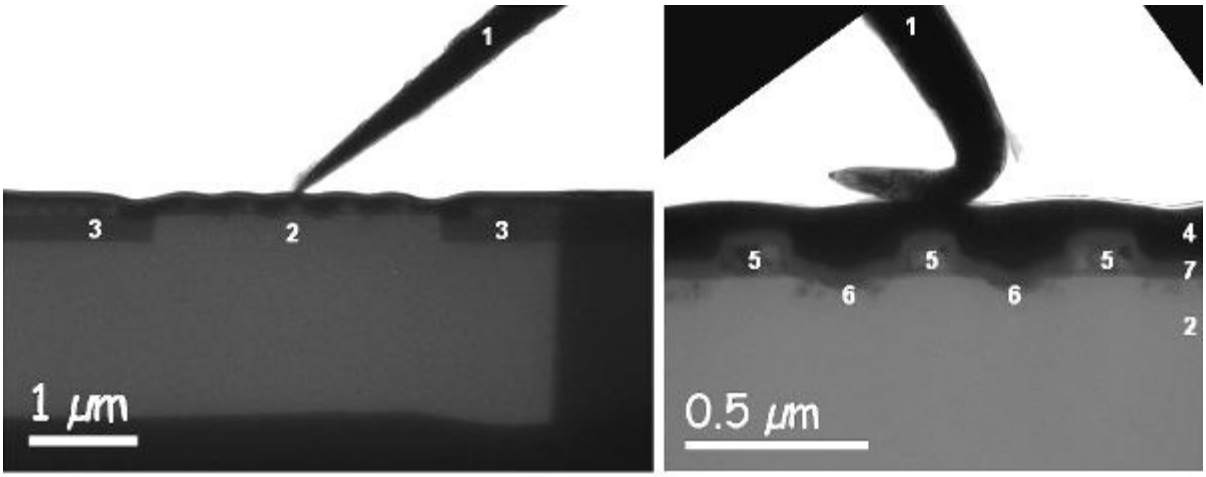

Figure 1. Contacting the FET: **Left:** The needle (1) is connected to the electron transparent FIB-lamella, which consists of a bulk-silicon pad (2) containing 5 FET structures surrounded by insulating oxide regions (3) **Right:** Bending of the needle enlarges the contact area with the platinum bar (4) and increases the elasticity of the whole connection. The gate contact (5) and the drain/source contact holes (6) were coated with amorphous silicon (7) before the FIB-cutting of the lamella was started

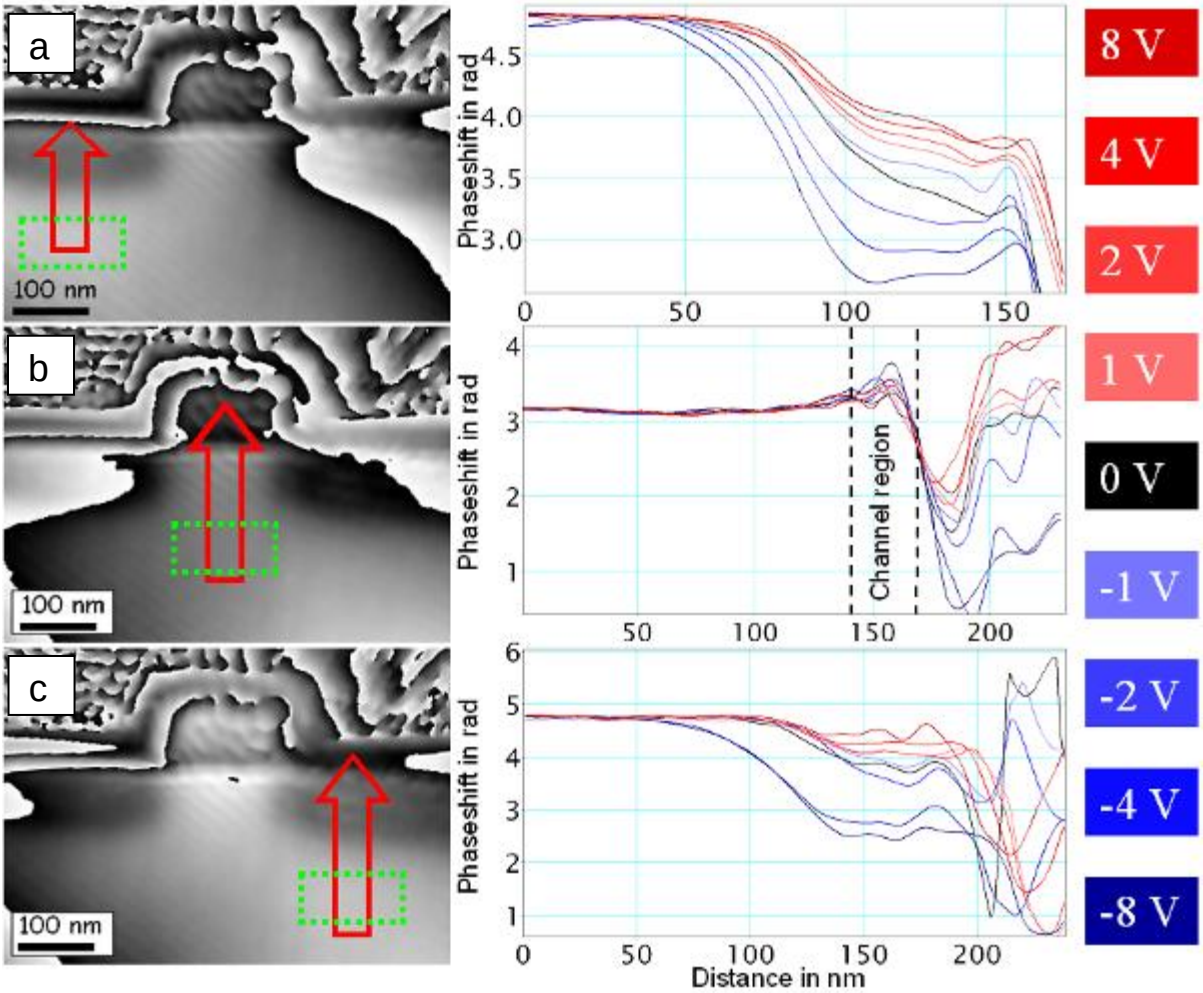

Figure 2. Measurement of phase shift beneath drain (a), gate (b) and source (c) under different biasing **Left:** Same phase image, three times differently corrected: The green dotted rectangle frames the region that was planished by adding a respective phase wedge. The red arrows indicate region and direction of the phase profiles shown next to the respective image. **Right:** Phase profiles for different voltages applied at the tungsten probe.

Static and Dynamic Electric and Magnetic Imaging

IM.5.P115
Focused ion beam specimen preparation for electron holography of electrically biased thin film solar cells

M. Duchamp[1], M. den Hertog[2], R. Imlau[1], C.B. Boothroyd[1], A. Kovacs[1], A.H. Tavabi[1], R.E. Dunin-Borkowski[1]

[1]Research Centre Juelich, Institute for Microstructure Research, Juelich, Germany
[2]CNRS, Institut Neel, Grenoble, France

martial.duchamp@gmail.com
Keywords: Electron holography, biased TEM specimen, thin film solar cell, FIB

Thin films of hydrogenated Si (Si:H) can be used as active absorber layers in solar cells deposited on low cost substrates using plasma-enhanced chemical vapour deposition [1]. In order to improve the efficiencies of such solar cells, the nature of the defects that act as charge recombination centres and decrease the internal electric field in the active Si layer needs to be understood. Chemical analysis using transmission electron microscopy (TEM) reveals diffusion of ZnO and/or B from the top layers into the active Si layer [2, 3]. Measurements of bulk electrical properties suggest that the diffusion of dopants creates a conductive path between the two electrical contacts of the cell, resulting in a short circuit and degrading the carrier collection and overall cell efficiency. The carrier separation processes in thin film Si:H cells are driven both by diffusion and by the internal electrical field generated by the ~20 nm-thick *n* and *p*-doped Si:H layers that are deposited on both sides of the ~2 µm-thick intrinsic Si layer. In order to understand the recombination mechanism and the internal electric field in such an *n-i-p* stack, direct observation of these two quantities at the nanometre scale is needed. Carrier collection can be mapped with the required spatial resolution by recording the electron beam induced current (EBIC) signal, while the internal electric field can be measured using off-axis electron holography [4]. Previous attempts to measure internal electrical fields in solar cells have been limited by poor signal-to-noise ratio and difficulties in interpreting measured holograms. These limitations can be overcome by measuring the electron holographic phase shift as a function of applied electrical bias *in situ* in the TEM. An EBIC signal can then also be measured, either at 0V or in the presence of a forward or reverse bias.

One of the major limitations for the preparation of electrically biased TEM specimens of solar cells is the lack of a reliable and routine procedure that provides both high specimen quality (with few defects introduced by TEM specimen preparation) and high conductivity of the electrical contacts [5]. Here, we propose a fully focused ion beam (FIB) based approach that can be used to prepare a TEM specimen for electron holography of a thin film solar cell using conventional lift-out specimen preparation and a home-made MEMS chip. Our procedure allows an electrically biased TEM specimen to be prepared in less than a day with a high success rate. The novelty of our approach results from the use of: (1) an Omniprobe manipulator to transfer the specimen from the bulk solar cell to the homemade MEMS chip; (2) an FEI Omniprobe grid support to handle the MEMS chip; (3) ion-beam-deposited Pt to achieve low resistance electrical contacts without damaging the region of interest; (4) back-side ion milling to obtain a specimen that is suitable for electron holography.

Figure 1a shows the central part of a home-made MEMS support, onto which a TEM specimen of a solar cell has been attached using two ion-beam deposited contacts. Figure 1b shows a FIB-prepared solar cell ready for electron hologram acquisition. The use of back-side milling has minimised any curtaining effects that would have resulted from uneven milling due to defective regions in the solar cell, which is now only present on the top contact. The final electrically biased TEM specimens showed a strong decrease in electrical resistance from 2.4 to 1kΩ when the ion energy was decreased from 8 to 2 kV for the final cleaning step.

Preliminary electron holography experiments were performed in Lorentz mode in a Titan TEM equipped with an image C_S corrector and a double biprism. For the present experiments, a voltage of 80 V was applied to the upper biprism. An electron hologram acquired from the intrinsic Si region in the solar cell is shown in Fig. 2a. The interference fringes in the FIB-prepared specimen have sufficient contrast to reconstruct the amplitude and phase, as shown Figs 2b and c, respectively. The present specimen preparation technique is applicable for *in situ* electrical biasing of any region of interest in a bulk sample, for both EBIC and electron holography studies. Furthermore, the use of FIB milling allows a wide variety of specimen geometries to be fabricated.

1. R .Biron *et al.*, New progress in the fabrication of n-i-p micromorph solar cells from opaque substrates, Sol. Energ. Mat. Soc C. 114 (2013) 147
2. M. Duchamp *et al.*, Compositional study of defects in microcrystalline silicon solar cells using spectral decomposition in the scanning transmission electron microscope, Appl. Phys. Lett. 102 (2013) 133902
3. M. Duchamp *et al.*, Electron energy-loss spectroscopy of boron-doped layers in amorphous thin film Si solar cells, J. Appl. Phys. 113 (2013) 093513
4. D. Cooper *et al.*, Field mapping with nanometer-scale resolution for next generation of electronic devices, ACSNano 11 (2011) 4585
5. S. Yazdi, Towards electron holography of working transistors, PhD Thesis of Imperial College London (2012)
6. The authors acknowledge financial support from the European Union under the Seventh Framework Programme under a contract for an Integrated Infrastructure Initiative. Reference 312483 – ESTEEM2.

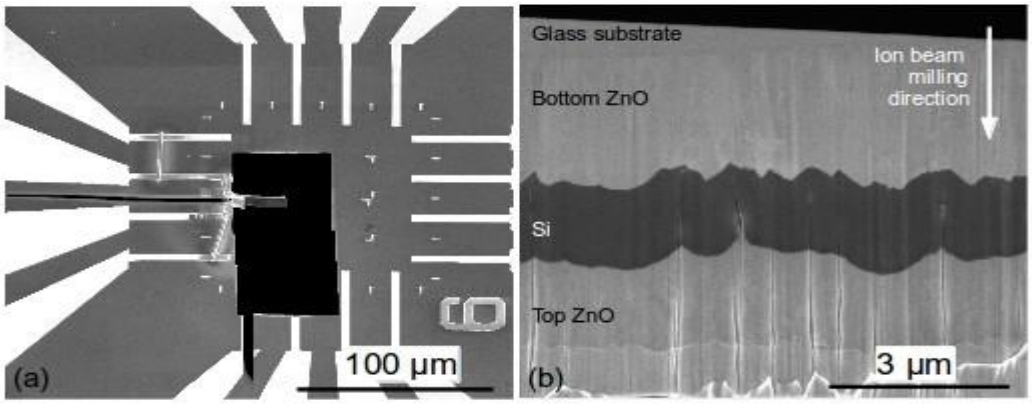

Figure 1. (a) Scanning electron micrograph of the central part of a home-made MEMS support, on which a TEM specimen of a solar cell is attached. (b) FIB-prepared TEM lamella of a solar cell ready for TEM examination. The ion beam milling direction is opposite to the growth direction of the sample (i.e., back-side milling)

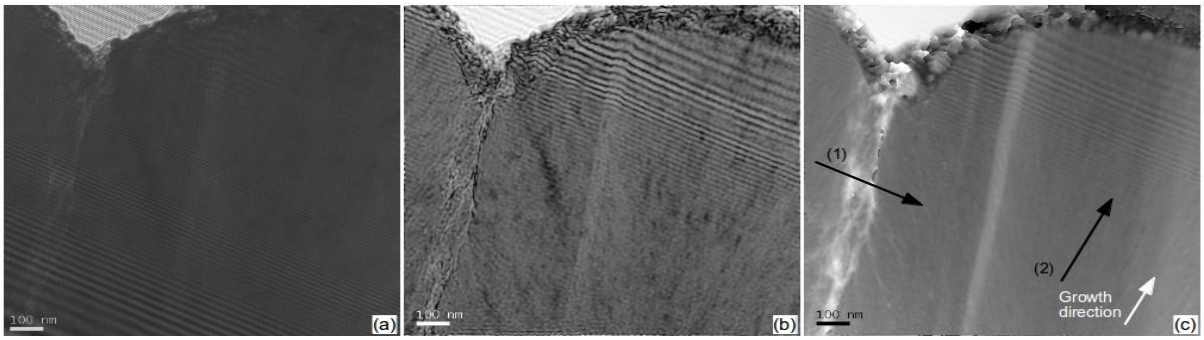

Figure 2. (a) Off-axis electron hologram recorded from the specimen shown in Fig. 1, which is in a geometry suitable for *in situ* electrical biasing. (b) Amplitude and (c) unwrapped phase images reconstructed from the hologram shown in (a). Arrows (1) and (2) indicate regions from which the 50-pixel-wide line profiles show in Fig. 3 were obtained. The white arrow indicates the growth direction of the solar cell.

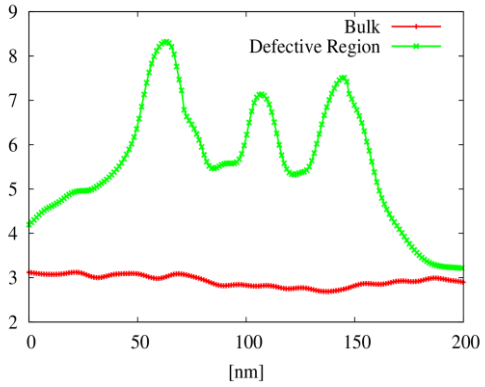

Figure 3. Linescans of the phase shift in radians, obtained from the phase image of the solar cell shown in Fig. 2c.

Static and Dynamic Electric and Magnetic Imaging

IM.5.P116
Fabrication and investigation of electrostatic condenser twin aperture for EMCD experiments

A. Pritschet[1], J. Zweck[1]

[1]Universität Regensburg, Physik, Regensburg, Germany

josef.zweck@physik.uni-regensburg.de
Keywords: EMCD, phase plate, aperture, simulation, beam cross-over

At the EMC2008 we have proposed a modified experimental setup [1] for overcoming the quality and orientation requirements in EMCD (Electron Magnetic Chiral Dichroism) [2] experiments. Our proposed changes to the setup are the exchange of a standard condenser aperture with a *twin aperture* (see Figure 1), which consists of two holes; each equipped with a ring electrode (Boersch phase plate [3]) allowing to adjust a phase difference between the transmitted beams.

Now we present a twin aperture prototype – together with a customized condenser aperture holder which is fabricated from a 25µm thick platinum foil. Figure 2 illustrates the fabrication process and Table 1 states the layer thicknesses. The choice for this substrate and thickness is based on the encounter of threefold astigmatism and other charging effects (see Figure 3) during the usage of thin (≤ 2µm) twin apertures fabricated from Si_3N_4 membranes. By means of Monte Carlo simulations of electron trajectories [4] the thickness of 25µm is determined to be sufficient for absorption of 200keV electrons in the Pt foil. Figure 4 shows the penetration probability derived from this simulation.

Furthermore we conduct theoretical and experimental investigations regarding the electron optical characteristics of these devices.

Using finite element simulations [5] we derive analytical models for the phase shift depending on the aperture plane coordinate and the applied potential at the ring electrodes. Using Fourier optics we investigate the wave function of a focused spot in the sample plane, which is the Fourier transform of the aperture function assuming an incident plane wave. The aperture function takes into account the aperture shape, our phase shift model and aberrations.

These calculations show that aberrations and deviations from a constant phase shift model [3] have negligible influences on the wave function in the sample plane in regions close to the optical axis (see Figure 5).

Using different experimental techniques we take a closer look on charging effects in thin twin apertures which we intend to avoid now by using a thick Pt-based device. After overcoming these effects we demonstrate the successful observation of an electron beam cross-over in the sample plane (Figure 6) with a diameter (=full width at half maximum) of ≈ 7nm. The cross-over shows no interference fringes as predicted by theory due to instabilities of the microscope.

1. A. Hasenkopf and J. Zweck, Proceedings of EMC 2008 – Late Breaking Posters (2008)
2. P. Schattschneider, S. Rubino, C. Hébert J. Rusz, J. Kunes, P. Novák, E. Carlino, M. Fabrizioli, G. Panaccione and G. Rossi, Nature 441 (2006), p. 486 – 488
3. T. Matsumoto and A. Tonomura, Ultramicroscopy 63 (1996), p. 5 – 10
4. D. Drouin, A. R. Couture, D. Joly, X. Tastet, V. Aimez and R. Gauvin, Scanning 29 (2007), p. 92 – 101
5. J. E. Guyer, D. Wheeler and J. A. Warren, Computing in Science & Engineering 11 (2009), p. 6 – 15

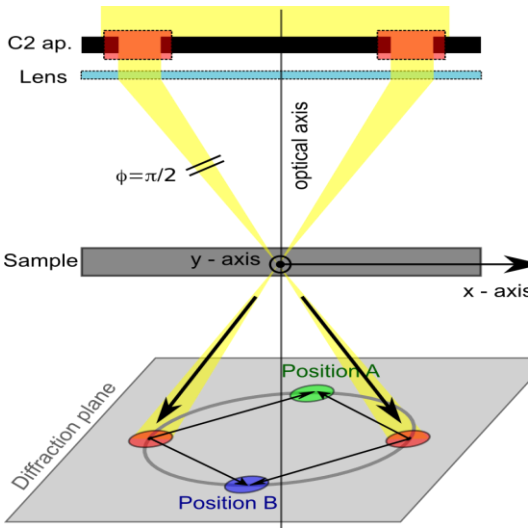

Figure 1. Schematic setup. Each aperture hole is equipped with a phase plate (red rectangle). The two transmitted beams by the aperture are equivalents to Bragg beams in the intrinsic method and define a Thales circle with measurement positions **A** and **B**.

Layer	Pt	SiO	Au	SiO	Au
Thickness [µm]	25	0.4	0.1	0.4	0.1

Table 1. Layer thicknesses of fabricated twin aperture.

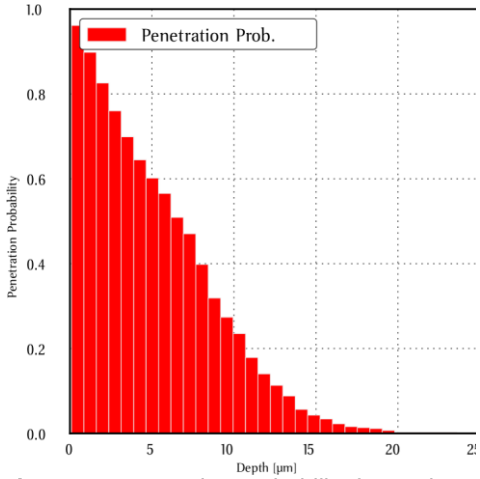

Figure 4. Penetration probability for 200keV electrons in platinum derived from electron trajectory simulations.

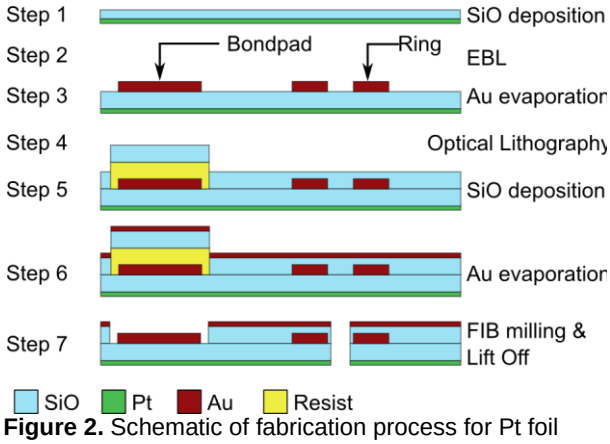

Figure 2. Schematic of fabrication process for Pt foil substrate (layer thicknesses not drawn to scale).

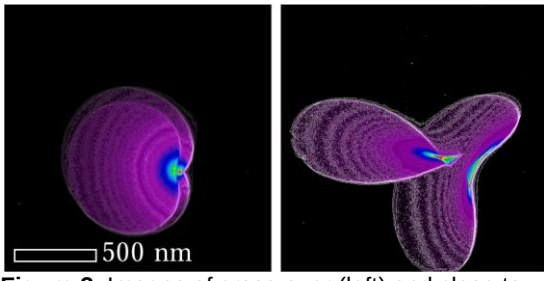

Figure 3. Images of cross-over (left) and close to cross-over (right). Charging effects introduce strong threefold astigmatism and increase spot diameter drastically.

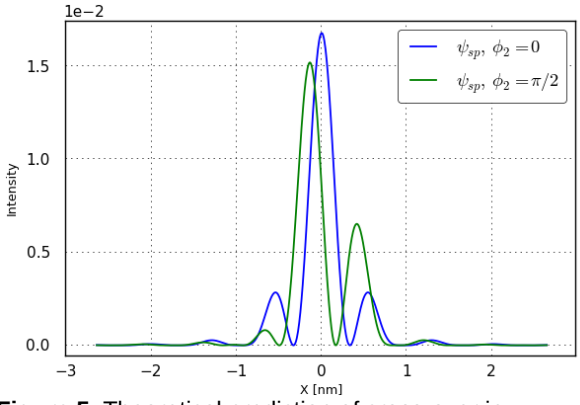

Figure 5. Theoretical prediction of cross-over in sample plane for 200keV electrons.

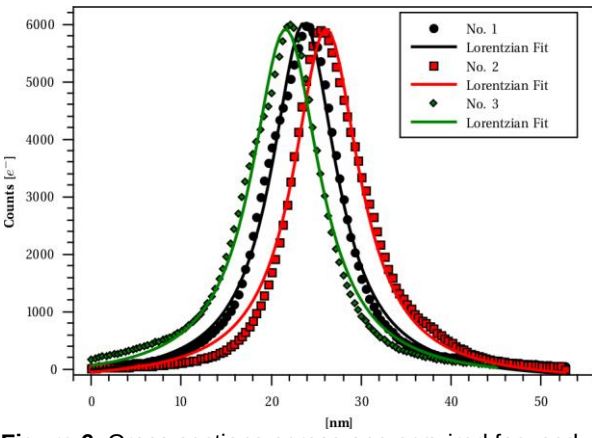

Figure 6. Cross sections across one acquired focused spot along different directions at 200kV. FWHM ≈ 7nm.

3D Imaging and Analysis

IM.6.117
STEM-EDX nano-tomography in a TEM

K Lepinay[1,2], F Lorut[2], R Pantel[2], T Epicier[1]

[1]MATEIS, umr CNRS 5510, Bât. Blaise Pascal, INSA de Lyon, F-69621 Villeurbanne Cedex
[2]STMicroelectronics, 850 rue Jean Monnet F-38926 Crolles Cedex, France

thierry.epicier@insa-lyon.fr
Keywords: nano-tomography, STEM-EDX, chemical 3D, CMOS transistor, microelectronic, nanowire

Performing 3D experiments at a nanometric level in a Transmission Electron Microscope (TEM) has almost become a routine technique in Materials Science. Basically, tomography in the TEM is performed as it is in X-ray tomography: a series of tilted projections on the object of interest is acquired over a large angular domain; after in situ and post-mortem alignment, these images are used as an input for dedicated algorithms enabling the volume to be reconstructed [1, 2]. The development of tilting tomography in Materials Science has indeed been slowed down, compared to tomography in Biology, because conventional TEM (bright-field) imaging does not generally fulfil the 'projection requirement' in the case of crystalline materials; when tilted, any crystalline object experiences contrast variations due to Bragg diffraction effects, which makes that the intensity in projections is not proportional to the "mass-thickness". As a consequence, the reconstruction cannot properly render the actual 3D structure of the sample. Practical approaches were possible when acquisition of signals independent from elastic diffraction became available to allow realistic tilting sequences: this has been achieved thanks to STEM-HAADF (Scanning TEM, High Angle Dark Field imaging) [3] and EFTEM (Energy-Filtered TEM) [1, 4].

Very interestingly, these two techniques, which have been extensively used and developed for nano-tomography during the last decade, offer the additional advantage to provide chemical information. In HAADF, incoherent scattering yields to a contrast varying as roughly Z^2, which thus permits to discern phases with sufficiently different mass-thicknesses. In EFTEM, elemental maps can be acquired using ionisation edges of different elements. However, each of these techniques has drawbacks: for materials with similar atomic density and atomic numbers, HAADF cannot provide a sufficient contrast for evaluating the chemistry. Concerning EFTEM, several images need to be acquired at each tilting position (at least 3 per element), and the method is very time consuming. It was then tempting to think about tomography using EDX (Energy-Dispersive X-ray) elemental mapping. But this idea remained a dream for a long time because EDX mapping is usually by far been much longer than STEM-HAADF of even EFTEM imaging [4].

This situation has recently changed owing to major technical improvements, all available on the same commercial instrument, regarding (i) the new generation of EDX analysers (the so-called SDDs: Silicon Drift Detectors), (ii) high brightness field- emission electron sources, (iii) the parallel coupling of several (4) detectors around the sample, owing to an optimized geometry of the pole pieces [5]. The aim of this contribution is to give some recent illustrations of nano-tomography performed in a TEM using the STEM-EDX technique. Several experiments will be presented, which were all carried out on the FEI-Tecnai OSIRIS microscope installed at ST Microelectronics in Crolles, F; accordingly, most results will concern devices for applications in microelectronics.

The first example presented here concerns an advanced 28nm FDSOI transistor (Figure 1 a-b) [6]). STEM-EDX nano-tomography was performed on FIB-milled needle of 150 nm of diameter (Figure 1 c)). The reconstructed volume is shown Figure 1 e) to g): information could be easily extracted from the volume to re-project single slices or sub-stacks of slices from any directions as in classical tomography but with a direct chemical meaning. Figure 2 refers to multi-gate devices such as gate-all-around nanowires, a perspective beyond the end of the CMOS roadmap. An efficient failure control in conventional 2D-TEM would require being able to prepare thin foils in any direction of such (small) devices: not only this procedure will be time-consuming, but it is not known a priori which viewing orientation would better reveal the possible defects. 180° EDX-tomography on FIB-prepared needles allows the device to be examined without any restriction, nor shadowing effect according to the 3D reconstruction.

Results (i.e. benefits and issues) will be discussed in terms of irradiation effects and mechanical instabilities, which are obviously key issues in all experiments. Most acquisitions were carried out under the following typical conditions: i) beam energy 120 kV, probe size and current typically 0.5 nm

and 1 - 2 nA respectively, ii) tilt series over 180° every 2 to 5°, iii) EDX maps about (500-800) pixels², dwell time between 500 and 1000 µs. All these parameters lead to acquisition times of a few minutes per map, and a total duration of 6 to 8 hours. We also aim at comparing STEM-EDX nano-tomography with other complementary techniques, such as HAADF and EFTEM as already evoked, but also Atom Probe Tomography [8], a very efficient technique for chemical analysis in 3D.

1. P.A. Midgley, M. Weyland, *Ultramicroscopy*, 96 (2003) 413-431.
2. G. Möbus, B.J. Inkson, *Materials Today*, 10-12 (2007) 18-25.
3. P.A. Midgley, M. Weyland, chap. 8, pp. 353-392 in *Scanning Transmission Electron Microscopy,* S.J. Pennycook, P.D. Nellist (eds.), Springer Science+Business Media, LLC 2011.
4. G. Möbus, R.C. Doole, B.J. Inkson, *Ultramicroscopy*, 96 (2003) 433-451.
5. P. Schlossmacher, D.O. Klenov, B. Freitag, and H.S. von Harrach, *Microscopy Today* 18(4) (2010) 14-20.
6. K. Lepinay, F. Lorut, R. Pantel, T. Epicier, *Micron*, 47, (2013), 43-49.
7. K. Lepinay, F. Lorut, A. Pofelski, R. Coquand, R. Pantel, T. Epicier, 18th Microscopy of Semi-Conducting Materials (MSM XVIII) 2013, Oxford, UK, 7-11 April 2013, to appear.
8. T.F. Kelly, M.K. Miller, *Review of Scientific Instruments*, 78, 3, (2007) article # 031101.

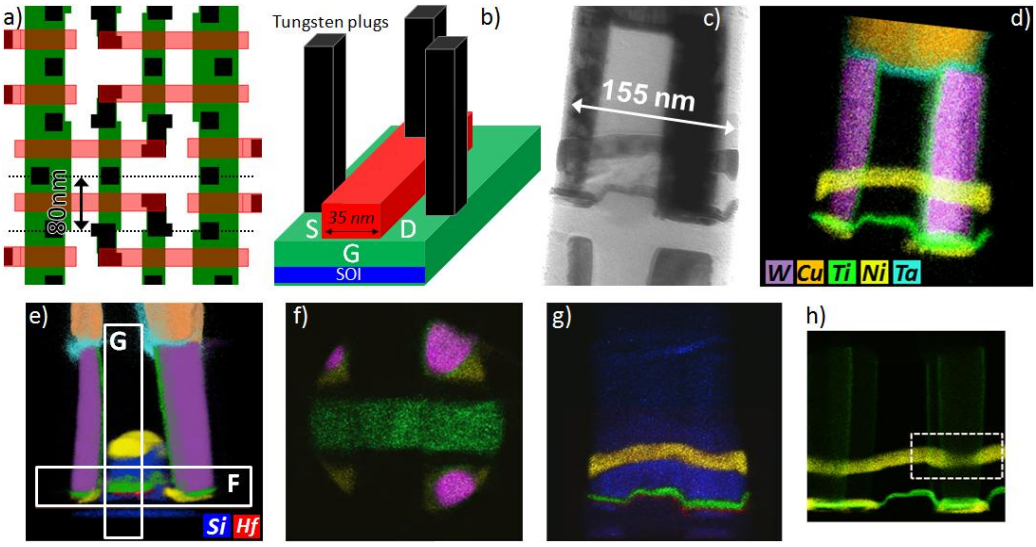

Figure 1. 3D STEM-EDX analysis of a 28nm FDSOI transistor. a): SDRAM layout (top view; active silicon is shown in green, the gate stack in red and the tungsten plugs in dark). b): schematic representation of a transistor. c): TEM image of the FIB tip (thickness about 150 nm). d): composite EDX map of the complete projection (acquisition at 120 keV, probe current 1.2 nA, tilt step 2° from -90 to 90°, 5 min. per map with size of 800x800 pixels²). e-g): 3D rendering of the chemical tomogram and volume extractions (45 nm - 150 slices -) along two perpendicular directions (frames F and G corresponding respectively to projections shown in f) and g)). H): typical usual 2D EDX map of Ti and Ni showing the shadowing effect produced by the W plug (to be compared to g)).

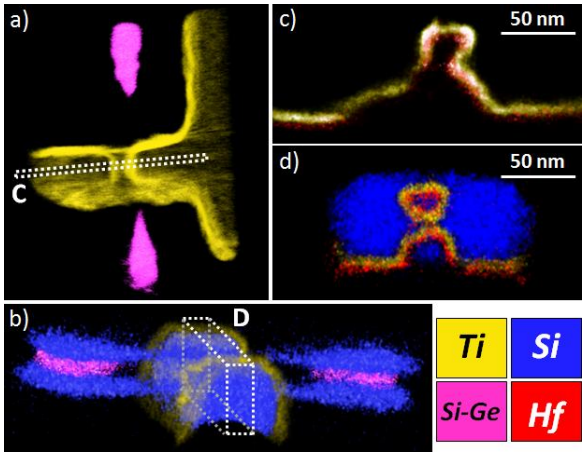

Figure 2. 3D chemical analysis of a complex device showing a failed system (a) and c)) and a well-processed one (b) and d)). Dotted frames in a) and b) show 'virtual' TEM lamellae extracted with any desired thickness and in any orientation to produce projections shown in c) and d). The visualization in d) demonstrates the correct and continuous high-K metal gate deposition all around the nanowire, contrarily to case c). The 3D resolution can be estimated around 3-4 nm (see details in [7]).

3D Imaging and Analysis

IM.6.118
Vascular geometry and optimality calculation by 3D morphometry SEM analysis

B. Minnich[1], S. Margiol[2], J. Frysak[2], E.W.N. Bernroider[2]

[1]University of Salzburg, Cellbiology & Physiology, Salzburg, Austria
[2]Vienna University of Economics and Business, Inst. Information Management and Control, Vienna, Austria

bernd.minnich@sbg.ac.at
Keywords: scanning electron microscopy, 3D morphometry, vascular optimality

Scanning electron microscopes (SEMs) are potential tools for morphological research. They have a great resolution and a high depth of focus, which gives SEM micrographs pseudo three-dimensionality. Adversely, the high depth of focus prevents accurate dimensional or spatial measurements of imaged microstructures from either the SEM video-display, printed micrographs or from photo-negatives. Macroscopic objects are viewed close up using binocular vision. Binocular vision is also used in microscopy where stereophotogrammetry and related techniques applying stereo paired images, and a variety of hardware tools calculate the third dimension (z-coordinate) using the parallax.

A method (3D-morphometry, *ComServ*, Austria) for dimensional and angular measurements of microstructures imaged in the SEM was first developed in our lab in 1999 [1]. It uses digitized stereo paired images frame-grabbed (slow scan) directly from the SEM's photo-display, vector equation-based algorithms for the calculation of spatial coordinates and derived distance- as well as angular measurements. It offers dynamic data exchange to open source software together with online graphs of frequency distributions of measured variables. Formulas for central perspective depth computation allow the overall error to be less than 1.0%. Meanwhile (2013), the method was further improved and the new java based software M^3 is suitable to be used with Windows 7 and 8 operating systems. A modern graphical user interface (GUI) (Fig.1), a new data interface (open office) is supported and an improved usability facilitates measurement processes [2].

This technique is currently used to analyse (a) the geometry of microvascular trees in terms of vascular parameters (i.e. diameters, interbranching distances, branching angles and intervascular distances) and (b) to determine bifurcation indices and area ratios followed by a calculation of optimality principles which are given in arterial bifurcations respectively venous mergings. Moreover the program now allows to generate anaglyphic 3D images (Fig.2) and to calculate optimality principles underlying the construction and maintenance of such delicate vascular networks (i.e. principle of minimal lumen volume, minimal pumping power, minimal lumen surface and minimal endothelial shear force) [3-4] (Fig.3).

In our current research we use M^3 to examine developmental and regression processes of the microvasculature of different organs in various animals such as the South African clawed toad (*Xenopus laevis Daudin*) [5-7] and also to explore the angioarchitecture of the *vasa vasorum* of the human great saphenous vein (*Vena saphena magna*) which plays a critical roll for bypass crafting during coronary surgery in men [8].

1. Minnich B. *et al*, Journal of Microsccopy 195 (1999), p. 23-33.
2. Minnich B. *et al*, in "Current microscopy contributions to advances in science and technology", eds. A Mendes Vilas and J D Alvarez, Formatex, (2012), p. 191-199.
3. LaBabera M., Science 249 (1990), p. 992-1000.
4. Murray C.D., Journal of General Physiology 9 (1926), p. 835-841.
5. Lametschwandtner A. *et al*, Archives of Histology & Cytology 73(1), (2010) p. 55-64.
6. Lametschwandtner A. *et al*, Italian Journal of Zoology 78(1) (2011), p. 27-34.
7. Lametschwandtner A. *et al*, Anatomical Sciences International 87 (2012), p. 88-100.
8. Kachlik D. *et al*, Central European Journal of Medicine 3(4) (2008), p. 475-481.

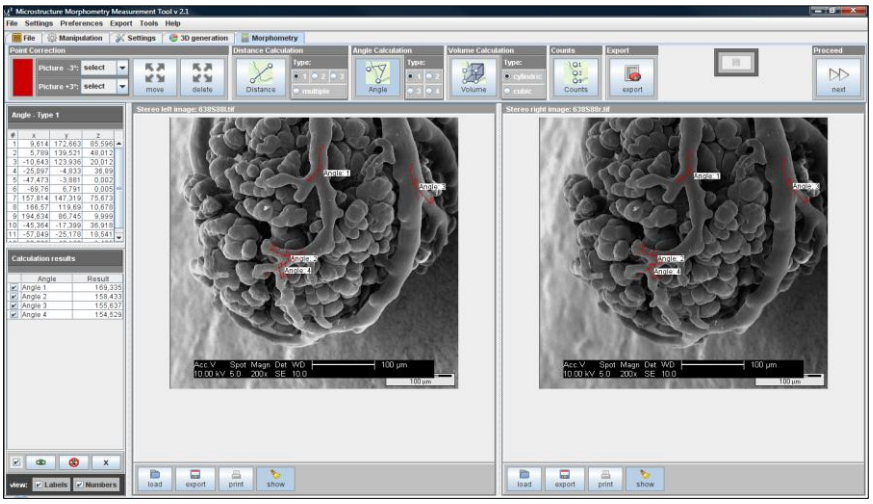

Figure 1. M3 graphical user interface (GUI) showing the morphometry screen while measuring branching angles of feeding arteries of the spleen of the adult *Xenopus laevis* Daudin.

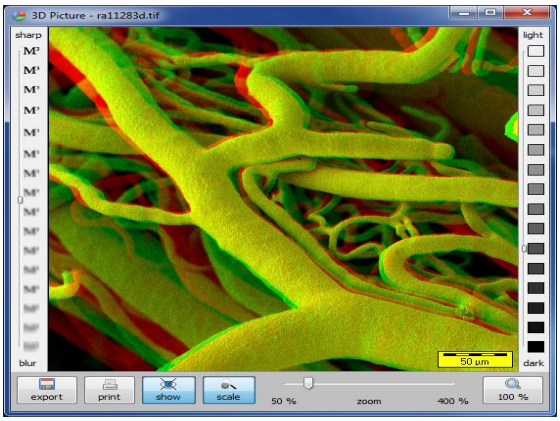

Figure 2. Anaglyphic 3D image representing a vascular corrosion cast of a microvascular network examined under an ESEM (FEI XL-30).

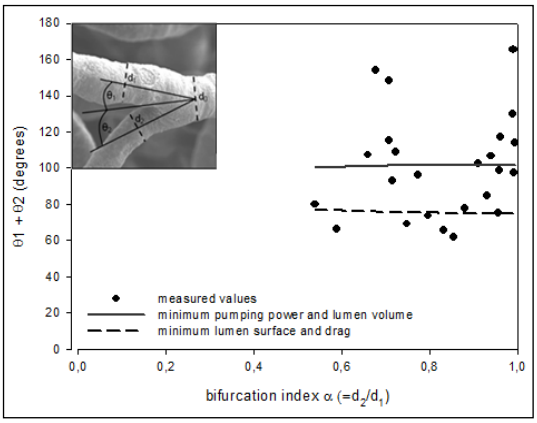

Figure 3. Scatterplot showing an optimality diagram of the brain microvascular bed (rhombencephalon) of the sterlet (*Acipenser ruthenus*). Vascular bifurcation with indications of vessel diameters and branching angles (insert).

3D Imaging and Analysis

IM.6.119
Simulation of the FIB-SEM Imaging Process and Segmentation of FIB-SEM Data Sets

T. Prill[1], K. Schladitz[1], D. Jeulin[1]

[1]Fraunhofer ITWM, Image Processing, Kaiserslautern, France

torben.prill@itwm.fhg.de

Nanoporous materials play an important role in modern batteries, as well as fuel cells. Furthermore, the microstructure is crucial in determining the performance of the porous materials. Yet the microstructure is too fine to be resolved with micro-CT, thus the method of choice is focused ion beam nanotomography(FIB-SEM). FIB tomography yields high quality 3D images of materials microstructures at the nanometre scale combining serial sectioning using a focused ion beam with scanning electron microscopy (SEM). However, SEM images represent the projection of a slice of unknown thickness. In FIB tomography of highly porous media this leads to shine-through artefacts , where structures in deeper slices are visible through the pore space, preventing automatic segmentation of the solid component (see Fig.2 for an example).

To overcome these difficulties, we simulate the SEM process[1]. Monte-Carlo techniques yield accurate results, but are too slow for FIB-SEM requiring hundreds of SEM images for one dataset. Nevertheless, a quasi analytic description of the specimen and acceleration techniques cut down the computing time by orders of magnitude, allowing the simulation of FIB-SEM data. Based on simulated FIB-SEM image data (see Fig. 1), segmentation methods for the 3D microstructure of highly porous media from the FIB-SEM data have been developed and evaluated.

With the synthetic data at hand, an algorithm was developed, which solves the segmentation problem, i.e. extract the 3D microstructure, from the FIB-SEM data. Based on well known morphological operations, a new method was developed for the reconstruction of highly porous structures from FIB-SEM data[2].

In an initial preprocessing step, the FIB-SEM image stack is precisely aligned. This is necessary, since the segmentation will be working with the variation of the grey value of individual pixels through the stack. This will be referred to as the z-profile of the pixel. Also, the image is corrected for shading artefacts and the contrast is enhanced.

For the matrix detection, features are extracted from the z-profiles of every pixel. A morphological gradient image with a linear structuring element (SE) is generated and thresholded, detecting the beginning of the matrix phase. Additionally, minima in the profile are detected, indicating the ending of the matrix phase in the z-profile. In the next step, pixels likely belonging to the matrix phase are marked by extending the thresholded gradient image to the minima. Then the marker image, together with a usual morphological gradient image, is used as input for a constrained watershed transformation where foreground and background are eroded and then used as initial basins for the transformation. This fits the initial basins to the edges in the image, resulting in a refined and final segmentation (see Fig.2,3).

For the first time, the method was validated with synthetic data generated by the simulation of the FIB-SEM process. With the ground truth available, the misclassification rate as well as other error measures, such as covariance and granulometry by openings could be determined. The results of the validation show that it outperforms any other method so far documented in literature.

This segmented data can then be used to simulate and optimize the macroscopic properties of nanoporous materials.

1. T. Prill and K. Schladitz, Simulation of FIB-SEM images for analysis of porous microstructures, Scanning 00, (2012), 1 – 7.
2. T. Prill, K. Schladitz, D. Jeulin, M. Faessel, Morphological segmentation of FIB-SEM data of highly porous media, Journal of Microscopy, accepted (2013)

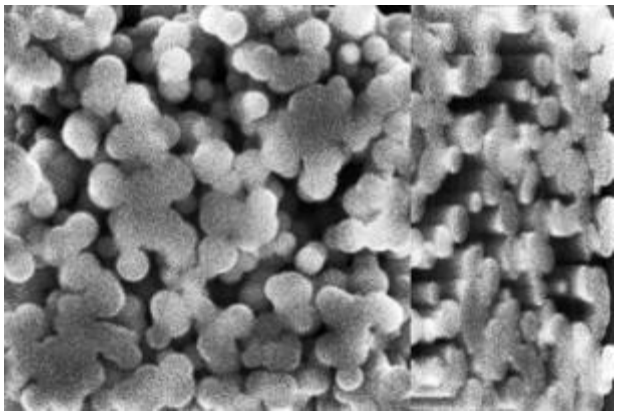

Figure 1. Simulated FIB-SEM data set of a porous carbon microstructure; left: the first slice of the FIB-SEM data set, right: crossection view through the image stack

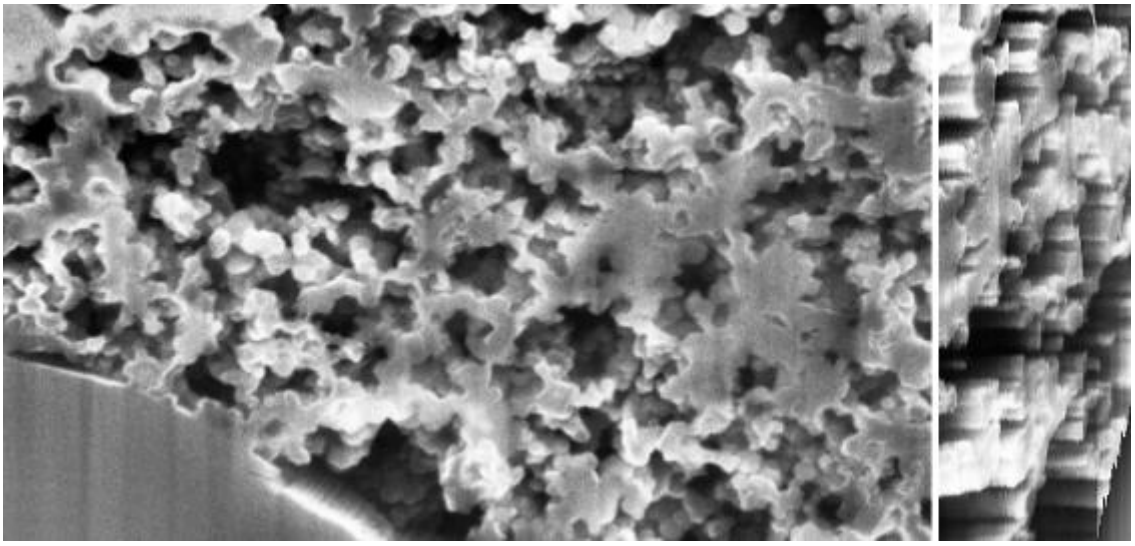

Figure 2. FIB-SEM data set of a porous carbon microstructure; left: the first slice of the FIB-SEM data set, right: crossection view through the image stack

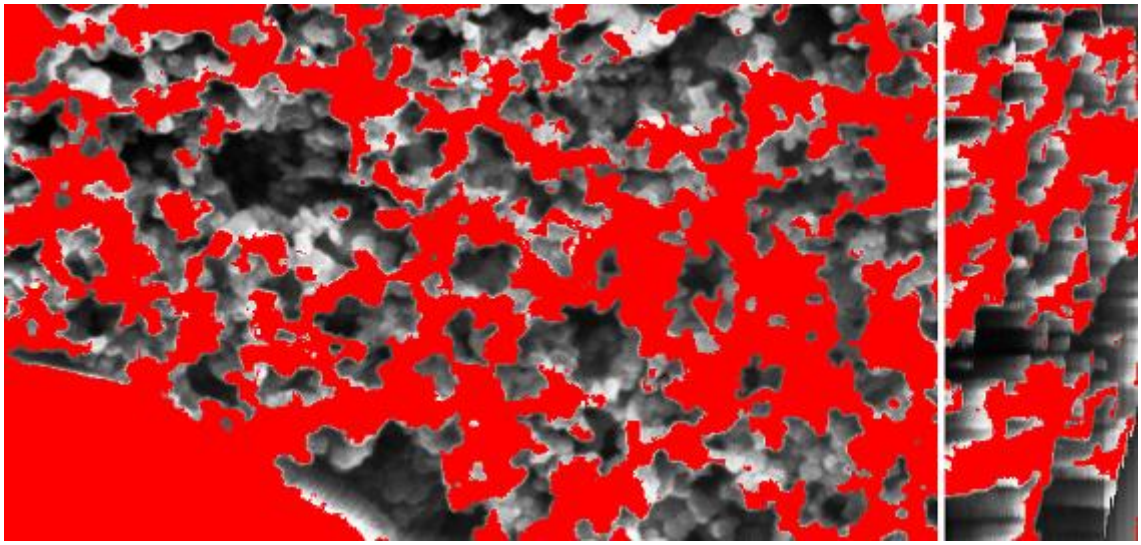

Figure 2. FIB-SEM data set with the segmentation as overlay (red); left: a slice view, right: a cross section view

3D Imaging and Analysis

IM.6.120
Combined STEM tomography and HRTEM analysis of PbSe-carbon nanotube hybrid structures

B. Winter[1], J. Schornbaum[2], B. Butz[1], S.P. Schießl[2], J. Zaumseil[2], E. Spiecker[1]

[1]FAU Erlangen-Nürnberg, Center for Nanoanalysis and Electron Microscopy (CENEM), Erlangen, Germany
[2]FAU Erlangen-Nürnberg, Institute of Polymer Materials, Erlangen, Germany

benjamin.winter@ww.uni-erlangen.de
Keywords: electron tomography, high-resolution transmission electron microscopy, PbSe quantum dots, single-walled carbon nanotubes, hybrid material, optoelectronic device

Hybrids of semiconductor quantum dots (QDs) with size-tunable absorption and single-walled carbon nanotubes (SWNTs) with high charge carrier mobilities form ideal building blocks for optoelectronic devices. Coupling near-infrared absorbing PbSe QDs to SWNTs transforms the photoexcited states of the QDs into charge separated states. Due to the fast charge transport in SWNTs a dramatic increase of photosensitivity is expected. Thus stable PbSe-SWNT hybrid structures are promising materials for the fabrication of highly sensitive near-infrared photodetectors [1,2].
PbSe-SWNT hybrid structures were obtained by a facile synthetic route described in detail in Ref. [3]. Adding partly debundled SWNTs to a lead precursor solution leads to the nucleation of lead oleate on the SWNT sidewalls. The injection of a selenium precursor solution results in a PbSe-SWNT hybrid without any molecular linker. Raman spectroscopy indicates that the sp^2-carbon lattice of the SWNTs is not chemically modified by the PbSe QDs [3]. This implies that the QDs are non-covalently attached to the SWNTs and charge transport along the SWNT is not significantly affected.
The size and shape of the QDs as well as the interface between the QDs and the SWNTs highly influence the electrical and optical properties of the hybrid material. Therefore, a detailed structural and chemical characterization using several TEM techniques has been carried out [3]. Aberration-corrected HRTEM, scanning TEM (STEM), STEM tomography and energy-dispersive X-ray spectroscopy (not shown) were performed using an aberration-corrected Titan³ 80-300 microscope operated at 80 kV acceleration voltage in order to minimize electron-beam induced damage of the SWNTs. From the low-magnification STEM image in Figure 1.a) it can be seen that many PbSe QDs are attached to SWNT bundles. STEM tomography reveals the three-dimensional morphology of individual QDs and their connection to the SWNTs (see Figure 1.d)), as had been shown in a similar way for CdSe-SWNT hybrids by Hungría et al. [4]. It can be seen that PbSe QDs partially grow around the SWNT bundles forming an intimate contact. The HRTEM images clearly indicate a preferred orientation of the {002} lattice planes of the single crystalline PbSe QDs perpendicular to the longitudinal axis of the SWNT bundles (Figure 2.a)). Combining HRTEM and STEM tomography for the same PbSe QD makes it possible to identify the zone axes of the PbSe QDs in the reconstructed volume (see Figure 2.). This method opens a new route to discrete tomography of nanocrystals in which STEM tomography contributes the 3D shape and HRTEM the relative orientation of the crystal lattice.

1. N. Cho, K.R. Choudhury, R.B. Thapa, Y. Sahoo, T. Ohulchanskyy, A.N. Cartwright, K.-S. Lee, P.N. Prasad, Adv. Mater. 19 (2007), p. 232.
2. D. Wang, J.K. Baral, H. Zhao, B.A. Gonfa, V.-V. Truong, M.A.E. Khakani, R. Izquierdo, D. Ma, Adv. Funct. Mater. 21 (2011), p. 4010
3. J. Schornbaum, B. Winter, S. P. Schießl, B. Butz, E. Spiecker, J. Zaumseil, Small (2013), submitted.
4. A.B. Hungría, B.H. Juárez, C. Klinke, H. Weller, P.A. Midgley, Nano Res. 1 (2008), p. 89.This research was financially supported by the Excellence Cluster “Engineering of Advanced Materials” (DFG EXC 315) and the Alfried Krupp von Bohlen und Halbach-Stiftung. B. W. gratefully acknowledges the DFG Research Training Group 1161 “Disperse Systems for Electronic Applications” and J. S. the Erlangen Graduate School in Advanced Optical Technologies (SAOT) within the framework of the German Excellence Initiative (DFG GSC 80).

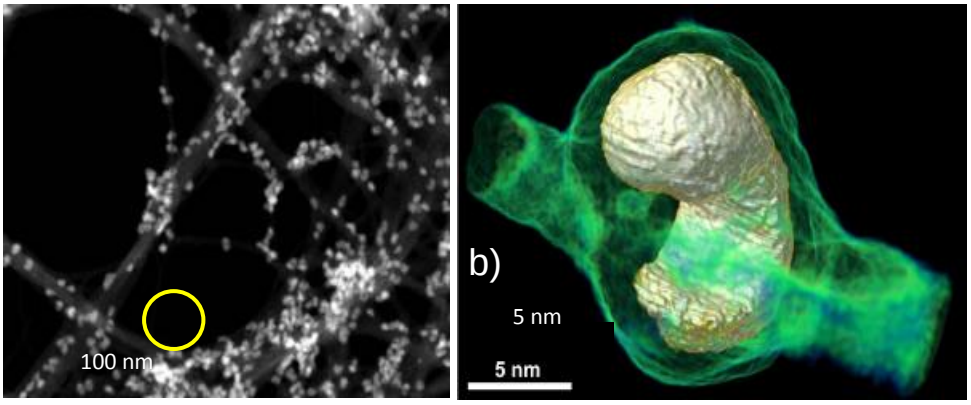

Figure 1. a) STEM overview image of the PbSe-SWNTs hybrid with the investigated QD encircled in yellow. b) Reconstructed volume (STEM tomography) showing that the PbSe QD (silver-yellow surface rendering) grows around a bundle of SWNTs (green-blue volume rendering).

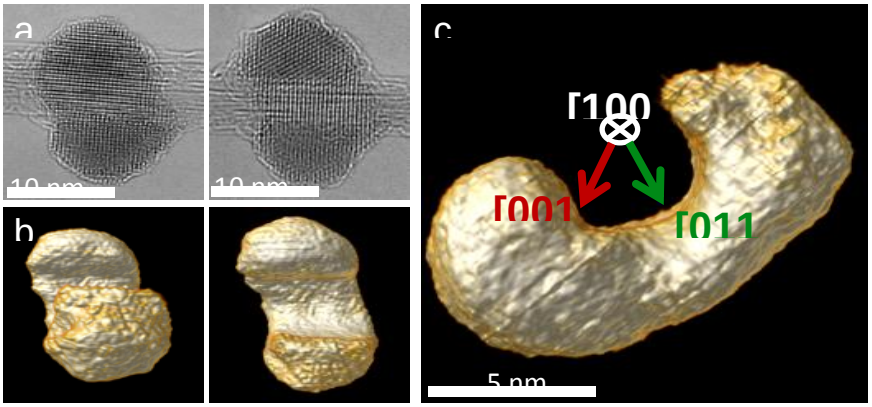

Figure 2. a) HRTEM images of the PbSe QD of Figure 1.b) tilted into different zone axes (left image view along [001]; right image view along [011]; [100] tilt axis horizontally positioned in the image plane). b) Parallel projection view of the reconstructed PbSe QD (surface rendering) along to the two zone axes from a). c) Parallel projection view of the reconstructed PbSe QD (surface rendering) along the [100] tilt axis. The arrows indicate the orientation of the [001] and [011] zone axes of the HRTEM images.

3D Imaging and Analysis

IM.6.121
Three-dimensional particle reconstruction by depth sectioning in scanning transmission electron microscopy

E. Mudry[1], A. Rosenauer[2], J. Verbeeck[1], S. Van Aert[1]

[1]University of Antwerp, Antwerp, Belgium
[2]University of Bremen, Bremen, Germany

emeric.mudry@ua.ac.be
Keyword: ADF-STEM, three-dimensional imaging, parameter estimation

Thanks to recent progress in aberration correction, atomic resolution is now possible in High Angle Annular Dark Field Scanning Transmission Electronic Microscopy (HAADF-STEM). Unfortunately this impressive resolution is limited to two-dimensional images and information on the axial structure of the sample is still missing. Recently several methods [1,2] have been proposed to obtain three-dimensional information from a tilt-series. While efficient, this technique is limited to the small volume of the sample that remains in the field of view for all tilts. Earlier, van Benthem *et al.* [3] proposed the use of depth sectioning, where several images of the same sample are taken at different focus. In this way vertical structures can be observed directly, like in three-dimensional light microscopy [4]. This technique is easy to implement on commercial microscopes and does not necessitate a specific sample preparation. Unfortunately the vertical size of the probe is of the order of several nm, thus far too large to distinguish individual atoms [4]. Moreover non-linear interaction between atoms are particularly important in the propagation direction, hindering a direct interpretation of the set of measurements [5]. Besides this drawback, we think that this technique might allow useful measurements, providing a suitable data treatment and using enough *a priori* knowledge on the sample. In this work, we study the possibility to measure the atom position in a gold nanoparticle using a three-dimensional image. We first study the precision that can be achieved using the so-called Cramér-Rao lower Bound (CRLB). This theoretical tool gives a lower bound on the variance with which parameters can be estimated unbiasedly and can be derived from a parametric statistical model defining the expectation as well as the noise statistics [6]. To compute the expectation values, we used a multislice simulation of a column of 10 gold atoms imaged by a HAADF detector assuming an aberration-corrected STEM microscope with a semi convergence angle of 22 mrad. We described the noise as a Poisson statistic. Our study proves that, even in this ideal case, the precision that can be reached when estimating the atom vertical position is larger than the inter-atom distance for realistic dose values. However, when estimating only the center-of-mass of the column a precision of a few pm is reachable (see Figure 1). This theoretical study proves that depth sectioning cannot be used to estimate the position of every single atoms of a nanoparticle but can be used to estimate the position of each column. Based on this result, we developed a procedure for reconstructing a gold nanoparticle from an HAADF-STEM depth sectioning three-dimensional image. We first estimate the lateral position and atom numbers of each column of the particle from one of the two-dimensional images [7]. We then simulate with an accurate multislice algorithm, a focal series of each type of atom columns present in the particle, assuming the inter-atomic distance as identical as in a perfect crystal. These templates are then matched to the nanoparticle's image using a maximum likelihood procedure. A numerical example of this procedure is shown in Figure 2.

1. S. Van Aert, K. J. Batenburg, M. D. Rossell, R. Erni and G. Van Tendeloo, Nature 470 (2011), pp. 374–377.
2. B. Goris, S. Bals, W. Van den Broek, E. Carbo-Argibay, S. Gomez-Grana, L. M. Liz-Marzan and G. Van Tendeloo, Nature Mat. 11 (2012), pp. 930–935.
3. K. van Benthem, A. R. Lupini, M. P. Oxley, S. D. Findlay, L. J. Allen and S. J. Pennycook, Ultramicroscopy 106 (2006), pp. 1062 – 1068.
4. W. Van den Broek, S. Van Aert, D. Van Dyck, Ultramicroscopy 110 (2010), pp. 548 – 554.
5. E. C. Cosgriff, P. D. Nellist, Ultramicroscopy 107 (2007), pp. 626 – 634.6A. den Dekker, S. Van Aert, A. van den Bos and D. Van Dyck, Ultramicroscopy 104 (2005), pp. 83 – 106.7S. Van Aert, A. De Backer, G. T. Martinez, B. Goris, S. Bals and G. Van Tendeloo, Phys. Rev. B, 87, (2013) p. 0641078 The authors acknowledge financial support from the Research Foundation Flanders (FWO) through project fundings G.0393.11, G.0064.10 and G.0374.13.

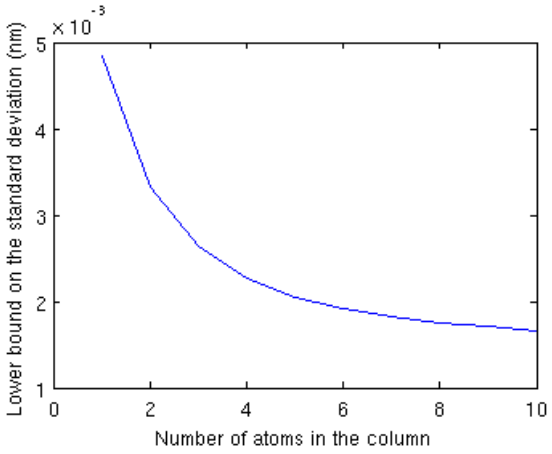

Figure 1. Lower bound on the standard deviation with which the vertical position of a gold atom column can be estimated from HAADF-STEM depth sectioning as a function of the number of atom in the column. The electron dose is 210 000 electrons, corresponding to a dwell time of 1 ms with a probe current of 40 pA.

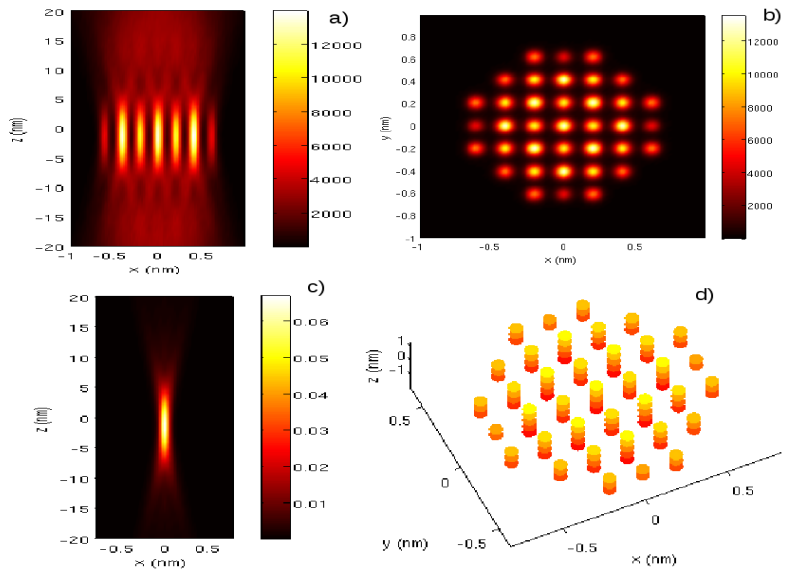

Figure 2. Particle reconstruction of an ellipsoidal gold nanoparticle from synthetic data of HAADF-STEM focal series. a) and b) (xz) and (xy) cut of the simulated depth sectioning of the nanoparticle. Colorbars scale in number of detected electrons. c) (xz) cut of the template for a column with 4 gold atoms. Colorbar scales in the detection probability for one electron dose. d) Reconstructed atom positions. Atoms with the same color are at the same vertical position.

3D Imaging and Analysis

IM.6.122
Non-linear electron tomography

C.T. Koch[1], W. Van den Broek[1]

[1]Ulm University, Institute for Experimental Physics, Ulm, Germany

Christoph.Koch@uni-ulm.de
Keywords: dynamical electron diffraction,

Tomography is generally considered as the problem of 3D reconstruction from 2D projections, and a large number of techniques have been developed to optimize electron tomography with respect to dose and control of projection parameters (e.g. refinement of projection alignment and actual tilt angles – see [1] for a recent review). Also, certain a-priori information of the object can be made use of, such as the fact that the object is sparse in some basis [2]. However, quantitative electron tomography must take into account the fact that electrons generally scatter multiple times within the sample, and that BF-TEM, HRTEM, HAADF-STEM, or EFTEM images are hardly linear projections of the underlying object.

In some cases, such as EFTEM tomography, or medium-resolution STEM tomography, a re-scaling of the data according to some exponential thickness–intensity relationship may help to improve the reconstruction significantly [3,4]. This re-scaling is applied only once to the experimental data, and a conventional linear reconstruction algorithm is used for the actual reconstruction. While these improved approximations of the imaging process can have a remarkable effect on the reconstruction results they still do not guarantee a truly quantitative result. In order to include non-linearity of the image formation process in iterative tomographic reconstruction schemes, it is necessary to consider this non-linearity in both forward simulation as well as back-projection, or at least treat the back-projection as a linear perturbation.

One of the most challenging areas in electron tomography is probably the reconstruction of the 3D arrangement of atoms. An obvious choice of recording method is HAADF-STEM, since it gives the most linear signal at atomic resolution [5]. However, HAADF-STEM requires high dose and also high accelerating voltage to produce a small enough probe, both of which are prone to produce knock-on damage. Also, a large tilt range is required for linear tomographic reconstruction algorithms if a high resolution parallel to the incident beam direction is desired.

In HRTEM the image contrast is highly non-linear and also delocalized, especially, in the presence of aberrations and/or objective lens defocus. Also, multiple scattering is much more obvious in HRTEM than in STEM. Figure 1 shows that multiple scattering of the incident electron beam within the sample actually helps to fulfill one of the requirements for compressive sensing, in that it increases the incoherence between the object space (atomic positions) and the image signal, especially at low accelerating voltage, where knock-on damage is expected to be low. If the imaging parameters are optimized, HRTEM can also be very efficient in the amount of signal detected per incident dose. Fig. 2 shows how a novel, non-linear reconstruction algorithm is able to invert the multiple scattering of electrons within the sample to recover the 3D scattering potential [6][7].

1. Pawel A. Penczek, *Methods Enzymol.* 482 (2010) 1–33
2. R. Leary,et al.,Ultramicroscopy(2013), http://dx.doi.org/10.1016/j.ultramic.2013.03.019
3. N.Y. Jin-Phillipp, C.T. Koch, P.A. van Aken, Ultramicroscopy 111 (2011) 1255–1261
4. W. Van den Broek, et al. *Ultramicroscopy* 116 (2012) 8–12
5. C. Chen et al, Nature 469 (2013) 74
6. W. Van den Broek and C.T. Koch, Phys. Rev. Lett. 109 (2012), p. 245502
7. The authors acknowledge the Carl Zeiss Foundation as well as the German Research Foundation (DFG, Grant No. KO 2911/7-1)

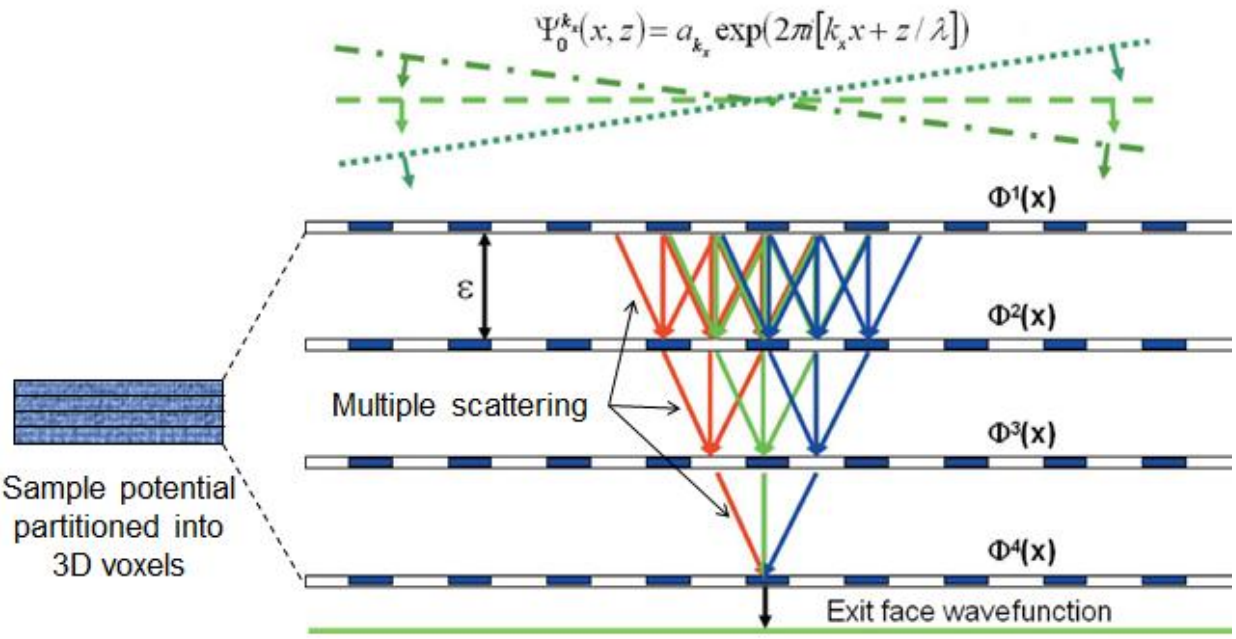

Figure 6. Diagram showing how multiple scattering of the incident electrons within the sample encodes non-local 3D information into the exit face wave function. Changing the angle of incidence of the illumination will change the phases and weights of different scattering paths, making it possible to retrieve the 3D scattering potential.

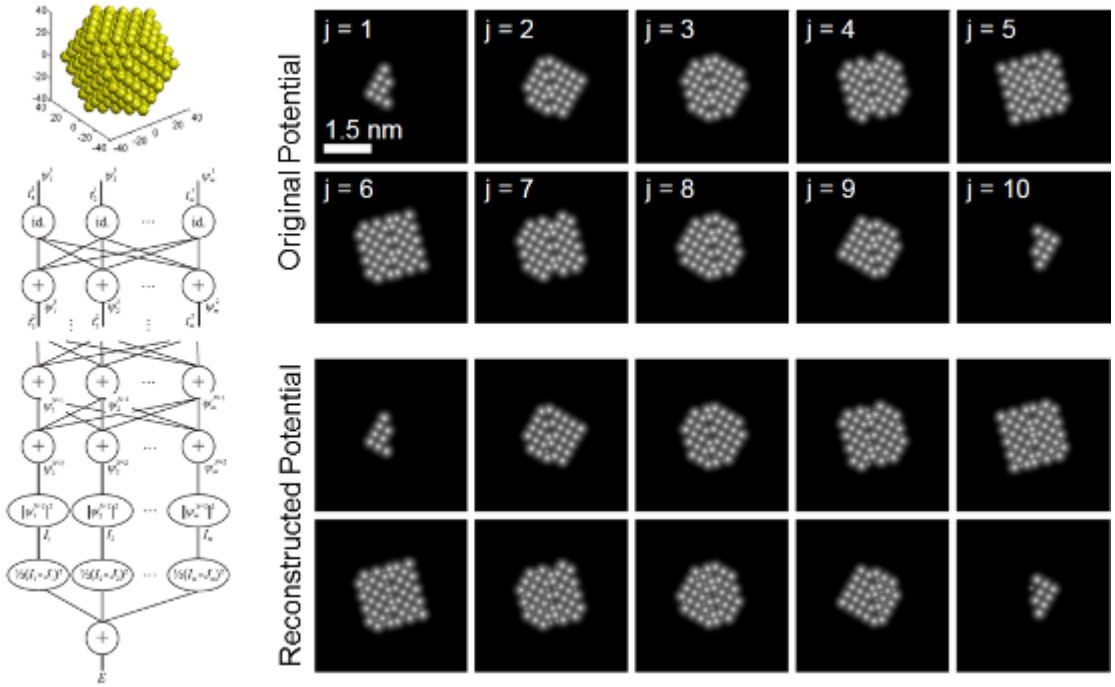

Figure 7. Two rows of images at the top right: potential slices through a Au nanoparticle containing 309 atoms (shown at the top left). Treating the (non-linear) multislice algorithm as an artificial neural network has helped to recover the content of these 10 slices from 40 kV HRTEM images simulated, as shown in the bottom 2 rows of images.

3D Imaging and Analysis

IM.6.P123
Sparta: A Single Particle Analysis Toolbox Built Around Speed and Interactivity

D. Tegunov[1], N. Braun[1], S. Weinkauf[1]

[1]Technische Universität München, Institute of Electron Microscopy, Department of Chemistry, Garching, Germany

dmitry.tegunov@tum.de
Keywords: electron microscopy, single particle analysis, classification, software, GPU computing

Three dimensional reconstruction of single particles is a complex process involving a wide range of methods, most notably image recognition, processing and statistical analysis. While attempts at full automation are in progress, many data sets are ill-suited for non-supervised approaches and require a large amount of human involvement. Due to limitations of old hardware architectures, previous software solutions offer little graphical user interaction. This often leads to obscurity and increases the risk of missing important information.

Furthermore, the amount of computational resources has to follow the demand for ever higher model resolution, which requires very large data sets. Modern GPU architectures [1] provide computational power at a fraction of the cost associated with a traditional CPU-based solution. With thousands of computational units and high memory bandwidth, they are better adapted to the parallel processing of large image sets.

Sparta, a new single particle analysis toolbox, has been written from scratch with these two challenges in mind. The underlying architecture relies on GPUs for all computationally intensive tasks and outperforms existing tools by up to two orders of magnitude when run on a single system (Figure 1). This increase in speed allows for improved interactivity within the interface, while also dramatically reducing the hardware costs.

Sparta's visual, real-time interactivity is perfectly suited for the analysis of heterogeneous data sets. When no initial structure is available and the input of classification parameters as well as the display of the obtained class averages are tedious, one usually starts with a large number of classes prior to performing further sub-classifications. Identification of angles showing significant structural variations within the corresponding projection images is very time-consuming and the risk of missing some of them is high, especially for inexperienced operators (Figure 2a). The fast, coherent and clear interface provided by Sparta encourages to experiment with a large set of parameters and classification hierarchies, thus enabling a fast identification of structural differences (Figure 2b).

While Sparta can be used as a stand-alone solution for model reconstruction, integration with existing pipelines is facilitated through native support for many popular file formats. Documented programming interfaces enable the integration of new processing algorithms into the same user interface, making Sparta a perfect testbed platform for future developments.

1. NVIDIA. NVIDIA's Next Generation CUDA™ Compute Architecture: Kepler TM GK110. (2012)
2. M van Heel, G Harauz, EV Orlova, R Schmidt and M Schatz. A new generation of the IMAGIC image processing system. J. Struct. Biol. 116 (1996), p. 17–24.

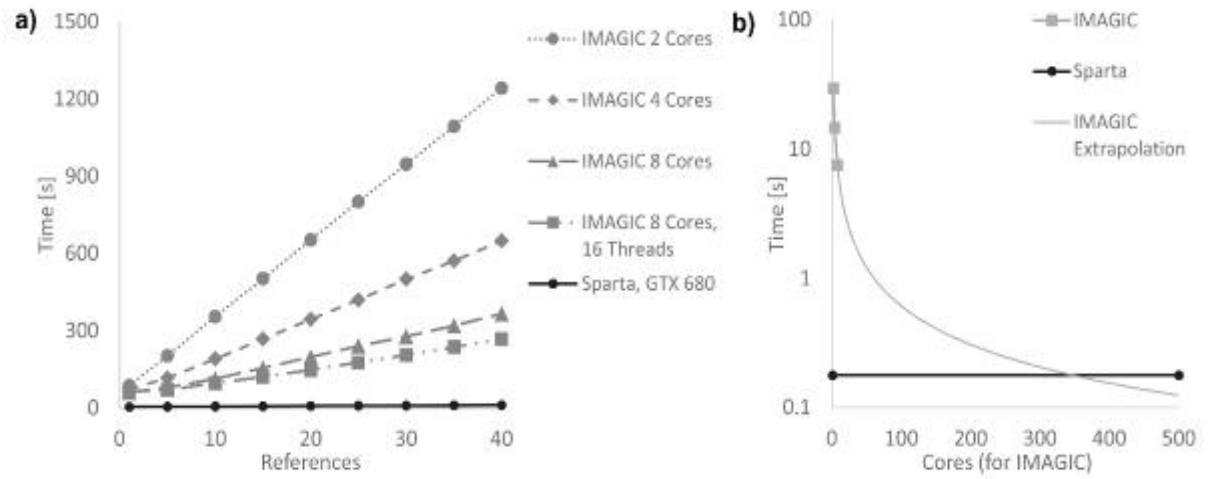

Figure 1: Performance comparison between the IMAGIC 5 package [2] (single machine, 2x Intel Xeon E5530, 12 GB DDR2 RAM) and Sparta (NVIDIA GeForce GTX 680, 2 GB DDR5 RAM) performing rotational multi-reference alignment on a stack of 16,000 128x128 px 16 bit images. **a)** Time cost for n references. **b)** Scalability of the procedure as expressed by the cost of increasing the number of references by one; extrapolation obtained by fitting the samples for 2, 4 and 8 CPU cores with a power-law function.

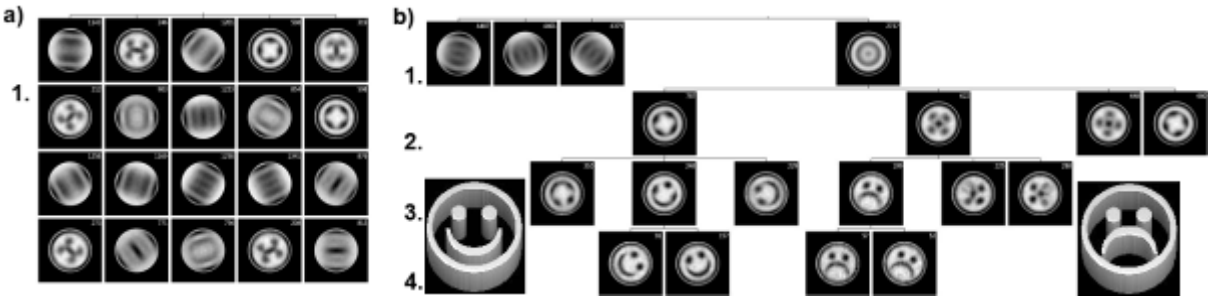

Figure 2: **a)** "classical classification": 20 class averages of a whole test dataset generated from random reprojections of two 3D-models of "smileys" **b)** "interactive, hierarchical classification": Four consecutive classifications, interactively lined up by the experimenter, enable a straightforward generation of meaningful class averages. Insets: surface representations of both 3D-Smileys.

3D Imaging and Analysis

IM.6.P124
Using entropy for evaluation of colocalization of multimodal and multichannel microscopic images

M. Čapek[1], D. Hadraba[1], J. Lišková[2], J. Michálek[1], B. Radochová[1], J. Janáček[1]

[1]Institute of Physiology ASCR, v.v.i., Dpt. Biomathematics, Prague, Czech Republic
[2]Institute of Physiology ASCR, v.v.i., Dpt. Biomaterials and Tissue Engineering, Prague, Czech Republic

capek@biomed.cas.cz
Keywords: collagen, SHG, colocalization, entropy

Collagen is an important component of the extracellular matrix (ECM) of connective tissue. Therefore, analysis of collagen deposition and remodeling is essential in tissue engineering. Second harmonic generation (SHG) imaging technique allows us to image non-centrosymmetric structures such as collagen in the ECM. The cells of human osteoblast cell line Saos-2 are able to grow extensively, and they can differentiate and produce ECM under specific conditions. They can be used for evaluation of biocompatibility of biomaterials for bone implants coatings, such as nanocrystalline diamond films (NCD) [1]. We have studied the production of type I collagen by Saos-2 after cultivation in differentiation medium. The native type I collagen fibers were visualized by SHG imaging, using a polarization filter with light planes rotated by 0°, 60°, and 120°, together with immunofluorescence staining and fluorescence microscopy, Figure 1. SHG signal provides information about collagen tissue that depends on direction of its fibers. When using the polarization filter under different angles, the excitation signal should interact more especially with collagen fibers that go along direction of the polarization angle. Thus, resulting SHG images are similar, but not the same, and should describe more precisely the morphology and formation of the fibers. However, as a result we get multimodal (fluorescence vs. SHG) and multichannel data (4 channels in this case, but even more can be obtained) that may be difficult to analyze. Colocalization analysis is understood as evaluation whether and how much two fluorescently labeled molecules are associated with one another. In our case we wish to analyze whether and how much amount of collagen mass detected in SHG data is produced by mass of Saos-2 cells detected in fluorescence data. Pearson's coefficient (PC) and Mander's coefficient (MC), e.g. [2], are probably the most popular approaches to colocalization analysis nowadays. They are restricted to a pair of images only; analysis of multichannel data is not easily possible. Moreover, when analyzing multimodal images, results obtained using them may be ambiguous. For example, when taking a look at Table 1-right column, we analyze here monomodal data (SHG 0° vs. SHG 60°) with distinct conclusion that images are well colocalized: PC $\rightarrow$ 1; MC $\rightarrow$ 1; scatter plot values are distributed along a linear function. A different situation is in Table 1-left column where we see the analysis of multimodal data (fluorescence vs. SHG 0°): PC = 0.5; MC $\rightarrow$ 0.5; scatter plot values are spread independently of the linear function. The conclusion about colocalization cannot be drawn here [2]. In the latter case we performed an additional "cross-correlation" analysis based on computing joint entropy of images using the discrete Kozachenko-Leonenko estimator, giving possibility to apply both multimodal and multichannel data [3]. We shifted the fluorescence image with respect to three SHG polarization images (1+3 multichannel analysis), ±10 pixels around the original position, pixel per pixel in both the x- and y-direction, computing the value of the entropy in each position using pixel values of all four images at the same time. The resulting mesh in Figure 3 shows values of entropy in the vicinity of the original position of the images. The mesh and corresponding line profiles demonstrate the maximum value of the entropy is not a random value, but it corresponds to a position of maximum similarity of the images; thus, all four images are truly colocalized. Conclusion: Multimodal and multichannel analysis of the vicinity of original position of images, based on Kozachenko-Leonenko entropy estimation, provides additional information about colocalization of images, and is useful in the real practice.

1. L. Grausova, A. Kromka A, Z. Burdikova, A. Eckhardt, B. Rezek, et al., PLoS ONE Vol. 6: e20943 (2011).
2. S. Bolte, F.P. Cordelières, J Microsc, Vol. 224 (2006), pp. 213-32.
3. J.D. García-Arteaga, J. Kybic, and W. Li, Comput Biol Med, Vol. 41(2011), pp. 960-70.
4. This research was supported by the Czech Science Foundation (P501/10/0340, P108/11/0794, 13-12412S), Technology Agency of the Czech Republic (TA02011193), the American Science and Information Center (AMVIS) (LH13028) and by support for long-term conceptual development of research organization RVO:67985823.

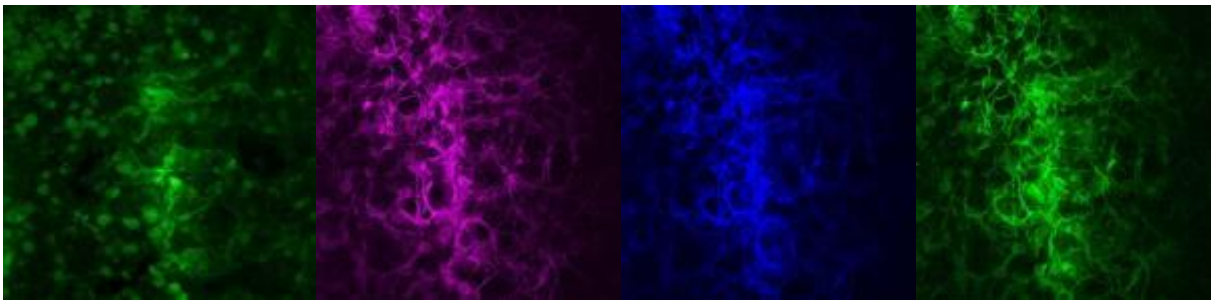

Figure 1. Microscopy images of human osteoblast cell line Saos-2. Left: a fluorescence confocal image (Leica SP2 AOBS); middle left: corresponding second harmonic generation (SHG) signal of collagen structures accompanying the cells using polarization filter with the light plane of 0°; middle right: SHG of 60°; right: SHG of 120° (Leica SP2 with a mode-locked Ti:Sapphire Chameleon Ultra laser (Coherent Inc., Santa Clara, California), tuneable from 690 to 1040 nm for TPE).

Fluorescence confocal vs. SHG (0°) image	SHG (0°) vs. SHG (60°) image
Pearson's Coefficient: r=0.5	Pearson's Coefficient: r=0.866
Manders' Coefficients (using threshold value of 32 for imgA and 43 for imgB): M1=0.641 (fraction of A overlapping B) M2=0.621 (fraction of B overlapping A)	Manders' Coefficients (using threshold value of 47 for imgA and 48 for imgB): M1=0.830 (fraction of A overlapping B) M2=0.832 (fraction of B overlapping A)
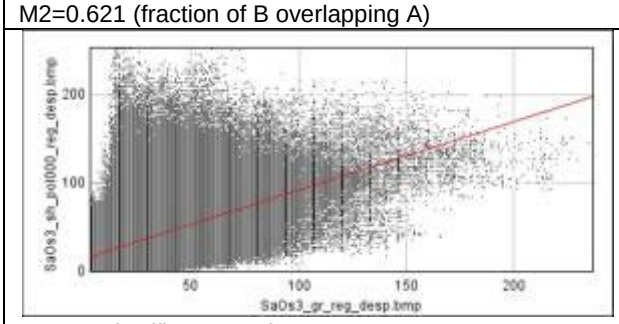	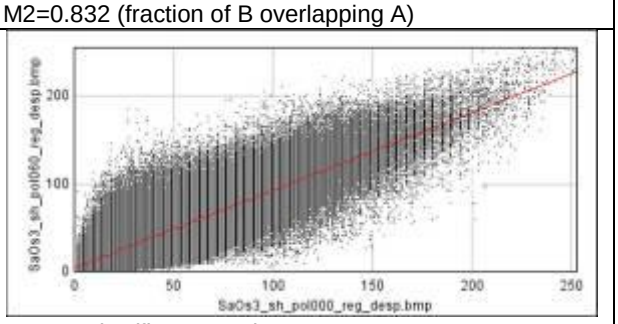
Scatter plot (fluorogram)	Scatter plot (fluorogram)

Table 1. Standard colocalization analysis of the images using JACoP plugin [2] of ImageJ software.

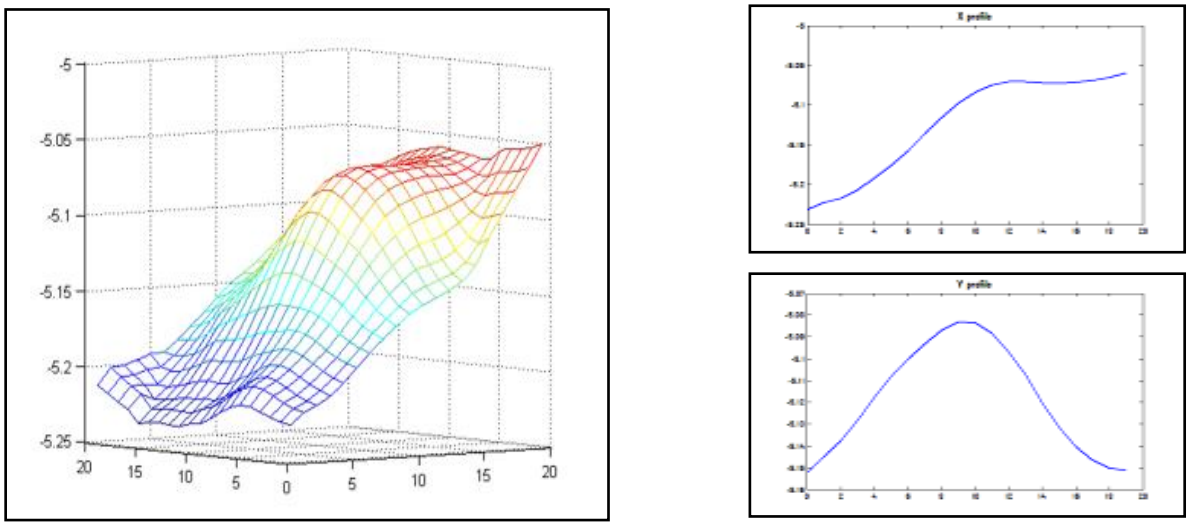

Figure 3. Left: mesh showing values of joint entropy of images in the neighbourhood of original position of the fluorescence image with respect to three SHG images (1+3 multichannel analysis) using Kozachenko-Leonenko entropy estimation; shifting ±10 pixels around the original position, pixel per pixel in both the x- and y-direction.

3D Imaging and Analysis

IM.6.P125
Block face imaging of tissues and cells and applications for 3D reconstruction

M. Dass[1]

[1]Carl Zeiss Microscopy GmbH, Microscopy Labs, München, Germany

martin.dass@zeiss.com
Keywords: tissue, cells, block face imaging, 3D reconstruction

Beside conventional 2D imaging in electron microscopy the imaging in 3D became an important part for researchers and scientists. Structures became a relationship to each other and handling of large data files opens new applications. There are different approaches on the market for 3D data acquisition. One of the most common one is electron tomography. This technique has advantages in high resolution on small structures but is limited to a maximum slice thickness of 500 nm caused by the limits of transmitted electrons under tilted conditions. One alternative approach is the block face imaging done by crossbeam systems or in our case with 3view® an ultramicrotome implemented in an scanning electron microscope (Figure 1).

This block face imaging method can be used for semi-automated analysis of any stained and resin embedded tissue, i.e. brain, muscle, lung or single cells [1,2]. A maximum sample size in x/y of around 600-800 µm can be analysed and also higher resolutions of biological membranes were achieved. The height of the sample in z can be around 1mm. We recommend a very well prepared sample which means a strong fixation on the sample holder and a cubic sample to prevent drift and vibrations during imaging.

For best image qualities the sample should be stained by heavy metals and well embedded as known from ultramicrotomy. The NCMIR protocol is one of the most efficient preparation protocols for 3view® experiments [3]. This protocol was developed for tissues and is a good basement for sample preparation also if the sample and application requires modifications in the preparation protocol. Nevertheless a strong staining with heavy metals and high vacuum conditions increases the signal to noise ratio and end up in a better image quality. We were able to visualize also conventional embedded samples under low kV imaging conditions.

The low kV imaging does came into account also on another point of view. The corresponding interacting volume depends on the accelerating voltage. Monte-Carlo-simulations with pure Carbon as example for biological material gave a penetration depth for 1kV electrons of around 10 – 15 nm (Figure 2). Calculations with the main staining agent Osmium end up in a penetration depth of around 5 nm. In this relation a resolving of membranes is possible. Regarding to this calculations a slice thickness between 15 and 200 nm can be selected. Practically we select 30-50 nm slice thickness for higher magnifications and 100-150 nm for overviews. In principle the smallest resolvable structure and changes in the ultrastructure came into account for the practical workflow. Another important point for stable image series depends on the charge of the sample and related beam current. In this case each sample should be checked during the first 10-20 slices if charge occur. We realized charge mainly in regions with pure embedding medium. Stained sample regions are more conductive than non-conductive embedding regions. To overcome this trouble there are different possibilities. Usage of low kV, changing beam current, short interacting times of the beam with the sample, fast acquisition times, or variable pressure modes (VP). In the case of VP modes higher accelerating voltages are necessary which increases the interacting volume and reduces the z-resolution. A direct comparison of VP images and high vacuum (HV) images represent better image qualities in the case of HV images caused by an better signal to noise ratio. Research on more conductive embedding materials is still going on.

Caused by the easy to handle block face imaging procedure there is a high potential and brought range of applications. Examples of imaged mouse kidney does give an impression of the workflow and image qualities (Figure 3). 3view® is a fast and stable image acquisition for 3D reconstruction.

K. Briggman, W. Denk, Current Opinion in Neurobiology, 16, 562-570 (2006)

1. J.W. Lichtman, W. Denk, Science, 334, 618-622, (2011)
2. T. Deerinck, E.A. Bushong, A. Thor, M.H. Ellisman, http://ncmir.ucsd.edu/sbfsem-protocol.pdf
3. We kindly acknowledge the help of customers and cooperation partners.

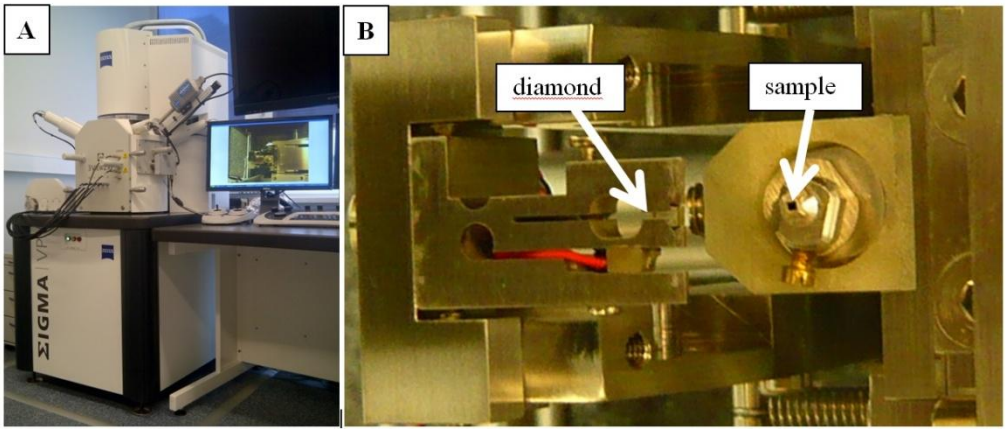

Figure 1. 3view mounted in a Carl Zeiss Sigma VP (A) and a closer look to the sample and diamond knife (B).

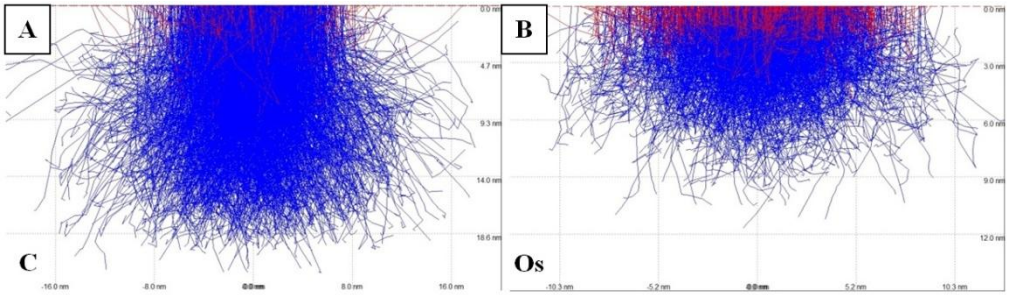

Figure 2. Monte Carlo Simulation – calculated penetration depth of electrons with 1 kV into Carbon (A) and into Osmium (B). Osmium represents the main component in stained biological samples.

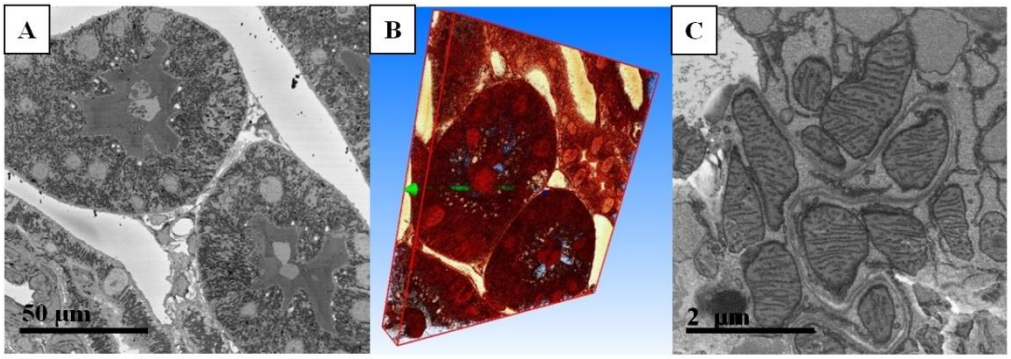

Figure 3. Mouse kidney – first image of a z-Stack image series is shown in (A) and a 3D model based on a fast grey value reconstruction (B). We were able to resolve cristae and membranes of mitochondria in higher magnifications (C)

3D Imaging and Analysis

IM.6.P126
Macro - and micro - CT analysis of porcine liver microvascular corrosion casts

L. Eberlova[1], V. Liska[2], H. Mirka[3], T. Gregor[4], Z. Tonar[5], M. Skala[2], A. Kralickova[5], R. Palek[2]
D. Glanc[2], M. Kralickova[5]

[1]Charles University, Anatomy, Pilsen, Czech Republic
[2]University hospital, Surgery, Pilsen, Czech Republic
[3]University hospital, Department of Imaging Methods, Pilsen, Czech Republic
[4]University of West Bohemia, New Technology and Materials Centre , Pilsen, Czech Republic
[5]Charles University, Embryology and Histology, Pilsen, Czech Republic

lada.eberlova@lfp.cuni.cz
Keywords: corrosion casts, micro-CT, 3D reconstruction

Corrosion casting is a classical, but still unsurpassed method of anatomical preparation of 3-D anatomical branching structures. Corrosion casting became very efficient for describing the morphology and anatomical distribution of blood microvessels. Recent development of X-ray microtomography (micro-CT) has brought resolution similar to routine histology, the tomographic modelling of vascular corrosion casts provides quantifiable three dimensional data on the vascular bed [1,2]. Detailed knowledge of the complex liver vascular anatomy is essential to improve current liver resection procedures [3].

Therefore we present a micro-CT (Figure 1) and macro–CT reconstruction of the porcine liver vasculature based on epoxy resin Biodur E20 (Biodur products, Heidelberg, Germany). Biodur E20 offers an excellent permeability through the entire microvascular bed, sufficient opacity and minimum shrinkage and fragility. Completing macro- with micro-CT scans enables to image the entire vascular bed, sophisticated software packages allow to separate the caval from the portal systems (Figure 2). Micro-CT scans allow also the stereological assessment, including quantification of volume fraction of microvessels, surface density and length density of the microvessels.

.

1. C. Debbaut, J. Vierendeels, C. Casteleyn, et al. Perfusion characteristics of the human hepatic microcirculation based on three-dimensional reconstructions and computational fluid dynamic analysis. J Biomech Eng. 2012;134:011003.
2. Lametschwandtner A, Minnich B, Stöttinger B, Krautgartner WD. Analysis of microvascular trees by means of scanning electron microscopy of vascular casts and 3D-morphometry. Ital J Anat Embryol. 2005;110:87-95.
3. Battaglia S, Fachinetti C, Draghi F, Rapaccini GL, de Matthaeis N, Abbattista T, Busilacchi P. Ultrasound examination of the liver: Variations in the vascular anatomy. J Ultrasound. 2010;13:49-56.
4. This work was supported by the Internal Grant Agency of the Ministry of Health of the Czech Republic under Project No. IGA MZ ČR 13326 and SVV No. 266 801.

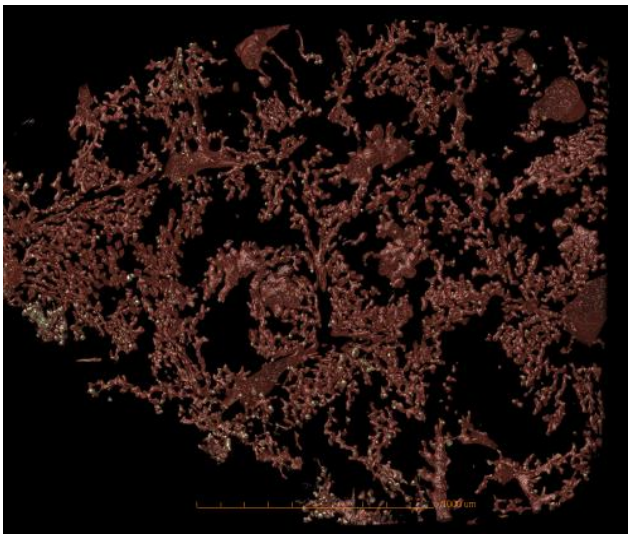

Figure 1. Micro-CT of the liver sinusoids, scale 1 mm

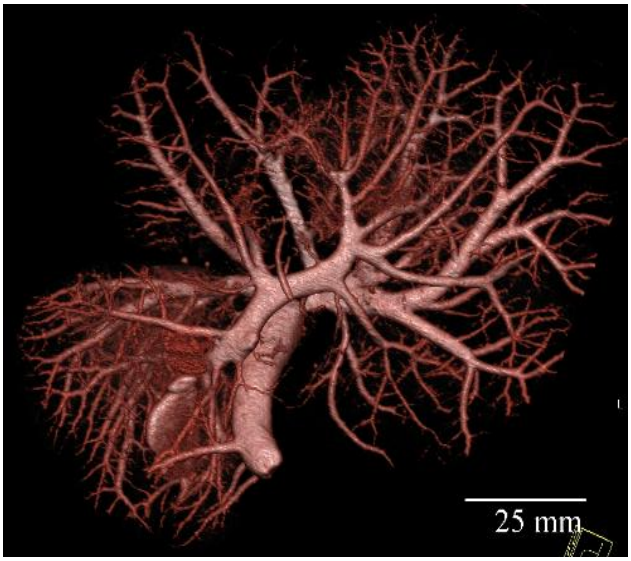

Figure 1. Branching of the portal vein, left lateral lobe, porcine liver, 3D volume rendering technique

3D Imaging and Analysis

IM.6.P127
3D X-ray microscopy for life sciences applications: high-resolution multiscale imaging of micro-anatomy, organismal diversity, and molecular expression

B. Metscher[1], A. Merkle[1,2], G. Müller[1]

[1]University of VIenna, Theoretical Biology, Vienna, Austria
[2]Xradia, Inc., Pleasanton, United States

brian.metscher@univie.ac.at
Keywords: micro-CT, tomography, biological imaging

Efforts in microscopy for life sciences research are driven by two opposing problems: the need for ever finer resolutions and the requirement to visualize tissues and structures in situ. At any given spatial scale, different imaging techniques have been developed for either direct 3D imaging or for reconstructing 3D information from 2D images. For organism-based biological research, the most relevant volumes of interest are in the sub-mm to cm range, with resolutions to around 1µm (or better). Several direct 3D imaging methods are effective in this size domain, particularly confocal microscopy, light sheet microscopy, and x-ray microtomography (microCT). The optical methods have clear advantages in available molecular markers and other visualization probes, but they require clearing of samples and have limits on sample size or thickness.

MicroCT has developed into a mature technology for applications in materials science and related fields, and it is now finding broader application in various areas of life sciences research, including microscopic analyses of unmineralized tissues at histological resolutions. The results obtainable with current lab-based microtomography systems can rival those commonly achieved by synchrotron facility users for whole organisms and other intact biological samples. Commercially available microCT systems can offer spatial resolutions down to less than 1µm in "micro" systems, which use projection-based imaging and microfocus x-ray sources, and to around 50nm in "nano" (or "ultra") systems, which employ x-ray focusing optics [1].

For animal embryos and other whole tissue samples, contrast-enhanced microCT imaging is a powerful complement to other imaging methods, including LM, TEM, and SEM. With simple contrast staining methods, high-resolution volume images of unsectioned specimens can be produced routinely for morphological, embryological, and even molecular studies. Because animal and plant tissues generally have very low opacities to x-rays above 1keV or so, contrast enhancement is a useful adjunct to microCT technology [2,3]. Stains based on elemental iodine are especially versatile (Figure 2B), and phosphotungstic acid imparts strong differential contrast to different animal tissues (Figure 1).

Using a modification to the usual antibody detection schemes that employ horseradish peroxidase-mediated chromogen reactions, we have developed a method for imparting x-ray density to immunoprobe staining [4]. By localized reduction of a soluble silver salt, the locations and quantities of a molecular probe can be visualized clearly in microCT images (fig 2C-E).

Because tomographic imaging records quantitative spatial and object density information, it naturally generates data suitable for various kinds of modeling and analysis. Current applications include functional studies in insects and quantitative modeling of various aspects of morphological development [5].

1. http://xradia.com/products/index.php
2. Metscher, B. D. 2009. *Developmental Dynamics* 238 (3):632-640.
3. Metscher, B. D. 2009. *BMC Physiology* 9:11
4. Metscher, B. D. and Müller, G. B. 2011. *Developmental Dynamics* 240 (10):2301-2308.
5. Metscher, B. D. 2013. *Microscopy and Analysis* 27(2):13-16.

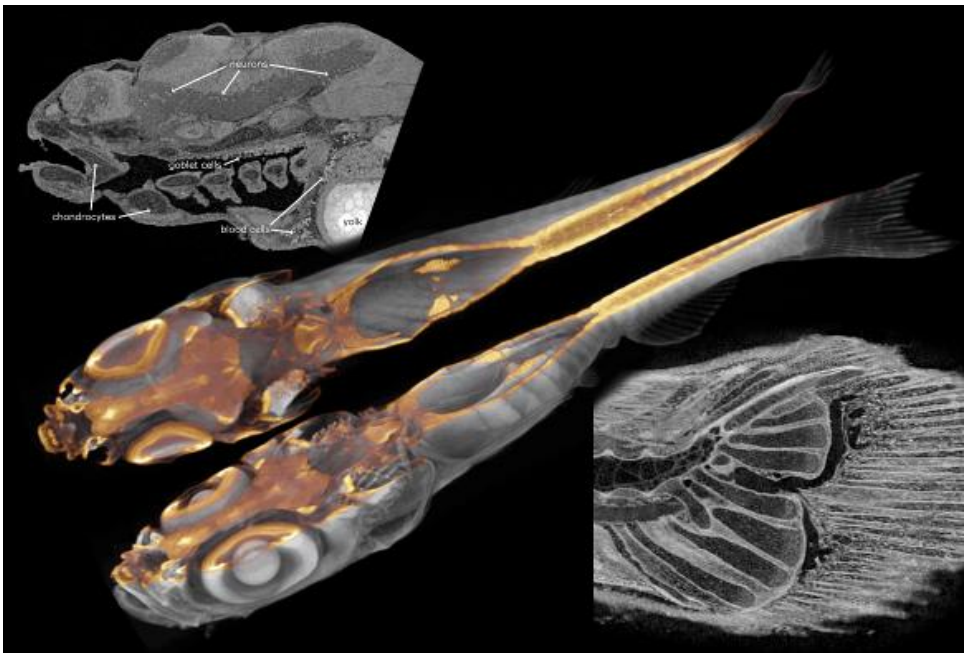

Figure 1. MicroCT images of 5-day zebrafish stained with phosphotungstic acid. Sagittal virtual sections through head (Xradia Versa) and tail (Xradia MicroXCT-200) showing histological details, and a volume-rendered cutaway of a mosaic image of a whole fish.

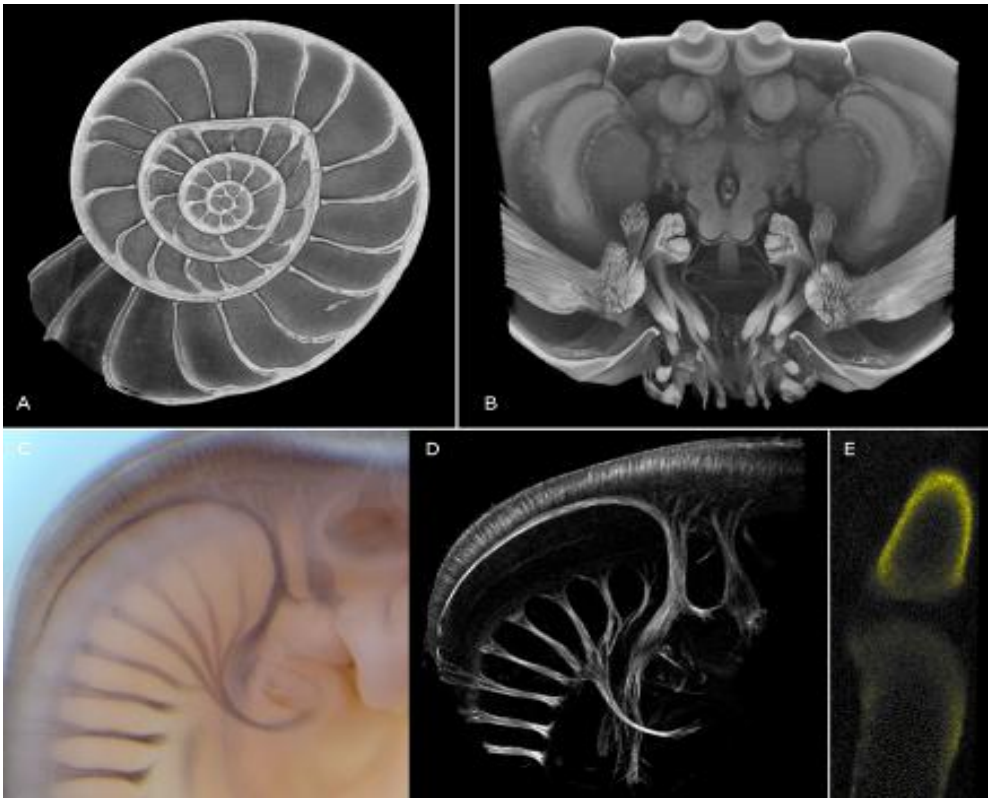

Figure 2. MicroCT imaging in diverse applications. A: fossil foraminiferan; B: neuropteran insect (*Pison*), iodine stained, cutaway of head; C, D: chick embryo immunostained for acetylated tubulin showing detail of developing nerves, LM (C) and microCT (D); E: chick hindlimb digit immunostained for type II collagen, microCT virtual section. Xradia MicroXCT-200 images.

3D Imaging and Analysis

IM.6.P128
Angular BSE Filtering for Topographic Information

D. Phifer[1], J. Pecher[2], P. Valasek[2], M. Petrek[2], T. Vystavel[2]

[1]FEI Company, Eindhoven, Netherlands
[2]FEI Company, Brno, Czech Republic

daniel.phifer@fei.com

SEM angular segmented solid state detectors can be used to filter topographic and compositional contrast with concentric ring detector segmentation designs [1]. Further subdivision of the topographic collection area into arches can yield additional information on the direction of sample surfaces and allow clear interpretation of topography. Since signal intensity is influenced by both sample topography and composition, the ability to separate one from the other is a useful parameter for potentially estimating scale of topography. Solid state detector diodes have been introduced with the ability to address concentric segment rings around the beam exit to separate high angle and low angle electrons (as shown in Figure 1). This works quite well to distinguish between composition and density on the inner rings closest to the beam and topographic information which is more prominent on the outer rings [1]. The relative direction of the surface collected is seen as uniform shading from one side of the image to the other. Segmentation into arch-shaped collection areas of the outer topographic rings allows collection of highly shadowed images which can be used for image analysis and potentially to quantify topography. Conventional segmentation of the detector such that there are 4 “quadrant” segments does not allow separation of atomic number effects on the topographic information as the inner (composition) and outer (topographic) information are both within a given signal collection area. Since BSE distribution is dependent on both composition and topography, the effect of a high atomic number region with topography may be exaggerated in respect to an adjacent low atomic number region due to the combined signal brightness and contrast. Direct signal is used for calculating height of topography based on contrast and brightness differences in the standard algorithms. The inability to separate brightness due to composition from that of topography could skew results if brightness and contrast are used as the determining factor for feature height, even when this is compared to a reference “off-axis” or 5th segment signal. This could be a contributing factor for why most surface model data is not so accurate with off-axis in the 3 or 5 segment BSE configurations [2]. Subdividing the outer “topographic” rings of concentric ring detector into three 60 degree “arch” segments allows separation of composition information (on the center ring) and allows characterization of directional information from “more pure” topographic content. An example of this is shown in Figure 2, where images from the inner ring and the three segments are shown. Shadowing is based on the direction of the sample surface and detector segment view of a sample orientation. Signal angular collection utilizing the unique BSE crystal segmentation provides new sample surface information. It is yet to be seen if angular filtering truly has the potential to create more accurate surface height representations in SEM imaging where composition can be removed from the equation or conversely used to refine the signal interpretation to yield better estimations because of the compositional signal differences. Software algorithms need to be developed to process this information whereby the ability to separate signal in this way can provide new insight into topographic surface characterization. This development presents a new opportunity to use direction-rich data for surface mapping and height measurements.

1. T. Vystavel, XIVth International Conference on Electron Microscopy (2011).
2. A. Agrawal et al, European Conference on Computer Vision (ECCV) (2006) p21.

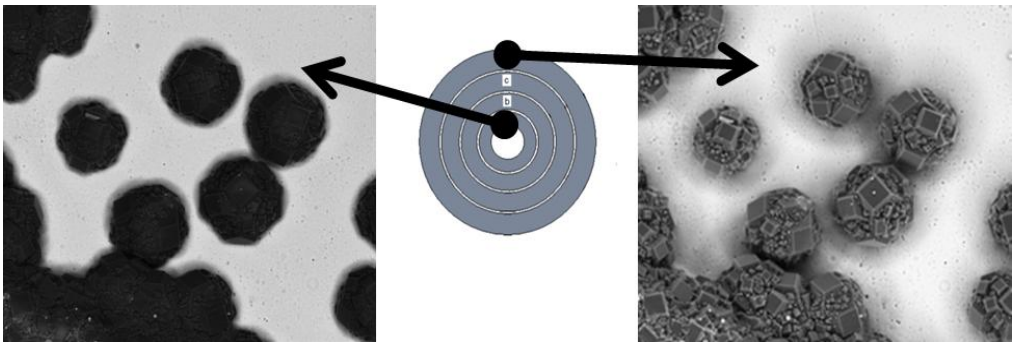

Figure 1. Angular filtering with concentric ring BSE segmentation clearly separates the atomic information form the innermost segment (right image) and topographic from the outer most segment (left image) content. Field width is ~23 microns.

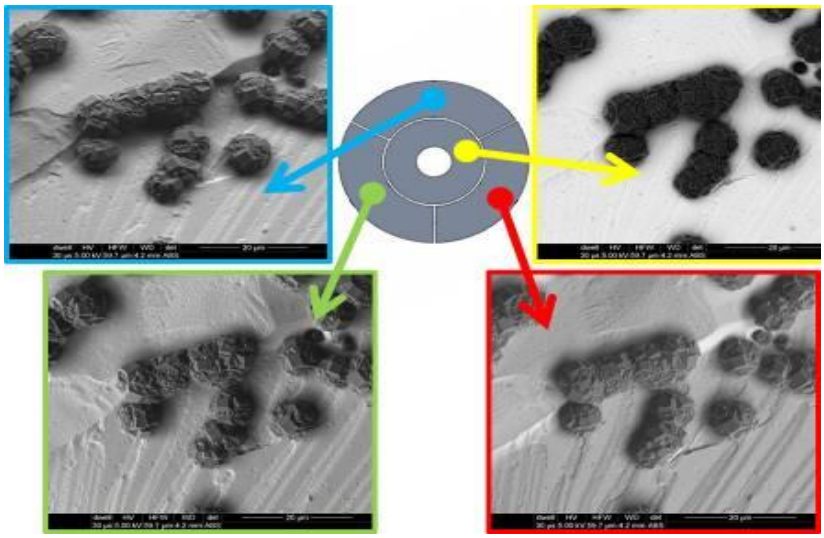

Figure 2. With an angular segmentation of the outer detector segments, separation of the topographic component is possible with angular direction yielding perspective shadows. This new information can be used to interpret the direction of slope in an image area in relation to neighboring pixels.

3D Imaging and Analysis

IM.6.P129
Electron tomography of Au nanorods at the atomic scale

B. Goris[1], S. Bals[1], G. Van Tendeloo[1]

[1]EMAT, University of Antwerp, Antwerp, Belgium

bart.goris@ua.ac.be
Keywords: Electron tomography, Au nanorods, Atomic resolution

To understand the properties of advanced nanostructured materials, understanding of the three dimensional (3D) structure is indispensable both at the nanometer and the atomic scale. Electron tomography enables us to reconstruct this 3D information based on a series of two dimensional (2D) projection images acquired using electron microscopy. When using conventional electron tomography, the quality of the final reconstruction is predominantly determined by the number of 2D projections that is used.

Recently, several novel reconstruction algorithms have been developed that exploit some prior knowledge concerning the sparsity of the reconstructed object during the reconstruction process [1, 2]. At the nanoscale, one can often assume that the reconstructed object has a sparse gradient since many nanoparticles have a uniform density. This method, sometimes referred to as a total variation minimization (TVM) reconstruction technique, is used to create a 3D reconstruction of Au nanorods. A 3D visualization of this reconstruction is displayed in Figure 1 revealing a faceted morphology. The presence of these facets cannot be determined from a reconstruction based on a regular reconstruction algorithm such as the simultaneous iterative reconstruction technique (SIRT). The presence of specific surface facets has important consequences on the catalytic properties of the nanorods. However, to correctly index these surface facets, a reconstruction at higher magnifications, in which the atomic lattice can be resolved, is required.

At the atomic scale, prior knowledge about the sparsity of the object itself can be exploited. This enables the calculation of a 3D reconstruction of the atomic structure of different Au nanorods. As a result, the influence of the synthesis method on the surface facets composing the final morphology of these Au nanorods can be determined at the atomic scale [3]. In Figure 2, it is shown that Au nanorods grown with cetyltrimethylammonium bromide (CTAB) surfactant exhibit {100} and {110} facets whereas the {520} facets are dominant for nanorods synthesized with Gemini surfactant. In addition to these results, also deviations from a perfect crystal lattice can be observed resulting in a 3D strain field. This information may be crucial for a better understanding of the relationship between the local structure and the properties of the nanostructures. As a first example we have applied this approach to Au nanorods, but the methodology is also valid for structures that contain multiple chemical elements. In this manner, the atomic interfaces and intermixing of different atom types can be investigated in 3D leading to precise information concerning the local atomic lattice of the investigated samples [5].

1. Z. Saghi, et al., Nano Letters 11 (2011), p. 4666-4673
2. B. Goris, et al., Ultramicroscopy 113 (2012), p. 120-130
3. B. Goris, et al., Nature Materials 11 (2012), p. 930–935
4. B. Goris acknowledges financial support from the FWO-Flanders (Fonds voor Wetenschappelijk Onderzo - - provision of the samples.

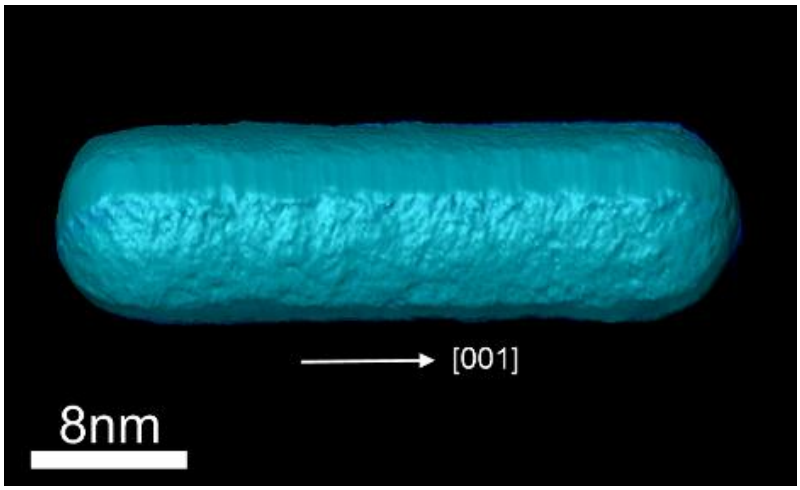

Figure.: Visualization of tomographic reconstruction of Au nanorod created using a total variation minimization based reconstruction algorithm. Different surface facets are observed in this reconstruction.

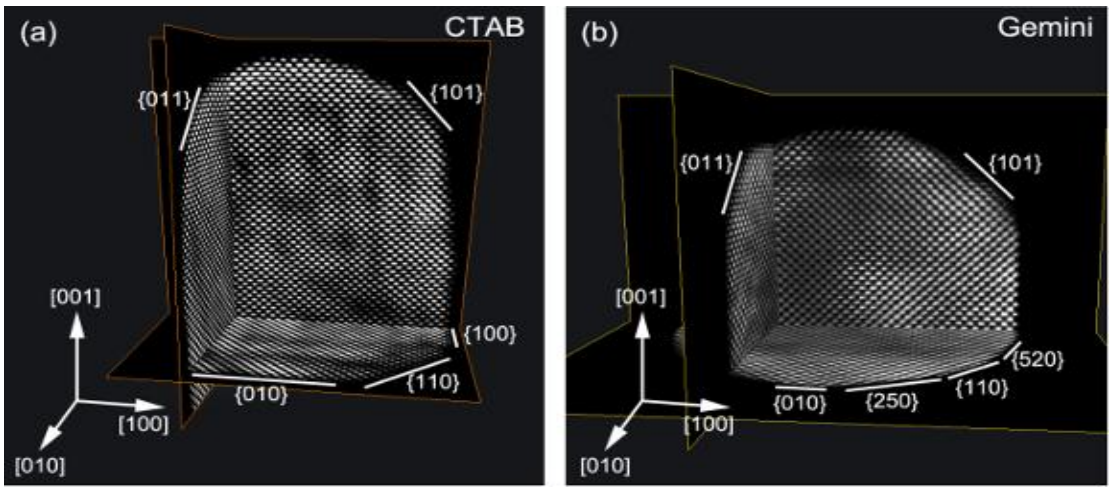

Figure 2. (a) Three orthogonal slices through the reconstruction of a nanorod grown with CTAB. It can be seen that {110} and {100} facets compose the morphology of the rod while {520} facets are present at the rods synthesized with Gemini surfactant.

3D Imaging and Analysis

IM.6.P130
3D reconstruction of lipid droplets in lipase deficient macrophages

D. Kolb-Lenz[1], B. Radovic[2], G. Leitinger[1], D. Kratky[2]

[1]Institute of Cell Biology, Histology and Embryology, Medical University of Graz, Graz, Austria
[2]Medical University of Graz, Institute of Molecular Biology and Biochemistry, Graz, Austria

dagmar.kolb@medunigraz.at
Keywords: macrophages, lipid droplets, ATGL -/-, HSL -/-, ATGL -/- HSL -/-, LAL -/-, Transmission electron microscopy, electron tomography.

Macrophages are a very good model system for studying lipid metabolism due to their high capacity for lipid accumulation. Ultrastructural analysis of lipid droplet formation in macrophages might help understanding foam cells formation, a major player in development of atherosclerosis.
We analyzed lipid droplet ultrastructure in macrophages obtained from different lipase deficient mouse models: ATGL -/- (Adiopse triglyceride lipase), HSL -/ - (Hormone sensitive lipase), ATGL –/- HSL -/- double knock out and LAL -/- (Lysosomal acid lipase).
Without exogenous lipid loading we saw accumulation of lipids in macrophages of all strains compared to wild type. In ATGL - /- we investigated many classical large lipid droplets with a leaflet. A small number of lipid droplets was observed in HSL -/- however this seems to be normal because in WT we also see similar lipid accumulation. In comparison to these single knock outs electron microscopy (EM) revealed significant ultrastructural differences in double knock outs. Lipid droplets appeared to cluster thereby losing their spherical shape. In LAL -/- neutral lipids generally accumulate in lysosomes which can readily be distinguished from LD´s due to double layer membranes around the accumulated lipids. After loading with VLDL we see normal lipid droplet formation and many clusters of lipid loaded lysosomes. By using different EM approaches and especially serial sectioning we were able to visualize heterogenous ultrastructure in the lysosomes.
High resolution analysis of lipid droplets in macrophages deficient of different lipases revealed different ways of lipid accumulation.

3D Imaging and Analysis

IM.6.P131
STEM tomography investigation within a combined optimization approach of mesoporous titania used as catalyst support

B. Winter[1], V. Novák[2], E. Ortel[3], B. Butz[1], B. Paul[3], P. Kočí[2], M. Marek[2], R. Kraehnert[3], E. Spiecker[1]

[1]FAU Erlangen-Nürnberg, Center for Nanoanalysis and Electron Microscopy (CENEM), Erlangen, Germany
[2]Institute of Chemical Technology, Department of Chemical Engineering, Prague, Czech Republic
[3]Technical University Berlin, Department of Chemistry, Berlin, Germany

benjamin.winter@ww.uni-erlangen.de
Keywords: electron tomography, catalysis, nanocasting, multi-scale mathematical modelling, diffusion, reaction, synthesis

For industrial and environmental applications, supported catalysts represent one of the most important types of catalyst material. The efficiency and performance of the catalytic converters depend on their synthesis, design, intrinsic catalytic and mass-transport properties [1]. The porous catalyst support should have a preferably large surface area providing enough space to bind many active metal nanoparticles enabling high reaction rates per catalyst volume and as high diffusion rates of the reactants to the active centers as possible. A precise analysis of the porosity and pore morphology of the support material and the position and quantity of nanoparticles enable to understand the properties of the catalyst and help to optimize its pore system. So, experimental results combined with computational approaches to catalyst design, intrinsic catalytic and mass-transport properties enable virtual prototyping and optimization of the pore system of solid catalysts for a given application [2].

Here, a procedure to predict and optimize the combined reaction-transport performance of a mesoporous TiO_2 catalyst support (see Figure 1.) is demonstrated. It combines the results from the characterization of a template-assisted synthesis of catalyst thin film layers by means of transmission electron microscopy (TEM) and small angle X-ray scattering (SAXS) with multi-scale mathematical modeling utilizing experimentally acquired, 3D computer-assisted reconstructions of the porous media.

Scanning TEM (STEM) tomography enables to reconstruct the three-dimensional catalyst pore system with nanometer resolution (see Figure 2.). The reconstructed volume is directly used to determine the pore size distribution and interconnectivity applying the maximum sphere inscription method (MSI) [3].The derived pore size distribution well agrees with results obtained from nitrogen sorption measurements (see Figure 3.a) and b)). Furthermore, the digital 3D reconstruction of the pore system is directly used as input data for the simulation of transport and reaction processes within the porous layer. Thus, the effective diffusivities and tortuosity factors along different directions in the reconstructed pore system obtained by diffusion simulation of CO transport in the reconstructed templated mesoporous TiO_2 layer are determined (see Figure 3.c)). Such computational analysis facilitates optimizing the performance of the catalyst based on its realistic 3D reconstruction. This method can generally be applied to a wide range of porous catalytic layers or membranes, where internal transport limitations significantly affect the macroscopic performance [2].

1. E. Ortel, S. Sokolov, C. Zielke, I. Lauermann, S. Selve, K. Weh, B. Paul, J. Polte, R. Kraehnert, R. Chemistry of Materials 24 (2012), p. 3828.
2. V. Novák, E. Ortel, B. Winter, B. Butz, B. Paul, P. Kočí, M. Marek, E. Spiecker, R. Kraehnert, J. of Catalysis (2013), submitted
3. V. Novák, F. Stepanek, P. Kočí, M. Marek, M. Kubicek, M. Chemical Engineering Science 65 (2010), p. 2352.

This work has been financially supported by the German Research Foundation (DFG) within the framework of the priority program SPP 1570 (project DFG SP 648/4-1 “3D analyses of complex pore structures using electron tomography and high-resolution TEM”) as well as by the Czech Science Foundation, project GACR P106/10/1568. Vladimír Novák is grateful for a fellowship of the German Academic Exchange Service (DAAD, Deutscher Akademischer Austauschdienst). Ralph Kraehnert acknowledges generous financial support of BMBF (FKZ 03X5517A) and of Einstein-Stiftung Berlin. Furthermore, the Cluster of Excellence EXC 315 “Engineering of Advanced Materials” at the Friedrich-Alexander University Erlangen-Nuremberg is gratefully acknowledged for instrumental support.

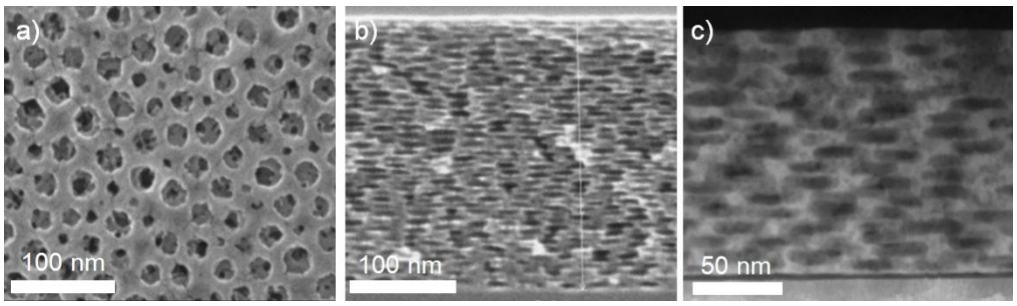

Figure 1. SEM images in a) top view and b) cross section direction and c) STEM image of the mesoporous titania catalyst support.

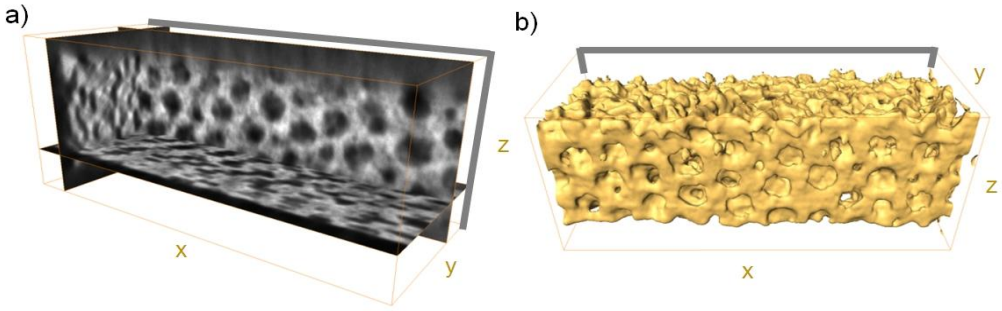

Figure 2. 3D reconstruction of the mesoporous TiO_2 derived from STEM tilt series (angular range: -71° – +63°). a) Ortho slices and b) surface rendering (pore walls appear as solid) of the reconstructed volume pores (volume size about 368 x 155 x 154 nm³). The x–z slice clearly shows the quasi periodic arrangement of the pores. Grey lines indicate in both images the x–z orientation of the Si substrate onto which the titania film was coated.

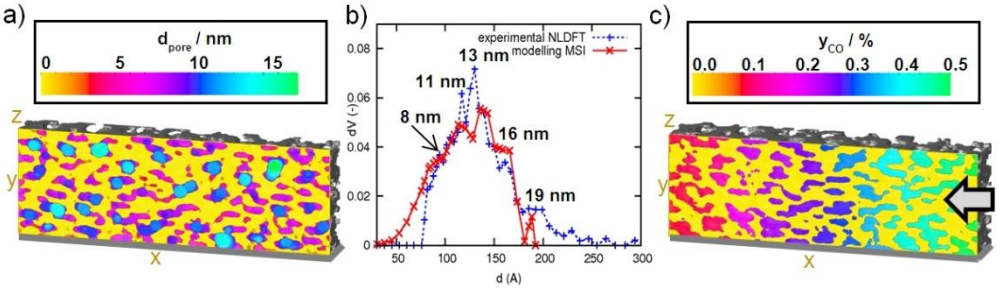

Figure 3. a) Local pore size distribution of the templated pore system obtained from MSI. Color coding indicates the diameter of the largest inscribable sphere at a given position. The visualisation corresponds to a cross section view of the sample. b) Pore size distribution of mesoporous templated TiO_2: Comparison between volumetric pore size distributions obtained from the MSI (tomography) vs. independently obtained N_2 sorption data evaluated by non-local density functional theory (NLDFT) method. c) Concentration profiles of CO for the x-direction (indicated by grey arrow) in the reconstructed pore system obtained by diffusion simulation of CO transport in the reconstructed model (model with imposed concentration gradient from right $y_{0,\,CO}$=0.5 % to left $y_{1,\,CO}$ = 0.1 %). Substrate orientation is the x–z plane. Simulated system size of 340 x 113 x 72 nm³ with discretization step 0.377 nm (volume cut out from tomogram shown in Figure 2.).

3D Imaging and Analysis

IM.6.P132
Whisker like oxide formation and its growth mechnism on pure iron nano powder

J. Gluch[1], C. Jung[1], L. Röntzsch[2], E. Zschech[1,3]

[1]TU Dresden, Dresden, Germany
[2]Fraunhofer IFAM, Dresden, Germany
[3]Fraunhofer IZFP, Dresden, Germany

juergen.gluch@tu-dresden.de
Keywords: TEM, SEM, tomography, whisker, iron oxide

In this study, we focus on the historic steam-iron-process for hydrogen generation. The cyclic manner of the redox reactions can also be implemented as storage for hydrogen, where hydrogen generation is represented by the reaction of highly reactive nano-sized iron powder (sponge) with water steam and hydrogen storage is represented by the reaction of magnetite powder with hydrogen: $3\ Fe + 4\ H_2O \leftrightarrow Fe_3O_4 + 4\ H_2$. Since the early use of the steam-iron-process a crucial disadvantage is the decrease of storage capacity after repeated storage cycles. The oxidation of nanosized pure iron powder at temperatures up to 750 K in a wet atmosphere results in a complex growth pattern of oxides, which was previously reported for stainless steel [1]. Depending on temperature and atmosphere, whiskers grow to a length of up to several micro meters.

All experiments were carried out at the micro- and nanoscale. The starting material for the redox cycle reaction is hematite powder (Fe_2O_3) that forms loose agglomerates in the range up to 100 micro meters. The size of the individual powder particles is in the range of few 10 nm to some 100 nm (Figure 1a and b). We designed a reaction chamber that fits into the beam path of an X-ray microscope (Xradia nanoXCT-100). It allows investigations on powder particle agglomerates in the diameter up to 16 µm. Using this attachment, the morphology change of powder particle agglomerates during repeated half reactions of the steam iron process can be imaged directly. Results from in-situ X-ray radiography and tomography tests inside the micro reactor chamber will be shown. The spatial resolution of the X-ray microscope is in the range of the particle size, which makes it difficult to observe fine details. Especially the formation of thin platelets and whiskers like features cannot be recorded with this device and was only visible through imaging by scanning electron microscopy and analytical transmission electron microscopy (ZEISS Libra 200 Cs MC). It shows the changed structure and the whiskers (Figure 1c). A multi-layer oxide develops at elevated temperatures. This oxide layer exhibits complex structures and microstructures. In tomographic x-ray reconstructions this oxide appears to form a closed skin around the powder agglomerate particles (Figure 1d) and thus decreases the reactivity during repeated cycles of the redox reaction.

This oxide thin is up to 250 nm thick and it is covered with platelet like features growing at random over the surface. These platelets seem to be hexagonal in shape.

There are also a large number of whisker growing over the entire surface. To investigate the growth mechanism and possible routes for prevention of oxide skin formation we continue TEM characterisation.

1. R.L. Higginson and G. Green, Corrosion Science 53 (2011) p.1690-1693
2. This work is funded by the European Union (ERDF) and the Free State of Saxony via the ESF project 100087859 ENano.

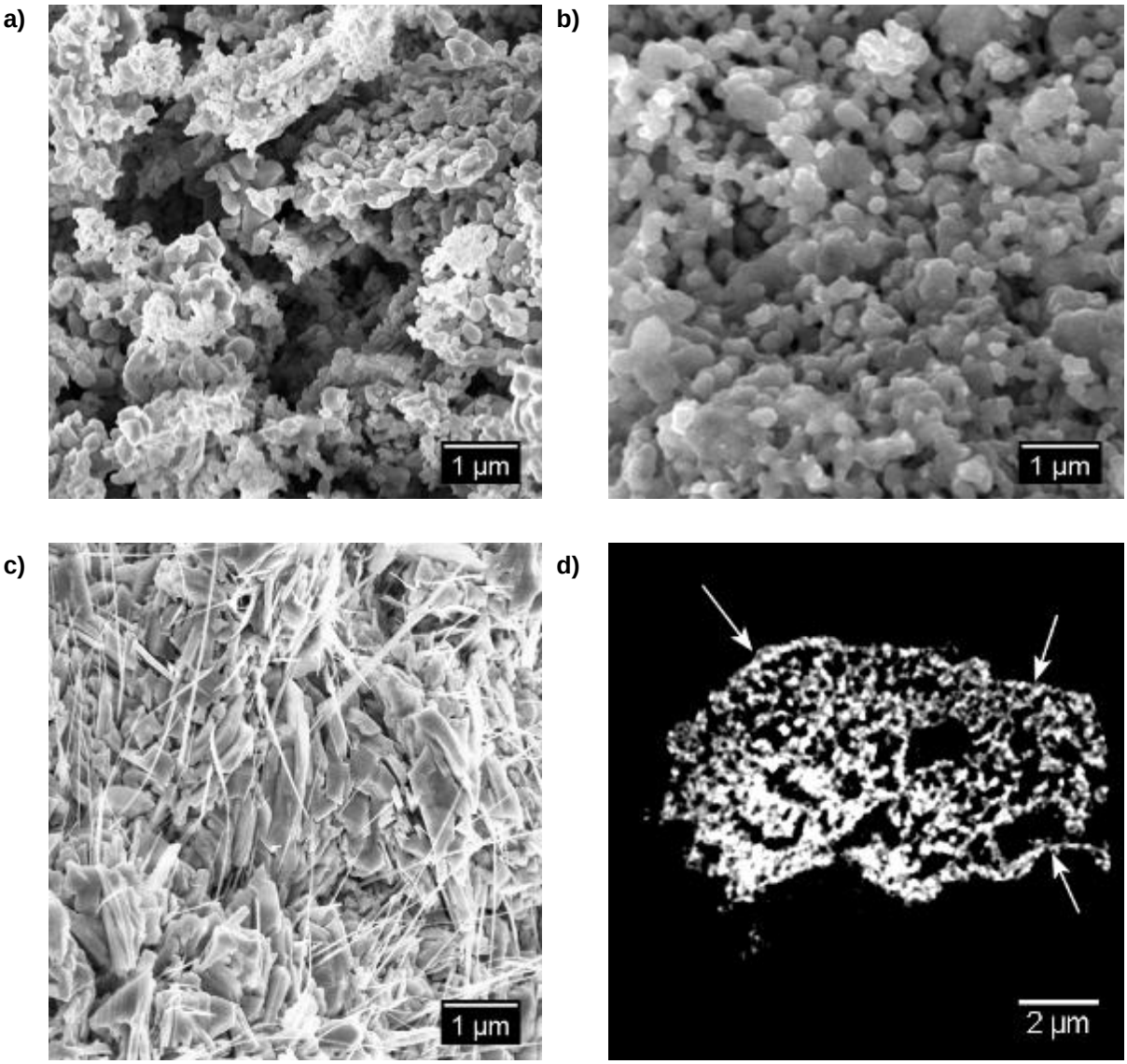

Figure 1. SEM images a) initial iron oxide powder (hematite) before, and b) after initial reduction in pure hydrogen. c) particles and whisker after oxidation in wet atmosphere d) tomographic cross section through powder agglomerate after one full redox cycle. The arrows point at position where the formed oxide skin is easy to be seen.

3D Imaging and Analysis

IM.6.P133
Resolution Extension in Missing-wedge-free Dark-field Tomography

D. Tyutyunnikov[1], C. Koch[2], P. van Aken[2]

[1]Max-Plank Institute, StEM, Stuttgart, Germany
[2]University, Experimental Physics, Ulm, Germany

tyutyunnikov@is.mpg.de
Keywords: transmission, electron, microscopy, tomography, charge-flipping, reconstruction algorithm

Transmission electron microscopy (TEM) is a powerful tool to investigate the atomic structure and morphology of nano- and micro-objects. Elastic electron scattering provides information about the outer contour of objects as well as their inner structure up to atomic resolution. However, TEM images are, at least in the kinematic (single scattering) approximation, projections of the object along the electron beam direction. To reveal the three-dimensional (3D) structure one needs to record a number of different projections by either tilting the sample or the electron beam [1]. The 3D morphology of the object is then reconstructed using a tomographic reconstruction algorithm. A very common problem in conventional bright-field (BF) tomography is the missing-wedge, an artifact which arises due to a limited range of tilt angles at which projections can be acquired.

Figure 1 shows the reciprocal-space representation of a simple cube. Figure 2b shows how a dark-field tilt series samples reciprocal space. Even for a tilt range much smaller than what is commonly used in BF tomography, the complete 3D volume can be swept by the Ewald sphere, preventing the appearance of missing-wedge artifacts. However, far away from the Bragg-condition the scattering signal becomes very weak, requiring long exposure times, making it difficult to acquire the necessary data for very high resolution along the vertical axis. In this work we report how the 3D shape of the object and its inner structure can be reconstructed from a very limited range of tilt angles. This approach is based on charge-flipping of the real-space potential which is widely used in crystallography [2] and can be applied to retrieve the morphology of small nanoparticles. The input data for this approach requires only a limited k_z -range in Fourier space (see Fig.1). Instead of acquiring diffraction patterns intensities [3] we propose to record the complex scattering signal in dark-field imaging mode [4], combined with DF focal series reconstruction as we have recently applied for mapping strain [5].

Our approach was verified by kinematical simulations for different conditions and different arrangements and shapes of particles, also including noise. The stability of the algorithm regarding the density and range of measured reciprocal space information was investigated and will be presented as well. In figure 2 one can see the results of the reconstruction for two separated particles. The reconstructed object is very close to the original one. The difference between flipping the real-space object potential or its derivatives will be shown and compared quantitatively. The convergence of the algorithm is discussed and the ways towards its optimization will be presented. The reconstruction of the real sample (MgO nanoparticle) based on this approach by using dynamical image simulations is currently in progress.

1. C.T. Koch, V.B. Özdöl, K. Ishizuka, Microscopy and Analysis May (2012) 5-8
2. Gábor Oszlányi and András Sütő, Acta Cryst. (2008). A64, 123–134
3. R. Dronyak et al., Appl. Phys. Lett. (2010) 96, 221907
4. Lionel Cervera Gontard, PhD thesis, 2007
5. C.T. Koch, B. Özdöl, P.A. van Aken, Appl. Phys. Lett. (2010) 96, 091901

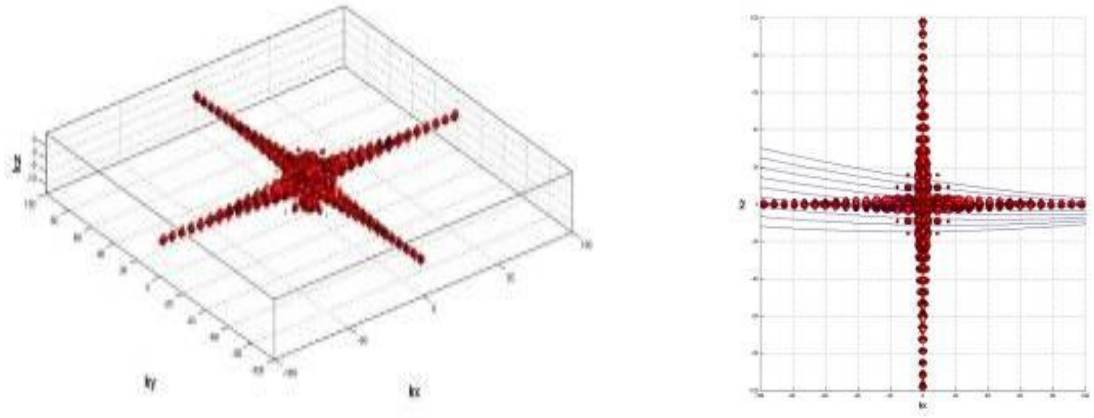

Figure 1. a) The modulus of the reciprocal-space representation of a cube with limited k_z -range. b) The principle of dark-field tomography: the intersection of Ewald sphere with the diffraction signal is indicated by blue arcs.

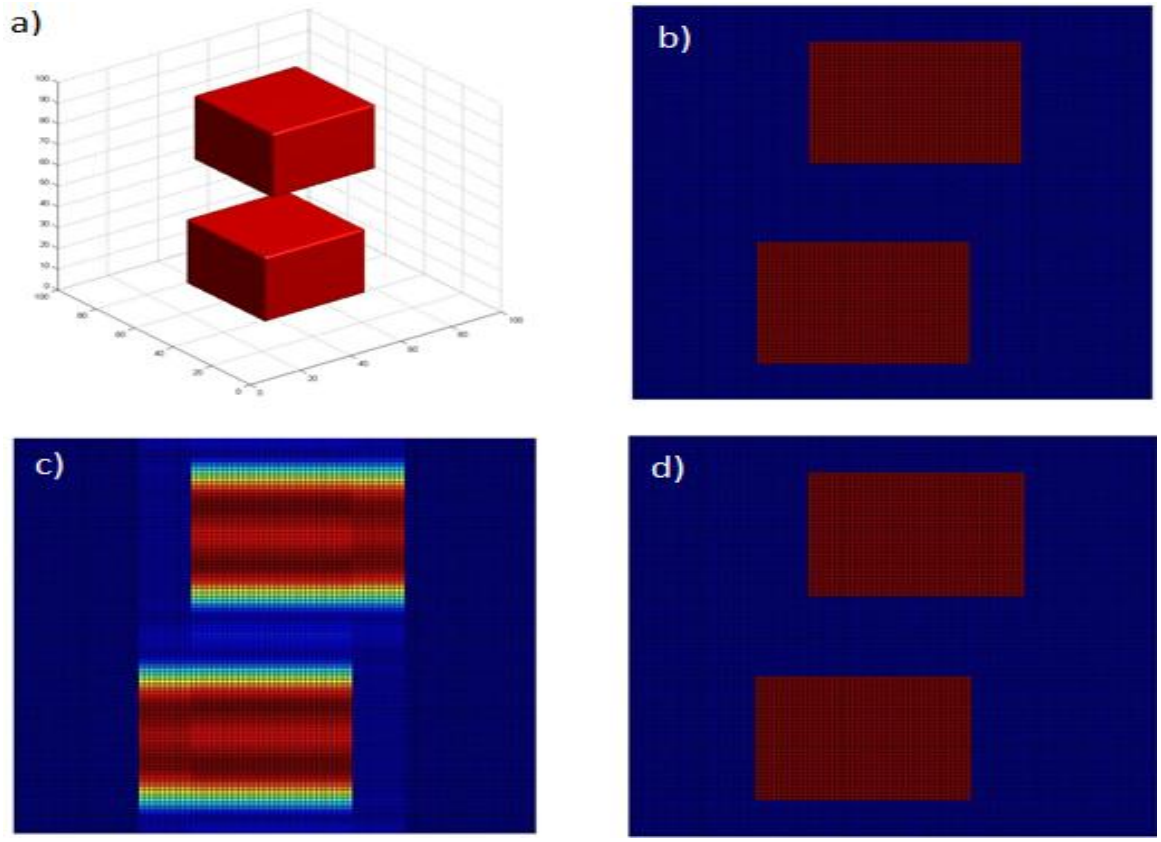

Figure 2. a) Isosurface of the 3D model of 2 particles. The modulus of a vertical slice through the 3D real-space volume of scattering potential: b) the original object, c) after limiting the data along k_z in Fourier space, d) after 400 iterations of the reconstruction algorithm.

3D Imaging and Analysis

IM.6.P134
New applications in Atom Probe Tomography

H.-U. Ehrke[1], J.W. Valley[2], T. Ushikubo[2], M.K. Miller[3], H. Takamizawa[4], Y. Shimizu[4], L.M. Gordon[5] D. Joester[5], A.D. Giddings[6], D.J. Larson[6]

[1]Cameca GmbH, Unterschleissheim / Munich, Germany
[2]University of Wisconsin, Department of Geoscience, Madison, WI, United States
[3]Oak Ridge National Laboratory, Oak Ridge, TN, United States
[4]Tohoku University, Institute for Materials Research, Tohoku, Japan
[5]Northwestern University, Dept. of Materials Science & Engineering, Evanston, IL, United States
[6]Cameca Instruments Inc., Madison, WI, United States

ulrich.ehrke@ametek.de
Keywords: Atom Probe Tomography, nano-scale, spectrometry

Recent innovations in atom probe tomography (APT), including laser-pulsed field evaporation and focused ion beam-based specimen preparation, have enabled a wide range of new applications [1]. This presentation provides a survey of those advances, including analysis of metal-oxide-semiconductor (MOS) transistor dopant distribution, geological dating of individual zircon crystals, quantum dot (QD) self-assembly in III-V multi-layer device structures, analysis of biological materials and nano-scale phase behavior of metallic glasses.

The structural variability in MOS transistors has substantially increased due to the reduction in lithographic feature size which occurs with each device generation. APT provides elemental mapping to correlate electrical performance with dopant concentration. For example in 65 nm-node n-MOS transistors, the channel dopant concentration, as imaged in Figure 1, has been positively correlated with the threshold voltage [2].

In geological materials, APT is now providing unique information for understanding the thermal history and mechanisms of mineral reaction, mineral exchange and radiation damage. In zircon crystals, precipitates containing Y and Pb are readily observed, as shown in Figure 2. The $^{207}Pb/^{206}Pb$ ratios for nm-scale domains (<2×10^4 atoms Pb) average 0.17±0.04 and 0.43±0.14 for 2.4 and 4.0 billion year old zircons respectively [3], in agreement with SIMS ratios (0.1684 and 0.4269) derived from much larger analysis volumes (hundreds of μm^3).

QDs are self-assembled nanostructures that have unique electronic properties, determined by their physical structure. The high spatial resolution and chemical sensitivity of APT has made it possible to image QDs in InAs/GaAs multi layers [4]. QDs may form into a pillar arrangement when the strain field from one QD layer influences the growth of subsequent layers; however the apparent helical distribution shown in Figure 3 has never previously been reported.

On the biological side, APT has revealed oriented collagen fibers in the dentin of elephant tusks. Figure 4 is a mass spectrum from an apatite-derived calcium and phosphate species, additional inorganic substituents, and carbon/nitrogen containing fragments of organic macromolecules [5].

In metallic glass research, the glass forming ability of high Fe-content glasses for low-cost transformer applications is improved by small copper additions, as imaged in Figure 5. After thermal annealing for 30 minutes at 729 K, $Fe_{75.3}C_{7.0}Si_{3.3}B_{5.0}P_{8.7}Cu_{0.7}$ glasses phase separate into α-Fe precipitates, ultrafine spheroidal ε-Cu-rich precipitates, silicon-depleted $Fe_3(P,B,C)$, and Fe_3C volumes [6].

1. T. F. Kelly and D. J. Larson, *Annual Reviews of Materials Research* 42 (2012) 1.
2. H. Takamizawa et al., *Applied Physics Letters* 100 (2012) 253504.
3. J. W. Valley et al., *Abstracts American Geophysical Fall Meeting* (2012) V12A-05.
4. A. D. Giddings et al., *Phys. Rev. B* 83 (2011) 205308.
5. L. M. Gordon, L. Tran and D. Joester, *ACS Nano* 6(12) 2012 10667.
6. Part of this research was sponsored by ORNL's Shared Research Equipment (ShaRE) User Facility, which is sponsored by the Scientific User Facilities Division, Office of Basic Energy Sciences, US Department of Energy.

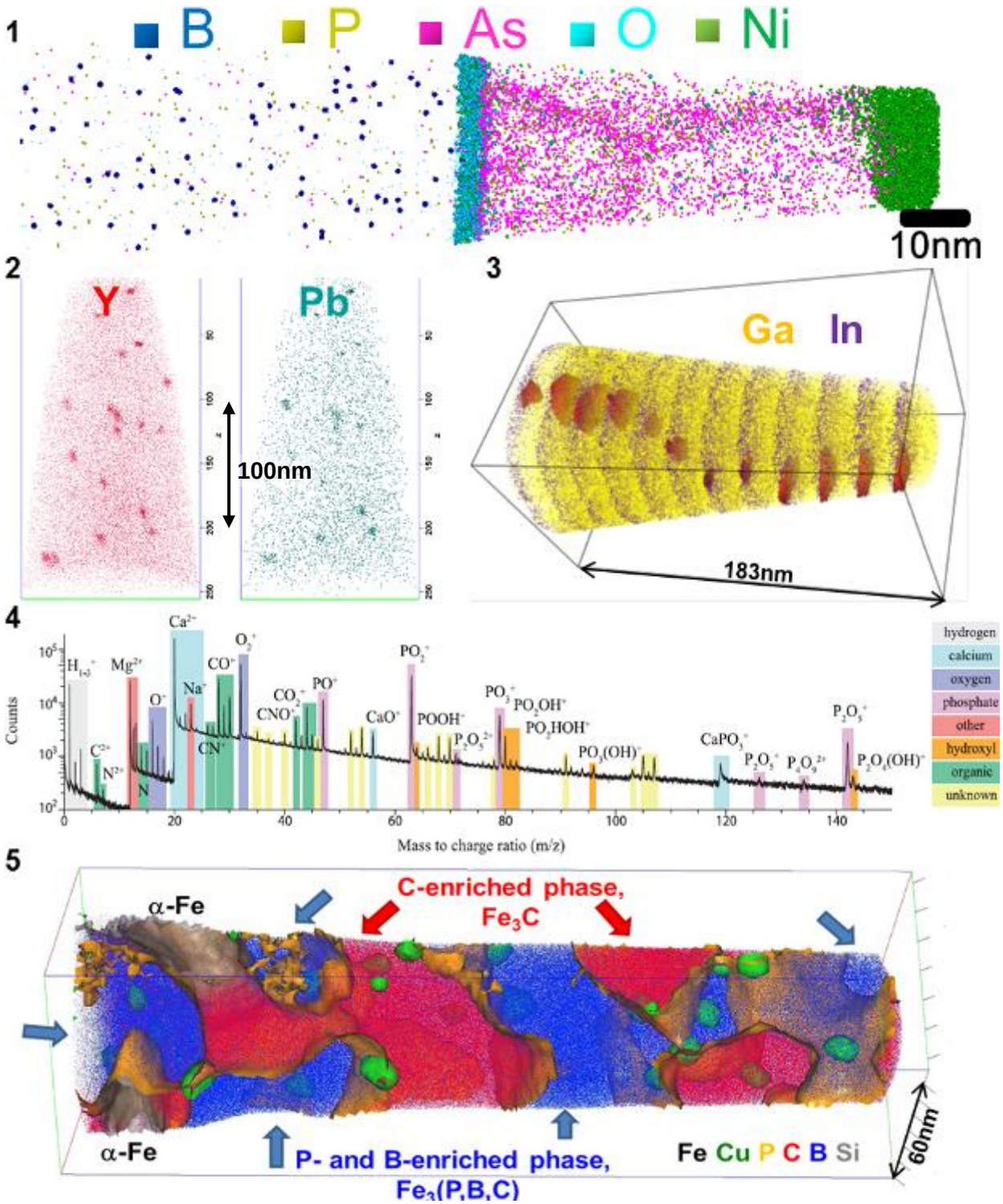

Figure 1. Atom map showing the dopant distribution in a MOS transistor.
Figure 2. Atom maps showing the Y and Pb distribution in a zircon mineral.
Figure 3. Atom map showing the arrangement of quantum dots in GaAs/$Ga_{1-x}In_xAs$ multi layers, iso-concentration surfaces for x > 15% are highlighted in red.
Figure 4. Mass spectrum from a nano-scale fibre within elephant tusk dentin.
Figure 5. Atom map with various composition surfaces highlighting the complex nano-structure observed in this particular metallic glass.

3D Imaging and Analysis

IM.6.P135
Combined SIMS-SPM instrument for high sensitivity and high resolution elemental 3D analysis

Y. Fleming[1], T. Wirtz[1], M. Gérard[1], P. Philipp[1], U. Gysin[2], T. Glatzel[2], E. Meyer[2], U. Maier[3]
U. Wegmann[3]

[1]CRP - Gabriel Lippmann, Belvaux, Luxembourg
[2]University of Basel, Department of Physics, Basel, Switzerland
[3]Ferrovac GmbH, Zürich, Switzerland

philipp@lippmann.lu

Owing to its excellent sensitivity, its high dynamic range and its good depth resolution, Secondary Ion Mass Spectrometry (SIMS) constitutes an extremely powerful technique for analyzing surfaces and thin films. In recent years, considerable efforts have been spent to further improve the spatial resolution of SIMS instruments. As a consequence, new fields of application for SIMS, e.g. nanotechnologies, biology and medicine in particular, are emerging [1-2]. State-of-the-art SIMS instruments allow producing 3D chemical mappings with excellent sensitivity and spatial resolution. However, several important artifacts arise from the fact that the 3D mappings do not take into account the sample's surface topography. The traditional 3D reconstruction assumes that the initial sample surface is flat and the analyzed volume is cuboid. The produced 3D images are thus affected by a more or less important uncertainty on the depth scale and can be distorted. Moreover, significant field inhomogeneities arise from the surface topography as a result of the distortion of the local electric field. These perturb both the primary beam and the trajectories of secondary ions, resulting in a number of possible artifacts, including shifts in apparent pixel position and changes in intensity. In order to obtain high-resolution SIMS 3D analyses without being prone to the aforementioned artifacts and limitations, we developed an integrated SIMS-SPM instrument, which is based on the Cameca NanoSIMS 50 [2]. This instrument, an in-situ combination of sequential high resolution Scanning Probe Microscopy (SPM) and high sensitivity SIMS, allows topographical images of the sample surface to be recorded in-situ before, in between and after SIMS analysis. Hence, high-sensitivity high-resolution chemical 3D reconstructions of samples are possible with this extremely powerful analytical tool [3-4]. In addition, this integrated instrument allows a combination of SIMS images with valuable AFM (Atomic Force Microscopy) and KPFM (Kelvin Probe Force Microscopy) data recorded in-situ in order to provide an extended picture of the sample under study. The known information channels of SIMS and AFM/KPFM are thus combined in one analytical and structural tool, enabling new multi-channel nanoanalytical experiments. This opens the pathway to new types of information about the investigated nanomaterials.

1. Y. Fleming, T. Wirtz, U. Gysin, T. Glatzel, U. Wegmann, E. Meyer, U. Maier, J. Rychen, Appl. Surf. Sci. 258(4), 1322-1327 (2011).
2. T. Wirtz, Y. Fleming, U. Gysin, T. Glatzel, U Wegmann, E. Meyer, U. Maier, and J. Rychen, Surf Interface Anal. 45 (1), 513-516 (2013).
3. T.Wirtz, Y. Fleming, M. Gerard, U. Gysin, T. Glatzel, E. Meyer, U. Wegmann, U. Maier, A. H. Odriozola and D. Uehli, Rev. Sci. Instrum. 83, 063702 (2012).
4. C. L. Nguyen, T. Wirtz, Y. Fleming and J. B. Metson, Appl. Surf. Sci. 265, 489-494 (2013).

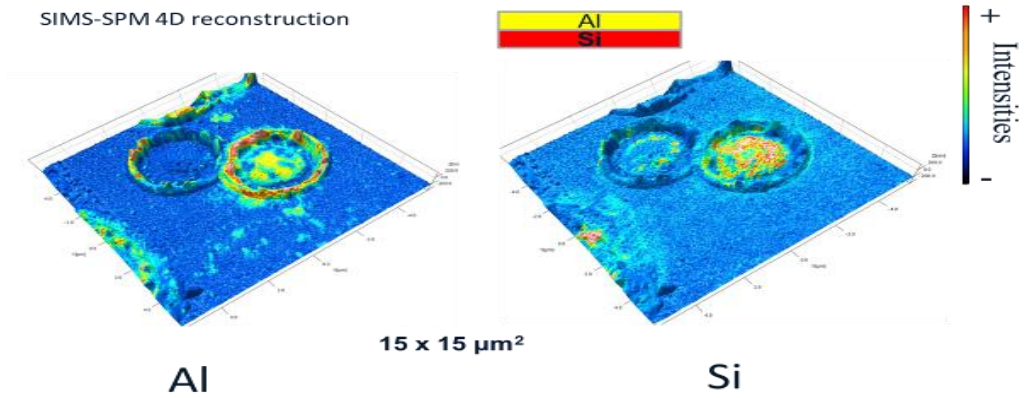

Figure 1. Interaction of streamer with metallic multi-layers in heptane environment (Field of view: 15 x 15 µm): (a) Combined SIMS-SPM 3D reconstruction of the $^{27}Al^-$ secondary ion signal, (b) Combined SIMS-SPM 3D reconstruction of the $^{28}Si^-$ secondary ion signal.

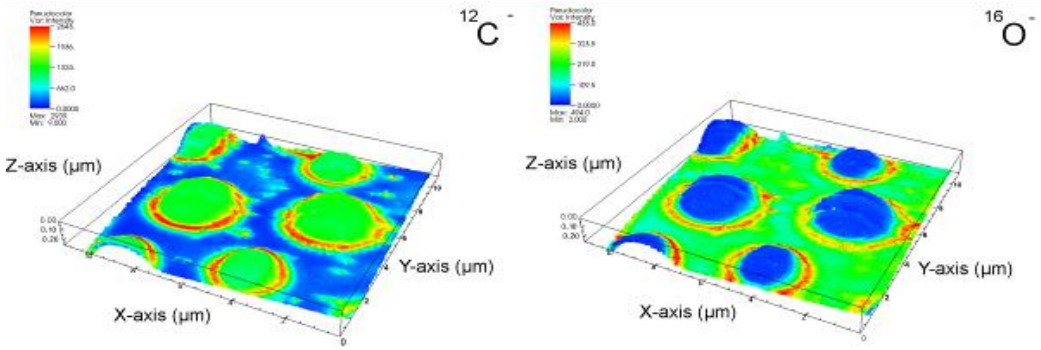

Figure 2. PS/PMMA blend (Field of view: 22.3x17.3 µm^2): (a) Combined SIMS-SPM 3D reconstruction of the $^{12}C^-$ secondary ion signal. (b) Combined SIMS-SPM 3D reconstruction of the $^{16}O^-$ signal, which is characteristic of PMMA [3].

3D Imaging and Analysis

IM.6.P136
A compact solution for Eucentric Positioning inside the FIB/SEM

S. Kleindiek[1], K. Schock[1], S. Zaefferer[2]

[1]Kleindiek Nanotechnik, Reutlingen, Germany
[2]Max-Planck-Institut für Eisenforschung, Microstructure Physics and Alloy Design, Düsseldorf, Germany

stephan.keindiek@kleindiek.com
Keywords: eucentric, tilting, EBSD, ECCI, SEM, FIB

Recently, more and more emphasis has been placed on 3D reconstructions from data obtained by scanning electron microscopy (SEM) methods. Various detectors are used to gather different types of information. In combination with a focussed ion beam (FIB), layers of the sample are removed in order to investigate the next "slice" of the sample. Often it is necessary to tilt the sample to different angles for milling and data collection - even more so if multiple data collection methods are to be utilized in parallel (EDX, EBSD, etc.).

Although the sample stages built in to typical FIB/SEM systems allow eucentric tilting, these stages are large and cumbersome and often do not deliver the precision necessary to reliably image a large number of slices at different tilt angles. Using the Eucentric 5-Axis Table (E5AT), it is possible to address any tilt angle between ±90° quickly and reproducibly with an absolute accuracy of 0.2°.

Any feature within the substage's XY travel range (10 mm x 10 mm) can be addressed; the additional rotation axis allows (re-)orienting the sample to align a given feature to the viewers preference. Once the feature of interest is positioned at the eucentric hight, the substage can tilt to the desired angle while keeping the feature in focus.

One application for this is a new imaging method developed at the Max Planck Institut für Eisenforschung in Düsseldorf, Germany: Electron Channeling Contrast Imaging (ECCI). This method requires the sample to be repositioned two times for each image. The first position is facing the EBSD camera in order to map the area of interest. Subsequently, the sample must be oriented in such a fashion that the crystallographic planes of the sample are facing the electron column at a small working distance for back scatter imaging. The correct tilt and rotation for this orientation are derived from a custom built software and the data from the EBSD map. The method allows visualizing features in the material’s structure that could previously only be detected in TEM.

1. I. Gutierrez-Urrutia, S. Zaefferer, D. Raabe Scripta Materialia, Volume 61, Issue 7, October 2009, Pages 737-740,

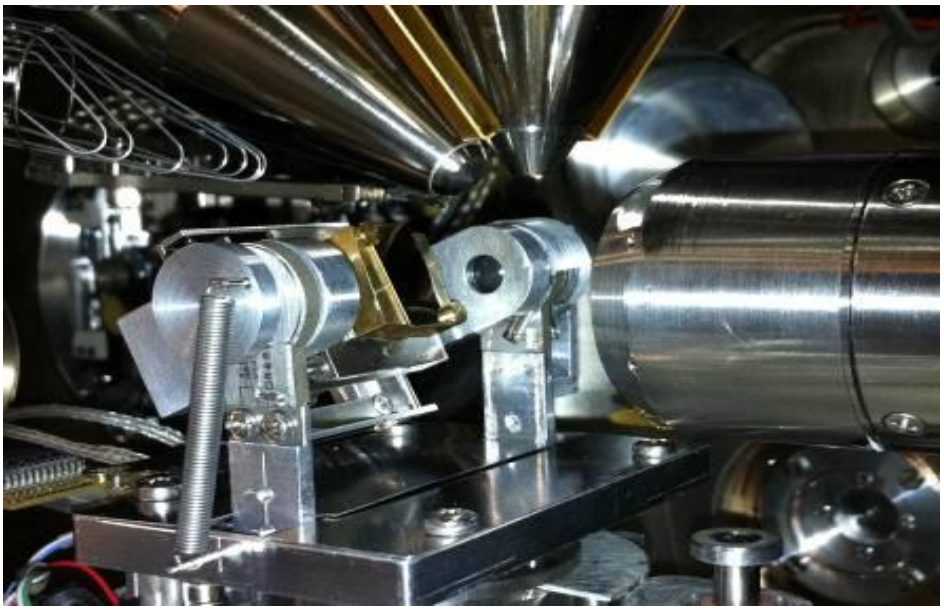

Figure 1. Five axis stage in a Zeiss 1540 XB.

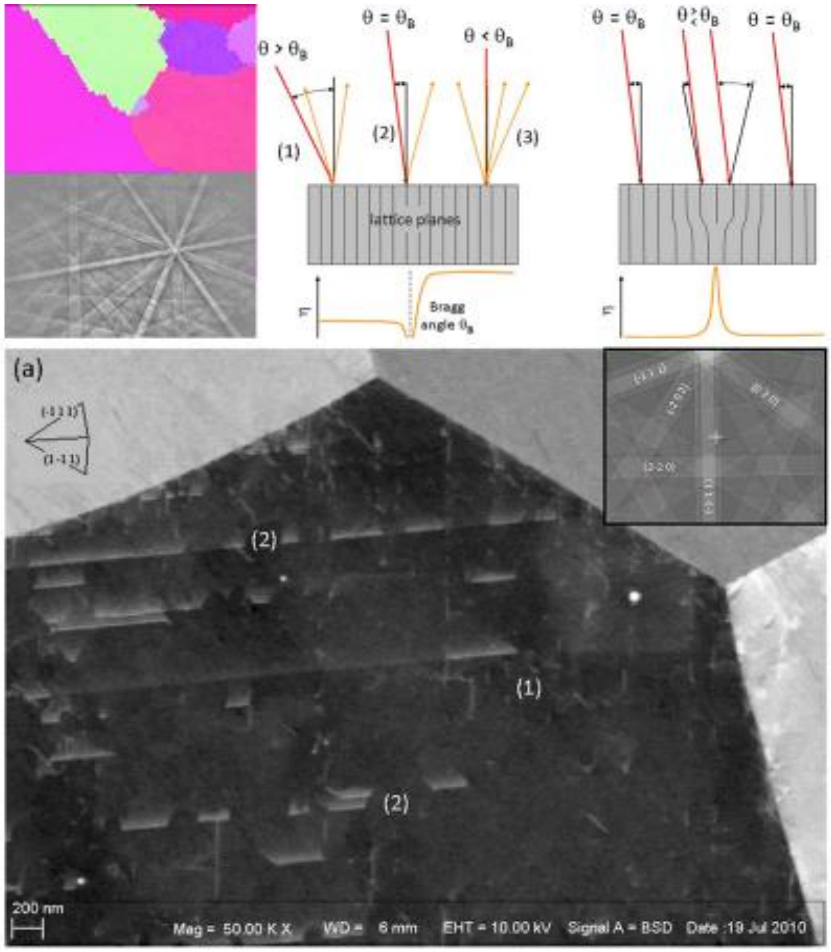

Figure 2. EBSD, ECCI

3D Imaging and Analysis

IM.6.P137
Recent Advancements in Laboratory X-ray Microscopes for 3D to 4D Imaging and Analysis

A. Merkle[1], J. Gelb[1], L. Lavery[1]

[1]Xradia, Pleasanton, CA, United States

amerkle@xradia.com
Keywords: nanoscale x-ray microscopy, x-ray tomography, in-situ XRM

Three-dimensional X-ray microscopy (XRM) has emerged as a powerful imaging technique that reveals three-dimensional microstructure from a range of materials. The non-destructive nature of X-rays has made the technique widely appealing, with the potential for characterizing sample changes in "4D," delivering 3D microstructural information on physically the same sample over time, as a function of sequential processing conditions or experimental treatments. This has led to a new generation of functional studies (Figure 1), with applications spanning the life sciences, physical sciences, geosciences, and electronics industry, and is in a state of rapid expansion [1]. Recently, laboratory-based X-ray sources have been coupled with high resolution X-ray focusing and detection optics from synchrotron-based systems to acquire tomographic datasets with resolution down to 50 nm [2]. This signifies an improvement of at least one order of magnitude in spatial resolution relative to the limits of 'optic-free' laboratory computed tomography (CT) techniques. Observing the evolution of microstructure on the same region of a single sample can rapidly benefit computational models of materials, by avoiding the requirement to extrapolate based on statistical samplings from a large number of like specimens. This talk will explore both the implementation of laboratory XRM characterization and analysis in several leading applications examples in materials imaging. Several examples of *in situ* and '4D' experiments will be presented, including crack propagation in ceramics, porosity and permeability characterization, polymer electrolyte fuel cell (PEFC) electrode characterization, deformation of polymer foams under load, and the evolution of defects in electrode materials in Lithium ion batteries. By incorporating X-ray focusing lenses, laboratory nanoscale XRMs are now enabling unprecedented high-resolution studies of soft and hard materials alike without the need for synchrotron radiation [2]. This is made possible largely through the use of Fresnel zone plates, which are diffractive imaging objective lenses capable of focusing X-ray radiation. Analogous to typical transmission light or electron microscopes, condenser and objective lenses in the Xradia nanoscale UltraXRM focus and magnify the object onto a detector in the image plane (Figure 2). As a result, the UltraXRM system provides laboratory access to 3D and 4D X-ray microscopy down to the 50 nm spatial resolution scale, with ultimate voxel sizes down to 16 nm, and fields of view up to 65 µm. Soft materials, ranging from polymers to biological tissue, consistently pose challenges in generating contrast by several techniques, X-ray absorption included. Employing the Zernike method, however, enhances the visibility of grain boundaries and material interfaces when absorption contrast is low, enabling visibility of microstructures without staining. We demonstrate the application of both absorption and phase contrast techniques on such materials, including polymer electrolyte fuel cells [1, 3-4] and superconducting materials. Using the Xradia microscale VersaXRM, battery electrodes in commercially-packaged cells may be characterized nondestructively with sub-micron resolution, enabling characterization of the electrode microstructures. The tunable contrast enhancement mechanism within the VersaXRM combines optimized absorption contrast, for a uniquely flexible laboratory X-ray microscope imaging and analysis platform for modern *in situ* and 4D studies. [5]. Using this approach, researchers may characterize the changes in this microstructure as a function of operational parameters, such as charge state, thermal environment, pressure/fracture, etc., either *ex situ*, *in situ* or *in operando* [6-9]. From their lightweight properties to unique storage capabilities, polymer foams have emerged as a unique material for many industrial application. While these materials are widely utilized for their functional parameters, much about the long-term microstructural behavior remains a mystery, and degradation mechanisms are not very well understood. Using laboratory XRM, the deformations within the foam microstructure may be directly observed in 3D. This enables the 4D mapping of parameters such as elastic moduli and hysteresis curves, along with the direct observation of strut/pore deflections and responses to mechanical loading [10]. Using the XRM technique with an *in situ* compression cell (Deben, UK), the deflections of pores within a polymer foam may be directly observed in 3D [10]. Measurements of these deflections may be subsequently

correlated to the loading pressures, for direct measurements of material's mechanical properties in conjunction with finite element analysis or fluid dynamics models.

1. A.P. Merkle, J. Gelb, Microscopy Today March (2013), p. 18.
2. A. Tkachuk, et al. Z. Kristallogr. 222 (2007) p. 650.
3. W.K. Epting, J. Gelb, S. Litster Advanced Functional Materials 22 (2011), p. 550.
4. W.K Epting, S. Litster, Int. Journal of Hydrogen Energy, 37 (2012) p. 8505.
5. J. Gelb, Adv. Mat. Proc. 170 (2012), p. 14.
6. S.C. Chao, et al., J. Electrochem. Soc. 158 (2011), p. A1335.
7. S.C. Chao, et al., Electrochem. Comm. 12 (2010), p. 234.
8. J. Nelson, et al., J. Am. Chem. Soc. 134 (2012), p. 6337.
9. P. Shearing, et al. ECS Interface, 20 (2011), p.43.
10. B.M. Patterson, et al., Microscopy & Analysis 26 (2012), p. 4

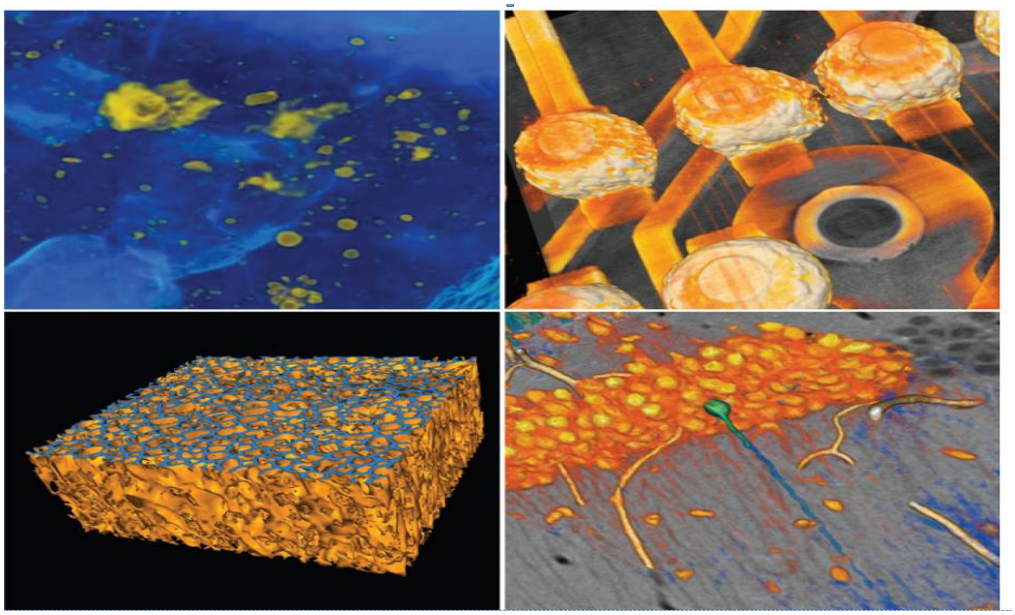

Figure 8. Xradia XRM 3D Datasets: Geology (upper left): carbonaceous chondrite meteorite that landed on April 22, 2012, at Sutter's Mill, CA. Image width = 9 mm. Courtesy of Prof. Qing-Zhu Yin, UC Davis. Electronics (upper right): microelectronic device with short circuit between two bumps. Image width = 600 µm. Courtesy of S.T. Crolles. Materials Science (lower left): soft porous polymer with urethane backbone (blue) imaged in situ under varying temperature and compression. Image width = 200 µm. Courtesy of Natl. Chemical Laboratories, India. Life Science (lower right): mammalian brain tissue section showing individual neuron cells. Image width = 260 µm. Courtesy of the Natl. Center for Microscopy & Imaging Research at UC San Diego. Images from Microscopy Today [1].

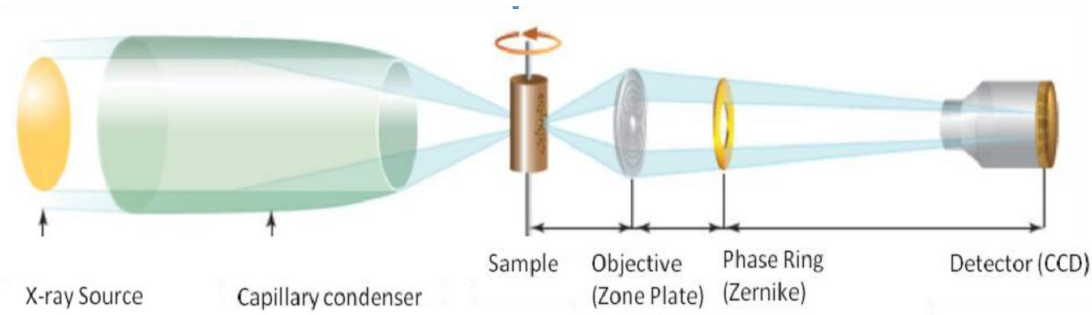

Figure 9.X-ray optical schematic of the Xradia UltraXRM-L200, achieving 50 nm spatial resolution with an 8 keV laboratory source

Sample Preparation Methods

IM.7.138
Diamond knife versus Gallium Ions

J. Wagner[1,2], A. Zankel[1,2], H. Reingruber[1], C. Mayrhofer[1], H. Schroettner[1,2], J. Rattenberger[1,2]

[1]Graz Centre for Electron Microscopy, Graz, Austria
[2]Graz University of Technology, Institute for Electron Microscopy and Nanoanalysis, Graz, Austria

julian.wagner@felmi-zfe.at
Keywords: 3D, ESEM, FIB, EDXS, tomography

The functionality of materials obviously depends on a precise control of the size, shape, crystal structure and composition of the material being synthesized. In order to characterize solids in an appropriate way many sophisticated analysing methods were established and combined. The demand for these highly developed investigation techniques arise because micro- and nanotechnology present many exciting opportunities.

At the beginnings of 3D-FIB EDXS the acquisition time for a three dimensional reconstruction of a certain volume was restricted to a treatable number of counts per second depending on the EDXS-system being used [1, 2, 3]. Today nearly all established X-ray detecting systems are able to handle 100000 counts and more per second. Therefore the time for gathering morphological and chemical information is nearly diminished to the cutting procedure. Gatan, Inc. (Pleasanton, CA, U.S.A.) provided an automated slice and view device for 3D microscopy based on an ultramicrotome developed by Denk et al. [4] that can be used inside the sample chamber of an environmental scanning electron microscope (ESEM). The method is called serial block face scanning electron microscopy (SBFSEM) [5] and was originally developed for studying biological samples, which offer a good cutting performance. However the maximum size of the reconstructed sample volume is often limited by the used microscopic method. Slice and viewing volumes lager than 10 µm³ using FIB techniques is generally a time consuming process and may cause drift problems due to the long slicing processes [6, 7].

This work presents results from two different approaches concerning applications in the field of microscopic serial sectioning. An aluminum-copper alloy (EN AW-2024 T351 by AMAG, Ranshofen, Austria) was used to compare the results acquired by SBFSEM and 3D-FIB-EDXS.

For the ESEM (FEI ESEM Quanta 600) experiment an X-Max silicon drift detector (SSD) from Oxford Instruments Analytical Ltd., UK was used for fast recording of the elemental maps. The total reconstructed volume is about 42.7 µm x 34.5 µm x 20.0 µm at a voxel size of 100 nm x 100 nm x 100 nm. The recording time for the 200 elemental maps (slices) was 22 hours. This comparatively short recording time was rendered possible by the combination of high detector count rates (75 kcps - kilo counts per second) and the fast and automated slicing process of the *in situ* ultramicrotome.

For the FIB (FEI Nanolab Nova200) experiment a Bruker-AXS system (Berlin, Germany, 10 mm2 SDD, Quantax400) was used with a total acquisition time of 53 hours for 200 elemental maps (sample volume: 40 µm x 30 µm x 20.0 µm) (“Figure 1, 2, 3”). Final data visualization was performed using the Amira 3.1 software (Mercury Computer Systems SA) (“Figure 4”) .

1. B. J. Inkson et al., Journal of Microscopy, Vol. 201, Pt 2, (2001), p. 256.
2. L. Holzer et al., Journal of Microscopy, Vol. 216, Pt 1, (2004), p. 84.
3. P.G. Kotula et al., Microsc. Microanal. 12 (2006), p. 36.
4. W.Denk, H.Horstmann PLoS Biol 2(11) (2004), p.329.
5. H. Reingruber, A. Zankel, C. Mayrhofer, P. Poelt, J. Membr. Sci. 372 (2011) p. 66.
6. M. Schaffer et al., Ultramicroscopy 107 (2007), 587.
7. M. Schaffer et al., Michrochimica Acta and X-ray Microanalysis, Plenum, New York, (1992).

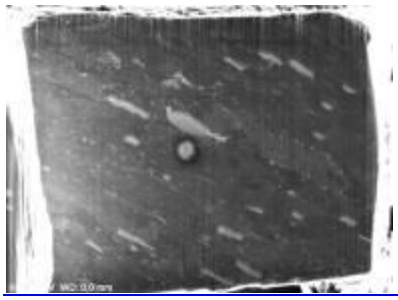

Figure 1. SE image of the Aluminium-alloy sample

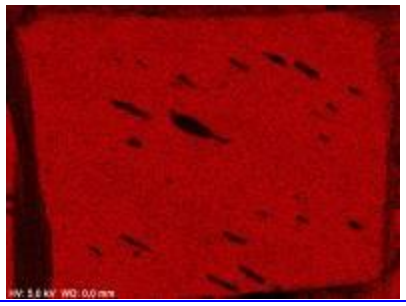

Figure 2. Aluminium distribution

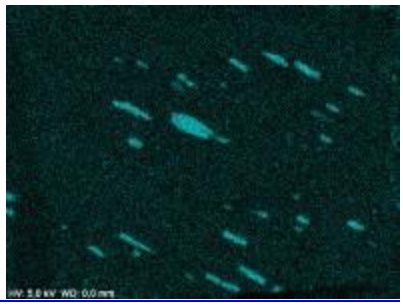

Figure 3. Magnesium distribution

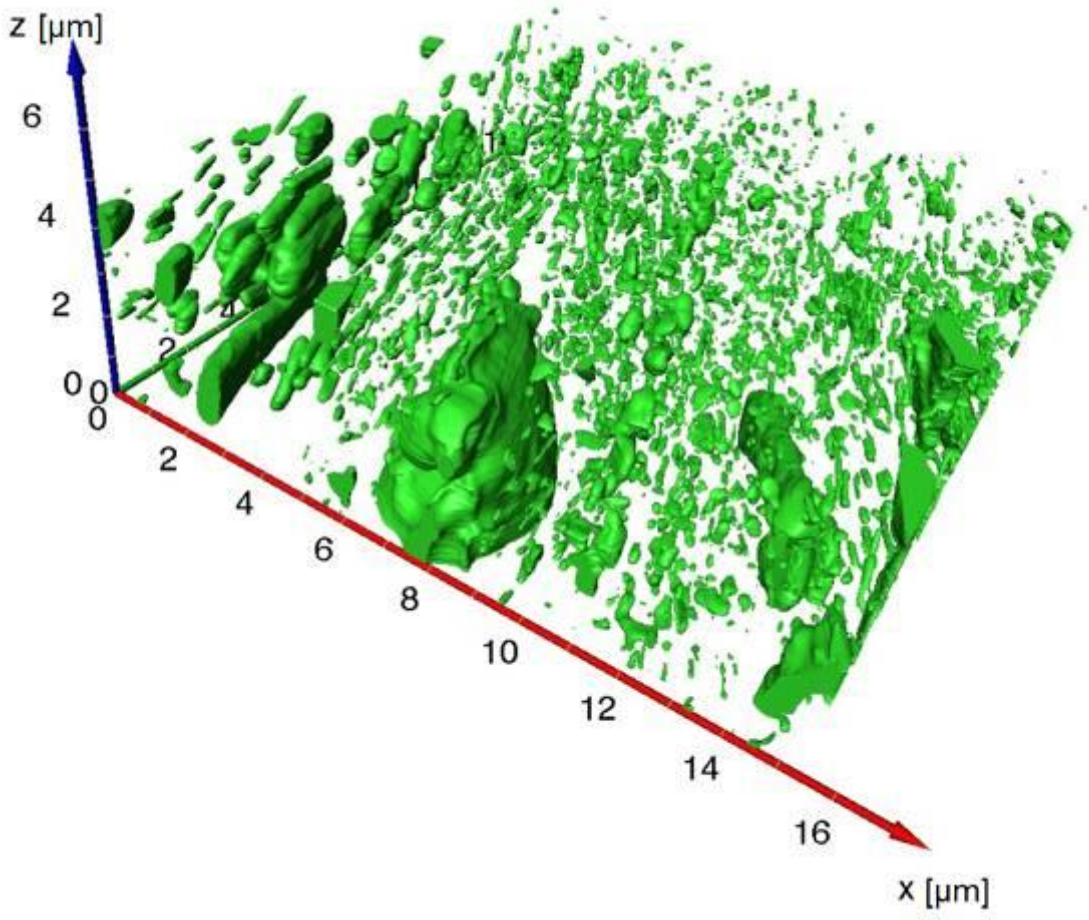

Figure 4. 3D-reconstruction of the Al_2CuMg phase (SBFSEM)

Sample Preparation Methods

IM.7.139
Combining laser and focussed ion-beam micromachining: Target preparation to large depths and at high ablation rates

M. Ebert[1], M. Krause[1], T. Höche[1]

[1]Fraunhofer Institute for Mechanics of Materials IWM, Center for Applied Microstructure Diagnostics CAM, Halle Saale, Germany

Martin.Ebert@iwmh.fraunhofer.de
Keywords: focussed ion beam, laser machining, material science

Microstructure diagnostics at 3D integrated microelectronics chips and MEMS is increasingly becoming faced with the need for target preparation techniques allowing to assess large depth. While Ga^+ focussed ion-beam machining has reached a very high level of sophistication in terms of reliability and spatial resolution, attainable ablation rate are limited to about 3 µm³/s (for an ion current of 10 nA). Inductively coupled plasma sources, as used in the Xe plasma FIB yield three orders of magnitude higher ablation rates, while laser ablation rates are another three orders of magnitude higher [1]. Therefore, it is reasonable to combine FIB machining with a preceding laser ablation in order to attain both the required ablation rate and the requested spatial resolution.

Following this line of argumentation, Carl Zeiss Microscopy GmbH has recently launched the Auriga Laser [2], featuring a diode-pumped solid-state ns-laser ($Nd:YVO_4$) with an average output power of 2 W at 355 nm. The laser source is attached via a scanner unit (scan field 45 x 45 mm²) to the load lock of a FIB workstation. This setup provides the opportunity that debris, which occur as a consequence of laser machining, will not reach the main chamber of the microscope.

In this contribution, we present results of a study aiming at the optimization of laser micromachining for stainless steel (1.4301) sheets. By varying output power, repetition rate, scan speed, and scan regime, laser machining was optimised in terms of attainable depth and width. As shown in Fig. 1, rather smooth flanges could be obtained. As illustrated by Fig. 2, depth of up to 600 µm can be readily reached by laser ablation within a processing time of about 25 min. Heat affected zones were evaluated by preparing TEM-Lamellae to find out which impact laser machining would have on the close-to-surface microstructure of the analysed sample. The laser-ablated flanges were also analysed by Electron Backscatter Diffraction.

1. S. Martens, et al. Proc. Intl. Conf. on Thermal, Mechanical, and Multiphysics Simulations and Experiments in Micro-Electronics and Micro-Systems, EuroSimE 2010, p. 82-90.
2. microscopy.zeiss.com/microscopy/en_de/products/fib-sem-instruments/auriga-laser.html
3. The authors acknowledge support by Carl Zeiss Microscopy GmbH during the evaluation of the Auriga Laser. This work was supported in part by the FhG Internal Programs under Grant No. Attract 692 280.

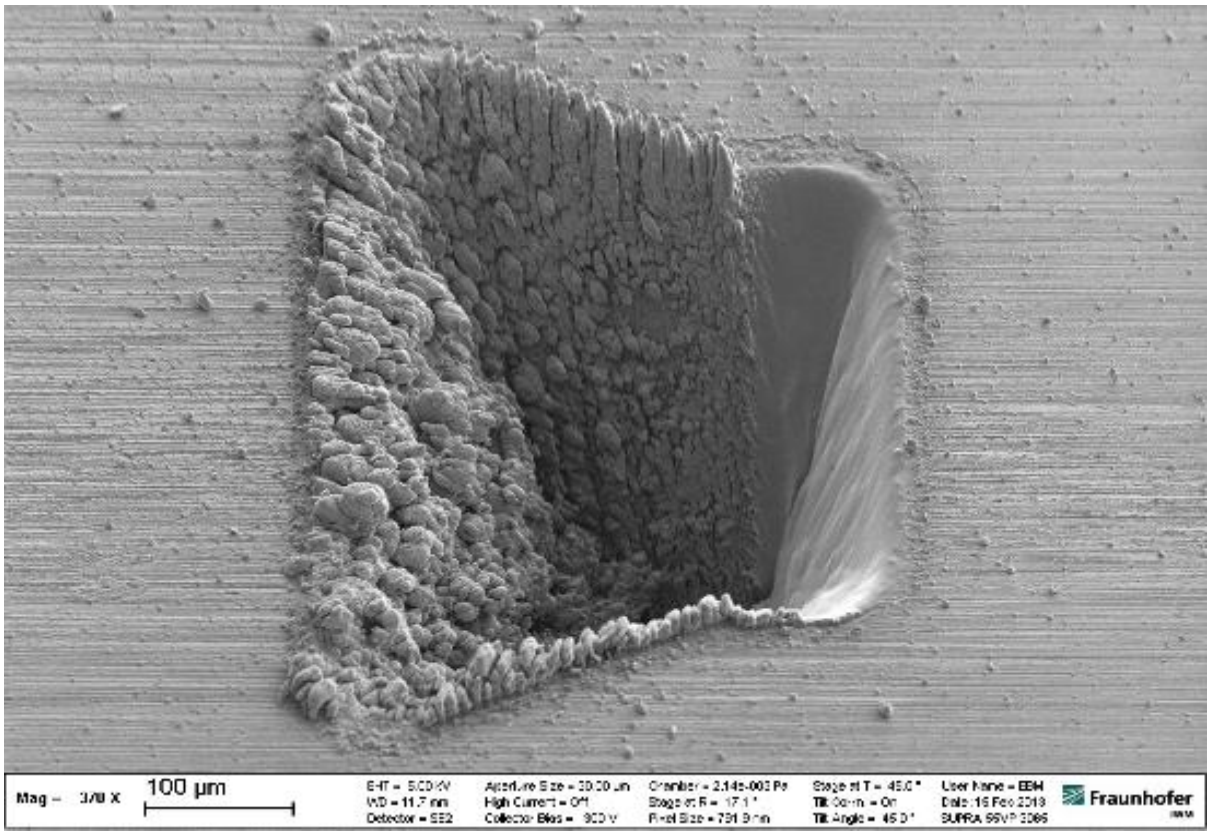

Figure 1. Laser machined structure with a very smooth sidewall investigated on the Auriga Laser by Carl Zeiss

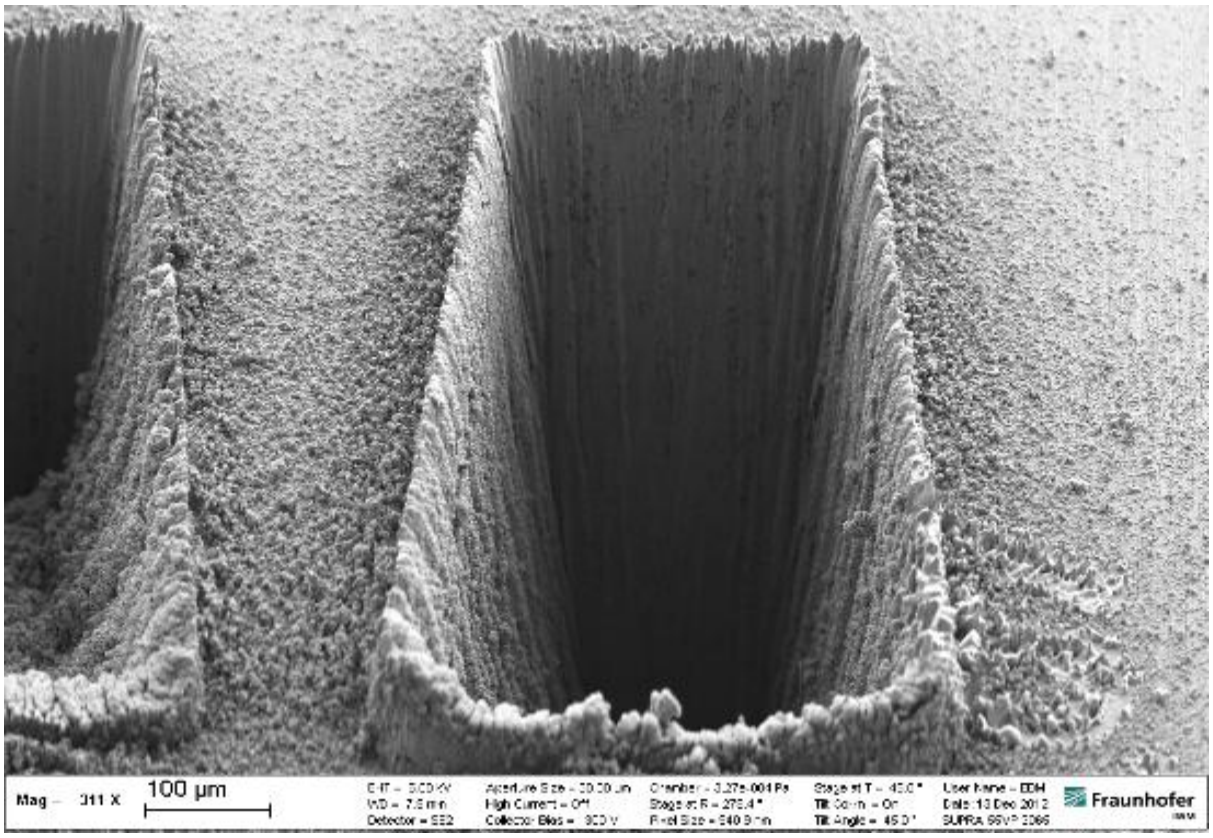

Figure 2. Laser machined structure with a 600 µm deep sidewall investigated on the Auriga Laser by Carl Zeiss

Sample Preparation Methods

IM.7.140
Using the X^2-Holder to Create Thin TEM-lamella by FIB

W. van Mierlo[1], A.C. Robins[2], U. Kaiser[1]

[1]Universität Ulm, ZE Materialwissenschaftliche Elektronenmikroskopie, Ulm, Germany
[2] E.A. Fischione Instruments, Inc., Horley, United Kingdom

willem.van-mierlo@uni-ulm.de
Keyword: FIB, TEM, Sample preparation

A new tiltable sample holder has been recently developed that facilitates the easy preparation of thin TEM lamellae with sufficient quality for HRTEM in our group [1]. Using this holder, two grooves in a direction at a high angle to each other are milled on either side of the lamella. Where both grooves overlap, an electron transparent window is created (figure 1). In contrast to the traditional method, however, the electron transparent window is on all four sides bounded by the thick lamella, which provides a sturdy frame around the electron transparent area. The frame increases the stability of the lamella significantly, making it possible to create large areas (tens of μm^2) of uniform thickness. The application of this technique to different sample types and geometries will be demonstrated.

To increase sample quality for very thin samples (< 20 nm), a post-FIB low voltage (500 V) argon polishing step can be performed. This however requires a slight modification of the lamella geometry to make the electron transparent area accessible to the argon beam and to reduce contamination. This modified geometry has been used in a Fishione Nanomill system to produce a high quality thin Lanthanum-Strontium-Aluminate sample. The 500 V final polishing step removed the ~ 5nm thick amorphous layer present after FIB preparation (5 kV final polishing) virtually completely as lattice fringes are visible up to the edge of the sample (figure 2).

As the electron transparent area is surrounded on all sides by thick material, the determination of the thickness of the electron transparent area is more difficult. A correct determination of the local thickness also greatly helps producing lamellae with a uniform thickness over a large area. We use a method based upon the intensity of the back scattered electron (BSE) signal [2]. For an accurate determination of the thickness it is essential that the background signal coming from the sample holder is minimized. Some modifications to the original design of the holder have been made, that minimizes the number of back-scattered electrons, but still ensure good sample holder conductivity to minimizing sample drift due to charging. In addition Monte Carlo simulations have been performed to determine the influence of detector position on the BSE signal as function of maximum electron penetration depth. These simulation show that the detector position has to be taken into account, otherwise this can lead to a ~ 20 % error in thickness determination (figure 3).

1. L. Lechner, J. Biskupek and U. Kaiser, *Microscopy and Microanalysis* 18 (2012), p. 379–384
2. R. Salzer, A. Graff, M. Simon and F. Altmann, *Microscopy and Microanalysis* 15 (2009), p. 340–341
3. This research was supported by the Deutsche Forschungsgemeinschaft (DFG) and the state of Baden-Württemberg within the SALVE (Sub-Ångström Low Voltage Electron Microscopy) project.

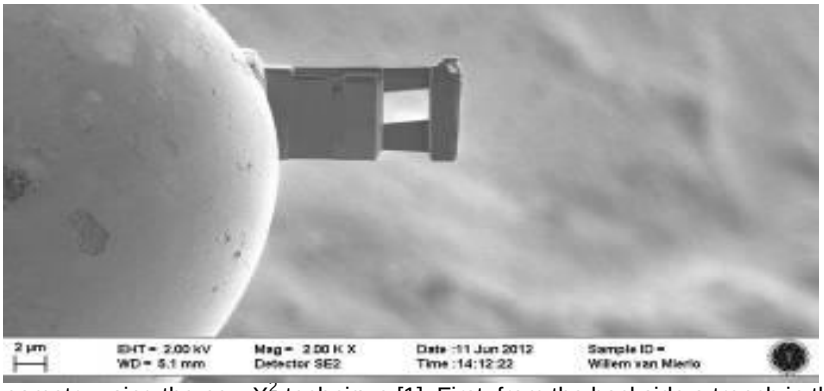

Figure 1: Milling geometry using the new X^2-technique [1]. First, from the backside a trench in the lamella is cut. After final polishing of the back side at a low voltage, the sample is tilted over ~ 90° and then is thinned from the front side the sample. An electron transparent window is created where both grooves overlap (see the bright window inside the lamella).

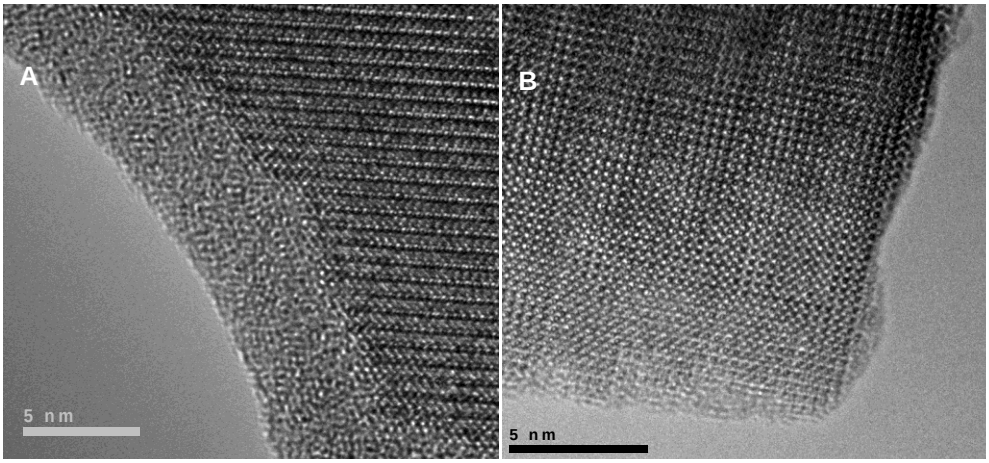

Figure 2: Improvement of sample quality after low-voltage argon-milling. A) Edge of the electron transparent window after final polishing with 5 kV Ga. B) After final polishing with argon at 500 V using the Fishione nanomill. The effect of low voltage Ar thinning step is seen by the complete reduction of the amorphous layer at the edge.

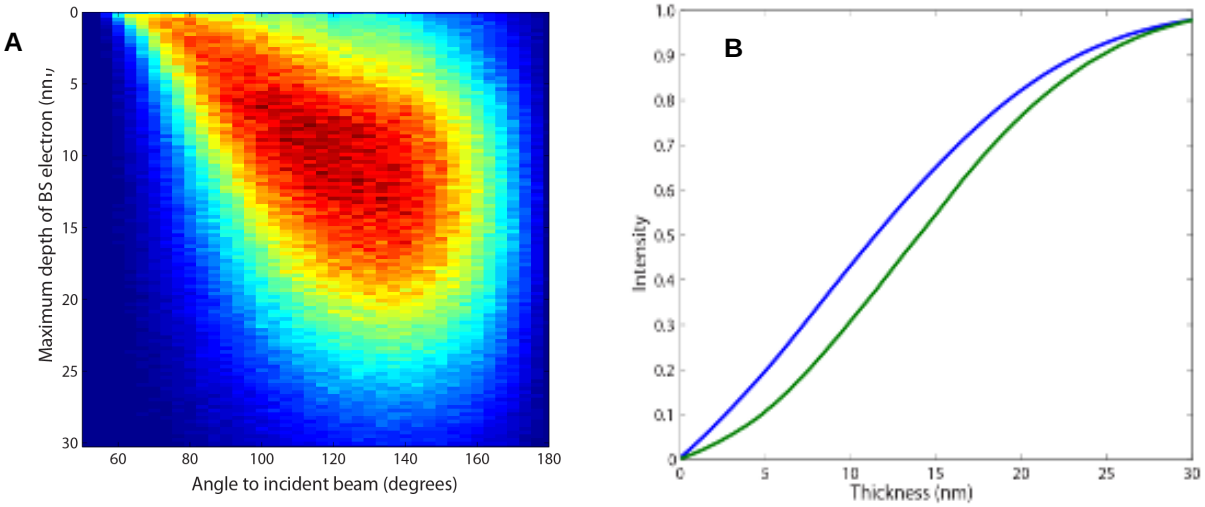

Figure 3: Results of Monte Carlo simulations showing the influence of the detector position on the maximum depth in the sample from which a detected back-scattered electron originates. A) Intensity distribution of back scattered electrons as function of back scattered angle (relative to incident beam) and maximum depth the back scattered electron penetrated into the target. Blue is low intensity, red is high intensity B) Difference between determined thickness with (green line) and without (blue line) taking into account the finite collection angle of the detector Not taking into account the finite collection angle leads to a ~ 20% underestimating of sample thickness.

Sample Preparation Methods

IM.7.141
CLEM Workflow in an Electron Microscopy Facility

R. Santarella-Mellwig[1]

[1]EMBL, Electron Microscopy Core Facility, Heidelberg, Germany

santarel@embl.de

Robust sample preparation is key to any multiuser, high-end Electron Microscopy Facility. At the EMBL our facility is permanently hosting 10 to 15 projects in parallel, and provides service to approximately 50 users per year. Each of these users face a number of different challenges when it comes to sample preparation and have different levels of experience. Our goal is to assist by standardizing methods and developing a toolbox to help projects become feasible and more efficient.

In recent years correlative light and electron microscopy (CLEM) has become a highly fashionable method using fluorescent markers to locate the region of interest (ROI) by light microscopy (LM) and combining it with the high-resolution data from achieved from the electron microscope. Our Facility is using a number of different CLEM methods and has played an active role in developing strategies to capture and study dynamic events at high-resolution.

Catching a rare event in a living cell or organism to later perform ultrastructural analysis at the exact moment of interest is not trivial. One method we are using is live-cell imaging followed by fixation. On cultured cells, the fixation can be performed with either chemical fixatives or by high-pressure freezing. The correlation is performed by recording the position of the cell of interest relative to a system of coordinates pre-existent onto the cultured surface [1], or by adding landmarks while performing the LM imaging [2]. For correlative studies on larger specimens such as starfish oocytes or *C.elegans* embryos, we have also implemented specific techniques where the sample is processed inside micro-capillary tubes [3].

Not only can the fluorescence be imaged on living specimens but also after fixation and sample preparation for EM, as demonstrated in 2011 by Kukulski et al. [4]. This is second method that has been developed at the EMBL and allows one to directly visualize fluorescence labels on a thick section. Imaging the section on the LM allows for a more rapid screening of the ROI in several cells. By using fluorescent fluorospheres as bi-functional fiducials, one can relocate the points of interest in the LM and then in the EM with high precision. This technique has become extremely popular with increasing demand and is an excellent example of transfer from scientific group to core facility.

1. I. Romero-Brey, A. Merz, A. Chiramel, J.Y. Lee, P. Chlanda, U. Haselman, R. Santarella-Mellwig, A. Habermann, S. Hoppe, S, Kallis, P. Walther, C. Antony, J. Krijnse-Locker, R. Bartenschlager. Three-dimensional architecture and biogenesis of membrane structures associated with hepatitis C virus replication. *PLoS Pathog.* 2012;8(12):e1003056.
2. J. Colombelli, C. Tängemo, U. Haselmann, C. Antony, E.H. Stelzer, R. Pepperkok, E.G. Reynaud. A correlative light and electron microscopy method based on laser micropatterning and etching. *Methods Mol Biol.* 2008;457:203-13.
3. D. Joseph-Strauss, M. Gorjánácz, R. Santarella-Mellwig, E. Voronina, A. Audhya, O. Cohen-Fix. Sm protein down-regulation leads to defects in nuclear pore complex disassembly and distribution in C. elegans embryos. *Dev Biol.* 2012 May 15;365(2):445-57.
4. W. Kukulski, M. Schorb, S. Welsch, A. Picco, M. Kaksonen, J.A. Briggs. Precise, correlated fluorescence microscopy and electron tomography of lowicryl sections using fluorescent fiducial markers. *Methods Cell Biol.* 2012;111:235-57.

Sample Preparation Methods

IM.7.142
A cryo high-vacuum shuttle for (correlative) cryogenic electron microscopy

S. Tacke[1], V. Krzyzanek[1,2], R. Reichelt[1], J. Klingauf[1]

[1]University of Muenster, Institute for Medical Physics and Biophysics, Muenster, Germany
[2]Institute of Scientific Instruments of the ASCR, v.v.i., Brno, Czech Republic

s.tacke@uni-muenste.de
Keywords: cryo high-vacuum shuttle, cryo-preparation, cryo correlative light and electron microscopy

Preservation of the native state during preparation is a prerequisite for an unadulterated view on the specimen. Offering the possibility of the direct, unaltered portrayal of hydrated objects like organelles [1,2], viruses [3], bacteria [4,5] or eukaryotic cells [6], cryogenic techniques, e.g. cryo-electron microscopy (cryo-EM), became increasingly popular. The prerequisite of cryo-EM techniques is the embedding in vitreous (amorphous) ice [7]. Besides offering a snapshot of the pristine architecture of the specimen, the physical fixation method also accompanies with some challenging requirements for the subsequent handling: Maintenance of the temperature below the recrystallization temperature of -138°K [7] and the avoidance of any contamination, e.g. additional ice. Especially in the case of cryo-electron tomography (cryo-ET) [8,9], quantitative scanning transmission electron microscopy (q-STEM, [10,11]), or correlative cryo light and electron microscopy [12] the handling becomes demanding due to the complex postprocessing [13] or the highest requests to the purity of the specimen [14].
In the past, several concepts were introduced and they are now commercially available. Owing to miscellaneous disadvantages of the existing systems, either by not offering a high-vacuum environment or limiting the application to a restricted workflow, some improvements are still desirable. To the best of our knowledge, a cryo high-vacuum transfer system for (scanning) transmission electron microscopes (STEM and TEM accordingly), comparable to the EM VCT 100 (Leica Microsystems Inc., [15]) for scanning electron microscopy, has not yet been invented.
Here, we present a cryo high-vacuum system (CHVS) for cryogenic (correlative) experiments which streamlines the handling of frozen-hydrated specimen by considering the problems identified above. Figure 1 shows the main parts of the CHVS: the storage unit, the cryo high-vacuum shuttle and the “plug & play” docking device in combination with the cryo-holder (CT3500, Gatan Inc.) for the electron microscope.

However, once mounted to modified cryo-holder cartridges, up to eight standard EM grids can be transferred to the cooling stage of the storage unit (Figure 1a)). Afterwards, the cartridges can be transferred to the electron microscope or any other device which was extended by the docking device for the cryo high-vacuum shuttle. A constant vacuum level of $7\pm2 \times 10^{-5}$ Pa and a temperature of approximate 90 °K guarantee a contamination free transfer (Figure 2b). Finally, screwed to the pre-cooled cryo-holder, the entire transfer process of the capsules takes 5 minutes (Figure 1c)). In order to observe the transfer process to the cryo-holder inside the microscope chamber, a CCD camera was installed beside the docking device.

Providing the back and forth exchange of the cartridge, the cryo-holder can maintain at cryogenic temperatures throughout the day. Additionally, we believe that this system is the missing link for the correlation of different types of experiments, e.g. cryo-STEM, q-STEM, cryo-EM, cryo atomic force microscopy or cryo light microscopy. With this progress, we aim for better quantitative studies of organic and inorganic samples like proteinaceous specimen, DNA-protein complexes, thin films and nanoparticles as well as correlative studies of cells like neurons or subcellular components like synaptic vesicles [16].

1. S. Takamori et al, Cell 127 (2006), p. 831.
2. D. Nicastro et al, Journal of Structural Biology 129 (2000), p. 48.
3. S. Jun et al, Structure 19 (2011), p. 1573.
4. J. L. S. Milne and S. Subramaniam, Nature Reviews Microbiology 7 (2009), p. 666.
5. A. J. Koster et al, Journal of Structural Biology 120 (1997), p. 276.
6. O. Medalia et al, Science 298 (2002), p. 1209.
7. J. Dubochet et al, Quarterly Reviews of Biophysics 21 (1988), p. 129.
8. D. Vanhecke et al, Journal of Microscopy 242 (2011), p. 221.
9. R. Glaeser and R. Hall, Biophysical Journal 100 (2011), p. 2331.
10. J. S. Wall and J. F. Hainfeld, Annual Review of Biophysics and Biophysical Chemistry 15 (1986), p. 355.
11. A. A. Sousa and R. D. Leapman, Ultramicroscopy 123 (2012), p. 38.
12. J. Plitzko et al, Current Opinion in Biotechnology 20 (2009), p. 83.
13. A. Rigort et al, Journal of Structural Biology 172 (2010), p. 169.
14. S. Müller et al, Ultramicroscopy 46 (1992), p. 317.
15. R. Wepf et al, Microscopy and Microanalysis 10 (Suppl. 2) (2004), p. 970.
16. This research is supported by the DFG Grants RE 782/11-1,-2. Vladislav Krzyzanek acknowledges the support by the grant CZ.1.07/2.3.00/20.0103 (EC and MEYS CR). We kindly acknowledge the help of the precision mechanical workshop, especially Martin Wensing. R. Reichelt initiated the project but unfortunately he passed away to early to see the results.

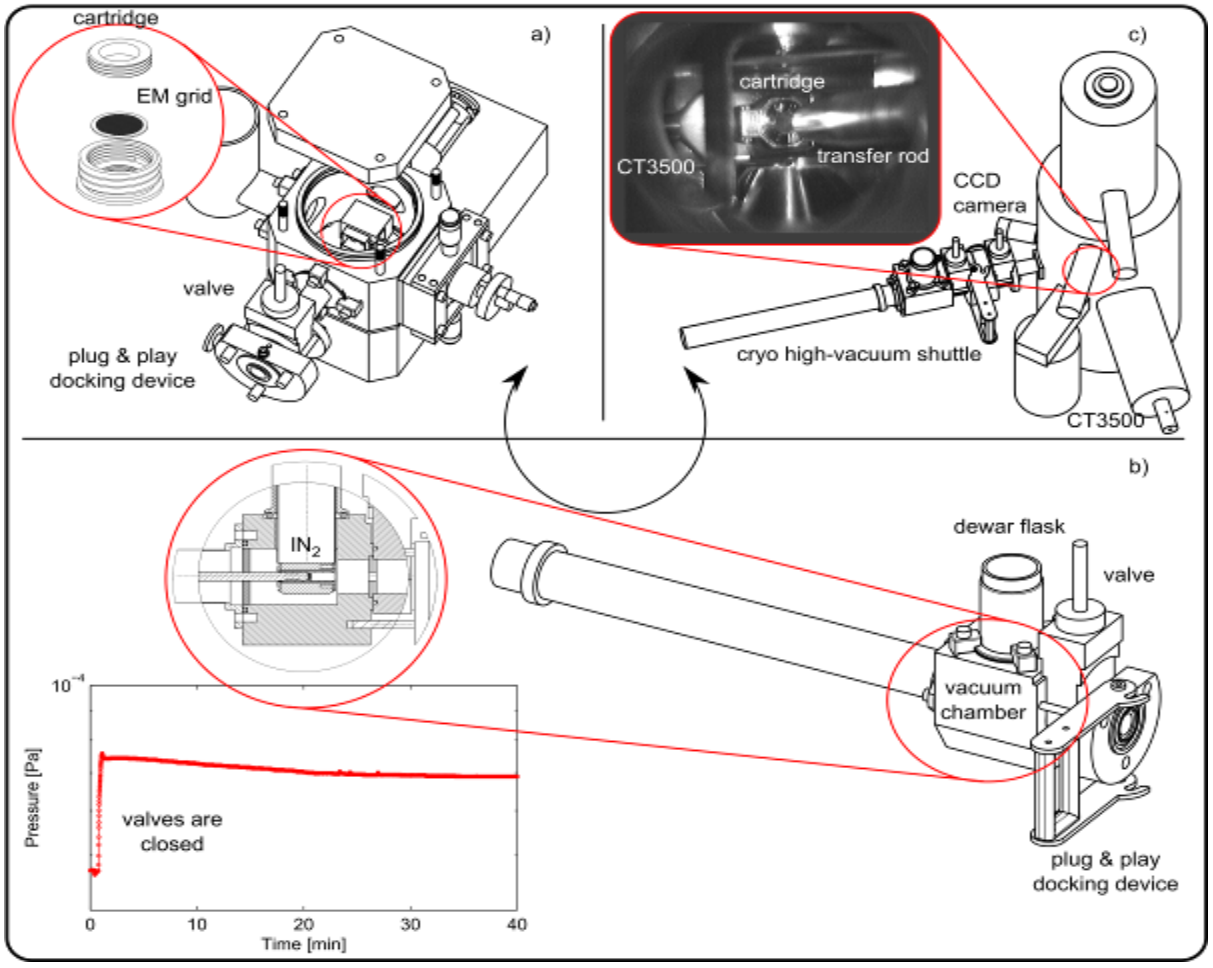

Figure 1. Schematic overview of the CHVS. a) Storage unit: Close up shows the modified cartridge which is finally mounted to the CT3500. Additionally, the small circle highlights the cooling stage. b) Cryo high-vacuum shuttle with general components: The top left close up shows the anti-contaminator of the cryo high-vacuum shuttle. On the left side: Vacuum level after disconnecting the shuttle from the docking device. c) Transfer of the capsule to the CT3500 inside the electron microscope (S-5000, Hitachi Ltd., Japan) visualized by a CCD camera

Sample Preparation Methods

IM.7.143
High-pressure freezing of adherent cells for frozen hydrated sectioning; a novel method

R. Mesman[1]

[1]Radboud University Nijmegen, Microbiology, IWWR, Faculty of science, Nijmegen, Netherlands

r.mesman@science.ru.nl

Cryo Electron Microscopy Of Vitreous Sections (CEMOVIS) allows the observation of samples in a frozen hydrated state, providing close to native ultrastructural details. However with the commonly used carriers for high-pressure freezing and cryo-sectioning (copper tubes, dome shaped carriers and membrane carriers), adherent grown cells need to be detached from their substrate by scraping or trypsinizing before freezing. This detachment procedure can introduce artifacts and unwanted changes in the cellular ultrastructure. If cells were to be cultured on a support that can be both frozen and sectioned, formation of these artifacts can be prevented. Here a new method is presented for high-pressure freezing adherent growing cells for frozen-hydrated sectioning and CEMOVIS. Cells were cultured on golden grids, containing a carbon coated Formvar film, and frozen on top of a membrane carrier (figure 1). This provides the grids with the structural support needed to withstand the strain of trimming and cryo-sectioning. The method has been successfully tested on representatives of the two different types of high-pressure freezers, those using a pressure chamber (HPM010, EMHPF, Wohlwend Compact 01/02, HPM100) and those directly pressurizing the sample (EMPact series). In sections from HepG2 hepatocytes frozen using this method, the ultrastructure appears well preserved. Cellular organelles and cell-cell contacts can be readily discerned. Though there is only one layer of cells within each section, the Formvar film on which the cells were grown can be easily identified and traced throughout the section, which facilitates finding the cells (figure 2). Another advantage is that the time required to prepare a specimen for freezing is much reduced. Furthermore, since the cells are cultured on a flat translucent surface, cells can be imaged by fluorescence microscopy before freezing, making this method readily compatible with correlative microscopy. In short, this method provides samples for cryo-electron microscopy with minimal disturbance of the cellular ultrastructure, bringing CEMOVIS one step closer to the ultimate goal; observing cells at high resolution in the native state.

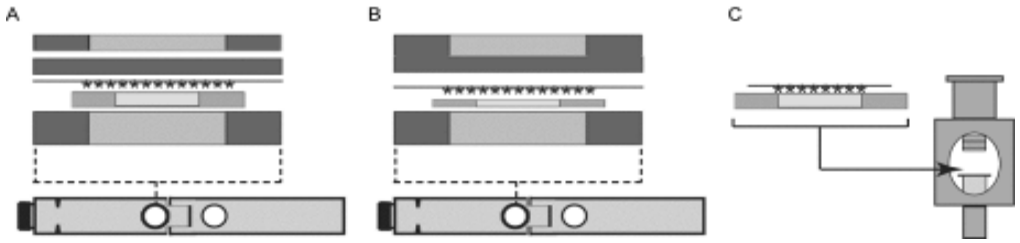

Figure 1. Freezing the grid / MC sandwiches in the EMHPF and EMpact
Specimen stacks for freezing the grid / MC sandwiches in the platelet holder (A,B) or the EMPact (C). (A) Specimen stack for the 200 µm deep MC consists of a 400 µm thick ring, followed by the MC. After filling the MC the grid is placed cells(*) down on the MC. The sandwich is closed with a lecithin coated 200 µm thick plate followed by a 200 µm thick ring to ensure a total height of 1 mm. (B) Specimen stack for the 100 µm deep MC, here the stack is closed off with a lecithin coated 0/300 (Type B) platelet to ensure a total height of 1 mm. (C) For freezing the grid/MC sandwich in the EMPact, the grid should lie in the center of the MC. The sandwich is carefully loaded into the pod and the pod is tightened with a force of 30Ncm.

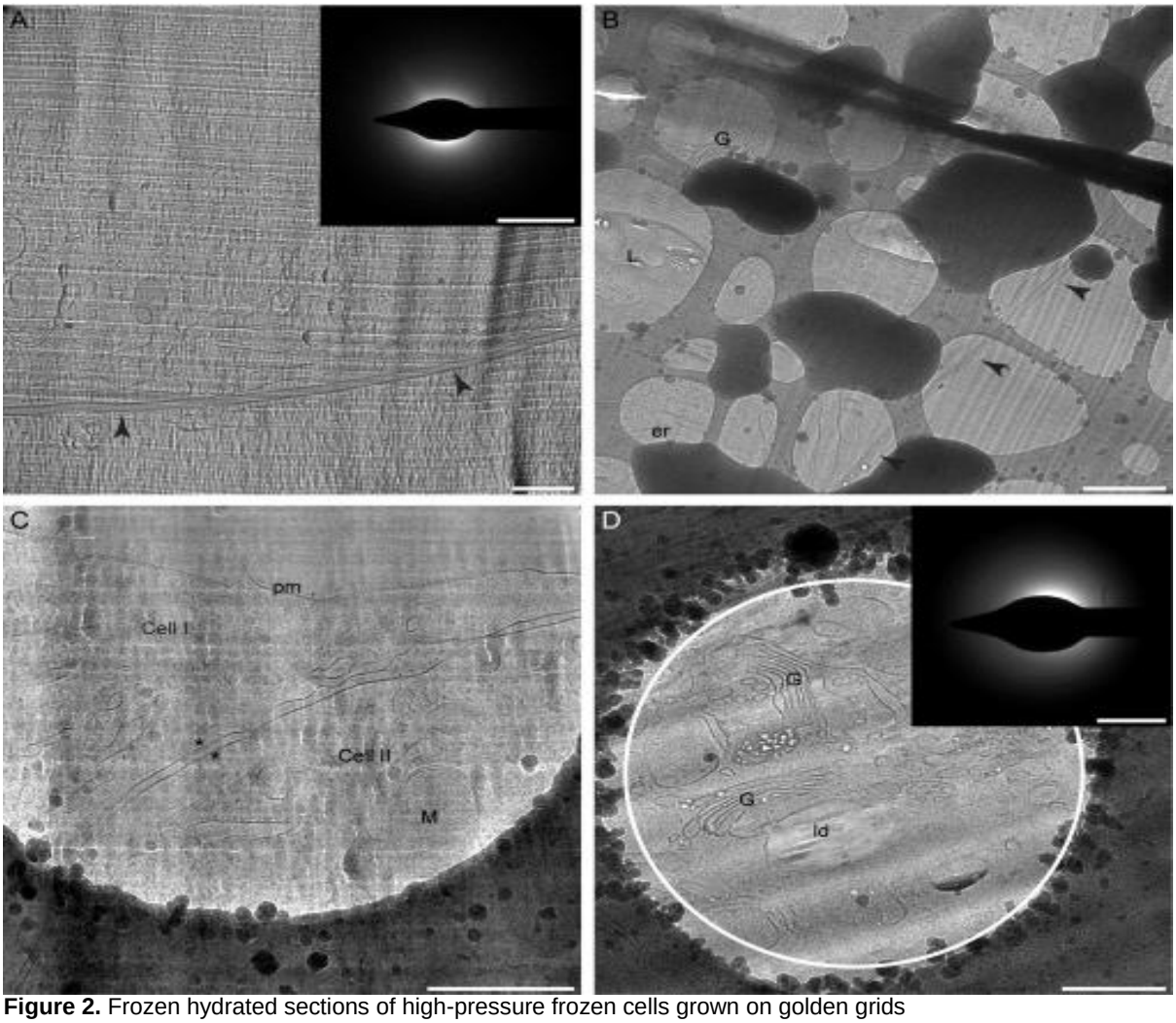

Figure 2. Frozen hydrated sections of high-pressure frozen cells grown on golden grids
The formvar film can be easily identified within the sections (arrowheads) which facilitates finding cells within the section. (A) Section from a sample where culture medium containing dextran was only applied to the the cell-side of the grid. Crevasses appear more prominent below the Formvar film, likely due to the different sectioning properties. The sample appeared to be vitreous in the diffraction pattern (inset). (B-D) Sections from a sample with dextran on both sides of the grid. (B) Since sections were cut without the use of a cryosphere, some suffered from ice contamination though cells could still be identified between the ice crystals. (C) As cells were at 80% confluence, cell-cell contacts were frequently observed. (D) Cellular components could be readily identified, again the sample appeared to be vitreous in the diffraction pattern (inset). Diffraction pattern taken before the image in panel D, white ring indicates the selected area aperture.
All micrograph scalebars indicate 500 nm, scalebars for diffractograms indicate 5nm. er: endoplasmic reticulum, G: Golgi, L: lysosome, ld: lipid droplet, M: mitochondria, pm: plasma membrane, *: desmosome.

Sample Preparation Methods

IM.7.P144
The effects of different surface preparation techniques on EBSD measurements

J Donik[1], M. Godec[1], D. Nolan[2]

[1]Institute of Metals and Technology, Ljubljana, Slovenia
[2]BlueScope Steel Ltd., Wollongong, Australia

crtomir.donik@imt.si
Keywords: EBSD, sample preparation, corrosion protection films

Microstructural morphology and crystallographic orientation aspects of protective coatings on steel sheet have been investigated by means of electron backscatter diffraction (EBSD). The aim of the present study was to determine the effects of different surface preparation techniques on the quality of EBSD results for these steel coating layers. The study investigated four different preparations techniques, including; a) the ion polishing method using Gatan PECS of pre-prepared mechanically polished surface, b) the cross-section polishing with ions using a JEOL Cross Section polisher, c) electro-polishing of mechanically polished sample, and d) mechanically prepared sample. The results demonstrated that, for this type of composite material, with a relatively hard substrate material combined with a much softer coating layer, the first three methods all yield very good sample surface condition, even in the cases where some deformation or inhomogeneity of composition and phase content is evident. Some details in the microstructures, especially with respect to the intermetallic layer between substrate and coating, are best revealed by the cross-section ion polisher. The only disadvantage of this technique is the potential for a curtaining effect, which might suppress evidence of misorientation in some grains. Some typical examples, such as the identification of grains and subgrains, grain size distribution, deformation fields and the texture components, are given in the study.

Sample Preparation Methods

IM.7.P145
Tips and tricks in Ultramicrotomy

C. Mayrhofer[1], A. Zankel[2], H. Plank[2], G. Kothleitner[2]

[1]Austrian Centre for Electron Microscopy and Nanoanalysis, Graz, Austria
[2]Graz University of Technology, Institut of Electron Microscopy und Nanoanalysis, Graz, Austria

claudia.mayrhofer@felmi-zfe.at
Keywords: Ultramicrotomy, electron microscopy, 3D, oscillating knife, atomic force microscopy, nanoflat surfaces

Sample preparation is a very important and crucial step for several microscopic methods such as light microscopy (LM), transmission electron microscopy (TEM), scanning electron microscopy (SEM) or atomic force microscopy (AFM). With a shift toward ever decreasing sample features and details [1], the need for compatible, artifact-free preparation techniques has grown. Microtomy allows for the sample preparation of many materials and the characterization of inner structures, facilitating well-defined specimen sectioning for either ultra-smooth surfaces (block-faces), or ultrathin sections [2]. Typical applications are the generation of 1) smooth surfaces for reflection-LM, AFM, infrared or Raman spectroscopy; 2) the production of semithin sections with typical thicknesses of about 2 microns for conventional LM; and 3) ultrathin cuts with thicknesses of 100 nm and less for TEM. Depending on the application and material, ultramicrotomy can often comprise pre-preparative steps like hardening, embedding, staining for contrast enhancement or cooling down below room temperature.

Besides the professional equipment needed for all this, the demands and challenges for high-quality samples require skilled personal, long-time experience and the employment of a few tricks. In this work we present a small selection of special methods and techniques to highlight some of the outstanding possibilities with ultramicrotomy.

As a relatively new method, serial block-face scanning electron microscopy (SBEM) [3] allows for a rather quick and efficient three-dimensional reconstruction of specimens in life and materials science. Here an ultramicrotome is integrated in a variable pressure scanning electron microscope (VPSEM), enabling serial sectioning and imaging for different types of materials. The resulting stack of SEM-type images allows three-dimensional investigations and reconstructions of the internal structures, according simulations and the derivation of physical quantities. Frequently, it is required to prepare extremely small block-faces. In this contribution we show, how final block-faces of about 200 x 300 μm^2 can be prepared site-specifically from an aluminium sample rod with a length of about 12 mm and a diameter of 2-3 mm by a multistep procedure (overview is given in “Figure 1”) [4,5].

New demands for the block-face smoothness have led to the development of an ultrasonic oscillating knife (Diatome, Switzerland) [6]. It offers the advantage to section materials at room temperature, which normally require cryo temperatures. Also, the elimination of cyclic compression and relaxation during slicing (“Figure 2”) results in much more homogeneous block-face surfaces for AFM, as well as in thinner sections for TEM investigations (less than 20 nm can be achieved). We demonstrate the aforementioned effects for the case of cellulose samples needed for AFM investigations. To study *in situ* the enzymatic cellulose degradation [7], the requirement was to obtain an average roughness of less than 10 nm. It will be shown that such materials can only be sliced in a reliable and reproducible way when an oscillating knife is employed (“Figure 3”).

1. G.H.Michler: Electron Microscopy of Polymers, Springer Verlag Berlin 2008.
2. L.C.Sawyer, D.T.Grubb, G.F.Meyers: Polymer Microscopy, Springer Verlag Berlin 2008.
3. W.Denk, H.Horstmann PLoS Biol 2(11) (2004), p.329.
4. A.Zankel, H.Reingruber, H.Schroettner, G.I.T. Imaging & Microscopy 02 (2011), p 35.
5. H.Reingruber, A.Zankel, C.Mayrhofer, P.Poelt, J. Membr. Sci. 372 (2011) p. 66.
6. J.S.Vastenhout , J.D.Harris, Microscopy Today, 2006, p. 20.
7. P.Bubner, J.Dohr, H.Plank, C.Mayrhofer, B.Nidetzky, The journal of biological chemistry 287 (2012) p. 2759.

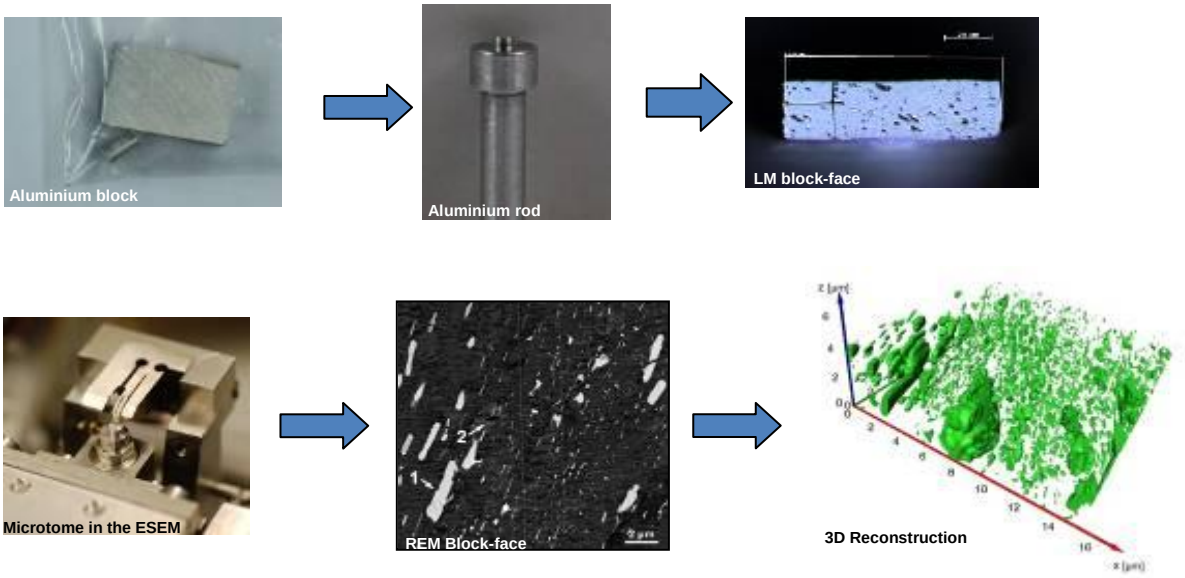

Figure 1. Ultramicrotome in the ESEM: “Aluminium going 3D”

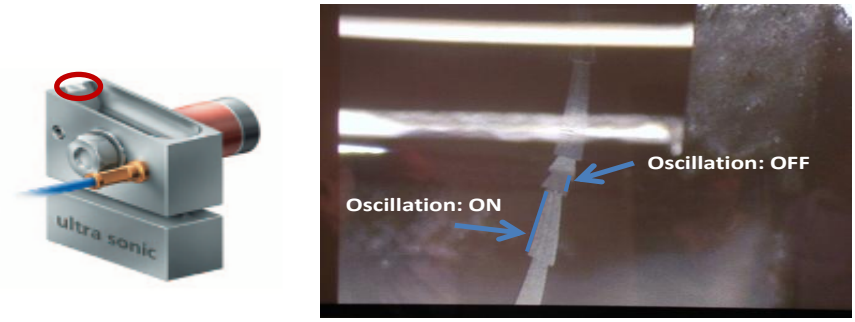

Figure 2. Elimination of compression for thin slices with ultrasonic-knife, turning oscillation on (less compression / relaxation) and off (implementation as a conventional diamond-knife)

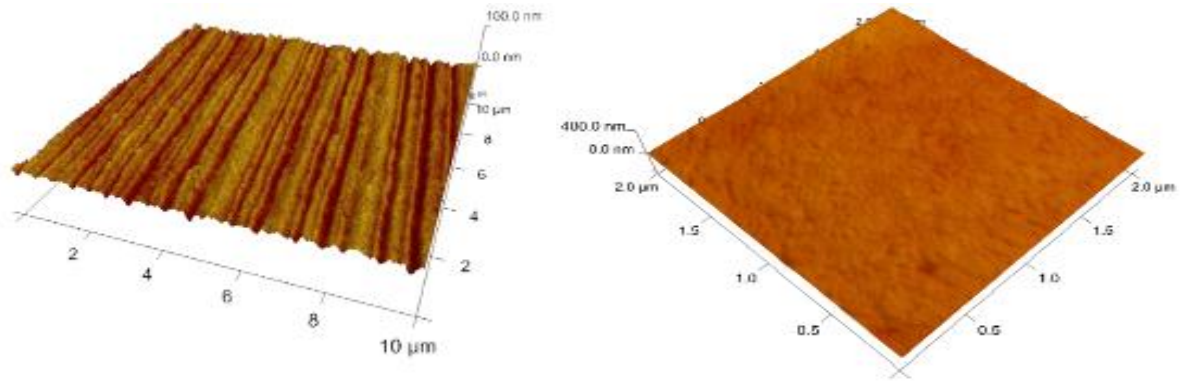

Figure 3: Block-face of cellulose prepared via conventional (left) and oscillating knifes (right)

Sample Preparation Methods

IM.7.P146
Comparison of TEM lamella preparation techniques on titania nanotube-arrays / metal Ti interface

M. Gec[1], M. Krivec[1], K. Žagar[1], L. Suhadolnik[1], D. Jenko[2], G. Dražić[1], M. Čeh[1]

[1]"Jozef Stefan" Institute, Department for nanostructured materials, Ljubljana, Slovenia
[2]. Institute of Metals and Technology, Ljubljana, Slovenia

medeja.gec@ijs.si
Keywords: TEM sample preparation, TiO_2 nanotube-array, Ion Slicer, Focused ion beam (FIB)

Titania based nanostructures are nowadays extensively used in many fields, like photocatalysis, gas sensors and photovoltaics. Immobilized titania nanostructures are considered to be the most suitable choice for different applications due to the potential toxicity of titania at nano scale. Thin TiO_2 layers are in most cases fixed to a specific substrate with different techniques: dip-coating, spin-coating, wash-coating, etc. One among possible coating techniques is an electrochemical oxidation of titanium foil which produces perfectly self-aligned TiO_2 nanotube assemblies with a stable substrate/TiO_2 contact. Titania nanotube-arrays were produced by anodization process using commercially available titanium foil. The titania nanotubes were synthesized according to the procedure reported by Shankar et al. [1].

Special attention was designated to preparation of these specimens, particularly the nanotubes/metal interface for transmission electron microscope (TEM). A comparison between conventional ion milling (PIPS), ion slicing (Ion Slicer) and focused ion beam (FIB) is presented.

Conventional ion-milled specimens were prepared longitudinally by mechanical polishing on a diamond-lapping film (DLF) in cross-section geometry down to a thickness of ~5 µm, Figure 1a. An automatic Allied MultiPrep System was used for tripod polishing of TEM specimens. Afterwards, the specimens were Ar-ion thinned at an accelerating voltage 4 keV and then the voltage was reduced, down to 0.8 keV, using an incidence angle of 8^o to perforation in a Gatan, PIPS.

Preparation of thin foils by means of argon ion-slicing using Ion Slicer is a method that enables a quick preparation of high quality specimens for TEM. The TEM samples prepared by this method were first cut to rectangular slice into 2.8 mm in length and 0.8 mm in width and glued together face to face, followed by polishing in cross-section geometry down to a thickness of 115 µm. After the sample was processed by the above two steps, it was mounted onto the Ion Slicer holder, partially masked with a shield belt. Additionally, the samples were milled with the Ar-ion beam at the accelerating voltage of 6 keV and 2.5^o tilt angle, and finally polished at the accelerating voltage of 2 keV and tilt angle 0.8^o to perforation in a JEOL EM-09100IS Ion Slicer [2]. Sample before and after argon ion-slicing is shown in Figure 2a, 2b.

For TEM sample preparation using FIB **(**FEI Helios Nanolab650) TEM sections of the TiO_2 nanotube-array were prepared with the in-situ, lift-out technique [3]. To avoid “curtain effect” inside the metal titanium part of the interface the cross-section was prepared from the top of the substrate (metal) which was previously thinned down to 2 µm using tripod polishing. Pt protective strap was deposited on the area of interest. The specimen was milled using 30 KeV Ga ions to form a lamella, Figure 3a, 3b. Using the in-situ micromanipulator (Omniprobe), the TEM lamella was lifted-out and positioned on a Cu lift-out grid with wide post, Figure 3c. The metal titanium / titania nanotube array interface clearly shows the specific morphology and size of lamellae. The interface itself is dense without any pores or cracks, Figure 3d. Afterwards, selected parts of the TEM lamella were thinned with 30 keV Ga ions to a thickness of around 50–70 nm and subsequently polished with 5 keV and 2 keV Ga ions to remove the amorphised layer. In this way the prepared specimens were thin enough for TEM observation.

All three methods were found to be efficient for preparation of the TEM cross-sections of metal/oxide interface. Ion-milling method with a modified procedure requires an experienced operator for preparation of top quality samples. However, a very small thinned area may create a problem for observation. Samples prepared by ion-slicer method were not so transparent but nevertheless exhibited relatively large useful areas. Preparation with FIB could be automated and could be done quite fast (within few hours); still an experienced operator with lot of practice is required.

1. K. Shankar, “et al”, Nanotechnology 18 (2007), p. 65707-65718.
2. D. Jenko, Materials and technology 45 (2011), p. 303–310
3. M. Gec, “et al”, Proceedings of the 15th European Microscopy Congress, 16th-21st September 2012, Manchester, United Kingdom, Royal Microscopical Society, (2012)
4. Acknowledgements: The financial support the research leading to these results has received funding from the European Union Seventh Framework Programme [FP7/2007-2013] under grant agreement n°312483 (ESTEEM2).

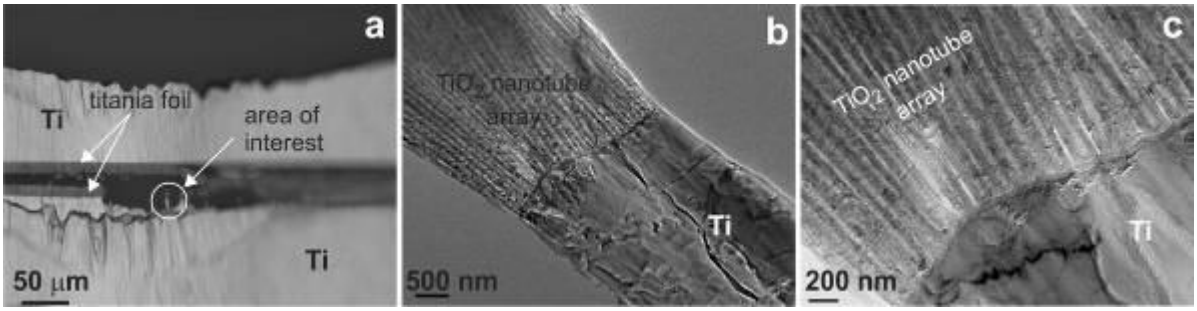

Figure 1. (a) Optical micrograph of ion-thinned specimens of TiO_2 nanotube array. (b, c) TEM micrograph of TiO_2 nanotube array interface

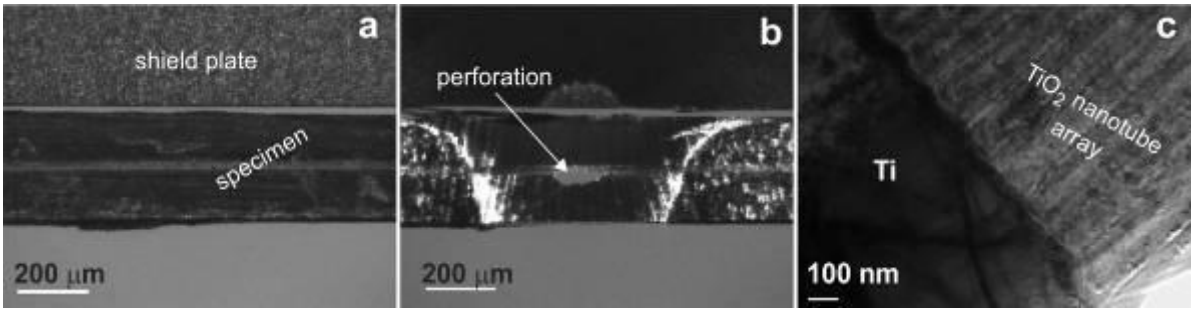

Figure 2. The Ion Slicer technique for preparation of a cross-section TiO_2 nanotubes material: (a) images before start milling and (b) images after milling. (c) TEM micrograph of TiO_2 nanotube array interface

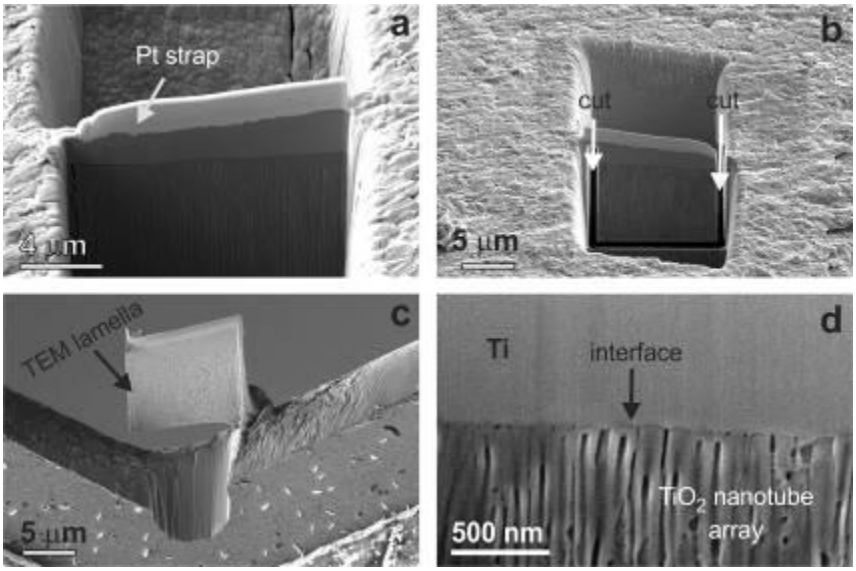

Figure 3. The FIB in-situ lift-out technique for preparation of a cross-section TiO_2 nanotubes material: (a) sectioning of a thin lamella using focused Ga ions at 30 keV. (b) lamella with cut-offs just before the lift-out (c) the TEM lamella, fixed at wide post of Lift-out grid and prepared to the final thinning (d) details of metal titanium/TiO2 nanotubes interface

Sample Preparation Methods

IM.7.P147
Osmium, epon and immunogold labeling - friend or foe?

A. Klingl[1,2], M. Debus[1,2], D. Märte[1]

[1]Philipps-Universität Marburg, Zellbiologie, Marburg, Germany
[2]LOEWE-Zentrum für synthetische Mikrobiologie (Synmikro), Elektronenmikroskopie, Marburg, Germany

andreas.klingl@synmikro.uni-marburg.de
Keywords: Immunogold labeling, epon, osmium tetroxide

For studies concerning the ultrastructure of microorganisms (Bacteria, Archaea, and unicellular Eukarya), cells or tissues, it is essential to preserve them in a close to natural state [1]. This can be achieved by the application of high-pressure freezing, freeze substitution and subsequent embedding in a resin polymer [2]. In the special case of the diatom *Phaeodactylum tricornutum*, the combination of cryo-preparation with suitable freeze substitution media is crucial because of the high number of membranous structures within this organism [3]. As an example, the plastid of *P. tricornutum* is the result of a so called secondary endosymbiosis and is therefore surrounded by four membranes. For a better visibility of membranes, freeze substitution is performed with acetone containing 0.2 up to 2% OsO_4, 0.5% uranyl acetate and small amounts of water [4]. Additionally, and in contrast to the general procedure for immunogold labelling on thin sections, the cells were usually embedded in epon resins. After slight modifications of substitution protocols, the localization of proteins, GFP-fusion proteins and sugars is still possible after this treatment with the advantage of optimal structural preservation (Figure 1).

As a proof of principle, the above mentioned substitution medium as well as ethanol containing glutaraldehyde, formaldehyde and uranyl acetate were also used for the processing of high-pressure frozen eukaryotes like the plant pathogen *Ustilago maydis* and several Bacteria and Archaea. In the latter case for example, the localization of the major S-layer protein Msed_1806 of the crenarchaeal species *Metallosphaera sedula* TH2 at the surface of the coccoid cells was successful (Figure 2)[5].

It could further be shown, that high-pressure freezing seems to be a key step in preservation of epitopes to overcome the negative effects of OsO_4 and epon on antigenicity. In almost all cases, the localization of the respective proteins or sugars was not possible when cells were chemically fixed with glutaraldehyde.

1. A. Klingl, C. Moissl-Eichinger, G. Wanner, J. Zweck, H. Huber, M. Thomm and R. Rachel. Arch Microbiol 193 (2011), 867.
2. R. Rachel, C. Meyer, A. Klingl, S. Gürster, T. Heimerl, N. Wasserburger, T. Burghardt, U. Kueper, A. Bellack, S. Schopf, R. Wirth, H. Huber and G. Wanner. Meth Cell Biol 96 (2010), 47.
3. N.H. Gonzalez, G. Felsner, A. Klingl, F.D. Schramm, U.-G. Maier and K. Bolte. PLoS ONE 6 (2011), e25316.
4. C. Buser and P. Walther. J Microsc 230 (2008), 268.
5. A. Klingl. PhD thesis, University of Regensburg (2011).
6. We kindly acknowledge K. Bolte, F. Hempel, M. Johannsen and R. Rachel for their support.
7. This work was supported by the state of Hessen (SYNMIKRO).

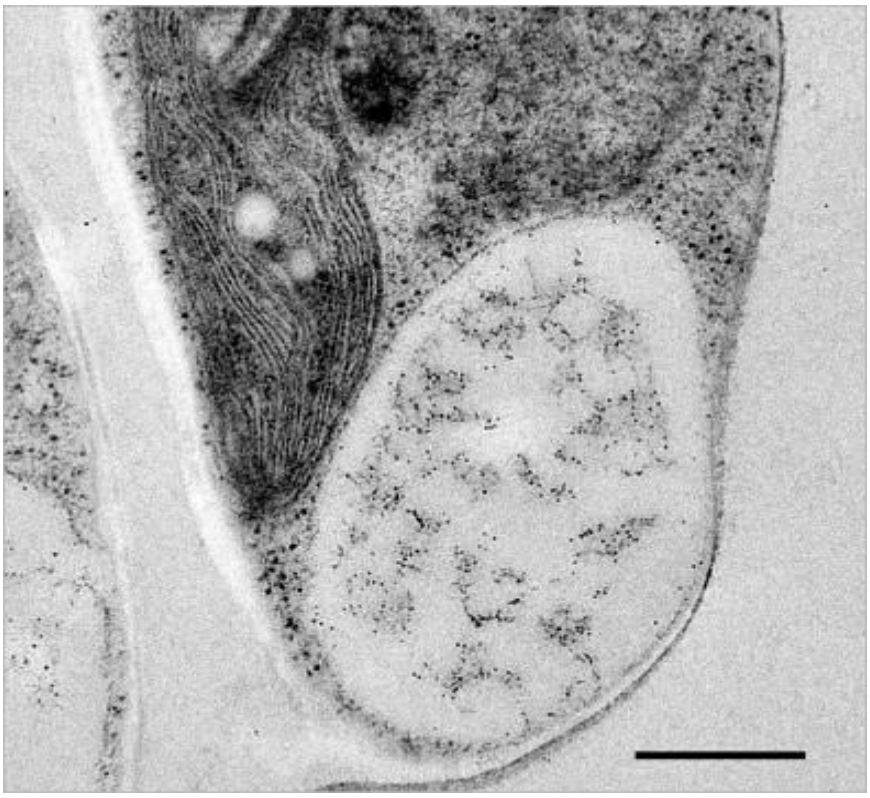

Figure 1. Transmission electron micrograph of a high-pressure frozen *P. tricornutum* cell showing the marbled vacuole. Within this compartment, the sugar chrysolaminarin could be localized with a mouse anti-betaglucan antibody (1:10000) in combination with a gold-coupled secondary antibody goat anti-mouse IgG + 5 nm gold (1:20). Freeze substitution: A.O.U.H.; scale bar: 500 nm.

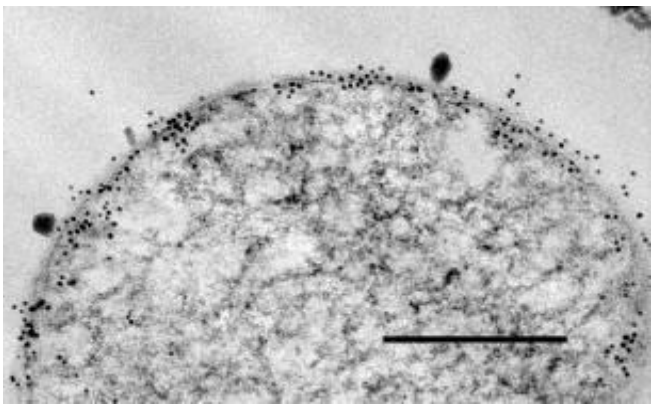

Figure 2. Ultrathin section of *M. sedula,* strain TH2. The major subunit of the S-layer protein Msed_1806 could be localized at the cell surface. Primary antibody: rabbit anti-Msed1806 (1:500); secondary antibody: goat anti-rabbit IgG + 6 nm gold (1:20). Freeze substitution: E.G.F.U.; scale bar: 200 nm.

Sample Preparation Methods

IM.7.P148
Low-energy Ar^+-polishing of FIB prepared GaN-SiC interfaces for Cs-corrected STEM

A. Lotnyk[1], D. Poppitz[1], J. Gerlach[1], B. Rauschenbach[1]

[1]Leibniz Institute of Surface Modification, Physics, Leipzig, Germany

andriy.lotnyk@iom-leipzig.de
Keywords: low energy ion milling, Cs-correction, STEM

For high-resolution aberration-corrected (Cs-corrected) scanning transmission electron microscopy (STEM) the quality of prepared TEM samples is crucial, because the image resolution and the quality of TEM data depends essentially on the thickness and surface quality of the TEM sample. Depending on the high voltages used for TEM work, TEM specimens should be as thin as 10 nm or less for low voltage TEM work (80 kV and lower) and they have to be as thin as 30 nm or less for medium voltage TEM work (e.g. 300 kV). Nowadays, widely used focused ion beam (FIB) preparation technique with standard FIB configuration using conventional lift-out method cannot be employed in fabrication of such thin TEM samples. The samples after FIB preparation are often too thick (more than 50 nm using even the 5 kV low voltage thinning step) for TEM studies. In addition, damage and amortization of the specimen surface during the milling process occurs. This damaged layer is a disorder of the original structure of the sample surface. To overcome these disadvantages of the FIB preparation, a low-energy Ar^+-polishing post FIB lamella treatment can be applied [1].

In the present work, we focus on TEM sample preparation of GaN-SiC interfaces for analysis in Cs-corrected STEM at 80 kV and 300 kV. For FIB lamellae preparation we have used standard FIB lift-out method. Afterwards, the FIB lamellae were further prepared by a focused low-energy Ar^+-polishing (less than 1 keV) in a NanoMill (Fischione) low energy ion mill system. The last step was plasma cleaning of a TEM lamella for 10 min in a Gatan Solarus plasma cleaning system. A Zeiss Auriga DualBeam system was applied for FIB preparation using *in situ* lift-out method. TEM observations were performed with a probe Cs-corrected Titan^3 G2 60-300 microscope equipped with HAADF, BF, DF, ABF and Super-X EDX detectors as well as with GIF Quantum Gatan imaging filter. The TEM was operated at 80 kV and 300 kV.

Figure 1 shows thickness measurements by means of energy filtered TEM of a porous GaN layer grown on a 6H-SiC (0001) substrate by IBA-MBE [3]. The brightness of colours in Figure 1 shows different thicknesses in the sample: the brighter the thicker. Since the brightness of the image does not change so much, the thickness of the TEM sample after NanoMill step is rather uniform. The thickness of the TEM sample at the SiC-GaN interface is in the range of 9 - 11 nm.

Figure 2a) shows a HRSTEM image of the interface between GaN thin film and SiC substrate. The image in Figure 2a) was taken from an interface region of the sample shown in Figure 1. The atomic structure of the GaN-SiC interface as well as defects in the GaN thin film close to the interface is clearly resolved in Figure 2a) and Figure 2b), respectively.

Another example of successfully post-treated FIB lamella with a low-energy Ar^+-polishing for atomic resolution STEM investigations at medium-kV is given in Figure 3. Figure 3a) shows a bright-field STEM image of a dense GaN layer produced on a 6H-SiC (0001) substrate by IBA-MBE. Different defects at the GaN-SiC interface can be seen in the image. EFTEM thickness measurements showed that the TEM lamella has a specimen thickness of only 25 - 30 nm throughout the whole length of the lamella (not shown here). Figure 3b) gives a HAADF-HRSTEM image of the GaN-SiC interface. The atomic columns in the GaN and SiC as well as at the GaN-SiC interface are clearly resolved.

The combination of FIB with focused low-energy argon ion milling in the "NanoMill" system enables to prepare routinely high quality TEM lamellae of GaN-SiC interfaces. The samples using this approach are well suited for (HR)TEM and (HR)STEM studies as well as for atomic EDX and EELS analyses at 80 kV and at 300 kV.

1. T. Mehrtens, S. Bley, P.V. Satyam and A. Rosenauer, Micron 43 (2012) p. 902.
2. J. W. Gerlach, T. Ivanov, L. Neumann, Th. Höche, D. Hirsch and B. Rauschenbach, J. Appl. Phys. 111 (2012), p. 113521.
3. The financial support of the European Union and the Free State of Saxony (LenA project) is greatly acknowledged.

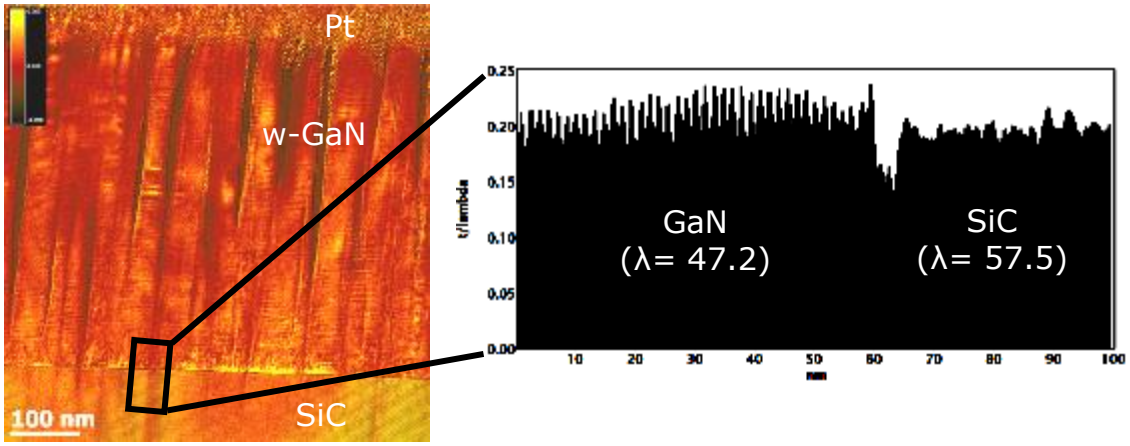

Figure 1. Thickness measurement by energy filtered TEM. From t / lambda, the thickness of a sample (t) can be calculated.

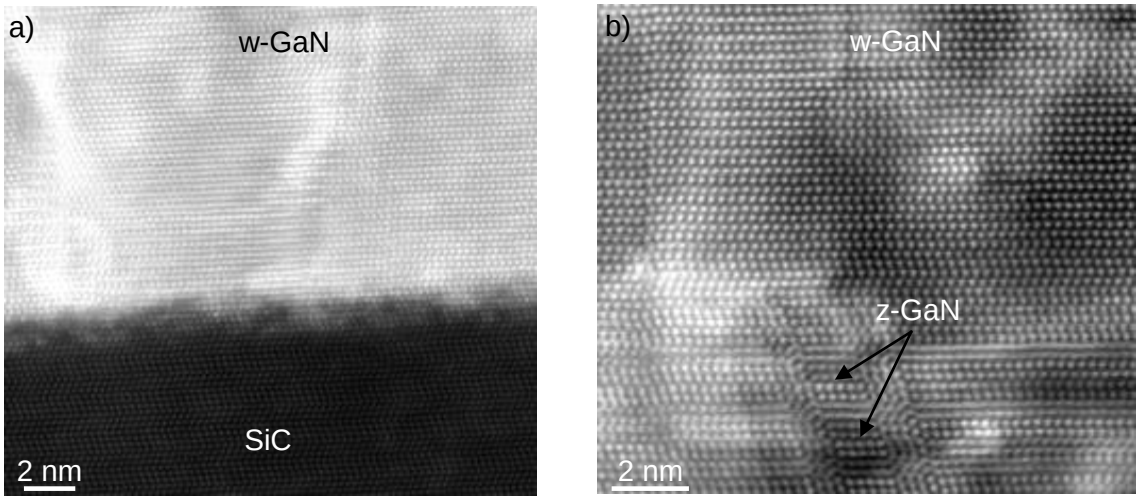

Figure 2. HAADF-HRSTEM images taken at 80 kV of a) the GaN-SiC interface and b) defects and intergrowths in GaN close to the GaN-SiC interface. For STEM analysis, the FIB lamella was prepared along the a-axes of both GaN and SiC.

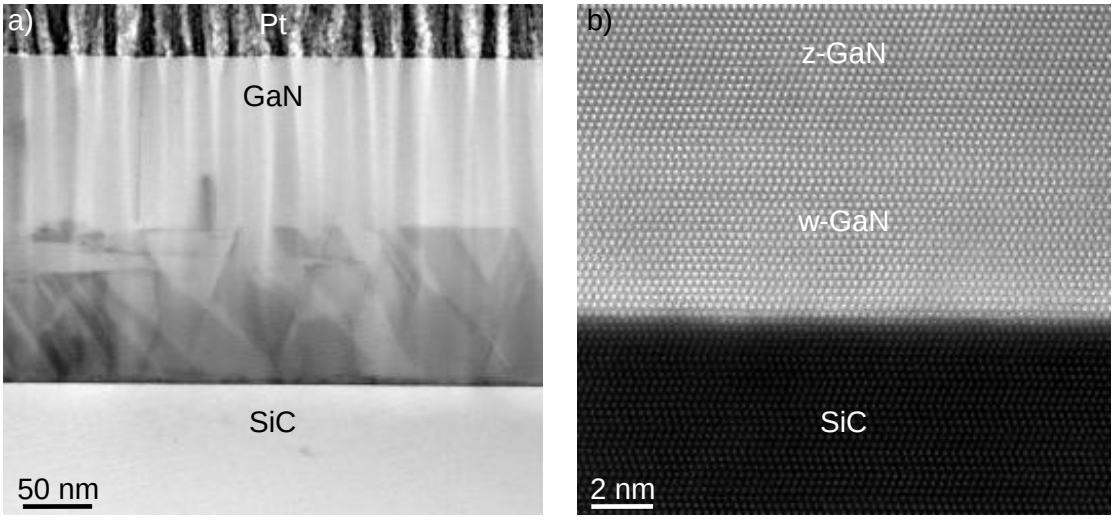

Figure 3. a) BF-STEM image of a GaN thin film grown on a 6H-SiC (0001) substrate. b) HAADF-HRSTEM image of the GaN-SiC interface. The STEM investigations were performed at 300 kV. For STEM investigations, the TEM lamella was cut along the a-axes of both GaN and SiC.

Sample Preparation Methods

IM.7.P149
Scanning Electron Microscopy of biological samples without metal coating: Utilizing bulk conductivity for enhanced preparation flexibility

H.-J. Ensikat[1], M. Weigend[1]

[1]Nees Institute for Biodiversity of Plants, Bonn, Germany

ensikat@uni-bonn.de

Our studies of plant surfaces by scanning electron microscopy induced several requirements that exceeded the possibilities of the standard CP-drying preparation. The study of contaminations and drop-surface interactions on superhydrophobic samples, material contrast imaging with backscattered electrons, and various other applications motivated us to develop a line of tailored preparation and microscopy techniques.

Several of these methods provide the samples with sufficient internal electrical conductivity that they can be imaged without metal coating in a conventional high-vacuum SEM. Our methods use some surprising properties of the samples. The low water permeability of plant surfaces, the low vapour pressure of some liquids, and the protonic conductivity of some liquids and of ice at cryogenic temperatures enabled the design of unusual but often simple methods. The presented methods range from imaging of fresh hydrated plant samples over cryo-SEM to special chemical treatment of bio-organic material to obtain the necessary conductivity. The proton conductivity occurs in liquids such as water or glycerol as well as in solids such as ice at temperatures above -100°C, and in chemically treated dry organic material at room temperature.

Sample Preparation Methods

IM.7.P150
Developments in Broad Argon Beam Systems to Complement Developments in TEMs and SEMs

M. Hassel-Shearer[1], T. Hosman[1], A. Pakzad[1], C. Spence[1]

[1]Gatan Inc, Pleasanton, United States

mhassel-shearer@gatan.com
Keywords: Broad Argon Beam System, Cathodoluminescence, Amorphous Layers

Sample Preparation is the quiet necessity required to release the exceptional performance of the recent generation of Corrected TEMs and SEMs. Revealing the details in samples for these microscopes requires improvements in the performance of broad Argon beam tools to reduce the damage layer to ~1 nm or less for both TEMs and SEMs. In general, the focus on sample prep as a means of minimizing damage has been on improving samples for the current ultra high resolution TEMs.

Focused Ion Beam tools are frequently used to prepare thin lamella for TEMs. However, even the lower accelerating voltages used leave an amorphous layer or Ga implanted into the lamella that degrades the resolving power of a corrected TEM. Recent argon tools have improved optics to permit lower energy polishing to meet this challenge of reducing the amorphous layer. An additional complimentary step with an aligned broad argon beam can reduce or eliminate the effect of the Ga.

For SEMs, often the area of interest is an internal interface. Broad Argon Beam based tools that provide cross sectional capabilities enable the revealing of these interfaces consisting of materials made with considerably different physical properties. Using the same argon guns and taking into consideration the same need to prepare low damage surfaces has resulted in improved imaging and analytical results for high resolution SEMs, specifically ultra low voltage SEMs that image and analyze the near surface region.

At the same time, these tools have been developed to truly permit reproducible and full unattended recipe operation. This includes not just changing the polishing parameters, but real time image analysis to determine when to change polishing parameters or stop the process. Examples of such unattended operations will be presented for TEM and SEM through images and analytical techniques, including energy filtered TEM and CL and EBSD for SEM samples, illustrating the usage of sub 500 electron volt final polishing performance for both TEM and SEM applications

Sample Preparation Methods

IM.7.P151
Preventing aggregation of nanoparticles during the drying procedure for TEM sample preparation

B. Michen[1], D. Vanhecke[1], B. Rothen-Rutishauser[1], A. Petri-Fink[1]

[1]Adolphe Merkle Institute, Marly, Switzerland

dimitri.vanhecke@unifr.ch

Nanomaterials have been promised a great future in various fields of applications. Because their physical and chemical properties depend very much on their size and shape, their characterization is of utmost importance. When nanomaterials are dispersed in a fluid an in-situ observation technique such as dynamic light scattering (DLS) is often used to probe the dispersion state of colloids. This technique is very precise in determining mean particle size and its distribution as long as it remains monomodal. However, when multimodal distributions evolve, for example, induced by aggregation the quantification becomes challenging due to the assumptions made in the applied models.

Alternatively, transmission electron microscopic (TEM) analysis can provide model-free data. However, in order to obtain TEM samples of nanoparticles in a fluid, the solvent (mostly water) must be removed. Drying effects will take place, which leads to the accumulation and aggregation and hence introduces bias or artifacts in the analysis. It is not possible to differentiate nanoparticle aggregates caused by drying effects from aggregates which were formed prior to drying (e.g. due to colloidal instability of the system). Thus, TEM has long been thought to be unsuitable for quantitative investigations of nanoparticles and colloidal aggregates of nanoparticles in liquids. Here, we present a simple protocol that circumvents the drying issue by stabilizing the colloidal system with a protein, namely bovine serum albumin (BSA). TEM samples with various ratios of proteins to nanoparticles have been prepared that resulted in different spatial distributions of nanomaterials on the TEM grid as shown in Figure 1. When a sufficient high protein concentration was used, the resulting TEM images allow for automated data collection on a large number of nanoparticles which is in very good agreement with data obtained from dynamic light scattering and thus, the actual dispersion state.

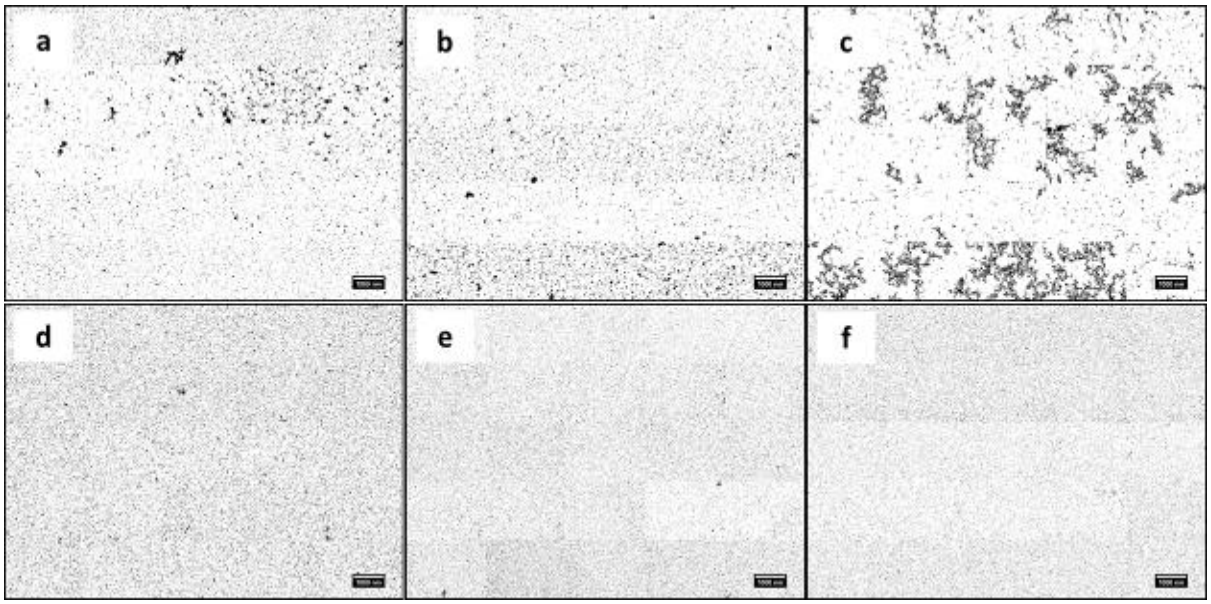

Figure 1. shows TEM mosaic images (each composed of 5x5 single images) of gold nanoparticles prepared at various concentration ratios of BSA to nanoparticles. In a) 25 images of the control sample are presented that do not contain BSA. The concentration ratio is steadily increasing from b) to f). When the control in a) is compared to e) and f) we observe an improved homogeneity in the distribution of the gold nanoparticles indicating that the accumulation of particles due to drying effects was not taking place.

Sample Preparation Methods

IM.7.P152
Sub-10 nm nanomodification of GaAs nanowires with Helium ion microscope

E. Ubyivovk[1], Y. Petrov[1], O. Vyvenko[1], A. Bouravleuv[1], G. Cirlin[1]

[1]St.-Petersburg State University, Physics, St. Petersburg, Russian Federation

ubyivovk@gmail.com
Keywords: nanostructure, nano-modification, nanowires

The development of the methods of local modification of the crystalline nano-objects without damaging their crystal structure can open a great opportunity for the study of more subtle physical effects and to manufacture new types of nano-devices.

The most direct way to modify the shape of nanowires including the drilling of nanoholes is ion beam sputtering of the material. This technique when used with commonly available Ga-FIB does not allow one to modify the whiskers with the diameter of few tens of nm due to a big interaction volume caused, In turn, by a big ion mass and strong ion backscattering. Another problem of nanomodification is a damage of treated surface.

In this work we performed experiments on nanomodification of GaAs nanowire with lighter ions-Helium – with the help of Scanning Helium Ion Microscope (HeIM) - Zeiss Orion (Fig. 2). In spite of the fact that sub 10-nm sputtering in HeIM was previously described [1], destruction of lattice and formation of amorphous layer nearby treated area is still not clearly understood.

The samples under the modification were GaAs nanowhiskers of different crystal structure (sphalerite, wurzite, core-shell etc) with the thickness of 50-100 nm and the lengths of 1-10 um.

The experiments included the drilling the openings under diverse angles with respect to crystal axes and the analysis of the resulting structure with HR-TEM (Fig. 2).

For the first time we showed that holes with the diameter as small as 10 nm surrounded with the amorphous layer is 2-5 nm thickness can be easy obtained by proper chosen parameters of the experiments. More detailed description of the experimental procedure, its advantages and limitation will be presented at the Conference.

1. Experimental data presented in this work were obtained using the equipment of Interdisciplinary Resource Center for Nanotechnology St. Petersburg State University, Russia [2]. This work is supported by a grant RFBR No. 12-02-01132-a.
2. .D. Winston, B.M. Cord, B. Ming, D.C. Bell and all J. Vac. Sci. Technol. B 27, 2702 (2009)
3. .Htpp://nano.spbu.ru

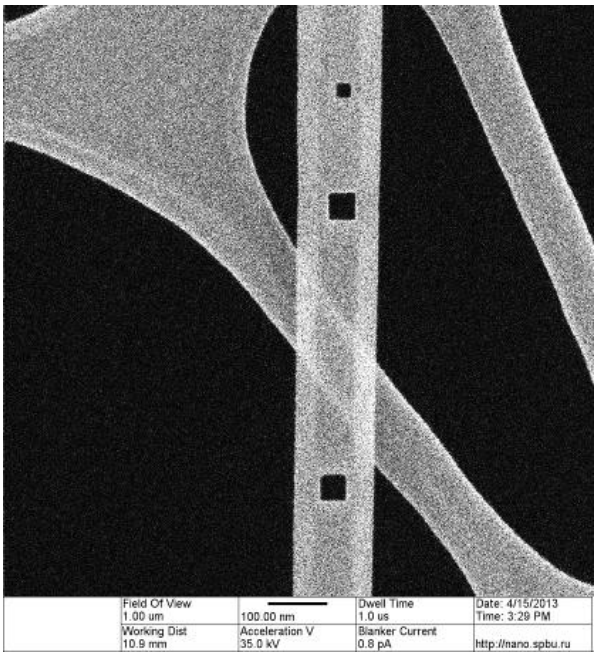

Figure 1. HeIM image nanomodification of GaAs nanowire.

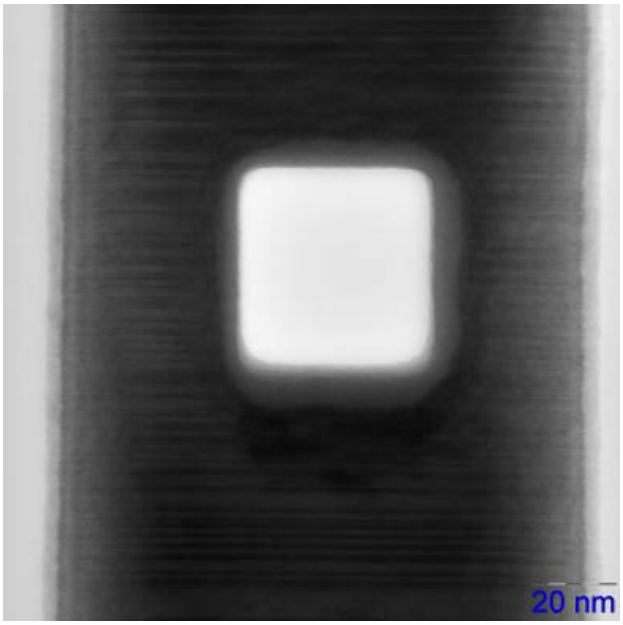

Figure 2. TEM image nanomodification of GaAs nanowire.

Sample Preparation Methods

IM.7.P154
Focused Ion Beam nanofabrication employing multiple Ion Species from Liquid Metal Alloy Ion Sources

S. Bauerdick[1], A. Nadzeyka[1], P. Mazarov[1], L. Bruchhaus[1], R. Jede[1]

[1]Raith GmbH, Konrad-Adenauer-Allee 8, 44263 Dortmund, Germany

bauerdick@raith.de
Keywords: FIB, ion source, nanofabrication

Focused ion beam (FIB) systems and combined FIB-SEM microscopes are widely used for sample preparation and various analytical tasks. Moreover, focused Ion Beam Lithography (IBL) can have significant advantages over other nanolithography techniques, like direct, resistless, and threedimensional patterning, while at the same time delivering the in-situ process control by cross sectioning and inspection that a FIB instrument typically affords. Since the type of ion has dramatic consequences on the nature of the interaction mechanism with the sample and thus the resulting nanostructures, we have extended the unique ion column and
Gallium source towards the long-term stable delivery of multiple species for a nanometer-scale focused ion beam employing a liquid metal alloy ion source (LMAIS). The column is equipped with an ExB filter capable of selecting from various ion species of one source [1, 2]. This provides single and multiple charged species of different mass (Figure 1) without changing the source, e.g. Si, Ge and Au, resulting in significantly different interaction volumes. We present the capabilities of the multiplespecies IBL instrument including excellent long-term current stability (Figure 1) and sub-20 nm beam resolution for various ions like Si (Figure 2) and Au. The characteristics and applications of different species will be discussed in terms of imaging, patterning and functionalization. From nanofabrication point of view – besides the lateral beam resolution – aspects like depth of interaction, sputter yield, available beam current and stability are equally or more important and depend on different application requirements. Advantages of the IBL setup in general for long-term and large area patterning will be shown by challenging nanofabrication examples like X-ray zone plates [3], large area gratings [4], and waferlevel nanopore devices for DNA sequencing [5, 6]. With the new ion species besides Gallium some of these applications can be further improved, e.g. less contamination in high resolution milling processes using Si, faster milling using Au or varying the implantation depth from Au double charged to Au clusters for optimizing functionalization or catalytic seeding. On-going investigations include photonics and plasmonics, nanopore membrane devices as well as selective growth of graphene [2, 7], whereas more fundamental studies of ion and matter interaction, directed self-assembly or growth of nano-scaled materials are possible as well.

1. B. R. Appleton et al., Nucl. Instrum. Methods B 272 (2012), 153.
2. S. Tongay et al., Appl. Phys. Lett. 100 (2012), 073501.
3. A. Nadzeyka et al., Microelectr. Engineering 98 (2012), 198.
4. S. K. Tripathi et al., J. Micromech. Microeng. 22 (2012) 055005.
5. J. Edel, T. Albrecht in “Nanopores for Bioanalytical Applications: Proceedings of the First International Conference” (ROYAL SOC OF CHEMISTRY) (2012), 57.
6. J. Edel et al., Anal. Chem. 85 (4) (2013), 2449.
7. M. G. Lemaitre et al., Appl. Phys. Lett. 100 (2012), 193105.

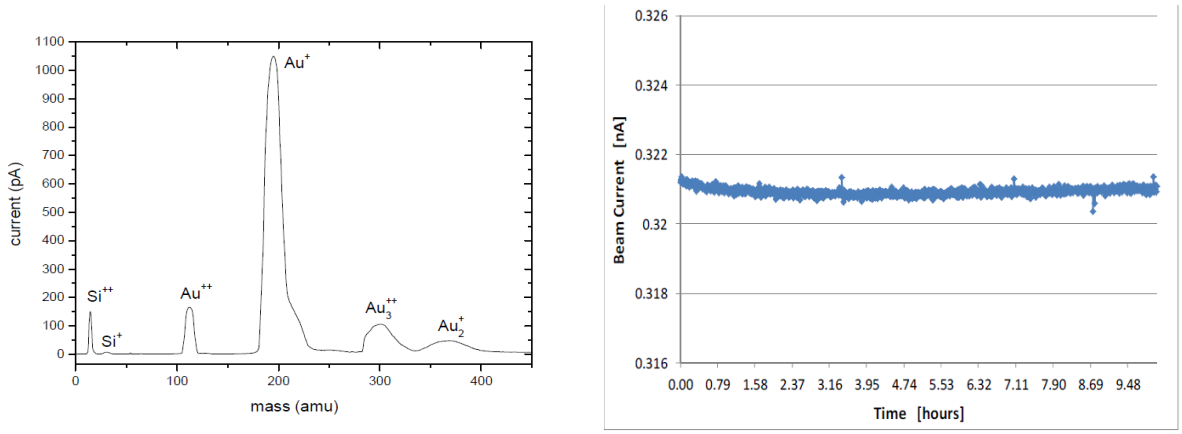

Figure 1. Mass spectrum (showing ions of different charge and mass) and stability measurement over 10 h of a AuSi Liquid Metal Alloy Ion Source (LMAIS).

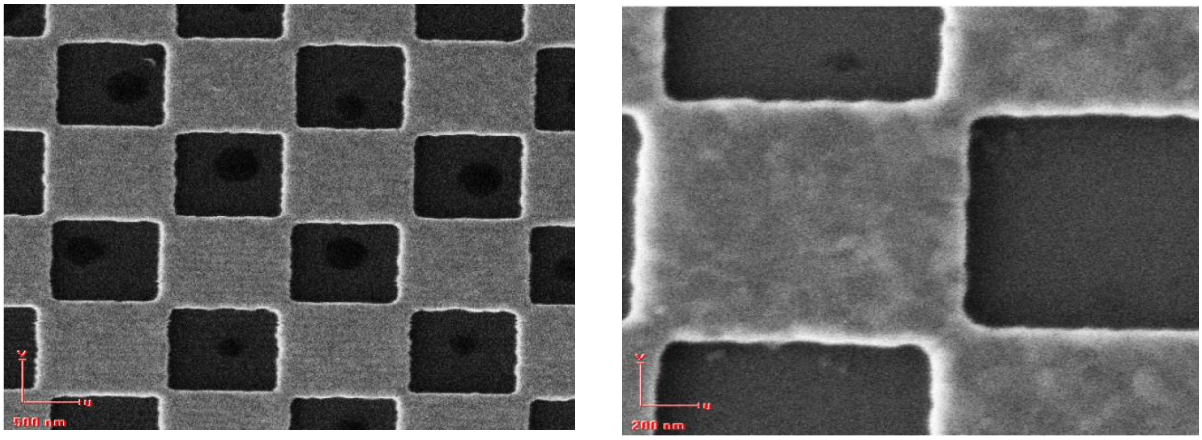

Figure 2. Secondary electron images obtained by scanning a focused Si^{++} ion beam over a sample of gold squares on silicon. The beam diameter is about 8 nm and can be applied to fabricate 10 – 15 nm features

Static and Dynamic Electric and Magnetic Imaging

LBP.IM.P01
Electrostatic properties of insulators in three-dimensions using transmission electron holography tomography.

L.C. Gontard[1], R.E. Dunin-Borkowski[2], T. Kasama[3]

[1]CSIC, Instituto de Ciencia de Materiales de Sevilla, Seville, Spain
[2] Forschungszentrum Jülich, Ernst Ruska-Centre for Microscopy and Spectroscopy with Electrons and Peter Grünberg Institute, Jülich, Germany
[3]Technical University of Denmark, Center for Electron Nanoscopy, Kgs. Lyngby, Denmark

lionel.cervera@icmse.csic.es

Electron holography tomography (EHT) [1,2] is applied here to measure quantitatively in three-dimensions inside and outside one sample of sapphire (Al_2O_3) the electrostatic potential, the electric field, the charge density and the accumulated charge. Sapphire is an insulator and when electron bombarded during transmission electron microscopy observation the sample will emit secondary electrons; if there is not external supply of electrons through a conductive path the sample accumulates an electric charge and an electric potential and electric field can be measured inside and outside the sample [3].

The electrostatic potential for insulating specimens has in first approximation two terms $V(x,y,z) = V_o(x,y,z) + V_c(x,y,z)$ where $V_o(x,y,z)$ in the so-called mean inner potential [4] and $V_c(x,y,z)$ is the potential that accounts for the contribution of the accumulated net charge (both free and bound charge). In our experiments we have made the assumption that the potential is time-independent, i.e., that the sample accumulates a constant charge, supported by the fact that the reconstructed data obtained are coherent with the physical properties expected.

EHT can be used to recover the modulation of the phase of the electron wave of a sample in three-dimensions, $\Delta\phi(x,y,z)$. Furthermore, the potential can be calculated like $|V(x,y,z)| = \Delta\phi\,(x,y,z)/C_E$, where C_E called the interaction constant is a specimen-independent value.

From the electrostatic potential, other electrostatic properties can be easily calculated using Maxwell equations.

The electric field can be computed with the equation

$$\vec{E}(x,y,z) = -\vec{\nabla}V(x,y,z)$$

Neglecting polarization effects the associated volume charge distribution obeys Poisson's equation

$$\nabla\cdot\vec{\nabla}V(x,y,z) = \nabla^2V(x,y,z) = -\frac{\rho(x,y,z)}{\varepsilon}$$

where $\rho(x,y,z)$ is the charge density, ε is the permitivitty of the material (approximately $8.85\cdot10^{-11}$ [F/m] for alumina), $\nabla\cdot$ is the divergence operator and ∇^2 the Laplacian operator. In vacuum there is not charge, $\rho_{vacuum}(x,y,z) = 0$ and Laplace's equation

$$\nabla^2V(x,y,z)_{vacuum} = 0$$

Finally, the total charge Q_R accumulated in the samples is computed as the volume integral over the region *R* of observation.

$$Q_R = \iiint_R \rho(x,y,z)\,dxdydz = -\varepsilon_o \iiint_R \nabla^2V(x,y,z)\,dxdydz$$

Figure 1 shows the experimental results obtained applying EHT to a tip of sapphire. Using the binding approximation as described in [4] the mean inner potential of neutral sapphire V_o is estimated to be 14 Volts.

The total potential $(V = V_o + V_c)$ reaches a maximum value of 12.5 Volts inside the tip and decreases towards the surface to a minimum value of 8 Volts. V_o of an homogeneous sample must be spatially invariant but the experiment here shows that the potential is not constant. $V(x,y,z)$ is lower at every point than the calculated V_o for neutral sapphire and decreases at the surface of the sample. The accumulation of a positive electric charge induced by the electron beam adding a potential $V_c(x,y,z)$ that decreases V_o [5]. The electric charge dsitribution is not homogeneous and accumulates closer to the surfaces of the sample (see Figure 1C).

The total charge is of 0.098 fC (equivalently to removing 614 electrons from the sample) confirmed by the presence of an electric field surrounding the sample. This electric field is always perpendicular to the surface and reaches a maximum value of 0.7 V/nm or 7MV/cm at the end of the tip which is lower than the breakdown voltage of sapphire.

1. A.C. Twitchett-Harrison, T.J.V. Yates, R.E. Dunin-Borkowski and P.A. Midgley, Ultramicroscopy 108 (2008) p. 1401.
2. D. Wolf, H. Lichte, G. Pozzi, P. Prete and N. Lovergine, Applied Physics Letters 98 (2011), 264103.
3. L.C. Gontard, J.R. Jinschek, H. Ou, J. Verbeeck and R.E. Dunin-Borkowski, Applied Physics Letters 100 (2012) 263113.
4. M. Gajdardziska-Josifovska and A.H. Carim in "Applications of electron holography. In *Introduction to Electron Holography"*, eds. L.F. Allard, D.C. Joy and E. Voelkl, (Plenum Press, New York) (1999), p. 267.

5. R.E. Dunin-Borkowski, S.B. Newcomb, T. Kasama, M.R. McCartney, M. Weyland, P.A. Midgley, Ultramicroscopy 103 (2005) p. 67.
6. We kindly acknowledge for funding to the EC project REGPOT AL-NANOFUNC.

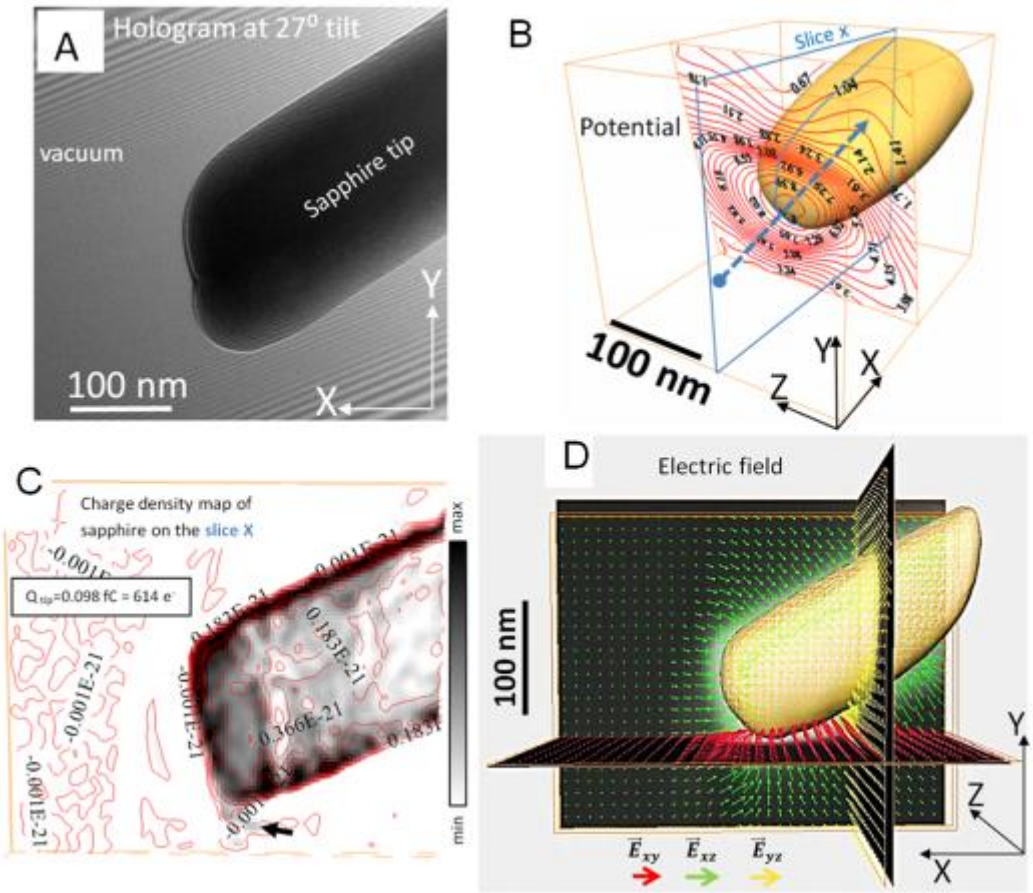

Figure 1. (A) Hologram of a tip of sapphire tip acquired in a microscope FEGTEM Titan and using a biprism. (B). Orthoslice of the three-dimensional distribution of electrostatic potential (in Volts) inside and outside the tip shown in (A). (C) Charge density distribution (C/nm^2) corresponding to the otrhoslice *Slice x* shown in (B). (D) Vectorial representation of the three-dimensional electrostatic field outside the tip.

Advances in Light and Electron Optics

LBP.IM.P03
Developing a Quantum Electron Microscope - employing the Interaction-Free Measurement to Reduce Radiation Damage

C. Kohstall[1], B. Klopfer[1], J. Francis[1], C. Kealhofer[1], G. Skulason[1], T. Juffmann[1], M. Kasevich[1]

[1]Stanford University, Physics, Stanford, United States

christoph.kohstall@gmail.com

We develop a new electron microscope based on the interaction-free measurement principle [1,2]. Such a Quantum Electron Microscope (QEM) [3], see Figure below, may enable imaging of biological samples with radiation doses so small that they are non-lethal. The realization of the QEM will require precise control over the quantum motion of free electrons. On this poster, we discuss our approach to build a QEM including the realization of an electron resonator and an electron amplitude beam-splitter. On top of the QEM application, these developments will advance the electron analogue to photon quantum optics.

1. A. C. Elitzur and L. Vaidman, *Found. Phys.* **23**, 987 (1993)
2. P. Kwiat, H. Weinfurter, T. Herzog, A. Zeilinger, and M. A. Kasevich, *Phys. Rev. Lett.* **74**, 4763 (1995)
3. W. P. Putnam and M. F. Yanik, *Phys. Rev. A* **80**, 040902(R) (2009)

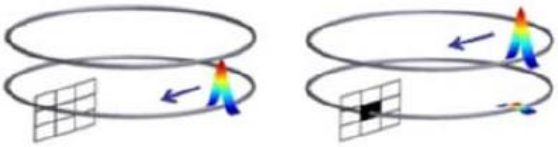

Figure: Interaction-free measurement as proposed in Ref. [3]. Say the electron starts circulating in the upper ring and the upper and lower rings are coherently coupled. After the characteristic coupling timescale, if there is no absorber in the lower ring (left), the electron will completely transfer to the lower ring. If there is an absorber (right), there is no coherent build-up of the electron wave function in the lower ring and it stays in the upper ring, which is a manifestation of the quantum Zeno effect. As the electron can now be measured in the upper ring, the existence of the absorber is inferred without having interacted with the electron. Fig. from ref. [2].

Quantitative High-Resolution TEM/STEM and Diffraction

LBP.IM.P04
Multi-CTF decomposition of the power spectrum of the zero-loss energy filtered and non-filtered images of amorphous carbon films

I. Lazic[1], S. De Carlo[1,2], R. Matadeen[2]

[1]FEI Company, R&D, Eindhoven, Netherlands
[2]NeCEN, Gorlaeus Laboratory, Leiden, Netherlands

ivan.lazic@fei.com

The contrast transfer function (CTF) describes the imaging formation process for weak phase/weak amplitude objects in TEM. In conventional image modeling, the effects of inelastic scattering are simply neglected or only partially included. Nevertheless, the accuracy of the description of the image formation of thin samples (<30nm) [1-4], as well as the energy Zero-Loss filtered imaging, is relatively high [5]. In the case of non-filtered imaging of relatively thicker samples (> 30nm) this approach gives unsatisfactory results. As the simplest example, the rotationally averaged power spectra (PS) of the amorphous carbon specimens (rotationally averaged Thon rings) cannot be reproduced using only a single CTF approach, especially when the low frequency part of the PS is considered. Application of a single CTF interpretation to address the discrepancy between experimental PS of the amorphous carbon and CTF theory using Zero-Loss energy filtered images has been attempted [6]. However the agreement for the low frequency part of the spectrum remained very poor and unexplained.

Here, we suggest that multi-CTF decomposition is required to be able to understand the lower frequency contributions in the PS. Extra signal in the lower frequencies of experimentally obtained PS's appears to be fully due to the inelastically scattered electrons. These electrons possess their own, independent, but very incoherent CTF components, which still contribute to the final image background.

We provide a clear theoretical insight supporting the introduction of the multi-CTF decomposition. The experimental PS of non-filtered and Zero-Loss energy filtered images of amorphous carbon will be decomposed and explained within this presentation. A semi-empirical approach will be used to de-couple the DQE of the detector and the incoherence's caused by the source and the sample itself.

1. R. H. Wade and J. Frank, *Optik* **49**, (1977) 81-92
2. R. H. Wade, *Ultramicroscopy* **3**, (1978) 329-334
3. R. H. Wade, *Ultramicroscopy* **46**, (1992) 145-156
4. R.J. Hall, E. Nogales, R.M. Glaeser, *Journal of Structural Biology*, **174** (2011) 468–475
5. M. Vulović et. al., *Journal of Structural Biology*, **183** (2013) 19–32
6. I. Angert, E. Majorovits, R. R. Schröder, *Ultramicroscopy*, **81** (2000) 203-222

Environmental and in situ SEM / TEM

LBP.IM.P05
Atmospheric scanning electron microscope (ASEM) with open sample space observes evaporation processes

M. Suga[1], H. Nishiyama[1], Y. Konyuba[1], C. Sato[2]

[1]JEOL, Akishima, Japan
[2]National Institute of Industrial Science and Technology (AIST), Biomedical Research Institute, Tsukuba, Japan

msuga@jeol.co.jp
Keywords: ASEM, aggregation, crystallization

The atmospheric scanning electron microscope (ASEM): ClairScope (JASM-6200) is able to directly observe a sample in liquid or gas in the atmosphere [1]. Its sample space is open to the air allowing observation of rapid volume change phenomena such as evaporation processes [2]. In ASEM, the SEM has been redesigned to be placed upside down: the gun is set at the bottom whereas an ASEM dish with a sealed SiN window is placed onto a sample stage at the top as shown in Fig. 1. A thin SiN film is only 100 nm in thickness which is transparent to electrons and can withstand atmospheric pressure. For SEM imaging, the electron beam is scanned upward onto the sample in the ASEM dish through the SiN window and the backscattered electrons from the sample through the SiN window are captured by a detector situated below. Above the dish, optical microscope (OM) with immersion lens is set to realize quasi-simultaneous observation. In this presentation, we report important applications of observing evaporation processes.

Morphology difference in TiO_2 aggregation processes depends on solvent, that were observed during drying process. TiO_2 particles (<100 nm) were suspended in two solvents: one is water and the other is ethanol. Small amount of suspensions were dropped on the SiN film of the ASEM dish, and their natural drying processes were observed using ASEM in situ. The suspension in water was monitored in Fig. 2. As water evaporated, distribution of TiO_2 particles became non-uniform, and network like structure appeared (Fig. 2 a, b). When water was completely evaporated, large cracks appeared (Fig. 2 c, d). On the other hand, for the suspension in ethanol, rather uniform morphologies were observed during evaporation process (Fig. 3 a, b). When it was completely dried, no cracks were observed and its surface was rather uniform (Fig. 3 c, d). These differences may be caused by solvent-mediated interactions among the particles as well as by the interactions between particles and the substrate. The observation of evaporation-induced phenomena in situ by ASEM would be useful to understand various processes in material science.

Formation of copper sulfate crystals were observed using ASEM in situ. Copper sulfate was crystallized in 10 µL copper sulfate solution (173 mg/mL, 45 °C). Crystallization was induced by evaporation and temperature decrease on an open ASEM dish. Images captured at an interval of 120 sec are shown in Fig. 4a and b. A bright hexagonal object with parallel opposite sides grew during observation; it was confirmed as a blue copper sulfate pentahydrate crystal by OM. Crystal growth was highlighted by subtracting images in Fig. 4c and d. Maximum outward growth was about 3.9 µm in Figure 4c, while other areas grew less than 0.5 µm during this 120 sec observation, exhibiting anisotropic growth. Fig. 4d shows growth of crystal at later time course from 216 to 224 s after Fig. 4a. In the 8 sec, the crystal grew rapidly by about 0.84 µm as indicated by arrows. This implies that later growth could be faster than earlier growth. Origins of non-time-constant anisotropic growth of crystals are considered to be dislocation structure, random surface adsorption, physical incorporation of impurities, lattice strain, deformation, etc. ASEM's capability to observe such phenomena in situ at high resolution would be valuable to clarify such process.

ASEM is not only valuable in the materials field, but also in life science including cancer research [3], diagnosis [4] and basic biological research [5]. Especially, since it has ability to observe evaporation process, it is applicable for screening of protein crystallization, which is critical for drug development [6].

1. 1. H. Nishiyama et al., J. Struct. Biol. 169, (2010) p.438-449.
2. 2. M. Suga et al., Ultramicroscopy 111, (2011) p.1650-1658.
3. 3. T. Murai et al., J. Biol. Chem. 286 (2011) p.1999-2007.
4. 4. C. Sato et al., Biochem. Biophys. Res. Commun. 417, (2012) p.1213-1218.
5. 5. Y. Maruyama et al., J. Struct. Biol. 180, (2012) p.259-270.
6. 6. Y. Maruyama et al., Int. J. Mol. Sci. 13, (2012) p.10553-10567.
7.

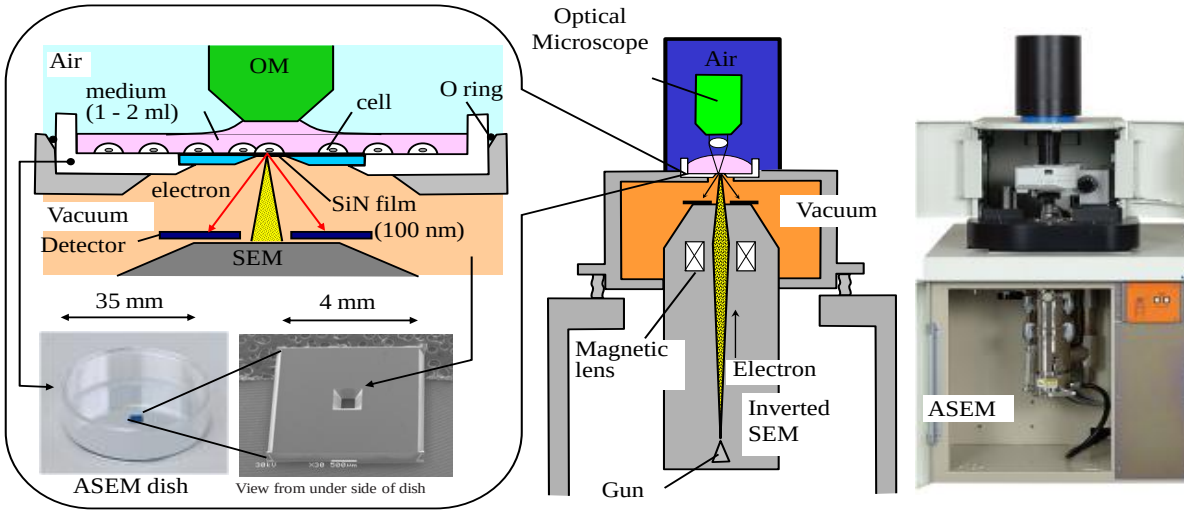

Figure 1. Configuration of the "Clairscope" ASEM. A sample space of the ASEM is open to the air, which is separated from vacuum by electron beam transparent SiN film. See text for the details.

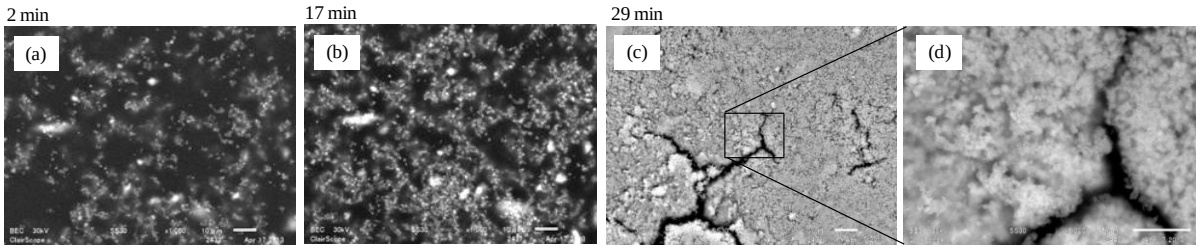

Figure 2. TiO_2 particles suspended in water monitored in situ during drying process by ASEM. Network like aggregations (a, b) were appeared during evaporation. After complete dry, cracks (c, d) were observed. Scale bar: a - c: 10 µm, c: 5 µm.

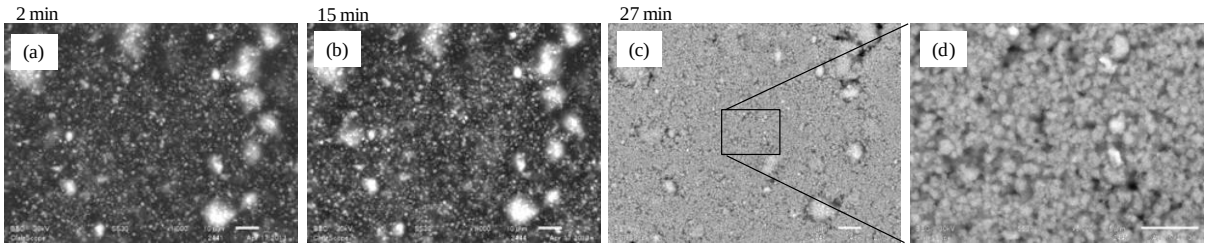

Figure 3. TiO_2 particles suspended in ethanol monitored in situ during drying process by ASEM. Distribution of TiO_2 particles were rather uniform except for big aggregates (a, b) during evaporation. After complete dry, no cracks were observed (c, d). Scale bar: a - c: 10 µm, c: 5 µm.

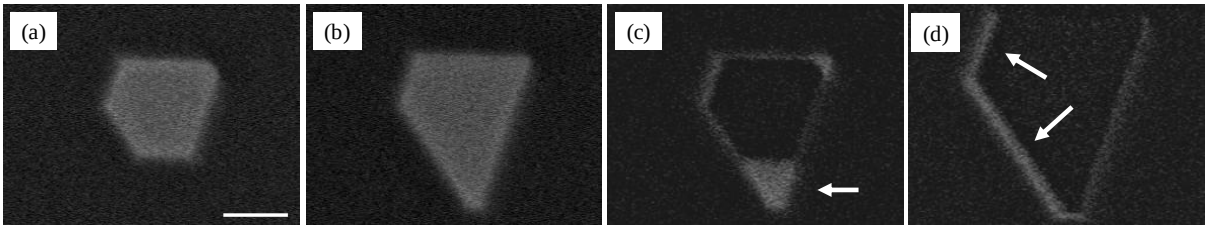

Figure 4. In situ ASEM observation images of copper sulfate crystals with time interval of 120 sec (a, b). Subtracted image of b minus a to emphasize crystal growth in 120 sec (c). Anisotropic growth was indicated by an arrow (c). Subtracted image of 224 sec after a minus 216 sec after a (d). See rapid growth indicated by arrows within only 8 sec (d). Scale bar: 5 µm.

Quantitative High-Resolution TEM/STEM and Diffraction

LBP.IM.P06
Factors influencing high quality low voltage TEM imaging of biological routinely stained specimen

I.-M. Sintorn[1,2], R. Nordström[2], L. Haag[2], E. Coufalova[3], M. Drsticka[3]

[1]Swedish University of Agricultural Sciences, Centre for Image Analysis, Uppsala, Sweden
[2]Vironova AB, Solna, Sweden
[3]Delong Instruments, Brno, Czech Republic

ida.sintorn@it.uu.se
Keywords: electron transmittance, carbon film thickness, image intensity

Low-voltage TEM imaging requires sufficient electron transmittance. One advantage of low-voltage TEM is the increased electron scattering resulting in higher contrast. Principally this implies that negative stain contrast agents may not be needed which would be beneficial since they inherently reduce the electron transmittance. However, negative stains are not only used to increase the contrast when imaging biological specimens. They also help in fixation and protect the specimen from dehydration. Hence, a requirement to acquire high quality images of biological specimen using a low-voltage TEM is fixation/staining while maintaining enough electron transmittance. This identifies and a few factors that can be investigated in order to acquire images of biological specimens using low-voltage TEM: supporting film, choice (molecular weight) of stain and thickness of stain layer. Here we have focused on the first factor, the supporting film. More specifically, we have focused on the thickness of amorphous carbon films since such supports tend to have negligible influence of the specimen, and the negative stains generally distribute evenly (which to our experience is not the case when using very thin graphene grids).

We here present a small study where the influence of the thickness of the carbon supporting film on electron transmittance has been investigated. The electron transmittance for two thicknesses of carbon films (EMS grids >30 nm and KC S6 grids <10 nm) has been measured at a range of energies, from 5 keV to 100 keV in an LVEM 5 (5keV), and a Tecnai Spirit BioTwin (20 to 100keV). The transmittance was derived as the ratio of the mean intensity values of images acquired with and without the grids inserted into the electron beam. How the transmittance for the two carbon film thicknesses varies for different electron voltages is shown in Figure 1.

To illustrate how the final low-voltage TEM image quality is influenced by the carbon film thickness, thick and thin carbon film grids containing BK virus-like particles stained with 2% UAc were prepared and imaged at 20 keV in a Tecnai Spirit BioTwin microscope at magnifications ranging from 6000 to 87000. Example images of the EMS and KS C6 grids are shown in Figure 2 together with their corresponding histograms.

In conclusion: reducing the carbon layer thickness from ~30 nm to <10 nm results in a significant increase in electron transmittance showing the following benefits:

- Improved image quality
- Reduced risk for dehydration effects
- Rapid and reproducible preparation procedures
- Conventional nsTEM procedures can be utilized
- Reduced chromatic aberration originating from the non-elastic scattering of the incident beam in the sample

1. This work was carried out jointly by the Centre for Image Analysis at Uppsala University and Swedish University of Agricultural Sciences, Vironova AB, and Delong Instruments, as part of the Eurostars miniTEM project, in which a low-voltage TEM with built in automated acquisition and analysis functionally is being developed.

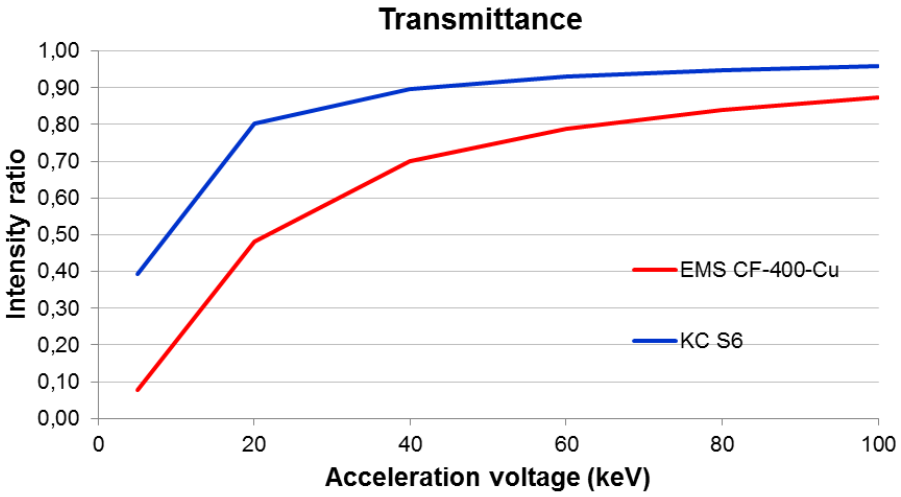

Figure 1. Electron transmittance of KC S6 grids (blue) and EMS CF-400-Cu grids (red) at energies from 5 to 100 keV. The values are derived as the ratio of the mean intensity values of images acquired with the grid inserted in the electron beam and images acquired with no grid inserted.

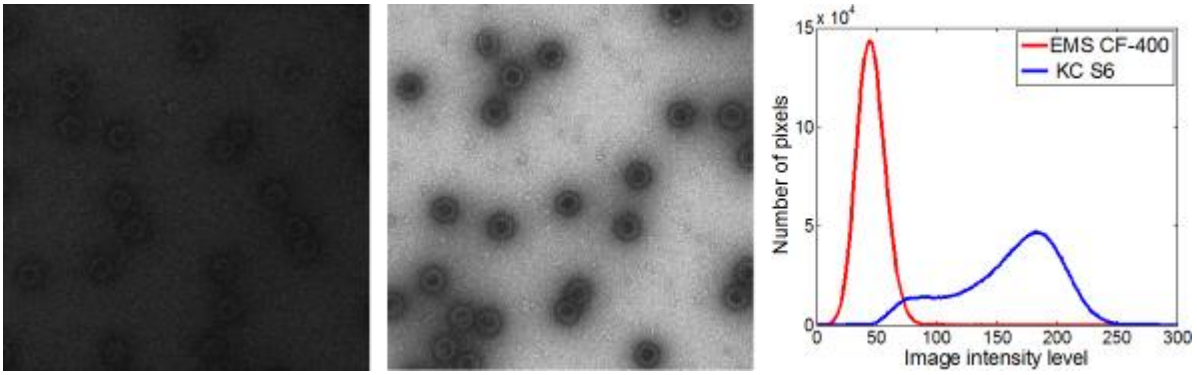

Figure 2. Example images of rBK viruses acquired at 20keV and 60 000 magnification on an EMS CF-400 grid (left),and KC S6 grid (middle). The corresponding histograms (right) are shown in red for EMS CF 400 and blue for KC S6. The images were acquired as 16bit images whereof the intensity range [0 300] is displayed here.

Advances in Light and Electron Optics

LBP.IM.P07
Strain measurement of semiconductor device by moiré fringes in STEM

Y. Kondo[1], N. Endo[1]

[1]JEOL Ltd., EM Business unit, Akishima Tokyo, Japan

yukikon1@za2.so-net.ne.jp

In scanning transmission electron microscopy (STEM), when the spacing for an STEM raster is similar to one for a crystal lattice or the multiple of it and the probe size is smaller than the crystal lattice spacing, the moiré fringes appears due to under-sampling effect. Since we can arbitrarily select the raster spacing and the rotation angle of the raster direction unlike a TEM moiré method [1-3], we can intentionally make the moiré fringes with wider spacing than crystal lattice that is wide enough to be visible even at lower magnification. The moiré fringe bends in strained region in a crystal. And the lattice strain can be measured by the curvature of the fringe, because the spacing and direction of the moiré fringe can be definitely expected by geometrical calculation. D. Su and Y. Zhu observed of a dislocation in a crystal that generates with very large strain, utilizing the STEM moiré fringes method [4]. However, the detection of a small strain, which is utilized for a strained silicon device, has been remained untouched. It is important to measure the strain in strained silicon device, because the device has high speed mobility of electrons, resulting in high processing speed. In this paper, we report the results of the method to detect and quantify the small strain in the practical silicon device over the region wide enough for the device characterization.

The sample and the microscope we used were a 150-nm-thick FIB-made semiconductor device and JEM-ARM200F. Figure 1 (a) and (b) shows HAADF images of the device around Si-Ge mixed crystal regions, showing parallel moiré fringes generated with the raster and the lattice fringes due to Si (220) reflection. Figure 1 (a) includes the strained region under the gate of device located between Si-Ge regions. The fringes bend rapidly just under the gate of the device, which implies that the region under the gate is strongly strained. Around Si-Ge crystal, the fringes gradually bend, which tells us that the strain occur not only the region under the gate, but wider region of the device around the Si-Ge crystal. The non-strained region located right of each image shows straight moiré fringes, because the region does not contain strain. Thus, the moiré fringes allow us to grasp the distribution of the strain.

To measure the curvature of the fringe, we utilize the phase analysis method of holography, which is similar to the way in high resolution transmission electron image [5]. The phase map is reproducible from the moiré fringes (carrier fringes), the result of phase analysis shows amount of lattice displacement which is the integrated strain map. The derivative of the integrated strain map shows the map of strain. In our experiment, the integrated strain of the lattice fringe almost parallel to the horizontal scanning raster. Therefore, the strain map reproduces in the vertically differentiated integrated strain map. Figure 2 (a) shows the HAADF image of silicon device showing the tilted moiré fringes. These moiré fringes are rotation moiré fringes caused in scanning raster and the l attice fringes due to Si [111]. The raw strain map affected by slow and slight displacement of the sample during image acquisition, since the acquisition time is rather long. To reduce the affection, the right quarter region was used as a reference, because the region does not have strain. The accurate strain map can be obtained by the subtraction of raw map by the map of reference region. In Fig. 2(b) and 2(c), a reproduced and subtracted integrated strain and strain maps are shown. Amount of strain under the gate was measure as 1.9 % from the strain map shown in Fig. 2(c).

To measure the amount of noise for this method, we performed a blank test on the non strained single crystal of silicon with the same manner. The HAADF image showing moiré fringes is shown in right region of Fig. 3 and the strain map is shown in left panel. The standard deviation of the strain was measured to be ± 0.2 % at present stage. However, the accuracy might be improved with better contrast of moiré fringes and less noise by further improvement of this technique. In conclusion, the strain distribution of a crystal can be reproduced from only a medium magnification STEM image serving a wide field which is striking for strained device characterization.

1. G. A. Bassett, J. W. Menter and D. W. Pashley, *Proc. R. Soc. Lond. A 19* (1958) 246, 1246, 345-368.
2. Goro Honjo and Katsumichi Yagi, *J. Vac. Sci. Tech.* (1969) , 6 , 4, 576 – 582.
3. D W Pashley, M J Stowell, M H Jacobs and T J Law, *Phil. Mag.* (1964), 10, 127-158.
4. Dong Su and Yimei Zhu, *Ultramicroscopy* (2010), 110(3), 229-233.
5. M.J. Hÿtch, E. Snoeck and R. Kilaas, *Ultramicroscopy* (1998), 74, 3, Pages 131–146.

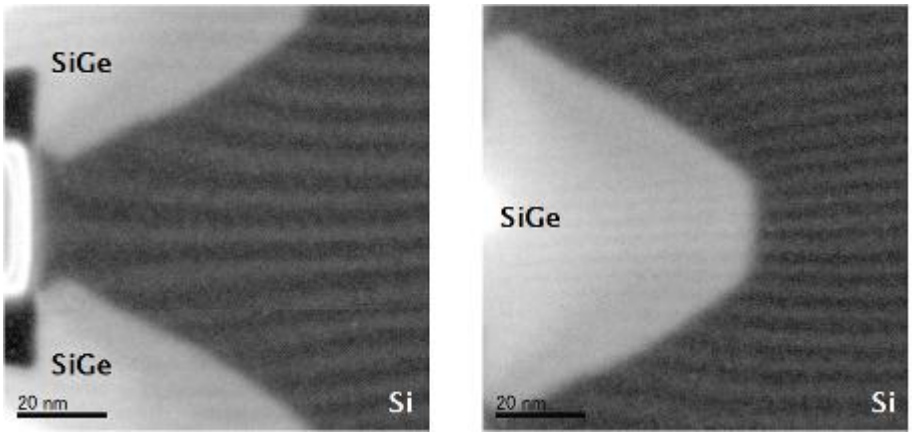

Figure 1. STEM moiré fringes of Si substrate under the gate (a) and Si-Ge crystal (b).

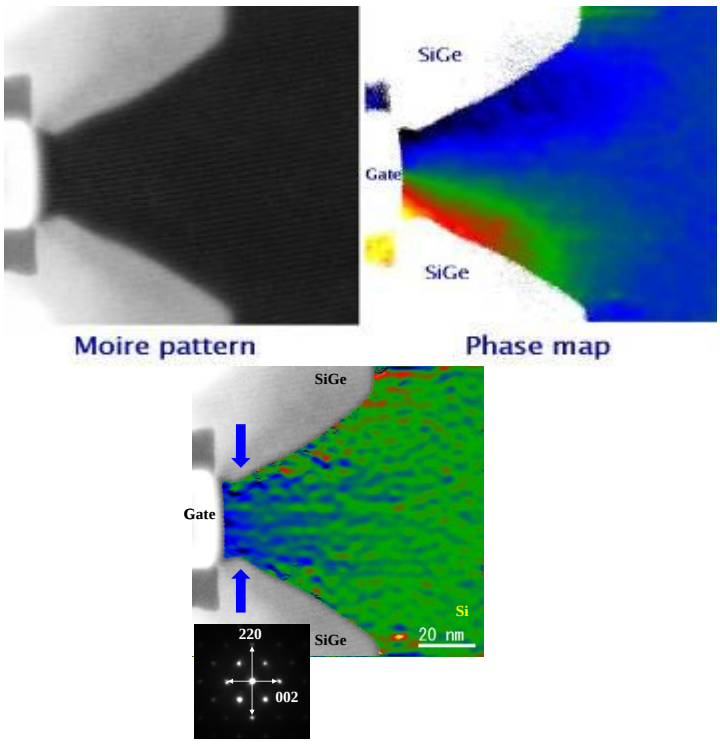

Figure 2. (a) HAADF image of moiré fringes (b) Phase map of moiré fringes (c) Strain map of strained silicon device.

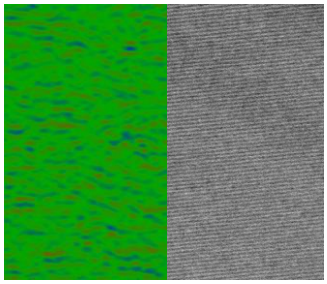

Figure 3. (a) Strain map reconstructed STEM from Fig. 3 (b), (b) moiré fringes of Si single crystal without strain.

Static and Dynamic Electric and Magnetic Imaging

LBP.IM.P08
Algorithm for Analysis of a Data Cube of Electron Micrographs

A. Knápek[1], Z. Pokorná[1]

[1]Institute of Scientific Instruments of AS CR, v.v.i., Brno, Czech Republic

knapek@isibrno.cz
Keywords: SLEEM, crystallographic orientation, grain boundary recognition

Scanning Low Energy Electron Microscopy (SLEEM) is an imaging technique, which uses low energy electrons while providing very good image resolution [1]. Reflectivity of very slow electrons in the range 0–30 eV can be correlated with the electronic structure of the material, aiming at determination of the local crystallographic orientation [2]. Since SLEEM is a 2D imaging method, a suitable algorithm is needed to analyse the image signal in dependence of the beam energy as the third dimension. Crucial task is to detect grain boundaries in polycrystals. Recent algorithms [3, 4], performing the task for the traditional EBSD method, are not able of correcting for artefacts connected with the specimen contamination.

The input data of the algorithm can be considered a 3D matrix. Indices x and y are coordinates in the two-dimensional image function $f(x,y)$, which is acquired for a range of beam energies (usually 0 – 30 eV) that represent the third dimension of the matrix. Problems connected with the input data that impede recognition of grain boundaries include first of all a certain inconsistency caused by variations in the impact angle of electrons as well as in the detection efficiency, both in dependence of distance from the optical axis. Second problem relates to the low S/N ratio, which prevents us from implementing any algorithm based on a lookup table. Fluctuations originate mainly from the statistical noise because of a short dwell time, combined with the quantization noise of the A/D convertor. Further problems relate to the low contrast between grains as well as to presence of white spots representing residual oxide contamination.

The devised algorithm is designed to work in static and dynamic mode. The static mode consists of 7 basic steps and achieves crystallographic information for the particular beam energy. The algorithm consists of the image acquisition, affine transformation in order to compensate for image distortions mapped in advance on a reference sample, enhancement of contrast, Gaussian filtration in order to smooth the image, detection of grain boundaries using the Canny edge detector [5], localization and removal of white spots, and localization of a particular grain and its boundaries in the image. This mode provides data about grain boundaries but insufficient information is provided to determine the crystallographic orientation.

The dynamic mode extends the static one. Instead of using the Canny edge detector in the fifth step, Sobel operators are used [5]. These operators provide less of the detected boundary points which was found convenient when passing through the data cube. Having accumulated the grain representations at particular energies, it is necessary to smooth the boundary network by removing the unconnected and isolated pixels. In contrast to the static mode, the dynamic mode not only collects data for the grain border representation but also measures the signal intensity for a particular grain yielding the dependence of the electron reflectivity vs. beam energy, which is essential for determination of the crystallographic orientation [2].

The example presented in this contribution reveals boundaries as high brightness gradient features on SLEEM images of polycrystalline copper using a specifically designed sequence of detection and filter algorithms.

Using EBSD as an auxiliary tool (fig. 1. d.), it is possible to determine, which crystallographic orientations provide sufficient boundary contrasts at particular beam energies. Experimental evaluation has been performed for the grain no. 146, as shown in table 1. Here value 1 stays for a grain neighbourhood exhibiting contrast sufficient to detect the common boundary. Zeros stays for undetectable boundaries. The situation was examined at three beam energies and the boundary was established when at least one “1” appeared in the column of the table.

Fig. 1 a, b and c shows three images obtained at various energies using the SLEEM. The backscattered electrons obviously form energy dependent grain image signal because of different reflectivity, characteristic for the grain orientation. Detecting the grain boundary where the image signal exhibits gradient exceeding a preselected threshold, we compile the boundary representation

for particular electron energy. Finally, the three representations are merged yielding the complete boundary map – see Fig. 1.h.

This research has been financially supported by the TA CR grant no. TE0102011 and by the CSF grant no. P108/11/2270.

8. 1. I. Müllerová and L. Frank. Scanning low energy electron microscopy. Advances in Imaging and Electron Physics. Elsevier, 2003, vol. 128, pp. 309–443.
9. 2. Z. Pokorna et al. Characterization of the local crystallinity via reflectance of very slow electrons. Applied Physics Letters, 2012, vol. 100, no. 26, pp. 261602–261602.
10. 3. M. Bartozzi, A.P. Boyle, D.J. Prior. Automated grain boundary detection and classification in orientation contrast images. Journal of Structural Geology, 2000, vol. 22, pp. 1569-1579.
11. 4. R. Heilbronner. Automatic grain boundary detection and grain size analysis using polarization micrographs or orientation images. Journal of Structural Geology, 2000, vol. 22, pp. 969-981.
12. 5. B. Jähne, H. Scharr, and S. Körkel. Principles of filter design. In Handbook of Computer Vision and Applications. Academic Press, 1999.

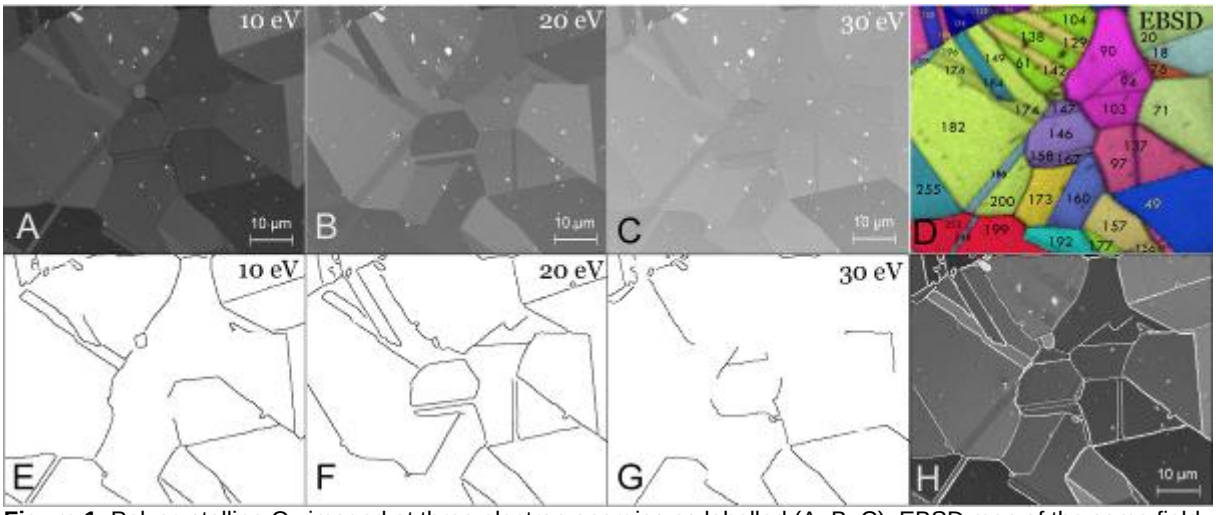

Figure 1. Polycrystalline Cu imaged at three electron energies as labelled (A, B, C), EBSD map of the same field of view with numbered grains (D), grain boundary representations resulting from automatic evaluation of the micrographs (E, F, G), final merger of the boundary representations (H).

grain no. (orientation)	**147** (14,9,23)	**103** (9,8,26)	**97** (8,5,27)	**158** (14,9,23)	**200** (8,1,15)	**186** (11,5,15)	**182** (9,1,17)	**174** (8,1,15)	**beam energy**
146 (11 7 18)	0	0	1	0	1	1	1	1	10 eV
146 (11 7 18)	1	1	1	1	1	1	1	1	20 eV
146 (11 7 18)	1	0	1	0	1	0	1	1	30 eV

Table 1. Grain no. 146 (11,7,18) edges with neighbouring grains at various beam energies.

Advances in Light and Electron Optics

LBP.IM.P09
Collection of signal electrons in Low Energy SEM

I. Konvalina[1], I. Müllerová[1]

[1]Institute of Scientific Instruments of the ASCR, v. v. i., Electron Microscopy, Brno, Czech Republic

ivo.konvalina@isibrno.cz
Keywords: signal collection, low energy SEM, trajectory simulations

Modern scanning electron microscopes (SEM) are equipped with a field emission gun and the specimen is usually immersed in a strong magnetic field in order to reach high resolution. Low energy SEM equipped by a beam deceleration system, e.g. cathode lens (CL) [1], can obtain spot size below 10 nm for landing energy of units of eV [2]. Low energy SEM with a cathode lens has to be combined with a focusing lens. Magnetic or immersion-magnetic focusing lenses (with weak or strong magnetic field in the specimen plane, respectively) are used in our simulations. These two alternatives are compared with regard to their influence on signal electrons.

Recent SEM are equipped with several detectors to maximize the collection of signal electrons. The commonly used Everhart-Thornley detector [3], side-attached near the specimen plane is replaced with an “in-lens” detector (TLD – through the lens detector). The detectors of backscattered electrons (BSE) and transmission electrons (TE) are used as well.

The BSE detector is placed below the objective lens. The field of the cathode lens not only decelerates the primary beam electrons to low landing energies but also accelerates the signal electrons towards the BSE detector. BSE emitted under a large polar angle are collimated towards the optical axis and are detected. Angle-resolved detection of BSE in low energy SEM can be performed e.g. using a detector split into several concentric annuli that can in addition be subdivided into angular segments. Elastically reflected BSE escaping through the central bore of the BSE detector may be detected by the TLD detector placed inside the objective lens.

Transmitted electrons (TE) are detected by the TE detector below the sample. TE can be imaged by a bright-field (BF) and dark-field (DF) detector. The DF signal may subdivided into annular dark-field (ADF) and high-angle annular dark-field (HAADF) images (also called Z-contrast images) [4]. The TE detector is divided into the BF circular detector in the center and several concentric annuli around it for DF mode imaging. The relative size of the TE detector can be varied by changing the strength of the cathode lens field and the field of magnetic objective lens.

A simulated arrangement of TLD, BSE and TE detectors is shown in Figure 1. Trajectories of signal electrons were traced in the EOD software [5] that allows simulating trajectories of electrons in combined magnetic and electrostatic fields. Simulations were done for primary beam energy of 10 keV, the energy of traced electrons was equal to the landing energy ($E_{BSE} = E_{TE} = E_L$), BSEs and TEs were emitted from the sample under a range of polar angles $\theta = 0°– 90°$ with 1° step.

The range of polar angles of detected signal electrons for the TLD, BSE and TE detectors, as a function of the landing energy is shown in Tables 1 and 2. The data were calculated for systems consisting of the cathode lens in combination with the focusing immersion-magnetic lens or the focusing magnetic lens, the primary beam energy was $E_P = 10$ keV, landing energy varied from 10 keV to 5 eV. The simulation results show a strong influence of magnetic and electrostatic fields on the collection of signals electron in low energy SEM.

1. I. Müllerová and L. Frank, Adv. Imag. Elect. Phys. 128 (2003), p. 309.
2. I. Konvalina and I. Müllerová, Nucl. Instr. Meth. Phys. Res. A 645 (2011), p. 55.
3. T.E. Everhart and R.F.M. Thornley, J. Sci. Instr. 37 (1960), p. 246.
4. J. Liu, J. Electron Microsc 54 (2005), p. 251.
5. J. Zlámal and B. Lencová, Nucl. Instr. Meth. Phys. Res. A 645 (2011), p. 278.
6. This work was partially supported by EC and MEYS CR (project No. CZ.1.07/2.4.00/31.0016).

13.

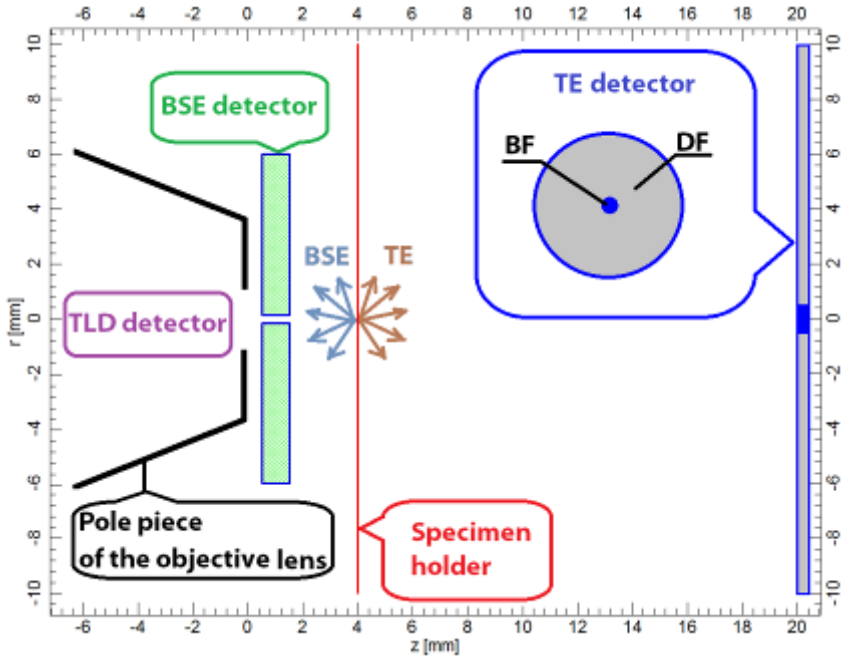

Figure 1. Arrangement used in simulations.

E_L (eV)	Detected polar angles θ (deg)			
	TLD detector	BSE detector	TE detector	
			BF mode	DF mode
10000	0 – 3	3 – 49	0 – 4	4 – 39
5000	0 – 4	4 – 78	0 – 5	5 – 90
1000	0 – 8	8 – 90	0 – 12	12 – 90
500	0 – 11	11 – 90	0 – 19	19 – 90
100	0 – 21	21 – 90	0 – 26	26 – 90
50	0 – 29	29 – 90	0 – 45	45 – 90
10	0 – 73	73 – 90	0 – 90	---
5	0 – 90	---	0 – 90	---

Table 1. Range of detected polar angles of signal electrons of TLD, BSE and TE detectors as a function of the landing energy; calculated for the focusing immersion-magnetic lens combined with the cathode lens, primary beam energy E_P = 10 keV, energy of traced electron E = E_L.

E_L (eV)	Detected polar angles θ (deg)			
	TLD detector	BSE detector	TE detector	
			BF mode	DF mode
10000	0 – 4	4 – 67	0 – 1	1 – 32
5000	0 – 4	4 – 90	0 – 2	2 – 39
1000	0 – 7	7 – 90	0 – 3	3 – 81
500	0 – 9	9 – 90	0 – 4	4 – 90
100	0 – 17	17 – 90	0 – 10	10 – 90
50	0 – 23	23 – 90	0 – 13	13 – 90
10	0 – 48	48 – 90	0 – 31	31 – 90
5	0 – 90	---	0 – 46	46 – 90

Table 2. Range of detected polar angles of signal electrons of TLD, BSE and TE detectors as a function of the landing energy; calculated for the focusing magnetic lens combined with the cathode lens, primary beam energy E_P = 10 keV, energy of traced electron E = E_L.

Advances in Light and Electron Optics

LBP.IM.P10
Scanning Low Energy Electron Microscopy for the determination of crystallographic orientation of polycrystalline metal grains

Z. Pokorna[1], A. Knápek[1]

[1]Institute of Scientific Instruments, Academy of Sciences of the Czech Republic, v.v.i., Electron Microscopy , Brno, Czech Republic

zuzana.pokorna@isibrno.cz
Keywords: SLEEM, crystallographic orientation, polycrystalline metal, cathode lens

Scanning Low Energy Electron Microscopy (SLEEM) is a Scanning Electron Microscopy technique in which electrons of an arbitrarily low incident energy (10^3–10^0 eV) are used [1]. It makes use of the cathode lens principle [2], allowing to preserve a very good image resolution even at the lowest incident electron energies.

In the incident electron energy range 0–30 eV, electron reflectivity can be correlated with the electronic structure of the material [3], from which the local crystallographic orientation of the specimen may be determined [4]. In this range, each grain exhibits a unique reflectivity curve (see Fig.1), which is indicative of its particular crystallographic orientation. Our work aims at high-speed semiautomated crystallographic orientation determination with a high lateral resolution and surface sensitivity.

The experiments were carried out on polycrystalline and single crystal samples of high purity copper and aluminium. The samples were ex situ cleaned by solvents and inserted into an ultra-high vacuum Scanning Low Energy Electron Microscopy (UHV-SLEEM III) apparatus. They were subsequently in situ cleaned by several cycles of argon ion sputtering and flashing to 400–450°C. The surface cleanliness was verified by Auger Electron Spectroscopy (AES). The samples were then imaged at very low electron energies in the range from 0 to 30 (or 45) eV with a step of 0,3 eV. The image data were then used to estimate the reflectivity curves of the specimens. The experiment was performed for a variety of specimen tilts in the range of ±2° and for several working distances.

Factors that influence the measured reflectivity are discussed in detail. The state of the specimen surface, such as roughness or the presence of hydrocarbon adlayers and native oxide, is an influence on its own [5]. The geometry of experimental setup (specimen tilt, distance of the studied point from the optical axis, working distance) is given special attention as both the signal and its collection efficiency hinges on it. This particular cathode lens setup with a central-bore scintillation detector allows also discerning the in-plane orientation of a crystal face, as shown for the twin grains in Fig. 2. This is probably due to the strongly directional reflectivity distribution of the specimen – a result of diffraction effects [6] – which causes a portion of the signal to disappear in the central bore of the scintillation detector. This effect is more pronounced in denser crystal faces. The ability of this method to discern between twins (grains of identical orientation, but rotated about an axis perpendicular to the surface) , is illustrated in Fig. 3. The very low energy electron reflectivity is a promising method for the determination of local crystallographic orientation.

1. Müllerová, Ilona, and Luděk Frank. "Scanning low-energy electron microscopy." *Advances in imaging and electron physics* vol. 128 (2003): 309–443.
2. Müllerová, Ilona, and Luděk Frank. "Use of cathode lens in scanning electron microscope for low voltage applications." *Microchimica Acta* 114, no. 1 (1994): 389–396.
3. Bauer, Ernst. "LEEM basics." *Surface Review and Letters* 5, no. 6 (1998): 1275–1286.
14. 4. Pokorná, Zuzana, Š. Mikmeková, I. Mullerová, and Luděk Frank. "Characterization of the local crystallinity via reflectance of very slow electrons." *Applied Physics Letters* 100, no. 26 (2012): 261602–261602.
15. 5. Herlt, H.-J., and E. Bauer. "A very low energy electron reflection study of hydrogen adsorption on W(100) and W(110) surfaces." *Surface science* 175, no. 2 (1986): 336–368.
16. 6. Pendry, John Brian. *Low energy electron diffraction: the theory and its application to determination of surface structure*. Vol. 2. London: Academic Press, 1974.
7. This research was supported by TACR grant No. TE01020118 and by CSF grant GAP108/11/2270. The presentation of this research work was supported by the EC and the Ministry of Education, Youth, and Sports of the Czech Republic, project CZ.1.07/2.4.00/31.0016.

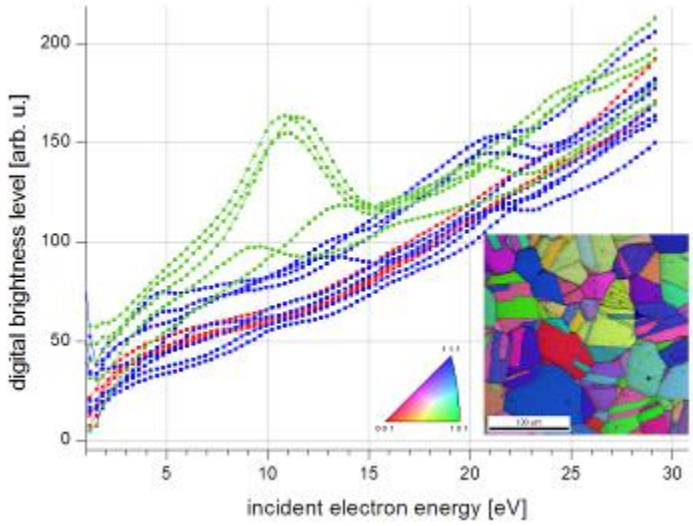

Figure 1. The reflectivity of differently oriented Cu grains close to basic orientations at incident energies 0–30 eV.

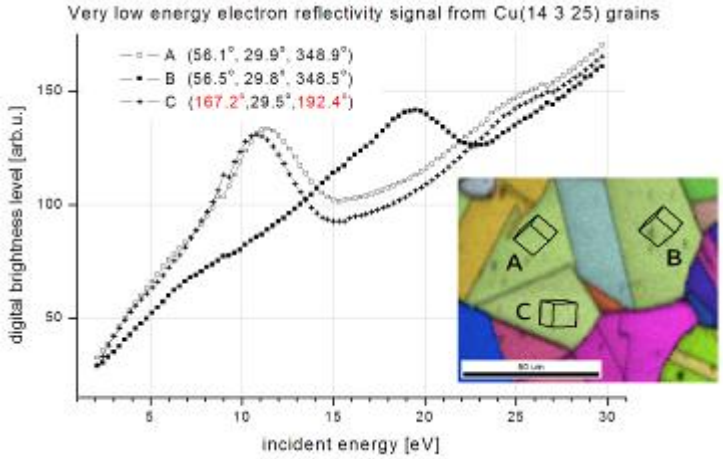

Figure 2. The reflectivity of twin grains in polycrystalline copper. The Euler angles (Bunge) are given in the inset.

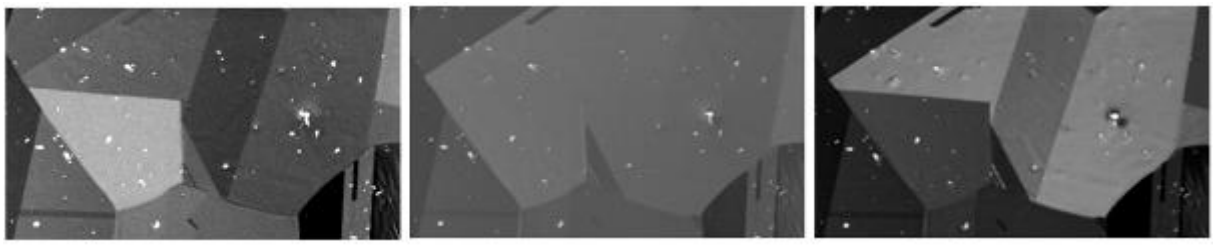

Figure 3. Twin grains in polycrystalline Cu at incident energies 17.1 eV, 14.1 eV, 10.8 eV.

Soft Matter, Polymers, Composites

MS.1.001
In-situ Dynamic SPM Studies of Organic Semiconductor Thin Film Growth on Test Patterns

S. Chiodini[1], A. Straub[1], S. Donati[1], F. Borgatti[1], C. Albonetti[1], F. Biscarini[1,2]

[1]Consiglio Nazionale delle Ricerche, Istituto per lo Studio dei Materiali Nanostrutturati (CNR-ISMN), Via P. Gobetti 101, 40129 Bologna, Italy
[2]Life Science Dept., Università di Modena e Reggio Emilia, Via Campi 183, 41125 Modena, Italy

fabio.biscarini@unimore.it

The physics of organic field effect transistors is correlated with the organization of the organic semiconductor at multiple length scales. In the case of molecular semiconductors, which are deposited asthin films on device test patterns by high- or ultra-high vacuum sublimation, this organization arises from the nucleation and growth phenomena occurring at timescales which are often not easily accessed by standard ex-situ characterization. We use in-situ dynamic scanning probe microscopy (SPM) to study the early stages of growth of a conjugated oligomer semiconductor, viz. sexithienyl (T6), on silicon oxide/silicon wafer as well as on test patterns with Au electrodes. In our experiment a thermal beam of T6 molecules from a Knudsen cell is produced in an ultra-high vacuum chamber directly under the tip of a variable temperature SPM. Non-contact AFM imaging of the same area at different times yields a movie depicting the growth of the ultra-thin film. The coexistence of quasi-layer-by-layer and 3D growth modes, the latter promoted by heteronucleation on surface defects, is observed. By performing the experiment at different temperatures, we extract the relevant molecular energy barriers of T6 thin film growth: desorption energy (0.53 eV), thickness-dependent diffusional barriers (0.15-0.20 eV), Erlich-Schwoebel barrier from 6 meV for the first monolayer to 120 meV for the third one. The latter is cause of the transition from layer-by-layer to island growth, which appears to be universal occurrence in organic semiconductor growth with implications in the charge transport in organic field effect transistors.

Soft Matter, Polymers, Composites

MS.1.002
Characterization of codeposited pentacene/perfluoropentacene on different substrates by transmission electron microscopy

B. Haas[1], K.I. Gries[1], T. Breuer[2], G. Witte[2], K. Volz[1]

[1]Philipps-Universität Marburg, Materials Science Center and Faculty of Physics, Marburg, Germany
[2]Philipps-Universität Marburg, Faculty of Physics, Marburg, Germany

katharina.gries@physik.uni-marburg.de, benedikt.haas@physik.uni-marburg.de
Keywords: perfluoropentacene, organic semiconductors, electron microscopy

Over the last several years organic semiconductor materials gain more and more importance. Two examples for such materials are pentacene (PEN) and perfluoropentacene (PFP). PEN is a polycyclic aromatic hydrocarbon ($C_{22}H_{14}$) with a HOMO-LUMO gap of approximately 2.1eV. Because of its high hole mobility it acts as an p-type semiconductor. The unit cell of PEN crystals contains two nonequivalent PEN molecules and crystallization takes always place in a triclinic crystal structure. The different phases, like for example the Campbell [1] and the thin film [2] phase, that have been observed for PEN differ in the parameters of the triclinic unit cell.

In case of PFP ($C_{22}F_{14}$) the hydrogen atoms are replaced by fluorine atoms. The strong electronegativity of fluorine results in an inverted quadrupole moment of PFP from PEN. PFP acts as a n-type semiconductor and crystallizes in a monoclinic crystal structure. Also for PFP different polymorphs exist [3],[4]. The strong structural relation of PFP to PEN makes these two materials promising for p-n-junctions because high quality interfaces are expected in between.

Transmission electron microscopy (TEM) is a quite useful method to investigate such structures at a high resolution level und thus to analyse the quality of PFP:PEN composite materials.

In our work we investigated PFP:PEN codeposited films that have been grown on different substrates like alkali halides (sodium fluoride (NaF), potassium chloride (KCl)) and silicon oxide via organic molecular beam deposition (OMBD). Overview TEM images as well as atomic force microscopy images show that the samples grown on alkali halogenides consist of organic fibers lying on an organic background layer.

In the TEM we used electron diffraction to get information on the crystal orientation of submicrometer-sized regions. This gives indication of local orientation correlations that cannot be investigated by X-ray diffraction because of the spatial averaging.

Besides electron diffraction also high resolution TEM imaging is a method to identify and to distinguish between separated PEN or PFP films and mixed PFP:PEN phases. Figure 1 shows a high resolution TEM image of PEN:PFP grown on NaF substrate. During the preparation process the substrate was removed and should not contribute to the signals in TEM. Generating a linescan along the turquoise area in the high resolution image a lattice plane spacing of 3.76Å was determined. This corresponds well to the (020) PEN thin film planes. Figure 2 shows a high resolution TEM image of the same sample. In this case a lattice plane spacing of 3.61Å was determined. This spacing does not fit to PEN, PFP or residues of the NaF substrate. Thus, it is attributed to the mixed phase.

High resolution TEM of one of the fibers that developed in a PEN:PFP sample grown on KCl is shown in Figure 3 (a). The lattice plane spacing was again determined from a line scan (b) along the turquoise area in (a). The spacing of 13.1Å is quite large and may be related to one of the lattice constants of the mixed phase. In Figure 3 (c) another part of the fiber is displayed, showing that the orientation does not change along the fiber.

The presentation will summarize the influence of different substrates on the growth of codeposited PFP/PEN and discuss its implications on the understanding of the film formation.

1. R.B. Campbell, J.M. Robertson and J. Trotter, Acta Crystallographica 15 (1962), p. 289.
2. S. Schiefer, M. Huth, A. Dobrinevski and B. Nickel, Journal of the American Chemical Society 129 (2007), p. 10316.
3. Y. Sakamoto, T. Suzuki, M. Kobayashi, Y. Gao, Y. Fukai, Y. Inoue, F. Sato and S. Tokito, Journal of the American Chemical Society 126 (2004), p. 8138.
4. I. Salzmann, S. Duhm, G. Heimel, J.P. Rabe, N. Koch, M. Oehzelt, Y. Sakamoto and T. Suzuki, Langmiur 24 (2008), p.7294.

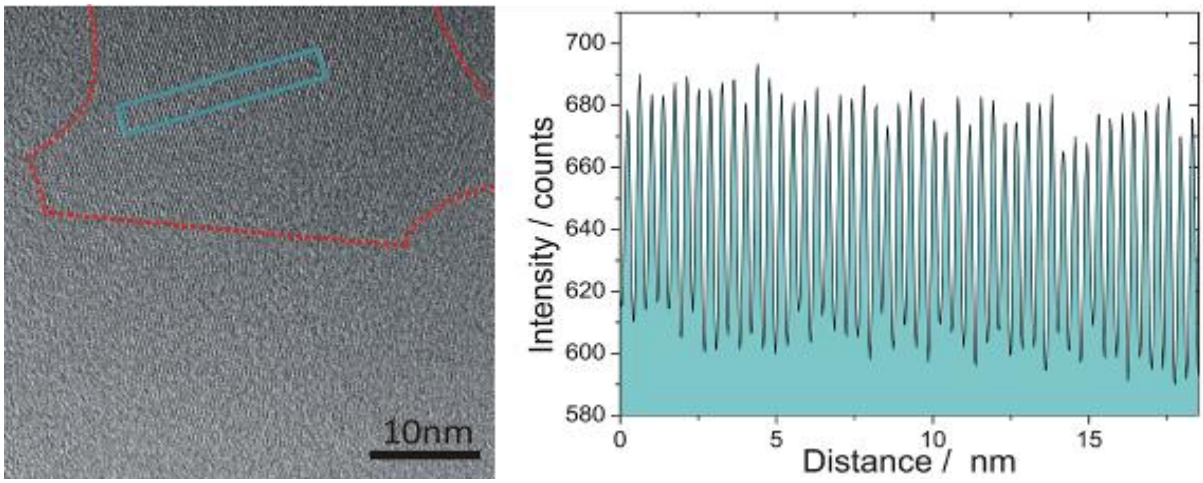

Figure 1. High resolution TEM image of a PEN:PFP/NaF sample. From the linescan along the turquoise area a lattice plane spacing of 3.76Å can be determined. This corresponds well to the (020) PEN thin film planes.

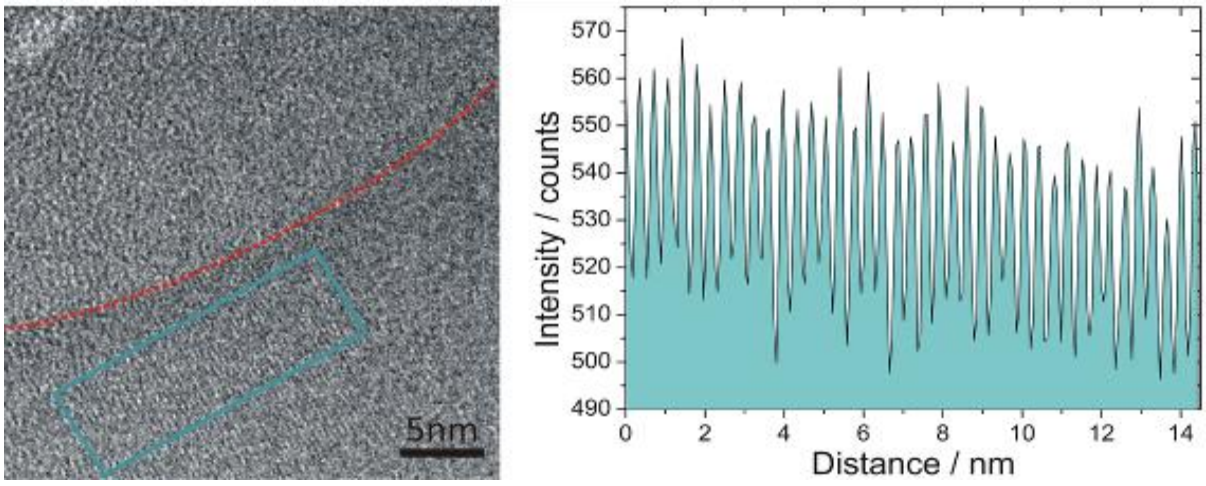

Figure 2. High resolution TEM image of a PEN:PFP/NaF sample. From the linescan along the turquoise area a lattice plane spacing of 3.61Å can be determined. This spacing does not fit to PEN or PFP and is attributed to the mixed phase.

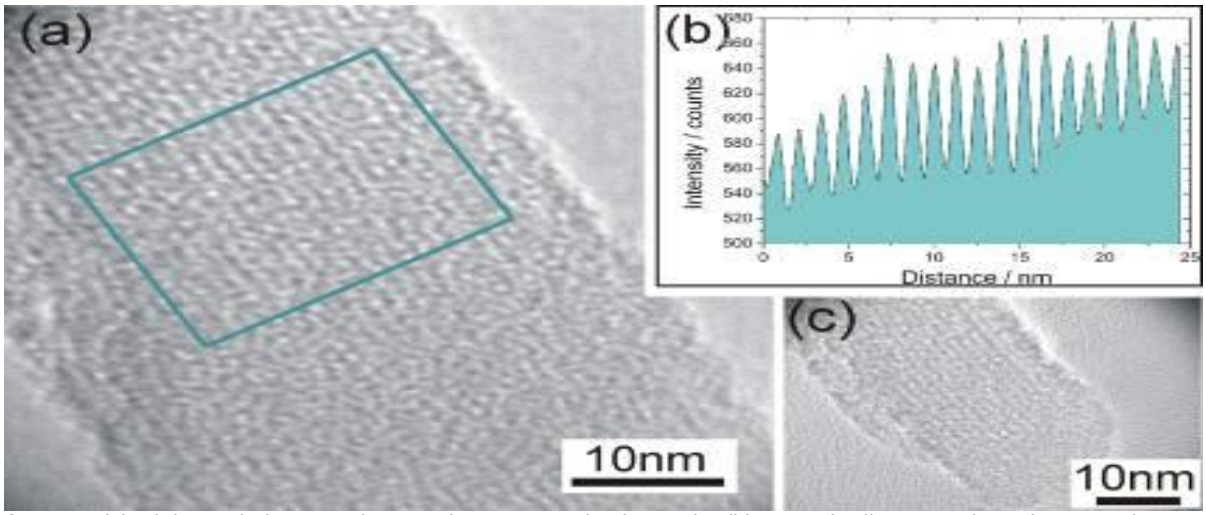

Figure 3. (a) High resolution TEM image of a PEN:PFP/KCl sample. (b) From the linescan along the turquoise area in (a) a lattice plane spacing of approximately 13.1Å can be determined. (c) A high resolution TEM image of another part of the fiber shows that the orientation does not change along the fiber.

Soft Matter, Polymers, Composites

MS.1.003
Characterization of the production process of nanoimprinted organic devices by analytical TEM

J. Kraxner[1], I. Letofsky-Papst[1,2], T. Rothländer[3], P. Hütter[3], B. Stadlober[3], W. Grogger[1,2]

[1]Graz Centre for Electron Microscopy (ZFE), Graz, Austria
[2]Institute for Electron Microscopy (FELMI) of the TU Graz, Graz, Austria
[3]Joanneum Research, Materials-Institute for Surface Technologies and Photonics, Weiz, Austria

johanna.kraxner@felmi-zfe.at
Keywords: organic electronics, nano-imprint lithography, analytical TEM

Organic electronics is a field of research with growing interest in the last years. Many applications are already entering industrial commercialization, but the search for new materials and the improvement of the used processes are still in progress. Organic electronics is a promising technology especially for applications, where large-area coverage, diversity in substrates, including flexible ones, and low temperature processing is important. As the device demands emerge to more advanced products such as smart objects and intelligent sensor networks, the performance parameters of the involved circuits become more and more challenging. Parameters like the switching speed, integration density, driving voltage and fabrication yield of circuits are crucial to be optimized. The miniaturization of the structures is a substantial requirement, achieving faster devices with a lower driving voltage and higher integration density.

The organic thin film transistor (OTFT) is a prominent device to optimize the production processes as well as the used materials. The transistor as a key element in logic circuits needs to be controlled as good as possible to be able to build more complex structures. In case of OTFTs the switching speed can be enhanced by an increased charge carrier mobility, and by a decrease of the channel length and the parasitic capacitance. A downscaling of the channel length and also a reduction of the parasitic capacitance is achieved by the usage of the self-aligned process schematically shown in Figure 1. The critical dimensions of the device can be downsized to the sub-micrometer regime and the parasitic capacitance is minimized by a decreased overlap between gate and source/drain electrode, which is the main contribution to the parasitic capacitance. This decrease in overlap can be dramatically enhanced by using the self-aligned technique [1].

The first step in the process (shown in Figure 1A) is to apply a structured gate electrode on the substrate. The gate electrode is either structured by a hot embossing process (HE-NIL) [2] or by an ultraviolet light induced crosslinking of a polymer (UV-NIL) [3]. The process is also suitable for flexible substrates, depending on the different temperature steps involved. In the next steps a dielectric layer and a UV curable positive resist are applied (Figure 1B and 1C). Now the gate structures are transferred into the photoresist by UV exposure through the substrate, using the gate electrode as a photo-mask (Figure 1D). Thereby a precise alignment of the source and drain electrodes with respect to the gate electrode, as well as a minimized overlap can be achieved. This step is followed by a development step, removing the exposed regions (Figure 1E). The source and drain material is applied (Figure 1F) and finally the remaining resist whit the source/drain material on top, is lifted off (Figure 1G) and the semiconductor material is added (Figure 1H).

With regard to the optimization of organic electrical devices, electron microscopy provides an excellent method to systematically study the various manufacturing steps and their influence on the devices. The first challenge is the TEM specimen preparation which is done mainly by using a focused ion beam (FIB) instrument. Due to the fact that soft materials are difficult to be prepared, windows of the regions of interest are milled out, thereby the remaining material provides mechanical stability. In Figure 2A a lamella of one channel can be seen. Figure 2B shows the thinned regions, in this case both sides of the transistor channel. Thereby the overlap of the source and drain electrodes with the gate can be seen easily (Figure 2C, 2D). Experiments with specimens prepared by means of ultramicrotomy were also performed but delamination of the different layers, introduced artefacts, and target preparation are huge problems. Therefore lamellas prepared by using a FIB instrument were analysed by scanning TEM (STEM), energy filtered TEM (EFTEM)as well as Electron Energy Loss Spectroscopy (EELS) and Energy Dispersive X-ray Spectroscopy (EDXS) are in order to gain a deeper understanding of the device (see Figure 1D). Questions concerning the quality of the imprint or the structure transfer of the imprint as well as the identification of any residuals could be answered. Especially with the on-going transformation to all printable materials the analytical methods become

more and more important due to the lack of differences (e.g. contrast) between the different materials. At the moment we are using PET (polyethylene terephthalate) as substrate, copper as gate electrode material, PVCi (poly(vinyl cinnamate)) as dielectric material, gold as source/drain material and pentacene as semiconductive layer. Moreover a variety of different resist materials is used during the process. Problems concerning the output of each process step, e.g. the complete removal of the resist in the transistor channel, can be monitored. The tasks get more challenging as the materials get more similar in atomic composition. In these cases questions concerning the layer thickness or shape of the structured features can only be answered by analysing either the plasmon region or the C K edge fine structure to differentiate between the materials. In this study we will present analytical results of organic materials. Despite the low contrast between the different materials we are able to clearly visualize all materials individually. This is possible by careful analysis of the corresponding features in the EEL spectrum: On the one hand the fine structure of the C K edge was used for calculating ratios of the σ* and π* peaks. On the other hand we found that the accurate determination of the plasmon peak energies was very useful to assist the distinction between the different organic materials.

1. U. Palfinger, C. Auner and H. Gold, Advanced Materials 22 (2010), 5115-5119
2. U. Haas, H. Gold, A. Haase, Applied Physics Letters 91 (2007), 043511
3. C. Auner, U. Palfinger and H. Gold, Organic Electronics 10 (2009), 1466-1472

4. The authors want to thank the Nanoinitiative Austria (FFG) for financial support. This work was done in the NILaustria cluster, in the project NILechoII 830269. Furthermore we want to thank the specimen preparation team and Thomas Haber.

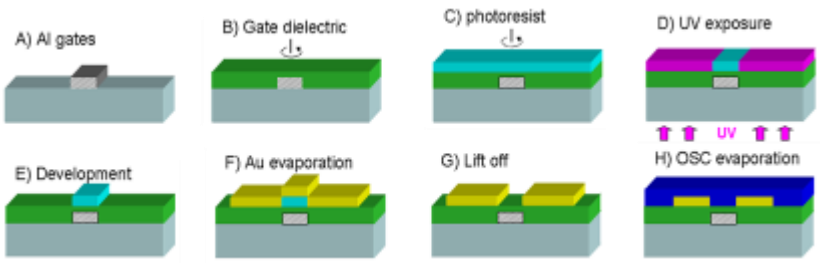

Figure 1. Process scheme of the self-aligned process [1]

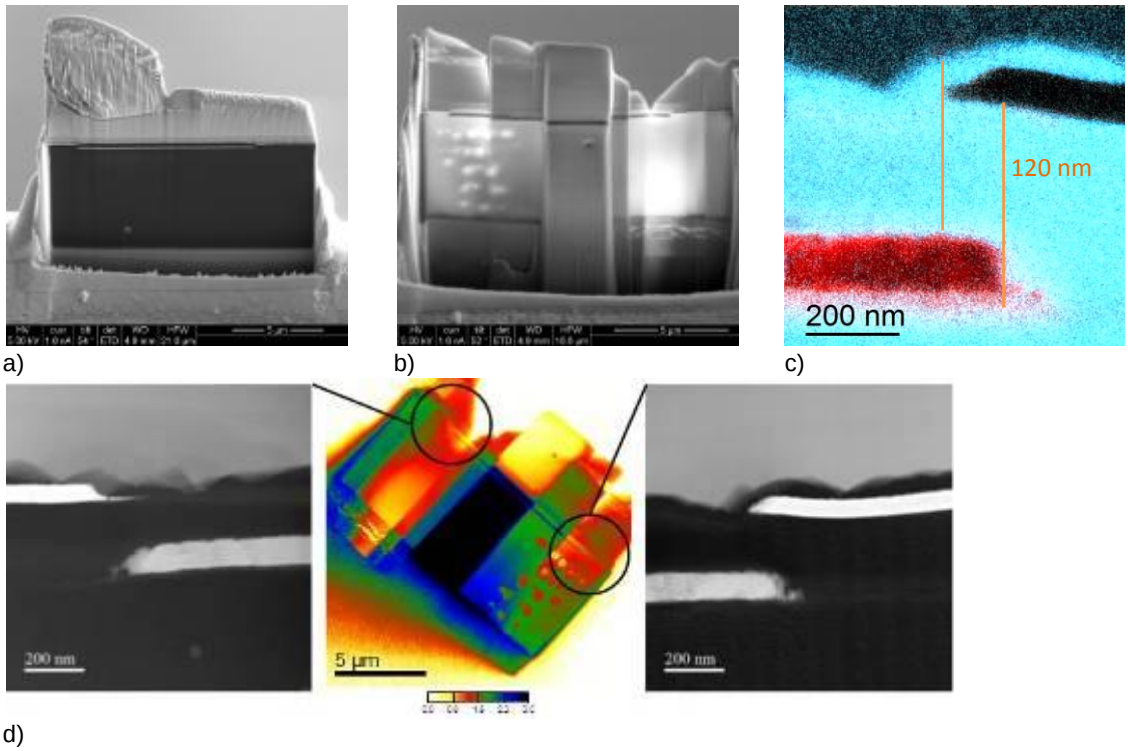

Figure 2. a) FIB lamella of an OTFT channel b) lamella after performing a window milling c) superposition of elemental maps: C…blue, Cu… red O…white, black represents Au and the protecting Pt layer d) relative thickness maps of the whole lamella as well as a close up of the two overlap regions.

Soft Matter, Polymers, Composites

MS.1.004
Observation of nucleated polyoxymethylene crystallization by means of in-situ polarized-light microscopy and in-situ scanning electron microscopy

M. Slouf[1], T. Vackova[1], S. Krejcikova[1], L. Novak[2], T. Vystavel[2]

[1]Institute of Macromolecular Chemistry, Academy of Sciences of the Czech Republic, Prague 6, Czech Republic
[2]FEI Czech Republic, s. r. o., Brno, Czech Republic

slouf@imc.cas.cz
Keywords: in-situ microscopy, nucleated crystallization, synthetic polymers

Polyoxymethylene (POM) is a synthetic polymer, which ranges among engineering thermoplastic materials [1]. It is frequently used for production of precise components requiring high stiffness, low friction and dimensional stability. Due to POM semicrystalline character, its final performance can be fine-tuned by adding various *nucleating agents* or *nucleants*. These are substances facilitating formation of the polymer crystal nuclei, shortening the crystallization process, decreasing the average size of spherulitic crystals (spherulites), and influencing physical properties of the material [2,3].

Although POM is produced in mass-scale (kilotons per year, ref. [1]), there are just a few reports dealing with nucleation of POM crystallization [3-6]. In this work, we employed our recently-developed sandwich method [7,8] and prepared POM sandwich composites (Figure 1). The prepared samples included polymer without nucleant (sandwich denoted as POM/0), sandwich with a layer of vacuum-sputtered gold nanoparticles (POM/Au), polymer with a layer of sorbitol derivative (sandwich POM/DBS), and polymer with a layer of talc microparticles (POM/Talc). The impact of nucleants on the crystallization of POM was evaluated both after the crystallization was finished (Figure 1; "static" sandwich method, described in our previous studies [7-9]) and during the crystallization process (Figure 2, "dynamic" or in-situ sandwich method; described in this contribution).

In a typical experiment, the sandwich composite was cut perpendicularly to the nucleant layer. The resulting sandwich cross-section, similar to that from static sandwich method (Figure 1; [7,8]), was observed in a polarized-light microscope (PLM; Nikon Eclipse 80i) equipped with a heating stage (Linkam THMS 600/TMS 9). The sample was molten (heated at 20 °C/min, held at 180 °C for 5 min) and isothermally crystallized (cooled at 80 °C/min, held at 154 °C till the end of crystallization). Samples with no nucleant (Figures 3a-e) showed random growth of spherulites. Samples with a nucleant layer exhibited intensive crystallization starting at the central layer, which was either quite sharp (Figures 3f-j) or smeared due to melt flow (Figures 3k-o, more frequent). The increase in overall intensity of polarized light with time (Figure 3; [9]), was proportional to the increase in crystallinity and could be interpreted in terms of Avrami theory (Figure 4; [10]). The overall rate of crystallization increased in the row: POM/0 = POM/Au < POM/DBS < POM/Talc (Figure 4a). The Avrami parameters ($t_{1/2}$,n,k; [9-11]) were obtained by fitting the experimental data with Avrami equation (Figure 4b) and their changes corresponded to computer simulations (Figure 4c). The results were verified by differential scanning calorimetry and in-situ SEM (not shown).

In conclusion, we demonstrated that the sandwich method can be used for in-situ observation of nucleated polymer crystallization. As the sandwich samples are quite small, the evaluation of crystallization kinetics is based on microscopy. The microscopic approach brings the following advantages: (i) direct observation of crystallization process and (ii) low consumption of polymers and nucleating agents, which makes it possible to prepare more samples and average the results.

1. S. M. Sinker in "Engineered materials handbook 2: Engineering plastics" eds. J. N. Epel, J. M. Margolis, S. Newman, R. B. Seymour (ASM International, Materials Park,OH) (1985), p. 100.
2. C. Mathieu, A. Thierry, J. C. Wittmann, B. Lotz, Polymer 41 (2000) p. 7241.
3. L. Jiang, F Jiang, J. Yang, R. Li, Y. Hu, Advanced Materials Research 466-467 (2012) p. 31.
4. Y. Shu, L. Ye, X. Zhao, Polymer-plastics Technology and Engineering 45 (2006) p. 963.
5. R. Nowacki, E. Piorkowska, Journal of Applied Polymer Science 105 (2007) p. 1053.
6. R. Masirek, E. Piorkowska, European Polymer Journal 46 (2010) p. 1436.
7. E. Pavlova, M. Slouf, H. Sandova, J. Baldrian, A. Sikora, F. Lednicky, R. Masirek, E. Piorkowska, Journal of Macromolecular Science B 49 (2010) p. 392.
8. M. Slouf, A. Sikora, E. Pavlova, H. Vlkova, J. Baldrian, T. Base, E. Piorkowska, Journal of Applied Polymer Science 125 (2012) p. 4338.
9. T. Vackova, M. Slouf, N. H. Vu: European Microscopy Congress 2012, Manchester, UK (2012) PS1.4.
10. M. Avrami, Journal of Chemical Physics 9 (1941), p. 177.
11. A. T. Lorenzo, M. L. Arnal, J. Albuerne, A. J. Muller, Polymer Testing 26 (2007) p. 222.

12. Support through grants GACR P205/10/0348 and TACR TE01020118 is acknowledged.

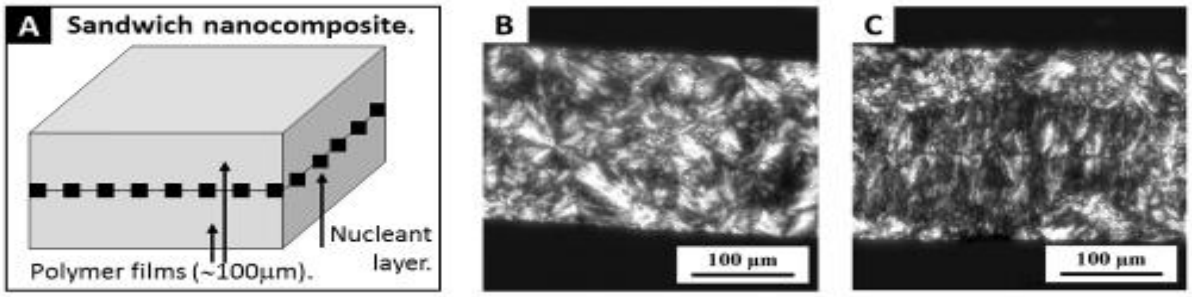

Figure 1. Static sandwich method: (a) sandwich preparation, (b) polarized-light micrograph of empty sandwich, POM/0, and (c) polarized-light micrograph of sandwich with talc layer POM/Talc. The micrograph (b) documents random growth of spherulites, while the micrograph (c) displays preferential growth of spherulites from the central talc layer (transcrystallization, refs. [7,8]), indicating strong nucleation effect.

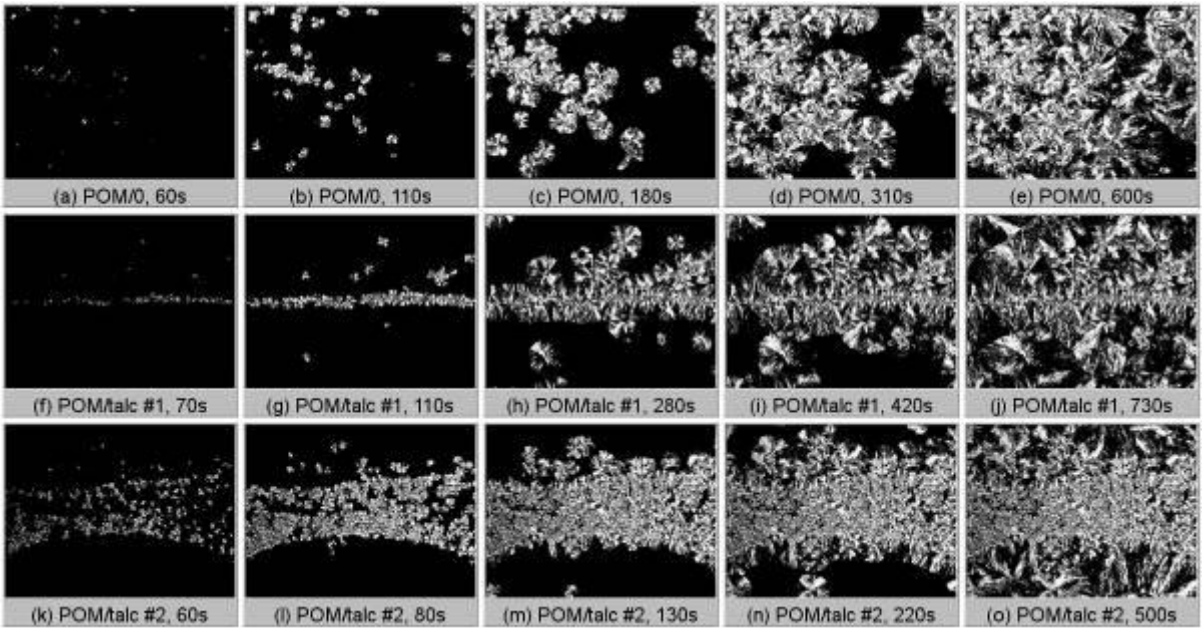

Figure 2. Dynamic sandwich method: polarized-light micrographs showing isothermal polymer crystallization in sandwich composites (a-e) without nucleant, (f-j) with sharp layer of talc, and (k-o) with molten layer of talc; real width of all images is 655 um.

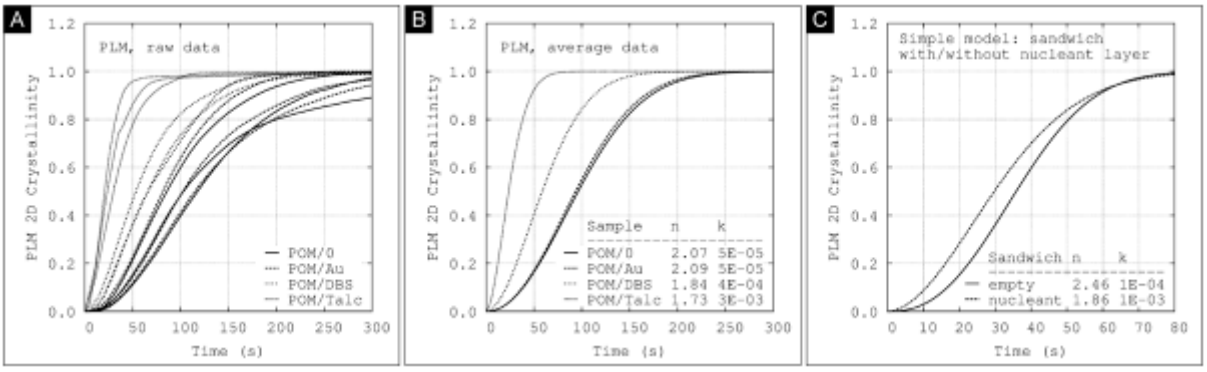

Figure 3. Kinetics of crystallization; overall crystallization as observed on PLM micrographs as a function of time: (a) raw data, (b) averaged data and (c) simplified model data. According (a) and (b), the strongest nucleation effect was observed in POM/Talc sandwich. Avrami coefficients from experiment (b) and from preliminary, simplified model (c) exhibited the same trend (decrease in *n* and increase in *k*) in the presence of a nucleating agent layer; more precise computer modelling is in progress.

Soft Matter, Polymers, Composites

MS.1.005
Morphological transitions in polymer vesicles upon bilayer swelling with small hydrophobic molecules in water

C. Parmenter[1], R. Chen[2], D. Cheung[3], S. Bon[2]

[1]University of Nottingham, Nottingham Nanotechnology and Nanoscience Centre, Nottingham, United Kingdom
[2]University of Warwick, Department of Chemistry, Coventry, United Kingdom
[3]University of Strathclyde, Department of Pure and Applied Chemistry, Glasgow, United Kingdom

christopher.parmenter@nottingham.ac.uk
Keywords: polymersomes, cryo-EM, swelling, DPD simulation

Attempts to scaffold surfactant based vesicles via polymerisation in the bilayer have often been shown to yield localised polymerisation and the formation of beads, due to possible phase separation between growing polymer and the molecules of the bilayer [1]. It has also been observed that other vesicle systems undergo re-arrangement and phase separation in response to the inclusion of solvents [2-3]. In order to minimise phase separation, a monomer with similar chemistry to the bilayer forming molecule can be selected. To achieve this, polymeric vesicles, also known as polymersomes, were swollen with compatible monomers, and the resulting dispersions analysed by cryogenic electron microscopy (cryo-EM). In parallel, these systems were modelled using dissipative particle dynamics (DPD) simulations and the effect of the momomer on the bilayer predicted. Through these combined approaches it was our aim to establish if phase separation occurs prior to polymerisation in polymersomes.

By the use of Cryo-EM, we have established that unilamellar polymer vesicles dispersed in water made from poly((ethylene oxide)$_{45}$-block-(methyl methacrylate)$_{164}$), poly((ethylene oxide)$_{45}$-block-(methyl methacrylate)$_{170}$), or poly(n-butyl methacrylate)$_{81}$-block-(2-(dimethylamino)ethyl methacrylate)$_{20}$ were smooth in appearance. However, when exposed to small hydrophobic molecules, here methyl methacrylate (MMA) and n-butyl methacrylate (n-BMA), they underwent morphological transitions. The monomers were added in the presence of a radical scavenger to rule out polymerisation. Upon swelling some of the bilayers increased as expected for the uptake of monomer, however, around 60% of the polymersomes lost their original simple bilayer morphology and transformed into more complex coil-like and patchy colloidal structures, which can be observed in both TEM (Figure 1&2) and SEM images (Figure 3).

The results of the DPD simulations on a model flat bilayer showed that transitions can occur upon bilayer swelling, which is accompanied by a change in the mechanical bilayer properties (Figure 4). The transition involves the formation of water pockets in the interior regions of the bilayer. Co-existence of the various morphologies in the experiments suggests an activation barrier towards morphological changes and a possibility of multiple meta-stable states. The latter indeed is supported by the existence of multiple minima in the surface tension as a function of bilayer area, as found in the simulations.

We feel that these results have an impact on, for example, the area of drug delivery, as polymersomes used in vivo as delivery vehicles may undergo such transitions, which would lead to different drug release profiles. Further details on this work are available in a recently accepted advanced preview [4].

1. M. Jung, D. H. W. Hubert, P. H. H. Bomans, P. Frederik, A. M. van Herk and A. L. German, Adv. Mater., 2000, 12, 210–213.
2. E. Br¨uckner and H. Rehage, Prog. Colloid Polym. Sci., 1998, 109, 21–28.
3. M. Jung, D. H. W. Hubert, E. van Veldhoven, P. M. Frederik, M. J. Blandamer, B. Briggs, A. J. W. G. Visser, A. M. van Herk and A. L. German, Langmuir, 2000, 16, 968–979.
4. C.D. J. Parmenter, R. Chen, D. L. Cheung and S.A.F. Bon, Soft Matter, 2013 DOI: 10.1039/c3sm50184a

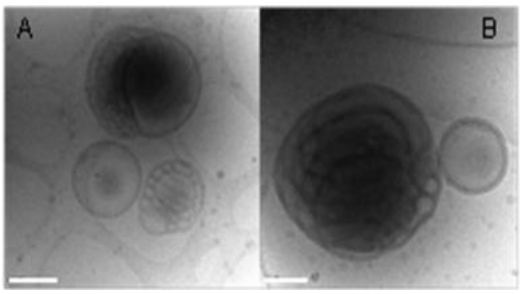

Figure 1. Cryo-TEM of PEG_{45}-b-$PMMA_{164}$ polymersomes swollen with MMA in water, showing coil and patch structures. Scale bars 500nm (A) and 200 nm (B).

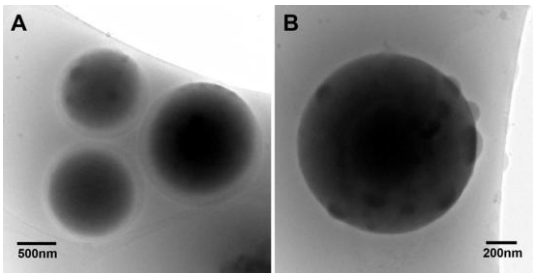

Figure 2. Cryo-TEM of PBMA-b-2DMAEMA polymersomes swollen with MMA in water displaying patchy structures.

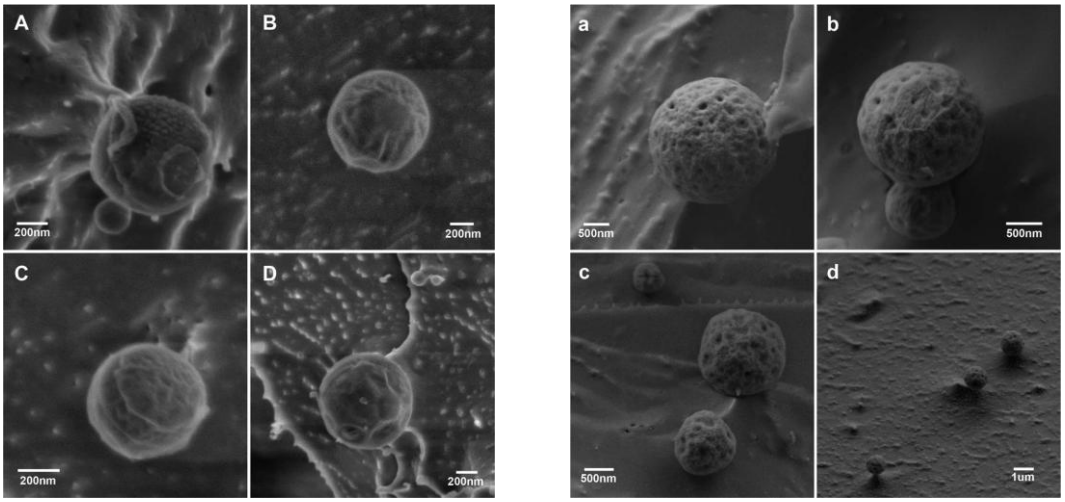

Figure 3. Cryo-SEM images of PEG_{45}-b-$PMMA_{170}$ swollen with MMA (A-D) showing coiled structures A and C and globular patchy structures D and PEG_{45}-b-$2DMAEMA_{20}$ swollen with BMA (a-d) displaying clear changes to the surface of a patchy nature.

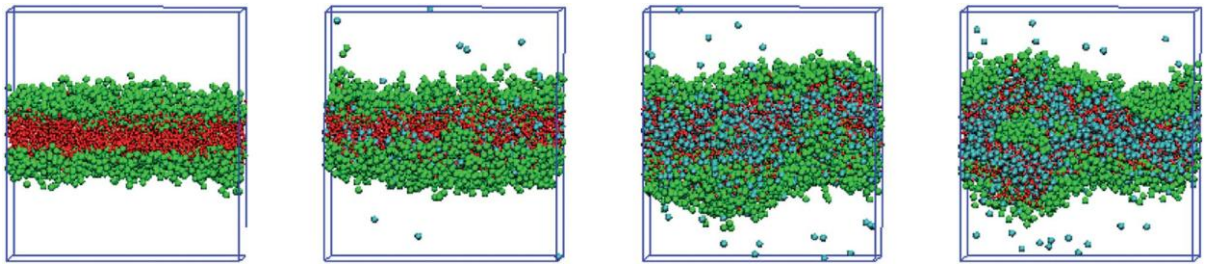

Figure 4. Simulation snapshots for 0, 500, 2500 and 3000 hydrophobic molecules (left to right). Head group beads shown in green, tail groups in red and hydrophobic monomers in blue (for clarity solvent beads not shown). As the concentration of the monomers increases they give rise to the formation of solvent pockets, which could be observed as patches and coils.

Soft Matter, Polymers, Composites

MS.1.006
Low temperature thermotropical dynamical processes in multiphase polymer systems by cryo AFM.

N. Matsko[1], V. Mittal[2]

[1]Graz Centre for Electron Microscopy, Graz, Austria
[2]Chemical Engineering Department, the Petroleum Institute , Abu Dhabi, United Arab Emirates

nadejda.matsko@felmi-zfe.at
Keywords: cryo AFM, thermotropical dynamic, polymers

The effect of thermotropical dynamical processes (e.g. processes, which are determined or changed by temperature) in soft materials is a subject of considerable interest and controversy not only in condensed matter physics, but also in the experimental electron microscopy. For example, the interpretation of TEM micrographs of thin sections based on the *a priori* assumption that since the specimen is of constant thickness (after ultramicrotomy) the image shows mass contrast only [1].

However, the detailed study of (bio-)polymer block face as well as of the section surfaces by AFM, represents numerous evidence that sample topography after ultramicrotomy varies from few to hundreds nanometers and strongly depends on the type of the sample material (Figure 1). Difference in the section thickness cause an additional input in the TEM amplitude image contrast and therefore has to be taken into account for the adequate TEM image interpretation. Appearance of the pronounced topographical contrast in the section surface results from thermotropical dynamic in soft materials and can be mainly attributed to the volumetric and enthalpy relaxation in amorphous polymers near or after the glass transition, which took place during material production and/or sample preparation for microscopical analysis. The glass transition is the reversible transition in amorphous materials (or in amorphous regions within semicrystalline materials) from a hard “glassy” and relatively brittle state into a molten or rubber-like state. If a glass-forming material is cooled below the glass transition temperature (Tg), its structure begins to depart from the equilibrium as a result of the decreasing molecular mobility, since the molecules are not able to reach their equilibrium conformations in the time scale of the cooling [2]. This may change the crystal structure, the degree of crystallinity, the perfection of the crystals, the orientation of both crystalline and amorphous phase, their contiguous structural morphology, the number of tie chains between the crystallites and as a consequence the entire phase volume.

In order to get an insight into the thermotropical dynamical processes, the analysis of the structural relaxation in specimens that are either in the amorphous or in the liquid crystalline state (or in a mixture of them) has been carried out (Figure 2). Cryo AFM (SNOTRA) [3] provides an opportunity to observe an evolution of the sample ultrastructure as a function of temperature *in situ*. The unique ability of the instrument to visualize structural changes over a wide range of temperatures (−120°C to +50 °C) with subsequent serial-section 3D reconstruction yields detailed information about polymer packing density, morphology and orientation of chains without contrast enhancing procedures, which is usually required for conventional EM studies. The results indicate that the different phases behave independently, exhibiting self-governing (and well different) glass transitions and with their own structural relaxations. Moreover, it seems that the changes in local order associated with a densification of the liquid-like packing lead to the development of some kind or local alignment, which favors the subsequent liquid-crystallization. Thermotropic effects investigated in this field can be caused by a phase separation process, by a phase transition between an isotropic and an anisotropic (liquid-crystalline) state and by strongly differing temperature dependencies of domains and matrix.

1. D. B. Williams, C. B Carter. Transmission Electron Microscopy: A Textbook for Materials Science. (Springer, Berlin) (2009), p. 375.
2. J. P. Fernandez-Blazquez, A. Bello, E. Perez. Polymer Bulletin (2007), 58, p.941.
3. A. Efimov, H. Gnaegi, R. Schaller, W.Grogger, F. Hofer, N. Matsko. Soft Matter (2012), 8, p. 9756.
4. We are very grateful to Ferdinand Hofer for fruitful discussions.

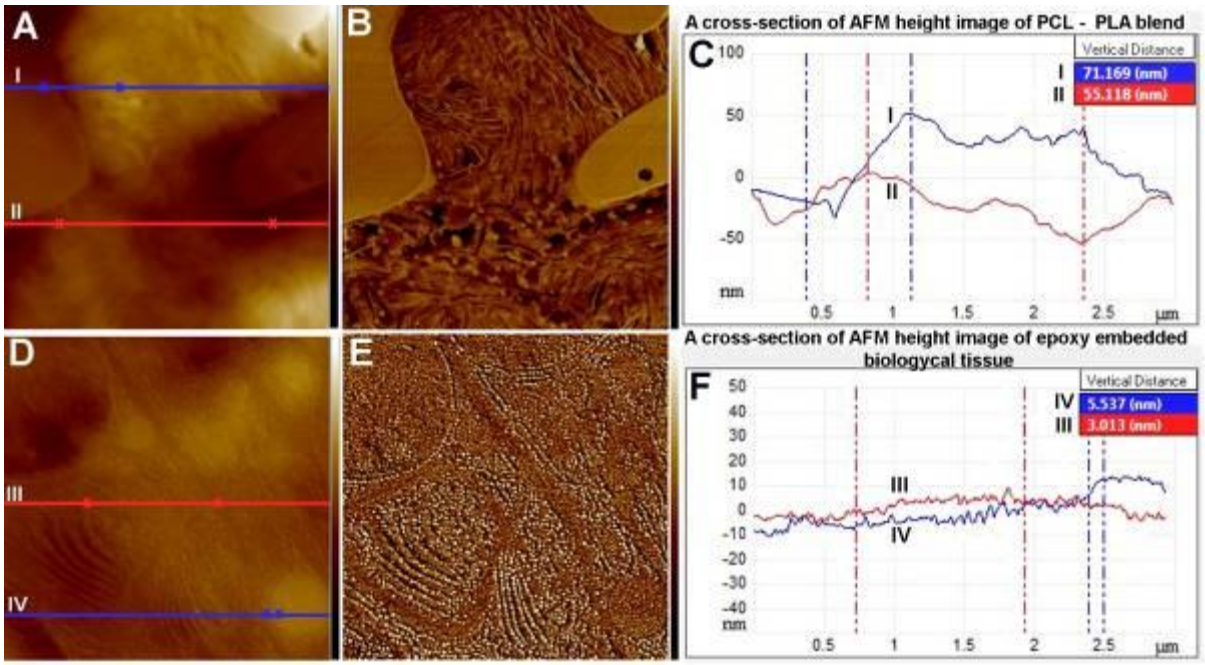

Figure 1. AFM height and phase images of the Poly[oxy(1-oxohexane-1,6-diyl)-Polylactid polymer blend (A, B), and epoxy embedded biological tissue (D, E). (C, F) Corresponding line profiles of the block face surfaces. Phase variations: 0-100° in (B) and 0-10° in (E).

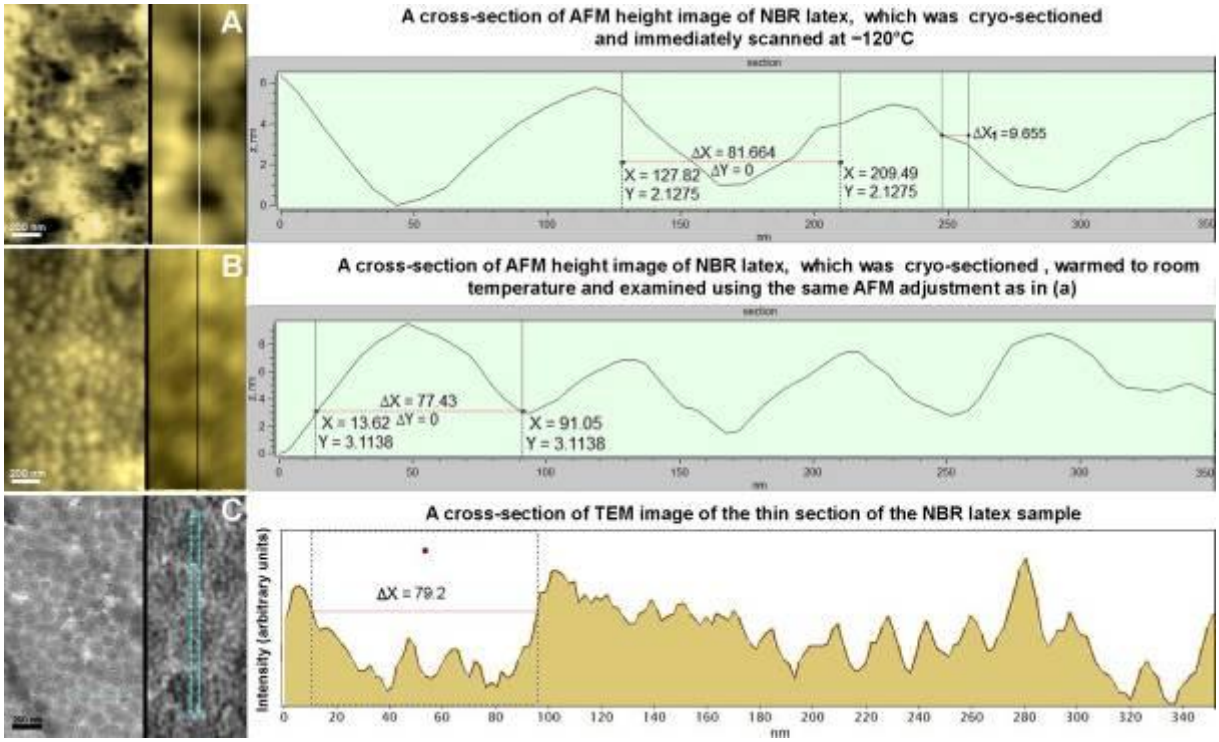

Figure 2. The morphology of a line profiles of a nitrile butadiene-rubber (NBR) latex sample characterized by cryo-AFM and TEM. (A) A topographical AFM image of an epoxy embedded latex stripe that was mounted in the cryo-chamber of SNOTRA, cryo-sectioned and immediately scanned at −120°C. (B) Immediately afterwards, the same sample was warmed to room temperature and then examined using the same AFM adjustment parameters and the same tuning fork sensor. (C) A TEM bright field image of the thin section of the NBR latex sample, which was examined without contrast enhancing procedures.

Soft Matter, Polymers, Composites

MS.1.P007
Strings in homochiral solutions

S. Stovbun[1], A. Skoblin[1], I. Litvin[1], M. Grishin[1], B. Shub[1]

[1]Semenov Institute of Chemical Physics, Department of kinetics and catalysis, Moscow, Russian Federation

j.a.litvin@gmail.com, s.stovbun@chph.ras.ru
Keywords: chirality, string, homochiral solution, superhelicity

Solutions of chiral and achiral trifluoroacetic alkanolamines (TFAAA) in a variety of organic solvents and water were investigated. Homochiral solutions get cured and turn into a gel-like mass on concentrations (10^{-3}-10^{-2}) mol/L which is more than one order less than the percolation threshold. Microscopy techniques revealed an irregular grid of strings which are anisometric structures with diameters about d ~ 1 μm, lengths L ~ 0.5 cm, aspect ratios L/d ~ (10^2-10^4), diameter being constant and strings being rectilinear on lengths >~ (10-100) d which points on the rigidity of the strings [1].

Achiral and racemic solutions with such concentrations don't get cured and in vaporized solutions TFAAA get condensed into isometric granules.

Single strings in solutions were obtained in capillaries which points that the strings are basic objects while the gels are formed due to the presence of the irregular grid of the strings. Such grids establish non-sedimenting mechanical skeletons (calculation shows that a single string should sediment over ~10^3 seconds), Figure 1.

The morphology of the strings is found to be highly dependent on the solvent (dense strings in cyclohexane, rarefied ones in heptane, branching ones in water).

Optical and atomic force microscopy revealed the following structural features. The thinnest (d ~ 0.01-0.1 μm) strings have helical structure [2]. Most of the thicker ones are formed by helically intertwisted thinner strings (Figure 2) which have helical structure themselves (Figure 3). Thus, the superhelicity phenomenon takes place; it is observed on several hierarchy levels. The diameter d and the step length h of a growing helix depend on the individual story of the string; they were observed in the ranges of d ~ (0.01-10) μm and h ~ (0.01-50) μm.

X-ray diffraction techniques revealed a crystalline packing of strings in samples with evaporated solvent. That packing differed with the TFAAA used and didn't depend on the solvent. This points that the identical (for specified TFAAA) long-range order and, perhaps, crystalline structure is formed in the solution, in thin (probably, elementary) strings which, in turn, give rise of the "thick" strings. Solvent molecules are not embedded into the molecular grid of a thin string which can be naturally interpreted as a consequence of solvent molecules being disproportional to the grid size. Because of this such thin strings (consisting of TFAAA molecules only) should be considered as elementary ones. Its grid is based on the complimentary interactions of homochiral TFAAA molecules; its diameters (estimated from the pictures of untwisted "thick" strings) d < 0.1 μm.

Interactions of elementary strings that enable twisting to form thicker ones probably originates from van der Waals forces. Diversity of microscopic strings' morphologies is most likely caused by different ratios of van der Waals forces between elementary strings (the latter depending on the solvent) to elastic forces rising because of superhilicity and corresponding mechanical strain.

1. S.V. Stovbun, Russian Journal of Physical Chemistry B Vol. 5 No. 4 (2011), pp. 546-553
2. S.V. Stovbun, A.M. Zanin, A.A. Skoblin, A.I. Mikhailov, R.G. Kostyanovskii, M.V. Grishin, B.R. Shub, Russian Journal of Physical Chemistry B Vol. 5 No. 6 (2011), pp. 1019-1022

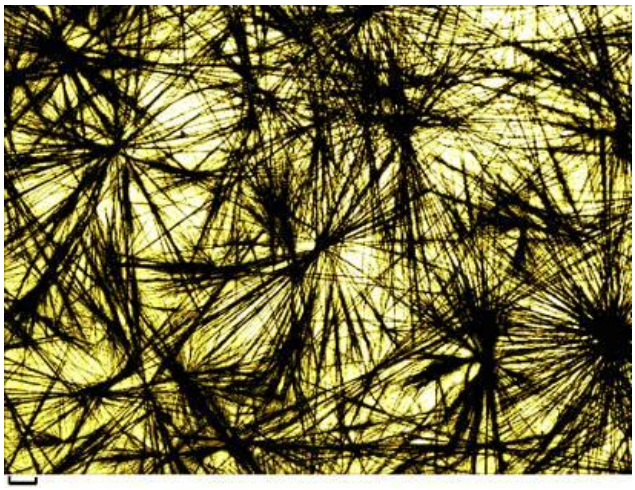

Figure 1. Mechanical skeleton of a gel formed by the strings. Scale bar corresponds to 100 μm.

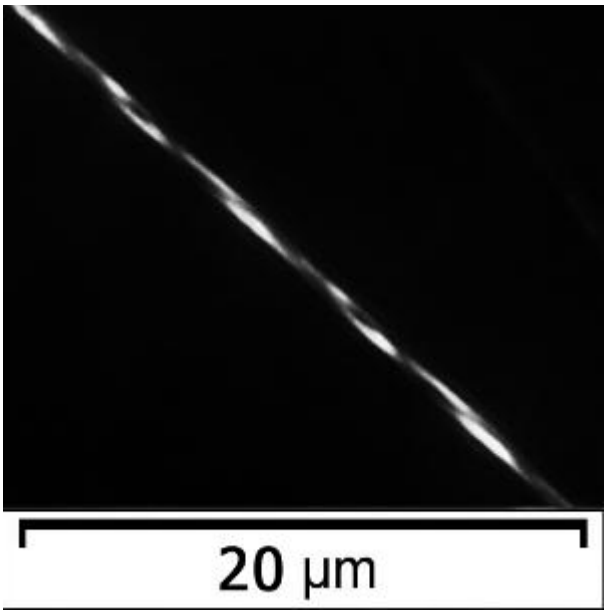

Figure 2. Helical structure of a solitary string.

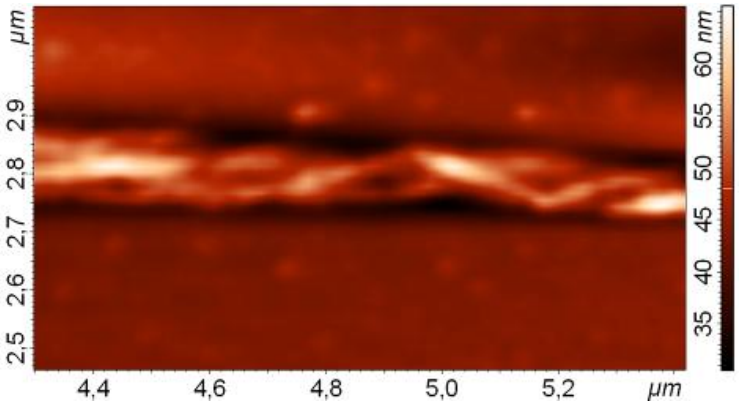

Figure 3. A thinner string consisting of intertwisted strings with the diameters of about 50 nm. AFM

Soft Matter, Polymers, Composites

MS.1.P008
Characterization of inorganic-organic cement materials

C. Miret[1], A. Malchere[1], T. Douillard[1], G. Foray[1], L. Joly-Pottuz[1]

[1]INSA Lyon, MATEIS, Villeurbanne, France

lucile.joly-pottuz@insa-lyon.fr
Keywords: composites, multi-scale characterization

For environmental issues and energy consumption diminution, building materials with high performances are presently widely studied. These materials can be described as organo-mineral composites with a complex texture of the organic/inorganic hydrated co-matrix. As final material properties are governed by this complex structure, a characterisation of the geometrical features and the texture of each phases could help in formulating new durable construction materials. Furthermore these materials evolve in time, for example by hydratation processes leading to the formation of hydrates or by a filmfication of latex. It is thus necessary to characterize the evolution of the materials during time by a characterization of the fresh state and solid state.

To fully study their microstructure, a multiscale characterization (from mm to nm) is required. Several tools of electron microscopy can be envisaged for the analysis at these different scales: scanning electron microscope (SEM), environmental scanning electron microscope (ESEM), transmission electron microscope (TEM). Furthermore a 3D characterization can now be envisaged with the development of the 3D tomography in the Focused Ion Beam (FIB) microscope. Nevertheless, protocols have to be carefully defined so that the microstructural observation of the material may be feasible without hindering the material microstructure.

Different cements were characterized in this study and the latex used has been varied in terms of size and stabilization. A characterization at different scale reveals differences in the microstructure of the samples. SEM images showed that the spatial organization of hydrates can vary depending on the latex used: hydrates can intermingle and form clusters of flattened beads (mean diameter: 3 microns) (confirmed by TEM observation), while in other samples they were distributed in distinct zones (Figure 1). TEM characterization was also very useful to discriminate the C-S-H hydrates formed: foil-like (figure 2a), tubular structure (figure 2b) typical of the outer-product, fibrillar structure of the inner product and some thin sheets (figure 2d).

The advantage of FIB characterization is the possibility to have a 3D characterization of the sample. It was used to study the organization of the latex around the mineral grains. In the case of small latex particles, the filmfication is not completed and some of particles are well distributed around amorphous grains (Figure 3a). In the case of big latex particles, their presence can promote the presence of nanoporosity in the sample. This was observed by FIB 3D reconstruction (Figure 3b).

The coupling of SEM, TEM and FIB characterizations is of much interest to fully characterize the complex structure of cement. FIB technique and 3D reconstruction will allow to go further on the characterization and is very complimentary with SEM and TEM characterizations [1].

The authors acknowledge St Gobain CREE for financial support and to the CLYM (Centre Lyonnais de Microscopie) for the access to the 2010F and NVision 40 microscopes.

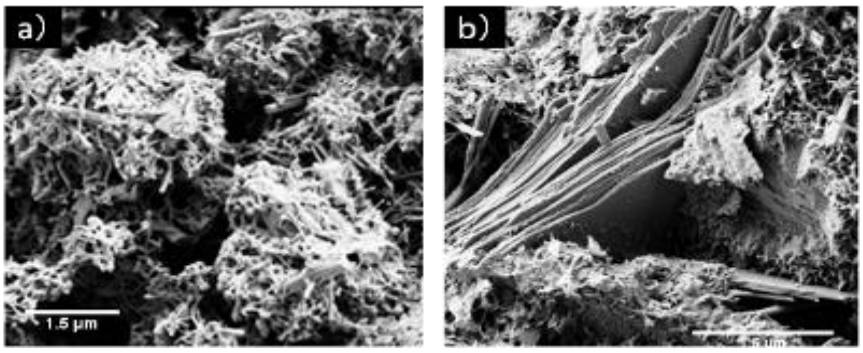

Figure1. SEM images showing two hydrates structures depending on the latex used: a) beads of hydrates, b) hydrates distributed around portlandite crystals (scale 1.5□m)

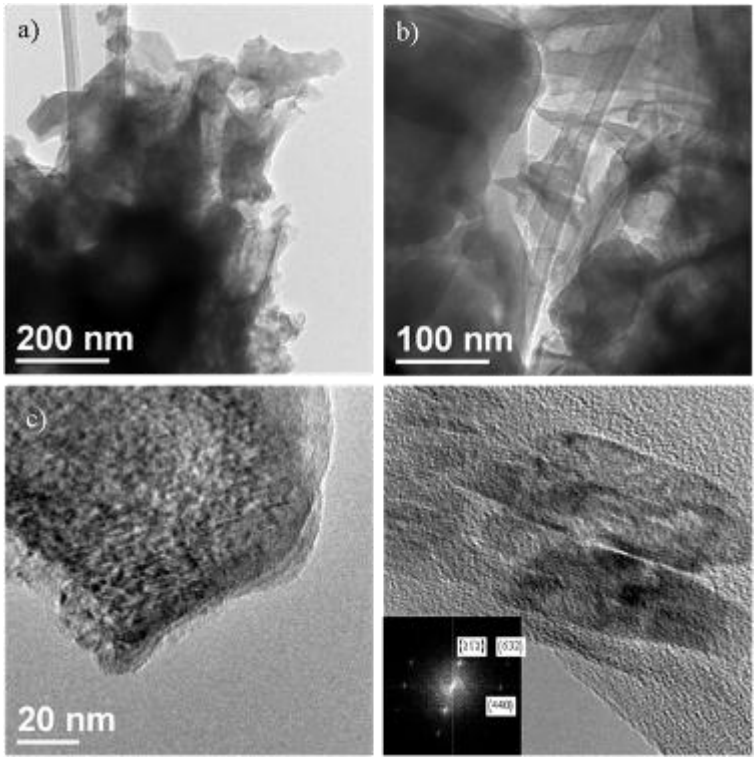

Figure 2. TEM characterization of the different morphologies of C-S-H :a): foil-like, b) tubular structure, c) fibrillar structure and d) thin sheets

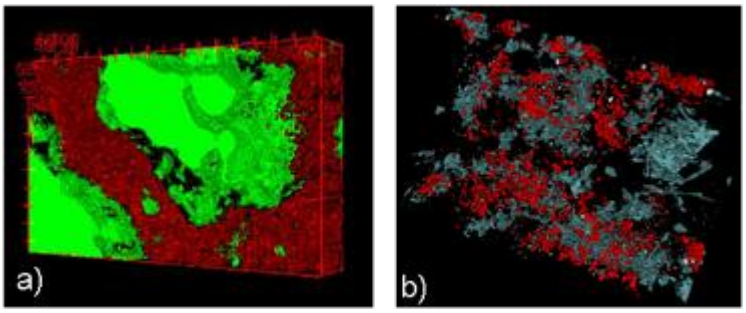

Figure 3. a) distribution of the latex particles around the mineral grains ; **b)** distribution of porosities due to the presence of latex (red) and hydrates (b)

Soft Matter, Polymers, Composites

MS.1.P009
Analytical electron microscopy investigations of B_4C-Al ceramic - metal composites produced by pressureless melt infiltration technique

P. Kaya[1], G. Arslan[1], S. Turan[1]

[1]Anadolu University, Material Science & Engineering, Eskisehir, Turkey

pkaya1@anadolu.edu.tr
Keywords: Pressureles melt infiltration, composite, TEM,

Ceramic-metal composite materials generally combine the hardness and light weight of ceramics with the toughness of metals as in B_4C-Al composites [1]. Interphase phenomena in ceramic-metal system are of significant importance in materials science and the technologies related to metal/ceramic joining and fabrication of metal-ceramic composites [2]. Several processing techniques, including powder metallurgy, casting, infiltration, directed metal oxidation, etc., have been developed to produce ceramic–metal composites. Pressureless melt infiltration is generally considered to be a more attractive technique to produce ceramic-metal composites due to its cost effectiveness and easiness when compared with more conventional methods such casting and powder metallurgy [3].

For this purpose porous pellets were produced by using B_4C powder, which were then pressureless melt infiltrated with a 2024 Al alloy in an Ar gas atmosphere. For analytical transmission electron microscopy (TEM) investigations electron transparent sample were prepared by ion beam milling. 200 kV field emission transmission electron microscope (JEOL 2100F) attached with an energy filter (GATAN GIF TRIDIEM), parallel electron energy loss spectrometer (PEELS), a high angle annular dark field scanning transmission electron microscope (STEM HAADF) detector and an energy dispersive x-ray (EDX) spectrometer (JEOL JED-2300T) was used for the characterization of interphase boundaries in composite. General microstructure and existing phases were determined by using X-ray diffraction (Rigaku Rint 2200, Tokyo, Japan) and scanning electron microscope (Zeiss Supra 50 VP) attached with energy dispersive X-ray spectrometer (EDX, Oxford, England). XRD results showed that main reaction product is Al_3BC phase. Figure 1 shows the microstructure of the composites. Because of the existence of light elements, it is difficult to carry out detailed elemental analyses of the reaction products by using SEM-EDX. Therefore, advanced TEM techniques were used. In this presentation, results of analytical investigations will be presented.

1. Cermet materials prepared by combustion synthesis and metal infiltration, Joseph B. Holt et al, U.S. Patent No 4,988,645
2. M.Aizenshtein, N.Froumin, M.P.Dariel, N.Frage, Materials Science and Engineering A, 474 (2008) 214-217
3. Development of Si3N4/Al composite by pressureless melt infiltration, Akhtar Farid, GUO Shi-ju, Trans. Nonferrous Met. SOC. China 16, (2006), 629-632

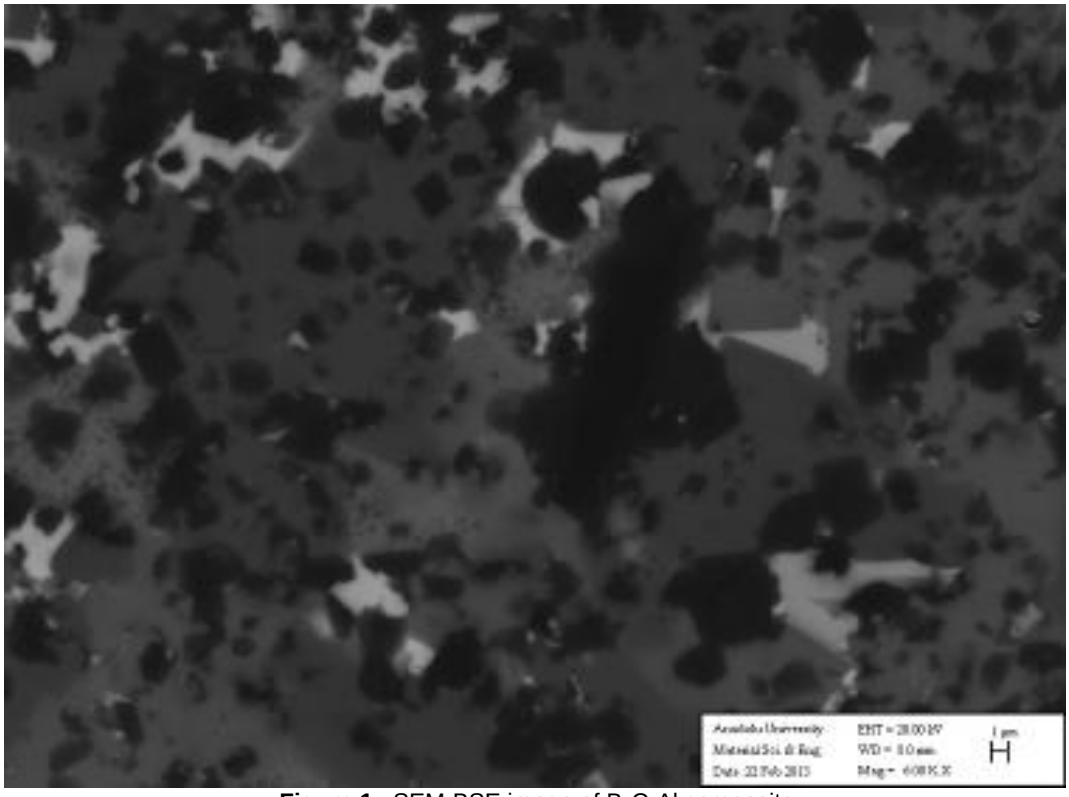

Figure 1.. SEM-BSE image of B_4C-Al composite

Soft Matter, Polymers, Composites

MS.1.P010
Morphological investigation of Ziegler-Natta catalysts

R. Selleri[1], M. Casinelli[1]

[1]LyondellBasell, Material Science, Ferrara, Italy

roberta.selleri@lyondellbasell.com
Keywords: Ziegler-Natta catalyst, ESEM/EDS, AFM, TEM, morphology

The Ziegler Natta catalysts, discovered in 1954 by Karl Ziegler and Giulio Natta (Nobel Prize in Chemistry 1963 awarded *"for their discoveries in the field of the chemistry and technology of high polymers)* are the basis for industrial production of polyolefins. Starting from the earlier titanium trichloride based catalysts, the discovery of magnesium chloride as the election support for titanium tetrachloride and of the routes to obtain a control of particle morphology represented the most important breakthrough for the development of modern catalysts. Nowadays the complete control of morphology from the support to the catalyst and, finally, to the growing polymer particles represent a key point in leading industrial polymerization processes [1].

The current work presents a morphological study based on an interdisciplinary approach involving different microscopy techniques, made possible by the set up of a new sample preparation procedure. The combination of the complementary information has brought about a deepen awareness of the observed morphology.

In the present work, ESEM/EDS, AFM and TEM evaluations have been applied under inert atmosphere and the obtained results will be presented (Figures 1, 2 and 3).

1. G. Cecchin, E. Marchetti and G.Baruzzi, Macromol.Chem.Phys.(2001),202 p.1987-1994

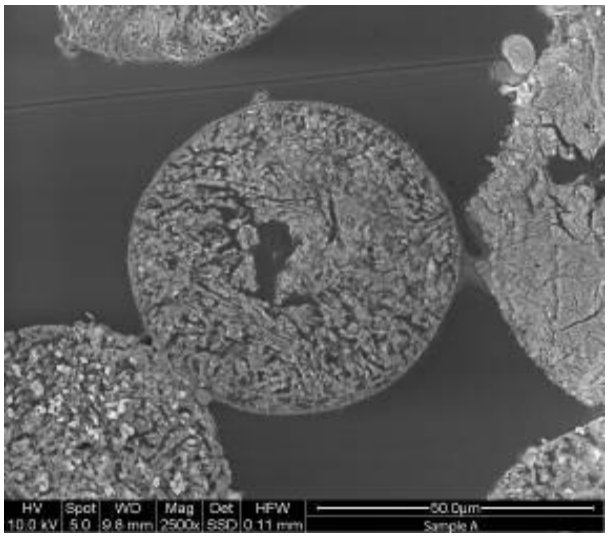

Figure 1. Sample A: ESEM image

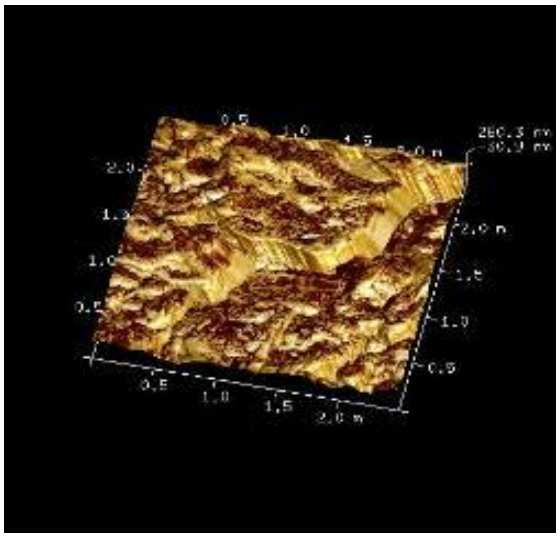

Figure 2. Sample A: AFM image

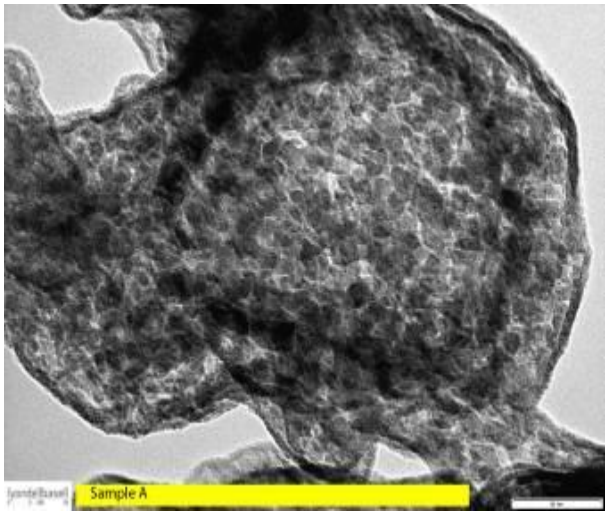

Figure 3. Sample A: TEM image

Soft Matter, Polymers, Composites

MS.1.P011
High performance carbon nanotube reinforced crosslinked high density polyethylene

E. Roumeli[1], E. Pavlidou[1], G. Vourlias[1], D. Bikiaris[2], K. Chrissafis[1]

[1]Aristotle University of Thessaloniki, Physics, Thessaloniki, Greece
[2]Aristotle University of Thessaloniki, Chemistry, Thessaloniki, Greece

hrisafis@physics.auth.gr
Keywords: carbon nanotubes, polyethylene, nanocomposite

Carbon nanotubes (CNTs) have exceptional mechanical, thermal and electric transport properties which make them ideal candidates as reinforcing and conducting fillers of composites for a wide range of applications [1, 2]. The outstanding strength and stiffness of CNTs are some of the most appealing properties that CNT-based nanocomposites are intending to achieve and an effective load transfer between the matrix and the filler may be the key to prepare composites with such superior properties [3, 4]. Crosslinked high density polyethylene (PEX) is a chemically or physically modified polyethylene that extends its use by raising its operating limit at much high temperatures and improving its mechanical properties due to the formation of a 3D structure [5, 6]. Since PEX is currently produced in large quantities for various types of applications, the further enhancement of its properties is of high interest. Therefore, the aim of the present work was to reinforce crosslinked high density polyethylene with small quantities of multi-walled carbon nanotubes (MWCNTs) in order to prepare nanocomposites of superior mechanical performance and examine the load transfer between the matrix and the fillers in tension.

PEX was prepared using the silane two-step process in which a high density polyethylene grafted with vinyl trimethoxysilane is mixed with a catalyst masterbatch containing the same polymer along with dibutyltin dilaurate (DBTDL), internal lubricants, stabilizers and various antioxidants and then the product is exposed to moisture in order for the final crosslinking to occur. Purified multi-walled carbon nanotubes were purchased from Chengdu Organic Chemicals Co. Ltd. The inner and outer diameters of MWCNTs were less than 2-5 nm and 8 nm respectively and they have 2.1 g/cm^3 density. Mixtures of PEX and 0.5, 1, 3 and 5 wt% MWCNTs were solid-state mixed for 6 hours in a Retsch centrifugal ball mill (model S 100) and then, they were melt-mixed for 10 min at 200^{o}C in a Haake-Buchler Rheomixer (model 600). Following that, the prepared materials were hot pressed and then rapidly cooled by immersion in water at 25^{o}C. For the examination of mechanical properties an Instron 3344 dynamometer was used, in accordance with ASTM D638 using a cross-head speed of 50 mm/min. The dispersion of MWCNTs and the morphology of the failure surfaces of all nanocomposites after tensile testing were examined using scanning transmission electron microscopy (SEM, TEM). The SEM system was a JEOL JSM 840A-Oxford ISIS 300 SEM with accelerating voltage 20 kV, probe current 45 nA and counting time 60s and the TEM system was a JEOL 120 CX microscope operating at 120 kV.

The dispersion of MWCNTs in the polymer matrix was studied with TEM and two typical images of the nanocomposite with 1 and 5 wt% MWCNTs are presented in Figures 1-2. While a fine dispersion can be revealed in the case of low filler content, for the high filler loading the formation of some nanotube bundles with size up to 200 nm cannot be avoided. However, the aggregated tubes seem to be well dispersed in the polymer matrix. The results of the mechanical properties tests of PEX and its nanocomposites reveal an obvious enhancement of all the studied properties. The addition of 0.5 % MWCNTs leads to a 100 MPa enhancement of Young's modulus while a further increase of MWCNTs content leads to elastic modulus values higher than neat PEX but somewhat lower than the nanocomposite with 0.5 % MWCNTs. However, the nanocomposite with 5% MWCNTs had the highest elastic modulus (985 MPa) which is 310 MPa higher than the neat polymer's. The stress at yield values seem to follow the same trend; in the case of 0.5% MWCNTs the stress at yield is 3.4 MPa higher than that of neat PEX. For the nanocomposites with 1-3% MWCNTs, the stress at yield remains almost the same as for the nanocomposite with 0.5% MWCNTs, while for the nanocomposite with 5% MWCNTs the stress at yield is much higher (9.8 MPa higher than in neat PEX). It seems that the small amounts of MWCNTs (up to 1 wt %) lead to a notable increase of 6.9 MPa for the stress at break while a higher MWCNTs concentration causes a reduction of the ultimate stress, which reaches the same level as neat PEX. The elongation at break of the nanocomposites presents a similar trend to the ultimate stress values. Up to 1% MWCNTs the elongation at break values are higher than in neat PEX,

while for higher filler content they are drastically reduced. Therefore, it seems that two competitive mechanisms act upon the incorporation of MWCNTs in PEX: a tendency to enhance the mechanical properties of PEX by load transfer and a drive to form aggregates or bundles that reduces the positive effect on these properties.

The characteristic fibrillar structure of PEX at failure was observed in all its nanocomposites. Upon failure, most of the MWCNTs were broken while a few were pulled out of the matrix as shown in Figures 3-4. Many of the tubes and bundles have fallen back onto the broken surfaces as a loosen network and they seem to be interconnecting the polymer lumps. The nanotubes and their bundles bridging across the cracks suggest that stress release and absorption of the fracture energy is possible and therefore the fillers may result in a toughness improvement. Also, some of the MWCNTs become loosened or curved, probably due to relaxation after fracture or uneven crack separation [4,7]. This interesting and typical breakage observation of the MWCNTs upon tensile stretching indicates a strong interfacial adhesion between MWCNTs and PEX matrix and a sufficient load transfer from the polymer to nanotubes [3, 4].

In conclusion, from the examination of the mechanical properties and observations of the failure surfaces of novel nanocomposites of crosslinked high density polyethylene reinforced with MWCNTs, a significant improvement of mechanical properties was found and it was suggested that two competitive mechanisms seem to govern the incorporation of MWCNTs in PEX: a tendency to enhance the mechanical properties of PEX by load transfer and a drive to form bundles that reduce the positive effect on these properties. Evidence of both these competitive mechanisms was found by SEM observations of the failure surfaces and TEM images of the dispersion of MWCNTs.

1. R.S. Ruoff, D.C. Lorents, Carbon, 33 (1995) 925-930.
2. J.N. Coleman, U. Khan, W.J. Blau, Y.K. Gun'ko, Carbon, 44 (2006) 1624-1652.
3. L.S. Schadler, S.C. Giannaris, P.M. Ajayan, Applied Physics Letters, 73 (1998) 3842-3844.
4. P.M. Ajayan, L.S. Schadler, C. Giannaris, A. Rubio, Advanced Materials, 12 (2000) 750-753.
5. S. Venkatraman, L. Kleiner, Advances in Polymer Technology, 9 (1989) 265-270.
6. J.E. Ritums, A. Mattozzi, U.W. Gedde, M.S. Hedenqvist, G. Bergman, M. Palmlöf, Journal of Polymer Science Part B: Polymer Physics, 44 (2006) 641-648.
7. V.G. Hadjiev, M.N. Iliev, S. Arepalli, P. Nikolaev, B.S. Files, Applied Physics Letters, 78 (2001) 3193-3195.

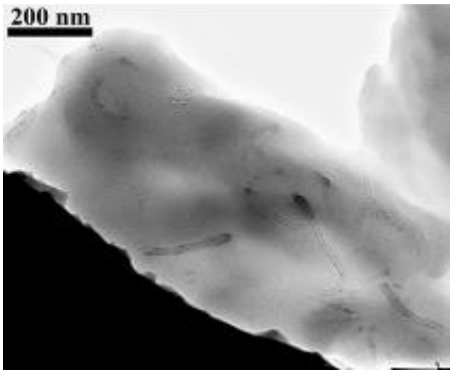

Figure 1. TEM image of PEX/1% MWCNTs

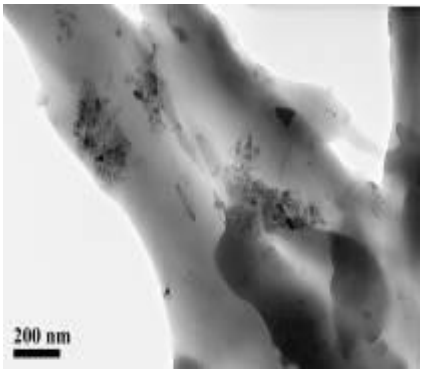

Figure 2. TEM image of PEX/5% MWCNTs

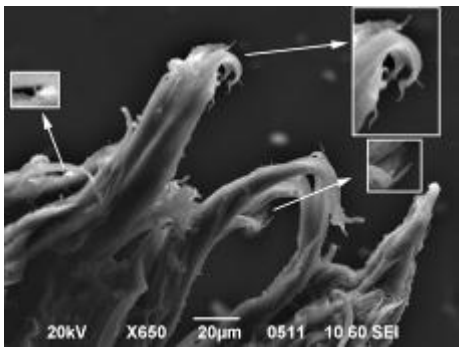

Figure 3. SEM image of the fracture surface after tensile testing of PEX nanocomposite containing 5% MWCNTs.

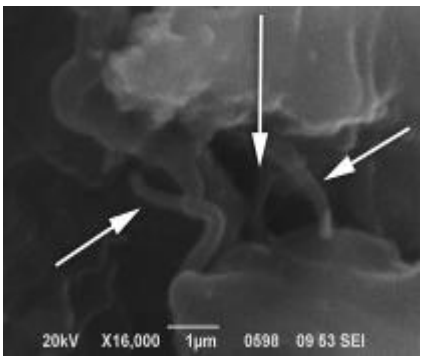

Figure 4. SEM image of the fracture surface after tensile testing of PEX nanocomposite containing 3% MWCNTs.

Soft Matter, Polymers, Composites

MS.1.P012
Applications of low-energy STEM for the investigation of carbon-based materials for organic solar cells

M. Pfaff[1], E. Müller[1], T. Volkenandt[1],D. Gerthsen[1]

[1]Karlsruhe Institute of Technology, Laboratory for Electron Microscopy, Karlsruhe, Germany

marina.pfaff@kit.edu
Keywords: low-energy STEM, Z-contrast, thickness and density determination

High-angle annular dark-field scanning transmission electron microscopy (HAADF STEM) is a promising technique for imaging carbon-based materials for organic solar cells because it provides a particularly sensitive composition (Z-)contrast at low electron energies. Furthermore, low-keV STEM can be generally applied to quantify thickness or material density of the investigated samples if the composition of the material is known.

The experiments were carried out with the field-emission-gun scanning electron microscope of a dual-beam FEI Strata400S. A standard semiconductor STEM detector with several ring-like segments was used which is positioned below the sample. Pronounced atomic-number contrast can be obtained in the high-angle annular dark-field (HAADF) STEM mode where only electrons are collected which are scattered into high angles after interaction with the nucleus of the sample atoms. This leads to a strong Z-contrast which is even more pronounced at low electron energies. For comparison, transmission electron microscopy (TEM) images were taken with a Philips CM 200 FEG/ST microscope at 200 keV.

The low-keV HAADF STEM intensity is not only sensitive towards the chemical composition but depends also on the sample thickness and primary electron energy. The energy dependence is demonstrated by Figures 1a-c which shows HAADF STEM images taken at different electron energies of an approximately 100 nm-thin film containing a blend of poly-(3-hexylselenophene-2,5-diyl):C61-butyric acid methyl ester (P3HS:PCBM), which is a material system for photoactive layers in organic solar cells [1]. A contrast inversion is clearly visible by comparing Figures 1a and 1c. To interpret the images a semiempirical formalism for the calculation of the HAADF STEM image intensity was developed [2]. The calculated intensities of PCBM and P3HS are plotted in Figure 2 as a function of the electron energy assuming a 100 nm-thin film. The contrast inversion is well predicted. The intensities show a characteristic maximum at about 8 keV which corresponds to minimum contrast between PCBM and P3HS (Figure 1b). On the basis of the calculations, the bright needle-like structures in Figure 1c are composed of P3HS. A degradation of resolution is visible in the image taken at 4.5 keV (Figure 1a) which suggests the choice of an electron energy higher than the contrast inversion energy for optimized imaging conditions.

Figure 3 shows a comparison of a 15 keV HAADF STEM image and two conventional bright-field TEM images. The sample consists of a blend of poly-(3-hexylthiophene-2,5-diyl):[6,6]-phenyl C61-butyric acid methyl ester (P3HT:PCBM). High contrast between the P3HT and PCBM domains is obtained in the 15 keV HAADF STEM image (Figure 3a). Simulations of the P3HT and PCBM HAADF STEM intensities in analogy to Figure 2 show that P3HT exhibits a lower intensity compared to PCBM. In contrast, in-focus bright-field TEM (Figure 3b) does not provide any structural features due to the small difference of mass thickness of the compounds. Large defocus values (Figure 3c) reveal some contrast. However, large defocus values degrade the resolution to a few nanometers and lead to strong delocalization of the image information which impedes the interpretation of the TEM images and the accurate size determination of the structural features [3].

The semiempirical formalism is not only useful for image interpretation or for the evaluation of optimum imaging conditions, it can be also used to determine either the sample thickness or the density of the sample material for a material with known composition. For this purpose the energy-dependent maximum of the HAADF STEM intensity is exploited. At the intensity maximum a well-defined relation exists between electron energy E, sample thickness t, density ρ, atomic number Z and atomic mass number A given by $t = f \cdot (A \cdot E^2)/(\rho \cdot Z^2)$, whereby the factor f depends on the collection angles of the HAADF detector. Experimentally, the intensity maximum is determined by varying the electron energy until the contrast due to thickness variations is minimized. This is exemplified by the determination of the density of fluorenyl hexa-peri-hexabenzocoronene (FHBC) [4] which is not known up to now. In principle it is sufficient to determine the contrast inversion energy for only one sample with a precisely known thickness. To enhance the quality and the reliability of the

measurement it is nevertheless useful to examine a set of samples with different known thicknesses. Figure 4 shows a plot of the sample thickness vs. the electron energy at contrast inversion, i.e. the energy at the maximum HAADF STEM intensity, for several FHBC films with different thicknesses. The density was then calculated from the prefactor of the quadratic fit function resulting in a value of 1.04±0.29 kg/m³.

1. M.F.G. Klein et al., Journal of Polymer Science Part B: Polymer Physics 50 (2012) p. 198.
2. M. Pfaff et al., Journal of Microscopy 243 (2011) p. 31.
3. M. Pfaff et al., Microscopy and Microanalysis 18 (2012), p.1380.
4. W.W.H. Wong, Advanced Functional Materials 20 (2010) p. 927

5. Acknowledgments: We thank Dr. D. Jones and Dr. W. W. Wong (Bio21 Institute, University of Melbourne) for providing FHBC, and M. F. G. Klein and Dr. A. Colsmann (Light Technology Institute, Karlsruhe Institute of Technology) for the fabrication of organic solar cell absorber layers. The project is funded by the German Research Foundation (DFG).

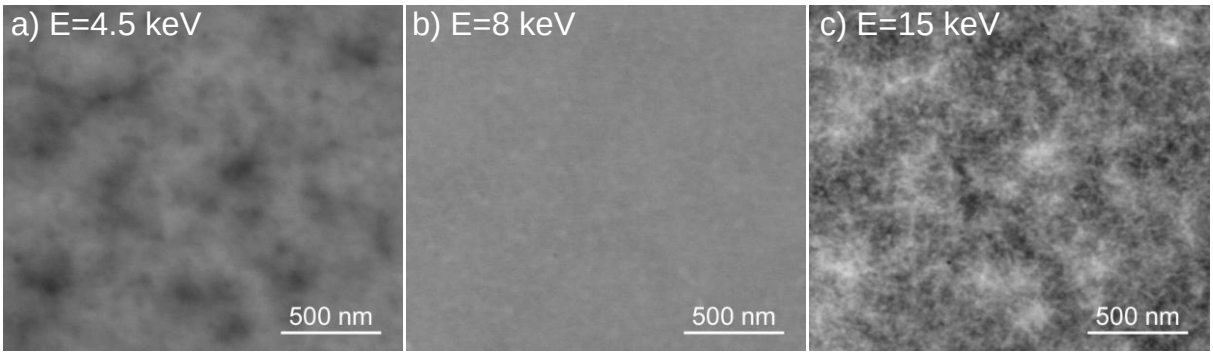

Figure 1. a)-c) HAADF STEM images of a P3HS:PCBM film taken at different electron energies, which show contrast inversion.

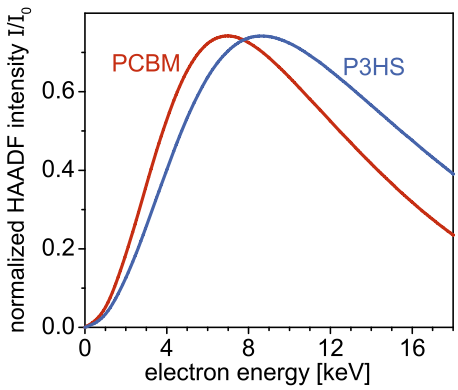

Figure 2. HAADF STEM intensity normalized with the intensity of the incident electrons calculated for 100 nm-thin films of P3HS and PCBM.

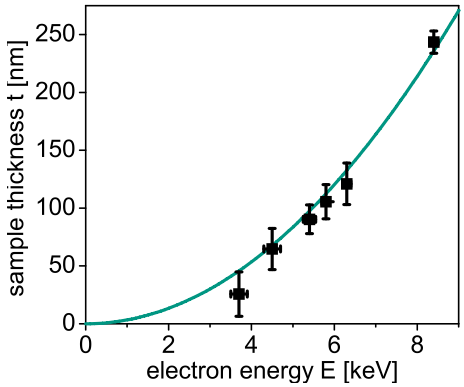

Figure 4. Relation between sample thickness and electron energy for different pure FHBC films at the intensity maximum (contrast inversion point).

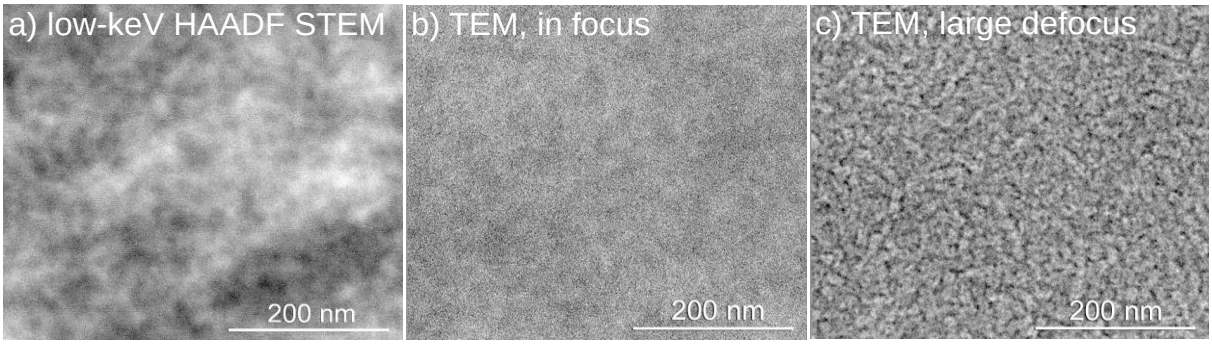

Figure 3. a) HAADF STEM image of a P3HT:PCBM film taken at 15 keV; b) In-focus TEM image taken at 200 keV; c) TEM image with an underfocus of 10 µm. (The images are taken at different sample positions.)

Soft Matter, Polymers, Composites

MS.1.P013
Conjugated polymer blend nanofibers

A.S. Sarac[1]

[1]Istanbul Technical University , Department of Chemistry, Istanbul, Turkey

sarac@itu.edu.tr
Keywords: conjugated polymer, nanofiber, scanning electron microscopy

Multi-functional micro and nano structures of conjugated polymers have received great attention (electrical, optical and magnetic material & devices) Polypyrrole and Polyaniline have advantages i.e.,easy polymerization, high conductivity and good thermal stability;but disadvantages of brittleness and hard processibility,which can be overcomed by the production of their nano composites and blends[1] .

In this study nanofibers of well dispersed poly(anthranilic acid)/ poly(vinyl pyrrolidone) (PANA/PVP) and polyanthranilic acid /polyacrylonitrile(PANA/PAN) blends are obtained by electrospinning .Electrospun nanofibers are characterized in terms of chemical composition, surface morphology, and electrical properties by using NMR, FTIR-ATR, UV-Visible Spectrophotometer (Figure 1A), and Electrochemical Impedance Spectroscopic (EIS) measurements .

SEM images indicated that homogeneous nanofibers of PANA/PVP blends with different weight ratios via electrospinning solutions of DMF or DMF/EtOH mixture (50/50 %w) are obtained. Incorporation of PANA and PVP was confirmed via UV vis spectroscopy and FTIR-ATR spectroscopy. SEM micrographs and the measured diameters of fibers (Figure 1B) indicated that the average diameter decreases from 1110 nm, to 240 nm with the increase of ratio of PANA/PVP in EtOH/DMF. Moreover, in DMF solution average fiber diameter changes from 770 nm to 180 nm with the increase of ratio of PANA/PVP. The low average nanofiber diameters result from the relatively low molecular weight of conductive polymers. Nanofibers also exhibit small diameters when the solutions have higher conductivity due to high solvent polarity. [1, 2]
A linear relationship was obtained between the conductivity values and increase of PANA concentration.

Electrochemical Impedance Spectroscopic measurement was carried out in electrospinning solutions or on nanofibers with Parstat 2263 Electrochemical Analyzer between 0.01 Hz and 100 kHz. Three-electrode system was used consist of nanofiber mat (or Pt in solution) as a working and Pt as a counter and silver as a reference electrode.

PANA increased the charge density of polyacrylonitrile solution, thus stronger elongation forces were imposed to the jets because of the self-repulsion of the excess charges under the electrical field. This yielded electrospun nanofibers with a substantially straighter shape and smaller diameter. The EIS data were fitted with an equivalent electrical circuit (EC) giving a good correlation (Figure 2). SEM analysis of nanofibers showed smaller diameter than for the other nanofibers bearing less ionic groups. Polyathranilic acid as a charge carriers resulted an important influence on the conductivity of nanofibers.

1. S.Cetiner, F. Kalaoglu ,H.Karakas ,A.S. Sarac . Textile Research Journal, 80(2010) 1784
2. S.Cetiner, S. Sen,B.Arman,A.S. Sarac,J.Appl. Polym. Sci,127 (2013)3830

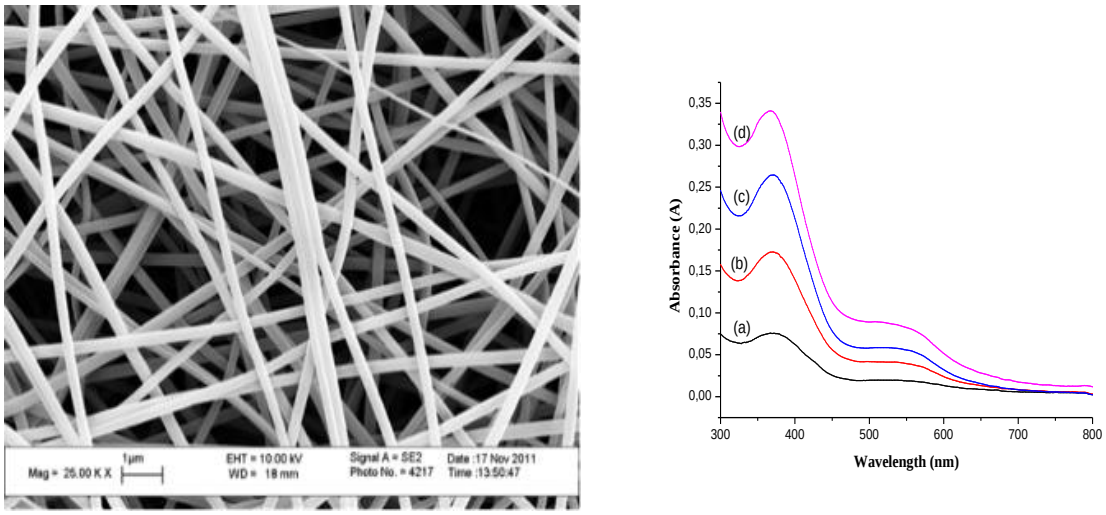

Figure 1. a)UV vis spectra of PANA/PVP with weight ratio of (a) 1/30 (b) 1/20, (c) 1/15, (d) 1/10, in EtOH/DMF mixture ,b)SEM-micrograph of fibers. Weight ratios PANA:PVP = 1:15 ; solvent EtOH/DMF=50/50 (w/w)

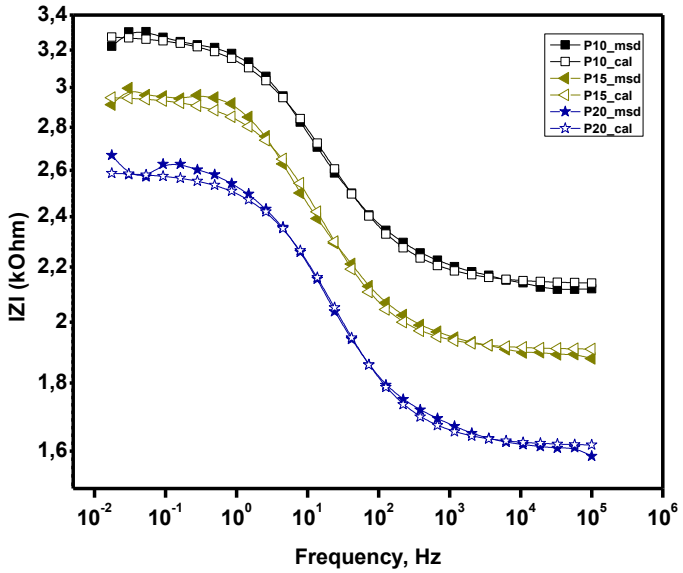

Figure 2. Bode Magnitude plots of PANA/PAN coated nanofibers on ITO-PET in 1 M HCl (measured and calculated data from the EC model well fitted).

Soft Matter, Polymers, Composites

MS.1.P014
In-situ dynamic SPM studies of organic semiconductor thin film growth on test patterns

S. Chiodini[1], A. Straub[1], S. Donati[1], F. Borgatti[1], C. Albonetti[1], F. Biscarini[2]

[1]National Council of Research (CNR), Institute for the Study of Nanostructured Materials (ISMN), Bologna, Italy
[2]Modena and Reggio Emilia University, Life Science, Modena, Italy

The physics of organic field effect transistors is strongly correlated with the organization of the organic semiconductor at multiple length scales. In the case of molecular semiconductors, which are deposited on device test patterns by high- or ultra-high vacuum sublimation, this organization arises from the nucleation and growth phenomena occurring at timescales which are often not easily accessed by standard ex-situ characterization. We use in-situ dynamic scanning force microscopy to study the early stages of growth of a conjugated oligomer semiconductor, viz. sexithienyl (T6), on a technologically-relevant substrate, silicon oxide/silicon wafer and on test patterns with Au electrodes.

In an ultra-high vacuum chamber a Knudsen cell produces a thermal beam of T6 molecules directly under the tip of a variable temperature SPM. Non-contact AFM images of the same sample area is acquired at different times to be mounted into a movie depicting the growth of the ultra-thin film. The coexistence of quasi-layer-by-layer and 3D growth modes, the latter promoted by heteronucleation on surface defects, is observed. By performing the experiment at different temperatures, we extract the relevant molecular energy barriers of T6 thin film growth: desorption energy (0.53 eV), layer-dependent diffusional barriers (0.15-0.20 eV), Erlich-Schwoebel barrier (0.070 eV). The latter is cause of the transition from layer-by-layer to island growth, which appears to be universal occurrence in organic semiconductor growth with important implications in the charge transport in organic field effect transistors.

Soft Matter, Polymers, Composites

MS.1.P015
Pentacene thin films for organic spintronics

P. Graziosi[1,2], M. Prezioso[1,3], I. Bergenti[1], A. Riminucci[1], D. Brunel[1,4], C. Newby[1,5], F. Li[6], Y. Zhan[1,6] M. Fahlmam[6], M. Ghidini[7], D.J. Busquets Mataix[2], D. Pullini[8], A. Dediu[1]

[1]CNR, ISMN, Bologna, Italy, Italy
[2]Universitat Politecnica de Valencia, Valencia, Spain, Spain
[3]University of California, Department of Electrical and Computer Engineering, Santa Barbara - USA, Italy
[4]CEA, IRAMIS, Service de Physique de l'Etat Condensé (CNRS URA) 2464, France, France
[5]Cornell University, Materials Science and Engineering Department, Ithaca - USA, United Kingdom
[6]Linkoping University, Department of Physics, Chemistry and Biology, Sweden, Sweden
[7]University of Parma, Italy, Italy
[8]Centro Ricerche Fiat, Orbassano, Italy, Italy

patrizio.graziosi@gmail.com

The utilization of high mobility organic semiconductors in spintronics is expected to provide a breakthrough improvement in the device operation. Pentacene is a reference material of choice for most OFET investigations and thus is among the main candidates for spintronic applications. We present here the study of the growth dynamics of pentacene on ferromagnetic oxide surfaces, namely on La0,7Sr0,3MnO3 (LSMO) manganites, with a link to vertical pentacene based spin valves prototype devices. It is important to mention that no magnetoresistance has been detected in similar geometry with cobalt electrodes [1].

Pentacene (Pn) films in the thickness range of 3-100 nm were thermally evaporated in UHV conditions on LSMO films at several deposition temperatures. A strictly diffusion limited, thermically activated (Arrhenius-type) growth was found. The molecule diffusion was found to have a strongly anisotropic character. Pentacene molecules form very wide and extended flat islands having size of a few microns. These large structures are delimited by quite high steps and show terraced features. The step height was estimated independently via AFM characterizations and Near Edge X-ray Absorption Fine Structure (NEXAFS) studies and constitutes 1.5 nm, corresponding to 70° angle between molecule axis and surface plane [2].

Pentacene film formation on LSMO layers is quantitatively understood by involving pentacene molecules diffusion on the bare substrate; stable nuclei formation when a certain critical number of molecules meet; nuclei growth, migration, coalescence; molecule diffusion on top of nuclei. A □T of about 15°C (from 30°C to 45°C) is sufficient to break the interaction, pentacene develops a weak interaction with the substrate. Pentacene growth appears to be a strictly diffusion limited, a thermally activated, Arrhenius type, process [3].

Vertical prototype spin valve devices are presented based on the Pentacene/LSMO interface and on the Pentacene/Alq_3/LSMO engineered interface, where not only the tuned morphology but also the modified interface energetic are shown to play a major role.

1. T. Ikegami, I. Kawayama, M. Tonouchi, S. Nakao, Y. Yamashita and H. Tada, Appl. Phys. Lett. 92 (2008) 153304.
2. F. Li, P. Graziosi, Q. Tang, Y. Zhan, X. Liu, V. Dediu and M. Fahlman Phy. Rev. B 81 (2010) 205415.

3. P. Graziosi, Material engineering in hybrid spintronic devices, PhD thesis, 2010.

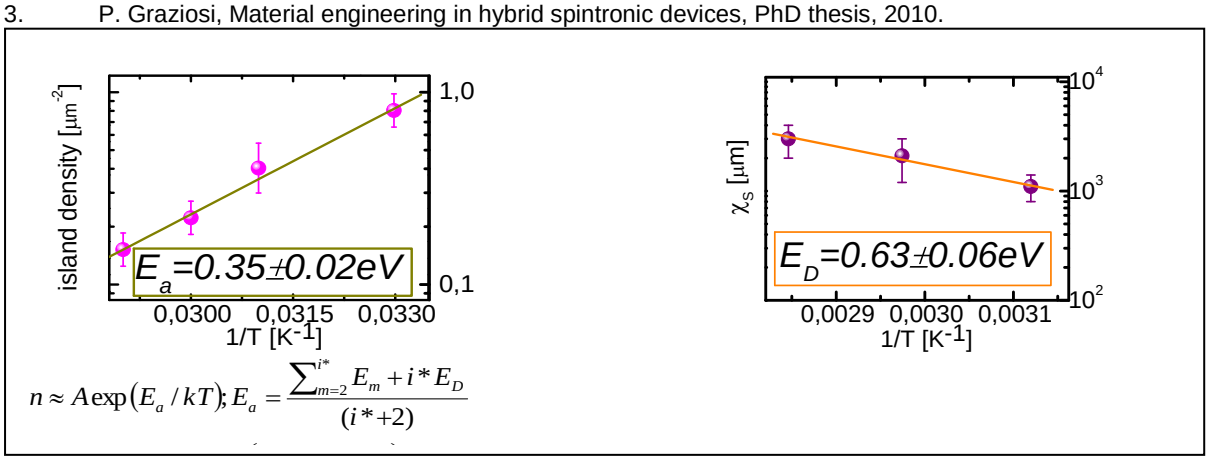

Figure 1. Arrhenius plots of the pentacene stable islands density and diffusion length obtained from 2 ML coverage of the LSMO surface, detected by AFM.

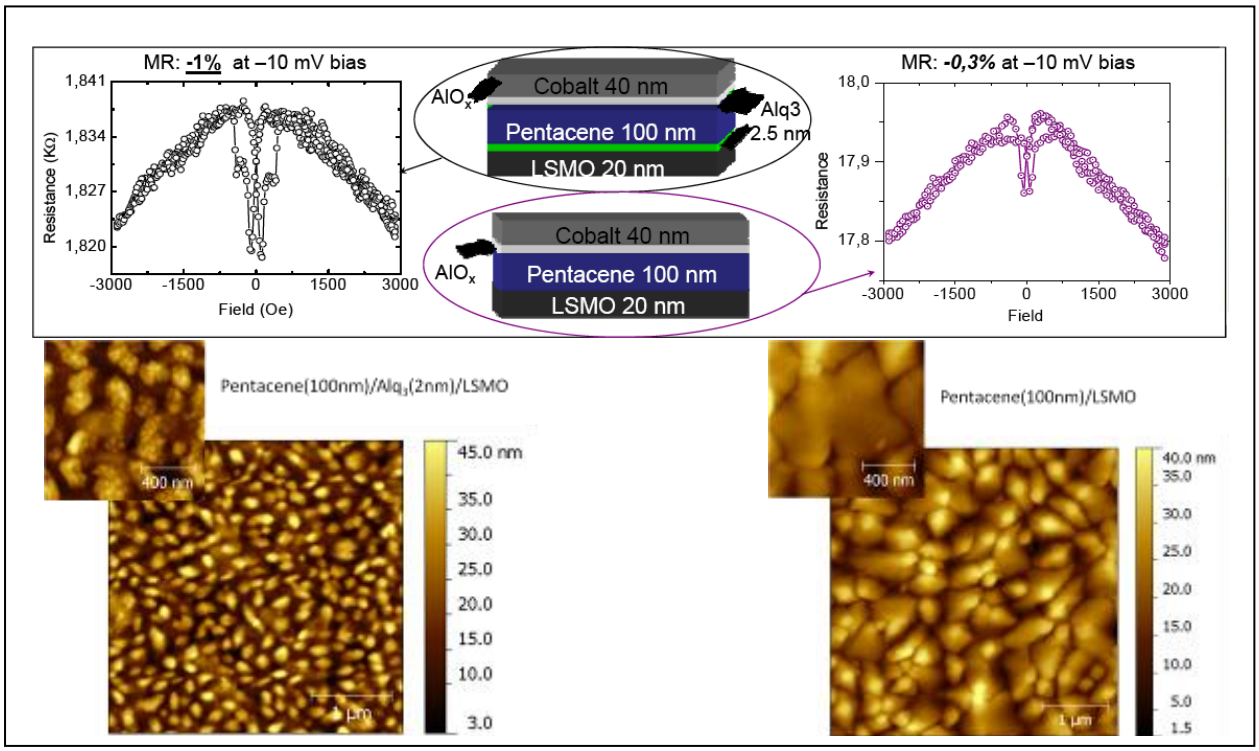

Figure 2. Prototype spin valve devices based on bare pentacene (right) and on Alq_3-tailored interfaces (left) as described in the sketch. In the bottom row the respective AFM images are shown.

Soft Matter, Polymers, Composites

MS.1.P016
Focused ion beam processing of low melting polymers: new perspectives due to optimized patterning strategies

R. Schmied[1], A. Orthacker[1], B. Chernev[2], G. Trimmel[3], H. Plank[2]

[1]Center for Electron Microscopy, Graz, Austria
[2]University of Technology, Institute for Electron Microscopy and Fine Structure Research, Graz, Austria
[3]University of Technology, Institute for Chemistry and Technology of Materials, Graz, Austria

roland.schmied@felmi-zfe.at, harald.plank@felmi-zfe.at
Keywords: soft matter, thermal stress, focused ion beam

During the last decade focused ion beam (FIB) processing became of increased importance due to its unique possibilities of site specific specimen manipulation. So far, FIB processing has been well established for transmission electron microscopy related ultrathin lamella preparation, but also gained importance as a method for 3D metrology and 3D surface structuring from the micro- to the nanoscale [1]. Due to its flexibility and straightforward implementation character, it represents a rapid prototyping tool for science and technology. Aside from these undoubted advantages, FIB processing entails unwanted side effects, such a spatially confined ion implantation, surface or bulk amorphization [1] and partial high thermal stress [2,3]. While the former two are intrinsic properties and therefore invariable, local heating effects have been shown to depend strongly on the patterning strategy. The reduction of this technically induced heating is of particular relevance for low melting materials such as polymers and biological material [4,5] but requires an improved understanding of the thermal effects during scanning.

As a starting point we discuss briefly a recently introduced alternative patterning strategy, which strongly reduced local temperatures by a decoupling from technically induced effects [6]. As a second point different polymers are subjected to this alternative process and compared to classical strategies. Characterization includes morphology via scanning electron microscopy (SEM), atomic force microscopy (AFM) and Kelvin force microscopy (KFM) as well as chemistry via Raman spectroscopy (RS). It will be shown that for FIB processing the materials can be roughly divided into two classes: 1) polymers that would mainly undergo cross-linking (CL) when exposed to thermal stress; and 2) others that would rather react by scissioning (SC) under the same conditions. This kind of reaction to thermal stress has a great influence on the morphology received when patterning.

Based on these results, spatially resolved simulations of the temperature evolution have been performed ranging from single ion events towards full patterning processes (Figure 1). The comparison with the experimental data suggest that CL materials increase their rigidity due to thermally induced cross linking while SC polymers reveal an increasing mobility on the micro-and nanoscale, which finally leads to extremely rugged surface structures. The careful adaption of the alternative patterning strategy to material related peculiarities, observed during FIB single pulse events, allows finally for strongly improved morphological stability (Figure 2). Finally, it is shown that the new patterning strategies decrease chemical degradation as well, which is of high interest for the final application or subsequent processes.

The study demonstrates the capabilities of FIB processing for low melting materials by using adapted scan strategies which can be easily implemented in most FIB systems. By that, new possibility for FIB based rapid prototyping on low melting materials might open up which have been considered as very complicated or even impossible before.

1. J. Mayer, et al., MRS Bulletin 2007, 32, 5, 400 – 407
2. N. Shukla, et al., Appl. Surf. Sci. 2009, 256, 2, 475 – 479
3. C.A. Volkert, A.M. Minor, MRS Bulletin 2007, 32, 5, 389 – 399
4. M.F. Hayles, et al., J. Micr. 2007, 226, 3, 263 – 269
5. J. Brown et al. in “Introduction to ion beam biotechnology”, Springer, New York, 2006F.
6. R.Schmied et al., RSC Adv., 2012, 2 (17), 6932 – 6938

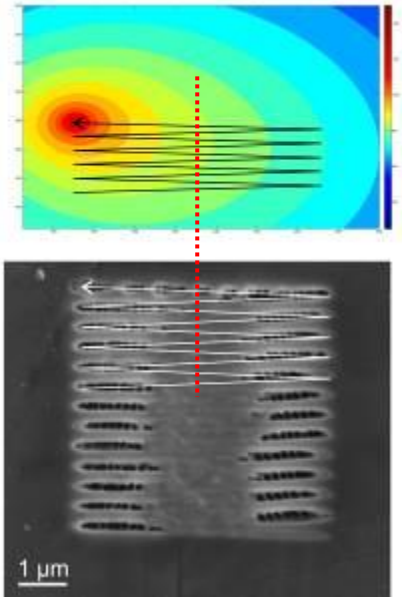

Figure 1. Simulated temperature evolution (top) during zig-zag scanning which reveals asymmetric temperature distributions and residual towards the center of the scanning lines (dotted red line). The correlated experiments (bottom) show a blurry area at the center which stems from temperature assisted material creeping. For higher temperatures closer to the end of the line, the material is immediately evaporated leading to deep trenches.

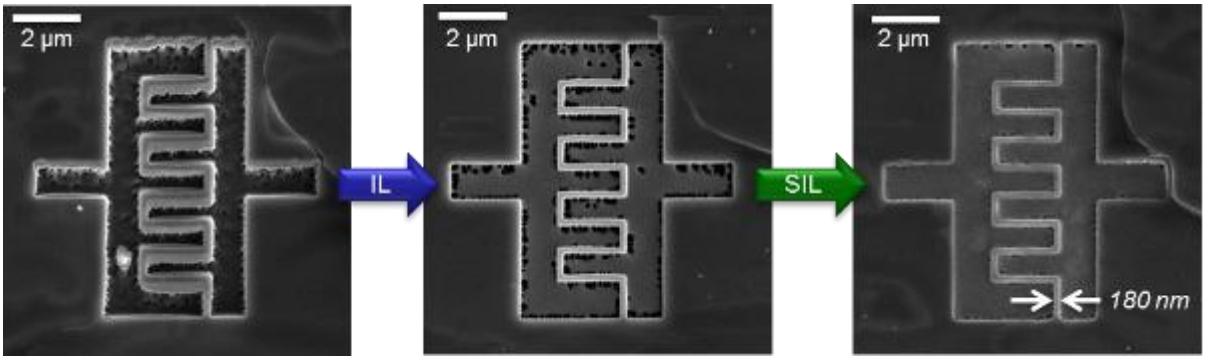

Figure 2. FIB processed polymer sample structured via classical approaches (left). While the introduction of an alternative interlacing (IL) strategy improves the morphological stability, the full potential is only exploit after parameter adaption to material dependent properties via smart interlacing (SIL) processing.

Soft Matter, Polymers, Composites

MS.1.P017
Ultra-structure of oil/water emulsions

L.H.S. Jensen[1], C. Loussert[2], B. Humbel[2], A.F. Horn[3], C. Jacobsen[3], N.S. Nielsen[3], A. Horsewell[4]

[1]Technical University of Denmark, Center for Electron Nanoscopy, Kgs. Lyngby, Denmark
[2]Université de Lausanne, Electron Microscopy Facility, Lausanne, Switzerland
[3]Techical University of Denmark, National Food Institute, Kgs. Lyngby, Denmark
[4]Technical University of Denmark, Department of Mechanical Engineering, Kgs. Lyngby, Denmark

losj@cen.dtu.dk
Keywords: emulsions, cryo-SEM, freeze substitution

Addition of fish oil to industrial food products is of interest to both the food industry and consumers for reasons such as health benefits and added commercial value. Fish oil is rich in long chain omega-3 fatty acids, which contain a large number of double bonds. This causes the omega-3 fatty acids to be highly susceptible to oxidation. This feature limits the shelf-life of fish-oil enriched food products. Strategies for limiting oxidation and thus increasing the shelf-life of potential products are necessary for commercial production. One such strategy is to add the oil as an emulsion rather than as pure fish-oil. Studies so far have indicated that emulsification of the fish oil changes the oxidative stability of the product but whether emulsification is an advantage or not seems to depend on the food matrix to which the emulsion is added [1, 2]. It is therefore of interest to look at the pure emulsions to assess what determines the oxidation. It has been proposed that oxidation is, to some extent, dependent on the structure of the emulsion; including oil droplet size distributions and the thickness of the interface between oil and water. This interface can be stabilized by food grade emulsifiers such as proteins and phospholipids from milk.

The main objective of this study is to characterize fish oil/water emulsions focusing on oil droplet size distribution and characterization of the oil/water interface (thickness and organization). Because of the expected size of the interface layer, a few nm, electron microscopy appears to be the technique of choice to study these samples. We analysed several oil/water emulsions, stabilized by sodium caseinate as emulsifier, prepared in different ways: chemical fixation combined with/ room temperature embedding in resin, cryofixation combined with/ freeze substitution, and cryofixation combined with / cryo imaging (freeze-fracture cryo-SEM).

The high water content of these samples is the first problem to solve for the analysis of the samples. Therefore we developed agar pockets for encapsulation or used capillary tubes for conventional protocols (e.g. chemical fixation and room temperature embedding). Chemical fixation of these samples is challenging because of the need to minimize ultra-structural modifications of the samples especially during the dehydration step which can induce artefacts like collapsing and shrinkage. The chemical fixation appears to be a promising way to prepare the emulsions. Indeed, we obtained a first view of the emulsions and the organisation of the interface layer surrounding the oil droplets. Cryofixation is a preparation method, which allows observing the sample in a “close to native” state, and we could observe the oil/emulsifier/water interface more precisely. We observed that freeze fractured frozen samples observed in cryo-SEM (Figure 1) are really similar to the freeze substituted samples (Figure 2). With TEM we could even observe the network of protein surrounding the oil droplets (Figure 2).

With this work, we wish to demonstrate the need of combining different microscopic approaches to access the ultrastructure of the oil/water emulsions due to their complexity and instability.

1. N.S. Nielsen and C. Jacobsen. Int J Food Sci Tech 44 (2009) 1536-1546
2. M. B. Let, C. Jacobsen and A. S. Meyer. J Agric Food Chem 55 (2007) 7802-7809
3. The micrographs were recorded at Electron Microscopy Facility, Université de Lausanne and Center for Electron Nanoscopy, Technical University of Denmark.

4. This research was supported by the Danish Food Industry Agency under the Ministry of Food, Agriculture and Fisheries

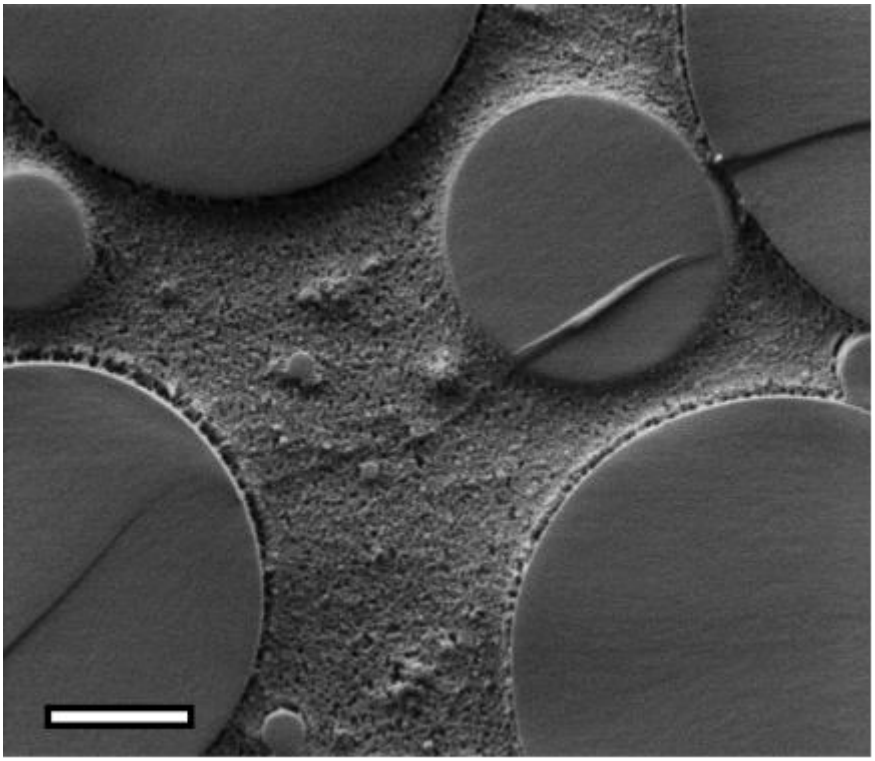

Figure 1. Emulsion containing 70% fish oil and 2.8% sodium caseinate. Freeze fracture cryo-SEM. Scalebar 2 µm.

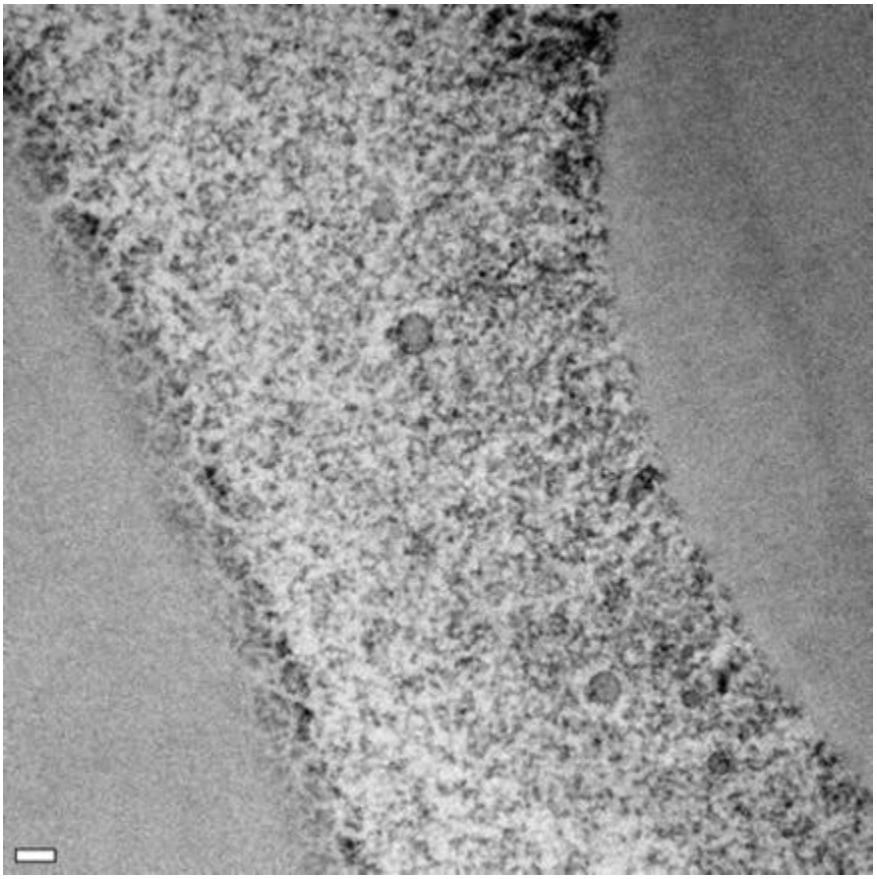

Figure 2. Emulsion containing 70% fish oil and 2.8% sodium caseinate. The micrograph depicts the edge of two oil droplets and the protein containing water phase between them. Freeze substitution, TEM. Scalebar 100 nm.

Ceramics, Oxides, Geomaterials

MS.2.018
The impact of electron microscopy on revealing phase separation mechanisms in alloy thin films.

G. Radnóczi[1], F. Misják[1], D. Biro[2], P.B. Barna[1,2]

[1]Research Centre for Natural Sciences, HAS, This Films, Budapest, Hungary
[2]Sapientia-Hungarian University of Transylvania, Faculty of Technical and Human Sciences, Târgu-Mures, Hungary

radnoczi@mfa.kfki.hu
Keywords: alloy films, phase separation, growth mechanism, spinodal decomposition, TEM

The structure zone diagram and growth mechanisms of one component thin films has been worked out on the basis of electron microscopic evidences and is summarized in [1]. These mechanisms describe atomic arrangements only on the growth surface, usually recalled as kinetic segregation resulting in nucleation and growth of phases on the growth surface including their mutual overgrowth, repeated nucleation and successfully treat the effect of contaminants. A similar and comprehensive knowledge would be necessary for the films composed from two and more components. As direct observation of atomic movements is not possible we have to come to these processes by indirect methods, by deducing – aided by simulations- from all possible structural details the atomic processes leading to the formation of the structure under investigation. These structural details include the formed phases, their morphology (size and shape of grains), orientation relations (texture), surface properties as well as very local analytical information on the distribution of components and impurities. Transmission electron microscopy is one of the most direct methods for providing the above nm or even atomic scale structural information. The scope of the present investigation is to model of the growth mechanism and the basic atomic mechanisms and kinetics of self organized formation of nanostructures in two component films based on structural information provided basically by TEM. We have chosen binary systems to show on practical examples the role of TEM in revealing the phase separation processes in them. Thin films of practically non-mixing components were co-deposited. $(Ti_{1-x}Al_x)_{1-y}Y_yN$ and $Ti_{0.45}O_{0.20}N_{0.35}$ thin films were grown at 550^{o}C and 400^{o}C by reactive unbalanced magnetron sputtering in N_2+Ar and N_2+Ar+ O_2 gas mixtures, respectively [2, 3]. Structural characterization was carried out by conventional TEM using a Philips CM-20 microscope at 200 keV and high resolution measurements were carried out using a JEOL 3010 microscope at 300 keV. For chemical analysis of the films a NORAN Energy Dispersive Spectrometer attached to the CM20 microscope and a Gatan TRIDIEM Electron Energy Loss Spectrometer (EELS) on the JEOL 3010 microscope were applied.

TiN and AlN are both close packed cubic and hexagonal structures, correspondingly. They are non-mixing at the growth temperature in the whole composition range. Due to these circumstances, very special substructure can develop in TiN based alloy films. Structural characteristics typical for one phase growth (V-shaped columnar morphology and texture) have been observed also in $(Ti_{0.41}Al_{0.57})Y_{0.02}N$ thin films. The columns are composed of 3~5 nm in size fcc (TiN) and hcp (AlN) crystallites forming alternating stacks and exhibiting epitaxial relation of $\{111\}_{TiN}$ and $<110>_{TiN}//\{0002\}_{AlN}$ and $<11\text{-}20>_{AlN}$. The formation mechanism of these columns must include the growth of supersaturated solid solution of one phase hcp TiAlN, followed by a phase separation through decomposition. Only this mechanism can generate identically oriented crystallites within the columns.

Oxygen is one of the most common contaminant growing nitride films. Oxygen doping can modify both the morphology and texture of the TiN films. It has been found that beyond 15 at% oxygen doping the columnar morphology is preserved, however, the <111> texture is changed to the <001>. The detailed structure analysis of the $Ti_{0.45}O_{0.20}N_{0.35}$ oxynitride films discovered a substructure in the bulk of the TiN(O) single crystal columns. In the cross sectional TEM images it is showing up in form of fibre-like morphology and in a honeycomb-like supernetwork in the plane view TEM specimens. Electron microscopy revealed that initial phase separation by spinodal decomposition occurred in the intra-grain structure of $(Ti_{0.41}Al_{0.57})Y_{0.02}N$ films. This process, taking place still as a growth event is responsible for the formation of the epitaxial two phase nanocomposite within each column in which the similarity of the lattices of separating phases plays important role.

The observed growth morphologies for the $(Ti_{0.41}Al_{0.57})Y_{0.02}N$ films correspond to columnar morphology and the corresponding texture is developing by competitive crystal growth. In the $Ti_{0.45}O_{0.20}N_{0.35}$ films the texture changes from <111> to <100> and an intra-grain superstructure appears by a surface segregation mechanism as the oxygen content increases.

1. I.Petrov, P.B. Barna, L. Hultman, J.E. Greene, J. Vac. Sci. Technol. A21(2003)S117-127
2. L. Székely , G. Sáfrán, V. Kis, F. Misják, M. Moser, P. H. Mayrhofer, P. B. Barna; to be published
3. M.F. Hasaneen, D. Biro, L. Székely, P. Nemes-Incze, P.B. Barna, Vacuum 86 (2012) 2105-2108
4. The Hungarian National Science Foundation (OTKA, K-81808 project) is acknowledged for financial support. F. Misják also acknowledges the financial support from the János Bolyai Research Scholarship of the Hungarian Academy of Sciences.

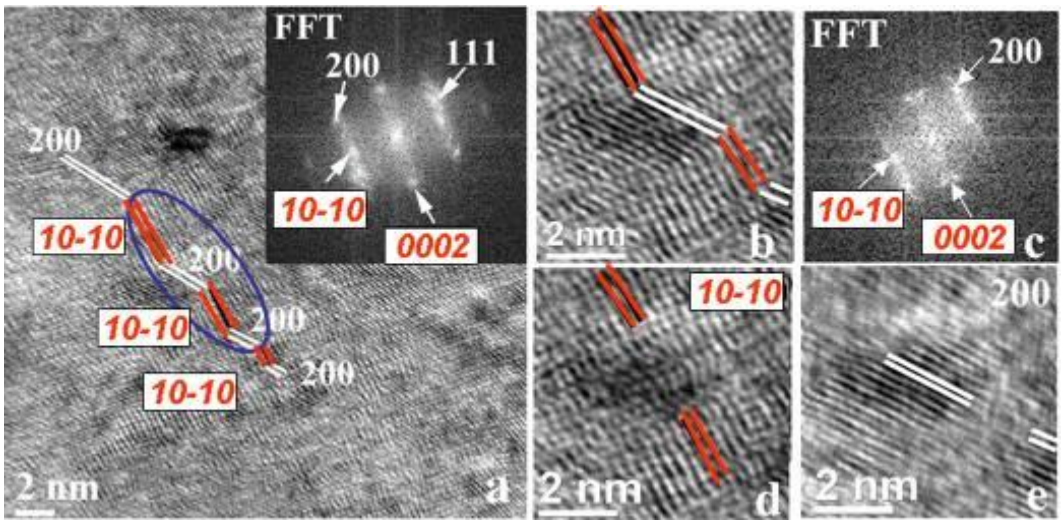

Figure 1. The HREM image of the $(Ti_{0.41}Al_{0.57})Y_{0.02}N$ film with inserted FFT pattern (a), the HREM image with two pairs of alternately stacked hcp and fcc nanocrystals (b) and corresponding FFT pattern (c); (d) and (e) are complementer HREM images taken with the hcp and fcc reflections, respectively.

Ceramics, Oxides, Geomaterials

MS.2.019
Cation stoichiometry, microstructure and properties tuned by oxygen vacancies in epitaxial manganite and manganite-based heterostructures

Z. Li[1], M. Bosman[2], W. Zhu[3], Z.-L. Dong[1]

[1]Nanyang Technological University, Materials Science and Engineering, Singapore, Singapore
[2]Institute of Materials Research and Engineering, Singapore, Singapore
[3]Nanyang Technological University, Singapore, Singapore

zldong@ntu.edu.sg
Keywords: cation stoichiometry, epitaxial, $La_{0.8}Sr_{0.2}MnO_3$ films

$La_{1-x}Sr_xMnO_3$ is viewed as one of the key building blocks of oxide spintronics devices due to its rich physical properties. However, when manganite and other materials are engineered together, the induced interfacial dead layer can reduce the device performance such as the tunneling current or magnetoelectric coupling effect. In this study, transmission electron microscopy and synchrotron-based spectroscopic techniques were used to demonstrate that the oxygen vacancies during film growth can serve as a critical factor in tuning the cation stoichiometry in pulsed laser deposited $La_{0.8}Sr_{0.2}MnO_3$ films. When the oxygen vacancies are induced, A-site cations (La/Sr) are in excess near film/substrate interface [1]. Simultaneously, SrO rocksalt monolayer is formed due to the migration of the Sr cations. Consequently, a gradient of Mn nominal valence is observed along the film growth direction according to the electron energy loss spectroscopy results. Figure 1 shows the comparison of Mn $L_{2,3}$ edge spectrums near film/substrate interface and film surface. The lattice image of the manganite film was shown in Figure 2, indicating good crystalline quality. This finding suggests that the oxygen pressure serves as one extrinsic tuning parameter for the interfacial dead layer and hence control over device properties. Furthermore, we studied the oxygen pressure-mediated microstructure and multiferroic properties of the $La_{0.8}Sr_{0.2}MnO_3/BaTiO_3$ superlattices. By atomic-resolution electron microscopy, piezoelectric force microscopy and magnetic properties measurements, we demonstrated that the degradation of multiferroic properties in the superlattices is strongly correlated to the local strain fields and cation off-stoichiometry induced by cation defects. When the defects which include pure edge dislocations and planar defects are eliminated by increasing oxygen pressure during growth, near bulk ferroelectric and ferromagnetic properties can be achieved. In summary, our work suggests that controlling the oxygen pressure during growth is crucial to achieving better interfaces, surfaces and microstructures, paving the way for the fabrication of complex oxide devices with high performance.

1. Z. P. Li, M. Bosman, Z. Yang, P. Ren, L. Wang, L. Cao, X. J. Yu, C. Ke, M. B. H. Breese, A. Rusydi, W. G. Zhu, Z. L. Dong, and Y. L. Foo, Advanced Functional Materials, 22 (2012), p 4312.
2. The authors are thankful for financial support from the Nanyang Technological University research scholarship and Singapore Ministry of Education AcRF Tier 2 grant (Reg No 200604393R).

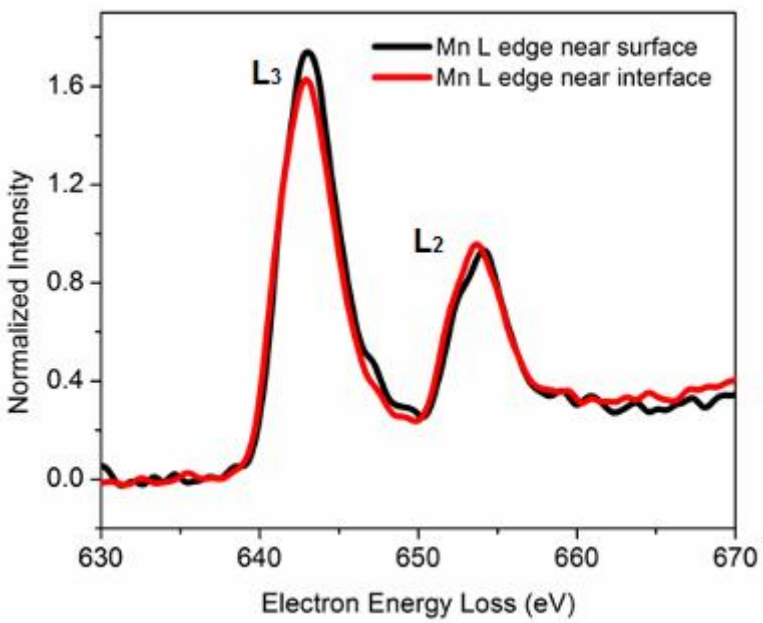

Figure 1. The EELS profiles of Mn $L_{2,3}$ edges taken near the $La_{0.8}Sr_{0.2}MnO_3/SrTiO_3$ interface and near LSMO surface of the sample grown under low oxygen pressure.

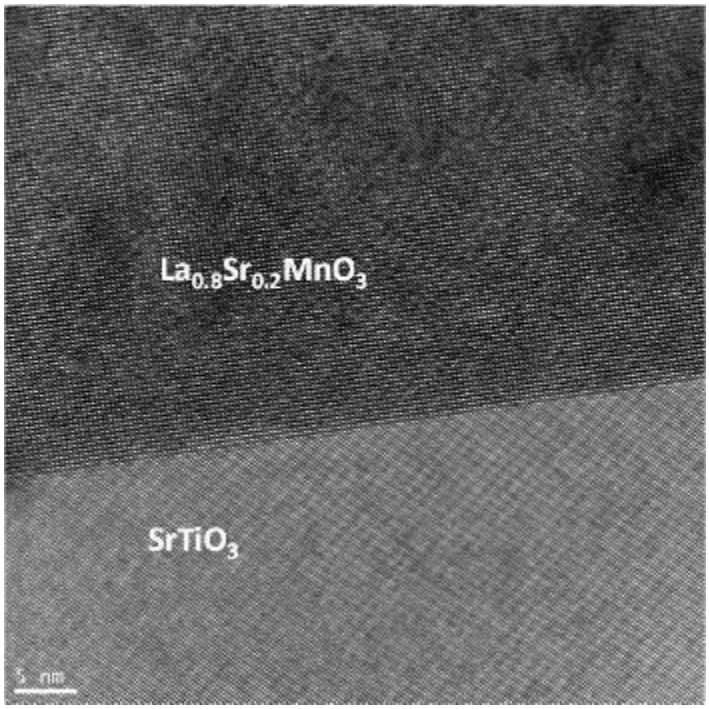

Figure 2. The high resolution TEM image of the interface between $La_{0.8}Sr_{0.2}MnO_3/SrTiO_3$.

Ceramics, Oxides, Geomaterials

MS.2.020
Cation diffusion and phase formation at Sm_2O_3/CeO_2- and Gd_2O_3/CeO_2-interfaces

C. Rockenhäuser[1], B. Butz[2], D. Gerthsen[1]

[1]Laboratorium für Elektronenmikroskopie, Karlsruhe, Germany
[2]Center for Nanoanalysis and Electron Microscopy (CENEM), Department Werkstoffwissenschaften, Erlangen, Germany

rockenhaeuser@kit.edu
Keywords: doped CeO_2, Sm diffusion, Gd diffusion, phase transformation, transmission electron microscopy (TEM), energy-dispersive x-ray spectroscopy (EDXS)

Due to their high oxygen conductivity the intensely studied Samarium (Sm) and Gadolinium (Gd) doped CeO_2 systems are promising candidates for different applications [1], e.g. as electrolyte in solid oxide fuel cells [2], or as catalysts [3]. However, basic characteristics of the Sm- and Gd-doped CeO_2 are not yet well understood. In particular, interdiffusion coefficients of Sm- and Gd-ions in CeO_2 are not known which were determined in this study at application-relevant temperatures between 970 °C and 1170 °C. For this purpose, Sm_2O_3 and Gd_2O_3 films with 150 nm thickness were deposited on dense, polycrystalline CeO_2 substrates by pulsed laser deposition (PLD). After deposition, annealing at temperatures between 970 °C and 1270 °C was conducted for up to 100 h in an oxidizing atmosphere. Analytical and structural characterization was performed by transmission electron microscopy (TEM). Interdiffusion profiles were acquired by energy-dispersive X-ray spectroscopy and electron energy-loss spectroscopy in an FEI TITAN^3 80-300. Structure determination was performed by comparing Fourier transforms of high-resolution TEM images and selected area electron diffraction patterns with simulated of diffraction patterns. Fig. 1 shows the microstructural evolution of the Gd_2O_3 films on CeO_2 as a function of annealing temperature. A reaction layer (RL) with increasing thickness is formed between the Gd_2O_3 film and the CeO_2 substrate after annealing at temperatures between 970 °C and 1170 °C for 100 h (Figs. 1a-d) whereas the Gd_2O_3 film is completely consumed after annealing at 1270 °C for 100 h (Fig. 1e). Structure determination yields the fluorite structure for CeO_2 and the bixbiyte Ia3 structure for Gd_2O_3 and the RL. Concentration profiles were acquired between the Gd_2O_3 films and the substrate (Fig. 3a after, e.g., annealing at 1070 ^oC). Concentration-independent diffusion coefficients D were evaluated by fitting the diffusion couple solution of Fick's second law $C(x,t) = \frac{C_0}{2} erfc(\frac{x}{2\sqrt{Dt}})$ to the experimental concentration profiles with the Gd-concentration C which depends on the position x and time t. Assuming an Arrhenius-type behaviour for the diffusion coefficients $D = D_0 \exp(\frac{-H}{k_b T})$, an activation enthalpy H=2.29 eV/atom and a frequency factor D_0=9.09·10^{-11} cm^{2}s^{-1} is determined from the fit of a straight line in the Arrhenius plot Fig. 3b. Sm_2O_3 on CeO_2 shows a different behavior. For low annealing temperatures, a direct interface between the monoclinic Sm_2O_3 film and CeO_2 is retained (Fig. 2a after annealing at 970 ^oC for 100 h) with small reaction volumes with bixbyite structure at the interface (Fig. 2b after annealing at 1070 ^oC for 100 h). Fig. 4a shows an interdiffusion profile between monoclinic Sm_2O_3 and CeO_2 after annealing at 1070 ^oC. At higher temperatures continuous RLs with bixbyite structure (RL 1) and the cubic $I2_13$ structure (RL 2) and increasing width are formed (Figs. 2c,d after annealing at 1170 ^oC and 1220 ^oC for 100 h). RL1 and RL2 have a homogeneous cationic composition (see concentration profile Fig. 4b) instead of a concentration gradient as in the Gd-samples. The Sm_2O_3 has inhomogeneous cationic composition and a separation between RL I and RL II is not observed after annealing at 1270 ^oC (Fig. 2e). From the samples with direct monoclinic Sm_2O_3/CeO_2-interface diffusion coefficients were determined for temperatures between 970 °C and 1170 ^oC. Shorter annealing times were used for higher annealing temperatures to prevent formation of a continuous RL in the bixbyite structure. The Arrhenius plot (Fig. 4c) yields an activation enthalpy for interdiffusion of 2.69 eV/atom and a frequency factor of D_0=8.268·10^{-10} cm^{2}s^{-1}. In summary, interdiffusion at the Gd_2O_3/CeO_2-interface proceeds faster than at the Sm_2O_3/CeO_2-interface.

1. Dirstine et al., Journal of the Electroceramic Society 126 (1979) p. 264.
2. Mai et al., Solid State Ionics 177 (2006) p. 2103.
3. Laosiripojana et al., Journal of Catalysis 276 (2010) p. 6.
4. Acknowledgement: We thank Dr. N. Schichtel and Prof. J. Janek (University of Giessen) for the PLD deposition of Gd_2O_3 and Sm_2O_3 films.

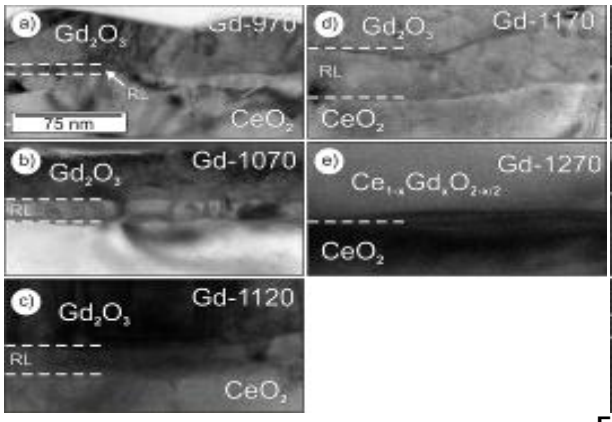

Figure 1. Cross-section bright-field TEM images of the interface region between Gd_2O_3 thin film and CeO_2 substrate after annealing at a) 970 °C, b) 1070 °C, c) 1120 °C, d) 1170 °C, and e) 1270 °C for 100 h.

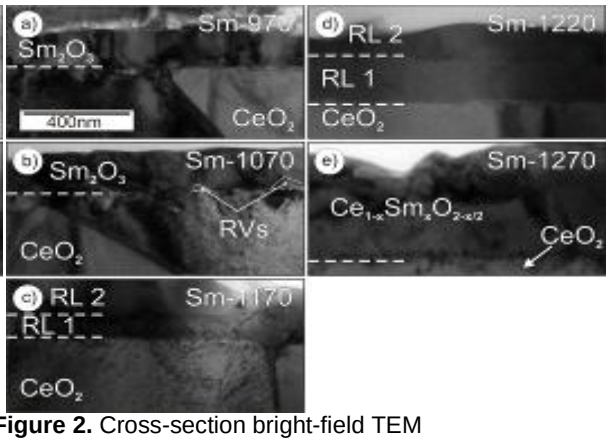

Figure 2. Cross-section bright-field TEM images of the interface region between Sm_2O_3 thin film and CeO_2 substrate after annealing at a) 970 °C, b) 1070 °C, c) 1170 °C, d) 1220 °C, and e) 1270 °C for 100 h.

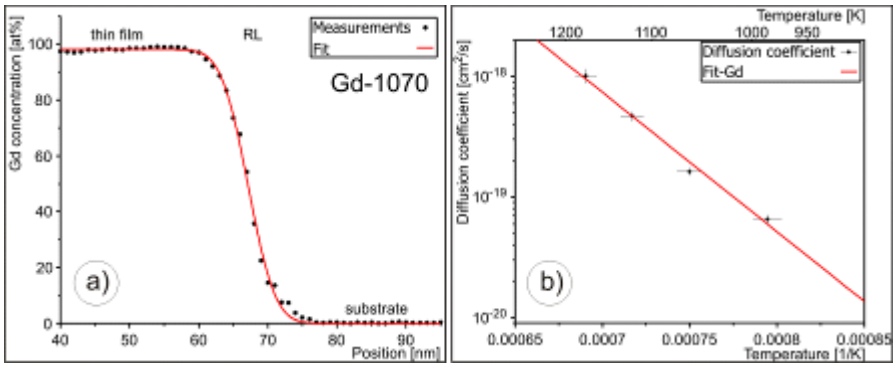

Figure 3. a) Gd-concentration profile across the RL after annealing at 1070 °C for 100 h, and b) Arrhenius plot of the diffusion coefficients as a function of the inverse temperature.

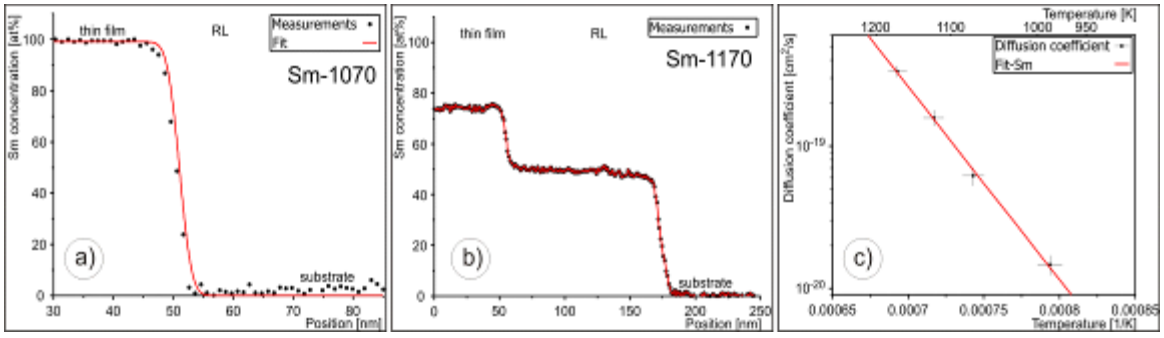

Figure 4. Sm-concentration profiles across the RL after annealing at a) 1070 °C, and b) 1170 °C, for 100 h and c) an Arrhenius plot of diffusion coefficients as a function of the inverse temperature.

Ceramics, Oxides, Geomaterials

MS.2.021
Detection and imaging of light elements in Mg-Al-spinel

M.M. Müller[1], H.-J. Kleebe[1]

[1]TU Darmstadt, Geomaterial Science, Darmstadt, Germany

mueller@geo.tu-darmstadt.de
Keywords: Spinel, LiF, probe-corrected imaging

$MgAl_2O_4$ is considered a promising material for optical applications and hence object to research for more than 40 years worldwide [1-3]. The densification mechanism of $MgAl_2O_4$ (hereafter termed spinel) doped with lithium fluoride (LiF) as transparent ceramic has been intensively studied.

Optical transparency requires densification to a value near the theoretical density since residual porosity, which acts as scattering source, has to be eliminated. In addition, impurities and secondary phases have to be removed to avoid scattering or absorption of the transmitted radiation (i.e. visible or IR light). LiF greatly reduces the sintering temperature and facilitates enhanced densification at low temperatures. However, the basic mechanisms behind the sintering process are still not fully understood, as neither LiF nor an additional secondary phase is detectable in the final product.

Based on individual studies Reimanis, Kleebe and Rozenburg [4-6] postulated three major processes during sintering of spinel with LiF including (i) Enhanced volume diffusion by incorporation of O-vacancies (ii) Dissolution – Reprecipitation and (iii) Wetting – Dewetting: At this early stage of sintering, the densification mechanism can be described by a classical liquid phase sintering process facilitating particle rearrangement. At temperatures above 1000°C, no secondary phase is detectable along grain boundaries. In a recent work it was shown that these mechanisms occur simultaneously interacting with each other [7], however, the verification was made by indirect methods as for example the double fringe technique introduced by D.R. Clark [8] for the wetting-dewetting mechanism as shown in Figure 1. In this presentation we will show exemplarily the reason for the twice changing mean inner potential creating the double Fresnel fringes as an example of the high potential of probe-corrected microscopes in the applied transmission electron microscopy and material science. Using an ARM 200F operating at 200kV a series of high resolution STEM-EELS investigations were performed at a polycrystalline spinel sample, sintered at 900°C, consistently showing an incorporation of fluorine in the first two atomic layers near the grain boundaries as depicted in Figure 2. This means that a) the double Fresnel fringes cannot only be created by an amorphous layer of a secondary phase but also by additional incorporated elements and b) the wetting mechanism occurs much earlier in the sintering process then postulated.

1. R. J. Bratton, *Am Ceram Soc Bull,* 47 [9] (1968) pp. 883-887.
2. D. W. Roy, *P Soc Photo-Opt Inst,* 297 (1981) pp. 13-18.
3. M. Shimada, T. Endo, T. Saito, and T. Sato, *Materials Letters,* 28 [4-6] (1996) pp. 413-15.
4. I. E. Reimanis and H. J. Kleebe, *,* 98 [12] (2007) pp. 1273-78.
5. I. E. Reimanis, K. Rozenburg, H. J. Kleebe, and R. L. Cook*,* 90 [7] (2007) pp. 2038-2042.
6. K. Rozenburg, I. E. Reimanis, H. J. Kleebe, and R. L. Cook, 91 [2] (2008) pp. 444-450.
7. M.M. Müller and H.-J. Kleebe, J. Am. Ceram. Soc., 95 [10] (2013) pp. 3022-3024.
8. D. R. Clarke, Ultramicroscopy 4 (1979) pp. 33-44.

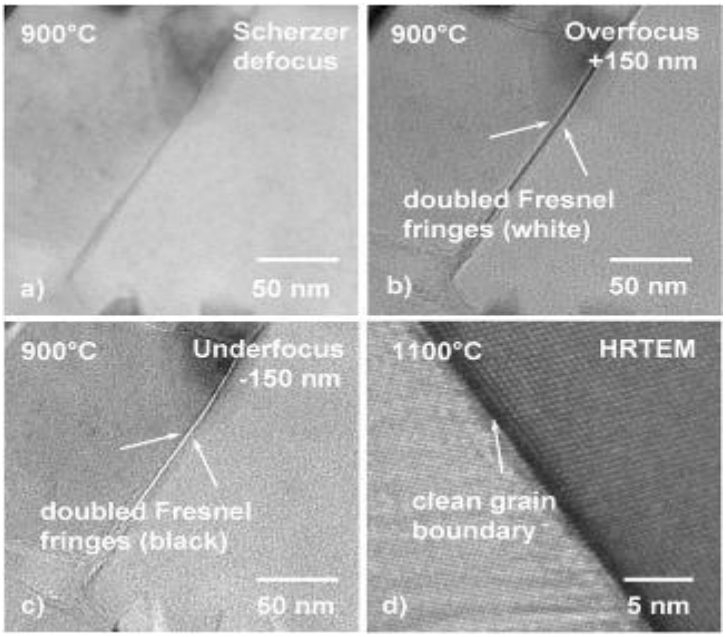

Figure 1. Defocus series of a spinel-spinel grain boundary. The material was sintered at 900°C [a,b,c] and 1100°C [d]. The double fringes occurring at 900°C indicate a twice changing mean inner potential which was interpreted as a wetting of the grain boundary. At higher temperatures no wetting was observed.

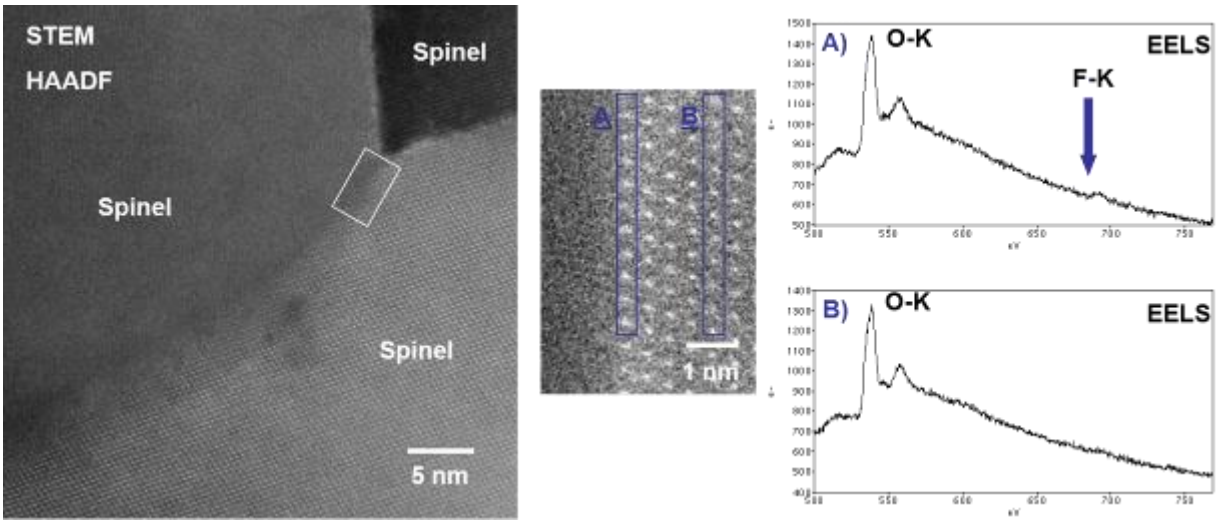

Figure 2. HR-STEM image of a spinel-spinel grain boundary. When applying the defocus technique double Fresnel fringes occurred but even in highest magnification no wetting could be shown. Instead, by using STEM EELS techniques, an incorporation of fluorine in the first two atomic layers was observed at a sintering temperature of 900°C.

Ceramics, Oxides, Geomaterials

MS.2.022
$BaTiO_3$ nanotube arrays by hydrothermal conversion of highly ordered TiO_2 nanotube carpets.

K. Bejtka[1], A. Chiodoni[1], A. Lamberti[1], N. Garino[1], S. Bianco[1], E. Ambrosio[1], M. Quaglio[1], C.F. Pirri[1,2]

[1]Italian Institute of Technology, Center for Space Human Robotics, Torino, Italy
[2]Politecnico di Torino, Department of Applied Science and Technology, Torino, Italy

katarzyna.bejtka@iit.it
Keywords: TiO_2 nanotubes, $BaTiO_3$, piezoelectric materials, nanostructures, anodic oxidation electron microscopy

The demand for well controlled synthesis routes for nanostructured piezoelectric materials, as 1D nanostructures of ferroelectric perovskites, has significantly increased during the last decade. Several synthesis methods, as hydrothermal synthesis, sol-gel deposition in templating structures and electrospinning [1] have been explored to prepare nanostructured materials. A promising and interesting approach to obtain 1D piezoelectric nanostructures is the hydrothermal conversion of 1D nanostructured precursors. The present work presents the morphological and structural characteristics of barium titanate ($BaTiO_3$) nanotubes synthesized by different conversion methods of TiO_2 nanotubes (NT). Vertically oriented TiO_2 NT arrays were previously synthesized by anodic oxidation of a titanium foil into an ammonium fluoride based electrolytic solution. The crystalline phase and morphology of the film were investigated, evidencing the formation of a highly ordered 1D NTs carpet with length ranging from few hundred nanometers up to several tens of micrometers (Figure 1).

In a first set of experiments, nanotube arrays of $BaTiO_3$ were obtained by a low temperature hydrothermal conversion of the TiO_2 nanostructures, following the synthesis procedure proposed by Yang and coworkers [2]. The morphology and crystal structures of the resulting $BaTiO_3$ NTs were characterized by Field Emission Scanning Electron Microscopy (FESEM), Transmission Electron Microscopy (TEM), X-ray diffraction (XRD) and Raman spectroscopy. The XRD measurement indicates that the TiO_2 template has been converted to $BaTiO_3$ after hydrothermal treatment. Figure 2 presents a FESEM micrograph of the nanotube arrays, showing that the ordered nanotubular structure was preserved. The top view is reported in the figure inset. In the second part of the work a simpler approach has been investigated, exploring different methods to favor the infiltration of TiO_2 nanotubes with solutions containing various barium salts. A heat treatment was then applied to promote barium incorporation into the TiO_2 structure in order to obtain the conversion into $BaTiO_3$ nanotubes. The $BaTiO_3$ NT arrays obtained by the second route resulted in the incorporation of barium into the structure, whilst the morphology of the highly ordered 1D TiO_2 NTs carpet was preserved. The morphological and structural characteristics of the obtained NTs will be compared with their functional properties, e.g. the piezoelectric response evaluated by nanoindentation.

1. P.M. Rørvik, T. Grande and M.A. Einarsrud, Adv. Mater. 23 (2011), p.4007.
2. Y. Yang, X. Wang, C. Sun and L. Li, Nanotechnology 20 (2009), p. 055709.

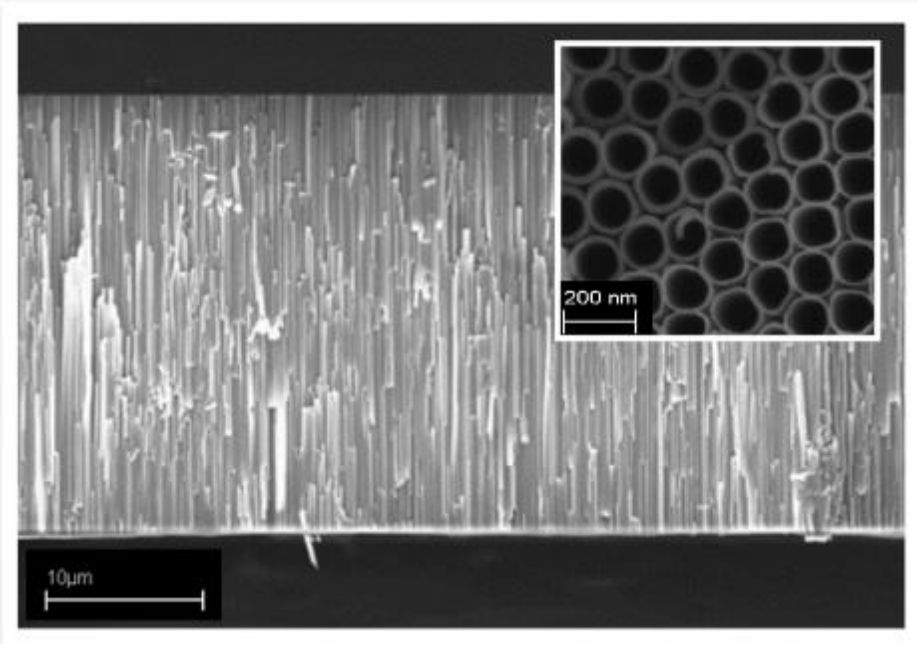

Figure 1. FESEM micrograph showing the cross sectional view of vertically oriented TiO_2 nanotubes array (the top view is reported in the inset).

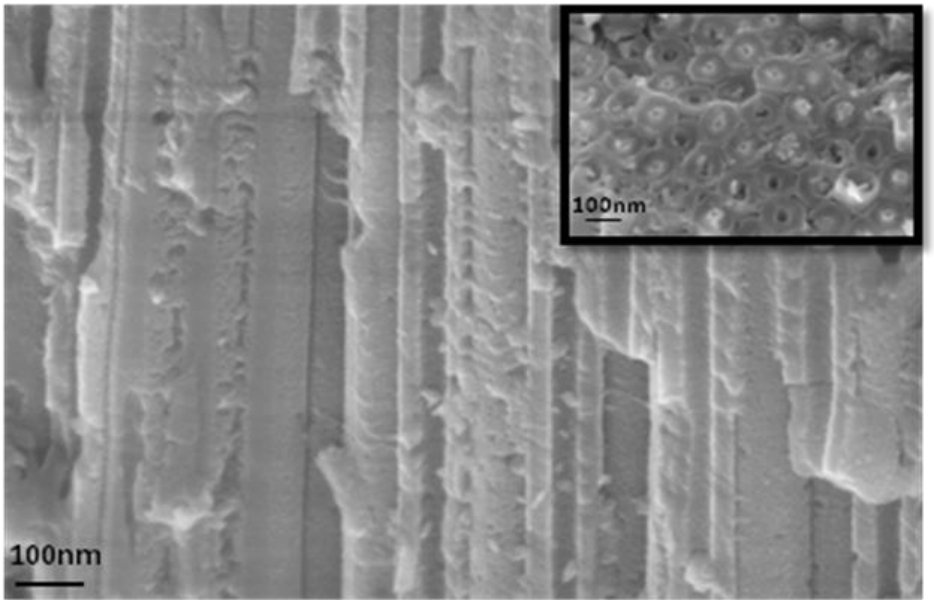

Figure 2. FESEM micrograph showing the cross sectional view of vertically oriented $BaTiO_3$ nanotubes array (the top view is reported in the inset).

Ceramics, Oxides, Geomaterials

MS.2.023
A reliable method for sizing constituent particles in pigment-grade titanium dioxide

R. Theissmann[1], M. Kluwig[1], T. Koch[1]

[1]KRONOS International, Inc., Research & Development, Leverkusen, Germany

ralf.theissmann@kronosww.com
Keywords: nanoparticle, metrology, particle sizing, white pigment, TiO_2

Titanium dioxide is a naturally occurring oxide of titanium. It has the highest refractive index of any material known to man, even the diamond, and is one of the whitest materials on earth. When ground into a fine powder, it transforms into a pigment that provides maximum whiteness and opacity. TiO_2 pigments are used in paints and coatings, plastics, paper, building materials, cosmetics, pharmaceuticals, foods and many other commercial products.

Upcoming regulations on national, European and international level upon the classification of nanoparticulate materials create the demand for standardized and reliable characterization methods [1]. For the time being, most scientific efforts are focused on model systems, such as spherical Au-nanoparticles [2]. Yet, industrial materials, which are the target of all classification and regulatory efforts, require approaches, which take into account the difficulties that go along with irregular shapes, broad size distributions and strong aggregation and agglomeration effects. In other words, robust, reproducible and statistically reliable methods are required, which can be applied to a broad range of materials.

This contribution introduces an operation procedure which was developed for the sizing of pigment-grade TiO_2 particles as they are produced in the order of up to 5.5 million metric tons a year world wide by the titanium dioxide Producing industries. The relevant steps of the procedure summarize as follows:

1. Samples are prepared by thorough mixing and imbedding in a hot mounting resin. Efficient mixing is done in the suitable dry mixing system, the fast mounting process prevents the separation of the specimen and the resin and a segregation or sedimentation of the different size-fraction within the sample. An optimum in terms of homogeneity is achieved in a representative sample!
2. A representative section through the sample is obtained via cutting, grinding and polishing. The preparation of the section ensures, that no particles are overlapping. Aggregated (fused) particles can readily be discriminated from agglomerated particles. The use of appropriate “oxide polishing suspensions” allows the preparation of particle sections surfaces for particle sizes down to 20nm.
3. An optimum choice for the recording conditions is found by balancing secondary electrons and backscattered electrons for image formation. Backscattered electrons contribute the contrast between the particles of interest and the hot mounting resin, secondary electrons emphasize the particle edges. An optimum is generally obtained by adjusting the acceleration voltage, working distance and the proper mixing of the detector signals.
4. A manual, semiautomatic or automatic acquisition procedure may be used for data collection, depending on sample properties, e.g. charging. This way, for pigmentary-.size particles in the Mie-scattering regime, several ten thousand particles can be recorded at reasonable acquisition times.
5. Modern image evaluation software allows efficient image processing, which includes noise reduction, shading correction, contrast optimization, edge detection or shape segmentation. In all cases, the need for reliability and reproducibility, requires stable image quality and a defined order of the image processing steps. Based on a processed image, an automated detection of particles in the image is done based on gray-value thresholding. Combined with a gray-value filtering (mean gray-value and its standard deviation), faulty detected “particles” can be eliminated.
6. Based on the obtained statically relevant dataset of several ten thousand detected particles, selection or discrimination of particles can be achieved by filtering. Most important particle property is its characteristic form, which can be expressed in terms of a “formfactor”, a

"convexity" or an "aspect ratio". A variety of other characteristics are available and can be chosen to match the necessity of the desired investigation. In the case of TiO_2-pigments described here, two different shape characteristics (formfactor and convexity) are an adequate choice for filtering.

Based on the almost fully automatable procedure described in the steps 1 through 6, a highly reproducible workflow for the evaluation of particle-size distributions (or likewise the distribution of any other characteristic particle properties) can be obtained based on relevant, number based counting statistics. In the special case of white TiO_2-pigment with a mean size in the range of Mie-Scattering regime, it turns out that there is no practical need for stereological corrections [3]. This is attributed to the combination of the characteristic, spheroidal particle shape, the properly chosen penetration depth of the electron beam (i.e. the acceleration voltage) which matches the characteristic length-scale of the particle diameters and the preparation procedure, which mechanically removes particles that have little hold in the matrix, i.e. are sliced close to the bottom.

1. Commission recommendation of 18 October 2011 on the definition of nanomaterial. Official Journal of the European Union 275:38-40.
2. Report of Investigation: Reference Material 8011 J. A. Small, R. L. Watters, Jr., National Insitute of Standards & Technology (2012).
3. 3D particle size distributions from 2D observations: stereology for natural applications, D. L. Sahagian, A. A. Proussevitch, J. of Volcanology and Geothermal Research 84 (1998) P. 173–196

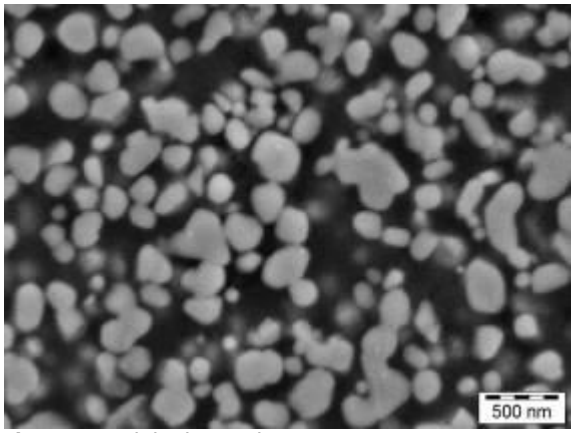

Figure 1. Original SEM-image

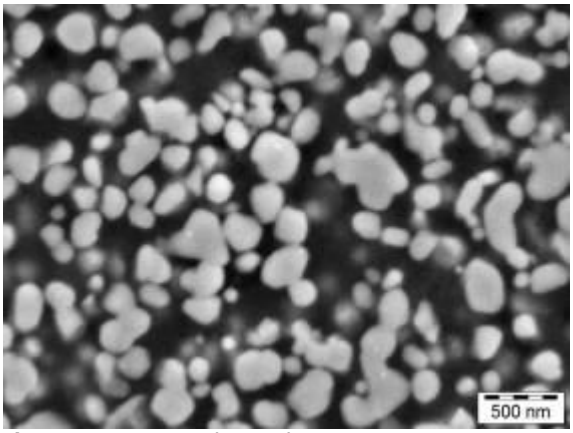

Figure 2. Processed SEM-image

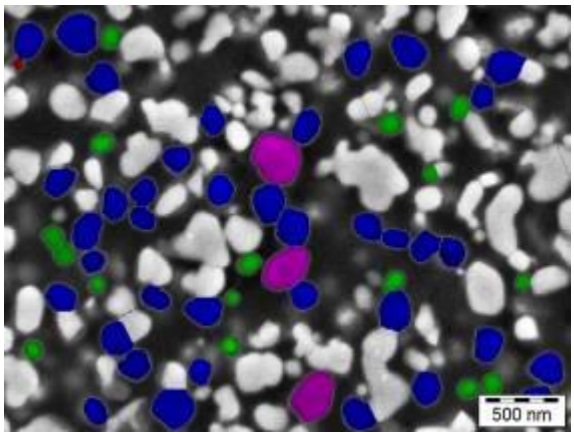

Figure 3. Processed SEM-image with detected constituent particles

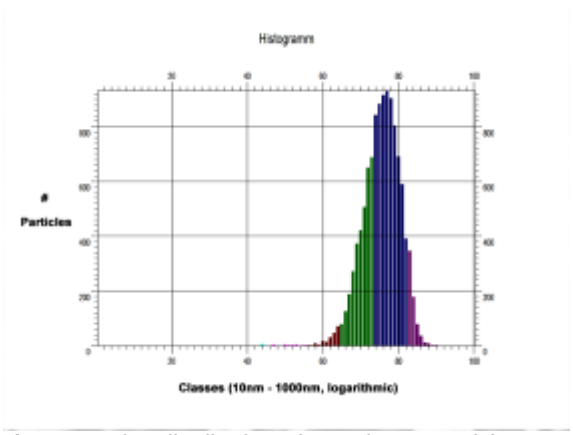

Figure 4. Size distribution of constituent particles; the ordinate gives the particle-count for each bin, the # of the bin is given on the abscissa; a logarithmic binning scheme of 100 bins is chosen between 10nm and 1000nm

Ceramics, Oxides, Geomaterials

MS.2.P024
Twinning and inclusions in chrysoberyl from Pratinhas, Brazil

S. Drev[1], A. Rečnik[1], N. Daneu[1]

[1]Jožef Stefan Institute, Ljubljana, Slovenia

sandra.drev@ijs.si
Keywords: chrysoberyl, twinning, inclusions, asterism, electron microscopy

Chrysoberyl ($BeAl_2O_4$) is a rare mineral usually found in metamorphosed pegmatites, granites and silicic volcanoclastic rocks [1]. It is orthorhombic with unit-cell parameters *a* = 5.481Å, *b* = 9.415Å and *c* = 4.428Å. Besides single crystals, contact twins and cyclic twins on (130) planes are common. The most famous chrysoberyl twin occurrences are in phlogopite mica matrix in Russia (Urals) [2] and in pegmatite matrix or in alluvial or colluvial gravels in Brazil (Bahia, Corrego Alegre, Espirito Santo) [3]. The reasons for the formation of chrysoberyl twins were not studied before. In our previous analyses of growth twins and related planar defects in various synthetic materials [4] and natural minerals [5,6] we showed that the formation of such defects is not accidental, but chemically triggered already in the nucleation stage of the crystal growth. In order to reveal the reasons for the formation of chrysoberyl twins, we studied contact {130} twins in natural crystals from Pratinhas locality in Bahia (Brazil) by electron microscopy methods. A typical heart-shape contact twin, as used for our studies, is shown in Figure 1a. The crystal is oriented along the [001] orientation and the {130} boundary, which divides the crystal into two equivalent halves, is clearly visible. For transmission electron microscopy (TEM) analyses, a block of 2x2 mm was cut from the crystal centered across the twin boundary parallel to the [001] direction. The block was inserted and glued into a brass ring, which was subsequently cut into about 500 μm thick slices. The slices were thinned down to 100 μm, dimpled down to 20 μm in the centre and perforated using Ar ions (PIPS, Gatan, Netherlands). The samples were analyzed with TEM (JEM-2100, Jeol, Japan) equipped with a detector for energy-dispersive spectroscopy (EDS).

A low-magnification image of the (130) twin boundary in chrysoberyl oriented along the [001] zone axis is shown in Figure 1b. In this orientation, the twin boundary is usually a straight interface, occasionally interrupted by short steps to nearby parallel planes. Diffraction patterns were recorded in both crystal domains and across the twin boundary (Figures 1c-d). The common {260} reflections (marked in Fig. 1e) confirm that the twin lies parallel to the {130} planes of the chrysoberyl structure. A typical HRTEM image of the twin boundary was taken in a thin part of the TEM sample (Fig. 1f). The contact between the two twin domains is sharp and no secondary phase was observed on the contact, as expected in analogy to the {301} twins in rutile [5]. Besides the twin boundary, we also observed numerous nano-sized precipitates in bulk chrysoberyl. The density of precipitates was similar in all regions of the analyzed TEM sample. HRTEM analysis of the precipitates (Figure 2) revealed that they lie parallel to the two equivalent {120} planes of chrysoberyl, which intersect at an angle of 98.7°. These precipitates are probably the reason for the origin of 4-ray asterism in rare and precious chrysoberyl gems. We performed also some preliminary EDS analyses in bulk chrysoberyl, across the precipitates and at the twin boundary (Figure 3). The results reveal that bulk chrysoberyl contains a small amount of iron, which is a common impurity in natural chrysoberyl crystals. The spectrum taken across the precipitate revealed that it is enriched in Ti. In combination with structural analysis, the precipitates could be rutile or some high-pressure TiO_2 polymorph. Ti and Fe enrichment was detected also in the region near the twin boundary as a consequence of diffusion and segregation processes.

1. G. Franz and G. Morteani, Be-minerals: synthesis, stability, and occurrence in metamorphic rocks. Reviews in Mineralogy and Geochemistry, Vol. 50, No. 1 (2002), p. 551-589.
2. C. Palache, H. Berman and C. Frondel, The system of Mineralogy, Seventh edition, Vol.1, (1944), p. 834.
3. K. Schmetzer, Russian Alexandrites, (2010), p. 144.
4. A. Rečnik, S. Bernik and N. Daneu, Microstructural engineering of ZnO-based varistor ceramics. Journal of Material Science, Vol. 47, No.4 (2012), p.1655–68.
5. N. Daneu, H. Schmid, A. Rečnik and W. Mader, Atomic structure and formation mechanism of (301) rutile twins from Diamantina (Brazil). American Mineralogist, Vol. 92, No. 11-12 (2007), p. 1789-1799.

6. N. Daneu, A. Rečnik, T. Yamazaki and T. Dolenec, Structure and chemistry of (111) twin boundaries in $MgAl_2O_4$ spinel crystals from Mogok. Physics and Chemistry of Minerals, Vol. 34, No. 4 (2007), p. 233-247.

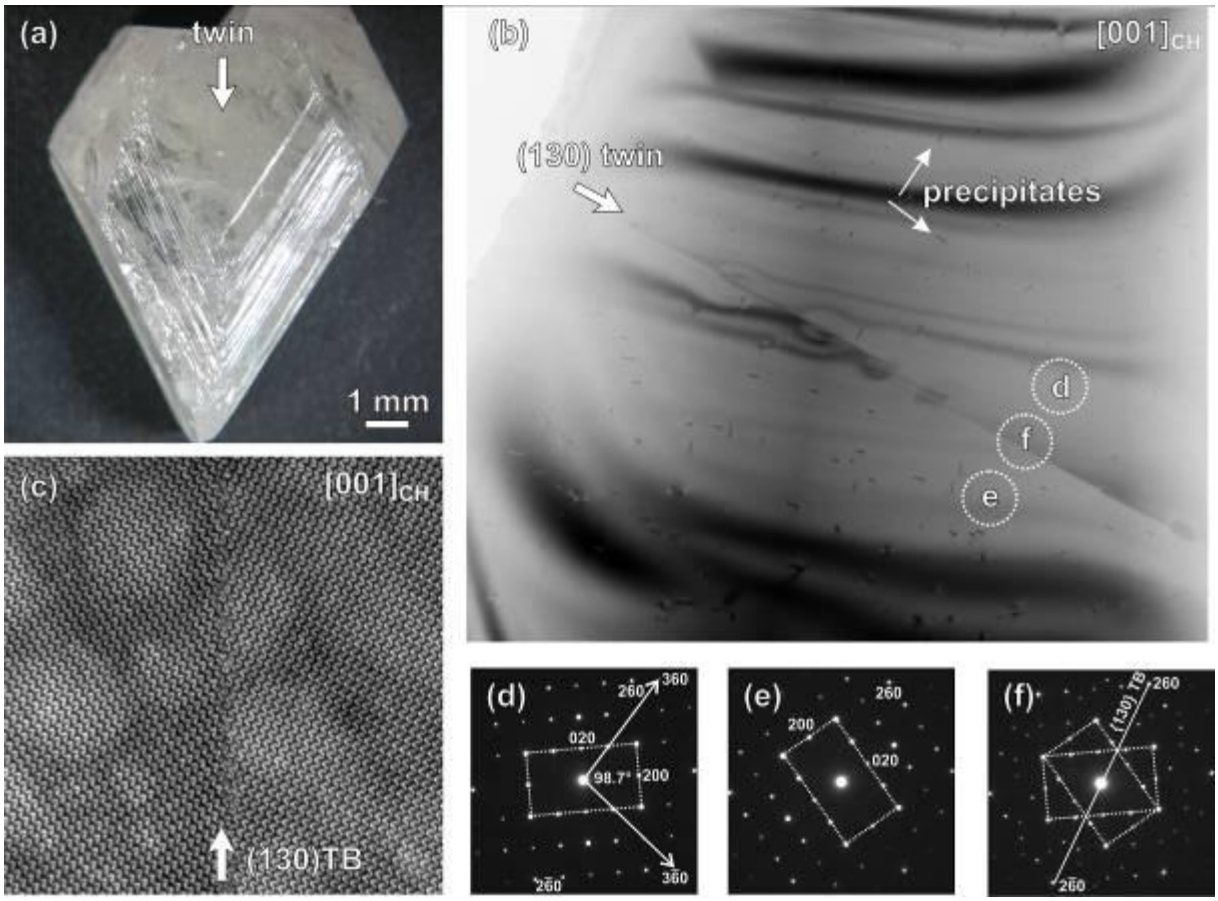

Figure 1. (a) Chrysoberyl with a well-defined contact twin boundary. (b) Low magnification TEM image of the twin boundary in chrysoberyl. Many nano-sized inclusions following two directions are visible in the bulk chrysoberyl. (c-e) Diffraction patterns taken in both crystal domains and across the twin boundary confirm that it lies parallel to {130} planes of the structure. (f) HRTEM image of the twin boundary.

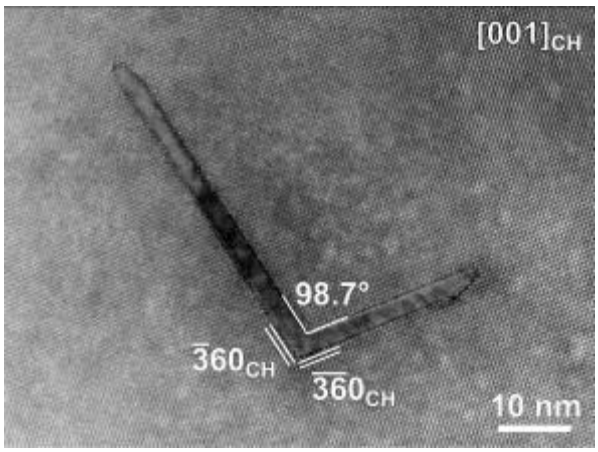

Figure 2. HRTEM image of a typical knee-shaped precipitate in chrysoberyl. The edges of the precipitate lie parallel to {120} planes of chrysoberyl, which form an angle of 98.7°.

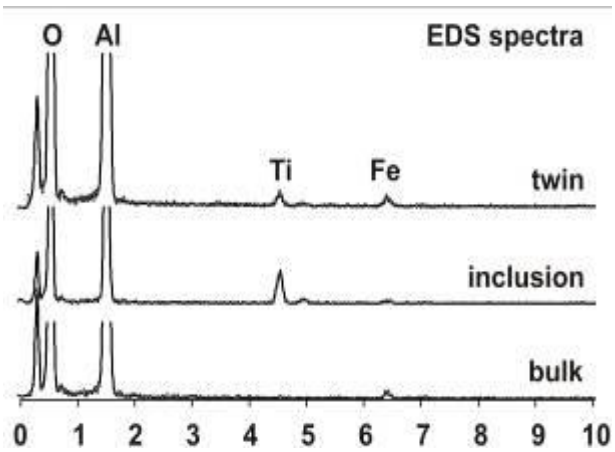

Figure 3. EDS spectra taken in bulk chrysoberyl, across the inclusion and across the {130} twin boundary reveal that bulk chrysoberyl contains some Fe, the inclusion is enriched in Ti, while the region near the twin boundary contains increased amount of Ti and Fe.

Ceramics, Oxides, Geomaterials

MS.2.P025
In situ mechanical polarization of polycristalline $BaTiO_3$ in the ESEM with subsequent EBSD investigations

A. Reichmann[1], K. Reichmann[2], M. Stefan[3], A. Zankel[3], P. Pölt[3]

[1]Austrian Centre for Electron Microscopy and Nanoanalysis, Graz, Austria
[2]Graz University of Technology, Christian Doppler Laboratory for Advanced Ferroic Oxides, Graz, Austria
[3]Graz University of Technology, Institute for Electron Microscopy, Graz, Austria

angelika.reichmann@felmi-zfe.at
Keywords: domain wall motion, tensile stage, ferroelectric

$BaTiO_3$ belongs to the class of ferroelectric materials, the electric analogs of ferromagnetics. It crystallizes in the simple perovskite structure, where the barium ions are positioned at the corners of a cube. The centre of this cube is occupied by the smaller titanium ion, which is coordinated by six oxygen ions forming an octahedron. For temperatures above 127°C the unit cell is cubic (unit cell parameter a=0,401 nm at 150°C) and $BaTiO_3$ is paraelectric. On cooling below 127°C it undergoes a first order phase transition and the central titanium ion, the surrounding oxygen ions and the barium ions move away from the centre of the unit cell. This causes a tetragonal distortion of the unit cell (a=0,399 nm and c=0,403 nm at room temperature) “Figure 1”. As a result the positive and negative charges separate and a permanent dipole moment is created, which leads to a spontaneous polarization along the c-axis of the unit cell.

The symmetry changes from cubic to tetragonal and $BaTiO_3$ becomes ferroelectric. In ceramics these dipoles are not randomly oriented within the grains [1]. To minimize energy due to mechanical stresses inside the grain and between individual grains (most of them caused by the phase transition at 127°C), unit cells with the same orientation of the polar axis form so-called domains. Two different types of boundaries between two domains are possible in tetragonal $BaTiO_3$: 90° und 180° domain walls. Only the 90° domains have the capability to reduce the elastic energy for the tetragonal structure [2]. There are two types of domain structures in coarse grained $BaTiO_3$, one called herringbone, which is the most common in unpoled ceramics, and the other square net pattern [3].

The ferroelectric behavior is based on the fact that the direction of the polar axis (and the direction of the c-axis) can be changed by an external electric field, so called poling. Also mechanical stress can induce a preferred orientation of the overall polarization. In this work domain wall motion of polycrystalline $BaTiO_3$ was recorded under mechanical stress in situ in the ESEM (Environmental Scanning Electron Microscope). The samples were imaged by crystal orientation contrast, an easy and quick method for the investigation of the microstructure of ceramic materials, enabling the observation of respective changes during in situ experiments. Crystal orientation contrast caused by orientation anisotropy of backscattered electrons can generate images in which grains of different orientations in polycrystalline material have different grey levels [4]. Even ferroelectric domains can be observed because of their differing polarization axes giving rise to twin boundaries.

Commercially available samples of $BaTiO_3$ ceramics were used for this investigation. From such sintered pellets rectangular blocks of 7x7x5 mm^3 were cut with a diamond wire saw and then one of the 7x7mm^2 faces was ground on silica carbide paper, finished with 4000 grit and then polished using a 0.25 µm diamond paste. The surface was mechanically fine polished using 0.04 µm SiO_2 emulsion to obtain the smooth surface required for good-quality OC (orientation contrast) images. The compression tests were carried out in an ESEM Quanta 600 FEG from FEI using the low vacuum mode and equipped with a slightly modified tensile stage from Deben (load cell: 1250 N, “Figure 2"). To determine the orientation of the grains before and after the compression experiments, EBSD (Electron Backscattered Diffraction) measurements were performed. Domain wall motion was observed at a stress exceeding 33 MPa resulting in mechanical poling “Figure 3”.

1. J. Holterman, P. Groen in “An introduction to piezoelectric materials and components”, Stichting Applied Piezo, Apeldorn (2012)
2. R. Waser, U. Böttger, S. Tiedke, „Polar Oxides“, Wiley-VCH Verlag GmbH, Weinheim (2005), p. 30ff
3. G. Arlt, P. Sasko, Journal of applied physics, 51 (1980), p. 49564
4. J. Goldstein et al. in “Scanning Electron Microscopy and X-Ray Microanalysis”, Springer, New York (2003), p. 250ff

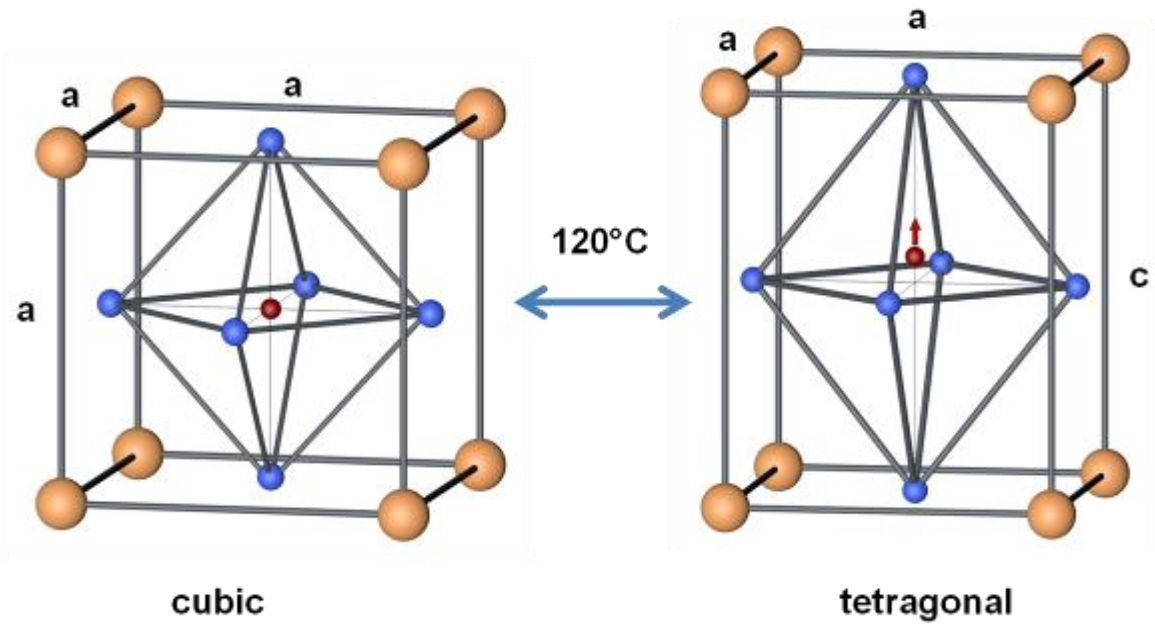

Figure 1. Unit cells of cubic and tetragonal $BaTiO_3$, yellow: Ba^{2+}, blue: O^{2-}, red: Ti^{4+}

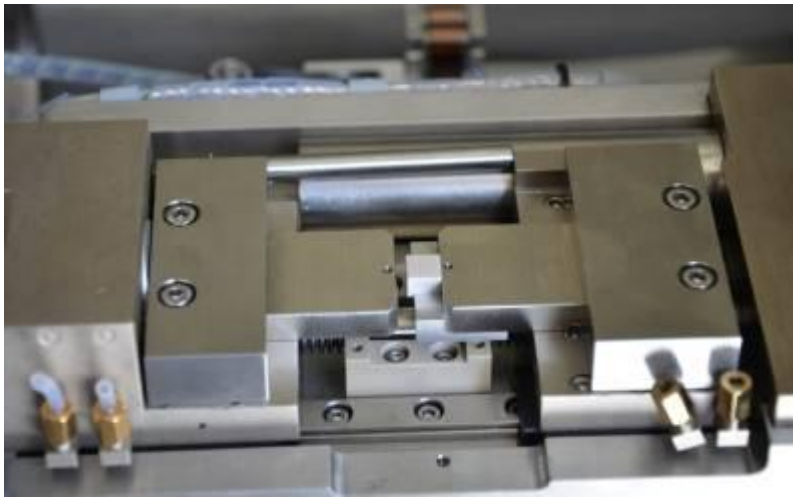

Figure 2. Tensile stage from Deben, with the ceramic sample mounted on it

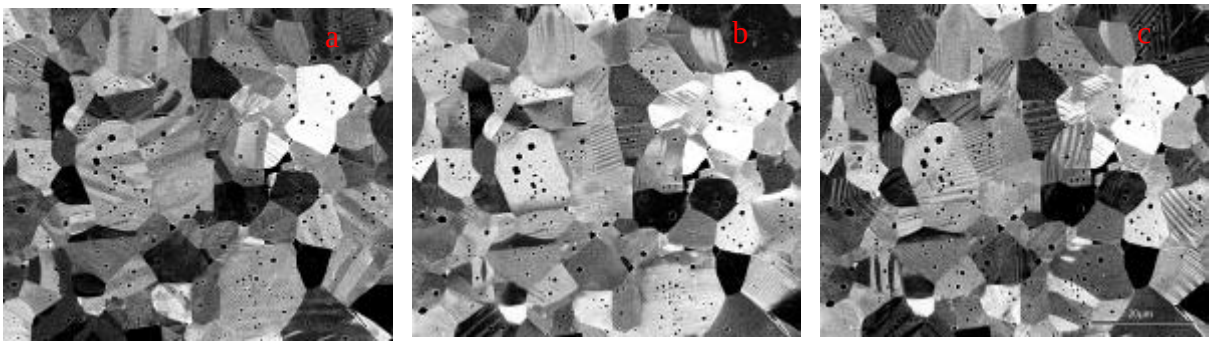

Figure 3.SEM-images of $BaTiO_3$ before (a), during (b) and after (c) compression

Ceramics, Oxides, Geomaterials

MS.2.P026
HAADF-STEM Imaging and Simulation of $(Sb_{1/3}Zn_{2/3})GaO_3(ZnO)_3$

S.-M. Hühne[1], J. Garling[1], H. Schmid[2,1], W. Assenmacher[1], W. Mader[1]

[1]Institut für Anorganische Chemie, Universität Bonn, Römerstraße 164, 53117 Bonn, Germany
[2]INM-Leibniz-Institut für Neue Materialien, Campus D2 2, 66123 Saarbrücken, Germany

huehne@uni-bonn.de
Keywords: zinc oxides, HAADF-STEM, simulation

A high temperature (1350 °C) processing route in sealed Pt tubes was used for the synthesis of $(Sb_{1/3}Zn_{2/3})GaO_3(ZnO)_3$ from appropriate powder mixtures of pure binary oxides as starting materials. $(Sb_{1/3}Zn_{2/3})GaO_3(ZnO)_3$ consists of an alternate stacking of octahedral layers $[(Sb_{1/3}Zn_{2/3})O_2]^-$ and $[(GaZn_3)O_4]^+$ units corresponding to CdI_2 and wurtzite structure type motifs, respectively. Inversions of the ZnO_4 tetrahedra occur (i) at the octahedral layers and (ii) halfway in the wurtzite type domains where trigonal bipyramidal coordinated cations constitute the boundary.

Crystal structure determination by single-crystal X-ray diffraction revealed the space group $R\bar{3}m$ with lattice parameters a_0 = 3.2366(3) Å; c_0 = 41.793(8) Å, and the structural characteristics as known from other members with general formula $ABO_3(ZnO)_m$ [1]. The composition of the octahedral layer can be refined without constraint to a ratio of Sb/Zn = 1/2. Electron diffraction and HRTEM clearly indicate ordering of these cation positions by presence of superstructure reflexions and contrast modulations of the cation columns in relevant orientations [2]. This indicates a real structure of $(Sb_{1/3}Zn_{2/3})GaO_3(ZnO)_3$ present on a local scale that is averaged by stacking disorder of the octahedral layers $[(Sb_{1/3}Zn_{2/3})O_2]^-$ as indicated by streaks parallel to 000*l* (Figure 2.). The cation ordering within the octahedral layers can be described by a model deduced earlier for single defect layers in ZnO doped with antimony [3]. The observed ED patterns, neglecting diffuse intensities by non-periodicity, can be described with corundum-like, well ordered octahedral layers $[(Sb_{1/3}Zn_{2/3})O_2]^-$ periodically translated by a 3_1 screw axis. This leads to a structure model with discrete positions for all ions in $P3_112$ with a = 5.6 Å and c = 41.8 Å (Figure 1.), where the Sb ions along the c-axis are stacked in ABC sequence.

To confirm the deduced structure model of $(Sb_{1/3}Zn_{2/3})GaO_3(ZnO)_3$ HAADF-STEM imaging was carried out in an advanced analytical TEM/STEM system (JEOL JEM-ARM 200CF) equipped with cold field-emission gun (C-FEG), probe Cs-corrector, X-ray (JED 2300) and electron spectrometer (GATAN GIF Quantum ER) attachments. The present setup provides sub-Å resolution capability in high-angle annular dark-field (HAADF) STEM imaging, whereas bright-field (BF) and particularly annular bright-field (ABF) with increased sensitivity for light elements enable the elucidation of true atomic structures by imaging both cation and anion sites [4]. The QSTEM software package [5] was used for simulation of HAADF images (Figure 3.).

HAADF imaging reveals the periodic order of antimony and zinc in the octahedral layers with columns of the heavier Sb atoms giving rise to bright Z-contrasts. The intensity ratio of the Zn and Sb columns can be measured to 0.42. This corresponds to an exponent of 1.7 ($Int_{(Zn)}/Int_{(Sb)}=30^{1.7}/51^{1.7}$= 0.41), which is in excellent agreement with theoretical predictions [6,7]. In some areas the stacking of the octahedral layers corresponds well with the structure model in $P3_112$. However, the stacking of larger regions does not correlate to the ABC stacking, i.e. stacking disorder occurs. This leads to an averaging of the Sb cation positions and in turn to streaks in SAED patterns at $\{h\bar{h}0l\}$, $h \neq 3n$, $n \in \mathbb{Z}$ (Figure 2.).

Currently, compounds of this structure type draw much attention and are considered promising materials systems for various technological applications such as transparent conducting materials, field emission applications, and as color pigments.

1. N. Kimizuka, T. Mohri and M. Nakamura, J. Solid State Chem. 81 (1989), p. 70-77
2. J. Garling, Diploma Thesis, University Bonn (2012)
3. A. Recnik, N. Daneu, T. Walther and W. Mader, J. Am. Ceram. Soc. 84 (2001), p. 2657-68
4. H. Schmid, E. Okunishi and W. Mader, Ultramicroscopy 127 (2013), p. 76-84
5. C. Koch, Dissertation, Arizona State University (2002)
6. R. F. Klie and Y. Zhu, Micron 36 (2005), p. 219
7. P. D. Nellist and S. J. Pennycook, Ultramicroscopy 78 (1999), p. 111
8. We thank E. Arzt for continuous support through INM

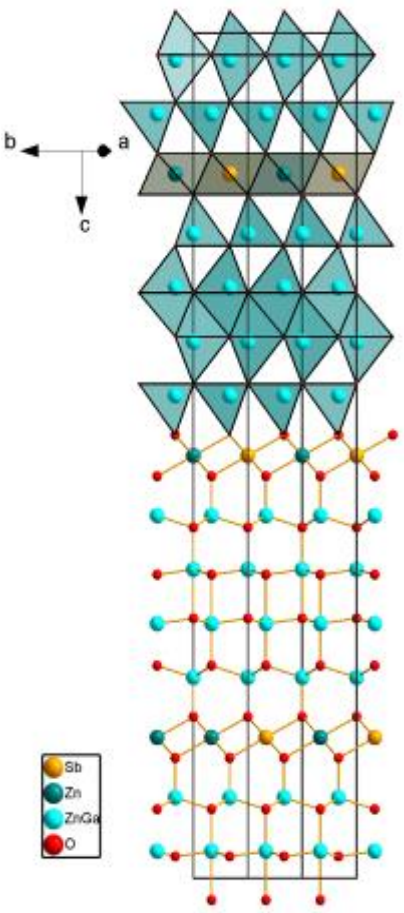

Figure 1. Crystal structure of $(Sb_{⅓}Zn_{⅔})GaO_3(ZnO)_3$ in $P3_112$ in $\langle 1\bar{1}00 \rangle$ zone axis, drawn as ball and stick model and as polyhedron representation, respectively.

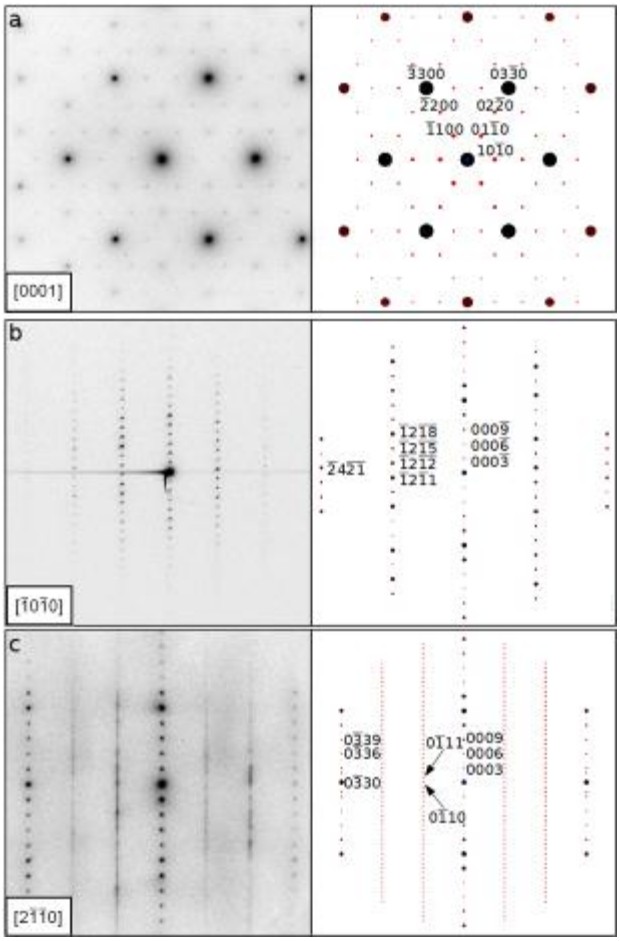

Figure 2. Electron diffraction patterns of $(Sb_{⅓}Zn_{⅔})GaO_3(ZnO)_3$ in principal orientations using the structure model in $P3_112$ and calculated patterns. Diffuse scattering in (c) is caused by stacking disorder of the octahedral planes.

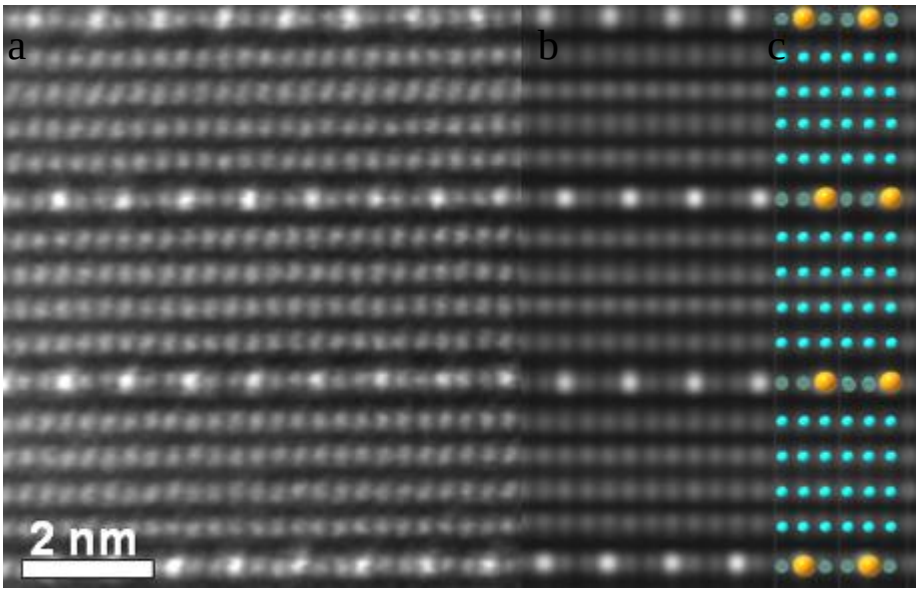

Figure 3. HAADF image (a), simulated HAADF image (b) and structure model (c) of $(Sb_{⅓}Zn_{⅔})GaO_3(ZnO)_3$ in *a*-axis orientation.

Ceramics, Oxides, Geomaterials

MS.2.P027
Electron Diffraction study of a novel high temperature phase in the system Fe-Zn-O

S. Eichhorn[1], W. Mader[1]

[1]Universität Bonn, Institut für Anorganische Chemie, Bonn, Germany

eichhorn@uni-bonn.de
Keywords: ZnO, $ZnFe_2O_4$, electron diffraction

The existence of phases $ABO_3(ZnO)_m$ in the system ZnO-Fe_2O_3 is known up to a composition of $Fe_2O_3(ZnO)_{12}$ at 1350 °C [1][2]. These phases share the structural characteristics of the better known compounds $InFeO_3(ZnO)_m$ [3] which exist in the range $m \geq 1$. $ABO_3(ZnO)_m$ compounds consist of wurtzite layers separated by planes of AO_6 octahedrons fully occupied with A^{3+} cations such as In^{3+}, Lu^{3+}, Sc^{3+}. In the center of the wurtzite layers tetrahedral layers of B^{3+} ions exist. At both of the cation layers the polarity of the ZnO layers is inverted. The crystal structures of compounds with low ZnO content were verified by single crystal X-ray diffraction [4].

We obtained a novel phase in the system ZnO-$ZnFe_2O_4$-Fe_2O_3 prepared by solid state reaction of ZnO and $ZnFe_2O_4$ powders at 1600 °C in an alumina crucible at air. The reaction product was quenched in water to conserve the metastable high temperature phase. XRD proves the layer structure of $Fe_2O_3(ZnO)_7$, however, EDXS measurements show a transition metal content of 30% Fe and 70% Zn instead of 22% Fe and 78% Zn as derived from the formula. Hence, the correct formula should be written as $Fe_2O_3(Zn_{1-x}Fe_xO)_7$ with ca. 8% of the iron distributed as Fe^{2+}.

Figure 1 shows a bright field image of ZnO inversion layers at the nanometer scale separated by basal IDBs which are clearly visible. The spacing between two basal IDBs is ca. 2.45 nm with eight intensity maxima located between two IDBs as shown in the corresponding profile (Figure 2). This confirms the formation of the $Fe_2O_3(Zn_{1-x}Fe_xO)_7$ structure and the results of XRD. Because of the structural similarities to $InFeO_3(ZnO)_7$ a space group $R\bar{3}m$ and thus diffraction patterns of a rhombohedral crystal were expected as in Figure 3, where a SAED pattern in [0001] direction is shown with the $(11\bar{2}0)$ reflection marked. HOLZ reflections are present because of the long *c* axis of ca. 75 Å and the *-h+k+l = 3n* reflection condition of the rhombohedral centering. Figure 3 and Figure 4 are diffraction patterns which correspond to the same orientation of the ZnO sub-lattice. However, additional superstructure reflections are visible in the diffraction patterns of the new phase $Fe_2O_3(Zn_{1-x}Fe_xO)_7$ (Fig. 4) caused by a symmetry reduction. The viewing direction is [001] in a monoclinic crystal system. Figure 5 shows a SAED pattern in [100] and figure 6 a SAED pattern in [010] of $Fe_2O_3(Zn_{1-x}Fe_xO)_7$. The observed superstructure is visible in the [100] direction as satellites to the main reflections having a periodicity of 34 Å. The periodicity of the (00*l*) reflections corresponds to a 24 Å lattice plane spacing matching the (000*l*) lattice planes of $InFeO_3(ZnO)_7$. Figure 6 displays a pattern along the [010] direction which shows the monoclinic angle β = 94.7° and a lattice plane spacing of 2.66 Å according to the (100) reflection.

The material offers great opportunities for the study of its structural and magnetic properties and of the origin of the superstructure by HRTEM and HAADF methods.

1. Oliver Köster-Scherger, *Dissertation*, Universität Bonn, 2008.
2. N. Kimizuka, M. Isobe, M. Nakamura, T. Mohri, J. Solid State Chem. 103 (1993) p. 394
3. N. Kimizuka, T. Mohri, Y. Matsui, K. Siratori, J. Solid State Chem. 74 (1988) p. 98

4. I. Keller, W. Assenmacher, G. Schnakenburg, W. M

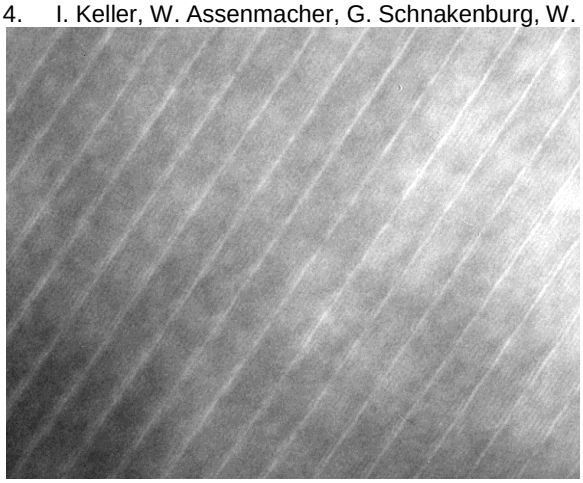

Figure 1. Bright Field Image of $Fe_2O_3(Zn_{1-x}Fe_xO)_7$ in [100] direction. FeO_6 basal IDBs are marked.

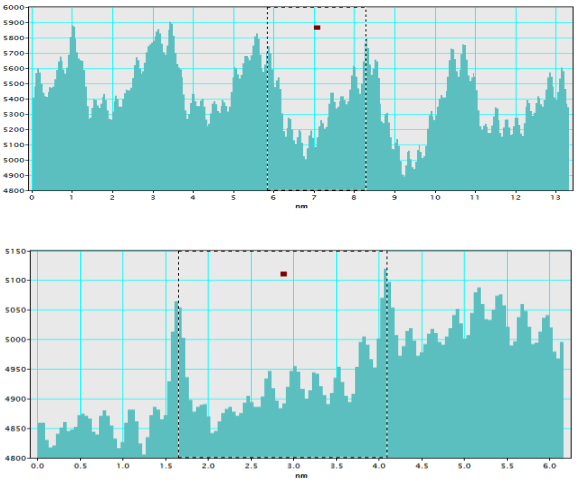

Figure 2. Corresponding intensity profile to fig. 1. Distance of two IDBs is 24.5 Å confirming the structure of $ABO_3(ZnO)_7$.

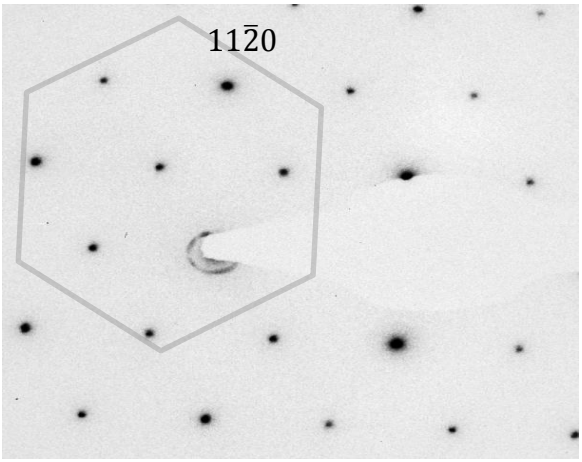

Figure 3. SAED pattern of $InFeO_3(ZnO)_7$ in [0001] direction. $\mathbf{11\bar{2}0}$ reflection is marked. HOLZ reflections are present in between.

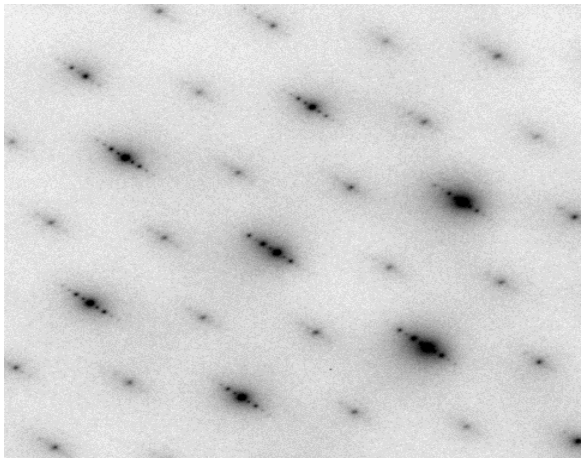

Figure 4. SAED pattern of $Fe_2O_3(Zn_{1-x}Fe_xO)_7$ in [001]. Superstructure reflections are caused by a symmetry reduction. HOLZ reflections have low intensity.

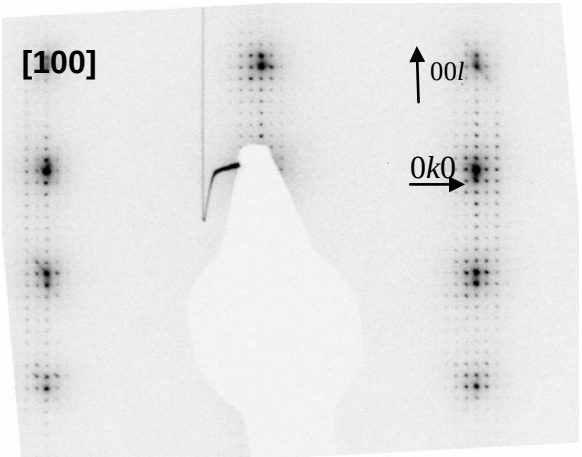

Figure 5. SAED pattern of $Fe_2O_3(Zn_{1-x}Fe_xO)_7$ in [100]. Periodicity of <00l>reflections is 24 Å, of <0k0> reflections is 34 Å.

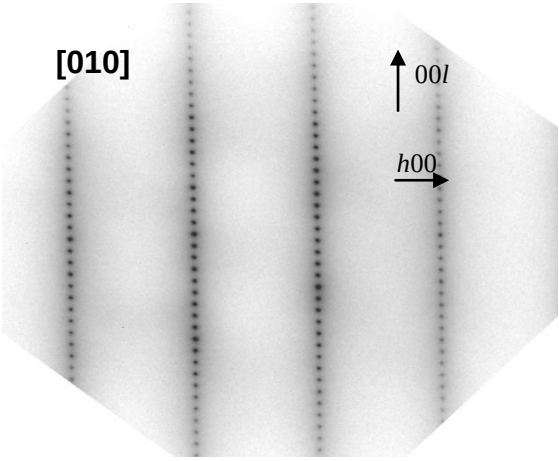

Figure 6. SAED pattern of $Fe_2O_3(Zn_{1-x}Fe_xO)_7$ in [010]. Periodicity of <00l>reflections is 24 Å, of <h00> reflections is 2,66 Å. The monoclinic angle is derived from $\beta^* = 85{,}3°$

Ceramics, Oxides, Geomaterials

MS.2.P028
Grain growth anomalies and their effect on domain structure in Barium Titanate

K. Reichmann[1], M. Naderer[1], A. Reichmann[2]

[1]Graz University of Technology, CD-Laboratory for Advanced Ferroic Oxides, Graz, Austria
[2]Austrian Centre for Electron Microscopy and Nanoanalysis, Graz, Austria

k.reichmann@tugraz.at
Keywords: abnormal grain growth, ferroelectric domains, orientation contrast imaging

Barium Titanate is a classical ferroelectric material that is widely used as dielectric in multilayer ceramic capacitors. In the ferroelectric state, which is observed below the Curie-Temperature of about 127°C, each unit cell of the compound develops a dipole moment, whose direction can be changed by an external electric field. This feature is responsible for the large relative permittivity of the material but also for a typical domain pattern inside each grain. Domains are regions of parallel orientation of the dipoles. Within the tetragonal phase of Barium Titanate 90° and 180° orientations between different domains are possible. The domain structure is given by the minimization of stray field energies (180° domain walls) and elastic energies (90°domain walls) [1]. The dielectric properties of barium titanate ceramics with respect to temperature, electric field, frequency and time strongly depend on the substitution of minor amounts of other ions (sometimes impurities in the ppm range) for Ba or Ti. In some cases such dopants influence domain structure and domain wall motion, which in turn affects the permittivity and a large fraction of the dissipation factor [2]. Thus an understanding of the domain structure of ferroelectric ceramics greatly assists the control of dielectric properties. In this study we investigate the effect of Zirconium Oxide contamination on the microstructure and the domain structure of Barium Titanate. This Zirconium Oxide could be introduced as contamination from milling media that are used for milling the material after solid state synthesis. Barium Titanate powder (BESPA BT-4-A from Nippon Chemical Industrial) with an average grain size of 0.3 µm was milled in a planetary mill (Fritsch Pulverisette 4) in 250 ml beakers made of yttrium stabilized zirconium oxide with 5mm milling balls made of the same material as the beakers with water as suspending liquid for six hours. In order to exaggerate the abrasive wear of the milling media the ratio between Barium Titanate powder and milling balls was chosen out of the recommended range. 15 g of Barium Titanate powder was milled with 500 g of milling balls. The main rotor was operated at 300 /min the planetary rotors were set at -600 /min. The powder was dried after milling, mixed with poly-ethylenglycol as binder, sieved and pressed in a 13 mm diameter pellet die with 150 MPa. After debindering these pellets were sintered at 1280°C for two hours. For comparison pellets from Barium Titanate powder as received without milling were sintered in the same run. The sintered samples were grounded on silica carbide paper, finished with 4000 grit and then polished using a 0.25 µm diamond paste. The surface was mechanically fine polished using 0.04 µm SiO_2 emulsion to obtain the smooth surface required for good-quality OC (orientation contrast) images. The orientation contrast imaging was done with an ESEM from FEI using the low vacuum mode. Figure 1 shows the microstructure and domain distribution of the sintered Barium Titanate without milling step. The sample exhibits a homogeneous microstructure with an average grain size of 2.1 µm. The domains show a typical 90° herringbone pattern. Figure 2 shows the microstructure and domain distribution of the sintered Barium Titanate after the milling step. Abnormal grain growth with a preferred growth direction can be observed. Many grains exhibit a “coffee bean” shape with a twin boundary dividing the grain in two halfs. The domain pattern, which is much coarser than in the reference sample, usually crosses this twin boundary but exhibits a change in domain orientation.

1. R. Waser, U. Böttger, S. Tiedke, in „Polar Oxides“, Wiley-VCH Verlag GmbH, Weinheim (2005), p. 30ff.
2. A.J. Moulson, J.M. Herbert in “Electroceramics”, Second Edition, John Wiley & Sons, Chichester (2003), p. 311ff.

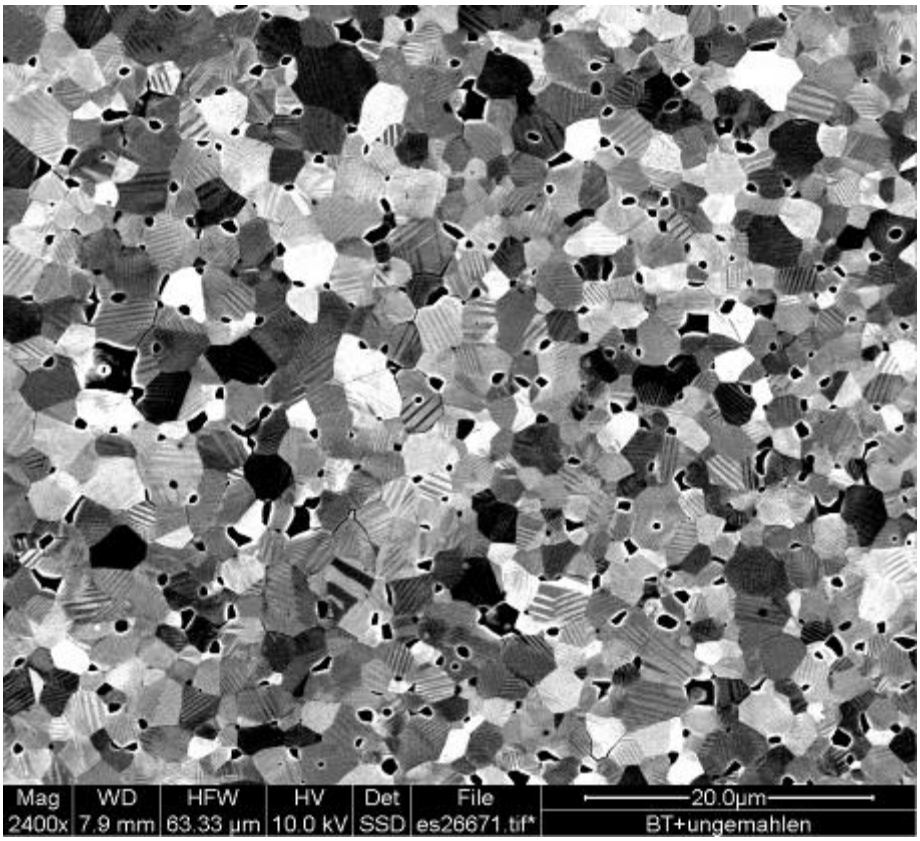

Figure 1. Microstructure and domain distribution of sintered Barium Titanate without milling step.

Figure 2. Microstructure and domain distribution of sintered Barium Titanate after the milling step.

Ceramics, Oxides, Geomaterials

MS.2.P029
ZrO_2-CuO nanoparticles revealed by HRTEM and SAED

A. Tonejc[1], M. Ivanda[2], A. Tonejc[1], M. Bijelić[1], L. Mikac[2], G. Štefanić[2], S. Musić[2]

[1]Faculty of Science, Department of Physics, Zagreb, Croatia
[2]Rugjer Bošković, Division of Materials Chemistry, Zagreb, Croatia

andelka@phy.hr
Keywords: ZrO_2–CuO nanoparticles, High Resolution Transmission Electron Microscopy (HRTEM), Selected Area Electron Diffraction (SAED)

In this article we report on HRTEM and SAED examinations of samples ZrO_2–CuO having 0.0 and 0.2 mol % CuO content and performed calcination at temperatures 400 and 500^0C (samples named ZCuO-400, ZCuO2-400, ZCuO-500, ZCuO2-500). Measurements were done on JEOL JEM 2010 200kV high resolution transmission electron microscope. Previously the samples were examined by low frequency Raman spectroscopy (LFRS) [1] and other characterization methods [2].

LFRS can be applied to nanoparticles having spherical microstructure and having a constant that depends on the ratio of the longitudinal and transversal velocities of sound within the particles.

The particle size distribution measured by LFRS and HRTEM is in very good agreement for a number of materials whether the particles are amorphous, nanocrystaline, nanocrystaline in amorphous matrix in thin films or in the form of powder [3,4].

In Figure 1. we give evidence about the existence of amorphous nanoparticles, what is evidenced in BF as well in SAED, were the first amorphous ring (A) is very well observed. By prolonged heating, monoclinic (M) and tetragonal ZrO_2 (sample ZCuO-400) can be observed in SAED.

The samples ZCuO-400 and ZCuO2-400 are fully amorphous (Figures 1b. and 2b.), but with heating in EM during observation by SEAD, the first spot of new phase appeared in amorphous part of the sample. The monoclinic ZrO_2 (-111) with d=0.314 nm and (111) with d=0.284 nm could be identified. In Figure 1c. in the same region of the sample, amorphous spherical and crystalline particles as well as the holes (H) are observed in HRTEM image. For lower magnification particle size distribution, the size of particles are D=(6.7$\pm$0.3) nm, while hole sizes are H=(5.7$\pm$0.3) nm. The crystalline phases are identified by SAED in Figures 1b. and 2b. as amorphous (A) and monoclinic ZrO_2 (M).

In Figure 2a. (sample ZCuO2) particle sizes are smaller, D=(3.4$\pm$0.6) nm. This result is in accordance with previous measurements, obtained on series of samples having different doping concentration of CuO, in which the particles sizes increase with increasing calcination temperatures [1]. Also, the results show that with increasing doping concentration, nanoparticles become smaller, as observed in In_2O_3 doped with Sn (ITO) [5].

1. L. Mikac, M. Ivanda, G. Štefanić, S. Musić, K. Furić and A.M. Tonejc, J. Molecular Structure 993 (2011), p. 198.
2. G. Štefanić, S. Musić, M. Ivanda, J. Alloys Comp. 491 (2010), p. 536.
3. M. Ivanda, A. M. Tonejc, I. Djerdj, M. Gotić, S. Musić, G. Mariotto and M. Montagna, in "Springer Lecture Notes in Physics: Nanoscale Spectroscopy and Its Application to Semiconductor Research", Eds: Y. Watanabe, S. Heun, G. Salviati and N. Yamamoto (Springer, Berlin) (2002), p. 24.
4. M. Ivanda, K. Furić, S. Musić, M. Gotić, D. Ristić, A. M. Tonejc, I. Djerdj, M. Mattarelli,. M. Montagna, M. Ferrari, A. Chiasera, Y. Jestin, G. C. Righini, W. Kiefer and R.R. Goncalves, J. Raman Spectroscopy 38 (2007), p. 647
5. J. Popović, B. Gržeta, E. Tkalčec, A. M. Tonejc, M. Bijelić, C. Goebert, Materials Science&Engineering B-Solid State Materials for Advanced Technology, 176 (2011) p.93.

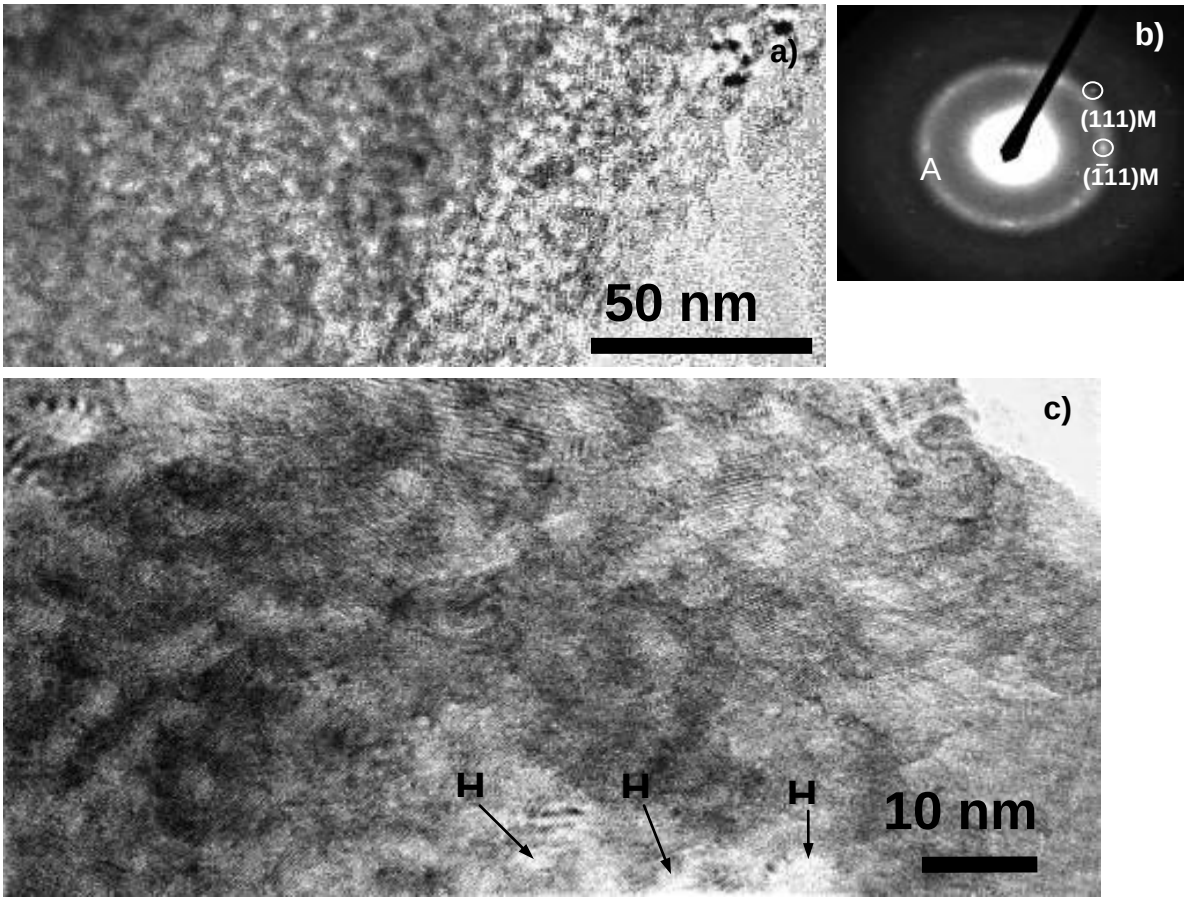

Figure 1. ZCuO-400: a) and c) nanocrystalline-amorphous sample with holes H; b) SAED-amorphous ring A.

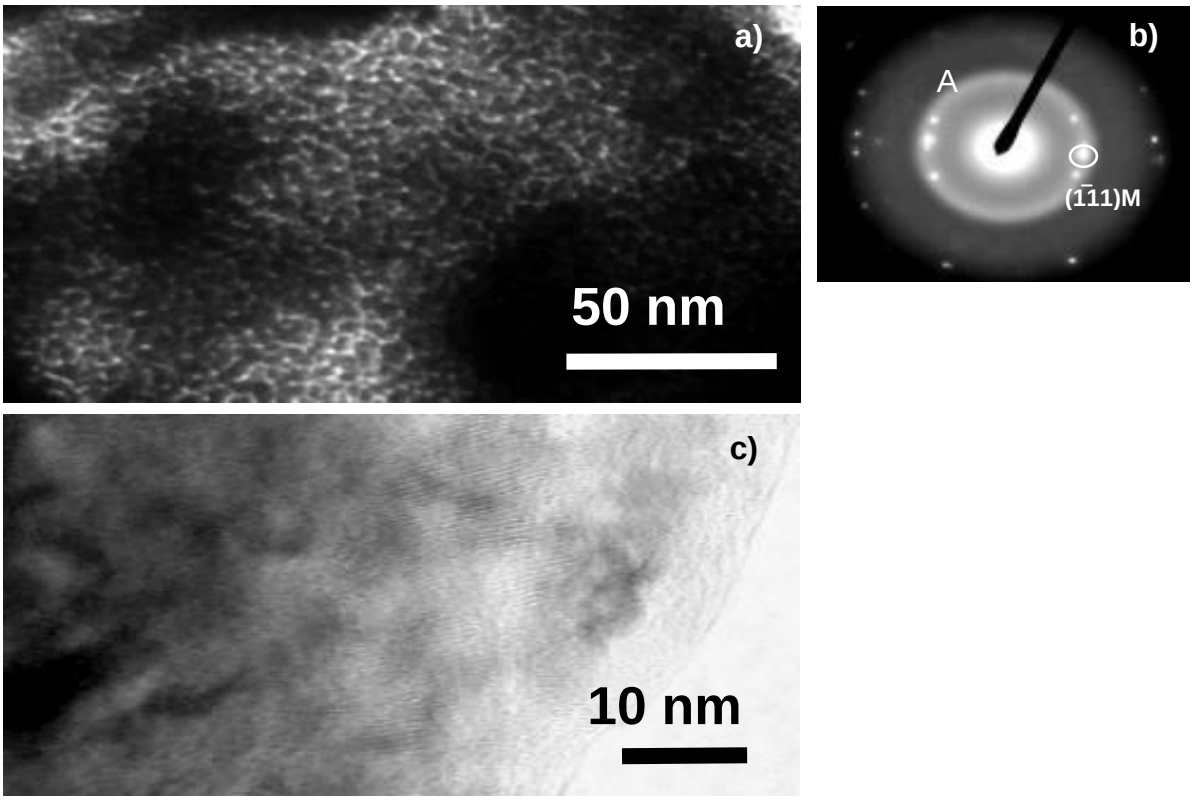

Figure 2. ZCuO2-400: a) and c) nanocrystalline-amorphous sample with holes; b) SAED-amorphous ring A.

Ceramics, Oxides, Geomaterials

MS.2.P030
SEM observation of gold in quartz vein from Atud ancient gold mine in central Eastern Desert of Egypt

A. S. Khalil[1], A. A. Zahran[1]
[1]Mining and Metallurgy Department, Tabbin Institute for Metallurgical Studies (TIMS), Helwan, POB 109, Cairo, Egypt

askhalil2004@yahoo.com
Keywords: Ancient Gold Mines, Quartz Veins, Gold Specks, Scanning Electron Microscope

The wealth of gold in Pharaonic Egypt is legendary. The Eastern Desert of Egypt was long known as a gold mining district of the empire providing the precious metal since ancient times. Gold mining in this area dates back to predynastic times (*ca* 3500 BC) and continued during Old to New Pharaonic dynastic Kingdoms (2700 to 1070 BC) and later different times throughout the history of Egypt. This area is belonging geologically to the Precambrian basement of the Arabian Nubian shield which extends from the river Nile eastwards towards the Arabian Peninsula. It extends as a belt parallel to the Red Sea coast for a distance of about 800 km along Egypt's eastern edge hosting all the known locations of gold deposits in Egypt which is about 250 gold mining sites spread over the whole area [1].

The gold was extracted from quartz veins of various dimensions in open-pit and underground workings. The quartz veins are sheet like body of crystallized silica precipitated from hydrothermal fluids in shear zones, faults and fractures within the metasidements and related rock of basaltic and dioritic origin [2]. The native gold is spatially associated with these veins and occurs in most cases as minute specks and discrete scattered flakes within the vein or as small inclusions in sulphides particularly pyrite and arsenopyrite [3].

The Atud area (latitude 25° 00' 10" N and longitude 34° 24' 10" E) located at 638 km (as the crow flies) south east of Cairo and 58 km west of the town of Mersa Alam on the Red Sea coast "Figure 1a." is one of several ancient dominant gold vein deposits in central Eastern Desert of Egypt. This area is centred on *Jabal* (hill) Atud shown from a bird's eye view perspective in "Figure 1b." and a corresponding geological map in "Figure 1c." and depicted in a photograph in "Figure 1d.". In this area a number of gold-bearing quartz veins are concentrated mainly in three localities, referred to as the main Atud. The average thickness of the veins in Atud is about 70 cm. The gold content of the mineralized veins varies considerably even in the same vein, it may reach a maximum of 467–1203 ppm. However, the average does not usually exceed 11–30 ppm [4]. The mine was first excavated during Pharonic time but no ore is produced since then, between 1953 and 1969, the Egyptian Geologic Survey and Mining Authorities (EGSMA) performed underground prospecting work in the main Atud site through three expeditions [5].

In this study we report SEM and EDS investigation of a sample cut using a geological hammer and crowbar from a quartz vein "Figure 1e." which cropped out inside surface of the first level entered from the northern side of the mine shown in "Figure 1f.". The samples for microscopic observations were cut from the bulk sample then grind, polished and ultrasonically cleaned. The SEM used in this study is FEI Inspect-S50 supplied with Quantx Bruker EDS spectrometer. The samples were observed at low vacuum of 0.45 Torr and the SEM operated at 20 keV accelerating voltage.

Depicted in "Figure 2a." illustrating gold specks of various morphologies, our observations showed that these specks ranged in maximum-lengths from 3.4 μm to 9.2 μm. A typical obtained EDS spectrum from such specks is shown in "Figure 2b.". However, due to the erratic presence of specks and their distribution of sizes, more specks must be measured to obtain a reliable histogram. In addition we should not exclude that gold may occur in "invisible form" as solid solution or submicron specks which is harder to observe. The possible origin of this gold mineralization in Atud area was related to fluid phase separation, sulphidization and carbonatization of the host dioritic rocks during hydrothermal alteration and mineralization [5]. In conclusion, we had demonstrated the versatility of using SEM-EDS in the assessment of a gold bearing quartz vein in Atud ancient mine.

1. D. Klemm, R. Klemm and A. Murr, African Earth Sciences, 33 (2001) p. 643.
2. A. A. Hussein, in "Geology of Egypt", ed. R. Saied, (Balkema, Rotterdam, Holland) (1990), p. 511.
3. A. G. Shazly, Egyptian Mineralogy, 10 (1998) p. 51.
4. N. G. Botros, Ore Geology Reviews, 19 (2002) p.137.
5. H. Z. Haraz, Journal of African Earth Science, 35 (2002) p.347.

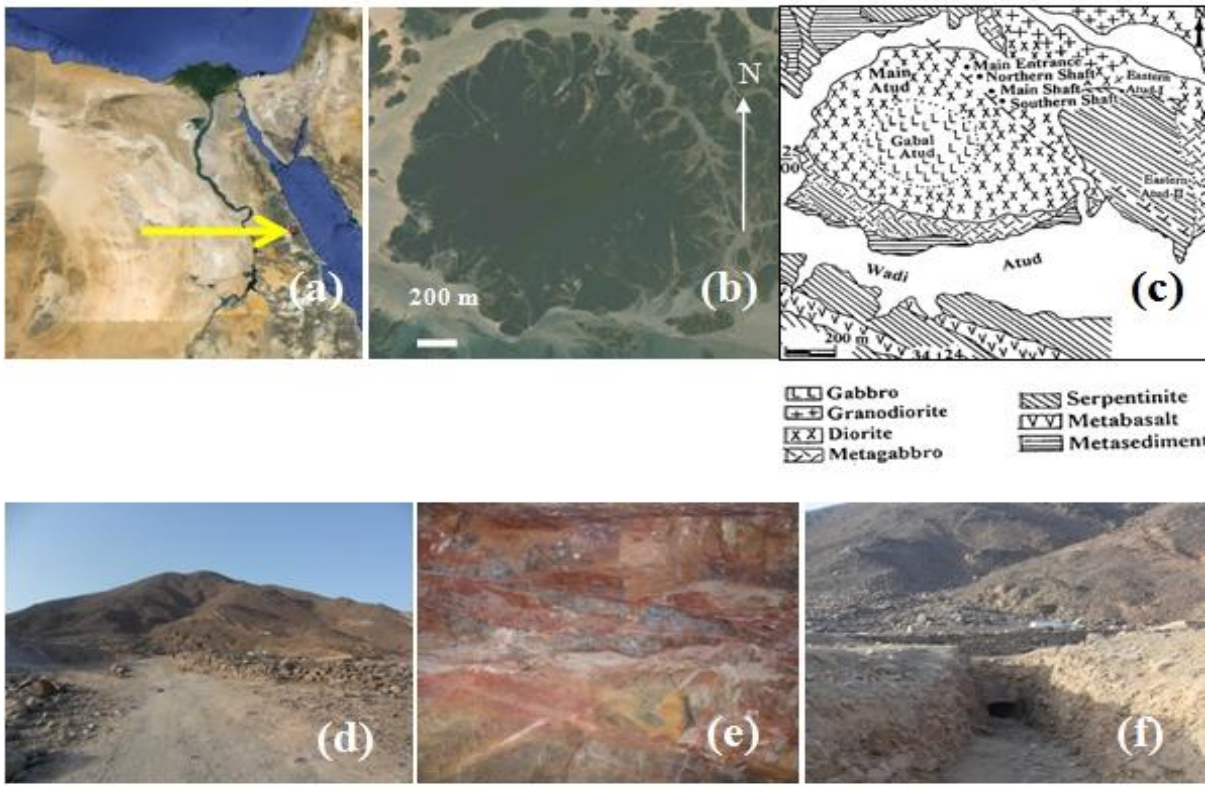

Figure 1. (a) A location map of Egypt with an arrow pointing to the Atud area in central Eastern Desert (Google Maps). In (b) a view at eye altitude of 6 km of the *Jabal* Atud (Google Earth) and in (c) a geological map of *Jabal* Atud [5]. In (d) the north side of *Jabal* Atud and in (e) the gold bearing quartz vein from the first level entered from the northern entrance shown in (f).

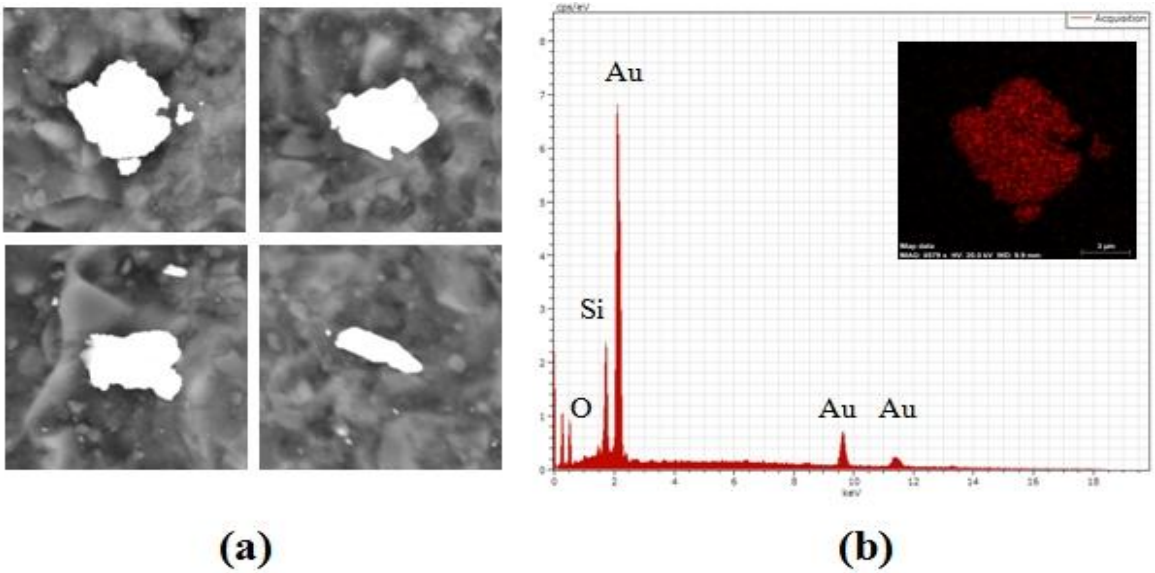

Figure 2. In (a) backscattered electron micrographs each has a side of 20μm (magnification of x5000) depicting the different morphologies of observed gold specks and in (b) EDS spectra obtained from the gold speck shown in the first micrograph in (a), with the inset showing the Au elemental mapping of this speck

Ceramics, Oxides, Geomaterials

MS.2.P031
Aberration-Corrected Microscopy and Spectroscopy of SiAlON Ceramics

H. Yurdakul[1], J.-C. Idrobo[2], E. Okunishi[3], S.J. Pennycook[2], S. Turan[4]

[1]Dumlupinar University, Materials Science & Engineering, Kutahya, Turkey
[2]Oak Ridge National Laboratory, Materials Science and Technology Division, Oak Ridge, TN, United States
[3]Jeol Ltd., Tokyo, Japan
[4]Anadolu University, Materials science and Engineering, Eskisehir, Turkey

hyurdakul@anadolu.edu.tr
Keywords: Cs-corrected STEM, atomic-resolved EELS, SiAlON, Ceramics

SiAlONs are new generation solid-solution ceramics derived from the same crystal structures of α-β/Si_3N_4 [1]. Depending on the sintering dopants, the desired engineering properties of SiAlONs for many kind of applications from cutting tools to white light emitting diodes (LEDs) can be tailored by microstructure, primarily consisting of two distinct polymorphs (α and β), triple junction phases and grain boundaries [2-4]. Therefore, the atomic-scale characterization is a key step in further developing and designing the SiAlONs. However, over the past three decades, although many researches have been shed light on the micro- to atomic-scale observations of SiAlONs, the atomic-resolved STEM knowledge from α- and β-SiAlON unit-cells as well as grain boundaries has been lacking.

Here, we report the atomic-scale imaging and spectroscopy of gas pressure sintered Yb, Ce and Yb-Ce containing single and double rare-earth cation doped α/β-SiAlONs as well as TiN reinforced β-SiAlON ceramics using Z-contrast and EELS techniques in different type of state of the art aberration-corrected STEMs [5-6]. The results demonstrate that: *(i)* Yb and Ce dopants were preferentially incorporated into the β-SiAlON crystal structure at the atom-specific lattice locations, with higher solubility for Yb than Ce; *(ii)* this observation was also confirmed in the Yb-Ce co-doped system; *(iii)* Ce atoms without any co-doped cation were present in the triangular-like host sites of α-SiAlON unit-cell, accommodating much more atoms than Ce-doped β-SiAlON; *(iv)* Yb and Ce atoms were periodically and differently arranged in the grain boundaries, explaining that they are in semi-crystalline nature, not completely amorphous; and (v) Ti atoms were incorporated into the β-SiAlON unit-cell.

In conclusion, our atomic-resolved microscopy and spectroscopy results demonstrate direct visualization of the sites and solubility of rare-earth and transition metal atoms in α-β SiAlON unit-cells and grain boundaries. This capability offers new atomic-level engineering insights into how appropriate rare-earth types and SiAlON host polymorphs should be chosen for nanoscopic tailoring of both next-generation SiAlON-based structural materials and optical ceramics. We expect our observations of impurity sites and solubilities in SiAlON polymorphs and grain boundaries represents the first step towards a new paradigm for atomic-scale guidance in the production of rare-earth and transition metal atoms doped materials for a wide variety of applications.

1. T. Ekström and M. Nygren, J. Am. Ceram. Soc. 75 (1992), p. 259.
2. H. Mandal, J. Eur. Cer. Soc. 19 (1999), p. 2349.
3. K. Shioi et al., J. Am. Ceram. Soc. 93 (2010), p. 465.
4. R. J. Xie, N. Hirosaki and M. Mitomo, J. Electroceram. 21 (2008), p. 370.
5. S. J. Pennycook *et al.,* Phil. Trans. R. Soc. A 367 (2009), p. 3709.
6. S. J. Pennycook, B. Rafferty, P. D. Nellist, Microsc. Microanal. 6 (2000), p. 343.
7. This research was supported by The Scientific and Technological Research Council of Turkey (TUBITAK) through 2214-International Doctoral Research Fellowship Program (H.Y.), by National Science Foundation through Grant No. DMR-0605964 (J.C.I.), Oak Ridge National Laboratory's SHaRE User Facility (J.C.I.), which is sponsored by the Office of Basic Energy Sciences, US Department of Energy, and the Office of Basic Energy Sciences, Materials Sciences and Engineering Division, US Department of Energy (S.J.P.). We also would like to thank MDA Advanced Ceramics (Eskisehir, Turkey) for the provision of the samples produced from the project with a contract number of 3040287-Technology and Innovation Funding Programmes Directorate (TEYDEB), Turkey.

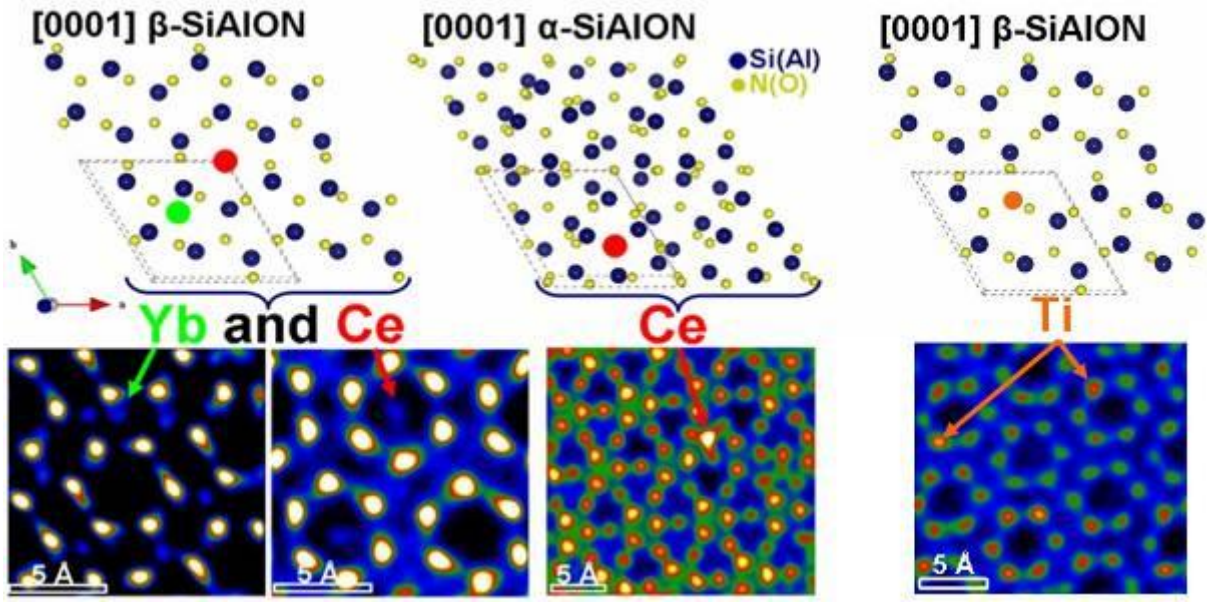

Figure 1. Z-contrast HAADF images of interstitial Yb and Ce rare-earth atoms in α- and β-SiAlON unit-cells as well as substitutional Ti atoms within β-SiAlON crystal structure through Cs-corrected STEM. Please note that unit-cells are shown by dashed parallelograms.

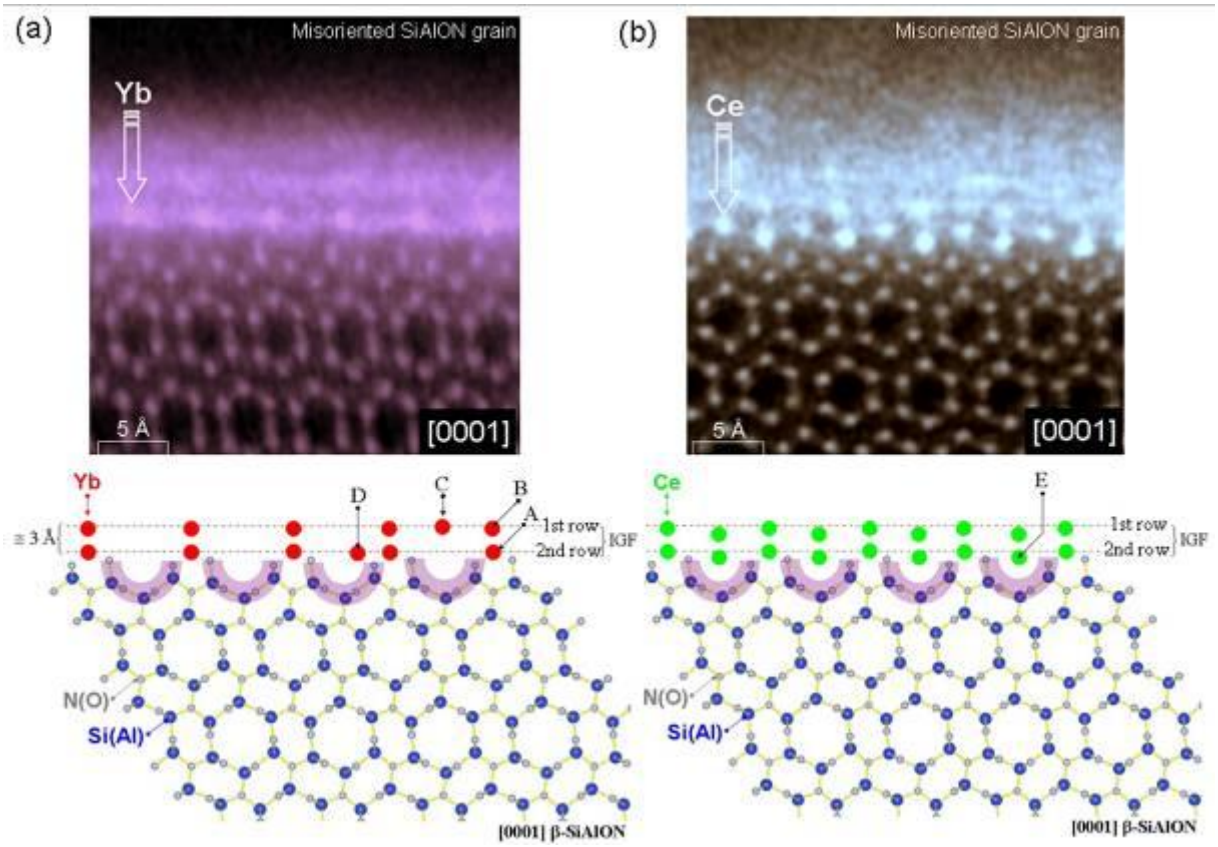

Figure 2. The Z-contrast images obtained from (a) Yb and (b) Ce doped systems using aberration-corrected STEM showing the IGF structures between [0001] β-SiAlON and misoriented SiAlON grains. Here, rare-earth element specific atomic-sites for Yb and Ce are atomically visualized in semi-crystalline IGFs with approximately 7-8 Å thicknesses. Evaluation of specific atomic positions (marked with arrows in the simulation part of Fig. 2(a-b)) on the rows of IGF, it can be deduced that Yb and Ce atoms are attached to the surface of [0001] β-SiAlON grain at the “A”, “B”, “C”, “D” and “E” atomic sites.

Ceramics, Oxides, Geomaterials

MS.2.P032
Deformation behaviour of $KNbO_3$ under compression between room temperature and 900°C

A.F. Mark[1], M. Castillo-Rodriguez[2], W. Sigle[1], P.A. van Aken[1]

[1]Max Planck Institute for Intelligent Systems, Stuttgart Center for Electron Microscopy, Stuttgart, Germany
[2]Universidad de Sevilla, Departamento de Física de la Materia Condensada, Seville, Spain

alison.mark@is.mpg.de
Keywords: dislocations, domain walls, $KNbO_3$, in situ TEM

Potassium niobate ($KNbO_3$) is a versatile ferroelectric perovskite and a strong candidate to replace lead-containing perovskites in electromechanical devices. A detailed understanding of the mechanical properties of this material and how they relate to its ferroelectric behaviour is key to its becoming a reliable component of these devices.

Previous work on strontium titanate revealed that it has unexpected ductile to brittle to ductile variations in its mechanical behaviour as the test temperature is increased [1,2]. Differences in the slip characteristics and dominant dislocations were observed in three temperature regimes [3,4]. It is not known how common this behaviour is across the perovskite family of materials, i.e. if $KNbO_3$ behaves in the same way. Also, since $KNbO_3$ is ferroelectric it has the added complication of domains and their boundaries, domain walls. It is not known how these interact with dislocations, if the mechanical behaviour is affected. Also, since the switching of the ferroelectric depends on movement of the domain walls the presence of dislocations might affect the switching process, probably detrimentally.

Compression tests have been performed on single crystals of potassium niobate at temperatures between 25°C and 900°C. The stress and strain response of the crystals has been tracked and the deformed crystals have been examined in detail. The damage level for each specimen has been determined using optical and scanning electron microscopy. Transmission electron microscopy has been performed to observe and characterize the dislocations and domain walls for all the specimens for which TEM sample preparation was possible. In addition, in-situ heating experiments have been performed to observe the interaction between domain walls and dislocations.

The initial response of $KNbO_3$ to strain is the development of characteristic domain structures (Figure 1). The in-situ tests reveal that specific domain structures also develop during heating of the material. The interaction of the domain walls with dislocations was also observed in the in-situ tests. Further straining in the compression tests reveals distinct differences in the behaviour of $KNbO_3$ at different temperatures. The level of damage increases with test temperature; the material behaves in a brittle manner at the higher temperatures (700°C–900°C). Differences in the domain wall and the dislocation structure are also observed (Figure 2).

1. D. Brunner, S. Taeri-Baghbadrani, W. Sigle and M. Rühle, J. Am. Ceram. Soc., 84 (2001) p.1161.
2. S. Taeri, D. Brunner, W. Sigle and M. Rühle, Z. Metallkd., 95 (2004) p. 433.
3. D. Brunner, Acta Mater., 54 (2006) p.4999.
4. M. Castillo-Rodríguez and W. Sigle, Scr. Mater., 64 (2011) p. 241.

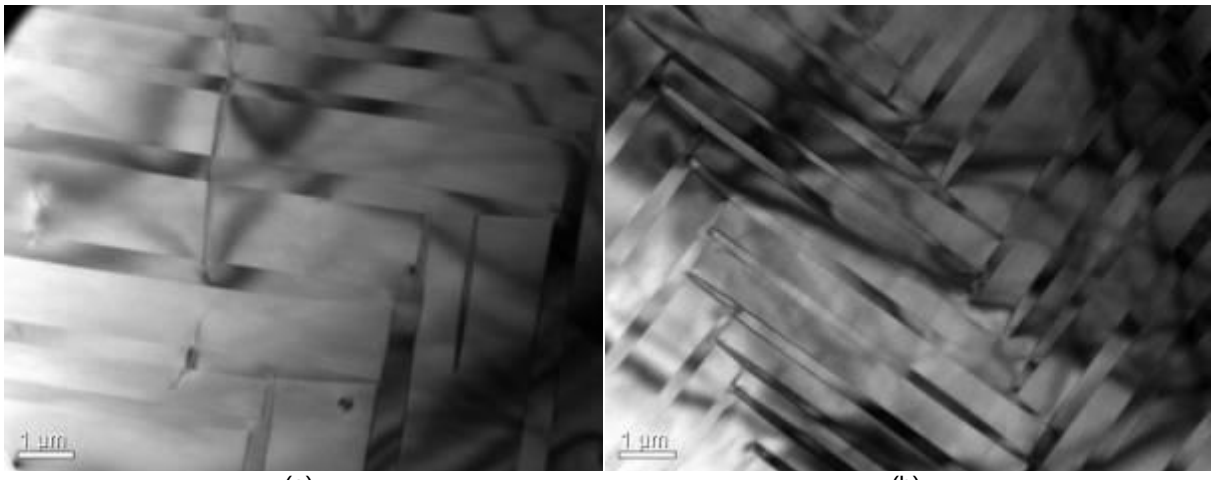

(a) (b)

Figure 1. Domain patterns observed in single crystal $KNbO_3$ after compression at room temperature. The amount of strain applied is higher in (b) than in (a).

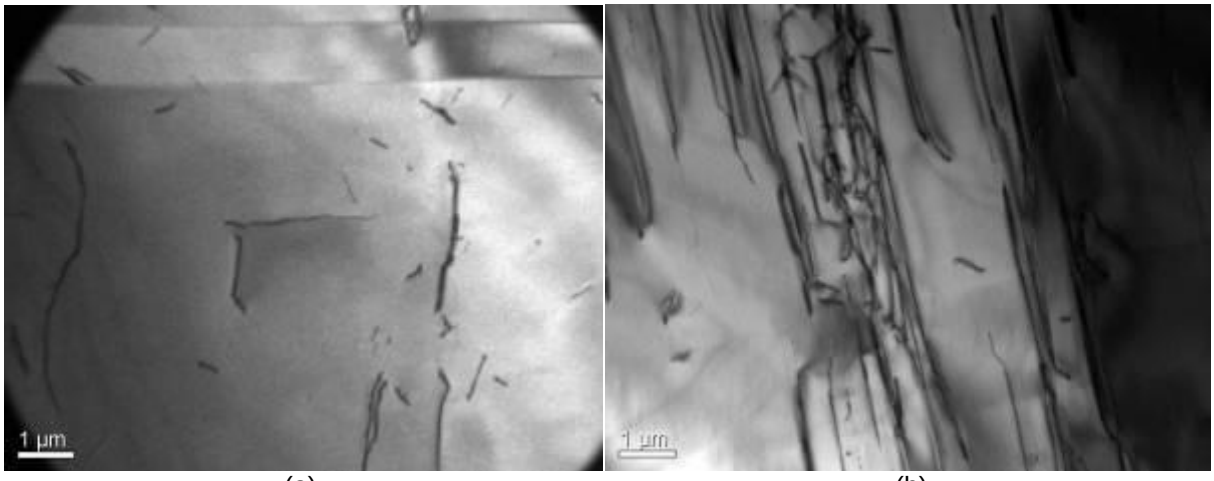

(a) (b)

Figure 2. Dislocations and domain walls observed in $KNbO_3$ after compression at (a) 700°C and (b) 900°C.

Ceramics, Oxides, Geomaterials

MS.2.P033
Characterization of local phases of $BaTiO_3$ ceramics by high-resolution electron energy loss spectroscopy

N.-H. Cho[1], H. Yun[1], S.-M. Moon[2], X. Wang[3]

[1]Inha University, Materials Science and Engineering, Incheon, Korea, Republic of
[2]Samsung Electronics Co., Ltd, Suwon, Korea, Republic of
[3]Tsinghua University, Beijing, China

nhcho@inha.ac.kr
Key words: $BaTiO_3$, Phase, EELS.

The electrical features of $BaTiO_3$ ceramics have been known to be crucially determined by the crystal system of their grains. Therefore, it is important to identify the relation of the tetragonal-cubic phase transition with local structural and chemical conditions. The variation in the electron energy structure of $BaTiO_3$ in terms of phase transition has been reported by some theoretical research groups [1,2]. Nevertheless, little electron-beam-related experimental researches have been carried out to identify the energy band structure of $BaTiO_3$, which can be related with the tetragonal-cubic phase transition.

The $BaTiO_3$ ceramics used in this study was prepared by a routine-sintering method. The purity of $BaTiO_3$ powder was 99.8%. $BaTiO_3$ powders were die-pressed under 200 MPa. The powder compact was heat-treated at 1360^{o}C in air for 4 h and then air-quenched to room temperature. To investigate the phase distribution within a nanoscale $BaTiO_3$ powder, ~50 nm-sized $BaTiO_3$ powders were prepared by the hydro-thermal method. In-situ X-ray diffraction examination was carried out to obtain structural information of the tetragonal and cubic phases of the ceramics. In-situ EELS measurements were also performed from a particular region in the sintered $BaTiO_3$ ceramic specimen; the tetragonal and cubic phase transition was induced by keeping the TEM specimen at particular temperatures in a heating stage. EELS spectra were acquired at room temperature and 150^{o}C, respectively.

Conventional TEM investigation was carried out using an electron microscope operated at 300 keV (TITAN TM 80-300, FEI company). The electron probe diameter was below 1 nm. For the evaluation of the electronic structure of the $BaTiO_3$ ceramics, the energy-loss near-edge structure (ELNES) of Ti $L_{2,3}$ were measured; the EELS measurement was carried out with the Gatan GIF 2002 system (parallel EELS).

The crystal structure and lattice parameters of the $BaTiO_3$ ceramics were confirmed in terms of temperature; the calculated results are summarized in Table 1. In the XRD data, the cubic phase appears to have lattice parameters (a, b and c axis) larger than those for the tetragonal phase condition. It is expected that in $BaTiO_3$, crystal field effect is stronger in a tetragonal phase than in a cubic phase. It was found that the fine structure of the titanium $L_{2,3}$ edge and their satellite peaks are sensitively varied with the tetragonal-cubic phase transition. Figure 1 shows the spectra taken from the tetragonal and cubic phases of $BaTiO_3$ ceramic; spectra (a) and (b) were obtained from the same region of $BaTiO_3$ ceramic specimen at room temperature and 150^{o}C, respectively. The peak splitting of Ti L_3 edge of tetragonal-phased $BaTiO_3$ ceramics was widened due to the increased crystal field effect compared to that of cubic-phased $BaTiO_3$. The satellite peaks were also shifted to higher energies by about 0.8 eV for tetragonal-phased $BaTiO_3$ with respect to the cubic-phased $BaTiO_3$ ceramics.

The phase distribution within nanoscale $BaTiO_3$ powders, in other words, the presence of tetragonal (or cubic) phases in terms of the distance from the surface was investigated by EELS techniques. Figure 2 shows the spectra recorded at positions 1, 4, 7 and 20 nm, away from the surface, respectively, in the $BaTiO_3$ powders. All the spectra are aligned such that the maximum of the first peak (Ti L_3 t_{2g} peak) is located at the same value in the spectra and these are denoted by vertical dotted lines. The L_3 edge splitting of the core region was found to be little smaller than that of shell region. In particular, the energy gap between the two peaks t_{2g} and e_g varied significantly with changing the distance between the probed position and the surface from 1 to 20 nm. These results suggest that EELS technique can be used to identify the local phase of sintered $BaTiO_3$ ceramic.

1. Bagayoko, D., Zhao, G.L., Fan, J.D. & Wang, J.T. (1998). J. Phys.: Condens. Matter. 10, 5645.
2. Cohen, R. & Krakauer, H. (1990). Phys. Rev. B42, 6416.

	25 °C	150 °C
a (Å)	3.9924	4.0459
b (Å)	3.9924	4.0459
c (Å)	4.0309	4.0459
c/a	1.009	1
Space group	P4mm	Pm3m

Table 1. Lattice parameters of $BaTiO_3$ ceramics. These values were obtained when the ceramics were at room temperature and 150°C, respectively.

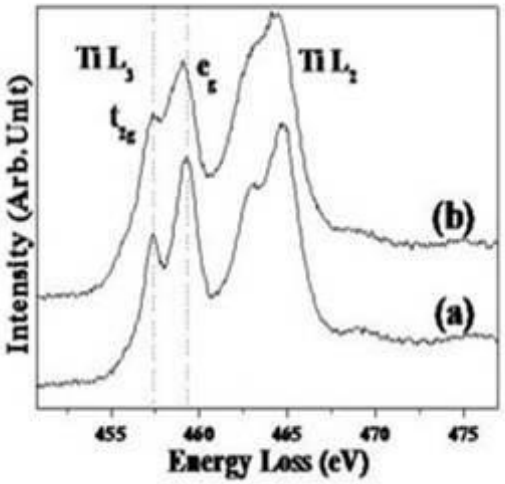

(Figure 1)

Figure 1. EELS spectra of Ti $L_{2,3}$ edge of $BaTiO_3$ ceramics. The ceramics were at room temperature (a) and 150°C (b), respectively.

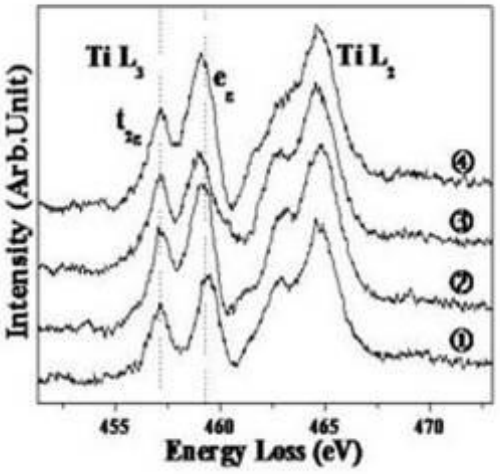

(Figure 2)

Figure 2. EELS spectra of Ti $L_{2,3}$ edge of nanoscale $BaTiO_3$ powders. (a) The EELS measurements were carried out at positions 1(①), 4(②), 7(③) and 20 nm(④) away from the surface, respectively.

Ceramics, Oxides, Geomaterials

MS.2.P034
Dimensional and phase characterization of titanium oxide nanoparticles

V. Zhigalina[1], A. Lizunova[2,3], S. Sulyanov[1], N. Kiselev[1], V. Ivanov[2,3]

[1]Shubnikov Institute of Crystallography RAS, Moscow, Russian Federation
[2]LLC "RUSNANO Metrology Center", Moscow, Russian Federation
[3]Moscow institute of physics and technology, Moscow, Russian Federation

anna.lizunova@gmail.com
Keywords: nanoparticles, LEC TiO_2, HRTEM

Titanium dioxide (TiO_2) nanoparticles are used in a wide range of industrial and consumer goods including paints, (photo)catalysis, adhesives, ceramics, cosmetics and pharmaceuticals, food colorants, gas sensors, solar cells [1]. The nanoparticles properties are determined by the crystal structure, size, morphology and state of agglomeration and strongly depend on the method of synthesis. Titanium dioxide exists in three main polymorphs: anatase, rutile and brookite. It is known that anatase phase possesses more stable crystal structure for particles size smaller than 30 nm and has a higher toxic activity in different vital processes than the rutile one [2].

In the present study the nanoparticles were synthesized by target laser ablation (LEC) from a micron size TiO_2 powder [3]. Pulsed laser ablation is known to prepare high purity nanoparticles with the narrow size distribution and a shape close to spherical. The most significant characteristic of the obtained titanium dioxide powder is a low agglomeration of the nanoparticles.

The TiO_2 powder was investigated by a high resolution transmission electron microscopy (HRTEM), selected area electron diffraction (SAED) and X-ray diffraction methods. An X-ray powder pattern was obtained at X'PERT PRO diffractometer in X-ray K_α line of copper. TEM, HRTEM and SAED were performed in a FEI Tecnai G^2 30 ST at 300 kV and a JEOL JEM-2100 at 200 kV.

Bragg peak parameters were measured by pseudo-Voigt function fitting. Two phases with tetragonal rutile (*$P4_2/mnm$*, a = 4.601(4) Å, c = 2.954(5) Å) and tetragonal anatase (*I41/amd*, a = 3.786(1) Å, c = 9.499(4) Å) lattices were revealed with the anatase phase being prevalent. The powder diffraction pattern had one faint unidentified peak which can be related to the brookite phase.

TEM study of the TiO_2 powder confirmed that the nanoparticles had almost spherical shape (Fig. 1a). Analysis of the electron diffraction patterns showed that an amount of the present anatase phase was several times higher than for the rutile one (Fig. 1b). These data were in a good agreement with previously obtained RFA data. The diameters of more than 3000 particles were measured. The size distribution of nanoparticles followed the log-normal curve and the mean diameter was 18 nm.

HRTEM study of single nanoparticles developed their monocrystalline structure (Fig. 2). Yet some particles had structural defects such as blocks and twin boundaries. In some cases thin amorphous layer of 1-2 nm was observed due to the electron beam irradiation. Lattice parameters were investigated by SAED and fast Fourier transforms (FFT) of HRTEM images. The crystal structure and diameter of 500 anatase particles (Fig. 2a) with sizes in the range of 5-45 nm and 57 rutile particles (Fig. 2b) with sizes in the range of 6-35 nm were determined. The average diameter of the anatase phase differed from the rutile one not more than 5% and was about 19 nm.

The investigated nanosized titanium oxide particles regardless of their size had nearly spherical shape and a narrow size distribution. They had monocrystalline structure with a tetragonal lattice of mostly anatase phase. There is no significant correlation between particle size and crystal structure of the TiO_2 nanoparticles.

1. Xiaobo Chen and Samuel S. Mao, Chem. Rev. 107 (7) (2007), p.2891
2. J.Jiang et al. Nanotoxicology 2(1) (2008), p.33
3. Yu Kotov *et al*. Technical Physics. 72 (2002), 11, p.76

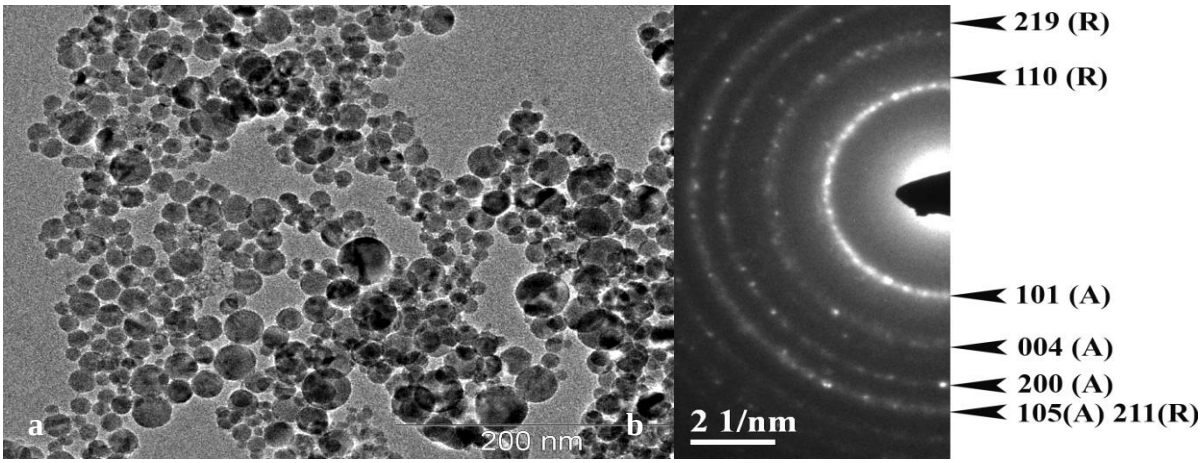

Figure 1. TEM image of TiO_2 nanoparticles (a) and their electron diffraction pattern (b).

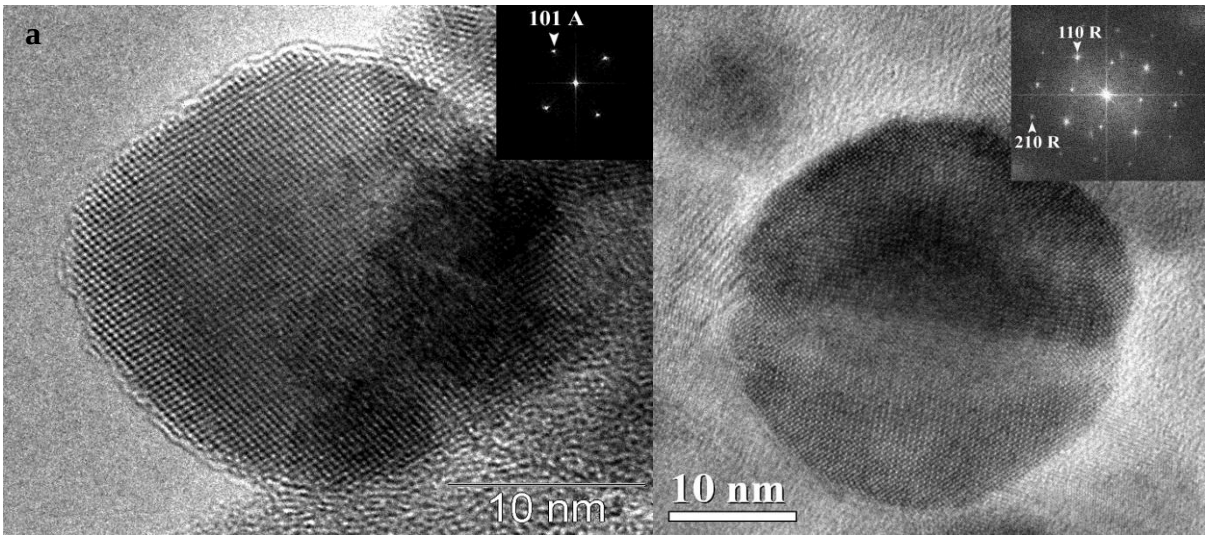

Figure 2. HRTEM images of single TiO_2 nanoparticles: anatase (a) and rutile (b) phases and their FFTs.

Ceramics, Oxides, Geomaterials

MS.2.P035
Characterization of partial smelting in earthenware ceramics through high resolution microscopy methods

M. Emami[1,2], R. Trettin[2]

[1]Art University of Isfahan, Conservation, Isfahan, Iran, Islamic Republic of
[2]University Siegen, Building material chemistry, Siegen-Germany, Germany

emami@chemie.uni-siegen.de
Keywords: Ceramic, ,Sintering, Partial smelting, AFM, ESEM, LM

Sintering is a well known terms in the ceramic science. Ceramic materials are the objects which must be sintered for getting their better physico-chemical properties, and consequently proved to be in thermodynamically meta-stable condition. Sintering has mostly been investigated as a mechanism not a result. Sinter temperature is the temperature by means of this the grain boundaries have to be damaged in order to build a smelt. Archaeological earthenware objects among them are interesting objects which consist of different mineralogical phase constituents and also different sinter temperature due to the kiln construction in the antiquity. Characterization of sinter structure helps also archaeologist for better understanding about the technology in the past. Indeed, ceramic technology is the oldest human tradition, but the newest scientific knowledge and therefore investigation on old objects can obtain better interpretation for characterization of technical ceramic's manufacturing process nowadays [1]. Sintering is not a process that quickly happened; rather it took place via partial smelting of the grain boundaries in the matrix [2]. According to this point of view, sintering and partial smelting of the matrix must study together, consequently. Sintering is discussed here as result and partial smelting as the process. In many cases we talk about good firing and sintering whereas the heat transfer process was not carried out completely. According to the crystalline phase composition and their decomposition, it will be noticeable for us to explain the state of the objects as in partial smelting zone or smelting zone. Investigation regarding to the partial smelting state is considerable because in this state the matrix is exposed to maximum mass diffusion through the crystalline phase decomposition [3]. Different samples have studied by means of their application for characterization of sintered texture. The samples are prepared as thin section and observed by polarization light microscopy for determining the crystalline phase constituents due to their typical petrographical features. The samples have also analyzed by environmental scanning electron microscope in order to gain the topographical data about the grain boundaries in micro area furthermore determining chemical composition of the matrix after sintering [3,4]. Mineralogical phase decomposition can also investigated for understanding about the mass transport and hence secondary mineralization through out of the sintering. Quantitative X-ray fluorescence analyses on crystalline phases have been carried out after phase refining method based on Rietveld process to obtain the exact crystallographic preferred orientation. The samples are investigated via atomic force microscopy in order to characterize the grain boundaries and their defect through sintering via partial smelting [5]. All of the samples are from 5100 BC and they seem to have optimal firing because of the solidity of their body. Archaeological objects are preferred objects because they made by well processed soil and clay from their original region, furthermore their manufacturing techniques are actually primitive and therefore caused the better visibility of texture. One of the most interesting factors in such objects is the thin layer of coating covered the samples (slip) [6]. To characterize the coating layer high resolution microscopy methods (AFM) carried out to determine the grain boundaries between the surface and the slip. According to the chemical analysis and petrographical investigation, partial smelting is a reaction which would be controlled by different mineralogical parameter. In this case the ratio between Gehlenite/Anorthite, is an important thermodynamic interaction. On the other hand partial smelting of clay minerals causes the better adherence of texture. In the earthenware materials mostly appeared 2-3% clay minerals which are not the secondary mineralization, but also they are remaining of partial smelting. Partial smelting is also detectable through AFM on grain boundaries (Figure 1).

1. M-A. Emami, T. Kowald and R. Trettin, Materials and Manufacturing Processes, issue 24, vol. 9, (2009), p. 934-941
2. M. Maggetti, Ch. Neururer and D. Ramseyer D., Applied Clay Science, vol. 53, (2011), p. 500-508.
3. M-A. Emami and R. Trettin, Journal of Advanced Microscopy Research, vol. 5, issue 11, (2010), p. 181-189.
4. R. Martineau, A.V. Walter-Simonnet, B. Grobety and M. Bautier, Archaeometry, vol. 49, (2007), p. 23-52.
5. M-A. Emami, J. Volkmar, and R. Trettin,R., Surface Engineering, issue 24, vol. 2, (2008), p. 129-137
6. M-A. Emami, R. Trettin, Surface Engineering, vol. 29, issue 2, (2013), pp. 134-139

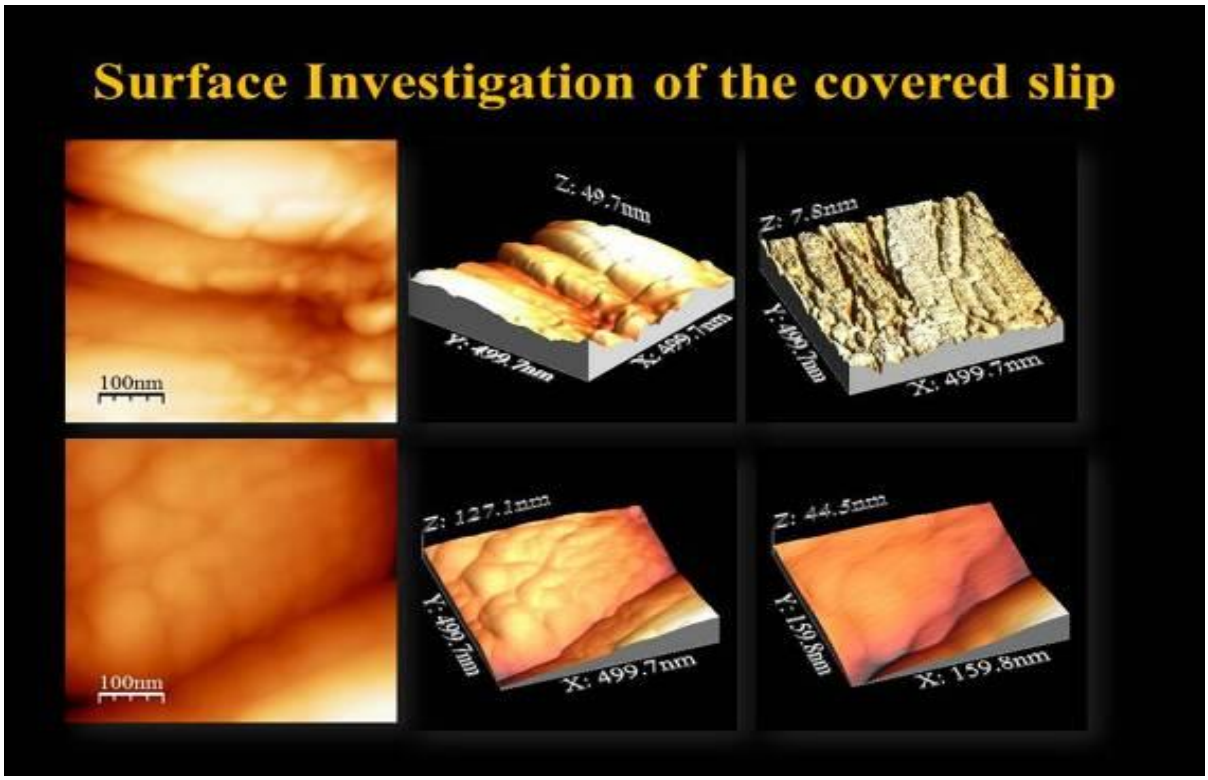

Figure 1. Surface characterization and partial smelting of the grain boundaries

Functional Materials

MS.3.036
Cross sectional imaging of high mobility graphene heterostructure devices

S. Haigh[1], A. Mishchenko[2], A. Gholinia[1], A. Geim[2], K. Novoselov[2], R. Gorbachev[2]

[1]University of Manchester, School of Materials, Manchester, United Kingdom
[2]University of Manchester, School of Physics and Astronomy, Manchester, United Kingdom

Sarah.haigh@manchester.ac.uk
Keywords: graphene, FIB, TEM

Recent progress in combining different 2D crystals in a single electronic device has produced new structures with unique properties. Multilayer heterostructures combining separate layers of graphene with hexagonal boron nitride are of particular interest with potential application in next generation high speed electronics [1-3]. Imaging of suspended 2D crystals using transmission electron microscopy (TEM) and scanning transmission electron microscopy (STEM) has provided fundamental scientific insights into defect formation, edge structure, doping and plasmonic properties [4,5]. However, when many separate 2D crystals are superimposed in projection, these plan view TEM images become difficult to interpret. Scanning tunnelling microscopy of 2D materials on surfaces has demonstrated that their behaviour is critically dependant on the presence of neighbouring atomic species [6]. This technique allows correlation of atomic surface structure with spectroscopic measurement of the local electronic density of states for 2D crystals on different substrates but is not suited to the study of encapsulated interfaces. Consequently little is known about the behaviour of 2D crystals when covered by additional layers and encapsulated deep below the surface. The increasing complexity of the latest devices requires a new approach to characterising two dimensional materials when layered into multi-component systems.

We have studied multilayer graphene/BN heterostructures where single layer and bilayer graphene sheets are individually contacted and encapsulated between insulating spacer layers. The multilayer stack begins with a thick (~ 50 nm) BN flake deposited on top of an oxidised Si wafer. Each subsequent layer is prepared on a separate wafer, de-bonded and transferred on top of the target device. The freshly deposited layer can be then shaped by reactive plasma etching and annealed (300°C in Ar/H_2) in order to remove processing residues. Because the graphene layers are separated by insulating BN spacers, each of them can be connected with Au/Ti contacts and the electrical properties studied independently [1]. Charge transport properties of these devices depend critically on the separation of the graphene layers and transport measurements therefore provide a route for estimation of the spacer layer thickness. However, more detailed structural data is highly desirable.

Here we report on recent work using a Focused Ion Beam (FIB) Scanning Electron Microscope (SEM) to extract thin cross sectional slices from the active region of several multi-layered graphene – based heterostructure devices with the desired location identified using secondary electron SEM imaging. The extracted cross sections have been imaged at high resolution using aberration corrected STEM combined with chemical analysis using electron energy loss spectroscopy and energy dispersive x-ray spectroscopy. Our side view observations (Fig 1) confirm the location of individual graphene sheets encapsulated between the separate BN layers and also allow precise measurement of interlayer spacings and interface roughness. Our side view imaging approach also allows comparison to the electrical device characteristics of individual layers measured before slice extraction. Through analysis of the local interlayer separation and layer roughness we observe a clear correlation between interface roughness and the electronic quality of encapsulated graphene [7]. We also report on the cross sectional imaging of devices that incorporate other 2D crystal such as tungsten disulphide and which have recently demonstrated significant improvements in device characteristics [8]. This work proves the concept of heterostructures assembled with atomic layer precision and reports their first side view TEM images. This novel approach offers the potential for correlation of measured transport properties for individual layers with local structural data and therefore provides a route to better understanding of the unique properties of 2D crystals when integrated into complex devices.

1. Britnell, L. *et al*. Field-effect tunneling transistor based on vertical graphene heterostructures. *Science* 335, 947-950 (2012).
2 Ponomarenko, L. A. *et al.* Tunable metal-insulator transition in double-layer graphene heterostructures. *Nature Phys.* 7, 958-961 (2011)
3. Wang, H. *et al.* BN/Graphene/BN transistors for RF applications. *IEEE Electron Device Lett.* 32, 1209 1211 (2011)..
4. J. H. Warner. *et al,* Dislocation Driven Deformations in Graphene. Science, 337, 209 (2012).
5. Meyer, J.C. *et al.* Experimental analysis of charge redistribution due to chemical bonding by high resolution transmission electron microscopy. Nature Mater. 10, 209-215 (2011).
6. Xue, J. et al. Scanning tunnelling microscopy and spectroscopy of ultra-flat graphene on hexagonal boron nitride, Nature Mater. 10, 282-285 (2011)
7. Haigh S. J. *et al.* Graphene-based heterostructures and superlattices: Cross-sectional imaging of individual layers and buried interfaces, Nature Mat. 11, 764–767 (2012)
8. Georgiou et al, Vertical field-effect transistor based on graphene–WS2 heterostructures for flexible and transparent

electronics, Nature Nano, **8**, 100–103 (2013) doi:10.1038/nnano.2012.224
9. The authors gratefully acknowledge funding from the EPSRC under grant number EP/G035954/1 and from the Defense Threat Reduction Agency.

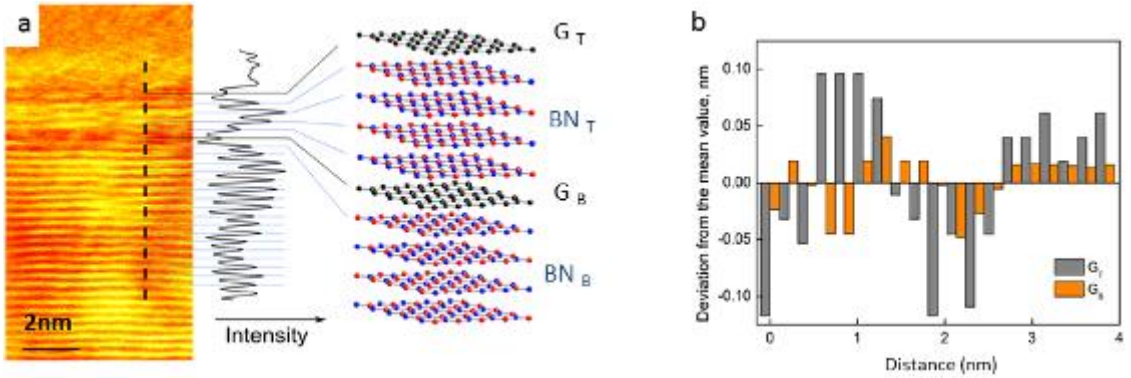

Figure 1. High resolution side view imaging of graphene/BN heterostructure devices. (a) Aberration corrected STEM image and schematic structure for one of our graphene heterostructured devices in which two independently contacted graphene flakes (G_T and G_B) are separated by a four layer boron nitride spacer (BN_T) and supported on a 20nm BN substrate (BN_B). (b) Estimate of the atomic roughness for each graphene layer using the deviation of layer position from horizontal.

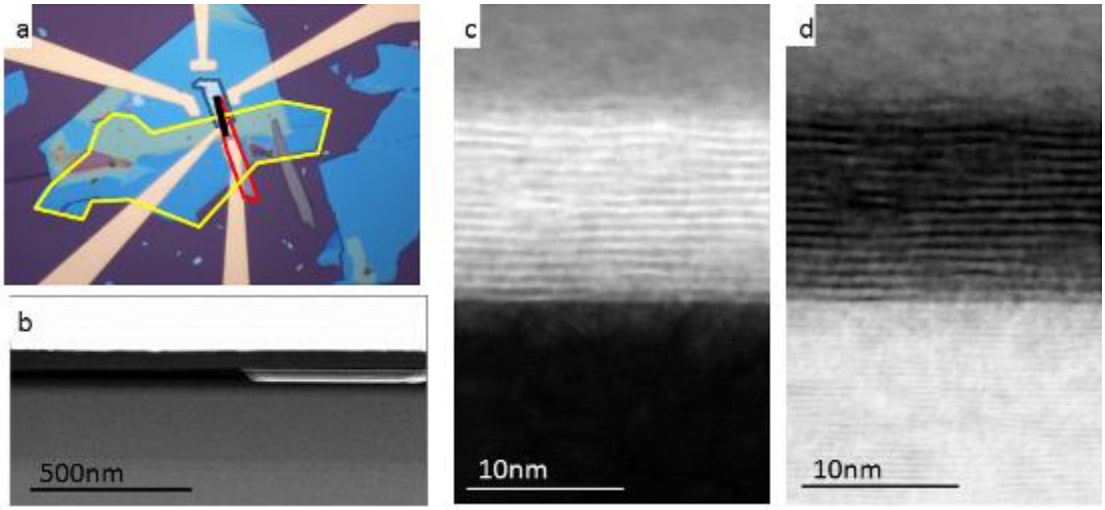

Figure 2. Imaging the encapsulated tungsten disulphide tunnelling barrier between two graphene sheets. (a) Optical image of device before extracting the cross section. High angle annular dark field STEM images showing (b) termination of tungsten disulphide layer within the slice and (c) lattice planes in barrier layer. (d) The complementary bright field STEM image for (c)

Functional Materials

MS.3.037
Toroidal plasmonic eigenmodes in oligomer nanocavities detected by EFTEM

W. Sigle[1], B. Ögüt[1], R. Vogelgesang[2], N. Talebi[1], P.A. van Aken[1]

[1]MPI for Intelligent Systems, Center for Electron Microscopy, Stuttgart, Germany
[2]Carl von Ossietzky University of Oldenburg, Oldenburg, Germany

ogut@is.mpg.de
Keywords: Surface plasmon resonances, EFTEM, toroidal modes.

Miniaturization has become one of the pillars of modern technology due to the trend of the electronic devices' diminishing down to the nanoscale since the beginning of the last decade. Using light for information technology in such devices is impeded by the diffraction limit of light. Converting light into surface plasmons could be a way to circumvent this limit because plasmons have much smaller wavelengths. Therefore plasmonics has become an astonishingly expanding field of technology, which offers numerous possibilities for applications beyond the diffraction limit of light.

Many plasmonic applications are based on electric-dipole and higher-order multipole resonances, as well as magnetic resonances. Here, by energy-filtering transmission electron microscopy (EFTEM) supported with 3D finite-difference time domain (3D-FDTD) simulations we detect the signatures of *toroidal* resonances in oligomer nanocavities at optical wavelengths, which could not be captured by conventional optical microscopy techniques due to their nearly radiation-free nature. Figure 1 displays a schematic illustration of a toroidal moment. A toroidal moment is composed of a combination of electrical and magnetic field loops revolving in radial and azimuthal directions, respectively [1].

Figure 2 illustrates the power of an electron beam to excite various plasmonic eigenmodes, normally requiring different optical excitation setups, all at once. Figures 2a–c display the acquired EFTEM images, corresponding peak maps, and the results of 3D-FDTD simulations, respectively. Modes (ii) and (iii) reveal the modes having magnetic and electrical dipolar character, accordingly, whereas modes (i) and (iv) correspond to toroidal modes. Even if the central hole is removed, evidence of toroidal behaviour persists, which would be totally impossible to capture with an optical microscopy technique [1].

We believe that toroidal moments have a big potential for novel innovations in the future, such as Purcell effect engineering [2] and data storage and processing [3].[4]

1. B.Ögüt, N. Talebi, R. Vogelgesang, W. Sigle and Peter A. van Aken, Nano Letters, **12** (2012) p. 5239.
2. K.J. Vahala, Nature 424 (2003) p.839.
3. K.S. Choi, H. Deng, J. Laurat and H.J. Kimble, Nature, 452 (2008) p. 67.
4. The research leading to these results has received funding from the European Union Seventh Framework Programme [FP7/2007- 2013] under grant agreement n°312483 (ESTEEM2).

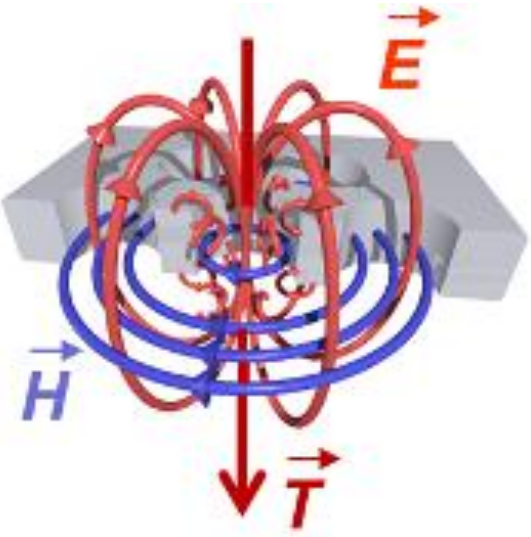

Figure 1. Illustration of a toroidal moment in a plasmonic nanocavity system formed by electric (red) and magnetic fields (blue) whirling in radial and azimuthal directions, respectively.

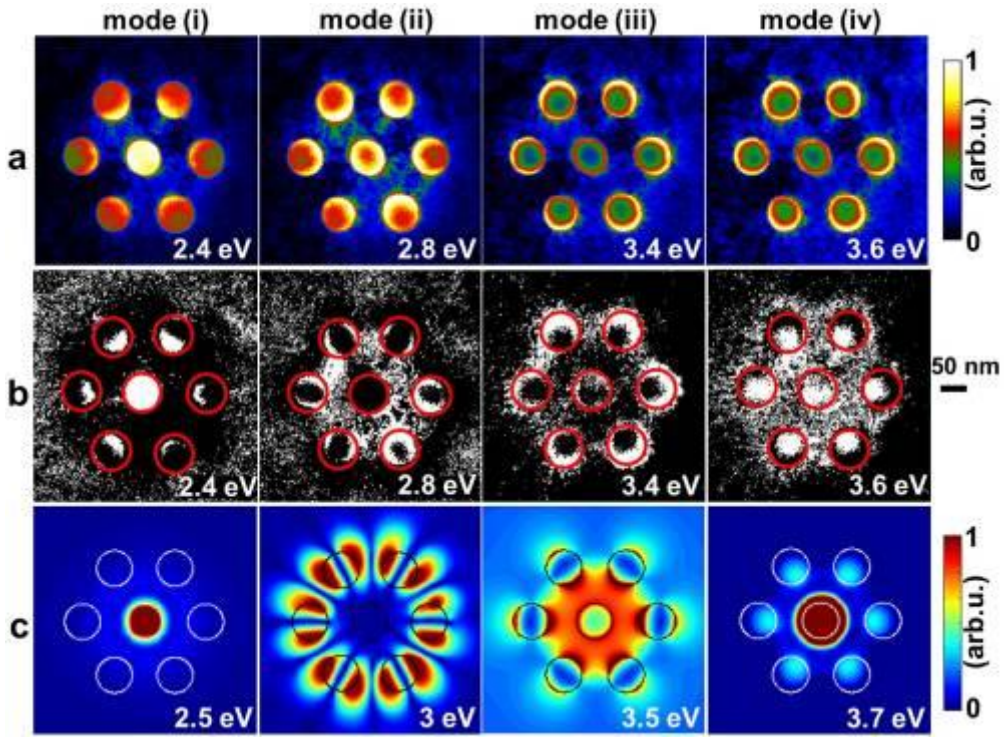

Figure 2. (a) Collection of modes acquired by EFTEM at energy losses of (i) 2.4, (ii) 2.8, (iii) 3.4, and (iv) 3.6 eV. The color code indicates the energy-loss probability in EFTEM images increasing from blue to yellow. (b) Peak maps obtained from the acquired images in (a). (c) Simulated modes with FDTD. Displayed is the modulus of the electric field (|*Ez*|), color coded increasing from blue to red, at (i) 2.5 eV, (ii) 3 eV, (iii) 3.5 eV, and (iv) 3.7 eV. The scale bar applies to all images.

Functional Materials

MS.3.038
Insight into the structural and electrical properties of individual $BaTiO_3$ nanorods

K. Zagar[1], F. Hernandez-Ramirez[2,3], J.D. Prades[3], J.R. Morante[2,3], A. Recnik[1], S. Sturm[1], M. Ceh[1]

[1]Jozef Stefan Institute, Department for Nanostructured Materials, Ljubljana, Slovenia
[2]Catalonia Institute for Energy Research (IREC), Barcelona, Spain
[3]University of Barcelona, Department of Electronics, Barcelona, Spain

kristina.zagar@ijs.si
Keywords: 1D nanostructures, electron microscopy, humidity nanosensors

One-dimensional $BaTiO_3$ nanostructures in the form of nanorods are a potential candidate for energy-harvester systems and sensors. In order to explore possible potential applications of $BaTiO_3$ nanostructures, we report on the template-assisted growth and the structural characterization of $BaTiO_3$ nanorods, the prototyping of functional devices based on them, and the preliminary assessment of their electrical performances [1].

$BaTiO_3$ nanorods were synthesized using sol-gel electrophoretic deposition (EPD) technique [2]. The stoichiometric $BaTiO_3$ sol was deposited into the anodic aluminium oxide (AAO) template while a potential of 30 V was applied between the AAO/Al working electrode and platinum counter electrode. After the deposition samples were annealed at 700 °C for 1 h with subsequent AAO template removal. Resulting $BaTiO_3$ nanorods were characterized by electron microscopy techniques. To study electrical properties, $BaTiO_3$ nanorod devices were fabricated by focused ion beam nanolithography techniques using $[(CH_3)_3CH_3C_5H_4Pt]$ injector to deposit platinum [3].

Obtained $BaTiO_3$ nanorods had diameters ranging from 150 to 200 nm, with an average length of 10-25 μm. The $BaTiO_3$ nanorods were always polycrystalline and composed of well-crystallized nanosized $BaTiO_3$ grains with a pseudo-cubic structure and grain sizes ranging from 20 to 50 nm (Figure 1(a)). A high-temperature hexagonal $BaTiO_3$ polymorph, that was observed as intergrowth of more or less ordered sequences of (111) twins with the perovskite matrix, was present as a minor phase (Figure 1(b)). Its formation was most probably triggered by reduction of Ti^{4+} to Ti^{3+} as a consequence of the local reducing environment, due to the decomposition of the organic precursors during the annealing process.

For the electrical characterization the prototype device was formed by integration of individual $BaTiO_3$ nanorod into simple circuit architecture. Four-probe electrical measurements performed on individual $BaTiO_3$ nanorods revealed the resistivity values between 10 and 100 ohm·cm, which corresponds to typical values for oxygen-deficient $BaTiO_3$. The measurements of electrical resistivity of single nanorods in varying humidity environment showed reproducible response, thus demonstrating that $BaTiO_3$ nanorods can be integrated in more complex circuit architectures with functional capacities of a humidity nano-sensor (Figure 2).

1. K. Zagar, F. Hernandez-Ramirez, J. D. Prades, J. R. Morante, A. Recnik and M. Ceh, Nanotechnology 22 (2011), p. 385501.
2. K. Zagar, A. Recnik, S. Sturm, A. Gajovic M. And Ceh, Mater. Res. Bull. 46 (2011), p. 366.
3. F. Hernandez-Ramirez, J. D. Prades, R. Jimenez-Diaz, T. Fischer, A. Romano-Rodriguez A, S. Mathur and J. R. Morante, Chem. Phys. 11 (2009), p. 7105.
4. This work was performed under Grant No. 1000-06-310008 and supported by the MHEST of Republic of Slovenia. The research was also supported by the Framework 7 program under the project S3 (FP7-NMP-2009-247768) and European Union Seventh Framework Programme [FP7/2007-2013] under grant agreement n°312483 (ESTEEM2).

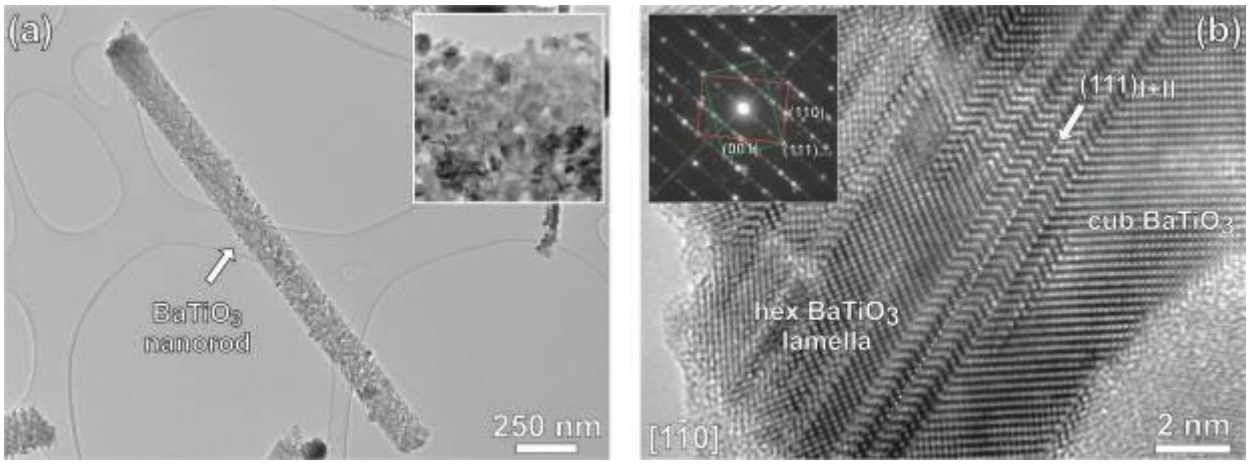

Figure 1. (a) Bright-field image of a uniformly shaped and polycrystalline $BaTiO_3$ nanorod. The inset in the upper right corner shows a higher-magnification bright-field TEM image of polycrystalline $BaTiO_3$ nanorod with grain sizes in the range from 20 to 50 nm. (b) HRTEM image of slabs of hexagonal $BaTiO_3$ polymorph intergrown with cubic $BaTiO_3$ as seen in the $[1\bar{1}0]$ zone axis. The inset presents the SAED corresponding to the hexagonal polymorph.

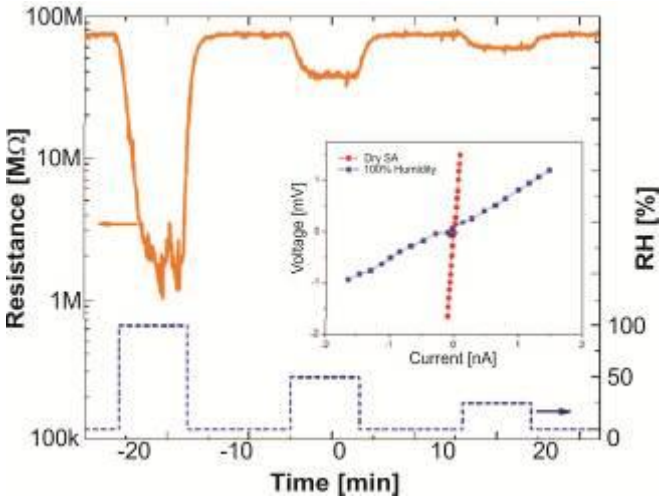

Figure 2. Sensing response of a $BaTiO_3$ nanorod towards pulses of 100, 50 and 25 % of relative humidity (RH) measured at room temperature. Synthetic air was used herein as carrier gas. The inset shows I-V curves obtained in dry and humid (100 % RH) air. A sharp and reversible modulation of the electrical response was observed.

Functional Materials

MS.3.039
Atomic resolution interface study of VN and Cu films on MgO using spherical-aberration corrected TEM

G. Dehm[1], Z. Zhang[2]

[1]MPI für Eisenforschung, Düsseldorf, Germany
[2]Erich Schmid Institut für Materialwissenschaft, Leoben, Austria

dehm@mpie.de
Keywords: Friedel oscillation, misfit dislocation, atomic structure

Interfaces strongly influence the functional and mechanical properties of materials. Recent advancements in TEM instrumentation permit to image the structure of material defects at atomic resolution and with elemental sensitivity by correcting the spherical aberration of the objective lens. In the present talk this benefit will be illustrated using two different material systems. The first system is a ceramic-ceramic structure consisting of VN on MgO, while the second is Cu on MgO. While for VN on MgO the misfit is quite low with 0.7% Cu on MgO possesses a large mismatch of 14.1%. For both systems the interface structure is analyzed with respect to its atomic structure using a 200 kV field emission TEM/STEM (JEOL 2100F) equipped with an image-side C_S-corrector.

Determination of the atomic positions with picometer precision reveals subtle periodic oscillations in the VN (Fig. 1) and Cu (Fig. 2) adjacent to the interface, while this is not observed for MgO. The analysis of the atomic displacements for VN on MgO reveals that the interplanar spacings oscillate adjacent to the interface in a similar way for both experimental measurements and DFT calculations [1]. The interfacial chemistry derived from ELNES with subnanometer spatial resolution revealed a V- and O-enriched interface where V-O bonds are likely to be formed at the interface, resulting in a slightly reduced V valence state.

For Cu on MgO the variations of the interplanar spacing adjacent to the interface show a damped oscillation similarly as for VN on MgO. Again, at the MgO side the oscillations are not pronounced as compared to the Cu side. The experimental measurement shows the oscillations down to around 13 layers. This phenomenon, we believe, is the Friedel oscillation occurring at the interfaces, which is similar to the Friedel oscillation present at the metal surface as observed in literature by scanning tunneling microscopy. The origin for the oscillatory interplanar spacing, i.e. contractions and expansions in lattice plane spacing, is most likely attributed to the repulsive or attractive atomic forces between the layers induced by electronic charge redistributions.

The possible impact of the interface structures observed by TEM on the material properties is briefly discussed.

1. Z. Zhang, B. Rashkova, G. Dehm, P. Lazar, J. Redinger, R. Podloucky, *Unveiling the atomic and electronic structure of the VN/MgO interface*, Phys. Rev. B 82, 060103(R), 2010 1-4.

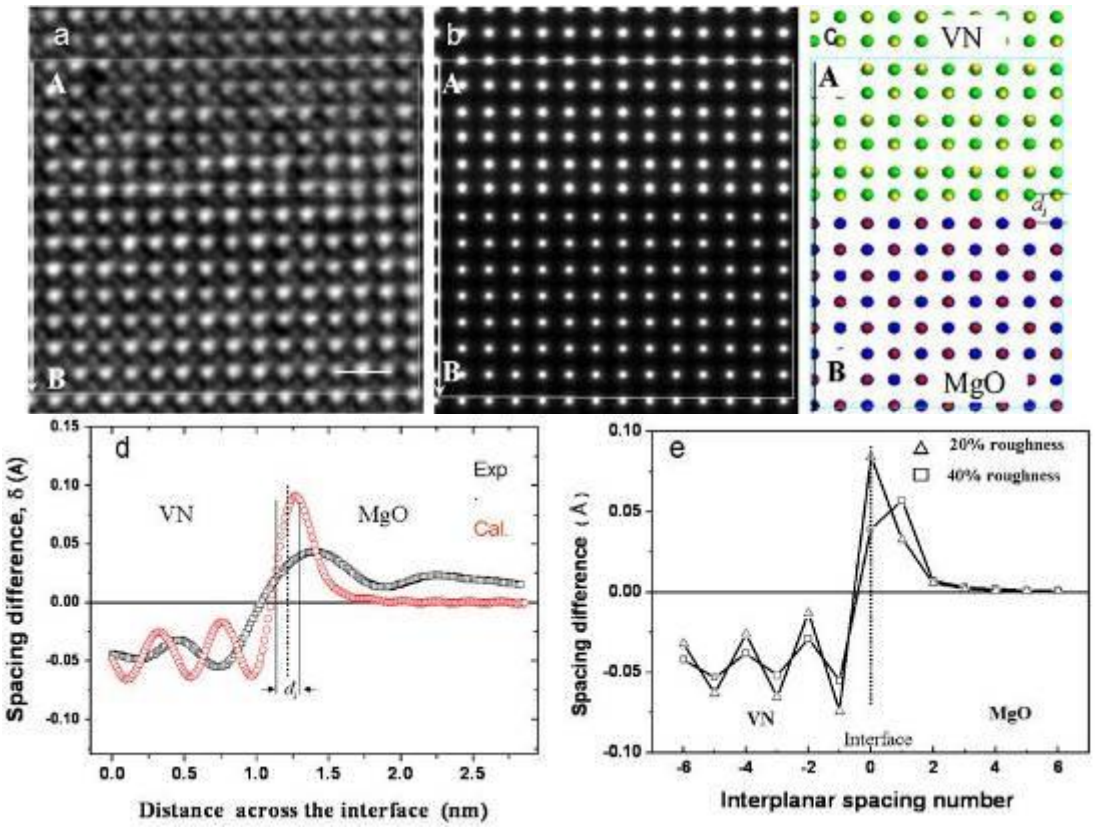

Figure 1. (a) A HRTEM image of the VN/MgO interface recorded along [100] (thickness: ~ 3.3 nm). A simulated potential image is shown in (b) based on an atomic model (c) obtained from ab-initio calculation. The spacing difference (d) obtained by averaging over a rectangular area of around 3.0 nm from A to B in (a), (b) is plotted as a function of distance covering 13 spacing of d_{002}, where the red and black curves denote the calculated (no roughness) and experimental results, respectively. The interfacial spacing d_i is indicated. Panel (e) shows the effects of an assumed mono atomic step roughness (20%, 40% roughness) Images and diagrams from [1].

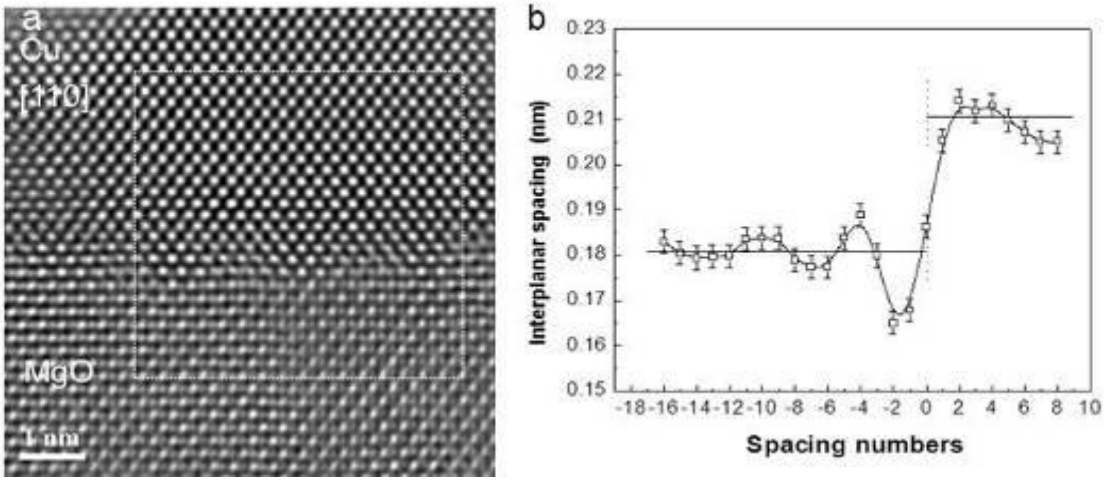

Figure 2. (a) HRTEM image of the Cu-MgO interface with a cube-on-cube epitaxial relationship, recorded along the [110] direction using a small negative C_S in which the individual O, Mg and Cu atomic columns are clearly imaged as bright dots (thickness: 2.0 - 3.0 nm). Paired dislocation components projected from the <100> misfit direction network are visible, and separated by coherent regions giving a little brighter contrast. (b) The (d_{002}) interplanar spacing is plotted as a function of interplanar spacing numbers across the interface. The thin lines denote the bulk Cu d_{002} and Mg d_{002} spacing, respectively.

Functional Materials

MS.3.040
Application of electron holography for characterization of magnetic domain patterns in Ni-Mn-Ga films

K. Vogel[1], C. Behler[2,3], D. Wolf[1], S. Sturm[1], A. Diestel[2], A. Backen[2], S. Fähler[2,4], L. Schultz[2], H. Lichte[1]
[1]Technische Universität Dresden, Triebenberg Labor, Dresden, Germany
[2]IFW Dresden, Institute for Metallic Materials, Dresden, Germany
[3]Technische Universität Dresden, Institute for Solid State Physics, Dresden, Germany
[4]Chemnitz University of Technology, Institute of Physics, Chemnitz, Germany

Karin.Vogel@triebenberg.de
Keywords: electron holography, magnetic shape memory alloys

Electron holography is a powerful tool for investigation of magnetic specimens because the phase of the electron wave is sensitive to magnetic fields within or around the sample. Here we apply electron holography to characterize the magnetic domain patterns in Ni-Mn-Ga films grown on MgO substrates with Cr buffer layers. Magnetic shape memory (MSM) alloys of the Ni-Mn-Ga system are considered to have a high potential for application in new actuator and sensor devices due to the large magnetic-field-induced strain [1,2]. Since the basic mechanism of the MSM effect is a reorientation of martensite variants in an external magnetic field, a ferromagnetic martensite with a large magnetocrystalline anisotropy is required.

In order to investigate the magnetic structure and its correlation with the microstructure of the Ni-Mn-Ga films we prepared cross-sections of two different orientations by FIB milling (Figure 1). In a previous work, the films had been investigated by means of atomic and magnetic force microscopy [3] and a high out-of-plane lamellar magnetic contrast was observed perpendicular to the twin boundaries on the surface of the 14M modulated films. This suggests the formation of magnetic band domains with antiparallel out of plane magnetization. According to these results we expect to find 180° domain walls in the (010) cross section while we expect quasi-90° domain walls in the (100) cross-section.

For the holographic investigations we used a Philips CM200 TEM equipped with a Lorentz lens and a Möllenstedt biprism. For acquisition of electron holograms the specimen was tilted away from the zone axis for some degrees in order to get an orientation that provides low diffraction contrast, which is an important precondition for the correct interpretation of phase images. From the holograms the complete electron wave in amplitude and phase was reconstructed. The results of the holographic reconstruction for the (100) cross-section are shown in Figure 2. In the amplitude image, the twinned microstructure is still slightly visible due to some remaining diffraction contrast (Figure 2a). The equi-phase lines in Figure 2b show the change of the magnetization direction at the twin boundaries. Obviously the direction of magnetization follows the magnetic easy axis as expected for a material with large magnetocrystalline anisotropy. The stripe-like shape of the magnetic domains becomes visible in the color-coded phase gradient image in Figure 2c.

The holographic results for the (010) cross-section are shown in Figure 3. The amplitude image shows very low diffraction contrast and the twins are only slightly visible. The phase image (Figure 3b) and the color-coded gradient image (3c) show magnetic domain walls perpendicular to the film surface. The direction of magnetization changes by nearly 180° across the wall. The observed deviations from this angle might be caused by several reasons, e.g. projection effects or charging of the sample, and will be the subject of further investigations. The shape of the equi-phase lines indicates that the 180° domain walls do not continuously run from top to bottom of the film. These observations are in agreement with the magnetic domain model [3] developed on the basis of the magnetic force microscopy results.

1. S. J. Murray, M. Marioni, S. M. Allen, R. C. O´Handley, T. A. Lograsso, Applied Physics Letters **77** (2000) p. 886.
2. A. Sozinov, A. A. Likhachev, N. Lanska, K. Ullakko, Applied Physics Letters **80** (2002) p. 1746.
3. A. Diestel, A. Backen, V. Neu, L. Schultz and S. Fähler, Scripta Materialia 67 (2012) p. 423.
4. We acknowledge the support of this work by the DFG priority programme SPP 1239, the funding by the European Union (EFRE) and the Free State of Saxony via the project 13923/2379 ECEMP, the funding by the European Union (ERDF) and the Free State of Saxony via the ESF project 100087859 ENano, and also financial support from the European Union under the Seventh Framework Programme under a contract for an Integrated Infrastructure Initiative. Reference 312483 - ESTEEM2.

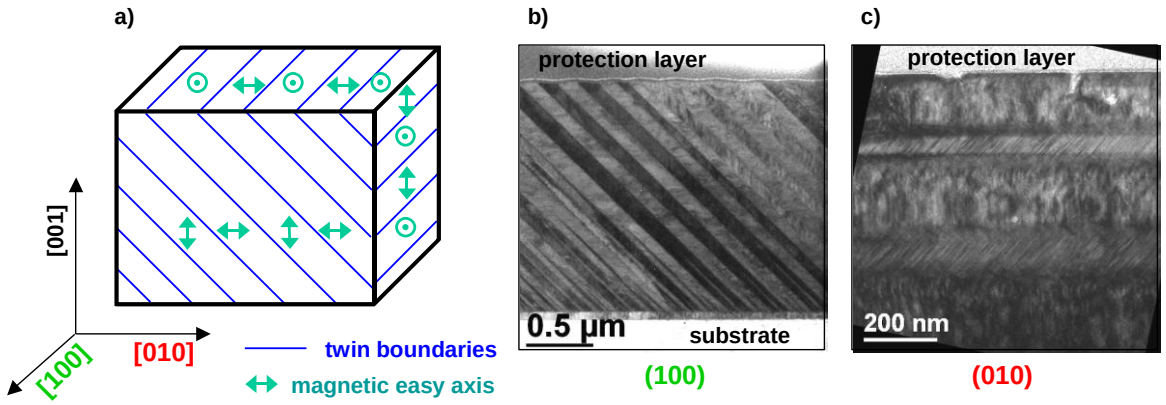

Figure 1. Orientations of the FIB cross-sections in the MSM film. 1a: Schematic drawing of the film and the twinned microstructure with possible orientations of the magnetic easy axis c_{14M}. 1b and 1c: TEM bright-field images showing the twins in (100) and (010) cross-sections perpendicular to [100] and [010] directions, respectively. In (100) cross-section, quasi-90° magnetic domain walls, and in (010) cross-section, 180° walls are expected.

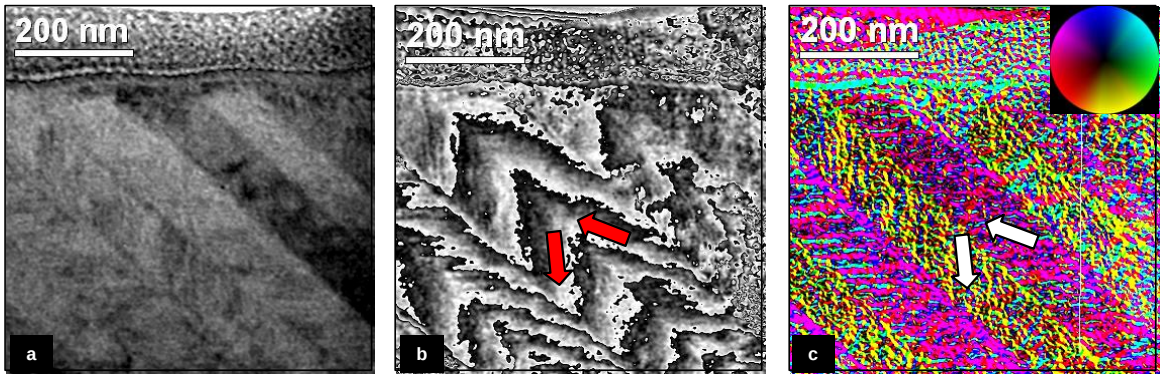

Figure 2. Holographic results for the (100) cross-section revealing quasi-90° domain walls. In the amplitude image (2a) the twinned microstructure is visible. Since the sample was slightly tilted out of the zone axis to minimize dynamic effects, the diffraction contrast is low, except for the two dark appearing twins in the upper right part of the image. The equi-phase lines in 2b show the change of the magnetization direction at the twin-boundaries (remark: the upper right part of the phase image can not be interpreted due to the large diffraction effects). The color-coded phase gradient image (2c) shows the stripe-like shape of the magnetic domains. The color-wheel and the arrows indicate the direction of magnetization.

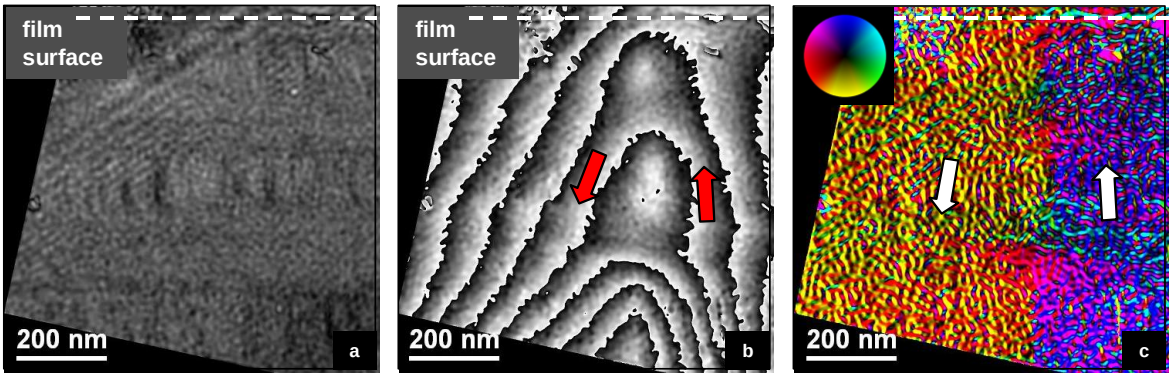

Figure 3. Holographic results for the (010) cross-section showing 180° domain walls perpendicular to the film surface. Amplitude image (3a), phase image (3b) and color-coded gradient image (3c). Deviations from 180° presumably due to projection and charging effects.

Functional Materials

MS.3.041
Morphing nanodisks to nanotriangles - a plasmonic EEL study

F.P. Schmidt[1,2], H. Ditlbacher[1], A. Hohenau[1], U. Hohenester[1], F. Hofer[2], J.R. Krenn[1]

[1]University of Graz, Department of Physics, Graz, Austria
[2]Graz University of Technology, Institute for Electron Microscopy and Nanoanalysis, Graz, Austria

franz.schmidt@uni-graz.at

Surface plasmons are collective electron oscillations, which are propagating at a metal-dielectric interface. They are generated at optical frequencies and show confinement into areas much smaller than the wavelength of light, which causes a strong increase of the electric field intensities. This enhancement is especially pronounced in case of nanometer sized metal particles. Various applications, ranging from novel light sources, photovoltaics to sensor devices take advantage of the extraordinary optical properties of such metallic nanoparticles. Electron energy loss spectroscopy (EELS) in combination with scanning transmission electron microscopy (STEM) allows probing the evanescent fields of such localized surface plasmons with nanometer resolution [1]. Alternatively energy filtered transmission electron microscopy (EFTEM) can be used to map localized surface plasmons as it was shown in previous works [2, 3], providing similar information as with STEM-EELS. Because of the capability of the transmission electron microscope used in this study (FEI Tecnai F20) to reach better energy resolution in STEM-EELS than in EFTEM mode, we used the scanning mode to optimize energy resolution down to 0.12 eV. A monochromated 200 keV electron beam was used to excite surface plasmons on different nanostructures, while the electron energy-loss was measured in order to get spatially resolved spectral information from the near-infrared, the visible and the UV range. Nanostructures of different geometries were designed using electron beam lithography (EBL), a technique suitable of creating thousands of nanostructures in just a few minutes. The EBL processing was realized on a 15 nm thin silicon nitride membrane. This material exhibit a band gap of about 8 eV, leading to no extra EEL signal in the optical range. 30 nm silver nanostructures were prepared and an additional 18 nm silicon oxide film was evaporated in order to reduce degeneration of the silver surface. EEL measurements were generated on a FEI Tecnai F20, equipped with a monochromated field emission gun and a high resolution Gatan Image Filter. Starting with single nanodisks, where we found a new type of plasmonic excitation, the so called breathing mode [4], we continue our study by morphing the shape of a disk to a triangle ("Figure 1"). Only with the help of theoretical calculations, which are in good agreement with the experiment, we are able to understand and interpret our findings [5]. We show which localized surface plasmons found in a single nanotriangle can be linked to plasmonic eigenmodes in a nanodisk, and how other LSPs differ in these 2 basic geometries. We will discuss the importance of plasmon hybridization in the context of mixing fundamental modes to a hybridised excitation. In the second part of this work we deal with the question how symmetry breaking of a nanodisk by creating designed defects ("Figure 2") affects the plasmonic behaviour of such nanodisks. A systematic change of designed defects in a nanodisk is realized by using electron beam lithography and a comparison of a comprehensive EEL-study is presented.

1. J. Nelayah *et al*, Nature Physics 3 (2007), 348.
2. B. Schaffer, U. Hohenester, A. Truegler and F. Hofer, Physical Review B 79 (2009), 041401.
3. W. Sigle, J. Nelayah, C.T. Koch and P.A. van Aken, Optics Letters 34 (2009), 0146-9592.
4. F.P. Schmidt, H. Ditlbacher, A. Hohenau, U. Hohenester, F. Hofer and J.R. Krenn, Nano Letters 11 (2012), 5780.
5. U. Hohenester and A. Truegler, Comp. Phys. Commun. 183 (2012), 370.
6. The authors gratefully acknowledge funding from the Austrian Science Fund under grant number P21800-N20 and the Graz Centre for Electron Microscopy.

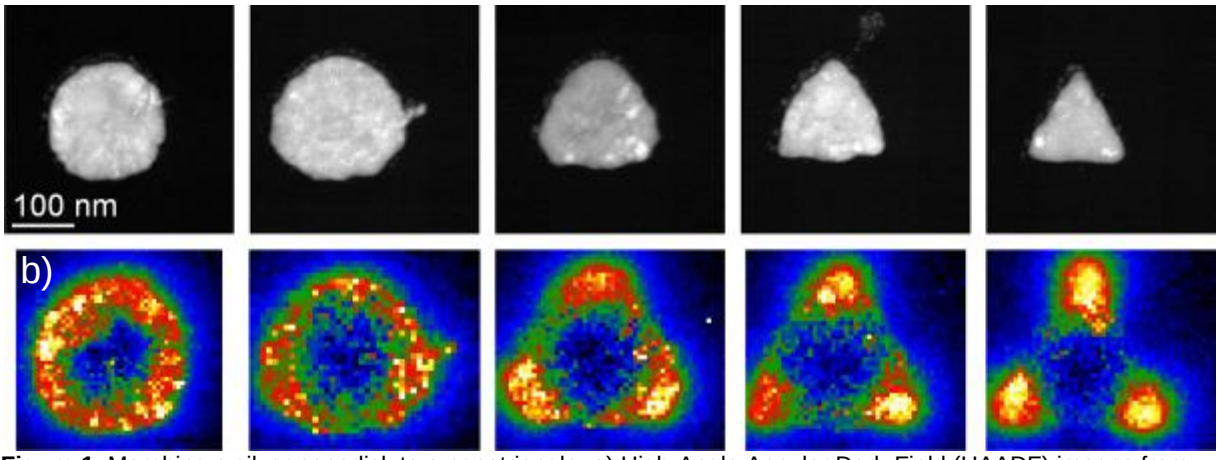

Figure 1. Morphing a silver nanodisk to a nanotriangle. a).High-Angle Annular Dark-Field (HAADF) images from 30 nm thick silver nanoparticles, ranging from nanodisk (left) to nanotriangle (right). Particles are prepared with electron beam lithography (EBL) on a 15 nm thin Si_3N_4 membrane. b) Corresponding EEL-maps from particles shown in a), where the electron energy-loss intensity of the plasmonic dipole excitation is shown as function of the lateral position.

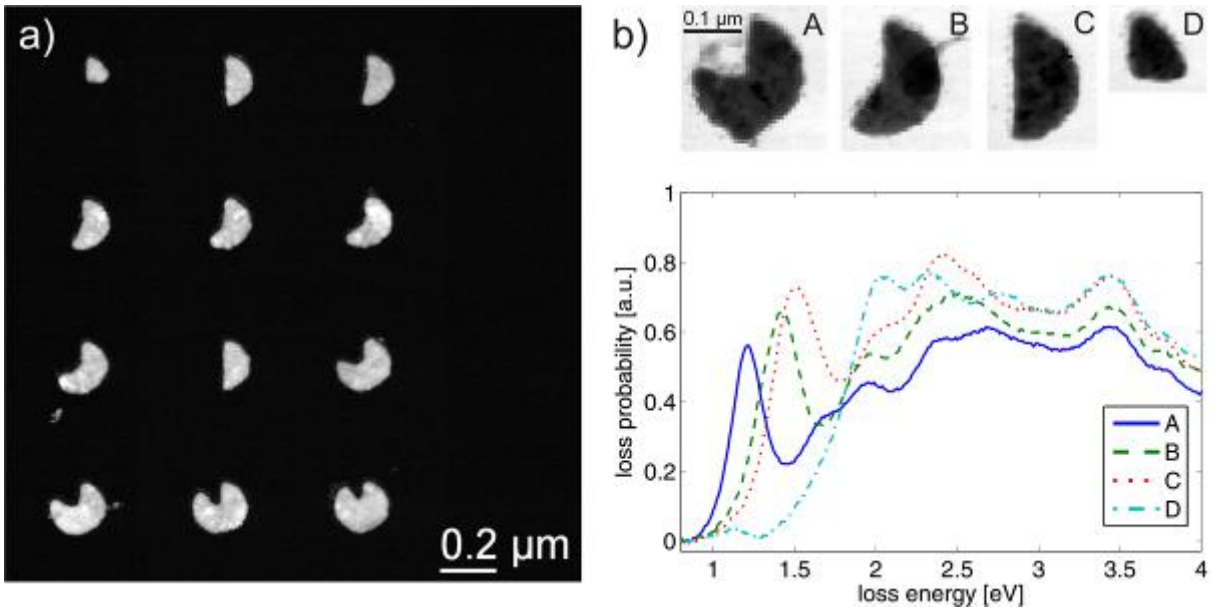

Figure 2. Nanodisks with designed defects. a) HAADF image of silver nanostructures of 30 nm thickness on a 15 nm thin Si_3N_4 membrane, coated with a 18 nm SiO_2 layer for better stability of the silver film. Particles were prepared using EBL. b) Spectrum images A, B, C and D of selected particles, prepared under same condition as particles in a) (top). Extracted EEL spectra A, B, C and D from spectrum images shown above (bottom).

Functional Materials

MS.3.P042
Line defects in TiO_2 single crystals and their influence on ionic and electronic transport

M. Kelsch[1]

[1]Max-Planck-Institut for Intelligent Systems, Stuttgarter Center for Electron Microscopie, Stuttgart, Germany

kelsch@is.mpg.de
Keywords: Dislocations, point defects, space charge zones

Point defects play a critical role in ionic solids. In fact, many physical properties are influenced by these zero dimensional defects. Therefore, studies on point defects have a paramount importance in the field of solid state ionics. By the advent of nano-ionics, it was found that the interplay of point defects and interfaces (such as grain boundaries and hetero-interfaces) could result in different properties compared to the bulk properties [1]. Thus, it is important to study also the interplay of point defects with other extended defects. The energetically least costly extended defects are line defects (dislocations), which take an intermediate place between point defects and frozen interfaces as far as thermodynamics and kinetics are concerned. TiO_2 was chosen as the model material not only for its versatile technological applications but also owing to its mobile cation and anion defects which are essential for dislocation generation.

Dislocations were created in TiO_2 single crystals by compressing at 1200 ^oC with 40 MPa for 5 min. TEM revealed that dislocations preferably lie on {110} which is one of the commonly observed slip systems for TiO_2 [3], as shown in Fig.1-3. The plan view specimens in Figs. 1 and 3 were cut out from a TiO_2 single crystal using a Well diamond wire saw to 2 mm square. These specimens were mechanically ground from the back side to a thickness of 70 µm and then further thinned and polished to less than 20 µm thickness in the dimpled area with a Gatan dimple grinder. The specimens were then mounted on a clamp type DuoPost and put it in a Precision Ion Polishing System (PIPS™691). Finally the specimens were thinned with Ar^+ to electron transparency.
The cross sections of the specimen as shown in Fig. 2 were prepared using an Allied Multiprep™ System. A wedge of material is prepared using a specially designed tripod specimen holder for polishing. Finally the specimens were thinned with Ar+ to electron transparency. TEM investigations were performed with a Philips CM200 microscope operated at 200 kV and large tilting angles. The point-resolution was 2.7 Á.

To understand the effect of dislocations on the electronic and ionic transport, electrical properties were studied parallel and perpendicular to the slip planes i.e., in [001] and [110] directions, respectively. For the [001] direction, the dislocations enhance the conductivity at high oxygen partial pressures (pO_2) from 1 – 10^5 bar, cf. Fig. 4. Wagner-Hebb type polarization measurements (green symbols in Fig. 2) on these samples revealed an increase in the hole conductivity by half an order of magnitude, and an increase by 3 orders of magnitude in ionic conductivity (oxygen vacancies and/or Ti interstitials) compared to the pristine crystals without dislocations. The sample measured along [110] did not show any conductivity change despite the presence of dislocations. Under reducing conditions, i.e. pO_2 below 10^{-12} bar there is no change in the n-type electronic conductivity, irrespective of the measurement axis. Furthermore, oxygen tracer experiments and SIMS analysis indicate that Ti interstitials make larger contributions to the increased ionic conductivity than oxygen vacancies.

The enhanced ionic and hole conductivities of [001] crystals at high pO_2 and unchanged n-type conductivity at low pO_2 can be well explained in the framework of negatively charged dislocation cores and space charge accumulated layers for positive carriers. This model can also explain the unchanged conductivity along [110], as the space charge zones do not overlap in this direction.

The present observations on TiO_2 single crystals demonstrate an alternative way to modify the ionic and electronic conductivities of ionic solids. A potential advantage of such a technique could be a spatial variation of ionic and electronic conductivity by locally generating dislocations, e.g. by nano indentation.

1. J. Maier, Nat. Mater. 4 (2005) 805.
2. K.K. Adepalli, R. Merkle, M. Kelsch, J. Maier, Adv. Funct. Mater. (2013) doi: 10.1002/adfm.201202256.
3. W.M. Hirthe, J.O. Brittain, J. Am. Cer. Soc. 45 (1962) 546

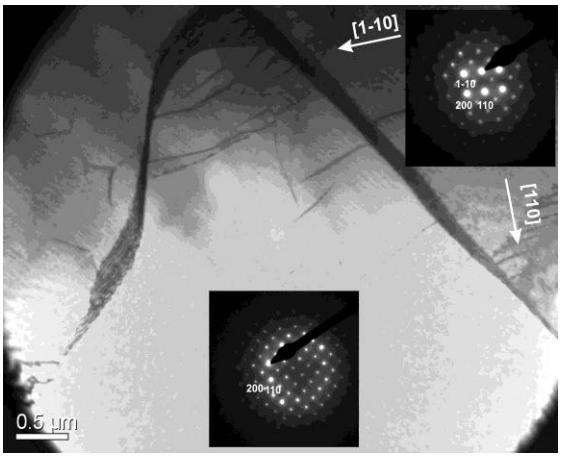

Figure 1. TEM bright field image of a plan view [001] sample with electron beam parallel to [001], from ref. [2].

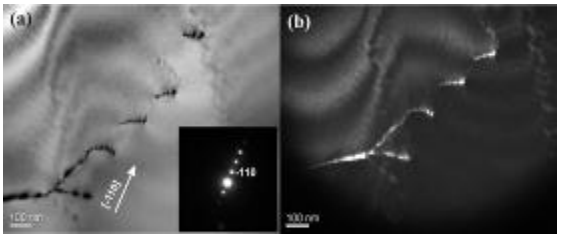

Figure 2. a) TEM-BF image of the T_{001} sample prepared from cross-section, two beam condition with -110 diffraction spot excited (electron beam parallel to [110]). b) DF image using -110 diffracted beam.

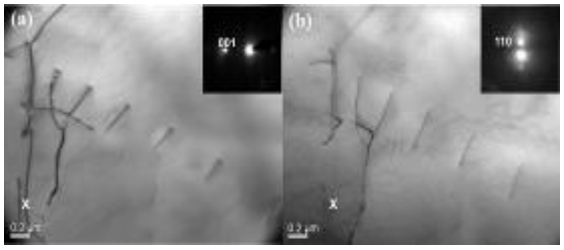

Figure 3. TEM-BF images of the T_{110} plan view sample with electron beam parallel to [110]:
a) two beam condition with 001 and b) 110 diffraction spots excited.

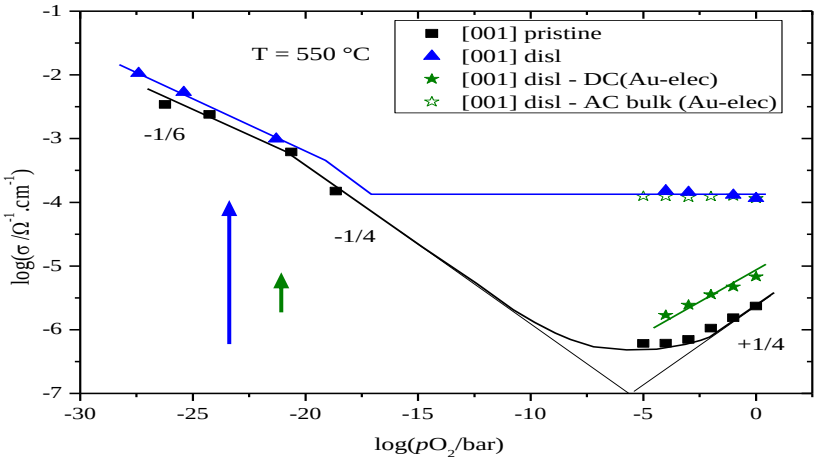

Figure 4. Conductivity of untreated (pristine) TiO_2 compared to a crystal with high dislocation density [2].

Functional Materials

MS.3.P043
Linking EELS studies of multiferroic Ca-doped $BiFeO_3$ with theoretical DFT calculations

Z. Chen[1,2], W. Sigle[1], G. Cao[2], C. Ma[2], H. Yang[2], J. Li[2], P.A. van Aken[1]

[1]Max Planck Institute for Intelligent Systems, Stuttgart Center for Electron Microscopy, Stuttgart, China
[2]Beijing National Laboratory for Condensed Matter Physics, Institute of Physics, Chinese Academy of Sciences, Beijing, China

zhen.chen@is.mpg.de
Keywords: $BiFeO_3$, multiferroics, Ca-doping, EELS, first-principles calculations, oxygen vacancy.

Lead-free multiferroic $BiFeO_3$ has high magnetic and ferroelectric ordering temperatures and has gained much interest due to its rich electric and magnetic phenomena and potential technological applications. In Ca-doped $BiFeO_3$ ($Bi_{1-x}Ca_xFeO_{3-\delta}$) enhanced magnetoelectric coupling has been found at low dopant concentration (x = 0.085) [1]. In addition, novel electric modulated insulator–conductor transition [2] and prominent optical properties like electrochromism [3] have also been observed. It has been revealed that oxygen vacancies exist in a wide range of Ca-doping samples and this oxygen deficiency is important to understand the novel properties [2-4]. In this study, we performed electron energy loss spectroscopy (EELS) and first-principles calculations to investigate the evolution of the electronic structure of $Bi_{1-x}Ca_xFeO_3$ with calcium doping. A series of $Bi_{1-x}Ca_xFeO_{3-\delta}$ ($0 < x \leq 0.5$) polycrystalline samples have firstly been analyzed by high-resolution transmission electron microscope (HRTEM) and electron diffraction [5]. A superstructure modulation along the ***a***-axis direction with different wavelengths for different Ca-doping was found and could be interpreted by oxygen vacancy ordering. We carried out EELS measurements in an FEI Tecnai F20, a Zeiss EM912, and a VG HB501UX. The O-K edge spectra were simulated by Wien2k [6] using *GGA+U* method with U = 4.0 eV. Figure 1 shows the O-K edge spectra for the compounds without Ca-doping and with Ca concentrations x = 0.1–0.5 at an energy resolution of about 1.0 eV. The intensity of peak B decreases with increasing Ca doping. Peak C has a similar shoulder structure for all the doped samples but appears broadened at higher Ca concentrations. According to the first-principles calculations and the simulations of O-K edge spectra of $BiFeO_3$ and $Bi_{0.5}Ca_{0.5}FeO_3$ (Figure 2), we revealed that peak A and its low-energy shoulder originate from O-2*p* states hybridized with Fe-e_g and Fe-t_{2g} orbitals, respectively, and peak B arises from O-2*p* states hybridized with Bi-5*p* and/or Ca-4*s* orbitals, which explains the decrease of peak B with increasing Ca concentration. From the experiments it is not clear whether the occupation of the Fe-3*d* orbitals changes or not with increasing Ca doping. For this, a better energy resolution is required. For the pristine phase $BiFeO_3$, the simulated O-K edge fits well with the experimental one except for the relative intensity of peak B which results from the overestimation of the hybridization of O-2*p* and Bi-5*p* orbitals by the DFT method. For $Bi_{0.5}Ca_{0.5}FeO_{3-\delta}$, oxygen vacancies have to be introduced to achieve the insulating state. Hence, we constructed a two-unit-cell superstructure with δ = 0.25 and relaxed all the internal crystalline parameters to obtain an energetically stable structure. We can predict the lower intensity of peak B in the x = 0.5 compound in the simulated O-K edge spectrum compared with the pristine phase, however, the low-energy shoulder of peak A in the simulated spectrum is too high which may be due to the improper consideration of the complex Fe–O coordination introduced by oxygen vacancies [4]. The detailed analyses of oxygen concentration and occupation states of Fe are in progress.

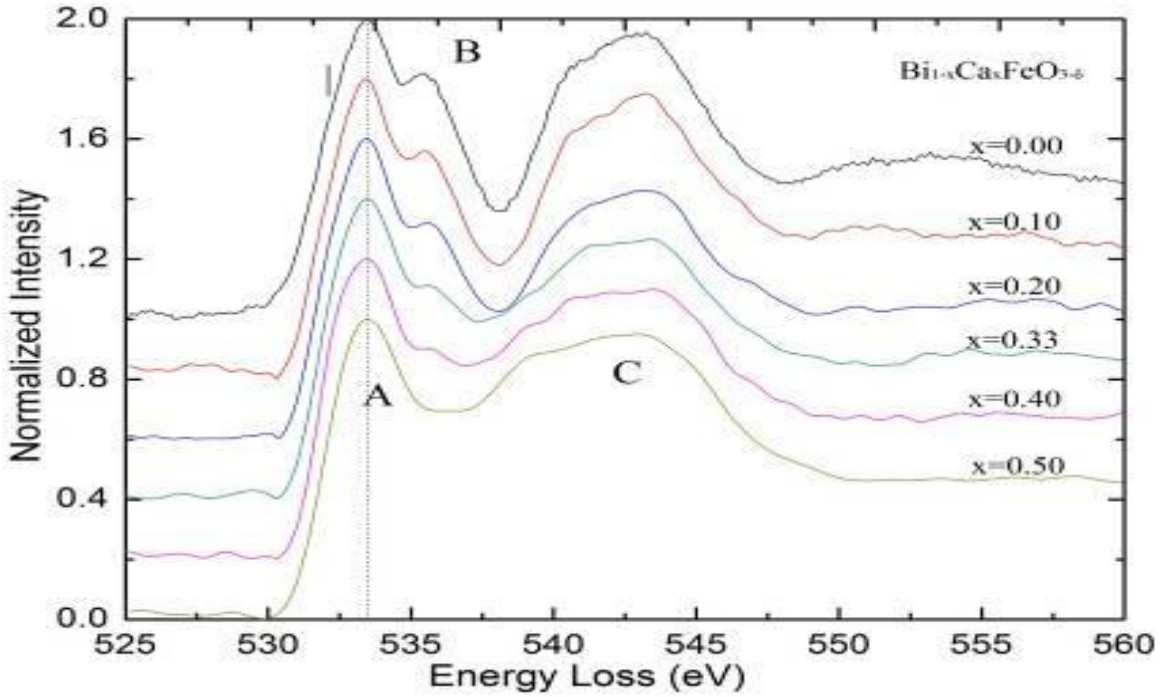

Figure 1. O-K edge EELS of $Bi_{1-x}Ca_xFeO_{3-\delta}$ ($0 \le x \le 0.5$).

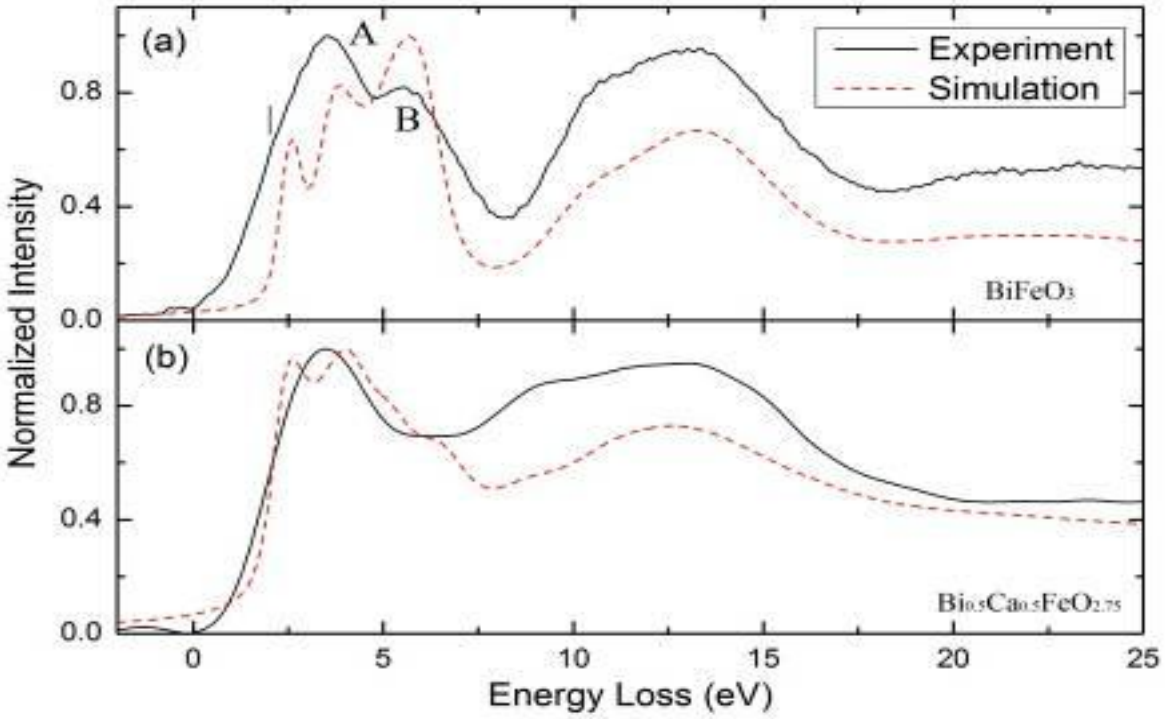

Figure 2. Experimental and simulated O-K edge for (a) $BiFeO_3$ and (b) $Bi_{0.5}Ca_{0.5}FeO_{2.75}$.

Functional Materials

MS.3.P044
Stabilisation mechanisms of particles in aluminium single films and foams

K. Heim[1,2], G.S. Vinod Kumar[1,2,3], F. Garcia-Moreno[1,2], M. Wollgarten[1], J. Banhart[1,2]

[1]Helmholtz Zentrum Berlin für Materialien und Energie, Berlin, Germany
[2]Technische Universität Berlin, Berlin, Germany
[3]SRM University, Kattankulathur, India

korbinian.heim@helmholtz-berlin.de
Keywords: aluminium foams, particle stabilisation, oxygen

When foaming metals, a minimum content of solid particles (e.g. >10 vol.% SiC) has to be present in the melt to stabilise the gas filled bubbles [1]. Oxygen in the blowing gas was found to support stabilisation by reducing the rate of bubble ruptures by increasing the oxygen concentration in the foams [2]. What the precise interactions between particles, melt and the solid-gas interface (oxygen layer) are and how they stabilise such foams is still under dispute [3]. In the present study we used a model system in order to discuss stabilisation of metallic foams: single metallic films were pulled from molten AlSi9Mg0.6 (all values in wt.%) containing different types of particles (20 vol.% SiC or 6 vol.% TiB_2) using circular molybdenum wire frames in a controlled atmosphere (possible oxygen concentration: 10^{-8} – $2.1x10^5$ ppm). For comparison, foams based on the same melts were produced via external gas injection using air or argon [4]. A further novel material based on Al-Mg containing sub-µm-sized $MgAl_2O_4$ spinel particles was foamed via the so-called 'Formgrip process' [5, 6]. The embedding of stabilising particles at the surfaces of foam bubbles and single films made in atmospheres containing different oxygen levels was analysed by Scanning Electron Microscopy (SEM). We found that particles in foams blown with argon gas and in films pulled at a reduced oxygen atmosphere (<2000 ppm O_2) are partial covered by the surface. In contrast, particles in air injected foams and in films pulled at ambient atmosphere are completely covered, compare figure 1. Cross sections of such particles were further examined by cutting out lamellae using a Focused Ion Beam (FIB, Zeiss Crossbeam 1540 EsB), see figure 2a). The same lamellae were further polished until electron transparency was sufficient for investigating the oxide surface by Energy Filtered Transmission Electron Microscopy (EFTEM, Zeiss LIBRA 200 FE) to elucidate their role in stabilisation. A correlation between the oxygen concentration during film pulling and the oxide layer thickness (ranging up to 35 nm) was not found. However, only films pulled at ambient atmosphere are able to form a connected oxygen layer in contrast to a discontinuous oxide formation for films pulled at oxygen reduced atmospheres, see figure 2b) and c). To investigate the distribution of fine $MgAl_2O_4$ particles (0.1–1 µm) a tomographic data set of the solid-gas interface was obtained by cutting slices in steps of 25 nm using FIB. We found that most of the $MgAl_2O_4$ particles tend to stay at the cell wall surface where they are totally embedded at the solid-gas interface. TEM images of the cell wall cross section of the oxide layer prepared by FIB reveal particles down to 50 nm size connected to the oxide layer, see figure 3. The close analogy of the model system 'single metallic films' to full metal foams allows us to investigate stabilisation criteria in the simpler system. In this regard we assume that the formation of a continuous oxide layer at the film or foam surface is mandatory to capture solid particles that stabilize liquid films.

1. D. Leitlmeier, H.P. Degischer, H.J. Flankl, Advanced Engineering Materials 4 (2002), p. 735-740.
2. N. Babcsán, D. Leitlmeier, H.P. Degischer, J. Banhart, Advanced Engineering Materials 6 (2004), p. 421-428.
3. J. Banhart, Advanced Engineering Materials 8 (2006), p. 781–794
4. S.W. Ip, Y. Wang, J.M. Toguri, Canadian Metallurgical Quarterly 38 (1999), p. 81-92.
5. V. Gergely, B. Clyne, Advanced Engineering Materials 2 (2000), p. 175-178.
6. G. Vinod Kumar, M. Chakraborty, F. Garcia-Moreno, J. Banhart, Metallurgical and Materials Transactions A (2011), p. 1-11.

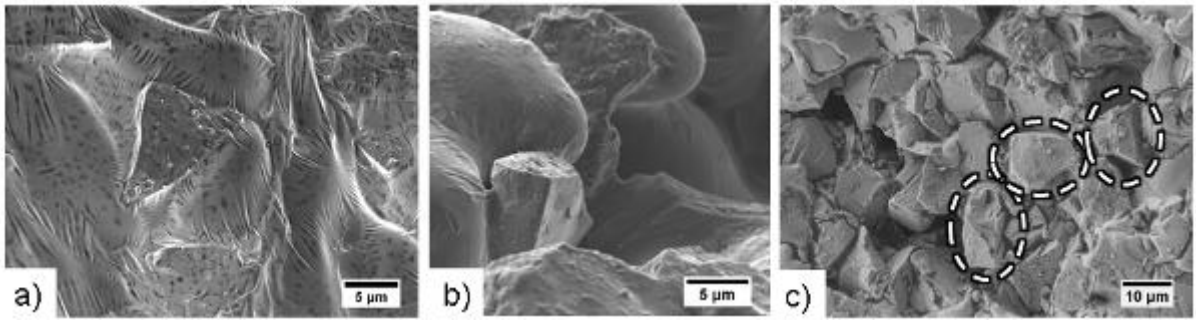

Figure 1. SEM images of SiC particles covering the solid-gas interface of films pulled at a) ambient atmosphere and b) at an oxygen reduced atmosphere (200 ppm O_2). c) Loosely connected SiC particles at the surface of an external argon injected foam (indicated by dashed circles).

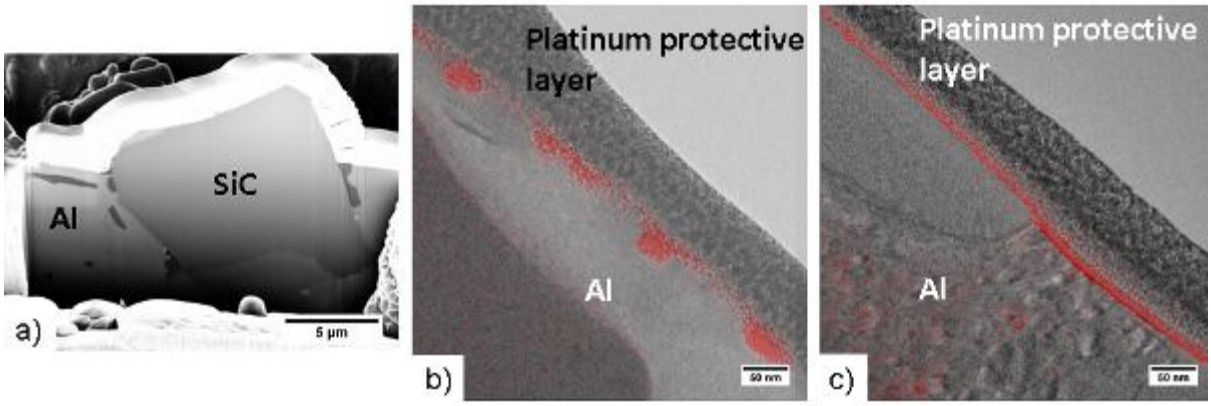

Figure 2. a) Cross section of a partial embedded SiC particle in AlSi9Mg0.6 pulled at 200 ppm O_2 and cut using FIB. Position of oxides, as revealed by EFTEM are indicated by red spots, of the same material pulled at b) 1000 ppm O_2 showing the formation of an interrupted layer and c) at ambient atmosphere with a clear continuous oxide layer.

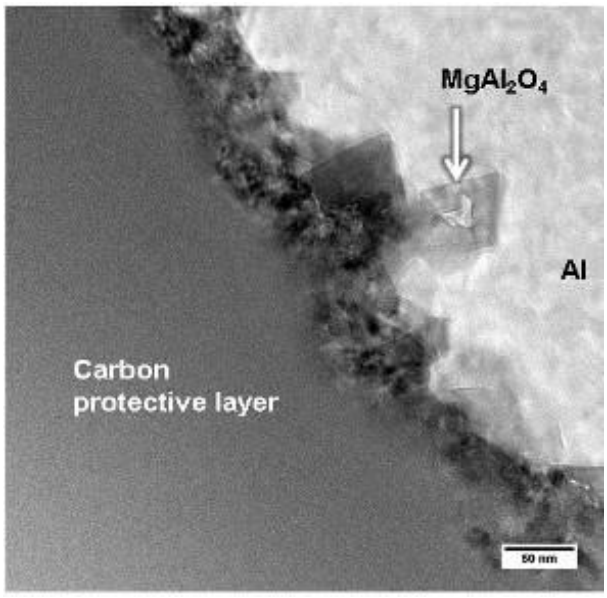

Figure 3. TEM image of nano-sized $MgAl_2O_4$ particles embedded at the oxidised surface.

Functional Materials

MS.3.P045
Spatial distribution of Thulium in Tm^{3+}-doped oxyfluoride glasses and glass-ceramics

A. de Pablos-Martín[1,2], C. Patzig[1], T. Höche[1], A. Durán[2], M. Pascual[2]

[1]Fraunhofer Institute for Mechanics of Materials IWM, Nanomaterials & Nanoanalytics, Halle, Germany
[2]Institute of Ceramic and Glass (CSIC), Madrid, Spain

araceli.de.pablos-martin@iwmh.fraunhofer.de
Keywords: oxyfluoride glass-ceramics, rare-earth ions.

The synthesis of rare-earth (RE) ion-doped oxyfluoride glass-ceramics is a promising way to obtain crystalline phases with very low phonon energies, like LaF_3,[1] $NaLaF_4$,[2] and $NaYF_4$,[3] embedded in a glassy matrix. In such transparent materials, the latter crystal phases act as hosts for the RE ions, thus enhancing radiative optical-emission processes, like up- and down-conversion emissions [4], yet still keeping the good mechanical properties of silicate matrices.

Until now, the verification of the incorporation of RE ions in nanocrystalline phases in glass-ceramics is mainly based on optical techniques, such as luminescence spectroscopy and luminescence decay curves. However, the possibility to perform elemental distribution mappings of RE elements would allow to directly localizing RE ions in the glass and glass-ceramics. Thus, the aim of this work is to complete our previous studies [1], adding unexcelled spatial resolution by using Transmission Electron Microscopy techniques (TEM) and Energy Dispersive X-Ray Spectroscopy (EDXS).

In this work, a glass of composition 55 SiO_2–20 Al_2O_3–15 Na_2O–10 LaF_3 (mol %), doped with 1 mol % Tm_2O_3, and the corresponding glass-ceramic were structurally characterized through TEM, STEM and EDXS (Figure 1). Tm^{3+} ions provide interesting optical properties to the glass, like blue up-conversion emission from the excitation in the near infrared range.

Based on previous works, the elucidation of the LaF_3 nano-crystallisation mechanism in Tm_2O_3 doped-oxyfluoride glass-ceramic has been improved by the application of TEM techniques described in this contribution. The parent glass contains amorphous La- and F-enriched phase separation droplets of ca. 30 nm diameter, also containing Si, Al, and O. The doping ion Tm^{3+} is partly incorporated in the phase-separation regions. Al is present, likely as Al_2O_3, in a thin shell surrounding the droplets. Upon annealing, growth of 10-20 nm LaF_3:Tm crystallites within these phase separation droplets takes place (Figure 1a,c), which are trapped in a volume determined by the size of the preceding phase-separation droplets. The LaF_3 nano-crystals act as host for part of the Tm^{3+} ions (Figure 1c). The remaining volume not occupied by the crystals is filled with Al, while silicon relocates itself towards the periphery (Figure 1b). In this final stage, further crystal growth is inhibited, due to the increase of viscosity in the periphery of the crystals (Figure 2). The possibility to actually being able to map the distribution of Tm in a radiation sensitive sample is well worth mentioning, since it is only made possible through a combination of proper sample preparation, cutting-edge analytical transmission electron microscopy at 80 kV acceleration voltage and, particularly, the application of a dedicated EDXS detector system (FEI Super X). Moreover, thanks to the advance STEM/EDSX analysis it was possible to discern between a thin aluminum layer around the crystals, and a second shell of Si, which inhibit further crystal growth, enabling the nano-crystal size. The verification of the inclusion of Tm^{3+} ions into the LaF_3 structure through EDX elemental mappings is a great advance in the development of rare earth doped glass-ceramics, since it is the key feature of these materials for their application in optical devices.

1. A. de Pablos-Martín, D. Ristic, S. Bhattacharyya, T. Höche, G.C. Mather, M. O Ramírez, S. Soria, M. Ferrari, G.C. Righini, L.E. Bausá, A. Durán, M.J. Pascual, J Am Ceram Soc, 96 (2013) 447-457.
2. A. de Pablos-Martin, M.O. Ramirez, A. Duran, L.E. Bausa, M.J. Pascual, Opt Mater, 33 (2010) 180-185.
3. G. Dominiak-Dzik, R. Lisiecki, W. Ryba-Romanowski, L. Krajczyk, J Alloy Compd, 511 (2012) 189-194.
4. A. de Pablos-Martin, A. Duran, M.J. Pascual, Int Mater Rev, 57 (2012) 165-186.
5. This work was supported in part by the FhG Internal Programs under Grant No. Attract 692 280.

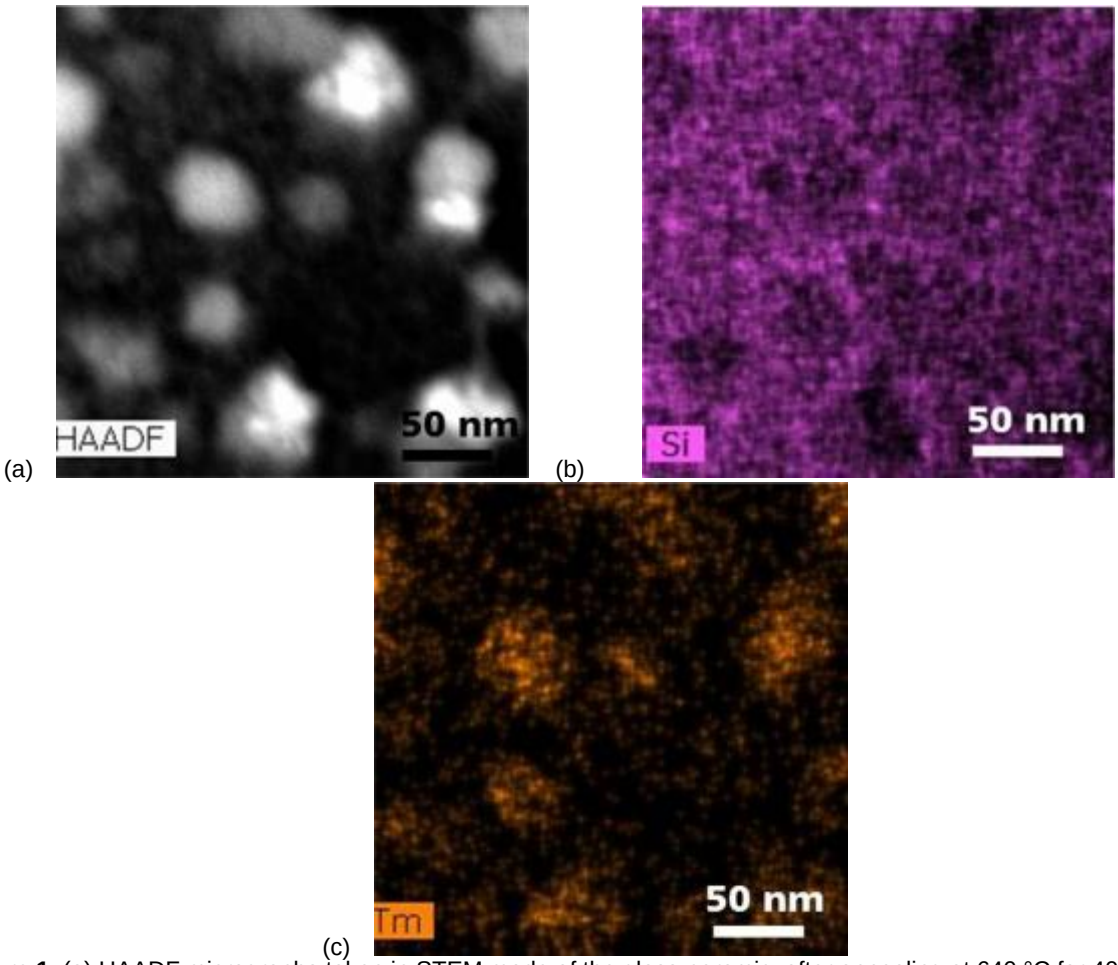

Figure 1. (a) HAADF micrographs taken in STEM mode of the glass-ceramic after annealing at 640 °C for 40 h and the corresponding EDXS mappings of (b) Si, (c) Tm.

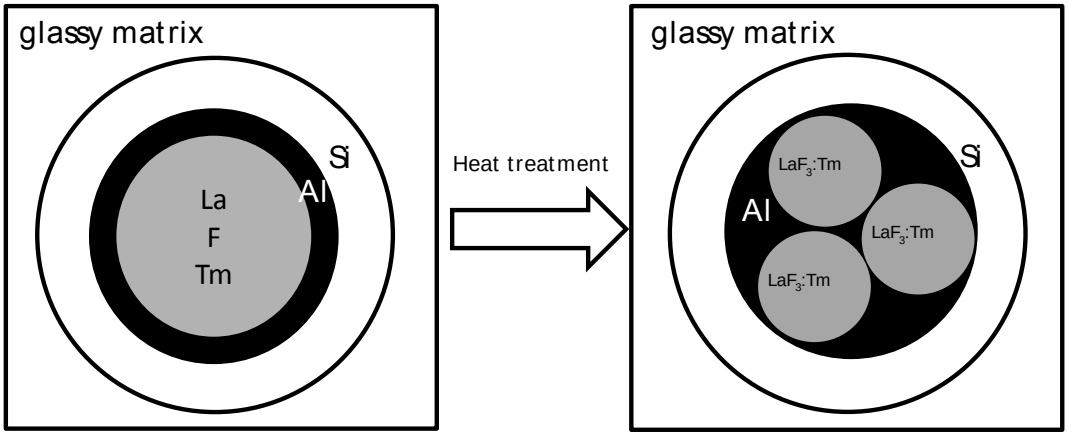

Figure 2. Scheme of the nano-crystallisation mechanism in the studied Tm^{3+} doped glass

Functional Materials

MS.3.P046
Beam size and analytic resolution of the FEG-EPMA JEOL JXA-8530F

J. Nissen[1], D. Berger[1]

[1]Technische Universität Berlin, Zentraleinrichtung Elektronenmikroskopie, Berlin, Germany

joerg.nissen@tu-berlin.de
Keywords: FEG-EPMA, Monte Carlo Simulation

The spatial resolution of EDX- and WDX- element analysis in the SEM is limited mainly by the size of the interaction volume. Therefore an Electron Probe Microanalyser (EPMA) with a thermionic electron emitter is sufficient in many cases. To increase the spatial resolution necessary for modern applications with nanostructures it is required to work with lower acceleration voltages (below 5 kV) of the primary electrons. Then the interaction volume is decreased efficiently and a higher spatial resolution is expected. But it should be kept in mind that electron beams from a thermionic source might not be focused very well for low acceleration voltages. Consequently, element analysis with the Field Emission Electron Probe Microanalyser (FEG-EPMA) is the method of choice.

Even for a FEG, the minimum achievable beam diameter is inversely proportional to the acceleration voltage. But the size of the interaction volume increases linearly with it. Therefore the acceleration voltage should be chosen very carefully to balance both effects and to achieve the best possible spatial resolution. Moreover the beam size depends on the beam current.

To get reliable information on the beam size of our FEG-EPMA JEOL JXA-8530F we recorded SE- and BSE-images of a gold-on-carbon high resolution sample by varying the accelerating voltage (3, 5, 8, und 15 kV) and the probe current in steps from 10 pA to 100 nA. Using the FEI-programme “Image”, we measured the contrast profile of the gold insulars edges in the SE- und BSE-images. The rise of these profiles (1 - 99 % criterion for comparison with Monte Carlo simulations) gives information on the probe diameter, e.g., 15 nm for 15 kV at 10 pA or 31 nm for 8 kV at 1 nA. Usually resolution measurements using profile scans are evaluated using the 16% - 84% criterium. But for the comparison with Monte Carlo simulations, the 1% - 99% criterium has to be chosen, since Monte Carlo simulations assume complete absorption of the electrons inside the sample. Results of the measured probe diameters are shown in “Figure 1”. These results accord with the data provided by JEOL.

In the next step the size of the interaction volume has to be regarded. Obviously it can not be measured directly. Therefore we made measurements on especially crafted model samples. For the first sample a silver layer (500 nm) was sputtered on a silicon wafer substrate. Furthermore, we sputtered a gold layer of 75 nm thickness and another 500nm Ag-layer (“Figure 2”). On the layers cross-section, a profile scan with 15 kV and 1nA was measured at a probe diameter of 22 nm. Considering the 1/99 criterion, we get a spatial resolution of 360 nm for the AuMα-signal (2.12 keV) and 200 nm for the AuLα-signal (9.68 keV) (“Figure 3.”).

Radial Xray distribution curves simulated with the Monte Carlo program Casino (version 2.48) confirm these results (“Figure 4.”). Decreasing the voltage to 5 kV, the current was 1 nA, we get an enhancement of resolution to 120 nm for the AuMα-signal. The estimated resolution using Monte Carlo simulation, however, is about 60 nm. Considering the probe diameter of 38 nm, we expect a resolution of about 100 nm. The measured resolution is worse due to fluorescence of AgLα-Xray (2.98 keV) widening the Au-Mα-signal (M_{abs}: 2.31 keV). In another test, we sputtered a 75 nm gold layer on a silicon wafer substrate. An additional 275nm thick carbon layer was deposited on the gold (“Figure 5”). In this case the cross-section profile scan was measured with 5 kV (1 nA) only. Having no fluorescence from Si-Kα (1.74 keV) we should get a better resolution and indeed 90 nm was achieved (“Figure 6”). Thus, measurement and Monte Carlo simulation (“Figure 7”) nearly coincide.

In conclusion, the FEG-EPMA has a very good analytical spatial resolution smaller than 100 nm significantly increased compared to EPMAs with thermionic electron emitter. To achieve the optimum analytical resolution the minimum beam diameter at low acceleration voltages and the actual size of the interaction volume has to be taken into account. The latter might be derived from measurements at model systems or by Monte Carlo simulations.

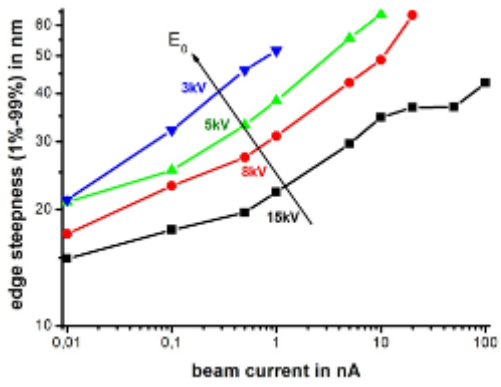

Figure 1: Probe diameter as a function of beam current and HV

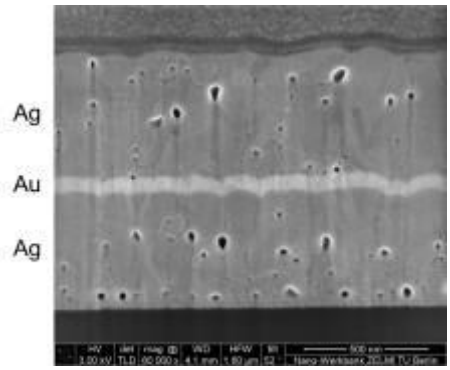

Figure 2. FIB-cross-section of Ag/Au/Ag-layers

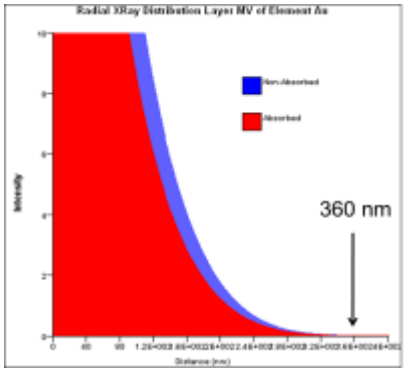

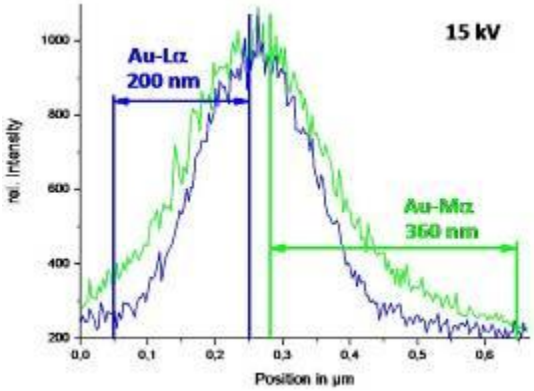

Figure 3. Profile scan on the Ag/Au/Ag-layers

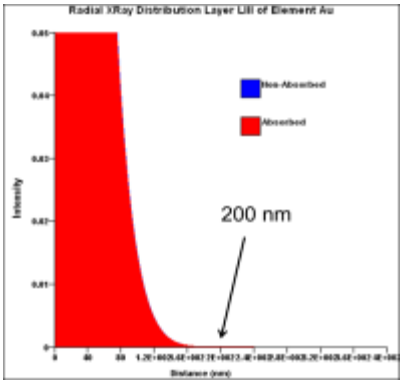

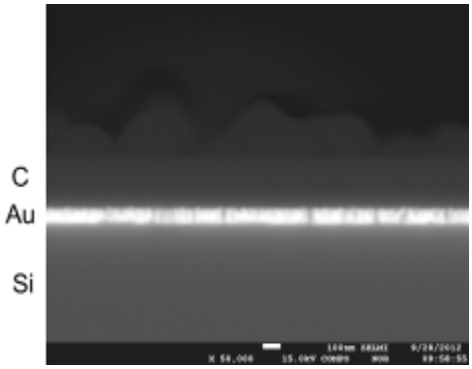

Figure 4. Radial Xray Distribution (RXD) simulation curves of AuMα and AuLα at 15 kV

Figure 5. Cross-section of Si/Au/C-layers

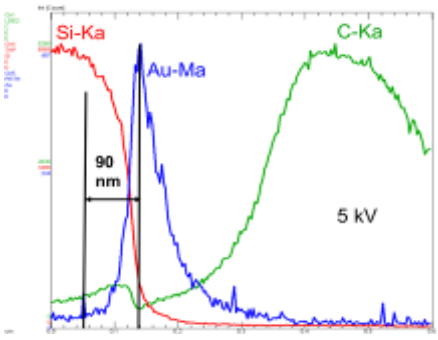

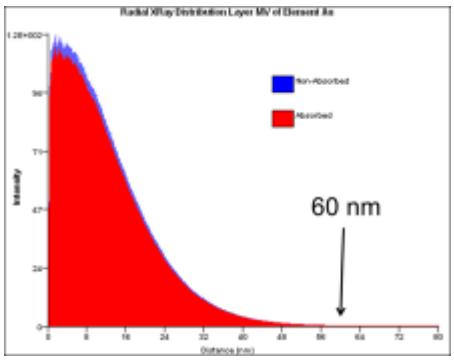

Figure 6. Profile scan on the Si/Au/C-layers

Figure 7. RXD simulation curve of AuMα at 5

Functional Materials

MS.3.P047
Characterization of cerium-doped LYSO scintillating crystals

E. Santecchia[1], G. Barucca[1], A. Di Cristoforo[1], D. Rinaldi[1], E. Tiberi[1], P. Mengucci[1]

[1]Università Politecnica delle Marche, SIMAU, Ancona, Italy

e.santecchia@univpm.it
Keywords: scintillating crystals, LYSO, mechanical properties, transmission electron microscopy (TEM), X-ray diffraction (XRD)

During the last decade, scintillating crystals have become of particular interest as promising candidates for applications in energy physics, security, diagnostic and medical imaging. Many oxyorthosilicate based materials showing high scintillating properties have been studied in the past.

Among them lutetium-yttrium oxyorthosilicate cerium-doped crystals are largely employed for positron emission tomography (PET) and single-photon emission computed tomography (SPECT).

Even though lutetium oxyorthosilicate (LSO) appears to be the best scintillating material for PET application, it has some characteristics that makes it unsuitable for mass production process such as high melting temperature and high cost of the oxide Lu_2O_3 (starting material). The addition of yttrium, leading to the $Lu_{2(1-x)}Y_xSiO_5$ (LYSO) system is able to reduce both the growth temperature and the material cost. Moreover, the addition of cerium as a dopant to the LYSO system, leads to crystals with a comparable light yield and a slightly longer time of decay (50 ns) to LSO, making this system the perfect candidate for scintillating applications. Lutetium yttrium oxyorthosilicate is considered a solid solution of two different silicates, Lu_2SiO_5 and Y_2SiO_5, and in the formation of the final compound, the concentration of the solid solution can be indicated as percentage of the Y/Lu ratio. Mechanical properties have a great importance in the exploitation of scintillating crystals at industrial scale, since they provide the designer a degree of workability in terms of cutting, shaping, mounting and assembling [1]. Aim of the present work is to correlate the microstructure of twelve lutetium-yttrium oxyorthosilicate cerium-doped $Lu_{2(1-x)}Y_{2x}SiO_5$:Ce with x=0.1 (LYSO) crystals to their mechanical behaviour. In particular, this work reports the very preliminary results obtained by transmission electron microscopy (TEM) observations and X-ray diffraction (XRD) techniques on samples submitted to thermal annealing and mechanical testing. X-ray diffraction measurements were carried out by a Bruker D8 Advance diffractometer, using Cu-Kα radiation in Bragg-Brentano geometry, while a Philips CM200 transmission electron microscope at 200 kV was used for TEM observations. Samples for TEM investigations were prepared by the conventional thinning procedure. Six out of the twelve samples were submitted to an annealing treatment in air consisting of the following steps: a) a linear temperature increase (1°C/min) from room temperature to 300°C, b) an isothermal treatment for 10 h at 300°C and c) slow cooling at a linear rate (0.5°C/min) down to room temperature. The ultimate tensile strength (σ_{UTS}) and the Young modulus (E) of all the samples were measured by applying a four-point bending load [2]. Mechanical testing showed a slightly decrease of the mechanical properties for the annealed samples. XRD measurements performed on the not-annealed samples showed peaks exclusively attributable to the LYSO matrix (Figure 1.). On the contrary, a TEM observation performed on an annealed sample evidenced the presence of small coherent precipitates uniformly distributed inside the sample, as reported in Figure 2. taken in two beam condition close to the [010] zone axis orientation. Further TEM investigations and X-ray diffraction measurements are in progress, in order to obtain a complete correlation between crystals mechanical properties and their microstructure.

1. D. Chiriu, N. Faedda, A. Geddo Lehmann, P.C. Ricci, Physical Review B 76 (2007) 0541121.
2. L. Scalise, D. Rinaldi, F. Davì, N. Paone, Nuclear Instruments and Methods in Physics Research A 654 (2011) 121.

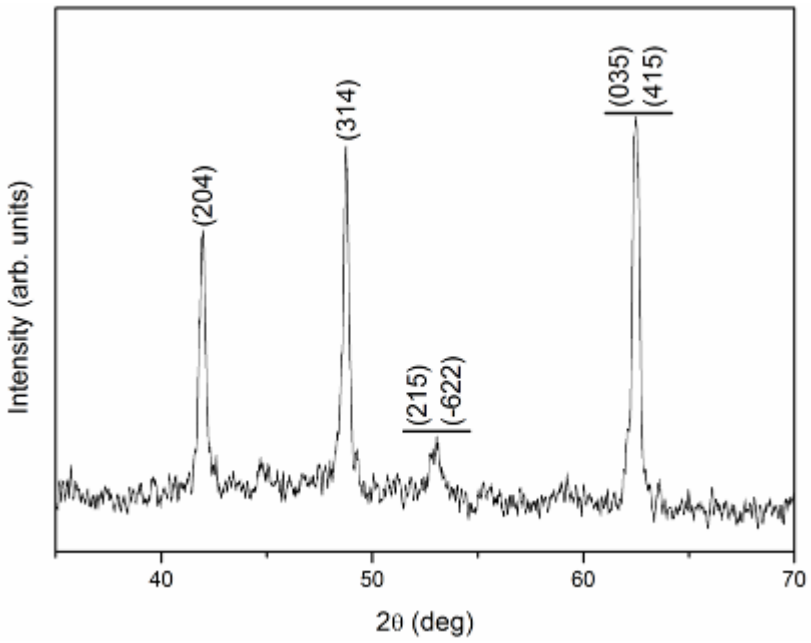

Figure 1. XRD spectrum of a not-annealed LYSO crystal.

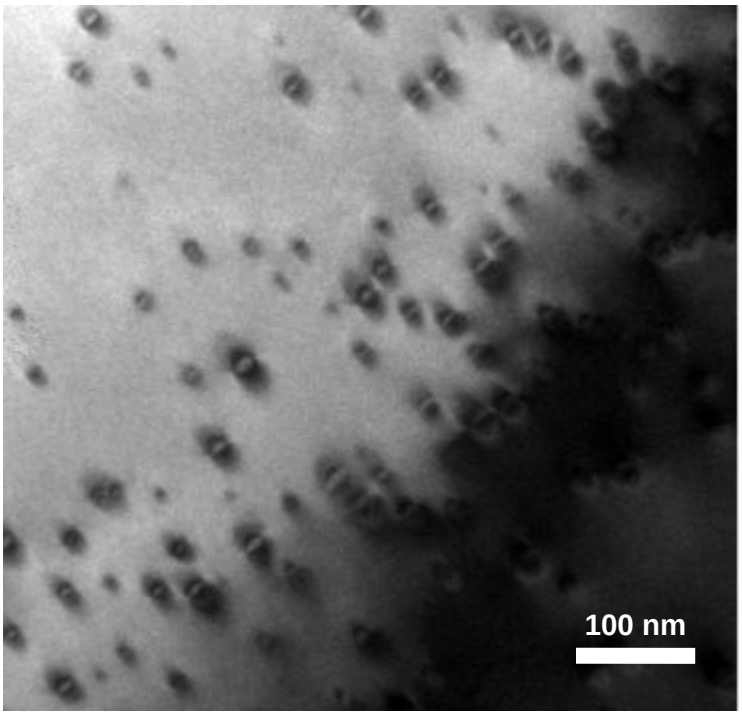

Figure 2. TEM micrograph of an annealed sample.

Functional Materials

MS.3.P048
TEM observations on different length scales for characterization of AlN texture and columnar growth

U. Schürmann[1], V. Hrkac[1], S. Marauska[2], A. Petraru[3], V. Duppel[4], V.S.K. Chakravadhanula[5]
C. Kübel[5], B. Wagner[2], H. Kohlstedt[3], L. Kienle[1]

[1]Institute for Materials Science, Christian Albrechts University , Synthesis and Real Structure, Kiel, Germany
[2]Fraunhofer Institute for Silicon Technology ISIT, Itzehoe, Germany
[3]Institute of Electrical and Information Engineering, Christian Albrechts University, Nanoelectronic, Kiel, Germany
[4]Max Planck Institute for Solid State Research, Stuttgart, Germany
[5]Karlsruhe Institute of Technology (KIT), Karlsruhe Nano Micro Facility (KNMF), Karlsruhe, Germany

usc@tf.uni-kiel.de
Keywords: piezoelectric material, AlN, HRTEM, ACOM

In the framework of the collaborative research center SFB 855 magnetoelectric (ME) materials are developed as strain-mediated piezoelectric-magnetostrictive nanocomposites for sensor applications. These sensors are considered as excellent candidates for biomagnetic interfaces enabling non-invasive medical imaging as magneto-encephalography or cardiography (MEG, MCG). For the piezoelectric component aluminum nitride (AlN) thin films exhibit outstanding performance [1]. The piezoelectric properties of AlN are directly associated with the crystal orientation and thus the morphology. For sensor applications highly c-textured films are desired with the film normal parallel to the polar crystal axis [0 0 0 1]. Modern TEM techniques, particularly automated crystal orientation mapping (ACOM) allow a detailed investigation of the morphology at different lengths scales ranging from nano- to the micron size [2,3]. The dominant color (figure 1b) and the diffraction patterns of the marked areas prove a columnar growth of AlN in [0 0 0 1] direction. However, several columns are misaligned from [0 0 0 1] orientation. These morphological defects can also be identified by PFM (piezo-response force microscopy) measurements from similar regions but on larger scale. Furthermore, a closer inspection of the orientation maps of figures 1c-d shows that the azimuthal rotation of the columns around the [0 0 0 1] direction is not subject to any restriction. Intrinsic features of the rotation at the grain boundaries and defect structures such as stacking mismatch boundaries (SMB, [4]) can be analyzed quantitatively by high resolution microscopy and (precession) electron diffraction. Moreover, a detailed study on defect structures was performed along the basal view ([0 0 0 1] zone axis. As depicted in the HRTEM micrograph in figure 2a, domain boundaries appear as strongly pronounced periodic contrast along the {2 -1 -1 0} planes (see also correlated FFT). The enlarged view of the domain boundary shows a convincing agreement between experimentally obtained and simulated high resolution contrast. In figure 2b and 2c, the polyhedral representation of the AlN structures are compared for the defect-free and the domain boundary case. In the bulk wurtzite type structure, the AlN tetrahedrons are linked by common corners. At the interface of the domain boundary the tetrahedrons share one common edge.

1. P. Muralt, J. Am. Ceram. Soc. **91**(2008), p.1385
2.. E. F. Rauch, M. Veron, J. Portillo, D. Bultreys, Y. Maniette and S. Nicolopoulos, Microsc. Anal. **93** (2008), S5
3. A. Kobler, A, Kashiwar, H. Hahn and C. Kübel, Ultramicroscopy **128** (2013), 68-81.
4. Y. Xin, P. D. Borwn, C. J. Humphreys, T. S. Cheng, C. T. Foxon, Appl. Phys. Lett., **70** (1997), p. 10
5. Funding by the German Research Foundation (DFG) as part of the Collaborative Research Center 855 “Magnetoelectric Composites – Future Biomagnetic Interfaces” (SFB 855 subprojects C2 and Z1) is gratefully acknowledged. The authors would like to thank Prof. B. Lotsch for enabling the TEM experiments and Christin Szillus for the FIB preparation.

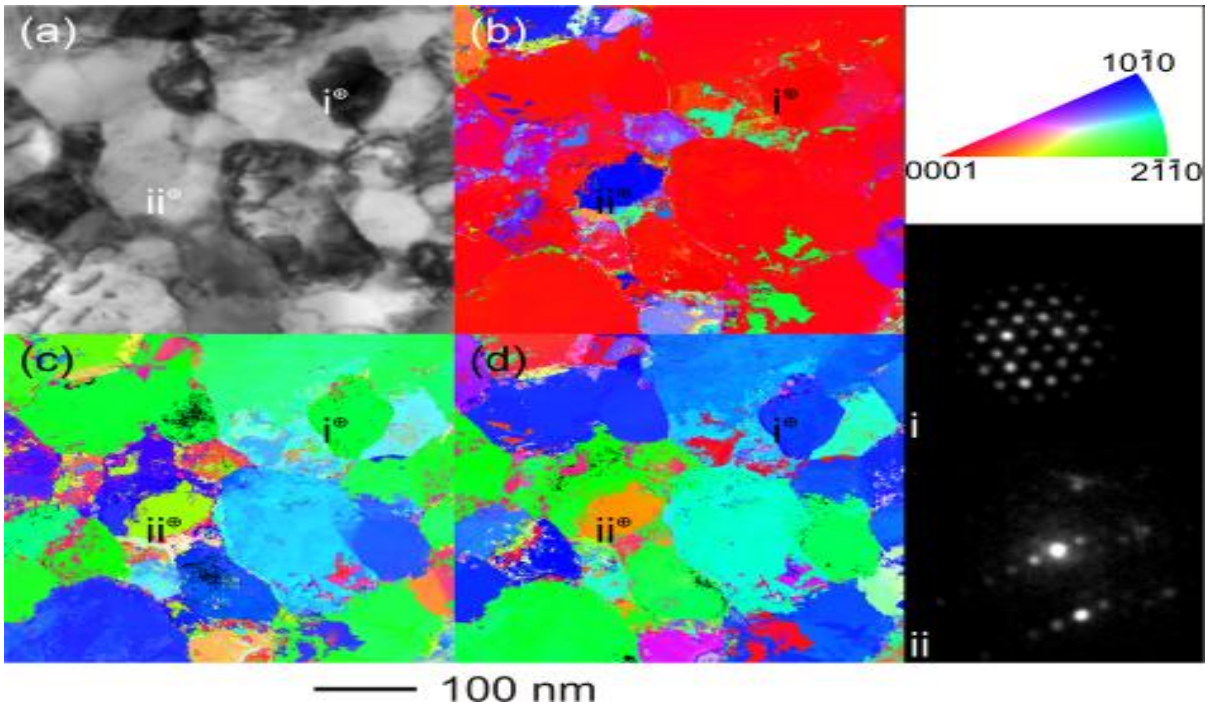

Figure 1. Automated crystal orientation mapping of AlN along the basal view. (a) Virtual bright field image. Orientation map along the out-of-plane z-direction (b), and two in-plane directions (c) x-direction, (d) y-direction. (Right) Color code of the stereographic triangle (hexagonal point group: 6*mm*) for all three maps. Diffraction patterns of area i) and ii).

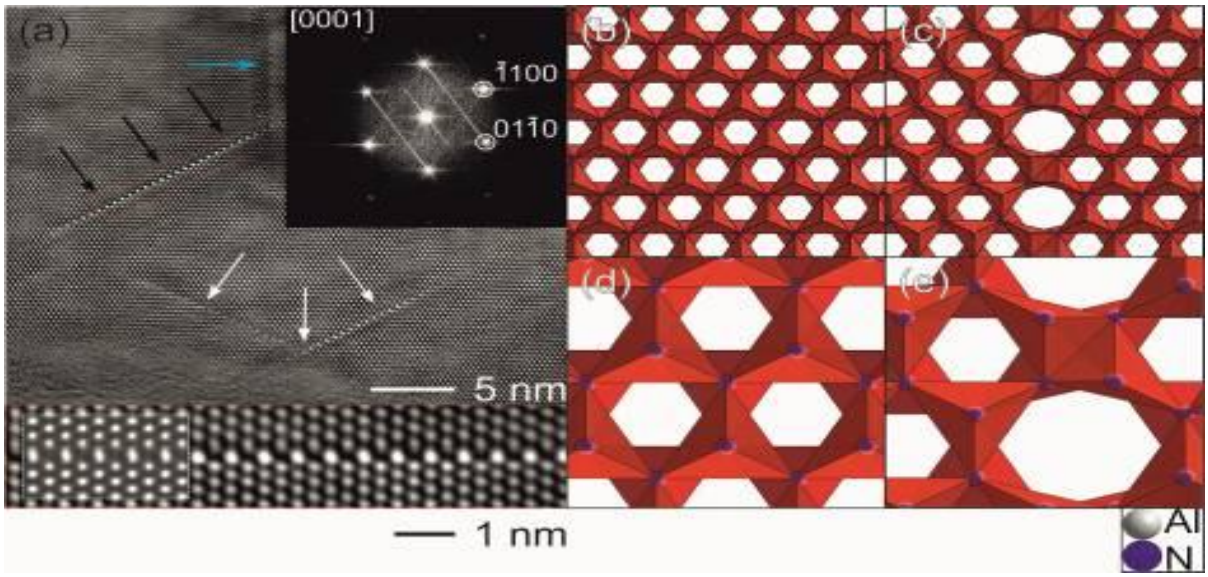

Figure 2. (a) HRTEM micrograph along the [0 0 0 1] zone axis with inserted FFT. Arrows mark the stacking mismatch boundaries. The enlarged panel at the bottom shows a stacking mismatch boundary with a simulation as inset (objective lens defocus | specimen thickness) of (-45 nm | ~5.5 nm). Schematic for the defect-free bulk structure (b) and the structure at the SMB (c) along the [0 0 0 1] zone axis. (d) and (e) corresponding enlarged views.

Functional Materials

MS.3.P049
TEM analysis of the influence of the synthetic polypeptide c25-mms6 on the cobalt ferrite nanoparticle growth

W. Hetaba[1,2], A. Wolff[2], N. Mill[2], M. Wissbrock[3], N. Sewald[3], A. Hütten[2]

[1]Vienna University of Technology, USTEM, Wien, Austria
[2]Bielefeld University, Department of Physics, Bielefeld, Germany
[3]Bielefeld University, Department of Chemistry, Bielefeld, Germany

walid.hetaba@tuwien.ac.at
Keywords: Nanoparticles, TEM, EELS

In recent years, biomimetic syntheses of nanoparticles have attracted great interest. Polypeptides play an important role in bio-inspired nanoparticle synthesis, as they are able to control the inorganic crystal growth [1]. To improve our understanding of the interaction between the polypeptide and inorganic crystals, we prepared cobalt ferrite nanoparticle solutions with and without the synthetic polypeptide c25-mms6 [2]. The influence of the polypeptide was investigated by comparing these two sorts of nanoparticles at different growth stages using transmission electron microscopy (TEM) and electron energy loss spectrometry (EELS). The investigations were conducted using an FEI TECNAI G^2 TF20 transmission electron microscope operated at 200 kV. Figure 1. (left) shows an image of a nanoparticle synthesised with c25-mms6 at a stage where its synthesis is still incomplete. It can be seen that the particle consists of several highly oriented subunits. In Figure 1. (right), a nanoparticle synthesised without the polypeptide is shown for the purpose of comparison. In contrast to the c25-mms6-enhanced particle, no such subunits were observed. Figure 2. (left) shows a hexagonal nanoparticle at the end of its growth process. Additionally, the corresponding diffraction pattern is presented in Figure 2. (right). Only two different orientations are present, namely the [111] and the [-211] zone axes. Together with diffraction patterns acquired at different growth stages, this suggests that the particle surfaces are {111} planes, despite the fact that this plane is usually energetically unfavourable. However, our investigations indicate that the polypeptide c25-mms6 adsorbs onto these specific crystal faces, thus lowering the surface energy. Furthermore, a change of the nanoparticle shape from irregular morphology to hexagonal shape is observed. The composition of the nanoparticles was determined by EELS using a Gatan GIF Tridiem attached to the transmission electron microscope. Quantification of Co and Fe was performed with standard procedures [3]. Analysis of the energy loss spectra shows that using the polypeptide c25-mms6 results in stoichiometric $CoFe_2O_4$ and Co_2FeO_4 nanoparticles. Without c25-mms6, the nanoparticles consist of non-stoichiometric compositions between $Co_{1.3}Fe_{1.7}O_4$ and $Co_{1.7}Fe_{1.3}O_4$. Both approaches have in common that smaller particles are Fe-rich while bigger particles are Co-rich. The results of this study show that the synthetic polypeptide c25-mms6 is not necessary for the formation of cobalt ferrite nanoparticles, but in fact controls the size and phase of the nanoparticles by changing the kinetics of the formation process [2]. It allows the formation of stoichiometric nanoparticles with {111} surfaces.

1. J.M.Slocik and R.R.Naik, Chem. Soc. Rev. 39 (2010), p. 3454.
2. A. Wolff et al., J. Nanopart. Res. 14 (2012), p. 1161.
3. R.F. Egerton, Rep. Prog. Phys. 72 (2009), p. 016502.

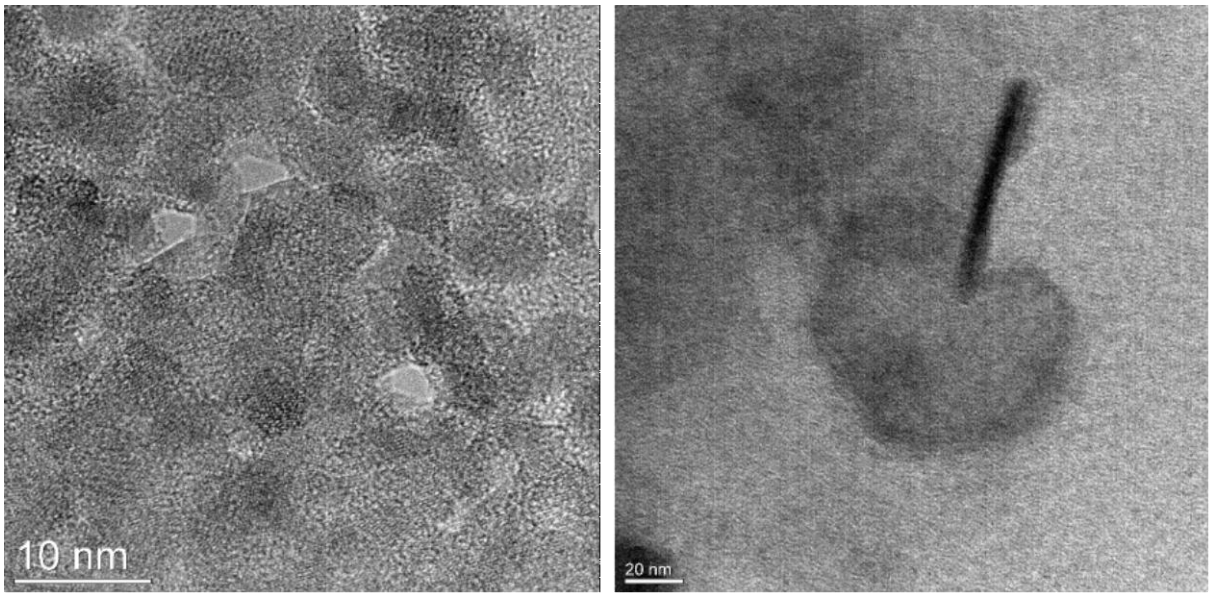

Figure 1. Left: HRTEM image of a nanoparticle synthesised using the polypeptide c25-mms6. The subunits the nanoparticle is formed of can be seen easily. Right: TEM image of a nanoparticle synthesised without the use of c25-mms6.

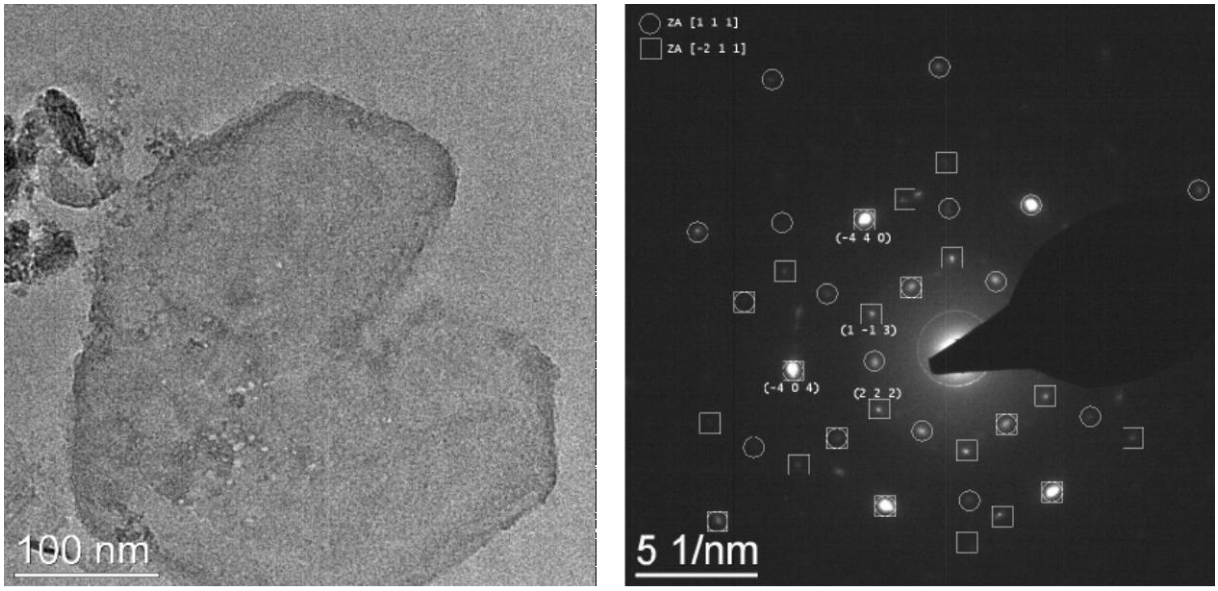

Figure 2. Left: TEM image of a nanoparticle formed by use of c25-mms6 exhibiting roughly hexagonal shape. Right: Corresponding diffraction pattern. The diffraction spots are indexed, only the [111] and the [-211] zone axes (ZA) appear.

Functional Materials

MS.3.P050
Three dimensional characterization of nanofilamentous growth of transition metal oxide dopants in organic semiconductors

A.K. Kast[1], D. Donhauser[2,3], L. Dieterle[2,3], M. Pfannmöller[1], E. Mankel[2,4], R. Lovrincic[2,3], M. Kühn[2,4] W. Kowalsky[2,3], R.R. Schröder[1,2]

[1]CellNetworks, BioQuant, Universitätsklinikum Heidelberg, Cryo-EM, Heidelberg, Germany
[2]InnovationLab GmbH, Heidelberg, Germany
[3]Institut für Hochfrequenztechnik, Technische Universität Braunschweig, Braunschweig, Germany
[4]Technische Universität Darmstadt, Materials Science Institute, Surface Science Division, Darmstadt, Germany

anne.kast@bioquant.uni-heidelberg.de
Keywords: organic semiconductors, tomography, p-type doping

Organic semiconductor devices are typically limited by low intrinsic conductivity and high charge injection barriers at the contacts which can be overcome by electrochemical doping. Wide bandgap materials like 4,4′-Bis(N-carbazolyl)-1,1′-biphenyl (CBP), which are commonly used in organic light emitting diodes, can be p-type doped with transition metal oxides like MoO_3 in a co-evaporation process. Often high doping ratios, exceeding 10 vol%, need to be applied due to low doping efficiencies of 1-2% [1]. Here we investigate the morphology of CBO:MoO_3-composites with films of varying dopant/matrix ratios. Bright-field transmission electron microscopy (TEM) and electron spectroscopic imaging (ESI) [2] of CBP films doped with 10 and 33 vol% MoO_3 revealed that at room temperature MoO_3 forms agglomerations. For 10 vol% doping concentration these agglomerations are about 1nm in diameter and typically spaced about 7 nm apart. A much larger doping concentration of 33 vol% leads to an increased densitiy of MoO_3 agglomerates of similar diameter as before. Electron-tomography revealed that for 10 vol% doping concentration MoO_3 forms filament-like agglomerates preferentially oriented along the growth direction of the film [3], as seen in Fig. 1. A large part of the filaments extends throughout the film thickness. The presence of these large clusters can explain the low doping efficiency discussed above. The 3D reconstruction of a sample with greatly reduced dopant concentration (0.6 vol%) in Fig. 2 shows that MoO_3 filaments – again with similar diameter – still form during co-evaporation. However, a significant decrease in filament number as well as possible fragmentation of the filaments is observed. Electrical measurements parallel and orthogonal to the growth direction of the filaments indicate an anisotropic charge transport for 10 vol% MoO_3 doping concentration. In contrast, measurements of the sample with 0.6 vol% dopant concentration show an isotropic behavior. These conductivity measurements can consistently be explained with the morphologies observed from electron tomography. Continuous filamentous transition metal oxide clusters can lead to an increased conductivity in the direction of the filaments (Fig. 1) whereas for lower dopant concentration the discontinuous clusters do not contribute to a preferred direction of conductivity.

1. S. Hamwi, J. Meyer, T. Winkler, T. Riedl, W. Kowalsky, Applied Physics Letters 94 (2009), 253307.
2. M. Pfannmöller et al., Nano Letters, 2011, 11, pp 3099–3107.
3. D. Donhauser, M. Pfannmöller, L. Dieterle, K. Schultheiß, R.R. Schröder, W. Kowalsky, M. Kröger, Advanced Functional Materials (2012)
4. The authors gratefully acknowledge funding from the BMBF under grant numbers FKZ 03EK3505K, FKZ 13N10794, FKZ 13N10721, FKZ 13N10723.

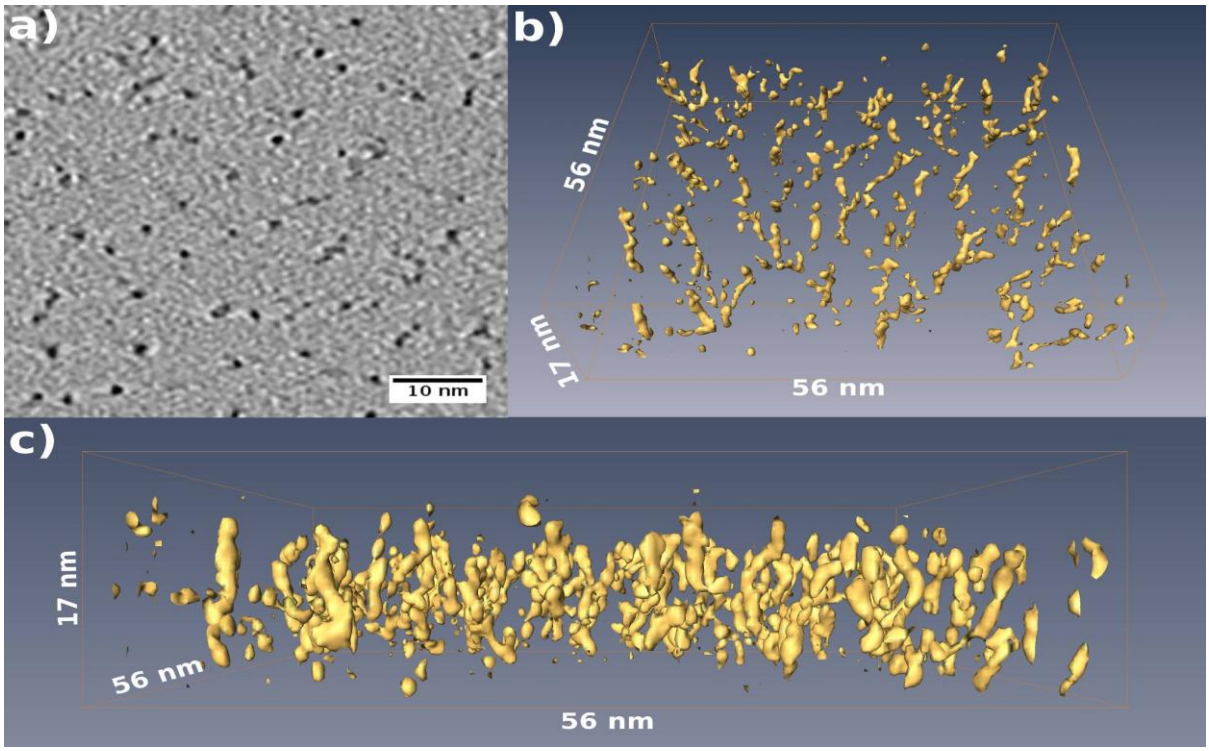

Figure 1. a) Grey-scale image of xy-plane of 10 vol% MoO_3:CBP. Three dimensional representation of the MoO_3 filaments, b) segmentation in 3D and c) side-view of yz-plane.

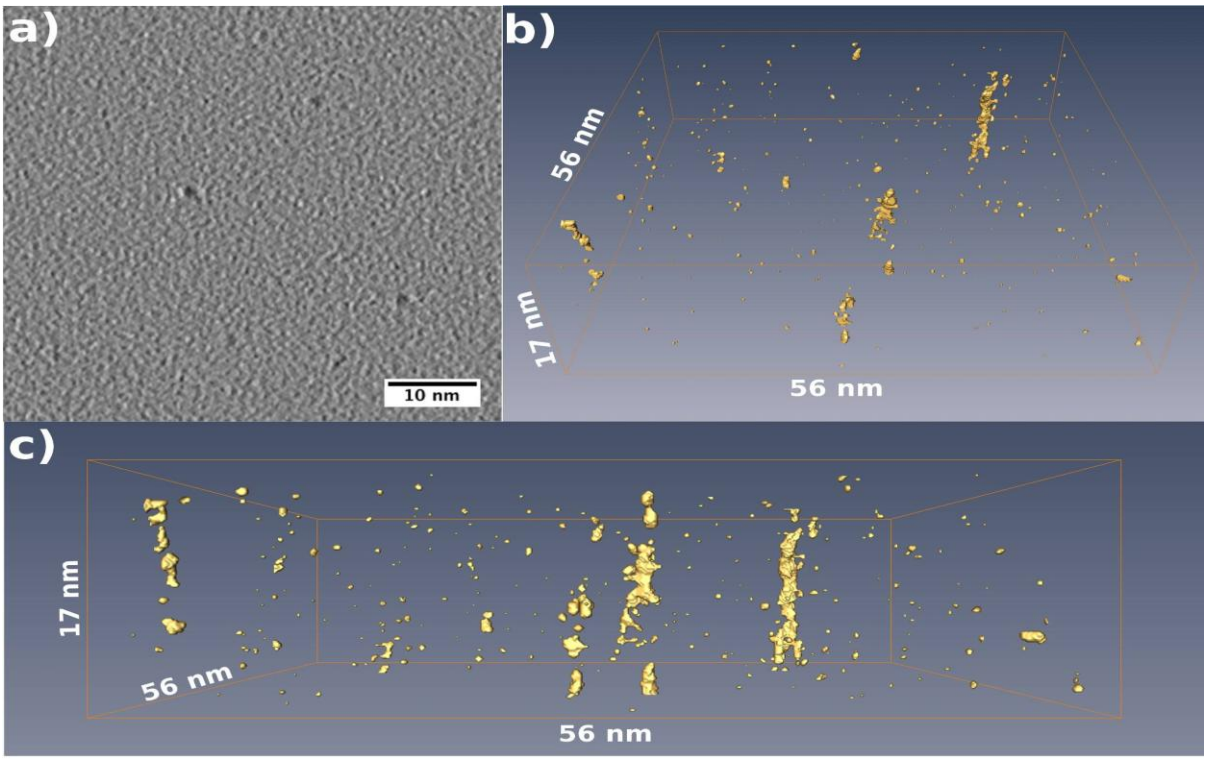

Figure 2. a) Grey-scale image of xy-plane of 0.6 vol% MoO_3:CBP. Three dimensional representation of the MoO_3 filaments, b) segmentation in 3D and c) side-view of yz-plane

Functional Materials

MS.3.P051
SEM study of microstructure of Fe-Mo powders prepared by ball milling

J. Buršík[1], Y. Jirásková[1]

[1]Institute of Physics of Materials, Academy of Sciences of the Czech Republic, Brno, Czech Republic

bursik@ipm.cz
Keywords: Fe-Mo alloy, milling, mechanical alloying, microstructure

Mechanical alloying (MA) is a way of preparing various kind of materials in the form of powders. It is a high-energy processing (e.g. ball milling) where mechanical energy of high speed rotation is transferred to the material. During this process the induced strains lead to repeated fracturing and cold welding of source materials. As a result the alloy powder is formed from blended elemental powders [1]. The process of mechanical alloying with involvement of high energy transfer is able to produce various unstable forms of materials, such as amorphous, metastable and oversaturated alloys. Despite an extensive experimental research [2,3] there is still a lack of understanding of complex physical and chemical mechanisms of the structure and phase formation during MA. This work is focused on the study of microstructure of Fe-Mo powders as depending on the milling conditions and further thermal treatment.

A Fritsch Pulverisette 7 premium line planetary ball mill was used to prepare the samples. The starting materials for ball milling were crystalline Fe (150μm) and Mo (5μm) powders of high purity (99.8%). They were at first annealed at 873K for 100 hours and slowly cooled down in the mixture of Ar and H_2.Then the powders in the ratio $Fe_{80}Mo_{20}$ were placed in two vials and mixed without balls at 150rpm for 1 minute. After that, 10pcs of balls of 10mm in diameter were added in each vial. The material of vials and balls was zirconium oxide. One of the closing lids was equipped with sensors for temperature and pressure monitoring during the milling in air. The other one enabled milling under nitrogen gas. The speed of rotation was 450rpm, the ball-to-power ratio was 10:1 and the maximum milling time was 250 h. To avoid undesired sample overheating every 60 min of milling were followed by a 60min pause. Powder samples were taken out at preselected times of milling for microstructural analysis. Samples after the final milling time of 250 h were optionally annealed at vacuum furnace at temperatures ranging from 673 to 823 K.

An X'PERT-PRO diffractometer with Co Kα radiation was used to study the occurring structural changes during milling. A TESCAN LYRA 3XMU FEG/SEM×FIB scanning electron microscope (SEM) working at accelerating voltage of 15 kV with an Oxford Instruments energy dispersive X-ray (EDX) analyzer X-Max 80 and a Philips CM12 STEM transmission electron microscope (TEM) with an EDAX EDX and Phoenix software were used to follow the surface morphology and microstructure.

X-ray diffraction analysis yielded the volume fraction of coexisting phases and respective mean diameters of coherently scattering crystal regions. An essential decrease of crystal regions size occurs during initial 80 h of milling. It turned out that Mo begins to dissolve in Fe and vice versa already after 10 h of milling. The samples annealed for 250 h both in air (A) and nitrogen (N) consist of dominant (nearly 90 %) bcc-Fe(Mo) phase and the residual bcc-Mo(Fe) phase. The A and N samples differ in the Mo content dissolved in Fe. According to lattice parameter measurements, in the A sample 14.4 at.% Mo was detected in bcc-Fe(Mo), while in the N sample approximately 11.4 at.% Mo was found. The crystallite size was about 6 nm for bcc-Fe(Mo) and 8 nm for bcc-Mo(Fe) phase in both samples.

TEM observations (Figure 1) were made on powder samples deposited on holey carbon films. They show compact agglomerates with internal structure consisting of small crystal regions, the size of which correlates well with the results of X-ray diffraction. Point EDX analyses in TEM reveal compositional variations inside the agglomerates [4]. Both X-ray and EDX measurements confirm that the Mo content in the bcc-Fe(Mo) and the Fe content in the bcc-Mo(Fe) solid solutions exceed substantially the equilibrium solubility limit in both A and N samples.

SEM observations document the powder size decrease in the course of milling (Figure 2). It should be noted that in SEM micrographs we observe agglomerates and only TEM can visualize their internal microstructure. Figure 3 displays the smallest agglomerate size after milling for 250 hours. Annealing at relatively low temperatures does not substantially affect the overall look of studied powder samples from the viewpoint of agglomerate and crystallite size. Extensive EDX analyses in SEM after various heat treatments found a reasonable amount of Zr in all measurements, originated from the vials and

balls. Small ZrO_2 peaks were detected also in X-ray diffractograms. Point EDX analyses from single agglomerates (though encompassing a large number of crystallites each) have a large scatter. Average values are 76Fe-16Mo-8Zr (at. %) for A samples and 76Fe-17.5Mo-6.5Zr for N samples [5].

1. C. Suryanarayana, Prog. Mater. Sci. 46 (2001), p. 1.
2. F. Otmane, S. Bergheul, M. Zergoug and M. Azzaz, Defect Diff. Forum 312-315 (2011), p. 743.
3. E. Jartych, J. Magn. Magn. Mater. 265 (2003), p. 176.
4. Y. Jirásková, J. Buršík and I. Turek, J. Supercond. Nov. Magn. (2013), DOI 10.1007/s10948-012-2049-4.

5. We kindly acknowledge the financial support from the Czech Science Foundation (Project P108/11/1350).

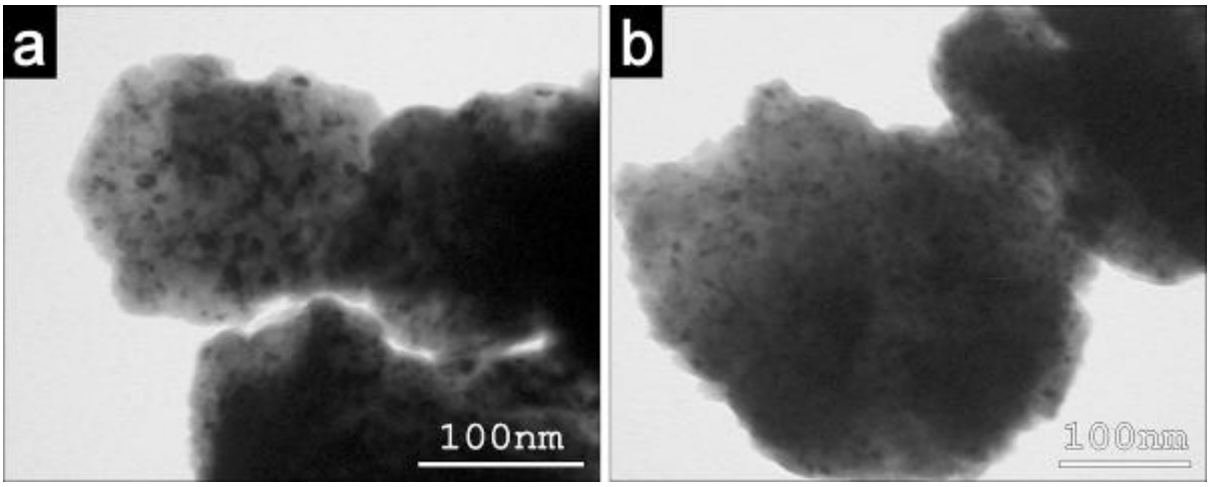

Figure 1. TEM micrographs of powder particles after 250 hours of milling in air (a) and in nitrogen (b).

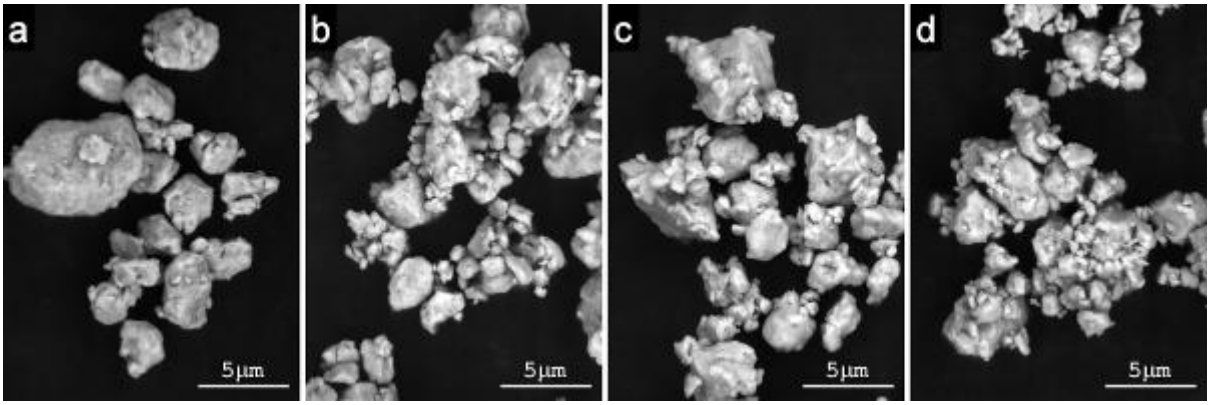

Figure 2. SEM micrographs of powders (backscatter electron images) in selected intermediate stages of milling: 60 hours in air (a), 60 hours in nitrogen gas (b), 120 hours in air (c) and 120 hours in nitrogen gas (d).

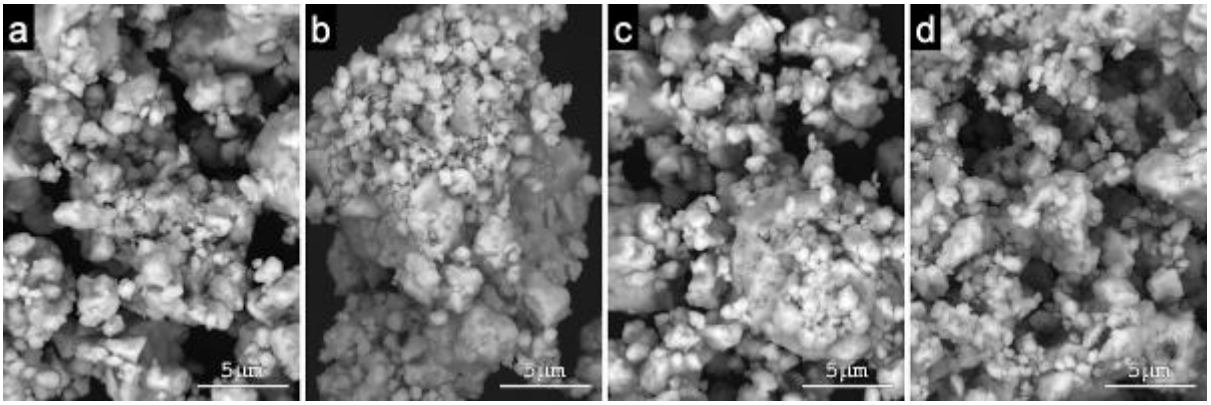

Figure 3. SEM micrographs of powders (backscatter electron images) after 250 hours of milling (in either air or nitrogen) followed by annealing at selected temperature: air, 723 K (a), nitrogen, 723 K (b), air, 773 K (c), nitrogen, 773 K (d)

Functional Materials

MS.3.P052
Characterisation of single stone impact defects of anticorrosive coated automotive steel plates

H. Schroettner[1,2], A. Schoenberger[3], J. Rattenberger[1], J. Wagner[1], S. Mertschnigg[1,2]

[1]Centre for Electron Microscopy and Nanoanalysis, Graz, Austria
[2]Institute for Electron Microscopy and Nanoanalysis/Graz University of Technology, Graz, Austria
[3]BMW AG, Munich, Germany

hartmuth.schroettner@felmi-zfe.at
Keywords: ESEM, FIB, IFM, EDXS, Corrosion

Corrosion protection is an important attribute of the quality of premium cars. To satisfy the customer and to guarantee the quality standardised testing of parts and prototypes are applied by the automotive industry. However, results of accelerating corrosion tests differ from corrosion data of field components. Additionally, results of corrosion issues in a late stage of the development process are difficult to handle for the production processes. Due to common problems it is necessary to detect stone chipping areas in an early stage of development due to a computerized simulation of stone chipping. The following work aims to stone impact and the corrosion progress starting from the stone chipping defect [1]. Induced damages of the coating system and the corrosion propagation were analysed using Pulsed-Phase-Thermography (PPT). After analysing results were correlated and verified with destructive analyses [2]. 3D surface measurement techniques [3] and destructive measurements were used to get information about the corrosion depth and the material removal behaviour of automotive parts. In a first step, steel plate samples in an as delivered condition from different types and combinations of anorganic and organic anticorrosion coatings were characterised on their surfaces and cross sections. These references were shot at from a mono stone impact test facility with defined profiles and weight of the impactor with varied velocity and angle. These impact defects were characterised with various methods. To gather a 3D-information of the defect surface measurements were made with an Infinite Focus Microscope (IFM) [3]. The IFM enables the measurement of three dimensional structures and volumes (see figure 1) using real colour information. Next the non-conductive surfaces were analysed inside an Environmental Electron Microscope (ESEM) using Energy Dispersive X-Ray-Spectrometry (EDXS) (see figure 2). Afterwards cross sections were made to investigate possible destruction or/and delamination of layers with ESEM/EDXS (see figure 3). Parallel different standardised corrosion tests were started and these specimens were characterised in the same way after the test cycles. To avoid mechanical or chemical influence on the corroded defects, additionally Focused Ion Beam (FIB) Slice & View technique was used (see figure 4).

1. A. Schoenberger, Master Thesis „Prognose des Steinschlags und der induzierten Korrosion am Fahrzeug“, (2012)
2. A. Schoenberger, S. Virtanen, V. Giese, C. Spießberger, H. Schroettner, J. Rattenberger, J. Wagner, Corrosion science 56, 168 – 175 (2012)
3. H. Schroettner, M. Schmied, S. Scherer, Modern Developments and Applications in Microbeam Analysis, 341, (2005)
4. A. Schoenberger, S. Virtanen, V. Giese, H. Schroettner, C. Spießberger, Materials and Corrosion, Volume 63, Issue 3, 195-199 (2012)
5. A. Schoenberger, S. Virtanen, V. Giese, C. Spießberger, H. Schröttner, J. Wagner, Materials and Corrosion 63, Title (2012)

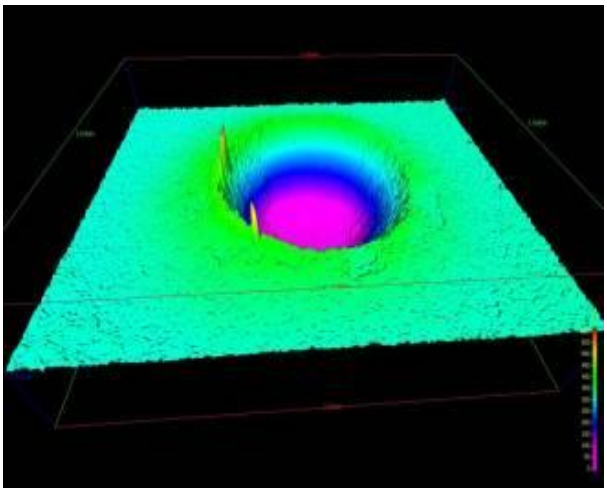

Figure 1. (left); IFM 3D surface model of a stone impact defect as false colour image

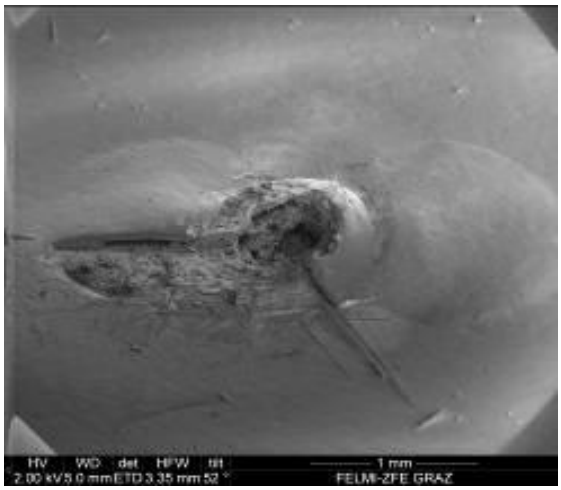

Figure 2. (right); ESEM SE image of the surface of a coated steel plate with a stone impact defect

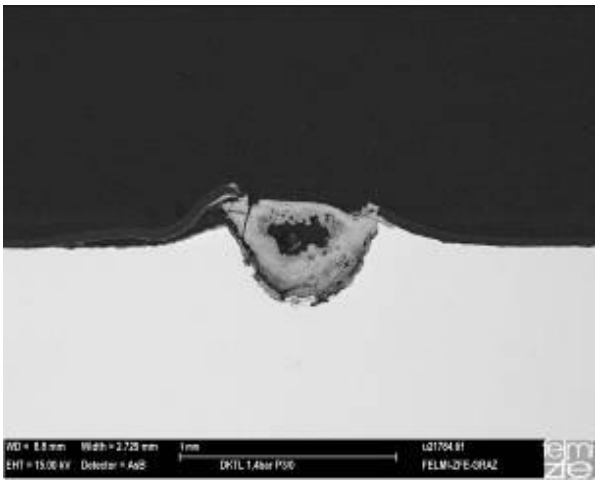

Figure 3. (left); SEM BSE image of a cross section through a stone chipping defect exposed in an accelerated corrosion test

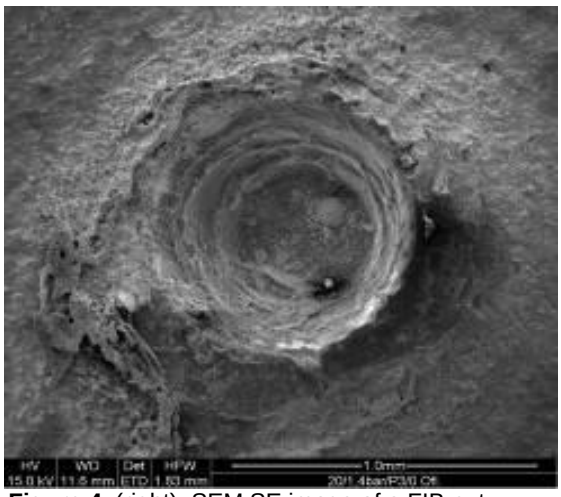

Figure 4. (right); SEM SE image of a FIB-cut through a stone chipping defect exposed in an accelerated corrosion test [5]

Functional Materials

MS.3.P053
Optimization and characterisation of metamorphic buffer layers for extended-InGaAs/InP photodetectors

S. Seifert[1,2], D. Franke[1], D. Zengler[2], F. Kießling[2], M. Lehmann[2]

[1]Fraunhofer Institute for Telecommunications, Heinrich Hertz Institute, Berlin, Germany
[2]TU Berlin, Institut für Optik und Atomare Physik, Berlin, Germany

sten.seifert@hhi.fraunhofer.de
Keywords: photodetector, InGaAs/InP, relaxation, weak-beam dark-field TEM, reciprocal space mapping

For non-contact temperature measurement from 40 °C to 80 °C detectors are needed, which detect thermal radiation up to a wavelength from 2.6 to 2.3 µm. In such detectors the active layer is usually a strongly strained extended-InGaAs (E-InGaAs) grown on InP substrate. The difference of the lattice constant between these both layers is at least $\Delta a/a = +1.5$ % (Fig. 1) which leads to the formation of misfit dislocations. To compensate the strong lattice mismatch between the active layer and substrate a metamorphic buffer layer [1-3] with altering composition is generally used. However, the thickness of total structures in such detectors is usually 15 – 20 µm [4], which is time-consuming and expensive. This work presents the improvement of material quality for E-InGaAs/InP photodetectors, which include metamorphic InAsP buffer layers (Fig. 1). The samples were successively optimized in several parameters such as strain relaxation of metamorphic buffer layers, reduction of total thickness and ideal number of layers.

Metal organic vapor phase epitaxy (MOVPE) growth of E-InGaAs detectors on (001) InP substrate has been performed in a horizontal Aixtron 200 reactor. InAsP metamorphic buffers were grown in order to compensate the lattice mismatch between the E-InGaAs and an InP substrate. Two types of metamorphic buffer layers were grown: step graded and linearly graded buffers. At the step graded buffer layers the number of steps as well as their thickness was varied and optimized by gradually changing the composition resulting in a stepwise adjustment of the lattice constant. In the case of linearly graded buffers the compositions were continuously changed.

To compare step graded with linearly graded buffers, two samples were analyzed by XRD. Figure 2a shows the reciprocal space mapping of sample A and sample B. Sample A has a step graded buffer. Since the layers are quite thick the mosaicity increased and it can be reflected in the broadening of the measured reflection (Fig. 2a) [5]. All measured reflection are on the relaxation line suggesting all the layers are completely relaxed. Sample B has a linearly graded buffer. The measured InGaAs reflection (Fig. 2b) is on the relaxation line. But the last layer before the E-InGaAs layer is not completely relaxed. This is shown in the measured reflection which is marked with 1 (Fig. 2b). Consequently under the used growth conditions, the step graded buffer is more suitable to achieve the required lattice constant.

To investigate the relaxation properties, TEM investigations were carried out on sample A and B. Figures 3a and b show weak-beam dark-field TEM images [6] of samples A and B, respectively. The utilized reflection is a (002). Here, some of the InAsP buffer layers followed by the E-InGaAs active layer are shown. The misfit strain in the buffer layers results in the nucleation of dislocations on a {111} plane. The bright lines in figure 3(a, b) show these misfit dislocations, where some of them bend at the interfaces (Fig. 3a). At the interface region between the last buffer layer to the E-InGaAs active layer no dislocations are observed. In the active layer of sample A the dislocation density is less than $6*10^7$ cm^{-2}. In sample B at the interface between the last buffer layer and the E-InGaAs layer defects are observed. In the active layer of sample B the dislocation density is more than $7*10^8$ cm^{-2}. Concluding, the presence of distinct interfaces within the buffer layer is necessary to prevent dislocation lines from advancing throughout the buffer structure towards the device layer.

To derive an ideal relationship between step number and layer thickness a step graded buffer was grown reducing the layer thickness stepwise. These samples were analyzed by XRD. Figure 4 shows the required layer thickness, so that the layer is completely relaxed at a certain strain. It is a minimum layer thickness resulted in a misfit of +0.1%. This is found to be a balance of the critical layer thickness [7, 8] and the reduction of lattice distortion. For the established InAsP buffer a reduced buffer of less than 4 µm overall thickness was grown with a detector structure on top. The total thickness of this structure is 7.5 µm.

1. Ch. Heyn, S. Mendach, S. Loehr, S. Beyer, S. Schnuell, W. Hansen: J. Crystal Growth 251, 832-833 (2003)
2. D.-S. Kim, S.R. Forrest, M.J. Lange, M.J. Cohen, G.H. Olsen, R.J. Menna and R.J. Pfaff: J. Appl. Phys. 80, 6229 (1996)
3. M.K. Hudait, Y. Lin, M.N. Palmisiano and S.A. Ringel: IEEE Electron. Device Lett. 24, 538 (2003)
4. Krier, Y. Mao: Infrared Physics & Technology 38, 397-403 (1997)
5. H. Lin, Y. Huo, Y. Rong, R. Chen, T. I. Kamins, J. S. Harris: J. Crystal Growth 323, 17-20 (2011)
6. E. P. Butler: Micron, Volume 5, Issue 3, 293-305 (1974-1975)
7. J.W. Matthews, A.E. Blakeslee: J. Crystal Growth 27, 118 (1974)
8. R. People, J.C. Bean: Appl. Phys. Lett. 47, 322 (1985); erratum: Appl. Phys. Lett. 49, 229 (1986)

9. This work was conducted within the HINT project (grant # 1N10880) funded by the German Federal Ministry of Education and Research under the KMU-Innovation program

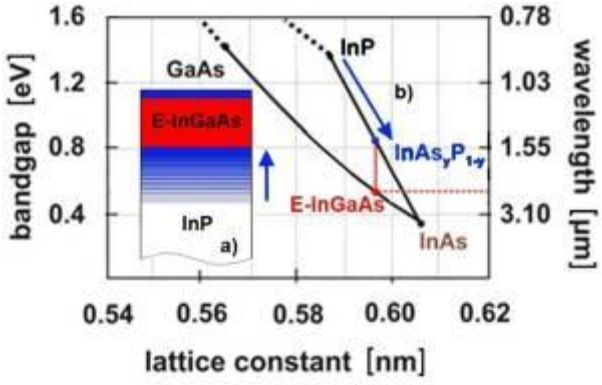

Figure 1. Schematic detector-structure (a). The As-concentration is increased within the buffer layer (b).

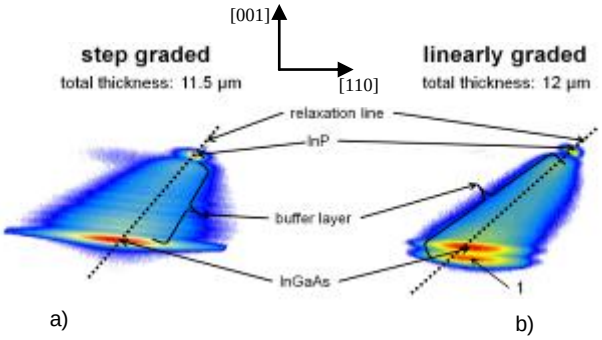

Figure 2. Reciprocal Space Mapping of the (115) reflexes of sample A (a) and sample B (b).

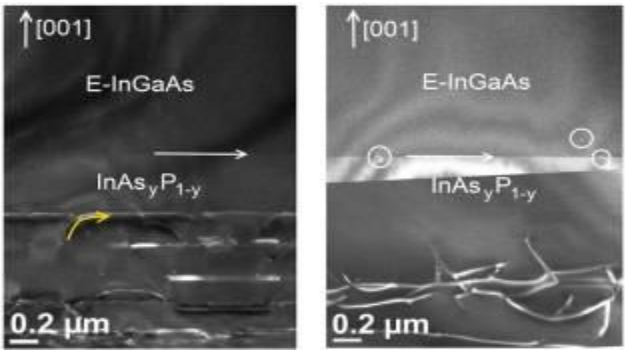

a) b)

Figure 3. Weak-beam dark-field cross-sectional TEM image of sample A and sample B. The white arrows show the interfaces between the last buffer layer and the E-InGaAs layer (a, b) and the interface between the E-InGaAs layer and the cap layer (b). The bending yellow arrow (a) shows a bending misfit dislocation. The circles (b) show defects in the E-InGaAs layer and at the interface.

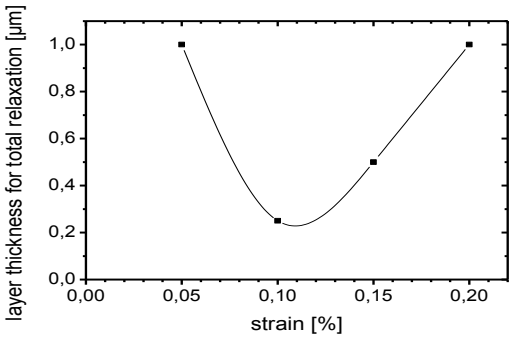

Figure 4. Relationship between strain and required layer thickness so that the layer is completely relaxed.

Functional Materials

MS.3.P054
Characterization of laser-deposited Ge-Sb-Te thin films by Cs-corrected STEM

U. Roß[1], A. Lotnyk[1], E. Thelander[1], B. Rauschenbach[1]

[1]IOM Leipzig, Leipzig, Germany

ulrich.ross@iom-leipzig.de
Keywords: phase-change materials, STEM, Cs-correction

Phase-change materials refer to a class of intermetallic glass-formers with a reversible crystallization process between the amorphous phase and an intermediate metastable crystalline phase, accompanied by a large change in optical and electric properties. Common uses include optical data-storage discs as well as electrical phase-change memory devices. While the application in optical data storage is well-developed, the exact mechanism of crystallization that enables the rapid switching between amorphous and metastable crystalline state is not fully understood[1].

In the work presented here, we make use of the pulsed laser-deposition process (PLD) in order to produce thin films of the prototypical phase-change material system $(GeTe)_x$-$(Sb_2Te_3)_{1-x}$ (GST) on single-crystalline silicon substrate covered by a silicon oxide buffer layer[2]. These films are investigated by probe Cs-corrected analytical transmission electron microscopy (TEM) and spectroscopy (EDX/EELS) using a Titan^2 G2 80-300 kV STEM microscope equipped with Super-X fourfold EDX detector arrangement and a Gatan GIF post-column filter, in order to assess deposited quality, optimize the deposition process and gain insight into the crystallization process.

Due to the inherent beam sensitivity of the sample material, we had to optimize a suitable TEM sample preparation technique. Using a Zeiss dual-beam FIB and a liquid nitrogen stage-cooled Fischione Nanomill low-energy argon ion mill, we are able to prepare 10-20 nm thin FIB-lamella suitable for EDX/EELS spectroscopy as well as for high-resolution TEM and STEM imaging with minimal damage to the pre-existing sample crystal structure. In order to minimize the influence of the electron beam during investigation, we strive to apply minimal beam currents at 80 kV acceleration voltage. Since low beam currents are especially detrimental to the signal-to-noise ratio of the spectroscopic techniques, a compromise between beam settings and beam exposure times during the measurements had to be found.

In order to assess the crystallization behaviour, the as-deposited films are irradiated locally with excimer laser pulses of varying fluences, resulting in grids of recrystallized GST in amorphous matrix (Figure 1.a)). FIB-lamellas are cut from the edges of these irradiated spots in order to access the amorphous-crystalline transition zone as well as both pure phases. Layer thickness and crystallinity were investigated by bright-field TEM and selected area diffraction (Figure 1.b)), confirming the formation of the metastable phase. High-angle annular dark-field STEM in conjunction with quantitative EDX mapping allows us to determine the local mass-thickness as well as elemental distribution. Figure 2. shows a separation of the Ge content from the Sb_2Te_3 phase. At high magnifications, individual crystallites can be imaged down to their local atomic arrangement depending on crystallite orientation (Figure 3.) without major changes of the crystal structure during investigation. EELS spectra are recorded both in EFTEM imaging as well as STEM mode (Figure 4.), revealing both individual high-loss elemental edges as well as low-loss features related to the local band structure.

We have therefore successfully applied the FIB/low energy ion milling sample preparation and TEM/STEM investigation in order to reliably assess the as-produced and laser-crystallized GST thin films with minimal damage to the sample structure.

1. A. Kolobov, P. Fons, A. Frenkel, A. Ankudinov, J. Tominaga, T. Uruga, Nat.Mat. 3 (703-708) 2004
2. H. Lu, E. Thelander, J.W. Gerlach, D. Hirsch, U. Decker, B. Rauschenbach, Appl. Phys. Lett. 101 2012) 031905.
3. The financial support of the European Union and the Free State of Saxony (LenA project) is greatly acknowledged.

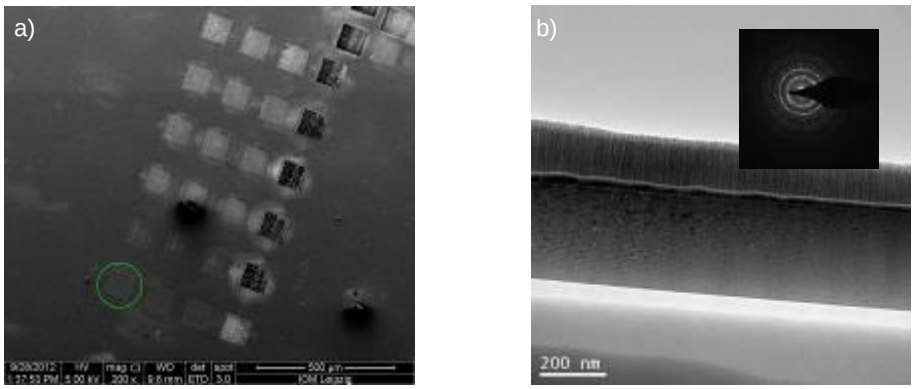

Figure 1. a) SEM surface image of GST film with laser-irradiated squares, green circle marks square selected for FIB preparation, b) bright-field image of amorphous-crystalline transition zone cut from area indicated in a), inset in b) shows local area electron diffraction pattern of the GST film.

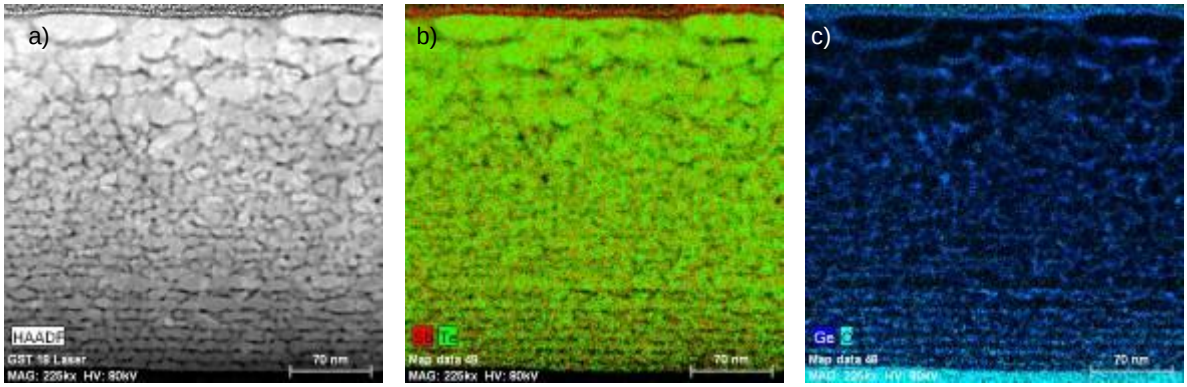

Figure 2. a) HAADF-STEM image of 50 mJ/cm² laser-recrystallized GST film as shown in Figure 1, b) EDX map of Sb/Te signal, c) EDX map of Ge/O signal

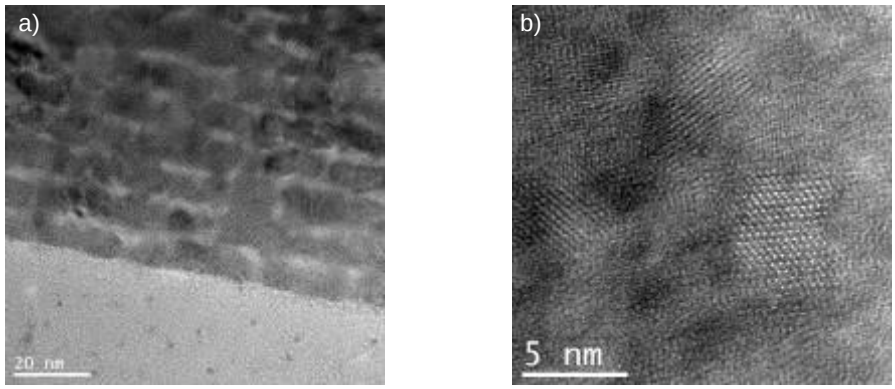

Figure 3. a) HRTEM image of interface SiO substrate – crystallized GST, b) HRSTEM image of GST crystallites

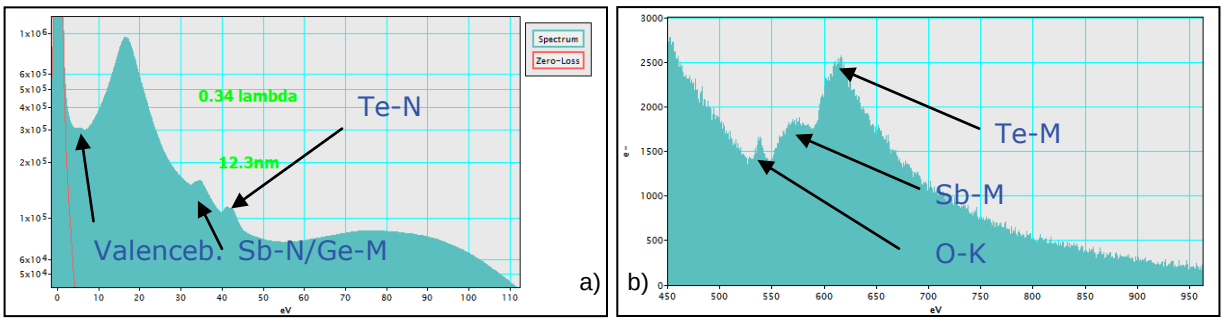

Figure 4. a) Low-loss region of GST EELS-spectrum from amorphous sample region, b) high-loss features (EELS edge fine-structure) from identical sample region.

Functional Material

MS.3.P055
HRTEM LaB_6: characterization of nano particles

J. Grinblat[1], R. Snovski[1], S. Margel[1]

[1]Bar Ilan University, Institute of Nano Technology, Ramat Gan, Israel

grinby@mail.biu.ac.il
Key words: LaB6, nano-materials, magnetic onion-like fullerene microspheres, Fourier transform.

The transmission electron microscope is one of the central techniques used for characterization of nano-materials. The performance of an electron microscope strongly depends on the properties and characteristics of the electron source. In the absence of a field emission gun, a high resolution transmission electron microscope with a conventional LaB_6 gun can be very effective in performing most of the routine works aimed at the characterization of nano-materials structure. This presentation exhibits a few examples of employing a JEOL JEM-2100 high resolution electron microscope for structural characterization of nano-materials. The studies were performed in TEM, HRTEM, STEM, EDS mode, using conventional selected area diffraction (SAED), dark field (DF) imaging techniques, nano-beam diffraction (NBD) or Fourier transform analysis (FFT) of the high resolution images. While exploiting the high level of the atomic imaging capability of this microscope and using computational FFT we are characterizing nano-materials and receive information at the level close to the sub-nanometer level. Few examples of non - standard applications are summarized herein [1]:

Magnetic poly(divinyl benzene)/Fe_3O_4 microspheres with a narrow size distribution were produced by entrapping the iron pentacarbonyl precursor within the pores of uniform porous poly(divinyl benzene) microspheres prepared in our laboratory, followed by the decomposition in a sealed cell of the entrapped $Fe(CO)_5$ particles at 300°C under an inert atmosphere. Magnetic onion-like fullerene microspheres with a narrow size distribution were obtained by annealing the PDVB/Fe_3O_4 particles at 500, 600, 800, and 1100°C, respectively, under an inert atmosphere. Characterization of the PDVB/Fe_3O_4 microsphere is shown in figure 1 displaying a bright field image (BF) of a microsphere obtained by annealing the $Fe(CO)_5$ entrapped within the PDVB particles at 300°C.

Figures 2 exhibit TEM micrographs of the composite microsphere obtained at 500°C, displaying the carbon graphitic coating. The the (DF) image display the spatial distribution of the graphitic carbon, the onion-like fullerenes that coat the magnetic nano-particles in the microsphere. This amazing phenomenon of fullerene formation can be observed at all temperatures ranging from 500 to 1100°C.

1. Ron Snovski, Judith Grinblat, and Shlomo Margel, Langmuir, 27 (2011), p.11071-11080.

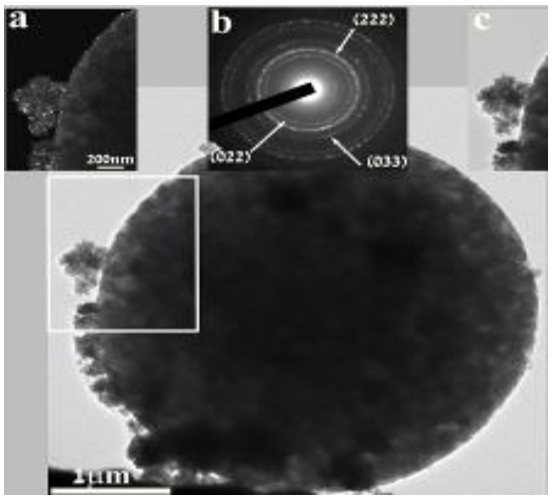

Figure 1.Bright field image of a microsphere obtained by annealing the $Fe(CO)_5$ entrapped within the PDVB particles at 300°C. DF image taken in the (220 and 311) reflection for the area marked by the white square (a). SAED from a 300nm area showing the ring diffraction of iron oxide (b).

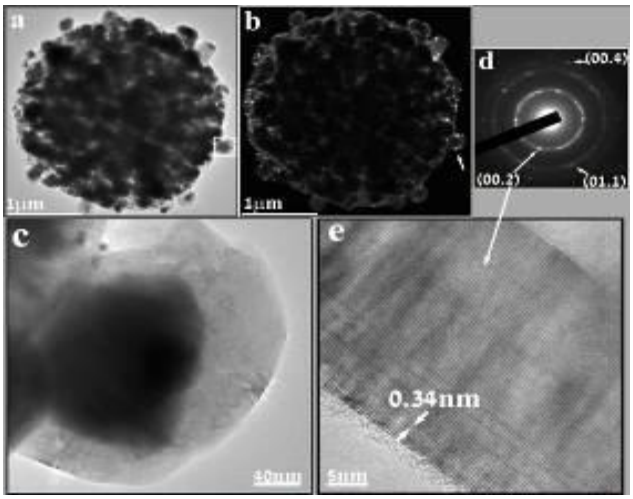

Figure 2. Bright field (a) DF (b) images of the $C/Fe_3O_4/Fe$ composite microsphere obtained at 500°C displaying the spatial distribution of the crystalline onion-like graphitic carbon. HRTEM image of the area marked by the white square, exhibiting the fullerene onion-like coating of the magnetic nano-particle (c). SAED from a 300nm area of the microsphere showing the ring diffraction pattern the hexagonal graphitic carbon (d). HRTEM image of the carbon coating (e).

Functional Materials

MS.3.P056
Structural and Morphological Characterization of Doped ZnO Nanowires

M. Fontana[1], A. Chiodoni[1], C. Ottone[1], V. Farias[1], E. Celasco[1], V. Cauda[1], C.F. Pirri[1,2]

[1]CSHR IIT@Polito, Torino, Italy
[2]Politecnico di Torino, DISAT, Torino, Italy

marco.fontana@iit.it
Keywords: ZnO, nanowires, doping, FESEM, TEM

Zinc oxide is a very interesting and promising material due to its functional properties: it is a piezoelectric wide band gap semiconductor which can be synthesized in a wide variety of nanostructures, such as nanowires, nanobelts, nanopods, nanoparticles. It is therefore an ideal candidate for the development of innovative miniaturized devices ranging over the field of nanotechnology [1].

The doping of ZnO with other chemical elements is crucial in order to control and to modulate its physical properties: p-type conductivity, band-gap tuning, enhanced piezoelectricity [2,3]. Some authors report on the doping of ZnO with transition metals as a way to achieve room temperature ferromagnetism, making ZnO a suitable material for spintronic applications [4].

In this work we report on the structural, chemical and morphological characterization of ZnO nanowires doped with Cr or with Mn by means of Field Emission Scanning Electron Microscopy (FESEM), Transmission Electron Microscopy (TEM), X-ray Diffraction (XRD) and X-ray Photoelectron Spectroscopy (XPS).

The synthesis of the doped nanowires was carried out through the hydrothermal method in a two-step synthetic approach. At first the substrates (silicon wafers) were coated with a thin film of oriented crystalline ZnO. This film acts as a seed layer for the further nucleation and growth of ZnO nanowires. The wire growth was carried out in a solution at 88°C for 1h, using zinc nitrate as the source of zinc, and chromium or manganese nitrates in order to introduce the dopants into the ZnO oxide crystalline structures.

The morphology of the samples was initially characterized by Field Emission Scanning Electron Microscopy: the aspect ratio, vertical alignment of the nanowires and the homogeneity of the samples were evaluated. Energy dispersive X-ray spectroscopy (EDX) and XPS were performed in order to reveal the presence of the dopants in the nanostructures, both in case of Cr and Mn doping. Further investigation of the structure of the doped nanowires was carried out by Transmission Electron Microscopy: high-resolution TEM imaging and selected area electron diffraction (SAED) of Cr-doped and Mn-doped samples were performed in order to analyze the crystalline structure of the nanowires, their orientation and the possible presence of defects due to the dopants.

The structural properties of the doped nanowires were finally correlated with their functional properties, showing the role of the dopants.

1. Z.L. Wang, Material Science and Engineering R 64 (2009), 33-71
2. V. Avrutin, D.J. Silversmith, H. Morkoc, Proceedings of the IEEE, 98 (2010), 1269-1280
3. A. Janotti, C.G. Van de Walle, Rep.Prog.Phys 72 (2009), 126501
4. U. Ozgur et al., J.Appl.Phys. 98 (2005), 041301

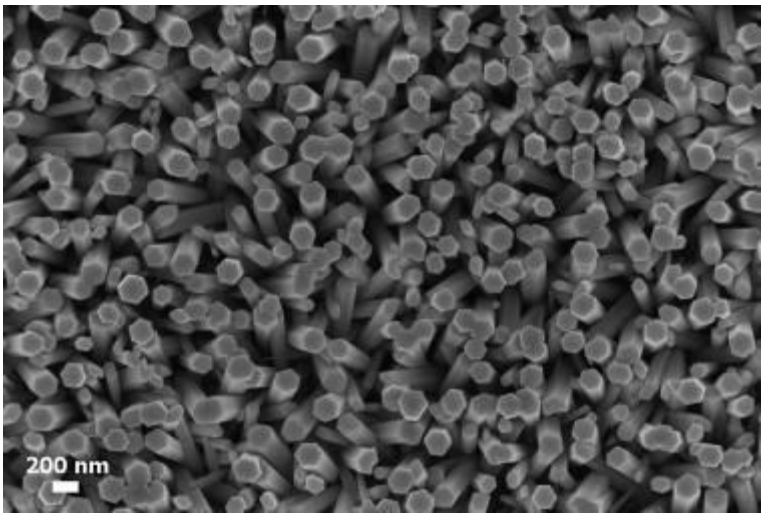

Figure 1. FESEM image of Cr-doped ZnO nanowires (top view)

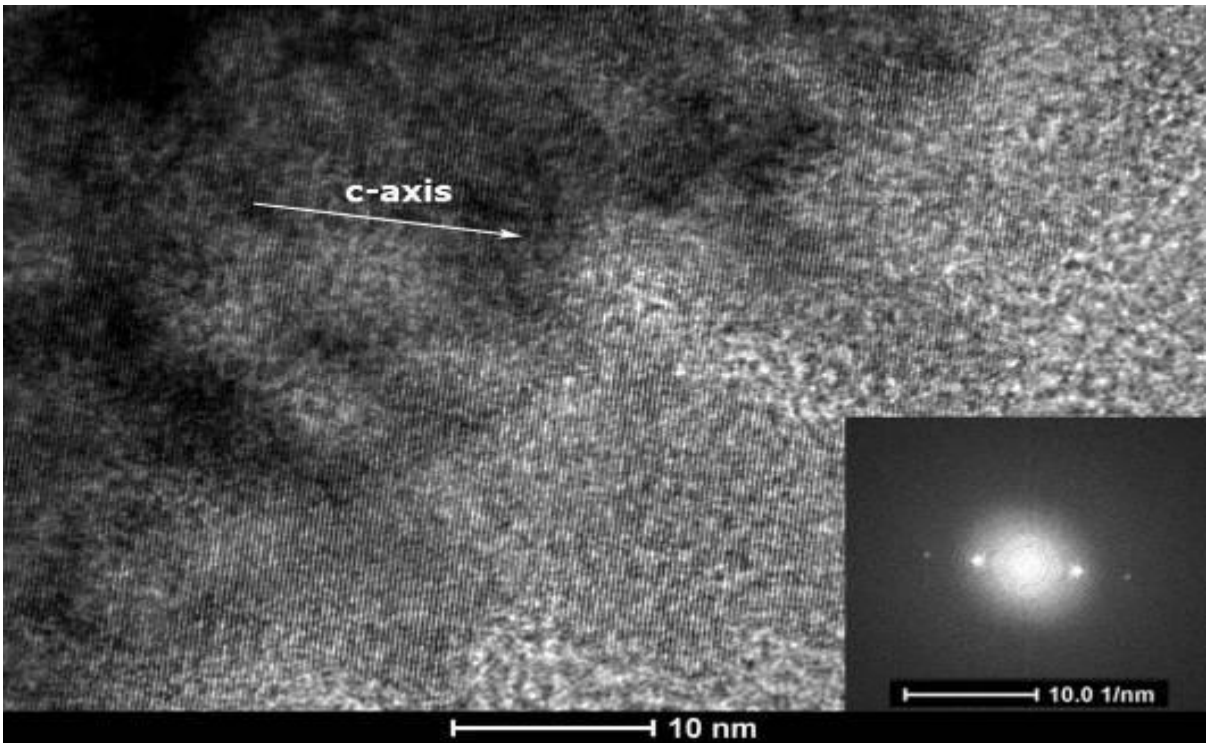

Figure 2. Bright field TEM image of a single Cr-doped nanowire. Inset: FFT of the image showing that the nanowire grows along the (002) direction.

Functional Materials

MS.3.P057
Complex Structures of “Sand” and “Chalk”

J. Rieder[1], J. Eiblmeier[1], M. Kellermeier[2], F. Glaab[1], W. Kunz[1]

[1]University of Regensburg, Institute of Physical and Theoretical Chemistry, Regensburg, Germany
[2]University of Konstanz, Physical Chemistry, Konstanz, Germany

julian.rieder@chemie.uni-regensburg.de
Keywords: biomimetic materials, nanostructures, inorganic self-assembly

In recent years, bio-inspired materials have aroused a great deal of interest due to their promising properties and potential relevance for various applications. Thereby, many studies were carried out in order to elucidate the influence of certain organic (macro)molecules and/or supramolecular matrices, as typically found in biomineralization processes, on the crystallization of naturally abundant minerals. By contrast, our current research is dedicated to explore such effects in purely inorganic environments, namely by using dissolved silica as an additive during mineralization of alkaline-earth carbonates. Under suitable conditions, these simple components can assemble into fascinating architectures, termed “silica biomorphs”, which display morphologies and structures very similar to those produced in biomineralization, such as periodically twisted filaments, flat sheets, or worm-like braids (see Figure 1) [1-3]. Moreover, this methodology allows us to prepare elaborate core-shell-shell nanoparticles in a straightforward one-step process, by slightly changing precipitation parameters (Figure 2) [4]. The formed particles were investigated in detail with HR-TEM and micro-EDX, in order to reveal compositional details.

On the other hand, silica-mediated self-organization mechanisms can also be observed in the absence of carbonate, simply by adding soluble metal salt crystals to alkaline silica sols. The resulting “silica gardens” also show stunning structures reminiscent of living forms such as trees or aquatic plants. Recently, we developed an experimental setup by which we could trace the evolution of relevant species in situ during growth of silica gardens prepared with iron- or cobalt salts [5]. Recently, we have extended this approach to study chemical gardens prepared with calcium salts (Figure 3), as the mechanisms occurring in this system are very similar to those underlying Portland cement hydration. Therefore, calcium-based chemical gardens might serve as model system for detailed analysis of the temporal evolution of dissolution and precipitation processes that occur in the inside of the C-S-H membrane. To characterize these processes, we utilized scanning electron microscopy (SEM) in combination with EDX to investigate structural and compositional details of the formed structures as a function of time.

1. J. M. García-Ruiz, S. T. Hyde, A. M. Carnerup, A. G. Christy, M. J. Van Kranendonk, N. J. Welham, Science 302 (2003), p. 1194
2. J. M. García-Ruiz, E. Melero-García, S. T. Hyde, Science 323 (2009), p. 362
3. M. Kellermeier, E. Melero-García, F. Glaab, J. Eiblmeier, L. Kienle, R. Rachel, W. Kunz, J. M. García-Ruiz, Chem. Eur. J. 18 (2012), p 2272.
4. J. Eiblmeier, M. Kellermeier, M. Deng, L. Kienle, J. M. García-Ruiz, W. Kunz Chem. Mat. (2013) DOI: 10.1021/cm4003959
5. F. Glaab, M. Kellermeier, W. Kunz, E. Morallon, J. M. García-Ruiz, Angew. Chem. Int. Ed. 51 (2012), p. 4317

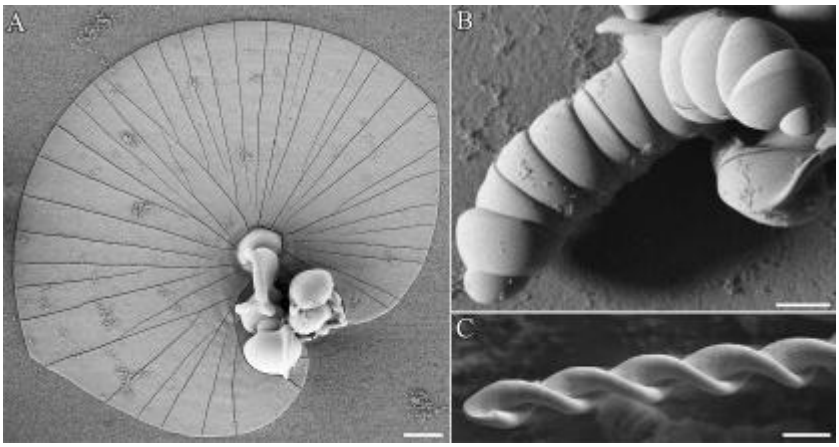

Figure 1. Overview of typical morphologies displayed by silica biomorphs: (A) Flat sheet-like objects, (B) worm-like braids, and (C) complex helical filaments. Scale bar is 20 µm.

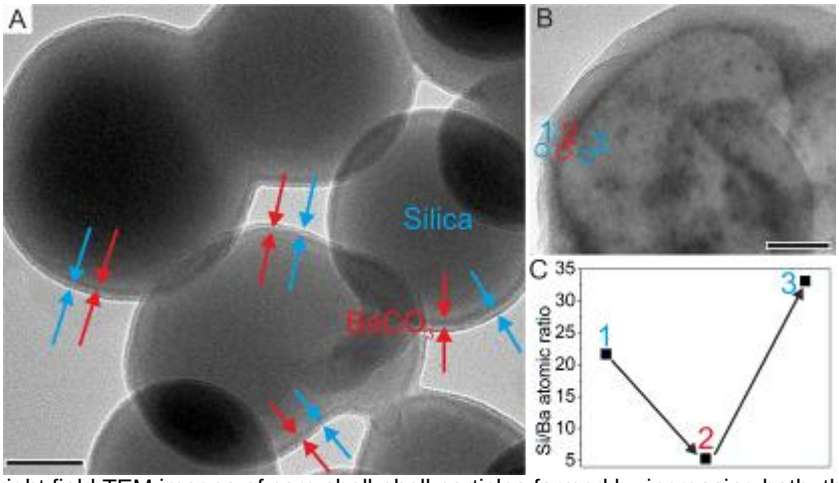

Figure 2. (A-B) Bright field TEM images of core shell-shell particles formed by increasing both, the carbonate and silica supersaturation. Red and blue arrows in (A) mark the interstitial $BaCO_3$ layer and the outer silica skin, respectively (scale bars are 40 nm). (C) Si/Ba atomic ratios calculated from three selected points (as defined by circles in (B)) along an EDX line-scan analysis over the rim of the composite particles. The arrows shall be a guide for the eye.[4]

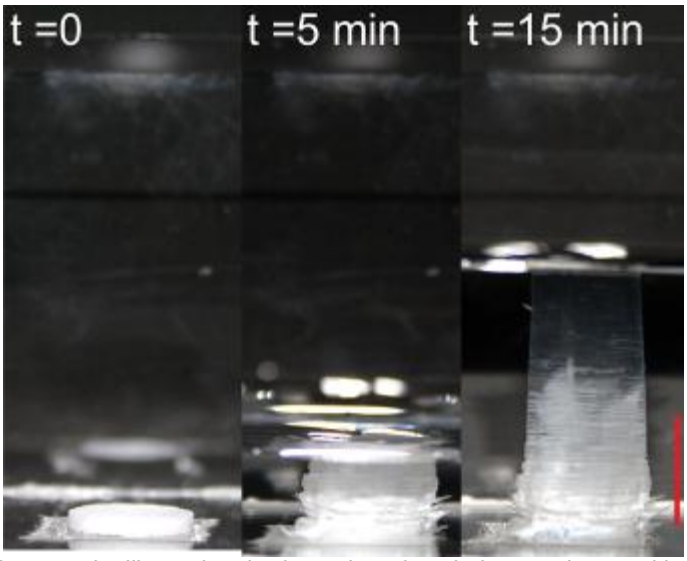

Figure 3. Sequence of photographs illustrating the formation of a tubular membrane with defined dimensions upon addition of diluted silica solution to a tablet of $CaCl_2$. Scalebar is 10 mm.

Functional Materials

MS.3.P058
Estimation of medium-range strain in 3D-stacked silicon-based integrated circuits using energy filtered CBED

U. Muehle[1], M. Gall[1], Y. Ritz[1], V. Sukharev[2], E. Zschech[1]

[1]Fraunhofer IZFP-D, Micro and Nano Evalulation, Dresden, Germany
[2]Mentor Graphics Inc., Fremont / CA, United States

uwe.muehle@izfp-d.fraunhofer.de

A current trend in semiconductor industry is 3D-stacking of integrated circuits using Through Silicon Vias (TSVs) in order to reduce floor space, to reduce power loss and to increase bandwidth. Due to the different coefficients of thermal expansion (CTE) of the involved materials, especially silicon as substrate and copper as the conducting via, transistors that are located next to a TSV in a range of some micrometers are affected by the resulting stress [1]. That means, this additional stress component and the stress in the transistor channel of MOSFETs – as performance booster in leading-edge devices [2] – and can influence the device performance. Strain measurements in channel regions of some 10 nm are necessary to understand the effect of strain on transistor performance – as one factor in addition to other sources like patterning effects, dopand fluctuations etc. – and to validate models used for performance simulation of 3D-stacked ICs [2].

Besides the direct imaging of strained lattice planes in HRTEM, the geometrical phase analysis (GPA) using inline holography [3] or off-axis holography [4] and diffraction-based methods are able to determine strain in crystalline materials. Whereas GPA requires a region with a well known strain situation in the vicinity of the ROI, for diffraction-based methods this reference region should be available for the TEM study without exchanging the specimen. Nano Beam Diffraction (NBD) is suitable for the determination of short-range strains in the silicon transistor channel [5, 6]. Conversion Beam Electron Diffraction (CBED) analysis uses a larger, medium-range region, i. e. strain measurements are performed on micrometer scale, but provides lattice parameter with high accuracy [7].

Usually the CBED measurement requires simulations of the High Order Laue Zone (HOLZ) pattern for exact adjustment of the actual acceleration voltage and of the strain state [8]. For well-defined stress states like a uniaxial strain state, the strain is usually calculated directly from the measured values. The reciprocal value of the Kikuchi line distance is proportional to the lattice plane. The use of an in-column energy filter improves the signal-to-noise ratio of the diffraction pattern, and the application of a sub-pixel peak fitting procedure leads to a precision better than 4×10^{-4}, covering the expected order of magnitude of strain (Fig. 1).

Measurements of lattice strain along a vertical line demonstrate that the level of strain beneath a transistor remains constant at a level of 0.3µm below the Si-upper edge. Based on the layout of the chip, locations 500nm below the bottom of the Shallow Trench Isolation (STI) were chosen for the strain measurement, for 3 transistors with different distances to the TVS. In addition, the strain course across the lamellae was measured (Fig. 2). The reference value was measured using an extraordinary lamella at a location where no strain due to influences of functional structures in the chip is expected.

The results were compared with simulations based on materials parameters and geometrical data of the whole TEM specimen. The measured strain values provide a basis for model validation and calibration.

1. Sukharev, V., Zschech, E.; AIP Conf. Proc. 1378 (2010); 21 - 49
2. Sun, Y., Thompson, S.E., Nishida, T.; Strain Effect in Semiconductor; Springer Science+Bus. Media; 2010
3. Koch, C.T., Burak Özdöl, V., and van Aken, P.; APL 96 (2010): 091901
4. Beche, A., Rouviere, J.L., Barnes, J.P., and Cooper, D.; Ultramicroscopy 111 (2011): 227-238.
5. Uesugi, F., Hokazono, A., and Tekeno, S.; Ultramicroscopy 111 (2011): 995-998.
6. Engelmann, H.J. et.al.; Proc. of 4th EMC, 2, 13 - 14 (2008)
7. Wittmann, R., Parzinger, C., Gerthsen, D.; Ultramicroscopy 70 (1998); 145 - 159
8. Stadelmann, P.A.; Ultramicroscopy 21 (1987): 131-146.
9. The authors gratefully acknowledge the financial support from the Semiconductor Research Corporation/Sematech 3D Enabling Center in Albany, NY, USA, under the Associated Task ID:2246.001
10. We kindly acknowledge valuable discussions with Riko Radojcic, Qualcomm Inc..

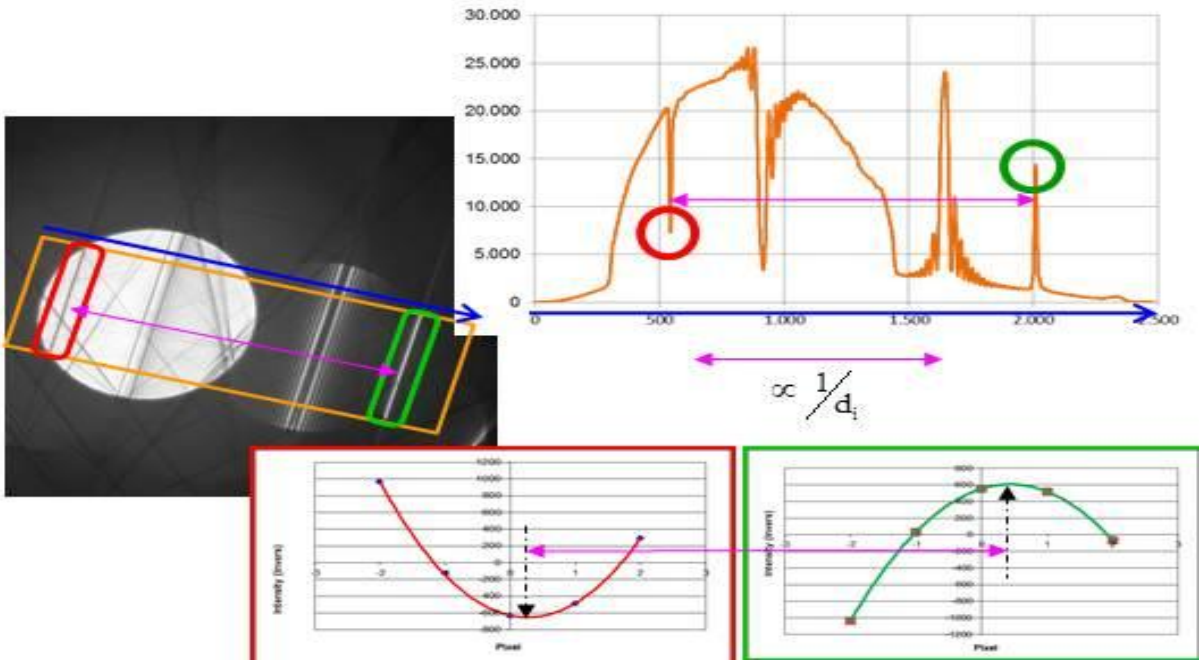

Figure 1. Methodology of strain measurement base on Kikuchi line spacing: left: CBED pattern Up: Intensity profile, bottom: fit with sub-pixel precision of dark and bright Kikuchi line, leading to reciprocal d values

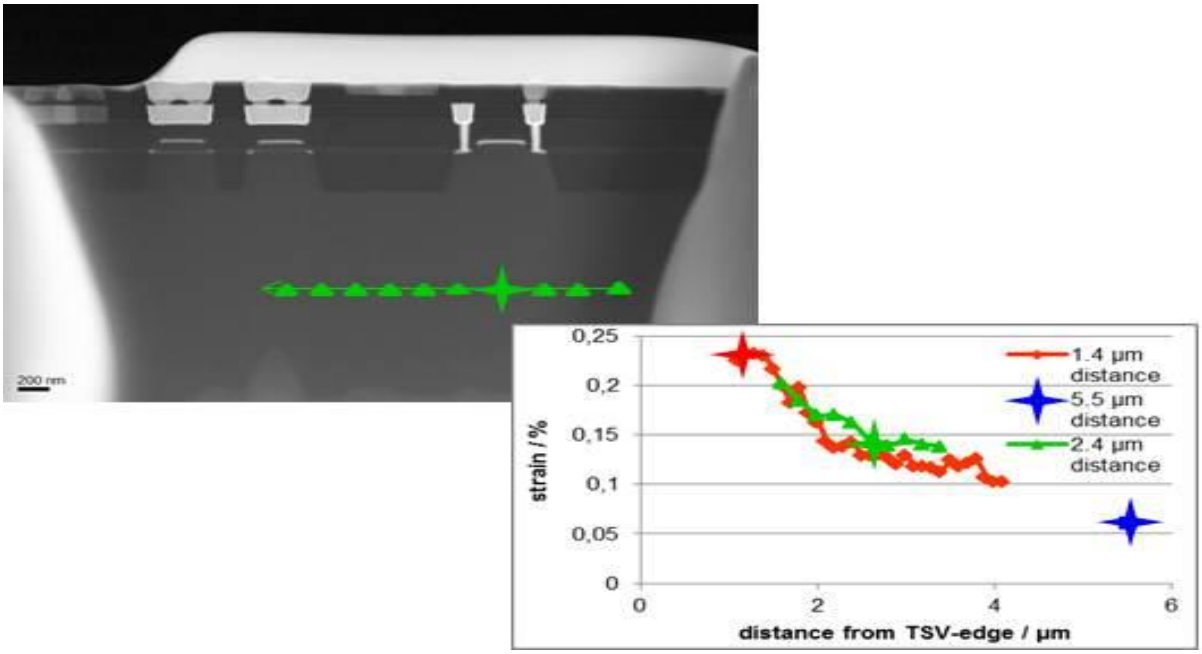

Figure 2. HAADF-STEM imaging of a transistor (left) with marked locations of measurement, and the trace across the TEM-lam.

Functional Materials

MS.3.P059
Hybridized metal slit eigenmodes as an illustration of Babinet's principle

B. Ögüt[1], R. Vogelgesang[2], W. Sigle[1], N. Talebi[1], C.T. Koch[3], P.A. van Aken[1]

[1]Max Planck Institute for Intelligent Systems, Stuttgart Center for Electron Microscopy, Stuttgart, Germany
[2]Carl von Ossietzky University of Oldenburg, Oldenburg, Germany
[3]Ulm University, Institute for Experimental Physics, Ulm, Germany

ogut@is.mpg.de
Keywords: Surface plasmon resonances, energy-filtering transmission electron microscopy, Babinet's principle

Surface plasmons are the collective electron oscillations propagating along the surface of a metal, whereas surface plasmon resonances are the corresponding eigenmodes in confined systems. These charge oscillations are the main ingredients in the field of plasmonics, offering potential applications in cancer research [1], surface enhanced Raman spectroscopy [2], and plasmonic computers [3]. In this study, we investigate surface plasmon resonances in rectangular single and double slits drilled into a free standing 100 nm thick silver film. For this purpose we acquired series of energy-filtered images (EFTEM) in the energy-loss range below 5 eV using the 200 kV SESAM microscope (Zeiss, Germany) equipped with a field emission gun, the in-column MANDOLINE filter, a symmetric electrostatic Omega-type electron monochromator, and ultra-stable high tension, facilitating an extraordinary dispersion, energy resolution, and isochromaticity [4, 5] during visualization of localized surface plasmon resonances (LSPRs) in rectangular slits. The image series were acquired in the energy-loss range between 0.4 eV and 5 eV with a step size of 0.2 eV where the monochromator slit and energy filter slit had a width of 0.2 eV. In order to gain a deeper insight into the electromagnetic behaviour, plasmonic eigenmode simulations of the rectangular slits were performed using the High Frequency Structure Simulator (HFSS 12, Ansoft, USA), which is based on the finite element method (FEM) and solves Maxwell's equations using an adaptive mesh refinement with tetrahedral mesh units. Fabry-Perot-like surface plasmon modes are visible for single and double rectangular slits. Different numbers of pronounced electric field intensity maxima were observed at different energies, which are attributed to LSPRs. In addition, coupling effects were observed for the case of double slits. In figure 1, simulated and experimentally observed plasmonic eigenmodes at around 1 eV in single and double slits are depicted. In the case of single slits, two electromagnetic field maxima are confined along the long slit walls. The theoretical result (figure 1d) shows that the electric field vectors resonate in phase. Therefore opposite electrical charges are deposited on the slit walls leading to a dipolar character. Corresponding experimental and simulated results for double slits show that the intensity is mainly concentrated along the connecting bridge. The simulated results for double slits show that opposite electrical charges are accumulated along the slit walls similar to the case in single slits, whereas the same electrical charge distribution is observed along the connecting bridge [6]. The reasons for this kind of behaviour as well as the difference of complimentary structures (slit versus rod) will be discussed in terms of electrical and magnetic charge coupling, too. In conclusion, we find excellent agreement between experimental and theoretical results which enables us to use the simulated field distribution for the interpretation of experimental data. From the experimental point of view, EFTEM is a powerful technique to investigate surface plasmon resonances from large areas with short acquisition times at high spatial resolution in the range of few nanometers which cannot be easily reached with optical methods [7, 8, 9,10].

1. S. Lal, S.E. Clare, N.J. Halas, Accounts of. Chemical Research 41 (2008), p. 1842.
2. K. Kneipp, Y. Wang, H. Kneipp, L.T. Perelmann, I. Itzkani, R. R. Dasari, M. Feld, Physical Review Letters 78 (1997), p. 1667.
3. R. Zia, J.A. Schuller, A. Chandran, M.L. Brongersma, Materials Today 9 (2006), p. 7.
4. C.T. Koch, W. Sigle, R. Höschen, M. Rühle, E. Essers, G. Benner, M. Matijevic, Microscopy and Microanalysis 12 (2006), p. 506.
5. E. Essers, G. Benner, T. Mandler, S. Meyer, D. Mittmann, M. Schnell, R. Höschen, Ultramicroscopy 110 (2010) p. 971.
6. B. Ögüt, R. Vogelgesang, W. Sigle, N. Talebi, C.T. Koch, P.A. van Aken, ACS Nano 5 (2011) p. 6701.
7. R. Vogelgesang, A. Dimitriev, Analyst 135 (2010), p. 1175.
8. The authors acknowledge Dr. J. Dorfmüller for helpful discussions, U. Eigenthaler and I. Lakemeyer for specimen preparation and M. Laudien for the support with the simulations.
9. This research has been supported by the European Union under the Framework 6 program under a contract for an Integrated Infrastructure Initiative, Reference 026019 (ESTEEM).
10. N. Talebi gratefully acknowledges Alexander-von-Humboldt foundation for financial support.

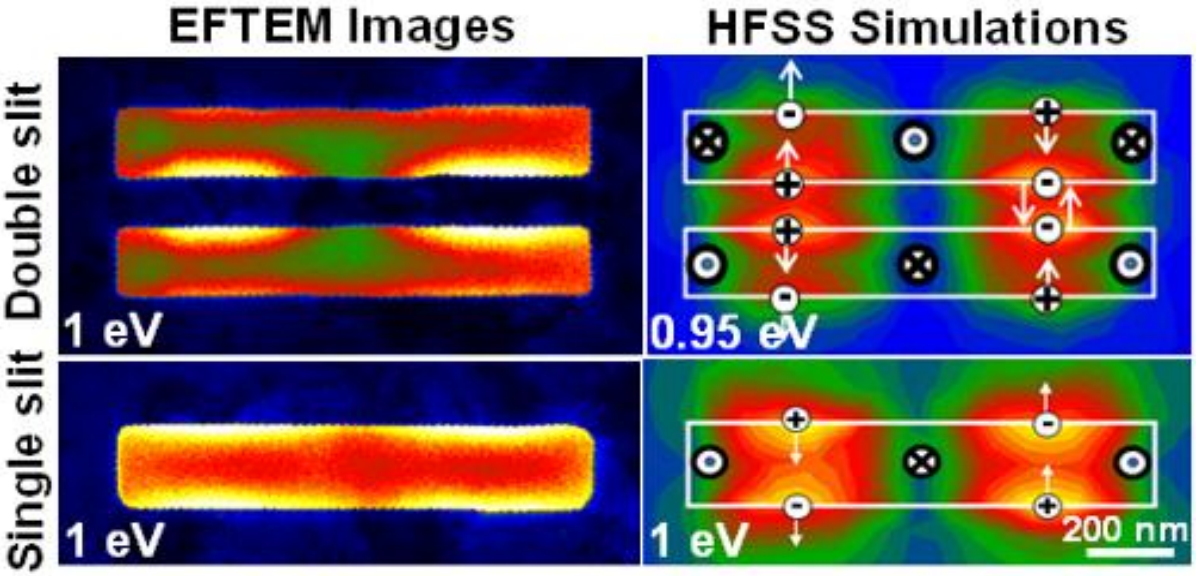

Figure 1. Plasmonic eigenmodes that have been simulated with High Frequency Structure Simulator (HFSS), and experimentally acquired with EFTEM imaging in the single slit and double slits at 1 eV [6]

Functional Materials

MS.3.P060
TEM investigation of adaptive martensite occurring in ultrafine-grained ferromagnetic Ni-Mn-Ga shape memory alloys

T. Waitz[1], C. Mangler[1], A. Kompatscher[2], P. Müllner[3]

[1]University of Vienna, Faculty of Physics, Physics of Nanostructured Materials, Vienna, Austria
[2]CiS Forschungsinstitut für Mikrosensorik und Photovoltaik GmbH, Erfurt, Germany
[3]Boise State University, Department of Materials Science and Engineering, Boise, United States

thomas.waitz@univie.ac.at
Keywords: TEM, lattice fringes, shape memory alloys

Ni-Mn-Ga alloys belong to a new class of ferromagnetic shape memory alloys that can show large and reversible magnetic field-induced strains. The phase stability and thus the functional properties of ferromagnetic shape memory alloys sensitively depend on their chemical composition. The $L2_1$ Heusler austenite of Ni-Mn-Ga alloys can transform to different martensitic structures including the non-modulated (NM) tetragonal lattice as well as modulated structures such as 6M, 10M and 14M [1]. In addition, crystal size at the nanoscale can significantly impact the formation of thermoelastic martensite [2,3]. It is the aim of the present paper to study the impact of grain size on the martensitic transformation of $Ni_{54}Mn_{25}Ga_{21}$ high temperature shape memory alloys.

$Ni_{54}Mn_{25}Ga_{21}$ alloys (prepared by induction melting in inert gas) were subjected to high pressure torsion followed by heating to 500°C to achieve an ultrafine-grained structure in the bulk material. Thin foils for transmission electron microscopy (TEM) were prepared by mechanical grinding followed by dimpling and ion milling. The TEM analysis was carried out using lattice fringe images and selected area diffraction (SAD) of small grains carefully tilted to specific beam directions (BD).

In their coarse grained state, $Ni_{54}Mn_{25}Ga_{21}$ alloys showed a martensitic phase transformation from the austenitic Heusler phase to the NM martensite. Contrary to that, in the case of the ultrafine grains (mean grain size about 140 nm) the austenite transformed to the modulated 14M martensitic structure. This is discussed using the concept of adaptive martensite i.e. nanotwins of the NM martensite that occur with a twinning periodicity of 7 atomic layers and a 2/5 ratio of the twin widths forming the metastable 14M martensitic structure [4,5].

Figures 1(a)-(c) show TEM lattice fringe images obtained by tilting the grains to the [201] zone axis of the 14M martensite and allowing the weak $\pm[020]$ satellite reflections to pass the objective aperture together with the transmitted beam (cf. the SAD pattern shown in Figure 1(d)). Fringes with a spacing of 1.48±0.02 nm dominate reflecting the seven layered $(\bar{5}2)_2$ stacking sequence expected in the case of a 14M adaptive martensite. However, frequently the periodicity of the contrast oscillations was interrupted; stripes of dark or bright contrast were encountered (e.g. near A in Figure 1(b) and (c)) that had a width larger than caused by the 14M martensite. Consequently, these stripes corresponded to larger twinning periodicities of the NM martensite. Near B in Figure 1(c), also rather thick twin variants of NM martensite were observed. This agrees with the concept of adaptive martensite where NM and 14M can coexist over a broad temperature range [5]. In the ultrafine grains, minimization of the transformation strain energy is most effectively facilitated by nanoscale twinning [2,3]. Therefore in ultrafine grained $Ni_{54}Mn_{25}Ga_{21}$, nanoscale twinning of the NM martensite yields the formation of the 14M lattice structure.

While most of the ultrafine grains contained a single variant of 14M martensite, some grains were also encountered that contained two twin related variants of the adaptive martensite (cf. Figure 2). The two variants were rotated by an angle of about 125°C around a common [201] zone axis and match at a common $(\bar{1}72)$ interface (indicated by dashed lines in the lattice fringes images of Figures 2(a) and (b)). These junction planes were rather straight and sharp (width less than 2 nm); each of the variants shows contrast oscillations frequently deviating from the perfect $(\bar{5}2)_2$ stacking sequence similar to those observed in grains containing a single variant of the martensite only (cf. Figures 1(b) and (c)). Based on the analysis of Figure 2, the twinning of the adaptive martensite was of type I. Twins with a similar crystallographic relationship were also observed in coarse grains of Ni-Mn-Ga alloys [6].

1. P. Entel et al., J. Phys. D: Appl. Phys. 39 (2006) p. 865.
2. T. Waitz, T. Antretter, F.D. Fischer, N.K. Simha and H.P. Karnthaler, J. Mech. Phys. Sol. 55 (2007) p. 419.
3. T. Waitz, K. Tsuchiya, T. Antretter and F.D. Fischer, MRS Bulletin 34 (2009) p. 814.
4. S. Kaufmann et al., Phys. Rev. Lett. 104 (2010) p.145702.
5. R. Niemann, U. K. Rößler, M. E. Gruner, O. Heczko, L. Schultz and S. Fähler, Adv. Eng. Mater. 14 (2012) p. 562.
6. M. Nishida, T. Hara, M. Matsuda and S. Ii, Mater. Sci. Eng. A 481–482 (2008) p.18.
7. Financial support from the Austria FFG COMET project MPPE A1.5 is gratefully acknowledged. PM acknowledges financial support from the National Science Foundation through project NSF-DMR 1207192.

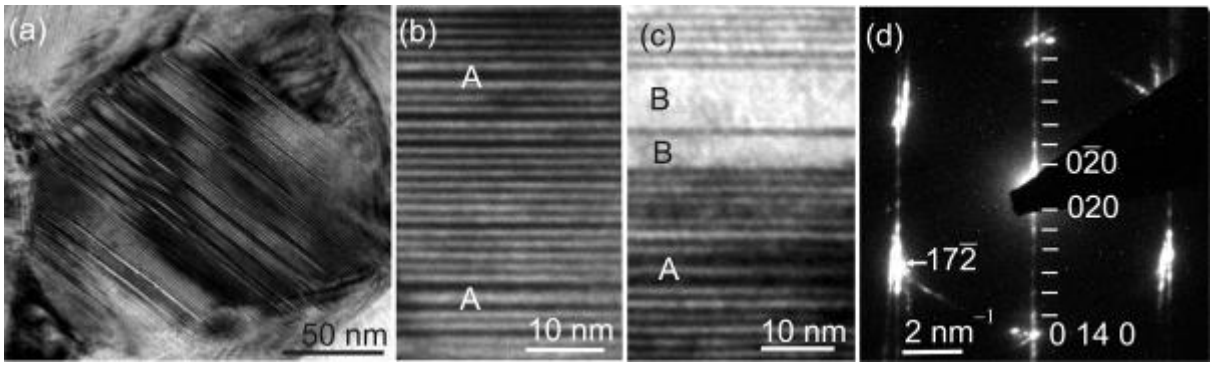

Figure 1. Ultrafine grained $Ni_{54}Mn_{25}Ga_{21}$. (a) TEM lattice fringe image of a grain containing a single variant of 14M martensite. (b) and (c) Contrast oscillations with a spacing of 1.48 nm arise by a 7 layer sequence of nanotwins of the NM martensite (corresponding to the $(\bar{5}2)_2$ stacking sequence of adaptive 14 martensite). These oscillations are frequently interrupted by oscillations with larger periodicities (near A). Areas with uniform contrast (near B) correspond to rather thick twins of the NM martensite. (d) SAD pattern. Six weak satellite reflections (indicated by lines) occur between the primary beam and the main ±[0 14 0] reflections. These satellite reflections are characteristic for the modulated 14M martensite. Weak streaks running parallel to [0 14 0] are caused by the stacking disorder. (**BD** = [201]).

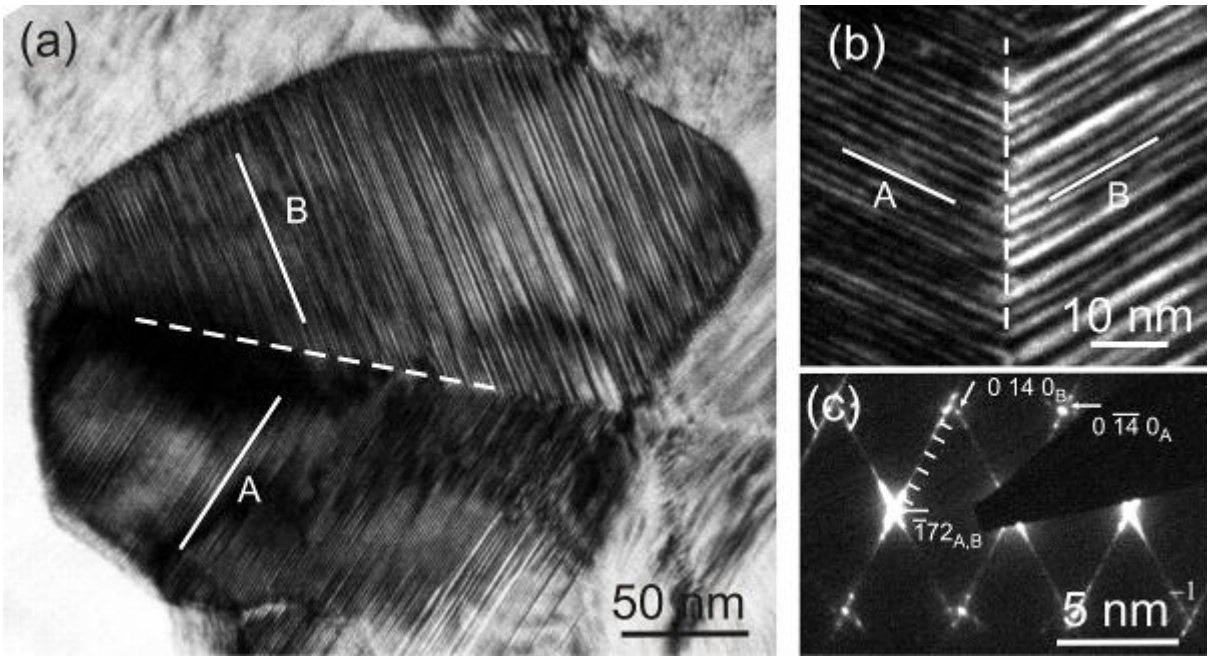

Figure 2. Ultrafine grained $Ni_{54}Mn_{25}Ga_{21}$ (a) TEM lattice fringe image of a grain containing two twin related variants A and B of 14M martensite. Solid and dashed lines indicate the (0 14 0) lattice planes and the junction plane of the variants, respectively, that all are in an edge-on orientation. (b) Detail of the junction plane that is almost straight and rather sharp. (c) Corresponding SAD pattern. Some of the satellite and main reflections are marked by lines and arrows, respectively. In agreement with a type I twin, variants A and B have a common $(\bar{1}72)$ junction plane and share a common zone axis. (**BD** = $[201]_A = [\bar{2}0\bar{1}]_B$).

Functional Materials

MS.3.P061
In this article, thermal buckling stability analysis of moderately thick functionally graded rectangular and square plate is studied. The equilibrium and stability equations are derived using two variable refined plate theory.

M. Bouazza[1], A. Boucheta [1], T. Becheri [1]

[1]Department of Civil Engineering, University of Bechar, Bechar 08000, Algeria., Department of Civil Engineering, Bechar, Algeria

bouazza_mokhtar@yahoo.fr
Keywords: Buckling; functionally graded plate; refined plate theory; thermal loading. The results are verified with the known data in the literature.

In this article, thermal buckling analysis of moderately thick functionally graded rectangular and square plate is studied. The equilibrium and stability equations are derived using two variable refined plate theory. The theory, which has strong similarity with classical plate theory in many aspects, accounts for a quadratic variation of the transverse shear strains across the thickness and satisfies the zero traction boundary conditions on the top and bottom surfaces of the plate without using shear correction factors. By using an analytical method, the stability equations are replaced by four equations. Solving the equations and satisfying the boundary conditions of simply supported edges, the critical buckling temperature is found analytically. Thermal buckling of functionally graded plate for three types of thermal loading, uniform temperature rise, linear temperature rise and non-linear temperature rise through the thickness are investigated. Finally, the effects of power law index and plate thickness on the critical buckling temperature of functionally graded rectangular and square plates are discussed in details.

The multilayered materials are used in many structures. In conventional laminated composite structures, homogeneous elastic laminae are bonded together to obtain enhanced mechanical and thermal properties. The main inconvenience of such an assembly is to create stress concentrations along the interfaces, more specifically when high temperatures are involved. This can lead to delaminations, matrix cracks, and other damage mechanisms which result from the abrupt change of the mechanical properties at the interface between the layers. One way to overcome this problem is to use functionally graded materials within which material properties vary continuously. The concept of functionally graded material (FGM) was proposed in 1984 by the material scientists in the Sendai area of Japan [1].

The FGM is a composite material whose composition varies according to the required performance. It can be produced with a continuously graded variation of the volume fractions of the constituents. That leads to a continuity of the material properties of FGM: this is the main difference between such a material and an usual composite material. The FGM is suitable for various applications, such as thermal coatings of barrier for ceramic engines, gas turbines, nuclear fusions, optical thin layers, biomaterial electronics, etc.

Many investigations have been carried out on the subject of mechanical and thermal buckling of structures. Developments of new materials such as functionally graded materials (FGMs), however, have necessitated more research in this area. The response of a functionally graded ceramic–metal plate was investigated by Praveen and Reddy using a finite element model that accounts for the transverse shear strains, rotary inertia, and moderately large rotations in the Von Karman sense [2]. In Ref. [3], Reddy et al. developed the relationship between the bending solutions of the classical plate theory and the first order plate theory for functionally graded circular plates. Bouzza et al reported mechanical and thermal buckling of rectangular and square functionally graded plates (FGPs) based on the classical plate theory [4,5]. They used energy method and reached to the closed-form solutions. They have also investigated thermal buckling of FGPs based on the first order displacement field [6-8]. They obtained buckling loads by solving the system of five stability equations. Najafizadeh and Eslami studied the thermoelastic stability of circular functionally graded plates [9,10].Ma and Wang employed the third order shear deformation plate theory to solve the axisymmetric bending and buckling problems of functionally graded circular plates [11]. Three-dimensional thermal buckling analysis of functionally graded materials, using finite element method, is reported by Na and Kim [12].

The purpose of this paper is to develop the two variable refined plate theory for thermal buckling analysis of functionally graded plates. The present theory satisfies equilibrium conditions at the top and bottom faces of the plate without using shear correction factors. Governing equations are derived from the principle of minimum total potential energy. Navier solution is used to obtain the closed-form solutions for simply supported FGM plate. To illustrate the accuracy of the present theory, the obtained results are compared with finite element method and results of the first-order shear deformation theory.

Refined plate theory for FG plates - Governing equations: The displacement field of a rectangular FGM plate, based on the two variable refined plate theory, can be expressed as

$$U(x,y,z) = u(x,y) - z\frac{\partial w_b}{\partial x} + z\left[\frac{1}{4} - \frac{5}{3}\left(\frac{z}{h}\right)^2\right]\frac{\partial w_s}{\partial x}$$
$$V(x,y,z) = v(x,y) - z\frac{\partial w_b}{\partial y} + z\left[\frac{1}{4} - \frac{5}{3}\left(\frac{z}{h}\right)^2\right]\frac{\partial w_s}{\partial y} \qquad (4)$$
$$W(x,y,z) = w_b(x,y) + w_s(x,y)$$

Constitutive relations: Consider a FGM plate made of ceramic and metal, the material properties of FGM such as material properties vary continuously across the thickness according to the following equations, which are the same as the equations proposed by Reddy et al. and Praveen et al. [3,4]:

$$E(z) = E_m + E_{cm}V_f(z) \qquad E_{cm} = E_c - E_m$$
$$\alpha(z) = \alpha_m + \alpha_{cm}V_f(z) \qquad \alpha_{cm} = \alpha_c - \alpha_m \qquad (7)$$
$$\nu(z) = \nu_0$$

Buckling analysis of FGM plates: The critical buckling temperature or temperature differences ΔT_{cr} with respect to the material gradient indexes of the plate are calculated for functionally graded squares plates with different relative thickness of the plate under uniform temperature rise, linear and nonlinear temperature distribution across the thickness using the two variable refined plate theory and are plotted in Figs. 3-5. It is clear that the critical temperature under non linear temperature rise is higher than that under linear temperature rise, which is higher than that under uniform temperature rise, whatever the gradient index k is. In all type of temperature cases (uniform, linear, nonlinear), the critical temperature change decreases, when the volume fraction index k a/h is increased. On the other hand, the critical temperature change increases, when the relative thickness of the plate a/h is decreased.

Conclusions: The thermal buckling analysis of functionally graded plates is carried out by using two variable refined plate theory. Material properties varied continuously in the thickness direction according to a simple power law distribution in terms of the volume fraction of a ceramic and metal. Numerical results of a simply isotropic square and rectangular plate under uniform and linear temperature rise compare well with those of the previous works. Further, the thermal buckling behavior under uniform, linear and nonlinear temperature rise across the thickness is analyzed for simply Al/Al2O3 FGM plates. The critical temperature decreases as volume fraction index is increased. In addition, the critical temperature increases when the geometric parameter b/h is decreased. The critical temperature under nonlinear temperature rise is higher than that under linear temperature rise and uniform temperature rise.

1. Koizumi M. FGM Activities in Japan. Composites 1997;28:1–4.
2. Praveen GN, Reddy JN. Nonlinear transient thermal elastic analysis of functionally graded ceramic–metal plates[J]. Int J Solids Struct 1998;35(33):4457–76.
3. Reddy JN, Wang CM, Kitipornchai S. Axisymmetric bending of functionally graded circular and annular plates[J]. Eur J Mech A/ Solids 1999;18(1):185–99.
4. Bouazza M, Tounsi A, Adda-Bedia E.A, Megueni A, Thermal buckling of simply supported FGM square plates, Applied Mechanics and Materials 61 (2011) 25-32.
5. Bouazza M, Ouinas D, Abdelaziz Y and Hamouine A. Buckling of thin plates under uniaxial and biaxial compression. Journal of Materials Science and Engineering B 2 (8) (2012) 487-492.
6. Bouazza M, Tounsi A, Adda-Bedia E.A, Megueni A, Thermoelastic stability analysis of functionally graded plates: An analytical approach, Computational Materials Science, Elsevier 49 (2010) 865-870.
7. Bouazza M, Tounsi A, Adda-Bedia E.A, Megueni A,Thermal buckling behavior of functionally graded material, Journal of Materials Science and Technology 18 (3) (2010)155-170
8. Bouazza M, Tounsi A, Adda-Bedia E.A, Megueni A, Stability analysis of functionally graded plates subject to thermal loads, Shell-like Structures-Advanced Structured Materials, Springer 15 (8) (2011) 669-680.

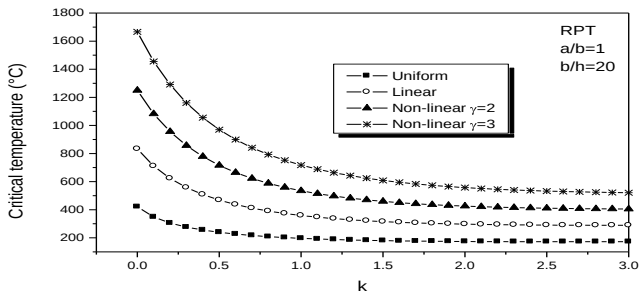

Figure 3. Critical buckling temperature of FGM plate under uniform linear and nonlinear temperature rise vs gradient index of the plate.

Functional Materials

MS.3.P062
In situ observation of the electron beam induced phase transformation of $CaCO_3$ to CaO as a function of the accelerating voltage (20-300kV)

U. Golla-Schindler[1], W. Schweigert[1], G. Benner[2], A. Orchowski[2], U. Kaiser[1]

[1]University Ulm, ZE Material Science, Ulm, Germany
[2]Carl Zeiss Microscopy GmbH, Materials Division, Oberkochen, Germany

ute.golla-schindler@uni-ulm.de
Keywords: SALVE, EELS, $CaCO_3$ first, second, third (Arial, 9pt, flush left)

$CaCO_3$ (calcite) is one of the important systems in the field of biomineralisation and the most common carbonate of the earth crust inevitable for the manufacture of cements. Limestone is the chief raw material, which when heated about 900° C forms CaO (lime) by the reaction: $CaCO_3 \rightarrow CaO + CO_2\uparrow$. Apparently $CaCO_3$ undergoes the same phase transformation to CaO by electron irradiation.

Therefore the new challenge arises to search for conditions and instrumental settings especially the applied accelerating voltage to study in situ the phase transformation on an atomic scale.

The accelerating voltage was reduced from 300 kV down to 20 kV by using a CM20 operating at 200 kV, equipped with a LaB6 cathode, a TITAN operating at 300 kV and 80 kV equipped with a field emission gun and an imaging-side Cs-corrector and the newly developed SALVE prototype microscope equipped with a field emission gun, an image-side Cs-corrector and a monochromator [1] operating at 20, 40 and 80 kV. At high accelerating voltages the radiation damage of $CaCO_3$ is starting immediately with the electron-radiation and can be divided up in three stages first the amorphisation of the crystalline structure, then producing holes and at least recrystalisation in a polycrystalline structure with significant volume and correlated mass loss during the reaction time. Figure 1 a), b) show a $CaCO_3$ crystal and the correlated FFT, where the lattice planes can be imaged without any radiation damage. Figure 1 c), d) show the same crystal after 25 min radiation with a dose rate of $4x10^4$ e/nm^{2}s, where a polycrystalline structure is grown with lattice spacing fitting the CaO structure. Exemplary a starting image taken with the Titan and a dose rate of $4x10^4$ e/nm^{2}s at 300kV accelerating voltage is presented in Figure 1 e), where the radiation damage results in fast hole ptoduction. However, the crystal structure of the original calcite is still present in the FFT of the cut-out. We found that reduced accelerating voltages below 80 kV slows down the radiation damage and gives the freedom to align the instrument to obtain information on the atomic scale before significant beam damage effects appear. The quantitative studies of volume-loss at 20, 40 and 80 kV delivered increasing volume loss with decreasing accelerating voltages. This effect at low accelerating voltages is counterbalanced by increasing contrast which allows the use of decreasing dose rates. To determine the mass loss quantitatively, the chemistry has to be known, therefore additionally EELS spectra were taken. Figure 2 show spectra taken with the SALVE microscope at 80kV a) of the C K, Ca L_{23} and b) O K-edges where the fading out signal of carbon confirms the phase transformation. The high stability of the instrument enables additionally to measure in situ the change of Ca ELNES during the phase transformation, which is correlated to bond length variation of Ca. The undistorted octahedral coordination of calcium with oxygen as binding partner is preserved, where solely the bond length change from 2,357 Å to 2,407 Å by 5 pm. As a result of the octahedral coordination the degenerated energy levels of the 3d shell split up into the t_{2g} and e_g energy levels by Δ. The value of Δ is influenced by the distances R between the cation in our case Ca and the surrounding ligands and can be described by: $\Delta = Q/R^5$ where Q is approximately a constant for cations of similar valence in the same transition series and identical charge on the ligands [2]. Finally we obtained for the ratio of energy level splitting for $CaCO_3$ and CaO $\Delta_{CaO} / \Delta_{CaCO3}$ experimentally 0,82 which agrees nicely with the theoretically prediction of 0,9.

1. U. Kaiser et al Ultramicroscopy 111 (2011), p.1239
2. R.G. Burns (1993) Mineralogical Applications of Crystal Field Theory. Cambridge University Press, New York
3. This work was supported by the DFG (German Research Foundation) and the Ministry of Science, Research and the Arts (MWK) of Baden-Wuerttemberg in the frame of the SALVE (Sub Angstrom Low-Voltage Electron microscopy and spectroscopy project.

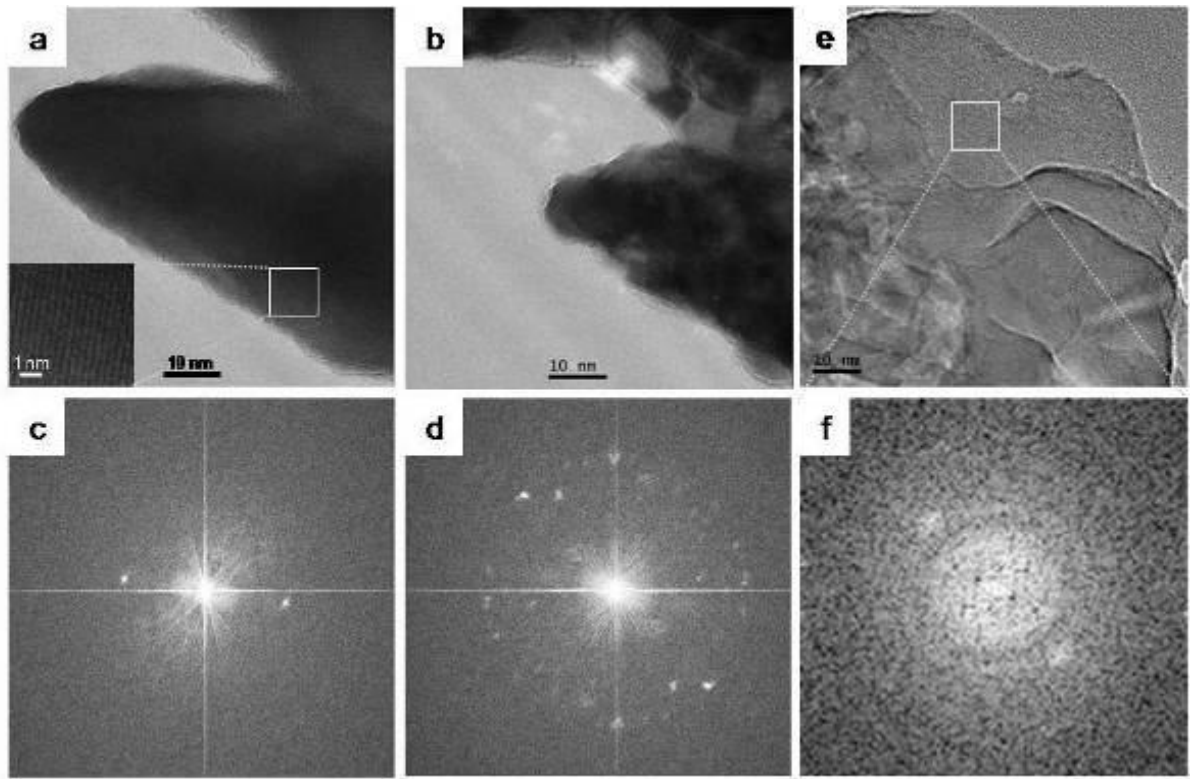

Figure 1. In situ study of calcite recorded with the SALVE at 20 kV (a-d) and Titan at 300kV (e,f) accelerating voltage and the corresponding FFTs, which shows the change of a single crystal structure to a polycrystalline structure after electron-irradiation. Please describe what we see in a,- f in more detail.

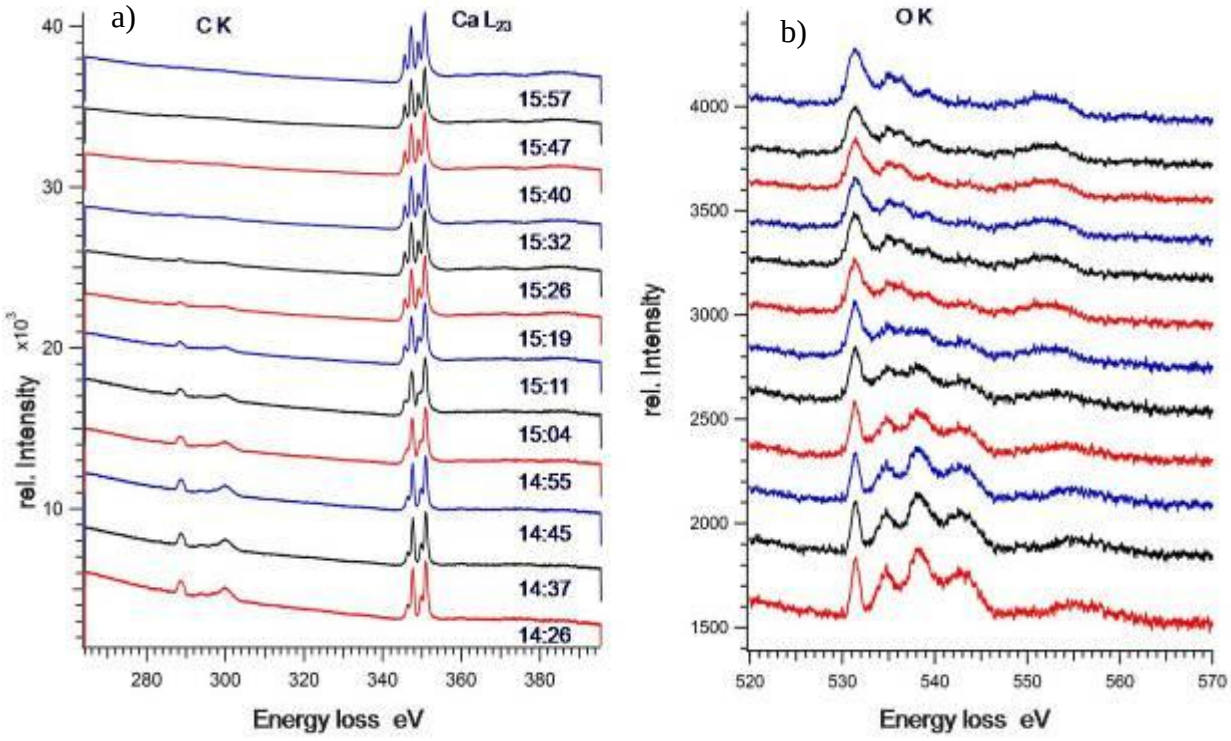

Figure 2. Electron energy loss spectra taken at 80kV during one phase transformation series of the a) C K, Ca L_{23} and b) O K-edges.

Functional Materials

MS.3.P063
Aberration corrected TEM and Super-X STEM-EDXS characterization of high electron mobility transistor structures

A. Graff[1], M. Simon-Najasek[1], F. Altmann[1], M. Dammann[2]

[1]Fraunhofer Institute for Mechanics of Materials IWM, Halle, Germany
[2]Fraunhofer Institute for Applied Solid State Physics IAF, Freiburg, Germany

andreas.graff@iwmh.fraunhofer.de
Keywords: GaN-HEMT, aberration corrected TEM, STEM-EDXS

GaN based high electron mobility transistor (HEMT) devices provide an outstanding performance for high frequency and high power applications as used in radar and next generation mobile telecommunication systems. The devices are based on GaN/AlGaN heterostructures with high mobility of charge carriers. The electron channel is contacted by ohmic source and drain metal structures. The channel switching is realized by a metal gate structure forming a Schottky contact to the upper AlGaN layer. The performance of the devices is strongly related to crystal defects and impurities within the epitaxial grown heterostructure, the interface perfection of the AlGaN/GaN electron channel and the metal/semiconductor interfaces of the gate. Furthermore structural and chemical changes during accelerated aging tests lead to a degradation of the electrical performance of such devices. Knowledge of reactions especially at the metallic gate is essential to understand the degradation mechanisms. In order to characterize the relevant hetero layer and interfaces, high resolution techniques for atomic level imaging and chemical analysis are required.

New developed TEM techniques allow aberration corrected imaging and superior sensitivity for STEM-EDXS analysis by new Super-X detectors with high acceptance angles. The new Super-X detector has been evaluated and applied to characterizing GaN-HEMT test structures before and after defined electrical treatment. Aged samples were selected by their electrical behavior after testing and potential defect sites under the gate were localized by emission microscopy. Electron transparent TEM cross sections were extracted from defect and reference positions by using focused ion beam (FIB) milling techniques. The lamellas were transferred in situ within a crossbeam system into self-made TEM grids with adapted clip holders for fixing the lamella (Figure 1a) [1]. To minimize sidewall defects and to further reduce lamella thickness all lamellas were finally polished by low energy FIB milling. Sample thicknesses lower than 80nm are regularly achieved using dedicated SEM based thickness mappings [2]. TEM investigations were performed at 300kV with an aberration corrected microscope (Titan G2 60-300, FEI) equipped with a high sensitive EDXS system (Super-X, FEI).

The gates are produced by depositing metal layer stacks onto the semiconductor surface where the SiN dielectric has been opened beforehand. The gate structure consists of layers of Nickel, Platinum and Gold. In the studied structures, metals grow with their (111) planes parallel to the flat GaN substrate surface. It was found that during the accelerated aging test a rough interface evolves (Figure 2), often starting at the edges of the gate semiconductor interface where pores are formed during the degradation. Thanks to the aberration correction imaging structures can be imaged without delocalization at the interfaces. Due to the sample thickness the superposition of lattice structures stays visible (Figure 2b). As a consequence of the electrical stress, interdiffusion of the metals can be identified. The gold tends to diffuse to the surfaces of the gate next to the GaN and SiN (Figure 3b). With the sensitivity of the new Super-X EDXS system in combination with the lateral resolution of the STEM it is possible to detect monolayers of impurities at the interfaces.

It is shown that the improved performance of the imaging and analytical TEM techniques gives a better insight into the microstructure of the GaN-HEMT transistor structures. It offers new possibilities to visualize load and aging related defects. These results can help to improve the performance, lifetime and reliability of GaN-HEMT devices by optimization of the manufacturing processes.

1. Altmann et al., Microscopy Microanalysis, 2011, 17 (Suppl 2), 626-627
2. Salzer et al., Microscopy Microanalysis, 2010, 16 (Suppl 2), 172-173

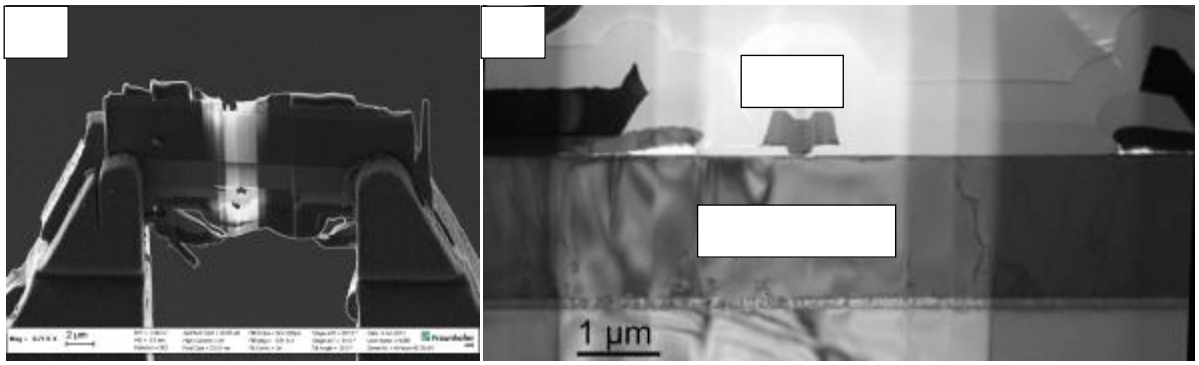

Figure 1. TEM cross section of a GaN transistor. a) FIB prepared sample in a special TEM magazine holder; b) TEM overview of the sample

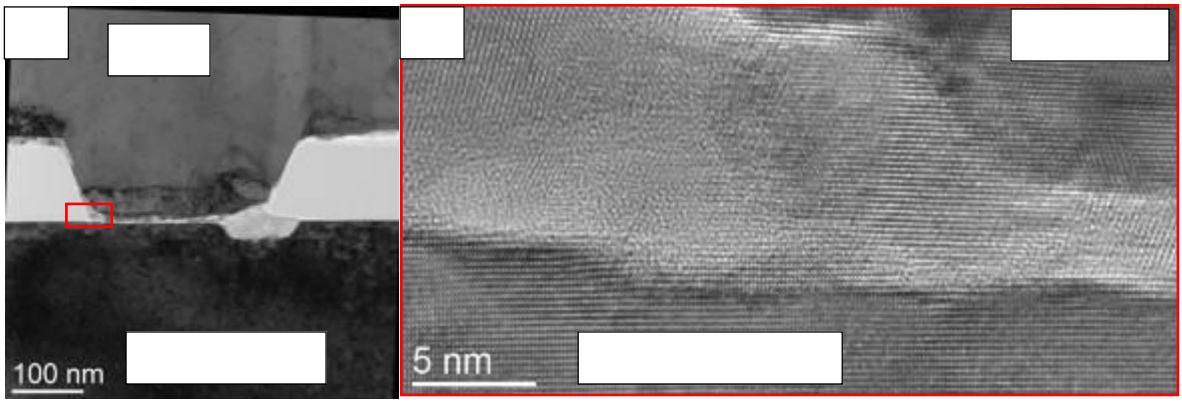

Figure 2. TEM cross section of a degraded transistor gate. a) TEM bright field of the metal/semiconductor interface; b) HRTEM detail of the left edge

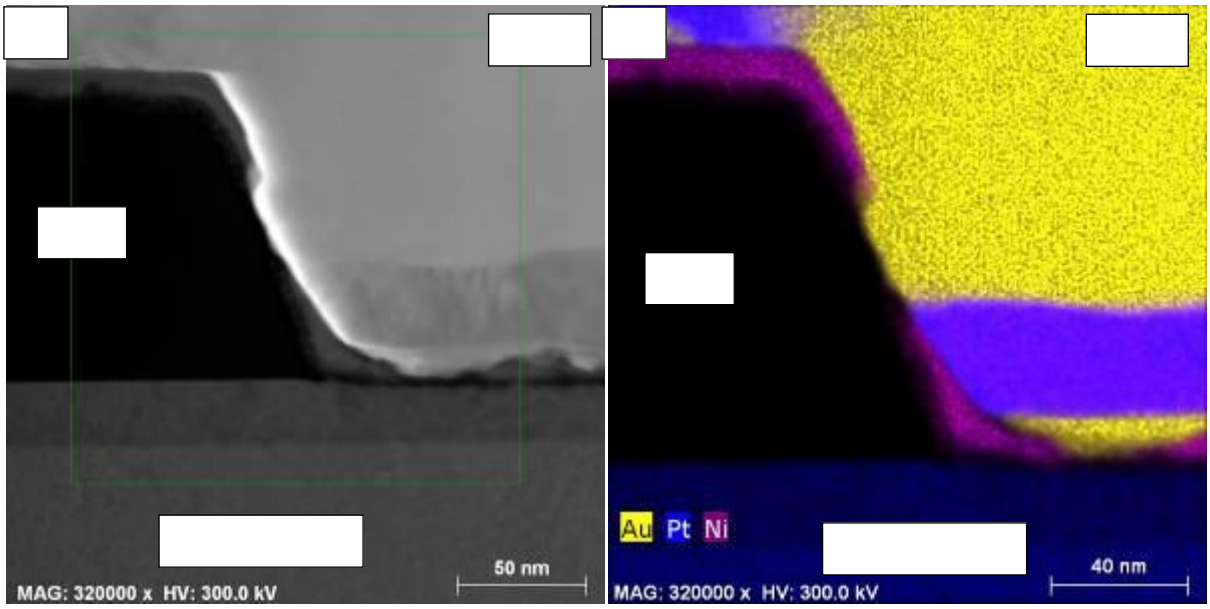

Figure 3. TEM cross section of a degraded transistor gate. a) STEM image of the left part of the gate; b) EDXS intensity map of characteristic X-rays of selected elements.

Functional Materials

MS.3.P064
The structure of supercrystals made by self-assembled nanoscaled Ag_2S hollow spheres and Ag_2S nanodiscs

R. Popescu[1], P. Leidinger[2], C. Feldmann[2], D. Gerthsen[1]

[1]Karlsruher Institut für Technologie, Laboratorium für Elektronenmikroskopie, Karlsruhe, Germany
[2]Karlsruhe Institute für Technology, Institut für Anorganische Chemie, Karlsruhe, Germany

radian.popescu@kit.edu
Keywords: Transmission electron microscopy, superscrystals, hollow spheres, nanodiscs

Supercrystals consisting of highly periodic arrangements of monodisperse nanoparticles were intensely investigated in the recent past due to their unique properties, which can differ from those of individual nanoparticles and bulk compounds [1]. For example, semiconductor and precious metal nanoparticles were utilized as so-called artificial atoms for a variety of functional superstructures [2]. While a reasonable number of 3D supercrystals were built with different types of massive nanoparticles, including Ag_2S, nanoscale hollow spheres have not been used as building blocks until now. In this work we study the structure of supercrystals which consist of nanoscale Ag_2S hollow spheres (HS) and Ag_2S nanodiscs (ND).

For the structural characterization we used scanning electron microscopy (SEM), high-resolution (HR) transmission electron microscopy (TEM), selected-area electron diffraction (SAED) and high-angle annular dark-field (HAADF) scanning TEM (STEM). The HSs and NDs were obtained by a microemulsion approach [3]. Samples for electron microscopy were prepared by evaporating ethanol-based suspensions on an amorphous carbon film. SEM was performed on a Zeiss Supra 40 VP equipped with a field emission gun (acceleration voltage 4–20 kV, working distance 3 mm). HRTEM and SAED were conducted on a Philips CM 200 FEG/ST at 200 kV, while HAADF-STEM images are taken with an aberration-corrected FEI Titan^3 80-300 at 300 kV.

In the following, the properties of supercrystals consisting self-assembled Ag_2S HSs and individual Ag_2S HSs are described. TEM (Fig. 1 a) and HAADF-STEM (Fig. 1b) images clearly evidence the hollow sphere structure of Ag_2S nanoparticles with an average outer diameter of ~ 37 nm, a wall thickness of ~ 10 nm and an inner cavity diameter of ~ 17 nm. Lattice fringes extend through the whole hollow sphere (image not shown here) indicate the single crystalline structure of the sphere wall. The measured fringe distance of 2.8) Å is compatible with d$(\bar{1}12)$ =2.84 Å in monoclinic α-Ag_2S/acanthite. The structure and composition of Ag_2S HSs is further confirmed by SAED, which demonstrates the presence of α-Ag_2S (Fig. 1c). The Ag_2S HS supercystals show regularly assembled building blocks (i.e. individual nanoscaled Ag_2S HSs) with a dense packing of hard spheres and overall dimensions of 10–30 micrometers (Fig. 1d). Herein, the individual Ag_2S hollow spheres are clearly visible (Fig. 1e,f).

Large tube-like supercrystals of 5–30 µm in length and about 500 nm in diameter are formed by self-assembling of Ag_2S NDs. Fig. 2a displays a side-view of a single tube-like supercrystal. Top-views of Ag_2S nanodisc arrays show a tube-like structure with an outer diameter of 400–500 nm and a lens-shaped inner channel with dimensions of about 200 nm x 50 nm (Fig. 2b). The TEM image in Fig. 2c clearly indicates the substructure of the nanodisc supercrystal. Accordingly, the tube-like superstructure is composed of individual nanodiscs that are deposited on top of each other. Notably, the parallel rows of stacked nanodiscs are slightly twisted along the longitudinal axis of the supercrystal resulting in a helix-like winding. Assuming that such winding increases the structural stability of the nanodisc assembly, its direct consequence is the presence of an inner channel, thus, a tube-like structure. According to Fig. 2c) and d), the nanodiscs are characterized by an average diameter of ~ 20 nm and a thickness of ~ 7 nm as schematically depicted in Fig. 2e. The HRTEM image in Fig. 2d illustrates the structure of a single Ag_2S nanodisc in detail. Lattice fringes across the whole nanodisc confirm the single crystallinity of the nanodiscs. The measured fringe distance of 2.4 Å is again compatible with the presence of monoclinic α-Ag_2S/acanthite (d(121) =2.44 Å). SAED patterns recorded from single nanodisc supercrystals indicate a remarkably high intensity of the $(\bar{1}12)$ reflection (Fig. 2f) which is preferentially aligned along a particular direction indicating a textured alignment of the disks. The high peak intensity of $(\bar{1}12)$ is also evident when comparing the SAED of nanodiscs with that of hollow sphere supercrystals (Fig. 2f and Fig. 1c). Since the single crystalline nanodiscs are well-assembled along the longitudinal axis of the tube-like supercrystal such a textural effect is not a surprise and can be explained assuming that the $(\bar{1}12)$ planes are parallel to the surface of the nanodiscs (scheme Fig. 2e). The orientation of the nanodiscs is also in agreement with the (121) lattice fringes in the HRTEM image Fig. 2d, because (121) is almost perpendicular to $(\bar{1}12)$

1. S. M. Rupich and D. V. Talapin, Nature Mater. 10 (2011), p. 815.
2. a) Z. Lu and Y. Yin, Chem. Soc. Rev. 41 (2012), p. 6874; b) R. C. Ashoori, Nature 379 (1996), p. 413.
3. D. H. M. Buchold and C. Feldmann, Adv. Funct. Mater. 18 (2008), p. 1002.

4. This work has been performed within the projects C1.4 and C4.5 of the DFG Research Center for Functional Nanostructures (CFN). It has been further supported by a grant from the Ministry of Science, Research and the Arts of Baden-Württemberg (Az: 7713.14-300).

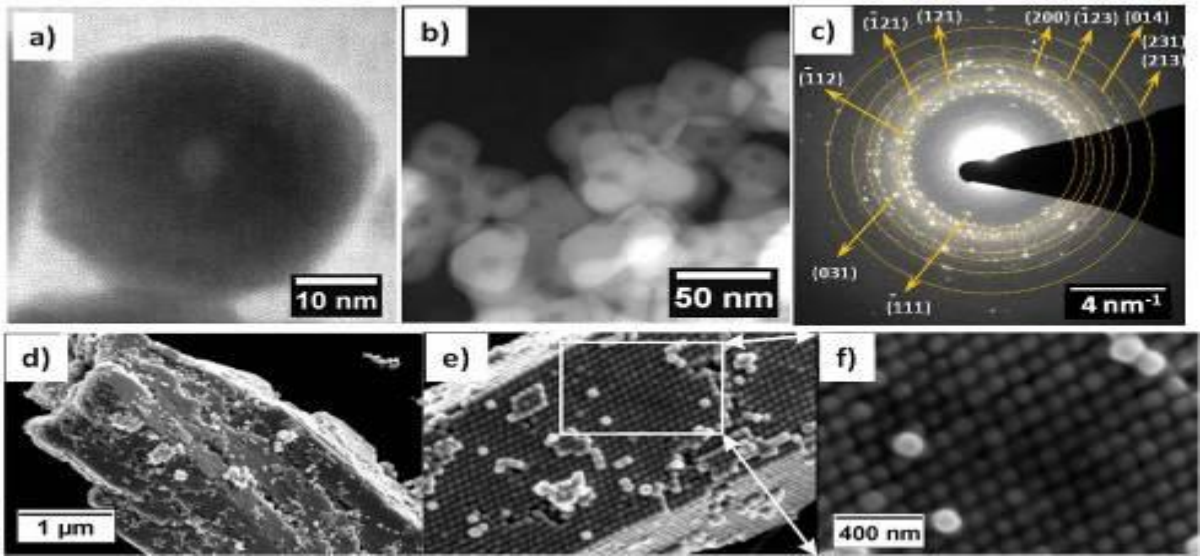

Figure 1. (a) HRTEM and (b) HAADF-STEM images of single Ag_2S HSs; (c) indexed SAED pattern of Ag_2S supercrystals (Miller indices correspond to bulk monoclinic α-Ag_2S/acanhite); (d) overview SEM image and (e,f) detail SEM images of Ag_2S hollow sphere supercrystals showing the dense packing of hollow spheres.

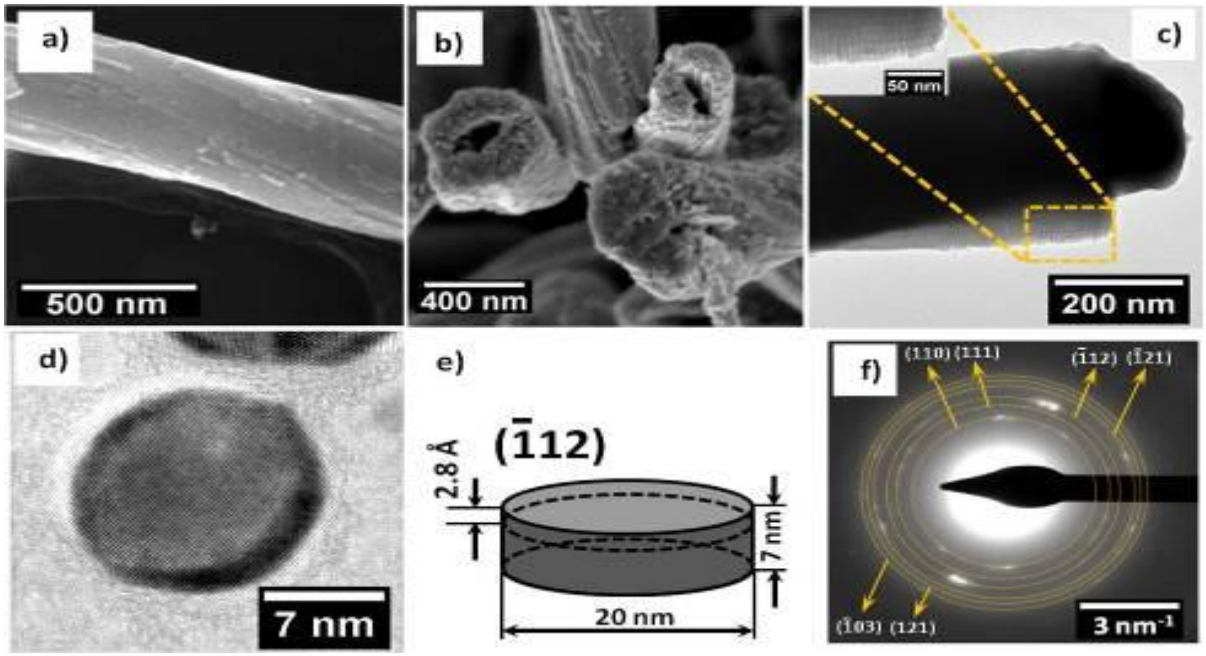

Figure 2. (a) Side-view and (b) top-view SEM images of Ag_2S nanodisk supercrystals; (c) TEM image showing stacked nanodiscs; (d) HRTEM and (e) schematic representation of a single Ag_2S ND; (f) indexed SAED pattern of Ag_2S ND supercrystals, which shows a strong $(\bar{1}12)$ texture (Miller indices correspond to bulk monoclinic α-Ag_2S/acanhite).

Functional Materials

MS.3.P065
Influence of the morphology and phase purity of barium titanate nanostructures on phase transition behaviour

A. Gajović[1], M. Plodinec[1], M. Dutour Sikirić[2], J. Šipušić[3], M. Čeh[4]

[1]Rudjer Boskovic Institute, Materials physics, Zagreb, Croatia
[2]Rudjer Boskovic Institute, Physical Chemistry, Zagreb, Croatia
[3]University of Zagreb, Faculty of Chemical Engineering and Technology, Zagreb, Croatia
[4]Institute Jozef Stefan, Nanostructured materials, Ljubljana, Slovenia

gajovic@irb.hr
Keywords: barium titanate nanostructures, TEM, Raman spectroscopy, phase transition

Last years, increasing attention has been dedicated to the synthesis of various $BaTiO_3$ nanostructures, such as nanoparticles, nanorods, nanowires and nanotubes, because dependence of their ferroelectric and piezoelectric properties on their dimension and size [1, 2]. The phase transition from ferroelectric to paraelectric phase in the case of perovskite materials is usually caused by structural phase transition. Typical example is $BaTiO_3$ (BTO) where phase transition from tetragonal to cubic phase induces the transition from ferroelectric to paraelectric state. Expected phase transition temperature is between 110 and 150 °C and depends on the different factors such as doping [3], grain and particle sizes and shapes [4], phase purity [5] etc. In this work the phase purity and morphology of the barium nanostructures were studied by transmission electron microscopy (TEM) techniques as the main method and the influence to the phase transition behavior was monitored by thermo-Raman spectroscopy.

For the synthesis of barium titanate nanostructures we apply hydrothermal method using different starting materials. For the synthesis different aqueous solutions of barium salts and titanium dioxide nanoparticles were hydrothermally treated with NaOH at different temperatures for different reaction times.

Obtained nanostructures were studied in details by high resolution TEM in combination with selected area diffraction (SAED) and energy dispersive X-ray spectroscopy (EDS) measurements. while X-ray powder diffraction (XRD) and Raman spectroscopy (RS) were used for determination of crystal structure and purity of the prepared BTO samples. Scanning electron microscopy (SEM) was used for the preliminary observation of morphology and the agglomeration of the nanostructures, while the size distribution of nanostructures was measured with dynamic light scattering (DLS). The results of DLS measurements were compared with size obtained from TEM images. With the aim to study ferroelectric phase transition in BTO, temperature dependent micro-RS measurements were done *in situ* at different temperature using Linkam heating stage.

Tetragonal phase of BFO, having *4mm* simetry with *c*/*a* axis ratio close to one, is hard or impossible to distinguish from cubic phase by using only XRD technique, so the phase purity and the crystal structure of the samples were determined by the combination of XRD and RS. It was observed that the purity and the structure of the samples depend on the starting salts and synthesis procedure. SEM and TEM measurements indicate that synthesized BTO have morphology of well crystalline nanoparticles and nanocubes of different sizes (Fig. 1), while in some cases nanowires (Fig. 2) were also present in the sample. EDS measurements showed that nanocubes were indeed BTO, while nanowires contained only titanium, oxygen and small amount od sodium indicated possible hydrogen titanete structure. RS was used for study of temperature dependent phase transitions to paralelectric (cubic), structure in BTO having different morphology and phase purity. The shift of phase transition to higher temperature then expected for BTO was observed in synthesized samples. The influence of the BTO nanostructures' morphology, sizes and the phase purity to the temperature of phase transitions will be discussed.

1. T. Yan, X. L. Liu, N.R. Wang and J. F. Chen, J. Cryst. Growth 281 (205) , p. 669.
2. Y. Y. Chen, B.Y. Yu , J. H. Wang, R. E. Cochran, J. J. Shyue, Inorg. Chem. 48 (2009), p. 681.
3. P. S. Dobal, A. Dixit, R. S. Katiyar, D. Garcia, R. Guo, A. S. Bhalla, J. Raman Spectrosc 32 (2001), p. 147.
4. Y. Shiratori, C. Pithan, J. Dornseiffer, R. Waser, J. Raman Spectrosc, 38 (2007), p. 1288 and 1300.
5. A. Gajović, J. Vukajlović Pleština, K. Zagar, M. Plodinec, S. Šturm, M. Čeh, J. Raman Spectrosc (2012), in press, doi: 10.1002/jrs.4206.

6. This work was supported by Croatian Ministry of Science Education and Sport project: 'Physics and applications of nanostructures and bulk matter', 098-0982904-2898, The research leading to part of these results has received funding from the European Union Seventh Framework Programme [FP7/2007-2013] under grant agreement n°312483 (ESTEEM2).

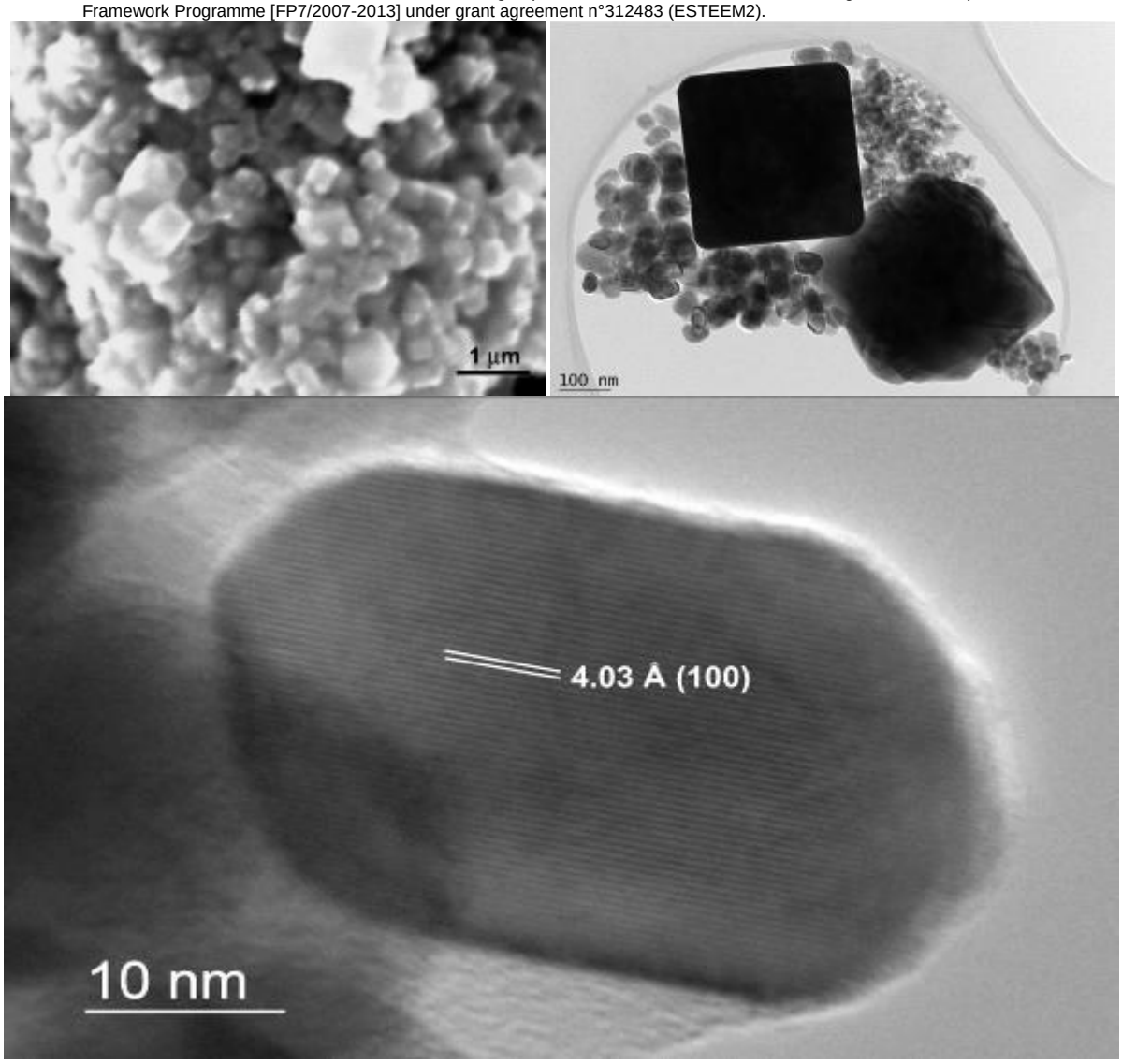

Figure 1. BTO having morphology of nanoparticles and nanocubes; a) SEM image, b) TEM image, c) HRTEM indicated BTO structure of nanoparticles.

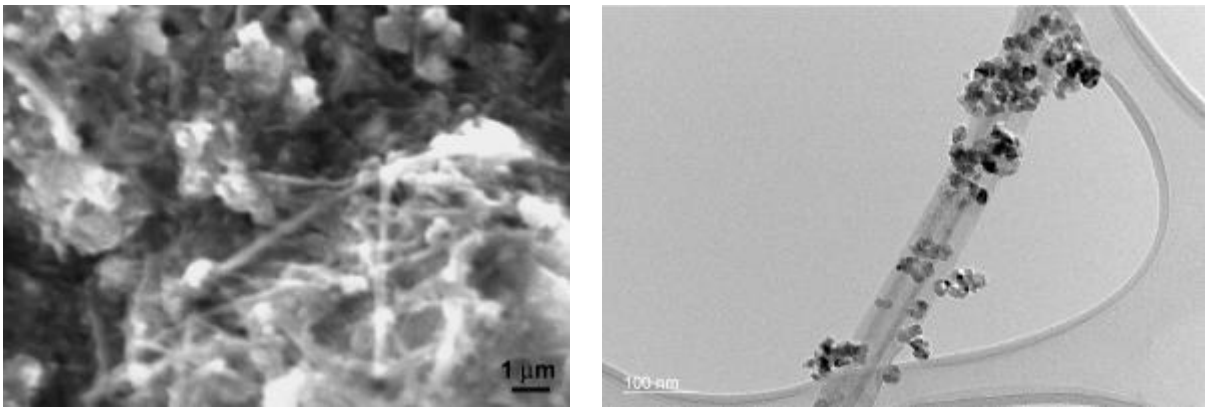

Figure 2. Sample containing nanowires - **a)** SEM image, **b)** TEM image

Functional Materials

MS.3.P066
Investigation of antioxidant activities of some flavonoid derivatives using aminophenyl modified glassy carbon sensor electrode

I.E. Mülazımoğlu[1], A. Demir Mülazımoğlu[1], E. Yılmaz[1]

[1]Necmettin Erbakan University, Chemistry, Konya, Turkey

iemulazimoglu@konya.edu.tr
Keywords: Flavonoid, antioxidant activity, chemical sensor electrode

Carrying on its development in the last 20 years and having quite a significant place in electrochemical studies, the modification of electrodes are extensively used today. Therefore, these modified electrodes come to the fore in determination of organic and inorganic species, especially in the determination of species that are of very little amount in natural samples. Modified electrodes can be prepared through appropriate media of an electrode surface and through electrochemical oxidation or reduction under the optimum conditions [1, 2], and they can also be physically prepared as in carbon paste electrodes [3]. Although the electrode modification is made in the aqueous medium [4, 5], there are recent studies in non-aqueous medium [6]. Because appointments are usually made in the aquatic environment during the studies, when thought to be more stable, aqueous media modification processes are preferred. However, determinations of some species in natural samples, such as phenolic compounds [3, 6], metals [7, 8], etc. can also be made in the aqueous medium using the sensor electrodes obtained after modification in the aqueous medium.

The electrochemical behaviors of 10 structurally different flavonoids (quercetin, galangin, chrysin, 3-hydroxyflavone, naringenin, luteolin, apigenin, flavone, kaempferol, and naringin) on a glassy carbon electrode (GCE) were studied by cyclic voltammetry. In the current study, nitrophenyl (NP) diazonium salt has been synthesized from p-nitrophenylamine. One millimolar prepared NP diazonium salt (in 100 mM tetrabutylammonium tetrafluoroborate) in acetonitrile was used to modify the glassy carbon electrode. Nitro groups have been reduced to amine groups in 100 mM HCl medium on the NP modified GCE surface. Although NP-modified GCE surface was electro-inactive, it is activated by reducing the nitro group into amine group. And then, aminophenyl (AP) modified GCE surface has been used for the determination of antioxidant activities of 10 flavonoid derivatives with cyclic voltammetry technique.

The aim of this work were: (a) to electrochemically modify GCE in non-aqueous media, (b) to characterize NP modified GCE electrode (NP/GCE), AP modified GCE electrode (AP/GCE), and flavonoid-grafted AP/GCE sensor electrodes in various medium by cyclic voltammetry (CV), electrochemical impedance spectroscopy (EIS), and scanning electron microscopy (SEM), (c) to investigate the effect of sweeping rate, and (d) to investigate the interaction of this modified electrode with some flavonoid derivatives by CV. AP/GCE sensor electrode has been used to examine its sensitivity against quercetin, galangin, chrysin, 3-hydroxyflavone, naringenin, luteolin, apigenin, flavone, kaempferol, and naringin by using the CV technique.

1. Zielinska D, Pierozynski B, J Electroanal Chem 625 (2009) 149
2. Yao H, Sun Y, Lin X, Tang Y, Huang L, Electrochim Acta 52 (2007) 6165
3. Mülazımoğlu IE, Yılmaz E, Desalination 256 (2010) 64
4. Cai CX, Xue KH, Xu SM, J Electroanal Chem 486 (2000) 111
5. Li X, Wan Y, Sun C, J Electroanal Chem 569 (2004) 79
6. Mülazımoğlu IE, Demir Mülazımoğlu A, Yılmaz E, Desalination 268 (2011) 227
7. TrojanowiczM, Kozminski P, Dias H, Brett CMA, Talanta 68 (2005) 394
8. Hu S, Xu C, Wang G, Cui D, Talanta 54 (2001) 115

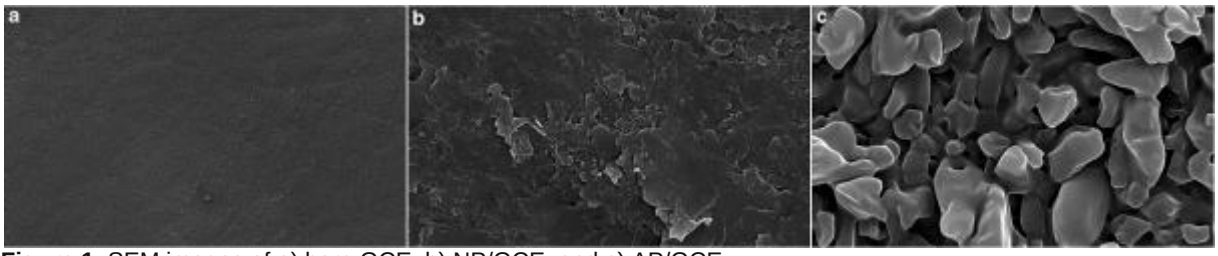

Figure 1. SEM images of a) bare GCE, b) NP/GCE, and c) AP/GCE

Functional Materials

MS.3.P067
Transmission electron microscopy study of defects in $BiFeO_3$ thin films

H. Deniz[1], A. Bhatnagar[1], E. Pippel[1], M. Alexe[1], D. Hesse[1]

[1]Max Planck Institute of Microstructure Physics, Halle (Saale), Germany

hdeniz@mpi-halle.de
Keywords: lattice defects, Aurivillius-type structure, $BiFeO_3$ films

A wide class of oxide materials with perovskite structure has been in the focus of intense research efforts lately due to fascinating properties they posses; such as ferroelectricity, colossal magnetoresistance, superconductivity, etc. $BiFeO_3$ (BFO) among them is the leading contender in the research of multiferroic compounds with its magnetic ordering and ferroelectric transition parameters well above room temperature. BFO has rhombohedral crystal structure that results in rich ferroelectric domain configurations in single-crystal thin films. Recently, a surface ("skin") layer has been put forward in order to elucidate some peculiar features observed for single crystals of bulk BFO [1]. Therefore, it is of great importance to grow defect-free high quality films of BFO in order to better understand/correlate structure-property relationships of this material. In this study, the surface of as-grown BFO films and defects of secondary phases were investigated by TEM to have a better understanding of its structure.

Single crystal $BiFeO_3$ thin films grown by pulsed laser deposition on scandate oxide substrates ($TbScO_3$, $GdScO_3$, etc.) have been investigated in high-resolution TEM and high angle annular dark field STEM (HAADF-STEM). Chemical composition of defects in the samples was studied using energy dispersive X-ray spectroscopy (EDX) scans in STEM. Defects having a layered structure, similar to bismuth-oxide layered perovskites [2], with a chemical composition different from the rest of the film have been observed (see figure 1a). Fast Fourier transform (FFT) analysis and image processing were used to elucidate the nature of these defects. They correspond to a new meta-stable phase in $BiFeO_3$ thin films.

EDX line scans across such defects revealed that the ratio of the atomic content of Bi to Fe is approximately 2:1 (figure 1b). High resolution HAADF images of such defects show that two rows of Bi atoms repeat themselves along the growth direction of BFO film and they are separated by a single row of Fe atoms. This structure is very different from the pseudo-cubic BFO film matrix where these defects are embedded in, closely resembling the crystal structure of Aurivillius-type ceramics, in particular Bi_2WO_6 (BWO). Layered perovskite ceramics consist of infinite 2D slabs of the ABO_3 perovskite structure which are separated by some other unit. In Aurivillius-type ceramics, separating units are Bi_2O_2 layers. BWO is the simplest case of Aurivillius-type ceramics where Bi_2O_2 layers are separated by a single WO_6 octahedron (see figure 2). BWO has an orthorhombic crystal structure with a space group *Aba2*. Its lattice parameters *a*, *b* and *c* are 5.436, 5.457 and 16.43 Å [3]. In our study, the estimated lattice parameters for the layered defects were $a \approx b \approx 5.338$ and $c = 16.18$ Å, respectively. This supports the fact that the structure of our layered defects closely matches that of BWO with a formula of Bi_2FeO_6 in our case.

1. X. Marti, P. Ferrer, J. Herrero-Albilos, J. Narvaez, V. Holy, N. Barrett, M. Alexe and G. Catalan, Phys. Rev. Lett. 106 (2011), 236101.
2. D. Hesse, N.D. Zakharov, A. Pignolet, A.R. James and S. Senz, Cryst. Res. Technol. 35 (2000), p.641.
3. R.E. Wolfe, R.E. Newnham and M.I. Kay, Solid State Comm. 7 (1969), p.1797.
4. Financial support by the FP7 project "IFOX" is gratefully acknowledged.

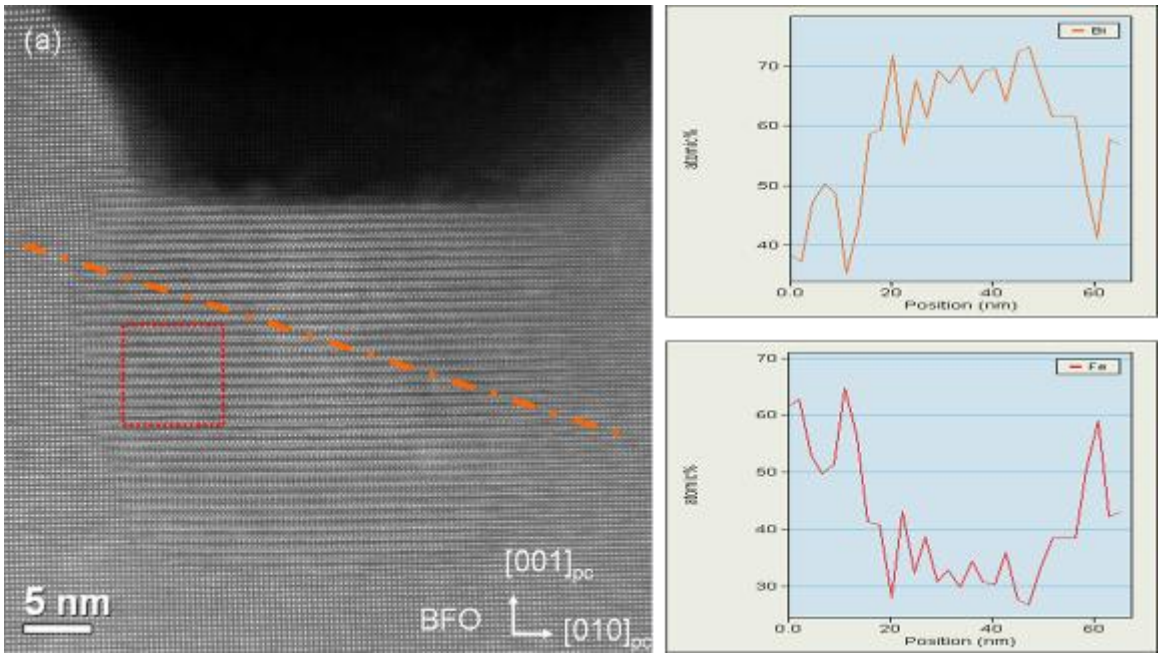

Figure 1. (a) High resolution HAADF-STEM image of a layered defect embedded in BFO film matrix. **(b)** The plots show atomic percentage of Bi and Fe contents obtained from EDX line scans along the orange colored line across the defect.

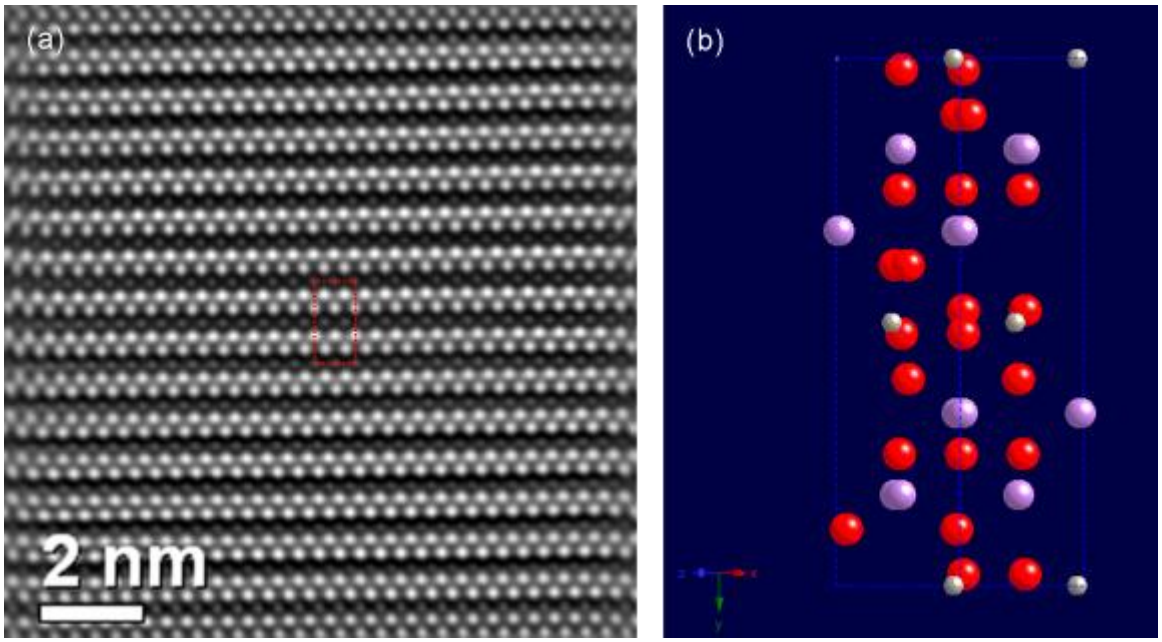

Figure 2. (a) Filtered and enlarged view of the red dotted box as-shown in the high resolution STEM image from figure 1. Bright rows of atoms and dark rows correspond to Bismuth and Iron, respectively. Red-dotted rectangle illustrates one unit cell of the new phase Bi_2FeO_6. **(b)** [101] projected crystal structure of Bi_2WO_6: Bi-lavender, W-grey and O-red.

Functional Materials

MS.3.P068
Modification of 2-amino-3-hydroxypyridine onto the glassy carbon electrode: determinations of Que, Gal, 3HF, and Chr

A. Demir Mülazımoğlu[1], E. Yılmaz[1], İE. Mülazımoğlu[1]

[1]Necmettin Erbakan University, Chemistry, Konya, Turkey

admulazimoglu@konya.edu.tr
Keywords: 2-amino-3-yydroxypyridine, flavonoid, surface modification, sensor electrode

Phenolic compounds are a complex group of substances that have attracted considerable attention due to their roles in providing flavor and color characteristics of food and in human health which are associated with their antioxidant activities [1, 2]. Many of the benefits associated with consumption of phenolic-rich foods are associated with their antioxidant activities [3]. The oxidation of flavonoids is of great interest because of their action as antioxidants with the ability to scavenge superfluous superoxide free radicals in the human body [4] by means of electron transfer processes. Among the wide variety of techniques [5, 6] used to detect antioxidants, electrochemical methods have the advantage of their high sensitivity, low cost, and inherent portability [7]. All flavonoids are electroactive, easily subject to either oxidation or reduction electron transfer reactions; hence, they can be investigated by electrochemical methods. The redox potentials of flavonoids determined by cyclic voltammetry are considered good measures of their antioxidant capacities.

Flavonoids, with high antioxidant activity in fruits and vegetables, are natural vegetable dyes synthesized from phenylalanine. They are very essential for human health due to their activity as free radical acceptors. In this study, the availability in the determination of quercetin (Que), galangin (Gal), 3-hydroxyflavone (3HF), and chrysin (Chr) of a modified glassy carbon (GC) sensor electrode using 2-amino-3-hydroxypyridine (AHP) was examined separately and simultaneously by cyclic voltammetry (CV). Surface characterization of modified electrodes was performed using CV, electrochemical impedance spectroscopy, and scanning electron microscopy techniques. The usability of the modified electrode was examined in the determination of some flavonoids by square wave voltammetry. From the experimental results, it was found out that Que, 3HF, and Chr; Gal, 3HF, and Chr; and 3HF and Chr can be determined simultaneously by using an AHP-modified GC sensor electrode. Also, these molecules can easily be determined separately by using the modified electrode.

The purposes of this study are (1) to obtain a new surface by modifying the glassy carbon (GC) electrode surface using AHP, (2) to characterize the obtained surface using electrochemical, spectroelectrochemical, and microscopic techniques, (3) to the check whether the molecule is bound to the GC electrode surface as diffusion-controlled and to support this graft through the SEM technique, (4) to investigate whether the new surface obtained is sensitive to the four different flavonoid derivatives both through cyclic voltammetry (CV) and square wave voltammetry (SWV), and (5) to investigate the usability of the developed electrode in the quantitative determination of used flavonoid derivatives simultaneously or separately.

1. Vermerris W, Nicholson R, Phenolic compound biochemistry, (2008) Springer, Berlin
2. Shahidi F, Ho CT, Phenolic compounds in foods and natural health products. (2005) The American Chemical Society, Urbana
3. Sawa T, Nakao M, Akaike T, Ono K, Maeda H, J Agric Food Chem 47 (1999) 397
4. Zhang J, Stanley RA, Adaim A, Melton LD, Skinner MA, Mol Nutr Food Res 50 (2006) 996
5. Chew LY, Khoo HE, Amin İ, Azrina A, Lau CY, Food Anal Methods 5 (2012) 126
6. Berker KI, Güçlü K, Tor İ, Demirata B, Apak R, Food Anal Methods 3 (2010) 154
7. Makhotkina O, Kilmartin PA, J Electroanal Chem 633 (2009) 165

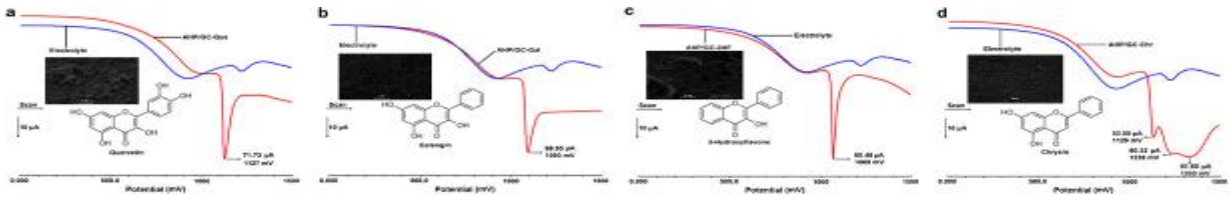

Figure 1. Square wave voltammograms and SEM images of flavonoids (1 mM) onto the AHP/GC electrode surfaces. **a)** Que, **b)** Gal, **c)** 3HF and **d)** Chr.

Functional Materials

MS.3.P069
DTO modified glassy carbon electrode at non-aqueous media: investigation of electrochemical behaviors of Que on the electrode surface

E. Yilmaz[1], A. Demir Mülazımoğlu[1], İE. Mülazımoğlu[1]

[1]NE University, A K Education Faculty, Chemistry, KONYA, Turkey

eciryilmaz@konya.edu.tr
Keywords: Modified electrode, quercetin, non-aqueous media, sensor electrode

Electrochemical and spectroelectrochemical measurements leading to the determination of kinetic parameters for antioxidants (e.g., redox potential, number of electrons transferred, electrode reaction rate constant, *etc.*), are very relevant, not only for evaluating the antioxidative abilities of flavonoids [1], but also for understanding their reaction mechanisms. The half-wave potential (E1/2) is a useful parameter for supplying information on the scavenging activity of the flavonoids. This has been rationalized on the basis that both electrochemical oxidation and hydrogen-donating free radical scavenging involve the breaking of the same phenolic bond between oxygen and hydrogen, producing the phenoxy radical and hydrogen, in an electron and proton transfer reaction. Thus a flavonoid which has a low value of $E_{1/2}$ is a good scavenger [2, 3]. Quercetin (Que) is one of the most abundant plant-derived polyphenols and is widely consumed with a human diet [4]. Most flavonoid molecules have the same structure as Que, except that they have a specific sugar molecule in place of one of Que hydroxyl groups on the C ring, which dramatically changes the activity of the molecule.

Electrochemical oxidation of Que, as an important biological molecule, has been studied in non-aqueous media using cyclic voltammetry, electrochemical impedance spectroscopy and scanning electron microscopy. To investigate the electrochemical properties of Que, an important flavonoid derivative, on a different surface, a new glassy carbon electrode has been developed using dithiooxamide (DTO) as modifier in non-aqueous media. The surface modification of glassy carbon electrode (GCE) has been performed within the 0.0 mV and +800 mV potential range with 20 cycles using 1 mM DTO solution in acetonitrile. However, the modification of Que to both bare glassy carbon and DTO modified glassy carbon electrode surface was carried out in a wide +300 mV and +2800 mV potential range with 10 cycles. Following the modification process, cyclic voltammetry has been used for the surface characterization in aqueous and non-aqueous media whereas electrochemical impedance spectroscopy has been used in aqueous media. Scanning electron microscopy has also been used to support the surface analysis. The obtained data from the characterization and modification studies of DTO modified and Que grafted glassy carbon electrode showed that the developed electrode can be used for the quantitative determination of Que and antioxidant capacity determination as a chemical sensor electrode. In this study, the electrochemical mechanism of oxidation of Que was investigated, for a wide range of non-aqueous solution conditions onto the DTO modified GCE surface, using CV, EIS and SEM techniques. Information on the mechanism of Que oxidation obtained from results at studies may play a crucial role in understanding its antioxidant activity. This study precedes studies initiated to find out the ability of Que determination in natural samples. The DTO/GCE electrode was used for the first time in non-aqueous media. This modified electrode was found to be very sensitive to Que molecules and could be used for the determination of Que in the future studies. The next step in our study is to use this modified GCE sensor electrode for the quantitative determination of Que using voltammetric techniques, and with this in mind, different plants are going to be collected and then varying antioxidant derivatives are going to be extracted from these plants. From the extract Que is going to be quantified by different voltammetric, spectroscopic and microscopic techniques (cyclic voltammetry, differential pulse voltammetry, square wave voltammetry, X-ray photoelectron spectroscopy, raman spectroscopy, ellipsometry, scanning electron microscopy, *etc.*) in these natural samples.

1. Hotta, H., Sakamoto, H., Nagano, S., Osakai, T., Tsujino, Y., Biochim. Biophys. Acta, 1526 (2001) 159.
2. Janeiro, P., Brett, A.M.O., Electroanalysis, 17 (2005) 733.
3. Rice-Evans, C.A., Miller, N.J., Paganga, G., Trends Plant Sci., 2 (1997) 152.
4. Hertog, M.G.L., Hollman, P.C.H., Katan, M.B., Kromhout, D. Nutr. Cancer, 20 (1993) 21.

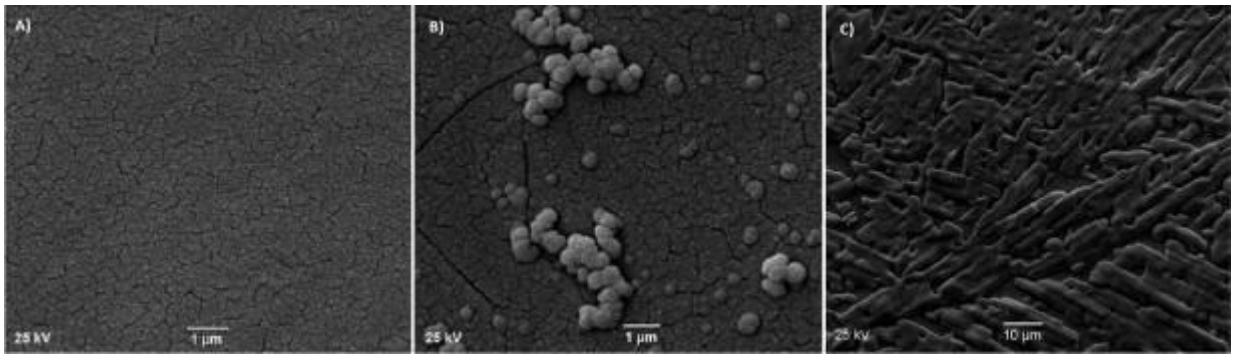

Figure 1. SEM images of (A) bare GCE, (B) DTO/GCE and (C) DTO/GCE-Que

Functional Materials

MS.3.P070
Electrostatic potential mapping in topological insulators by inline electron holography

C. Ozsoy Keskinbora[1], C.T. Koch[2], H.M. Benia[3], B. Bussmann[1], K. Kern[3], P.A. van Aken[1]

[1]Max Planck Institute for Intelligent Systems, Stuttgart Center for Electron Microscopy, Stuttgart, Germany
[2]Universität Ulm, ELIM: Electron and Ion Microscopy, Ulm, Germany
[3]Max Planck Institute for Solid State Research, Nanoscale Science, Stuttgart, Germany

ozsoy@is.mpg.de
Keywords: inline holography, topological insulators, space charge

Bi_2Se_3 has been known since decades as an insulating material that has good thermoelectric properties. In 2009 Xia *et al.* revealed a remarkable new characteristic [1]: Bi_2Se_3 is a clear experimental example of topological insulators. The bulk insulating Bi_2Se_3 bears a single singly-degenerate surface state within the band gap having a Dirac cone-like dispersion. As a consequence, Bi_2Se_3 became one of most popular materials that could be used to concretize quantum computers [2]. However, most of the time, the topological surface state of Bi_2Se_3 coexists with a two-dimensional electron gas (2DEG) at the surface. The electronic properties of the 2DEG in the reciprocal space have been studied using mainly Angle-resolved photon emission spectroscopy (ARPES)[3]. However, real-space observation and characterization of the 2DEG has not been reported. Here, we use electron holography method with sub-nm spatial resolution to investigate the 2DEG. This technique is able to map the mean inner potential distribution, since the holographically measured phase-shift is proportional to the projected potential according to equation (1)

(1).

From variations in the mean inner potential the charge density may be obtained, according to Poisson's equation (2)

(2).

In this study, the exit wave function has been reconstructed using inline electron holography. For this purpose, first a focal series comprising 11 bright-field (BF) images was recorded using the Zeiss SESAM (Carl Zeiss NTS GmbH, Germany). In order to achieve high spatial coherence the illuminated semi-convergence angle was set to 30 µrad. The defocus was changed in a cubic fashion in order to have small defocus variations of 300 nm close to Gaussian focus and still span the range of -30 µm to +30 µm defocus. Inline holograms recorded at large defocus encode low spatial frequency information in the phase shift with better signal-to-noise properties than those with just a small defocus. A 7 eV energy-selecting slit was used to remove the contribution from inelastically scattered electrons. The full-resolution wave reconstruction (FRWR) code [5] has been used for the focal series reconstruction of the amplitude and phase of the exit face wave function. The resulting phase map is shown in Figure 1b. The spatial resolution was limited to 0.8 nm by the objective aperture but was sufficiently high to resolve the quintuple layers which are spaced 0.9 nm apart.

Figure 2a shows the potential profile across the (0001) surface of Bi_2Se_3. In our specimen prepared by ultramicrotomy this surface seems to always be covered by an amorphous layer. Extracting this layer and also removing the sharp potential increase expected for a crystallographically sharp onset of the mean inner potential, smoothed to the resolution determined by the objective aperture, we obtain the mean inner potential profile from the surface towards the inside of the specimen (Figure 2b).). In the presented work, these potential profiles will be discussed in detail.

1. Y. Xia, D. Qian, D. Hsieh, L. Wray, A. Pal, H. Lin, A. Bansil, D. Grauer, Y. S. Hor, R. J. Cava, and M. Z. Hasan, Nat Phys 5 (2009),p 398–402.
2. M. Z. Hasan and C. L. Kane, Rev. Mod. Phys 82 (2010), p 3045–3067.
3. H. M. Benia, C. Lin, K. Kern, and C. R. Ast, *Phys. Rev. Lett.* 107 (2011), p. 177602.
4. M. Bianchi, D. Guan, S. Bao, J. Mi, B. B. Iversen, P. D. C. King, and P. Hofmann, Nat Commun 1 (2010), p. 128.
5. C.T. Koch, Ultramicroscopy 108 (2008), p. 141–150.

6. The research leading to these results has received funding from the European Union Seventh Framework Programme [FP7/2007-2013] under grant agreement n°312483 (ESTEEM2).

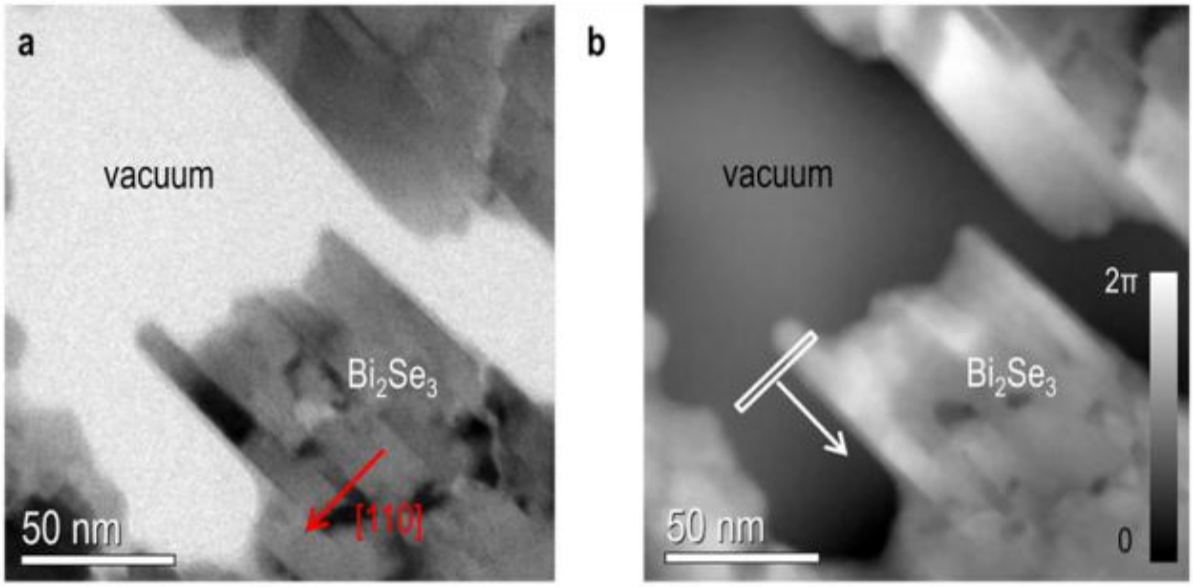

Figure 1 a) TEM bright-field image b) Phase map recovered using inline electron holography.

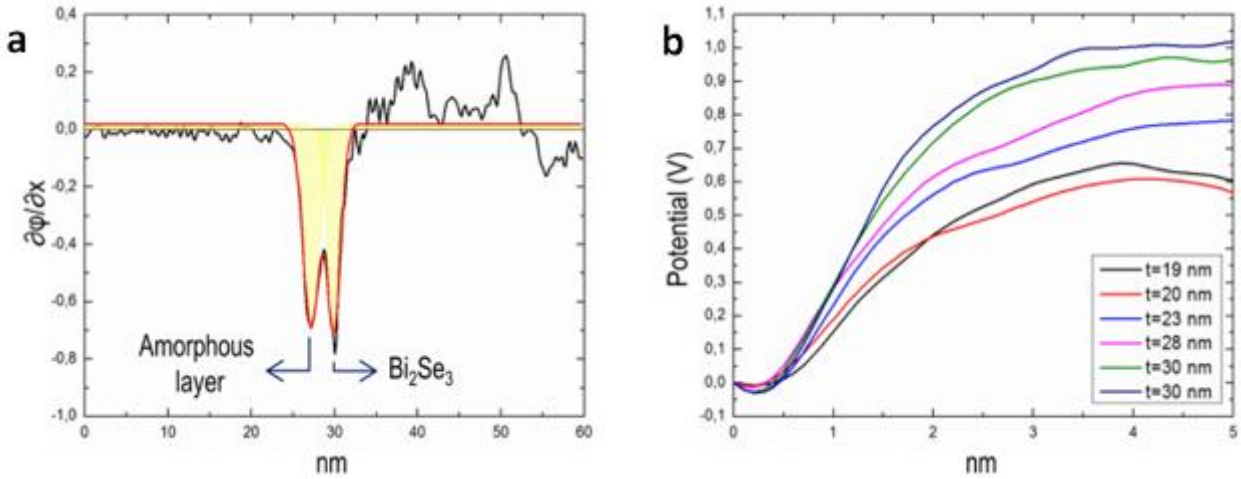

Figure 2 a) Profile of the gradient of the phase across the surface of the basal plane of Bi_2Se_3. b) Potential profiles from the surface towards the bulk material, after removing the potential step at the specimen surface.

Functional Materials

MS.3.P071
Analysis of crystal orientation in AlN layers grown on m-plane sapphire

A. Mogilatenko[1,2], J. Stellmach[3], M. Frentrup[3], F. Mehnke[3], T. Wernicke[3], M. Kneissl[3], M. Weyers[1]

[1]Ferdinand-Braun-Institut, Leibniz-Institut für Höchstfreqeunztechnik, Berlin, Germany
[2]Humboldt University of Berlin, Institute of Physics, Berlin, Germany
[3]Technische Universität Berlin, Institute of Solid State Physics, Berlin, Germany

Keywords: scanning nanobeam diffraction, III-nitrides, semipolar layers

Most of today's III-nitride based device heterostructures are grown along the c-axis direction of the wurtzite structure (so called c-plane layers). However, optoelectronic devices obtained on the basis of c-plane nitrides suffer from spontaneous and piezoelectric polarisation fields which appear in the noncentrosymmetric wurtzite structure along the polar c-axis. Thus, growth of so-called non-polar (i.e. m-plane (10-10) or a-plane (11-20)) as well as semipolar (i.e. (11-22), (10-13), etc.) nitride layers has been intensively investigated in the last decade [1]. Whereas most of the recent studies focus on the growth of nonpolar and semipolar GaN layers, less attention has been given to AlN. The AlN-based heterostructures are especially important for light emitters operating in deep ultra-violet (UV) spectral range (below 280 nm), which e.g. can be used for water purification, gas sensing and medical diagnostics.

Our study reports on the structure of AlN layers grown on m-plane (1-100) sapphire by metal organic vapour phase epitaxy. Using high-resolution transmission electron microscopy (HRTEM) and scanning nanobeam diffraction (SNBD) [2] we will show that variation of V/III ratio during the nitride deposition allows tuning of the layer orientation: from a preferentially oriented semipolar (11-22) AlN layer at a V/III ratio of 1050 to a layer consisting of differently oriented crystallites at a V/III ratio of 630.

Figure 1 shows three major orientations observed in the AlN layers on m-plane sapphire: semipolar {11-22}AlN and {10-13}AlN as well as non-polar m-plane {1-100}AlN. These orientations are present simultaneously in AlN layers grown at the V/III ratio of 630 (Fig. 2a) in accordance with XRD results. Basal plane stacking faults (BSF) are frequently observed in these crystallites with a different inclination angle depending on the crystallite orientation. The different crystallite orientation is visible in Fig. 2b showing exemplary crystallographic orientation maps obtained by SNBD. In the obtained images the (11-22)AlN layer appears at the interface to the sapphire substrate, whereas differently oriented crystallites are visible above this layer. We attribute the presence of a semipolar (11-22)AlN layer at the substrate interface to the projection effect in the TEM specimen and not to an initial formation of a uniformly (11-22)-oriented interfacial layer. Except for the (11-22)-orientation, all the other orientations present in the sample are governed by a common relationship along one direction, i.e. [11-20]AlN || [0001]Al_2O_3 (see the green coloured area in Fig. 2b), which has been previously observed in GaN layers [3]. This in-plane relation results in a lattice mismatch of about 4%.

An increase of the V/III ratio to 1050 leads to a predominant formation of (11-22)AlN layers with a BSF density of about $2\text{-}4\cdot10^5$ cm^{-1} (Fig. 3a). Atom force microscopy shows that these layers exhibit a complex surface morphology with a periodic undulation along [1-100]AlN and a number of additional dot like structures on the layer surface [4]. The lateral size and height of these dot-like structures strongly depend on the reactor pressure. Cross-sectional TEM analysis reveals that these structures can be attributed to differently oriented crystallites (Fig. 3b,c), which might randomly nucleate on the m-plane sapphire surface, coalesce with (11-22)AlN nuclei during the further growth and protrude from the surface of (11-22)AlN layers due to the different growth rates.

1. U. Schwarz, M. Kneissl, phys.stat.sol (RRL) 1 (2007), p. A44.
2. measured using ASTAR system of NanoMegas installed at TEM/STEM JEOL 2200 FS (FEG, 200kV)
3. P. Vennegues, T. Zmartin, N. Grandjean, J. Appl. Phys. 108 (2010), p.113521.

4. J. Stellmach, M. Frentrup, F. Mehnke, M. Pristovsek, T. Wernicke, M. Kneissl, J. Cryst. Growth 355 (2012), p. 59.

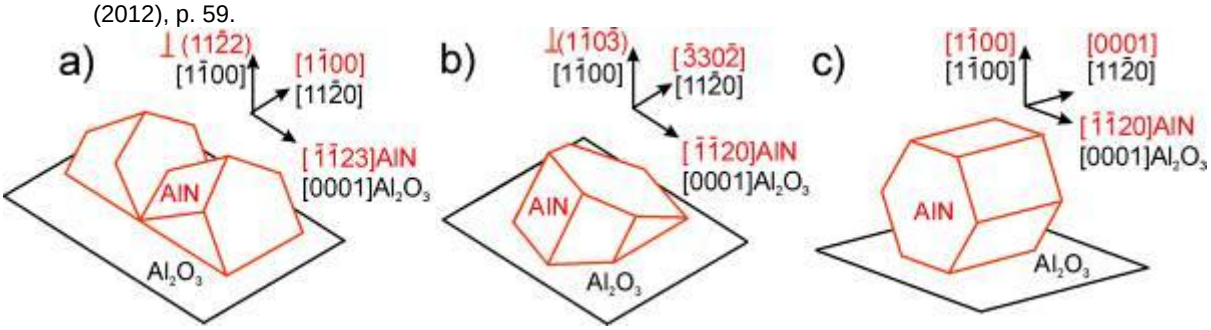

Figure 1. Sketch of different epitaxial orientation relations observed in AlN layers grown on m-plane sapphire: a) semipolar (11-22) orientation; b) semipolar (10-13) orientation; c) non-polar m-plane (1-100) orientation.

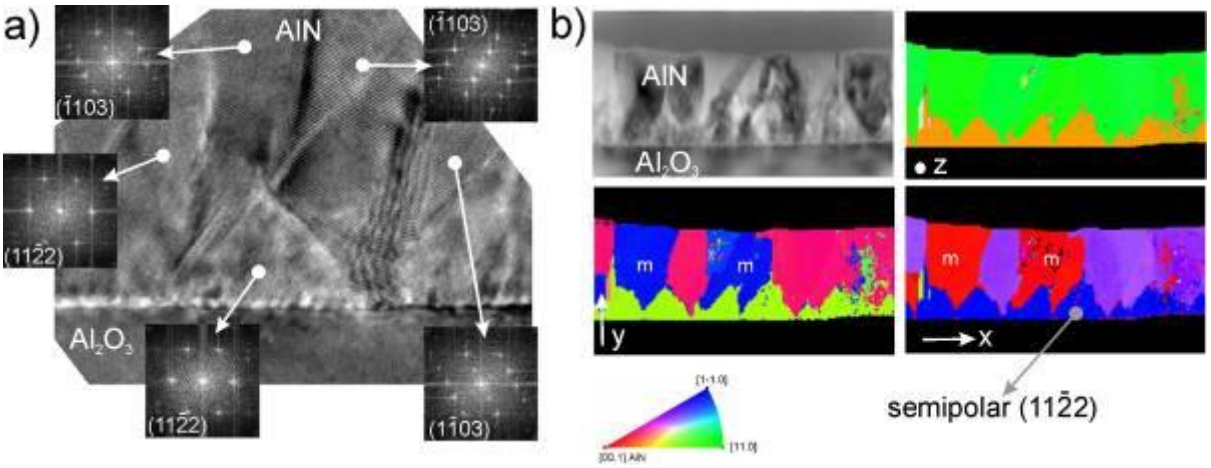

Figure 2. Structure of AlN layers grown on m-plane sapphire at a III/V ratio of 630: a) cross-sectional HRTEM image showing differently oriented crystallites (the different growth planes are indicated in the corresponding Fourier spectra); b) cross-sectional crystallographic orientation maps obtained by SNBD and the corresponding color zone selector (m-plane oriented crystallites are indicated in the maps).

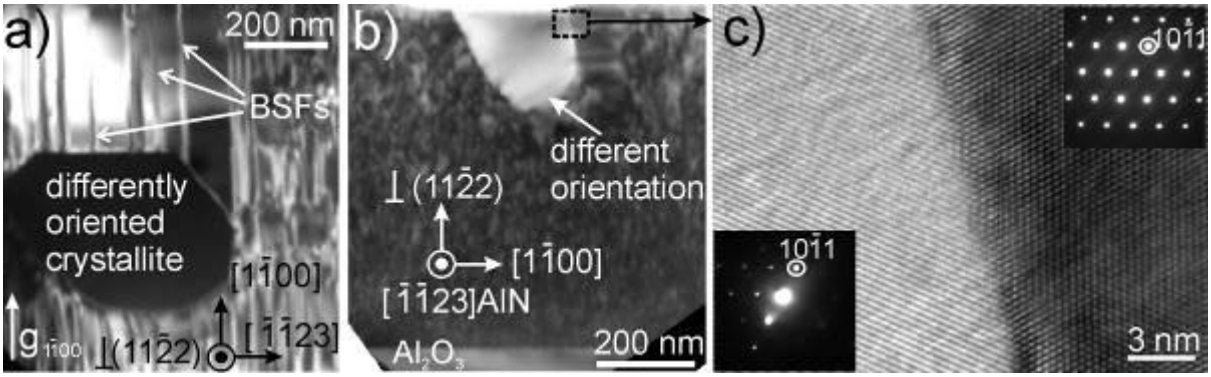

Figure 3. Structure of AlN layers grown on m-plane sapphire at a III/V ratio of 1050: a) plan-view dark-field image of (11-22)-oriented AlN layer containing BSFs and an embedded crystallite of a different orientation; b) cross-sectional bright-field image obtained in zone axis showing semipolar (11-22)AlN with an embedded crystallite of a different orientation; c) HRTEM image of a region marked in (b) with the corresponding diffraction patterns show that the crystallite is rotated in the (10-11) plane with respect to the semipolar (11-22)AlN matrix.

Functional Materials

MS.3.P072
Electron-beam-hardening of nanoscaled amorphous silica

M. Mackovic[1], E. Spiecker[1]

[1]Department of Materials Science and Engineering (WW7), Center for Nanoanalysis and Electron Microscopy, Erlangen, Germany

mirza.mackovic@ww.uni-erlangen.de
Keywords: nanoscaled amorphous silica, in situ transmission electron microscopy, mechanical testing

Materials are traditionally strengthened by controlled creation of internal defects and boundaries, which inhibit dislocation motion [1]. Such strategies unalterably compromise ductility, the ability of a material to plastically deform without fracture. Due to absence of long-range periodicity in amorphous materials dislocations are not available and therefore plasticity has to rely on other mechanisms that govern the irreversible deformation, such as local plastic rearrangements [2]. It was shown by in situ mechanical testing in a transmission electron microscope (TEM) that nanoscaled amorphous silica exhibits enormous ductility even at or near room temperature [3]. By means of molecular dynamics simulations the authors revealed an interesting mechanism, involving electron-beam-induced generation of structural and bonding defects that facilitate bond-switching events in the silica network, the rotation and reorientation of SiO_4 clusters, finally accommodating viscous flow.

Here we report on an experimental approach for hardening of nanoscaled amorphous silica, achieved by electron-beam irradiation inside of a TEM. The silica spheres investigated here were synthesized by the Stöber-Fink-Bohn (SFB) method [4], being monodisperse, amorphous and without any obvious impurities. The in situ compression in the TEM was carried out using a Hysitron Picoindenter^{TM} (PI-95), equipped with a flat punch. Before every in situ compression experiment, the silica spheres were irradiated with the electron beam (e-beam), using a specific beam current density and afterwards compressed either with or without e-beam irradiation. Displacement-controlled in situ compression under e-beam irradiation (beam on) confirmed severe ductility, without any evidence of shear banding or fracture, as shown in figure 1. These results agree well with the results reported previously by Zheng et al. [3], who used an identical experimental set-up and comparable in situ compression experiments of sol-gel derived silica spheres. Beyond that, we carried out in situ compression experiments, where the silica spheres were compressed without e-beam, after e-beam irradiation with different beam current densities (see figure 2). After specific e-beam irradiation the e-beam was switched off and the compression was carried out at different times (beam-off 30 and 300 s) after switching off the e-beam. In particular, by using such experiments, the aim was to show the impact of specific beam current densities and the e-beam effect on time scale on the deformation behavior of the silica spheres. As can be seen in figure 2 the load-displacement curves for beam-off experiments clearly show that the silica spheres exhibit more elasticity and less plasticity, compared with beam on experiments (see figure 1). This is not surprising, since the e-beam softens the silica spheres and thus enables more plastic flow. More interesting is the comparison of the maximum loads for different beam-off experiments and for low and high beam current densities (see bottom in figure 2). Namely, using a low beam current density during e-beam irradiation, followed by a compression with beam off (A in figure 2) significantly lower maximum loads are observed, compared to the experiments, where the silica spheres are irradiated with a higher beam current density (B in figure 2) and compressed with beam off. Even if the compression was carried out after 300 s beam off (C in figure 2) the maximum loads were in a comparable range as in the case for 30 s beam off. This clearly indicates that the e-beam makes the silica permanently stronger. Moreover, our results suggest that the hardness of nanoscaled amorphous silica spheres can be tuned selectively by using a specific e-beam irradiation, by a selective choice of the beam current density.

The results in the present study may help for tuning and improvement of the mechanical stability of amorphous silica, where functionality and mechanical resistance is needed at the same time.

1. K. Lu, L. Lu, S. Suresh, *Science* 324 (2009) 349-352.
2. M. Tsamados, A. Tunguy, C. Goldenberg, J.L. Barrat, *Physical Review E* 80 (2009) 026112-1-17.
3. K. Zheng, C. Wang, Y.Q. Cheng, Y. Yue, X. Han, Z. Zhang, Z. Shan, S.X. Mao, M. Ye, Y. Yin, E. Ma, *Nature Communications* 1 (2010) doi:10.1038/ncomms1021.
4. W. Stöber, A. Fink, E. Bohn, *Journal of Colloid and Interface Science* 26 (1968) 62-69.
The authors would like to thank M. Hanisch and R.N. Klupp-Taylor for providing the silica spheres. The financial support by the German research foundation (DFG) via the priority program SPP 1594

"Topological Engineering of Ultra-Strong Glasses" and the Cluster of Excellence EXC 315 "Engineering of Advanced Materials" is gratefully acknowledged.

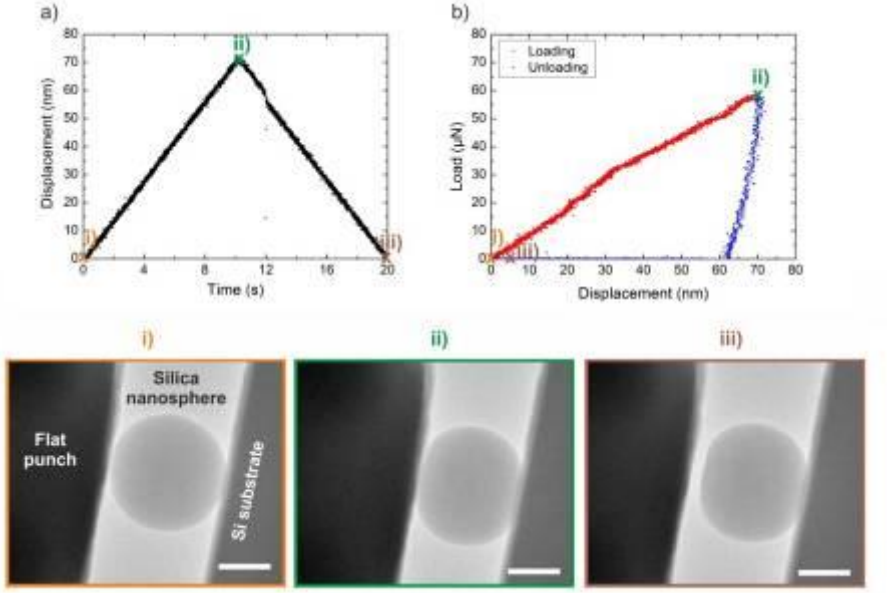

Figure 1. Displacement-controlled in situ compression of silica nanospheres under electron beam irradiation (beam on). In a) the used displacement profile is shown, while b) shows the simultaneously acquired load-displacement data. TEM images i-iii) are extracted from the in situ movie at different stages of the compression experiment, as marked in a) and b), respectively. The scale bars are 200 nm.

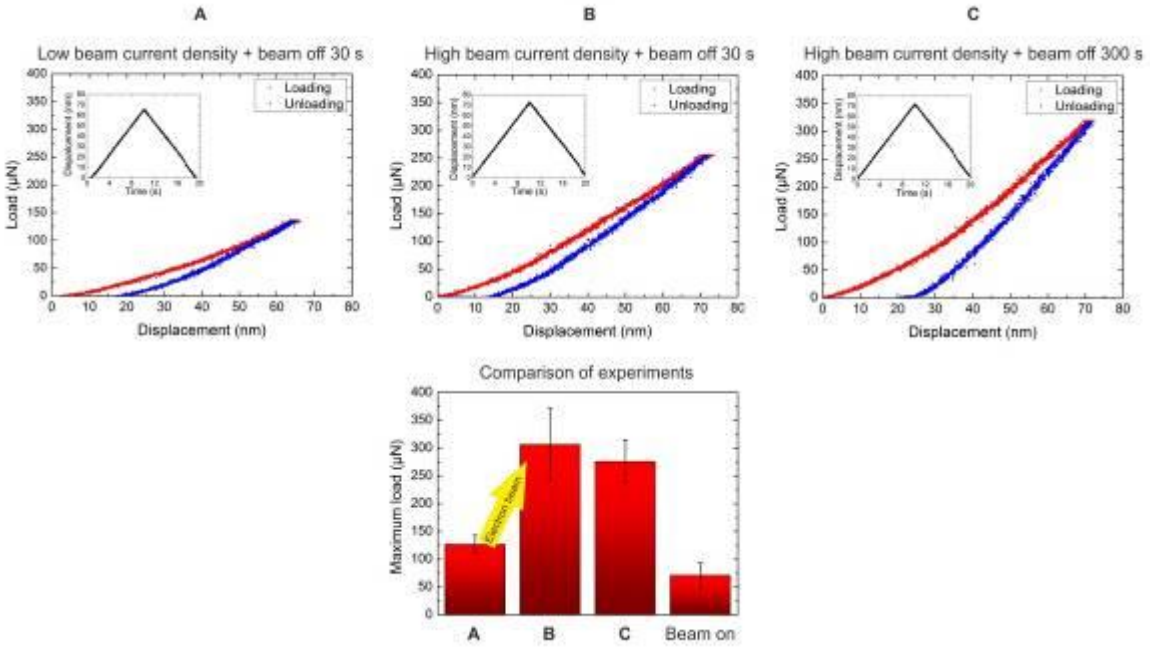

Figure 2. Displacement-controlled in situ compression of silica nanospheres without electron beam irradiation (beam off), after illumination with different beam current densities: A) illumination with low beam current density and compression after beam off 30 s; B) illumination with high beam current density and compression after beam off 30 s; C) illumination with high beam current density and compression with beam off 300 s. The used displacement profiles are shown as insets in A, B and C. The figure at bottom compares the different experiments (A, B and C), while also the beam on experiments are plotted as reference.

Functional Materials

MS.3.P073
TEM and other chracterizations of $PbNb_2O_6$ for high temperature piezoelectric applications

U. De[1]

[1]Kendriya Vihar, C-4/60, Kolkata, India

ude2006@gmail.com

Materials with much higher Curie temperature than that of presently popular piezo-electric materials like barium titanate ($BaTiO_3$) and lead zirconate titanate (PZT) are often needed. A high temperature piezo-electric material like Lead Meta-Niobate, $PbNb_2O_6$ (PNO), must be used in the ultrasonic imaging system that can "view" nuclear fuel rods under molten metal (often, liquid sodium) in a Fast Breeder Reactor (FBR). This helps eliminate mis-alignment of the rods and ensures highrer safety of FBRs that simultaneously produce energy and nuclear fuel. One has to look for such fuels due to the limited stock of natural uranium globally and some countries in particular. PNO is piezoelectric only in its orthorhombic phase. It is one of the potential functional materials – in form of sensors and actuators – also for other high temperature applications like car exhaust. We have perfected the steps for the preparation of the meta-stable orthorhombic PNO, avoiding the competing rhombohedral phase and other compounds, leading to Curie temperatures (vide next paragraph), higher than those in recent reports. Check of no second phase has been concluded from XRD Rietveld Analysis and, at granular level, by High Resolution Transmission Electron Microscopy (TEM) on different grains. We discovered that starting materials govern the end product in PNO preparation. Microstructure of our ceramic PNO in orthorhombic and rhombohedral phases has been studied. Lattice planes and ferroelectric domains show up clearly in TEM pictures. Real part, Z´, and imaginary part, Z˝, of electrical impedance, Z, (related to real and imaginary parts of permittivity) have been measured in an Impedance Spectrometer - up to ~ 700 ºC over 20 Hz to 5.5 MHz range. The real part of permittivity peaks sharply, at (580 ± 1)°C at 5.5 MHz and at (573 ± 1)°C at 20 Hz, indicating the Curie Temperatures. Differential Scanning Calorimetry [1] showed an interesting endothermic minimum at ~ 570ºC during heating in orthorhombic PNO but not in non-piezoelectric (rhombohedral) PNO, confirming the Curie temperature. Electron diffraction rings from the two phases (Figure 1) are indeed very different, and the symmetry of the pattern is lower in the rhombohedral sample than in the orthorhombic sample.

1. K.R. Sahu, and Udayan De, Thermochimica Acta 2009; 490: 75.

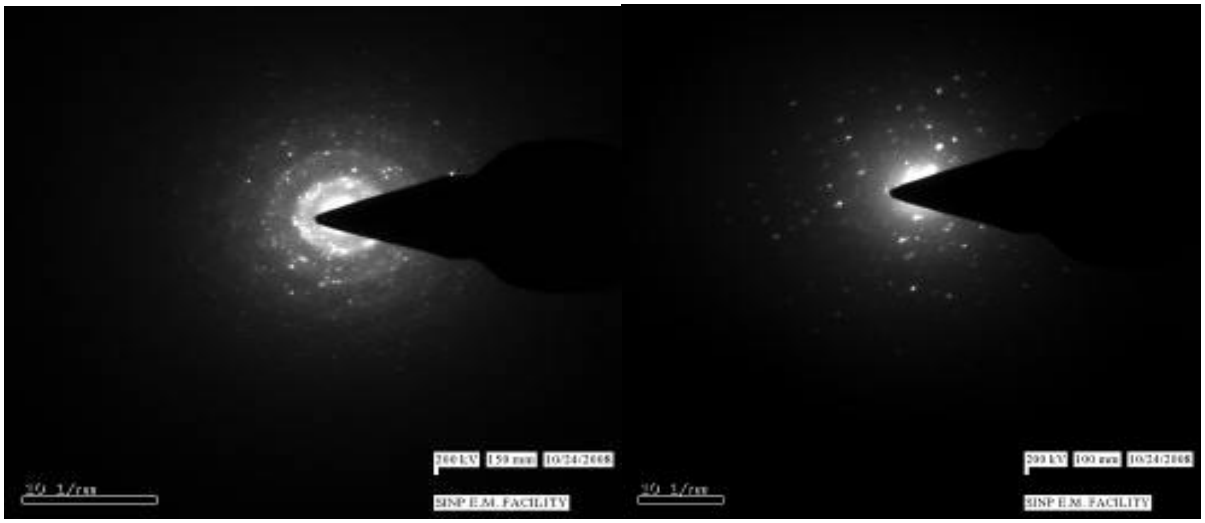

Figure 1. Diffraction rings seen by 200 kV Transmission Electron Microscopy of orthorhombic PNO (left figure) and of rhombohedral PNO (right figure).

Functional Materials

MS.3.P074
Characterization of ZnO nanowire arrays obtained using a template assisted approach.

K. Bejtka[1], A. Chiodoni[1], M. Fontana[1], C. Ottone[1], V. Farías[1], V. Cauda[1], C.F. Pirri[1,2]

[1]Italian Institute of Technology, Center for Space Human Robotics, Torino, Italy
[2]Politecnico di Torino, Department of Applied Science and Technology, Torino, Italy

katarzyna.bejtka@iit.it
Keywords: metal oxide, ZnO, nanowire, nanowire arrays, template assisted growth, electron microscopy

Semiconductor oxides have attracted much attention as they possess a range of interesting properties, making them suitable for a variety of applications, including piezoelectric field-effect transistors and diodes, self-powered nano-generators and nano-sensors [1].

ZnO is considered a very important semiconductor because of its wide bandgap, good optical, electrical and piezoelectric properties [2]. This material can be grown in a reproducible way with a variety of nanostructures, e.g. nanowires (NWs), nanorings, nanobows and other forms. This variety provides a range of peculiar properties that are unique for many applications in nanotechnology [3].

Recently, ZnO nanowires have been synthesized using porous templates (e.g. anodic alumina or polycarbonate) with different methods, such as electrodeposition [4], sol-gel [5] and electrophoresis [6]. The use of templates in combination of these methods results in the growth of nanowires with diameter above 50 nm. The wire diameter can be further controlled by combining two templates, e.g. anodic alumina with mesoporous silica (4-12 nm in diameter).

In this study we report on the characteristics of ZnO nanowires synthesised by combining the use of the template approaches described above with a low temperature aqueous chemical growth method [7]. The growth mechanism of nanowires will be discussed and the Field Emission Scanning Electron Microscopy (FESEM) and Transmission Electron Microscopy (TEM) characterization will be shown.

The first type of structures uses commercial and self-anodized alumina membranes with pore diameter 200-300 nm and 50 nm, respectively. FESEM images reveal the complete filling of the template channels and an enlargement of their diameter, producing NWs with larger diameter than the respective template. The X-ray spectrum reveals that the structure corresponds to ZnO and crystalline alumina. The TEM images of a single NW show that the external side of the NW is amorphous. The template can be removed by chemical etching with sodium hydroxide, whilst the NWs maintain the template shape. However, the etching attacks the nanostructured material surface, generating a granular surface, as inferred from the SEM micrograph in figure 1.

The second group of structures, which uses flexible polycarbonate membrane (150-200 nm pore size) shows inert behavior during the synthesis, yielding to a wurtzite crystalline ZnO NWs, as evident by both X-ray and electron diffraction pattern at TEM.

In the third group of structures the wire diameter was reduced by use of double templating of self-anodized alumina membranes with mesoporous silica. Figure 2 shows TEM characterisation revealing that small crystals are formed in the pores of the mesoporous silica. The size of these nanocrystalline structures is below 5 nm.

This study demonstrates that the template-assisted method allows the filling of a variety of porous matrices with ZnO when inert templates take part. In contact with the alumina surface the precursor solution reacts with the template and a mixture of crystalline Al_2O_3 and ZnO fills the amorphous alumina channels. The interface between the two oxides phases is at present not well understood.

1. M. Choi, D. Choi, M-J. Jin, I.S. Kim, S-Y. Kim, J-Y. Choi J-Y, et al. Adv. Mater. 21 (2009), p. 2185.
2. C. H. Liu, W. C. Yiu, F. C. K. Au, J. X. Ding, C. S. Lee, and S. T. Lee, Appl. Phys. Lett. 83 (2003), p. 3168.
3. R. Mohammed, J. Song , O. Nur , Z.L. Wang, and M. Willanderet, Adv. Funct. Mater. XX (2010), p. 1.
4. M. J. Zheng, L.D. Zhang, G.H. Li, W.Z. Shen, Chemical Physics Letters 363 (2002), p. 123.
5. G. S. Wu, T. Xie, X.Y. Yuan, Y. Li, L. Yang, Y.H. Xiao and L.D.Zhang, Solid State Comm. 134 (2005), p. 485.
6. Y. C. Wang, I.C. Leu, M.H. Hon, J. of Appl. Phys. 95 (2004), p. 1444.
7. X. Hu, Y. Masuda, T. Ohji, K. Katoet, Thin Solid Films 518 (2009), p. 906.

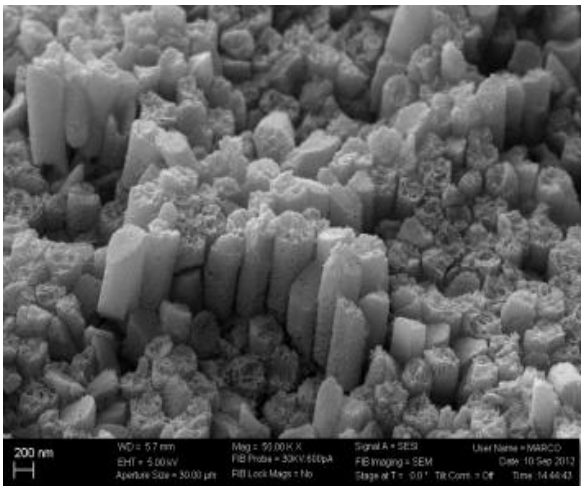

Figure 1. SEM image showing the morphology of the ZnO-Al_2O_3 NWs after template etching.

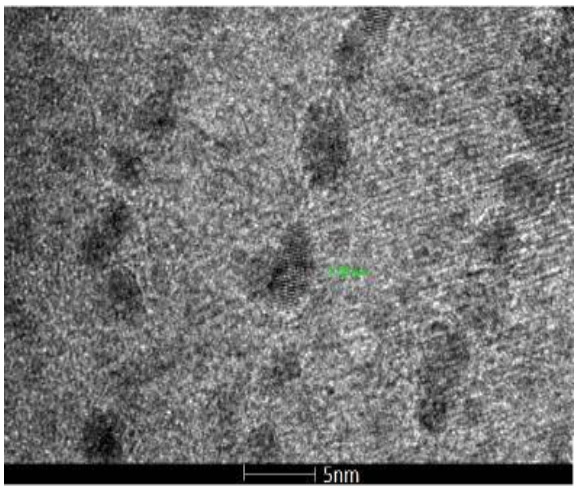

Figure 2. TEM micrograph showing the cross sectional view of vertically oriented ZnO nanowire array.

Functional Materials

MS.3.P075
Towards the 3D investigation of pore space in molecularly imprinted polymers (MIPs)

G. Neusser[1], S. Eppler[1], P. Walther[2], B. Mizaikoff[1], C. Kranz[1]

[1]University Ulm, Institute of Analytical and Bioanalytical Chemistry, Ulm, Germany
[2]University Ulm, Central Facility of Electron Microscopy, Ulm, Germany

Molecular imprinted polymers (MIPs) are polymer films or polymer particles containing selective binding sites for an analyte molecule (so-called template) within the synthetic polymer network [1]. The template molecules are mixed with functional monomers, which are able to interact with the template, forming a so-called pre-polymerization complex. These complexes are co-polymerized in the presence of crosslinker monomers. After polymerization, the template molecules are removed, resulting in a rigid polymer network with binding sites, which are complementary in size, shape and functionality to the template molecule. These binding pockets are highly selective for the template molecule, and hence many applications like specific sensing layers, imprinted membranes, selective extraction matrices for separation and chromatography and antibody mimicking can be envisaged [1].

The pore space and interconnectivity of pores are crucial for the efficiency of MIPs. Pore volume, diameter and surface area are usually investigated by Brunauer-Emett-Teller (BET) measurements [2] of bulk samples. Transmission Electron Microscopy (TEM) was used in an attempt to visualize binding pockets [3], however the structure of pores within a specific MIP and the imaging and investigation of interconnectivity has not yet been demonstrated.

In this study we present first results towards the investigation and visualization of pore space in MIP particles using focused ion beam – electron microscopy (FIB/SEM) tomography. As a model MIP the beta-blocker drug propranolol was imprinted using methacrylic acid as functional monomer and divinylbenzene (DVB) or a mixture of DVB and ethylenglycoldimethaacrylate (EGDMA) as crosslinker with azobisisobutyronitrile as radical initiator to create a bulk polymer. Adding EGDMA as a second crosslinker yields a polymer with modified structure and polarity. In addition, as a control non-imprinted polymers (NIP) were prepared in absence of the template molecule, respectively. After grinding and sieving, the MIP particles were treated with osmium tetroxide and uranyl acetate using freeze substitution and Epon embedding [4,5] to enhance contrast in secondary electron (SE) images. This procedure is usually applied for biological samples and was used here to visualize of pore space and reduce adverse effects due to local heating.

Prior to the 3D investigations using auto slice & view routine, several embedded MIP particles were examined by cross-sectioning perpendicular to the surface (Fig 1, B- F). SE images show contrast between the Epon and the polymer matrix of the MIP (cloudy dark and bright areas), with the MIP polymer blotched by bright spots. The bright spots can be attributed to the metal loading (Os and U).

Figure 2 shows a 3D model of a reconstructed section of a MIP particle. The pores seem to be elongated with a limited interconnection between the pores, which may be attributed to the embedding and preparation process. Hence, alternative sample preparation will be presented in order to enhance the contrast between polymer matrix and Epon epoxy and therefore improving the visualization of the pore space.

1. F. Meier, B. Mizaikoff, in Artificial Receptors for Chemical Sensors, (2010), 391-437. (Ed.: Vladimir M. Mirsky, Anatoly K. Yatsimirsky).
2. A. M. Rosengren, B. C. G. Karlsson, I. A. Nicholls, Int. J. Mol. Sci.,14, (2013) 1207-1217.
3. D. M. Hawkins, E. A. Ellis, D. Stevenson, A. Holzenburg, S. M. Reddy, J. Mater. Sci. 42 (2007) 9465-9468
4. C. Villinger, H. Gregorius, C. Kranz, K. Hoehn, C. Muenzberg, G. von Wichert, B. Mizzaikoff, G. Wanner, P. Walther, Hist. Cell Biol. 138/4 (2012) 549- 556
5. C. Walther, A. Ziegler, J. Microsc. 208 (2002) 3-10.

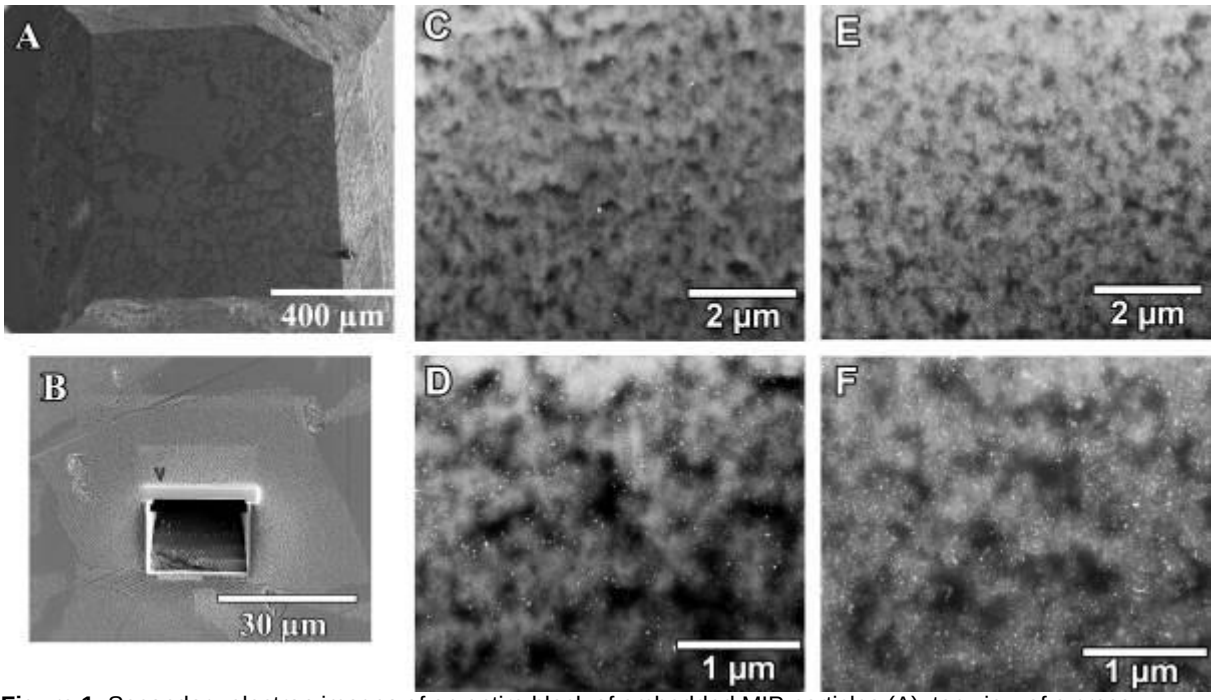

Figure 1. Secondary electron images of an entire block of embedded MIP particles (A), top view of a cross-section within a MIP particle (B), exemplary images of the front of cross-sections in different MIP particles showing pore space (dark areas) and local enrichment of Os and U: MIP polymerized by DBV only (C&D), MIP polymerized with a mixture of DBV and EGDMA (E&F).

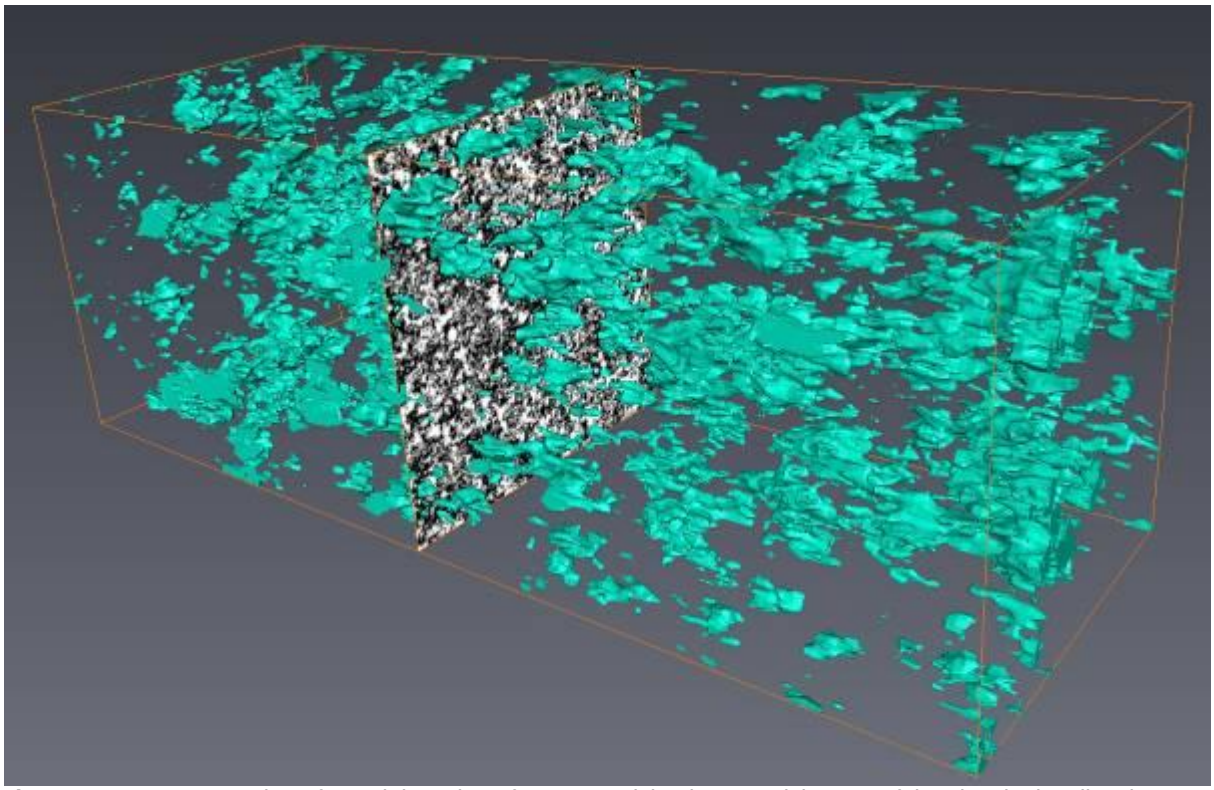

Figure 2. 3D reconstruction of a serial section of a MIP particle, the greenish parts of the sketch visualize the pores: length of the box 1.4 x 1.4 x 3.7 µm, MIP polymerized with a mixture of DBV and EGDMA.

Functional Materials

MS.3.P076
Acquisition of EEL spectra of the Si-III, Si-IV and Si-XII high-pressure phases

M. Schade[1,2], F. Heyroth[2], H.S. Leipner[2]

[1]Martin-Luther-Universität Halle-Wittenberg, Zentrum für Innovationskompetenz SiLi-nano, Halle, Germany
[2]Martin-Luther-Universität Halle-Wittenberg, Interdisziplinäres Zentrum für Materialwissenschaften, Halle, Germany

Under stresses larger than 10 GPa, crystalline silicon (Si-I) undergoes phase changes resulting in metastable high-pressure phases (HPP) [1]. During both indentation and scratching experiments, pressures of up to 12 GPa can be achieved, whereas after unloading the metastable Si-III, Si-IV and Si-XII phases can be formed. Since these structures exhibit different structural and electric properties, a fundamental knowledge of them is necessary in order to investigate their industrial applicability. Furthermore, silicon high pressure phases have been found after fs-laser irradiation of crystalline silicon [2] or the annealing of amorphous silicon (a-Si) [3], respectively. Since their localization via electron diffraction methods is possible but challenging, a more convenient way may be the use of a spectroscopic method like electron energy loss spectroscopy (EELS). Its main advantage is the changed fine structure of the Si $L_{2,3}$ edges comparing a-Si, Si-I and the diverse HPPs. However, the preparation of electron transparent samples is quite difficult due to the reverse transformation of the HPPs at temperatures above 175 °C. Silicon HPPs have been prepared by means of scratching or indentation of Si(100) surfaces applying slow unloading rates lower than 1.5 mN/s. Afterwards, the formation of the Si-III and Si-XII phases has been verified by registering loading-displacement curves as well as by Raman spectroscopy. The EELS investigations have been performed in a VG HB 501 UX scanning transmission electron microscope equipped with a Gatan ENFINA 1000 parallel electron energy loss spectrometer. The microscope was operated at an acceleration voltage of 100 kV. Ultra-thin samples (thickness < 60 nm) were necessary in order to achieve a sufficient spectral intensity. The electron transparent preparation of the samples has been described in [4]. Best samples have been achieved using focused ion beam (FIB) technique and classic plan view preparation including pulsed Ar^+ ion milling, respectively. The prepared samples were first inspected by electron diffraction in order to verify the presence of the silicon HPPs in the ultra-thin sample regions. Due to their particular crystal structures, each HPP exhibit unique lattice plane distances that are different from those of the phase Si-I. This is clearly visible in the diffraction pattern in Figure 1 acquired from a crystallite in the Si-XII phase. After preparation, the plan view samples exhibited mainly the Si-III and Si-XII phases, whereas the FIB samples contained mainly the Si-IV and Si-XIII phases. Both latter phases transformed from the two former ones due to local heating of the samples above 175 °C during Ga^+ ion milling inside the FIB machine. Subsequently, all samples were investigated by EELS. Therefore, EEL spectra of the Si $L_{2,3}$ edge of a-Si and the phase Si-I have been acquired at first as a reference since these both and the HPPs coexist in the investigated sample volume (cf. Figure 2). The spectra experimentally acquired from the various HPPs have been compared to *ab initio* density functional theory calculations. This results in both the assignment of the individual peaks in the acquired EEL spectra and the evaluation of the threshold energies for each investigated high pressure phase. Hence, different Si HPPs can be distinguished using EELS.

1. A. George, Properties of Crystalline Silicon, INSPEC, London, 1999, p.104.
2. M. Schade, O. Varlamova, J. Reif, H. Blumtritt, W. Erfurth, H. S. Leipner, Anal. Bioanal. Chem. 396 (2010) 1905.
3. T. Mchedlidze, M. Beigmohamadi, B. Berghoff, R. Sohal, S. Suckow, T. Arguirov, N. Wilck, J. Mayer, B. Spangenberg, M. Kittler, Phys. Status Solidi A 208 (2011) 588.
4. M. Schade, W. Fränzel, H. S. Leipner, Materials Science Forum Vol. 725 (2012) pp 199-202
5. We kindly acknowledge the help from B. Haberl (ANU Canberra) with indentation experiments.
6. We kindly acknowledge financial support by the BMBF under grant No. 03 SF 0352.

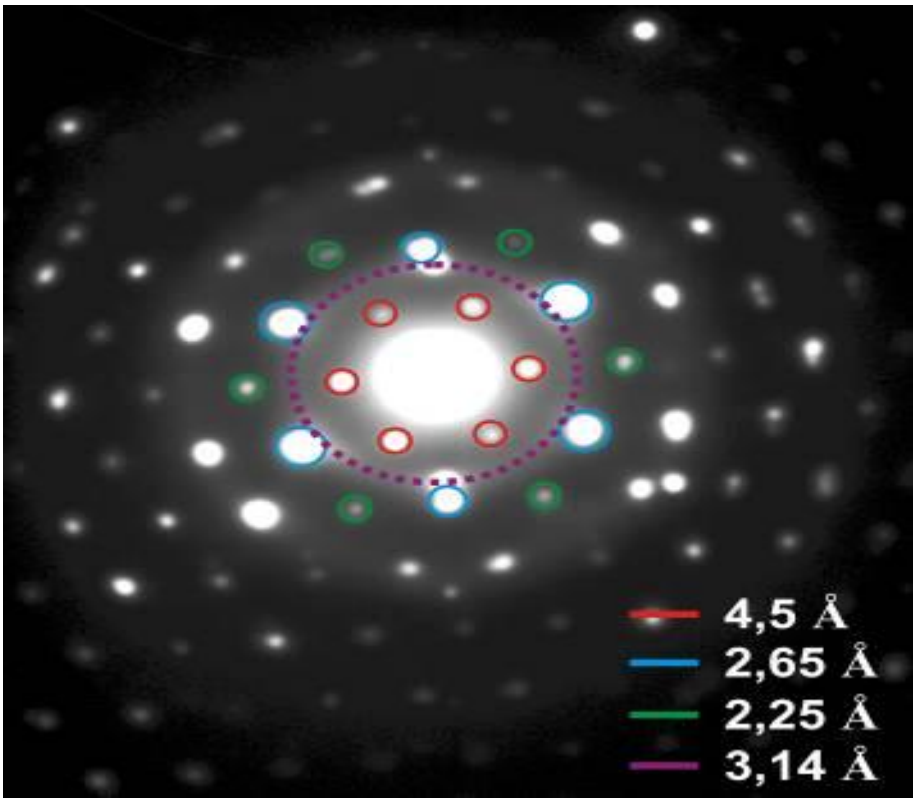

Figure 3. Diffraction pattern of a crystallite in the Si-XII phase. The purple circle indicates {111} planes of the Si-I phase.

Functional Materials

MS.3.P077
Morphological and Compositional Analysis of Organic LEDs with Silicon QDs as Active Layer (SiLEDs)

C. Kübel[1,2], M.-F. Florian[3,4], R. Julia[5], A.K. Powell[5], G.A. Ozin[6,4], U. Lemmer[3,4]
V.S.K. Chakravadhanula[7]

[1]Karlsruhe Nano Micro Facility (KNMF), Eggenstein-Leopoldshafen, Germany
[2]Karlsruhe Institute of Technology (KIT), Institute of Nanotechnology (INT), Eggenstein-Leopoldshafen, Germany
[3]Karlsruhe Institute of Technology (KIT), Light Technology Institute (LTI), Karlsruhe, Germany
[4]Karlsruhe Institute of Technology (KIT), DFG Center for Functional Nanostructures (CFN), Karlsruhe, Germany
[5]Karlsruhe Institute of Technology (KIT), Institute of Inorganic Chemistry, Karlsruhe, Germany
[6]University of Toronto, Department of Chemistry, Toronto, Canada
[7]Helmholtz Institute Ulm for Electrochemical Energy Storage / Kalrsruhe Institute of Technology, Institute of Nanotechnology, Eggenstein-Leopoldshafen, Germany

cvskiran@kit.edu
Keywords: Organic LEDs, Silicon QDs, SiLEDs

Quantum dot light emitting diodes (QD-LEDs) feature great scientific and economic potential. Compared to their purely organic counterparts, the organic emissive layer of these devices is replaced by solution-processable functionalized quantum dots (QDs). QDs and QD-LEDs feature a wide spectral tunability and high color purity. Furthermore, as the efficiency of these devices is not intrinsically limited by spin statistics as in case of purely organic LEDs, they have the potential to reach much higher efficiencies. This, together with recently reported all-inorganic QD-LEDs without need for encapsulation, shows the great potential of this novel generation of LEDs in terms of efficiency and stability of the devices.

Even though a lot of work has been published on QD-LEDs, including the young field of silicon quantum dot based light emitting diodes (SiLEDs) [1], an in-depth study of the morphological properties of full devices before and after device operation is lacking in literature. Nevertheless, it is crucial to learn more about the degradation processes in order to further improve on the currently limited device life times. For purely organic LEDs, device failure is often related to migration or diffusion of elements forming non-conductive barriers, which lead to higher internal resistance and, as a consequence, destroy the device. However, no comparable data is available on the degradation properties related to morphological or compositional changes in QD-LEDs.

Here, we describe the results of a complete morphological and compositional study of SiLEDs using an image corrected FEI Titan 80-300 operated at 300kV. Initial BF-TEM and HAADF-STEM imaging was performed under strict low-dose conditions (dose <100 e/nm²), but as the morphology of the organic multilayers is stable even at significantly higher doses, a more detailed compositional analysis by EFTEM and STEM-EDX mapping could be performed for the various 2.5-35 nm thick organic layers. The resulting elemental distribution for C, N, O, S, Si and F is in very good agreement with the nominal composition of the different layers (Figure 1 and 2).

A comparison of as fabricated and electrically driven SiLEDs as well as SiLEDs prepared using monodisperse and polydisperse SiQDs [2] has been carried out to correlate morphological and compositional features with the degradation behavior and was combined with electroluminescence and photoluminescence life time studies. This analysis showed that the morphology and composition of the SiLED is very well preserved during normal operation of the devices even though the electroluminescence is reduced to 20% during this operation, which is attributed to atomic scale processes within the SiQDs themselves. In contrast, at high voltage/current, significant electromigration of SiQDs into the hole blocking layer TPBi is observed, whereas no change for the other organic layers is observed. For non-size separated SiQDs, device life times are significantly reduced compared to SiLEDs build from monodisperse SiQDs. This seems to be related to both percolating path of larger nanoparticles inside the SiQD layer as well as diffusion/electromigration of extremely small nanoparticles into the hole blocking layer. We expect that these results are not only valid for SiLEDs but also transferable to other QD-based LEDs.

1. F. Maier-Flaig, M. Stephan, T. Bocksrocker, M. Bruns, C. Kübel, J. Rinck, A.K. Powell, G.A. Ozin, U. Lemmer, Nano Lett., 13 (2013),475-480; DOI: 10.1021/nl3038689.
2. M. Mastronardi, F. Maier-Flaig, D. Faulkner, E. Henderson, C. Kübel, U. Lemmer, G.A. Ozin, Nano Lett., 12 (2012), 337-342; DOI: 10.1021/nl2036194.

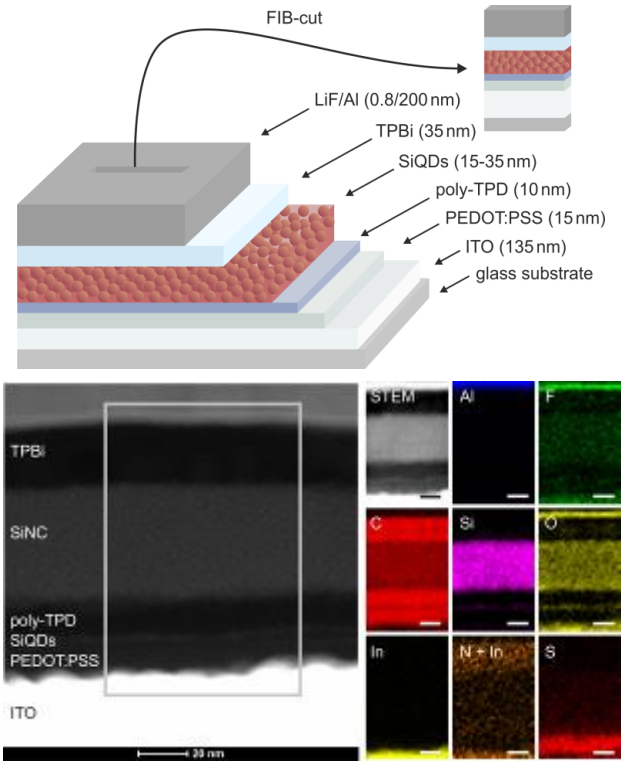

Figure 1. Schematic representation of the SiLED stack and HAADF-STEM cross-section image with corresponding EDX maps (scale bars 20 nm)

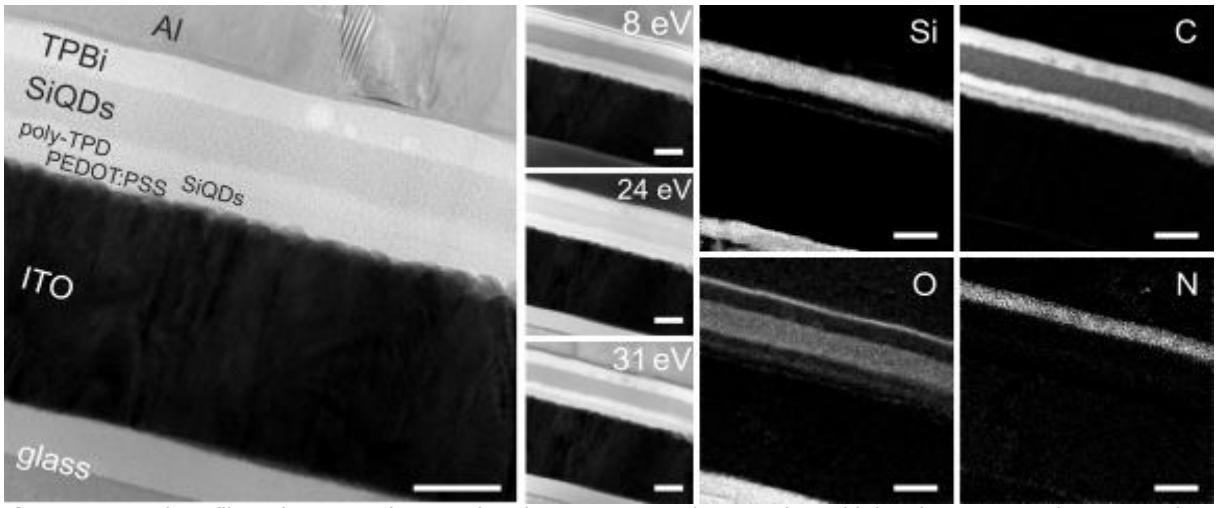

Figure 2. Zero-loss filtered BF-TEM image of a SiLED cross-section together with low-loss EFTEM images and elemental maps for silicon, carbon, oxygen and nitrogen (scale bars 50 nm).

Functional Materials

MS.3.P078
Crystallisation and boron redistribution in CoFeB / MgO systems with Ru and Ta cap layers for magnetic tunnel junctions during annealing studied by HRTEM and EELS

H. Schuhmann[1], P. Peretzki[1], M. Walter[2], V. Zbarskyy[2], M. Seibt[1], M. Münzenberg[2]

[1]Universität Göttingen, IV. Physikalisches Institut, Göttingen, Germany
[2]Universität Göttingen, I. Physikalisches Institut, Göttingen, Germany

schuhmann@ph4.physik.uni-goettingen.de

In recent years, magnetic tunnel junctions (MTJ) with crystalline MgO tunnel barrier and amorphous CoFeB (a-CoFeB) electrodes received much attention. Due to their large tunnelling magnetoresistance (TMR) ratio at room temperature, they are used as sensor element for harddrive read heads.

For industrial application the use of amorphous electrodes in MTJ is favorable due to its better growth flexibility. After annealing at temperatures up to 600°C [1] high TMR were achieved because of partial crystallization of the a-CoFeB. During annealing, boron atoms diffuse out of the CoFeB into adjecent layers which is a prerequisite for its crystallization into bcc CoFe using the MgO as a template [2]. Hence, a-CoFeB crystallization can be controlled by choosing cap layers acting as a boron sink or diffusion barrier. Here, the influence of the cap layer material on boron redistribution was studied by electron energy loss spectroscopy (EELS) and on the crystallization process of a-CoFeB by HRTEM. This study was applied to a model system consisting of a MgO substrate, electron-beam sputtered MgO (5nm), CoFeB (5nm or 100nm) and capped by respectively a 10nm Ru layer or a 10nm Ta + 3nm Ru layer. TEM images of samples with thick CoFeB layers (Figure 1) show a crystalline bcc (001) CoFe region at the interface to the MgO and, in the case of the Ru cap, an additional polycrystalline layer at the interface to the hcp-Ru layer. No noticeable EELS B-K-signal is observed in the MgO or at its interface region. In samples with thin layers (Figure 2), a-CoFeB also crystallizes into bcc CoFe at the interface to the MgO. Furthermore, the MgO and the MgO interface region did not show any presence of boron or boronoxide in EELS (Figure 3), which has been concluded as a prerequisite for high TMR [3]. This B and BO_x segregation is often found in MTJ systems with a radio frequency sputtered MgO barrier [2,4-6]. In contrast to the thick CoFeB sample, an approximately 1nm thick amorphous interlayer between c-CoFe and the Ru cap layer is visible, consisting of non crystallized CoFeB. Here, the Ta+Ru cap layer sample did not show this amorphous interlayer and the CoFeB is completely crystallized in bcc (001) CoFe. The boron diffuses from the CoFeB into the adjacent Ta layer were the boron concentration decreases rapidly with distance to the CoFe. This high boron concentration is not visible in the Ru cap layer sample. From these measurements it can be concluded that Ru serves as a diffusion barrier for boron. As a consequence, boron accumulates in an amorphous interlayer in absence of another boron sink. Ta, however, seems to be a sink for boron which promotes CoFeB crystallization into a fully crystalline layer. In summary, we can conclude that our e-beam sputtered MgO barriers are free of any B or BO_x contamination which leads to a high TMR. In addition, it was shown that Ta sputtered on a-CoFeB is a cap layer material which does not disturb the crystallization process of CoFe during annealing and acts as an important sink for boron.

1. S. V. Karthik *et al*, J. Appl. Phys. 111 (2012), 083922
2. D. K. Schreiber *et al*, J. App. Phys. 109 (2011)103909
3. J. D. Burton *et al*, Appl. Phys. Lett., 89, (2006) 142507
4. J. J. Cha *et al*, Appl. Phys. Lett. 91 (2007) 062516
5. J. J. Cha *et al*, Appl. Phys. Lett. 95 (2009) 032506
6. S. V. Karthik *et al*, J. Appl. Phys. 106 (2009) 023920

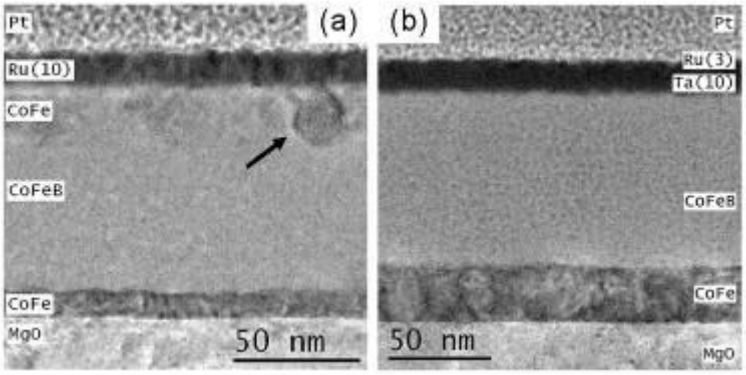

Figure 1. TEM images of samples with thick CoFeB layer with Ru (a) and Ta+Ru cap layer (b). The lower c-CoFe layer is clearly visible in both samples. A second polycrystalline CoFe region is present in the Ru cap sample at the interface to the cap layer (see arrow).

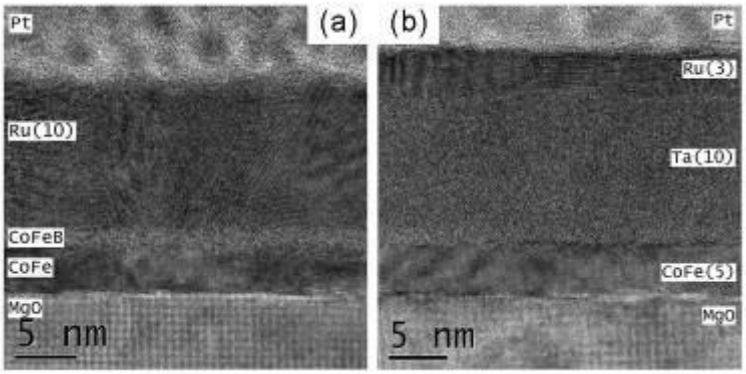

Figure 2. TEM images of samples with thin CoFeB layer. Amorphous interlayer between CoFe and Ru consisting of a-CoFeB (a). Fully crystallized CoFeB with boron containing Ta cap layer (b).

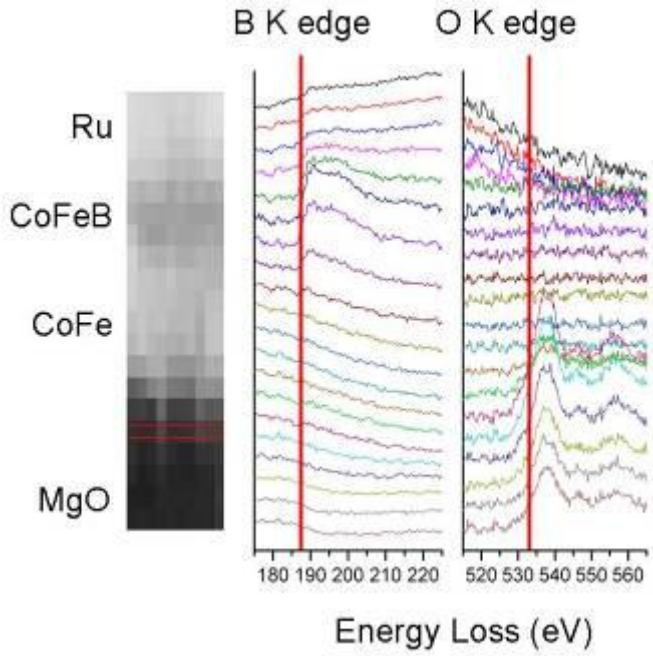

Figure 3. EEL spectra of the B-K and O-K edge from the MgO into the Ru cap. The absence of B and BO_x at the MgO and its interface is clearly visible from these spectra. Boron is only present in the amorphous interlayer between the Ru cap and the CoFe. Corresponding HAADF signal at the left.

Functional Materials

MS.3.P079
TiO_2 nanotubes arrays as active material for energy harvesting and storage devices

A. Chiodoni[1], K. Bejtka[1], A. Lamberti[1], S. Bianco[1], A. Sacco[1], N. Garino[1], C. Gerbaldi[2], M. Quaglio[1] C.F. Pirri[1,2]
[1]Istituto Italiano di Tecnologia - IIT, Center for Sapce Human Robotics, Torino, Italy
[2]Politecnico di Torino, Dipartimento di Scienza Applicata e Tecnologia, Torino, Italy

angelica.chiodoni@iit.it
Keywords: TiO_2, nanotubes, electron microscopy, dye sensitized solar cells, Li-ion batteries

TiO_2 nanotubes (NTs) are nowadays attracting increasing interest in applications such as dye-sensitised solar cells (DSCs) as they offer the possibility to modify the standard architecture based on mesoporous layers of TiO_2 nanoparticles by introducing vertically aligned nanostructures, characterised by a large sensitised surface area and anatase crystalline structure, able to improve the charge percolation through the anode because of the strongly interconnection of the nanocrystals [1,2]. The same nanostructures are also attracting interest as anodes in Li-ion batteries. In fact, TiO_2 represents an alternative anode material to graphite, due to its high specific surface area and pore volume, to the reduced cost and to the reduced environment impact [3,4].
In this work we report on the morphological, structural and functional characterization of vertically aligned TiO_2 nanotubes arrays prepared by anodic oxidation. Two different annealing procedures are presented.

In the first procedure, TiO_2 nanotube arrays with different lengths were fabricated by anodic oxidation of Ti foil, followed by an annealing step in furnace 450°C for 30 minutes. Stoichiometry, crystalline phase and morphology of the TiO_2 NTs were investigated by means of TEM, FESEM, Energy Dispersive Spectroscopy (EDS) and X-ray diffraction, evidencing the formation of a highly ordered 1D NT array, with a pure anatase crystalline structure (figure 1).

Free-standing NTs membranes were detached by the metal substrate to be tested as photoanodes in DSC (1) and as anodes in Li-ion batteries (2) [refs].

1) Transparent photoanodes were fabricated transferring the membranes on FTO/glass sheet with an adhesion layer made of TiO_2 nanoparticle (NP). DSCs were assembled employing a microfluidic housing system. The cell performances and the electron transport properties as a function of the tubes length were characterized by I-V electrical measurements, incident photon-to-electron conversion efficiency, electrochemical impedance spectroscopy and open circuit voltage decay. A comparison with the charge transport properties evaluated in nanoparticle-based photoanode showed an increase of the electron lifetime and the diffusion length, yielding an overall power conversion efficiency up to 7.56% [5].

2) The electrochemical response in laboratory-scale lithium cells with TiO2 NTs as anode was highly satisfying, showing good stability and capacity retention after prolonged cycling along with improved durability (> 1100 cycles). High surface area, short diffusion path and fast kinetics of the TiO_2 nanotube arrays are considered to be responsible for the noticeable electrochemical performance [4].

Due to the high annealing temperature (450°C), not compatible with the most common polymeric substrates, TiO_2 nanotubes cannot be used for the fabrication of flexible devices. However, the flexibility is becoming a key characteristic for future devices, because it can provide devices able to adapt to different configuration.

In the second procedure, low temperature water treatment is proposed as a way to overcome this limitation, obtaining the crystallization starting from amorphous metal-oxide nanostructures [6]. In the present work, this easy approach is improved exploiting water vapour as phase transformation environment in order to crystallize the amorphous TiO_2 NTs layer (figure 2) and open the way to future highly-efficient TiO_2 NTs based flexible photoanodes. Stoichiometry, crystalline phase and morphology of the TiO_2 NTs were investigated by means of TEM, FESEM, EDS and X-ray diffraction, in order to put in evidence the characteristic of the TiO_2 nanotubes before and after the water vapour treatment and confirm the successful crystallization of the nanostructures.

1. J.M. Macak, H. Tsuchiya, A. Ghicov and P. Schmuki, Electrochemistry Communications 7 (2005) p. 1133.
2. A. Lamberti, A. Sacco, S. Bianco, D. Manfredi, F. Cappelluti, S. Hernandez, M. Quaglio and C.F. Pirri, Phys. Chem. Chem. Phys. 15 (2013) p.2233.
3. T. Djenizian, I. Hanzu and P. Knauth, J. Mater. Chem. 21 (2011) 9925.
4. A. Lamberti, N. Garino, A. Sacco, S. Bianco, D. Manfredi and C. Gerbaldi, Electrochimica Acta (2013) Accepted Manuscript
5. A. Lamberti, A. Sacco, S. Bianco, D. Manfredi, F. Cappelluti, S. Hernandez, M. Quaglio and C.F. Pirri, Phys. Chem. Chem. Phys. 15 (2013) 2233.
6. D. Wang, L. Liu, F. Zhang, K. Tao, E. Pippel and K. Domen, Nano Lett. 11 (2011) 3649

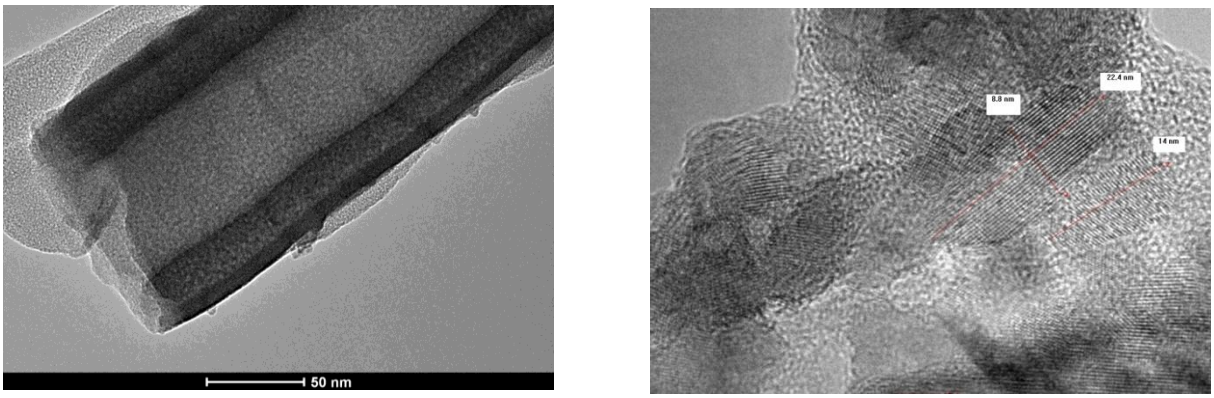

Figure 1. TEM and HRTEM images showing the morphology and the crystalline quality of TiO_2 NTs annealed at 450°C for 30 minutes

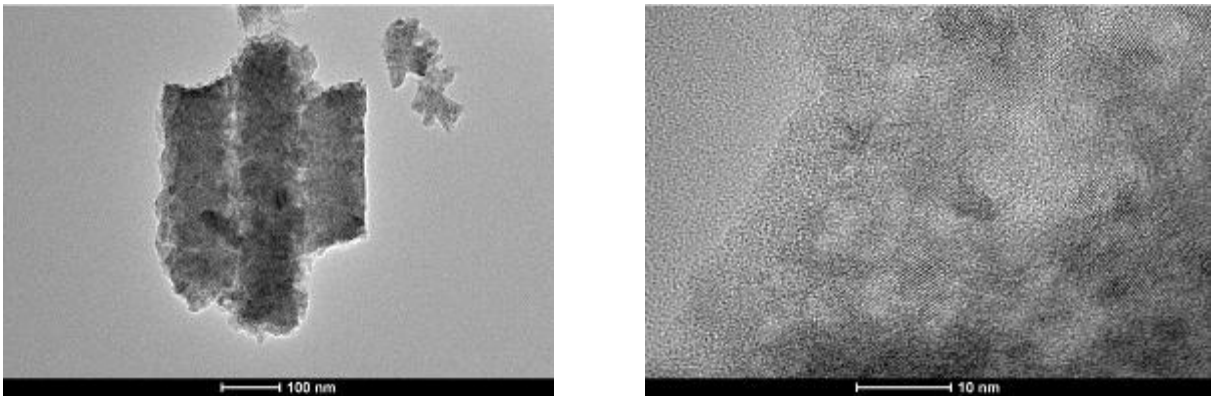

Figure 2. TEM and HRTEM images showing the morphology and the crystalline quality of TiO_2 NTs treated with water vapour

Functional Materials

MS.3.P080
Structural characterization of polyelectrolyte multilayer hollow capsules by SEM

V. Krzyzanek[1], U. Keller[2], N. Sporenberg[3], M. Schönhoff[3]

[1]Institute of Scientific Instruments of the ASCR, Electron Microscopy, Brno, Czech Republic
[2]University of Münster, Institute of Medical Physics and Biophysics, Münster, Germany
[3]University of Münster, Institute of Physical Chemistry, Münster, Germany

krzyzanek@isibrno.cz
Keywords: Cryo-SEM, quantitative imaging, hollow capsules

Polyelectrolyte hollow capsules are promising material that can be used for example as a drug delivery system in medical applications and release applications [1]. They can be prepared from polyelectrolytes on silica spherical particles by using the layer-by-layer self-assembly method [2] and, consequently, dissolving the silica core with dilute hydrofluoric acid. Poly(allylamine hydrochlorid) (PAH) and poly(sodium 4-styrene sulfonate) (PSS) were used as a base material for the wall of the capsules. The capsules presented here with a diameter of ~400 nm consist of 5 bilayers of PAH/PSS polyelectrolytes (Figure 1a). The wall permeability is a crucial property for, e.g., drug delivery applications, and can be readily measured by confocal laser scanning microscopy and nuclear magnetic resonance diffusion experiments [3]. Dimensions of our capsules are rather small in comparison to typically studied ones, and therefore, electron microscopy is essential tool for detailed structure characterization.

A high-resolution field-emission scanning electron microscope was employed to investigate the structure details of the capsule wall. The capsules before the core dissolution process were investigated in the air-dried state. Both secondary electron (SE) and back-scattered electron (BSE) micrographs were recorded simultaneously (Figure 1b). The BSE micrograph may be used for rough estimation of the thickness of the capsule wall, since the density of silica core is ~2 times higher than the density of the polyelectrolyte wall. Monte Carlo simulations of electron scattering in planar films show that at 20 keV electron energy the BSE yield from silica is ~3 times stronger than that from polymeric materials.

Because the hollow capsules are damaged during their air-drying process due to the surface tension forces, cryo-techniques had to be employed. Here, we used the freeze-drying techniques developed and used mainly for investigations of biological samples [4] to retain the intact shape of the capsules. Capsules were rapidly frozen into liquid ethane, subsequently freeze-dried at vacuum, and finally rotary coated with very thin metal layer for high-resolution imaging (Figure 1c). This technique allowed for the first time to observe the capsules at high resolution in their intact shape and enabled to find new features, e.g., holes within size ≥10 nm in their capsule wall [5].

In addition, a quantitative annular dark-field (ADF) imaging mode [6-8] is applied for quantitative investigations of the mass-thickness mapping of the wall using the high-resolution SEM S-5000 (Hitachi, Japan) in the transmission mode. The first images (Figure 1d) prove the clear dependence of the ADF signal to the thickness wall.

1. A.L. Becker et al., Small 6 (2010), p. 1836.
2. G.B. Sukhorukov et al, Polym. Adv. Technol. 9 (1998), p. 759.
3. R.P. Choudbury et al., J. Phys. Chem. B 112 (2008), p. 13245.
5. A. Cavalier et al, “Handbook of Cryo-Preparation Methods for Electron Microscopy”, CRC Press, Boca Raton 2009.
6. V. Krzyzanek et al., Soft Matter 7 (2011), p. 7034.
7. V. Krzyzanek and R. Reichelt, Microscopy & Microanalysis 13 (Suppl. 3) (2007), p. 80.
8. H. Nusse et al., in Proc. Microscopy Conference MC2011, Kiel (2011).
9. S. Tacke et al., in Proc. Microscopy Conference MC2013, Regensburg (2013).
10. The authors gratefully acknowledge the support from EC and MEYS CR (grant Nr CZ.1.07/2.3.00/20.0103) and from the DFG (grant Nr. RE 872/11).

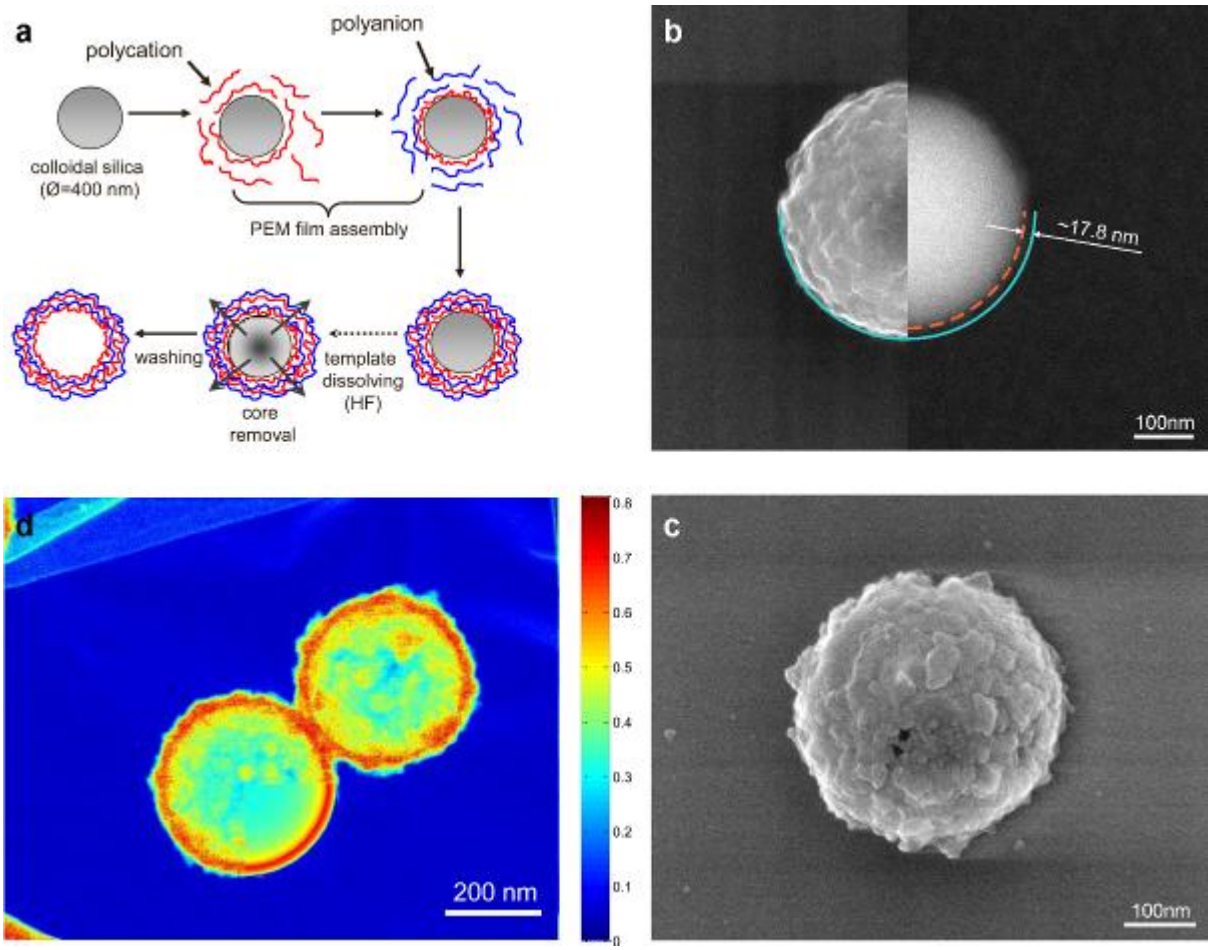

Figure 1. Polyelectrolyte multilayer hollow capsules: (a) Graphical illustration of the capsule preparation. (b) Air-dried hollow capsules before dissolving the core: SE (left half) and BSE (right half) micrographs acquired simultaneously. The BSE micrograph may be used for a rough estimation of the thickness of the capsule wall; the dashed red line indicate the core/wall interface and the solid green line indicate the wall/vacuum interface, respectively. (c) SE micrograph of freeze-dried hollow capsule. (d) ADF micrograph of hollow capsules on very thin amorphous carbon film recorded at very low electron dose; the colour scale is recalculated to the fraction of elastically scattered electrons, the right bottom segment is a theoretical model.

Functional Materials

MS.3.P081
Controlled morphological transformation of hollow oxide nanostructures upon *in situ* annealing in a transmission electron microscope

L. Molina-Luna[1], S. Schildt[1], M. Buffière[2], K. Du[3], C.-H. Choi[3], H.-J. Kleebe[1], S. Konstantinidis[4] S. Rony[4,5], C. Bittencourt[4], A.-A. El Mel[4]

[1]Technische Universität Darmstadt, Department of Material- and Geosciences, Darmstadt, Germany
[2]IMEC, Heverlee, Belgium
[3]Stevens Institute of Technology, Department of Mechanical Engineering, Hoboken, United States
[4]University of Mons, Chimie des Interactions Plasma-Surface (ChIPS) CIRMAP, Research Institute for Materials Science and Engineering, Mons, Belgium
[5]Materia Nova Research Center, Mons, Belgium

molina@geo.tu-darmstadt.de

Hollow oxide nanostructures are materials with a high technological potential for applications in various fields ranging from nano-optics, catalysis, sensing, energy storage, microreactors to drug delivery. Currently, there is an interest in the development of methods to fabricate hollow oxide nanostructures of a wide variety of materials [1]. Among these hollow structures, oxide nanotubes are considered as potential building blocks for nanoelectronics. Up-to-now, the majority of the synthesis methods produce oxide nanotubes which suffer from short length and poor organization. Recently, a fabrication method of highly organized ultra-long metal oxide nanotube (length-up to several centimeters) based on the thermal oxidation of metal nanowire arrays selectively grown on nanograting template structures has been developed [2]. Figure 1 shows scanning electron microscope images of highly organized copper oxide nanotubes as-prepared on a nanograted silicon substrate. This route, based on the nanoscale Kirkendall effect, is also extendable to periodic zero-dimensional hollow nano-objects [2].This novel fabrication method yields oxide nanotubes in a planar configuration and opens-up the way to further nanodevice construction and characterization.

In this contribution we present an extensive structural study of the morphological transformation of oxide nanotubes upon *in situ* annealing in a transmission electron microscope. Based on this, the role of oxygen on the fundamental mechanisms occurring during the formation of such oxide nanotubes will be discussed. These results show the structural transformation and copper ions diffusion inside an oxide nanotube due to the effect of heating.The experiments were performed to temperatures higher than 600°C and done using a dedicated Gatan 652 heating holder. Figure 2 (a) shows a TEM bright-field image of periodic Cu nanoparticles created inside an oxide nanotube. Figure 2 (b) is the corresponding TEM dark-field image. Further *ex situ* studies using spatially resolved scanning transmission electron microscopy in combination with electron energy-loss spectroscopy revealed the chemical nature of the Cu based surrounding core-shell structure.

1. Fan, H. J. *et al.* Monocrystalline spinel nanotube fabrication based on the Kirkendall effect. *Nature Mater.* 5, 627-631 (2006).
2. El Mel, A. A. *et al.* Highly ordered hollow oxide nanostructures: The Kirkendall effect at the nanoscale. *Small*, in press.DOI: 10.1002/smll.201202824
3. Chun, S R *et al.* Joining copper oxide nanotube arrays driven by the nanoscale Kirkendall effect. *Small*, in press.DOI: 10.1002/smll.201202533

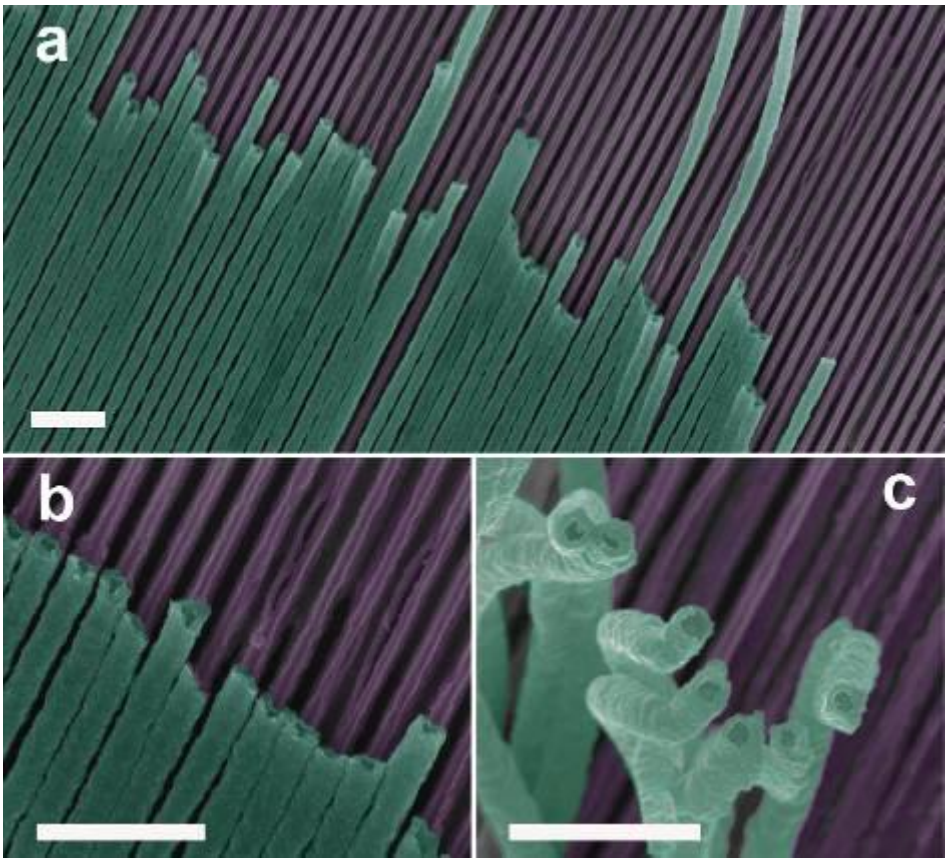

Figure 1. (a,b) False colored SEM micrographs of highly organized copper oxide nanotubes as-prepared on the nanograted substrate. c) SEM micrograph of oxide nanotubes disengaged from the silicon substrate. Scale bar: 1µm.

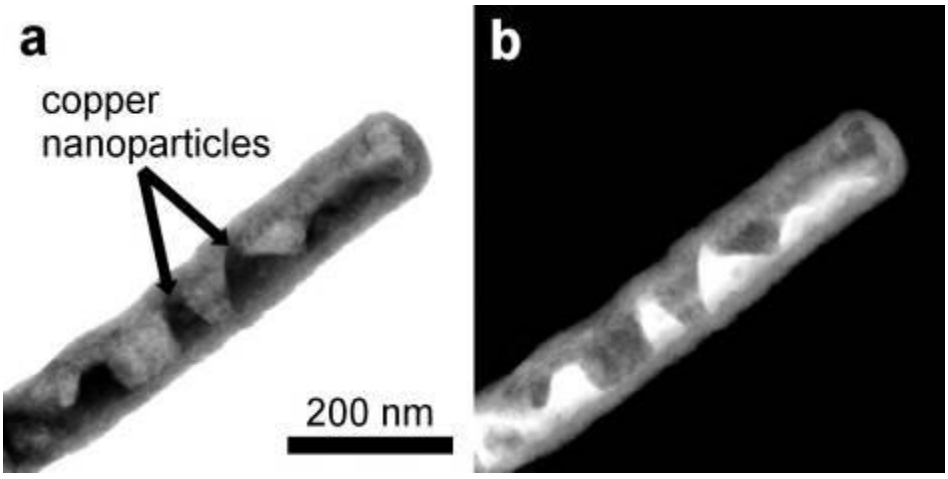

Figure 2. (a) TEM-bright field image of periodic Cu nanoparticles created inside an oxide nanotube (b) Corresponding TEM

Functional Materials

MS.3.P082
Influence of processing parameters and retained austenite on the subsurface microstructure of martensitic steel

P. Stemmer[1,2], S. Goeke[3], W. Theisen[4], D. Biermann[3], A. Fischer[1,2]

[1]University Duisburg-Essen, Materials Science and Engineering, Duisburg, Germany
[2]CENIDE Center for Nano Integration Duisburg Essen, Duisburg, Germany
[3]Technical University Dortmund, Institute of Machining Technology, Dortmund, Germany
[4]Ruhr-Universität Bochum, Chair of Materials Technology, Bochum, Germany

priska.stemmer@uni-due.de
Keywords: surface integrity, phase transformation,

With advances in technology the requirements for technological applications e.g. bearing surfaces are increasing. In many applications the tribological systems are run under mixed or boundary lubrication, which might lead to higher friction coefficients and wear. However, an extended durability for those components is claimed as well. For Co- and Fe-based alloys microstructural alterations were proven to provide ultra-mild sliding wear conditions during steady state even under such conditions [1] [2]. Such alterations include grain refinement and strain induced phase transformations. As a result the generation of a beneficial tribolayer may be enabled as a result of the interaction of altered surface material and constituents of the interfacial (lubricant, wear particles) as well as surrounding media (environment) [3]. While within Co- and Fe-based austenitic materials the tribolayer is supported by a strain induced shear zone reaching from the µm-sized bulk material toward the nm-sized subsurface zone, Fe-based martensites take benefit from their high strength in combination with compressive stresses introduced by a strain induced transformation of retained austenite.

A current research project aims at the reduction of the running-in phase by generating such a subsurface microstructure that supports the generation of a stable tribolayer. This should then lead to an earlier transition from run-in to steady state and result in ultra-mild sliding wear (< 3 nm/h). For this purpose the influence of machining process parameters and varying ratios of retained austenite are investigated as to the subsurface constituents in a first step. Thus samples of the case hardening steel 18CrNiMo7-6 have been case-hardened to different contents of carbon in the case leading to fractions of retained austenite from 2 to 20 % after quenching. These were milled by means of different processing parameters. Afterwards the subsurface gradients of microstructure are analyzed by scanning electron microscopy (SEM) and transmission electron microscopy (TEM). As a result of the SEM evaluation a thin layer of some 100 nm thickness stands out against the martensitic microstructure indicating a phase transformation (Fig. 1).
This contribution presents the subsurface microstructural gradient in relation to the milling parameters.

1. Pourzal R. VDI Verlag GmbH, Reihe 17, Nr 285 (2012)
2. Hahn et al. Wear 267 (2009) 916-924
3. Büscher R. VDI Verlag GmbH, Reihe 17, Nr. 256 (2005)

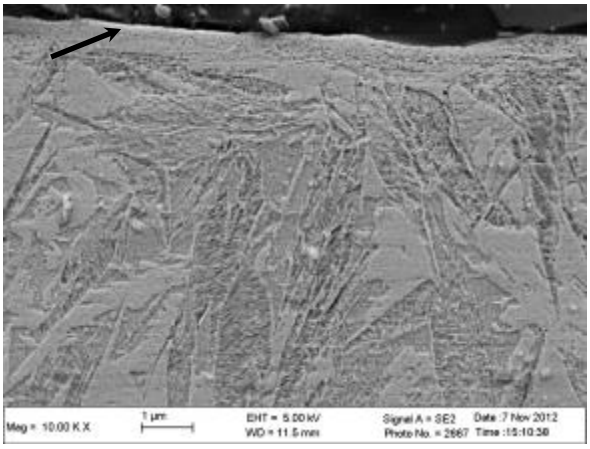

Figure 4. SEM cross-sectional micrograph of machined surface of martensitic steel exhibiting transformed layer below the surface.

Materials for Energy Technology

MS.4.083
Understanding the behaviour of a CoB catalyst for sodium borohydride hydrolysis: An electron microscopy study

A. Fernández[1], G.M.Arzac[1], D.Hufschmidt[1], T.C.Rojas[1], M.C.Jiménez[1]

[1]Instituto de Ciencia de Materiales de Sevilla (CSIC – Univ. Seville), Calle Américo Vespucio 49, 41092 Sevilla, Spain

asuncion@icmse.csic.es
Keywords: Hydrogen generation, Co-B catalysts, TEM, SEM, sodium borohydride

Sodium borohydride ($NaBH_4$, SBH) is a stable, non-flammable and non toxic hydride that permits a safe and versatile generation of hydrogen. SBH solutions at high pH (fuel) are stable and only produce hydrogen when in contact with suitable catalysts (on demand H_2 generation). The release of hydrogen can be carried out in a controlled way in ambient conditions, which makes it suitable to feed a PEMFC (Polymer Exchange Membrane Fuel Cell) for small scale and portable applications [1]:

$$NaBH_4 + 2H_2O \rightarrow 4H_2 + NaBO_2$$

Among metal based catalysts, the Co-B materials are the most investigated owing to its reactivity and low cost. In this work the Co-B based catalyst was prepared by chemical methods (reduction of cobalt salts by SBH) in powder form and also supported on pre-treated stainless steel homemade monoliths. The monoliths were prepared for its use in a continuous working reactor designed and built to allow a constant and adaptable generation of hydrogen (in the range of 0.3-1.7 L/min) over a long period of time.

The exact microstructure of these catalysts was not well known and was usually considered as an amorphous material. Herein we present an exhaustive study which shows a new and complete microstructural view of a Co·B-based material together with the chemistry of the cobalt and boron involved. By using nanoscale-resolution microscopy and spectroscopy techniques (i.e. scanning TEM (STEM), high angle annular dark field detector (HAADF) and electron energy loss spectroscopy (EELS)), we have elucidated the role of boron compounds as stabilizers in a complex microstructure, which also explains its high catalytic performance and long-term stability. The catalyst is proposed to be made up of 1–3 nm hcp Co nanoparticles embedded in amorphous Co_xB (x=1, 2, 3), Co_xO_y, $Co(BO_2)_2$, and B_2O_3 phases alternatively or all together [2]. Figure 1 shows some selected results as the HAADF image in STEM mode, accompanied of the localized EELS spectra as obtained from the spectrum imaging data.

Special interest was also laid on deactivation, reactivation and durability of the supported catalyst working under high conversion conditions in our continuous reactor [3]. A deactivation of the catalyst was observed after long time of use, depending largely of the mode of experiment (start/stop cycles, continuous run). The deactivation and the intents of reactivation of the Co-B catalysts were studied and will be discussed in terms of borate formation and elimination (see Figure2). For this study the use of a SEM-FEG microscope with EDX mapping facilities will be presented showing the capabilities for working with pieces of monoliths coming directly from the reactor.

We can conclude that catalysts for practical applications and reactors in hydrogen generation reactions are systems with a complex microstructure were electron microscopy, together with other techniques, are very efficient tools to determine their behaviour and to draw-up the best operation conditions. Nevertheless the borohydride in this system acts both, as a fuel for the hydrogen generation, and as a reduction agent that can modify the catalysts “in operando“ conditions what is also giving an example of how the microstructural analysis should be always considered in the context of the operation behaviour.

1. B.H. Liu, Z.P. Li, J. Power Sources, 187 (2009), p. 527.
2. G.M. Arzac, T.C. Rojas, A.Fernández, Chem. Cat Chem, 3 (2011) p. 1305.
3. *G. M. Arzac, D. Hufschmidt, M. C. Jiménez de Haro, A. Fernández, B. Sarmiento, M. A. Jiménez, M.M. Jiménez, International Journal of Hydrogen Energy37 (2012) p. 14373.*
4. We kindly acknowledge the financial support from Abengoa Hidrógeno S.A., MINECO (Project CTQ2012-32519), “Junta de Andalucía” (TEP217) and the EC (CT-REGPOT-2011-1-285895, AL-NANOFUNC)

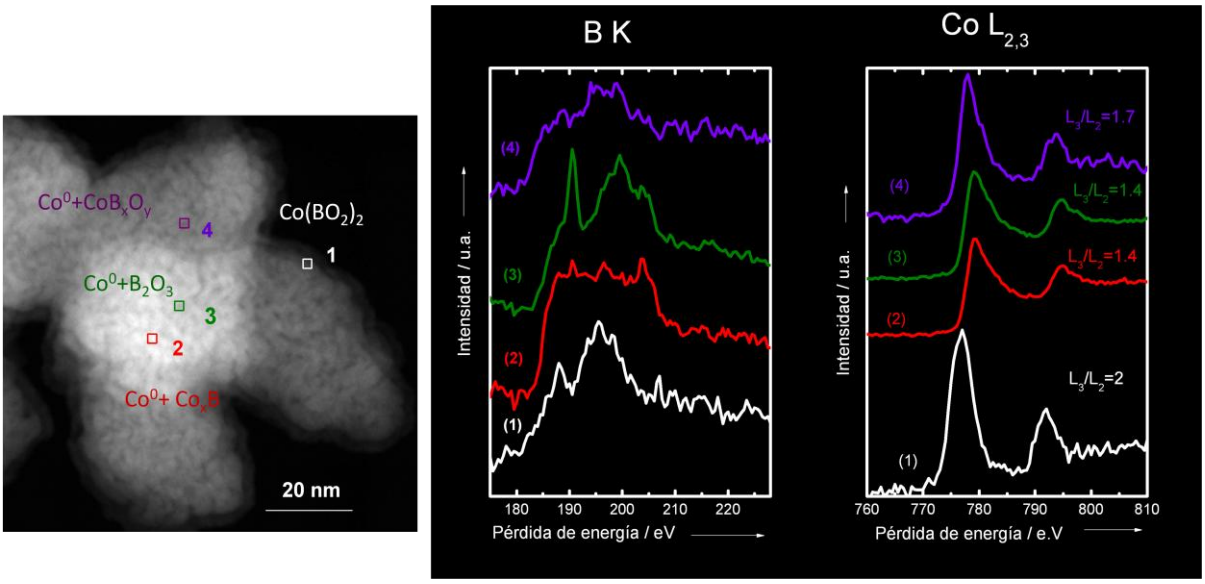

Figure 1.STEM/SI study on the prepared Co·B catalyst. Left) HAADF image, centre) EELS B K-edge spectra, and right) EELS Co $L_{2,3}$ spectra for the zones as defined in the left figure

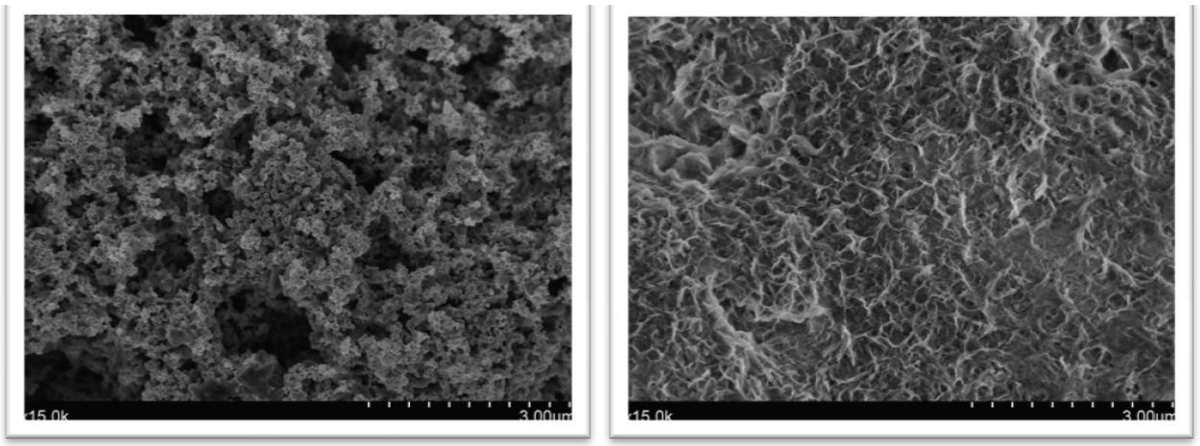

Figure 2.SEM micrographs from the catalysts supported in a steel monolith: As prepared (left) and after total deactivation showing a borate layer (right).

Materials for Energy Technology

MS.4.084
Imaging LiBC by phase-contrast scanning transmission electron microscopy

F. Krumeich[1], M. Wörle[1], P. Reibisch[1], R. Nesper[1]

[1]ETH Zurich, Laboratory of Inorganic Chemistry, Zurich, Switzerland

Keywords: aberration-correction, STEM, Li visibility

The visualization of light elements is a particular challenge for electron microscopy as the contrast in most methods strongly depends on the scattering potential of the specimen. Although it was found possible to estimate Li in $LiCoO_2$ by HRTEM [1], recently scanning transmission electron microscopy (STEM) bright field methods have produced more promising results. In particular, annular bright field STEM is utilized for such investigations, e.g. for detecting Li in battery materials [2]. Phase-contrast STEM also is a suitable tool for the detection of light element positions, as demonstrated e.g. for O in $SrTiO_3$ [3]. Thus, we evaluated this method for the investigation of LiBC, an interesting compound in different aspects consisting of light elements only. Phase-contrast STEM (PC-STEM) imaging [4,5] represents an increasingly important alternative to the well-established HRTEM method. The image contrast in both methods is coherently generated and thus depends not only on illumination and collection angles but on defocus and specimen thickness as well.

Hexagonal platelets of LiBC were synthesized from the elements by heating at 1523 K in inert atmosphere [6]. Boron and carbon form planar hetero graphite layers of the isoelectronic hexagonal BN type. These BC six-ring layers are stacked ecliptically such that B and C alternate along the *c* axis. Li is intercalated between these layers *($P6_3/mmc$; a* = 275.2 pm; *c* = 705.8 pm) [6]. The STEM investigations were performed on a dedicated STEM microscope (Hitachi HD-2700CS with cold-field emitter, V_{acc} = 200 kV). An aberration-corrector (CEOS) optimizes the performance of the probe-forming objective lens resulting in a resolution better than 0.1 nm [7]. In the phase contrast mode, a variant of the bright field (BF) STEM method using a small BF detector, mainly diffracted beams contribute to the image. Image simulations were performed by multi-slice calculations with the EMS program [8] taking the parameters of the microscope and the crystallographic data of LiBC [6] into account.

The hexagonal structure of LiBC was investigated in projection along the *c* axis. For this, the orientation of the selected crystal area was adjusted in the nano diffraction mode (Figure 2a). The focus dependency of PC-STEM imaging is demonstrated in Figure 1 where a contrast inversion is observed. Higher magnified images recorded at a small defocus value reveal an arrangement of rings of six bright spots that are mostly centered by a fainter spot (Figure 2b,c). The comparison with simulated images allowed us to assign the bright spots to the positions of the B and C atoms while the faint central spot corresponds to the Li position (Figure 2d). Defects in the BC substructure have not been observed, but there are frequent positions in the center of the BC hexagons that are obviously not occupied by Li atoms as they appear dark (Figure 2c). Its semiconducting behavior makes it less likely that empty Li positions are an intrinsic property of the LiBC structure but may be induced by the measurement: the enhanced mobility of Li^+ might be caused by the electron beam. In NMR studies, Li mobility was found to be very small up to 500 K [9]. As the LiBC structure is slowly destroyed during the measurement and is finally getting amorphous after a few minutes, vacancy formation is most likely due to the action of the electron beam (Figure 1b) [10].

1. Y. Shao-Horn *et al.*, Nature Mater. 2 (2003) p. 464.
2. E. Okunushi, H. Sawada, Y. Kondo, Micron 43 (2012) p. 538.
3. S. J. Pennycook *et al.*, MRS Bull. 31 (2006) p. 36.
4. H. Rose, Optik 39 (1974) p. 416.
5. F. Krumeich *et al.*, Micron (2013). DOI: 10.1016/j.micron.2013.03.006.
6. M. Wörle *et al.*, Z. Allg. Anorg. Chem. 621 (1995) p. 1153
7. H. Inada *et al.*, J. Electron Microsc. 58 (2009) p. 111.
8. P. Stadelmann, Ultramicroscopy 21 (1987) p. 131.
9. T. Langer *et al.*, Z. Naturforsch. 67b (2012) p. 1212.
10. Electron microscopy investigations were performed at the electron microscopy center of ETH Zurich (EMEZ).

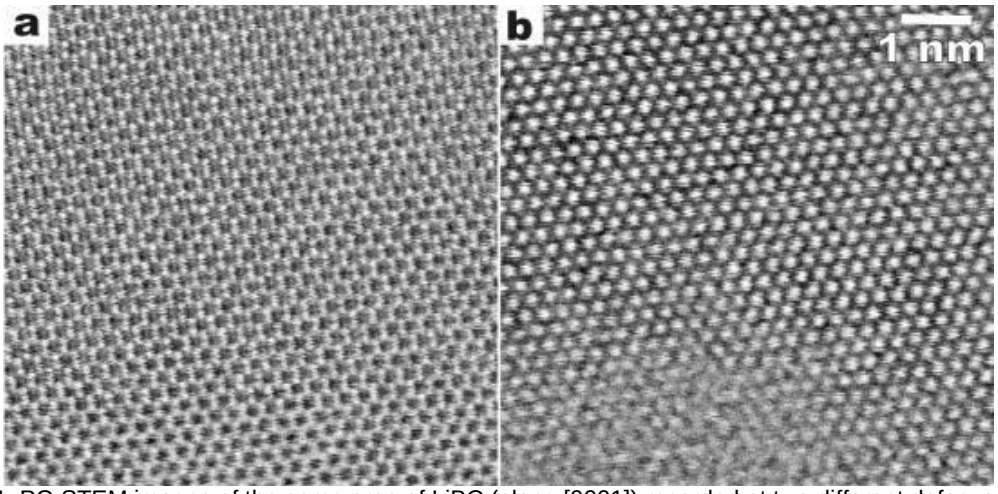

Figure 1. PC-STEM images of the same area of LiBC (along [0001]) recorded at two different defocus values *f* (□*f* ≈ 20 nm) show a contrast inversion. The lower left part in (b) is already affected by amorphization of the structure in the electron beam.

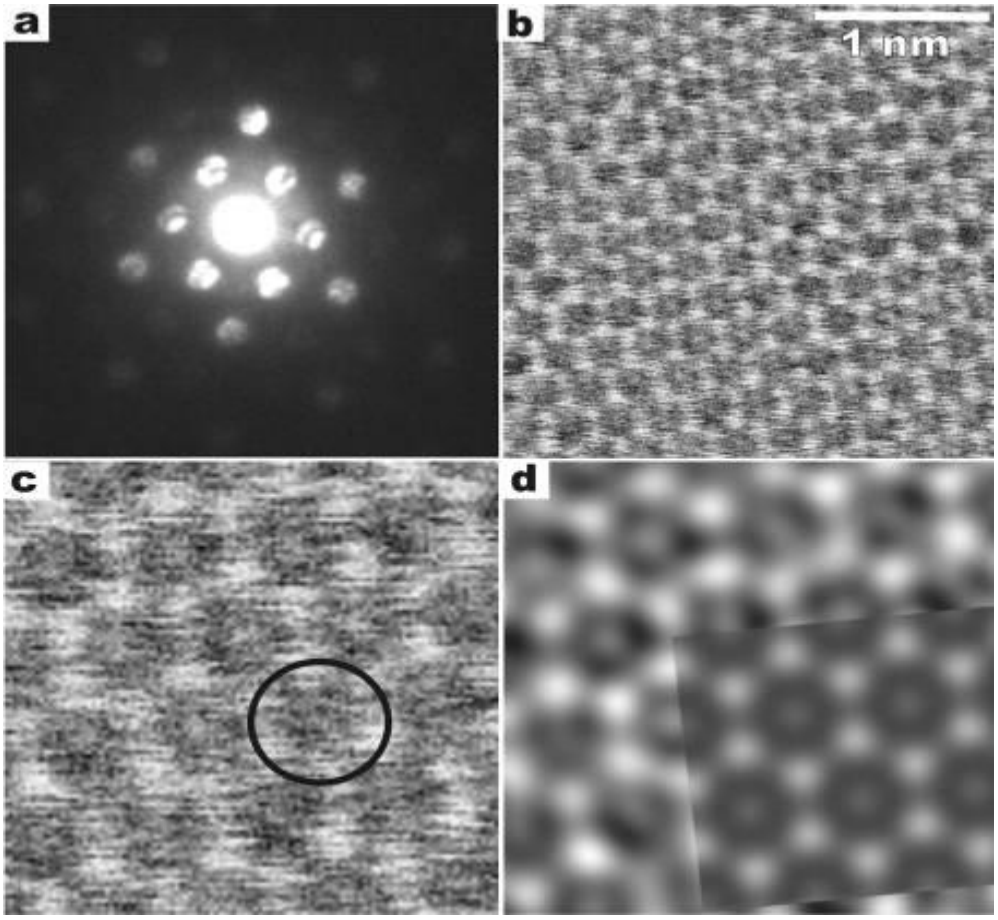

Figure 2. LiBC along [0001]. (a) Nanodiffraction pattern. (b) PC-STEM image as obtained. (c) Magnified section of (b). The circle marks an empty Li position. (d) Fourier filtered image (c) with a simulation fitted in. The simulation was calculated using the multi-slice algorithm of the EMS program for a defocus of *f* = 5 nm and a thickness of 5.6 nm [7]. Microscope parameters: V_{acc} = 200 kV; C_s = 10 □m; C_c = 1.6 mm; variation of Δ*f* = 5 nm, reciprocal diameter of the objective aperture D^{-1} = 25.4 nm^{-1}; beam semi convergence = 1.5 mrad.

Materials for Energy Technology

MS.4.085
Electron microscopic and electrochemical characterization of Li-air battery materials

S. Eswara Moorthy[1], M. Marinaro[2], J. Bernhard[1], J. Biskupek[1], D. Geiger[1], L. Jörissen[2], M. Wohlfahrt-Mehrens[2], U. Kaiser[1]

[1]Electron Microscopy Group of Materials Science, University of Ulm, 89081 Ulm, Germany, Germany
[2]Centre for Solar Energy and Hydrogen Research BW, 89081 Ulm, Germany, Germany

santhana.eswara@uni-ulm.de
Keywords: Li-air battery, TEM, pore structure

Lithium-based batteries are one of the most important groups of rechargeable batteries in portable electronic devices owing to their high gravimetric energy-density. An increasing scientific and technological interest in further improving the energy-capacity and the number of charge-discharge cycles has provided significant impetus for further innovations in the field of Li-Air batteries [1, 2]. However, one of the most severe limitations in the commercialization of the Li-Air batteries is that the oxygen reduction reaction (ORR) during discharging and oxygen evolution reaction (OER) during charging must have fast kinetics. In order to enhance the ORR and OER reaction kinetics and to suppress any parasitic reactions, innovations in developing suitable electrocatalysts as well as suitable characterization techniques are necessary. In the current work, we employed electron microscopy (TEM and SEM) as well as Focused Ion Beam (FIB) techniques to characterize the reaction products and the electrocatalysts in order to gain a deeper understanding of the underlying reactions and their mechanisms to improve reaction efficiencies. The SEM images of the gas diffusion electrode at pristine, discharged and recharged states and corresponding galvanostatic curve (up to 500 mA.h/(g carbon)) are shown in Figure 1. Discharging the battery forms lithium peroxide on the cathode. Upon recharge, it disappears. Our SEM results are consistent with XRD results which show Li_2O_2 peaks in discharged case but not in recharged case. These results are also consistent with Electrochemical Impedance Spectroscopy results. Another set of electrodes, in this case discharged up to 1000 mA.h/(g carbon) were also investigated. These results are shown in Figure 2. Formation and dissolution of lithium peroxide upon discharging and recharging are evident from these figures. The size of the lithium peroxide crystals are in the range of 250-350 nm and the morphology is rather smooth. Determination of the pore structures and tortuosity [3] in the gas diffusion electrode is important to design and develop an optimal electrode structure to facilitate the oxidation and reduction kinetics. In order to obtain the 3-D morphology of the pores in the electrode, FIB tomography methods were employed. Our first results showed that sufficient contrast between the carbon electrode and the background is indispensable for the reconstruction of the pores. Therefore, the discharged and recharged electrodes were vacuum-impregnated with commercial epoxy. Furthermore, we are characterizing numerous candidates for bifunctional electrocatalysts. There are two major classes of electrocatalysts viz., noble metal based and oxide based, that are being investigated. In our contribution, we will share our latest results from this on-going research work on mechanistic understanding of electrochemical reaction products and optimized imaging conditions.

1. M. Armand and J.-M. Tarascone, Nature, (2008), 451, 652-657
2. J. Christensen et al, J. Electrochem. Soc., 159(2), (2012), R1-R30
3. M. Ender, J. Joos, T. Carraro and E. Ivers-Tiffée, J. Electrochemical society, 159(7), A972-A980 (2012)
4. The authors gratefully acknowledge funding from the German Federal Ministry of Education and Research (BMBF) under the project ‘Strom aus Luft und Li’.

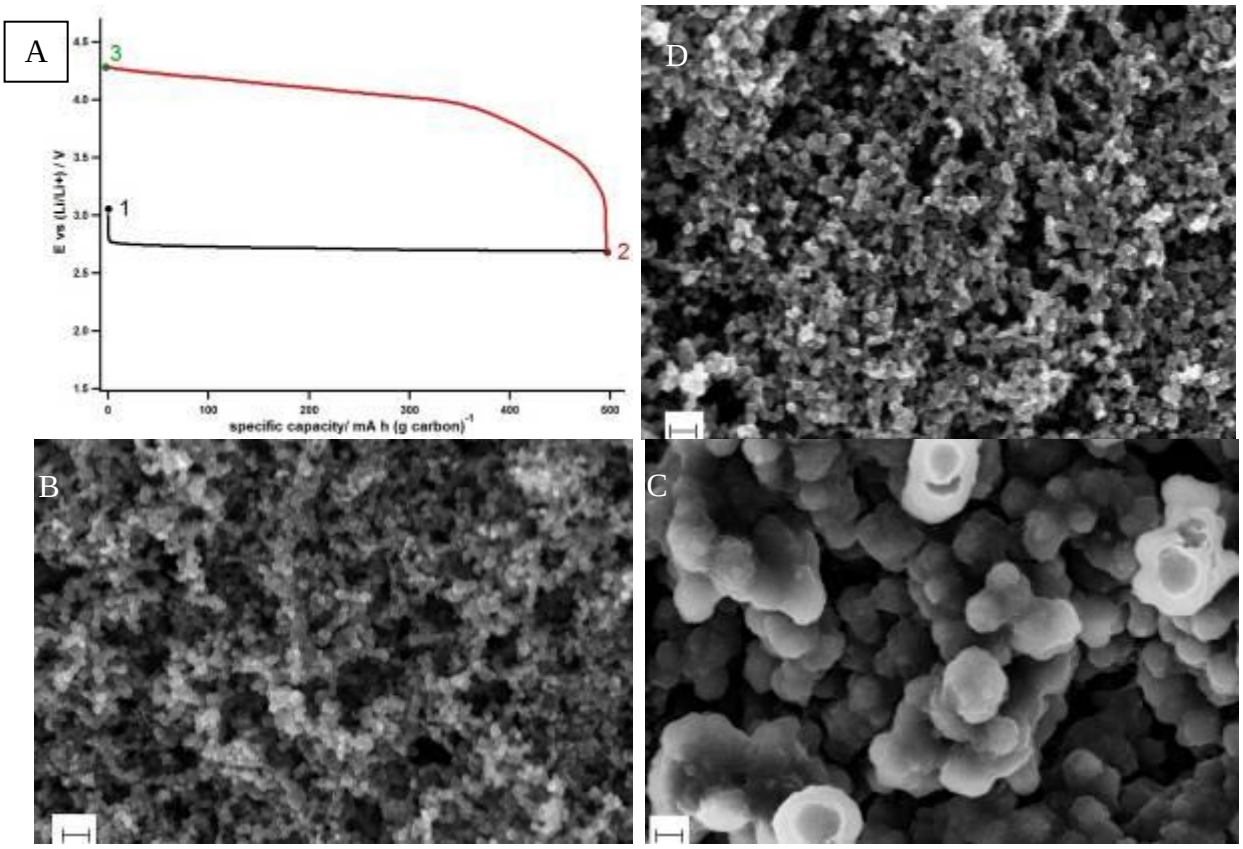

Figure 1. The galvanostatic discharge/charge curve (A) and microstructures of pristine (B), discharged (C) and recharged (D) electrodes. The scale bars correspond to 200 nm.

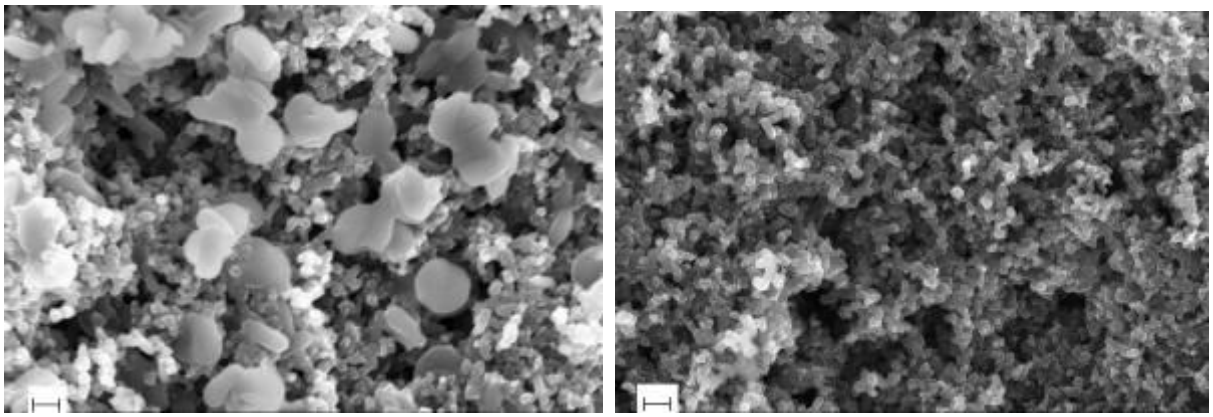

Figure 2. Microstructure of the discharged (left) and recharged (right) electrodes. The formation of lithium peroxide crystals on the discharged electrode (up to 1000 mA.h/ g carbon) in the form of large crystals with smooth morphologies are clearly visible. The scale bars correspond to 200 nm.

Materials for Energy Technology

MS.4.086
Quantification of oxygen vacancies in fuel-cells materials using atomic level EELS analysis

P. Longo[1], M. Chisholm[2], M. Varela[2], A. Lupini[2], R. Twesten[1]

[1]Gatan, Inc., Pleasanton, CA, United States
[2]Oak Ridge National Laboratory, Materials Science and Technology Division, Oak Ridge, Tennessee 37831, USA, United States

plongo@gatan.com
Keywords: EELS, quantification, DualEELS, fuel-cells materials, STEM

Fuel cells are promising systems for efficient energy conversion technology. Electrical energy is produced through a chemical reaction between oxygen and a fuel (typically H). In solid oxide fuel cells, O ions move through a solid electrolyte via O vacancies hopping to react with the fuel. The density and distribution of O vacancies in electrolyte influence the performance of the overall device. Quantifying these O vacancies, down to the unit cell level, provide insight into the physical properties and chemical interactions that occur across different regions in fuel cell materials. This insight would help overcome performance barriers such as limited lifespan and low temperature operation that have prevented the widespread commercial use of fuel cells as energy converters.

Here we present an EELS based approach for direct quantification of oxygen vacancy concentration using electron energy-loss spectroscopy and a model based analysis approach [1]. For this study, a specimen of $SrTiO_3$/$SrCoO_x$ (STO)/(SCO) was analyzed. O vacancies can be easily observed in the SCO area as alternating dark contrast in the Sr-O atomic planes as shown in the analog ADF STEM image in Figure 1a. The distance between these planes varies from 0.32nm and 0.38nm where the oxygen vacancies are present. A similar spacing variation has been previously reported for LSCO thin films [2], where it was found to be the result of structural relaxation. Here elemental and compositional analysis was carried out using atomic level EELS analysis. Data were acquired using a Nion UltraSTEM operating at 200kV equipped with a cold-FEG and a Gatan Enfinium ER EELS spectrometer. For the results shown in this abstract, EELS spectra were acquired in single range mode using an exposure time as low as 8 ms per spectrum in order to limit the electron beam damage. O, Sr and Co EELS intensity maps are shown in Figures 1b-d. The effects of the presence of the structural relaxation typical of O vacancies can be observed in the Sr elemental map in Figure 1c as alternating dark contrast. However, O vacancies can be directly observed in the O elemental map in Figure 1b as alternating dark and bright stripes and can be quantified using a model based approach [1]. This is possible because the edges from Sr $L_{2,3}$ at 1940eV, Co $L_{2,3}$ at 779eV and O K at 532eV, in the SCO area, can be all recorded in the same EELS spectrum given the high-dynamic range available in the latest generation of EELS spectrometers as shown in Figure 2. The O concentration varies from 54% to 52%, the latter in the area where the O vacancies are observed. Consistency of these results was also verified using a more conventional approach with a standard material containing the same elements Co, Sr and O. The stripes in the O elemental map fade during the acquisition; this is due to electron beam damage. In addition the image contrast at the interface seems to be affected by misfit strain.

These preliminary results demonstrate the consistency and the accuracy of the EELS quantification routine. Other materials containing O vacancies are currently under investigation using the same approach, and the results will be also presented. These materials range from GdCeOx, LaSrCoOx to LaSrMnOx. They are being investigated using means of acquisition in DualEELS™ mode where the low- and high-loss regions of the EELS spectrum are acquired nearly simultaneously under the same experimental conditions [3]. Having the low-loss contribution allows correction for the effects of multiple scattering that affects the shape of the edges and allows absolute quantification of the O content. Acquiring data in DualEELS™ mode opens up new avenues for the characterization of such materials and will allow crucial quantitative compositional information to be obtained.

1. P.J. Thomas et al., Microscopy and Microanalysis 18, (2012), p. 968
2. Y-M Kim et al., Nature Materials 11 (2012), p. 888
3. A.J. Gubbens et al., Ultramicroscopy 110 (2010), p. 962
4. We kindly acknowledge the U.S. Department of Energy, Basic Energy Sciences and Engineering Division to support this research (MFC, MV, ARL)

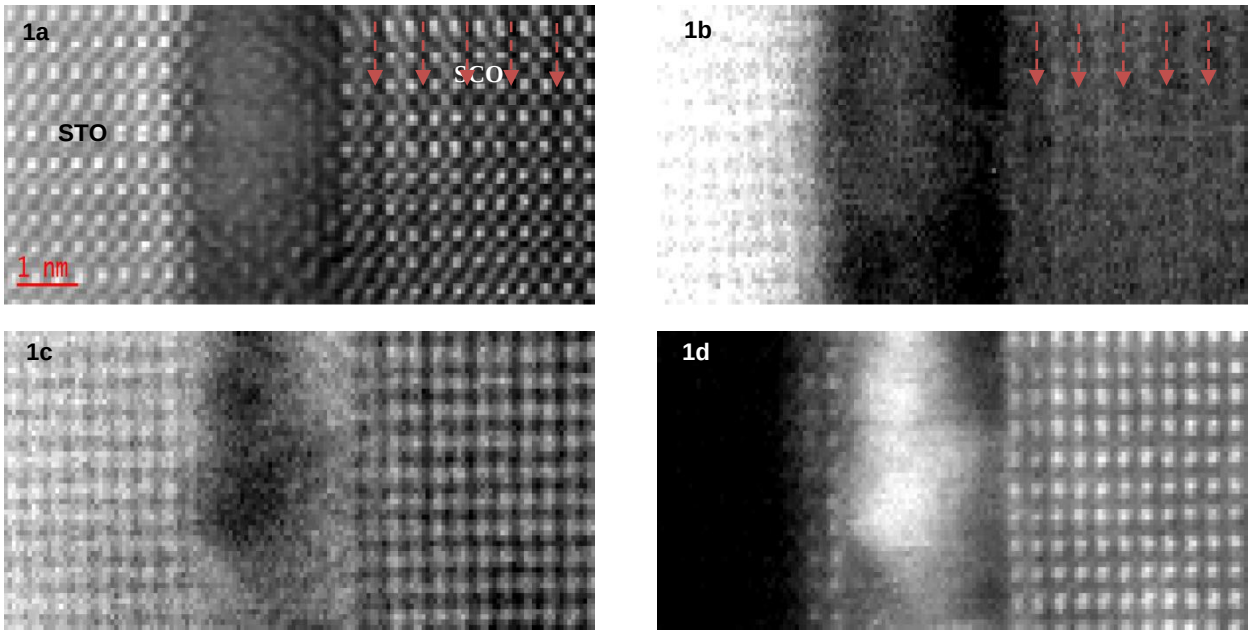

Figures 1. a): ADF STEM image taken simultaneously during the acquisition of the spectrum imaging. The alternating dark contrast shows where the O vacancies are expected; b) O elemental map showing the presence of O vacancies in the dark stripes; c) Sr and d) Co elemental maps. The red arrows in the ADF STEM image and the O elemental map indicate where the O vacancies are present.

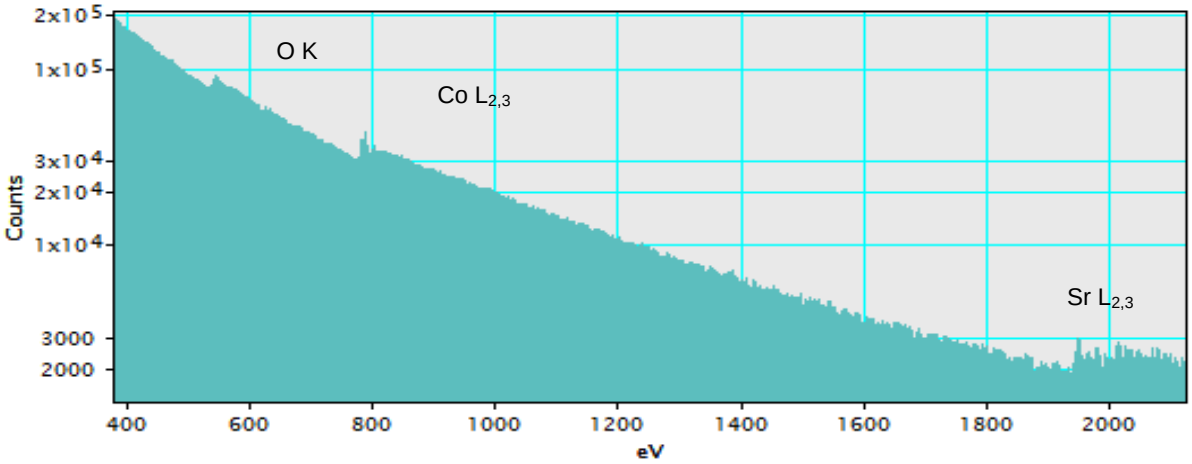

Figure 2. EELS spectrum in log-view extracted from the SCO region extending from 400eV to 2400eV. All the edges from Sr $L_{2,3}$ at 1940eV, Co $L_{2,3}$ at 779eV and O K at 532eV recorded in the same spectrum, allowing the relative composition to be accurately determined.

Materials for Energy Technology

MS.4.087
Investigation of carbonates in oxygen-transporting membrane ceramics by analytical transmission electron microscopy

A. Feldhoff[1], O. Ravkina[1], T. Klande[1]

[1]Leibniz University Hannover, Institute of Physical Chemistry and Electrochemistry, Hannover, Germany

armin.feldhoff@pci.uni-hannover.de
Keywords: perovskite, carbonate, electron energy-loss spectroscopy

Mixed oxygen-ionic and electronic conductors (MIECs) can be used as oxygen-transporting membranes in gas separation, which is needed in concepts for energy conversion technologies as solid oxide fuel cells and “clean-coal“ oxy-fuel combustion with less environmental pollution as compared to alternative approaches. These applications require chemical stability of the membrane material against carbon dioxide in the gas atmosphere. Already tiny carbonate scales on membrane surfaces, which are then impermeable for oxygen, must be avoided by proper choice of the material. Out-performing membrane ceramics with respect to total oxygen flux are based on perovskite-type oxides containing the alkaline-earth elements barium and strontium [1]. These constituents, however, form carbonates during membrane operation under CO_2-containing atmosphere [2, 3]. An example is given in Figure 1 with the out-performing cobalt-free $Ba_{0.5}Sr_{0.5}Fe_{0.8}Zn_{0.2}O_{3-\delta}$ perovskite, which was operated for two hours at 1023 K while sweeping with carbon dioxide on the oxygen-release side. A reaction zone with severe damage to the perovskite structure is noticed. Alternative materials, which avoid barium and strontium offer better chemical stability on the cost of lower oxygen flux [4].

A reliable analytical tool to identify tiniest carbonate scales on membrane surfaces is given by electron energy-loss spectroscopy (EELS) in the energy-filtering transmission electron microscope (EFTEM). The carbon-K and the oxygen-K ionization edges of carbonate and perovskite-type oxide phases show characteristic spectral signatures to distinguish them on the nanometer scale in properly prepared membrane cross-sections like shown in Figure 2. Here we study if partial cationic substitution of alkaline-earth elements can conserve high oxygen flux and give sufficient chemical stabilization. The TEM-based analytical method is applied to MIEC membranes after long-term operation (i.e. > 100 hours) of oxide ceramic membranes under technologically relevant conditions in presence of carbon dioxide. In the prominent perovskite $SrCo_{0.8}FeO_{3-\delta}$ (SCF) strontium was partially substituted by lanthanum to yield $La_{1-x}Sr_xCo_{0.8}FeO_{3-\delta}$ (LSCF) with x down to 0.4, and oxygen permeation experiments were correlated to the microstructure analysis. The later shows different amounts of carbonates at the CO_2-exposed sweep side of the membrane. Effects on total oxygen flux and chemical stability towards CO_2 as seen by oxygen permeation experiments are also discussed.

1. T. Klande, O. Ravkina, A. Feldhoff, *J. Eur. Ceram. Soc*. 33 (2013) 1129.
2. M. Arnold, H. Wang, A. Feldhoff, *J. Membr. Sci.* 293 (2007) 44.
3. J. Martynczuk, K. Efimov, L. Robben, A. Feldhoff, *J. Membr. Sci.* 344 (2009) 62.
4. Y. Wei, O. Ravkina, T. Klande. H. Wang, A. Feldhoff, *J. Membr. Sci.* 429 (2013) 147.

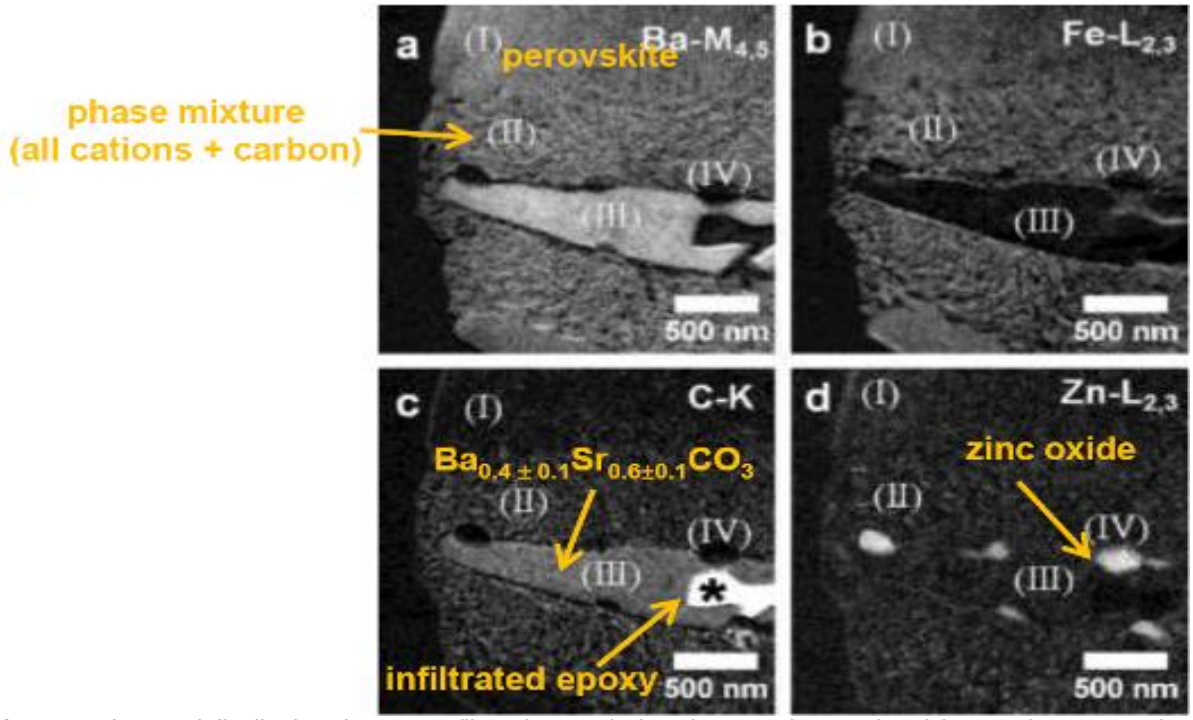

Figure 1. Elemental distributions by energy-filtered transmission electron micrographs of the reaction zone at the permeate side of $Ba_{0.5}Sr_{0.5}Fe_{0.8}Zn_{0.2}O_{3-\delta}$ perovskite after treatment with CO_2 for 2 h at 1023 K. High elemental concentration is shown by bright contrast: (a) barium, (b) iron, (c) carbon and (d) zinc. The asterisk (*) in (c) refers to a pore filled by epoxy due to TEM specimen preparation.

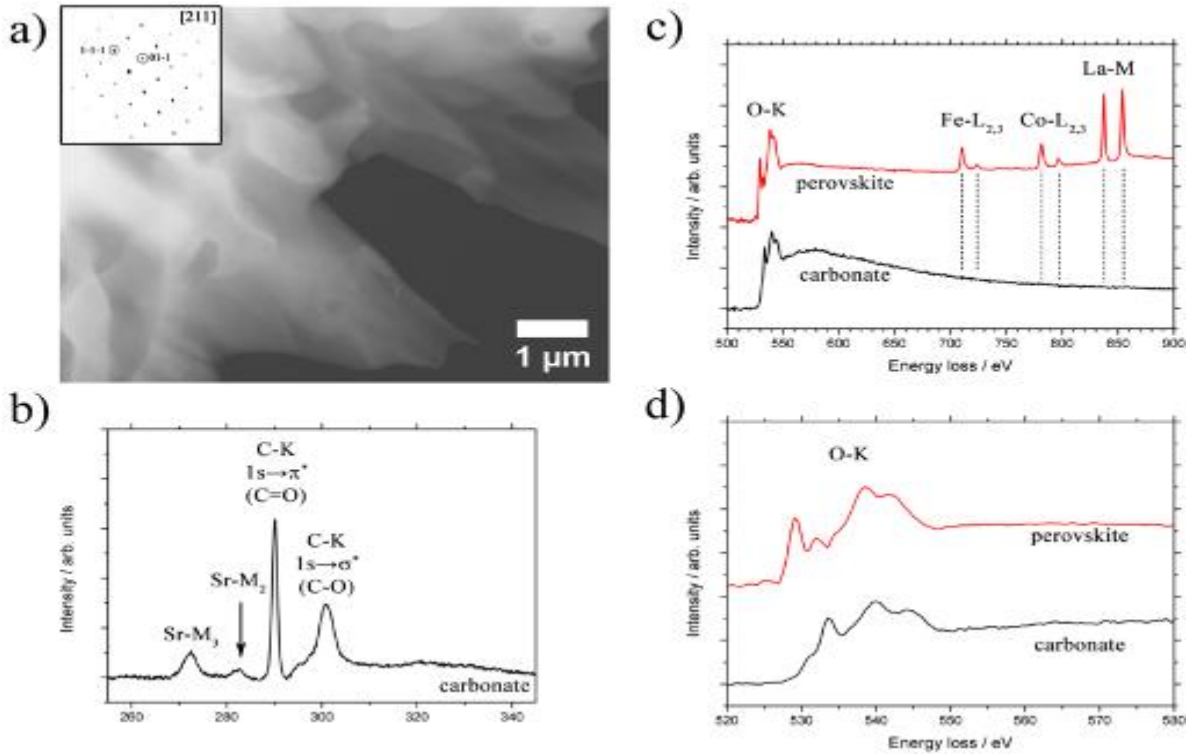

Figure 2. Transmission electron microscope analysis of sweep-side near region in $La_{0.2}Sr_{0.8}Co_{0.8}Fe_{0.2}O_{3-\delta}$ membrane after 200 hours of operation at 1173 K while sweeping with 100% CO_2: (a) High-angular dark field micrograph and selected area electron diffraction pattern, (b-d) electron energy-loss spectra of different locations showing signals from original perovskite and carbonate. Note different energy-loss scales.

Materials for Energy Technology

MS.4.088
Nanostructured Telluride based Thermoelectric Materials

T. Dankwort[1], M. Winkler[2], X. Liu[3], V. Duppel[4], U. Schürmann[1], J.D. König[2], H. Böttner[2], L. Kienle[1], W. Bensch[3]

[1]Christian Albrechts University, Institute for Materials Science , Kiel, Germany
[2]Fraunhofer-Institute for Physical Measurement Techniques, Thermoelectric Systems, Freiburg, Germany
[3]Christian Albrechts University, Institute of Inorganic Chemistry, Kiel, Germany
[4]Max Planck Institute for Solid State Research, Stuttgart, Germany

td@tf.uni-kiel.de
Keywords: Thermoelectric Materials, Nanostructured Tellurides, PED, HRTEM

Thermoelectric materials are promising candidates to tackle the problem of CO_2 emissions, when their efficiency is increased. Strategies to increase the figure of merit (ZT) for thermoelectric materials, include nanostructuring of the materials to reduce the thermal conductivity significantly. In this contribution we present recent results on two different important nanostructured materials, i.e. nanostructured Bi and Se double substituted GeTe (already known as phase change material, PCM) and superlattices of Bi_2Te_3/Sb_2Te_3.

Tellurium based PCM have a small band gap and a low thermal conductivity. Additionally, PCM´s are known to form complex nanostructures which make them ideal candidates for the application as thermoelectric materials [1]. To be able to control and understand the influence of the nanostructuring is an essential step in order to further reduce the thermal conductivity of these materials and hence to increase the ZT value.

$[GeTe]_{0.962}[Bi_2Se_{0.2}Te_{2.8}]_{0.038}$ and $[GeTe]_{0.937}[Bi_2Se_{0.2}Te_{2.8}]_{0.063}$ powder samples have been synthesized and compacted by spark-plasma sintering (SPS). Both samples were heat cycled. The high ZT value of $[GeTe]_{0.962}[Bi_2Se_{0.2}Te_{2.8}]_{0.038}$ remained stable but for the $[GeTe]_{0.937}[Bi_2Se_{0.2}Te_{2.8}]_{0.063}$ the ZT dropped from high to moderate ZT values after the first heating cycle due to a degradation of the electrical conductivity.

HRTEM micrographs have been recorded before and after the heat treatments of the $[GeTe]_{0.937}[Bi_2Se_{0.2}Te_{2.8}]_{0.063}$ specimen in order to identify real-structure property co-relationships. Before the heat treatments two major effects appearing on different length scales were noticed. Firstly, the precession electron diffraction (PED) measurements show a splitting of the reflections. Simulations show that the splitting is either due to a 91.3° rotation of domains or the formation of non-merohedral twins with a mirror plane along the {101} plane (figure 1a-c). Secondly, observed stripe like Moiré fringes appear on small nanometer sized areas in an ordered GeTe matrix (figure 1d). Preliminary simulations of the Moiré contrast indicate that the stripe like fringes rather arise from a change in the lattice constant than due to a rotation and/or translation of different GeTe grains. It is believed that the change of the lattice constant is due to an agglomeration of $Bi_2(SeTe)_3$. After the heat treatments the stripe like Moiré fringes vanished and planar defects were observed and also indicated via diffuse scattering in the FFT pattern (see figure 2) [1].

Artificial superlattices of Bi_2Te_3/Sb_2Te_3 as reported by Venkatasubramanian lead to a significant increase of the ZT value [2] with respect to bulk materials. However, the superlattice structure of Venkatasubramanian and thus the high ZT values have not been reproduced, in this form yet. In cooperation with the Fraunhofer IPM we show a similar superlattice structure prepared with the so-called nanoalloying approach [3] and report about the reproducibility of the thermoelectric performance.

1. U. Schürmann, V. Duppel, S. Buller, W. Bensch and L. Kienle, Cryst. Res. Technol. 46 (2011), p. 561
2. R. Venkatasubramanian, E. Siivola, T. Colpitts and B. O'Quinn, Nature 413 (2001), p. 597.
3. J.D. König, M. Winkler, S. Buller, W. Bensch, U. Schürmann, L. Kienle and H. Böttner J. Electron. Mater 40 (2011) p. 1266
4. Acknowledgment: The authors would like to thank Christin Szillus for the FIB preparation. Financial support by the DFG in the frame of the priority program SPP1386 "Nanostructured Thermoelectric Materials" is gratefully acknowledged.

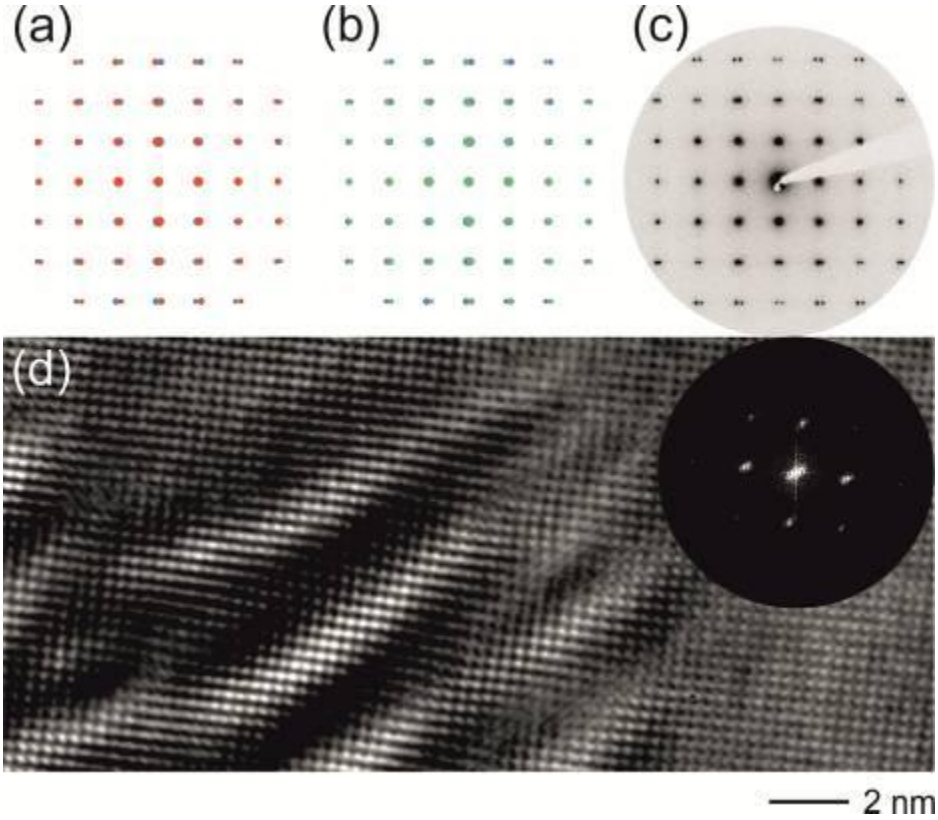

Figure 1. PED and Fourier filtered HRTEM micrograph of $[GeTe]_{0.937}[Bi_2Se_{0.2}Te_{2.8}]_{0.063}$ before the heat treatments. PED pattern of the sample shows a splitting of the reflections (c). Simulations indicate that the splitting is either due to a 91.3 ° rotation of different grains (a) or a twinning with a mirror plane along the {101} plane (b). HRTEM micrographs (d) show a stripe like Moiré contrast. The inset represents the corresponding FFT.

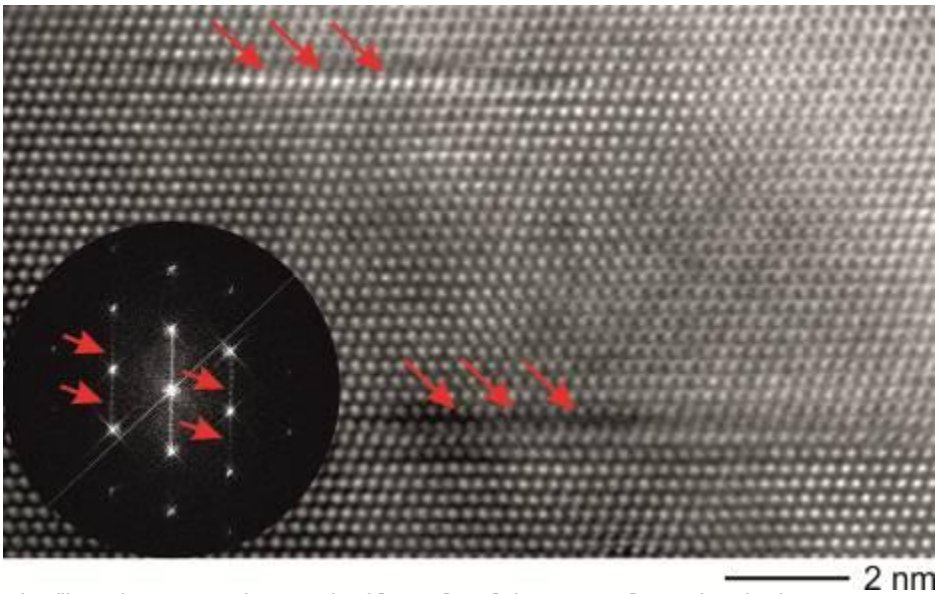

Figure 2. Fourier filtered HRTEM micrograph of $[GeTe]_{0.937}[Bi_2Se_{0.2}Te_{2.8}]_{0.063}$ after the heat treatments. Red arrows indicate planar defects. The inset represents the corresponding FFT. The diffuse intensities are due to the planar defects observed in the HRTEM micrograph [1].

Materials for Energy Technology

MS.4.089
Hydrogen storage behaviour of Pd-polymer composites

P. Mengucci[1], G. Barucca[2], G. Carotenuto[3], R. Checchetto[2], A. Di Cristoforo[1], A. Miotello[2], E. Santecchia[1]

[1]Dipartimento SIMAU, Università Politecnica delle Marche, Ancona, Italy
[2]Dipartimento di Fisica, Università di Trento, Trento, Italy
[3]Institute of Composite and Biomedical Materials, National Research Council, Napoli, Italy.

p.mengucci@univpm.it
Keywords: Hydrogen storage, metal hydrides, metal-polymer composites, electron microscopy.

Solid state hydrogen storage based on metal hydrides represents a viable way to obtain storage systems that are safe and efficient at the same time even though their practical implementation is mainly limited by the decrepitation phenomenon and the slow hydrogen sorption kinetics.

Composite materials constituted of a metal forming hydride dispersed into a porous matrix can be used to overcome those limitations. In particular, the confinement of nanometric particles (nanoconfinement) has been proved to enhance the thermodynamic and kinetic properties of the composite materials [1, 2]. The synthesis of nanoconfined composites can be performed by chemical and electrochemical methods as well as by laser ablation techniques, generally requiring considerable experience and expensive equipment [3]. In order to overcome those drawbacks we produced a metal-polymer composite material from commercially available components by using a simple polymerization procedure not requiring specific equipment. The metal-polymer system studied in this work is formed of Pd metal particles embedded in a polysilossane polymeric matrix. Polysilossane exhibits high hydrogen permeability while Pd forms the interstitial $PdH_{0.67}$ metal hydride.

Aim of this work is to study the hydrogenation properties of the obtained composites and to investigate the microstructural changes induced by the hydrogen absorption/desorption cycles.

The Pd particles (Sigma-Aldrich, Pd 99.9%, nominal surface area between 40 and 60 m^2/g) were manually dispersed into a self-curing acetic silicon polysilossane formulation (Saratoga). Three different compositions were prepared with a nominal Pd content (in wt%) of 5% (sample A), 15% (sample B) and 50% (sample C). The hydrogen sorption measurements were performed in a Sievert's type apparatus at three different temperatures: 60°C, 80°C and 100°C. For each temperature, the hydrogenation properties of the samples were evaluated at three different pressure values: 0.2 atm (low pressure), 1 atm (intermediate pressure) and 2 atm (high pressure).

The structural characterization was performed by X-ray diffraction (XRD), scanning electron microscopy (SEM) and energy dispersive microanalysis (EDS).

The pure Pd powder is formed of spherical particles with a diameter ranging from 200 nm to 400 nm. In the composite samples the Pd particles tend to form clusters whose mean size increases with the Pd content reaching a maximum value for sample C (Pd 50%), as shown in Figure 1.

After repeated hydrogen sorption cycles the structure of the samples is almost unchanged and even the crystalline state of the Pd particles remains unaltered suggesting the complete reversibility of the $Pd \leftrightarrow PdH_{0.67}$ reaction. Since the polymeric matrix always evidenced a negligible contribution to the hydrogen stored, the amount of hydrogen desorbed during the dehydrogenation process for the different samples was attributed only to the formation of the $PdH_{0.67}$ hydride.

The total amount of hydrogen desorbed by each sample, expressed as the H/Pd atomic ratio, is plotted in Figure 2. as a function of the desorption time. In Figure 2. the slope of the initial increase of each curve depends on the desorption kinetics, that ends at the beginning of the plateau, while the height of the plateau measures the total hydrogen absorbed amount. It is evident that the pure Pd powder always exhibits the fastest kinetics independently on the pressure and temperature values. However, in spite of the slowness of its reaction kinetics, sample A (Pd 5%) always stores the highest amount of hydrogen of all the other composites (Figure 2.). This behaviour is much more pronounced at high temperature and pressure values (Figure 2.b) where sample A stores a hydrogen amount even higher than the pure Pd powder, close to the stoichiometric limit of H/Pd=0.67. On the contrary, regardless of the temperature and pressure values sample C (Pd 50%) always shows the worst performance in terms of hydrogen stored amount (Figure 2.).

In conclusion, by limiting the hydrogen diffusivity during the sorption processes the polymeric matrix slows down the hydrogen kinetics of the composite samples. On the other side, the worsening of the

hydrogen storage capacity at the increase of the metallic content can be related to the formation of the Pd clusters that reduce the surface area exposed to H_2. In this respect, sample C (Pd 50%) still shows a “polymer-like” behaviour due to the fact that the metallic domains of its structure are not well interconnected so that hydrogen cannot migrate freely through them. In this way, the beneficial effect of the bulk-like system given by sample C is prevented.

Further work is in progress to deeper investigate the role of the polymeric matrix as well as the influence of the cluster size on the hydrogenation behaviour of the Pd-polymer composites.

1. C. Zlotea, M. Latroche, Colloids and Surfaces A: Physicochemical and Engineering Aspects, in press, available on line 1 December 2012.
2. M. Fichtner, Nanotechnology 20 (2009) 204009.
3. K.J. Jeon, H.R. Moon, AM. Ruminski, B. Jiang, C. Kisielowski, R. Bardhan, J.J Urban, Nature Materials 10 (2011) 52.

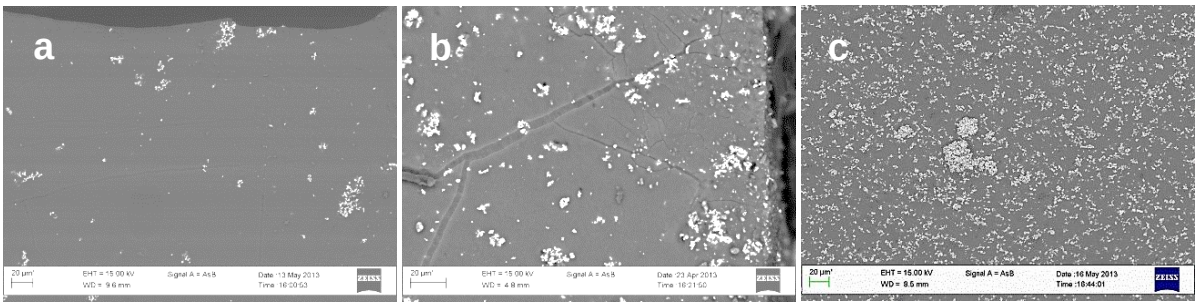

Figure 1. SEM images of the composite samples in the as-produced condition (in wt%): a) Pd 5%, b) Pd 15% and c) Pd 50%.

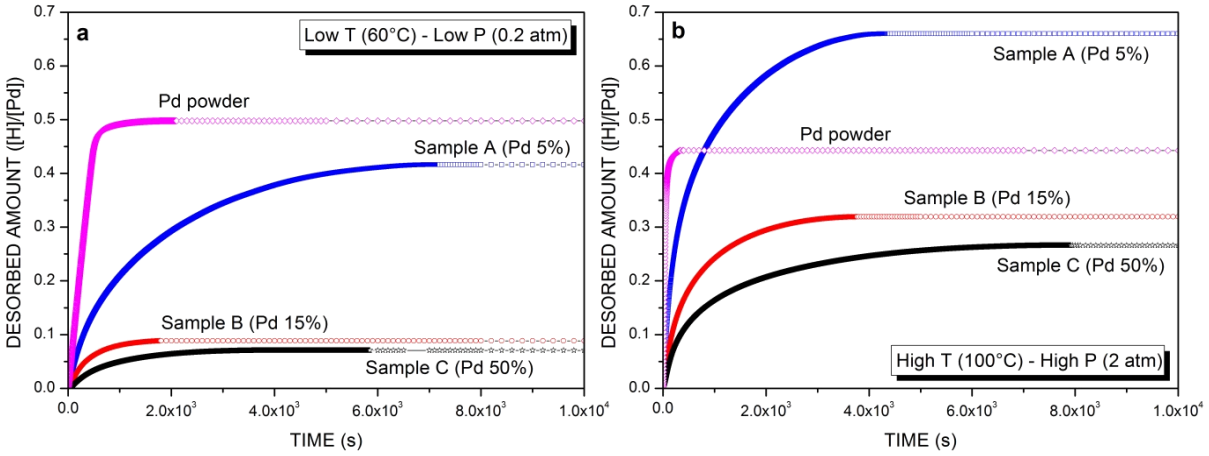

Figure 2. Hydrogen sorption kinetics of the composite samples: a) low temperature and low pressure values and b) high temperature and high pressure values. The Pd powder curves are reported as a reference.

Materials for Energy Technology

MS.4.090
Compacted Mg-based powders for hydrogen storage applications

A. Montone[1], D. Mirabile Gattia[1], L. Pasquini[2]

[1]ENEA, Technical Unit Materials Technology, Rome, Italy
[2]University of Bologna, Department of Physics and CNISM, Bologna, Italy

amelia.montone@enea.it
Keywords: magnesium hydride, compacted powders, electron microscopy

A cheap, abundant and environment-friendly attractive material for hydrogen (H_2) storage is magnesium hydride (MgH_2) [1]. Theoretical hydrogen storage capacity is about 7.6 wt% H_2 and it is an interesting material also for heat storage applications (-76 kJ/mol H_2) [2].

The application of materials for hydrogen-based technologies requires sufficiently fast H_2 absorption and desorption kinetics, which are normally sluggish in pure, microcrystalline Mg. A significant progress in this respect was gained by various materials engineering routes that yield a nanostructured material adding at the same time a suitable catalyst at the surface.

In particular, nanostructuring and catalyst dispersion through high-energy ball milling has emerged as a relatively simple, cost-effective, and scalable technique to produce MgH_2-based materials with fast H_2-sorption kinetics.

Furthermore the materials used for hydrogen storage should present good stability to cycling in terms of kinetics and capacity. The stability of these materials to cycling under hydrogen pressure have to be deeply studied.

For what concern the application of metallic hydrides inside tanks for hydrogen storage many authors proposed to fill the tanks with pellets instead of powders in order to avoid deterioration of the powders and to improve heat exchange. The pellet should be in contact with another material or with the heating or freezing system in the tank to have the suitable conditions in term of temperature for absorption and desorption cycling.

Quite recently, the ideas of nanostructuring, dispersion of catalyst and graphitic carbon, and powder compaction in pellet form, were combined to synthesize MgH_2/carbon based materials composites showing both improved H_2-sorption kinetics and increased thermal conductivity [3-5]. This success story finally led to the realization and appearance on the market of MgH_2/expanded natural graphite (ENG) composite H_2-storage tanks for stationary applications, in which a phase-change material can also be employed as a reservoir for the heat of transformation. Other strategies that make use of Al and Cu instead of ENG to obtain Mg-alloy/C composites were also studied with particular reference to their thermal conduction properties and their applications are presently under investigation [6].

In this work, we investigate the microstructure and morphology of pellets obtained by the compaction of ball-milled MgH_2-based powders mixed with expanded natural graphite and a suitable catalyst (figure 1).

The pellets are subjected to repeated hydrogen sorption cycles to measure hydrogen storage properties and its stability with cycling. Moreover, the effect of air-exposure on the hydrogen sorption behaviour is studied.

Electron microscopy observations of as-prepared and cycled pellets point to a dramatic modification of the material's microstructure upon repeated hydrogen cycling (figure 2). In particular, the appearance of MgH_2 particles depleted of the catalyst and the formation of hollow MgO shells are highlighted.

Kinetics measurements were carried out with a Sieverts' type apparatus. The compacted powder were cycled under hydrogen at 310°C and at H_2 pressures of 1.2 bar and 4.0 respectively, during desorption and adsorption run respectively.

1. .I. Jain, C. Lal, A. Jain, Int J Hydrogen Energy, 35 (2010) 5133-44
2. M. Felderhoff, B. Bogdanović, Int J Molecular Sciences, 10 (2009) 325-44
3. A. Chaise, P. de Rango, Ph. Marty, D. Fruchart, S. Miraglia, R. Olives, S. Garrier, International Journal of Hydrogen Energy, 34 (2009), p. 8589
4. C. Pohlmann, L. Rontzsch, S. Kalinichenka, T. Hutsch, B. Kieback, International Journal of Hydrogen Energy, 35 (2010), p. 12829
5. D. Mirabile Gattia, A. Montone, L. Pasquini, Int J Hydrogen Energy 38 (2013), 1918-1924
6. A. Khndewlal, F. Agresti, G. Capurso, S. Lo Russo, A. Maddalena, S. Gialanella, G. Principi, International Journal of Hydrogen Energy, 35 (2010), p. 3565

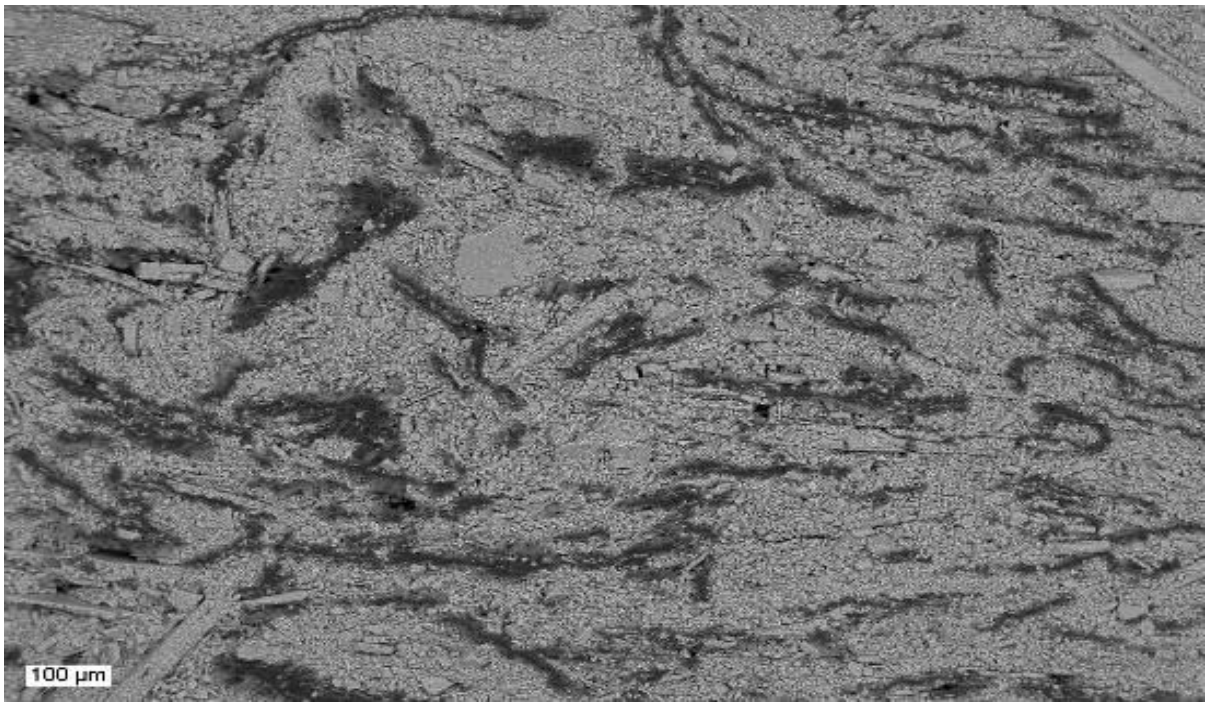

Figure 1. SEM image of as-prepared compacted MgH_2 with 10wt% Nb_2O_5 and 5 wt% ENG

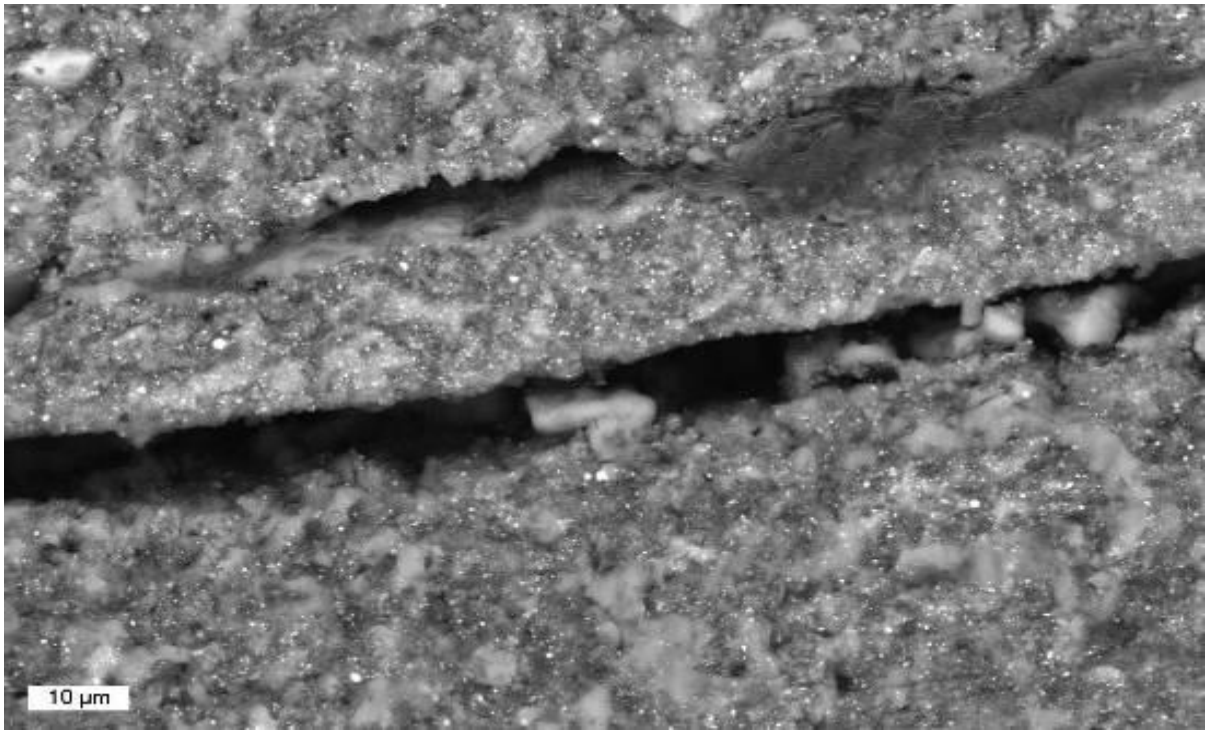

Figure 2. SEM image of compacted MgH_2 with 10wt

Materials for Energy Technology

MS.4.P091
Aberration-corrected STEM and EELS analyses of interfaces in wafer-bonded tandem solar cells

D. Häußler[1], L. Houben[2], R. Dunin-Borkowski[2], S. Essig[3], F. Dimroth[3], W. Jäger[1]

[1]Christian Albrechts Universität zu Kiel, Institute for Materials Science, Kiel, Germany
[2]Ernst Ruska Centre for Microscopy and Spectroscopy with Electrons, Jülich, Germany
[3]Fraunhofer Institute for Solar Energy Systems ISE, Freiburg, Germany

dih@tf.uni-kiel.de
Keywords: Multi-junction solar cell, bonding, aberration corrected STEM

Crystalline silicon based tandem solar cells are a promising way to circumvent the conversion efficiency limits of conventional single-junction photovoltaic cells. In such devices, the visible wavelength range of the solar spectrum is converted more efficiently by adding additional pn-junctions on top of a Si cell (Figure 1). High-quality III-V multi junction solar cells on Si can be fabricated by surface-activated wafer bonding at room temperature. In this way the formation of lattice-mismatch induced defects in the active solar cell layers can be reduced or completely avoided. In this approach, a 10 µm thin GaInP/GaAs dual junction solar cell is grown lattice-matched on GaAs and transferred to Si by direct wafer bonding (Figure 2). An essential stage of our treatment represents is the in-situ particle bombardment of the surfaces to be bonded aiming at cleaning and surface activation under high vacuum conditions (Figure 3). For testing the bonding concept, we have investigated two alternative concepts to perform these treatments: ion beam bombardment (IB) and atom beam bombardment (FAB). The FAB method has been successfully used as well for the bonding of other semiconductor systems [1,2]. In HR-TEM and EDXS cross-section investigations of the bonding interfaces between the GaAs middle-cell and the Si bottom-cell, amorphous interface layers with disadvantageous properties have been discovered for both treatments [3]. Here, we present the results of STEM and EELS investigations of the identical TEM cross-section samples (Figures 4, 5). The investigations were performed at a probe corrected FEI Titan 80-300 FEG TEM equipped with a CEOS double hexapole corrector. These analyses clearly benefit from reduced delocalization in STEM imaging and from the improved detection sensitivity in STEM-EELS. Across the bonding interface. Si, O, C, Ga and As signal intensities after background subtraction and normalization to the inelastic scattering cross-section are shown. The resulting normalized EELS signal is proportional to the area density of the elements. Error bars reflect the 68% confidence interval for the signal calculated as the combined effect of signal noise, background noise, and background extrapolation error. The elemental profiles reveal the presence of a gallium and silicon oxide amorphous double layer with a minor carbon contamination.

1. M.M.R. Howlader, T. Suga, F. Zhang, T.H. Lee and M.J. Kim, Electrochemical and Solid-State Letters, 13 (2010) p. H61.
2. T.R. Chung, L. Yang, N. Hosoda, T. Suga, Nuclear Instruments and Methods in Physics Research B I2 (1997) p. 203.
3. D Häussler et al. in: Proc. 15th European Microscopy Congress 2012 (Manchester, Vol. 1, Eds. D.J. Stokes, W.M. Rainforth, The Royal Microscopical Society 2012) p. 7

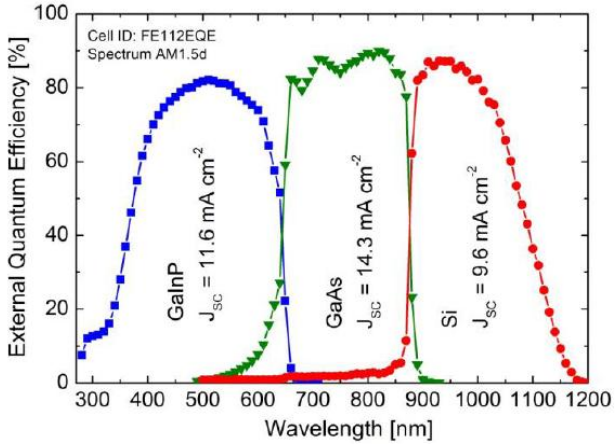

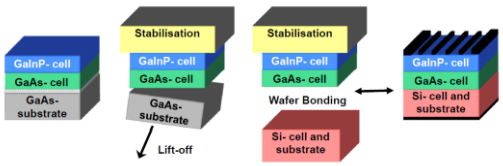

Figu
GaIr
after

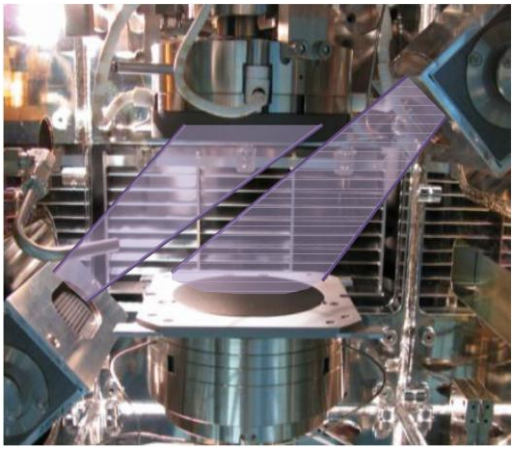

Figu

Figure 3. Vacuum chamber of the commercial equipment which is used for surface activation and bonding (schematic).

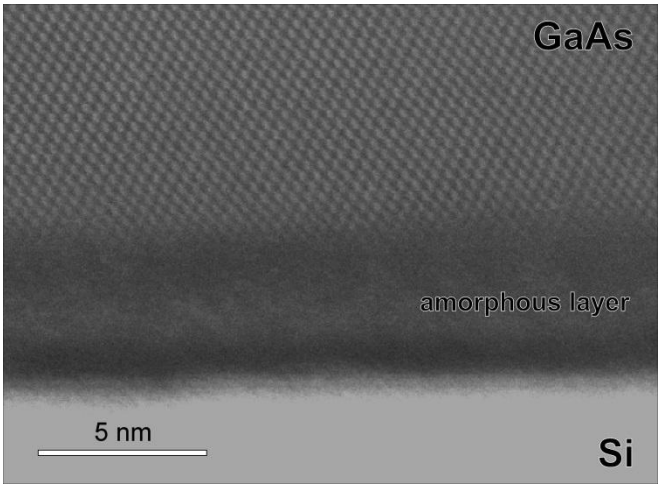

Figure 4. Cross-section HAADF-STEM image of the amorphous interlayer at the bonding interface between the GaAs middle-cell and the Si bottom-cell. III-V multi junction solar cell wafer-bonded on Si after atom bombardment treatment.

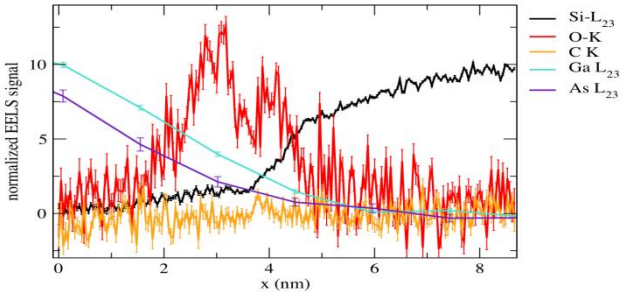

Figure 5. EELS profiles for a III-V multi junction solar cell wafer-bonded on Si after atom bombardment treatment taken

Materials for Energy Technology

MS.4.P092
Focused ion beam sample preparation of mechanically alloyed iron powders for atom probe tomography

F. Mendez-Martin[1], G. Ressel[1], H. Leitner[1]

[1]MontanUniversität Leoben, Department Physical Metallurgy and Materials Testing, Leoben, Austria

francisca.mendez-martin@unileoben.ac.at
Keywords: focused ion beam, atom probe tomography, steel powders

Higher temperature strength in steels can be achieved with addition of finely distributed Yttrium oxides by mechanical alloying. Nevertheless, the strengthening mechanism during mechanical alloying is still not clearly understood. In order to clarify the effects of Y and O distribution during the alloying process, 4 different manufactured powders were analysed.

Two different iron-rich powders have been analysed, see figure 1. The powder was mechanically alloyed for 12h and 48h using a Certony^{TM} attritor. The iron powder was produced by water atomization and was mixed with 0.5 wt% yttria powder with a d_{90} of 1.16 µm. The chemical composition is presented in table 1.

For the characterization of the different powder conditions, atom probe tomography (APT) has been used [1]. For APT measurements needle-shaped specimens are needed, with radii between 30 to 100 nm on the tip and an angle near to or lower than 10°. Traditional methods as chemically or electrochemically polishing [2] are impossible to use in powder material. Therefore, the method for preparation of needle-shaped tips for powder samples via focused ion beam (FIB) was chosen [3, 4]. A single grain of each powder was selected for a thick lift out in a wedge form and a platinum layer was deposited on the interesting zone, first via electron deposition and afterwards with ion deposition, to minimize gallium implantation. Multiple specimens were cut from the thick lift out wedge and welded on a micotip coupon, which provides the pre-tips for the APT measurements. Afterwards, the following annular milling at 30 kV, 5 kV and 2 kV were the last process, for the preparation of the APT tips free of Gallium implantation. The atom probe investigations were completed in a LEAP^{TM} 3000X HR of Cameca^{TM} with a Local Electrode system. The analyses were performed in voltage mode at 60 K in ultra-high vacuum. A pulse fraction of 15 % and 20 % was used. The atom probe measurements were evaluated with IVAS 3.4.3 software. The analysed volume was about 25x25x150 nm^3 and the different material conditions were compared.

The atom probe investigations reveal a clustered arrangement of Y and O atoms during mechanical alloying; see figure 2 a) and b). Yttrium atoms together with oxygen, rearrange during mechanical alloying to form clusters. Aluminium and manganese enrichments (see figure 2 c) and d)) could be also detected, which suggests that diffusion processes are active during the mechanical alloying process. These clusters are not only remnants of the Y_2O_3 powder, yttrium and oxygen dissolve in the matrix to rearrange afterwards at favourable sites as lattice defects, vacancies or dislocations to form clusters.

By using focused ion beam, needles-shape specimens for atom probe tomography could be prepared for two different grain size powder samples after 12 and 48 h of mechanical alloying. The atom probe investigations reveal fine distributed yttrium oxide clusters as well as yttrium dissolved in the matrix. Moreover enrichments of alloying elements as aluminium and manganese reveal that diffusion processes are active during mechanical alloying clarifying the mechanism during this process.

1. W.R. McKenzie, E.A. Marquis and P.R. Munroe, “Microscopy: Science, Technology, Applications and Education”, ed. A. Méndez-Vilas and J. Díaz (2010) p. 1800.
2. M.K. Miller, A. Cerezo, M. G, Hetherington and G.G.W. Smith, “Atom Probe Field Ion Microscopy”, ed. R.J. Brook, A. Heuer, T.J. Marks, D.A. Smith, A. Cheetham, S.P. Hirsch, J. Silcox, M.V. Tirrell, V.Vitek (1996) p.476.
3. M.K. Miller, K.F. Russel, K. Thompson, R. Alvis and D. J. Larson, Microscopy and Microanalysis 13 (2007), p. 428.
3. M.K. Miller and K.F. Russel, Ultramicroscopy 107 (2007), p. 761.

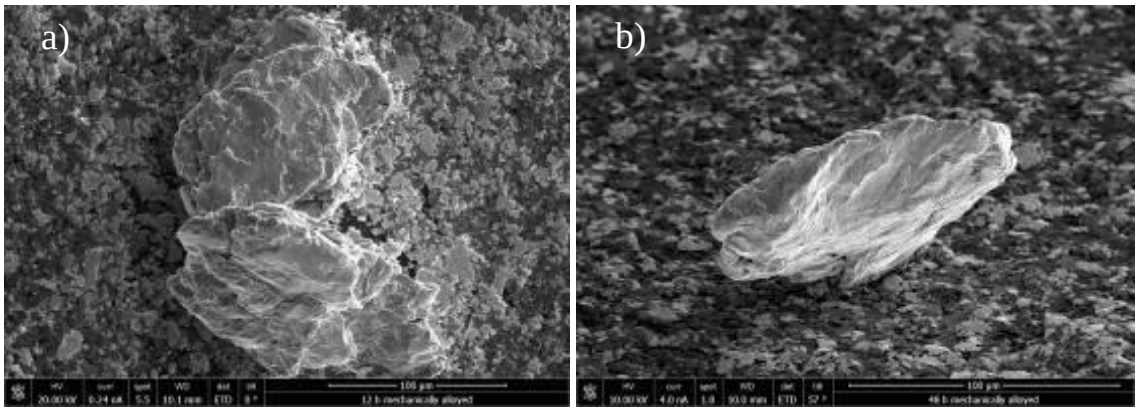

Figure 1. Powder after 12 h mechanically alloyed (a) and after 48 h mechanically alloyed (b).

	Fe	Al	Mn	Cr	Ni	Mo	W	Y_2O_3
12 h mechanically alloyed	bal.	0.34	0.14	0.09	0.05	0.01	0.8	0.12
48 h mechanically alloyed	bal.	0.1	0.16	0.24	0.1	0.01	0.05	0.13

Table 1. Chemical composition of the of the analyzed powders (at.%).

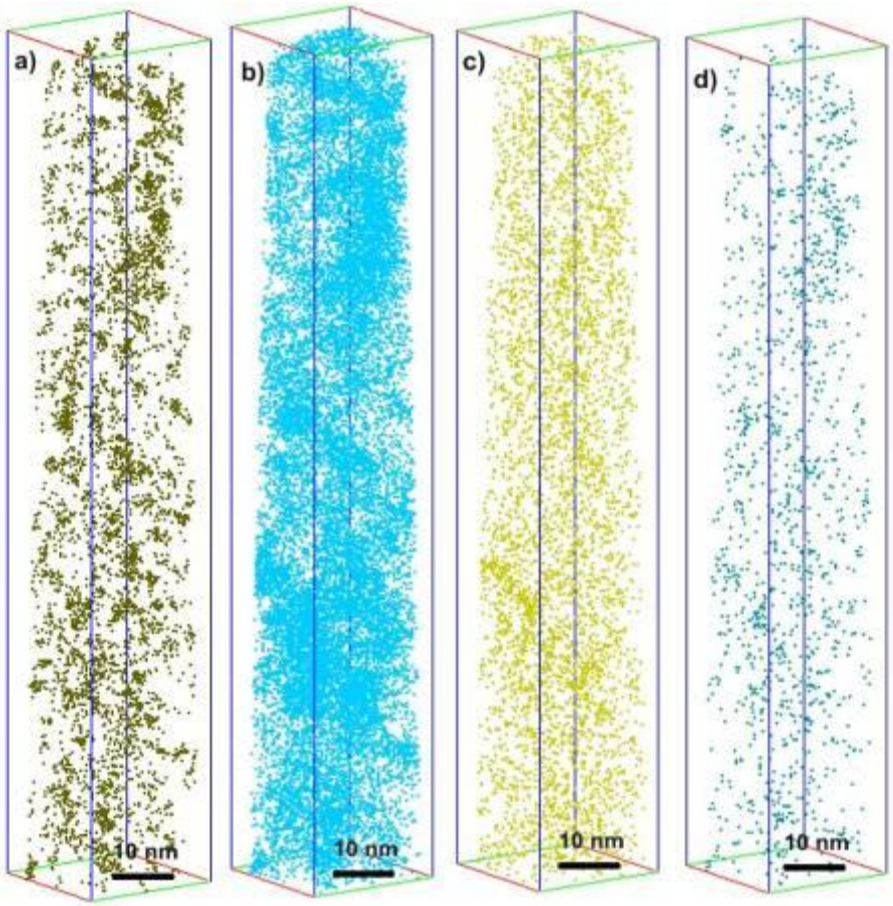

Figure 2. 3D atom maps of the 48 h mechanically alloyed condition. a) Y; b) O. 3D atom maps of the 48 h mechanically alloyed state, showing enrichments of Al and Mn at the Y-O clusters c) Mn and d) Al.

Materials for Energy Technology

MS.4.P093
Morphology studies of Si-SiO_2 nanocomposites using energy-filtered transmission electron microscopy

R. Hübner[1], D. Friedrich[1], D. Wolf[2], B. Liedke[1], B. Schmidt[1], K.-H. Heinig[1]

[1]Helmholtz-Zentrum Dresden-Rossendorf, Institute of Ion Beam Physics and Materials Research, Dresden, Germany
[2]Technische Universität Dresden, Triebenberg Laboratory, Dresden, Germany

r.huebner@hzdr.de
Keywords: silicon-rich silicon oxide, EFTEM imaging, EFTEM tomography, KMC simulation

Due to significant band gap widening by quantum confinement, Si nanosponge structures embedded in SiO_2 formed by spinodal decomposition of metastable silicon-rich silicon oxide are promising, advanced Si absorbers for 3rd generation solar cells. In thermodynamically metastable, silicon-rich oxide, i.e. SiO_x with $x < 2$, high-temperature annealing results in the formation of Si precipitations in a stoichiometric SiO_2 matrix. According to $SiO_x \rightarrow \frac{x}{2} SiO_2 + (1-\frac{x}{2})Si$, phase separation of SiO_x films with $1.2 \leq x < 2$ (Si excess of up to 40 at.-%) leads to disconnected Si nanoclusters, whereas for $x < 1.2$ (Si excess larger than 40 at.-%) phase separation results in percolated Si nanostructures with a sponge-like morphology [1].

To reveal such a sponge-like morphology in sputter-deposited SiO_x films for $x \sim 1$ after activation by rapid thermal annealing (RTA), energy-filtered transmission electron microscopy (EFTEM) imaging as well as EFTEM tomography were carried out and the results were compared with kinetic Monte-Carlo (KMC) simulations. To this end, 200 nm thick SiO_x layers were prepared at room temperature on p-type (100) Si wafers by magnetron sputtering in Ar plasma from two simultaneously operating Si and SiO_2 targets. During subsequent RTA in Ar or Ar + 5 % H_2 ambient, samples were heated up to 1150 °C and annealed for 30 s. Sponge-like nanostructures were investigated by EFTEM imaging using an image-corrected FEI Titan 80-300 microscope equipped with a Gatan Imaging Filter 863. For EFTEM tomography, a tilt series between ±70° was acquired in steps of 2° in a Philips CM200 FEG microscope with Gatan Imaging Filter 678. The tilt series alignment, i.e. the correction of residual displacements, was carried out using the IMOD software [2], while the tomographic reconstruction of the Si 3D morphology was performed with the Weighted Simultaneous Iterative Reconstruction Technique [3].

The contrast in zero-loss filtered high-resolution TEM images such as Figure 1 is caused by the coherent superposition of unscattered and elastically scattered electrons within the thin TEM lamella, and hence, related to the projected atomic structure. Consequently, Bragg-oriented Si nanocrystals larger than a minimum size are visible in Figure 1 and indicate phase separation of the SiO_x film with subsequent crystallization during RTA. Since large amorphous Si precipitates crystallize preferably, high-resolution TEM images allow the determination of a maximum Si structure size. For small Si structures, however, phase separation is also possible without crystallization. Such amorphous precipitates as well as not Bragg-oriented Si nanocrystals cannot be observed with high-resolution electron microscopy, leading to an underestimation of the Si phase fraction. Therefore, EFTEM analysis is a suitable alternative for Si morphology studies. In particular, valence-band plasmon energy-loss imaging is an appropriate approach, since the Si plasmon peak is, except the zero-loss peak, the most intense feature in the electron energy-loss spectrum. It has a narrow energy distribution of a few eV, and thus, allows to distinguish the Si phase from the SiO_2 compound [4]. As shown in Figure 2, the expected sponge-like Si morphology in phase-separated SiO_x has been proven by Si plasmon imaging, which particularly shows that Si filaments have diameters of a few nanometers with a narrow size distribution. This finding is in excellent agreement with large-scale simulations based on KMC (Figure 3). Although Si plasmon EFTEM images can show the Si phase distribution in a planar projection, they do not provide three-dimensional information. For example, a superposition of Si nanodots cannot be distinguished from a sponge-like morphology in a 2D projection. Therefore, EFTEM tomography was applied, revealing that the separation of silicon into percolated nanostructures is not obvious (Figure 4). Coarsening of the Si sponge accompanied by a loss of percolation may be the reason. Indeed, longer annealing at 1100 °C for 3 h leads to separated non-spherical nanoclusters [5]. However, an underestimation of the thinnest, presumably amorphous, Si filaments cannot be excluded. Prolonged electron irradiation during acquisition of the EFTEM tilt series might have an influence on the sponge-like morphology, too.

1. T. Müller, K.-H. Heinig, W. Möller, C. Bonafos, H. Coffin, N. Cherkashin, G. Ben Assayag, S. Schamm, G. Zanchi and A. Claverie, Appl. Phys. Lett. 85 (2004), p. 12.
2. J. Kremer, D. N. Mastronarde and J. R. McIntosh, J. Struct. Biol. 116 (1996), p. 71.
3. D. Wolf, A. Lubk and H. Lichte, Ultramicroscopy (2013), submitted.
4. S. Schamm, C. Bonafos, H. Coffin, N. Cherkashin, M. Carradaa, G. Ben Assayag, A. Claverie, M. Tencé and C. Colliex, Ultramicroscopy 108 (2008), p. 346.
5. A. Yurtsever, M. Weyland and D. A. Muller, Appl. Phys. Let. 89 (2006), p. 151920.
6. The authors kindly acknowledge TEM sample preparation by Annette Kunz and Martina Missbach.

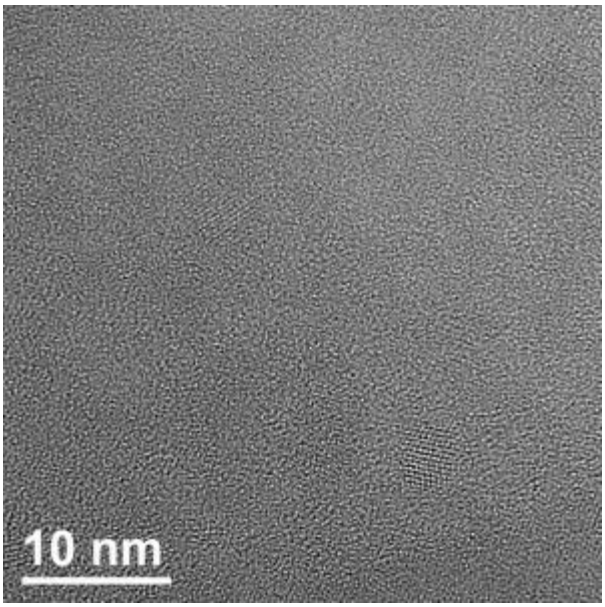

Figure 1. Cross-sectional zero-loss filtered high-resolution TEM image of a $SiO_{0.9}$ layer decomposed into Si and SiO_2 during annealing at 1100 °C for 30 s. Only Bragg-oriented Si nanocrystals can be clearly observed.

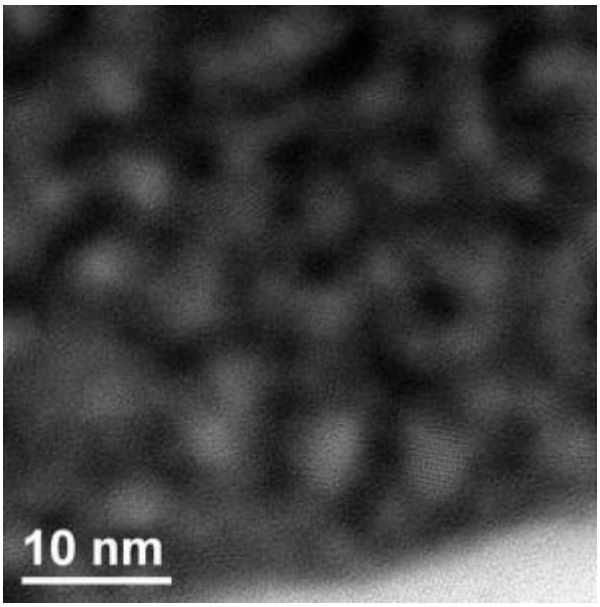

Figure 2. Cross-sectional Si plasmon EFTEM image of the same field of view as in Figure 1. Valence-band plasmon energy-loss imaging at E_{loss} = 17 eV allows to visualize both, crystalline as well as amorphous Si structures of various sizes.

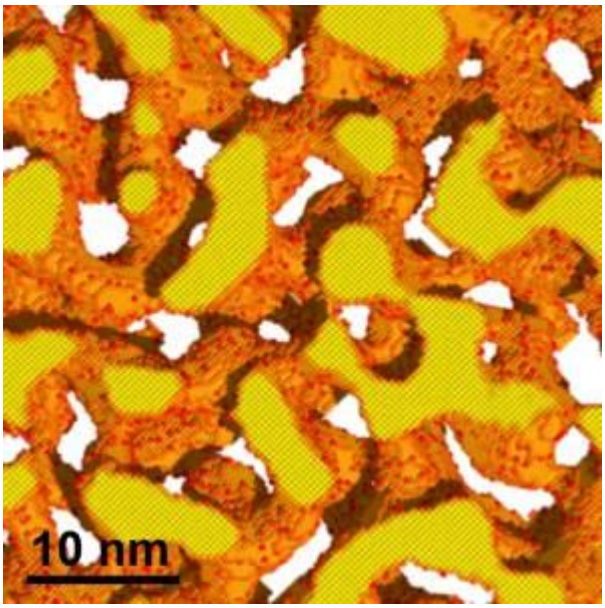

Figure 3. 3D morphology of an approximately 10 nm thick phase-separated $SiO_{0.9}$ film predicted by KMC simulation corresponding to annealing at 1100 °C for 30 s. The yellow areas represent a cut through silicon by slicing the simulation box, while the orange color visualizes the interface between Si and SiO_2, which is assumed to be transparent.

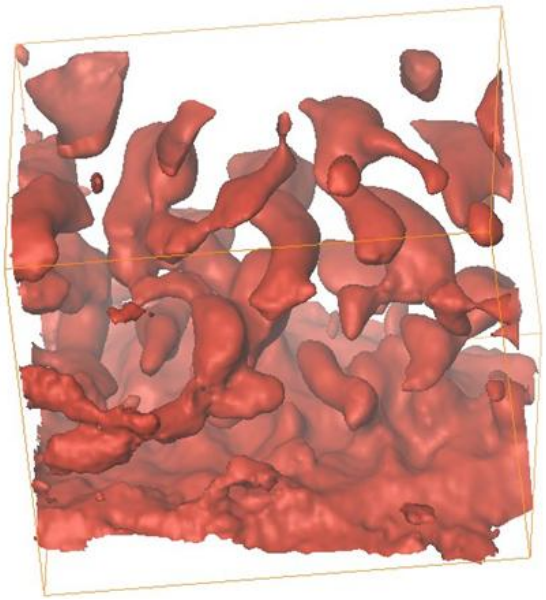

Figure 4. Si plasmon EFTEM tomography (E_{loss} = 17 eV) of phase-separated $SiO_{0.9}$ confirms a 3D sponge-like morphology as expected by spinodal decomposition. Si (red) and SiO_2 (transparent) are separated applying an intensity threshold resulting in ca. 30 vol.-% Si within a 28 x 31 x 24 nm³ volume.

Materials for Energy Technology

MS.4.P094
MgH_2/TiO_2 nanocomposite for application in solid state hydrogen storage: comparison from powder and pellet.

A. Montone[1], A. Aurora[1], V. Contini[1], G. di Girolamo[1], D. Mirabile Gattia[1]

[1]ENEA, Material Technology Unit, Rome, Italy

amelia.montone@enea.it

The interest in Mg-based hydrides for solid state hydrogen storage is associated to their capability of reversibly absorbing and desorbing large amounts of hydrogen. For this reason, the tailoring of hydrogen sorption kinetics of Mg hydride represents one of the most challenging opportunities for a safe storage and reliable use of hydrogen in on board applications. Furthermore, the low cost, high hydrogen capacity and the light-weight make these materials an interesting perspective for technological application. However, the main limitation is represented by the slow hydrogen sorption kinetic and the high thermodynamic stability, which do not allow an immediate technological use. However, it is known that the nanostructuration of MgH_2-based composite materials obtained by ball milling MgH_2 with different additives such as metals and their oxides [1,2], shows the best results in the direction of practical application due to its action of speeding up the kinetics and lowering both the working pressure and temperature.

Here we report a study of nanostructured composite materials obtained by ball milling MgH_2 with 5wt.% of TiO_2, which focused the attention on the structural and kinetic modifications promoted by long-term H_2 absorption and desorption cycles.

Both the crystalline structures of TiO_2, Rutile and Anatase, were explored on the basis of their different behaviour as additive [3] and in different cycling conditions mainly in term of temperature and H_2 charging and discharging pressure of cycling.

With the view to using this material in tank for hydrogen storage, the ball milled MgH_2/TiO_2 powder was enriched with 5wt.% of Expanded Natural Graphite (ENG) and then compacted in cylindrical pellets. The compaction and the addition of carbon-based additive in fact, increase the volumetric hydrogen storage density and improve the mechanical properties of compacted powders [4,5].

The samples were obtained by cold pressing MgH_2 + 5wt.%TiO_2 + 5wt.%ENG powder in a dye, under different loads and then subjected to repeated hydrogen sorption cycle.

The pellets, compared with the powder, show analogous kinetic performance even if the pressure of compaction revealed to be an important parameter for the efficiency and the mechanical stability of the compacted structure.

Kinetic and thermodynamic tests were performed using a Sievert's type gas reaction controller. Scanning Electron microscopy observations of as-prepared and cycled pellets allowed pointing out the distribution of the catalyst into the MgH_2 matrix and the analysis of the microstructural evolution occurring during and after cycling. The structural characterization before and after cycling was followed by X-ray diffraction.

1. G. Liang, J. Huot, S. Boily, A. Van Neste and R. Schulz: J. Alloys Comp. 292 (1999), p. 247–252.
2. W. Oelerich, T. Klassen and R. Bormann: J. Alloys Comp. 315 (2001), p. 237–242.
3. D.L. Croston et al. / Journal of Alloys and Compounds 492 (2010), p. 251–258
4. S. Garrier, A. Chaise , P. de Rango, P. Marty , B. Delhomme , D. Fruchart ,S. Miraglia, Int. J. Hydrogen Energy 36 (2011), p. 9719.
5. D. Mirabile Gattia, A. Montone, L. Pasquini, Int J Hydrogen Energy 38 (2013), 1918-1924

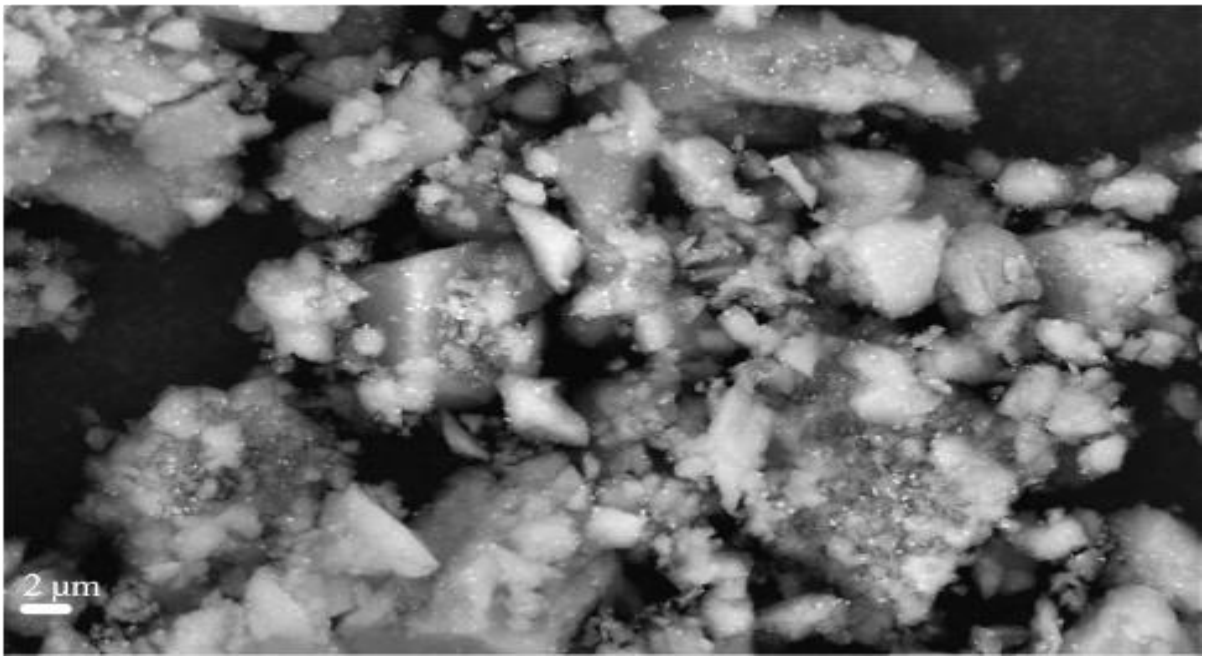

Figure 1. MgH_2 + 5wt.%TiO_2 (Anatase) after ball milling (10h in Ar at 6,0 bar)

Materials for Energy Technology

MS.4.P095
Structure and chemistry of CeO_2/YSZ interfaces investigated by TEM/STEM

K. Song[1], H. Schmid[2], V. Srot[1], E. Gilardi[3], G. Gregori[3], J. Maier[3], P.A. van Aken[1]

[1]Max-Planck Institute for Intelligent Systems, Stuttgart, Germany
[2]Leibniz-Institute for New Materials, Saarbrücken, Germany
[3]Max Planck Institute for Solid State Research, Stuttgart, Germany

ksong@is.mpg.de
Keywords: CeO_2/YSZ, interface, STEM, EELS, ELNES, Ce-$M_{4,5}$ edges

Ceria (CeO_2) and yttria stabilized zirconia (YSZ) are two typical candidates for electrolyte materials in solid oxide fuel cells attributed to their high ion conductivities. However, the conductivities of these materials are closely connected with high temperatures.Therefore, it is important to develop electrolyte materials which can conduct oxygen ions at lower temperatures. Recent experiments have shown that heterostructures consisting of alternating layers of Gd-doped CeO_2 and Y-doped zirconia (YSZ) exhibit higher ionic conductivity compared to either of the bulk materials[1]. However, the mechanism for the high ionic conductivity of the CeO_2/YSZ hetero structures is still unclear and under debate until now. Theoretical calculations indicate that the oxygen vacancy formation energy is considerably reduced at the interfaces and oxygen vacancies expected to segregate to the interfaces might provide highways for rapid ion conduction[2]. The aim of our work is to obtain insights into the structure and chemistry of interfaces between CeO_2 and YSZ by scanning transmission electron microscopy (STEM) combined with electron energy-loss spectroscopy (EELS).

Epitaxial CeO_2 films were grown on YSZ (111) substrates using pulsed laser deposition (PLD). TEM samples in cross-sectional geometry were prepared by the tripod polishing technique followed by Ar^+ ion-milling while cooling the specimen with liquid nitrogen. Investigations were carried out at 200 kV in an analytical TEM/STEM microscope (JEOL-ARM 200F) equipped with cold field-emission gun (C-FEG) and CEOS probe Cs-corrector. A post-column imaging energy-filter (GATAN GIF Quantum ER) attached to this system is used for EELS spectroscopy and electron spectroscopic imaging (ESI).

A bright-field (BF) STEM image of the cross-sectional view is presented in Figure 1a, showing the CeO_2/YSZ interface. The CeO_2 film epitaxially deposited on the (111) surface of YSZ is approximately 30 nm thick and continuous. Figure 1b shows a high-resolution, high-angle annular dark-field (HAADF)-STEM image of the interface. From the image it can be seen that the CeO_2 film and YSZ substrate have a cubic on cubic orientation relationship ((111) $<1\text{-}10>_{CeO2}$ // (111) $<1\text{-}10>_{YSZ}$). No reaction layers or other phases can be observed at the interface. Periodical misfit dislocations were observed at the interface with extra atomic planes appearing in YSZ. It is well known that the Ce-$M_{4,5}$ edges are valence sensitive to the ionic oxidation state. Since the possible presence of Ce^{3+} is seen as evidence of oxygen vacancy formation, oxygen states of cerium ions near the interface were investigated by electron energy-loss spectroscopy (EELS). Intensity ratios of Ce-$M_{4,5}$ white-lines as observed in energy-loss near-edge structures (ELNES) were used to determine the valence states of cerium. Measured spectra were compared with known reference spectra acquired from compounds containing cerium in Ce^{3+} or Ce^{4+} oxidation state. In addition, quantitative analysis has been performed on the Ce-$M_{4,5}$ edges to study the ratio of Ce^{3+} to Ce^{4+} as function of the distance from the interfaces.

1. S. Azad, O.A. Marina, C.M. Wang, L. Saraf, V. Shutthanandan, D.E. McCready, A. El-Azab, J.E. Jaffe, M.H. Engelhard, C.H.F. Peden, and S. Thevuthasan, Applied Physics Letters, 131906 (2005).
2. M. Fronzi,S. Cereda,Y. Tateyama,A. De Vita,and E. Traversa, Physical Review B **86**, 085407 (2012).
3. Financial support by the doctoral training program between MaxPlanck Society (MPG) and Chinese Academy of Sciences (CAS) is greatly acknowledged.

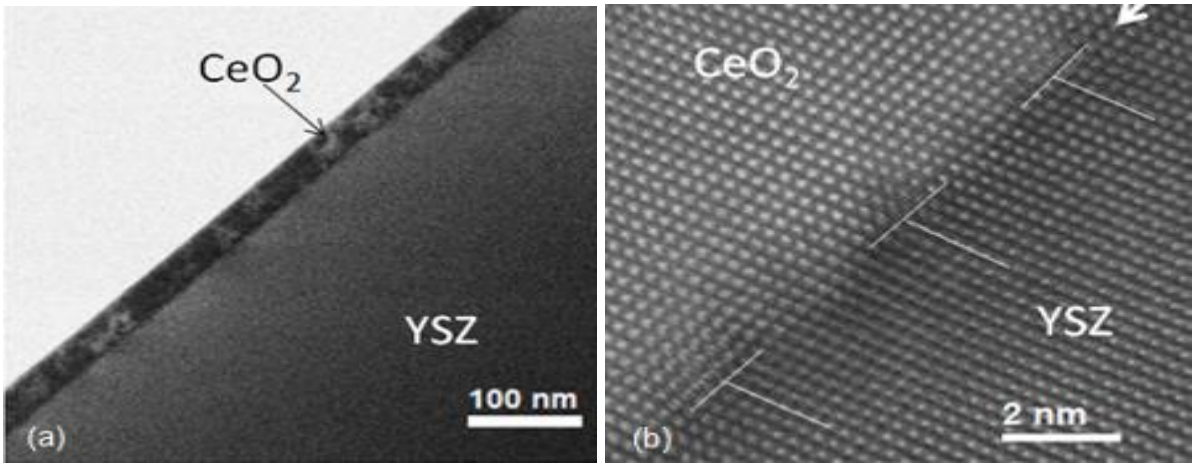

Figure 1.(a)Bright-field STEM image of CeO_2/YSZ interface. (b) High-angle annular dark-field (HR)STEM image of CeO_2/YSZ acquired along $(1\text{-}10)_{YSZ}$ direction. White arrow indicates the position of interface. Lattice mismatch is accommodated by periodically spaced misfit dislocations as indicated in (b).

Materials for Energy Technology

MS.4.P096
Microscopic and element-sensitive investigation on Pt and Pt alloy nanocatalysts

S. Selve[1], F. Hasché[2], M. Oezaslan[3,4], P. Strasser[3], D. Berger[1]

[1]TU Berlin, ZELMI, Berlin, Germany
[2]TU München, Technical Electrochemistry, München, Germany
[3]TU Berlin, Institute for Chemistry, Berlin, Germany
[4]Paul Scherrer Institut, Villingen, Switzerland

soeren.selve@tu-berlin.de
Keywords: morphology, nanoparticles, PEMFC

Optimizing of the catalytic properties and lifetime of nanoparticles is of great interest for the chemical industry. For instance, one of the promising technologies for clean energy conversion is the proton exchange membrane fuel cell (PEMFCs). The large-scale commercialization of PEMFCs is, however, hindered by the sluggish kinetics of the electroreduction of oxygen, insufficient catalyst lifetime and high costs of precious metal.[1] In particular, the degradation processes under operating fuel cell conditions, such as carbon corrosion, particle growth, loss of active surface area and metal dissolution, remain unclear to date.[2] Therefore, microscopic and spectroscopic techniques help to obtain a deep insight into the degradation processes of catalytically active nanoparticles in strongly corrosive and acid environments.

In this work, microscopic investigations on catalytically active Pt nanoparticles were performed to study interaction between particle-support for several Pt nanoparticles supported on carbon materials. Transmission electron microscopy (TEM) was used as imaging method with a high lateral resolution. The TEM results were compared with typical non-imaging characterization methods like X-ray diffraction (XRD). This study provides information about the precise localization of the PEM fuel cell nanoparticle catalysts, their morphology or crystal structure. The used electrocatalysts differ in their morphology, degree of graphitization of the carbon support, metal loading, BET (Brunauer−Emmett−Teller) surface area and initial particle size (see Figure 1). All catalysts were subjected two different electrochemical stability test protocols. The electrochemical stability tests revealed that the graphitization of the carbon support plays an import role towards improvement in durability and activity.[3-5] Beside the electrochemical durability in acidic electrolyte, a thermal induced particle growth via migration for various catalysts was examined under different gas environments. Ex-situ TEM and in-situ XRD were employed to trace out the changes in carbon morphology, particle size and particle density. A complex growth behavior for Pt nanoparticles induced by thermal annealing was observed by using in-situ high temperature XRD and was in line with the ex-situ TEM measurements, shown in Figure 2.[6] Based on these microscopic and spectroscopic results, the loss of catalytically active surface area was correlated with the catalyst structure and its interaction between particle and support. Our results highlighted that a strong particle-support interaction and a high graphitization improve the durability of nanocatalysts over the time under operating fuel cell conditions.

1. Debe, M.K., Nature 2012, 486 (7401), 43-51.
2. Shao-Horn, Y., Sheng, W., Chen, S., Ferreira, P., Holby, E., Morgan, D., Topics in Catalysis 2007, 46 (3), 285-305.
3. Hasché, F., Oezaslan, M., Strasser, P., Physical Chemistry Chemical Physics 2010, 12 (46), 15251-15258.
4. Hasché, F., Oezaslan, M., Strasser, P., Journal of The Electrochemical Society 2012, 159 (1), B25-B34.
5. Hasché, F., Fellinger, T.-P., Oezaslan, M., Paraknowitsch, J.P., Antonietti, M., Strasser, P., ChemCatChem 2012, 4 (4), 479-483.
6. Hasché, F., Oezaslan, M., Strasser, P., ChemPhysChem 2012, 13 (3), 828-834.

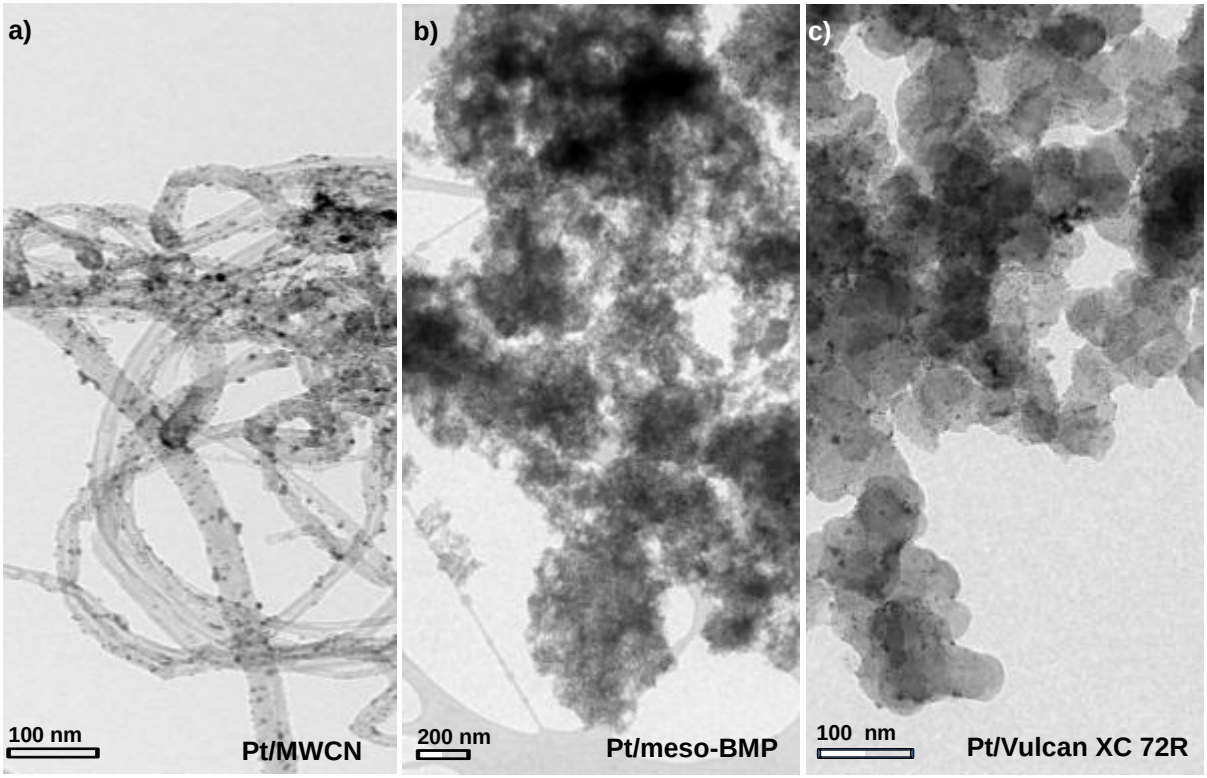

Figure 1. Microscopic investigations on several Pt nanoparticles supported on carbon. (a) Pt/multi walled carbon nanotubes (MWCNT), (b) Pt/meso-nitrogen doped carbon (meso-BMP) and (c) Pt/Vulcan XC 72R.

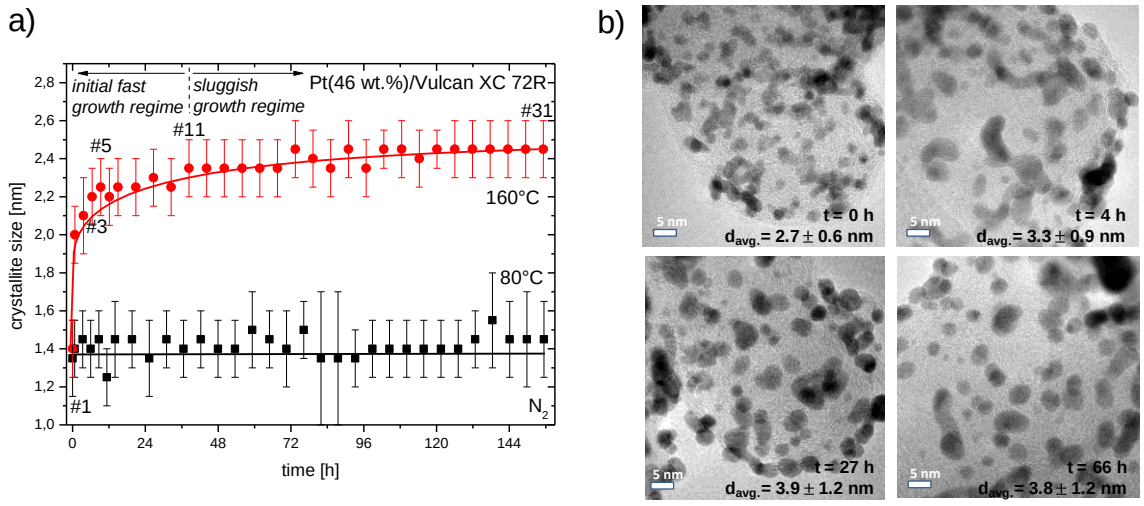

Figure 2. a) Crystallite size of platinum versus holding time at 80 °C (black squares) and 160 °C (red circles) for Pt(46 wt.%)/Vulcan XC 72R nanoparticle catalyst in N_2 atmosphere. The initial mean crystallite size was determined at 30 °C. (b) TEM images and mean particle sizes ($d_{avg.}$) for Pt(46wt.%)/Vulcan XC 72R (scale bar of 5 nm) nanoparticle catalyst after thermal treatment at 160 °C in N_2 atmosphere.

Materials for Energy Technology

MS.4.P097
Identification of an intermediate state during electrochemical lithiation of silicon using in-situ TEM techniques

T. Wuttke[1], B. Roos[1,2], C. Nowak[1,2], C. Volkert[1,2]

[1]Georg-August-Universität, Institut für Materialphysik, Göttingen, Germany
[2]Grad. Prog. for Energy Storage and Electromobility, Niedersachsen, Germany

twuttke@ump.gwdg.de
Keywords: lithiation, silicon, Li-ion-battery, intermediate state

In-situ TEM studies of structural changes during lithiation of active materials have recently become an important method for understanding intercalation mechanisms. We have developed an in-situ TEM battery setup which allows us to investigate the lithiation of Si. We observe that the formation of metastable amorphous lithiated Si is preceded by the growth of planar Li precipitates. We propose that the precipitates destabilize the Si lattice and allow the formation of the metastable amorphous phase rather than the stable crystalline phases. Figure 1(a) shows one of the silicon lamellae which was used as a cathode inside the TEM. The lamellae are prepared using common FIB techniques and are attached to TEM lift-out copper grids using electron beam Pt deposition. To prepare a lithium anode an electrochemically thinned tungsten wire is scraped across lithium metal. Figure 1(b) shows a dark field image of one of these wires. It can be seen that a layer of lithium metal remains at the tip of the wire. It takes about 1min to mount the wire into the STM-TEM holder and to transfer the holder into the high vacuum of the TEM. The surface of the lithium metal oxidizes during this time and forms various compounds like Li_3N, Li_2O and LiOH. These insulating compounds exhibit a high diffusivity for Li^+-ions and therefore act as solid state electrolytes. Figure 1(c) shows a sketch of the STM-TEM holder and the respective positions of both electrodes. The tungsten wire is mounted on a movable piezo actuator opposite to the Si-cathode which is attached to a conventional lift-out copper grid. The STM-TEM holder allows application of voltages of -10V to 10V between wire and copper grid. Currents can be measured with an accuracy of 100pA. The in-situ battery experiments were carried out in the following way: At first both electrodes are mechanically connected using the movable piezo actuator. The connection results in bending contours. Then a voltage of -10V is applied and the lamella continuously monitored. Figure 2(a) shows the lamella at the beginning of a battery experiment and Figure 2(b) 30min later. As can be seen in Figure 2(b) a line like defect has appeared which is visible due to the interruption of bending contours. Figure 2(c) shows the development over time of another line like defect. Further analysis of these defects shows that they are planar. This is proven by oscillating contrast in dark field imaging (Figure 3(a)). The planar defects can evolve into channel like amorphous structures during further lithiation (Figure 4(a)). High resolution TEM imaging reveals a sharp interface between the amorphous and the crystalline phase (Figure 4(b)). EELS measurement shows the Li K-edge at 57eV and the Si $L_{2,3}$-edge at 99eV energy loss (Figure 4(c)), indicating an amorphous lithiated Si phase, which is expected during the lithiation of silicon. The fact that this amorphous phase forms at the location of the planar precipitates suggests that the planar precipitates are nucleation sites for the amorphous phase. We envision the following two-step process (Figure 5):

1. Lithium dissolves in the crystal matrix and clusters in planar precipitates, at locations perhaps determined by mechanical stress.

2. The planar Li precipitates break the covalent bonds of the Si lattice, possibly accounting for the formation of metastable amorphous lithiated Si rather than the expected crystalline phases.

A similar process is suggested in the literature [1] and used to explain the unexpected shrinkage of Si-nanopillars. We provide the first direct observation of the proposed Li-based precipitates, which are similar in structure to H-based precipitates in silicon [2].

1. S. W. Lee, M.T. McDowell, J.W. Choi and Y. Cui, Nano Lett. 11 (2011), p. 3034.
2. N. Martsinovich, M.I. Heggie and C.P. Ewels , J. Phys.: Condens. Matter 15 (2003), p. 2815.

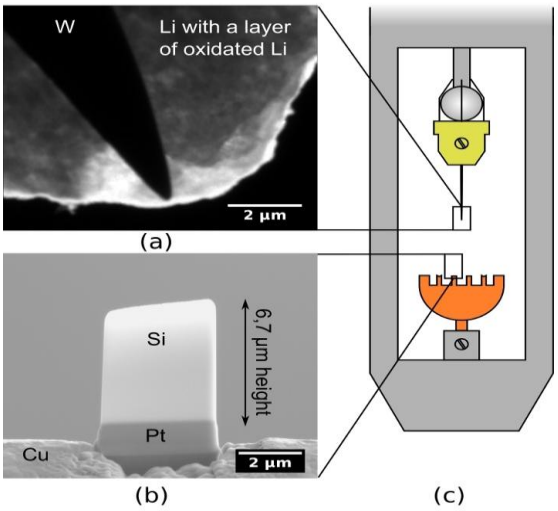

Figure 1. (a) A tungsten tip with lithium is used as anode. The layer of oxidated lithium acts as solid state electrolyte. (b) A Si-lamella used as cathode and is attached to a conventional TEM lift-out copper grid. (c) Sketch of the STM-TEM holder and the respective positions of both electrod

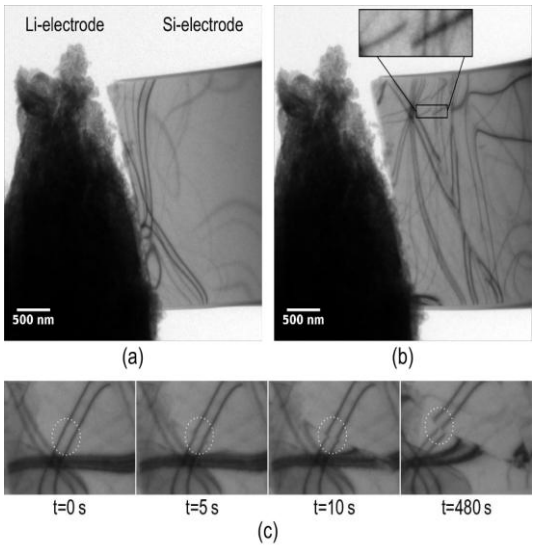

Figure 2. (a) The lamella at the beginning of an in-situ battery experiment. (b) A line like defect has appeared 30min later, visible due to the interruption of bending contours. (c) development over time of another line like defect.

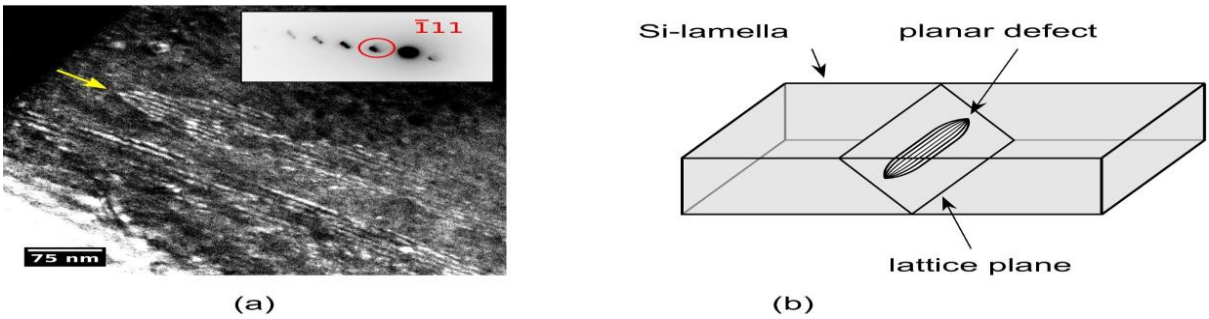

Figure 3. (a) Oscillating contrast reveals that the defects are planar. (b) Sketch to visualize the defect geometry.

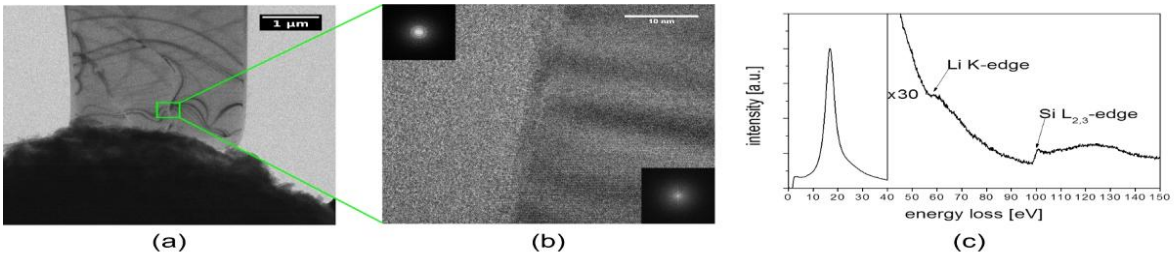

Figure 4. (a) The planar defects can evolve into channel like amorphous structures during further lithiation. (b) High resolution TEM imaging reveals a sharp interface between the amorphous and the crystalline phase. (c) EELS measurement shows the Li K-edge at 57eV and the Si $L_{2,3}$-edge at 99eV energy loss, indicating an amorphous lithiated Si phase, which is expected during the lithiation of silicon.

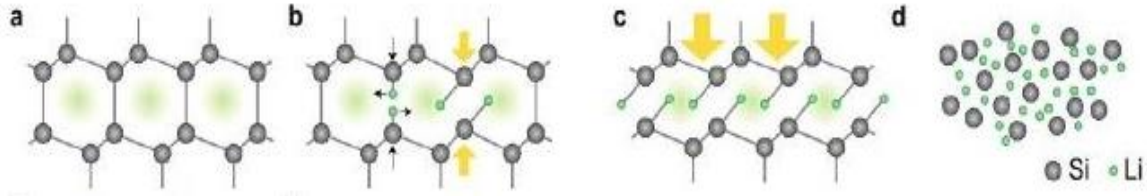

Figure 5. The amorphization of silicon begins with the formation of planar lithium precipitates. These break the covalent bonds of the Si lattice, possibly accounting for the formation of metastable amorphous lithiated Si rather than the expected crystalline phases. Model first proposed in [1].

Materials for Energy Technology

MS.4.P098
Correlated EDXS and EELS compositional analyses in Dy-doped Nd-Fe-B-based magnets

S. Sturm[1]

[1]IJS, Ljubljana, Slovenia

saso.sturm@ijs.si
Keywords: STEM/EELS/EDXS, Dy-Nd-Fe-B, hard magnet

The coercivity of Nd–Fe–B-based permanent magnets depends strongly on the microstructural features, such as the structure/chemistry properties of the matrix grains, the triple pockets (TPs) and the various internal interfaces. The partial replacement of the Nd by a heavy-rare-earth (HRE) element (Dy or Tb) as part of the grain-boundary diffusion process is known to have a large, positive influence on the coercivity, due to the formation of core-shell grains with a HRE-containing shell and a Nd–Fe–B-based core. It is believed that the shell, with its higher anisotropy field resulting from the HRE, hinders magnetisation reversal at the grain edges and leads to an increase in the coercivity of the magnet. To gain a deeper insight into the critical demagnetization processes in relation to the presence of HREs, it is vital to properly detect and quantify their location in the microstructure on the nanoscale.

In this study Dy-doped Nd–Fe–B-based magnets were used, allowing us to establish analytical procedures that facilitate the reliable quantification of HREs using transmission electron microscopy (TEM). The compositional analysis of the sample was obtained by using a scanning transmission electron microscope (STEM/TEM UHR Jeol 2010F) equipped with an energy-dispersive x-ray spectrometer (EDXS) (LINK ISIS EDS 300) and electron energy-loss spectroscopy (EELS) (Gatan PEELS 766).

The EDXS analysis of the matrix grain, which was performed with a large, 100x100nm analytical window, confirmed the expected concentrations of Nd and Fe. In addition, minor amounts of Pr, Co and Cu were identified. However, the presence of Dy could not be detected by EDXS. The problem of a reliable detection and quantification of small concentrations of Dy dopant in the Nd–Fe–B system by EDXS is related to the strong overlap of the Fe-K and Dy-L spectral lines. In addition, the reliability of EDXS analysis is further compromised by the overlapping spectral lines of elements that are required for the fine tuning of the Nd–Fe–B's magnetic properties and are typically present in small concentrations, for example, Co.

In contrast, the EELS Fe-$L_{2,3}$, Co-$L_{2,3}$ and Dy-$M_{4,5}$ ionization edges do not suffer from signal overlap and can therefore be reliably quantified. In addition, EELS offers the possibility for the detection and quantification of light elements, such as B and O. A serious overlap in EELS though can be found between the Pr-$M_{4,5}$ and Nd-$M_{4,5}$ edges, which are superimposed on the Cu-$L_{2,3}$ edge. To perform a complete compositional analysis of the Dy-doped Nd–Fe–B-based system we propose a correlated EDXS and EELS analytical procedure. Such a combined spectra acquisition facilitates not only a complete quantification of the most important elements (Nd, Fe and Dy), but also a full quantification of the minor (Co, Cu) and light elements (B, O) from the same specimen area.

Figure 1 shows a HAADF-STEM image of a Nd–Fe–B grain and the adjacent TP. Several EDXS and EELS line-scans were acquired across the interface. The TP is characterized by large amounts of Nd and Pr, about 42 at% and 13 at%, respectively. In addition, the concentration of Fe and Cu in the TP was found to be approximately 4 at%. While the concentration of these elements in the TP stays constant, the Co shows a gradual decrease in concentration from the interior of the TP towards the interface. The concentration of Co in the grain was found to be constant at around 2 at.%. The averaged background-subtracted EELS spectrum obtained from the 19 individual spectra acquired from the matrix grain is shown in Figure 2a. The presence of the Fe, Pr and Nd signals is clearly seen.In addition, the enlarged high-energy loss spectrum region clearly contains a Nd signal (Figure 2b). The average composition obtained by quantification of the EELS spectrum, applying theoretical cross-sections for selected elements, yields 80 at.% of Fe, 3 at.% of Pr and 15 at.% of Nd, which is roughly consistent with the EDXS results. In addition, the EELS analysis reveals that there is around 3 at.% of Dy present in the Nd–Fe–B grain close to the interface. The presented study confirms that correlated EDXS and EELS analysis can be successfully applied to fully quantify the Nd–Fe–B system, which includes a reliable analysis of small amounts of Dy.

1. This work was financially supported by the European Union as part of the Framework 7 program under a contract for a Small or medium-scale focused research projects (STREP), FP7-NMP-2012-SMALL-6, with the project title: Replacement and Original Magnet Engineering Options (ROMEO).

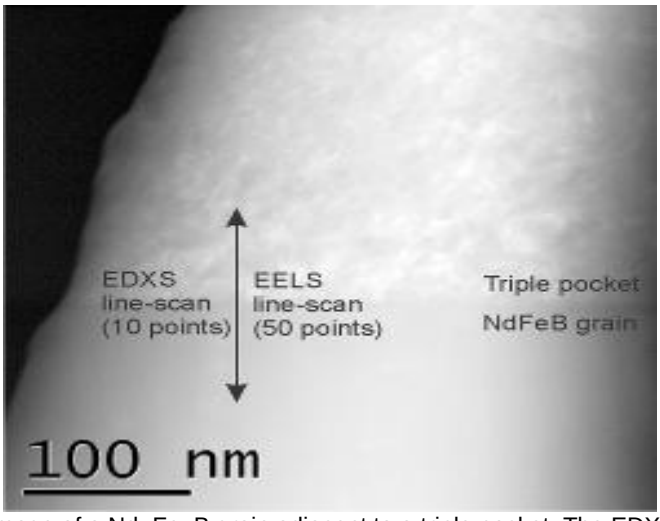

Figure 1. HAADF-STEM image of a Nd–Fe–B grain adjacent to a triple pocket. The EDXS and EELS line-scans are marked on the image.

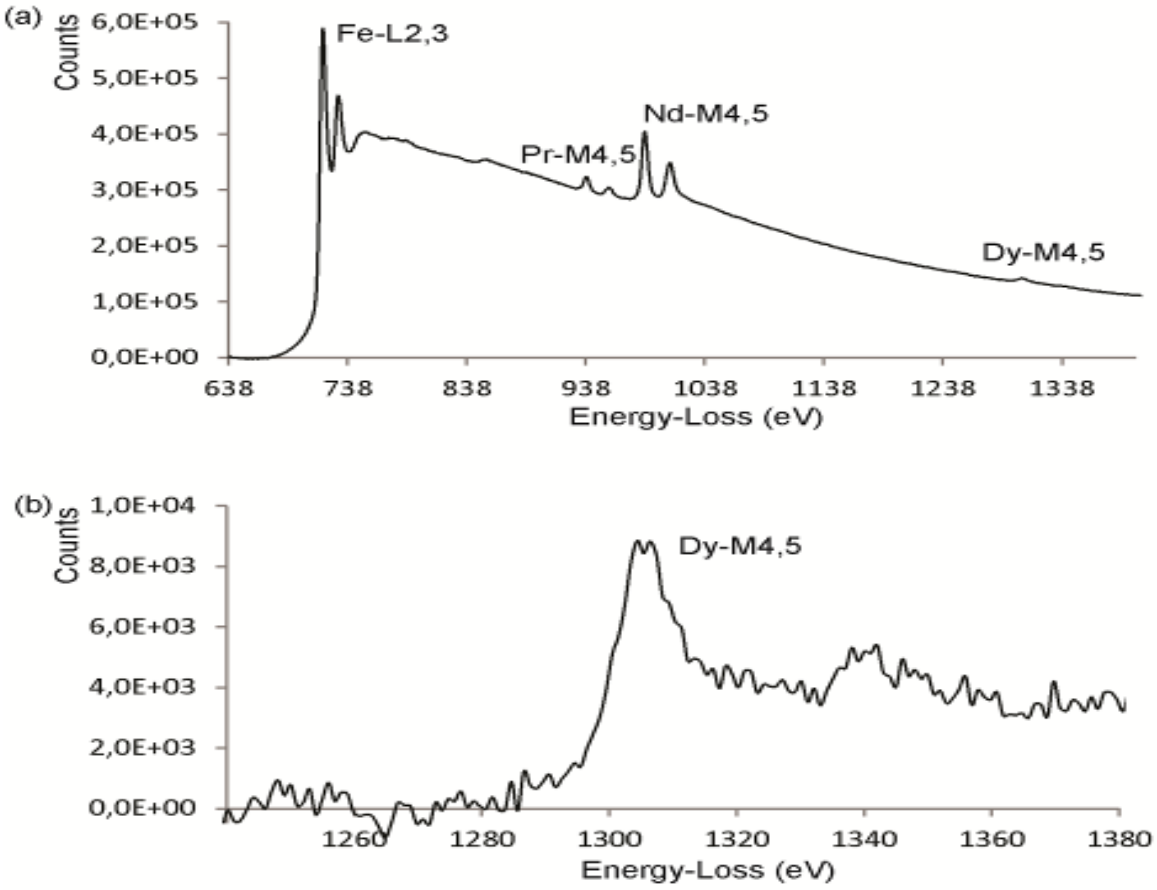

Figure 2. Background-subtracted (a) averaged EELS spectrum acquired from the Nd–Fe–B grain adjacent to the TP and (b) enlarged Dy-$M_{4,5}$ energy-loss region.

Materials for Energy Technology

MS.4.P099
Revealing the nanomorphology in organic solar cells with energy filtered TEM

W. Schindler[1], M. Wollgarten[1], H. Kropf[1], G. Chauliaras[1], K. Foustriopoulos[1]

[1]Helmholtz Zentrum Berlin für Materialien und Energie, Berlin, Germany

wollgarten@helmholtz-berlin.de
Keywords: EFTEM, organic solar cell, phase separation

In organic solar cells, the photoactive layer typically is a composite of an electron donor (D) and an acceptor (A) material. An entangled D/A heterojunction at the nanometer scale is crucial to yield high device performances. A key in the development and characterization of optimized D/A heterojunctions is a high resolution imaging method like transmission electron microscopy (TEM). However, conventional TEM imaging of D/A nanocomposites suffers from weak mass density and diffraction contrasts as the components are chemically similar and often amorphous.

Our approach to clearly identify and map the D and A phases is based on material-specific electron energy losses of the beam electrons passing the sample. With electron energy loss spectroscopy we found ($\pi+\sigma$) plasmon energies ranging from 22 to 26 eV for various donor materials like the small molecule zinc-phthalocyanine (ZnPc) [1] or the polymer PCPDTBT [2] and fullerenes as acceptor material. Custom-developed routines for the acquisition, correction and evaluation of an energy filtered (EF-)TEM image series in the plasmon regime allow the determination of the lateral D/A distribution with a spatial resolution < 5 nm independently of the existence of crystalline domains.

We used plasmon peak mapping to study phase separation in ZnPc/C_{60} mixtures which were prepared by multiple, sequential deposition of thin alternating ZnPc/C_{60} layers at substrate temperatures of 25 °C and 80 °C. Temperature induced agglomeration, as visualized in Figure 1 by mapping ultramicrotome cross-sections [3] of complete devices, correlated with a current density doubled to 15 mA/cm^2 and fill factor increased by half to 57%.

In another experiment, we applied plasmon peak mapping to wet processed polymer blends. The TEM samples were easily prepared by floating the 100 nm thick film from the glass substrate which was coated with water soluble PEDOT:PSS. Coarser phase separation was revealed in blend layers of the polymer PCPDTBT and the fullerene derivative $PC_{70}BM$ for increasing concentrations of the solvent additive diiodoctane (Figure 2). The mapped nanomorphologies can be correlated with data from studies on charge carrier dynamics and photovoltaic parameters of respective solar cells [2]. Furthermore, we prepared a TEM lamella using a focused ion beam (FIB) to reveal the vertical phase separation in an actual solar cell [4].

Last but not least, we demonstrate the feasibility of energy filtered TEM to investigate all-polymer mixtures whose components have indistinguishable plasmon energies but differ in sulfur content. The signal of the sulfur ionization edge, though at low intensity, successfully enables elemental mapping of the D/A morphology.

1. W. Schindler, M. Wollgarten and K. Fostiropoulos, Org. Electron. 13 (2012), pp. 1100-04.
2. S. Albrecht, S. Janietz, W. Schindler, J. Frisch, J. Kurpiers, J. Kniepert, S. Inal, P. Pingel, K. Fostiropoulos, N. Koch and D. Neher, J. Am. Chem. Soc, 134 (2012), pp. 14932-44.
3. We kindly acknowledge P. Schubert-Bischoff for preparing the cross sections with the Ultramicrotome.
4. We kindly acknowledge S. Albrecht, University of Potsdam, for providing the polymer solar cell.

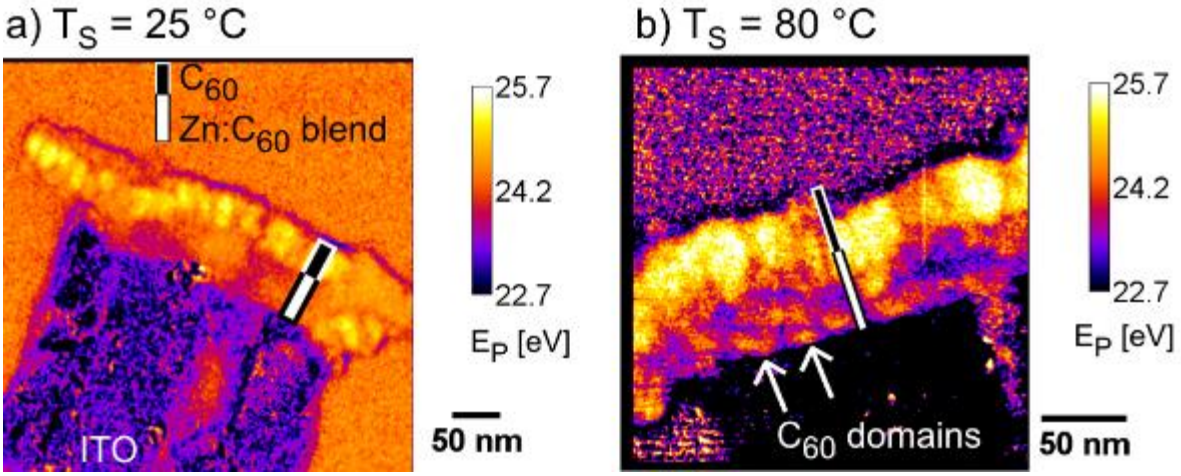

Figure 1 Plasmon peak mapping of ultramicrotome cross-sections of ZnPc/C_{60} solar cells with the nominal architecture ITO substrate / 48 nm ZnPc:C_{60} blend / 35 nm C_{60}. The blend in (a) was deposited at substrate temperature T_S=25°C and in (b) at T_S = 80°C, respectively. Map (b) reveals C_{60} domains (spots of higher plasmon energy E_P) in the blend layer indicating temperature induced phase separation.

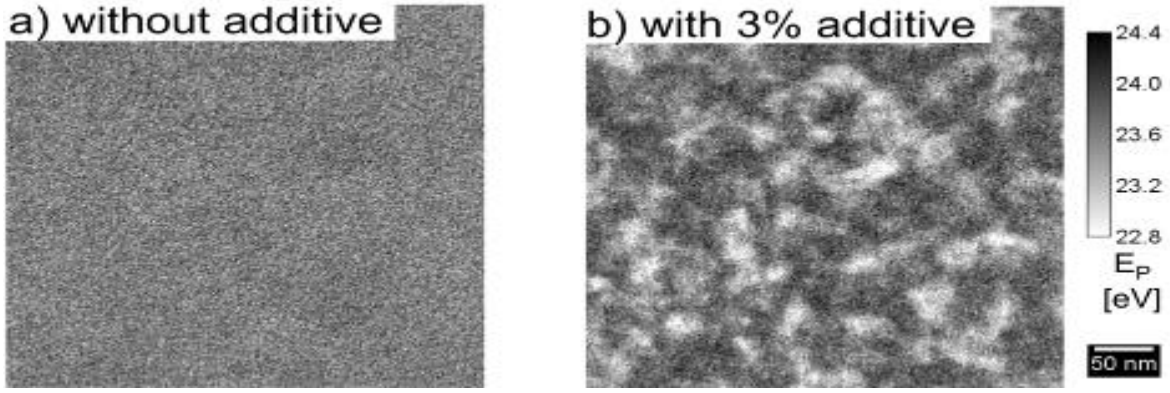

Figure 2. Plasmon peak mapping of blends of the polymer PCPDTBT and the fullerene derivative $PC_{70}BM$. While the blend without additive (a) shows good intermixing, the blend with 3% solvent additive (b) shows coarse separation of the two components (lower plasmon energy E_P corresponds to polymer-rich regions).

Materials for Energy Technology

MS.4.P100
TEM and FIB-based EBIC investigations to study photovoltaic properties of a complex oxide pn-heterojunction

P. Peretzki[1], P. Marín Perera[1], B. Ifland[2], P. Saring[1], C. Jooss[2], M. Seibt[1]

[1]Georg-August-Universität Göttingen, IV. Physikalisches Institut, Göttingen, Germany
[2]Georg-August-Universität Göttingen, Institut für Materialphysik, Göttingen, Germany

peretzki@ph4.physik.uni-goettingen.de

The perovskite-structured manganite $Pr_{1-x}Ca_xMnO_3$ (PCMO) combined with $SrTi_{1-y}Nb_yO_3$ (STNO) is presently explored as a model system for manganite-based pn-heterojunctions, using hole-doped PCMO and electron-doped STNO with different doping levels.[1] The used system is a potential candidate for high-efficiency photovoltaic devices, as it is expected that the rapid thermalization of low-energy photoexcitated charge carriers can be quenched by making use of hot-polaron type correlated states with long lifetimes and/or long diffusion lengths. This would open the possibility of converting a broader range of the solar spectrum than in conventional photovoltaics. PCMO can be epitaxially grown on STNO, as shown in Figure 1, and atomic scale PCMO-STNO interface design is expected to be crucial for controlling the charge transfer across the interface and thus photovoltaic properties.

Illumination- and temperature-dependent photovoltaic response has already been measured in the system.[2] Electron Beam Induced Current (EBIC) measurements provide a method for mapping the short-circuit current, from which the carrier diffusion length can be extracted.[3] It can be used for different specimen geometries, such as from top, in cross-section and in bevel-prepared specimens (see Figure 2) by combining SEM-based EBIC with Focused Ion Beam preparation in dual beam instruments.

However, EBIC is resolution-limited not only because of the SEM probe size but also because of the broad carrier generation volume, increasing with the electron beam energy, which is important especially in cross-sectional investigations of the photovoltaic response around the PCMO/STNO interface. Because of this, TEM lamellae are prepared from the material, which reduces the generation volume to a minimum. EBIC images were taken in cross-section under a perpendicular illumination for different electron beam energies, resulting in precise EBIC images of the PCMO/STNO interface, as shown in Figure 3.

1. G. Saucke et al., Phys. Rev. B 85 (2012) 165315.
2. A. Sawa et al., App. Phys. Lett. 85 (2005) 3375.
3. H. J. Leamy, J. App. Phys. 53(6) (1982) R51–R80.

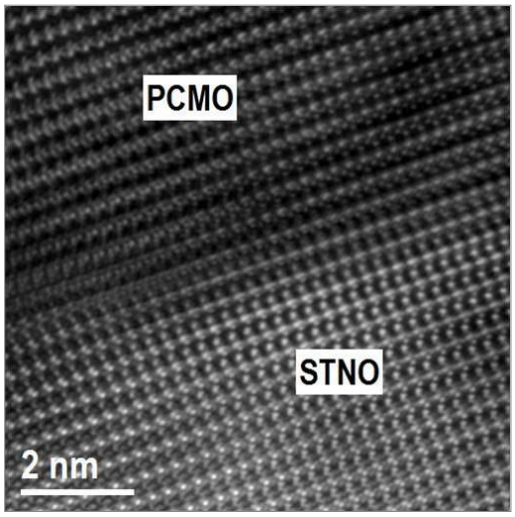

Figure 1. HRTEM image of a PCMO layer on STNO, showing the layer grew epitaxially on the substrate

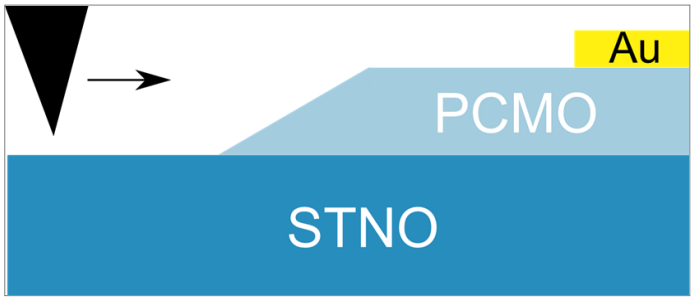

Figure 2. Sketch of the bevel structure used in EBIC experiments. The black triangle represents the electron beam scanned across the bevel.

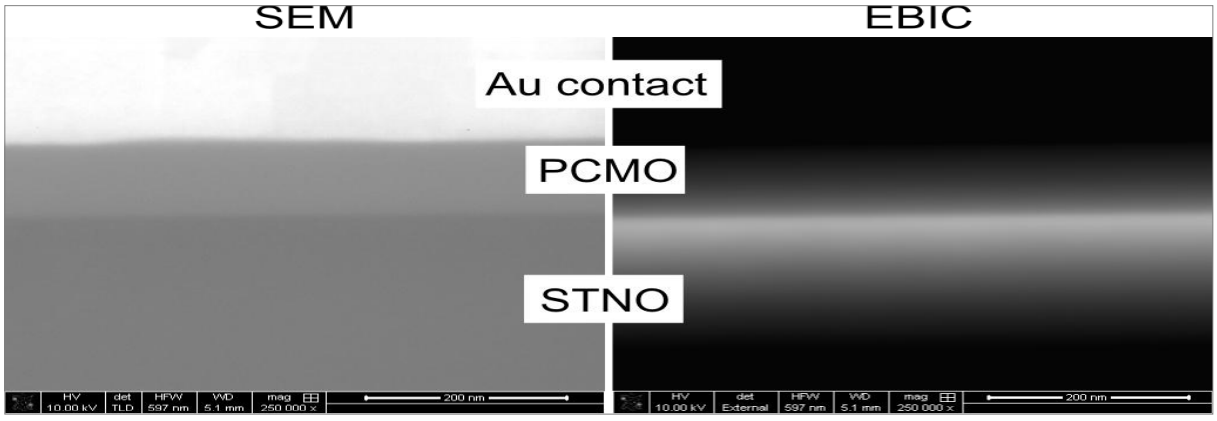

Figure 3. Simultaniously recorded SEM and EBIC images of a cross-section lamella, showing the PCMO/STNO interface with a Au contact grown on top

Materials for Energy Technology

MS.4.P101
Electron microscopy investigation of TiO_2 rutile nanowires for application in hybrid solar cells

S.B. Betzler[1], A.M. Folger[1], A. Wisnet[1], V. Falkowski[1], J. Weickert[2], L. Schmidt-Mende[2], C. Scheu[1]

[1]LMU Munich, Chemistry, Munich, Germany
[2]University of Konstanz, Physics, Konstanz, Germany

sophia.betzler@cup.uni-muenchen.de

TiO_2 is largely applied as electron acceptor material in hybrid and dye-sensitized solar cells, due its electronic properties. The performance of these solar cells can further be enhanced by increasing the donor-acceptor interfacial area, resulting in improved charge-carrier separation. Moreover, various studies report an improved conversion efficiency in dye-sensitized solar cells using TiO_2 based core-shell electrodes compared to the performance of plain TiO_2 electrodes [1-3]. This study focuses on the electron microscopic investigation of hydrothermally grown rutile TiO_2 nanowires, which offer a large interfacial area and a direct electron path to the electrode. Furthermore, by the sol-gel method and spin-coating technique prepared TiO_2 based core-shell structures are analyzed. A systematic investigation of the growth of rutile nanowires on fluorine-doped tin oxide is performed using scanning electron microscopy (cf. Fig. 1A). Thereby the effect of different synthesis parameters, such as the addition of various salts, on the morphology of the rutile nanowires is investigated. Furthermore transmission electron microscopy (TEM) is applied to analyze the defect structure occurring in single rutile nanowires during the hydrothermal growth (cf. Fig. 1B), as the defect structure could influence the performance of the wires. The analyses show that the defect structure originates from one single edge dislocation at the bottom of the wire, which forms the starting point of a defect cascade reaching to the top of the wire. Initial studies of TiO_2 based core-shell structures in hybrid solar cells focus on bilayers consisting of an about 100 nm thick TiO_2 anatase layer covered by an either amorphous or crystalline 10 nm thick Nb_2O_5 or Ta_2O_5 layer. However, first TEM measurements prove that the applied synthesis method also enables a homogeneous covering of the rutile nanowires by a 1-2 nm thick Nb_2O_5 shell. Future studies will focus on the analysis of diffusion processes occurring at the interface between TiO_2 and Nb_2O_5/Ta_2O_5.

1. A. Zaban, S.G. Chen, S. Chappel, B.A. Gregg, Chem. Commun. (2000), p. 2231.
2. Y. Diamant, S.G. Chen, O. Melamed, A. Zaban, J. Phys. Chem. B 107 (2003), p. 1977.
3. E. Palomares, J.N. Clifford, S.A. Haque, T. Lutz, J.R. Durrant, J. Am. Chem. Soc. 125 (2003), p. 475.

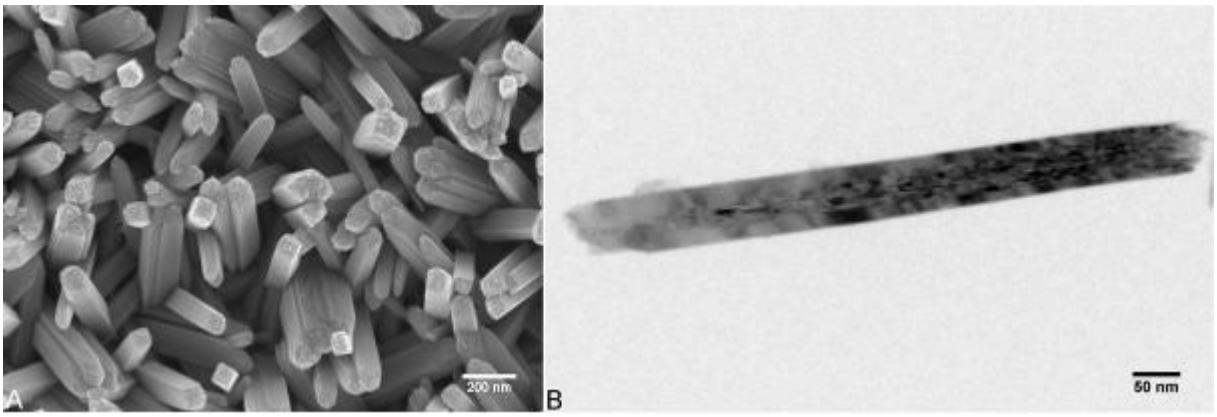

Figure 1. Electron microscopic images of rutile TiO_2 nanowires. A) Scanning electron microscope image of rutile nanowires grown on a fluorine-doped tin oxide substrate. B) Bright field TEM image of one rutile nanowire.

Materials for Energy Technology

MS.4.P102
Fabrication of Thin Film Nanocrystalline TiO_2 Solar Cells using Ruthenium Complexes with Carboxyl and Sulfonyl Groups

S. Erten - Ela, K. Ocakoglu[1]

[1]EgeUniversity, İzmir, Turkey

suleerten@yahoo.com
Keywords: Dye Sensitized Solar Cell, Nanocrystalline, Ruthenium Complex, Renewable Energy

The sun is our primary source to use of the photovoltaic effect in solar cells in the search for sustainable renewable energy sources. New generation solar cells employing thin film technology are promising technology. Solar cells based on nanocrystalline titanium dioxide sensitized with an organic or metalorganic dyes have attracted a great deal of interest since a 1991 research breakthrough. This type of organic solar cells are notable for achieving solar power-to-electricity conversion efficiencies exceeding 12% in the laboratory that implies low manufacturing costs. The TiO_2 film is generally deposited over a glass substrate with a conductive layer such as fluorine-doped tin oxide (FTO) by screen printing or doctor blading technique. Dye sensitized solar cells based on nanocrystalline TiO_2 electrodes have attracted intensive interest for scientific and industrial applications due to their high photo to electricity conversion efficiency and low production cost.[1-4].

In this study, In this paper, functionalized ruthenium complexes which have carboxyl and sulfonyl groups are reported. The products are characterized by H^1-NMR, UV–vis, FTIR, CV and AFM to determine the photophysical and electrochemical properties. Their photovoltaic properties have been tested in dye sensitized solar cells to understand the relationship between the molecular structures and efficiencies. Standard global AM 1.5 solar conditions, it is found that K314-sensitized solar cell shows higher efficiency and mostly promising. K314 based dye sensitized solar cell exhibit short circuit photocurrent density of 14.92 $mAcm^{-2}$, open circuit voltage of 570 mV, filling factor of 0.62 and overall conversion efficiencies of 5.09 %. Fig. 1 shows the ground state optimization of Ruthenium complexes.

1. B. O'Regan, M. Grätzel, Nature 353 (1991) 737.
2. S. Kolemen, A. Bozdemir, Y. Cakmak, G. Barin, S. Erten-Ela, M. Marszalek, J-H. Yum, S.M Zakeeruddin, M.K. Nazeeruddin, M. Grätzel, and Akkaya E.U, Chemical Science 2 (2011) 949.
3. .S. Erten-Ela, J. Brendel, M. Thelakkat, Chem. Phys. Lett., 510 (2011) 93
4. A. Yella, H. W. Lee, H. N. Tsao, C. Yi, A. K. Chandiran, Md. K. Nazeeruddin, E. W. G. Diau, C. Y. Yeh, .S. M. Zakeeruddin, M. Grätzel, Science 334 (2011) 629

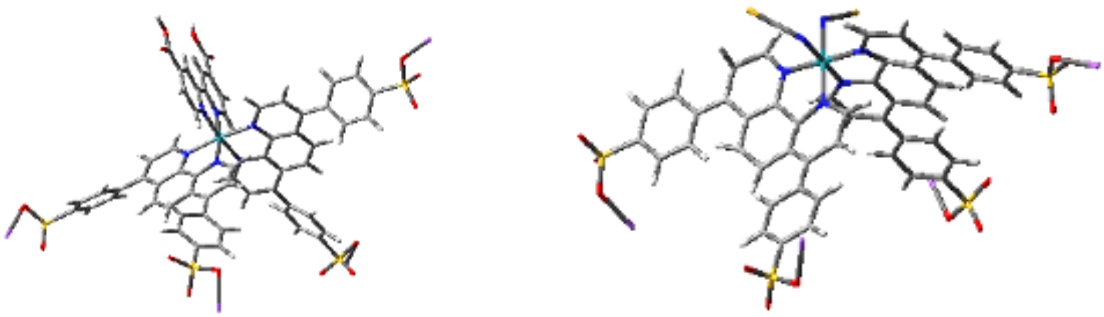

a.) **b.)**

Figure 1. Ground State Optimization at B3LYP/LANL2DZ

Materials for Energy Technology

MS.4.P103
TEM Investigation of Bi_2Te_3/Sb_2Te_3 Nanolaminate Structures Synthesized by Atomic Layer Deposition

V.S.K. Chakravadhanula[1,2,3], C. Kübel[2,3], K. Zhang[4,5], D. Nminibapiel[4,5], M. Tangirala[4,5]
H. Baumgart[4,5], V. Kochergin[6]

[1]Helmholtz Institute Ulm for Electrochemical Energy Storage / Kalrsruhe Institute of Technology, Institute of Nanotechnology, Eggenstein-Leopoldshafen, Germany
[2]Karlsruhe Nano Micro Facility, Eggenstein-Leopoldshafen, Germany
[3]Karlsruhe Institute of Technology (KIT), Institute for Nanotechnology (INT), Eggenstein-Leopoldshafen, Germany
[4]Old Dominion University, Norfolk, Department of Electrical and Computer Engineering, Virginia, United States
[5]Applied Research Center at Jefferson National Accelerator Laboratory, Virginia, United States
[6]MicroXact Inc., Virginia, United States

cvskiran@kit.edu
Keywords: Bi_2Te_3/Sb_2Te_3, Nanolaminate structures, Atomic layer deposition

High efficiency thermoelectric materials have been extensively investigated due to their potential application in power generation and refrigeration systems. The efficiency of thermoelectric materials is expressed by the figure of merit (ZT), $ZT = S^2 \sigma T / (\kappa_l + \kappa_e)$, where S is Seebeck coefficient, σ is electrical conductivity, T is the absolute temperature, and $\kappa_l + \kappa_e$ are the thermal conductivity due to the lattice and electron contribution. It is observed that higher thermoelectric efficiency can be obtained by increasing the electron conductivity and reducing the thermal conductivity. A decrease of thermal conductivity could be achieved by a low dimensional superlattice structure, due to the quantum confinement or phonon scattering. In the past Bi_2Te_3/ Sb_2Te_3 superlattice nanostructures have been attempted by using conventional techniques, such as pulsed laser deposition (PLD), metal-organic chemical vapor deposition (MO-CVD), and molecular beam epitaxy (MBE) at high temperature. However, high growth temperature results in the issues of interlayer outdiffusion and thermal lattice mismatch, which in turn adversely affects the thermoelectric performance. In contrast, the growth temperature of ALD is rather low in comparison with other thin film fabrication processes. In this paper we report on the fabrication of thermoelectric superlattice nanolaminate structures of alternating Bi_2Te_3 and Sb_2Te_3 ALD layers.

Trimethylsilyl telluride ($(Me_3Si)_2Te$), bismuth trichloride ($BiCl_3$) and antimony trichloride ($SbCl_3$) were utilized as chemical ALD precursors for telluride, bismuth and antimony, respectively. The results of field emission scanning electron microscopy (FE-SEM) indicate both metal tellurides exhibit the prevalent Volmer-Weber island growth mechanism with characteristic hexagonal crystallites revealing telluride-terminated surfaces. It is found that the addition of hydroxyl OH^- bonds at the native Si oxide surface of the substrate promotes ALD growth of metal tellurides by providing suitable nucleation sites and by preventing delamination of the hexagonal platelet shaped crystallites. The use of longer ALD pulse exposure times of chemical precursors during the ALD process enhances chemisorption and the number of nucleation sites. During subsequent ALD growth the individual nucleated islands coalesce into a continuous layer with smooth surface morphology. Transmission electron microscopic (TEM) studies (FEI Titan80-300) were performed to analyze the ALD deposited nanolaminate material. Cross-sectional analysis of these materials confirmed the Volmer-Weber type growth mechanism.

1. We acknowledge the help of Robby Prang in the FIB sample preparation.

Materials for Energy Technology

MS.4.P104
First high resolution transmission electron microscopy characterization of fcc→9R transformation in nanocrystalline palladium films due to hydriding

B. Aminahmadi[1], H. Idrissi[1,2], R. Delmelle[2], T. Pardoen[2], J. Proost[2], D. Schryvers[1]

[1]University of Antwerp, Physics- Electron microscopy for material science (EMAT), Antwerpen, Belgium
[2]Université catholique de Louvain, Institute of Mechanics, Materials and Civil Engineering, Louvain-la-Neuve, Belgium

behnam.amin-ahmadi@ua.ac.be
Keywords: Nanocrystalline Palladium, ∑3{112} twin boundary, 9R phase

Thin palladium (Pd) membranes constitute an enabling material in hydrogen permeation and sensing applications essential for hydrogen energy technology. These membranes must be as thin as possible to ensure high hydrogen permeability while remaining mechanically stable. It has been recently reported that the ductility of Pd thin films with an average grain size of 30 nm can be significantly improved due to the presence of coherent growth nanotwins [1].

In the present work, nanocrystalline (nc) Pd films with 150 nm thickness containing nanoscale growth ∑3{111} coherent TBs (CTBs) and ∑3{112} incoherent TBs (ITBs) were produced using sputter deposition and subjected to hydriding cycles. Figure 1(a) is a BF image of a plan-view FIB sample of the as-sputtered Pd film. The average in-plane grain size equals 26±1 nm while the cross-sections reveal a columnar morphological texture with an average elongated aspect ratio (height/lateral dimension ratio) of 3. Growth nanotwins are indicated by white arrows in Figure 1(a). In Figure 1(b), a <110> HRTEM image of a single grain is shown in which parallel ∑3{111} CTBs connected by ∑3{112} ITBs are recognized. The incoherent character of the ∑3{112} ITBs can be clearly distinguished in the Geometrical Phase Analysis (GPA) map of Figure 1(c) with an array of misfit dislocations located at the ∑3{112} ITBs. Figure 1(d) shows the evolution of the internal stress as a function of time during a complete hydriding cycle at P_{H2} = 97.5 mbar. This pressure is large enough to induce the α→β transformation in nc Pd. The initial volume of the Pd structure expands by about 10% during this phase transformation [2], which induces a plastic deformation within the Pd film.

After a hydriding/dehydriding cycle of Pd films, it was observed that ∑3{112} ITBs dissociate into two phase boundaries bounding a new and thermodynamically unstable 9R phase with the formation of single stacking faults every three {111} planes. Figure 2(a) shows a <110> oriented HRTEM micrograph of a straight band exhibiting two common {111} interfaces bounding a 9R phase in a hydrided Pd sample. However, care needs to be taken not to confuse a genuine 9R area with an overlapping region between twin and matrix, also causing an extra threefold periodicity in the <110> HRTEM images of an fcc lattice. The difference between both cases can be observed from the actual position of these 1/3 extra spots in the first rows next to the central <111> row. By analysis of the Fast Fourier Transform (FFT) of the HRTEM images, for a true 9R structure, observed along a $<110>_{fcc}$ direction, none of the spots in these rows coincides with the center normal to the <111> long period axis, as seen in the example of Figure 2(a). On the other hand, for the overlapping case, this normal crosses the middle spot in the adjacent row, as seen in Figure 2(b).

The sizes of the observed 9R regions and thus the dissociation width of the ∑3{112} ITBs are in the 5 to 30±1 nm range. Figure 3(b) shows an example of a smaller 9R region after hydriding indicating that not all regions involve extended dissociation. Figure 3(c) exhibits a GPA map of the region indicated by solid lines in Figure 3(b); the misfit dislocations located at the two 9R phase boundaries can be clearly observed. In the area indicated by dashed lines in Figure 3(b), the exact stacking is revealed from the HRTEM lattice micrograph, further enlarged in Figure 3(d) and which exhibits some stacking defects (due to secondary GB dislocations) within the perfect 9R sequence.

This is the first time the 9R structure is reported in nc Pd. This observation is unexpected when considering the high stacking fault energy (SFE) of Pd. This observation is explained by the influence of the hydrogen on the SFE of Pd and the high compressive stresses building up during hydriding.

1. H. Idrissi, B. Wang, M.S. Colla, J.P. Raskin, D. Schryvers and T. Pardoen, Adv. Mater. 23 (2011), P.2119.
2. M. V. Goltsova, and G. I. Zhirov, Met. Sci. Heat Treat. 49 (2007), P.141.
3. J. Wang, A. Misra, and J. P. Hirth, Phys. Rev. B 83, (2011) P. 64106.

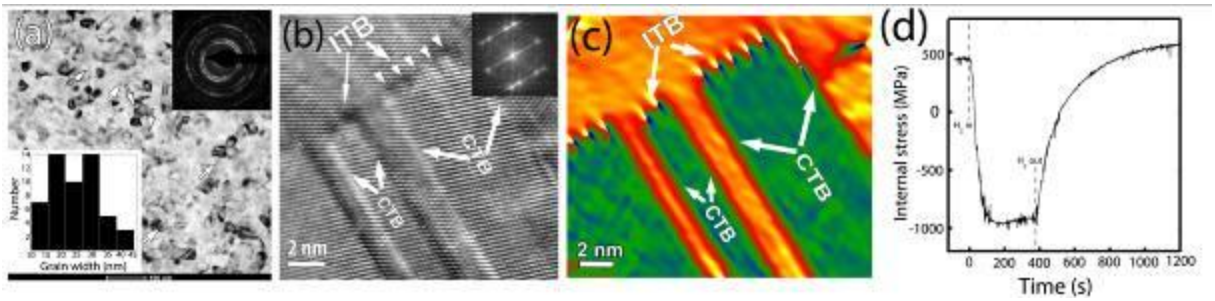

Figure 1. (a) BF micrograph of plan-view FIB specimen prepared from as-deposited Pd film. Growth twins are shown by white arrows. Upper-right inset SADP shows the fcc Pd crystalline structure. Lower-left inset shows the grain width distribution of as-deposited Pd film. (b) HRTEM micrograph of an as-deposited cross-section specimen showing ∑3{111} CTBs and ∑3{112} ITBs. (c) GPA map of the HRTEM image of Figure 1b (d) Evolution of the internal stress as a function of time during a hydriding cycle recorded at P_{H2}=97.5 mbar.

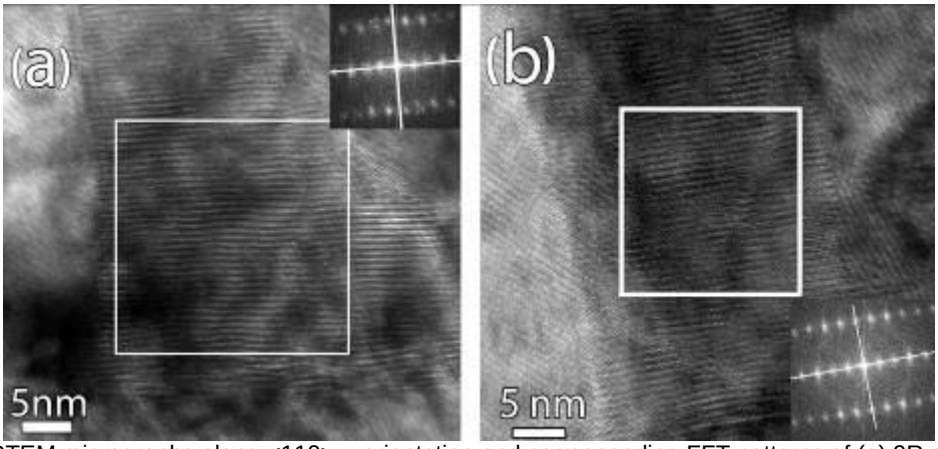

Figure 2. HRTEM micrographs along <110>$_{fcc}$ orientation and corresponding FFT patterns of (a) 9R structure and (b) overlap structure of twin and matrix for Pd thin film after hydriding. The FFT was performed from the regions indicated by white squares.

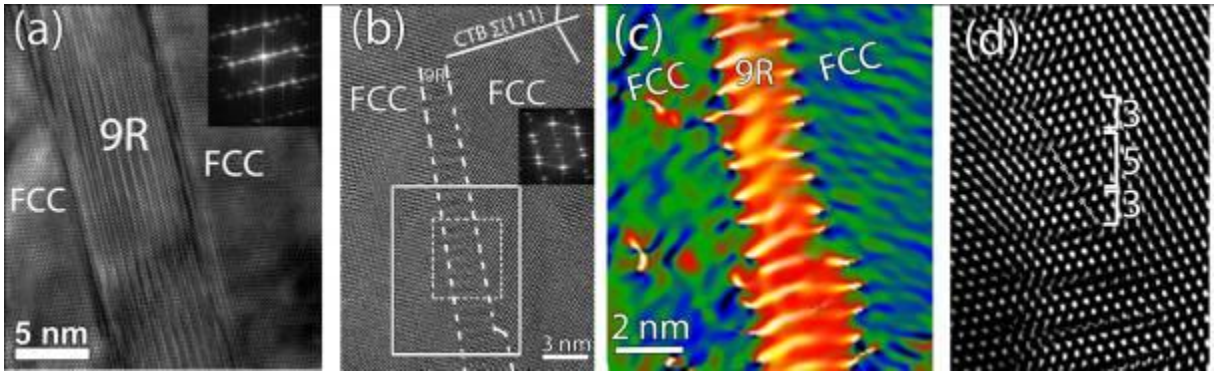

Figure 3. (a) <100> HRTEM image of a 9R band embedded in the fcc Pd matrix after hydriding. (b) <100> HRTEM image of narrowly dissociated ∑3{112} ITBs with the corresponding FFT pattern showing the local 9R structure. (c) collated GPA map of the region indicated by solid lines in the HRTEM image of (b). (d) Enlargement of the region of (b) indicated by dashed lines showing a (defected) atomic stacking sequence of the 9R phase.

Materials for Energy Technology

MS.4.P105
Real-structure effects of quaternary and quinary germanium antimony telluride thermoelectrics caused by doping with silver and indium

L. Neudert[1], T. Rosenthal[1], T. Schroeder[1], M. Doeblinger[1], O. Oeckler[2]

[1]University of Munich (LMU), Chemistry, Munich, Germany
[2]Leipzig University, IMKM, Leipzig, Germany

lukas.neudert@cup.uni-muenchen.de
Keywords: real structure, thermoelectrics, tellurides

$(GeTe)_nSb_2Te_3$ (GST) materials doped with silver or indium exhibit a high concentration of defects, which leads to pronounced real-structure effects and influences the thermoelectric properties. The occurrence of defect layers depends on n; their extension and relative orientation have been investigated by electron diffraction and HRTEM. The chemical composition was determined by EDX with spatial resolution. In the rocksalt-type high-temperature phase of GST materials, Te^{2-} occupies the anion position, whereas Ge^{2+}, Sb^{3+} and optionally In^{3+} and/or vacancies are randomly disordered on the cation position. Quenching the cubic high-temperature phase leads to metastable pseudo-cubic samples with layer-like defect ordering. Annealing at temperatures below the stability range of the cubic phase yields trigonal layered structures which are stable at ambient conditions and characterized by van der Waals gaps instead of cation defect layers in a fcc anion arrangement [1]. The efficiency of thermoelectrics is quantified by the figure of merit ($ZT = S^2\sigma T/\kappa$), depending on the Seebeck coefficient S, the electrical conductivity σ, the total thermal conductivity κ and the temperature T. Quenched ingots of $(GeTe)_nSb_2Te_3$ with n = 12, 19 yield ZT values up to 1.3 [2]. The substitution of one Ge^{2+} cation by two monovalent cations such as Li^+ or Ag^+ can be used to reduce the vacancy concentration and thus to stabilize the quenched modification. The nanostructure of the metastable pseudo-cubic phase can be tuned with a precise concentration of vacancies, simultaneously optimizing ZT by decreasing the thermal conductivity. For $(GeTe)_{11}Li_2Sb_2Te_4$, the rocksalt-type phase stable above 250 °C shows a low total thermal conductivity of 1.4 W/Km, yielding ZT = 1.0 at 450 °C. The chemical variation of compounds $Ge_{n-x}Ag_{2x}In_ySb_{1-y}Te_{1.5+n}$ (with $0 \le n \le 9$, $0 \le x \le 0.5$ and $0 \le y \le 1$) involves pronounced structural changes on various length scales, including the exsolution of tellurides like Ag_2Te or In_2Te_3. TEM investigations indicate a randomly disordered structure for quenched $Ge_{5.5}AgSb_{0.5}In_{0.5}Te_{7.5}$ with no vacancies and no short-range cation ordering (cf. Fig. 1A). In contrast, quenched $Ge_{3.25}Ag_{0.5}SbTe_5$ exhibits pronounced nanostructure with predominantly layer-like ordered vacancies (cf. Fig. 1B). Both X-ray and electron diffraction indicate that the rocksalt-type unit cell is slightly distorted. In the GeTe-type trigonal phase $Ge_7AgIn_{0.5}Sb_{0.5}Te_9$ (a = 4.20679(4) Å; c = 10.4595(2) Å, $R3m$), there are In- and Ag-rich nanodomains in a "matrix" with disordered defect layers (Fig. 2) which occasionally intersect and, in general, are randomly distributed. Since the volume of these nanodomains is very small, the overall structure as obtained by Rietveld refinement on X-ray powder data shows an "average" GeTe-type. The nano-scale inclusions or precipitates, respectively, should affect thermoelectric properties, e. g. by increasing phonon scattering [3]. The presence of twin domains in $Ge_7AgIn_{0.5}Sb_{0.5}Te_9$ as verified by electron diffraction (cf. Fig. 2A) results in real structures with a low thermal conductivity, additional vacancies may further improve it.

1. M. N. Schneider, T. Rosenthal, C. Stiewe, O. Oeckler, Z. Kristallogr. 225 (2010), 463.
2. T. Rosenthal, M. N. Schneider, C. Stiewe, M. Döblinger, O. Oeckler, Chem. Mater. 23 (2011), 4349.
3. J. R. Sootsman, D. Y. Chung, M. G. Kanazidis, Angew. Chem. Int. Ed. 48 (2009), 8616.

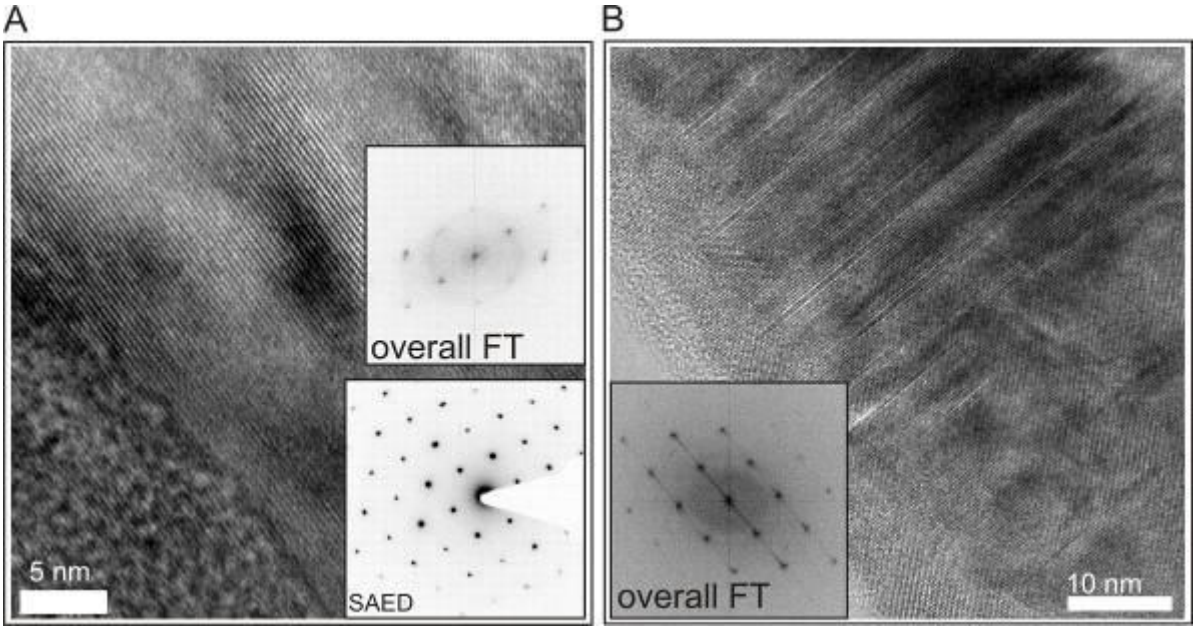

Figure 1. A: $Ge_{5.5}AgSb_{0.5}In_{0.5}Te_{7.5}$ with average GeTe-type structure with no apparent short-range order (no diffuse intensity in FT and SAED); B: $Ge_{3.25}Ag_{0.5}SbTe_5$ crystallite (<110> zone axis) with irregularly stacked defect layers, FT with pronounced diffuse intensity.

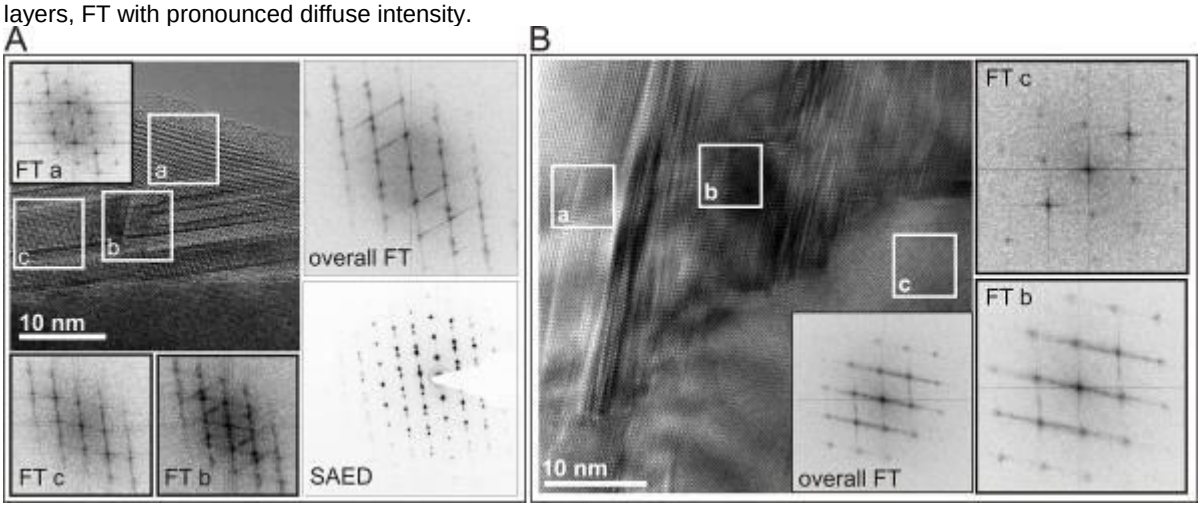

Figure 2. A: $Ge_7AgIn_{0.5}Sb_{0.5}Te_9$ crystallite (pseudocubic <110> zone axis) with differently oriented defect layers, diffuse streaks in the overall FT along <111>; the SAED indicates an obverse-reverse twinning of R-lattice; B: Ge- (a) or In-rich (c) sections show no defect layers (no diffuse streaks in the FT) whereas in region b (containing Ge and In) there is layer-like defect ordering perpendicular to <111>.

Materials for Energy Technology

MS.4.P106
Electron microscopy study of Yttrium-doped $Ba_{0.5}Sr_{0.5}Co_{0.8}Fe_{0.2}O_{3-\delta}$

M. Meffert[1,2], P. Müller[1,2], H. Störmer[1], C. Niedrig[3], S.F. Wagner[3], E. Ivers-Tiffée[3,2], D. Gerthsen[1,2]

[1]Karlsruher Institut für Technologie, Laboratorium für Elektronenmikroskopie, Karlsruhe, Germany
[2]Karlsruher Institut für Technologie, DFG Center for Functional Nanostructures, Karlsruhe, Germany
[3]Karlsruher Institut für Technologie, Institut für Werkstoffe der Elektrotechnik, Karlsruhe, Germany

matthias.meffert@kit.edu
Keywords: BSCF, Yttrium-doping, perovskite

ABO_3-type perovskite oxides have been identified as promising materials for application in oxygen separation membranes. Among these perovskites $Ba_{0.5}Sr_{0.5}Co_{0.8}Fe_{0.2}O_{3-\delta}$ (BSCF) has received particular attention due to its exceptional high oxygen permeation properties. However, a major obstacle for the application is the thermodynamic instability of the cubic BSCF phase at application-relevant temperatures. The desired cubic phase decomposes at temperatures below 900 ^{o}C, resulting in a slow decrease of oxygen flux making it unsuitable for long-term operation. It is assumed that the decomposition is initiated by the decreasing concentration of oxygen vacancies with decreasing temperature which requires an increase of the valence of the B-site cations to preserve overall charge neutrality. This leads to a change of the ionic radius of the B-site cations and a corresponding destabilization of the cubic BSCF phase. Therefore, the cubic phase decomposes into various secondary phases, like the hexagonal BSCF phase, Co-oxide, precipitates with plate-like morphology, which are composed of thin lamellae of the cubic and hexagonal phases, and barium cobaltites $Ba_{n+1}Co_nO_{3n+3}(Co_8O_8)$ with $n \geq 2$ (denoted BCO) [1-4].

To improve the long-term stability of the cubic BSCF phase B-site doping with monovalent transition metals was investigated. Recent studies show improved phase stability for Zr-doped BSCF with a dopant concentration as low as 3 at% [5]. Furthermore, Y-doped BSCF has been reported to even improve considerably the oxygen conductivity [6]. However, a detailed phase investigation with high spatial resolution is still missing. Therefore, undoped and Y-doped BSCF was investigated by transmission electron microscopy and scanning electron microscopy (SEM). Electron energy loss spectroscopy (EELS) was applied to study the valence of the Co-cations. Energy dispersive X-ray spectroscopy (EDXS) was used for composition analysis.

Y-doped BSCF powder was prepared using the mixed-oxide route. Mixed raw powders were calcined and isostatically pressed into compacts. After sintering and homogenization, the bulk samples were annealed at temperatures from 700 ^{o}C to 900 ^{o}C for 100 h in ambient air. Prior to the SEM investigation the bulk samples were polished up to a surface roughness of about 0.1 µm, followed by an etching process using a colloidal silicon dioxide suspension. Due to the different etching rates of the different BSCF phases, a surface topography develops resulting in secondary electron contrast. This contrast can be directly related to the different BSCF phases [3], which allows a quick large-scale characterization of the phase composition of numerous samples.

Figure 1 shows SEM images of etched (a) undoped and (b) 3 at% Y-doped BSCF bulk samples after annealing at 700 ^{o}C. Undoped BSCF contains a large volume fraction of secondary phases, mainly precipitates with plate-like morphology surrounded by the hexagonal phase with dark contrast as shown in Fig. 1(a). Furthermore, CoO precipitates could be observed. In contrast, Y-doped BSCF only shows the hexagonal phase which can be found exclusively at grain boundary regions (dark contrast in Fig. 1(b)). After 800 ^{o}C annealing, the hexagonal phase is only formed at triple points of grain boundaries in Y-doped BSCF. At 900 ^{o}C, secondary phases were not detected in Y-doped BSCF whereas undoped BSCF contains BCO-type lamellae and CoO grains. Therefore, Y strongly reduces the concentration of nucleation centers for the hexagonal phase compared to undoped BSCF.
However, Y does not fully suppress the formation of the hexagonal phase. Therefore, chemical analyses were performed to gain further insights into the decomposition process. EDXS mappings of a region containing the cubic BSCF phase and the hexagonal phase at a grain boundary (Figure 2) show a strong increase of Co and a depletion of Fe and Y whereas the Ba- and Sr-concentrations (mappings not shown here) only change marginally. The lack of Y in the hexagonal phase might be one reason for the improved phase stability because the formation of secondary phases requires a strong diffusion of B-site cations which might be suppressed by the large ionic radius of Y^{3+}.

Since the change of the Co-valence plays a major role in the decomposition process, the Co-valence state was investigated by EELS. Since the Ba-$M_{4,5}$ white-lines are superimposed on the Co-

$L_{2,3}$ white-lines, Co-valence determination cannot be performed by the measurement of the Co-$L_{2,3}$ white-line intensity ratio. Therefore, a new method was developed to characterize the Co-valence state in BSCF by determining the change in Co-$L_{2,3}$ white-line distance. This technique was elaborated on the basis of Co-$L_{2,3}$ white-line distance measurements of reference materials with known Co-valence state. This method allows to easily map the Co-valence over a comparably large region as shown in Figure 3(a). The corresponding sample area of the mapping is marked with a white frame in the HAADF-STEM image Figure 3(b). Figure 3(a) confirms the supposed different Co-valence states in the hexagonal and cubic phase. In the cubic phase of Y-doped BSCF the valence of cobalt is about 2+, whereas in the hexagonal phase the valence state of cobalt is elevated (≥2.6+).

1. S. Švarcová et al, SSI 178 (2008) p. 1787.
2. C. Niedrig et al, SSI 197 (2011) p. 25.
3. P. Müller et al, SSI 206 (2012) p. 57.
4. P. Müller et al, Chem. Mater. 25 (2013) p. 564.
5. S. Yakovlev et al, Appl. Phys. Lett. 96 (2010) p. 254 101.
6. P. Haworth et al, Sep. Purif. Technol. 81 (2011) p. 88.

7. This work has been performed within the project F.2 of the DFG Research Center for Functional Nanostructures (CFN). It has been further supported by a grant from the Ministry of Science, Research and the Arts of Baden-Württemberg (Az: 7713.14-300) and by the Helmholtz Association of German Research Centres through the portfolio topic MEM-BRAIN.

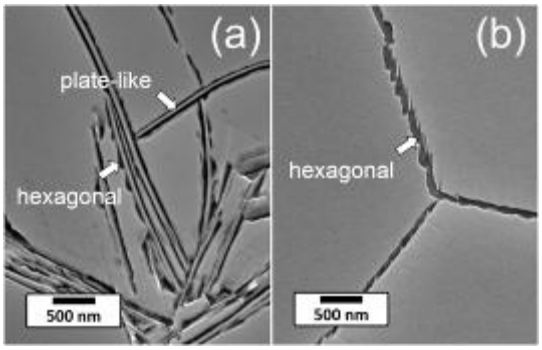

Figure 1. SEM micrographs of etched (a) undoped and (b) 3 at% Y-doped BSCF annealed at 700 ^{o}C for 100 h. The dark contrast corresponds to the hexagonal phase.

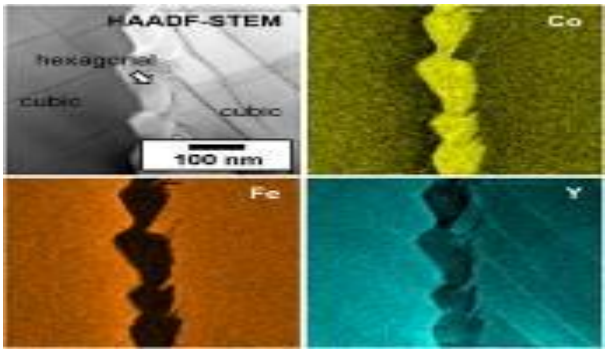

Figure 2. EDXS mappings of the Co-, Y- and Fe-distribution in cubic BSCF and hexagonal BSCF at a grain boundary in 3 at% Y-doped BSCF annealed at 700 ^{o}C for 100 h.

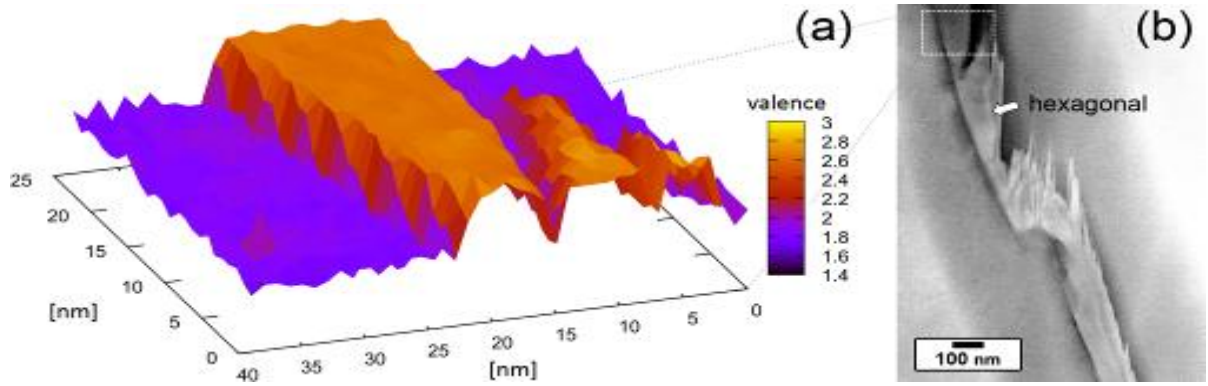

Figure 3. (a) EELS Co-valence mapping of a grain boundary region containing the hexagonal phase in 3 at% Y-doped BSCF annealed at 730 ^{o}C for 100 h. (b) Overview HAADF-STEM image. The white frame corresponds to the sample area where the Co-valence mapping was performed.

Materials for Energy Technology

MS.4.P107
Advanced TEM characterisation of nanoparticle based solar cells.

R. Imlau[1], M. Luysberg[1], A. Kovács[1], S. Muthmann[2], C. Leidinger[2], M. Nuys[2], J. Flohre[2]
K. Dörmbach[3], A. Pich[3], R. Dunin-Borkowski[1], R. Carius[2]

[1]Forschungszentrum Jülich, Ernst Ruska-Centre for Microscopy and Spectroscopy with Electrons and Peter Grünberg Institute 5, Jülich, Germany
[2]Forschungszentrum Jülich, Institute of Energy- and Climate Research 5 - Photovoltaics, Jülich, Germany
[3]DWI an der RWTH Aachen e.V., Aachen, Germany

r.imlau@fz-juelich.de
Keywords: α-Fe_2O_3, nanoparticle, solar cell, EELS

α-Fe_2O_3 nanoparticles (NPs) were embedded into a p-i-n amorphous silicon (a-Si) solar cell as a model system for NP-based solar cells, in which the NPs promote the photogeneration of charge carriers as a result of their high absorption coefficient and suitable band gap. The a-Si p-i-n structure is expected to provide a low defect density matrix, as well as the electric field that is required for charge carrier separation. Key issues for the solar cell performance are the quality of the NP absorber layer, which should have a low recombination rate, as well as effective charge extraction from the NP to the p and n contacts.

α-Fe_2O_3 NPs were synthesized in a wet chemical process without using organic ligands [1]. NP layers were prepared by spin coating on p doped layers, followed by further PECVD growth of intrinsic and n-type layers. All of the silicon layers in the a-Si solar cells were deposited using plasma-enhanced chemical vapour deposition [2].

Although a working solar cell was achieved a comparison of our prototype solar cell with a reference p-i-n junction deposited without NPs showed a significant deterioration of the I-V characteristics and no contribution of the NPs to the quantum efficiency.

In order to study the influence of the deposition process on the NPs, we investigated the structural and electronic properties of Fe_2O_3 NPs before and after embedding. We performed conventional transmission electron microscopy (TEM) using an FEI Tecnai F20 microscope operated at 200 kV and advanced scanning TEM (STEM) and electron energy-loss spectroscopy (EELS) using an FEI Titan TEM operated at 300 kV equipped with a condenser lens aberration corrector.

Figure 5a shows a bright-field TEM image of α-Fe_2O_3 NPs embedded in a p-i-n a-Si solar cell structure, examined in cross section. The NPs form a two-dimensional array and are separated from each other by a-Si. The a-Si contains voids both beneath and near to the NPs, which appear dark in the STEM image shown in Fig. 1b.

The chemical compositions and bonding states of the NPs were investigated using the StripeSTEM EELS technique [3], both before and after embedding. Figure 6a shows line scans of background-subtracted Fe L and O K edge intensities recorded across the surface of an α-Fe_2O_3 NP that was not embedded. No indication of an O-rich shell is observed. Figure 2b shows similar results after embedding, from the interface between a NP and the surrounding a-Si as indicated in Figure 5b. An O-rich shell of thickness (1 ± 0.3) nm is observed around the embedded NP. In
Figure 7, the O K edge onset energy of the shell is compared with that of α-Fe_2O_3. The pre-peak at 532 eV, which is characteristic for α-Fe_2O_3, is missing in the O-rich shell. This missing peak is consistent with the O being bonded to silicon. Moreover, the Fe L_2 and Fe L_3 edge energies and ratios stay constant, providing no indication of changes in the bonding state of iron. We conclude that the shell around the embedded α-Fe_2O_3 NPs consists of O-rich Si.

The observed O-rich shells around the NPs may inhibit carrier extraction and may therefore explain the lack of a contribution from the NPs to the quantum efficiency. A possible reason for the formation of the shell is the presence of a remaining surface layer of water after spin coating, which may lead to the formation of a thin O-rich Si layer during the early stages of growth of the intrinsic a-Si matrix.

1. M Ozaki, S. Kratohvil and E Matijevi, Journal of Interface and Colloid Science 102 (1984) p. 146
2. S. Muthmann and A. Gordijn, Solar Energy Materials and Solar Cells, 95 (2011) p. 2
3. M. Heidelmann, J. Barthel and L. Houben, Ultramicroscopy 109 (2009) p. 1447
We are grateful to Doris Meertens for TEM specimen preparation and to the BMBF for funding under grant number 03SF0402A.

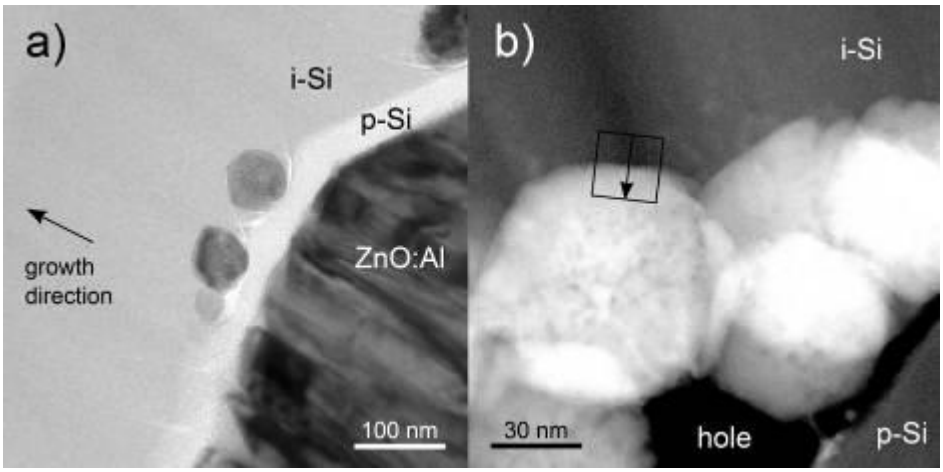

Figure 5. (a) Bright-field TEM image and (b) HAADF STEM image (inner detector angle 70 mrad) acquired from a cross-sectional specimen of α-Fe_2O_3 NPs embedded in a Si solar cell structure. The marked region and arrow in (b) indicate the area from which the STEM/EELS measurements in Fig. 2b were obtained.

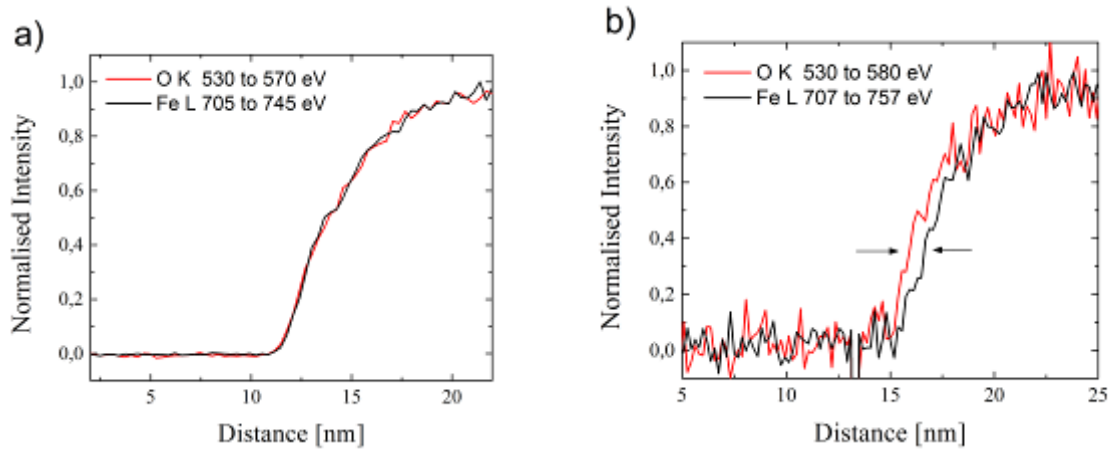

Figure 6. Integrated intensity profile determined from background-subtracted O K and Fe L EELS edges across the interface (a) between vacuum and a pristine NP and (b) between the a-Si interface and an embedded NP.

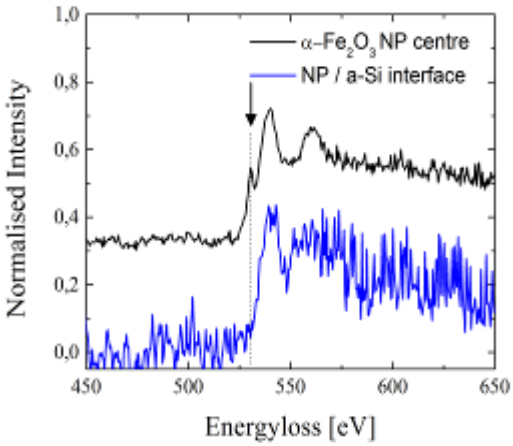

Figure 7. Background-subtracted EELS edges showing the O K edge onset recorded from an embedded α-Fe_2O_3 NP, both from its centre (black curve) and from the NP/a-Si interface (blue curve). The intensity was averaged over distances of 5 and 1 nm, respectively. The line and arrow mark a pre-edge peak at 532 eV that is characteristic for α-Fe_2O_3. The spectra have been shifted vertically for clarity.

Materials for Energy Technology

MS.4.P108
Electron beam induced dehydrogenation of nanocrystalline MgH_2 investigated by VEELS

A. Surrey[1,2], I. Lindemann[1,2], C. Bonatto Minella[1,2], L. Schultz[1,2], B. Rellinghaus[1]

[1]IFW Dresden, Institute for Metallic Materials, Dresden, Germany
[2]TU Dresden, Institut für Festkörperphysik, Dresden, Germany

a.surrey@ifw-dresden.de

There is an on-going quest for finding a hydrogen storage material that provides both high H_2 storage density and good H_2 absorption as well as desorption properties. Here, nanosized or nanoconfined hydrides promise improved thermodynamics and reaction kinetics. As for the structural characterization utilizing transmission electron microscopy (TEM), however, most materials degrade fast upon the irradiation with the imaging electron beam due to radiolysis. MgH_2 is one of the best studied binary hydrides due to its relatively high storage capacity of 7.6 wt.% H_2. Therefore, ball milled MgH_2 is used as a reference material for in-situ TEM experiments on submicron particles which are comprised of nano-crystals as revealed by XRD measurements. Special care is taken that the sample is not exposed the oxygen or water vapour from ambient air during the transfer from the glove box to the electron microscope. Therefore a vacuum transfer holder is used which successfully prevents the oxidation of the specimen. Valence electron energy loss spectroscopy (VEELS) is conducted using a monochromated FEI Titan^3 80-300 microscope. From the observation of the plasmonic absorptions in the low loss regime it is found that MgH_2 successively converts into Mg upon electron irradiation (see "Figure 1.") as it was observed in other studies [1,2]. After removing plural scattering using Fourier-log deconvolution the temporal evolution of the spectra is analysed quantitatively by fitting a function composed of two Lorentzians to each spectrum. As a result it can be shown that the signal of the MgH_2 plasmon follows an exponential decay which allows to determine a characteristic electron dose for the electron beam-induced dehydrogenation. From measurements for incident electron energies of both 80 keV and 300 keV characteristic electron doses are deduced. These characteristic doses are roughly 10^4 electrons/nm^2 and 10^6 electrons/nm^2 for 80 keV and 300 keV electrons, respectively (see "Figure 2."). This observation confirms that radiolysis is the major damaging mechanism. By a comparing the characteristic doses of individual particles a dependence on their thickness is found. This indicates that the electron beam-induced dehydrogenation is diffusion limited and as a consequence, reaction kinetics for individual particles can be investigated. This understanding is also crucial for TEM studies on other hydrides such as AlH_3.

1. M. Danaie, S.X. Tao, P. Kalisvaart, D. Mitlin, Acta Materialia 58 (2010), 3162–3172
2. K.-J. Jeon, H.R. Moon, A.M. Ruminski, B. Jiang, C. Kisielowski, R. Bardhan, J.J. Urban, Nature Materials 10 (2011), 286–290

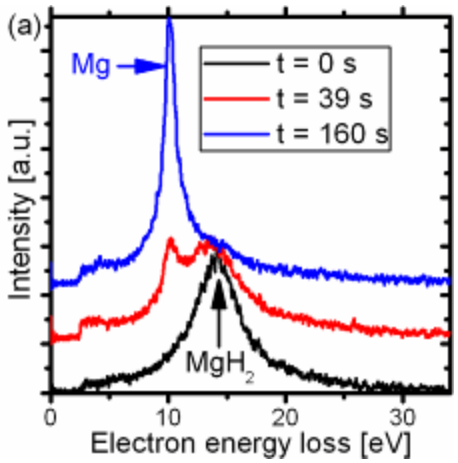

Figure 1. Temporal sequence of three subsequently obtained VEEL spectra of a submicron MgH_2 particle at three different stages during the exposure to the imaging electron beam in the electron microscope.

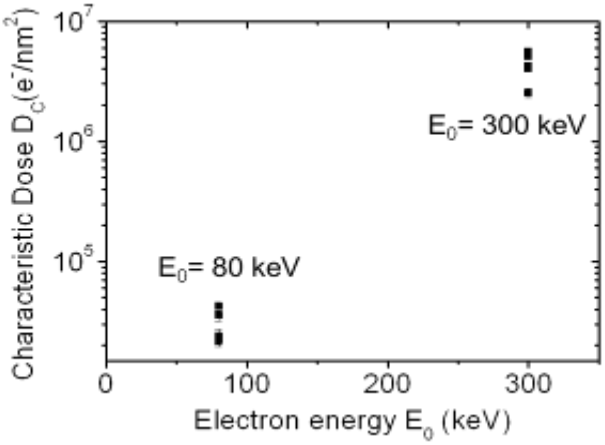

Figure 2. Characteristic electron doses for the electron beam induced dehydrogenation of 14 different MgH_2 particles with incident electron energies of 80 keV and 300 keV.

Materials for Energy Technology

MS.4.P109
The impact of defects on the EC performance of $LiFePO_4$ batteries - an EELS and NEXAFS study

M.E. Schuster[1], D. Teschner[1], F. Girgsdies[1], M.G. Willinger[1], J. Tornow[1], N. Ohmer[2], D. Samuelis[2] J. Popovic[2,3], M.-M. Titirici[3], R. Schlögl[1]

[1]Fritz-Haber-Institute der Max-Planck Gesellschaft, Anorganische Chemie, Berlin, Germany
[2]Max-Planck-Institut für Festkörperforschung, Stuttgart, Germany
[3]Max-Planck-Institut für Kolloid- und Grenzflächenforschung, Potsdam, Germany

manfred@fhi-berlin.mpg.de
Keywords: $LiFePO_4$, EELS, NEXAFS, cathode materials

The olivine-structured $LiFePO_4$ is considered as a highly promising cathode material for lithium battery due to its high operating voltage (~3.5 V vs. Li/Li^+) and its large theoretical gravimetric capacity (~170 mAh/g). Further advantages such as its low cost, safety advantages and non-toxicity are faced by major drawbacks such as low electron conductivity and the one-dimensionality of the Li^+ diffusion [1]. The performance of the cathode material strongly depends on the transport of Li into and out of the host material and its actual charging state in the host matrix.

In particular, reversibility in the intercalation of Li is crucial for achieving high performance of $LiFePO_4$; additionally, a stable structure is auspicial for long-term stability upon cycling. A correlation between electrochemical performance and the morphology and nanostructure of the $LiFePO_4$ is recognized, however still poorly understood. The structural and morphological heterogeneity of the synthesized material hampers to establish such a correlation by means of integral methods, while local characterization techniques are required. It will be shown in this work that electron microscopy characterization is especially suitable to establish such correlation.

By means of cross section preparation and by tuning the acceleration voltages in the TEM, small and big particles are separately characterized. Those results are compared with that obtained by integral methods such as XRD and NEXAFS. Modifications of the crystal structure as function of the particles size were investigated in this work by means of HRTEM and XRD, while changes in the electronic structure between Fe^{2+} and Fe^{3+} were studied by EELS and NEXAFS of the Fe $L_{3,2}$ edge
To study the mobility of Li in and out the surface and bulk region as function of the particles size, $LiFePO_4$ cathode materials at several charging and discharging stages were investigated by a combination of local (EELS) and integral (NEXAFS) methods. Variation on the surface and in the bulk of the fresh and cycled samples were accessed by TEY and FY NEXAFS measurements.

A comparative analysis of the completely charged sample by means of Fe $L_{3,2}$ edge EELS for particles with significantly different particle size is depicted in Figure 1. The lithiated phase and delithiated phase of $LiFePO_4$ differ in the onset of the O K-edge, due the formation of a pre-edge peak upon Li removal. This feature is related to unoccupied states with strong oxygen 2p character in $FePO_4$ and appears at around 528 eV [1]. Additionally, changes in the oxidation state of iron can be observed as a shift of the Fe L_3 peak maximum position. It can be clearly seen that the L_3 edge position shifts to higher energy losses as the sample thickness increases, indicating that Li is removed more easily from the bigger crystallites compared to the smaller $LiFePO_4$ nanoparticles.

HRTEM analysis revealed a higher defect content for the small crystallites while the crystalline structure of the several 100 nm big crystals seems to be unaffected by the cycling procedure. A turbostratic arrangement was found in the nanosized $LiFePO_4$ crystals hindering the mobility of the Li atoms during the charging/discharging process. This is especially crucial for the case of the olivine structured $LiFePO_4$ as the Li mobility is limited to one dimensionality.

In conclusion, this work [3] shows that turbostratic alignment of layers and therefore higher defect content is responsible for irreversible hosting of Li in the structure of small particles. This work is of relevance to optimize conditions for hydrothermal synthesis of $LiFePO_4$ battery materials towards formation of huge (several 100 nm – □m) sized crystallites which show reversible intercalation behavior.

1. M. K. Kinyanjui, P. Axmann, M. Wohlfahrt-Mehrens, P. Moreau, F. Boucher, U. Kaiser; J. Phys.: Condens. Matter 22 (2010) 275501
2. A.K. Padhi, K.S. Najundaswamy and J.B. Goodenough, J. Electrochem. Soc., 1997, 144, 1188
3. M. E. Schuster et al. in preparation.

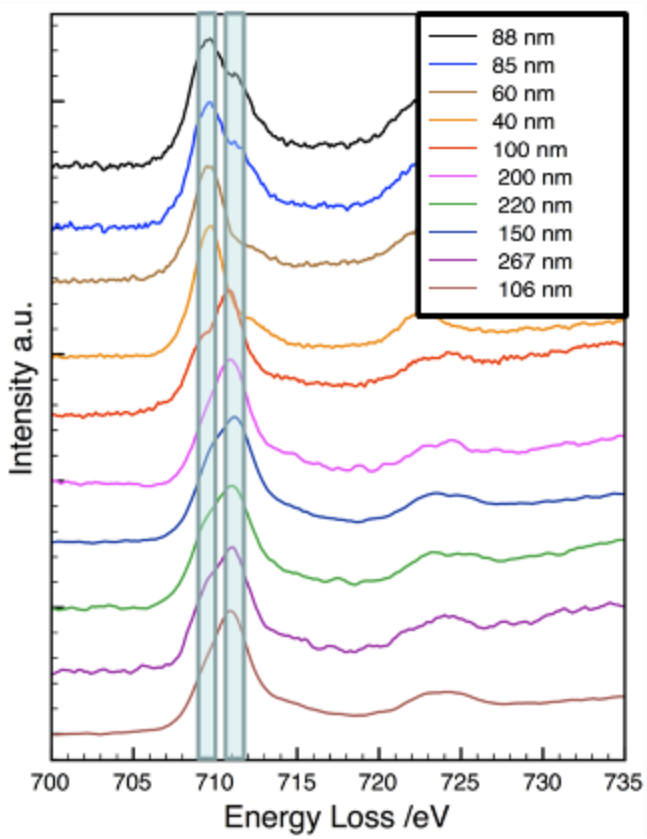

Figure 1. Fe L3,2 EELS, note the shift of the L3 edge position from top to bottom as function of the sample thickness (charged state 1st cycle)

Materials for Energy Technology

MS.4.P110
The Synthesis of Phenoxazine Dyes Comprising Anchoring Group and Their Performances in Dye Sensitized Solar Cells

N. Sünger[1]

[1]Ege University Solar Energy Institute, İzmir, Turkey

nspctrm@gmail.com

In recent decades, increasing attention has been paid to the development new efficient dyes for dye sensitized solar cells (DSSCs). As a source of renewable energy, DSSCs has potentially low-cost fabrication, economical and effective way to carry out the energy conversion from solar light to electricity and the possible solution for environmental concerns for the future energy demand. This potentials tempted scientists all over the world about the subject since O'Regan and Gratzel[1]. One of the crucial components in DSSCs, the photosensitizers have always attracted ever increasing attention. Due to the better cost performance compared to metal-complex sensitizers, the organic dyes exhibit the more brilliant future in commercial application. Intense effort focused at this area by synthetic organic chemists in according to achive better and better overall efficiencies. But generally synthetic routs for synthesising new materials involves mostly conventional heating which is inefficient and time consuming. Microwave synthesis represents a major breakthrough in synthetic chemistry, gives organic chemists more time to expand their scientific creativity. Insted of spending hours or even days synthesizing a single compound, chemists can now perform the same reaction in minutes[2-6].

In this study, organic sensitizers with phenoxazine core comprising donor, electron-conducting, and anchoring groups synthesized for sensitization titanium dioxide in dye sensitized solar cells. All synthetic steps for the construction of the dyes conducted under microwave irradiations which are N-alkylation, vilsmeier -haack Formylation, knoevenagel condensation. Under microwave irradiation phenoxazine reacts remarkably fast with a number of alkyl halides to give N-alkyl derivatives of phenoxazine especially compared to the traditional organic synthesis using reflux conditions. The reactions were carried out with high yield by simply mixing phenoxazine with an alkyl halide which was adsorb on potassium carbonate Vilsmeier -Haack Formylation and Knoevenagel Condensation reactions was also fast and high yielded. Phenoxazine dyes comprising anchoring groups were characterized by UV-Vis, IR, ^{1}H NMR techniques. The effect of different dye structures on the performance of the DSSCs was investigated systematically with photophysical, photovoltaic as well as photoelectrochemical methods. J-V and IPCE curves were evaluated for photovoltaic performances of phenoxazine dyes. Results showed that phenoxazine dyes exhibited promising photovoltaic properties.

1. B. O'Regan and M. Graetzel, Nature, 353, 1991, 737–740.
2. Oliver Kappe, C. *Chemical Society reviews* 37, 2008, 1127–39.
3. B. Hayes, CEM Publishing, 2003, 289 pp.
4. Bogdal, D., Pielichowski, J. & Jaskot, K. Synthetic Communications 1996, 1553–1560.
5. Tian, H. *et al. Chemical communications* 2009, 6288–90.
6. Deyu Wang, Sule Erten-Ela, Shaik M. Zakeeruddin, Ivan Exnar, Qing Wang, Peter Petchy and Michael Graetzel, Electrochemistry Communications, 11, 2009, 1350-1352.

Materials for Energy Technology

MS.4.P111
Normal Type and Inverted Type Bulk Heterojunction Solar Cells

S. Erten-Ela[1]

[1]EgeUniversity, İzmir, Turkey

suleerten@yahoo.com
Keywords: inverted type bulk heterojunction solar cell, normal type, fullerene

Bulk heterojunction solar cells are fabricated as normal type and inverted type. In normal type solar cell, A low work function cathode metal electrode is generally preferred to fabricate organic bulk-heterojunction solar cells and degrades rapidly without proper encapsulation because of oxidation of the highly reactive electrode. In inverted solar cell, metal oxide layers such as ZnO, TiO_2 onto fluorine doped tin oxide (FTO) substrate as an electron collecting contact are deposited. This approach requires an inversion in the ordering of layer deposition allowing for more stable metals such as Au to be used as back hole collecting electrodes. Metal oxide layers have the additional effect of acting as a hole blocking contact, along with enhancing electron extraction. Inverted bulk heterojunction solar cell devices are shown air-stability with this solar cell configuration[1-4].

In this study, normal-type and inverted-type bulk heterojunction solar cells are fabricated using P3HT polymer material as donor and C_{60} and PCBM as acceptor. ZnO cathode electrode material is prepared for solution-processed applications. ZnO layers are spincoated onto FTO substrates. The morphology of ZnO layers are investigated by means of Atomic Force Microscopy Images. The photocurrent-voltage (I-V) and IPCE results of inverted-type bulk heterojunction solar cells are reported in FTO/ZnO/P3HT:PCBM/Au and FTO/PEDOT/P3HT:PCBM device configurations. Active layer is blended in different weight ratio. Fig. 1 shows the schematic illustration of inverted-type bulk heterojunction solar cell device configuration.

1. Tang CW. Two-Layer Organic Photovoltaic Cell, Appl. Phys. Lett 1986;48:183-85.
2. Bouit PA, Rauh D, Neugebauer S, Delgado JL, Piazza ED, Rigaut S, Maury O, Andraud C, Dyakonov V, and Martin N. A Cyanine-Cyanine Salt Exhibiting Photovoltaic Properties, Org. Let 2009;11: 4806-9.
3. Bekci R., Karsli A., Cakir A.C., Sarica H., Guloglu A., Gunes S., Erten-Ela S., Comparison of ZnO Interlayers in Inverted Bulk Heterojunction Solar Cells, Applied Energy, 212;96;417-421.
4. Bekci R., Erten-Ela S., Nanostructured ZnO Cathode Layer on the Photovoltaic Performance of Inverted Bulk Heterojunction Solar Cells, Renewable Energy, 2012;43;378-382.

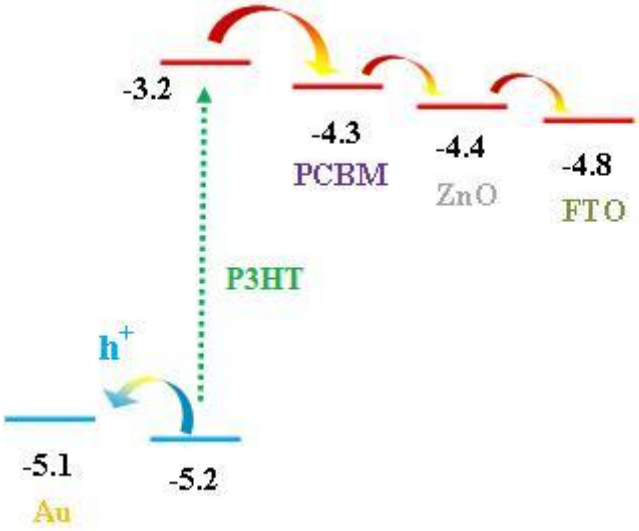

Figure 1. Inverted solar cell device structure and approximate energy level diagram**.**

Materials for Energy Technology

MS.4.P112
Chemical element mapping and metrology of γ’ and γ’’ nanoparticles in Inconel 718 superalloy for aeronautics and power generation.

A. Czyrska-Filemonowicz[1], P. Buffat[2], K. Kulawik[1]

[1]AGH University of Science and Technology, Int. Centre of Electron Microscopy for Materials Science, Krakow, Poland
[2]EPF-Lausanne, CIME, Lausanne, Switzerland

czyrska@agh.edu.pl
Keywords: ChemiSTEM, Inconel 718, nanoparticles

Inconel 718 (IN718) is a high strength, corrosion resistant nickel-iron based superalloy used for applications in the temperature range from -250 to 700 °C. Thanks to these properties, IN718 has wide application in power generation, aeronautics and aerospace. Its typical chemical composition of IN718 is: Ni-19Fe-18Cr-5Nb-3Mo-1Ti-0.5Al-0.04C (wt%). The IN718 microstructure consists of a γ matrix (Ni-based solid solution) strengthened by ordered face centred cubic γ' $Ni_3(Al,Ti)$-type and ordered body centred tetragonal γ'' Ni_3Nb-type nanoparticles (Figure 1). The primary strengthening mechanism for this alloy is a precipitation hardening by the γ' and γ'' particles and therefore properly sized and distributed precipitates are critical for good alloy performance. The aim of this study was to describe quantitatively IN718 microstructure, identify γ' and γ'' precipitates and examine their 3D shape and special distribution.

Microstructural investigation of Inconel 718 superalloy after various heat treatment was performed by electron microscopy (SEM, TEM, STEM-HAADF-EDX) and electron tomography techniques (FIB-SEM) taking advantage of recent developments in quantitative electron microscopy. Electron microscopy analyses were performed using a Merlin Gemini II of Zeiss, Tecnai G2 Twin and a probe Cs-corrected Titan G2 60-300 with EDX ChemiSTEM technology, both of FEI. The FIB-SEM tomography investigation was conducted by NEON CrossBeam 40EsB of Zeiss.

The distribution maps of the chemical elements collected by ChemiSTEM show that the γ'' phase contains Ni, Nb, Ti, whereas the γ' phase contains mainly Ni, Al and Ti. Comparing Al and Nb maps brings a clear contrast between the γ' and γ'' precipitates as well as the matrix (Figures 2, 3). This allows to precisely measuring their size and spatial distribution. Moreover, the high map signal/noise ratio brought by the ChemiSTEM optimization makes possible to extract the actual composition of the γ' and γ'' nanoparticles though they are buried in the matrix.

Electron microscopy and FIB-SEM tomography images revealed the 3D morphology of γ' and γ'' precipitates; the γ'' precipitates are nearly disc-shaped, while γ' particles are almost spherical. Tomographic images were used also for estimation of the volume fraction of both phases strengthening the superalloy. It appears that the main difference in the microstructure of the specimens subjected to different heat treatment variants is the presence of $\gamma' + \gamma''$ co-precipitates, what favourably contributes to better mechanical properties of the IN718 superalloy.

1. The authors acknowledge Pratt and Whitney, USA for providing the material for investigation and thank Dr Ioannis Alexandrou and Dr Anna Carlsson, FEI, for assistance in the research.

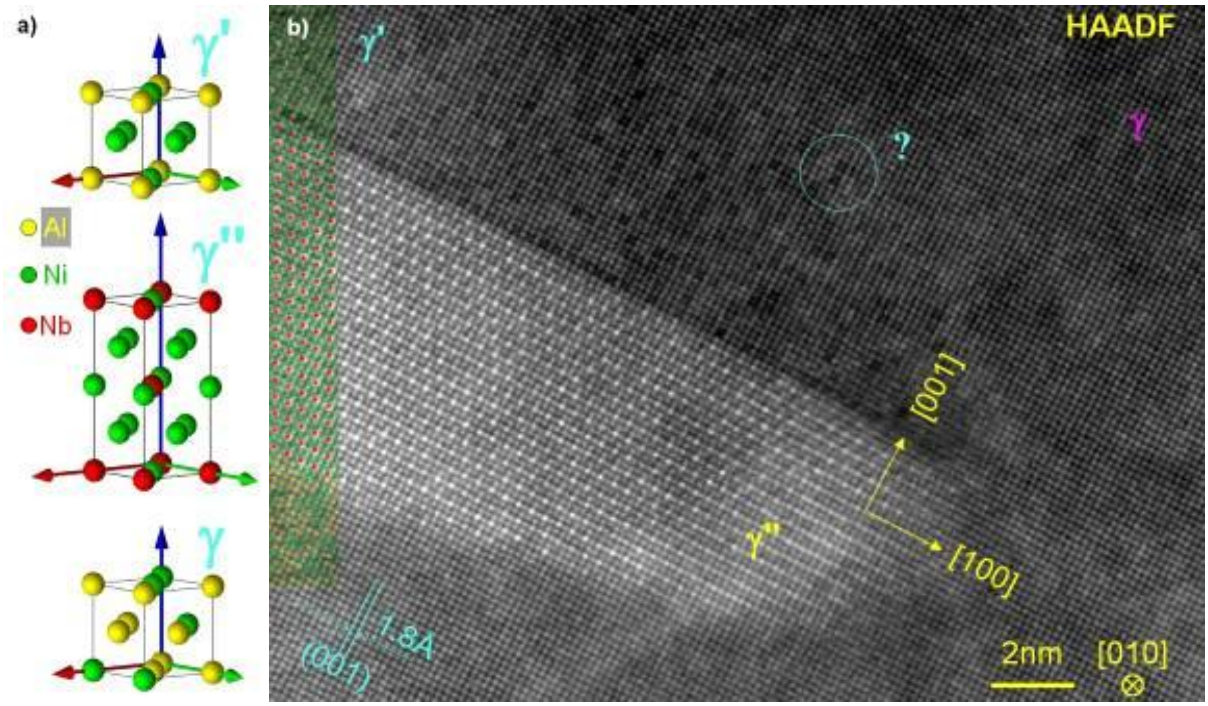

Figure 1. a) ball model of the □ matrix and the □' and □" phases; b) HAADF high-resolution STEM image of □' and □" precipitates in the □ matrix. All interfaces are coherent, but the □'/□" one as well as the □' precipitate contain defects at the atom column scale.

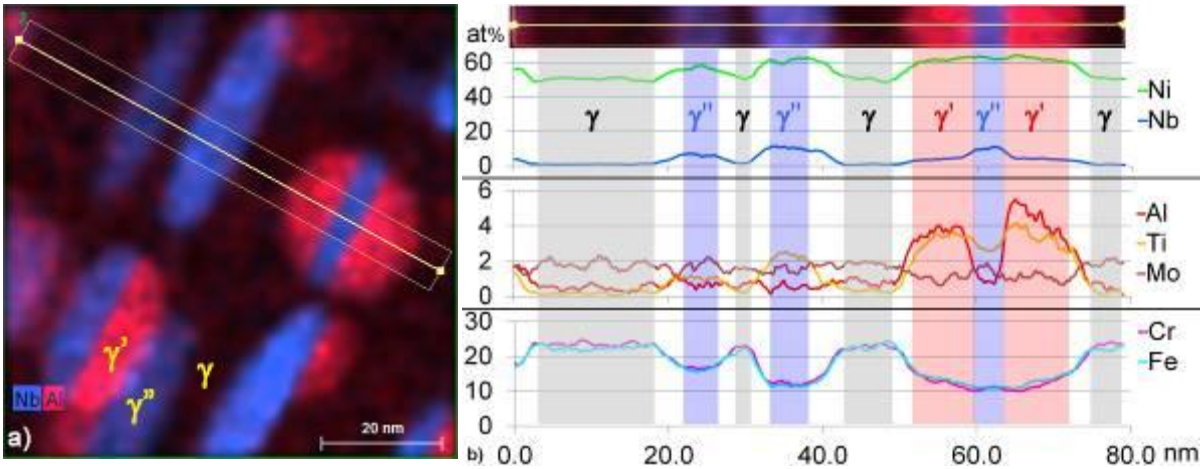

Figure 2. a) EDX ChemiSTEM map of Al (red) and Nb (blue) that distinguishes the □' and □" precipitates; b) Composition changes along a line scan across the three phases. Notice the unexpected presence of Nb in the □' phase.

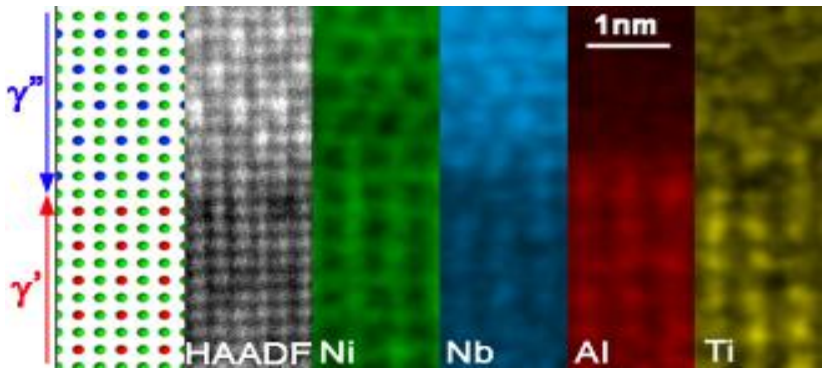

Figure 3. EDX ChemiSTEM maps of a □'/□" interface. The Nb substitute to Al in the □' phase

Materials for Energy Technology

MS.4.P113
Distribution of MgO nanocrystals in superconductor MgB_2 wires observed with TEM tomography

M. Song[1], S.J. Ye[1,2], M. Takeguchi[1], A. Matsumoto[1], K. Togano[1], T. Ohmura[1,2], H. Kumakura[1]

[1]National Institute for Materials Science, Surface Physics and Structure Unit, Tsukuba, Japan
[2]Kyushu University, Faculty of Engineering , Fukuoka, Japan

Minghui.SONG@nims.go.jp
Keywords: MgB_2, superconductor, tomography

MgB_2 has the highest critical temperature (T_c) of 39 K among metallic superconductors [1]. It has other benefit features also such as low weight, abundance and low cost of the start materials, easy to be fabricated into wires, sheets, and etc. For these reasons, the MgB_2 superconductor is considered to be a promising material for large-scale applications in electric power and magnetic field generation at around 20 K with low cost. However, one of the problems of the material is that the critical current density (J_c) is not high enough for practical use. It has been established that doping with carbon or nano-sized inclusions such as oxides can improve J_C and other superconductive properties of MgB_2. MgO is a kind of impurity in MgB_2 which is introduced in the fabrication process of the material and is difficult to be removed. The inclusions of MgO may become positive if they are in nano-size, with appropriate density and distribution because they can act as magnetic pinning centres. Therefore, to understand the size, density and distribution of inclusions of MgO and other impurities in MgB_2 is very important for the improvement of superconductive properties of the material. In the present work, we characterized the MgB_2 wires fabricated with internal magnesium diffusion (IMD) process [2] by means of 3-dimensional (3D) and conventional TEM in order to give a visualization of distribution of MgO nano-inclusions and correlate the size and distribution to superconductive properties of the wires.

Two kinds of MgB_2 wires, without and with addition of SiC, were fabricated by IMD process. The start materials were boron powder (purity 99.9%), magnesium (Mg) rod, and SiC powder. The Mg rod was coaxially inserted into an iron (Fe) tube. The other constitutes were packed into the gap between the Mg rod and Fe tube [2]. The composites were heat treated at 670 °C for 3 hours. The MgB_2 wires with addition of SiC exhibited much higher J_Cs than those without addition of SiC in the magnetic field from 8 to 12 T. The TEM thin film specimens were prepared from the fabricated MgB_2 wires by a focused ion beam instrument, JEM-9310FIB. The tilting series images were obtained in STEM HAADF mode. The observation for obtaining tilting series images were carried out with tilting angles from -69 to 69 degree in a step of 3 degree. The reconstruction of the tilting series images was performed using a software made by Gatan, Inc. JEM-2100F and JEM-3000F were used for the observation and analysis.

Figure 1 shows typical STEM images of the MgB_2 wires. 2 kinds of domains, here called as domain A and domain B, were observed in the MgB_2 wires. Domain A is composed of small crystal grains while domain B is in amorphous status. The crystal grains in the MgB_2 wires without addition of SiC were confirmed to be those of MgB_2 and MgO. The crystal grains in the MgB_2 wires with addition of SiC were identified to be those of MgB_2, MgO, and Mg_2Si. The elemental distribution was analyzed with EDS (energy dispersive X-ray spectroscopy) and EFI (energy filtering imaging). It was confirmed that domain A had elements of boron, Mg, O in the MgB_2 without addition of SiC, and of boron, Mg, O, C, Si in the MgB_2 with addition of SiC. Domain B is composed of boron in the two kinds of MgB_2 wires. It is noticed that the high composition areas of O are distributed surround the B domain. Since the areas are also the high composition areas of Mg, the O should exists in form of MgO. It is considered that the O may mainly come from the surface of the start materials of boron particles. The core of domain B should be the remained unreacted boron. The nano-sized MgO crystals shown bright contrasts in STEM HAADF observation because they have a higher mass-density than MgB_2 or Mg_2Si (density ρ in $g.cm^{-3}$: MgO 3.6; MgB_2 2.57; Mg_2Si 1.99). This made it possible to identify the distribution of MgO in STEM HAADF mode for 3D observation. The 3D observations revealed that the MgO

crystals appeared a layer-like distribution surround domain B in MgB_2 wires without addition of SiC, while they distributed more dispersedly in the wires with addition of SiC. It is suggested that in the sintering of MgB_2 in IMD process, Mg reacted firstly with O on the surface of boron particles to form MgO, and then reacted with boron to form MgB_2, finally the Mg was consumed and the unreacted boron was remained. As a result, the nano-crystals of MgO distributed surround domain B in a layer-like shape for the MgB2 without addition of SiC. The results implied that the addition of SiC slowed down the reaction of Mg with O and resulted in the dispersion of MgO. The dispersed nano-sized MgO crystals may act as magnetic pinning centers in the wires. Therefore, the MgB_2 wires with addition of SiC exhibited a higher J_C than those without addition of SiC.

1. J. Nagamatsu, N. Nakagawa, T. Muranaka, Y. Zenitani, J. Akimitsu, Nature 410 (2001) p.63.
2. J. Hur, K. Togano, A. Mastumoto, H. Kumakura, H. Wada, K. Kimura, Supercond. Sci. Technol. 21 (2008) 032001(4pp).

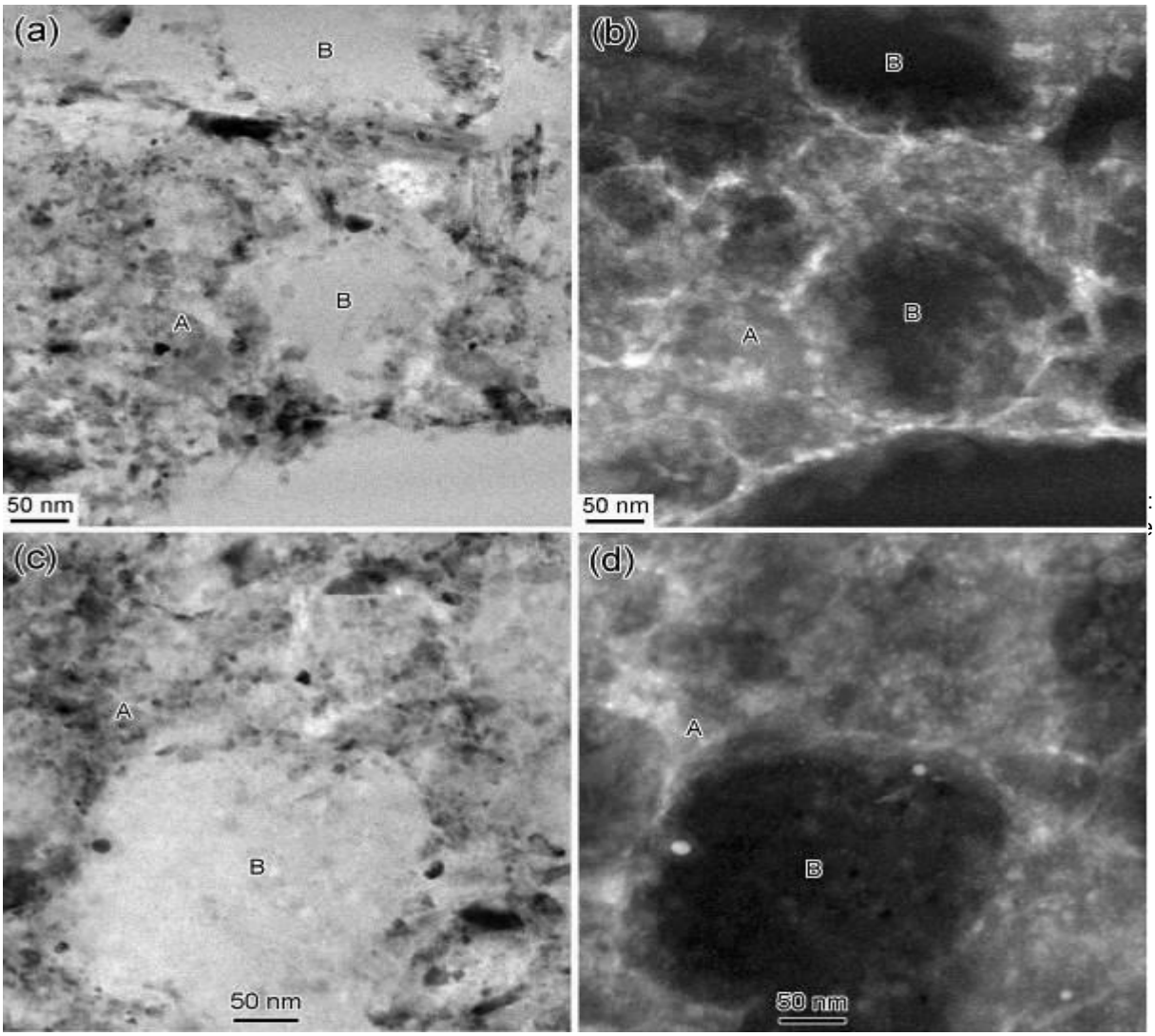

Thin Films and Coatings

MS.5.114
Perspectives on $Li_{3x}Nd_{2/3-x}TiO_3$ – a complex perovskite material with nano-chessboard contrast in TEM

R. Erni[1], A.M. Abakumov[2], A.A. Tsirlin[3], M.D. Rossell[1], D. Batuk[2], G. Nénert[4], G. Van Tendeloo[2]

[1]Electron Microscopy Center, Empa, Swiss Federal Laboratories for Materials Science and Technology, CH-8600 Dübendorf, Switzerland
[2]EMAT, University of Antwerp, B-2020 Antwerp, Belgium
[3]National Institute of Chemical Physics and Biophysics, 12618 Tallinn, Estonia
[4]Institut Laue Langevin, 6 rue Jules Horowitz, 38042 Grenoble, France

rolf.erni@empa.ch
Keywords: Chessboard materials, STEM, channelling contrast

An important problem in materials science and crystallography is the question about the occupation of the lattice if different atomic species compete for the same sites. Whether long- or short-range order is established amongst atomic species that are hosted by the same type of crystalline lattice sites, or whether a material decomposes into two phases, is essentially ruled by the chemical nature and the size difference of the atoms. Complexity is added if additional effects need to be encountered. This is exemplified in complex perovskite materials where tilting distortions of the oxygen octahedra and polar cation displacements can occur. The interplay of such effects can lead to remarkable structural features which in the case of $Li_{3x}Nd_{2/3-x}TiO_3$ are manifested in a striking nano-chessboard contrast in TEM images. However, the fact that this chessboard pattern does not unambiguously relate to the structural nature of the material is revealed by a gradually changing pattern contrast, from chessboard to a diamond-type pattern, when the imaging conditions or the sample thickness is varied, see Fig. 1.

We employed electron microscopy, X-ray and neutron diffraction in order to revisit the structure of $Li_{3x}Nd_{2/3-x}TiO_3$ and to reveal the true nature of the chessboard contrast in TEM images. While the pattern contrast in coherently formed TEM images strongly depends on the sample thickness and the objective focus, STEM images of thicker sample areas reveal an invariant diamond pattern. It was argued that the reason for the diamond pattern observable in so-called *Z*-contrast STEM images lies in an ordered phase separation into a Li-rich and a Li-depleted phase [1]. However, our STEM investigation show that this intuitive contrast interpretation of the *Z*-contrast STEM images is inadequate as the pattern contrast diminishes with increasing scattering angle, i.e. while the pattern contrast is most visible in incoherently formed bright-field (BF) and annular dark-field (ADF) STEM images, there is only a very faint pattern contrast observable under strong *Z*-contrast conditions in high-angle annular dark-field (HAADF) STEM, see Fig. 2. The dependence of the pattern contrast on the detection angle reveals that the true source of the residual pattern contrast in the supposedly *Z*-contrast images lies in the channelling conditions given by the local strain.

Electron diffraction provides a complementary method to tackle the intriguing structure of $Li_{3x}Nd_{2/3-x}TiO_3$ and reveals a basic perovskite lattice (p) whose main reflections are decorated by satellites. In addition, a set of weak reflections near $½½0_p$-positions can be observed which are out of phase with respect to the satellites. These “forbidden” sets of reflections and the satellites provide indication that a domain structure is present. Based on earlier work by Labeau *et al.* [2] on $ThNb_4O_{12}$, García-Martín *et al.* [3] proposed that similar to $ThNb_4O_{12}$ a quasiperiodic microdomain structure is responsible for the diffraction behaviour. The domains are supposed to be formed by twin boundaries which separate areas wherein the pattern of tilted TiO_6 octahedra is uniform.

Powder synchrotron X-ray (ID31, ESRF) and neutron diffraction (D2B, ILL) in combination with the TEM data allowed for a complete quantitative structure solution of the (3+2)-dimensional incommensurately modulated $Li_{0.15}Nd_{0.617}TiO_3$ structure. Unlike the model of García-Martín *et al.* [3] or any other previously suggested model, Rietveld refinement revealed that the primary modulation is related to rectangular domains with a quasiperiodic two-dimensional perturbation of the in-phase tilting pattern of the TiO_6 octahedra around the *c*-axis [4]. The refinement undoubtedly demonstrated the absence of the compositional modulation and the earlier proposed phase separation. Moreover, contrary to the phase separation model [1], our (3+2)-dimensional model of $Nd_{0.617}Li_{0.15}TiO_3$, whose domain structure is merely due to displacive modulations with a primary contribution of the frustrated TiO_6 octahedra tilting, reproduces the experimental electron diffraction pattern (see Fig. 3), the varying pattern contrast in TEM images as well as the residual channelling contrast in BF and ADF STEM.

1. B.S. Guiton and P. Davies, Nature Mater. 6 (2007) 586.
2. M. Labeau, I.E. Grey, J.C. Joubert, H. Vincent and M.A. Alario-Franco, Acta Cryst. B 38 (1982) 753. (1982).
3. S. García-Martín, F. García-Alvarado, A.D. Robertson, A.R. West and M.A. Alario-Franco, J. Solid State Chem. 128 (1997) 97.
4. A.M. Abakumov, R. Erni, A.A. Tsirlin, M.D. Rossell, D. Batuk, G. Nénert, G. Van Tendeloo, Chem. Mater., DOI: 10.1021/cm4012052.

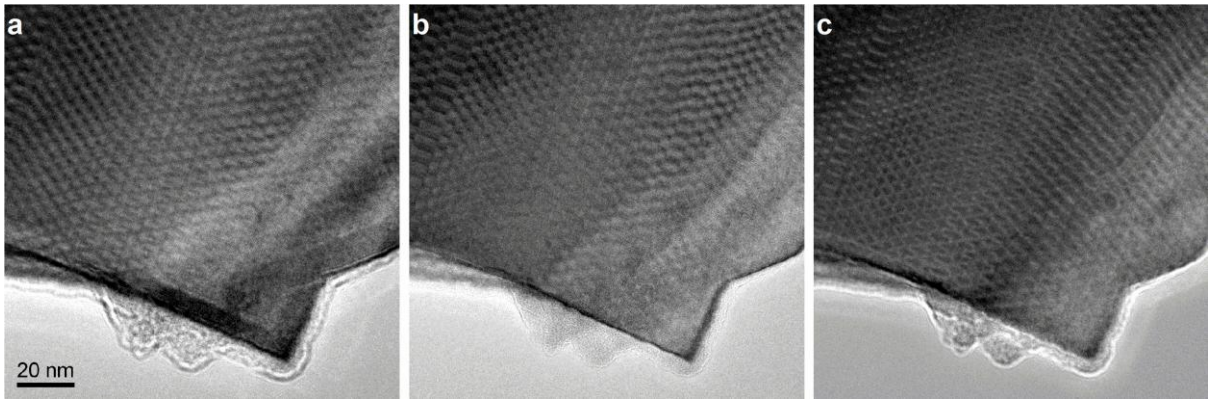

Figure 1. Dependence of the "chessboard" pattern on the imaging conditions of $Nd_{0.617}Li_{0.15}TiO_3$ in $[001]_p$ zone-axis orientation. The nominal defocus in (a), (b) and (c) is +1000 nm, +100 nm and -900 nm. The pattern contrast strongly depends on the local diffraction conditions (sample tilt), on the sample thickness and on the imaging conditions (defocus).

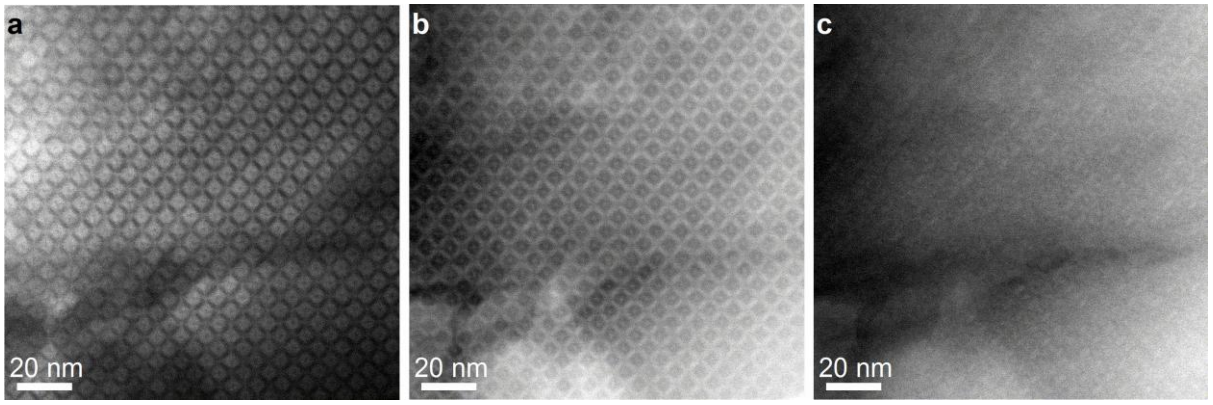

Figure 2. BF (a), ADF (b) and HAADF STEM (c) images of $Nd_{0.547}Li_{0.36}TiO_3$ in $[001]_p$ zone-axis orientation. The inner detection angles for the HAADF and the ADF STEM images are 100 and 35 mrad, respectively. As the contrast of the diamond pattern disappears with increasing dark-field detection angle, the pattern cannot be due to a compositional variation. STEM: 200 kV, semi-convergence angle: 10.8 mrad.

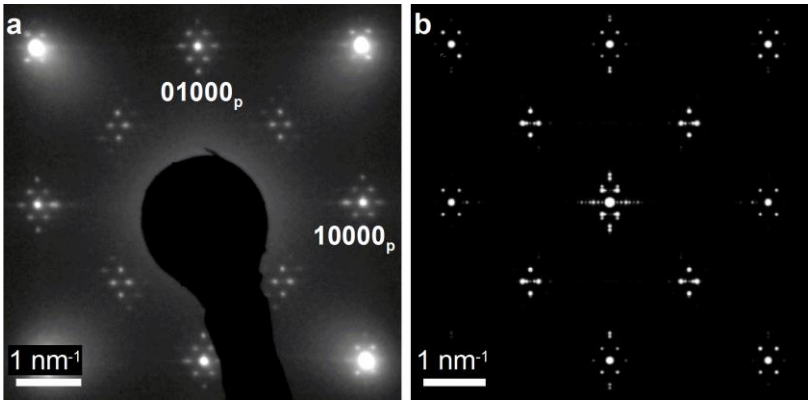

Figure 3. Experimental (a) and simulated (b) electron diffraction pattern of $Nd_{0.617}Li_{0.15}TiO_3$ in [00100] zone-axis orientation. The simulated ED pattern is based on a $40a_p x 40a_p x 2a_p$ commensurate approximant of the (3+2) dimensional quasiperiodic domain structure. The speckling along the vertical and horizontal directions in the center is due to the finite size of the approximant.

Thin Films and Coatings

MS.5.115
TEM study of interface's impact on hardening mechanisms in transition metal nitride thin films

M. Parlinska-Wojtan[1]

[1]University of Rzeszow, Center for Microelectronics & Nanotechnology, Rzeszow, Poland

magdalena.parlinska@univ.rzeszow.pl
Keywords: Hard coatings, Nitride thin films, Nanocomposites, Multilayers, TEM.

The aim of this study was to identify the types of interfaces and their impact on hardening mechanisms of differently structured transition metal nitride coatings, by direct transmission electron microscopy (TEM) observations. The investigated coatings have been divided according to their structure into three groups: columnar coatings, multilayers and nanocomposites. The microstructural aspects of all three groups have been extensively studied by TEM in as-deposited and heat-treated state or after indentation in order to better visualize the mechanisms governing the coating behavior during plastic deformation. Also the combination of different chemical compositions and their influence on the coating's microstructure has been analyzed.

TEM studies down to the atomic scale, of a compositionally graded TiAlSiN coating allowed putting some light onto the mechanism of formation of the nanocomposite structure. The images taken in the Ti-rich part of the coating showed crystalline columns with neat interfaces, followed by a progressive appearance first of a crystalline and then of an amorphous boundary phase as the Al+Si concentration was increasing. At the top part of the coating the well-known nanocomposite structure consisting of crystalline grains surrounded by an amorphous matrix was observed, Figure 1(a). In addition it could be shown that the nanocomposite structure, exhibiting high hardness, can only be formed with two phases having sharp interfaces such as TiN/SiN, Figure 1(c). It was not possible to make a hardness enhanced nanocomposite out of AlN and SiN. This was due to local epitaxy at AlN/SiN interfaces, investigated on a models system of AlN/SiN multilayers. Indeed, it was found that 0.7 nm of SiN, corresponding to about two monolayers, grew crystalline on AlN favoring epitaxy, Figure 1(b) – (e).
The nanocomposite structure is not the only way to achieve a hardness enhancement in these coatings: also columnar coatings can be hard, provided a sufficient density of dislocation barriers, not in form of column boundaries, is present. Two solutions to increase the density of dislocation barriers are presented: one consists in the introduction of compositionally graded multilayers, which distort the lattice but do not obstruct the columnar growth. The second solution is a phase modulated structure i.e. inside the columns zones of different phases are formed as it is the case for cubic and hexagonal NbN, which nevertheless has a columnar structure.

In multilayered coatings three types of interfaces, influencing their properties were observed: completely epitaxial, such as in AlN10 nm/SiN<0.7 nm layers or NbN/CrN interfaces in the growth direction, Figure 1(d), semi-coherent, with local epitaxy and non-coherent such as in TiN/SiN coatings. All of them were barriers for dislocation movement making thus these coatings harder that their reference columnar layouts.

To better visualize and identify the hardening mechanisms based on dislocation blocking in metal nitride coatings, plastic deformation was deliberately induced by nanoindentation.
Columnar and multilayered coatings have been extensively investigated by post-mortem TEM observations of indents cross-sections. In general, all coatings containing TiN, independently on their structure or layer thickness, deformed by shear sliding at grain boundaries. This mechanism was observed on two different scales: either multilayer pieces or individual grains were vertically displaced over distances of several nanometers. It was particularly well visible for the NbN/TiN and the TiN/amorphous-SiN combinations.

By microstructural observations it could be shown that the substrate governs the deformation induced by nanoindentation with a Berkovich indenter tip in columnar TiN coatings. In the case of columnar TiN deposited on a soft Si substrate during indentation the columns underwent shear sliding at grain boundaries and were pushed into the substrate forming steps at the interface Figure 2(a) & (b). If columnar TiN is grown on polycrystalline, hard WC-Co substrate, cracks at columnar boundaries are generated and the columns are bent, Figure 2(c). However, the columns, which grow on the soft Co matrix, are also pushed into it, similarly to the TiN/Si combination. Conversely, those columns, which grow on the hard WC grains are bent and internally fractured, Figure 2 (d).

1. W.-D. Münz, J. Vac. Sci. Technol. A 4/6 (1986) 2717.
2. W.D. Sproul, Science 273 (1996) 889.
3. S. Veprek, J. Vac. Sci. Technol. A 17 (5) (1999) 2401.
4. M. Parlinska-Wojtan, A. Karimi, T. Cselle, M. Morstein, Surf. Coat. Technol. 177, p. 376 (2004).
5. K.A. Rzepiejewska-Malyska, W.M. Mook, M. Parlinska-Wojtan, J. Hejduk, J. Michler JMR 24(3), p.1208, (2009)
6. M. Parlinska-Wojtan, S. Meier and J. Patscheider Thin Solid Films 518 (17) p.4890–4897, (2010)

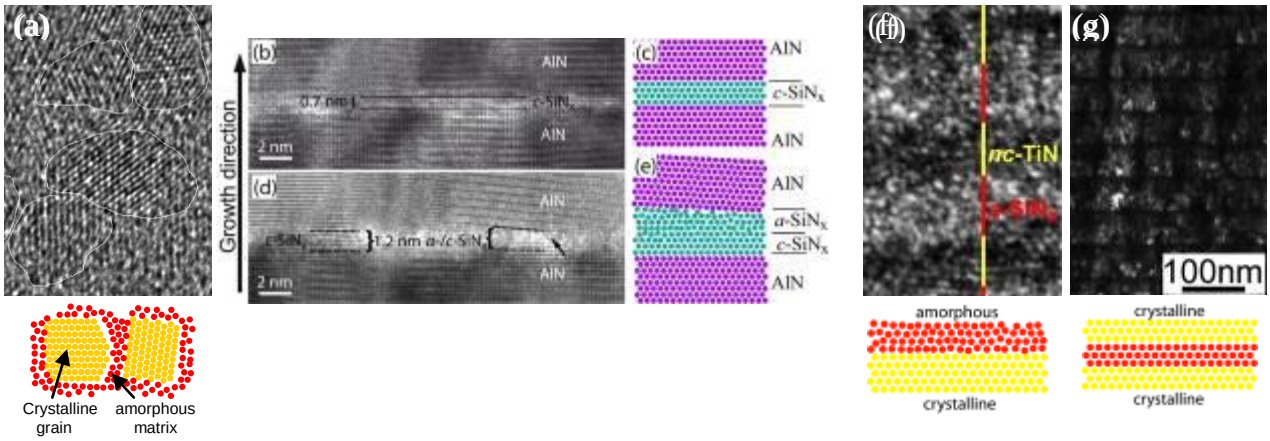

Figure 1. (a) HRTEM image of a TiAlSiN nanocomposite with a scheme of crystalline grains surrounded by an amorphous matrix; (b) & (d) Single crystalline AlN/SiN_x multilayers with two different SiN_x thicknesses together with (c) & (e) schematic models of the interlayer arrangement of the SiN_x atoms; (f) HRTEM image of a cross-section through a of TiN/amorphous-SiN multilayers with the respective layer thickness of 1 nm and a schematic representation of the atomic arrangement. (g) Dark field image of a cross-section through a multilayered NbN/CrN coating and a schematic representation of the atoms in the multilayers.

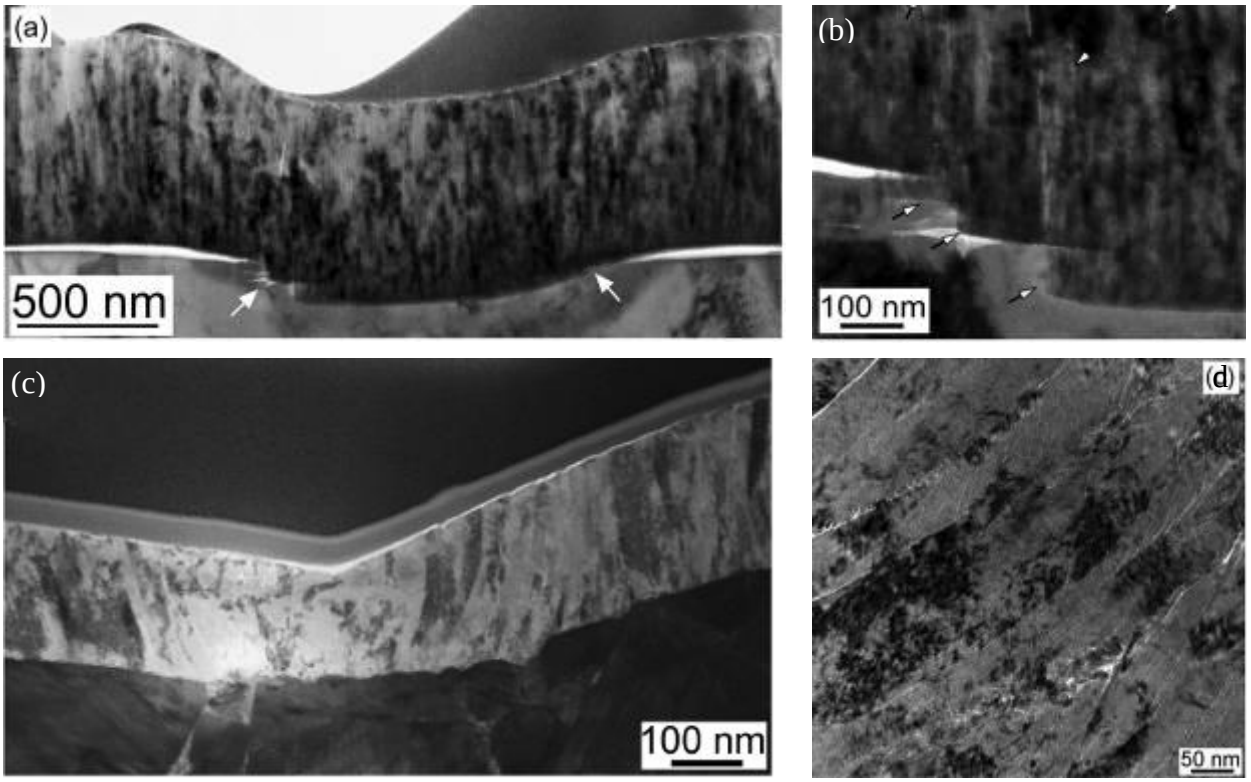

Figure 2. TEM bf images of cross-sections through a Berkovitch indent imprints in columnar TiN coatings grown on (a) soft Si (001) substrate; (b) hard polycrystalline WCCo substrate; magnified view of: (b) the steps formed by the columns pushed into the soft SI substrate due to grain boundary sliding; (d) Columns with intercolumnar and internal cracks.

Thin Films and Coatings

MS.5.116
Effect of Na-doping on the microstructure in Cu(In,Ga)Se_2 thin-film solar cells

L.A. Pfaffmann[1], A. Kast[1], D. Litvinov[1], E. Müller[1], W. Hempel[2], M. Powalla[2,3], D. Gerthsen[1]

[1]Laboratorium für Elektronenmikroskopie, Karlsruher Institut für Technologie, Karlsruhe, Germany
[2]Zentrum für Sonnenenergie- und Wasserstoff-Forschung Baden-Würtemberg (ZSW), Stuttgart, Germany
[3]Lichttechnisches Institut, Karlsruher Institur für Technologie, Karlsruhe, Germany

lukas.pfaffmann@lem.uni-karlsruhe.de
Keywords: Cu(In,Ga)Se_2, sodium-doping, EBSD, STEM, SEM

Polycrystalline chalcopyrites (chemical structure: $A^IB^{III}C^{VI}$) thin-films play an important role as solar cell absorbers. Especially solar cells based on Cu($In_{0.7}$,$Ga_{0.3}$)Se_2 layers are particularly promising because they have already reached an efficiency of 20.3% [1].

A typical CIGS-solar-cell layer stack consists of a substrate of glass or flexible foils, coated with Mo as the back contact. The p-n junction is located between the p-type CIGS layer and the transparent n-type window layer, which consists of a CdS buffer layer and the ZnO front contact.

During the fabrication, Na diffuses from the soda-lime-glass substrate into the CIGS layer which has positive effects during the growth process of the absorber layer and the efficiency of the solar cell [2]. Without Na, the formation of a $MoSe_2$ layer [3] is suppressed. This leads to the formation of a Schottky-type electrical contact instead of a contact with ohmic character.

To investigate the effects of Na, three samples with different Na-concentrations in the CIGS layer were prepared by inserting a Na-blocking and Na-doping layer below the Mo back contact as shown in the scanning electron microscopy image Figure 1. Secondary-ion-mass spectroscopy (SIMS) was applied to determine the Na-concentrations in the CIGS layer (0.008 at%, 0.342 at%, 0.523 at%). These samples were compared with a sample prepared by the standard procedure which contains 0.025 at% Na.

To reveal the difference of the microstructure between the CIGS layers, cross-sections were prepared by focused-ion-beam milling in combination with low-energy Ar^+-ion milling. This preparation technique yields thin lamellae for transmission electron microscopy (TEM) and cross-section samples for electron backscatter diffraction (EBSD) measurements with smooth surfaces and without artefacts.

Figure 2 shows high-angle annular dark-field cross-section STEM images of the interface region between the Mo back contact and the CIGS layer for all samples. The measurement of the thickness of the $MoSe_2$ layer, which is important for the electrical contact of the CIGS layer, shows a clear correlation between Na-content and thickness of the $MoSe_2$ layer. Its thickness increases from values below 25 nm for the sample with 0.008 at% Na to values above 150 nm for the sample with the highest Na-concentration.

The grain size was determined by the evaluation of EBSD maps from cross-sections (see Figure 3) and by etching the solar cell on top. The average grains size increases from 1.0 □m (0.008 at% Na), to 1.1 (0.025 at%), to 1.5 (0.342 at%), to 4.3 (0.523 at%) demonstrating again a strong influence of the Na-concentration. The EBSD maps also reveal the crystallographic orientation of the grains and facilitate the characterization of grain boundaries. A slight preference of the [010] grain orientation (green colour) perpendicular to the surface of the cross-section can be recognized in Figure 3 with increasing Na-content which is particularly obvious in the sample with the highest Na-content.

Clear effects of the increasing Na-concentration on the microstructure could be revealed. However, apart from the sample with the lowest Na-content, all other samples are characterized by efficiencies between 14,44 % and 15,10 % indicating that the increase of the grains sizes do not have a pronounced effect of the efficiency.

1. P. Jackson, D. Hariskos, E. Lotter, S. Paetel, R. Wuerz, R. Menner, W. Wischmann and M. Powalla, Prog. Photovolt: Res. Appl. 19 (2011) pp. 894–897
2. U. Rau, Advances in Solid State Physics 44 (2004) pp. 27-39
3. J. H. Sco_eld, A. Duda, D. Albin, B.L. Ballard, P.K. Predecki, Thin Solid Films, 260 (1995) pp. 26-31

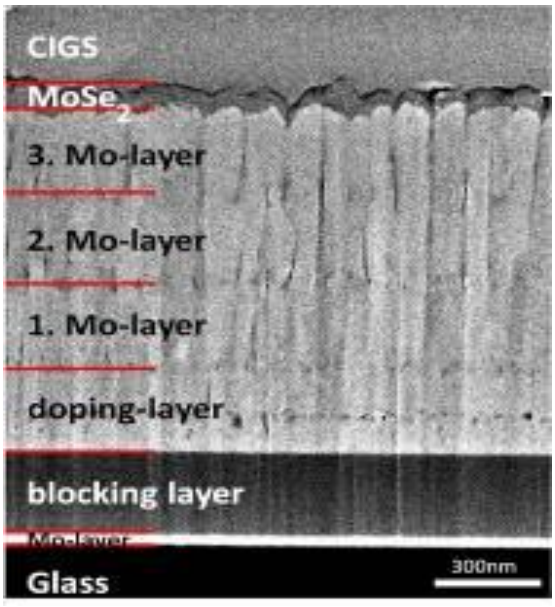

Figure 1. Scanning electron micro-graph of a cross-section of the modified back-contact

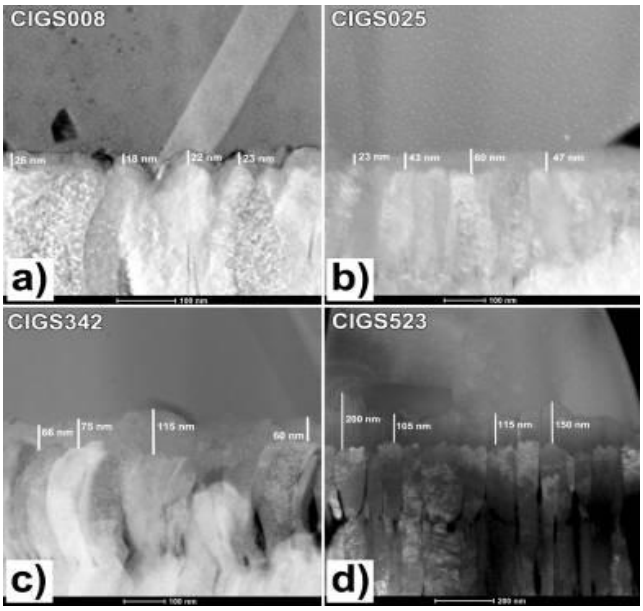

Figure 2. HAADF-STEM images of the Mo/$MoSe_2$/CIGS interface region of the samples with a Na-concentration of a) 0,008 at%, b) 0025 at%, c) 0,342 at% and d) 0,523 at%.

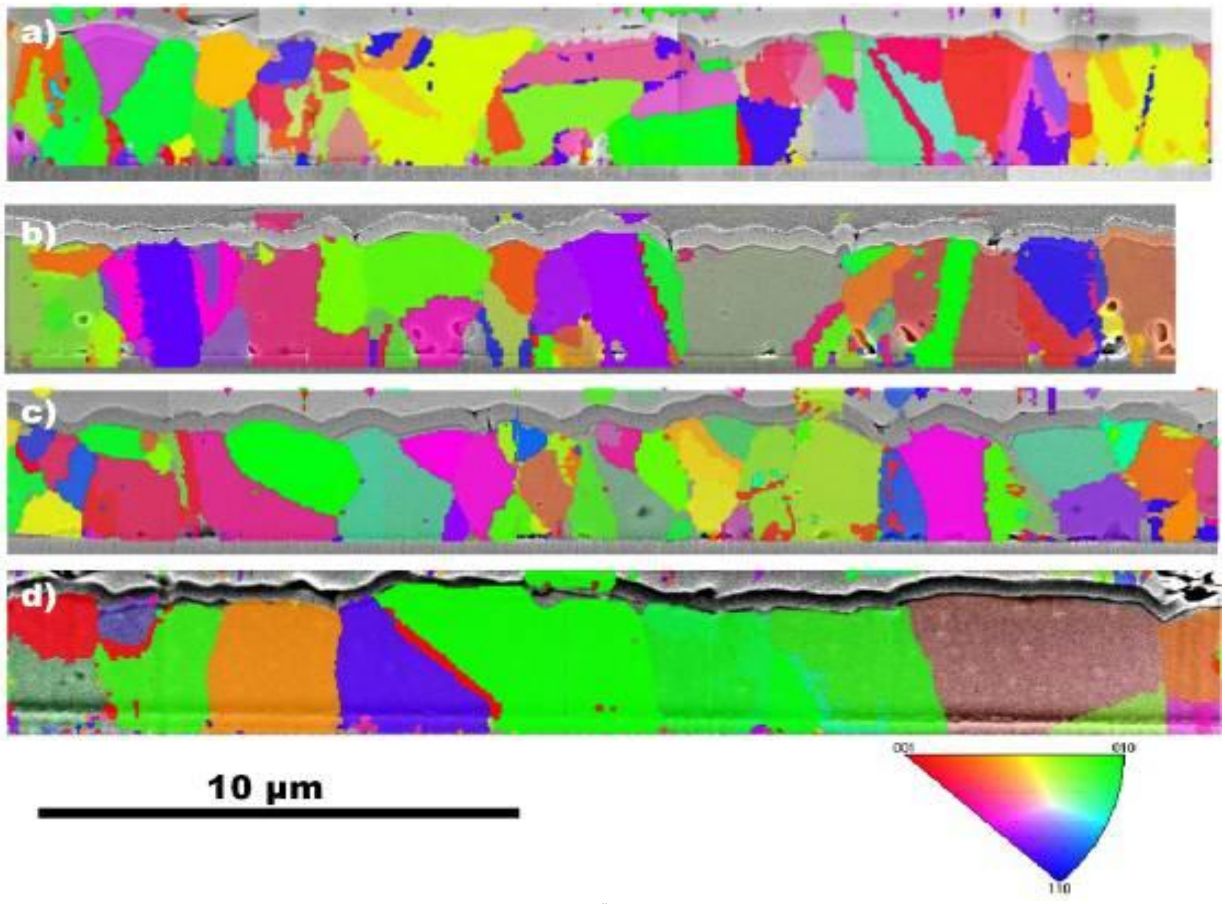

Figure 3. EBSD-maps of the samples with the sodium concentration of a) 0,008 at%, b) 0025 at%, c) 0,342 at% and d) 0,523 at% measured by SIMS. The orientation color scheme is given below the maps.

Thin Films and Coatings

MS.5.117
Competing Magnéli-like phases driven by substrate-induced strain in TiO_2 anatase thin films

R. Ciancio[1], A. Vittadini[2,3], A. Selloni[4], C. Aruta[5], F. Miletto Granozio[6,7], U. Scotti di Uccio[6,7] G. Rossi[1,8] E. Carlino[1]

[1]CNR-IOM, Trieste, Italy
[2]CNR-ISTM, Padova, Italy
[3]CR-INSTM, Padova, Italy
[4]Princeton University, CNR, Princeton, United States
[5]CNR-SPIN, Rome, Italy
[6]CNR-SPIN, Naples, Italy
[7]University of Naples "Federico II", Naples, Italy
[8]University of Milan, Milan, Italy

ciancio@iom.cnr.it
Keywords: anatase, HRTEM and STEM/HAADF, Density Functional Theory calculations

We used high-resolution transmission electron microscopy (HRTEM) experiments and simulation together with density functional theory (DFT) calculations to characterize the structure and defects in $LaAlO_3$-supported TiO_2 anatase thin films. Bright field TEM shows that the film is 40 nm thick and is split into two adjacent slabs of about 20 nm thickness each, characterized by different diffraction contrast (see Figure 1a). Closer HRTEM inspection shows that the two slabs have a modulated structure typical of the existence of crystallographic shear (CS) planes. In particular, we detected (103)- and (101)-oriented shear plane structures in the outer film region and in proximity of the film/substrate interface, respectively (see Figure 1b). Diffractograms taken over the two CS regions and displayed in Figure 1c and 1d, respectively, show a typical multiple-peak pattern, which indicates a superstructure-like behavior originating from the CS planes and defining two new superlattices. STEM/HAADF and Energy Dispersive X-ray Spectroscopy (EDXS) revealed the presence of Al interdiffusion from the substrate into the first 20 nm of the film[1].

By combining HRTEM results and relevant image simulations with DFT calculations we determined the atomic structure of the CS planes and show that they are based on the cubic TiO structure resembling the classical rutile-derived Ti_nO_{2n-1} Magnéli phases[2]. Figure 2a shows a HRTEM image focused at the (103) CS region; in Figure 2b a simulated image obtained from the (103) CS optimized structural model at 6 nm thickness and 74-nm underfocus values is displayed. A very good agreement is found between experiment and simulation, as highlighted by line profiles across the intensity maxima along the relevant segments of the two images. Differently from the previous case, although the orientation and spacing of the (101) CS planes in the theoretical model agree with the experimental ones, a discrepancy is observed in the linear arrangement of the brighter contrast spots running along the [100] anatase direction, as shown by the line scan profiles taken across the intensity maxima of representative segments of the two images (Figure 3a and 3b). Such a discrepancy may be related to the Al interdiffusion measured by HAADF and EDXS from the substrate over the first 20 nm film region[1,2]. DFT-derived thermodynamic predictions provided information on the stability of the observed structures as well as on the relations to the growth dynamics and to the matching with the bare substrate. Interestingly, we found that the crossover in the film between the two region hosting the two different Magnéli-like phases corresponds to the transition from a three-dimensional (3D) to a two-dimensional (2D) growth mode in the film structure as observed by in-situ reflection high energy electron diffraction (RHEED) during film growth[3].

Based on the experimental and theoretical evidences, we proposed a model for the peculiar growth mode of the overlayer and drew conclusions on the role of cation interdiffusion on film nucleation providing an explanation for the relative predominance of (103) and (101) CS planes in the body of the film and close to the interface with the substrate, respectively.

Our results shed light on fundamental processes useful also for tailoring the heteroepitaxial growth of TiO_2 anatase for device applications. In particular, we unveiled new effects which might be tailored to engineer new heterostructures with ad-hoc functionalities related to fundamental growth mechanisms.

1. R. Ciancio, E. Carlino, C. Aruta, D. Maccariello, F. Miletto Granozio and U. Scotti di Uccio, Nanoscale 4 (2012) 91.
2. R. Ciancio, E. Carlino, G. Rossi, C. Aruta, U. Scotti di Uccio, A. Vittadini and A. Selloni, Physical Review B 86 (2012) 104110.
3. R. Ciancio, A. Vittadini, A. Selloni, R. Arpaia, C. Aruta, F. Miletto Granozio, U. Scotti di Uccio, G. Rossi and E. Carlino, submitted to Journal of Nanoparticle Research.

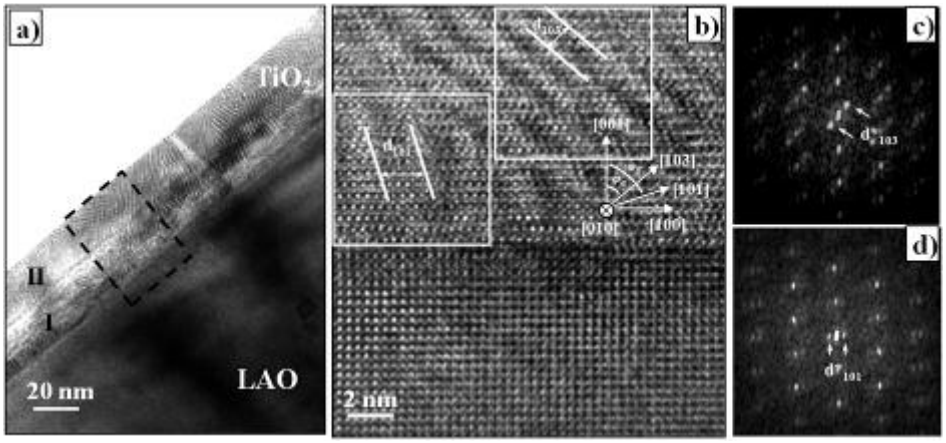

Figure 1. (a) Bright field TEM image of the TiO2/LAO film in the [010] TiO2 zone axis showing the splitting of the film into adjacent regions (I and II) with different diffraction contrast. (b) HRTEM image of the TiO2/LAO interfacial region, taken in the [010] zone axis, of the film showing the presence of two types of modulations characterized by different spacing (d101 and d103). Diffractograms taken over the region containing (c) (103) and (d) (101) CS planes. The satellite peaks around the (000) reflection are indicated by arrows in the two diffractograms.

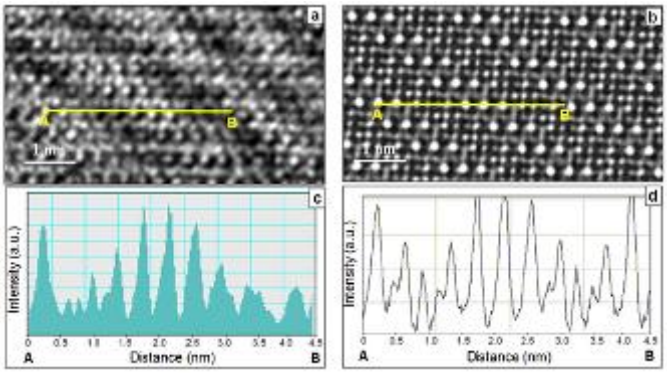

Figure 2. (a) HRTEM image focused at the film region containing (103) shear planes and taken in the [010] zone axis of the anatase film. (b) Simulated image obtained from the (103) CS modeled structure at 6 nm thickness and 74-nm underfocus values. Line scans across image intensity maxima calculated along the line of the (c) experimental and (d) simulated image.

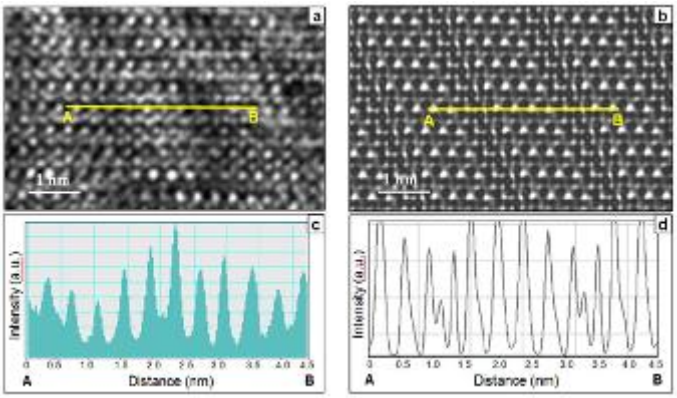

Figure 3. (a) HRTEM image focused at the film region containing (101) shear planes and taken in the [010] zone axis of the anatase film. (b) Image simulation calculated from the (101) CS modeled structure obtained at 6 nm thickness and 74-nm underfocus values. Line scans across phase maxima calculated along the line of the (c) experimental and (d) simulated image.

Thin Films and Coatings

MS.5.118
On the Huygens principle and crystallization of thin amorphous films according to “in situ” transmission electron microscopy data

A. Bagmut[1]

[1]National Technical University , Theoretic and Experimental Physics, Kharkov, Ukraine

agbagmut@mail.ru

On the basis of systematic electron diffraction and electron microscopy studies of species of crystallization of thin amorphous films on structural and morphological features, shared between the layered polymorphic crystallization [LPC], island polymorphic crystallization [IPC], dendrite polymorphic crystallization [DPC] and fluid-phase crystallization [FPC] [1,2]. This enabled to classify adequately a variety of crystallization processes in amorphous films.

The amorphous films were prepared by pulsed laser sputtering of rotating targets in vacuum and in oxygen atmosphere. Laser erosion plasma was deposited on the (001) surface of KCl crystals. Laser sputtering provided the formation of micro-babbles of sputtered substance in vapor-plasma flow, leading to the formation of micro-holes in the amorphous film. This allowed to analyze the spreading of crystallization line in the presence of barrier in the film. The films with thickness d ≈ 25-40 nm, transparent for an electron beam, were investigated. The obtained films were separated from the substrates in distilled water and placed on the micro grids for the electron microscopic investigations. Crystallization was initiated by local radiating influence of an electron beam on an amorphous film in a column of electron microscope ore by annealing of film in a muffle furnace on air. The film structure was investigated by electron diffraction methods and transmission electron microscopy. An example of LPC of amorphous film of HfO_2 is shown in figure 1a. The movement of crystallization line g - g' (dotted line in figure 1a and 1b) at velocity v_T took place during crystal growth. This line corresponded to the geometrical area of interaction of amorphous phase, crystalline phase, and external environment (air or vacuum). One can describe the movement of g - g′ line as propagation of light wave front in accordance with Huygens principle. Based on the Huygens principle, each point of crystallization line should be considered as formation centers of “flat’ secondary crystals formed by several unit cells of crystalline lattice. The secondary crystals grow in directions, having acute angles with external normal to the crystallization line. Such crystals also have similar orientation coincident with crystals orientation (identical streaking in figure 1b). Practical implementations of the Huygens principle to the periodic reactions taking place in the condensed matter, were proved by Leduc Stefan in [3]. The movement of the crystallization line g-g' in the direction v_T is a multiple of the unit cell size of the crystallized substance, and can be considered as a periodic process. Geometrical construction based on the Huygens principle, allowed to explain the diffraction of light and enveloping of various obstacles during light wave propagation. Such geometrical similarity is adaptable to the LPC mechanism and allows to understand the penetration of crystallization line into the geometrical shadow area formed by an obstacle (barrier h in figure 1b). Figure 1c and 1d illustrate the experimental confirmation of this idea. The holes h and h' serves as an obstacle to crystallization front propagation in the Cr_2O_3 amorphous film. TEM images shown in figure 1c and 1d, illustrate the propagation of crystalline phase, bypassing the hole h. The Cr_2O_3 single-crystalline layer is formed in the same orientation (zone axis [001] Cr_2O_3) behind the obstacle h (upper left corner in figure 1d). Such experimental investigations demonstrated the applicability of the Huygens principle to describe LPC of the amorphous films. One of the reasons for the implementation of a certain type of crystallization is the nature of the binding forces between the atoms of the elements. If dominated the covalent bonds, often the mechanism of LPC takes place. Metallic bond initiates the mechanism of IPC. In the case of LPC, the term “coherent” crystallization can be applied to the crystallization of thin film, as the single-crystal layer is provided by the same orientation (i.e. the “coherence”) of secondary nucleation centers. At the same time the LPC is an analog to the layer growth of the film on the substrate from the vapor phase (growth accordance to Frank and van der Merwe mechanism). As the result of the phase transformation on the mechanism of LPC, a crystalline film forms, where the dimensions of flat grains in the tangential direction by orders of magnitude are greater than its thickness. Island polymorphic crystallization is not a “coherent” crystallization. It is the analog of island film growth on the substrate from the vapor phase (growth accordance to Volmer and Weber mechanism). As the result of the phase transformation finely dispersed polycrystalline film is formed.

1. A. Bagmut, Technical Physics Letters 38 (2012), p. 488.
2. A. Bagmut, Functional Materials 19 (2012), p. 370.
3. S. Leduc, Théorie physico-chimique de la vie et générations spontaneés, Paris (1910), 202 p.

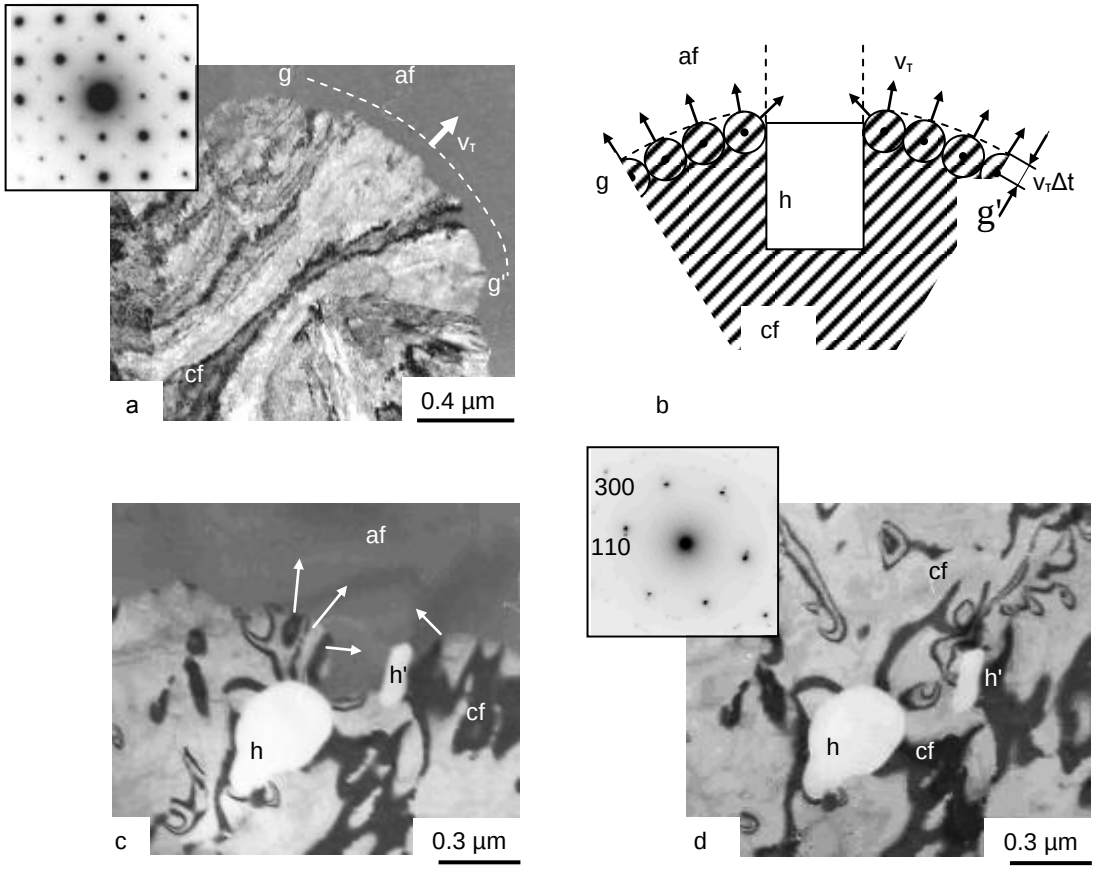

Figure 1. Layered polymorphic crystallization of amorphous films. a – crystallization of film of HfO_2 by annealing in a muffle furnace on air. b - the scheme of coherent crystallization, made by the analogy with the optical principle of Huygens. c, d - crystallization of amorphous film of Cr_2O_3 under the influence of the electron beam in vacuum. Crystallization line bypass the obstacles (holes h and h') by its moving. af - amorphous phase. cf - crystalline phase. The arrows indicate the direction of movement of the sections of the line of crystallization. In the upper left corner of the micrograph (a) and (d) the patterns of electron micro diffraction are shown (contrast is inverted).

Thin Films and Coatings

MS.5.119
In situ and *ex situ* transmission electron study of the crystallization kinetics of $Ag_4In_3Sb_{67}Te_{26}$

M. Bornhöfft[1,2], J. Benke[3], A. Kaldenbach[3], M. Wuttig[3], J. Mayer[1,2]

[1]GFE, RWTH-Aachen, Aachen, Germany
[2]ER-C, Jülich, Germany
[3]IA, RWTH-Aachen, Aachen, Germany

In optical data storage phase-change materials have been successfully established [1] and are promising candidates for non volatile electronic memory applications [2]. The crystallization kinetics is mainly defined by the writing speed and the stability of the phase-change data storage. Therefore sophisticated knowledge of the crystallization kinetics of phase-change materials is needed. Recent topics are the growth velocity of fast growth materials like $Ag_4In_3Sb_{67}Te_{26}$ (AIST) and the differences between as-deposited and melt-quenched AIST.

In the present work, the crystallization kinetics of AIST is investigated by *in situ* and *ex situ* heating. The *in situ* heating experiment is carried out with a Phillips PW 6592 *in situ* heating holder inside of a FEI Tecnai F20 transmission electron microscope (TEM). The *ex situ* heating is carried out inside of the heating furnace of a differential scanning calorimeter (DSC) for a high precision temperature control of ± 0.1 K.

The 30 nm thick amorphous AIST layer is embedded in a supporting multilayer stack on a 500 µm thick silicon substrate (“Figure 1.”). The 100 nm thick ZnS-SiO_2 capping layer on top of the AIST layer prevents oxidation. The 10 nm thick ZnS-SiO_2 layer below the AIST layer decreases together with the capping layer the necessary power to melt the AIST layer by laser irradiation. The 50 nm thick Si_3N_4 layer is an etch stop needed to prepare the TEM samples. The silicon substrate delivers sufficient heat dissipation for melt quenching. The AIST is either investigated in the as-deposited or in the melt-quenched state. Melt quenched amorphous marks (bits) are produced by laser irradiation of crystallized AIST. The AIST is crystallized beforehand in a furnace. To investigate the samples in a TEM the silicon substrate is removed by dimple grinding and etching with potassium hydroxide.

The *in situ* heating experiment is carried out with the AIST samples prepared by melt quenching. First of all the sample is heated from room temperature to 343 K and then heated to 383 K after the thermal drift has faded. The bits crystallize by inward growth from the crystalline rim towards the centre of the bit. The crystalline rim grows homogeneously into the bit. At 383 K the crystallization of a complete bit takes around 30 minutes after the heating starts. There is no nucleation observed inside the bit. This shows clearly the growth dominated crystallization behaviour of AIST. Bending contours created during crystallization follow approximately the crystal growth direction. The crystallized area shows little difference in morphology to its surrounding crystalline matrix (“Figure 2.”).

In the *ex situ* heating experiment the growth velocity of as-deposited AIST is quantitatively measured. The samples are annealed in the temperature range of 413.15 K-428.15 K. As soon as measurable grains have crystallized the samples are switched between TEM and further heating in the DSC. The grain size is measured in TEM brightfield images after each heating step. The morphology of the growing grains in the as-deposited layer is the same as the morphology of the area from the melt-quenched bit after crystallization. Bending contours in the growing grains are clearly visible. The average growth velocities are calculated from the measurements of several round grains in a few samples for every temperature. The grains are growing mainly homogenously round. The size of the diameter of the grains increases linear over time at a given temperature. The growth velocity increases exponential with increasing temperature. The *ex situ* heating will be also performed with melt-quenched AIST and compared to the as-deposited state.

1. E. Meinders, A. Mijiritskii, L. Pieterson and M. Wuttig in “Optical Data Storage: Phase-change Media and Recording”, ed. F. Toolenaar, (Springer, Netherlands) (2006), p. 18.
2. M. Wuttig and N. Yamada, Nature Materials 6, (2007), p. 824.
3. J. Heber, D. Schlom, Y. Tokura und R. Waser in “Frontiers in Electronic Materials”, ed. M. Wuttig, (Wiley-VCH, Deutschland) (2012), p. 175.
4. We kindly acknowledge the funding from the DFG in the framework of the SFB 917 “Nanoswitches”.

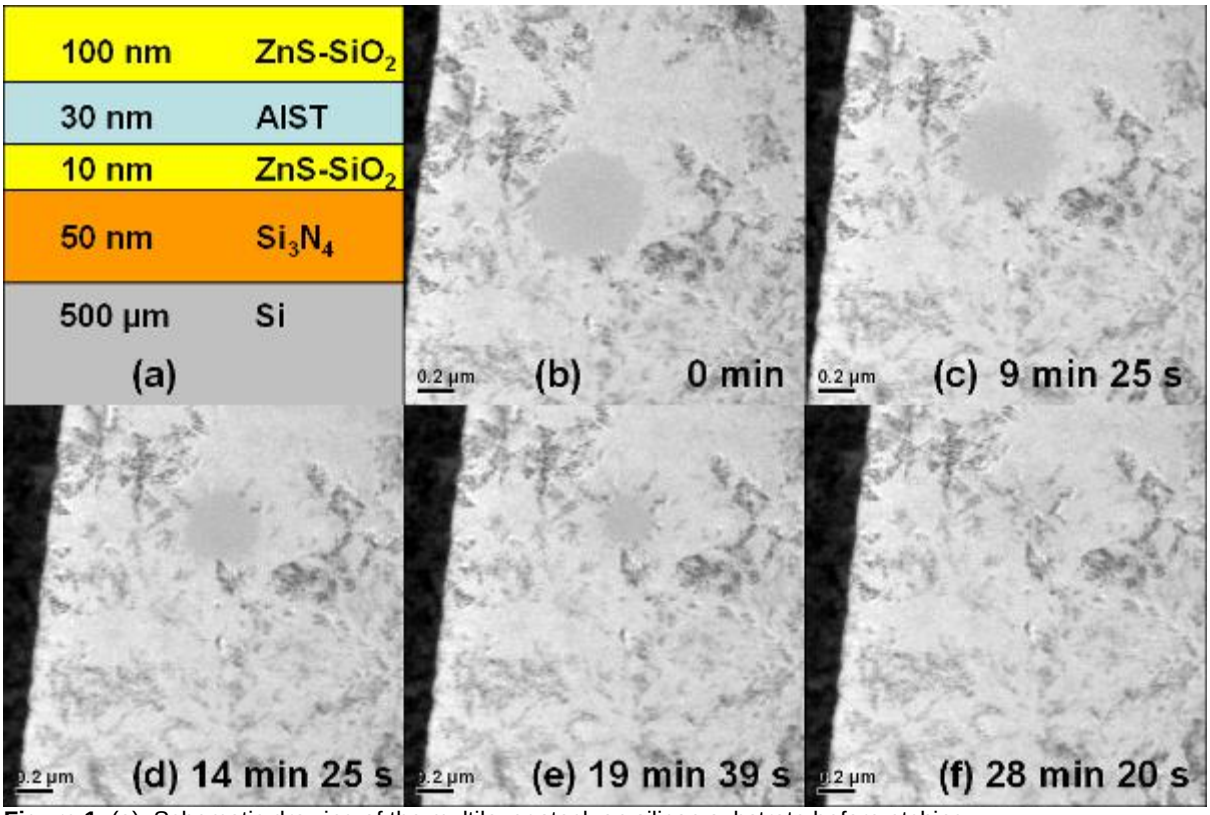

Figure 1. (a). Schematic drawing of the multilayer stack on silicon substrate before etching.
(b)-(f). Transmission electron microscope brightfield images of an amorphous melt quenched region within a crystalline $Ag_4In_3Sb_{67}Te_{26}$ layer heated *in situ* at 383 K. The displayed time is related to the start of heating [3].

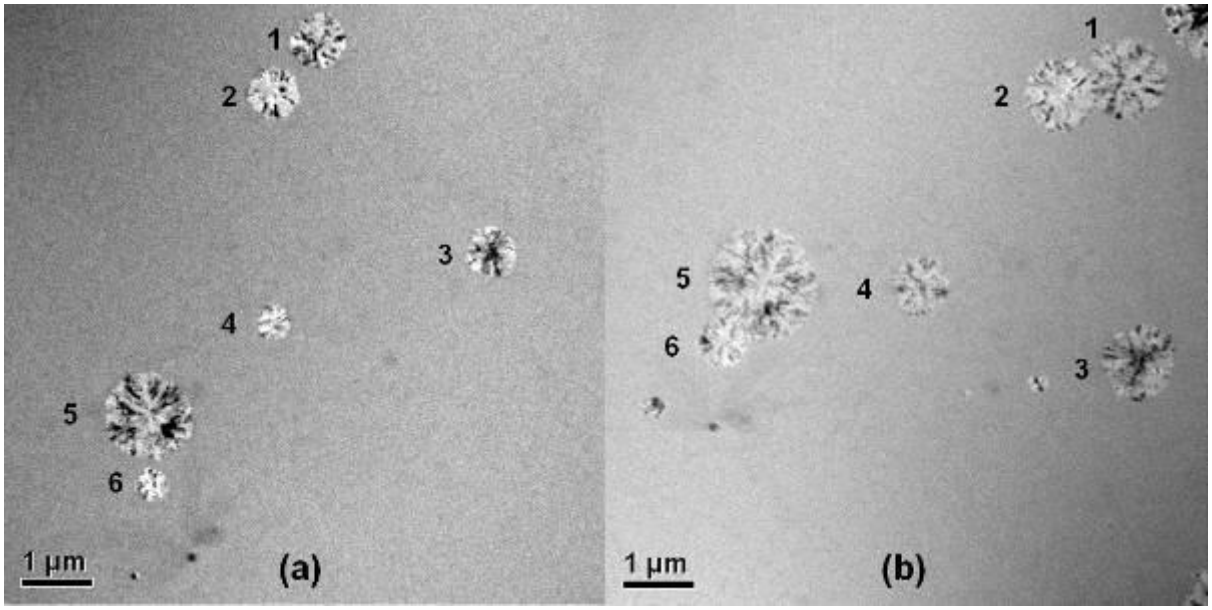

Figure 2. (a). Transmission electron microscope brightfield image of crystalline grains in a amorphous $Ag_4In_3Sb_{67}Te_{26}$ layer after 90 min *ex situ* heating in a furnace at 418.15 K.
(b). The grains from image (a) after 10 min additional heating (100 min in total) at 418.15 K.

Thin Films and Coatings

MS.5.120
A study of structural evolution of alkaline earth fluorides from amorphous to polycrystalline phase by in-situ TEM

X. Mu[1], A. Bach[2], W. Sigle[1], D. Fischer[2], M. Jansen[2], P.A. van Aken[1]

[1]Max Planck Institute for Intelligent Systems, Stuttgart Center for Electron Microscopy (StEM), Stuttgart, Germany
[2]Max Planck Institute for Solid State Research, Inorganic Solid State Chemistry, Stuttgart, Germany

xiaoke.mu@is.mpg.de
Key words: in-situ phase transformation, alkaline earth fluorides, pair distribution function, disordered solids

New metastable modifications, their existence and the development of new ways for their synthesis have been an important subject of solid state science in both theoretical and experimental studies. One such synthesis method is the so-called low-temperature atom beam deposition (LT-ABD) [1] that has been successfully applied to the synthesis of new halides [2], alloys [3], and nitrides [4]. Deposition onto a cooled substrate leads to amorphous thin films. During annealing the formation of metastable and stable crystalline phases can be studied. The study of these processes enhances the understanding of the kinetic processes of the phase evolution as well as of the energy landscape [5]. One recent success of the LT-ABD method is the discovery of a new polymorph of magnesium difluoride (MgF_2) [6]. In addition to MgF_2, the behavior of the structure evolution of other alkaline earth fluoride compounds and their mixtures are of interest, in particular because of the role of the cationic radius.

The pair distribution function (PDF) as an effective means to characterize amorphous and nanocrystalline materials is already routinely used in neutron and X-ray diffraction. It represents the atomic density distribution oscillating around the average atomic density in the material investigated. Similarly, methods to obtain the PDF by electron diffraction, especially in combination with electron energy filtering to eliminate inelastic scattering contributions, have been widely studied [7].

In this work we applied the LT-ABD technique combined with in-situ transmission electron microscopy to investigate the phase evolution of mixtures of CaF_2/BaF_2, and of MgF_2/BaF_2 from the low-temperature amorphous phase to crystalline phases. The results are compared with pure alkaline earth fluorides. The PDF analyses are the key method to characterize the initial amorphous phase and the structural distortions in the crystalline phases. Each material was directly deposited on a carbon support cooled to -150 °C, and afterwards transferred under vacuum and cooling to the TEM. Subsequently measurements were performed during the heating process up to 1000 °C.

Differing from the pure binary fluorides (CaF_2, SrF_2, BaF_2), we observed diverse structure evolutions in the quasi-binary mixtures due to addition of a second cation. The electron diffraction results show that the crystallization of an amorphous $(Mg_{0.3}Ba_{0.7})F_2$ sample starts at 320 °C and forms first crystalline BaF_2. Further at 450 °C, the ternary compound $MgBaF_4$ crystallizes, which correlates with the thermodynamic stable phases of the phase diagram. [8]. The situation is completely different for $(Ca_{0.5}Ba_{0.5})F_2$, where the amorphous sample firstly crystallized into a solid solution phase at 370 °C (fluorite-type), which decomposes at 480 °C into the pure phase CaF_2/BaF_2. Thus, compared to earlier studies [9] we are also able to stabilizes the metastable solid solution of $(Ca_{0.5}Ba_{0.5})F_2$ by our experiments. Corresponding PDFs were calculated from the diffraction data. This study reveals the phase evolutions of the investigated materials, by which the parameter field was experimentally explored.

1. D. Fischer, M. Jansen, J Am Chem Soc, 124 (2002), p.3488.
2. Y. Liebold-Ribeiro, D. Fischer, M. Jansen, Angew Chem Int Edit, 47 (2008), p.4428.
3. D. Fischer, M. Jansen, Z Anorg Allg Chem, 636 (2010), p.1917.
4. D. Fischer, M. Jansen, Angew Chem Int Edit, 41 (2002), p.1755.
5. M. Jansen, Angew Chem Int Edit, 41 (2002), p.3747.
6. A. Bach, D. Fischer, X.K. Mu, W. Sigle, P.A. van Aken, M. Jansen, Inorg Chem, 50 (2011), p.1563.
7. D.J.H. Cockayne, Annu Rev Mater Res, 37 (2007), p.159.
8. M. Rolin, M. Clausier, Rev Int Hautes Temp, 4 (1967), p.39.
9. A. Duvel, B. Ruprecht, P. Heitjans, M. Wilkening, J Phys Chem C, 115 (2011), p.23784.
10. F. Gingl, Z Anorg Allg Chem, 623 (1997), p.705.
11. X. Mu, S. Neelamraju, W. Sigle, C.T. Koch, N. Totò, J.C. Schön, A. Bach, D. Fischer, M. Jansen, P.A.v. Aken, submitted to Journal of Applied Crystallography, (2013).
12. Financial support for this work was received from the Deutsche Forschungsgemeinschaft, Schwerpunktprogramm SPP 1415.

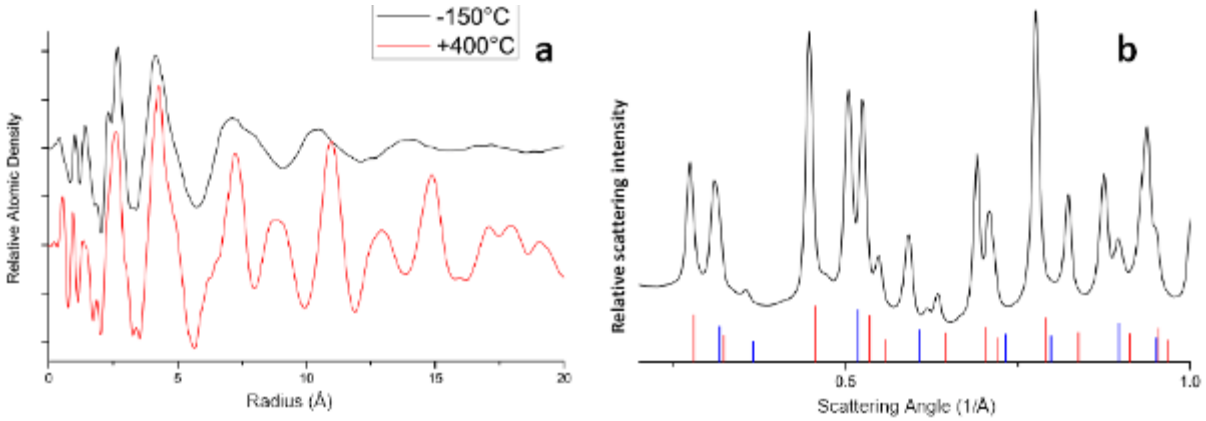

Figure. 1. Structure evolution of $(Ca_{0.5}Ba_{0.5})F_2$, (a) PDFs for the amorphous phase at -150°C (top, black) and the cubic-structure solid solution phase at +400°C (bottom, red). (b) Normalised structure factor of the phase-separated phase at +600°C (black); the sticks at the bottom represent calculated diffraction peaks (BaF_2: red, CaF_2: blue).

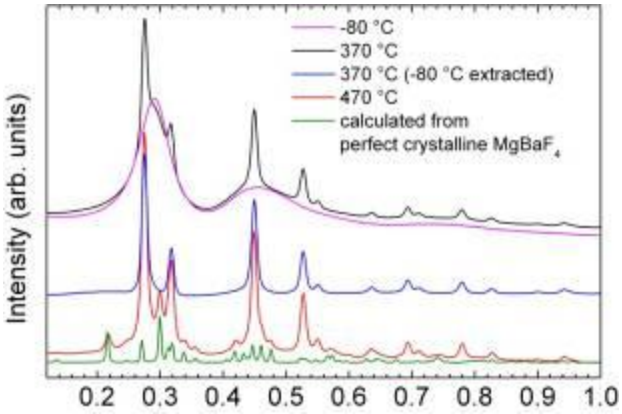

Figure 2. Experimentally measured electron diffraction patterns of the $(Mg_{0.3}Ba_{0.7})F_2$ film recorded at -80 °C (pink), 370 °C (black), and 470 °C (red) as well as the profile (blue) obtained by subtracting the -80 °C profile from the 370 °C profile and the diffraction profile calculated from database of the crystalline $MgBaF_4$ [10] (green).

	Amorphous phase	**Intermediate phase (metastable)**	**Stable phase**
$(Mg_{0.3}Ba_{0.7})F_2$	< 320 °C	320 – 450 °C amorphous + BaF_2 (fluorite-type)	> 450 °C $MgBaF_4$ + BaF_2 (fluorite-type)
$(Ca_{0.5}Ba_{0.5})F_2$	< 370 °C	370 – 480 °C solid solution $Ca_{0.5}Ba_{0.5}F_2$ (fluorite-type)	> 480 °C phase separated BaF_2 + CaF_2 (fluorite-type)
CaF_2	< 0 °C	None	> 0 °C Fluorite-type
SrF_2	< 0 °C	None	> 0 °C Fluorite-type
BaF_2	< 0 °C	None	> 0 °C Fluorite-type
MgF_2 [11]	< 185 °C	185 – 380 °C $CaCl_2$-type	> 380 °C rutile-type

Table 1. Summary of the structure evolution of the investigated alkaline earth fluorides (TEM results)

Thin Films and Coatings

MS.5.P121
Strain analysis of buried AlAs/oxide stressor layers by dark field holography

F. Kießling[1], T. Niermann[1], J.-H. Schulze[2], A. Strittmatter[2], U.W. Pohl[2], M. Lehmann[1]

[1]TU Berlin, Institut für Optik und Atomare Physik, Berlin, Germany
[2]TU Berlin, Institut für Festkörperphysik, Berlin, Germany

felix.kiessling@physik.tu-berlin.de
Keywords: transmission electron microscopy, dark field holography, strain analysis

Buried oxide stressor layers allow for site-controlled quantum dot (QD) growth, important, e.g., for single-photon emitters (SPE). The stressor is formed by partially oxidizing an AlAs layer beneath a GaAs layer. A locally varying strain field results from the length difference of Al-O and Al-As bonds which modulates the surface free energy of the GaAs (001) surface and thereby controls the QD-growth. This technique enables comparably thick buffer layers >100 nm between the buried stressor and the QD growth plane which enables growth of high quality QD for optical applications [1]. We used dark field holography (DFH) [2] in Lorentz mode to directly resolve the strain distribution within the layer structure over a large field of view. In DFH one interferes the image of the strained material on one side of the biprism with that of the unstrained bulk material on the other side. With the uniform thick specimen the strain gradient of the geometric phase can be directly obtained from the phase [3].

For specimen preparation focused ion beam (FIB, FEI Helios Nanolab 600) etching was used to fabricate an electron-transparent specimen (thickness of 100 to 200 nm) over the whole length of the mesa. Images were recorded by FEI Titan Berlin Holography Special 300 kV TEM at the TU Berlin equipped with a double biprism setup to reduce Fresnel fringes in the hologram.

The examined specimen was a rectangular mesa test structure with a buried oxidized AlAs layer [4]. Its layer sequence from substrate to surface comprises the stressor structure made of partially oxidized AlAs, a GaAs spacer layer, an InGaAs layer, and final capping layers. The stressor structure consists of a sandwich of $Al_{0.9}Ga_{0.1}As/AlAs/Al_{0.9}Ga_{0.1}As$ which was laterally oxidized from the mesa edges by water vapor [5] forming an oxide aperture (figure 1a). Upon oxidization, a volume reduction of the oxidized layer region takes place [4]. Figure 1b shows a cross section of the layer structure under bright field TEM conditions. The bright contrast region corresponds to the oxidized part of the AlAs layer. As revealed by Fourier transformation the oxidized region contained polycrystalline □-Al_2O_3 with a corresponding lattice constant of 7.93 Å (figure 1d). Interestingly, a separate oxide region was found at the tip of the oxide layer (figure 1c). This region shows less well defined contours and might have been evolved during overgrowth of the mesa structure.

Figure 2 shows the strain distributions along the growth direction (ε_{zz}) and along the in-plane direction (ε_{yy}) as obtained from DFHs of (1$\underline{1}$1) and ($\underline{1}$1$\underline{1}$). In all four subimages strain-free regions of the GaAs substrate were used for the interference in DFH which allowed for quantification of the strain components. Figure 2a reveals an area of compressive strain in growth direction directly above the opening of the oxidization front. Correspondingly, the in-plane component (figure 2b) shows tensile character in the same area. Above the oxidized layer a slight shear component (figure 2c) and a strong rotation (figure 2d) of the matrix were observed.

Our analysis reveals strong strain fields induced from the stressor layer which agrees well with calculations of the strain distribution based on continuum elastic models [4]. Most notably, local tensile surface strains of up to 1% can be created by such stressors which is important for selective QD nucleation above the mesa center.

1. A. Strittmatter et al., Applied Physics Letters 100 (2012) 093111.
2. M. Hÿtch et al., Nature 453 (2008) 1086.
3. M. Hÿtch et al., Journal of Physics: Conference Series 241 (2010) 012027.
4. A. Strittmatter et al., physica status solidi (a) 209 (2012) 2411.
5. K. D. Choquette et al., IEEE Journal of Selected Topics in Quantum Electronics 3 (1997) 916.
6. R. D. Twesten et al., Applied Physics Letters 69 (1996) 19.
7. This work is supported by the DFG Collaborative Research Centre 787 ‘Semiconductor Nanophotonics’.

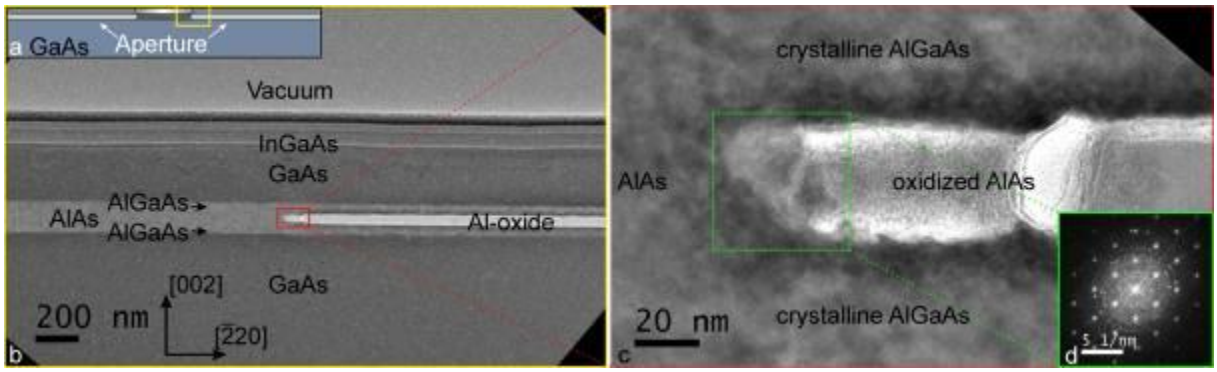

Figure 1. a) Sketch of the cross section of the mesa. b) Bright field conventional TEM overview of the middle of the mesa showing the right edge of the aperture. The oxidized layer is visible as bright contrast in the AlGaAs layer sandwich. c) Shows the oxidization front in the AlAs layer at higher magnification, d) the Fourier transformation of the marked area. The polycrystalline □-Al_2O_3 rings are visible as well as strong AlAs reflections.

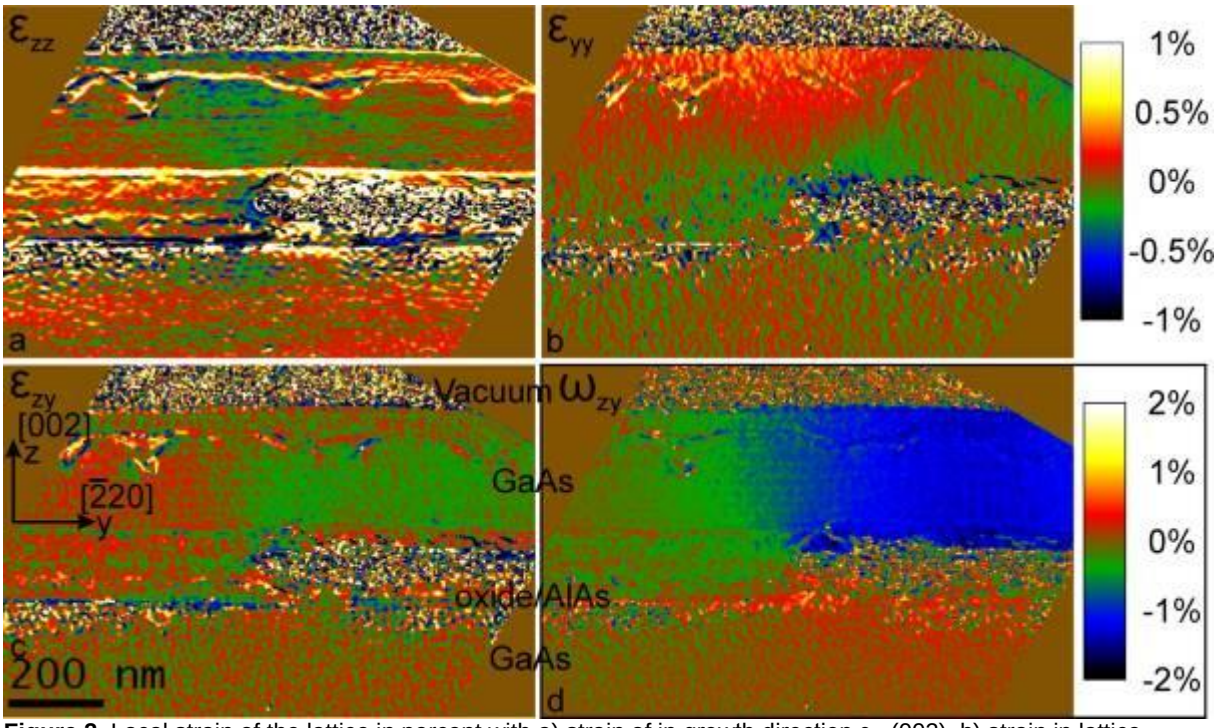

Figure 2. Local strain of the lattice in percent with a) strain of in growth direction ε_{zz} (002), b) strain in lattice direction ε_{yy} ($\underline{2}$20), c) shear component ε_{zy} and d) the rotation component ω_{zy}. The color in a), b) and c) corresponds to the upper scale bar, the lower scale bar corresponds to d).

Thin Films and Coatings

MS.5.P122
Composition dependence of morphology, electrical and mechanical properties of sputtered Cu-Mn alloy films

K. Nagy[1], F. Misják[1], P. Szommer[2], P. Lobotka[3], G. Radnóczi[1]

[1]Research Centre for Natural Sciences of HAS, Thin Film Physics, Budapest, Hungary
[2]Eötvös Loránd University, Budapest, Hungary
[3]Institute of Electrical Engineering, Bratislava, Slovakia

misjak@mfa.kfki.hu
Keywords: Cu-Mn alloy films, TEM, resistivity, hardness, structure

For large scale integrated electronic devices Cu-Mn alloy is perspective contact and interconnect material [1]. As a result of the continuous decrease of device sizes in semiconductor industry the idea of self organized processes emerged. Cu-Mn alloy has been found a promising multicomponent system for this process. For interconnect materials various requirements exist including low resistivity, excellent diffusion barrier property and acceptable adhesion strength. Therefore the investigation of structure and morphology of Cu-Mn alloy films and their effect on electrical and mechanical properties is fundamental for the development of a reproducible technology. Consequently, analysing electrical and mechanical properties vs. composition curves is a plausible way of phase analysis and film characterisation.

Cu-Mn alloy films were prepared by co-deposition in an ultra-high-vacuum DC magnetron sputtering system onto SiO_2 and SiO_x substrates at room temperature. The base pressure was $<1x10^{-5}$ Pa, while the sputtering gas was Ar at $2x10^{-1}$ Pa pressure. The thickness of the films was about 1µm. Deposition rate corresponded to 0.4 nm/s. Composition of the films was controlled by calibrating deposition rates as a function of sputtering power. Nanoindentation was carried out in a UMIS 2000 nanoindenter using a Berkovich tip. In plane sheet resistance was measured by a conventional four-point probe in the temperature range of ~80-323 K. Cross-sectional specimens were prepared using low-energy Ar ion milling preceded by mechanical grinding. Structural and chemical characterisation was carried out in Philiphs CM20 and JEOL 3010 electron microscopes.

Phase transformations appear on specific resistivity curves as changes in the derivative. Figure 1. shows the specific resistivity of Cu-Mn films as a function of composition. A single maximum exists at 80 at% Mn corresponding to 205 µΩcm. Beside pure fcc Cu and pure αMn phases three one phase regions can be distinguished by a linear behaviour. In the low Mn content zone up to ~20 at% Mn a Cu based solid solution is formed. Between ~40-70 at% Mn an amorphous disordered structure can be observed as shown on Figure 2. While form ~80 at% Mn content αMn type solid solution forms. Deviations from the linear characteristic mark the two phase zones of the system. In both zones larger crystallites of the majority phase are surrounded by an amorphous Cu-Mn phase. In the region of ~30-40 at% Mn, crystallites have Cu based fcc structure while at ~70-80 at% Mn, αMn based grains can be found.

The temperature dependence of temperature coefficient of resistivity (TCR) is shown on Figure 3 for all samples with the exception of pure Cu. Since lattice distortions significantly decrease the conductivity of Cu based solid solutions TCR curves exhibit the characteristics of weakly conducting metals. In the 40-80 at% Mn region the TCR turns negative indicating the non-metallic nature of the alloy films in this composition range. In this region a local minimum of TCR can be observed in the temperature range of 273-310 K presumably due to a magnetic transformation [2]. As Mn content increases the location of this minimum shifts to lower temperatures. Meanwhile the TCR values decrease with the composition in the amorphous range, they increase when crystallites appear at 80 at% Mn.

Nanoindentation measurement shows a good correlation with the revealed phase regions. In the nanohardness vs. composition curve (indicated on Figure 4.) a single minimum exists at 40 at% Mn, the border of the disordered region. The curve shows a monotonous increase of hardness in the Cu based fcc region and from 40 at% up to 100 at% Mn as well.

1. J. Koike et al., Journal of Applied Physics 102 (2007), p. 043527.
2. P. A. Beck, Progress in Materials Science 23 (1980), p. 1.
3. The authors acknowledge the financial support of the National Science Foundation under the grant number of OTKA-K81808. F. Misják also acknowledges the support by the János Bolyai Research Scholarship of the Hungarian Academy of Sciences. P. Lobotka acknowledges APVV grant agency under the contract APVV-0593-11.

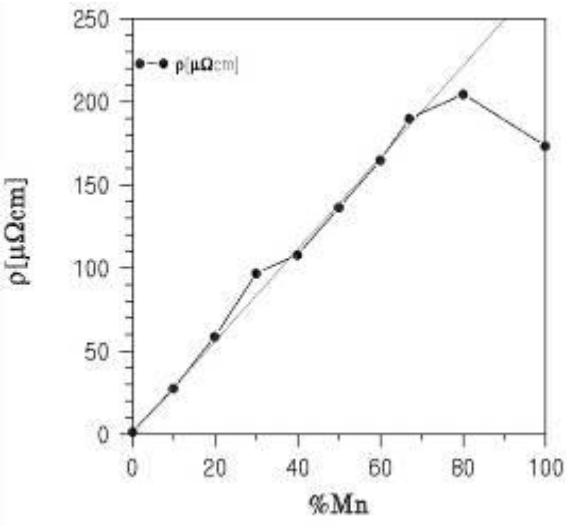

Figure 1. Specific resistivity of Cu-Mn alloy films as the function of composition at room temperature.

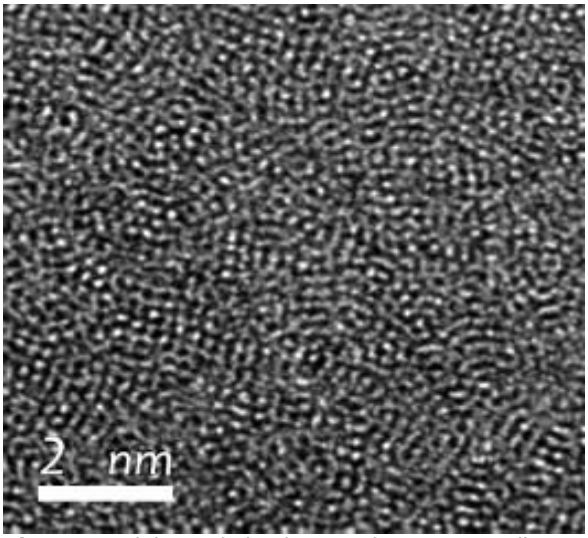

Figure. 2. High resolution image of 65 at% Mn alloy film.

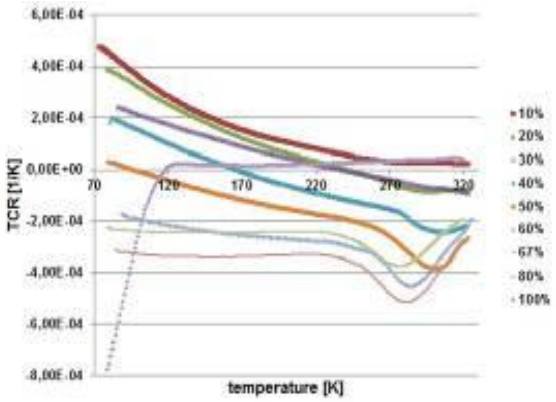

Figure 3. The temperature dependence of TCR of Cu-Mn alloy films in the temperature range of ~80-323 K.

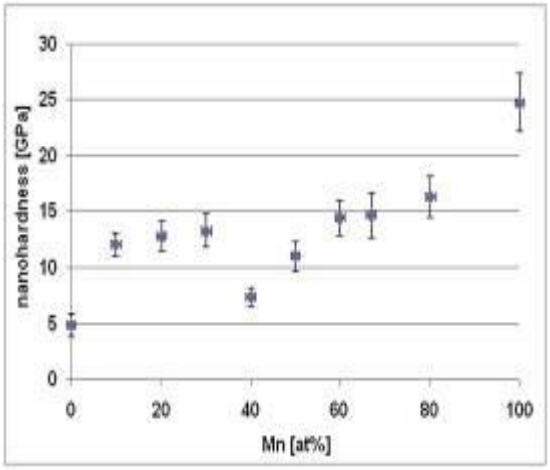

Figure 4. Nanohardness of Cu-Mn alloy films as a function of composition.

Thin Films and Coatings

MS.5.P123
TEM investigations of alumina coatings after corrosion experiments

I. Dörfel[1], M. Nofz[1], M. Feigl[2], C. Zietelmann[3]

[1]BAM Federal Institute for Materials Research and Testing, Materials Engineering, Berlin, Germany
[2]Fügetechnik Berlin-Brandenburg GmbH, Eberswalde, Germany
[3]BAM Federal Institute for Materials Research and Testing, Materials Protection and Surface Technology, Berlin, Germany

ilona.doerfel@bam.de
Keywords: alumina, coatings, corrosion,

Alumina coatings are demonstrated to protect metallic substrates against corrosion in order to increase their application area and lifetime. Thin coatings with thicknesses of around 400 nm were produced by a sol-gel-process on INCONEL 718 Ni-base superalloy substrates. For this coating system different corrosion experiments were performed to investigate the quality of the coating, the warranty of fitness for a particular corrosion type and the modification of the coating system during the tests. So, high- temperature corrosion experiments were done in different atmospheres like dry air or steam [1, 2, 3] at 800°C for 800 hours. Adhesion tests to evaluate the thermo mechanical properties of the coating-substrate system were performed by cyclic loading with a Nd:YAG Laser beam [4].

An established method to investigate corrosion processes during electro chemical influences to material is the electrical impedance spectroscopy. For this, samples were prepared by a spin-coating process and heat treated at 800°C for 30 minutes. Then they were brought in contact with a NaCl solution at room temperature for up to 180 hours. During the test time of few minutes an AC voltage was applied. As result of these investigations the polarization resistance of the samples increased with dwell time. This leads to the assumption, that material transport took place and the coating became denser by formation of an interlayer between substrate and coating or by deposition of corrosion products inside the coating. The aim of the TEM investigations was the comparison of the loaded and the unloaded samples to identify morphological and/or chemical differences between them and so to conclude on protection possibilities of alumina coatings on INCONEL 718 against corrosion in NaCl containing media. The TEM samples were prepared as cross-sections perpendicular to the coating surface by the focused ion beam method (FIB) by means of the in-situ lift out technique in a Quanta 3D instrument. To avoid surface damages, in front of the ion-beam-assisted deposition of a Pt bar an electron-beam-assisted Pt deposition was performed. The TEM investigations were carried out in an analytical STEM JEM 2200FS at 200 keV acceleration voltage. Beside images in TEM and STEM mode, HREM investigations, electron diffraction, energy filtered TEM (EFTEM) and EDX investigations were done. These results show small but visible morphological differences between the loaded and the unloaded samples. The superficial zone of the loaded sample shows a compacted region of 15 nm thickness, the superficial region of the unloaded sample does not show any compacting. Differences in the elemental distribution are also detected. So, the Cr-diffusion zone at the interface of the loaded sample shows a higher Cr content than this region of the unloaded sample. After the Cr-diffusion zone of the coating near the interface, an Al-rich region with a relatively sharp gradient is detected. In the unloaded sample the Al enrichment in this region is low and the gradient is flat. These features are demonstrated in the TEM images and EDX linescans in Figures 1 and 2. Thus, the assumption of material transport during exposure is supported. In the result the coating becomes more protective against corrosion by NaCl solution.

1. M. Dressler, M. Nofz, I. Dörfel, R. Saliwan-Neumann, Surface & Coatings Technol.202 (2008) p.6095
2. M.Dressler, M. Nofz, I. Dörfel, R. Saliwan-Neumann, Thin Solid Films 520 (2012) p.4344
3. M. Feigl, Thesis, TU Clausthal, 2011
4 M. Feigl, R. Pulz, R. Sojref, I. Dörfel, I. Feldmann, M. Sabel, B. Rehmer, M. Nofz, submitted to Mater.Sci and Engin. A
5. We kindly acknowledge the Deutsche Forschungsgemeinschaft (DFG) for financial support (NO 352/3-2 und PO 405/603) and Mrs. H. Rooch for sample preparation.

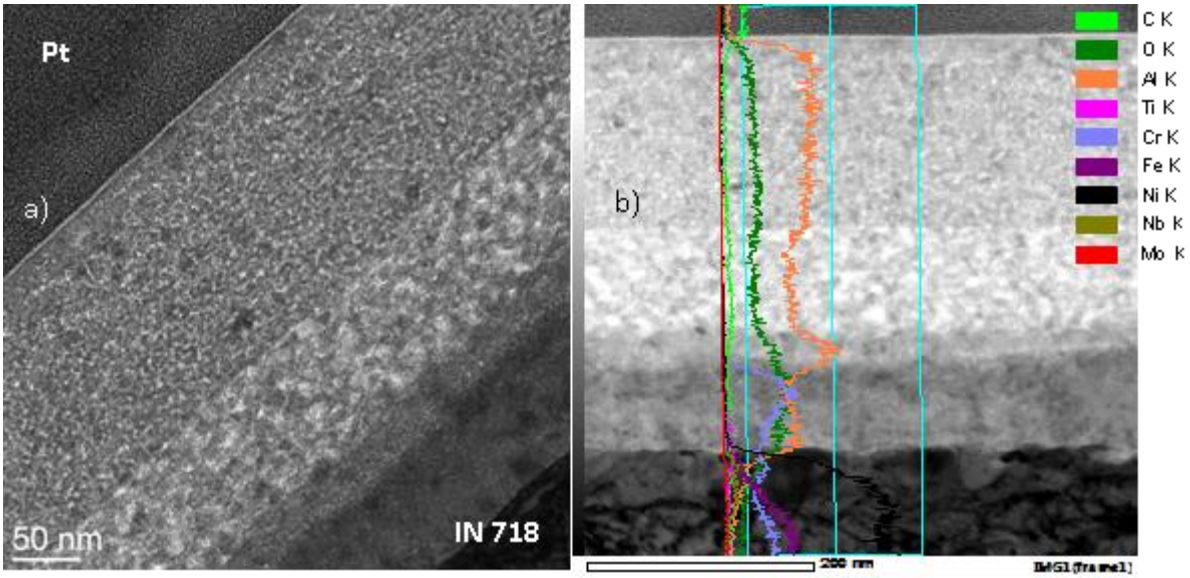

Figure 1. Loaded sample, a: TEM image, b: STEM bright field image with EDX linescan across the coating

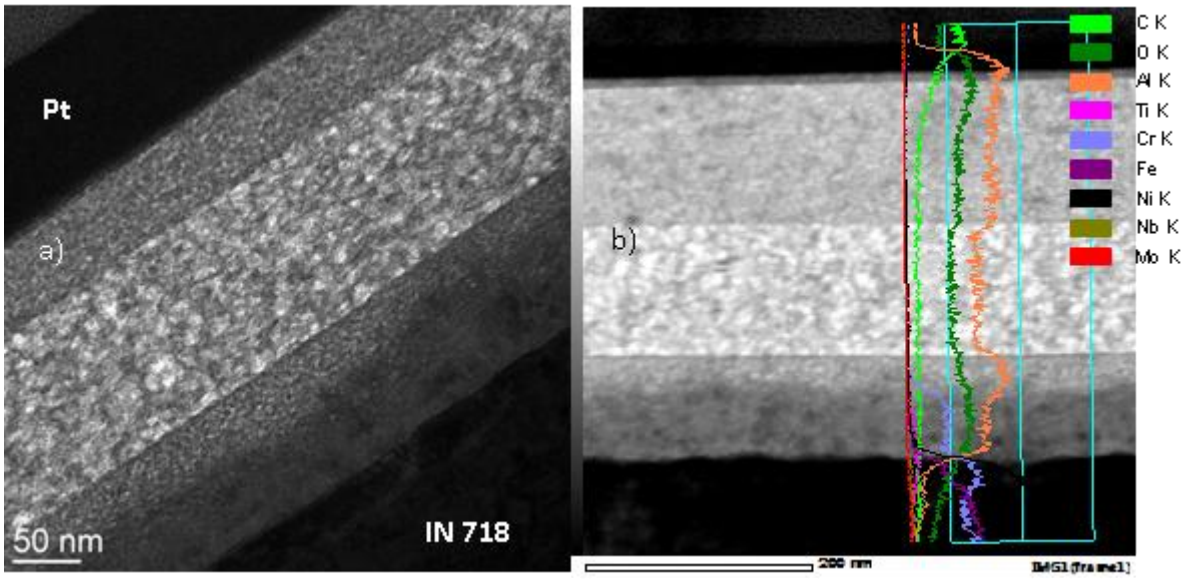

Figure 2. Unloaded sample, a: TEM image, b: STEM bright field image with EDX linescan across the coating

Thin Films and Coatings

MS.5.P124
Nucleation and growth studies in confined volumes

H. Gojzewski[1,2], F. Ghani[1], M. Regnat[1], H. Riegler[1]

[1]Max Planck Institute of Colloids and Interfaces, Department of Interfaces, Potsdam, Germany
[2]Poznan University of Technology, Institute of Physics, Poznan, Germany

hubert.gojzewski@mpikg.mpg.de
Keywords: nucleation, growth, spraying.

The aim of this project is to investigate how nucleation and growth occurs in droplets in sprays of solutions of a volatile solvent and a non-volatile solute during flight and/or or after their deposition on a solid substrate. Nucleation, precipitation and growth are processes ubiquitous in naturally and technologically occurring processes. Although they are of immense general technological relevance (metallurgy, combustion, spray drying, etc.) and fundamentally interesting, they are still not yet very well understood. There are several theoretical studies on nucleation and growth, but experimental data are rare [1]. Especially knowledge on fundamental solute aggregation processes in evaporating spray droplets, in particular regarding solute nucleation and early growth states, are virtually nonexistent.

Fundamental research on nucleation and growth with a strong inclination towards potential applications (improvement of spray drying respectively spray deposition) is the focus of this project. The research is, for instance, also motivated by potential applications in the preparation of organic photovoltaic cells by spray deposition. For the functioning of heterojunction organic photovoltaic cells, the cell structure on a nanometer scale is of utmost importance. Thus, optimized nucleation and growth processes, performed/controlled for instance via spray deposition, will lead to optimized cell structures with improved photovoltaic performance.

Solutions of different composition, respectively solute concentration, were prepared, nebulized, and the resulting spray was deposited on clean and hydrophilic SiO_2-substrates (Silicon-Wafers). The model solutes were non-volatile Metal-Phthalocyanines dissolved in conventional solvents and acids [2,3]. A high-frequency ultrasonic atomizer was used to generate sprays of micron size (1-2 µm). The deposition was performed in chamber of controlled humidity, temperature and the flight time/distance of the droplets. In the experimental setup the following experiments can be performed: 1) Complete solvent evaporation during droplet flight, 2) Partial solvent evaporation during droplet flight with solute enrichment but without reaching supersaturation before hitting the substrate, 3) Partial solvent evaporation during droplet flight with solute enrichment reaching supersaturation before hitting the substrate. The obtained deposits were investigated by atomic force microscopy (AFM). With appropriate experimental conditions we can prepare layers of individual (in some cases agglomerated) nano size aggregates (Fig. 1). The aggregate sizes, size distributions, morphologies and surface coverage can be tuned by the preparation system parameters, such as humidity, solute concentration and droplet flying distance. The different coverages, morphologies, etc. result from the different nucleation and growth scenarios.

1. R.P Sear, J. Phys.: Condens. Matter 19 (2007) 033101.
2. F. Ghani, I. Bochukov, K. Fostiropoulos, H. Riegler, Thin Solid Films 525 (2012) 177.
3. F. Ghani, J. Kristen, H. Riegler, J. Chem. Eng. Data 57 (2012) 439.
4. H.G. acknowledges the Polish Ministry of Science and Higher Education for the project "Mobilnosc Plus" No. 650/MOB/2011/0.

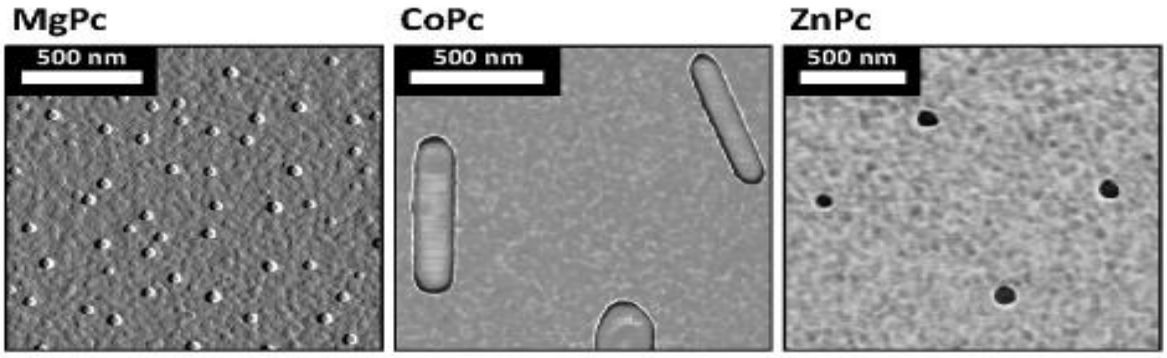

Figure 1. Atomic force microscopy images of metal phthalocyanines aggregates adsorbed on hydrophilic silicone surface as a result of spraying deposition of micro-sized droplets.

Thin Films and Coatings

MS.5.P125
The Influence of the Electron Beam on Potentiometry of GaN

J.B. Park[1], T. Niermann[1], M. Beleggia[2], M. Lehmann[1]

[1]TU Berlin, Institut für Optik und Atomare Physik, Berlin, Germany
[2]Technical University of Denmark, Center for Electron Nanoscopy, Kgs. Lyngby, Denmark

park@physik.tu-berlin.de
Keywords: GaN, p-n Junction, off-axis EH

Off-axis electron holography (EH) allows retrieving the phase modulation of the electron wave emerging from a thin sample in the transmission electron microscope. When the sample contains a p-n junction, such phase modulation is determined primarily by the potential difference at thermal equilibrium between the p- and n-regions: the built-in potential V_{pn} [1]. Here we measure the built-in potential of two GaN p-n junctions that differ in their acceptor density (Si-donor concentration: $N_d=2x10^{18}$ cm^{-3}, Mg-acceptor concentration: $N_a=6x10^{19}$ cm^{-3} in sample A and $N_a=2x10^{17}$ cm^{-3} in sample B), and we assess the influence of the electron beam on the measured V_{pn}.

The specimen is prepared by focused ion beam (FIB) at 30 kV by successive reducing the Ga-Ion current. We use the H-bar technique in two perpendicular directions for producing a square-shape needle specimen [2]. No further polishing steps such as Ar-Ion Milling are employed.

In absence of a magnetic field and under kinematic conditions the phase modulation is described by the equation $\varphi = \sigma \cdot V_{GaN} \cdot t_{total} + \sigma \cdot V_{pn} \cdot (t_{total} - t_{dead})$, where σ is an accelerating voltage dependent constant (=6.53x10^6 V^{-1}m^{-1} at 300 kV), V_{GaN} the mean inner potential of GaN, V_{pn} the built-in potential step and t_{total} the sample thickness penetrated by the electrons. The remaining phenomenological parameter, t_{dead} is the "electrically-inactive thickness", describing the effects of amorphous surface layers and the surface depletion layers created by the semiconductor-vacuum interfaces. For the amorphous layer a thickness of (19 ± 7) nm is used, which was determined from previous study. The surface depletion layers depend on the doping concentrations on either side of the junction, and on the position of surface states (if present) within the band gap; for the sake of simplicity, the surface depletion layers are neglected here.

Figure 1 shows the procedure to determine the thickness t_{total}. We measure the length w from a set of unwrapped phase images, each acquired with a different α-tilt angle. The thickness t is obtained by a fitting the measured w(α) data set with a sine function, since geometry dictates that $w=t \cdot \sin\alpha$. The thickness t_{total} can then be derived from $t_{total} = t/\cos\alpha$. For our samples we get $(t_{total} - t_{dead})$ = (416 ± 2) nm for the high p-doped sample A and $(t_{total} - t_{dead})$ = (397 ± 4) nm for the low p-doped sample B considering the amorphous layers described earlier.

The measurements yield dramatically low built-in potential values in the range of 0.22 V: about 15 times smaller than expected for GaN p-n junction specimens ($V_{pn,A}$= 3.39 V, $V_{pn,B}$= 3.24 V). Expectations are based on the bulk theory of p-n junctions with known doping concentrations [3].

In order to investigate the contribution of illumination to the built-in potential, we varied the electron dose rate while illuminating both specimens, and observed an enhancement of the measured built-in potential by reducing the electron dose rate: the built-in potential increases roughly by 18% in sample A and up to 41% in sample B (Figure 2). We interpret the results as beam-induced generation of electron-hole pairs in sufficient numbers to alter significantly the built-in potential.

Additionally, we observe a markedly different charging character on the specimen by modification of the surface properties, which might be closely connected to the variation of conductivity at the surface. In figure 3(b) the specimen is examined after FIB-preparation. The FIB-preparation produces normally a damaged amorphous surface, which can serve as a conductor. Thus, the effect of the charging with respect to the ground is minute. However, after a change of the surface properties by using the plasma cleaner to remove organic contamination, the stray fields around the specimen has clearly increased (Figure 3(c)). Removing the amorphous surface by wet-etching (KOH) leads to even stronger charging as can be seen from the stray fields (Figure 3(d)).

1. H. Lichte and M. Lehmann, Rep. Prog. Phys. 71 (2008), p. 1.
2. A. Lenk, Dissertation, Dresden (2008).
3. S.M. Sze in “Physics of Semiconductor Devices”, 2., John Wiley & Sons (1981), p.75.
4. This work is carried out as the DFG collaborative research center SFB787 semiconductor nanophotonics

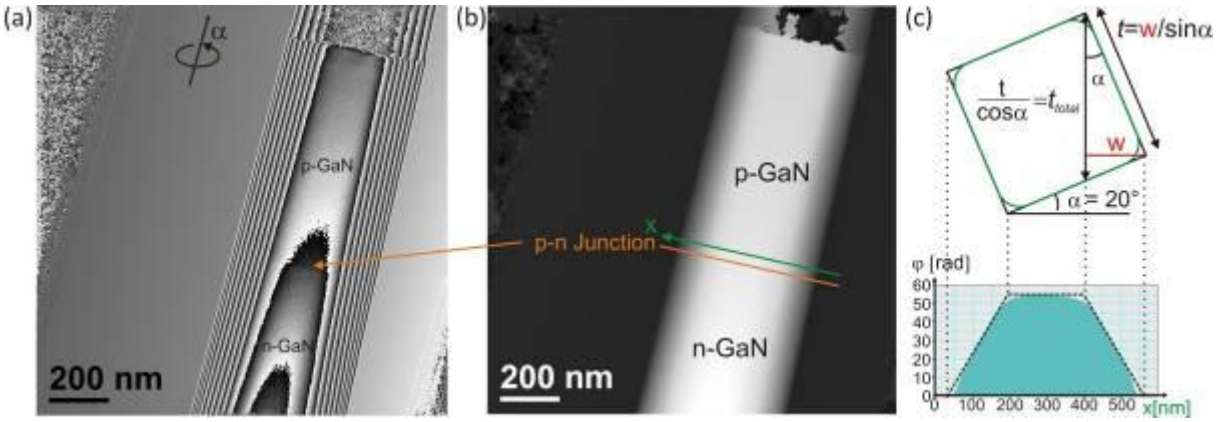

Figure 1. (a) Reconstructed phase of the FIB-prepared square-shape needle at α-tilt angle 20°. The phase variation at the p-n junction is clear visible. (b) Unwrapped phase. The gradually slope is observable at each edge due to the increase of the thickness. (c) Schematic diagram of the expected geometry of the needle with the corresponding profile of the phase along x (green arrow) is depicted.

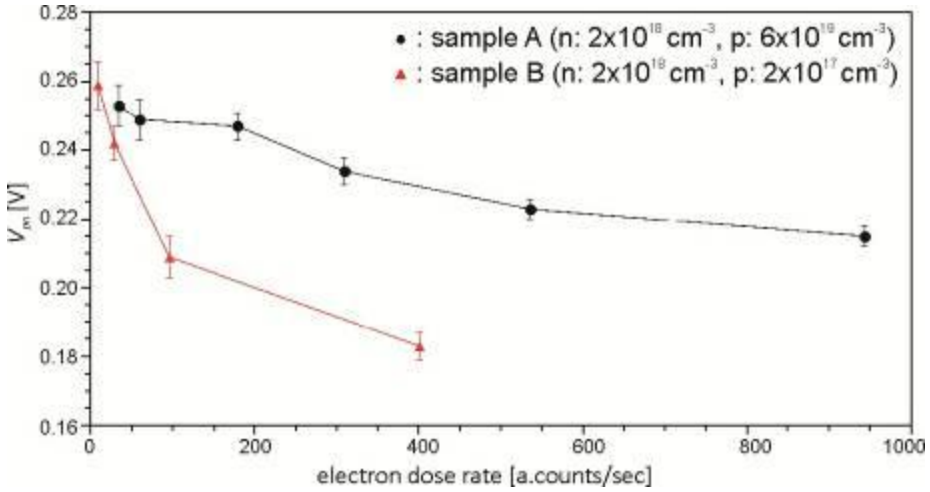

Figure 2. The built-in potential V_{pn} over the electron dose rate is showed from two different GaN p-n junctions, in which the doping concentration of p-GaN is changed.

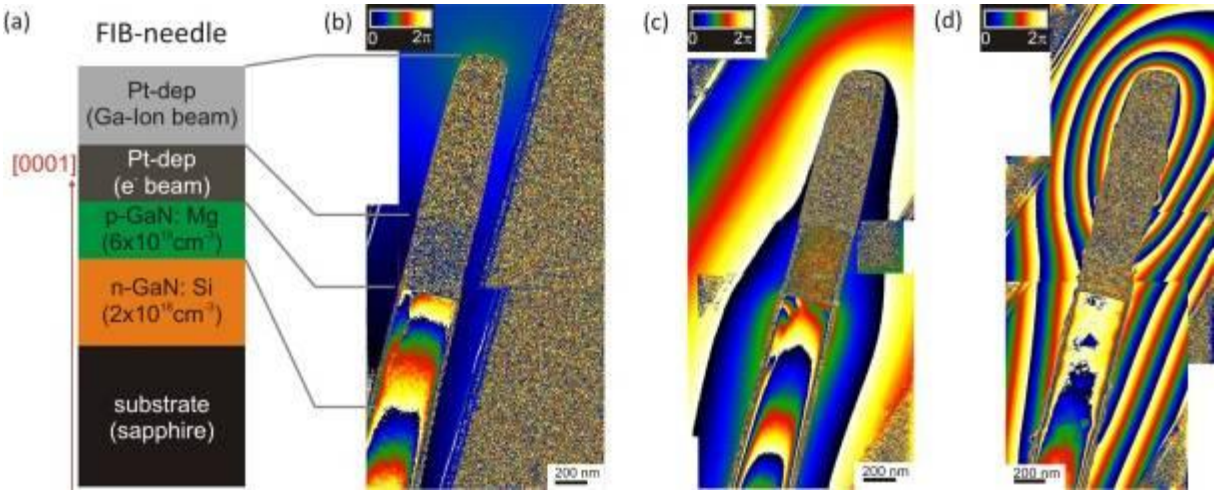

Figure 3. (a) The specimen structure. Each map of the reconstructed phases consists of several reconstructed holograms: (b) The reconstructed phase map of the needle after FIB-preparation. (c) After 5 min plasma cleaning treatment. (d) After 1 min KOH wet-etching.

Thin Films and Coatings

MS.5.P126
TEM study of PZT crystallization behaviour in multilayer heterostructures

O. Zhigalina[1], D. Khmelenin[1], K. Vorotilov[2], A. Sigov[2], I. Lebo[2]

[1] Shubnikov Institute of Crystallography, Electron microscopy, Leninskiy prospekt 59, 119333 Moscow, Russia, Russian Federation
[2]Moscow State Technical University of Radioengineering, Electronics and Automation, Vernadskiy prospekt 78, 119454 Moscow, Russia, Russian Federation

zhigal@ns.crys.ras.ru
Keywords: thin films, crystallization, laser annealing, grains, texture

Thin PZT ($PbZr_{0.53}Ti_{0.47}O_3$) films are one of the prominent materials for ferroelectric random access memory (FRAM), MEMS and other integrated ferroelectric devices [1, 2]. Chemical solution deposition (including sol-gel techniques) is widely used for formation of multicomponent thin film oxides due to good stoichiometric control and a relatively low temperature of oxide phase formation [3, 4]. The main strategy of the annealing procedure during the formation of ferroelectric film is to achieve an optimal crystalline structure at the minimum temperature of the heat treatment. Laser annealing has a number of advantages and can effectively influence the crystallization of multilayer heterostructures based on ferroelectric films [5,6].

In this work we have investigated and tried to compare PZT crystallization processes after traditional isothermal heat threatments at different temperatures and laser annealing.

Films 100—150 nm thick were deposited on Si— $Si0_2$(300 nm)—TiO_2(10 nm)—Pt(100 nm) wafers 100 mm in diameter by the chemical solution deposition method. After deposition of five layers the films were annealed at 550, 600, 650, 700, 750 and 900°C for 20 min. The PZT film thickness was about 160 nm. Laser annealing was performed using a KrF-excimer laser emitting light at the wavelength of λ=248nm. The pulse energies and the number of pulses within one crystallization process were varied over a range of 0.18-0.35 J/cm^2 and 100-500 pulses.

The study of film structure, phase and element composition was performed by TEM (FEI Tecnai G^2 30ST, equipped by HAADF STEM detector and EDX spectrometer, at accelerating voltage of 300 kV) and X-Ray diffraction.

Perovskite grain nucleation in PZT films occurs at about 550 °C: rounded (111) grains grow on the platinum surface with the same (111) orientation in this case. The height of perovskite grains comprises a half of the films thickness. Disordered perovskite grains (to the order of smaller size) and pyrochlore grains (2 ...15 nm) are formed in the bulk of the film as well. At annealing temperature of 600 °C the perovskite grains grow through the whole films thickness, the amount of pyrochlore phase is significantly reduced and practically disappears when the annealing temperature increases to 700 °C. At the same time the amount of (100) oriented perovskite grains increases and dominates over (111) oriented ones after annealing at 900 °C. The reason is the activation of diffusion processes in the layers of the heterostructure that leads in particular to the formation of TiO_2 inclusions on the Pt surface.

In the case of laser annealing it has been found that, in contrast to isothermal annealing, where nucleation on the platinum layer dominates, crystallization and the growth of spherical perovskite crystals occur in the film bulk. The perovskite phase crystals' size increases from 10 to 120 nm with increasing laser beam energy (Figure 1a-d).

1. N. Setter, D. Damjanovic, L. Eng, et al., J. Applied Phys. 100 (2006), p. 051606.
2. *C.J. Brinker and G.W. Scherer, Sol-gel science: the physics and chemistry of sol-gel processing, Academic Press, N.Y, 1990.*
3. *K.A. Vorotilov, M.I. Yanovskaya, E.P. Turevskaya, and A.S. Sigov*, *J. Sol-Gel Science and Technology. 16 (1999), p. 109.*
4. O.M. Zhigalina, P.V. Burmistrova, A.L. Vasiliev, V.V. Roddatis, A.S. Sigov, and K.A. Vorotilov, Ferroelectrics. 286 (2003), p. 311.
5. S.S.N Bharadwaja, F. Griggio, J. Kulik and S. Trolier-McKinstry Applied Physics Letters 99 (2011) p. 042903
6. D.N. Khmelenin, O.M. Zhigalina, K.A. Vorotilov, I.G. Lebo Physics of solid state 54 (2012) p. 999
7. This work is was performed in part using the equiopment of the Shared Facility Center of Shubnikov Institute of Crystallography, Russian acadevy of scienses

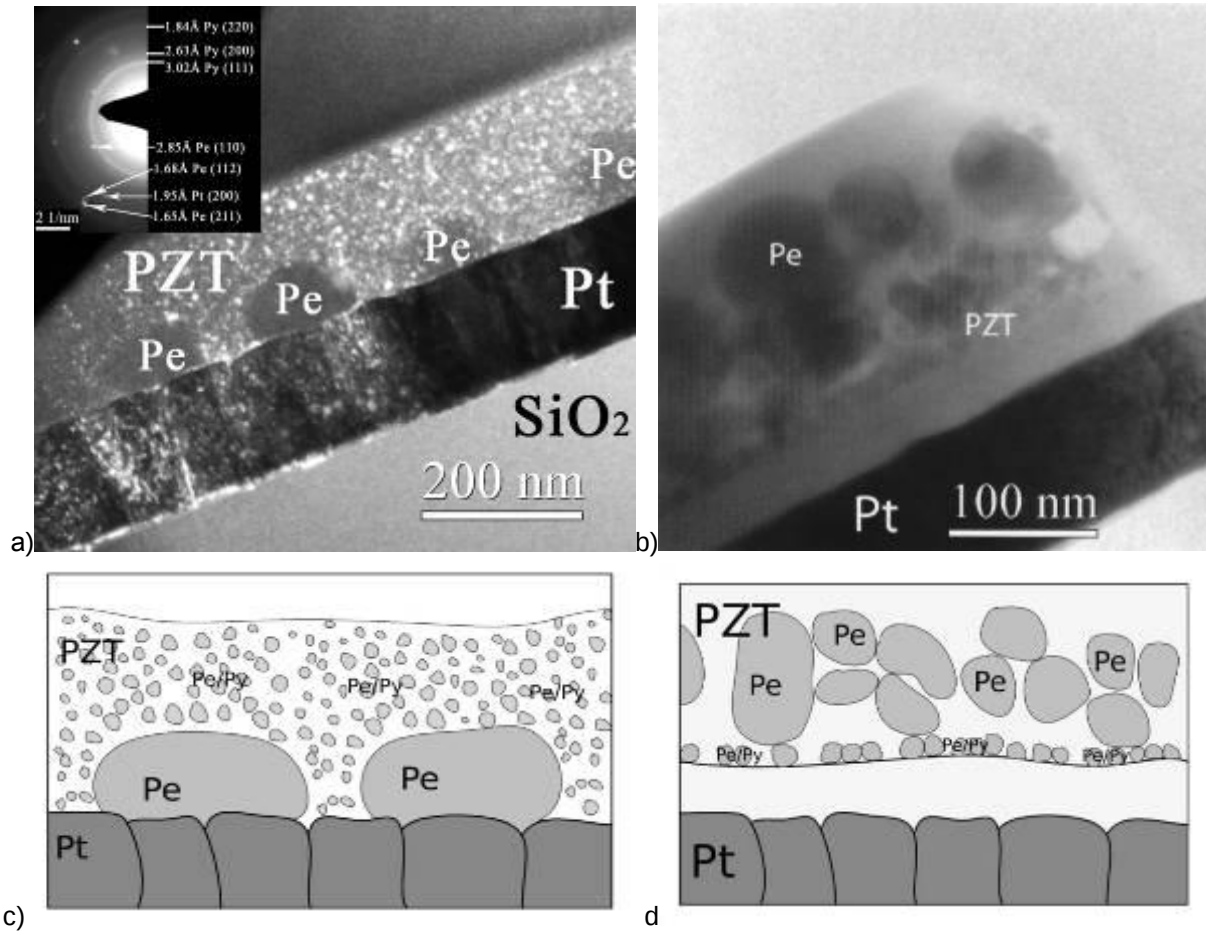

Figure 1. Cross sectional view of PZT/Pt/TiO_2/SiO_2/Si heterostructures:
a) dark field image and corresponding SAED pattern (crystallization at 550 °C),
b) bright field image (laser annealing with the energy preposition of 0.35 J/cm^2)
c), d) corresponding schemes of TEM images a), b).

Thin Films and Coatings

MS.5.P127
Scanning Tunneling Microscopy of Cu, Ag and Au Nanoformations on the Monocrystalline Surfaces

V. Karbivskyy[1], L. Karbovskaya[1], V. Vishnyak[1]

[1]G.V. Kurdumov Institute NAS of Ukraine, Spectroscopy of Solid State Surface, Kiev, Ukraine

karb@imp.kiev.ua
Keywords: microscopy, noble metals, nanostructures

Using high-vacuum high-resolution scanning tunneling microscopy we have investigated the processes of hexagonal-pyramidal Cu, Ag and Au structures formation after thermal sputtering of metals onto monocrystalline Si (1 1 1) and Si (1 1 0) surfaces (Fig. 1-3). It was found that under homogeneity of melt of deposited metals and vacuum not lower than 10^{-8} Pa there are formed self-ordered hexagonal-pyramidal nanostrucutres consisting of monoatomic layer planes each shifted by a distance of about 3 nm relatively to the growth start of the previous plane (Fig. 1-3). The mechanism of formation of hexagonal-pyramidal Cu, Ag and Au nanostructures is determined with a character of electron density behaviour at the edge of each monoatomic layer. Extreme atoms of planes have higher energy state and thereby growth of each next monoatomic plane starts not from the edge but at the distance of about 3 nm from it what is caused with relaxation of inhomogeneity of electron density of states at this distance and determines pyramidal shape of formations. During thermal deposition of silver (Fig. 2), after the formation of 3-4 monolayers, observe the formation of grain boundaries, which with further deposition begin to combine. The result of "two-dimensional" grain boundaries combine are the topological features in the form of wells (depth of ~ 0.4 Å). Annealing by heating to 300 °C, recreates intact structure 7x7.

By other metals deposition modes there was observed formation of conglomerates of nanoparticles with subsequent transformation of them into ellipsoidal particles and further nanocrystal formation.

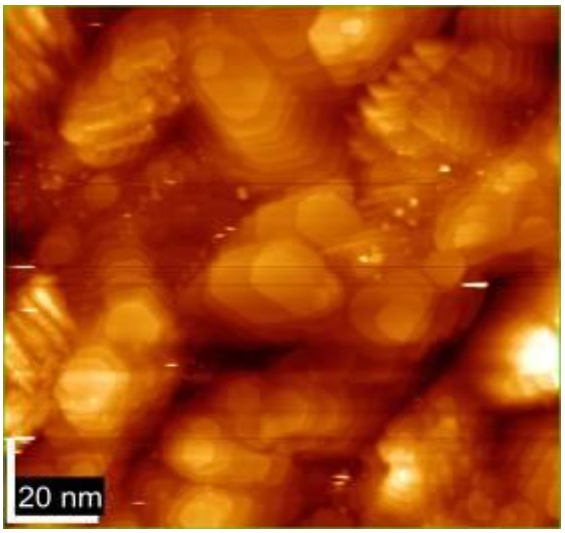

Figure 1. Au nanoformation on the Si (111) surface.

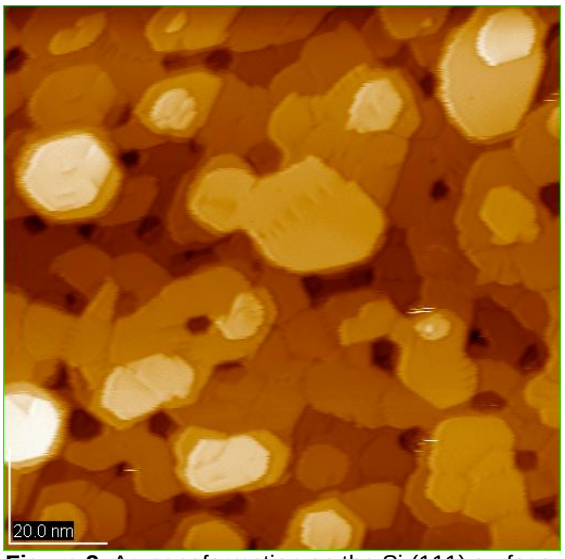

Figure 2. Ag nanoformation on the Si (111) surface.

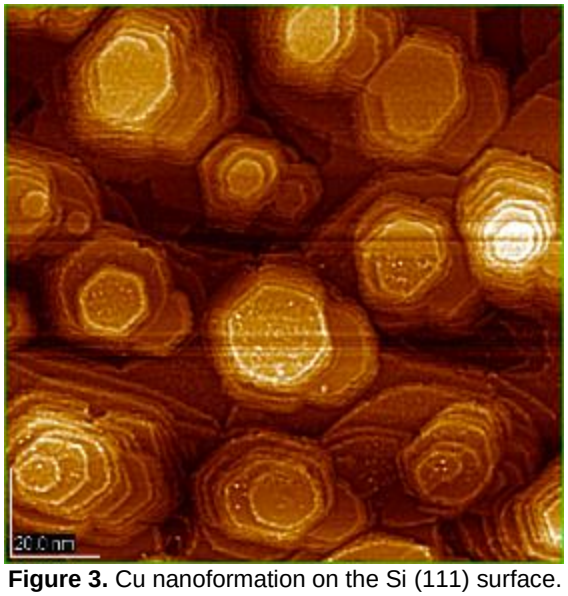

Figure 3. Cu nanoformation on the Si (111) surface.

Thin Films and Coatings

MS.5.P128
Spontaneous barrier layer formation in SiO_2/Cu-Mn alloy film interface

F. Misják[1], J. Yamasaki[2], Y. Yamamoto[2], J. Lábár[1], N. Tanaka[2], G. Radnóczi[1]

[1]Research Centre for Natural Sciences, Hungarian Academy of Sciences, Budapest, Hungary
[2]EcoTopia Science Institute, Nagoya University, Nagoya, Japan

misjak.fanni@ttk.mta.hu
Keywords: barrier layer, Cu-Mn films, amorphous alloy, HREM, EELS

The Cu-Mn system is a prospective contact or interconnect material for memory or IC applications. In the current technology for advanced semiconductor devices, copper is the main material of transistor interconnects. The high diffusion rates for elemental copper in silicon and silicon oxides have required the development of diffusion barriers. As the semiconductor industry moves to smaller sizes, for future technologies there will be a need to reduce the barrier width below 4 nm while retaining its diffusion integrity and adhesion properties. One possible way for reaching this dimension can be the utilization of self-organised processes simultaneously meeting preconditions like conformal coating, small thickness of the barrier layer and small lateral sizes. The idea of using self-forming barrier layers involves the deposition of a copper alloy directly onto the dielectric layers. Subsequent annealing (400 ^{o}C for 60 min as published in [1]) can lead to the segregation of the alloying metal to the copper/dielectric interface, where it chemically reacts with the dielectric forming a thin barrier layer. The most promising results in the literature relate to copper-manganese (Cu-Mn) as contact and self-forming barrier material. In this aspect, a detailed investigation of the Cu-Mn system is aimed at the background knowledge for technological developments. The basic intention of this work is the detailed understanding of the structure of 40-70 at% Mn composition region in the Cu-Mn thin film system and the possible reaction between the film and silicon oxide substrate layer.

Cu-Mn alloy films were co-deposited by DC magnetron sputtering from Cu and Mn targets onto SiO_x and SiO_2 substrate at room temperature. The background pressure of $5x10^{-8}$ mbar and sputtering gas (Ar) pressure of $2x10^{-3}$ mbar were used. The thickness of the films was around 500 nm, and a deposition rate of 0.4 nm/s was applied. Cross-sectional samples for HRTEM were prepared by Ar ion milling using low angle sputtering. HREM investigation was carried out in Philips CM20 and in C_s corrected JEOL electron microscopes equipped with EELS possibilities.

A typical structure characteristic of the investigated composition region (40-70 at% Mn) is shown in Figure 1. The HREM image shows disordered structure, neither the lattice of Cu nor that of αMn could be detected. Apparently the film possesses an amorphous nature. For establishing short range atomic arrangements radial distribution function of the sample has been calculated [2]. It shows good agreement with αMn atomic arrangements (Figure 2.) where all peaks and relative intensities are similar in the two structures. The phenomenon, that the atomic density of the amorphous alloy is somewhat lower than that of αMn may be due to the fact that Cu atoms are larger than Mn atoms manifested also in larger coordination distances for the alloy structure.

Investigating the interface of the layers and the silicon oxide substrate we could find that at the interface a ~4 nm thick layer formed (Figure 3.). Its appearance is very similar to the one observed after annealing at elevated temperature in [1]. EELS measurements (Figure 4.) of elemental distributions across the barrier layer show that this layer is composed of a mixed oxide of Si and Mn. The distribution of Cu suggests that the thin mixed oxide layer stops migration of Cu atoms in the direction of the dielectric substrate, thereby acts as a barrier layer. The temperature history of the film shown in Figure 3 is its unavoidable treatment at 150^{o}C for 60 min during the sample preparation process. This (treatment) is much lower than the annealing described in the literature and applied for forming of the barrier layer [1].

As a conclusion we can state that the structure of the high Mn content alloy films (40-70 at% Mn) is amorphous and has a short range order similar to □Mn. The very low temperature or spontaneous formation of the barrier layer in the SiO_2/Cu-Mn alloy interface suggests a possible way of the utilization of this phenomenon in IC applications. Self-forming and spontaneous barrier layers may be prepared by depositing first a few nm thick amorphous layer of high Mn content which ensures barrier formation, then continuing deposition with a low Mn content crystalline film [3] serving as interconnect material.

1. J. Koike et al. Journal of Applied Physics 102 (2007) p. 043527.
2. J. L. Lábár Microscopy and Microanalysis 14 (2008) p. 287-295.
3. Zs. Czigány, F. Misják, O. Geszti, G. Radnóczi, Acta Materialia 60 (2012) p.7226-7231.
4. The authors acknowledge the financial support of the National Science Foundation under the grant number of OTKA-K81808. F. Misják also acknowledges the support by the János Bolyai Research Scholarship of the Hungarian Academy of Sciences and the Japan Society for the Promotion of Science.

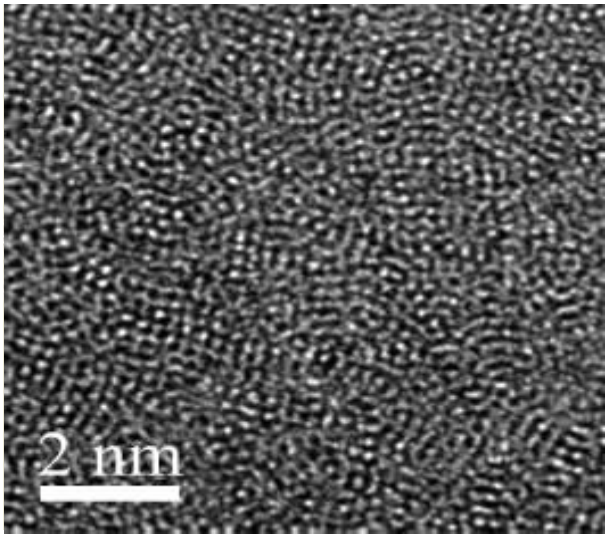

Figure 1. High resolution image of 65 at% Mn alloy film

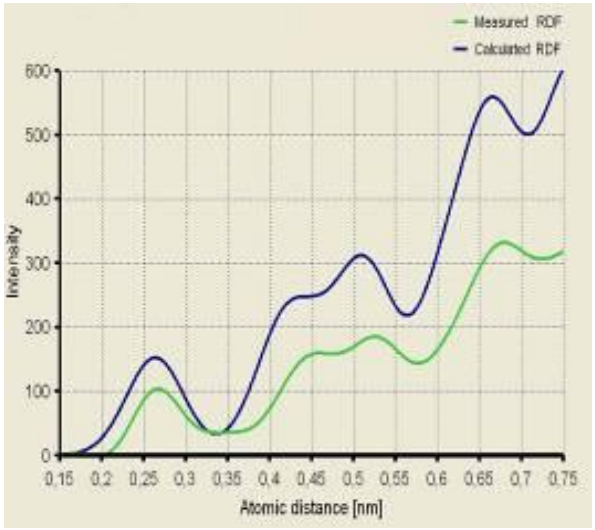

Figure 2. Radial distribution functions of Mn (blue) and that of the 65 at% Mn content Cu-Mn alloy film (green).

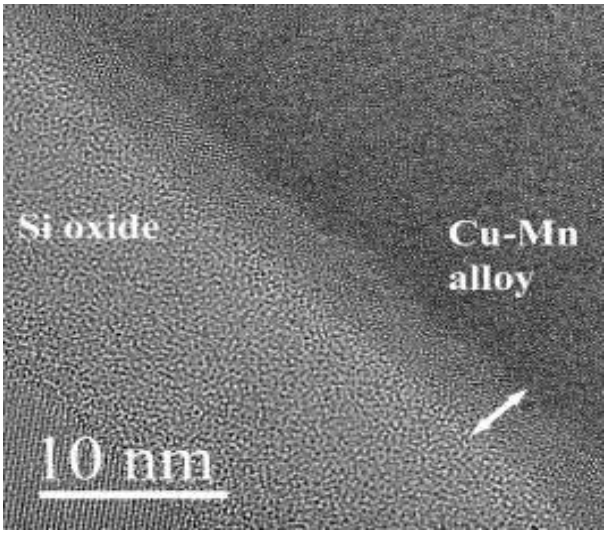

Figure 3. HREM image of a typical interaction layer (arrow) between the Cu-Mn alloy film and the Si oxide

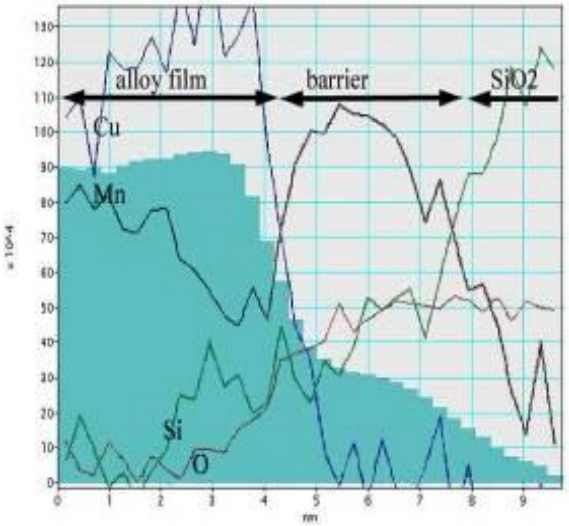

Figure 4. EELS elemental distribution profiles across the barrier layer (40 at% Mn sample)

Thin Films and Coatings

MS.5.P129
Controlling the orientation-relationship between Ni (111) and sapphire (0001)

Z. Fogarassy[1], G. Dobrik[2], L.K. Varga[3], L. Biró[2], J. Lábár[1]

[1]MTA TTK MFA, Thin Film Physics Department, Budapest, Hungary
[2]MTA TTK MFA, Nanostructures Department, Budapest, Hungary
[3]Institute for Solid State Physics and Optics, Wigner Research Center for Physics, Budapest, Hungary

labar.janos@mta.ttk.hu
Keywords: Ni, Sapphire, double-positioning

Epitaxial growth of Ni (111) on sapphire (0001) was studied during DC magnetron sputtering in ultrahigh vacuum. Commercial sapphire (0001) single crystal was used as a substrate. During growth the substrate temperature was 300-750^{o}C, and the growth velocity was 0.2 nm/s or 0.5 nm/s for the different samples. In some of case bias was also applied. The orientation relationship was investigated with transmission electron microscopy (TEM).

Our aim was to produce a good quality single crystal nickel (sc-Ni) thin layer, which can serve as an inexpensive substrate for graphene deposition. Earlier investigations reported only that the Ni (111) planes were parallel to the Sapphire (0001) and so to the substrate surface [1] and termed it epitaxial growth, although in-plane orientation was not studied.

In the present investigation two kinds of epitaxial orientations were detected in the same sample. In both cases the Ni (111) lattice planes were parallel with the Sapphire (0001) lattice planes, but the two different orientations are rotated to each other with 30 degrees around the axis perpendicular to the surface. The sapphire [10-10] is parallel either to the nickel [110] or to the [211]. In the first case the lattice misfit is -9.29 %, which means nickel needs to be compressed to fit to the sapphire and below this orientation will be called the “compressed” orientation. In the second case the misfit is +4.68 %, it will be called the “dilated” orientation. Figure 1.a shows a selected area diffraction pattern from a cross-sectional TEM sample, where both epitaxial orientations are present. The surface normal of the sapphire is marked by the arrows on the diffraction pictures. The sapphire diffraction is shown in Figure 1.b. Figure 1.c shows only the reflections that belong to the “compressed” orientation. Twin boundaries were found in both types of orientations. These twin boundaries are perpendicular or parallel to the surface as it can be seen in Figure 2.

In the sample grown at 550^{o}C temperature with 0.2 nm/s deposition rate, both kinds of orientations were present, but with larger flux (0.5 nm/s) only the “compressed” orientation formed. Using bias, it was possible to produce a Ni layer containing only the “dilated” orientation. In the sample with higher temperature (750^{o}C) and small flux, dominantly the “compressed” orientation appeared.

Earlier calculations on non-relaxed structures showed that the “compressed” orientation matches better to the sapphire surface than the “dilated” orientation, although the “dilated” orientation can also exist energetically [2]. However, the “compressed” orientation has a larger misfit than the other one and it stores a larger elastic energy. Our present experimental observations can be explained with the above reasoning. When the nucleus size is small then better adhesion will dominate and “compressed” orientation forms. When the nucleus size is larger, the orientation with the smaller misfit will be energetically more favorable and growth of the “diluted” orientation is preferred.

By controlling the initial nucleation density and the size of nuclei with temperature and deposition rate, it was possible to foster the formation of the pre-selected in-plane orientation of the nickel (epitaxial to the single crystal sapphire (0001) substrate) and to get single crystalline nickel with a single in-plane orientation only. Details are published separately [3].

1. Carlo M. Orofeo, Hiroki Ago, Baoshan Hu, and Masaharu Tsuji; Synthesis of Large Area, Homogeneous, Single Layer Graphene Films by Annealing Amorphous Carbon on Co and Ni; Nano Res. 4 (2011) 531–540.
2. W. Zhang, J.R. Smith, A.G. Evans; Acta Materialia 50 (2002) 3803–3816.
3. Zs. Fogarassy, G. Dobrik, L.K. Varga, L.P. Biró, J.L Lábár: Growth of Ni layers on single crystal sapphire substrates. Thin Solid Films, submitted for publication.

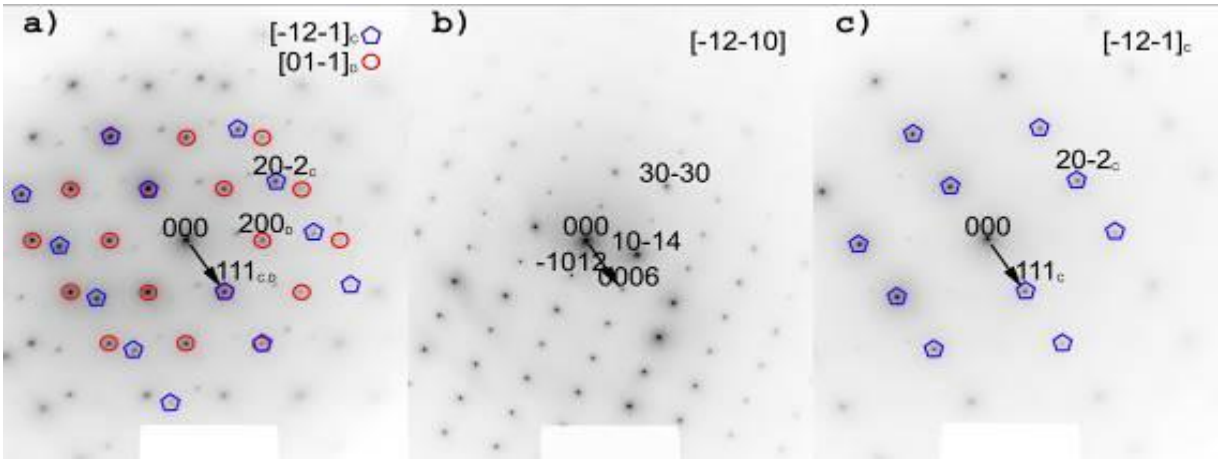

Figure 1. Selected area diffractions taken on a cross-section TEM sample. The direction of the sapphire surface normal is marked by the arrows. Diffraction a) shows a grain boundary area where both the “compressed” and “dilated” orientations are present. The reflections from the “dilated” orientation are marked by the circles, while those from the “compressed” orientations are marked with pentagons. Diffraction b) shows the reflections of the sapphire. Diffraction c) shows the reflections of the “compressed” orientation. The {111} planes coincide for both the “compressed” and the “dilated” orientations and are parallel to the (006) plane of sapphire.

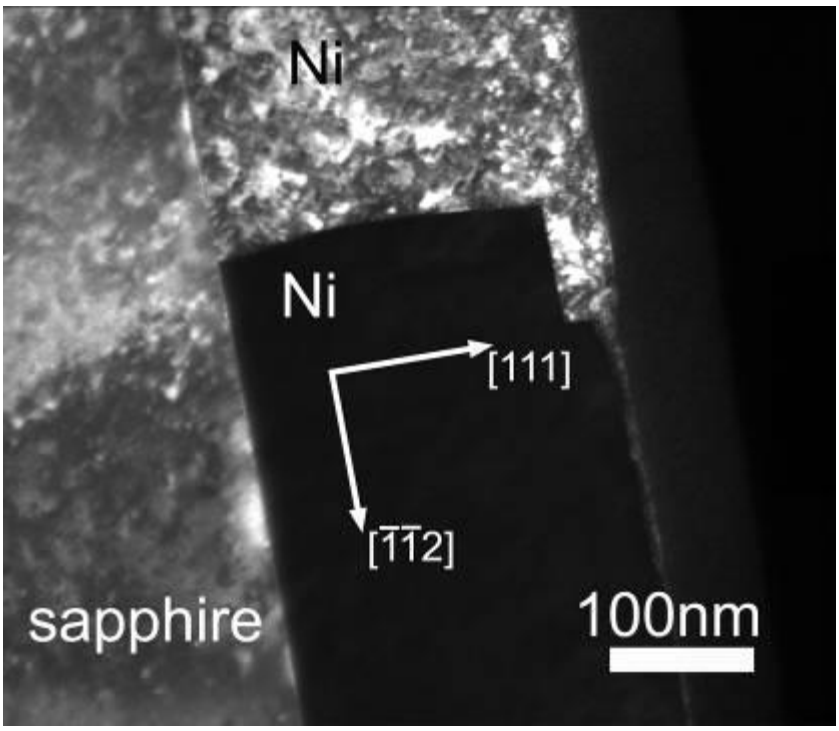

Figure 2. Dark field image taken on a cross-section TEM sample. The light (top) and dark (bottom) areas within the Ni layer show the twinned crystallites and the directions of their faceted grain boundary. It can be seen that the grain boundary is formed from facets of {111} and {211} planes, characteristic of the coherent and incoherent twins in fcc materials.

Thin Films and Coatings

MS.5.P130
Influence of persistent resistance changes on structure and chemical composition of metal-$Pr_{1-x}Ca_xMnO_3$-metal thin film heterostructures observed by TEM techniques

T. Kramer[1], O. Janik[1], J. Norpoth[1], M. Scherff[1], J. Maier[1], J. Hoffman[1], C. Jooß[1]

[1]University of Goettingen, Institute for Materials Physics, Goettingen, Germany

tkramer@ump.gwdg.de
Keywords: Resistive Switching, Manganites, Heterostructures

Resistive switching phenomena are observed in many metal-oxide-metal thin film heterostructures. Application of an external voltage of the order of one volt between the facing metallic top and bottom electrode can change the initial virgin state resistance (VS) of the heterostructure to a high resistance (HRS) or a low resistance state (LRS). The induced resistance change is persistent, i.e. the HRS or LRS remains after removing the applied bias. In order to microscopically explain the resistance changes, various models have been proposed, e.g., Mott transitions, Schottky barrier effects, trapping controlled space charge limited currents, or electro-chemical effects related to migration of oxygen cation vacancies.

We will show investigations of structural and chemical responses on electrical stimulation corresponding to different resistance states. For this purpose we use a FEI Titan 80-300 ETEM which has just been successfully installed. It is equipped with an imaging aberration corrector and a high-resolution Gatan Imaging Filter (GIF), allowing experiments with sub-1Å resolution. The monochromator enables spectroscopy with 0.2 eV energy resolution. This allows high resolution TEM, selected area diffraction or scanning TEM images for structural analysis as well as electron energy loss spectrometry (EELS) and energy filtered transmission electron microscopy (EFTEM).

We have selected the colossal resistance manganite $Pr_{1-x}Ca_xMnO_3$ (PCMO) sandwiched by precious metal electrodes (Pt, Au, Ag) or niobium doped $SrTiO_3$ (Nb:STO) as a model system for resistive switching. From the viewpoint of bulk properties, PCMO belongs to the class of perovskites, where the interplay of electron-electron, magnetic exchange and electron-phonon correlations gives rise to the formation of a rich variety of different structural and electronic phases.

Thin Films and Coatings

MS.5.P131
TEM investigation of droplets in TiAlN based coatings

I. Letofsky-Papst[1,2], M. Tkadletz[3], C. Mitterer[4], C. Michotte[5], W. Grogger[1,2]

[1]Graz University of Technology, Institute for Electron Microscopy and Nanoanalysis, Graz, Austria
[2]Graz Centre for Electron Microscopy, Graz, Austria
[3]Materials Center Leoben Forschung GmbH, Leoben, Austria
[4]Montanuniversität, Department of Physical Metallurgy and Materials Testing, Leoben, Austria
[5]CERATIZIT Luxembourg S.ár.l., Mamer, Luxembourg

ilse.papst@felmi-zfe.at
Keywords: EFTEM, TiAlN based coatings, droplets

Wear resistant coatings are widely used to improve the performance and lifetime of cutting tools. Often, these coatings are grown by cathodic arc evaporation, where a target is evaporated by a cathodic arc, thus creating a vapor phase which condenses together with reactive process gases on the substrates to be coated. An inherent drawback of this process is the formation of droplets, which are emitted from the target and incorporated into the coating, representing defects. These droplets affect the cutting performance as they act as diffusion paths, negatively influencing the oxidation resistance, as nuclei for cracks, and they increase the surface roughness of the coating.

The aim of the present work was to determine structure and chemical composition of droplets within a ~3 µm thick TiAlN based coating and a ~300 nm thick TiN base layer deposited onto cemented carbide substrates. Possible crack and oxidation triggering effects of these droplets have been determined for coatings loaded by dry sliding ball-on-disk tests performed at room temperature and at 700°C in ambient air. Coatings were investigated by transmission electron microscopy (TEM), where cross-sectional samples have been prepared within the wear tracks formed. Lamellas for TEM were prepared by means of an Orsay Physics Cobra Z-05 focused ion beam instrument (FIB). The TEM investigations were conducted using a monochromated TF20 TEM, Schottky cathode, operated at 200 kV, equipped for energy-dispersive X-ray spectroscopy (EDX) with a SiLi detector and an ultrathin window. For electron energy-loss spectroscopy (EELS) and energy-filtering (EFTEM), the TEM is equipped with a high-resolution Gatan imaging filter (GIF). All EELS measurements were recorded in scanning mode of the TEM using a probe diameter of about 1 nm.

Figure 1(a) shows a bright-field image of a part of a droplet in the room temperature sample. The EFTEM O K jump ratio image in (b) indicates oxygen-enriched areas in the under-dense regions surrounding the droplet, which originated from shadowing effects during film growth. EFTEM reveals further that the droplet is rich in titanium, within regions which contain more nitrogen (c) and less titanium (d) than the surroundings. In the RGB image, an oxidized area is seen (top right in (e)), which indicates oxidized wear debris formed in the dry sliding test. All EFTEM results have been confirmed by means of EDX and EELS (not shown). An SAED pattern (f) was taken from the nitrogen-rich region marked in the bright-field image (a), which could be clearly interpreted as the □-titanium phase (ICSD 43416) in [001] orientation.

The bright-field image for the 700°C sample is shown in Figure 2(a). In contrast to Figure 1, there is more oxygen detected in the surroundings of the droplet (see (b) and (e)). Titanium and nitrogen are homogenously distributed (c, d). The SAED pattern acquired from the marked region in the bright-field image (a) agrees well with $Ti_4N_{2.33}$ (ICSD 40951) in orientation.

In summary, the performed investigations revealed droplets consisting of a metallic Ti-rich core including nitrided areas originating from the nitrogen within the reactive deposition atmosphere. Cavities between droplets and genuine coating material were identified as oxidation sites and are more pronounced for the 700°C dry sliding test. Further, material accumulations were identified as worn coating material, which has also been oxidized within the tribological contact.

1 .R.L. Boxman and S. Goldsmith, Surface and Coatings Technology, 52, (1992), 39.
2. A. Hörling, L. Hulton, M. Odén, J. Sjolén and L. Karlsson, J. Vac. Sci. Technol., A 20(5), (2002), 1815.
3. P. Harlin, U.Bexell and M. Olsson, Surface and Coatings Technology, 203, (2009), 1748.

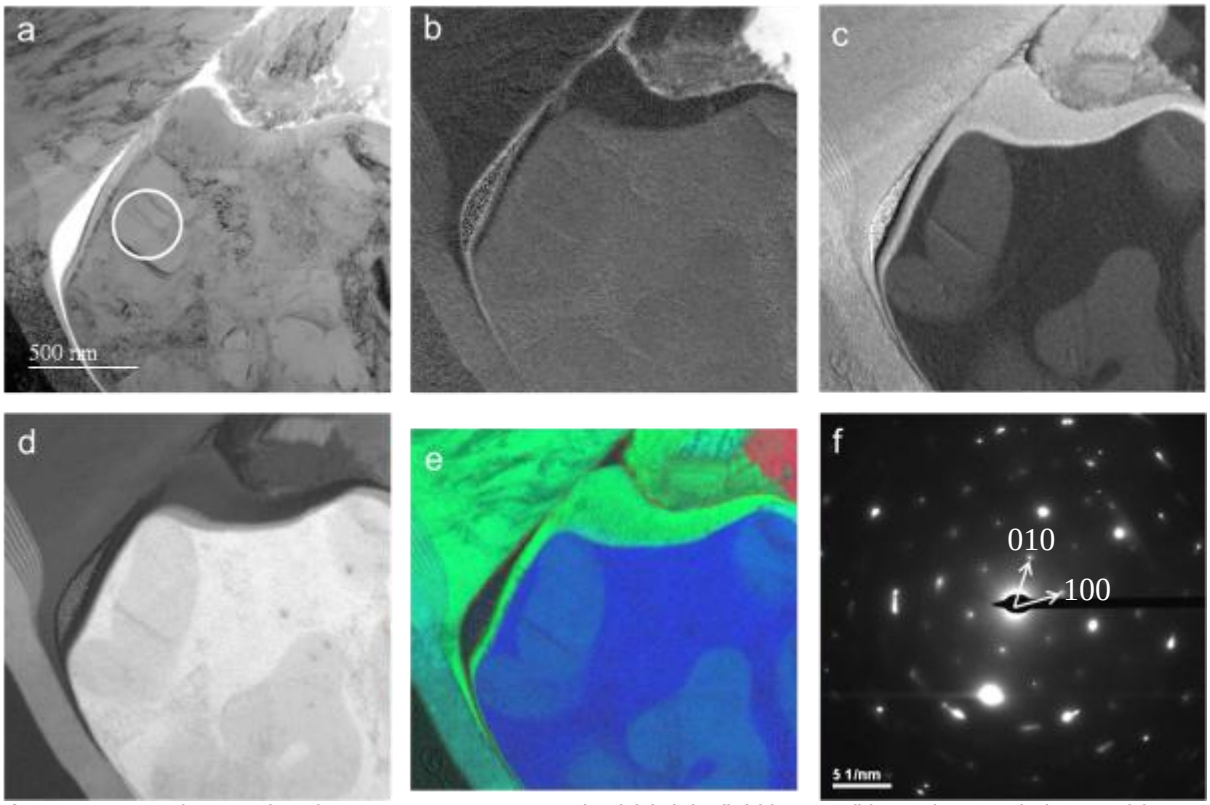

Figure 1. TEM micrographs of room temperature sample. (a) bright-field image, (b) O K jump ratio image, (c) N K jump ratio image, (d) Ti $L_{2,3}$ jump ratio image, (e) RGB image: red=O, green=N, blue=Ti, (f) SAED of marked region in (a).

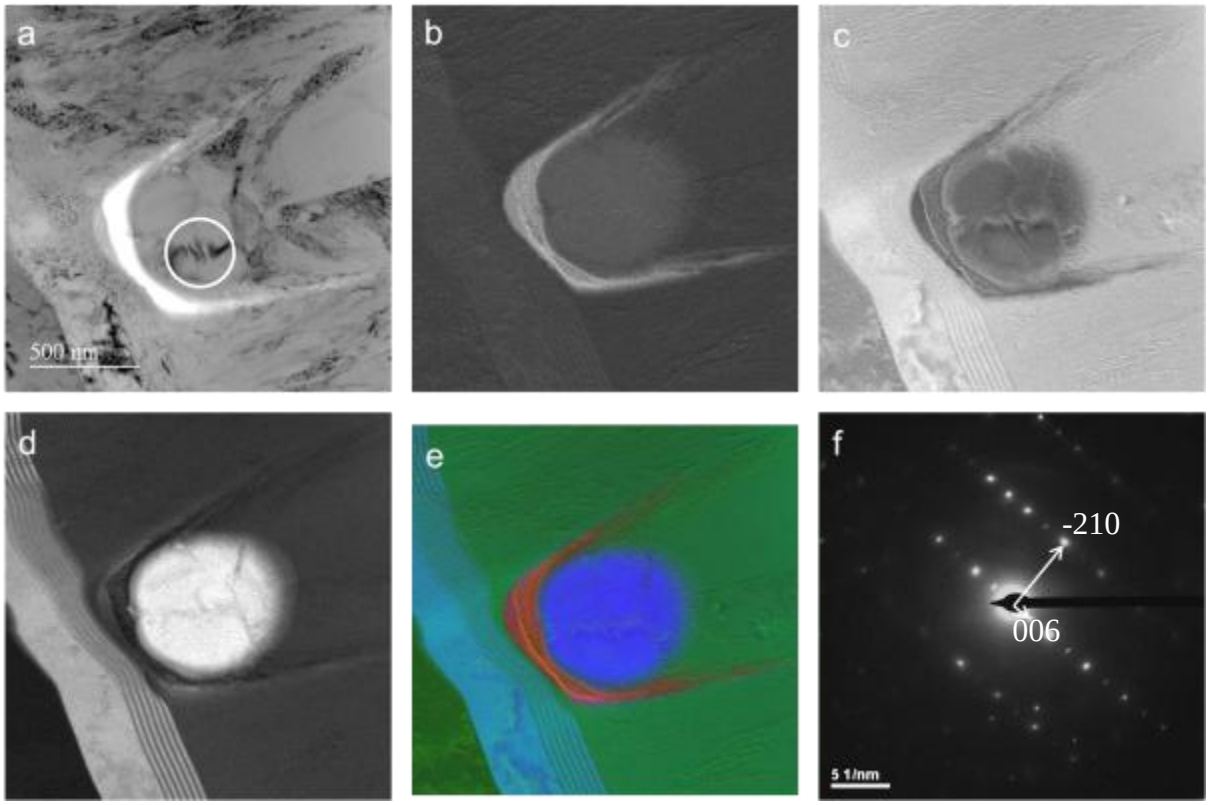

Figure 2. TEM micrographs of 700°C sample. (a) bright-field image, (b) O K jump ratio image, (c) N K jump ratio image, (d) Ti $L_{2,3}$ jump ratio image, (e) RGB image: red=O, green=N, blue=Ti, (f) SAED of marked region in (a)

Thin Films and Coatings

MS.5.P132
HRTEM studies of ultrathin NbN and NbTiN films for superconducting photodetectors

A. Łaszcz[1], M. Guziewicz[1], W. Słysz[1], A. Czerwinski[1], J. Ratajczak[1], J. Kątcki[1]

[1]Institute of Electron Technology, Warsaw, Poland

laszcz@ite.waw.pl
Keywords: thin films, superconductive photodetectors, HRTEM

Superconducting single-photon detectors (SSPD) are novel optoelectronic devices that are currently subject of intensive research and development. The SSPDs are typically meander-type nanostructures patterned in an ultrathin superconducting NbN or NbTiN films [1].

NbN phase was the first choice material for manufacturing of SSPDs due to its stable superconducting properties at relatively high temperatures and already well established technological procedures for the ultrathin film growth and processing [2-3]. However the NbTiN phase presents advantages over the NbN phase because an addition of Ti increases metallic electrical conduction properties of NbTiN and titanium is a good nitrogen getter as well [4].

Ultrathin NbN and NbTiN films presented in this work were deposited on Al_2O_3 (0001) substrates by a high-temperature reactive magnetron sputtering method. The NbN film was deposited from Nb target in N_2/Ar gas mixture at temperature of 850°C, while the NbTiN film was deposited by co-sputtering of Nb and Ti targets. The thicknesses of the deposited films were 4 nm for NbN and 5 nm for NbTiN. Both films were annealed in Ar at 1000°C using a rapid thermal annealing (RTA) process to improve their superconducting properties.

The obtained ultrathin films were characterized by high-resolution transmission electron microscopy (HRTEM) in the JEOL JEM-2100 microscope. TEM specimens were prepared by the focusing ion beam (FIB) cross-section method in the FEI Helios NanoLab system. The DigitalMicrograph (DM) software was applied for the measurements of atomic distances using the HRTEM images of as-deposited and annealed NbN and NbTiN films.

HRTEM images (Figure 1) showed in all cases that the films fabricated on the Al_2O_3 substrate have excellent epitaxial crystalline quality. To disclosure of lattice strains distribution in the NbN and NbTiN films the atomic distances were measured across and along the cubic NbN and NbTiN films according to the rules shown in Figure 2. Results of the atomic distance measurements are presented in Table 1.

Distances in as-deposited or annealed NbN films are higher than distances in as-deposited or annealed NbTiN films. For as-deposited NbN and NbTiN samples the distances measured across the films are higher than measured along the films (i.e. in the direction along the ultrathin film-substrate interface). For the annealed NbN film the distances measured across and along the film are practically the same, in contrast to the annealed NbTiN film where the distances measured across the film are lower than those measured along the film. Observed differences between the distances for NbN and NbTiN films can be related to different lattice strains formed during deposition and their relaxations due to annealing.

HRTEM studies showed that ultrathin NbN and NbTiN films due to heteroepitaxial growth on Al_2O_3 (0001) substrate have a great compatibility and integration of these films with optoelectronic circuitry give excellent potential for their application in SSPD devices.

1. C.M. Natarajan, M.G. Tanner and R.H. Hadfield, IOP Supercond. Sci. Technol. 25 (2012) p. 063001.
2. W. Słysz, M. Guziewicz, M. Borysiewicz, J.Z. Domagała, I. Pasternak, K. Hejduk, W. Rzodkiewicz, J. Ratajczak, J. Bar, M. Wegrzecki, P. Grabiec, R. Grodecki, I. Wegrzecka and R. Sobolewski, Acta Physica Polonica A 120 (2011), p. 200.
3. M. Guziewicz, W. Slysz, M. Borysiewicz, R. Kruszka, Z. Sidor, M. Juchniewicz, K. Golaszewska, J.Z. Domagala, W. Rzodkiewicz, J. Ratajczak, J. Bar, M. Węgrzecki and R. Sobolewski, Acta Physica Polonica A 120 (2011), p. 76.
4. A.M. Valente-Feliciano, H.L. Phillips, C.E. Reece and J.K. Spradlin, Proceedings of SRF2011 Chicago, THPO074 (2011), p.920.
5. This work was supported by the European Union within the European Regional Development Fund, through the Innovative Economy Grant (POIG.01.01.02-00-108/09, "MIME")

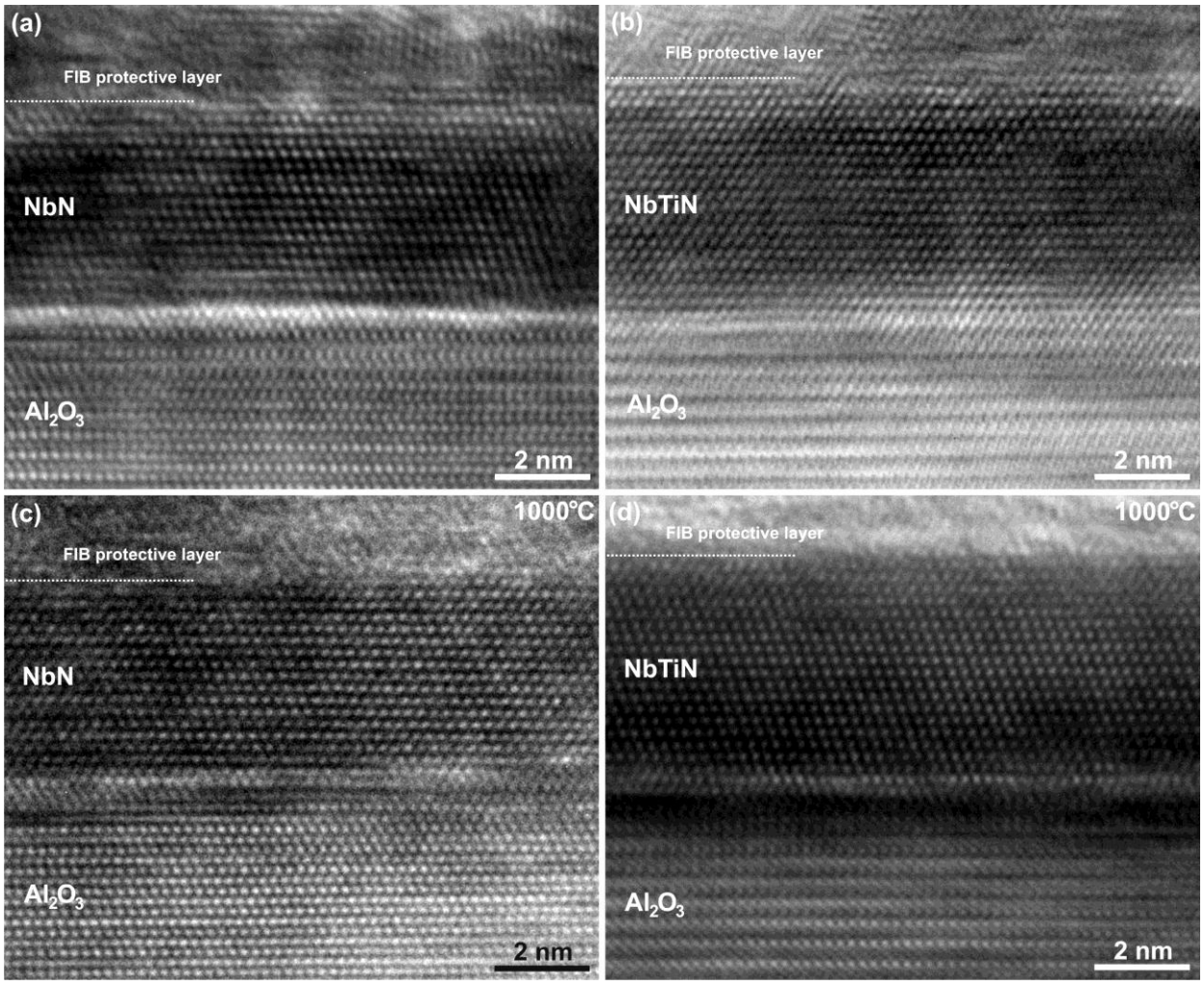

Figure 1. HRTEM images of: (a) NbN and (b) NbTiN as-deposited ultrathin films, and: (c) NbN and (d) NbTiN ultrathin films annealed at 1000°C. In all cases cubic NbN or NbTiN films were shown with (110) plane parallel to the plane of the figure.

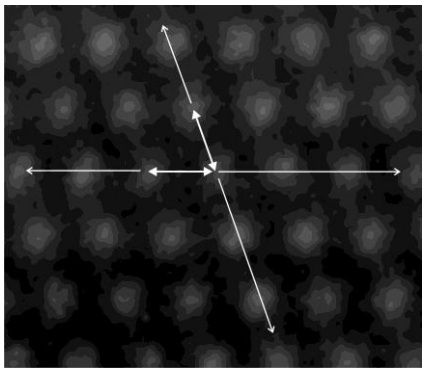

Figure 2. HRTEM image of annealed NbTiN film (high magnification fragment of Fig. 1d) with drawings related to two directions of atomic distances measurements: along (horizontal arrow) and across (inclined arrow) of the film.

sample →	as-deposited		annealed	
distance ↓	NbN	NbTiN	NbN	NbTiN
average distance measured across the film	0.2729 nm	0.2659 nm	0.2697 nm	0.2551 nm
average distance measured along the film	0.2648 nm	0.2612 nm	0.2695 nm	0.2640 nm

Table 1. Values of atomic distances for as-deposited and annealed NbN and NbTiN films. There were two directions of atomic distance measurements: across and along the films, according to the drawing shown in Figure 2. The average measured distance were calculated as a mean value of 10 distances measured across the film in 20 different places, and as a mean value of 30 distances measured along the film in 6 different places.

Thin Films and Coatings

MS.5.P133
Ni_xGe_y films synthetized by LPCVD using Ge_2Me_6 and Et_3GeH precursors

M. Klementova[1], F. Novotný[2], R. Fajgar[3], V. Dřínek[3]

[1]Institute of Physics of AS CR, v.v.i., Departement of Structure Analysis, Prague, Czech Republic
[2]Czech Technical University in Prague, Faculty of Nuclear Sciences and Physical Engineering, Prague, Czech Republic
[3]Institute of Chemical Process Fundamentals of the AS CR, v. v. i., Prague, Czech Republic

klemari@fzu.cz

Ni_xGe_y alloys are among the candidates for Ohmic`s contacts in electronic devices since they have a low processing temperature (below 250 °C) and possess low resistivity [1,2]. Samples were prepared by Low Pressure Chemical Vapor Deposition (LPCVD) using hexamethyldigermane Ge_2Me_6 and triethylgermane Et_3GeH precursors over Ni substrate at temperature of 500 °C. Samples were characterized by SEM/EDS, XRD, TEM/EDS, and Raman spectroscopy.

Ni_xGe_y films were prepared using two different germanium containing precursors Ge_2Me_6 and Et_3GeH, and their mixture. Morphology of the resulting deposits is porous and consisting of Ge nanowires when both pure Et_3GeH and pure Ge_2Me_6 are used. Using a mixture Ge_2Me_6/Et_3GeH yields Ni_xGe_y crystals several microns in size (Figure 1) besides the porous deposit and Ge nanowires. In the direction from the input of the quartz reactor to its output, the deposits on nickel substrates changed gradually from porous to well-developed Ni_xGe_y crystals; then islands of Ge nanowires merging into a continuous cover.

According to XRD, the Ni_xGe_y crystals belong either to orthorhombic phase $Ni_{0.67}Ge_{0.33}$ (ICSD-53743) or hexagonal phase $Ni_{0.64}Ge_{0.36}$ (ICSD-87906). In addition, a modulated structure of $Ni_{19}Ge_{12}$ ($Ni_{0.61}Ge_{0.39}$) corresponding to (ICSD-53749) was observed by TEM (Figure 2). All these phases are very close in composition and it is likely that their formation is influenced by the diffusivity of Ni from the substrate.

1. J. H. Park, P. Kapur, K. C. Saraswat, H. Peng, Appl. Phys. Lett. 91 (2007), p. 143107-1.
2. X. V. Li, M. K. Husain, M. Kiziriglou, C. H. de Groot, Microelectron. Eng. 86 (2009), p. 1599.
3. The study was supported by the Grant Agency of the Czech Republic under project No. 13-25757S.

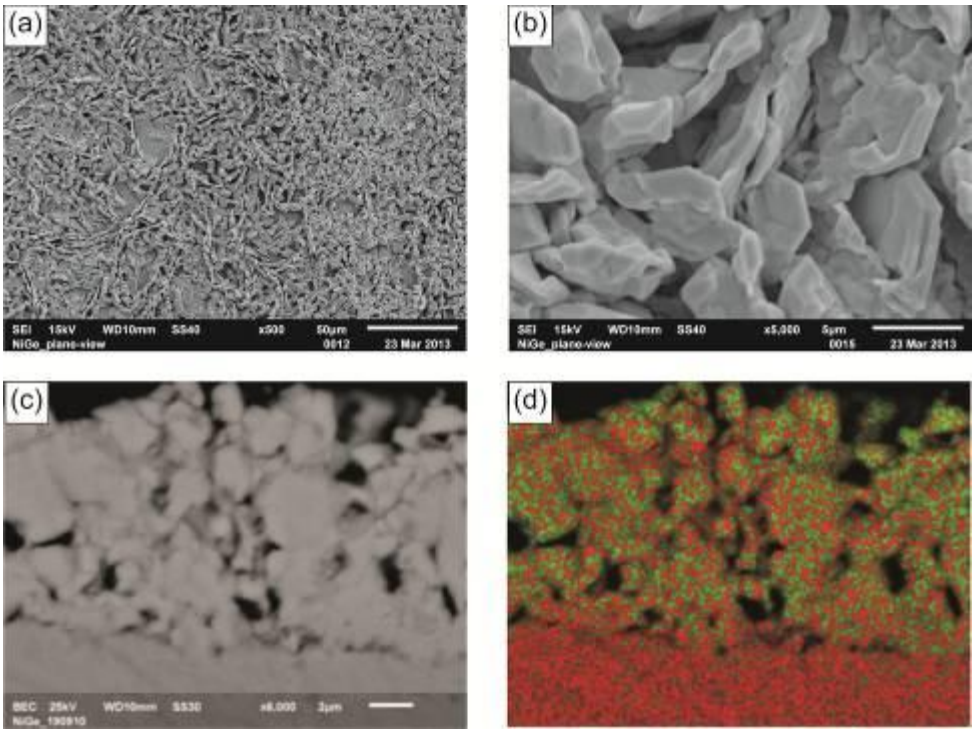

Figure 1. SEM observations of the deposit: (a), (b) plane view, (c) cross-section in BSE, (d) EDS mapping of the area shown in (c) - red - nickel, green - germanium.

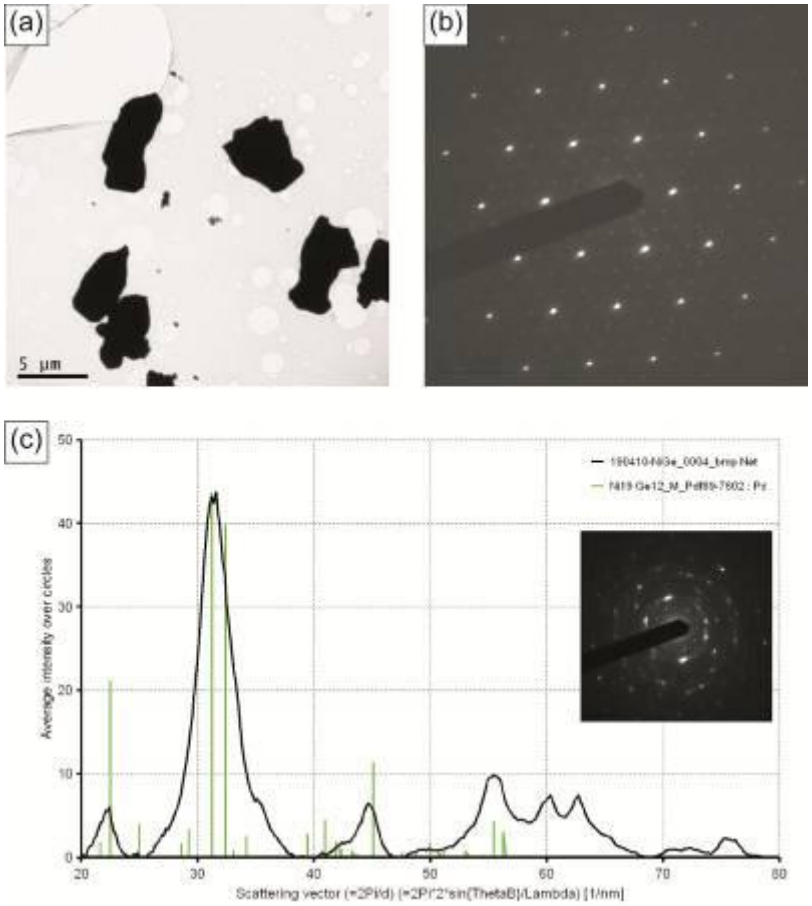

Figure 2. TEM observations of the deposit: (a) low-mag image, (b) SAED corresponding to $Ni_{19}Ge_{12}$ single crystal, (c) SAED corresponding to powder $Ni_{19}Ge_{12}$.

Thin Films and Coatings

MS.5.P134
Transmission electron microscopy characterization of the growth and properties of Al-Si-Cu-Fe approximant thin films

M. Garbrecht[1], S. Olsson[1], F. Eriksson[1], J. Birch[1], L. Hultman[1]

[1]Linköping University, IFM, Thin Film Physics Division, Linköping, Sweden

magnus.garbrecht@liu.se
Keywords: HR(S)TEM, approximants, quasicrystals

Quasicrystals and their associated approximant phases have drawn increased scientific attention during the past decade not only for the purpose of fundamental research, but due to their possible applications as bulk materials or thin films [1, 2]. Owing to their infinitely large unit cell, the determination of the local atomic structure of any quasicrystal is a challenging task to be performed by transmission electron microscopy (TEM). However, an associated approximant phase with comparable physical properties shares the local atomic arrangement and thus allows conventional structure analysis to be performed [3].

In the past, the cubic Al-Si-Cu-Fe α-approximant of nominal composition $Al_{55}Si_7Cu_{25.5}Fe_{12.5}$ has been prepared by, e.g., arc melting under pressurized Ar atmosphere, leading to bulk alloy ingots [4-6]. Recently, we showed that thin films of the Ψ-$Al_{62.5}Cu_{25}Fe_{12.5}$ quasicrystalline phase can be prepared by annealing a multilayer stack on a sapphire substrate [7]. Here, we show that the α-approximant with nominal composition $Al_{55}Si_7Cu_{25.5}Fe_{12.5}$ close to the icosahedral quasicrystalline phase can be grown identically by high-vacuum magnetron sputtering of individual Al, Cu, and Fe layers onto Si(100) substrates, yielding a total thickness of 400 nm [8]. The cubic α-approximant phase was formed by Si diffusion from the substrate into the thin films activated by subsequent annealing to temperatures close below 450° C, where the quasicrystal phase starts to form.

Figure 1 shows a low magnification overview HAADF-STEM micrograph of the film on the substrate with the electron beam parallel to the Si[110] direction (a), and an EDX spectrum confirming its chemical composition (b). The film of ~0.4 µm thickness consists of non-equiaxial grains with diameters of the order of ~100 nm showing no preferential orientation relationship with the substrate or each other. The substrate-film interface is rough as well as the surface of the film, but exhibits no amorphous oxide layer. HRSTEM micrographs in the [110] and [111] zone axes of an individual grain exhibiting strain are presented together with their respective electron diffraction patterns in Figure 2.

We present a detailed analysis of the growth process and resulting microstructure of the α-approximant thin film employing high-resolution (S)/TEM, EDX, electron diffraction methods and accompanying multi-slice simulations. All experiments were conducted at the Linköping double-corrected and monochromated FEI Titan^3 60-300 microscope equipped with a Gatan Quantum ERS GIF, high brightness XFEG source, and Super-X EDX detector, operated at 300 kV.

1. J-M. Dubois, S.S. Kang, A. Perrot, Mater. Sci. Eng. A 179/180 (1994) 122.
2. J-M. Dubois, Useful Quasicrystals, World Scientific Publishing, Singapore, 2005.
3. U. Mizutani, T. Takeuchi and H. Sato, J. Phys.: Condens. Mat. 14 (2002) 767.
4. A. Quivy, M. Quiquandon, Y. Calvayrac, F. Faudot, D. Gratias, C. Berger, R.A. Brand, V. Simonet, F. Hippert, J. Phys.: Condens. Matter 8 (1996) 4223.
5. T. Takeuchi, H. Yamada, M. Takata, T. Nakata, N. Tanaka, U. Mizutani, Mater. Sci. Eng. A 294 (2000) 340.
6. Z. M. Stadnik, T. Takeuchi, N. Tanaka, U. Mizutani, J. Phys.: Condens. Mat. 15 (2003) 6365.
7. S. Olsson, F. Eriksson, J. Birch, and L. Hultman, Thin Solid Films 526 (2012) 740
8. S. Olsson, F. Eriksson, J. Jensen, M. Garbrecht, J. Birch, and L. Hultman, submitted, 2013.

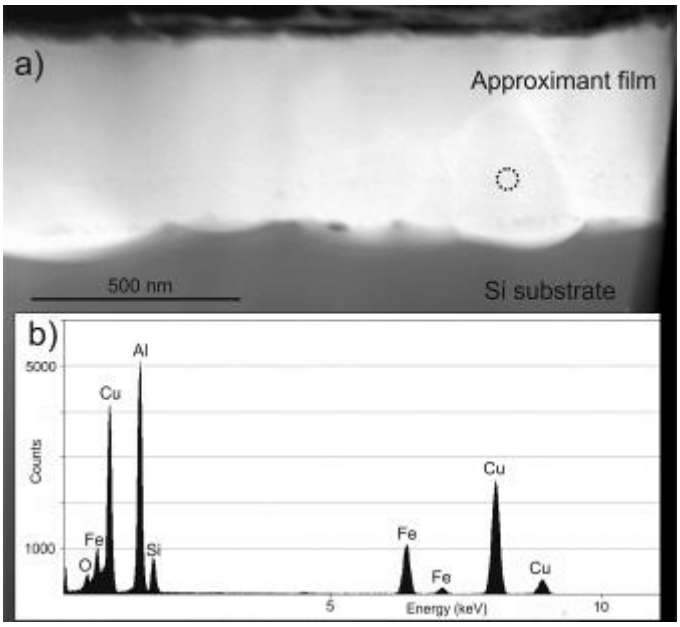

Figure 1. Low magnification overview HAADF-STEM of the approximant film (a), and EDX spectrum acquired from the encircled region (b).

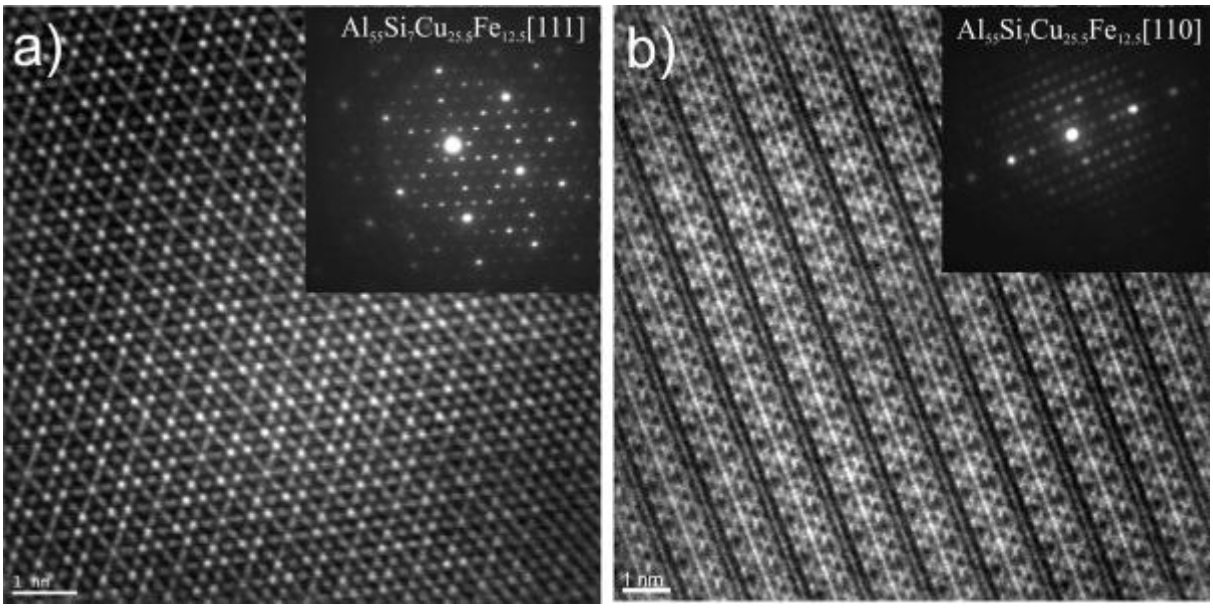

Figure 2. HAADF-STEM micrographs of the α-approximant thin films in [111] (a) and [110] (b) zone axis.

Thin Films and Coatings

MS.5.P135
New Low Voltage FE-SEM & AFM Techniques Offer Unprecedented Glimpse into Graphene

T. Groves[1], M.A. Fenner[2]

[1]Agilent Technologies UK Ltd, Wokingham, United Kingdom
[2]Agilent Technologies GmbH, Frankfurt, Germany

trevor_groves@agilent.com

Low voltage (<1kV) field emission scanning electron microscopy (LV-FESEM) provides a high quality easy to use imaging technique for energy-sensitive materials whilst still maintaining high imaging resolution. For non-conducting samples, the application of a thin conducting surface coating can sometimes be eliminated when a state of charge equilibrium is achieved on the specimen's surface and this approach has be successfully applied to graphene films deposited onto insulating substrates. It should be noted that applying a conductive coating can compromise with the imaging of graphene and is therefore not recommended.

The presentation will show low voltage imaging of graphene on a range of substrates. Secondary electron, backscattered electron and topographic imaging modes were used to study the surface morphologies of graphene samples at a broad range of magnifications. Reducing the incident beam voltage to 500 volts is shown as an effective method in controlling the electron charge caused by insulating substrates beneath single and multiple graphene layers. It will be demonstrated, with examples, that LV-FESEM imaging can successfully be employed in graphene-related research and can further be applied to quality checks, determining the number of graphene layers deposited on a substrate and visualizing impurity particles sometimes present in engineered graphene manufacture. [1-4].

High-resolution visualization of the surface morphology is a key feature of the Atomic Force Microscopy (AFM) technique and the capability of routinely resolving details at a single molecular level has been well demonstrated previously. Furthermore advanced AFM methods can be used to characterize the electrical properties of surfaces. In this presentation we describe Kelvin Force Microscopy (KFM) which is a single pass surface potential measurement. KFM offers a powerful experimental means to investigate the local electrical properties of both single layer graphene and few layer graphene films. The effect of the film thickness on the surface potential is detected and quantitative measurements are obtained. [5-6].

1. K.S. Novoselov et al, Science 306, (2004) p. 666.
2. F. Schwierz, Nat. Nano. 5, (2010) p. 487.
3. Y.-M. Lin et al, Science 327, (2010) p. 662.
4. J. Hass et al, J. Phys: Condens Matter 20, (2008) p. 323202.
5. S. Zhou, G.-H et al, Nat. Mat. 6, (2007) p. 770.
6. A. Bostwic et al, Nat. Phys. 3, (2007) p. 36.

Thin Films and Coatings

MS.5.P136
Nanocrystal orientation and superlattice array in Pbs-oleic acid thin films: The role of crystal habit and organic fibrils

P. Simon[1], L. Liebscher[2], I.A. Baburin[2], P. Formanek[3], F. Röder[4], J. Sickmann[4], S. Hickey[2]
A. Eychmüller[2], H. Lichte[4], R. Kniep[1], E. Rosseeva[1,5]

[1]Max-Planck-Institute, Inorganic Chemistry, Dresden, Germany
[2]Technical University of Dresden, Institut für Physikalische Chemie / Elektrochemie, Dresden, Germany
[3]Leibniz-Institut für Polymerforschung Dresden e.V., Dresden, Germany
[4]Technical University of Dresden, Institute of Structure Physics, Dresden, Germany
[5]University of Konstanz, Physical Chemistry, Konstanz, Germany

paul.simon@cpfs.mpg.de

With regard to the materials science aspects of nanocolloid structural chemistry, this study is of great interest in the attempt to answer two of the major topics being hotly debated. The first concerns the principles of the ordering of self-assembled films and the driving forces for this kind of self-assembly [1,2]. The second topic concerns itself with the optimisation of physical properties of such systems containing confined and isolated but nevertheless interconnected structures [3].

For the self-assembly processes of ligand capped nanoparticles a complex set of events should be taken into account, such as the attraction between the surface charges of the inorganic nanoparticles and a significant contribution from van der Waals forces between the organic surface chains which are further assisted by capillary forces evolving during the drying processes and steric effects caused by the shape of the individual nanoparticles. As soon as a structure has been established by the self assembly process, further ordering may be assumed to be prevented by fibrillation of the organic surfactant. By careful analysis of high-resolution bright field images it was found that the nanoparticles are interconnected by organic fibrils of oleic acid which are partially mineralised by PbS. These inorganic bridges on an atomic level together with organic fibrils are responsible for keeping the orientation of the nanoparticles fixed thus preventing the system from adopting a disordered or arbitrary arrangement. Recently, we were able to determine the 3D structure of a PbS - oleic acid superassembly showing an intermediate character between a high and low orientational ordering of nanoparticles, respectively [4]. In this system, the truncated octahedrally shaped PbS nanocrystals are stabilized by organic molecules and assembled into an fcc superlattice with long-range “translational” order, while still maintaining their preferable crystallographic orientation limited to shorter ranges. This situation is reminiscent of a special type of colloidal crystal classified as “mesocrystals” which represent superstructures of nanoparticles with certain mutual orientation relations

1. S. A. Harfenist, Z. L. Wang, M. M. Alvarez, I. Vezmar, R. L. Whetten. J. Phys. Chem (1996) 100, 13904-13910.
2. Z. L. Wang, S. A. Harfenist, I. Vezmar, R. L. Whetten, J.Bentley, N. D. Evans, K. B. Alexander. Adv. Mater. (1998) 10, 13-30.
3. D. V. Talapin, J.-S. Lee, M. V. Kovalenko, E. V. Shevchenko. Chem. Rev. (2010) 110, 389–458.
4. P. Simon, E. Rosseeva, I. A. Baburin, L. Liebscher, S.G. Hickey, R. Cardoso-Gil, A. Eychmüller, R. Kniep, W. Carrillo-Cabrera. Angew. Chem. Int. Ed. (2012) 51, 10776-10781.
4. We kindly acknowledge Prof. H. Lichte for the possibility to measure at the Triebenberg Laboratory at the TU Dresden, Germany

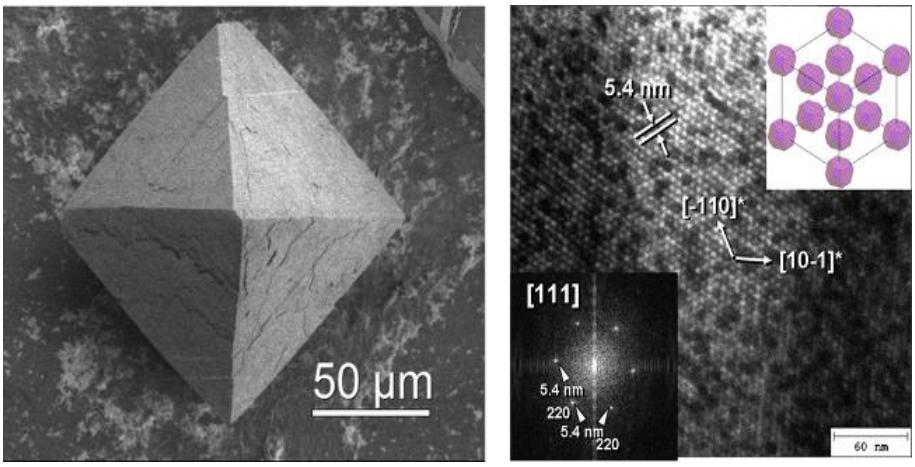

Figure 1.

Thin Films and Coatings

MS.5.P137
Characterization of amorphous and porous Silicon coatings by (S)TEM and EELS

R. Schierholz[1], J. Caballero-Fernández[1], V. Godinho[1], A. Fernández[1]

[1]Instituto de Ciencia de Materiales de Sevilla, Sevilla, Spain

Roland.schierholz@icmse.csic.es
Keywords: porous silicon, (S)TEM, EELS

We present a new way to produce porous amorphous silicon coatings by glancing angle magnetron sputtering of Si targets in noble gas atmospheres. A similar process was previously applied to produce SiO_xN_y-coatings [1]. This allows the production of a closed porosity in contrast to the previously most common way of chemical etching in HF-based solution, which leads to open porosity. Our way is environment friendly and up scalable. By varying the deposition parameters such as type of noble gas, the pressure, RF-power as well as applying an additional bias or substrate heating we are able to change the microstructure, which influences the refractive index, of interest for the microelectronic technology and optical applications. The microstructural and chemical investigation of coatings by TEM should lead to a better understanding of the growth mechanism and the influence of the deposition parameters.

Because the pore size lies in the range of ≈ 2 nm to ≈ 50 nm TEM is the appropriate way to characterize the pore size distribution. But TEM also suffers from the overlap of pores in projection so we apply tomography in addition to reveal the porosity in three dimensions. This helps to identify the closed pores and the complicated surface structure of the sample due to TEM sample preparation by ion milling. In addition we perform both, STEM-EELS and EFTEM experiments.

In Figure 1 shows STEM HAADF images of coatings deposited under (a) He- and (b) Ar-atmosphere. The coating is dense for the Ar- and porous for He-atmosphere. Pores align in columns towards the magnetron source. The corresponding EEL-spectra in (d) reveal only the Si plasmon peak for the dense coating while that of the porous coating in (c) contains two additional features, the He K-edge at ≈ 22 eV and the shoulder at ≈ 10 eV attributed to the pore-matrix interface plasmon [2]. Figure 2 shows an EFTEM spectrum image of another coating deposited under He-atmosphere with more separated. The spectrum extracted from position 1 at the wall separating two pores reveals the same shoulder and the image slice at 9 ± 2 eV is shown in (a) and demonstrates the excitation of the pore-matrix interface plasmon for the closed pores. The zero-loss filtered image is shown in (b) as well as a spectrum extracted from position 2 in between the major pores. This spectrum looks similar to that of the dense layer produced under Ar-atmosphere. Nevertheless the energy resolution and sensitivity of the spectra extracted from the presented EFTEM SI is too low to resolve the He-K-edge so we aim one getting more EELS data for quantification of He inside the pores [3].

1. V. Godinho, C. Rojas and A. Fernandez, Microporous and Mesoporous Materials 149 (2012) 142
2. M.-L. David, F. Pailloux, V. Mauchamp and L. Pizzagalli, Appl. Phys. Lett. 98 (2011) 171903
3. C. A. Walsh, J. Yuan and L. M. Brown, Philosophical Magazine A 80 (2000) 1507

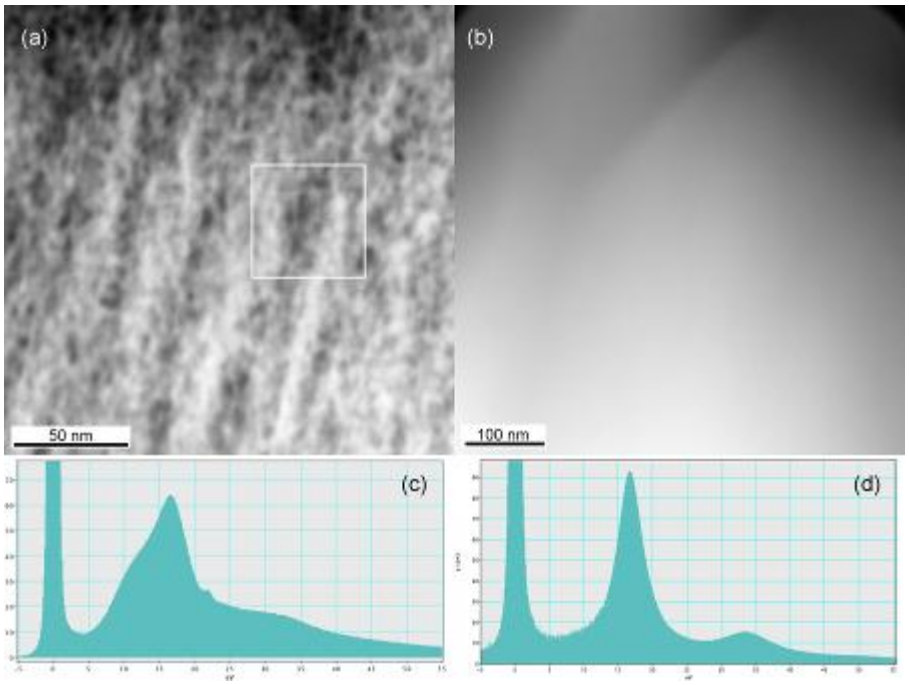

Figure 8. STEM HAADF images of coatings deposited under (a) He- (5·10-2 mbar) and (b) Ar-atmosphere ($7 \cdot 10^{-3}$ mbar). The corresponding EEL-spectra reveal only the Si plasmon peak for the dense layer in (d) while two additional features are present in the spectrum of the porous coating recorded in the area marked with the white square. At ≈ 22 eV the He edge is present and the shoulder at ≈ 10 eV originates from the interface plasmon [2].

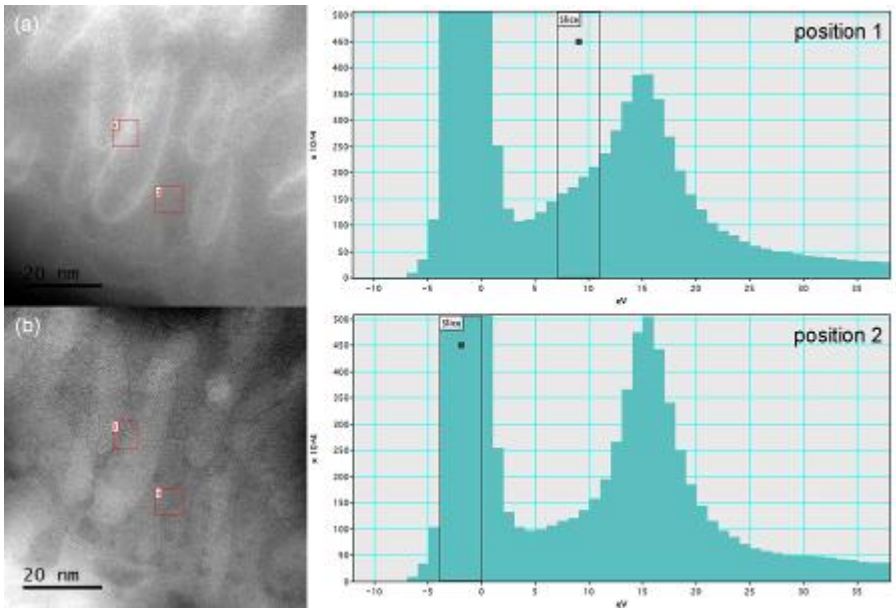

Figure 9. EFTEM spectrum image of a porous Si-coating prepared under He-atmosphere. The image slice at 9±2eV (a) reveals plasmon at the inner surface of the pores. The zero loss filtered image is shown in (b). The spectra extracted from position 1at the pore wall reveals the same shoulder as the spectrum in Figure 1 (c). For comparison the spectrum at position 2 is shown which reveals only the Si-plasmon peak as the spectrum of the dense coating in Figure 1 (d).

Thin Films and Coatings

MS.5.P138
TEM microstructural characterization of co-sputtered Zr-Cu thin films metallic glasses

M. Apreutesei[1], P. Steyer[1], L. Joly-Pottuz[1], A. Billard[2], F. Sanchette[3], C. Esnouf[1]

[1]INSA Lyon, MATEIS, Villeurbanne, France
[2]LERMPS-UTBM, Montbéliard, France
[3]UTT, LASMIS, Nogent, France

lucile.joly-pottuz@insa-lyon.fr
Keywords : thin films, metallic glass, amorphous structure

The bulk metallic glasses have been studied for a long time since they present exceptional mechanical properties at room temperature and excellent corrosion resistance. A new challenge presently is to transfer such properties in the form of coatings, so called thin films metallic glasses (TFMGs). These films are, indeed, expected to be used in a large range of applications : microelectronics, optoelectronics, biomedical, and military components, besides of their properties. The overall aim of the presented study was to investigate the mechanical properties of Zr-Cu thin films (from 13 to 90 at. % Cu), deposited using a magnetron co-sputtering method. The most important issue was, in fact, to investigate the glass forming ability (GFA) of these films. A structural characterization performed by XRD at room temperature revealed that within the [33, 85] at. % Cu range films are amorphous. Nevertheless, a deeper characterization of the films was needed since some studies already mentioned the presence of crystalline domains in some TFMGs [ref]. Transmission Electron Microscopy (TEM) characterization was performed on the [33, 85] at. % Cu range films in order to confirm the amorphous structure determined by XRD. Bright field images coupled with Energy Dispersive X-Ray Spectroscopy (EDS) and Selected Area Electron Diffraction (SAED) were performed on different regions of each films. Films containing 48.3 at. % Cu were found to be fully amorphous (Fig 1). Neither on the bright field images, nor on the SAED patterns, crystalline domains were observed. For films containing less or more copper, fine crystalline nanodomains appeared (Fig 2a). Such nanocrystallised phases may be explained by the presence of Zr-Cu intermetallic compounds ($Cu_{10}Zr_7$, $Cu_{51}Zr_{14}$), pure copper or zirconia artefacts. In the case of a low content of copper, SAED patterns coupled with EDX confirm mainly the presence of zirconia. For higher copper contents, intermetallic compounds or pure copper were identified. For a Zr-59.1 at% Cu film, both copper and $Cu_{10}Zr_7$ were detected. Furthermore, these crystals are in a crystallographic relationship with a common constitutive (111) Cu plan parallel to (215) of $Cu_{10}Zr_7$. These results confirm the interest of using TEM tools to fully characterize the thin films metallic glasses. Indeed owing to X-ray detection limitations, small nanodomains cannot be detected. Thus, characterization at smaller scale is required. Mechanical properties and microstructural characterizations will now be strongly correlated in order to better understand the properties of the thin films metallic glasses. It will, thus, be possible to improve their processing and enhance their properties.

1. K. Kondoh, J. Fujita, J. Umeda, T. Serikawa, Adv. Mat. Sc. Eng., 2008 (2008) ID 518354.
2. The authors acknowledge the CLYM (Centre Lyonnais de Microscopie) for the access to the 2010F microscope, the Franche Comte Region and the French Ministry of Research for financial support.

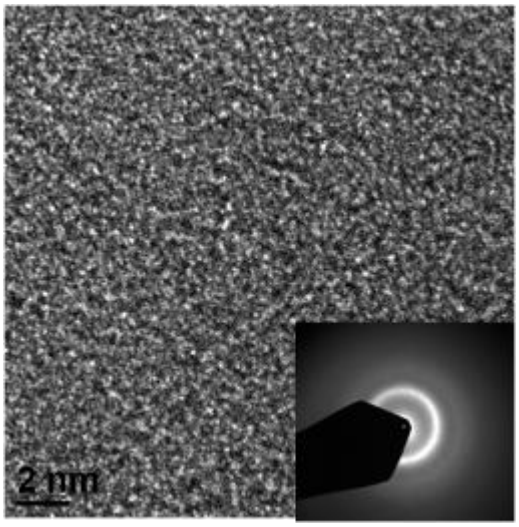

Figure 1. HRTEM plane view micrograph of Zr-48.3 at%Cu film with an inserted SAED (analyzed zone 400 nm in diameter)

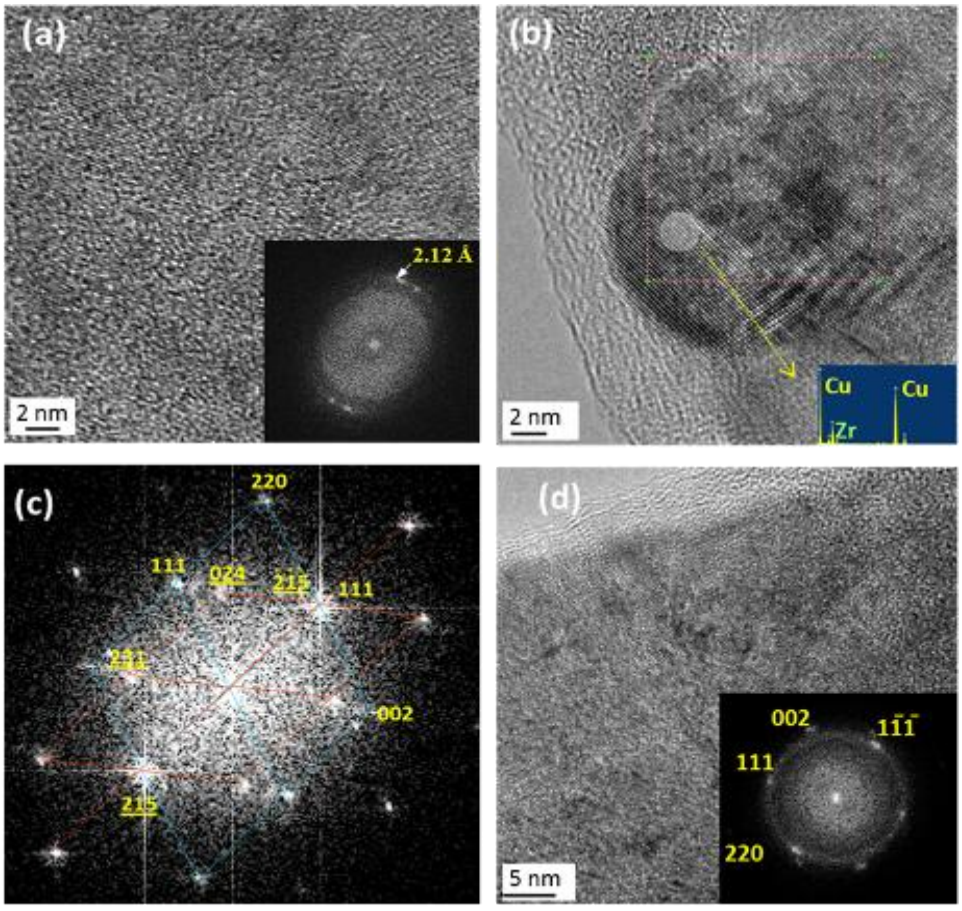

Figure 2. HRTEM characterization of different Zr-Cu thin films: a.) 40.1 at% Cu with an inserted Fourier transform diffractogram; b.) 59.1 at% Cu with an inserted EDX spectrum corresponding to the 2 nm highlighted circle ; c.) Indexed Fourier transform pattern acquired on region delimited by dotted line square of previous micrograph; non underlined numbers are corresponding to Cu indexation ([1-10] zone axis), while underlined numbers are attributed to $Cu_{10}Zr_7$ ([-742] zone axis); d.) 85.0 %Cu with an inserted Fourier transform diffractogram corresponding to copper nanocrystal

Thin Films and Coatings

MS.5.P139
Silicon nanostructures produced by self-masked plasma etching

G. Barucca[1], E. Santecchia[1], P. Mengucci[1], E. Tiberi[1], R. Di Mundo[2], R. d'Agostino[2], F. Palumbo[3]

[1]University Politecnica delle Marche, SIMAU, Ancona, Italy
[2]University of Bari, Department of Chemistry, Bari, Italy
[3]CNR, Institute for Inorganic Methodologies and Plasmas (IMIP), Bari, Italy

g.barucca@univpm.it
Keywords: silicon nanostructures, plasma etching, transmission electron microscopy (TEM), X-ray photoelectron spectroscopy (XPS)

Plasma etching is emerging as a reliable top-down self-masked approach for nano-texturing the surface of crystalline silicon on a wafer-scale. With this technique is possible to realize under maskless, or more precisely, under self-masked conditions, random distributions of non-geometrically shaped structures with wide tunability in terms of size [1,2]. In this work, we focus our investigation on the morphological, compositional and structural characteristics of the nanotextured silicon surfaces obtained by CF_4 fed plasma etching process. The aim is to understand the nature and formation mechanism of these structures. In particular, we have combined the morphological and structural information achieved by high resolution scanning electron microscopy (SEM) and transmission electron microscopy (TEM) observations with compositional data obtained by angle-resolved X-ray photoelectron spectroscopy (XPS) and energy-dispersive spectrometry (EDS) analyses.
Polished slabs of p-type crystalline silicon 1cmx1cm with a thickness of 725 µm were used as substrates for the etching experiments. Substrates were processed in a Reactive Ion Etching RF parallel plate plasma reactor. The plasma was ignited with a 13.56 MHz power supply (Caesar Dressler) through an impedance matching unit. The gas feed, consisting of CF_4, was inserted into the reactor through a shower head mounted in the upper electrode. The samples obtained at the input power of 100 W and 300 W were considered for the microscopic and spectroscopic analyses reported in this work.
SEM images of the CF_4 plasma-treated c-silicon surfaces are shown in Figure 1. The 100 W sample (a) presents sharp structures separated by an average distance of 100 nm. The 300 W sample (b) is markedly different. The structures, separated by an average distance of 200 nm, are significantly taller. Moreover the width of these structures is considerably larger, although it is difficult to quantify considering the particularly evident structure coalescence phenomenon (already present in the 100 W sample). Silicon, carbon, fluorine, oxygen and iron were detected in both samples by XPS analyses. Fe atoms/clusters come from the steel electrodes. The angle-resolved measurements show a significant variations in the surface percentages of carbon, fluorine, and especially silicon as function of the take-off angle (TOA), while oxygen and iron content remains fairly constant. In particular, with a gradual increase in TOA (namely analyzing sample layers closer to the surface), the silicon content decreases steeply, while fluorine and carbon content increases (especially the latter at 100W). Cross-section TEM images show that the samples surface is composed of crystalline cusps (darker) over which amorphous domains (lighter) are superimposed, Figure2. EDS results show that the crystalline regions are exclusively composed of silicon in both samples. Metal atoms (Fe) are only detected in the amorphous regions where silicon atoms are also present. Analyzing the 300 W sample, high resolution TEM images and selected area electron diffraction (SAD) patterns (inset of Figure 2.) show that the plumes are composed of amorphous material inside which some metallic nano-crystals are present.

1. C. Lee, S. Y. Bae, S. Mobasser, H. Manohara, Nano Lett. 2005; 5:2438
2. D. Muriasa, C. Reyes-Betanzo, , M. Moreno, A. Torres, A. Itzmoyotla, R. Ambrosio, M. Soriano, J. Lucas, P. Roca i Cabarrocas, Materials Science and Engineering B 2012; 177:1509

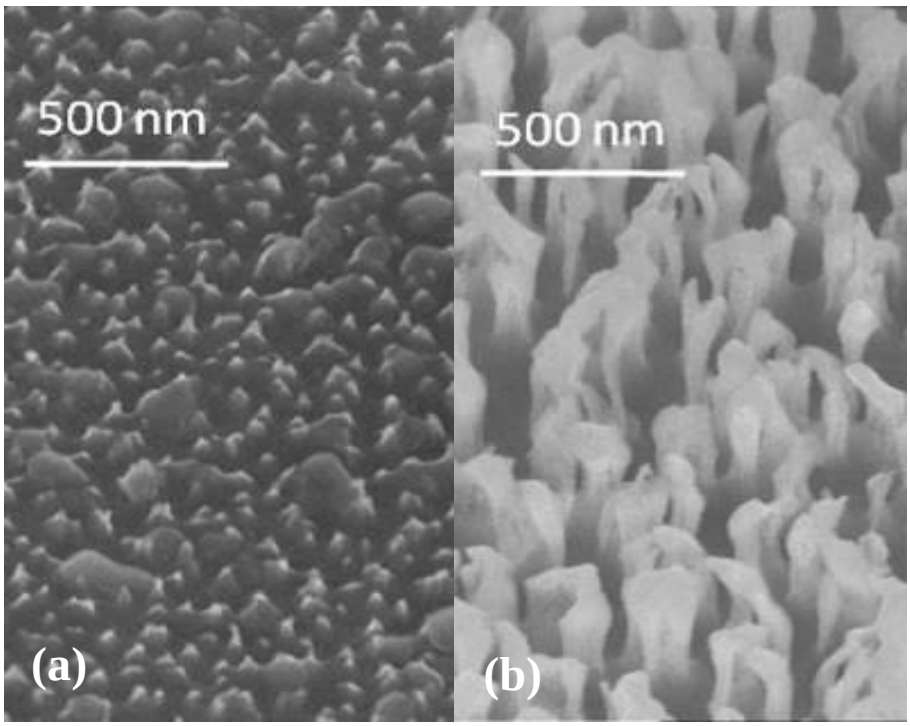

Figure 1. SEM images of the 100 W (a) and 300 W (b) sample.

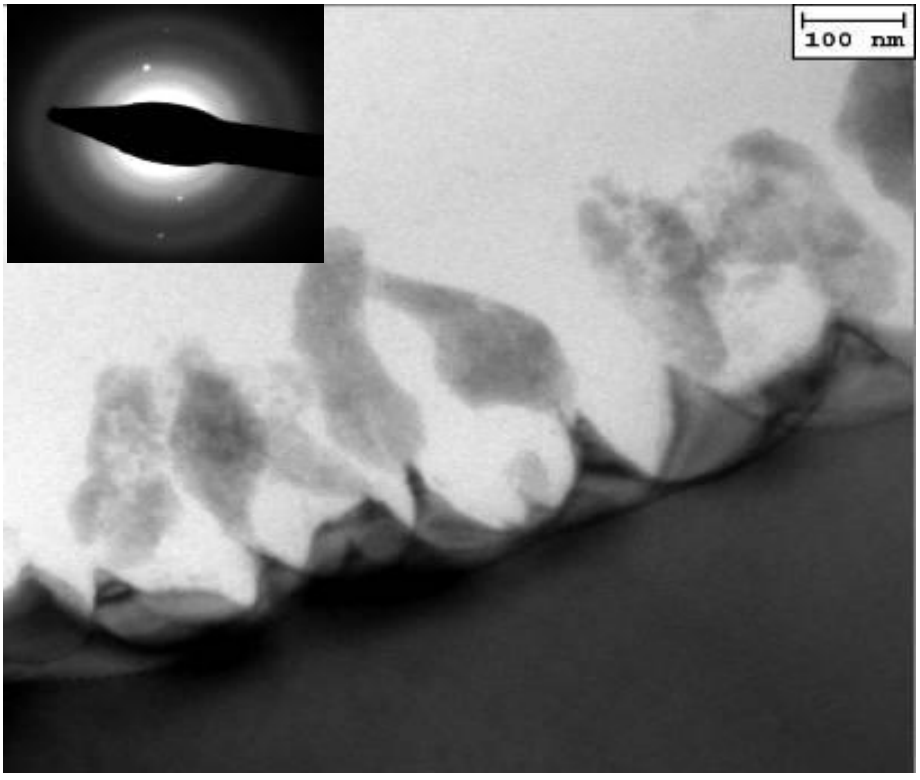

Figure 2. TEM cross section image of the 300 W sample. In the inset a SAD pattern of a plume is shown.

Thin Films and Coatings

MS.5.P140
HRTEM Image Simulation of Model Structures for Fullerene-Like Nanotructures

Z. Czigany[1]

[1]Institute for Technical Physics and Materials Science in RCNS of HAS, Thin Film Physics, Budapest, Hungary

czigany.zsolt@ttk.mta.hu
Keywords: HRTEM, fullerenes, image simulation, aberration correction, nanostructures

Carbon based amorphous and fullerene–like (FL) thin films have a great potential in applications due to their mechanical resiliency. However, high resolution transmission electron microscopy (HRTEM) imaging of fullerene-like structures in the solid phase is limited by the overlap of spherical nm-sized fullerene-like features as reported recently for CN_x [1] and CP_x [2] thin films. In this paper the prospects and limitations of HRTEM imaging is investigated by image simulations.

Model structures were created for CN_x and CP_x thin films using close packed clusters of nano-onions of encapsulated Goldberg polyhedra (of C_{60} C_{240} and C_{540}) and P doped randomized C_{20} fullerites [3], respectively. The 10at% P doping in the model for CP_x was implemented by application of $C_{18}P_2$ isomers [3].

HRTEM image simulations were made by the JEMS program (by P. Stadelmann) using the multislice method [4]. Conventional and C_s corrected HRTEM images were simulated with the parameters of FEI Tecnai G^2 (200 kV, equipped with ultratwin objective lens; point resolution of 0.19nm) and FEI Titan (300 kV) microscopes, respectively. Conventional HRTEM images were calculated at Scherzer defocus. For the C_s corrected HRTEM images optimized parameters were applied to minimize the point spread [5]. For 300kV acceleration voltage and $g_I \approx 15nm^{-1}$ information limit C_s=7.5µm and -4.5nm defocus were applied.

Results of conventional (non C_s corrected) HRTEM image simulations of a nano-onion ensemble in two orientations are shown in Fig.1. For small overlap of two 3 shell nano-onions faceting like artificial fringes appear at the shell coincidences which is demonstrated in a symmetric arrangement in Fig.1c. In general, if the overlap of two 3 shell nano-onions exceeds 50% the interpretation of the image is uncertain. Overlap of more than two onions results in amorphous-like appearance of the image (Fig.1d). The features in the image depend strongly on the defocus in agreement with experimental observations [1]. In C_s corrected image simulations (Fig.2 – simulated image of Fig.1b arrangement) the innermost shell is not visible even in the non-overlapping onions at the periphery of the cluster. At the overlapping central region of the cluster the structure has an amorphous-like appearance with a finer scale pattern compared to non C_s corrected images.

Simulated HRTEM images of clusters of $C_{18}P_2$ cages, containing 13, 20, 40, 60 and 90 cages for FEI Tecnai G^2 microscope at Scherzer defocus and FEI Titan microscope are compared in Figure 3. For the model clusters of close packed $C_{18}P_2$ molecules (built for FL-CP_x) the contrast of fringes is very similar for different cluster sizes and multiplicity of overlaps. An amorphous appearance dominates the image over a few nm specimen thicknesses. In the simulated C_s corrected images the slightest overlap, producing ~1.6nm specimen thickness, may provide an amorphous appearance of the structure with finer scale pattern compared to the non C_s corrected case.

The simulated HRTEM images of the above model structures are also in agreement with the experimental observation [1,2] and provide a general indication, that quite complex nanostructured materials may have amorphous-like appearance in real TEM observations – independent of the actual resolution [6].

1 Zs. Czigány, J. Neidhardt, I. F. Brunell and L. Hultman, Ultramicroscopy 94 (2003) 163
2 A. Furlan, G.K. Gueorguiev, Zs. Czigány, H. Högberg, S. Braun, S. Stafström, L. Hultman, Rapid Research Letter in Physica Status Solidi 2 (2008) 191
3 Zs. Czigány, Phys. Stat. Solidi B 250 (2013) 334
4 P.J. Stadelman, Ultramicroscopy 21 (1987) 131
5 K.W. Urban, C-L. Jia, L. Houben, M. Letzen, S-B. Mi, K. Tillman in New possibilities with aberration corrected electron microscopy (Editors: David Cockayne, Angus Kirkland, Peter Nellist and Andrew Bleloch) *Philosophical Transactions of the Royal Society* 367 (2009) 3735
6 OTKA-81808 and Bolyai János Research Scholarship of Hungarian Academy of Sciences

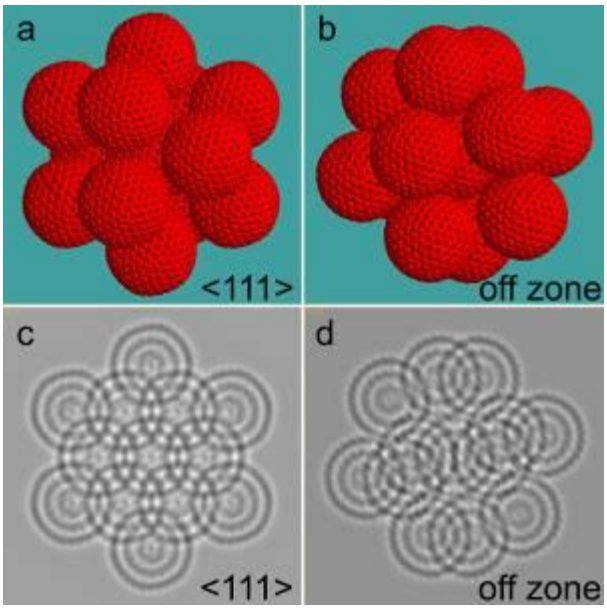

Figure 1. Close packed (fcc) clusters of 13 pieces of 3-shell nano-onions in different orientations are depicted in panels (a and b) and corresponding simulated HRTEM images calculated for FEI Tecnai G^2 microscope at Scherzer defocus (-43nm) are shown in panels (c and d). The panels are 8 nm wide. False fringes and confusion of shell structure can be recognized in the central region of the cluster for <111> and "off zone" orientations, respectively, due to multiple overlap.

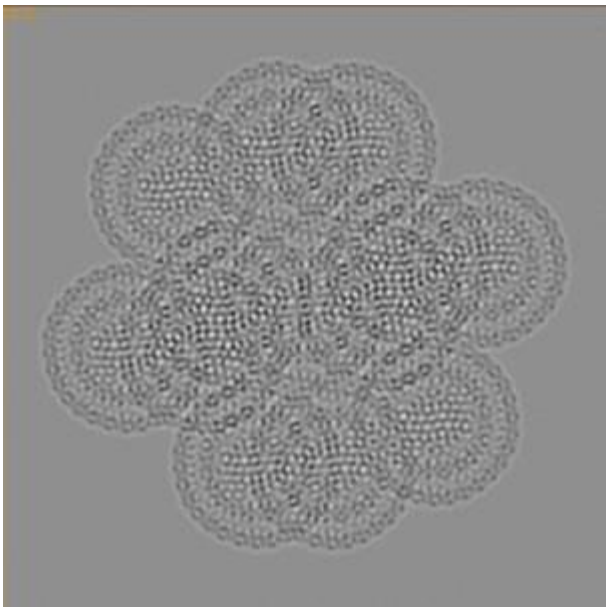

Figure 2. Simulated HRTEM image of a close packed (fcc) clusters of 13 pieces of 3-shell nano-onions in off zone orientation (Fig. 1b) calculated for FEI Titan microscope at C_s=7.5μm and Δf=-4.5nm (least confusion). The panel is 8 nm wide. The inner onion shells are not visible and the image has an amorphous appearance even in the non overlapping areas.

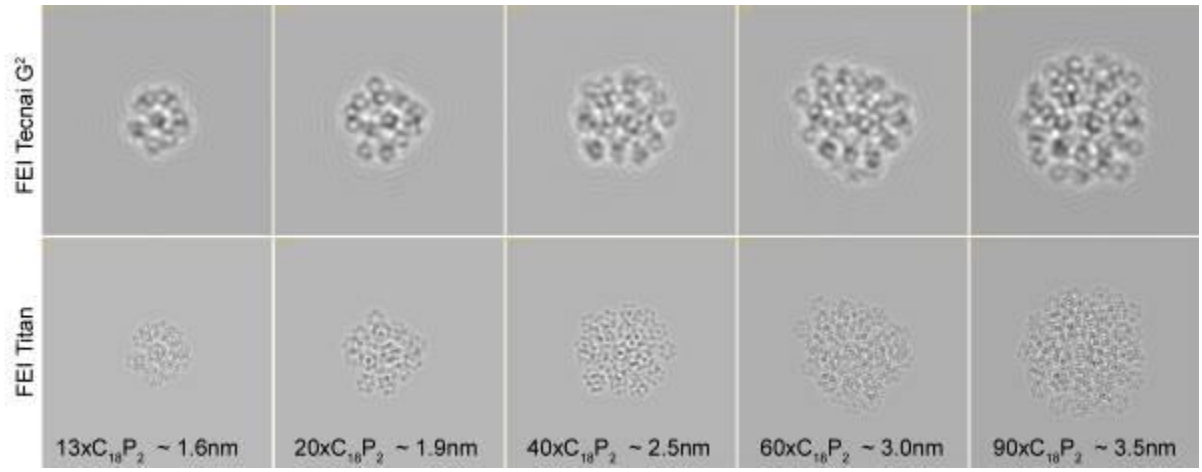

Figure 3. Simulated HRTEM images of $C_{18}P_2$ clusters containing 13, 20, 40, 60 and 90 cages for FEI Tecnai G^2 microscope at Scherzer defocus (upper line of images) and FEI Titan microscope (lower line of images). The panels are 5.5 nm wide. The corresponding cluster diameters are given in each panel. In all images of clusters for FEI Tecnai G^2 microscope small circles (resembling the projection of an individual C_{20} sized cage) can be recognized both at the periphery of the clusters and at the centre, where cage overlap is obvious. The image for C_s corrected (FEI Titan microscope) has very similar appearance having at finer scale reminding of an amorphous appearance.

Thin Films and Coatings

MS.5.P141
Microstructural investigation of magnetic CoCrPt:SiO_2 films

E. Santecchia[1], G. Barucca[1], P. Mengucci[1], G. Varvaro[2], A.M. Testa[2], E. Agostinelli[2], F. Springer[3] C. Brombacher[3], M. Albrecht[3]

[1]Università Politecnica delle Marche, SIMAU, Ancona, Italy
[2]CNR, Istituto di Struttura della Materia, Rome, Italy
[3]Chemnitz University of Technology, Institute of Physics, Chemnitz, Germany

e.santecchia@univpm.it
Keywords: magnetic films, transmission electron microscopy (TEM), X-ray diffraction (XRD)

Magnetic recording is today the dominant storage technology and CoCrPt:SiO_2-based systems with perpendicular magnetic anisotropy represent a very important resource for hard disk drives (HDDs) realisation [1,2]. In the present work, the correlation between the structural properties of granular CoCrPt:SiO_2 films with variable thickness and the magnetization reversal mechanisms are investigated.

$[(Co_{90}Cr_{10})_{80}Pt_{20}]_{92}:(SiO_2)_8$ thin films with a nominal thickness of 7.5, 10 and 17.5 nm (hereafter referred to as ML7.5, ML10 and ML17.5) were deposited by magnetron sputtering on 2.5-inch hard disk HOYA substrates, with a complex underlayer structure – Cr(2.5nm)/Ru(8nm)/Ru(12nm) – aimed to promote a perpendicular anisotropy and good microstructural properties; films were covered by a 4 nm protective overcoat of diamond-like carbon. Structural characterization were carried out by X-ray diffraction (XRD) and transmission electron microscopy (TEM) techniques. Magnetic measurements were carried out by using a vector vibrating sample magnetometer (vVSM, ADE-Technologies Model 10).

X-ray diffraction patterns of the samples show the presence of only two peaks. One peak labelled as Ru (002), is due to the underlying dual Ru layer, while the second peak is attributed to the (002) reflection of the hexagonal CoCrPt recording layer. The absence of any other Ru or CoCrPt peak suggests a preferential growth of both layers with the *c*-axis perpendicular to the substrate. The degree of preferential growth along the *c*-axis of CoCrPt and Ru layers was estimated by measuring the full width at half maximum (FWHM) of the corresponding rocking curves. TEM plan view observations reveal the granular nature of the CoCrPt films. Fine grains with an average size of 7 nm, well separated by amorphous-like material (Si-oxide), are clearly visible in all the samples, Figure 1. The analysis of angular and time-dependent magnetic measurements indicates that the magnetization reversal mechanism is determined by the coexistence of coherent and incoherent processes, with a tendency toward more coherent reversal processes (i.e. Stoner-Wohlfarth character) as the thickness of the magnetic layer increases. It is important to stress that the switch between coherent and incoherent process is connected to a lower or higher ferromagnetic exchange coupling among neighbouring grains. Looking at the plan view images of the samples the CoCrPt grains have the same lateral average size and degree of separation regardless of the film thickness. Therefore, to understand the nature of magnetic results, TEM cross section observations of the samples were performed, Figure 2.. Results show that all the samples can be considered as formed by an initial thin layer at the interface with the Ru underlayer, consisting of nanograins physically in contact among them; on top of such layer, well separated columnar islands grow, whose height increases with increasing thickness, with an intergrain distance remaining roughly constant through the entire film thickness. Such peculiar microstructural features are consistent with magnetic results.

1. K. Srinivasan, S.N. Piramanayagam, R.W. Chantrell, Y.S. Kay, Journal of Magnetism and Magnetic Materials 320 (2008) 3036.
2. H.S. Jung, M. Kuo, S.S. Malhotra, G. Bertero, Applied Physics Letters 91 (2007) 212502

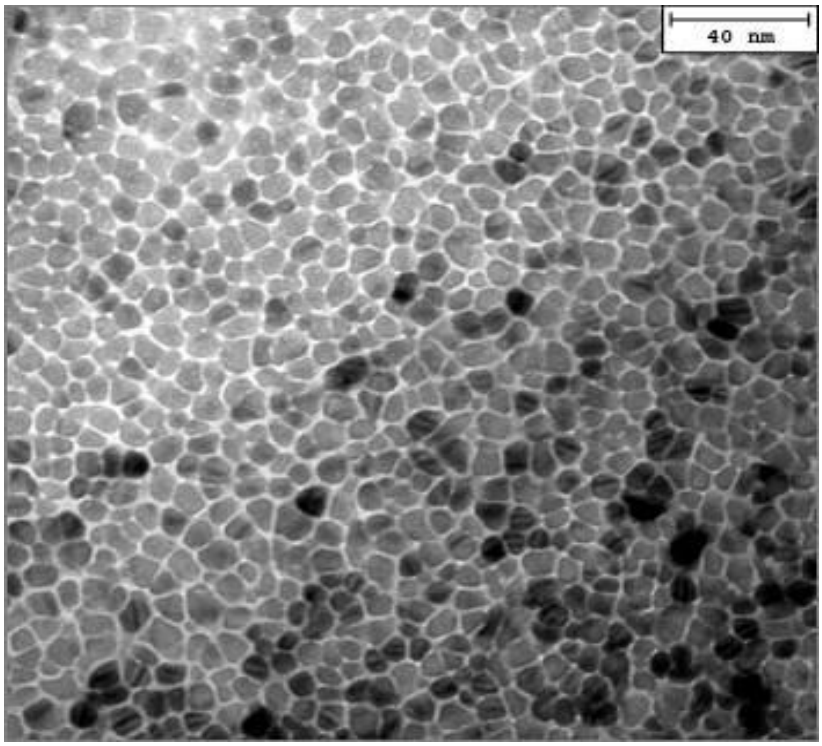

Figure 1. Typical TEM plan view image of a granular CoCrPt:SiO_2 film.

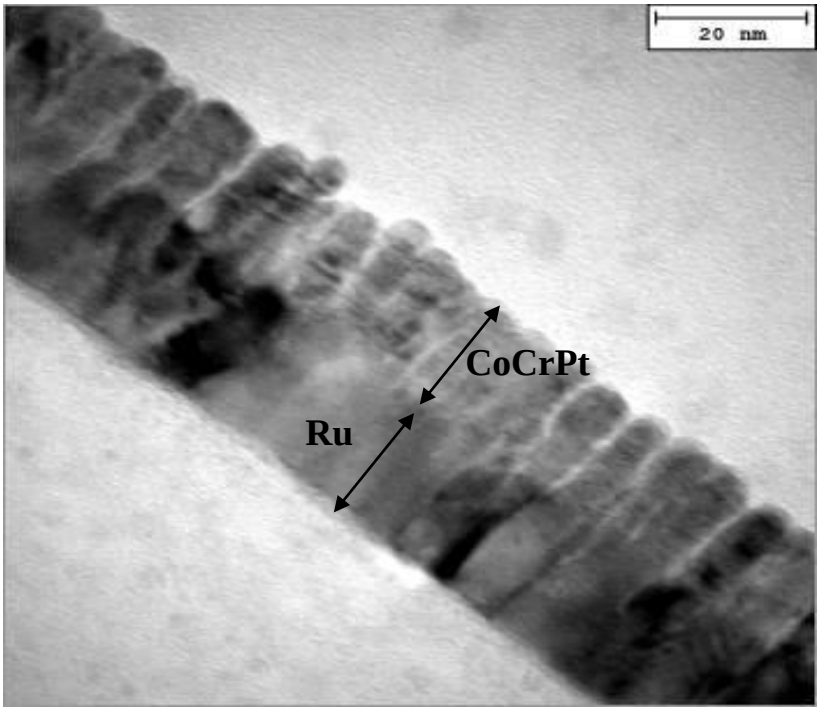

Figure 2. TEM cross section image of the ML17.5 sample. The dual Ru layer and recording layer are indicated.

Thin Films and Coatings

MS.5.P142
TEM investigation of the effect of silicon alloying on the microstructure and stability of amorphous and crystalline Al_2O_3-coatings

M.G.J. Müller[1], J. Mayer[1], F. Nahif[2], J.M. Schneider[2]

[1]Central Facility for Electron Microscopy, RWTH Aachen University, Aachen, Germany
[2]Materials Chemistry, RWTH Aachen University, Aachen, Germany

mueller@gfe.rwth-aachen.de

Alumina (Al_2O_3) is a very important polymorphic ceramic material with a wide range of applications due to excellent physical properties. Besides the thermodynamically stable α-Al_2O_3-phase it exhibits several metastable structures, the so called transition aluminas, such as γ-, η-, δ-, θ-, κ-, χ-Al_2O_3. Among these transition aluminas, the γ-Al_2O_3-phase exhibits comparable mechanical properties as the α-Al_2O_3-phase [1]. However, the phase transformation of the metastable γ-Al_2O_3-phase into the stable α-Al_2O_3-phase at high temperatures and the corresponding volume change may induce adhesive and/or cohesive failure and may hence limit coating lifetime. Therefore enhancing the thermal stability of γ-Al_2O_3 is of particular interest. One possibility to improve the thermal stability of γ-Al_2O_3 is to alloy it with a suitable alloying element. Different alloying elements, such as Y, Er, Ti, B, Mo, As, W, Sc, N, S or Si, and their effect on the thermal stability of transition aluminas have been discussed in literature [2, 3]. Based on the ab initio results of Jiang et al. [2], silicon has a stabilizing effect on γ-Al_2O_3. Hence silicon was chosen as an alloying element for Al_2O_3-layers in the present study.

To investigate the effect of Si-alloying on the thermal stability of the Al_2O_3-coatings crystalline and amorphous Al_2O_3-samples with and without silicon alloying have been deposited by using the Filtered Cathodic Arc (FCA) technique.

The unalloyed/Si-alloyed crystalline γ-Al_2O_3-coatings are a few micrometers thick ("Figure 1 a."). The samples were annealed ex situ in atmosphere to temperatures in the range of 1173.15 K to 1473.15 K. For TEM investigations thin cross sections of these samples were prepared by Focused Ion Beam (FIB) using a FEI Strata FIB 205 work station.

The TEM samples of the unalloyed/Si-alloyed amorphous Al_2O_3-coatings were prepared by conventional preparation techniques. The Si-wafer was removed by grinding, dimple grinding and etching with potassium hydroxide (KOH). A 50 nm thick Si_3N_4-layer was added as a etch stop between the Si-wafer and the Al_2O_3-layer to protect the Al_2O_3 against the etching of the KOH. The thickness of the Al_2O_3-layers is limited to a few hundred nanometres to ensure the electron transparency of the samples. The layers structure of the samples before and after the preparation is explained in "Figure 1 b." and "Figure 1 c.". The resulting TEM disc samples were annealed ex situ in an Ar-atmosphere at temperatures in the range of 873.15 K to 1373.15 K.

The TEM investigation of the crystalline and amorphous Al_2O_3-samples were performed by using a FEI Tecnai F20 microscope operated at 200 kV. For the TEM investigations conventional TEM methods, such as bright field imaging (TEM BF) and selected area diffraction (SAD), and Scanning TEM (STEM) techniques were applied to characterize the unalloyed and Si-alloyed nanocrystalline and amorphous samples. During the TEM study the investigation of the morphology, porosity and of the microstructure of the Al_2O_3-coating was of special interest. The TEM data suggest that the Si-alloying influences the morphology and the phase stability of both, the crystalline and the amorphous samples ("Figure 2." and "Figure 3.").

1. C. Täschner, B. Ljungberg, V. Alfredsson, Surface and Coatings Technology 108-109 (1998), p. 257 - 264.
2. K. Jiang, D. Music, K. Sarakinos, J. Phys.: Condens. Matter 22 (2010), p. 1 - 8.
3. O. Mekasuwandumrong, P. Tantichuwet, C. Chaisuk, Materials Chemistry and Physics 107 (2008), p. 208 - 214
4. The authors kindly acknowledge the financial support of the German Research Foundation within the project numbers MA 1280/30-2 and SCHN 735/14-2

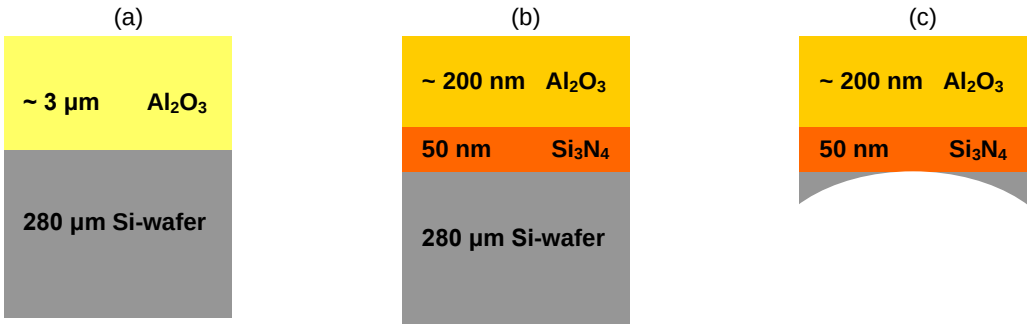

Figure 10. a) Coating structure of the unalloyed /Si-alloyed nanocrystalline Al_2O_3-layers (b) Layer structure of the unalloyed/Si-alloyed amorphous Al_2O_3-layers and (c) Layer structure of the unalloyed/Si-alloyed amorphous Al_2O_3-layers after dimple grinding and etching.

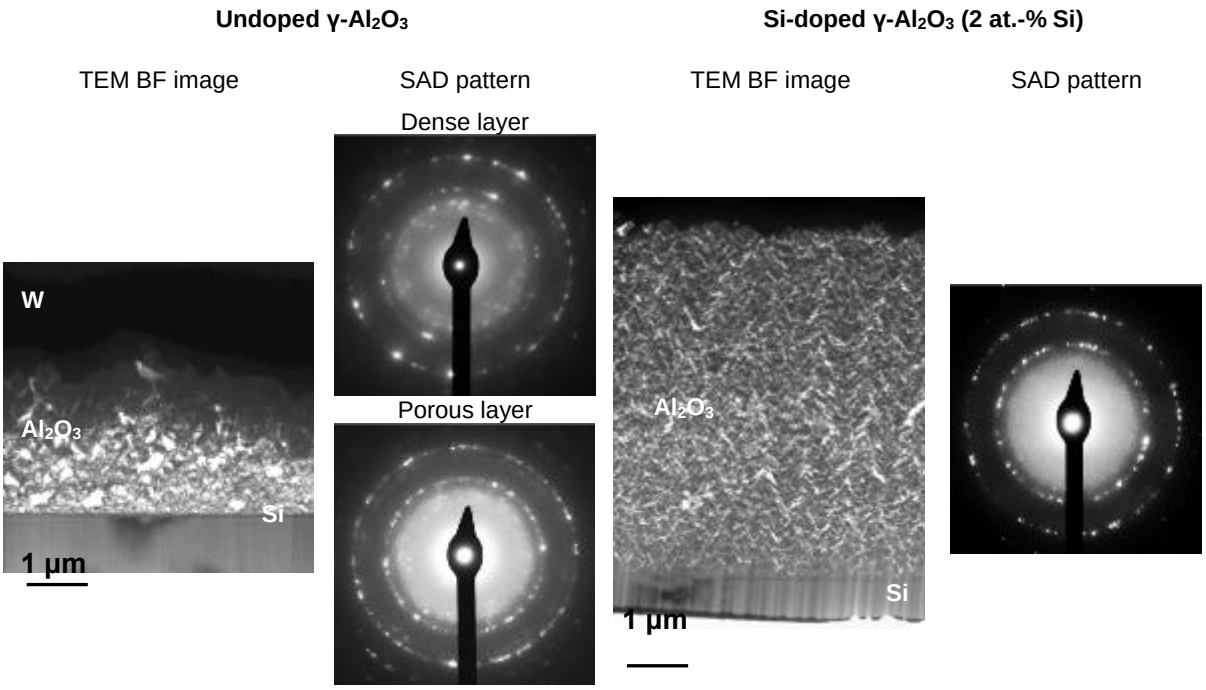

Figure 11. TEM BF overview images of the FIB lamellae of the undoped/Si-doped nanocrystalline Al_2O_3-samples after annealing to 1173.15 K and the corresponding selected area diffraction (SAD) pattern.

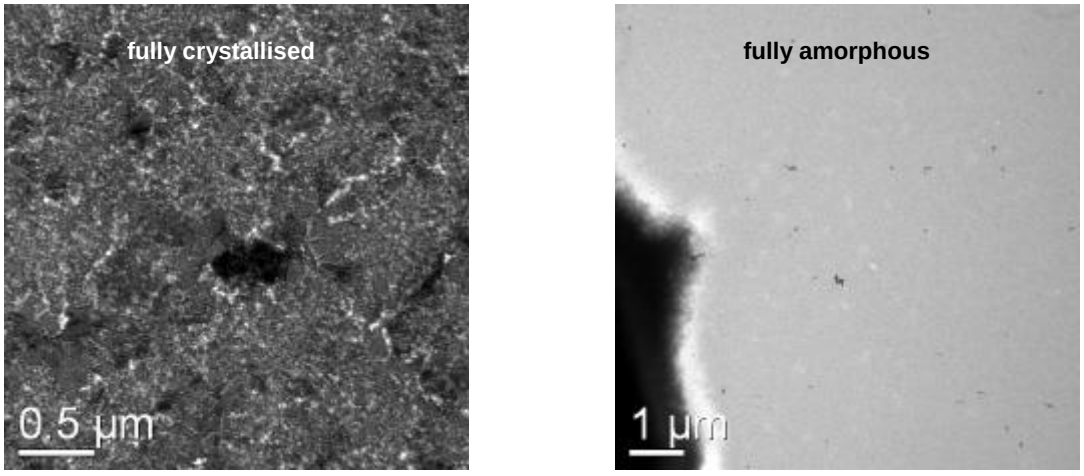

Figure 12. TEM BF images of the annealed undoped amorphous Al_2O_3-sample (923.15 K, on the left) and of the annealed Si-doped (2 at.-% Si) amorphous Al_2O_3-sample (1023.15 K, on the right).

Thin Films and Coatings

MS.5.P143
Nanoscale masking with UV excimer laser for bit patterned media

J. Szívós[1,2], G. Sáfrán[1], M. Serényi[1], E. Gergely-Fülöp[1]

[1]H.A.S., Institute for Technical Physics and Materials Science, Thin Film Physics, Budapest, Hungary
[2]University of Pannonia, Doctoral School of Molecular- and Nanotechnologies, Veszprém, Hungary

szivos.janos@ttk.mta.hu
Keywords: thin films, patterning, nanoscale structures, nano-mask fabrication

In order to pass recent thin film media, bit patterned media (BPM) is a promising candidate for future high density magnetic recording. In spite of a decrease of the domain size, the thermal stability can be improved and media transition noise reduced. There are several techniques targeting the 1 Tbit/inch^2 density (~25 nm dot size) such as electron beam lithography, nanostamping and colloid chemical methods. Our aim was to develop a novel method to prepare nanoscale masks applicable for BPM. Samples were covered with a monolayer of silica nanospheres and treated with UV laser (λ=248 nm) pulses. The intensity distribution of the laser-illuminated area (1.5 cm x 5 cm) has been measured by means of a GaN photodiode and the energy densities required for the formation of the various morphologies were determined. The nanospheres of 300 nm of diameter exhibit hexagonal arrangement as self-assembled by means of the Langmuir-Blodgett (LB) method. The nanospheres act as individual lenses focusing the laser light underneath. This provides highly intense spots for nano-size processing of the sample. Depending on the beam parameters, an ordered array of hillocks, pits or holes of ~120 nm diameter can be molded /Figure 1. (a)/ which are suitable candidates for direct- or mask patterning. Sputter deposited amorphous AlO_x layers, as potential masks, were used for laser patterning. The structure and morphology of the patterned films were characterized by Atomic Force-, and Transmission Electron Microscopy. After the LB film had been removed, as expected from the computer simulation of energy distribution /Figure 1. (a)/, regular patterns of hillocks and holes could be observed depending on the laser intensity /Figure 1. (b), (c) and (d)/. The formation of the observed patterns can be revealed by the cross sectional TEM results shown in Figure 2. An overview in (a) shows hillocks, they seem to be arranged equidistantly (~250nm) on the AlO_x surface at the places of local maxima of the laser pulse. Figure 2. (b) illustrates a hillock. In the formed hillock crystallization event took place with crystallite sizes about 50 nm and the formation of separate, small bubbles indicating moderate energy impact. An increase of the local energy is suggested to ignite plasma and thereafter gas release blowing up large single bubbles as it is demonstrated in (c). Further increase of the local pulse energy causes the burst of the bubble forming a crater at the surface of the AlO_x layer as it can be seen in Figure 2. (d). This refers to a series of holes observed by AFM in Figure 1. (b). The above results show that by applying silica nanosphere LB films and carefully controlled UV laser pulses suitable masks can be fabricated for nanopatterning various thin films including high recording density magnetic media.

1. This work was partially supported by the National Development Agency grant TÁMOP-4.2.2/B-10/1-2010-0025.

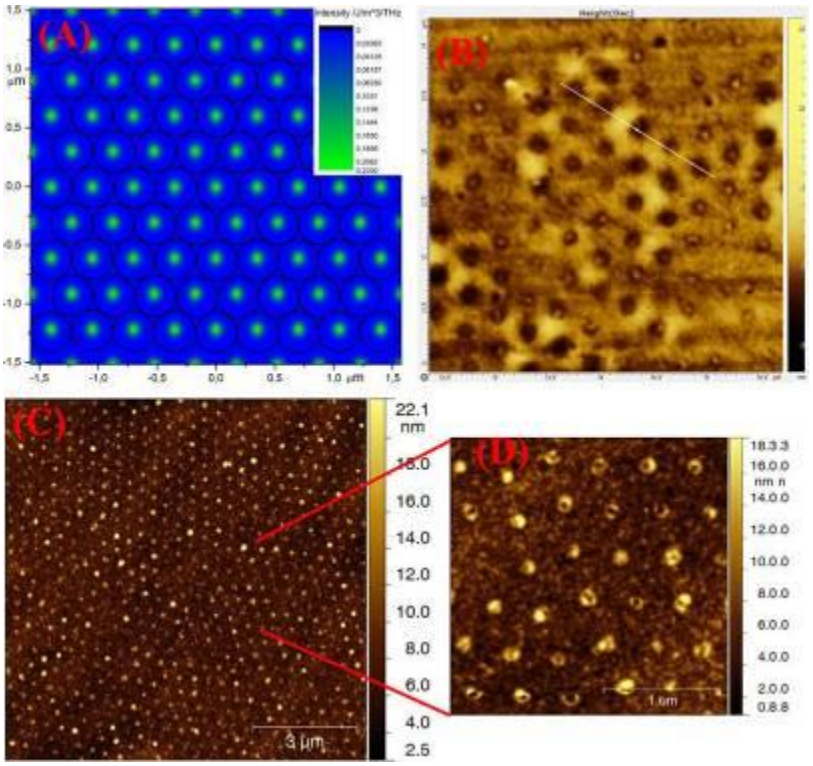

Figure 1. a) Simulation of the energy distribution of UV laser beam focused by self-assembled silica nanospheres; intensity rises from blue to green, b) AFM image of a fabricated hole pattern, c) and d) blown-up and blown-out nano-bubbles in a hexagonal array.

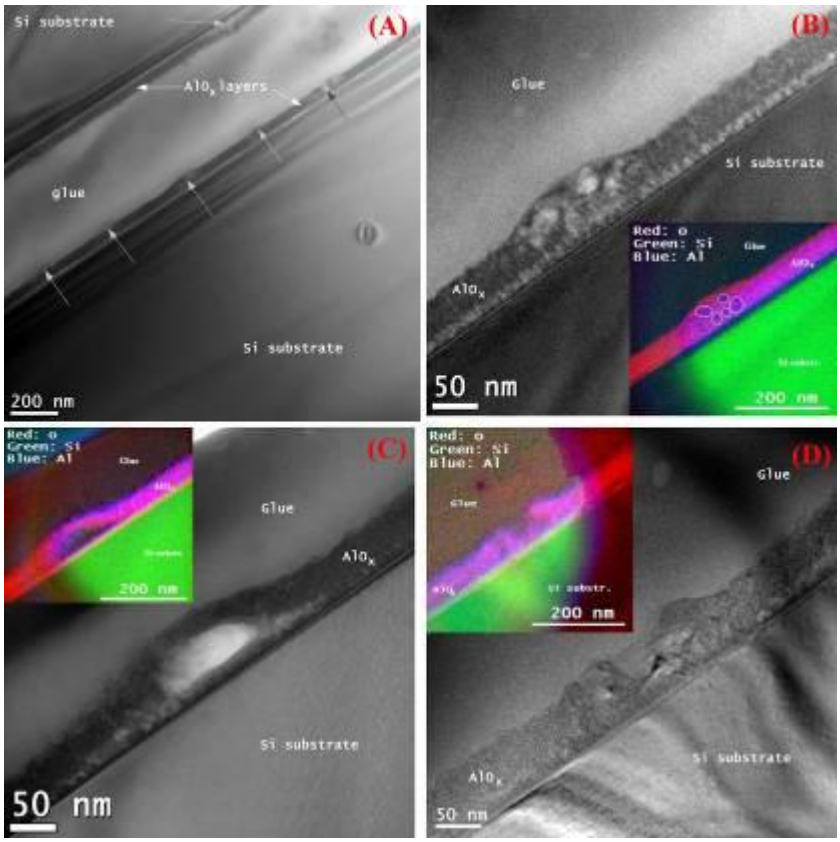

Figure 2. a) Cross-sectional TEM overview of a patterned AlO_x layer. The arrows indicate protruding features. b) A hillock is developed due to local recrystallization and formation of small discrete bubbles. c) Large single bubble due to increased laser energy. d) Cross-section of a crater resulted in a burst of bubble by the further increase of laser energy. The color insets are the EELS elemental maps depicting the distributions of O, Si and Al.

Thin Films and Coatings

MS.5.P144
Polycrystalline to single crystalline, ALD deposited ZnO layers

B. Pecz[1], Z. Baji[1], Z. Lábadi[1], A. Kovács[2]

[1]Institute for Technical Physics and Matl. Sci., Research Centre for Natural Sciences, Hungarian Academy of Sciences, 1121 Budapest, Konkoly-Thege u. 29-33, Hungary, Budapest, Hungary
[2]Ernst Ruska-Centre for Microscopy and Spectroscopy with Electrons and Peter Grünberg Institute, Forschungszentrum Jülich, D-52425, Germany , Jülich, Germany

pecz.bela@ttk.mta.hu
Keywords: ZnO, atomic layer deposition, transmission electron microscopy

ZnO is a wide bandgap (~3.37 eV at room temperature) semiconductor and one of the transparent conductive oxides (TCO) that has recently gained interest in solar cells as a replacement of indium tin oxide. For these kind of applications, the polycrystalline ZnO thin film is usually sputter deposited, but other deposition methods such as metalorganic chemical vapour deposition (MOCVD), molecular beam epitaxy (MBE) and atomic layer deposition (ALD) are applied when ZnO is to be used as a semiconducting layer. The principle of the ALD process is that the precursors are introduced into the vacuum chamber as separate pulses; therefore they only react with one another on the surface of the substrate, never in gas phase [1]. Consequently the growth can be controlled on an atomic level, and the grown layers are extremely conform and uniform. Due to this growth mechanism an epitaxial growth is quite straightforward although ALD is used most commonly for the deposition of oxides, nitrides, and other composite layers. ALD ZnO layers are usually deposited on Si and glass substrates, in which case the grown layers are polycrystalline. The crystalline structure and orientation of ALD ZnO depends on the deposition temperature and the substrate. The preferential orientation is typically (100) at lower deposition temperatures, and (002) above 220°C [2]. So far there have only been a few reports published on ALD deposited epitaxial ZnO layers [3-5] on GaN, or Al_2O_3 (sapphire). (In such a case the method is also called atomic layer epitaxy). In this work ZnO films are deposited using ALD on Si, sapphire and GaN substrates in a Picosun Sunale R-100 type ALD reactor. Di-ethyl Zinc (DEZ) and water were used as precursors for growth of ZnO. The deposition was carried out at 300°C and the nominal thickness of the layers was 40 nm. The grown layers are studied using conventional and aberration-corrected transmission electron microscopy (TEM). High-resolution TEM images were taken in a JEOL 3010 microscope at 300 kV, while the aberration-corrected TEM images were recorded in a FEI Titan microscope operated at 300 kV. The aberration functions were corrected up to fourth order. The spherical aberration function (Cs) was set up to be negative (~ -15 µm) in order to enhance the contrast of the images. The TEM specimens were prepared using conventional method, namely mechanical polishing and Ar ion milling. The specimen preparation process was finished using low-energy (< 1 keV) Ar ion milling in order to reduce the surface damage. Figure 1 is a cross-sectional bright-field (BF) TEM image that shows a ZnO layer grown on (111) Si. The amorphous layer on the Si surface is a native oxide. The growth of ZnO on amorphous SiOx is very similar to the case that the ZnO film is deposited on glass substrate. One can see that grains of ZnO are nucleated with different orientation and the long columns are grown toward the surface. As the method utilises water as oxygen precursor it is very difficult (if not impossible) to get silicon/ZnO interface without an amorphous oxide strip at the interface. Figure 2 is a BF TEM image of ZnO film deposited on single crystalline sapphire. Interestingly the ZnO is polycrystalline again despite the fact that it was grown on single crystalline substrate. The random growth of ZnO grains can be explained this case by the large misfit (15 %) between ZnO and sapphire.Figure 3 is a BF TEM image of an ALD deposited ZnO layer on GaN, which is single crystalline proved by selected area diffraction pattern (not shown here). The Fourier image of this high resolution image also shows a single crystalline like diffraction pattern in which someone cannot distinguish the reflections of GaN and ZnO due to the very small (1.8%) misfit. This study shows, that ALD can provide ZnO layers which are always crystalline, but the epitaxial properties strongly depend on the substrate crystal.

1. S. M. George, Chem. Rev. 110, (2010) 111–131
2. Zs. Baji, Z. Lábadi, Z.E. Horváth, I. Bársony, Thin Solid Films 520 (2012) 4703–4706
3. H.C. Chen, M.J. Chen, T.C. Liu, J.R. Yang, M. Shiojiri, Thin Solid Films 519 (2010) 536
4. L. Wachnicki, T. Krajewski, G. Luka, B. Witkowski, B. Kowalski, K. Kopalko, J.Z. Domagala, M. Guziewicz, M. Godlewski, E. Guziewicz, Thin Solid Films 518 (2010) 4556
5. C.S.Ku, J-M. Huang, C.M. Lin, H.Y. Lee, Thin Solid Films 518 (2010) 1373
6. This work has been supported by the Hungarian National Scientific Research Fund (OTKA) under Grant No. K75735

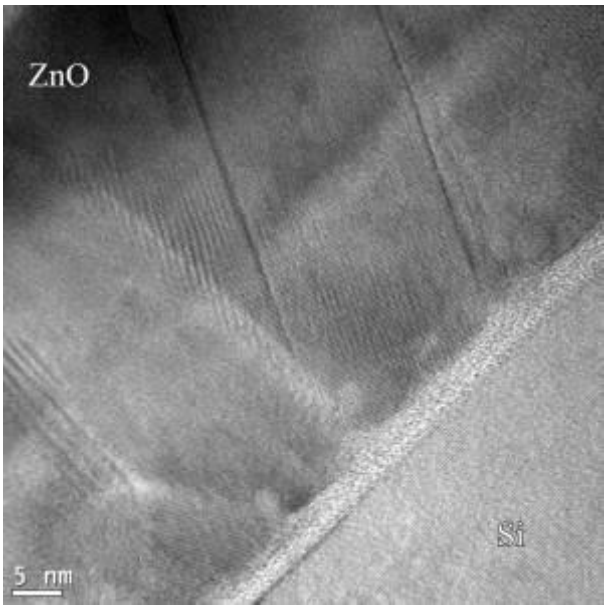

Figure 1. BF TEM image of ZnO deposited on (111) Si.

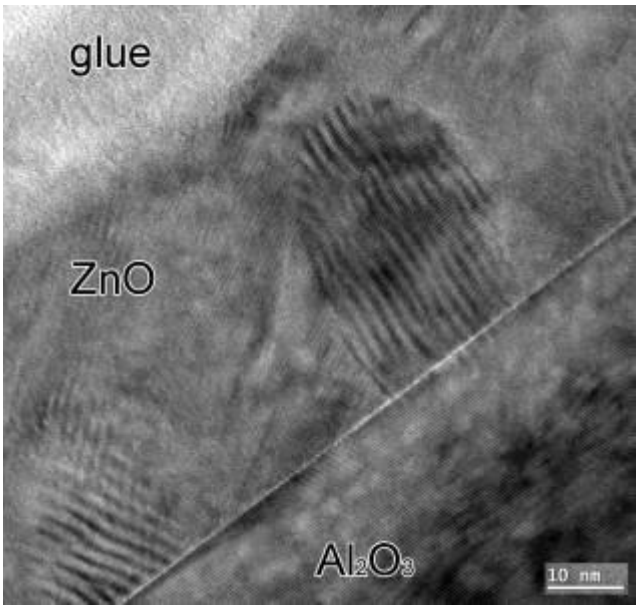

Figure 2. BF TEM image of ZnO deposited on (0001) Al_2O_3

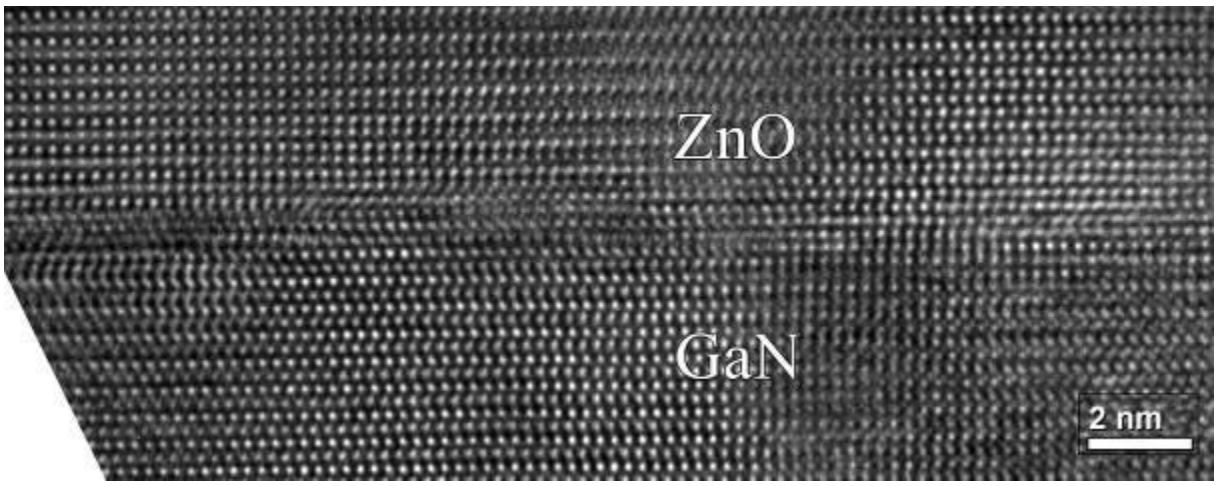

Figure 3. Aberration-corrected high-resolution TEM image showing an ALD grown ZnO on GaN.

Thin Films and Coatings

MS.5.P145
Substrate strain measurements by convergent beam electron diffraction in epitaxially grown $Ba(Fe_{1-x}Co_x)_2As_2$ thin films

P. Chekhonin[1], J. Engelmann[2], T. Gemming[2], B. Holzapfel[2], B. Rellinghaus[2], C.-G. Oertel[1]
W. Skrotzki[1]

[1]Technische Universität Dresden, Institut für Strukturphysik, D-01062 Dresden, Germany
[2]Leibniz-Institut für Festkörper- und Werkstoffforschung Dresden, IFW Dresden, D-01069 Dresden, Germany

paul.chekhonin@physik.tu-dresden.de
Keywords: CBED, strain, thin film, superconductivity

Superconductivity and antiferromagnetism in ironpnictides are affected by chemical doping, stress or strain [1]. Thin film growth on a substrate with slightly different lattice parameters is one way to produce an in-plane strain [2]. Epitaxial $Ba(Fe_{1-x}Co_x)_2As_2$ (Ba122) thin films with x = 0.06 have been produced by pulsed laser deposition (PLD) on a $MgAl_2O_4$ spinel substrate with a 30 nm thick iron buffer layer, also produced by PLD. Because of a small lattice mismatch between unstrained bulk substrate ($d_{100}/4$ = 0.2021 nm), bulk iron (d_{110} = 0.2027 nm) and bulk Ba122 ($d_{100}/2$ = 0.198 nm) strain is introduced to the 60 nm thick Ba122 layer. In addition, on top of the first Ba122 layer a second very thin iron layer (7 nm) and a 55 nm thick Ba122 layer were deposited by PLD (Fig. 1). TEM lamellae were cut by the focused ion beam technique. X-ray diffraction as well as electron diffraction experiments confirmed that the layers were epitaxially grown on the substrate.

It is a major task to clarify, whether the strain state in the Ba122 layer is dictated by the substrate or rather by the iron buffer layer in between. To provide an answer, the convergent beam electron diffraction (CBED) technique [3] in the transmission electron microscope (TEM) with an acceleration voltage of 200 kV was applied.

With the beam close to the spinel [1 12 0] direction Kossel patterns from the substrate were recorded at different distances to the spinel/iron interface. Approaching the spinel/iron interface, major changes are observed (Fig. 2): The higher order Laue zone (HOLZ) lines corresponding to lattice planes with a normal containing a [001] component start to split. HOLZ line splitting can be explained by the bending of the thin TEM lamella due to strain relaxation [4]. However, almost no splitting is observed for HOLZ lines if the corresponding lattice plane normal is close to the [010] direction. Therefore, only the latter HOLZ lines are used for analysis by comparing their change in position with Kossel patterns dynamically simulated with the software TEMStrain developed by A. Morawiec [5]. Two different assumptions are made in the simulation: The first “thin film” assumption considers the specimen as a completely relaxed (very thin) TEM lamella yielding a stress only along the [100] spinel direction. The second assumption considers the TEM lamella as an unrelaxed bulk specimen. Due to specimen symmetry in this case it is assumed that the stresses in the [100] and [010] direction are the same. For both assumptions there are no additional stress components. The change of the distance ratio L1/L2 (Fig. 2) in the measured patterns (as a function of the distance from the spinel/iron interface) and in the simulated patterns (as a function of the in-plane lattice parameter of spinel) is plotted in Fig. 3. To interpret the result, it is necessary to point to the lattice parameter where the simulated ratio L1/L2 is the same as the measured one (dotted lines in Fig. 3). Qualitatively both assumptions show an increase of the in-plane lattice parameters in spinel. Regarding the lattice parameters of the unstrained bulk materials it may be concluded that the 30 nm thick iron layer is not thin enough to adopt lattice parameters somewhere between the spinel substrate and Ba122. As a consequence, the strain in Ba122 is mainly determined by the iron buffer layer and not by the substrate.

1. J. Paglione and R.L. Greene, Nature Physics 6 (2010), 645.
2. K. Iida, J. Hänisch, R. Hühne, F. Kurth, M. Kidszun, S. Haindl, J. Werner, L. Schultz and B. Holzapfel, Appl. Phys. Lett. 95 (2009), 192501.
3. J.C.H. Spence and J.M. Zuo, in: “Electron Microdiffraction”, Plenum Press New York (1992), 125.
4. F. Pailloux, R.J. Gaboriaud, C. Champeaux and A. Catherinot, Mater. Sci. Eng. A288 (2000), 244.
5. A. Morawiec, J. Appl. Cryst. 40 (2007), 618.
Support of this work by the German Research Foundation (DFG) within the framework of the Research Training Group 1621 is gratefully acknowledged.

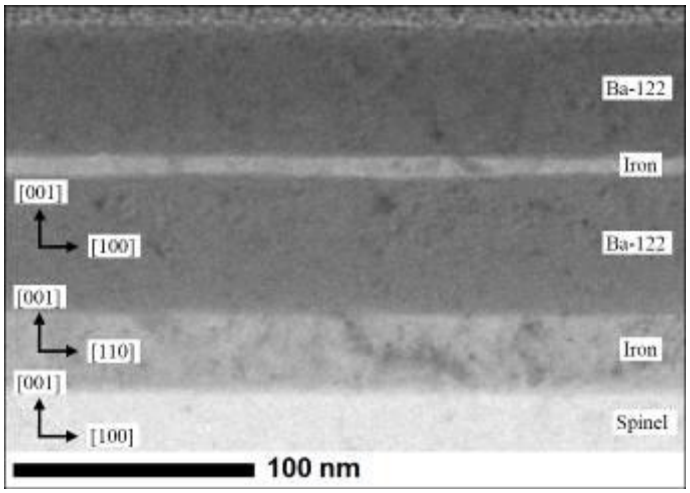

Figure 1. TEM bright field micrograph of the thin film. Beam is parallel to the [010] direction of spinel.

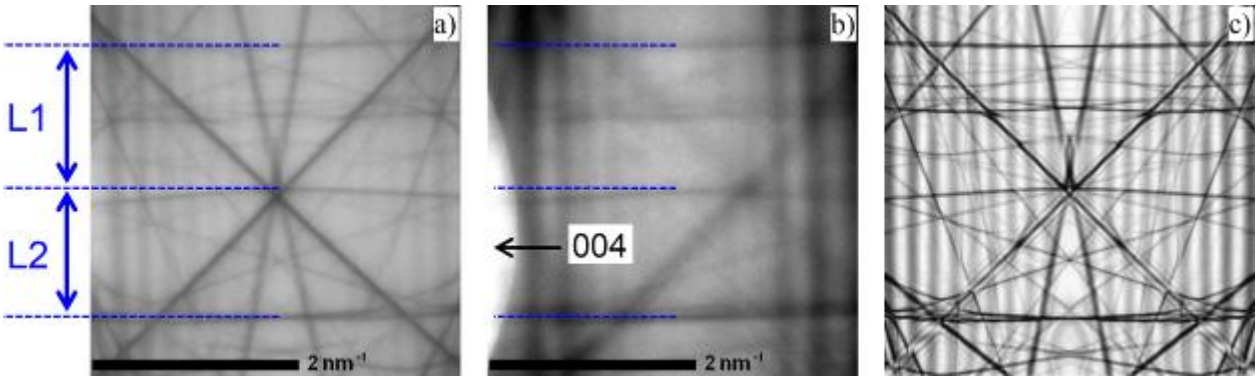

Figure 2. a) Kossel pattern taken 800 nm from the spinel/iron interface, b) Kossel pattern taken 50 nm from the spinel/iron interface and c) dynamically simulated pattern assuming unstrained spinel.

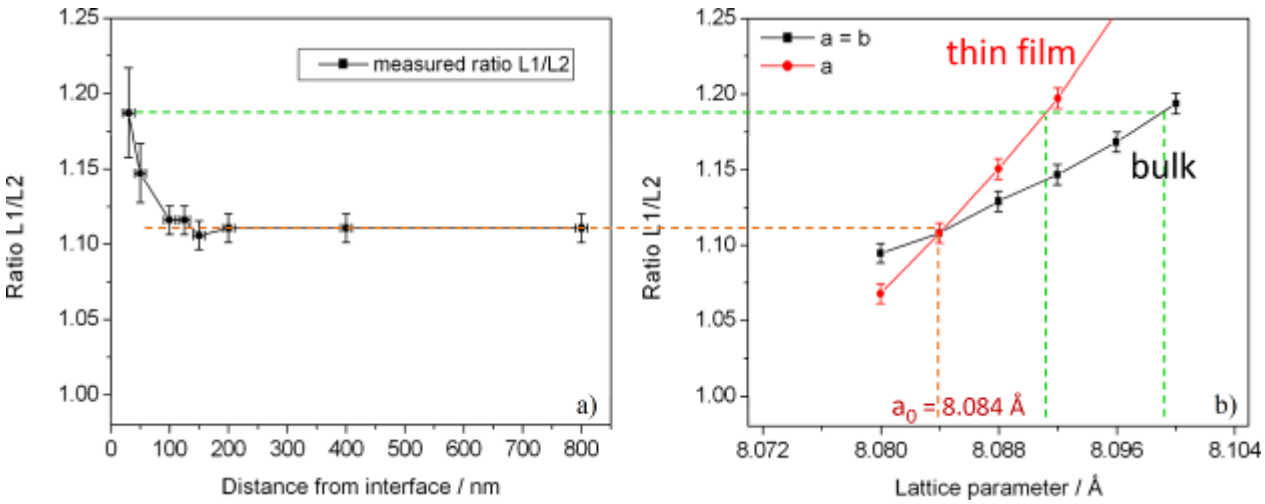

Figure 3. a) L1/L2 ratio of recorded Kossel patterns in spinel as a function of distance from the spinel/iron interface and b) L1/L2 ratio of simulated Kossel patterns as a function of the in-plane lattice parameter of spinel (variation of a = b in the “bulk” and variation of a in the “thin film” assumption).

Thin Films and Coatings

MS.5.P146
Microstructure of nanocomposite TiSiN and nanolayered TiSiN/TiAlN coatings

A. Miletić[1], B. Škorić[1], P. Panjan[2], M. Čekada[2], L. Kovačević[1], P. Terek[1]
[1]Faculty of Technical Sciences, Department for Manufacturing Engineering, Novi Sad, Serbia
[2]Jozef Stefan Institute, Department of Thin Films and Surfaces, Ljubljana, Slovenia

miletic@uns.ac.rs
Keywords: nanocomposite, nanolayered coatings, superhard

During the last few decades, hard coatings have been widely used for protection of mechanical components, particularly to increase the life of cutting tools. Among them, single-layer TiAlN stands up as the most commonly used coating for the protection of cutting and forming tools. TiAlN is based on fcc TiN structure and is characterized by high hardness (around 32 GPa), high stiffness (modulus of elasticity) and high oxidation resistance (up to 800 °C) [1]. Recently, nanocomposite and nanolayered coatings have attracted increasing interest. The most studied TiSiN nanocomposite coating consists of TiN nanocrystals embedded in an amorphous matrix of silicon nitride [2]. This coating exhibits superhardness (higher than 40 GPa) which is attributed to absence of dislocation activity in small crystals and suppression of grain boundary sliding by high cohesion strength between TiN and SiN_x phases. In addition, TiSiN nanocomposite coatings exhibit high oxidation resistance (around 850 °C) and high thermal stability (up to 1100 °C) [2]. Nanolayered coatings are composed of few nanometers thick layers (typically below 10 nm) of two or more different materials (eg. TiN/SiN_x). Their properties depend mostly on thickness of individual layers, number and width of interfaces [3,4].

In this research nanocomposite TiSiN and metastable TiAlN were combined in advance nanolayered TiSiN/TiAlN coating. Single-layer TiSiN and TiAlN were prepared for comparison. All coatings were deposited by magnetron sputtering in an industrial unit equipped with four sources. For the preparation of the TiSiN and TiAlN coatings two TiAl, and two TiSi targets were used, respectively. The nanolayered TiSiN/TiAlN coating was deposited from one pair of TiAl and one pair of TiSi targets positioned on both sides of the chamber. Coating microstructure was analyzed by scanning electron microscopy, conventional and high resolution transmission electron microscopy and X-ray diffraction. Chemical and phase composition were assessed by X-ray photoelectron spectroscopy. Mechanical properties were determined by nanoindentation technique.

According to the results of XRD and XPS measurements it appears that TiSiN and nanolayered TiSiN/TiAlN coatings are nanocomposites composed of crystalline and amorphous phases. The single-layer TiSiN coating is built of TiN crystals embedded in amorphous Si_3N_4 matrix, while the nanolayered TiSiN/TiAlN coating consists of crystalline TiN and Ti1-xAlxN phases along with amorphous Si_3N_4.

Both coatings are characterized by fine-grained morphology as can be seen in Figure 1 and in Figure 2. The TiSiN coating is composed of nanocolumns approximately 4 nm wide and few tens of nanometers long (Figure 1a). The fast Fourier transformation analysis of zones selected in HRTEM image revealed that each nanocolumn is composed of several nanocrystals. The results of FFT analysis of several zones of different nanocolumns are presented in Figure 1b. Nanolayered structure of TiSiN/TiAlN coating can be clearly distinguished from Figure 2. The TiSiN layer blocks the growth of TiAlN crystallites which are equiaxed and size around 5 nm. The SAED patterns shown in the inserts of Figure 1a and Figure 2a confirm nanocrystalline nature of both TiSiN and TiSiN/TiAlN coatings. The diffraction rings correspond to fcc TiN-like phases.

The hardness of 39 GPa was measured on nanolayered TiSiN/TiAlN coating. This is considerably higher from the value of 29.7 GPa which was estimated by applying the rule of mixture for the measured hardness of 46.3 GPa and 25.2 GPa of constituting TiSiN and TiAlN coatings, respectively. This high hardness value is attributed to hindering of dislocation motion due to grain size refinement along with blocking of grain boundary sliding by relatively sharp interfaces.

1. A. Horling, L. Hultman, M. Oden, J. Sjolen, L. Karlsson, Surface & Coatings Technology 191 (2005), p. 384.
2. S. Veprek, M.G.J. Veprek-Heijman, P. Karvankova, J. Prochazka, Thin Solid Films 476 (2005), p. 1.
3. , J.M. Molina-Aldareguia, L. Hultman, Journal of Applied Physics 97 (2005) 114327.
4. S.K. Kim, V. Van Le, Cathodic, Thin Solid Films 518 (2010), p. 7483.
5. This research was supported by the Serbian Ministry of Science and Technological Development and by the Slovenian Research Agency (ARRS) which the authors gratefully acknowledge.

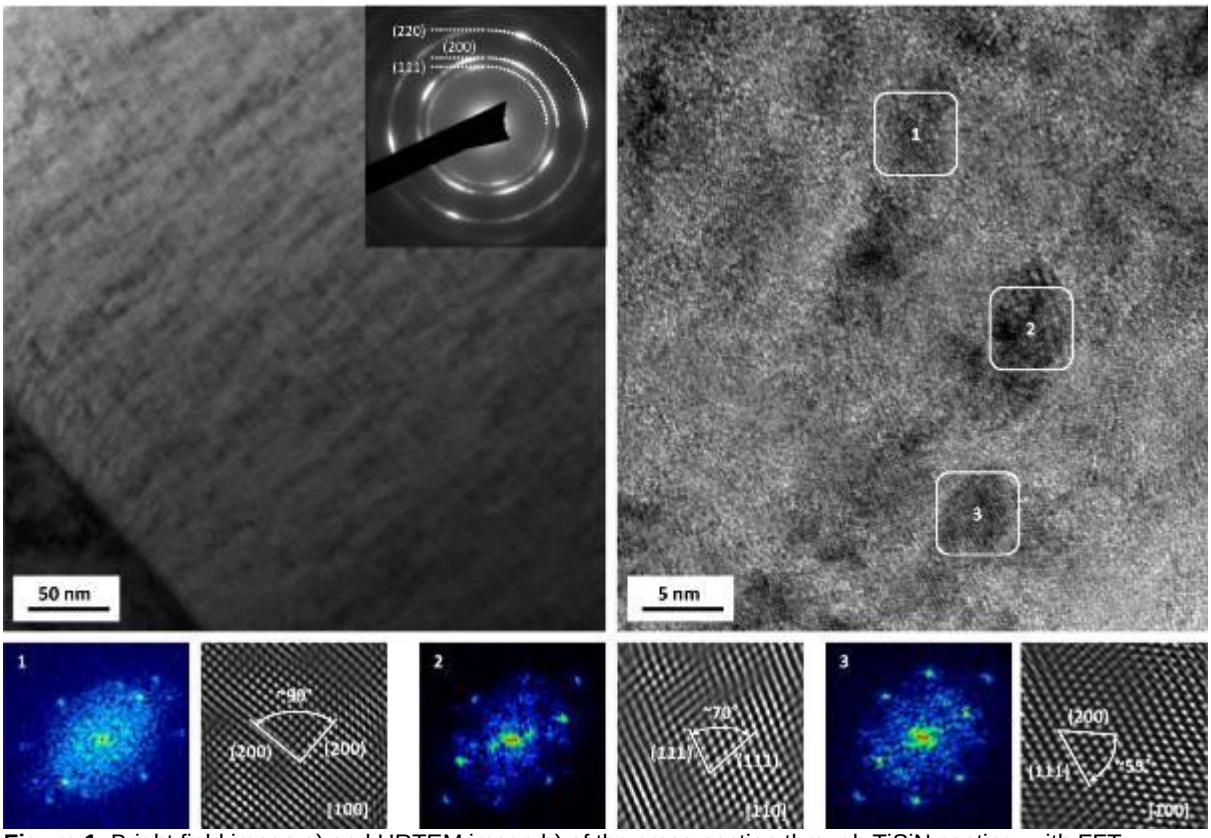

Figure 1. Bright field image a) and HRTEM image b) of the cross-section through TiSiN coating, with FFT patterns along with inverse FFT images. The SAED pattern is included in the figure a).

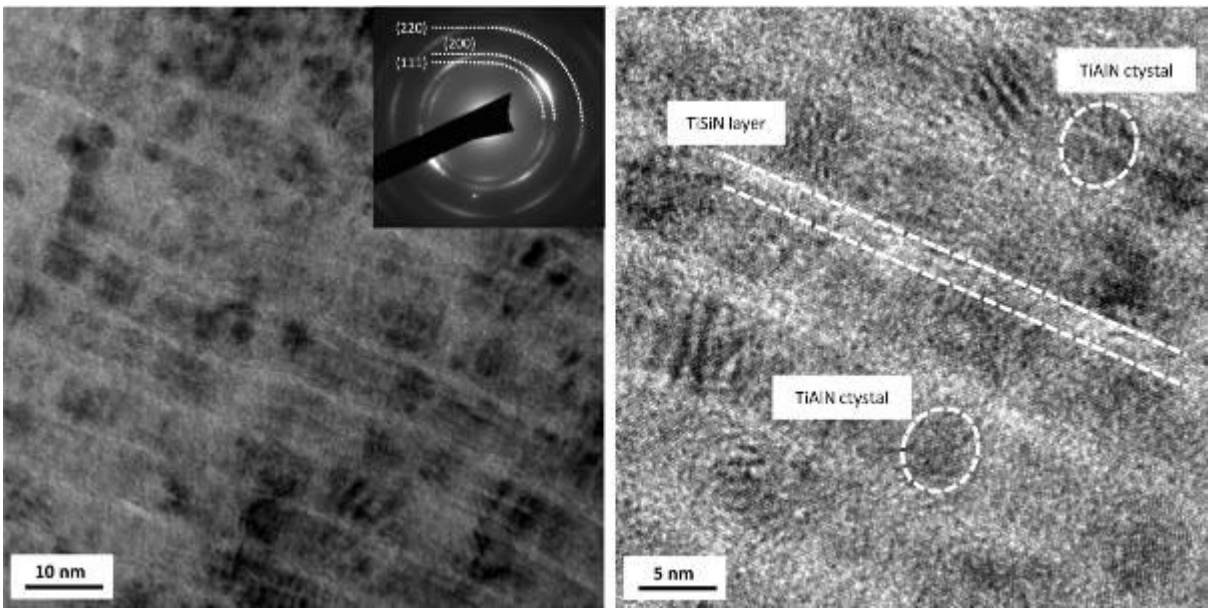

Figure 2. Bright field image along with the SAED pattern a) and HRTEM image b) of TiSiN/TiAlN coating

Thin Films and Coatings

MS.5.P147
TEM characterization of Fe_3Si/Ge/Fe_3Si thin film stacks grown epitaxially on GaAs(001)

B. Jenichen[1], U. Jahn[1], A. Trampert[1], J. Herfort[1]

[1]Paul-Drude-Institut, Berlin, Germany

jen@pdi-berlin.de
Keywords: MBE, spintronics, ferromagnet

Fe_3Si is a ferromagnetic metal with high Curie temperature (576°C) and lattice matched to GaAs and Ge. Fe_3Si films have already been grown on Ge and GaAs substrates by molecular beam epitaxy (MBE). Excellent magnetic properties with a small coercivity (0.9 Oe) and electrical properties with Schottky barrier height of 0.52 eV were obtained.[1,2] Spin transistors, consisting of Ge channel and ferromagnetic source/drain for spin injection were envisaged. Vertical structures like metal/Ge/metal are most promising for next-generation devices. Ge films on Si-terminated Fe_3Si films were recently grown by MBE on Ge(111) substrates.[3,4] In the present work we grow and analyze metal/Ge/metal structures on GaAs(001): Fe_3Si /Ge/ Fe_3Si layer stacks have been grown by MBE. This is an example for the overgrowth of a metal by a semiconductor, a difficult task due to chemical reactivity and poor wetting.

The structures have been characterized by transmission electron microscopy (TEM), electron backscattered diffraction (EBSD), and high-resolution x-ray diffraction (XRD). Interface quality and crystal properties of the films were studied in dependence of the substrate temperature T_S during Ge deposition. The first Fe_3Si epitaxial film on GaAs is always single crystalline. The structural properties of the Ge film and the second Fe_3Si layer depend on the substrate temperature during Ge deposition. Different orientation distributions of the grains in the Ge and the upper Fe_3Si film were found. The lowest substrate temperature T_S = 150°C during Ge deposition ensures smooth interfaces, and intermediate temperatures result in poly-crystalline films with small grain size. Growth at the highest T_S =350°C delivers smooth interfaces and single crystal films in a considerable part of the sample (about 80% of the area as shown by EBSD). In the remaining part however, islands with different crystallographic orientation are formed and the interfaces are damaged by chemical reaction below those islands.

Figure 1 demonstrates the high-resolution TEM image of a sample near the GaAs/Fe_3Si interface. The Ge layer of the sample was grown at the lowest substrate temperature of T_S = 150°C. As demonstrated previously [5] the GaAs/Fe_3Si interface is extremely smooth for the given growth conditions of the first Fe_3Si film. The Fe_3Si/Ge interface above however had a slightly increased roughness. First mono-layers of the Ge film grew well oriented, however the material above was not a single crystal any more. Figure 2 demonstrates the XRD curve of the sample near the GaAs 002 reflection. The curve could be simulated taking into account merely the first Fe_3Si film with a thickness of 9 nm. The contribution of the upper films could be neglected for high-resolution XRD near the GaAs 002 maximum. Although in the sample the upper Fe_3Si film was not single-crystalline as well as the underlying Ge film, the low temperature growth seems to be most promising for technological purposes on a larger scale, as temperature treatment of Ge after growth allows for recrystallization (solid phase epitaxy).

The overgrowth of a metallic Fe_3Si film with a Ge film up to now was demonstrated only recently using a Si-terminated Fe_3Si film on a Ge(111) substrate.[3] We have used the more common 001 orientation of the Fe_3Si film on the corresponding GaAs substrate for the overgrowth. We could avoid chemical reaction with the Ge. The quality of the Ge films largely depends on the substrate temperature during deposition, the structural quality of the following Fe_3Si film is influenced by the parameters of the Ge film itself.

1. M. Miyao, et al. Thin Solid Films 518 (2010), p. 273.
2. J. Herfort, et al. Applied Physics Letters 83 (2003), p. 3912.
3. K. Ueda, et al. Applied Surface Science 254 (2008), p. 6215.
4. S. Yamada, et al. Crystal Growth and Design 12 (2012), p. 4703.
5. J. Herfort et al. Physica E 32 (2006), p. 371

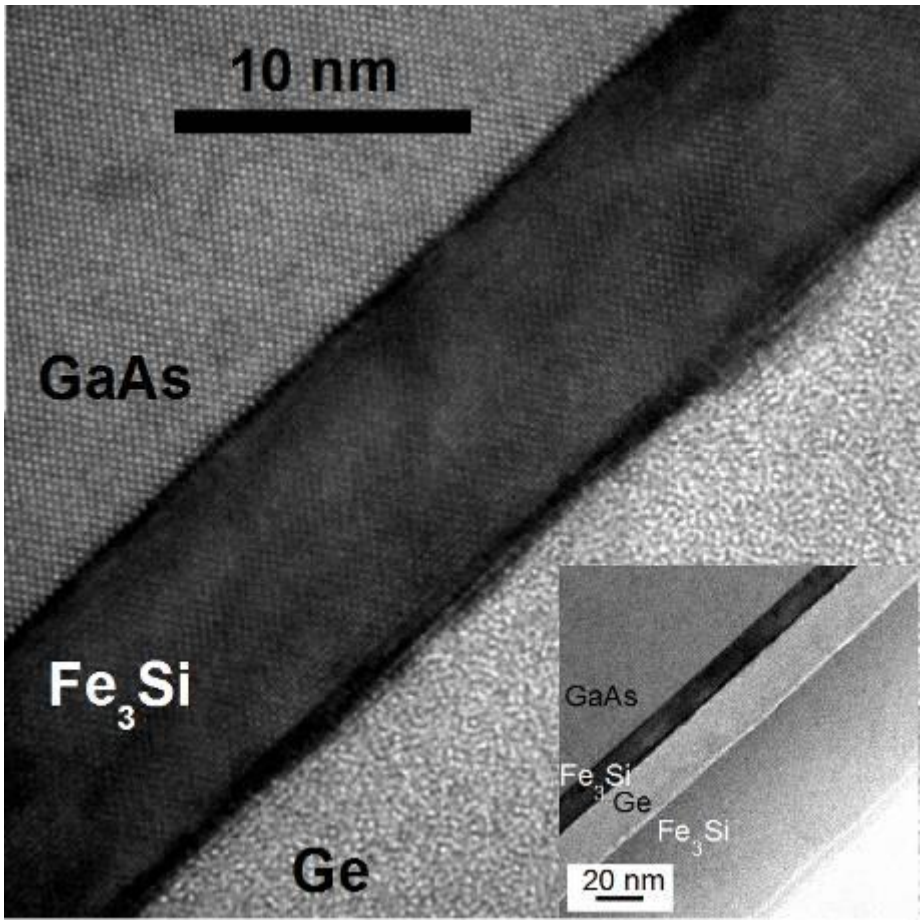

Figure 1. High resolution TEM image of a sample with GaAs/Fe_3Si and the Fe_3Si/Ge interfaces. The Ge layer of that sample was grown at the lowest substrate temperature of T_S= 150°C. The GaAs/Fe_3Si interface is smooth. The Fe_3Si/Ge interface has only a slightly larger roughness than the bottom IF. The inset shows the complete structure at lower magnification.

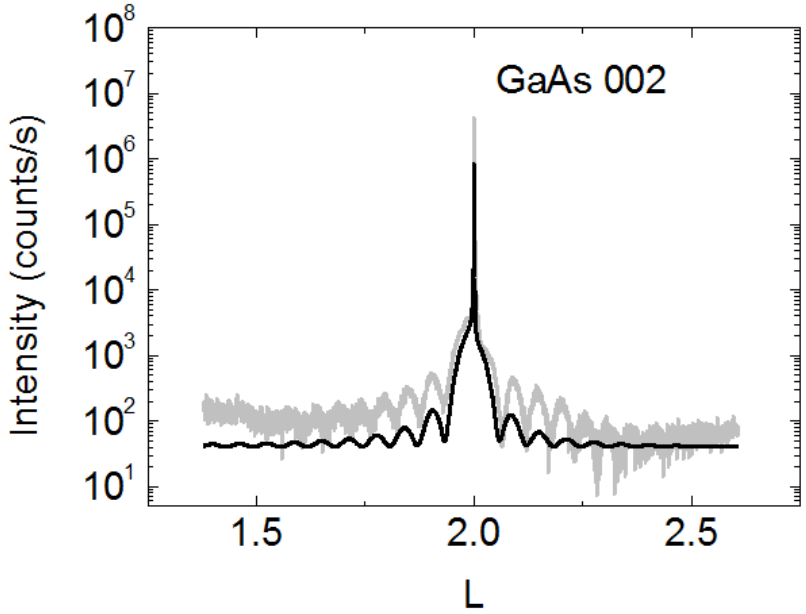

Figure 2. XRD curve of the sample shown in Figure 1 in the vicinity of the GaAs 002 reflection and the corresponding simulation. For the simulation only the first Fe_3Si film of 9 nm thickness had to be taken into account. The upper polycrystalline films could be neglected for high resolution XRD near the GaAs 002 reflection.

Thin Films and Coatings

MS.5.P148
Microstructure investigation of porous gallium-nitride thin films

D. Poppitz[1], A. Lotnyk[1], J. Gerlach[1], B. Rauschenbach[1]

[1]IOM Leipzig, Leipzig, Germany

Keywords: Cs-corrected STEM, FIB, GaN

Gallium nitride (GaN) is a scientifically very interesting and commercially used semiconductor. Because of its wide bandgap of 3.4 eV, GaN is suitable for use in optoelectronic devices. For industrial applications, GaN is usually produced as thin films with different thicknesses and textures. The thin films can be deposited on various single crystalline substrates like sapphire and SiC, where low lattice mismatch epitaxial relationships exist. In the present work, films of GaN were grown on 6H-SiC(0001) substrates by ion-beam assisted molecular-beam epitaxy (IBA-MBE), applying a hyperthermal ion-beam source equipped with an ion-beam focusing, magnetic lens [1, 2]. Using IBA-MBE, GaN thin films with different microstructures can be produced. The aim of this work is to characterize GaN thin films with porous microstructure by transmission electron microscopy (TEM). It should be noted that the porous thin films were deposited directly on 6H-SiC by IBA-MBE.

Focused ion beam technique (FIB) was used for preparation of TEM samples. After the FIB preparation, the TEM lamellae were thinned using focused low-energy argon ion milling in a NanoMill (Fischione) system. The TEM samples were polished in several steps using ion energies in the range from 900 eV to 200 eV. These steps are not only necessary to achieve a sample thickness lower than 30 nm, but also to remove amorphous surface layers and implanted gallium from the FIB process. The FIB lamella was prepared along the a-axis of GaN and 6H-SiC. TEM investigations were performed with a Titan^3 G2 60-300 probe Cs-corrected TEM (Co. FEI) equipped with HAADF, BF, DF, ABF detectors as well as with a Super-X EDX system for energy dispersive x-ray spectroscopy (EDX) and a Gatan imaging filter for electron energy loss spectroscopy and energy filtered TEM analysis. The microscope was operated at 80 kV or 300 kV acceleration voltages.

Figure 1a) shows a scanning electron microscopy (SEM) image of a GaN thin film grown on a 6H-SiC (0001) substrate at a substrate temperature of 750 °C. The film shows a rough and porous surface. The surface topography of the GaN films changes with changing substrate material and substrate temperature. Figure 1b) gives the cross-section of the sample presented in Figure 1a). It is shown, that the pores go through the film down to the 6H-SiC substrate. A similar structures were also observed for GaN thin film grown on 6H-SiC(0001) at a substrate temperature of 850 °C as well as on c-plane oriented sapphire at a substrate temperature of 700 °C and 750 °C. It should be noted that variations of the substrate temperature affect the pore size and shape.

TEM analysis (Figure 2a) confirms that the porous structure is present in the complete GaN film grown on the 6H-SiC substrate. In addition, defect-rich regions exist at the substrate-GaN-film interface. However, above a film thickness of 30 nm the defects density decreases strongly. Further, many stacking faults were observed in the GaN thin films as seen in Figure 2b). Figure 3 gives HRSTEM images of the interface region between the 6H-SiC substrate and the epitaxially grown GaN. Figure 3a) shows an almost defect free interface, where as various defect types like cubic inclusions of GaN, stacking faults and grain boundaries can be seen in Figure 3b). With local EDX analysis, the chemical composition of the GaN was confirmed.

In the present work, the microstructure of porous GaN thin films deposited by IBA-MBE on 6H-SiC were investigated. Using FIB and TEM, it was shown that the pores are present in the complete GaN thin films. HRSTEM studies reveal the defect structure of the GaN film as well as the presence of various defects at the interface between the GaN thin films and 6H-SiC substrates.

1. J. W. Gerlach, T. Ivanov, L. Neumann, Th. Höche, D. Hirsch and B. Rauschenbach, J. Appl. Phys. 111 (2012), p. 113521.
2. L. Neumann, J.W. Gerlach, B. Rauschenbach, Thin Solid Films 520 (2012), p. 3936.
3. The financial support of the European Union and the Free State of Saxony (LenA project) is greatly acknowledged.

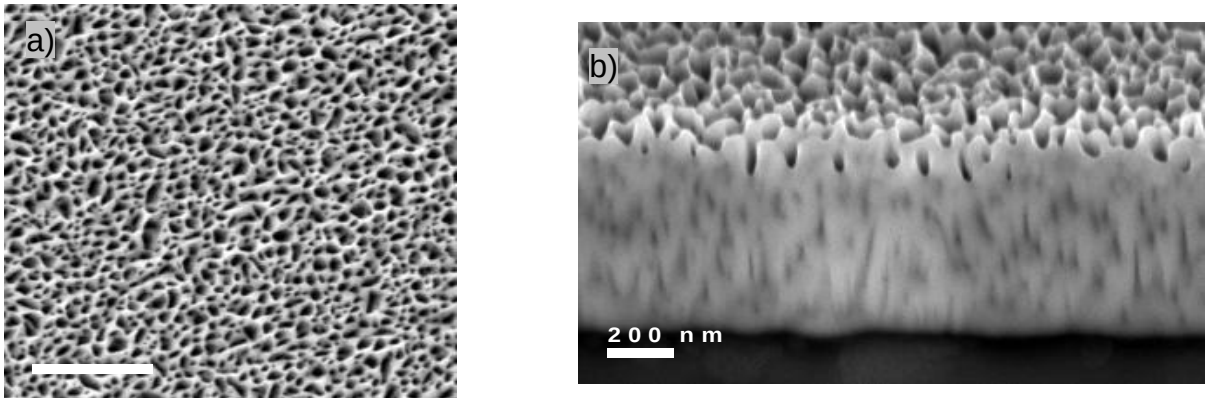

Figure 1. SEM images of a GaN film epitaxially grown by IBA-MBE on 6H-SiC (0001) at 750 °C a) top view on the porous surface topography b) FIB prepared cross-section.

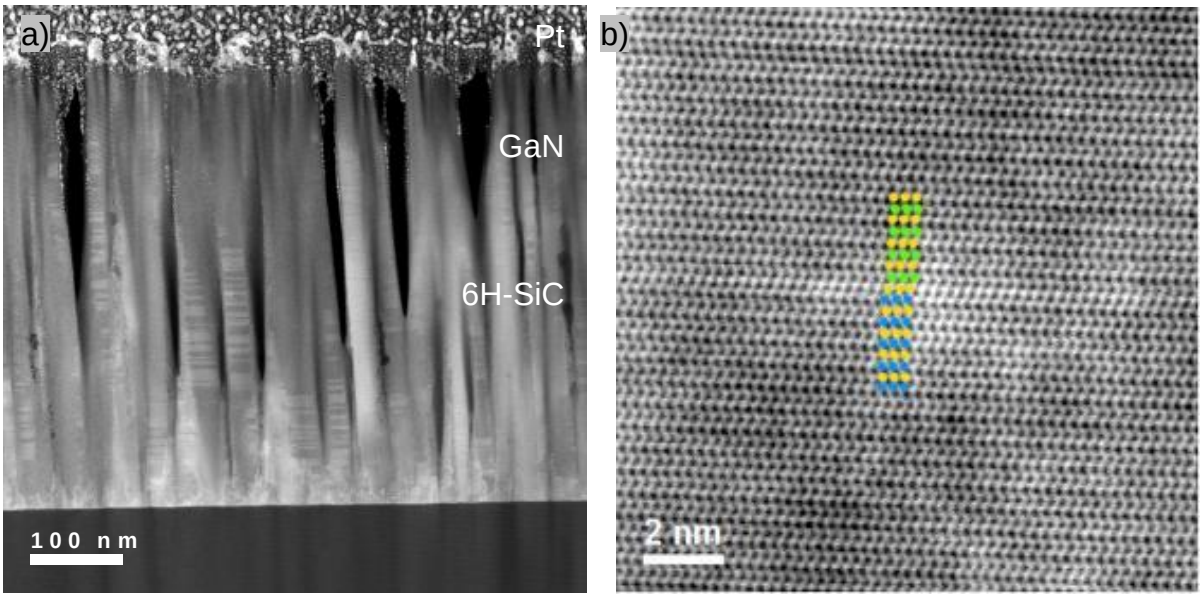

Figure 2. HAADF-STEM images of porous GaN thin films grown on 6H-SiC(0001) at 750 °C substrate temperature a) overview image, b) high resolution image of a stacking fault.

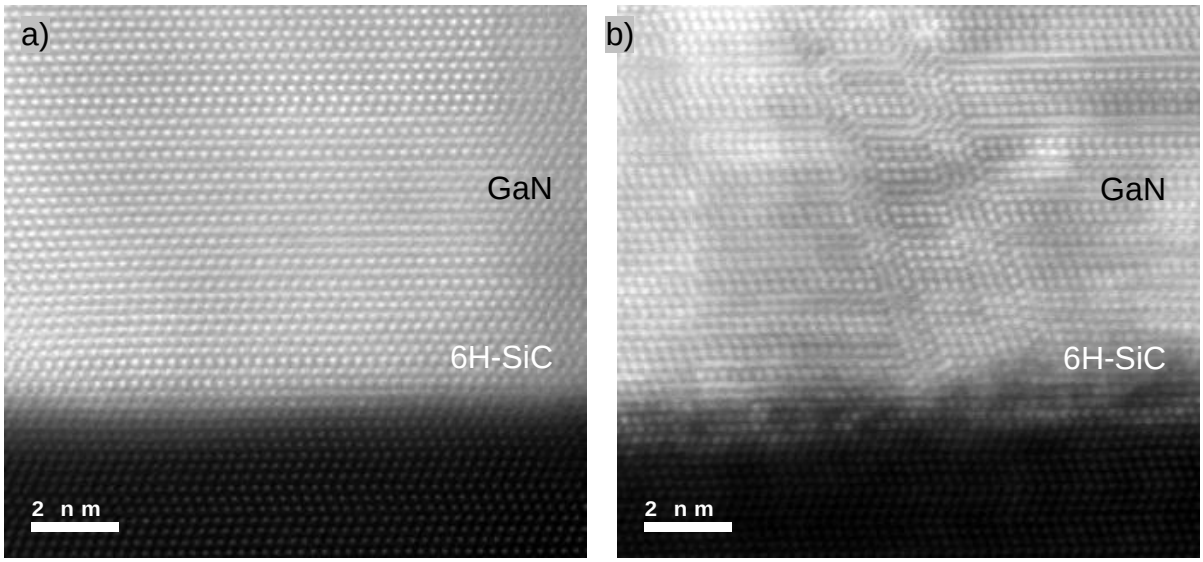

Figure 3. HAADF-STEM images of a) a nearly defect free region of the substrate (6H-SiC)/thin film (GaN) interface, b) another interface region with cubic inclusions and stacking faults.

Thin Films and Coatings

MS.5.P149
In situ and analytical transmission electron microscopy: mechanism of material transport and crystallization during the metal induced layer exchange (MILE)

B. Birajdar[1], S.M. Kraschewski[1], T. Antesberger[2], M. Stutzmann[2], P. Rosner[1], F. Gannott[3]
J. Zaumseil[3], E. Spiecker[1]

[1]Uni-Erlangen, CENEM, Erlangen, Germany
[2]TU München, Walter Schottky Institut and Physics Department, Garching, Germany
[3]Uni-Erlangen, LSP, Erlangen, Germany

Simon.M.Kraschewski@ww.uni-erlangen.de
Keywords: in situ electron microscopy, solar cells, crystallization

When an a-Si/metal/glass stack is heated at a temperature of 400-500 °C diffusion of Si into the metal layer followed by metal induced crystallization takes place eventually resulting in a new stacking order of type (metal+Si)/c-Si/glass with Si grain size up to 250 µm. This surprising phenomenon is called metal induced layer exchange (MILE) and can be exploited for fabrication of polycrystalline semiconductor thin films with great potential for applications in thin film solar cells and transistors. In this work *in situ* analytical electron microscopy is used for the improved understanding of the microscopic mechanism of material transport during MILE.

In our experiments Al or Ag (~50 nm) and a-Si (~100 nm) layers were subsequently deposited on quartz glass using thermal evaporation and electron beam evaporation, respectively [1]. For the TEM studies a CM30 (Philips) and a TITAN^3 80-300 (FEI) equipped with an EDXS detector (EDAX) were used. *In situ* heating of the plan view samples was carried out during light and electron microscopy.

A reflection light microscopy (LM) image of a typical a-Si/Al/glass stack annealed to 10 % layer exchange is depicted in Fig. 1(a). In the LM image primary crystalline Si grains appear dark and dendritic. The sizes of the primary Si grains in the samples range between 5 µm and 50 µm. An Al-K_α STEM EDXS elemental map around a 6 µm large crystalline Si grain marked by a box in Fig. 1 (a) is shown in Fig. 1(b). For various regions marked in Fig. 1(b) the vertical stacking of Al and Si is schematically illustrated on the right of the image. The non-reacted region, marked by the top most box in the right, has the geometry of the starting stack. The box below has the darkest contrast and is therefore almost devoid of Al. It indicates that this region consists of Si in the top layer, as well as in the bottom layer which initially consisted of Al. The third box from the top depicts a region consisting of crystalline Si in the bottom layer and a mixture of Si and nanocrystalline Al in the top layer. In total it can be concluded that the region comprising this early stage Si grain primarily contains Si and is thus severely depleted of Al. The lowest box, which like the topmost box lies in the non-reacted region, depicts an area consisting of Al layer in the bottom layer and Al in the top layer, which we named “push up” Al [1]. Such a push up Al/Al geometry with an epitaxial relationship was confirmed by diffraction contrast microscopy and HRTEM in cross section geometry [1,2].

The influence of a Ti barrier layer between a-Si and Al has been investigated, as it results in Si grain size enhancement up to 250 µm [3]. It was observed that during annealing first the Ti wets some of the Al grain boundaries and forms Ti rich phases there. As a consequence nucleation of Si crystallites is suppressed, which in turn leads to enhanced Si grain size.

In particular Ag metal layer was used to directly visualize the material transport by Z contrast imaging in STEM due to the large difference in atomic numbers of Ag and Si. Figure 2 shows the development of a Si nucleus in plan view HAADF STEM during an *in situ* experiment. Due to the large difference in the atomic number Ag appears bright and Si dark. Like in Al induced crystallization, Si grains are nucleated in the original Ag layer and grow dendritically as the smaller Ag grains were preferentially replaced by Si. In the red boxes of figure 2, it can be seen, that push up Ag appears in the direct vicinity of the Si nucleus and inhibits further growth of the Si nucleus in the radial direction. The radial growth of the c-Si grains takes place predominantly at places where the push up Ag is absent as can be seen in the blue box marked in figure 2. The replaced Ag was observed to concentrate over the larger Ag grains replacing the a-Si which appears to migrate towards the Si crystallites enabling them to grow primarily in the lateral direction. These processes which lead to incomplete layer exchange of the Ag and Si layers were found to depend on the annealing

temperature as well as the grain size distribution in the Ag layer. Lower annealing temperature of 500 °C lead to a more complete layer exchange in comparison to 550 °C annealing temperature.

1. B Birajdar, T Antesberger, M Stutzmann, E Spiecker, Phys. Status Solidi RRL 5, 172 (2011).
2. B Birajdar, T Antesberger, M Stutzmann, E Spiecker, Scripta Materialia 66, 550 (2012).
3. T Antesberger et al., Journal Of Applied Physics 112, 123509 (2012).

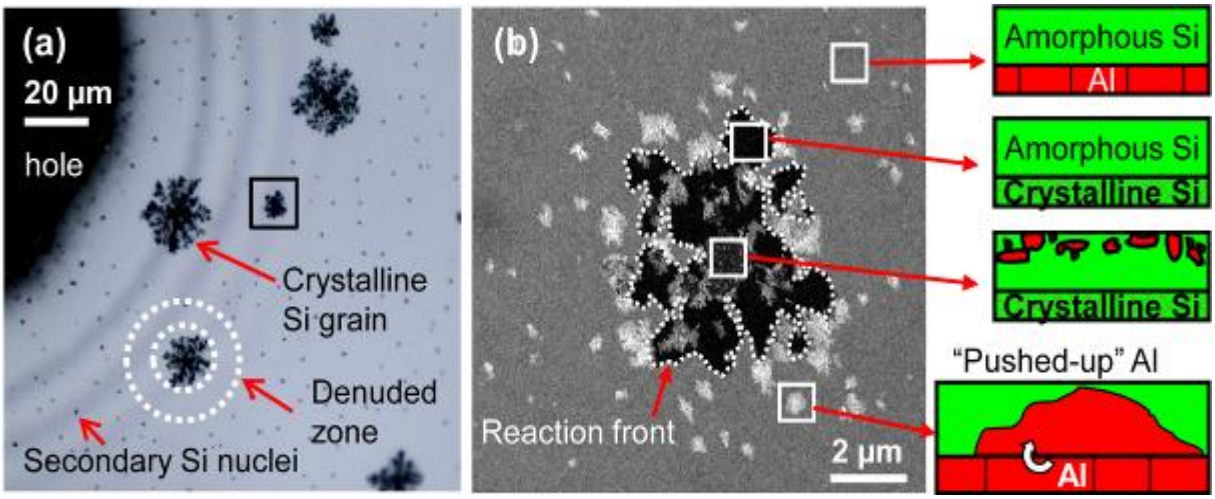

Figure 1.(a) LM image (reflection mode) of a 10 % ex situ reacted plan view TEM sample as viewed from the quartz substrate side. (b) Al K_α STEM EDXS elemental map of the region marked by a box in (a). The schematics of cross-section geometries corresponding to the various regions marked in Fig. 1(b) are shown on the right.

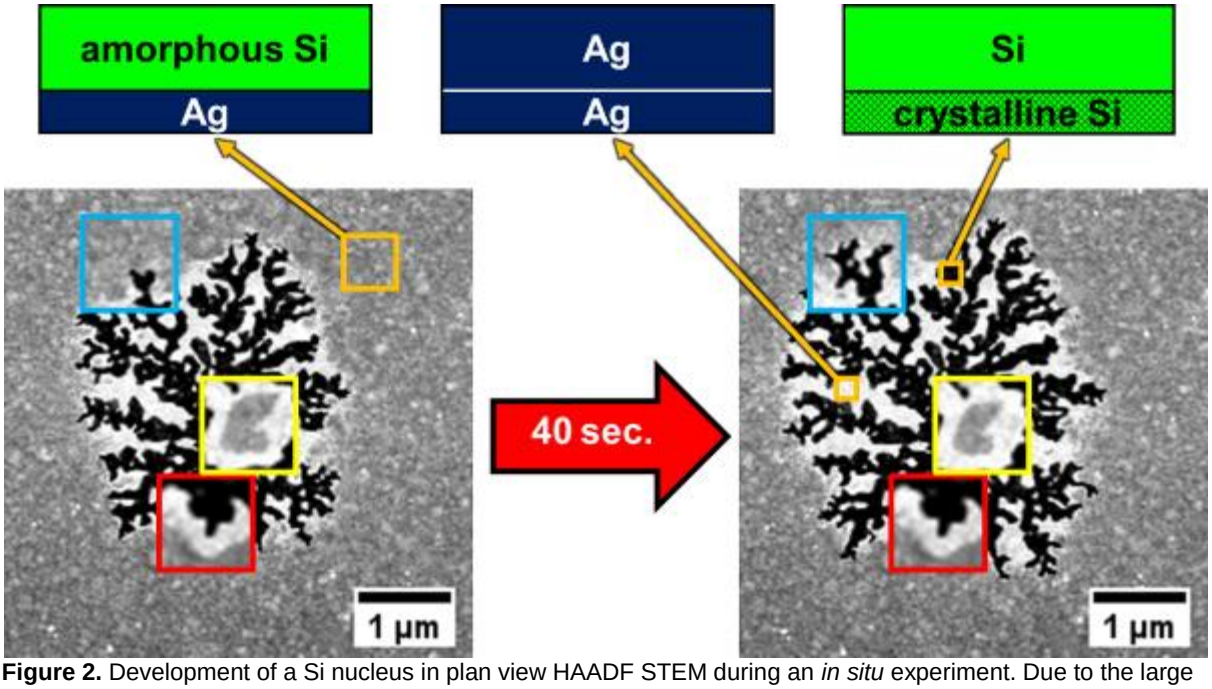

Figure 2. Development of a Si nucleus in plan view HAADF STEM during an *in situ* experiment. Due to the large difference in the atomic number Ag appears bright and Si dark. The red, blue and yellow boxes show enlarged regions indicating different effects during the growth of the Si nucleus.

Thin Films and Coatings

MS.5.P150
TEM/STEM EELS investigation of silicon oxidation under composite ion beam irradiation at room temperature

K. Prikhodko[1], B. Gurovich[1], E. Kuleshova[1], D. Komarov[1], D. Kozlova[1]

[1]National Research Centre "Kurchatov Institute", Moscow, Russian Federation

kirill@irmrnt.kiae.ru
Keywords: ion beam irradiation, silicon oxidation, low energy EELS, EFTEM

Recent time we have developed new technique to oxidize silicon by means of composite ion beam irradiation at room temperature using composite (protons and oxygen) ions ion beams with oxygen concentration ~10^{-4} [1]. To understand the nature of irradiation-induced oxidation at room temperature in this work we performed cross-section EELS TEM/STEM study of microstructure evolution for different ion fluences and irradiation conditions.

The mono-crystal Si (100) wafers were irradiated at room temperature by ions which were extracted from RF plasma by 1 keV pulse HV bias. Composition of the ion beam was controlled by the partial pressure of different gases in discharge chamber. The cross section samples were prepared by the conventional technique by Ar ion milling. The degree of silicon atoms oxidation state was controlled by the position of Plasmon peak of energy loss. EELS spectra were taken in STEM mode to get local information with small probe size.

At the first case we made a gas mixture from pure hydrogen and oxygen gases after deep camber aging ("dry" oxidation). The ion beam composition was controlled by the partial pressure of dry oxygen gas. At this case we have found the formation of porous silicon at the fluence of ~10^{18}cm^{-2} (Figure 1). According to EELS data analysis at this stage of irradiation the thickness of oxide layer did not exceed a few nanometers from the surface. Thus the nano-porous silicon was formed at these irradiation conditions. With increasing of the fluence the oxide thickness increased that is proved by the EELS study across the surface of the sample, but the average pores diameter dropped down and at ~ $1.1 \cdot 10^{20}$cm^{-2} pores disappeared at all and perfect silicon oxide layer was formed.

The second way to form the composite ion beam was to use residual gases in the discharge chamber while the rest was filled with hydrogen ("wet" oxidation). In this case the main residual gas was water because it was really difficult to get water-free conditions without special aging procedures. We didn't find big porous formation in silicon during irradiation in this case. The oxidation was quicker, probably due to the higher diffusion rate of OH ions because their small size, but the final thickness of SiO_2 (in both "dry" and "wet" cases) corresponded to the hydrogen projected range (Figure 2).

To study the depth dependence of pores formation region we performed samples irradiation with 3.8 keV energy ions at "dry" oxidation regime. The depth of pores formation for this energy of ions is more than the corresponded depth for 1keV irradiation (Figure 3). EFTEM O jump ratio map showed non uniform depth distribution of oxidation (Figure 4). The maximum oxygen concentration was observed up to 20 nm from the surface. In this region the silicon was fully oxidised (Si^{+4}) what was proved by the Plasmon peak position at EELS spectra (Figure 5). With increasing of the depth the Plasmon peak position smoothly moved to 16 eV (Figure 5) which corresponds to the virgin silicon (Si^0).

According to our understanding the proton induced vacancy production process played an important role during irradiation-induced silicon oxidation under composite ion beam irradiation. We can compare the experimental integrated EFTEM jump ratio oxygen distribution with the calculated one [2] (Figure 6). It is clear from Figure 6 that together with the presence of direct oxygen implanted area there is an inner maxima at the depth of preferable vacancy production from the proton component of ion beam. Due to the fact that we always observe the silicon oxidation to the depth up to the projected range of protons at high fluencies, we can conclude the radiation nature of the process of silicon oxidation at room temperature under composite ion beam irradiation.

Irradiation-induced silicon oxidation at room temperature can be used in wide range of nanotechnology applications (formation of sensors, transistors, etc.). We are grateful for financial support [3].

1. B.A.Gurovich, K.E.Prikhodko, E.A.Kuleshova, and D.A.Komarov, NIMB (2013). In Press (http://dx.doi.org/10.1016/j.nimb.2012.12.110)
2. Ziegler J.F., Biersack J.P., Ziegler M.D. The Stopping and Range of Ions in Matter, (Morrisville: Lulu Press Co., 2008) (http://www.srim.org)
3. This work is supported by the Russian Ministry of Science and Education (contract No.14.513.11.0008).

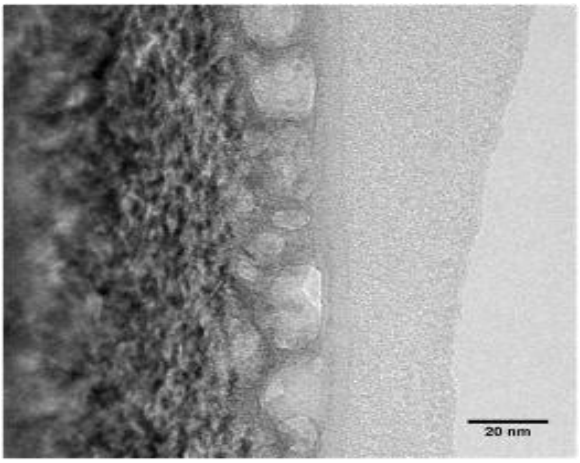

Figure 1. XTEM BF image of Si after 1 keV composite ion beam irradiation up to $9{,}4 \cdot 10^{17}$ cm^{-2} (“dry” regime).

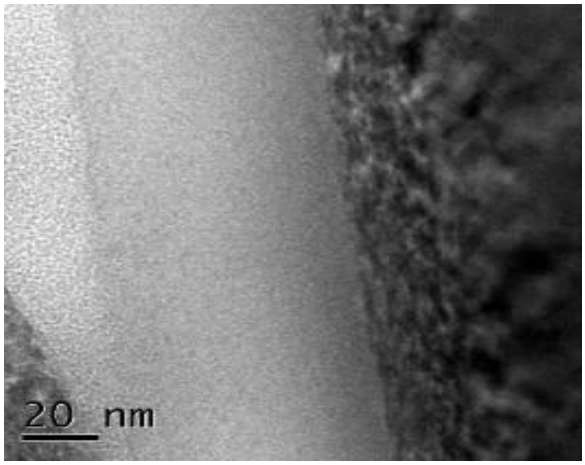

Figure 2. XTEM BF image of Si after 1 keV composite ion beam irradiation up to $1{,}2 \cdot 10^{20}$ cm^{-2} (“wet” regime).

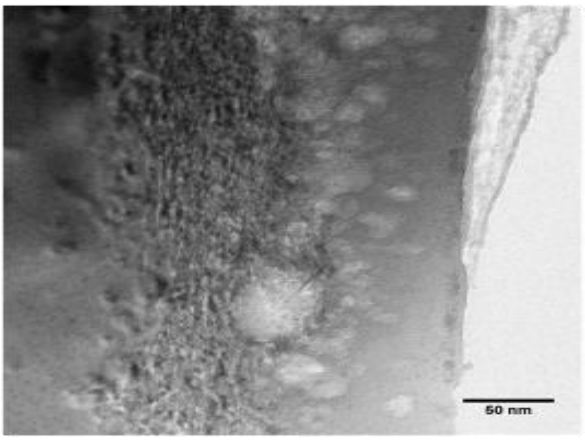

Figure 3. XTEM BF image of Si after 3.8 keV composite ion beam irradiation up to $2{,}9 \cdot 10^{19}$ cm^{-2} (“dry” regime).

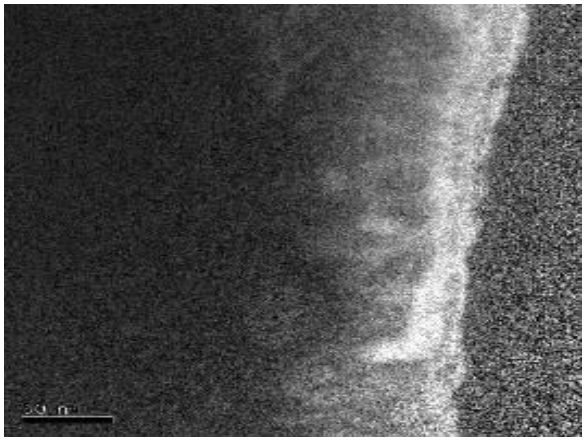

Figure 4. EFTEM oxygen jump ratio map of Si after 3.8 keV composite ion beam irradiation up to $2{,}9 \cdot 10^{19}$ cm^{-2} (“dry” regime).

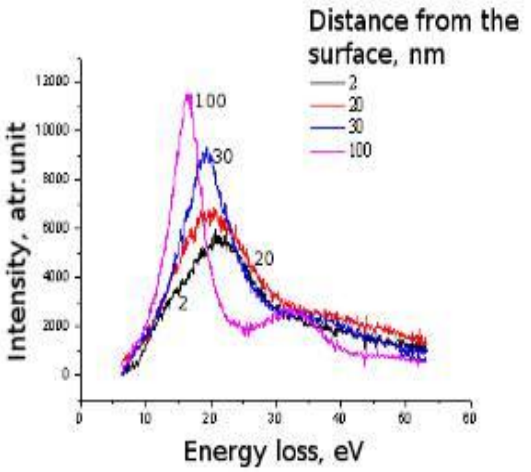

Figure 5. EELS Plasmon peak at different distances from the sample surface after 3.8 keV irradiation up to $2{,}9 \cdot 10^{19} cm^{-2}$ (“dry” regime).

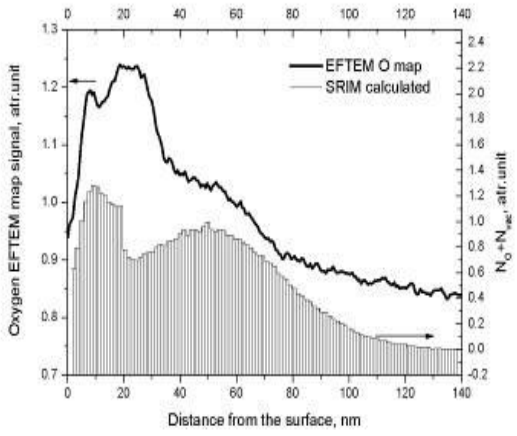

Figure 6. Integral EFTEM O signal from Figure 4 and calculated SRIM [2] distribution of normalised implanted O plus normalised vacancy after 3.8 keV composite ion beam irradiation (not to scale)

Thin Films and Coatings

MS.5.P151
Characterization and optimization of a barium titanate deposition process for fabrication of capacitive microelectrodes

S. Röhler[1], B. Schröppel[1], C.J. Burkhardt[1], A. Stett[1], D.P. Kern[2]

[1]NMI Natural and Medical Sciences Insititute, Reutlingen, Germany
[2]University of Tübingen, Institute of Applied Physics, Tübingen, Germany

This work presents high-resolution imaging and quantitative analysis of insulators with different analytical probes. Our aim is to develop a thin layer fabrication process for capacitive microelectrodes for neurotechnological applications. We use focused ion beam (FIB) milling to prepare lamellas for transmission electron microscope (TEM) imaging. The surface topography is measured with atomic force microscopy (AFM). To determine the atomic composition of the fabricated thin layers energy-dispersive and wavelength-dispersive X-ray spectroscopy (EDX and WDX) measurements are performed. Comparison of the AFM data with images acquired with helium ion microscopy (HIM) is in progress.

Due to continued miniaturization of implantable neural prosthetics the treatment of diseases where neural defects are involved is being improved. Deep brain stimulation is used to suppress Parkinson's disease [1], cochlear implants treat deafness [2] and retina stimulators are used to restore vision in blind patients [3]. These devices are equipped with electrodes that are in contact with the adjacent tissue. By applying voltage signals to the electrodes extracellular currents are generated to stimulate neurons. The electrodes of such implants must not degenerate while they are in use in order to achieve long-term stability. Any type of electrically induced corrosion must be suppressed. This can be achieved by using capacitive microelectrodes where faradaic (i.e. direct) currents are completely blocked. In in-vitro experiments it is possible to stimulate neurons with capacitive currents with spatial resolution down to 50 µm [4].

Capacitive microelectrodes are fabricated by depositing a thin insulating layer on top of a metallic electrode. Thereby the electrode is galvanically insulated from the tissue while capacitive charge transfer is still possible. Figure 1 schematically shows an in-vitro experiment where capacitive microelectrodes are used to stimulate neurons. By increasing the specific capacitance of the electrode (i.e. capacitance per area) the electrode size can be decreased whereby the spatial resolution is increased. Because of its high permittivity we chose barium titanate ($BaTiO_3$) that is deposited in an RF sputter process. For layers thinner than 1 µm permittivities of up to 700 are reported [5].

Table 1 shows the permittivity and the capacitance of a thin layer of sputtered $BaTiO_3$ after different annealing temperatures. Because of the low permittivity of the sample annealed at 200°C it must be assumed that it is not in a ferroelectric phase. This presumption is confirmed by the fact that in the TEM image (figure 2) no grains are visible in this $BaTiO_3$ layer. The critical grain size for ferroelectric behaviour of nanocrystalline $BaTiO_3$ samples is 10 – 30 nm [6]. AFM measurements (figure 3a) show that the surface is very smooth compared to a sputtered platinum layer (figure 3b) where the grains are clearly visible.

In EDX spectra the L series of barium overlaps with the K series of titanium (figure 4). Hence we used WDX to determine the composition of the sputtered layers because of its higher energy resolution. This analysis revealed that the compounds are very close to the stoichiometric ratio. No impurities could be detected.

Currently we are investigating whether it is possible to fabricate polycrystalline layers by varying the annealing process and changing the sputtering atmosphere. We expect to increase the permittivity by increasing the grain size. TEM images of these samples will be presented.

1. H. C. Walker, et al., J. Neurophysiol. 105 (2011), pp. 1112-1121.
2. B. S. Wilson, M. F. Dorman, Hearing Research 242 (2008), pp. 3-21.
3. E. Zrenner, et al., Proc. R. Soc. B 278 (2011), pp. 1489-1497.
4. M. Eickenscheidt, et al., J. Neurophysiol. 107 (2012), pp. 2742-2755.
5. A. Ianculescu, et al., J. European Ceram. Soc. 27 (2007), pp. 1129-1135.
6. Z. Zhao, et al., Phys. Rev. B 70 (2004), p. 024107.
7. This work was supported by the Federal Ministry of Education and Research (BMBF), grant 01GQ0834 (Bernsteinfocus Neurotechnology: Hybrid brain).

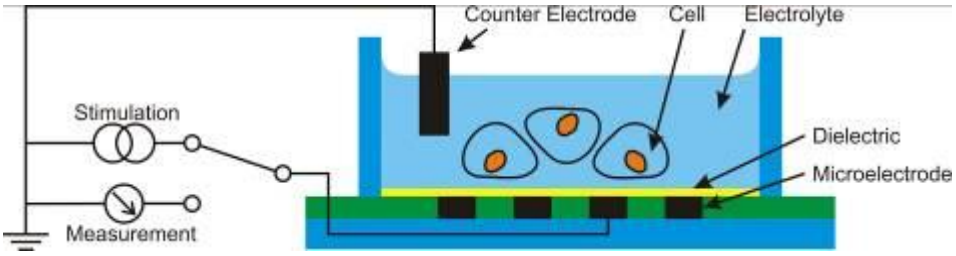

Figure 1. Schematic cross-sectional view of an in-vitro experiment in which capacitive microelectrodes are used.

Annealing temperature	200°C	400°C	600°C	800°C
Capacitance (µF/cm²)	0,167 ± 0,004	0,495 ± 0,015	1,069 ± 0,015	1,871 ± 0,047
Permittivity	15,1 ± 0,3	44,7 ± 1,3	96,6 ± 1,3	169,1 ± 4,2

Table 1. Measured capacitance and permittivity for $BaTiO_3$ thin layers (thickness: 80 nm).

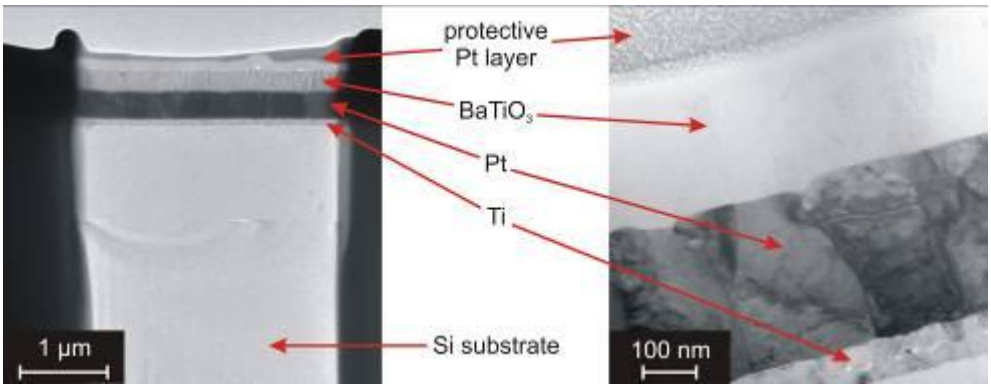

Figure 2. Brightfield TEM images of a Ti-Pt-$BaTiO_3$ layer stack annealed at 200°C after FIB sample preparation.

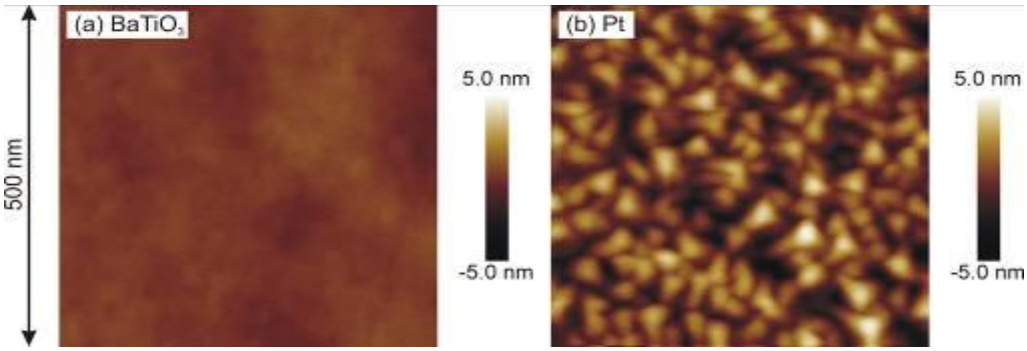

Figure 3. AFM topography measurements of $BaTiO_3$ (a) and Pt (b) for comparison.

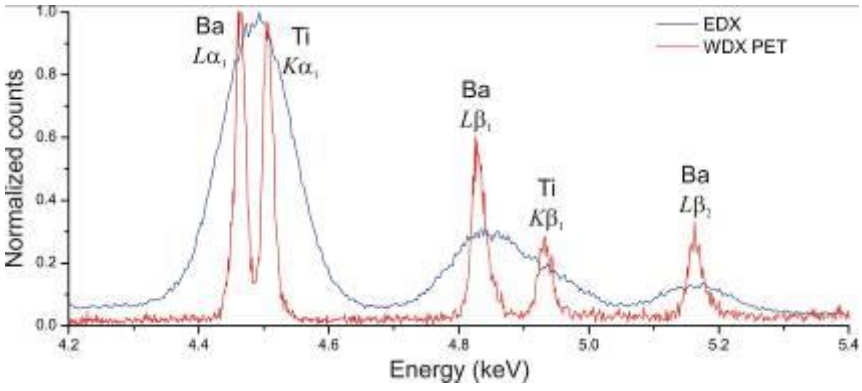

Figure 4. Comparison of EDX and WDX spectra of $BaTiO_3$

Thin Films and Coatings

MS.5.P152
In-situ inspection of nanogap structures fabrication by electromigration.

K. Bejtka[1], A. Chiodoni[1], P. Motto[2], I. Rattalino[1], G. Piccinini[2], D. Demarchi[2], C.F. Pirri[1,3]

[1]Italian Institute of Technology, Center for Space Human Robotics, Torino, Italy
[2]Politecnico di Torino, Department of Electronics, Torino, Italy
[3]Politecnico di Torino, Department of Applied Science and Technology, Torino, Italy

katarzyna.bejtka@iit.it
Keywords: electromigration, EIBJ, nanogap, electron microscopy

The fabrication of nanogaps has generated much interest for applications in molecular electronics, plasmonics, single molecule analysis and detection. A nanogap consists of a pair of metal electrodes separated by a nanoscopic space. A number of methods for fabricating nano-gap electrodes has been demonstrated, such as mechanical break junction, electrochemical deposition, electromigration and Focused Ion Beam (FIB). Electromigration induced break junction was established as an effective technique for nanogap fabrication between 1 and 30 nm in width, due to its reliability, reproducibility and high throughput capability [1]. This process is driven by the mass transport generated by the migration of ions in metals (e.g. in a metal wire), due to the momentum transfer between conducting electrons and diffusing metal atoms. The accumulation of ions at the anode and the void generation at the cathode can result in nanogap formation.Various models were developed to describe the electromigration process [2], they however use the information on the final shape and dimension of the gap as input parameters, and do not consider the behavior of the structure that is forming during the process. This work focuses on the in-situ monitoring by Scanning Electron Microscopy (SEM) of the electromigration process during the formation of nanogaps. This procedure leads to an improved understanding of the mechanism of the process and the behavior of the metal wire during the electromigration. Figure 1a shows a chip containing 8 micro-wires, which are designed to perform the fabrication of 8 nanogaps. The electromigration process is controlled by a custom-made electronic board [3]. While the voltage increases, the current is continuously measured. The values of the current and the resistance over time are used to take control decisions on the voltage applied. If the rate of electromigration is too fast, the voltage is reduced in order to slow down the wire deepening and avoid thermal run away and melting. This process is repeated until eventually the wire breaks into two parts, which are separated by a nanogap. The electromigration process was performed and inspected in a Zeiss AURIGA CrossBeam FIB/FESEM Workstation electron microscope. Kleindiek micromanipulators with tungsten tips were used to contact the sample with the electronic board [Figure 1b]. During the process, it was observed that initially the wire is thinning and holes are created at the grain boundaries that are present in the metal structure. The expected behavior is that nanogaps are normally created at this location, however, it was also observed that some of the openings slightly re-close after some time. The narrowest point of the gap remains at this location. Figure 2 shows the created nanogap at a magnification of 350 kX. The nanogap is visualized as a narrow break perpendicular to the wire longitudinal axis, approximately 5 nm in width in this case. The proposed results can be used for the validation of existing models.

1. Z.M. Wu, M. Steinacher, R. Huber and M. Calame, Appl. Phys.Lett. 91 (2007), p. 053118.
2. I. Rattalino, P. Motto, G. Piccinini and D. Demarchi, Physics Letters A 376 (2012), p. 2134.
3. P. Motto, A. Dimonte, I. Rattalino, D. Demarchi, G. Piccinini and P. Civera, Nanoscale Research Letters 7 (2012), p. 113.

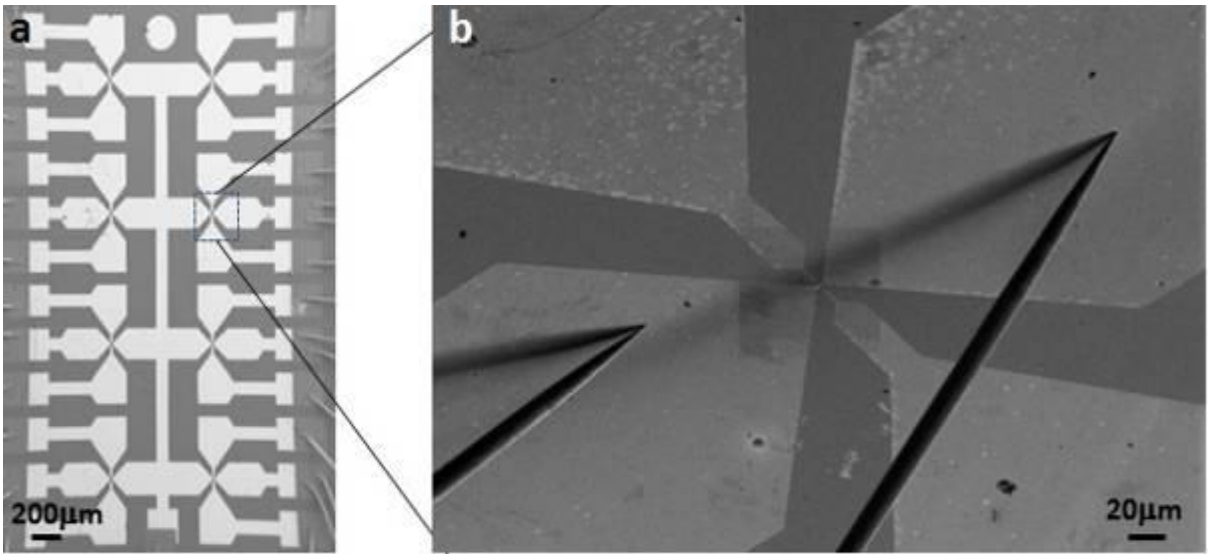

Figure 1. (a) FESEM micrograph showing the chip containing 8 micro-wires, (b) FIB micrograph showing the tungsten tips placed on the pads for electromigration.

Figure 2. FESEM micrograph showing the nanogap.

Thin Films and Coatings

MS.5.P153
Characterizing the atomic and electronic structure of the defects in CrN films by advanced TEM

Z. Zhang[1], R. Daniel[2], C. Mitterer[2], G. Dehm[1,3]

[1]Erich Schmid Institute of Materials Science, Austrian Academy of Sciences, Leoben, Austria
[2]Montanuniversität Leoben, Department of Physical Metallurgy and Materials Testing, Leoben, Austria
[3]Montanuniversität Leoben, Department of Materials Physics, Leoben, Austria

zaoli.zhang@oeaw.ac.at
Keywords: C_S-corrected HRTEM, EELS, electron diffraction,

Transition metal nitrides (TMN) have found wide-spread applications in the cutting- and machining-tool industry due to their extreme hardness, thermal stability and resistance to corrosion. The increasing demand of these nitrides requires an in-depth understanding of their structures at the atomic scale. This has led to numerous experimental and theoretical researches. Among TMNs, CrN exhibits fascinating structural, magnetic, and electronic properties that are of fundamental importance to condensed-matter physics [1-6]. Detailed studies of the structure of CrN will definitely reveal its unique property. On the other hand, it is inevitable to generate structural disorders during film deposition, where various defects can be introduced. Apparently, these defects involved will influence the properties of CrN films. Recently available aberration corrected TEM enables quantitative characterization and evaluation of materials structure. In this study, we apply C_S-corrected HRTEM, quantitative electron diffraction, and EELS analysis to understand the intrinsic structure of CrN films. The films used in this study were deposited by reactive direct current magnetron sputtering of a Cr target in an Ar+N_2 atmosphere at a constant total pressure of 1 Pa, a target power of 6 kW, and a temperature of 350°C.A TEM/STEM JEOL 2100F operated at 200 kV and equipped with an image-side C_S-corrector and a Gatan imaging filter (Tridiem) was used to characterize the film structure.

A comparative study is carried out. The first part of this paper will be ordered defects, i.e. nitrogen (N) vacancies, which were found at the Cr/CrN interface during growth of CrN on a Cr interlayer, used to provide sufficient adhesion to the Si(100) substrate. These ordered N vacancies result in formation of numerous stacking faults, which are accompanied by strong distortions in the crystal structure and a reduced lattice constant. The strain measurement indicates an isotropic distribution within the N-deficient layer (Figure 1). By a combination of HRTEM, EELS and ab-*initio* calculations, atomic and electronic structures are clarified. Moreover, a generalized relationship between the lattice constant and N vacancy concentration in CrN is established [5].

The second part is about randomly distributed defects in the films introduced during film deposition which are frequently encountered. To explore the defects in a quantitative way, a specimen consisting of three sublayers deposited under different substrate bias voltages, i.e. -40, -80 and -120 V, and having each 1 µm thickness, was chosen for visualizing the structural inhomogeneity. The cross-sectional bright field image shows no clear interface between the layers. Apart from C_S-corrected HRTEM image analysis, quantitative electron diffraction analysis was also performed. It reveals that the intensity ratios of (111), and (200) reflections (I_{111}/I_{200}) sensibly varies with the defect density. It is seen that the ratio noticeably increase from the layer grown at -40 V to the -80 V layer and to the -120 V layer as Figure 2 shows.

A high defect density also triggers a variation of electronic structure as observed by EELS measurements of different layers grown at different bias voltages. It is noted that a higher randomly distributed defect density in the film can also give a detectable change in the near edge fine structure, particularly reflected in the change of the N-K edge, as compared with 'perfect' bulk CrN.

1. B Alling et al et al, Physical Review B 82(2010), p.184430.
2. R Daniel et al, Acta Materialia 58(2010), p. 2621.
3. XY Zhang et al, Physical Review B 83(2011), p. 165205.
4. SM Wang et al , Physical Review B 86(2012), p. 064111.
5. Z L Zhang et al, Physical Review B 87 (2013), p.014104.
6. AS Botana et al, Physical Review B 85(2012), p. 235118.
7. Acknowledgements: Gabriele Moser and Herwig Felber are gratefully acknowledged for their help with sample preparation. B. Sartory, Materials Center Leoben Forschung GmbH, Leoben, Austria

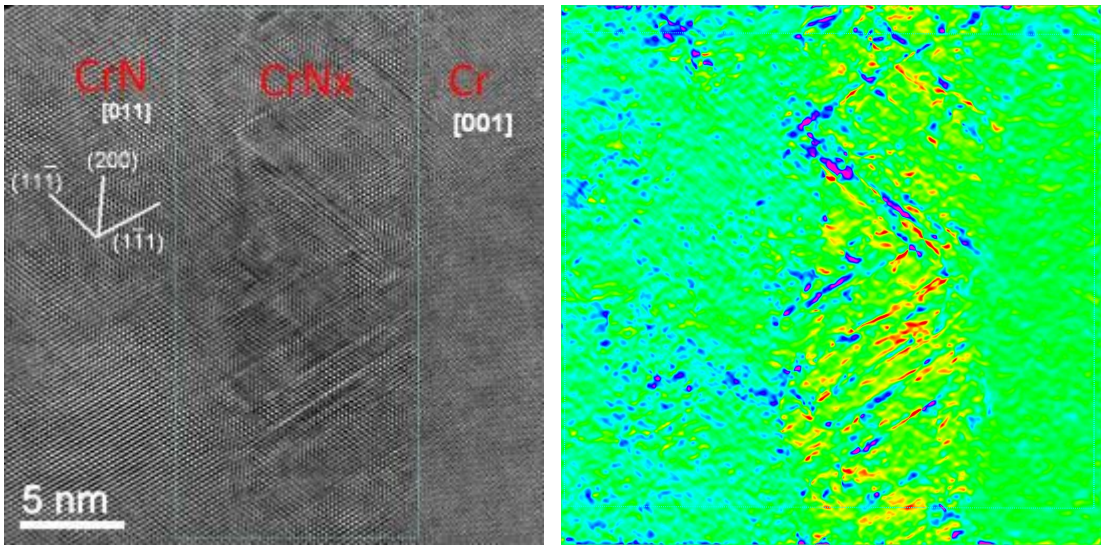

Figure 1. Left: a typical HRTEM image of the CrN/Cr interface along CrN [011] direction (Wien filtered), a defect layer between Cr and CrN originates from the ordered N-vacancies on {111} planes. Right: a strain map (e_{yy}) obtained by geometrical phase analysis, demonstrating the anisotropic distribution of strain within the defective CrN_x layer.

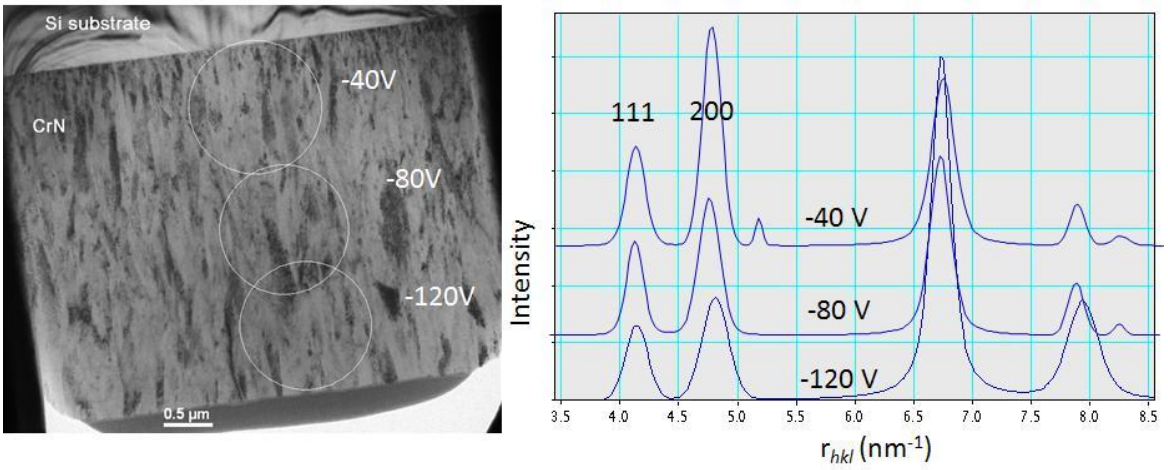

Figure 2. Left: A bright field image of a CrN layer on Si substrate prepared by focused ion beam method. The CrN layer is about 3 µm in thickness, deposited under different bias voltage, -40, -80 and -120 V. Right: The radial intensity distribution of ring pattern recorded at the different positions in the bright field image as schematically labeled. The plot indicates that the intensity ratio of (111) and (200) refections varies with the bias voltage. The detailed analysis gives a different ratio (I_{111}/I_{200}), which is 0.49, 0.57 and 0.6 at the respective layer deposited at a bias voltage of -40, -80 and -120 V.

Thin Films and Coatings

MS.5.P154
Optimizing EBSD setup for high lateral resolution to investigate thin $(FePt)_{1-x}Cu_x$-films

N. Jöhrmann[1], C. Brombacher[2], M. Albrecht[2], M. Hietschold[1]

[1]University of Technology, Solid Surfaces Analysis, Chemnitz, Germany
[2]University of Technology, Surface and Interface Physics, Chemnitz, Germany

nathanael.joehrmann@s2002.tu-chemnitz.de
Keywords: EBSD, t-EBSD, TKD, FePt

Thin FePt films are a promising candidate to raise storage densities in future magnetic storage devices, because FePt shows very high uniaxial magnetocrystalline anisotropy in its chemical ordered $L1_0$ phase. In this regard, films with (001) texture and small grains are required. The films were prepared by magnetron sputtering of Cu/FePt bilayers at room temperature on thermally oxidized Si(100) substrates, followed by rapid thermal annealing. The copper content and several annealing parameters were varied, to study their influence on texture formation and grain size evolution. To investigate the film morphology, EBSD (Electron Backscatter Diffraction) seemed a suitable method. However, due to the small grains in a range of 10 – 100 nm, it was necessary to adjust the EBSD setup for high lateral resolution. By optimizing the acceleration voltage [1], tilt angle and aperture an effective resolution of 10 nm was achieved. The EBSD results shown in Figure 1 prove, that increasing copper content leads to an enhanced (001) texture formation. Further experiments revealed that copper especially promotes nucleation of $L1_0$ (001) oriented grains [2], while a higher heating temperature mostly improves the crystallite growth.

For future investigations the achieved lateral resolution is still not sufficient. Therefore an approach with thinned samples and slightly changed setup called t-EBSD or TKD (Transmission Kikuchi Diffraction) as it was suggested by Keller and Geiss [3] was tested. The results are compared with the standard EBSD measurements and the advantages of the different approaches are discussed.

1. D.R. Steinmetz and S. Zaefferer, Materials Science and Technology 26 (2010), pp. 640-645
2. C. Brombacher et al., J. Appl. Phys. 112, 073912 (2012)
3. R. R. Keller und R. H. Geiss, Journal of Microscopy 245 (2011), pp. 245-251

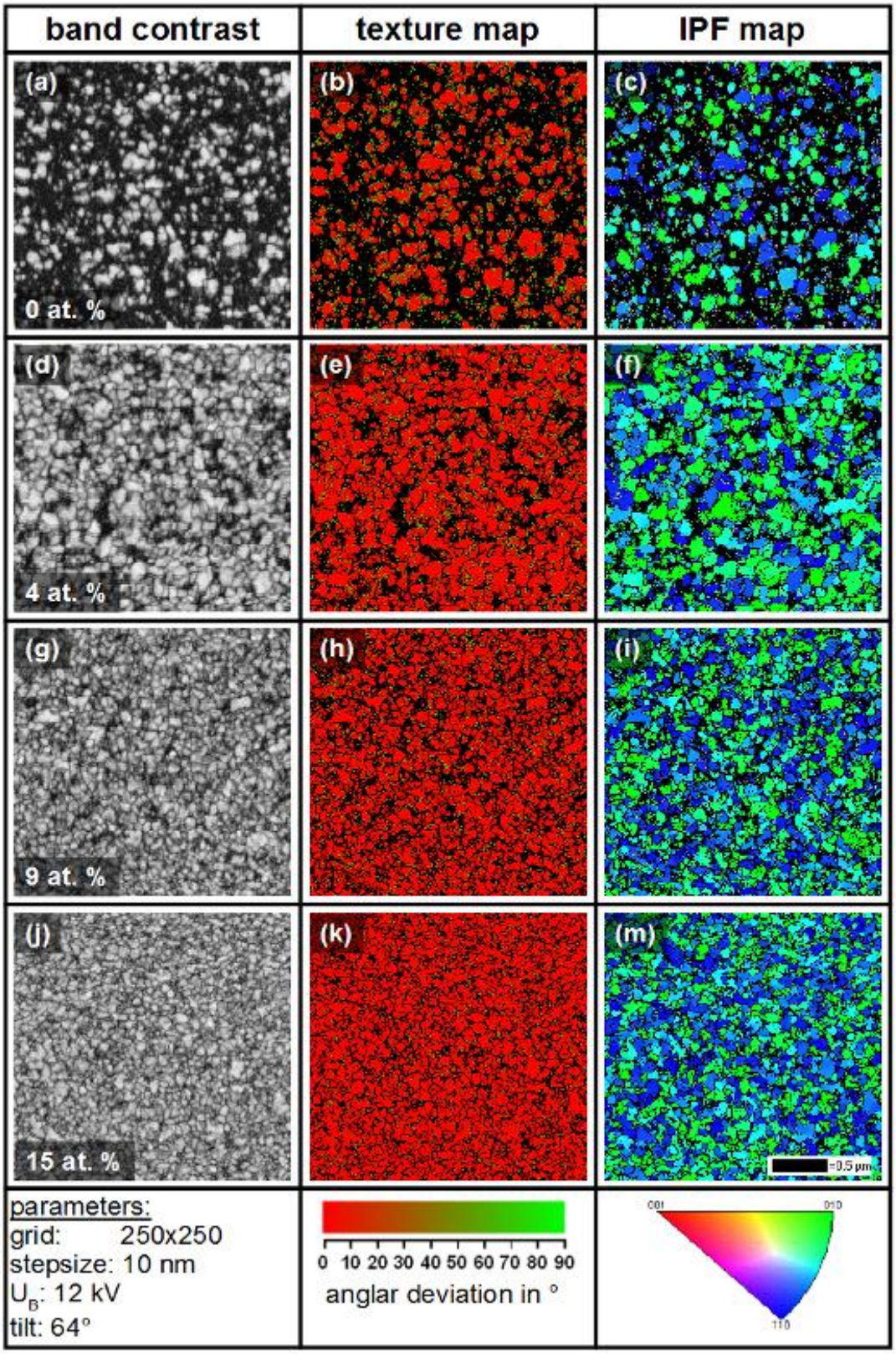

Figure 1. EBSD results for $(FePt)_{1-x}Cu_x$-films with various copper contents. The texture maps show the angle between the axis perpendicular to the sample surface and the (001)-orientation, while the IPF maps are coloured regarding to an axis parallel to the sample surface.

Thin Films and Coatings

MS.5.P155
Characterization of CrN films on MgO (100) by advanced TEM

K. Kormout[1], R. Daniel[2], C. Mitterer[2], G. Dehm[3], Z. Zhang[1]

[1]Erich Schmid Institute of Materials Science, Austrian Academy of Sciences, Leoben, Austria
[2]Montanuniversität Leoben, Department of Physical Metallurgy and Materials Testing, Leoben, Austria
[3]Max-Planck-Institut für Eisenforschung GmbH, Düsseldorf, Germany

karoline.kormout@oeaw.ac.at
Keywords: CrN, microstructure, HRTEM, EELS

CrN has – besides its application as wear-resistant coating – recently gained considerable interest due to its unique antiferromagnetic configurations for which it has been used as a prototype material for strong magnetostructural interactions. This has recently led to numerous experimental and theoretical studies [1-3].

The CrN films in this work were deposited by d.c. magnetron sputtering of a Cr target at a constant total pressure of 1 Pa. The microstructure of two different CrN thin films grown (i) as a single layer at -40 V bias voltage, a target power of 6 kW and a temperature of 350 °C with a thickness of 1.4 µm and (ii) as a bi-layer with a thickness of 10 nm with a 10 nm-thin Cr top layer grown at -80 V bias, a target power of 2 kW and a temperature of 500 °C was investigated by transmission electron microscopy (TEM). The chemical analysis was carried out by electron energy-loss spectroscopy (EELS). Conventional TEM was performed by a Philips CM12 at 120 kV. High-resolution TEM (HRTEM) investigations and EELS analyses were conducted on a TEM/STEM JEOL 2100F at 200 kV equipped with an image-side C_S-corrector (CEOS) and an energy filter (Tridiem, Gatan). Geometric phase analysis [4] was carried out to analyze the relative strain across the interface. TEM specimens were prepared by a standard procedure, mechanically ground and polished and then thinned from both sides till perforation by Ar^+ ion milling using a precision ion polishing system of Gatan (Model 691).
While a thin Cr(10 nm)/CrN(10 nm) bi-layer grew with a single crystalline microstructure, the CrN single layer with a thickness of more than 1 µm forms as a polycrystalline film with a columnar microstructure on MgO substrate. C_S-corrected HRTEM studies revealed that both layers were grown epitaxially on the MgO substrate at the initial stage. Interfacial misfit dislocations at the CrN/MgO interface were observed and detailed atomic structures at the interface are revealed. The geometric phase analysis across the CrN/MgO interface revealed strain changes from -14.7% to +16.6% with respect to the unstrained MgO lattice due to the presence of misfit dislocations. In two-dimensional relative strain maps the strain fields of pure edge type dislocations show a symmetrical shape with compressively stressed and stretched regions in x-direction and strain-free structure in y-direction (see centered dislocation in Figure 1). The map was calculated using the 111 and 200 reflections (Figure 1d).

In addition to the structural characterization, detailed EELS analysis was performed for the CrN single layer across the interface. The EEL spectra recorded at or close to the film-substrate interface (Figure 2a) show the evolution from the CrN film to the MgO substrate. This is reflected by a gradual change of the O-K, N-K and Cr-$L_{2,3}$ edges when crossing the interface. Because of the overlapping of the Cr-$L_{2,3}$ with the O-K edge, the multiple linear least-squares (MLLS) fitting was applied to the data to map out the respective Cr and O signals. A spatial distribution of the CrN and MgO components is shown in Figure 2b. It further reveals an interface width (from CrN to MgO) of about 4.3 nm.

1. S.M. Wang et al, Physical Review B 86 (2012), p. 064111.
2. Z.L. Zhang et al, Physical Review B 87 (2013), p.014104.
3. A.S. Botana et al, Physical Review B 85 (2012), p. 235118.
4. M.J. Hÿtch, Scanning Microscopy 11 (1997), p. 53-66.
5. Acknowledgements: Gabriele Moser and Herwig Felber are gratefully acknowledged for their help with the sample preparation.

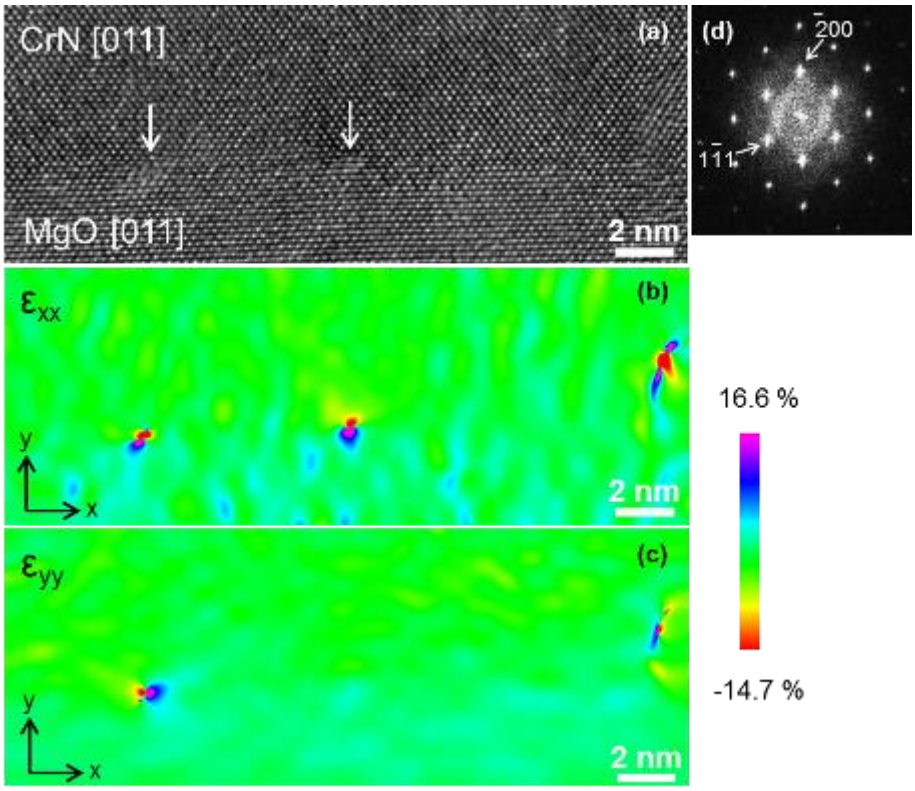

Figure 1: a) HRTEM image of the CrN/MgO interface of the bi-layer sample; b) relative strain map in x-direction and c) y-direction; d) power spectrum with selected reflections.

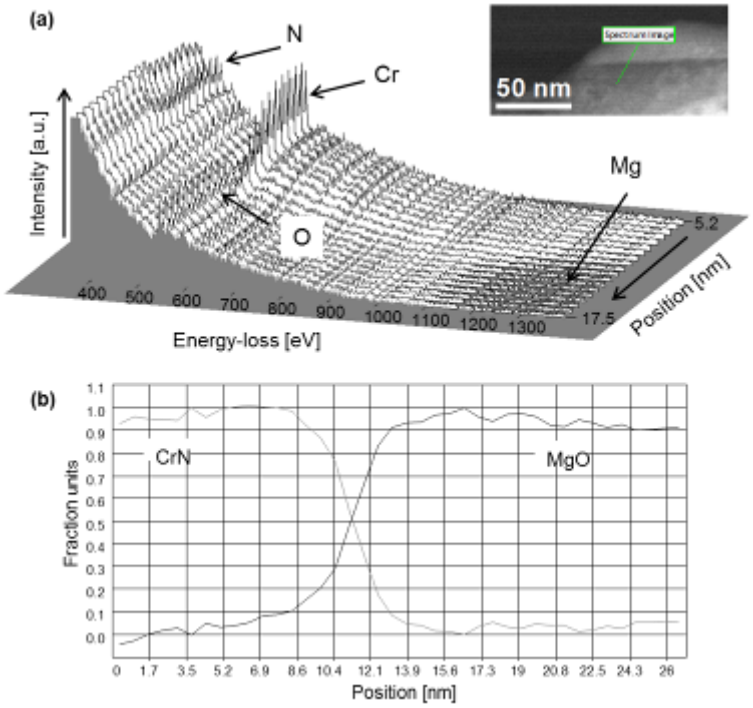

Figure 2. a) A section of line scan spectra at or close to the CrN/MgO interface with corresponding STEM image. The position of the spectra corresponds to the b) spatial distribution of the two components (CrN film and MgO substrate) across the interface obtained by MLLS fitting

Thin Films and Coatings

MS.5.P156
Mechanical properties of Cu tested by nanoindentation and orientation mapping

U.D. Hangen[1], R. Stromberg[1], D. Stauffer[1]

[1]Hysitron Inc., Aachen, Germany

uhangen@hysitron.com

Copper is being widely used in today's semiconductor devices and its mechanical properties are of large interest for the mechanical stability of the engineered structure. Moreover, the thermo-mechanical behaviour of copper is critical for the device reliability. Copper is a material with a large anisotropy of elastic properties. While the <100> direction has a modulus of 60 GPa, the <111> direction has a modulus of 192 GPa.

In the past, nanoindentation experiments have shown a low sensitivity to this anisotropy and usually an average value has been reported [1]. Recently, a sensitivity to the orientation has been found in the elastic deformation regime with sharp indenters at small force [2,3]. This finding has been surprising, but now plays an important role in the microstructures to mechanical property relationship of Cu thin film. The development of a nanoindentation device that combines the ability of low force mechanical testing in the SEM and a two axis rotation/tilting stage that allows orienting the sample to an EBSD mapping position is therefore of large importance for a direct correlation of local orientation and mechanical properties.

1. J.J. Vlassak and W.D. Nix, J. Mech. Phys. Solids, 42, 1223-1245, (1994).
2. S. N. Dub, Y. Y. Lim, and M. M. Chaudhri, JOURNAL OF APPLIED PHYSICS 107, 043510 2010
3. KB Yeap, E Zschech, U. D. Hangen, T. Wyrobek, L.W: Kong, A. Karmakar, X. Xu and I.Panchenko; Journal of Materials Research / Volume 27 / Issue 01 / 2012, pp 339-348

Thin Films and Coatings

MS.5.P157
Characterization of graphene layers functionalized through radical UV-grafting

A. Chiodoni[1], K. Bejtka[1], A. Chiappone[1], I. Roppolo[1], S. Porro[1], C.F. Pirri[1,2]

[1]Istituto Italiano di Tecnologia - IIT, Center for Sapce Human Robotics, Torino, Italy
[2]Politecnico di Torino, Dipartimento di Scienza Applicata e Tecnologia, Torino, Italy

angelica.chiodoni@iit.it
Keywords: graphene oxide, functionalisation, photo-reduction, UV-grafting, electron microscopy

Chemically-modified graphene was recently studied for many applications, including polymer composites, energy materials, sensors, field-effect transistors, biomedical applications [1]. Due to the presence of a range of reactive oxygen functional groups, chemical modification of graphene oxide (GO) has been a promising route to achieve mass production of functionalized graphene [2].

In particular, exploiting the richness of –OH groups typical of GO and its ability to be reduced under UV light in the presence of radicals [3], a new GO grafting/reduction process is here proposed for the production of functionalized graphene. This work reports a sequential two-step process to obtain the mentioned grafting/reduction process [4]. A scheme of the two-step reaction is shown in figure 1.

In the first step, initiator moieties are formed onto GO by UV irradiation of a GO–Benzophenone (BP) solution. BP abstracts hydrogen from the surface and creates a free radical. Contemporarily, GO is reduced to graphene under UV light. At this pointthe surface radical and the newly formed semipinacol radicals combine to form surface-bound initiators. The unreacted BP is then removed by solvent washing. The second step of graft polymerization is then achieved with a solution containing monomer and solvent. UV irradiation liberates the immobilized photoinitiatorsthat initiate graft polymerization from GO. This process avoids the homopolymer formation while the growth of grafted linear polymer chains is preferred, since there is no BP in the monomer solutions. Furthermore, the production of a photosensitive substrate after the first step allows grafting a large variety of monomers. In this work, acrylate and methacrylate monomers were used; in particular, fluorinated acrylic monomers were considered (e.g. perfluorobutyl acrylate). The materials were characterized at different steps by means of Transmission Electron Microscopy, (TEM), Field Emission Scanning Electron Microscopy (FESEM), Energy Dispersive Spectroscopy (EDS) and by infrared spectroscopy. X-ray photoelectron spectroscopy and thermogravimetic analysis were also considered to confirm the successful completion of each step. In figure 2, the TEM characterization of GO and grafted/reduced GO is reported. In figure 3, the TEM characterization of layers of graphene covered by the polymeric layer is reported with the elemental analysis obtained with EDS. The presence of fluorine demonstrate that the polymer grafting process was successful.This procedure to functionalize graphene allows the production of grafted graphene from low cost GO, which can be easily dispersed in common solvents to produce easily processable graphene-based conductive inks and coatings.

1. A.K. Geim and K.S. Novoselov, Nat. Mater. 6 (2007) p. 183
2. D.R. Dreyer, S. Park, C.W. Bielawski, R.S. Ruoff, Chem. Soc. Rev. 39 (2010) p. 228
3. Y.H. Ding, P. Zhang, Q. Zhuo, H.M. Ren, Z.M. Yang, Y. Jiang, Nanotechnology 22 (2011) p. 215601
4. H Ma, R.H. Davis, C.N. Bowman, Macromolecules 33 (2000) p. 331

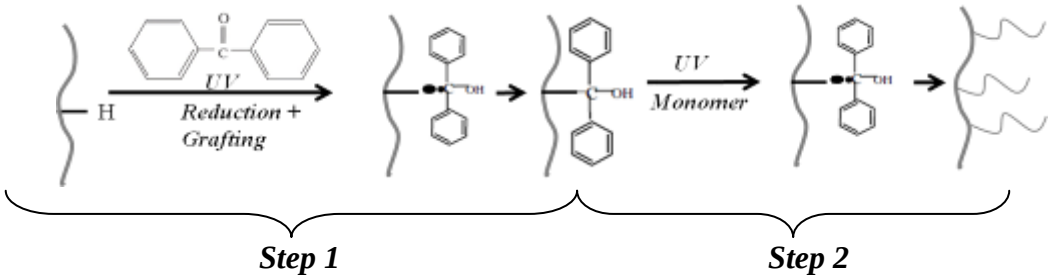

Figure 1. Scheme of the two-step reaction showing the GO reduction and functionalisation through BP mediated UV-grafting.

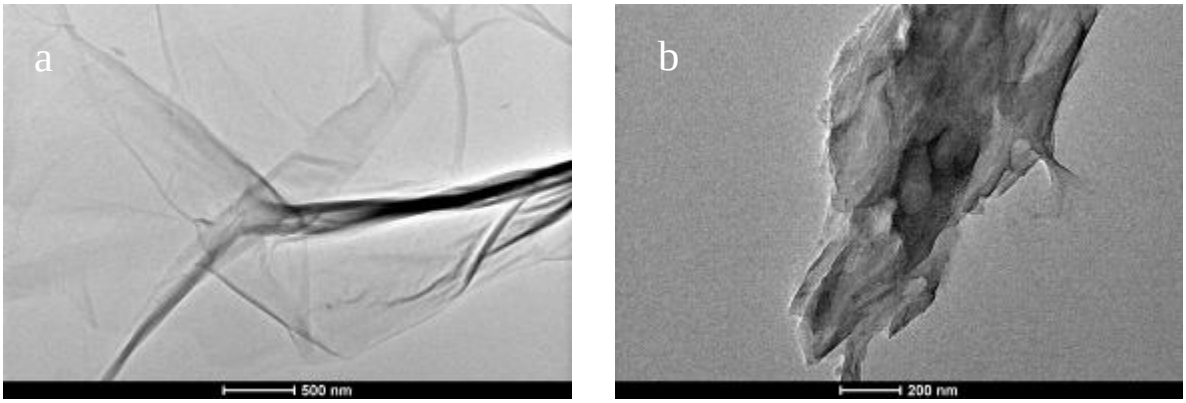

Figure 2. TEM images showing the morphology of the materials in the first step. a): GO as prepared. b): at the end of step 1, where BP is grafted to GO

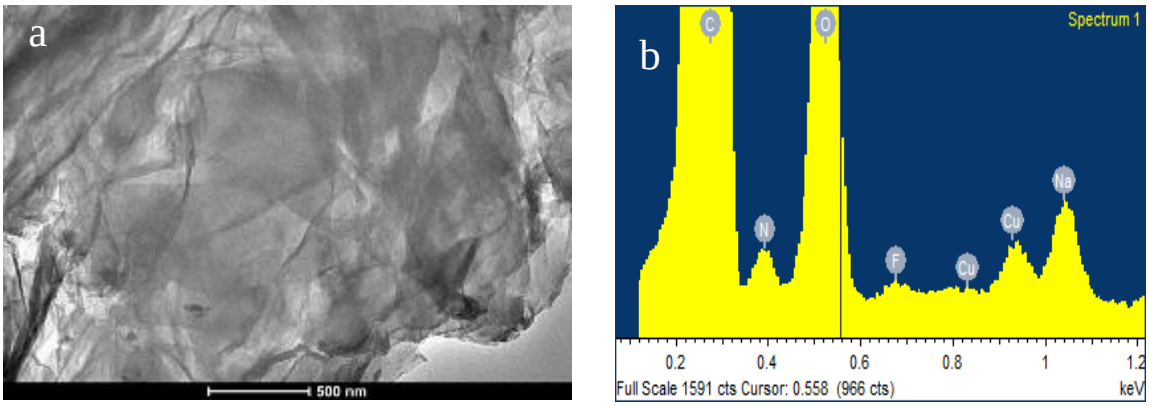

Figure 3. TEM (a) and EDS (b) characterization of the material at the end of step 2. The presence of the polymer on the graphene is confirmed by the presence of fluorine.

Alloys and Intermetallics

MS.6.158
Structural Defects in Advanced Alloys and Intermetallics

A. Dlouhý[1], L. Agudo Jácome[2], C. Somsen[2], E.P. George[3,4], G. Eggeler[2]

[1]Institute of Physics of Materials, Mechanical Properties, Brno, Czech Republic
[2]Ruhr-Universität Bochum, Institut für Werkstoffe, Bochum, Germany
[3]Oak Ridge National Laboratory, Materials Science and Technology Division, Oak Ridge, United States
[4]University of Tennessee, Materials Science and Engineering Department, Knoxville, United States

dlouhy@ipm.cz
Keywords: scanning transmission electron microscopy, high angular annular dark field, stereo pairs, dislocations

Advanced alloys and intermetallics combine high mechanical strength with excellent resistance to corrosion and oxidation in harsh environments. In the present study we investigate microstructural background of their mechanical strength. A focus is on directionally solidified NiAl-(Cr)-Mo eutectics, CoCrFeMnNi high entropy alloys and more conventional Ni-based superalloys single crystals. We first introduce a novel STEM HAADF technique which provides an insight into 3D arrangements of dislocation structures [1]. In order to demonstrate a potential of the technique, we first review some basic elements of classical stereo TEM. We then show how the method can be extended by working in the scanning transmission electron microscope (STEM) mode of a modern analytical based 200 kV TEM equipped with a field emission gun (FEG TEM) and a high angle annular dark field (HAADF) detector. Two STEM micrographs of a stereo pair combine into one anaglyph. When viewed with special coloured glasses the anaglyph provides a direct and realistic 3D impression of the microstructure, see Figure 1. The technique is then applied in order to resolve spatial dislocation arrangements in the series of structural materials. In particular, dislocation processes at the NiAl-Mo and NiAl-Cr interfaces in the directionally solidified NiAl-(Cr)-Mo eutectics are investigated in detail. Directionally solidified NiAl-(Cr)-Mo composites exhibit microstructures of major (NiAl matrix) and minor (Mo or Cr fibre) eutectic phases. Recent advances in processing have resulted in NiAl-(Cr)-Mo microstructures of unprecedented quality in terms of alloy purity and microstructural regularity. The NiAl-(Cr)-Mo microstructure was investigated by STEM before and after creep. The results of the analysis clearly show that the formidable high-temperature strength of NiAl-(Cr)-Mo in situ composites is associated with the presence of fine Mo or Cr fibres. Since fibres are essentially dislocation-free in the as-solidified microstructure, they can support the high stresses associated with dense dislocations structures. We show that later in creep life, dislocations can be transmitted from the NiAl intermetallic matrix through the interfaces into the reinforcing eutectic phase. These processes invert the strain accumulation kinetics at high temperatures and thus cause weakening of the material [2]. Similarly, a combination of dislocation slip and deformation twinning in new class of solid solution high entropy alloys results in unique deformation behaviour. An equiatomic CoCrFeMnNi high-entropy alloy, which crystallizes in the face-centered cubic (FCC) crystal structure, was produced by arc melting and drop casting. The drop-cast ingots were homogenized, cold rolled, and recrystallized to obtain single-phase microstructures with three different grain sizes in the range 4~160 μm. Quasi-static tensile tests at an engineering strain rate of 10^{-3} s^{-1} were then performed at temperatures between 77 and 1073 K. Yield strength, ultimate tensile strength and elongation to fracture all increased with decreasing temperature. During the initial stages of plasticity (up to ~2% strain), deformation occurs by planar dislocation glide on the normal FCC slip system, {111}<110>, at all temperatures and grain sizes investigated. Undissociated 1/2<110> dislocations were observed, as were numerous stacking faults, which imply the dissociation of several of these dislocations into 1/6<112> Shockley partials. At later stages (~20% strain), nanoscale deformation twins were observed after interrupted tests at 77 K, but not in specimens tested at room temperature where plasticity occurred exclusively by the afore-mentioned dislocations. The STEM HAADF analysis suggests that excellent ductility observed at 77K is due to a unique combination of dislocation and twinning deformation modes [3].

1. L. Agudo Jácome, G. Eggeler and A. Dlouhý, Ultramicroscopy 122 (2012), p. 48.
M. Dudová, K. Kuchařová, T. Barták, H. Bei, E.P. George, Ch. Somsen and A. Dlouhý, Scripta Materialia
65 (2011), p. 699.
2. F. Otto, A. Dlouhý, Ch. Somsen, H. Bei, G. Eggeler and E.P. George, Acta Materialia (2013) submitted for publication.
3. The authors acknowledge support provided by following funding bodies: IPM AS CR development program no. RVO:68081723 (AD), DFG Projects A1 and A2 of the collaborative research centre SFB/Transregio 103 (LA, ChS, GE) and U.S. Department of Energy, Basic Energy Sciences, Materials Sciences and Engineering Division (EPG).

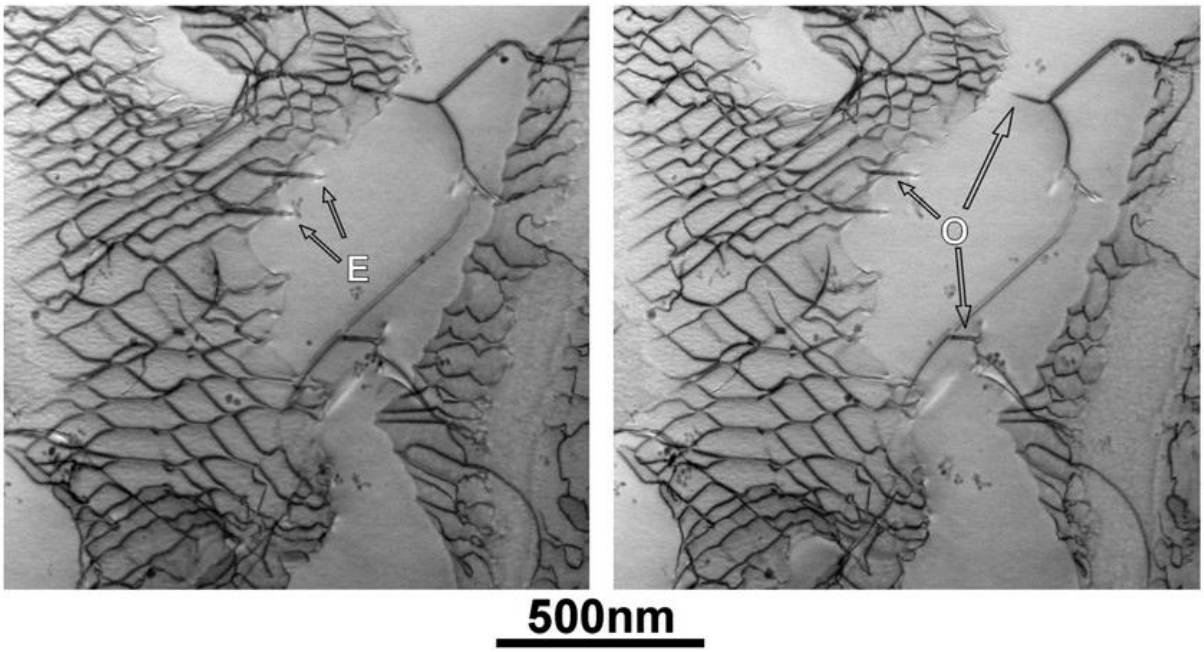

Figure 1. Stereo transmission electron microscopy of a crept Ni-base single crystal superalloy (LEK94, 160MPa, 1020°C, 2%). Corresponding stereomicrographs obtained using STEM HAADF technique (inverted contrast).

Alloys and Intermetallics

MS.6.159
Simultaneous strain and chemical mapping applied to Ni-based superalloys

J. Müller[1], F. Niekiel[1], E. Spiecker[1]

[1]Center for Nanoanalysis and Electron Microscopy (CENEM), University of Erlangen-Nürnberg, Erlangen, Germany

Julian.mueller@ww.uni-erlangen.de
Keywords: Strain mapping, CBED, Superalloy

The γ/γ'-interface plays an important role for the mechanical properties of γ'-strengthened Ni- and Co-based superalloys. Both alloys are composed of cuboidal γ'-precipitates of an ordered intermetallic phase coherently embedded in a solid solution matrix (γ). Even though both phases share a coherent interface a small residual misfit is present causing the γ-phase to be constrained in the bulk material. During creep deformation the rafted microstructure which is strongly depending on the misfit is evolving. In these superalloys the sign and magnitude of the misfit are key parameters in high-temperature creep since, for instance, they determine the orientation of the rafted structure with respect to the load direction. Therefore an accurate understanding of the strain distribution at the interface is of great importance.

To measure the misfit either averaging scattering methods using X-rays or neutrons or single point measurements with electrons by convergent beam electron diffraction (CBED) are used. While averaging scattering methods provide good statistics, almost all spatial resolution is lost. On the other hand, with electrons it is possible to measure on a nm-scale but difficult to obtain sufficient statistics. Often not only the lattice parameter but also the distribution of chemical elements across the interfaces have to be determined to account for e.g. segregation effects which can strongly influence the creep properties as well. In the case of superalloys, γ and γ' have almost the same lattice parameter but show different chemical compositions due to the different crystal structure. This chemical difference is another important factor determining the rafted microstructure of the deformed alloy.

To measure the lattice parameter across interfaces by performing CBED line scans in STEM mode an advanced approach was established, which ensures sufficient statistics with very high spatial resolution. Simultaneously EDX spectra are acquired in the exact same measuring point combining structural and chemical information (fig. 1). Difficulties by applying this method are caused by the strongly differing sensitivities of the CCD-camera and the EDX-detector making an accurate balancing of the measuring time necessary. This method also facilitates the evaluation of two dimensional strain fields at corners or other irregular shaped interfaces.

In this work the lattice misfit of a common Ni-based superalloy is investigated by means of the above mentioned CBED-EDXS analysis. The structural and chemical transition from the γ- to the γ'-phase could be clearly identified using the data from the EDX spectra and the CBED patterns (fig. 1 c) and d)). In a first approach the lattice misfit was estimated from the CBED patterns by comparing them with simulated patterns under the assumption that both phases are purely cubic. It was found that the results for the measured misfit are in very good agreement with values found in literature [1, 2] for similar Ni-based superalloys. In the next step we want to extend the method to the corner of a γ/γ'-interface and account for the tetragonal distortion and thin foil relaxation. First FEM simulations have already been carried out to estimate the thin film relaxation of the TEM-sample (fig. 2). They indicate that the thin foil effect on the in-plane strain several µm away from the hole of the sample could be neglected.

1. C. Schulze and M. Feller-Kniepmeier, Mater. Sci. Eng. 281 (2000), p. 204
2. R. Gills et al., Appl. Phys. A 74 (2002), p. 1446
3. The authors gratefully acknowledge the collaborative research center SFB/TRR 103 and the DFG training research group 1229 for financial support.

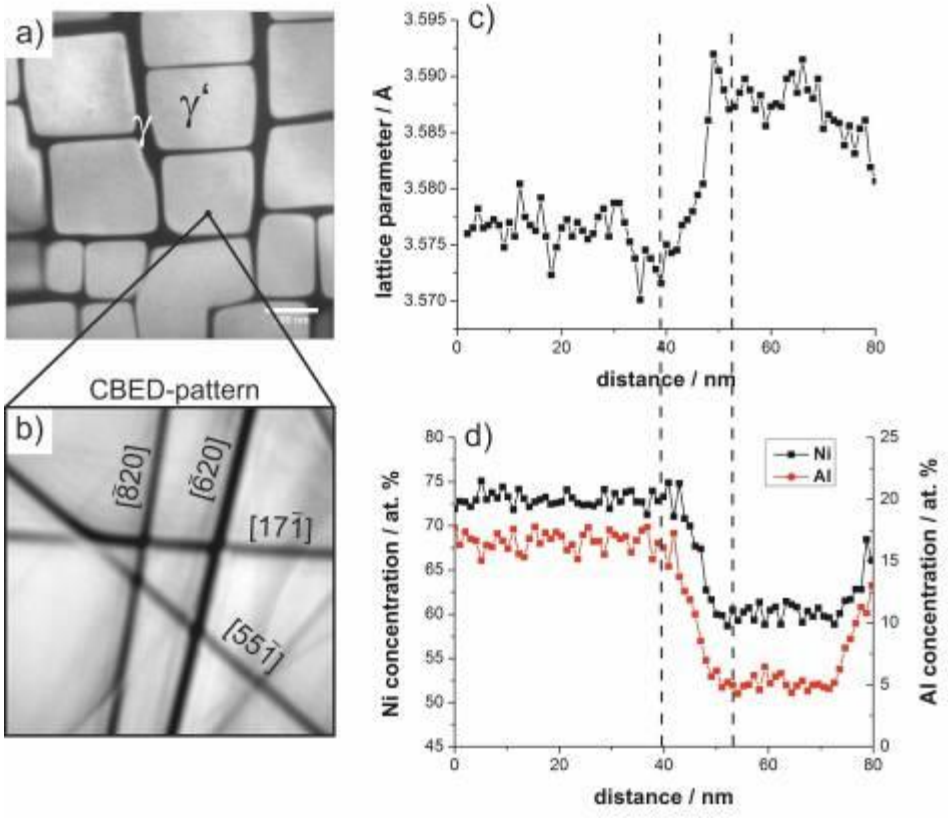

Figure 1. a) Dark field TEM image of the γ/γ'-microstructure in an undeformed sample. b) CBED-pattern observed in both phases. Structural c) and chemical d) transition evaluated from the line-scan. The broadening of the interface is due to tilting of the sample.

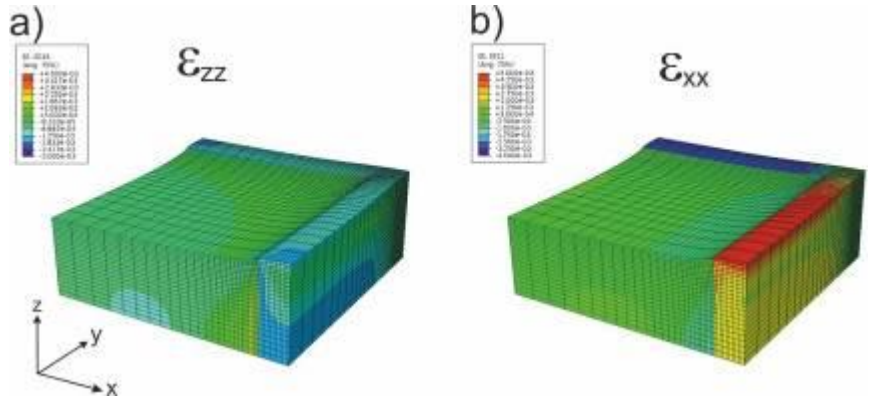

Figure 2. FEM simulations a) ε_{zz} and b) ε_{xx} for a 150 nm thick TEM-foil displayed with a scaling factor of 50.

Alloys and Intermetallics

MS.6.160
Site-occupation of Nb atoms in ternary Ni-Ti-Nb shape memory alloy

H. Shi[1], J. Frenzel[2], G. Martinez[1], S. Van Rompaey[1], S. Van Aert[1], D. Schryvers[1]

[1]University of Antwerp, Physics, Antwerp, Belgium
[2]Ruhr Universität Bochum, Werkstoffe, Bochum, Germany

nick.schryvers@ua.ac.be
Keywords: shape memory alloy, site occupation, aberration-correction, HAADF-HRSTEM, PED

In this work, aberration corrected High Angle Annular Dark Field - High Resolution Scanning Transmission Electron Microscopy (HAADF-HRSTEM) combined with Precession Electron Diffraction (PED) has been used to find Nb atoms both in the matrix and the Ti_2Ni phase in a $Ti_{45.5}Ni_{45.5}Nb_9$ shape memory alloy.

The atomic model of the ordered body-centered cubic (bcc) B2 crystal structure of the austenite matrix is shown in Figure 1(a). Figure 1(b) is the atom projection of the B2 structure along the [001] zone axis. In this viewing direction every atom column is a pure column, i.e. or Ni or Ti and their columns are alternatively arranged along the <110> directions. In order to find the preferential site for the Nb solute atoms in the ternary system, Z-contrast HAADF-HRSTEM images along <001> have been obtained from the Ni-Ti-rich matrix of the reference binary $Ni_{51.7}Ti_{48.3}$ material and the as-cast $Ti_{45.5}Ni_{45.5}Nb_9$ sample. Examples of these are shown in Figure 1(c) and (d), respectively. In Figure 1(e) and (f), refined parameterized empirical models using the quantitative method explained in [1] are shown which are in close agreement with the underlying experimental data of (c) and (d), respectively. Histograms of the estimated total scattered intensities are presented in Figure 1(g) and (h) indicating the distributions of the measured scattering cross sections for the atomic columns in these images. Although it is clear that the ensembles of atom columns belonging to one of both pure Ni or Ti sub-lattices in Figure 1(c) and (e) reveal important variations in intensity (Ti atom columns in white box, Ni in black box), the respective histograms can clearly be discriminated. Contrary, for the ternary Ni-Ti-Nb, the intensity histograms of the labeled Ni and Ti+Nb columns strongly overlap as shown in Figure 1(h). The comparison of the intensity histograms of the binary and ternary matrices shown in Figure 1(g) and (h), respectively, clearly indicates that the Nb atoms are located on the Ti sites.

An alternative HAADF-HRSTEM approach is used to determine the location of the Nb atoms in the Ti_2Ni (space group is Fd m) phase. This phase has a complex face centered cubic (fcc) based crystal structure with 96 atoms of which 64 Ti atoms occupy two Wyckoff positions 48 f and 16 c, and 32 Ni atoms occupying the 32 e positions. The projection structure model for one unit cell along the [001] and [011] zone axes are displayed in Figure 2(a) and (b), respectively. In both cases all atom columns are pure columns. The purple (dark) and green (light gray) atoms represent the 48 f and 16 c Ti atoms, the silver (white centered) atoms are the 32 e Ni atoms. Figure 2(c) and (d) are HAADF-HRSTEM experimental images of one unit cell along [001] and [011], respectively. In Figure 2(e) to (j) HAADF-HRSTEM simulated images using STEMsim [2] along [001] and [011] are presented for different occupation sites for the Nb atoms. According to the STEM Energy Dispersive X-ray Spectroscopy (EDX) data of this Ti_2Ni phase, Ni has a concentration of 33.7% ± 0.8% which corresponds with the 1/3 stoichiometric ratio of Ni in the Ti_2Ni phase. In a unit cell with 96 atoms this yields 32 Ni atoms, the remaining 64 being divided over 41 Ti and 23 Nb, again following the EDX data. In Figure 2(e) and (f) all Nb substitutes on Ti f sites, in (g) and (h) all Ti c sites are replaced by Nb, the remaining Nb atoms being placed on the Ti f sites while in (i) and (j) all Nb atoms substitute on Ni e sites, with Ni atoms replacing Ti on f and c sites accordingly. Comparing the indicated intensity profiles of the experimental images with those of the three simulated cases for the [001] zone axis it is clear that Nb atoms prefer to substitute for the 48 f Ti atoms. The same conclusion can be drawn from a qualitative comparison of the [011] experimental and calculated images.

PED was used to further verify that Nb atoms prefer to substitute the 48f Ti positions. In practice, reflections were extracted from a total of 6 PED patterns with different zone axes (<110>, <112>, <113>, <116>, <123> and <255>). Since in principle there are three possible symmetry positions (f, c and e) for the Nb atoms to occupy, 3 pairs of starting structure models are created to find the occupation preference of the Nb atoms between each two positions based on the PED refinement performed with JANA2006 software. The results show that the model with all Nb atoms occupying the Ti f site gives the lowest R-value, confirming the HAADF-HRSTEM conclusions.

1. S. Van Aert, J. Verbeeck, R. Erni, S. Bals, M. Luysberg, D. Van Dyck, G. Van Tendeloo, Ultramicroscopy 109 (2009) 1236-1244.
2. http://www.ifp.uni-bremen.de/electron-microscopy/software/stemsim/
3. We thank FWO and CONNEC for financial support

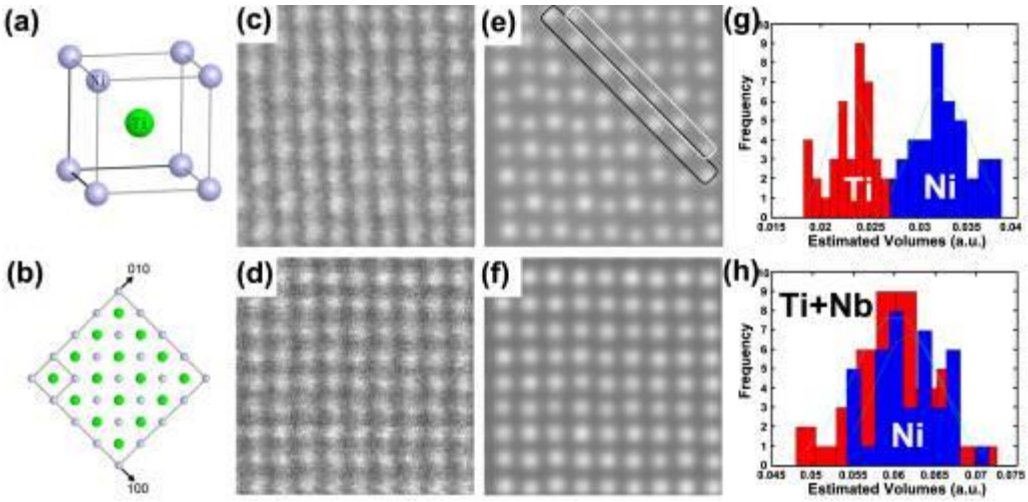

Figure 1. (a) Atomic structure model and (b) projection along [001] zone axis of binary TiNi. (c) HAADF-HRSTEM image of binary $Ti_{48.3}Ni_{51.7}$ and (d) ternary $Ti_{45.5}Ni_{45.5}Nb_9$. (e), (f) corresponding refined parameterized empirical models. (g), (h) histograms of total scattered column intensities in (e) and (f), respectively. The white and black boxes in (e) represent the Ti and Ni atom columns, respectively.

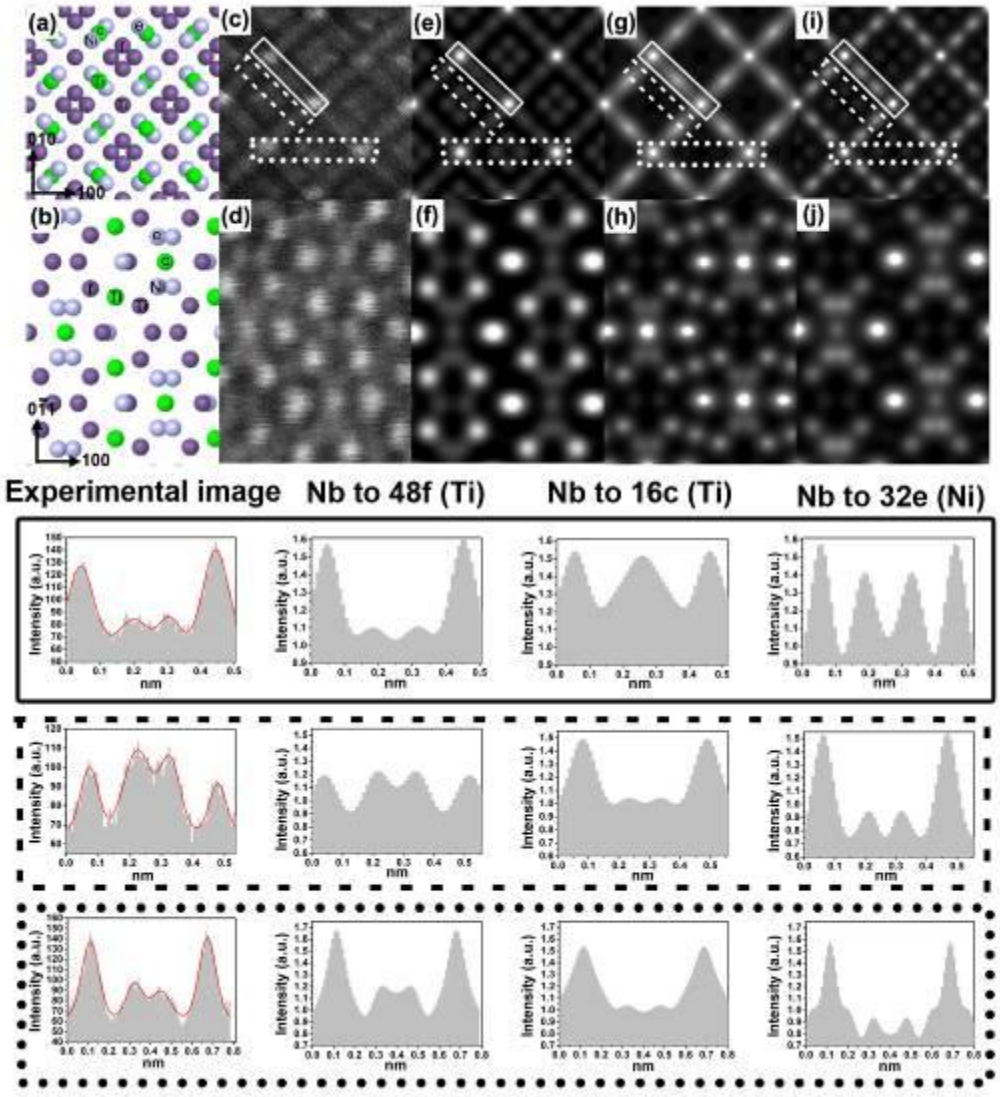

Figure 2. (a), (b) atomic projections along [001] and [011] zone axis of Ti_2Ni phase. (c), (d) corresponding experimental HAADF-HRSTEM images. (e) to (j) corresponding simulated images for different Nb occupations (48 f, 16 c and 32 e)

Alloys and Intermetallics

MS.6.161
Density changes in shear bands of a metallic glass determined by HAADF-STEM and EELS

H. Rösner[1], C. Kübel[2], M. Peterlechner[1], G. Wilde[1]

[1]Universität Münster, Institut für Materialphysik, Münster, Germany
[2]Karlsruhe Institute of Technology, Institut für Nanotechnologie, Karlsruhe, Germany

rosner@uni-muenster.de
Keywords: HAADF-STEM, EELS, metallic glass

The deformation process in metallic glasses is quite different from that in crystalline materials because there are no defects such as dislocations, twins or grain boundaries available that can act as deformation carriers for an easy flow mechanism. Deformation tests on metallic glasses have shown that when the applied load exceeds the elastic range the plastic flow is confined to narrow regions called shear bands [1]. In conventional TEM, shear bands are usually distinguished from the surrounding amorphous matrix as regions of lower contrast. Such shear bands are locally softer than the surrounding matrix allowing the accommodation of external shear stresses via slip. It is common belief that such shear bands are associated with a structural change like local dilatation, implying a volume change and thus a change in the density, ρ. An important issue is hence the quantification of free volume inside shear bands. It is the purpose of the present contribution to describe and discuss a new method for probing the local density of shear bands using analytical TEM resulting in new insight of shear bands in metallic glasses. In our approach [2] we use the relation of the dark-field intensity I/I_0 (scattered electrons collected by an high-angle annular dark-field detector) and the mass thickness: $\frac{I}{I_0} \propto \rho \cdot t$. The foil thickness, t, is calculated from the low-loss region of the electron-energy loss spectrum [3], which is acquired simultaneously to the HAADF signal. This new experimental approach yielded several new results for shear bands in metallic glasses:

(i) Shear bands can show either an increase or decrease in mass density relative to the surrounding matrix (see Figure 1).
(ii) Compositional changes are observed within the shear bands. The surrounding matrix was not observed to be affected.
(iii) High amounts of free volume (up to 6 % and more) are found for individual shear bands.
(iv) Mixtures of amorphous/crystalline or medium range ordered domains were found within the shear bands.

We associate the decrease in density mainly with an enhanced free volume in the shear bands and the increase in density with concomitant changes of the mass. This interpretation is further supported by changes in the zero loss/Plasmon signal (see Figure 2) originating from such sites. The obtained results indicate clearly that shear bands in one given sample can vary significantly with respect to their specific properties, e.g. their mass density. This fact highlights the importance of local imaging methods for their characterization and it also offers a direct explanation for the wide range of observations that are reported in the literature.

1. P.E. Donovan, W.M. Stobbs, Acta Metall. 29 (1981), p. 1419.
2. Submitted to Ultramicroscopy.
3. K. Iakoubovskii, K. Mitsuishi, Y. Nakayama, K. Furuya, Microsc. Res. Tech. 71 (2008), p.626.
4. We kindly acknowledge financial support by the DFG via SPP 1595 (Topological engineering of ultra-strong glasses).

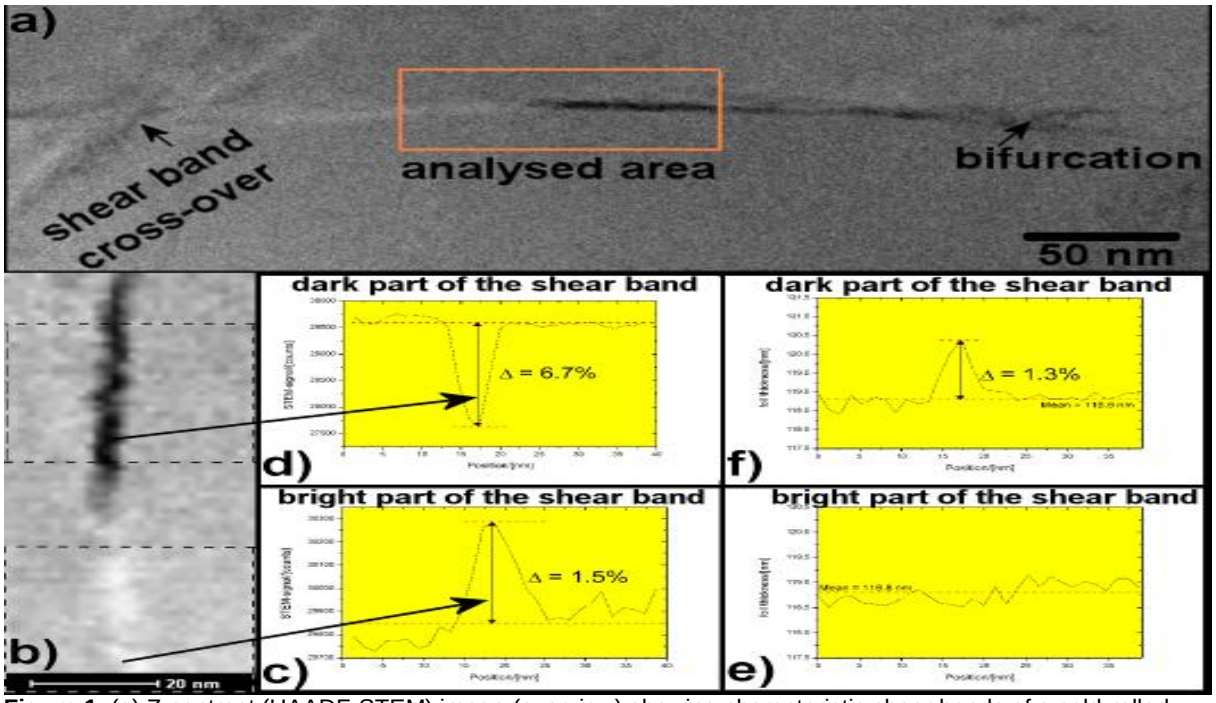

Figure 1. (a) Z-contrast (HAADF-STEM) image (overview) showing characteristic shear bands of a cold-rolled $Al_{88}Y_7Fe_5$ melt-spun ribbon. A cross-over of shear bands is seen on the left side. The horizontal shear band displays a contrast change from bright to dark in the box (analyzed area) and a bifurcation at the end. (b) HAADF detector signal corresponding to the box shown in (a) rotated 90° anti-clockwise. (c, d) Averaged profiles of the HAADF detector signal from the boxed areas indicated in (b). (e, f) Averaged profiles of the foil thickness from the boxed areas indicated in (b).

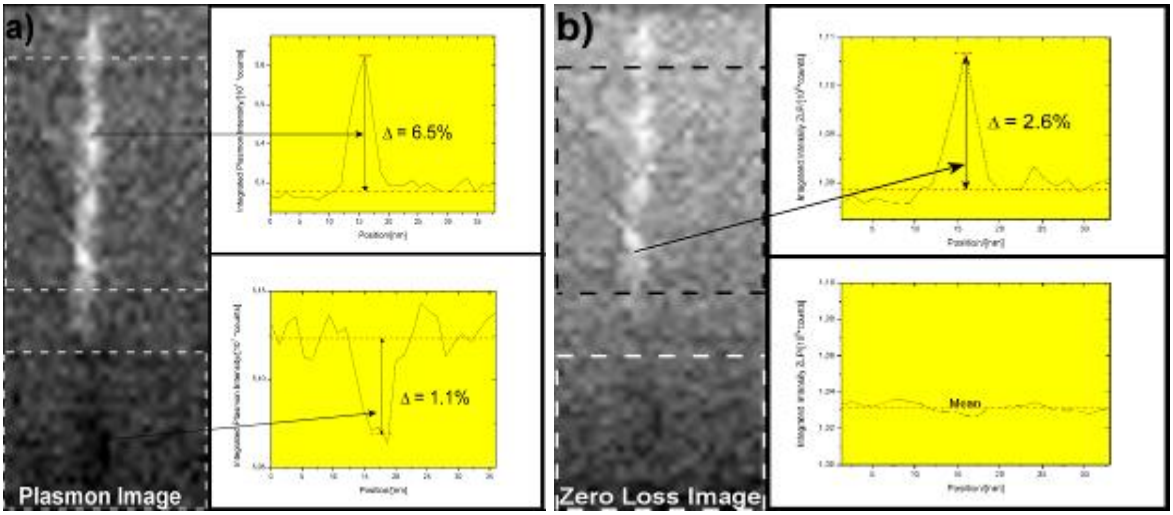

Figure 2. (a) Image of the Plasmon signal (energy window: 12-18 eV) extracted from the individual electron-energy loss spectra and corresponding profiles across boxed regions. Note the contrast inversion compared to the HAADF detector signal in Fig.1. (b) Image of the zero loss peak (ZLP) (energy window: 5 eV) extracted from the individual electron-energy loss spectra and corresponding profiles.

Alloys and Intermetallics

MS.6.162
Fluctuation electron microscopy of a bulk metallic glass

C. Gammer[1,2], D. Beitelschmidt[3], S. Pauly[3], D. Geist[2], J. Eckert[3], H.-P. Karnthaler[2], C. Rentenberger[2]

[1]LBNL, National Center for Electron Microscopy, Berkeley, California, Austria
[2]University of Vienna, Physics of Nanostructured Materials, Vienna, Austria
[3]IFW Dresden, Institute for Complex Materials, Dresden, Germany

christian.rentenberger@univie.ac.at
Keywords: fluctuation electron microscopy, bulk metallic glass, medium range order

Bulk metallic glasses (BMG) are currently the focus of intense research in the materials community due to their potential for structural applications [1]. The attractive properties as very high strength and high elastic limits are closely related to their atomic arrangement. Therefore, a quantitative description of the structure of BMG is necessary to understand their properties. Unlike crystalline materials, the structure of BMG is characterized by the lack of long-range periodicity as in an amorphous structure; still it is assumed that short-range order (SRO) and medium-range order (MRO) are present in BMG. Conventional diffraction methods, e. g. by X-rays or electrons are only sensitive to SRO involving atoms of neighbouring shells. In order to study atomic correlations beyond SRO, new methods are required that are sensitive to detect correlations of MRO (0.5 to 3 nm). Here, we use fluctuation electron microscopy (FEM) [2] to study atomic correlations of a BMG on the MRO scale. FEM is a spatially resolving diffraction technique that is sensitive to structural fluctuations on nanometer scale.

Samples of CuZrAlAg, a BMG produced by copper mould suction casting, were prepared by electropolishing to achieve TEM foils. FEM experiments by taking tilted dark-field images (cf. Fig. 1(a)) were carried out in a TEM operating at 120 and 200kV. The dark-field images show intensity variations due to local structural correlations on the MRO scale (cf. Fig. 1(b,c)). In order to measure MRO, dark-field images taken at different scattering vectors k were analyzed statistically by calculating the normalized variance V(k) of the image intensity I(k,r) [2]: $V(k)=(\langle I(k,r)^2\rangle/\langle I(k,r)\rangle^2)-1$, where <> means averaging over sample position r. Since V(k) depends on the imaging condition, the exact focus found by maximizing V(k) in the image as well as constant condensor settings and no specimen drift are mandatory. Before calculating V(k) the dark-field images were corrected for instrumental effects (e.g. modular transfer function, read-out noise) due to the acquisition using a CCD camera. In order to increase the reliability of V(k) a set of dark-field images was taken by varying the scattering vector k and the angle φ (cf. Fig. 2). The acquisition of dark-field images probing the reciprocal space between given values of k and φ was automated by a script running under “Digital Micrograph”. Averaging over φ was done in two alternative ways: (i) V(k) was calculated from images summed over φ or (ii) V(k) calculated for all images was averaged over φ. Both averaging methods lead to curves of the normalized variance as a function of k with similar characteristics but the absolute values are different (cf. Fig. 3). A peak in the curve indicates that intensity speckles in the images measured by the normalized variance are especially pronounced at a given k-value (4.2 nm^{-1}). The scattering vector of the maximum contains information of the MRO structure. It is interesting to note that in crystalline B2 ordered CuZr the strongest reflection corresponding to (110) has a very similar k-value indicating some similarity in the atomic correlations as in the MRO of the BMG (cf. Fig. 3).

In order to get information on the correlation length sets of dark-field images were taken with different objective apertures (2, 5, 10, 20 μm). Both the size of the objective aperture used to form the image and the wavelength of the electrons determine the resolution of the FEM images. By varying the resolution the sample is probed with respect to MRO on different length scales. The corresponding calculated V(k) curves show the same characteristics with a peak at 4.2 nm^{-1}; as an example the curves obtained from images taken with 5 and 10 μm objective apertures are shown in Figure 4. Plotting the peak values of V(k=4.2 nm^{-1}) as a function of resolution yields a curve containing two maxima (cf. Fig. 5). Two maxima in V as a function of resolution indicate the presence of two MRO correlation lengths of about 0.7 and 2.3 nm in the amorphous structure. The observed MRO correlation lengths can be linked to the size of individual clusters and to the correlation between similarly oriented clusters.

1. A. L. Greer and E. Ma, MRS Bulletin 32 (2007), p. 611.
2. M.M.J. Treacy, D. Kumar, A. Rogee, G. Zhao, P.R. Buseck, I. McNulty, L. Fan, C. Rau and J.M. Gibson, J. Phys.: Condens. Matter 19 (2007) 455201.
3. We kindly acknowledge financial support by the Austrian Science Fund (FWF):[P22440,J3397].

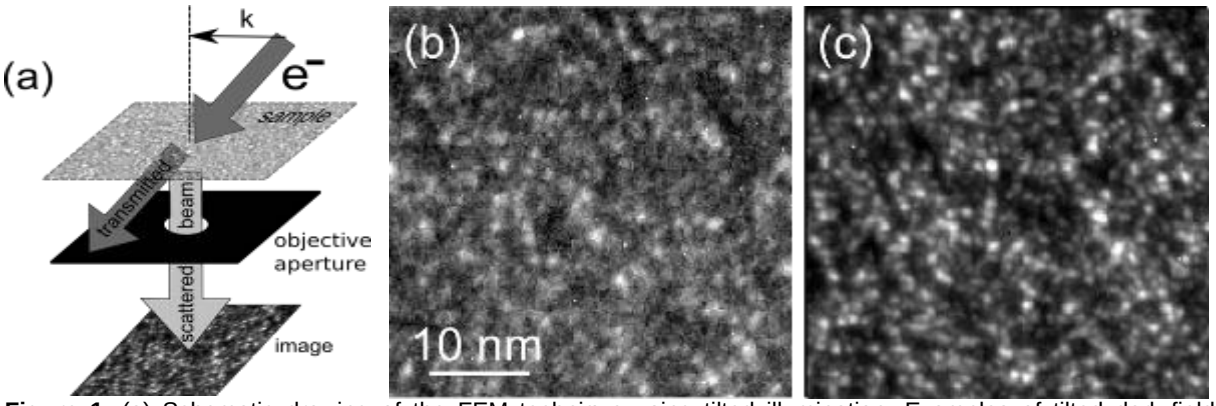

Figure 1. (a) Schematic drawing of the FEM technique using tilted illumination. Examples of tilted dark-field images showing low (b) and high values (c) of the normalized variance.

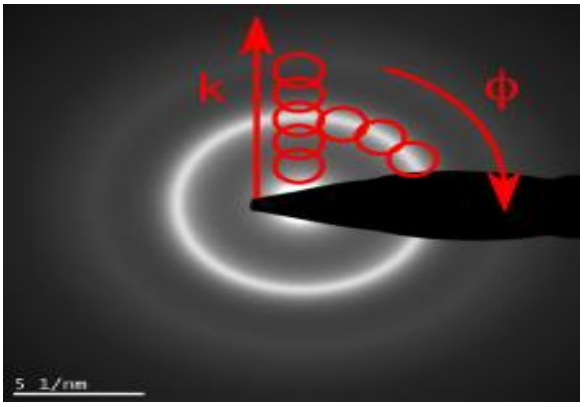

Figure 2. Diffraction pattern of CuZrAlAg bulk metallic glass is characterized by diffuse rings. For the FEM analysis a set of dark-field images is taken by varying the scattering vector k and the angle φ. The rings illustrate the different positions of the objective apertures used to form the dark-field images.

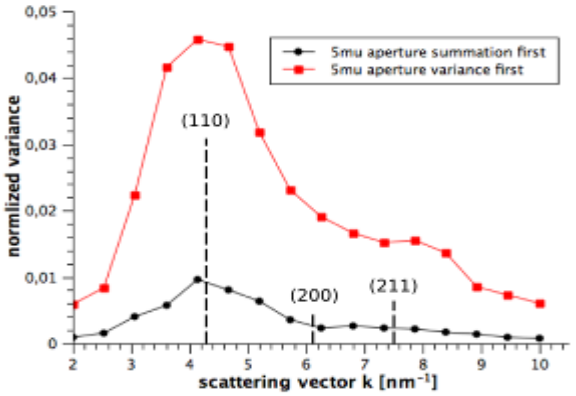

Figure 3. Plot of the normalized variance V(k) of the intensity of images taken with a 5 μm objective aperture. The two curves differ by the method of averaging over the angle φ. Lower values of V(k) are obtained by calculating V of images summed first over φ. The position of structure factors (hkl) of B2 ordered CuZr is indicated.

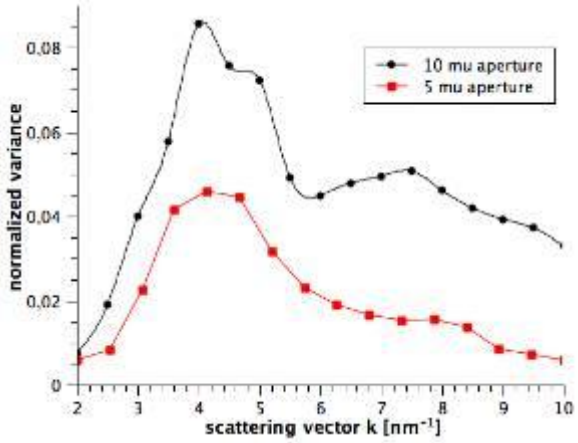

Figure 4. Plot of V(k) calculated from sets of dark-field images taken with different objective apertures (5 and 10 μm in diameter).

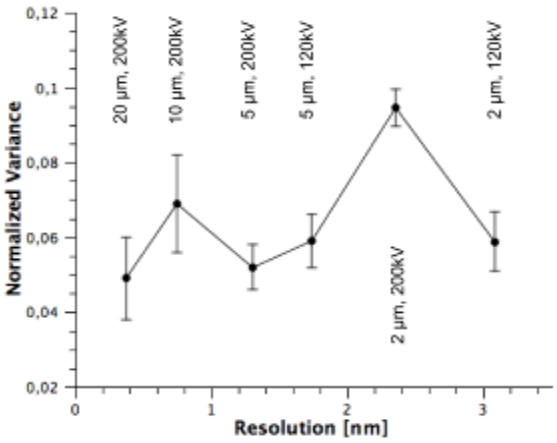

Figure 5. Plot of the normalized variance as a function of the resolution determined by the size of the objective aperture and the acceleration voltage.

Alloys and Intermetallics

MS.6.163
Metastable precipitation in the Al-Mg,Si,Cu system: an atomic STEM-EELS study

T. Epicier[1], M. Lopez-Haro[2], P. Bayle-Guillemaud[2]

[1]INSA-CNRS, MATEIS, umr5510 CNRS, Villeurbanne, France
[2]CEA-Grenoble, Institut Nanosciences et Cryogénie – UJF / SP2M, Laboratoire d'Études des Matériaux par Microscopie Avancée (LEMMA), Grenoble, France

thierry.epicier@insa-lyon.fr

Precipitation hardening is still an important and efficient way to improve the mechanical resistance of aluminium alloys. We focus here on the 6061 grade, namely with the composition Al - Mg 1 wt. % - Si 0.6 wt. % - Cu 0.25 wt. %. This system belongs to the so-called 6xxx series, based on the Al-Mg-Si system. It was previously shown [1,2] that a complex precipitation sequence occurs, which is greatly affected by the presence of any further addition of minor element(s), such as copper:

Low Cu quantity (i.e. 0,07 wt. %): o.s.s.s. □ zones GP □ □" □ [□' + Q'] □ [□ + Si]

High Cu quantity (0,9 wt. %): o.s.s.s. □ GP zones □ □ ' □ Q' □ [Q + Si]

o.s.s.s. mean over saturated solid solution; GP zones are aggregates of solute atoms, comparable to well-known Guinier-Preston zones – see for example original references cited in [3]). Labels □", □', Q', refer to metastable phases, whereas □ (Mg_2Si) Si and Q ($Al_xCu_2Mg_{12-x}Si_7$ [4]) refer to stable phases. Typically, at 573 K, the precipitation sequence can be summarized as [5]: □" → QP + QC → QC + Q' → Q' → □ where QP, QC are metastable phases closely-related to the □' in the Al-Mg-Si system [6]. Although a large number of (HR)TEM studies exist in the literature on this particular alloy (see the recent review [7]), their atomic structures are not accurately known. A major difficulty encountered is indeed that 'composite' particles frequently develop, the HRTEM contrast of which is perturbed by dynamical scattering, local misorientations and possible strain effects. In a recent study by means of STEM-HAADF imaging, a better structural description of some atomic arrangements could be obtained, thanks to Z-contrast images which are much less sensitive to the previous undesirable effects [8]. Starting from a model initially proposed by [6], we were able to refine atomic positions and suggest new atomic occupancies, as well as a different space group for the QC phase. But confirmation of these observations requires chemical analysis at the atomic level.

This is the purpose of the present work. We have carried out STEM-EELS (Electron Energy-Loss Spectroscopy) measurements at the atomic level, using a double Cs-corrected FEI-TITAN microscope recently installed at CEA-Grenoble, Minatec. To minimize as much as possible irradiation effects during 'column-by-column' analysis with a sub-Angström probe, we have performed these experiments at 80 kV. Results are illustrated by figures 1 and 2. In figure 1, we use the Q' phase as a 'standard' in order to ascertain the chemistry of expected Cu-columns, as deduced from the structure refined in the case of the stable phase (Q: $Al_xCu_2Mg_{12-x}Si_7$ [4]). In figure 2, EELS imaging reveals that the brighter dots resolved in the STEM-HAADF images are not those containing the higher content of Cu, but that they are Si-enriched. These experimental results, which would be probably impossible to obtain by another technique, will be used to refine the model of the QC phase [9].

1. W.F. Miao, D.E. Laughlin, *Metall. Mater. Trans. A*, 31A (2000) 361-371.
2. K. Matsuda, Y. Uetani, T. Sato, S. Ikeno, *Metall. Mater. Trans. A*, 32A (2001) 1293-1299.
3. O.B.M. Hardouin Duparc, *Metall. Mater. Trans. A*, 41A (2010) 1873-1882.
4. L. Arnberg, B. Aurivillius, *Acta Chem. Scand.*, A34, (1980), 1-5.
5. V. Massardier, T. Epicier, *Mat. Sci. Forum*, 396-402, (2002), 851-856.
6. C. Cayron, P.A. Buffat, *Acta mater.* 48, (2000), 2639-2653.
7. C.D. Marioara, S.J. Andersen, T.N. Stene, H. Hasting, J. Walmsley, A.T.J. Van Helvoort,
8. R. Holmestad, *Philos. Mag.*, 87, 23, (2007), 3385-341.
9. T. Epicier, C. Cayron, *Rev. Metall.* 109, (2012), 393-407.
10. Thanks are due to the CLYM (http://clym.insa-lyon.fr) for the access to the 2010F microscope, and to the French METSA network (www.metsa.cnrs.fr) for partial financial support.

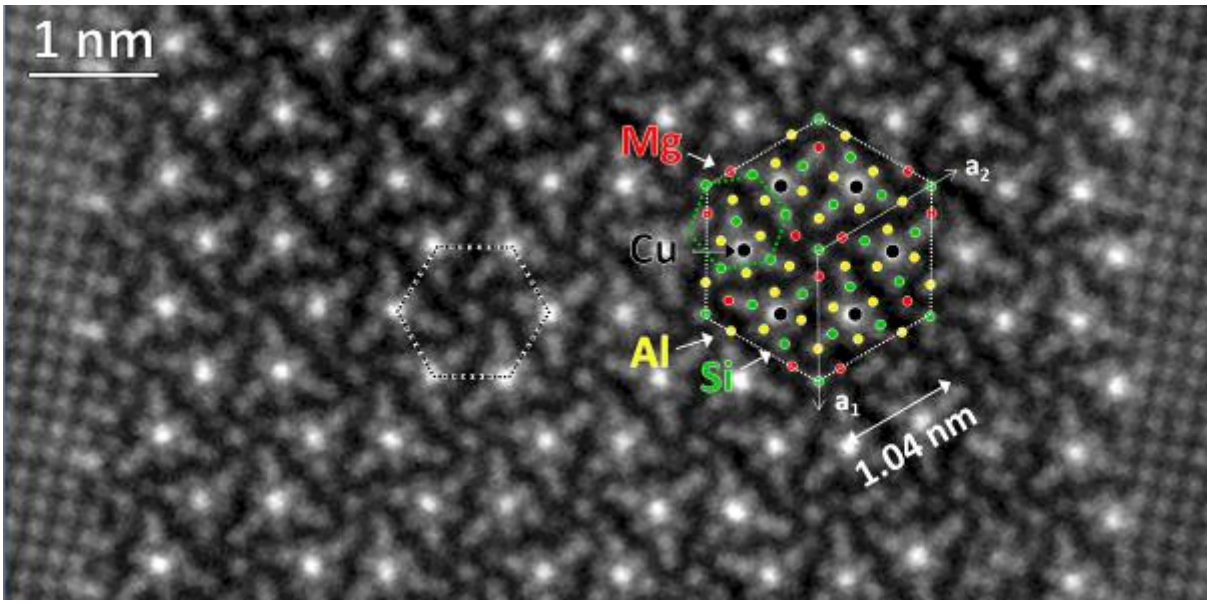

Figure 1. Atomic STEM image of a Q' precipitate, showing a one-to-one correspondence with the model of the stable Q hexagonal phase (P-6, with a = 1.04 nm, c ≈ 0.405 nm [4]); brighter dots image Cu sites.

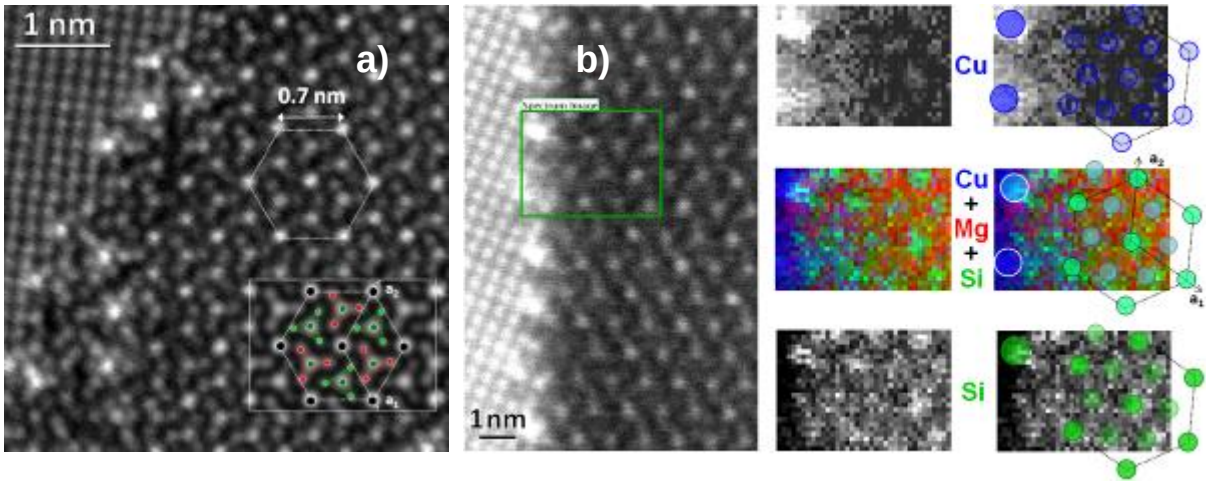

Figure 2. STEM-EELS analysis of the QC phase. a): STEM image and simulation corresponding to the refined model proposed in [8] (hexagonal P-6, a ≈ 0.7 nm, c = 0.405 nm): the hexagonal lattice at 0.7 nm is defined by brighter dots imaging mixed Cu-Si columns. b): STEM-EELS imaging of another QC precipitate showing the respective Cu, Si and composite Cu+Mg+Si *maps* (middle row). Both top and bottom maps show that the brighter dots (0.7 nm lattice) are Si-enriched and not Cu-enriched (note that Cu segregation at the precipitate-matric interface is clearly evidenced).

Alloys and Intermetallics

MS.6.164
In-situ TEM straining of tetragonal martensite in a Ni-Mn-Ga alloy

N. Zárubová[1], Y. Ge[2], O. Heczko[1], S.-P. Hannula[2]

[1]Institute of Physics, ASCR, Department of Functional Materials, Prague 8, Czech Republic
[2]Aalto University, School of Chemical Technology, Departement of Materials Science and Engineering, Aalto, Finland

zarubova@fzu.cz
Keywords: *in-situ* TEM straining, martensitic transformation, Ni-Mn-Ga shape memory alloy

Ni-Mn-Ga is a ferromagnetic shape memory alloy (FSMA) with many potential applications for sensors and actuators. This is based on the fact that large strains can be achieved by application of mechanical, magnetic or combined magneto-mechanical forces [1,2]. The magnetic-field-induced-strain (magnetoplasticity) in Ni-Mn-Ga is caused by the reorientation of martensite variants. The reorientation mechanism in Ni-Mn-Ga has been well explained from the phenomenological point of view [3-5], but there is a discussion about the microscopic mechanism, and only few TEM observations of the reorientation process have been published so far [6-8]. In the present study, the *in-situ* TEM straining tests were performed to follow in detail the reorientation of martensite variants of non-modulated tetragonal martensite (NM), with the aim to explain the mechanism of the twin boundary motion [9].

Foils of $Ni_{52.4}Mn_{27.3}Ga_{20.3}$ alloy (1.67 x 5.5 x 0.1 mm^3) were prepared from a single crystal with NM martensite structure. The central area of the foils was thinned until a hole appeared. The samples were strained in tension at room temperature in a JEM 1200EX microscope equipped with a double-tilt straining stage. The stress-induced processes were video-recorded, and then the structure was examined under stress using two-beam bright and dark field conditions. Some deformed foils were further cut to a 3 mm length and analyzed in a high-resolution Tecnai F20 200kV FEG microscope.

Figure 1a shows the crystallographic orientation of the three tetragonal martensite variants in the foil. M2 is the most favorably oriented variant relative to the external load and M3 is the least preferable one. Figure 1b illustrates two levels of twin hierarchy in the self-accommodated thermally induced martensite. Large domains, separated by incoherent boundaries, consist of internal twins, which form a lamellar structure. The internal twins, about a dozen of nanometers in size, are (101) compound twins, in agreement with the theory of tetragonal martensite. The interfaces between the internal twins (twin planes) are planar and coherent.

After applying the external load, detwinning process starts by movement of twinning dislocations along the internal twin boundaries. The variants oriented more favorably to the applied stress grow at the expense of the less favorable ones. The dislocation speed is very high at the beginning, and a large number of dislocations move simultaneously. As the process successively slows down, movement of individual twinning dislocations can be monitored due to the bow-like contrast, provided that the internal twins are inclined to the foil surface (Figure 1c). The twinning dislocations are starting and ending at the incoherent inter-domain boundaries. The nucleation process is shown in Figure 2a where the dislocations are generated at the intersection of the M3 plate with the domain boundary.

For the variant combination M2+M3 shown in Figures 2a,b the twin planes are ($)_{M2}$ planes. The direction of the Burgers vector of the twinning dislocations, b, is $[101]_{M2}$ as determined from the invisibility criterion, $g \cdot b = 0$ [8]. The pronounced changing contrast on the transforming plates (see Figures 2a,b) is the result of variations in the lattice displacement and twin plate thickness, both due to movement of twinning dislocations on successive twin planes (see the scheme in Figure 2c). The magnitude of the Burgers vector of the twinning dislocations can be determined from the variations of α-fringe contrast on the reorienting twin plates [6]. The changes in the contrast correspond to the phase differences $\alpha = 2\pi(g.b)$, $2\pi(g.2b)$, etc. produced by an array of twinning dislocations with the Burgers vector close to 1/12[101] gliding in the successive ( ) planes.

Our TEM observations agree well with the results of Ref. [6]. For operative reflection g = 022, a train of twining dislocations with the Burgers vector 1/12 [101] will yield a six-fold contrast, $\alpha = \pi/3$, $2\pi/3$, π, $4\pi/3$, $5\pi/3$, 2π. An example is shown in Figure 2b (see also [8]). Six levels of contrast are clearly visible on the transforming M3 plate in the image center. Segment 6 is without contrast, in agreement with $\alpha = 2\pi$ 6/12[101] [022] = 2π. The broad segments of equal contrast shown in Figure 2b often indicate an irregular distribution of the twinning dislocations (Figure 2c, case I), while their arrangement is very regular at the ends of the transforming plates (see double arrows in Figure 2b, and Figure 2c, case II). It is demonstrated in Figures 3a-d, where changes of the contrast with the operative reflection are illustrated. Figure 3d is a dark-field image in reflection 0012_{M2}. The α-contrast disappears in this reflection ($g \cdot b = 1$, $\alpha = 2\pi$) and individual twinning dislocations are visible as fine lines, without disturbance of the α-fringes. The distances between dislocations are about 30nm.

1. K. Ullakko, J.K. Huang, C. Kanter, R.C. O'Handley and V.V. Kokorin, Appl Phys Lett 69 (1996), p. 1966.
2. A. Sozinov, N. Lanska, A. Soroka and W. Zou, Appl Phys Lett 102 (2013), p. 021902.
3. P. Müllner and A.H.King, Acta Mater 58 (2010), p. 5242.
4. O. Heczko, L. Straka, I. Aaltio and S.-P. Hannula, Mater Sci Eng A 481-482 (2008), p. 283.

5. O. Heczko, N. Scheerbaum, O. Gutfleisch, “Magnetic shape memory phenomena”, in Nanoscale magnetic
materials and applications, Springer Science+Business Media (2009), p.399.
6. R.C. Pond, B. Muntifering and P. Müllner, Acta Mater 60 (2012), p. 3976.
7. Y. Ge, N. Zárubová, Z. Dlabáček, I. Aaltio, O. Söderberg and S.-P. Hannulal, Proc. ESOMAT 2009;04007 DOI:
10.1051/esomat/200904007.
8. N. Zárubová, Y. Ge, J. Gemperlová, A. Gemperle and S.-P. Hannula, Func Mater Lett 5 (2012), p. 1250006.
9. N. Zárubová, Y. Ge, O. Heczko and S.-P. Hannula, Acta Mater, submitted.
10. We kindly acknowledge the financial support of the Academy of Finland, Grant Agency of CR (contracts P107/11/0391, P107/12/0800) and Grant Agency of ASCR (contract IAA100100920). Operation of the JEM 1200EX microscope was supported by the grant MEYS of CR LM201126.

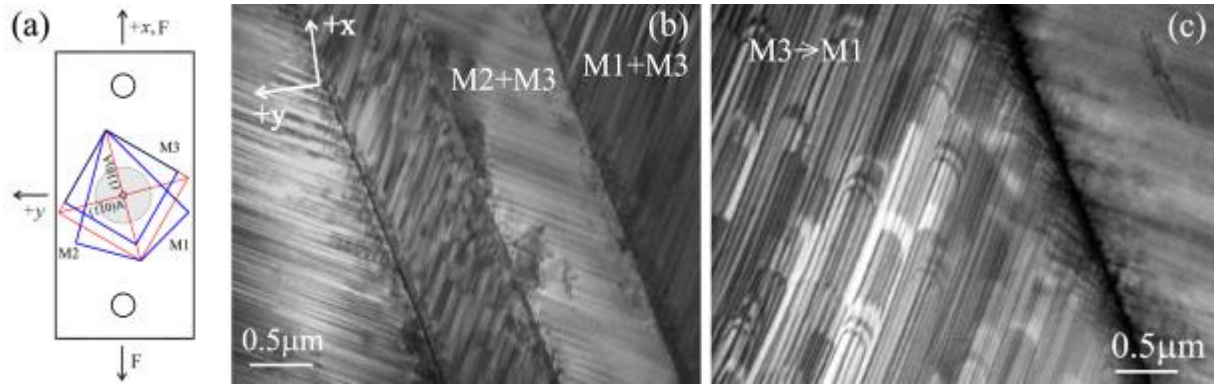

Figure 1. (a) Orientation of the parent austenite (red) and the martensite variants M1, M2, M3 (blue) in the foil. F – external load; *x, y* – tilt axes. (b) Structure of the thermally induced martensite. (c) A video frame recording the detwinning process M3→M1. The twinning dislocations are visualized by the bow-like contrast.

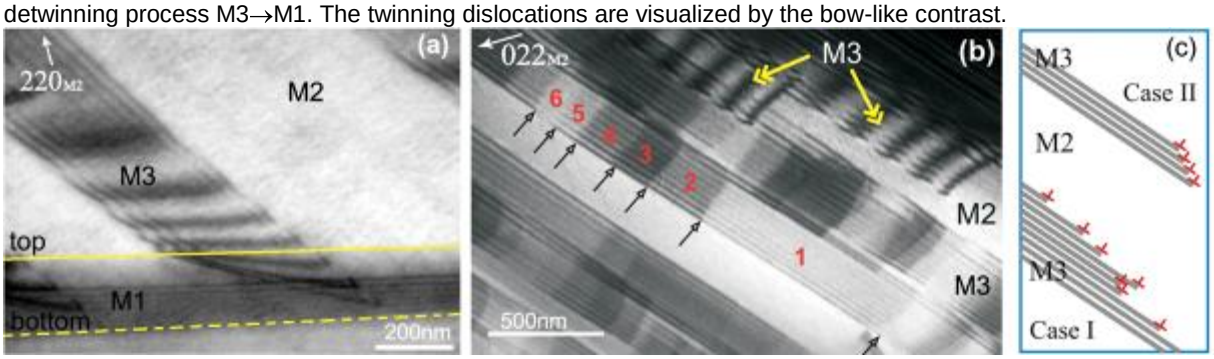

Figure 2. (a) Nucleation of twinning dislocations at the intersection of the M3 plate with the boundary between two domains. (b) Partly detwinned domain M2+M3. Plates of M3 variant reorient into M2 variant. Positions of the twinning dislocations and six levels of the contrast are marked by the black arrows. (c) A scheme of twinning dislocations gliding in parallel twin planes. The twin planes are perpendicular to the plane of the scheme.

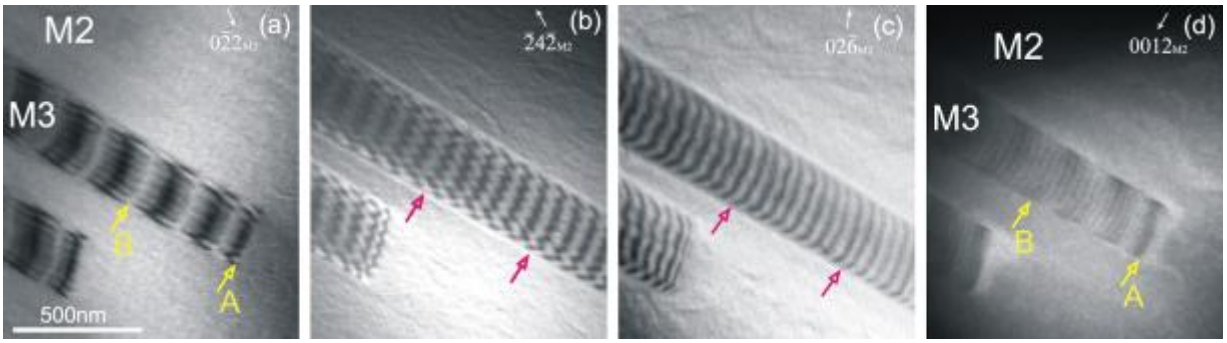

Figure 3. Contrast on reorienting M3 plates in various reflections. (a) **g**·**b** = 1/6; six-level contrast. (b) **g**·**b** = -1/3; three-level contrast. (c) **g**·**b** = -1/2; two-level contrast. (d) **g**·**b** = 1; α-contrast vanished; only dislocations are visible.

Alloys and Intermetallics

MS.6.P165
An EBSD approach for estimating the a´´ martensite fraction in ß titanium

D. Dietrich[1], E. Farghadany[2], A. Zarei-Hanzaki[2], H.R. Abedi[2], M.R. Yadegari[2], T. Lampke[1]

[1]Technische Universität Chemnitz, IWW, Chemnitz, Germany
[2]University of Tehran, College of Engineering, Tehran, Iran, Islamic Republic of

dagmar.dietrich@mb.tu-chemnitz.de
Keywords: Beta titanium alloy, deformation-induced martensite, mean angular deviation.

The newly developed β metastable titanium alloys (Ti-Nb-Ta-Zr alloys, TNTZ) exhibit superior biocompatibility due to properties such as reasonable bio-corrosion resistance, Young's modulus close to the bone stiffness, high strength, and good formability [1]. The stability of the β phase, which is controlled by chemical composition and deformation conditions, provides certain influences on the active deformation mechanism including dislocation slip, twining, crystallographic lattice rotation and martensitic transformation. The heat- and stress-induced α´´ martensitic transformation and reversion affect superelastic and shape memory behavior [2]. A recent study was focused on the correlation between strain rate sensitivity and deformation-induced α´´ phase volume fraction [3].

TNTZ (actually Ti-27.96 Nb-11.97 Ta-5.02 Zr-0.05 O-0.01 C-0.014 N) alloy samples in as-forged and annealed (850°C, 45 min) condition were subjected to an isothermal (25 - 500°C) compression test under strain rates between 0.3 and 0.003 s^{-1}. Cross-sections parallel to the loading axis were prepared with a vibration polishing surface finish for SEM/EBSD studies. The microstructure evolution changes from nearly unaffected ß grains at the sample edges and increasing twinning in a transition region to severe plastic deformation with α´´ phase formation in the sample centre (Figure 1). Deformation-induced martensite has been confirmed by XRD [3].

Of further interest is the volume fraction of martensite formation which was estimated by EBSD with a conventional indexing routine after Hough transformation. The approach is based on the specific lattice correspondence between α´´ and β phases. Assuming the crystal structure of the α´´ phase as simple tetragonal with the [100] and [001] directions parallel to the [011] and [100] directions in the cubic β phase [4], the martensitic phase may be obtained from a minute distortion in the primary β titanium. A comparison of the thus calculated lattice parameters (0.3295 nm and 0.4659 nm) with our XRD results of the orthorhombic α´´ phase (0.3289 nm, 0.4798 nm, and 0.4814 nm) [3] reveals that the α´´ phase can be considered as fcc structure with diminutive deviations. Accordingly, only the ß phase using the lattice parameters derived from XRD, was considered for indexing the electron backscatter diffraction patterns during EBSD analysis and the mean angular deviation (MAD value) was determined (Figure 2). The MAD distribution between 0 and 5° shows two peaks around 2.2° and around 3.2° (Figure 2 g-h). The first peak representing the β phase is broadened due to the occurrence of TNTZ solid solutions formation. The second peak is attributed to the α´´ phase which proves to be justified by correlating the different regions of the inhomogeneous microstructure (Figure 2).

The microstructure observed by electron channeling contrast [5], shows a large number of dislocation arrangements, slip lines, twins and martensite laths in the deformed material which are not present in the almost undeformed edge regions (Figure 1 and 3). Mainly in the transition region, some of the features (Figure 3a) have been attributed to fine twin lamellae showing a disorientation corresponding to the □ type Ti twinning system {112} <111> by EBSD. Deformation-induced martensite laths can be observed across the □ grains (Figure 3b). The increase of the martensite volume fraction has been relatively quantified by EBSD analysis.

1. J. Malek, F. Hnilica, J. Vesely, B. Smola , S. Bartakova, J. Vanek, Mater Design 35 (2012) 731.
2. M. Besse, P. Castany, T. Gloriant, Acta Mater 59 (2011) 5982.
3. E. Farghadany, A. Zarei-Hanzaki, H. R. Abedi, D. Dietrich, T. Lampke, M. R. Yadegari, J Mech Behav Biomed, submitted
4. H.Y. Kim, T. Sasaki, K. Okutsu, J.I. Kim, T. Inamura, H. Hosoda, S. Miyazaki, Acta Mater 54 (2006) 423.
5. R. Zauter, F. Petry, M. Bayerlein, C. Sommer, H.-J. Christ, H. Mughrabi, Phil Mag A 66 (1992) 425.

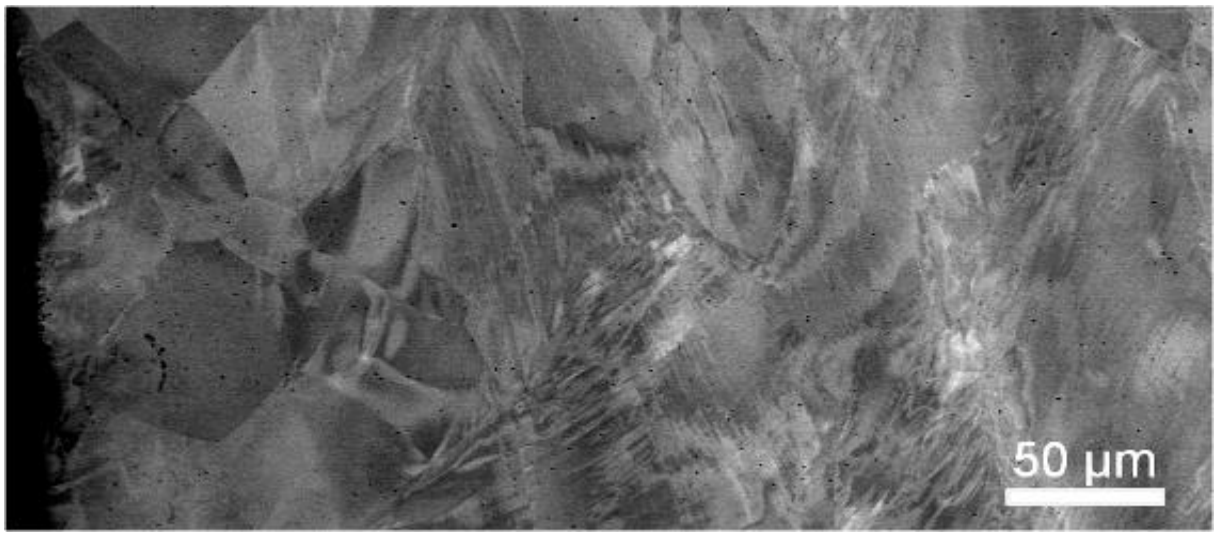

Figure1. Structural changes between the edge (left) and the centre (right) of a compression test sample.

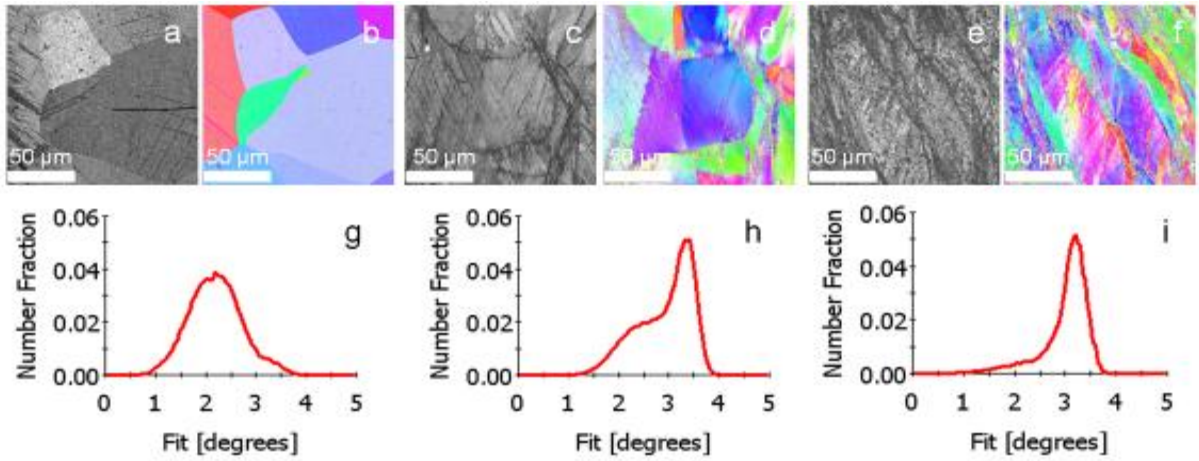

Figure 2a-i. EBSD pattern quality maps, crystal orientation maps and MAD distributions of 3 sample regions: almost undeformed (a, b, g), deformation-twinned (c, d, h) and severely deformed (e, f, i).

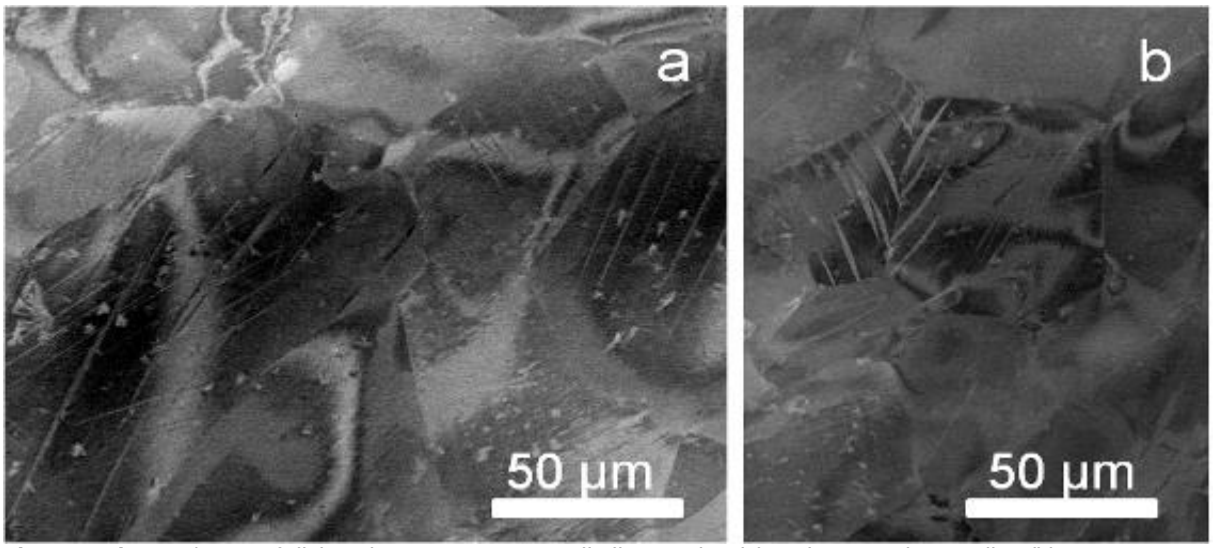

Figure 3a-b.SEM/ECCI of dislocation arrangements, slip lines, twins (a) and martensite needles (b).

Alloys and Intermetallics

MS.6.P166
Study of precipitation and recrystallization in Ti-Nb-Ta biomedical alloy during heat treatment

J. Malek[1], F. Hnilica[1], J. Veselý[1]

[1]UJP PRAHA a.s., Prague, Czech Republic

malek@ujp.cz

Materials for bioapplications (especially beta-titanium alloys) are nowadays intensively studied because of increasing demand on implants and other surgical devices [1,2]. Beta titanium alloys moreover posses low Young's modulus which is very important to avoid stress shielding effect [3-5]. In this work the effect of heat treatment on microstructure of Ti-35Nb-6Ta beta-titanium alloy was studied. The alloy was prepared via powder metallurgy (cold isostatic pressing and sintering). As sintered specimens were hot forged, solution treated and subsequently cold swaged into wires of a 5 mm diameter. Cold swaged specimens were subjected to annealing for various periods (0.5; 1; 2; 4; 8 and 16 hours) at different temperatures (i.e. 500; 550; 600; 650 and 700°C). The changes in microstructure were studied by using transmission electron microscopy (TEM) and electron back scattered diffraction (EBSD).

Precipitation of α-Ti (hcp) phase occurred in all annealed specimens at temperatures used for annealing α-phase instead of ω-phase (usually precipitates at lower temperatures) precipitates [6,7]. Changes in size and morphology of these precipitates depending on annealing conditions can be observed. In general there are two types of precipitates in specimens annealed at lower temperatures. Almost equiaxed precipitates with diameter about 1 micrometer especially placed along grain boundaries (Fig.1). These precipitates were probably present in microstructure before annealing and coarsened during annealing. Finer needle like (with size of few hundreds nm) precipitates can be observed (Fig.2). These are inside grains and were formed during annealing. Their size increases with increasing annealing time and temperature.

After cold swaging the microstructure is highly deformed and EBSD measurements are quite difficult. The deformation is in general localized along grain boundaries and in these areas the image quality (IQ) of EBSD is poor – see Fig.3. Recrystallization processes take place during annealing, but the effect is strongly depended on temperature used for annealing. At temperatures 500 or 550°C no recrystallization can be observed. On the other hand recovery takes place, because the areas along grain boundaries where EBSD image quality pattern was poor decreased in comparison with cold swaged specimen. After annealing 600°C/8h newly formed grains can be observed in formely highly deformed areas. The fraction of recrystallized areas increases with increasing temperature and longer time it can be seen (Fig.4) that after annealing at 700°C the microstructure consist mainly of newly formed fine grains. On the other hand after 0,5h annealing at 700°C only few recrystallized grains are present. As mentioned above precipitation takes place along with recrystallization, but needle – like precipitates are present only in original grains, but not in newly formed fine grains.

1. M. Niinomi, M. Nakai, J. Hieda; Acta Biomaterialia; 8; 2012; p. 3888.
2. M. Geetha, A.K. Singh, R. Asokamani, A.K. Gogia; Progress in Materials science; 54; 2009; p. 397.
3. X. Zhao, M. Niinomi, M. Nakai, C. Myiamoto, T. Furuhara; Acta Biomaterialia; 7; 2011; p. 3230.
4. Y.L. Hao, S.J. Li, S.Y. Sun, R. Yang; Materials Science and Engineering A; 441; 2006; p. 112.
5. M. Niinomi; J. Artif Organs; 11; 2008; p. 105.
6. J.I. Qazi, B. Marquardt, L. F. Allard, H.J. Rack; Materials Science and Engineering C; 25; 2005; p. 389.
7. Y. L. Zhou, M. Niinomi; Journal of Alloys and compounds; 466; 2008; p. 535.
This work was supported by Technology Agency of the Czech Republic (project No. TE01020069).

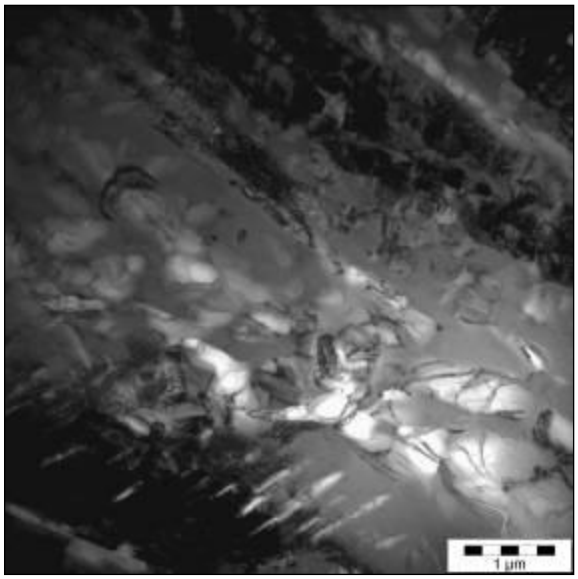

Figure 1: TEM image of coarse α-precipitates in specimen annealed at 600°C for 8 hours

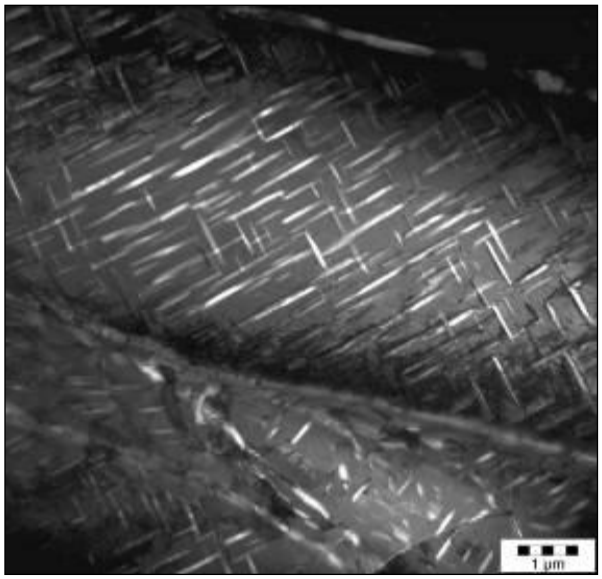

Figure 2: TEM image of fine needle-like α-precipitates in specimen annealed at 600°C for 8 hours

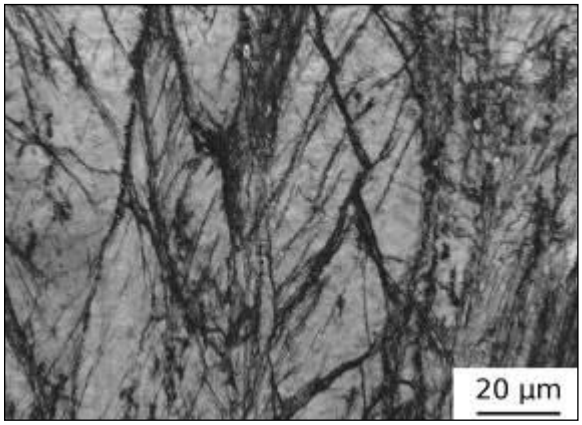

Figure 3. Map of Kikuchi band contrast (image quality) in cold swaged specimen

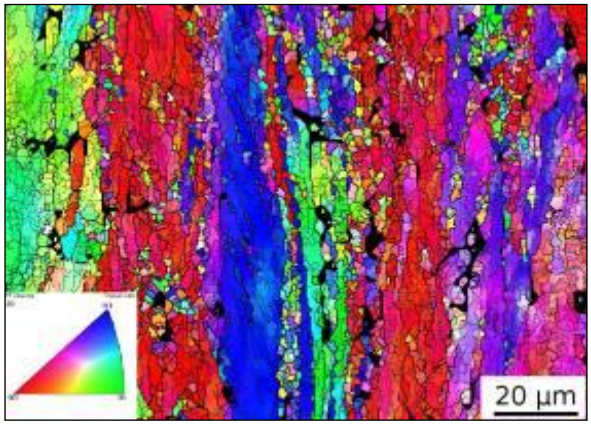

Figure 4: Inverse pole figure map of specimen annealed at 700°C for 4 hours

Alloys and Intermetallics

MS.6.P167
Rectification of EBSD results from large scale maps

J. Buršík[1]

[1]IPM ASCR, Brno, Czech Republic

bursik@ipm.cz
Keywords: EBSD, SEM, disorientation, microtexture

Most polycrystalline solid materials develop a texture, which causes anisotropy of many material properties as much as 20-50% of the property value [1]. Therefore, the determination and interpretation of texture is of fundamental importance in materials technology and understanding texture evolution in the course of various processing steps helps to understand and control the underlying mechanisms. Texture has been studied since methods of X-ray diffraction (and later neutron diffraction) appeared. Besides these well-established so called *macrotexture* techniques, in the last decades we can take advantage of analytical devices embedded in transmission or scanning electron microscopes, which are able to study the so called *microtexture*, i.e. local orientation with the resolution given by the interaction volume of electron beam with material. The technique based on electron backscatter diffraction (EBSD) [1,2] is rapidly evolving and it has become a frequent option of analytical add-ons mainly in the field of scanning electron microscopy (SEM). Then we can study orientation of individual grains even in submicron range, quality of grain boundaries, point-to-point orientation correlations, distribution of phases etc. For obtaining unbiased and accurate results the geometry of EBSD signal collection has to be carefully calibrated. Sample position (most simply a 70° tilt towards the vertical recording screen), diffraction pattern centre and sample-to-screen distance are the most important parameters. Both the calibration procedure and the evaluation of Kikuchi patterns suppose that the backscatter electron signal originates at the electron image centre, i.e. at the sample intersection with optical axis. This causes no problem when collecting EBSD maps at high magnification. This work discusses the catches of collecting large maps in SEM at low magnification. In such case a departure from the image centre means a change of signal path geometry and hence a position-dependent error of orientation evaluation. EBSD data post-processing is proposed, which removes the bias caused by geometrical effects. Let us take a rather extreme example of measuring an EBSD map at magnification as low as about 50× (horizontal view field 2.5 mm) with sample inclined by 70° towards the screen and with sample-to-screen distance of 23 mm. In that case the point at the image edge 1.25 mm off the centre (Figure 1) produces a Kikuchi pattern shifted by 1.25 mm. If the software does not compensate for the shift and expects the signal coming from the centre, it falsely interprets the pattern shift as an additional rotation of the volume under beam by angle τ. In our example τ=3.1°. It means that the apparent angular difference in our example measured between two points and reported by the software reaches up to 6.2° along the central horizontal line and even 7.6° between opposite corners. These are values markedly exceeding the angular resolution, which is on the order of 0.5° for standard EBSD platforms [2]. Figure 2 shows the position-dependent magnitude of angular deviation from the central beam. The above mentioned geometrical effect is less important at higher magnifications and of course it can be completely avoided if we scan by the stage and thus keep the geometry of signal collection invariable (on the other hand scanning by stage is slower and the positioning is less accurate compared to beam scanning). When using standard beam scanning to collect orientation maps at lower magnification, we always have to bear in mind that the local orientation evaluated by the system depends on the position even in the case of perfect single crystal: e.g. angular deviation of two points increases with their distance. This artefact mixes with the true changes of crystal grains orientation. Did we detect a continuous rotation while scanning across a large packet of subgrains or lamellas? It can have physical meaning, but we should be careful and consider different explanation as well. We worked with an Oxford Instruments Analytical system INCA Crystal (The Microanalysis Suite - Issue 15) and recently also with the AZtecHKL system (version 2.0). Until the correction for beam position is eventually built in the software by developers (which seems to be quite straightforward and the most correct solution) we find it useful to post-process the data from large scale EBSD maps collected at low magnification. Euler angles and coordinates of all points in a map were exported to a worksheet and an additional rotation was applied

depending on the magnification and point position. By this way we could improve the data quality and reach an uncompromised precision in microtexture analysis (see a demonstration in Figure 3) [3].

1. V. Randle and O. Engler, Introduction to Texture Analysis, Taylor & Francis, London, 2000.
2. A.J. Schwartz, M. Kumar, B.L. Adams and D.P. Field (Eds.), Electron Backscatter Diffraction in Materials Science, Springer Science+Business Media, New York, 2009.

3. We kindly acknowledge the financial support from the Czech Science Foundation (Project P108/11/2260).

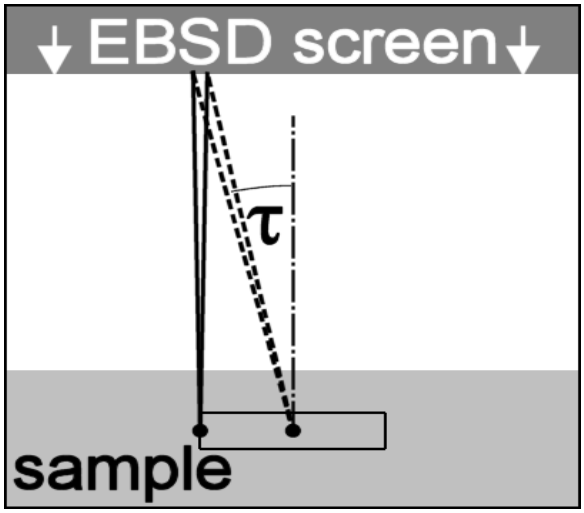

Figure 1. EBSD pattern collection geometry (top view, drawing not to scale). A pair of Kikuchi lines is generated at the edge of the mapped region. This is falsely interpreted by the system as a pair generated at the centre with additional tilt τ.

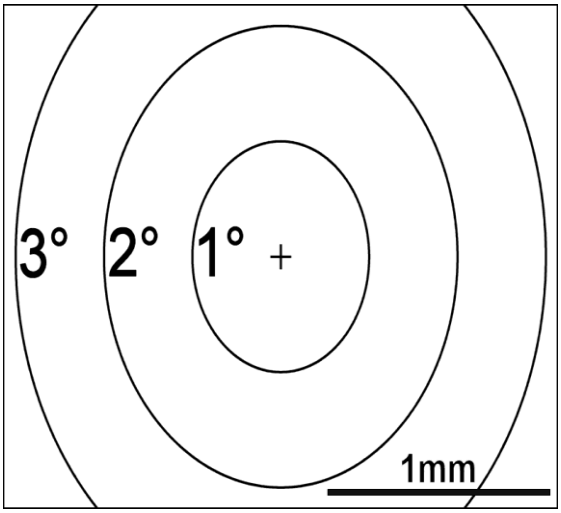

Figure 2. Magnitude of additional tilt due to signal collection geometry (plan view). Isolines are not circles due to sample surface tilt relative to EBSD screen. The values are calculated for sample tilt 70° and sample-to-screen distance 23 mm. With increasing magnification we are zooming in on the central part and the geometric effect becomes less important.

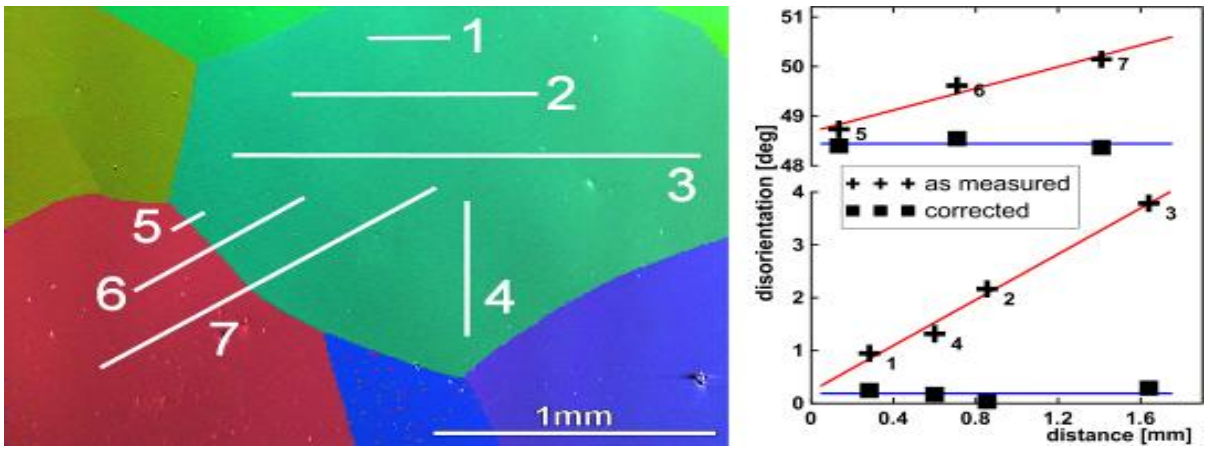

Figure 3. EBSD orientation map of a coarse grain annealed copper with several measurements of disorientation between line endpoints. Inside a single grain (measurements 1 to 4) the values reported by the analytical system increase nearly proportionally with the endpoints distance. This artefact is completely removed by our data post-processing (see the plot on the right). Similar situation occurs while measuring disorientations across a grain boundary (lines 5 to 7). After data post-processing we do not need to worry about the line length: all the measurements give almost the same result.

Alloys and Intermetallics

MS.6.P168
Relation between macroscopic shrinking and microstructural evolution in 17-4PH steel.

R. Sowa[1], A. Dziedzic[2], S. Arabasz[3], I. dul[4], M. Parlinska-Wojtan[1]

[1]University of Rzeszow, Center for Microelectronics & Nanotechnology, Rzeszow, Poland
[2]University of Rzeszow, Center for Innovation & KNowledge Transfer, Rzeszow, Poland
[3]Labsoft SA, warszawa, Poland
[4]WSK PZL-Rzeszow, Rzeszow, Poland

sowa.roamn89@gmail.com
Keywords: steel 17-4PH, Cu precipitation hardening, martensite, NbC precipitates,TEM

The investigated material is a corrosion-resistant, Cu precipitation hardened steel 17-4PH, which shrinks in an uncontrolled way, as a result of the following heat treatment: solution treatment at 1028C for 1 h (condition A), ageing at 540C for 4 h (condition H1025), [1-5]. The aim of this study is to clarify and understand the behavior of the material during the above defined thermal processes based on chemical analysis, microstructure combined with micro-hardness measurement and identification of phase transitions in subsequent stages of heat treatment.

The phase identification was made by X-ray diffraction (XRD) and microstructural imaging was performed using transmission electron microscopy (TEM), scanning transmission electron microscopy (STEM) and scanning electron microscopy (SEM). The chemical analysis was accomplished by energy dispersive X-ray (EDX), and the TEM lamella, were cut by focused ion beam (FIB) technique.

The results were obtained from four samples differing in the applied heat treatment, which is shown in Table 1. Sample 1 is derived from the state of delivery (condition A), sample 2 was again solution treated with the same parameters as before (condition A+A), Sample 3 underwent additionally ageing (condition A+A+H1025), while sample 4 was again solution treatment (condition A+A+H1025+A).

Analysis of the microstructure of the 4 samples shows distinct differences between the states. Figure 1 shows SEM images the cross-sections of the four samples, which were polished and subsequently etched to reveal the microstructure topography. Based on these photographs, it can be clearly seen, that the use of additional heat-treatment operations on samples 1, 2, 3 contributes to significant and irregular grain growth compared to the delivery condition, Figure 1 (a)-(c). Consequently, it is expected that a change of hardness and yield point will occur with a changing grain size. Furthermore, similarities in the microstructure of samples 2, Figure 1(b) and 4, Figure 1(d), such as the presence of lath martensite, in form of parallel stripes and residual austenite – distinct grain boundaries, can be cleary observed. This interpretation is in agreement with the TEM and STEM observations of internal microstructure (images not shown here), where finer grains are visible in sample 1 compared to sample 2. Sample 4 exhibits a large quantity of lath martensite, which contains many dislocations, Figure 1(e).

In all samples, the TEM and the STEM images reveal the presence of, Nb carbides with sizes varying from 50 to 150 nm, confirmed by chemical analysis, Figure 2(a). In the case of sample 3, a large quantity of Cu precipitates, which did not appear in samples 1 and 2 was observed. The Cu content was confirmed by chemical analysis, Figure 2(b). After the solution treatment, these precipitates almost disappeared in sample 4. However, in areas with a high density of dislocations, individual, residual copper precipitates could be identified by EDX. Analysis of the XRD diffractogramms allowed the identification and comparison of phases observed in SEM and TEM photographs, as well as relating the change of lattice parameters to the observed phase transitions and macroscopic shrinking of the material.

1. H.R. Habibi Bajguirani, Mat. Sci. & Eng. A 338, (2002) p. 142-159
2. H. Dong, M. Esfandiari, X.Y. Li Surface & Coatings Technology 202 (2008) p. 2969–2975
3. J. Wang, H. Zou, C. Li, S. Qiu, B. Shen Materials Characterization 57 (2006) 274–280
4. J. Wang, H. Zou, C. Li, Y. Peng, S. Qiu, B. Shen Nuclear Engineering and Design 236 (2006) 2531–2536
5. J. Wang, H. Zou, C. Li, S. Qiu, B. Shen Materials Characterization 59 (2008) 587–591

	Condition A 1028°C 1h	Additional Condition A	Aging = 551°C 4h	Condition A 1028°C 1h
Sample 1	Condition A			
Sample 2		Condition A+A		
Sample 3			Condition A+A+H1025	
Sample 4				Condition A+A+1025+A

Table 1.heat treatment procedure applied to the 17-4 PH steel samples

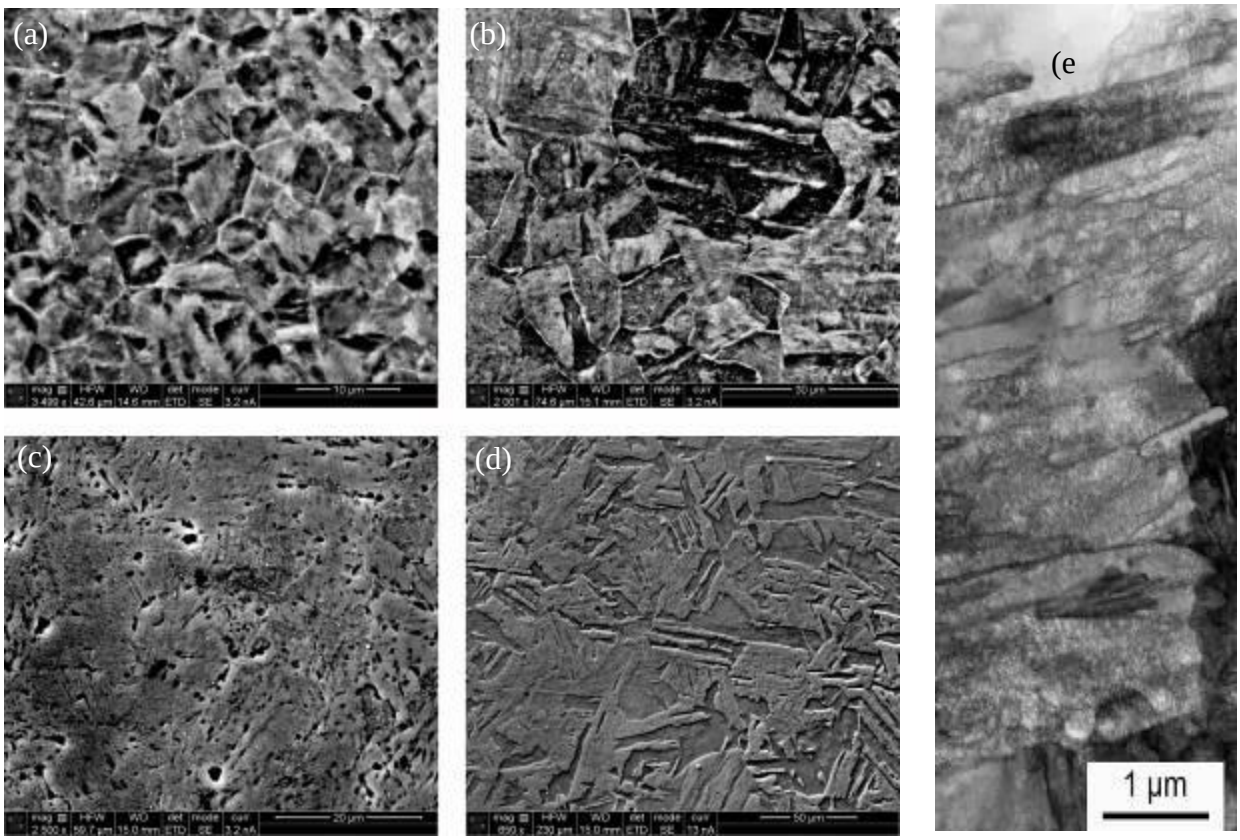

Figure 13. SEM micrographs of polished and chemically etched sample cross-sections illustrating differences between them: (a) Sample 1, condition A; (b) Sample 2, condition A+A; (c) Sample 3, condition A+A+H1025, (d) Sample 4, condition A+A+H1025+A. Please note that the scales on the images are different.

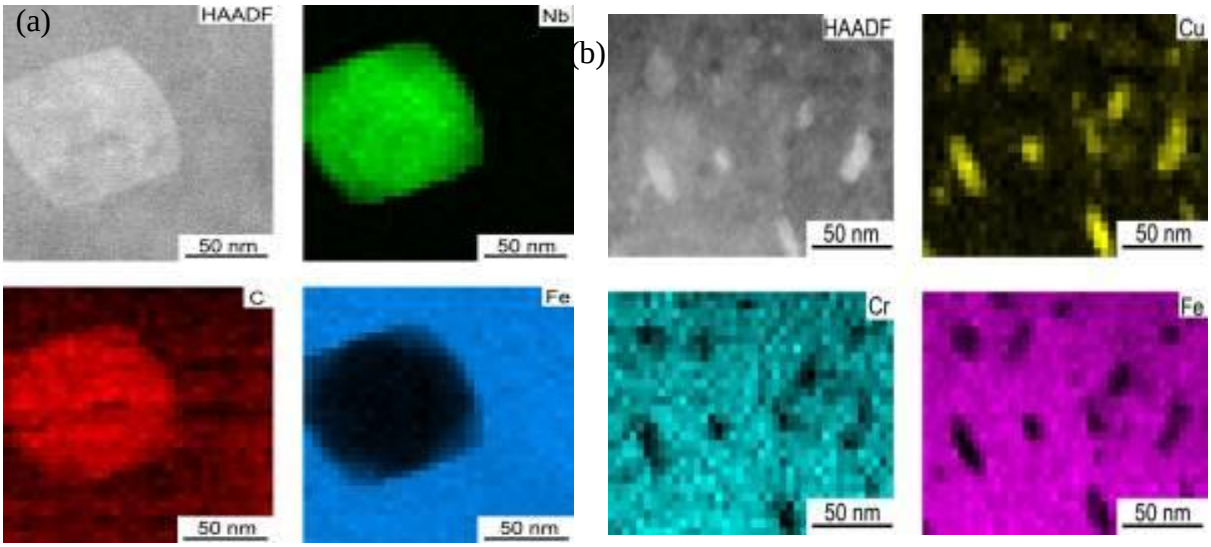

Figure 14. HAADF images and EDX maps of: (a) NbC precipitates present the microstructure of all 17-4PH steel samples; (b) Cu nanoprecipitates observed in the microstructure of sample 3.

Alloys and Intermetallics

MS.6.P169
Investigation of the HAADF-STEM contrast thickness for different camera lengths in metallic glasses

V. Schmidt[1], H. Rösner[1], M. Peterlechner[1], G. Wilde[1]

[1]Universität Münster, Institut für Materialphysik, Münster, Germany

vschm_02@uni-muenster.de

Shear bands are of utmost importance for understanding the plastic deformation behaviour of metallic glasses. They are associated with a structural change compared to the surrounding matrix due to local dilatation most likely resulting in enhanced free volume [1]. Thus the quantification of free volume inside shear bands is an important issue.

In this respect, we have developed a new experimental approach [2] to measure density changes using the relation of the dark-field intensity I/I_0 (scattered electrons collected by a high-angle annular dark-field (HAADF) detector) and the mass thickness:

$$\frac{I}{I_0} = \left[1 - \exp\left(-\frac{N_A \cdot \sigma \cdot \rho \cdot t}{A}\right)\right] = \left[1 - \exp\left(-\frac{\rho \cdot t}{x_k}\right)\right] \quad \text{(Eq. 1)}$$

Where N_A is the Avogadro's number, σ is the total scattering cross-section, ρ is the density, t is the foil thickness and A is atomic weight. x_k is the contrast thickness, which is defined as $A/(N_A \cdot \sigma)$.

The foil thickness t is obtained from the low-loss region of the electron-energy loss spectrum (EELS) [3], which is acquired simultaneously to the HAADF signal.

To obtain a small argument of the exponential function, which allows the linearization of Eq. 1 to $I/I_0 \approx \rho \cdot t/x_k$, the contrast thickness should preferably be large. This can be achieved by choosing small camera lengths. However, the camera length affects the scattering cross-section and thus the HADDF-STEM signal. Larger camera lengths show a better signal-to-noise-ratio. However, the collection angle for the EELS measurement has to be smaller than the convergence angle [3]. In the present study gain-corrected and normalized HAADF-STEM line scans using different camera lengths were compared taken on a FEI Titan 80-300 operated at 300 kV. Different systems of metallic glasses were examined using melt-spun $Al_{88}Y_7Fe_5$ as well as $Pd_{40}Ni_{40}P_{20}$.

We found that the HAADF-STEM signal was constant within the noise level for different camera lengths from 48 mm to 130 mm. Thus the linear approach works sufficiently accurate within this range. However for larger camera lengths a deviation in the HAADF-STEM intensity was observed.

Thus, it is concluded that a camera length of 130 mm was the best choice for simultaneous measurements of the HAADF-STEM and EELS signal.

1. P.E. Donovan, W.M. Stobbs, Acta Metall. 29 (1981), p. 1419.
2. Submitted in Ultramicroscopy
3. K. Iakoubovskii, K. Mitsuishi, Y. Nakayama, K. Furuya, Microsc. Res. Tech. **71** (2008), p.626.
4. D. Williams, C. Carter, Transmission Electron Microscopy (1996), p.685-688.
5. We kindly acknowledge financial support by the DFG via SPP 1595 (Topological engineering of ultra-strong glasses). Part of this work was carried out with support of the Karlsruhe Nano Micro Facility (KNMF), a Helmholtz research infrastructure at Karlsruhe Institute of Technology (KIT).

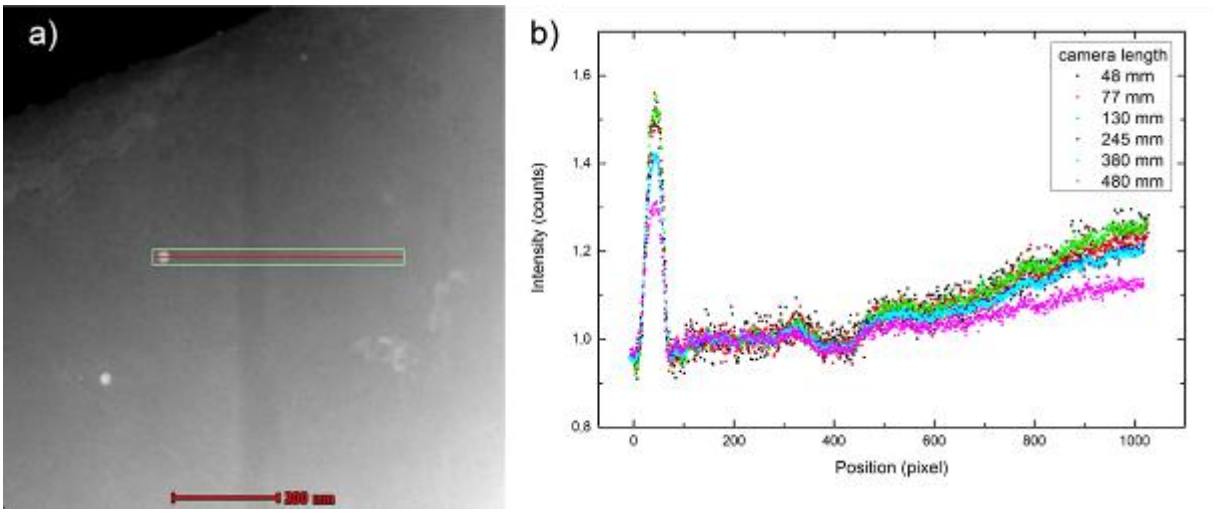

Figure 15. a) HAADF-STEM image of a shear band in $Al_{88}Y_7Fe_5$.The position of the line scan is indicated by the frame and integrated over the area. b) Gain-corrected and normalized intensities of the line scans shown for different camera lengths. Note the deviation for large camera length.

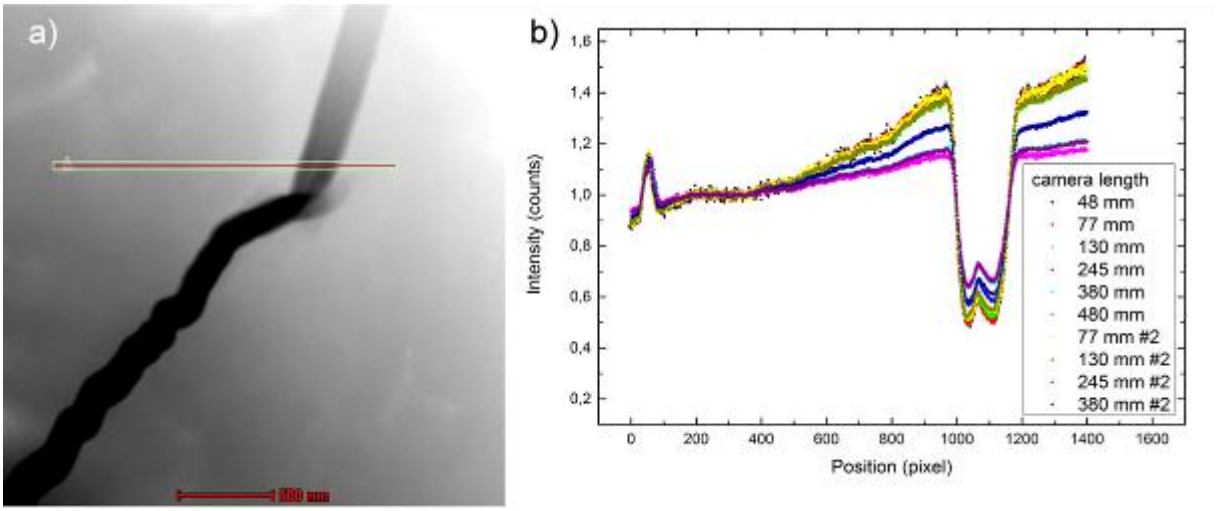

Figure 16. HAADF-STEM image (a) of a crack-initiated shear band in $Pd_{40}Ni_{40}P_{20}$. The line scan is integrated over the boxed area. b) Profiles repeated and compared with respect to different camera lengths. Larger camera lengths reveal an underestimation of the intensity change compared to the smaller ones.

Alloys and Intermetallics

MS.6.P170
Statistical analysis of nanocrystals embedded in the amorphous phase of a Co-Ti alloy studied by TEM

S. Noisternig[1], C. Gammer[1,2], D. Geist[1], H.-P. Karnthaler[1], C. Rentenberger[1]

[1]University of Vienna, Physics of Nanostructured Materials, Wien, Austria
[2]LBNL, National Center for Electron Microscopy, Berkeley, Austria

stefan.noisternig@univie.ac.at
Keywords: nanocrystals, amorphous phase, severe plastic deformation

Amorphous alloys combine desirable properties of both conventional crystalline alloys and oxide glasses. They exhibit e.g.: the maintenance of dimensional accuracy, room temperature strength and a high elastic strain as compared with their crystalline counterparts. Their big disadvantage is a very low tensile ductility. Nevertheless, most amorphous alloys are not intrinsically brittle and possess mechanisms for plastic flow [1]. In the present study we show that in an amorphous alloy small crystals exists and it is thought that they could have a positive influence on the macroscopic properties. A Co-23at.%Ti alloy is studied for crystallisation in its amorphous phase with a transmission electron microscope (TEM) using 200 kV. The aim is to determine the size and quantity of crystals in the amorphous phase. The amorphous phase is accomplished by severe plastic deformation using high pressure torsion. A crystalline Co-Ti specimen is compressed at 4 GPa between two anvils which are then turned against each other for 20 rotations. This induces lattice defects and increases the free enthalpy until it is higher than the free enthalpy of the amorphous state and the crystal turns into the amorphous phase. An area of approx. 530 nm² with a thickness of approx. 40 nm is considered in the amorphous phase of the Co-Ti specimen. Fig. 1 shows the considered area and a large crystalline area C on the left side due to the inhomogeneous deformation of the specimen. The local thickness is determined by local intensity measurements at different tilt angles of the specimen. A functional relation between the specimen thickness and the measured intensity in an amorphous specimen is given in [2]. One can obtain the local thickness as a fit parameter of the intensity - tilt angle relation. The nanocrystals embedded in the amorphous phase are studied by bright field and dark field images captured with the CCD-camera of the TEM (see Fig. 2 and 3). The contrast theories for the amorphous phase and that for the crystalline phase are quite different. The amorphous phase can be described by diffuse scattering [2] while crystals are described by diffraction. It is interesting to note that there are bright areas in the bright field images and also dark areas in the dark field images (cf. Fig. 2 and 3). If a crystal is far off a Bragg condition, it will cause a bright contrast in a bright field image because of the intensity loss of the incident electron beam in the surrounding amorphous phase due to diffuse scattering. Likewise the amorphous phase has a certain amount of intensity in the dark field image. Thus crystals which do not satisfy the selected diffraction conditions for the dark field image will cause a dark contrast compared to the surrounding amorphous phase. In order to recognize all crystals in the amorphous phase the specimen is tilted in little steps for the bright field images. Dark field images are taken with an objective aperture (20 µm) set on the first diffuse ring in the diffraction pattern as shown in Fig. 4 (There also lie diffraction spots of the nanocrystals.) By shifting the diffraction pattern along the ring all crystals with reflections included in the objective aperture are contained in tilted dark field images. A main task is to find a procedure for the evaluation of the images. There are about 15 images to evaluate for both imaging methods. The crystalline areas are segmented manually for the bright field images while the evaluation of the dark field images is done partly automatised by the application of digital image processing. Thereby the bright and dark areas in the dark field images are segmented separately. The procedure must allow manual changes and corrections because of overlapping crystalline areas in some images and differences of the image positions in the specimen. A combined mask image of bright field and dark field images is given in Fig. 5. The present results show that the nanocrystals have an average diameter of 7 nm. The value is obtained by a measurement of the crystal areas and the assumption of their circular forms. This is a valid approximation according to the observed morphology. The crystals cover approx. 1-2% of the considered volume of the specimen. Results for the dark field images exhibit smaller values than those for the bright field images which could be related to the different segmentation methods. Fig. 6 shows a comparison of the crystal diameters for both the bright field and dark field evaluation.

1. A. L. Greer, E. Ma, MRS Bulletin 32 (2007), p. 613.
2. L. Reimer, H. Kohl in "Transmission Electron Microscopy", 5. ed. , (Springer, New York) (2008), p.196.
3. We kindly acknowledge the support by the Austrian Science Fund (FWF): [P22440].

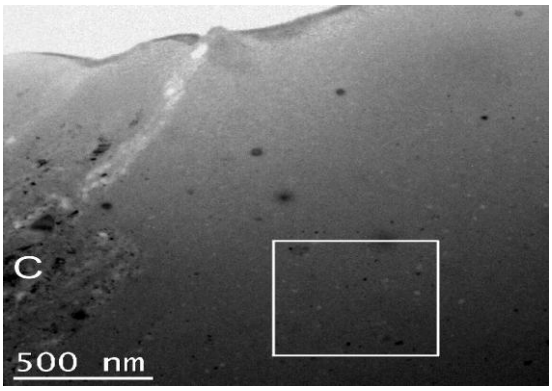

Figure 1. Amorphous phase with the evaluated area and a crystalline area C on the left side

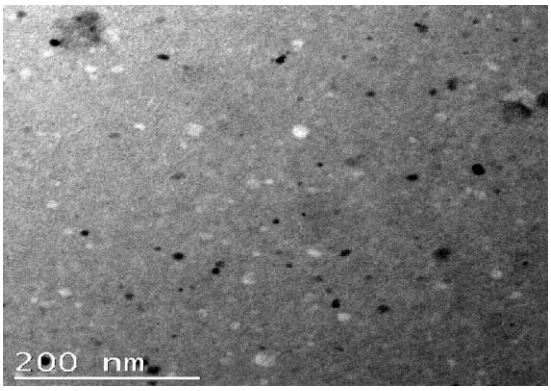

Figure 2. Bright field image of the evaluated area, showing dark but also bright nanocrystals

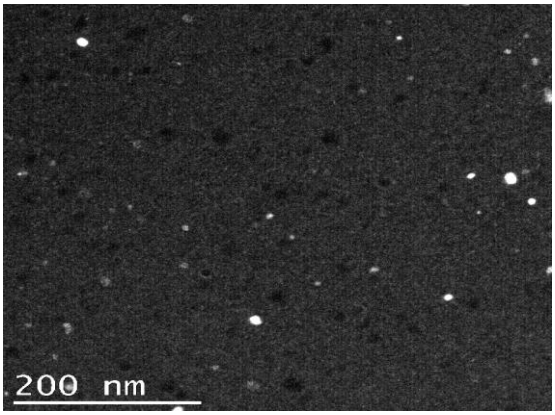

Figure 3. Dark field image of the evaluated area (same area as in Fig. 2), showing bright but also dark nanocrystals.

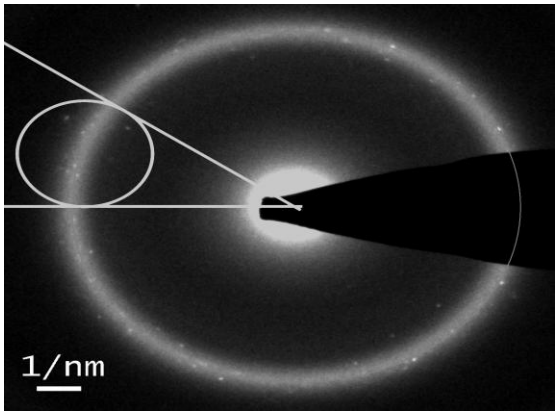

Figure 4. Diffraction pattern with marked objective aperture lying on the diffuse ring of the amorphous phase and containing spots of the nanocrystals

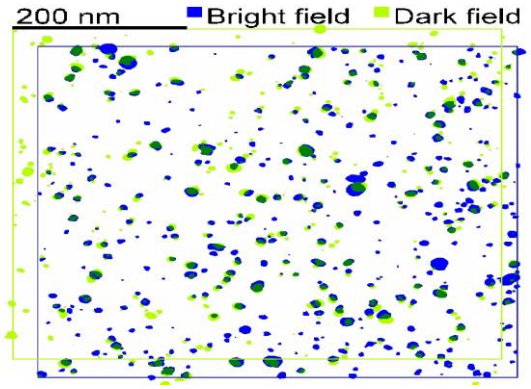

Figure 5. Combined mask image of the segmented bright field and dark field images of the nanocrystals

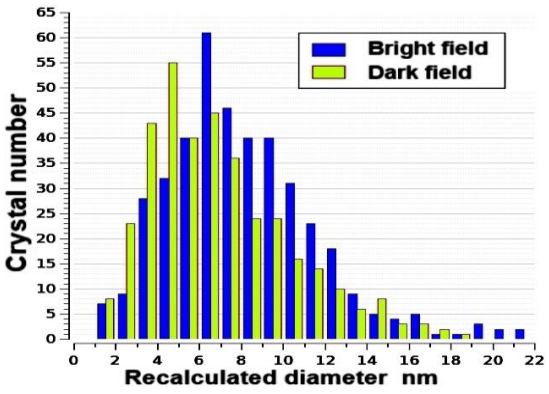

Figure 6. Frequency - diameter graph of the crystals for both the bright and the dark field evaluation

Alloys and Intermetallics

MS.6.P171
The SEM study of ADI material embrittlement in water and hydrogen environment

D. Labus[1], D. Rajnovic[1], S. Balos[1], M. Dramicanin[1], O. Eric Cekic[2], L. Sidjanin[1]

[1]Faculty of Technical Sciences, University of Novi Sad, Novi Sad, Serbia
[2]Innovation Centre, Faculty of Mechanical Engineering, University of Belgrade, Belgrade, Serbia

danlabus@uns.ac.rs
Keywords: ADI material, water, hydrogen, embrittlement, fracture mode

Austempered ductile iron (ADI) is advance material produced by austempering of ductile iron. Due to unique microstructure of ADI material, known as ausferrite (mixture of high carbon enriched, stable, retained austenite and ausferritic ferrite), its possess an excellent combination of mechanical properties, such as: high strength, ductility and toughness together with good wear, fatigue resistance and machinability. Consequently, ADI materials are used increasingly for many wear resistant and tough engineering components in different sectors including automotive, trucks, construction, earthmoving, agricultural, railway, etc [1, 2].

However, in recent years it is noticed that ADI materials in contact with water and other liquids exhibits a drop of tensile properties, that is, decrease in strength and even more critically, ductility [3-5]. This embrittlement phenomenon could potentially lead to catastrophic failure in practical applications. Furthermore, the embrittlement phenomenon is revertible [3]. After removing from water and drying, specimens revert their previous tensile properties. There are several explanations for degradation of the tensile properties. The most common is hydrogen embrittlement [3]. However, Masud *et al* [4] suggested that this process is not an electrochemical phenomenon and that H atoms are not responsible for the embrittlement. Furthermore, Caballero *et al* [5] also reported that hydrogen is not involved in embrittlement of ADI and that the water is substance which embrittle the ADI. As there is still some unknowns about influence of hydrogen on the embrittlement phenomenon further study is necessary.

For that reason, in this study a tensile test (EN 10002) of ADI materials in water and gaseous hydrogen environment was performed. The two different grades of ADI were used. The ADIs were produced from unalloyed ductile iron by austenitisation at 900°C for 2 hour, followed by austempering at 300 or 400°C for 1 hour. The microstructure was examined by “Leitz-Orthoplan” light microscope, while fracture mode has been examined by SEM JEOL JSM 6460LV, at 20kV.

The light micrographs of the ADI microstructure are given in Figure 1. The graphite spheroidisation was more than 90%, with average graphite volume fraction of 10.9%, nodule size of 25 to 30 μm and nodule count of 150 to 200 per mm^2, Figure 1a. The austempering at 300°C/1h produce ADI material with high strength but lower ductility, while 400°C/1h produced ADI with lower strength but with higher ductility, Table 1. This difference in mechanical properties is due to different morphology of obtained microstructures [1, 2]. The microstructure of both samples is fully ausferritic consisting of mixture of ausferritic ferrite and carbon enriched retained austenite. The increase of transformation temperature from 300 to 400°C changes the ausferritic morphology, from needle-like (Figure 1b) to more plate-like (Figure 1c), and amount of retained austenite from 16 to 31.4%, respectively. The results of tensile test (Table 1) in different environments showed that the ADI material exhibits the most pronounced decrease of tensile properties in the water. Testing in the hydrogen atmosphere showed that there is also some reduction of mechanical properties. This decrease is less pronounced compared to testing in the water. The SEM analysis of embrittled specimens revealed brittle fracture mode at a small specimens surface area, Figure 2. The rest of the surface exhibits mostly ductile fracture mode with some quasi-cleavage, Figure 3. The brittle fracture area at the surface indicates that the fracture was initiated in that zone. However, the appearance of brittle fracture is not typical for this type of ADI material. Partially, the fracture looks like as result of fatigue crack growth, with appearance of randomly oriented striations lines stretching from free specimens surface or free surface around graphite nodules, Figure 4a. This appearance could be attributed to the cyclic chemisorption of hydrogen into narrow region beneath specimens surface. Thus, causing embrittlement, then brittle fracture and finally, new free surface where chemisorption might start again. The high magnification of transgranular cleavage fracture in brittle zone can be seen in Figure 4b.

Based on obtained results it could be summarized that primary effect on ADI material embrittlement has hydrogen. Furthermore, embrittlement is more pronounced in liquid environments than in gaseous. The chemisorption of hydrogen atoms into the material surface cause the formation of brittle zone which acts as a weak place for the fracture nucleation.

1. R.A. Harding, Kovove Materialy 45 (2007), p. 1.
2. L. Sidjanin, D. Rajnovic, O. Eric and R. E. Smallman, Materials Science and Technology 26 (2010), p. 567.
3. S. Komatsu, Y. Osafune, Y. Tanaka, K. Tanigawa, S. Shibutani and H. Kyogoku, International Journal of Cast Metals Research 16 (2003), p. 209.

4. L. Masud, R. Martinez, S. Simison and R. Boeri, Journal of Materials Science 38 (2003), p. 2971
L. Caballero, M. Elices and R. N. Parkins, Corrosion 61 (2005), p. 51.
5. The authors gratefully acknowledge research funding from the Ministry of Education, Science and Technological Development of the Republic of Serbia under grant number TR34015.

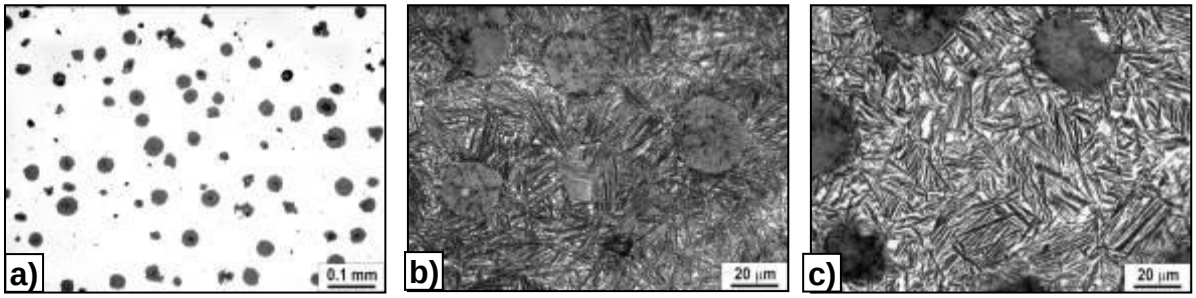

Figure 1. Microstructure of ADI: a) polished surface; b) 300°C/1h, c) 400°C/1h

Material	Proof strength, $R_{p0,2\%}$ [MPa]	Tensile strength, R_m [MPa]	Elongation, A_5 [%]	Environment
As-cast	326	473	22.2	dry
ADI-300°C/1h	1395	1513	3.8	dry
	-	1180	-	water
	1283	1504	4.5	hydrogen gas
ADI-400°C/1h	757	1042	14.2	dry
	727	838	3.5	water
	721	978	9.2	hydrogen gas

Table 1. Tensile properties in dry condition, water and hydrogen gas

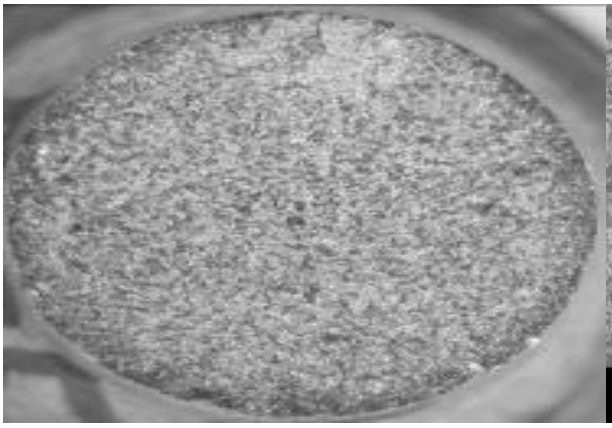

Figure 2. Fracture zones (arrow-embrittlement zone)

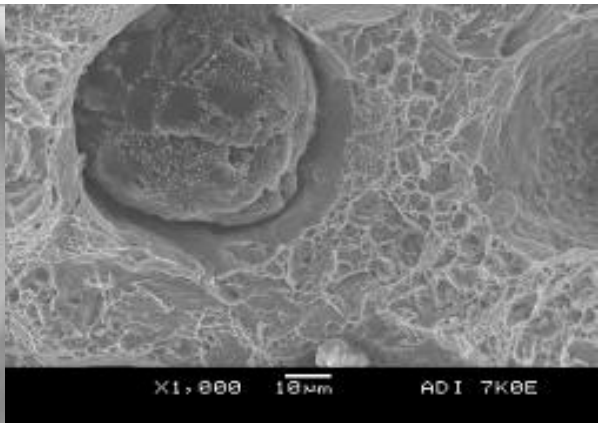

Figure 3. Fracture mode of ductile zone

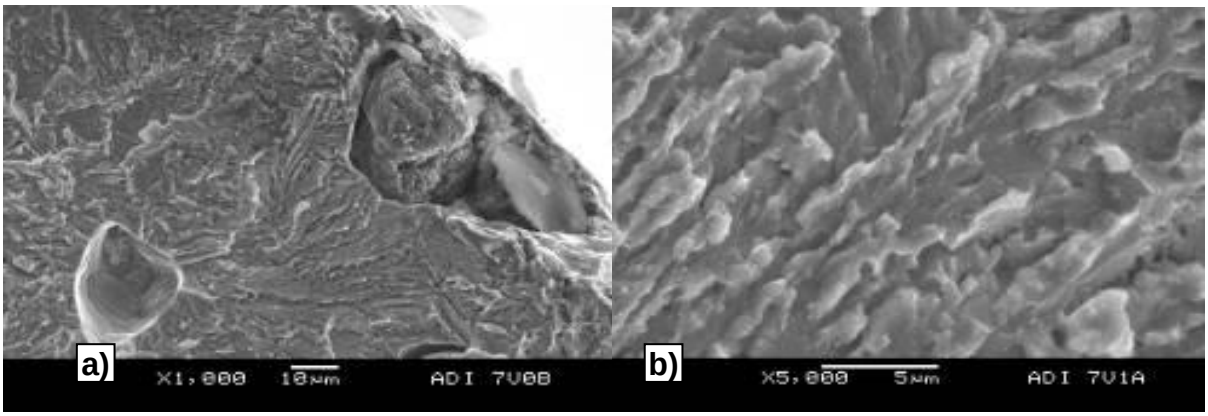

Figure 4. Fracture mode of embrittlement zone

Alloys and Intermetallics

MS.6.P172
Devitrification of Co_3Ti studied by in-situ heating in the TEM

C. Ebner[1], C. Gammer[1,2], D. Geist[1], H.-P. Karnthaler[1], C. Rentenberger[1]

[1]University of Vienna, Physics of Nanostructured Materials, Wien, Austria
[2]National Center for Electron Microscopy, LBNL, Berkeley, Austria

christian.ebner@univie.ac.at
Keywords: devitrification, amorphous phase, nanocrystals

The investigation of amorphous metallic alloys is of special interest from both, a scientific point of view and because of their specific potential applications. It is the aim of this work to study the transition from the amorphous phase to the crystalline one. Therefore the stability and the phase transition of intermetallic Co_3Ti, made amorphous by severe plastic deformation (SPD), are investigated by in-situ heating in the transmission electron microscope (TEM).

Intermetallic Co_3Ti with the nominal composition of Co-23at.%Ti was made by melting and mixing Co and Ti of 99.995% purity in an induction furnace. The alloy was annealed at 950°C for ~100h under a static Ar overpressure to achieve the $L1_2$ long range ordered phase. Disc shaped specimens were cut out of the rod formed alloy by spark erosion and deformed by SPD using the method of high pressure torsion (HPT) at a low deformation speed to avoid heating of the specimen. The deformation was performed using 3 different settings: 20 turns at a quasi-hydrostatic pressure of 4GPa, 80 turns at 4GPa and 20 turns at 8GPa.

The analysis in the scanning electron microscope of cross sections of the HPT deformed discs showed that only the samples deformed by 20 turns at 8GPa were amorphous in the outer regions, while all others, deformed at 4GPa, showed still a largely crystalline structure.

The TEM micrographs show that there are a few nanocrystals present in the amorphous matrix of the specimen deformed at 20 turns at 8GPa (cf. Fig. 1). These crystals have bright or dark contrast in bright field images, depending on their orientation respective to the incoming electron beam. Crystals orientated near Bragg condition scatter strongly and therefore they have a dark contrast relative to the amorphous matrix. Other crystals orientated in such a way, that they scatter the beam stronger in the forward direction show a brighter contrast in the image. The amorphous regions scatter mostly diffuse because of the lack of a periodic structure and therefore produce a contrast of medium intensity.

A differential scanning calorimetry (DSC) measurement was done to determine the temperature of the phase change from the amorphous to the crystalline phase. In an in-situ experiment the specimen was heated inside the TEM stepwise using a heating holder and images were taken for each temperature step at different times of the isothermal. Devitrification is occurring especially near the rim of the TEM foil. Fig. 2 shows a sequence of bright field images taken from the same area at 300°C, 400°C and 430°C. With increasing temperature the volume fraction of the crystalline phase increases; still the size of the crystals remains 10-50 nm due to the high nucleation rate. The nanocrystals contain planar defects as shown in Fig. 3(a), indicated by the arrows. In addition selected area (SA) diffraction patterns were taken to analyse the crystalline structure of the devitrified areas, cf. Fig. 3(b). The profile analysis with PASAD [1] shows clearly the occurrence of hcp Co crystals. The fact that it is not so easy to identify the nanocrystals containing the Ti rich phases (Co_2Ti, $Co_{2.1}Ti_{0.9}$) from the integrated profiles can be caused by their faults, small size, and complicated Laves structures, that all lead to a reduction of intensity and broadening of the lines. It is interesting to note, that the temperature at which the crystals start to grow is about 80K below the crystallization temperature of the bulk amorphous alloy as deduced from the DSC measurement. Therefore our results are in agreement with a surface induced phase transition, as known from surface melting. In addition, it seems that the nanocrystals already present in the amorphous matrix before heating, do not act as nucleation centers. This is concluded since the newly formed nanocrystals do not concentrate near the already existing ones, which themselves do not grow. The results of this in-situ study will be compared with those of bulk annealed samples.

1. C. Gammer, C. Mangler, C. Rentenberger and H.P. Karnthaler. Scripta Materialia 63, (2010), 312. doi:10.1016/j.scriptamat.2010.04.019
2. Acknowledgements: We would like to thank Prof. Dr. Ferdinand Hofer, Institute for Electron Microscopy of the TU Graz (FELMI) for the very fruitful cooperation and we acknowledge the support by the Austrian Science Fund (FWF): [P22440].

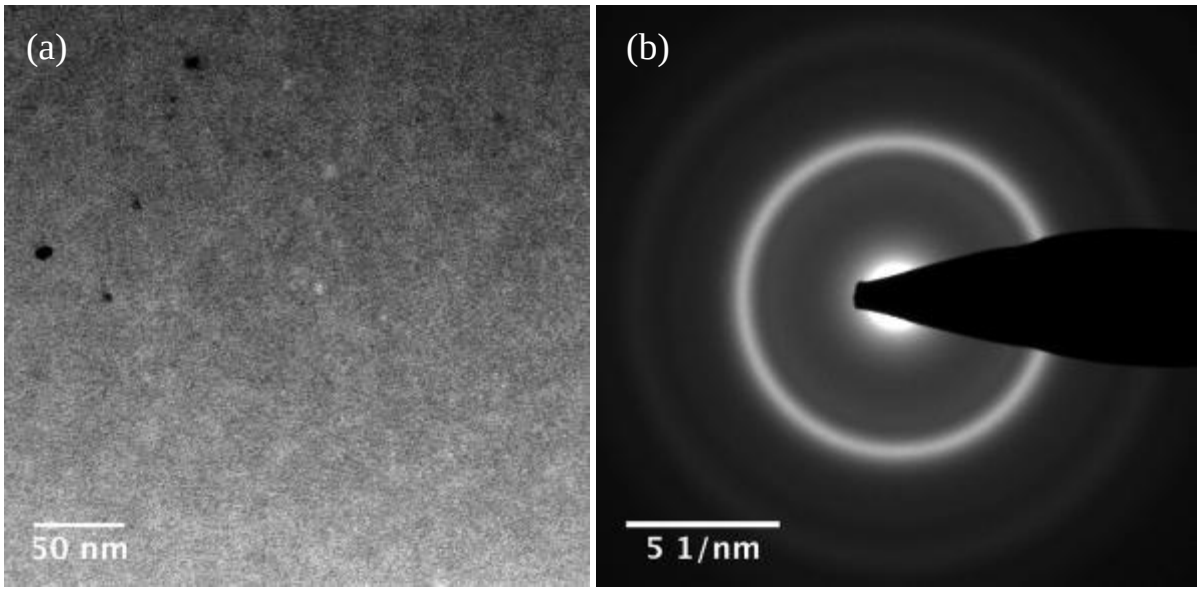

Figure 1. Amorphous Co_3Ti made by SPD. (a) TEM bright field image of the amorphous region showing a few nanocrystals that form during the deformation. (b) SA diffraction pattern of (a) showing amorphous rings.

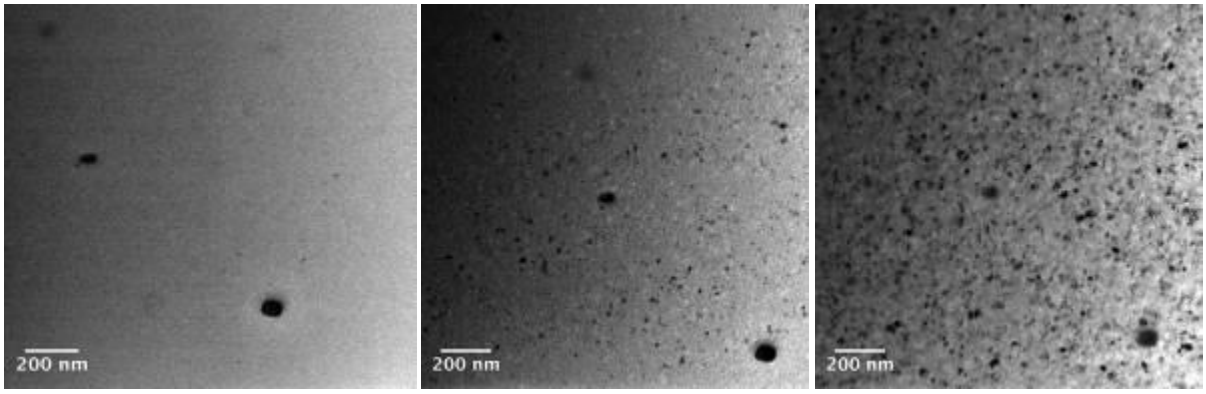

Figure 2. TEM bright field micrographs of the devitrification of amorphous Co_3Ti during in-situ heating, (a) observed at 300°C, (b) 400°C and (c) 430°C.

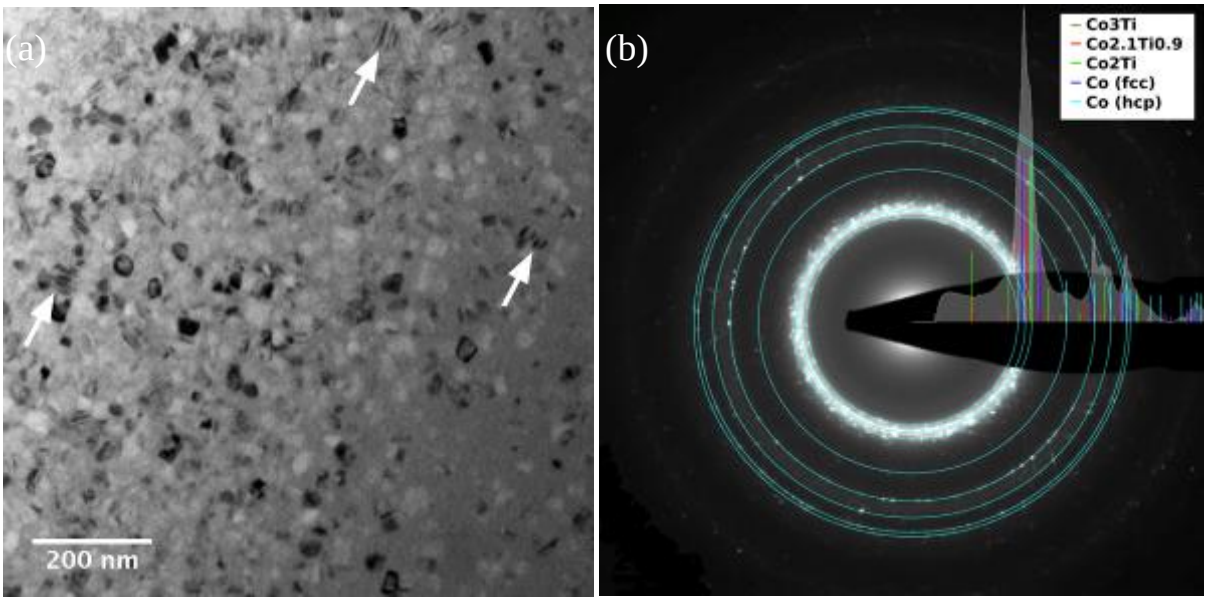

Figure 3. Devitrification of amorphous Co_3Ti after in-situ heating to 430°C observed at room temperature. (a) Bright field micrograph of the newly formed crystalline phase, arrows indicating planar defects present in the crystals. (b) SA diffraction pattern with PASAD [1] profile analysis compared with X-ray structure data.

Alloys and Intermetallics

MS.6.P173
The SEM study of cavitation damage of as-cast ductile iron

O. Eric Cekic[1], M. Dojcinovic[2], S. Balos[3], D. Rajnovic[3], L. Sidjanin[3]

[1]Innovation Centre, Faculty of Mechanical Engineering, University of Belgrade, Belgrade, Serbia
[2]Faculty of Technology and Metallurgy, University of Belgrade, Belgrade, Serbia
[3]Faculty of Technical Sciences, University of Novi Sad, Novi Sad, Serbia

olivera66eric@gmail.com
Keywords: ductile iron, cavitation resistance, surface morphology, pits

Cavitation is material damage caused by the formation and collapse of bubbles, in a liquid. The shock waves and microjets emitted during the collapses of vapor structures interact with neighboring solid surfaces and may cause the material damage [1-3]. During cavitation, the implosion of the bubbles formed in the liquid on the component surface erodes the surface. The cavitation is a source of concern in machine parts that are subject to vibratory forces while in contact with a liquid. Different materials offer different levels of resistance to cavitation. Cast iron is a material known to have relatively low resistance to cavitation. Examples of cast iron machine components that are susceptible to cavitation include, among others, housings of pumps and liners of engine cylinders. The cavitation erosion resistance of a material is commonly determined by mass loss measurements in the laboratory using an ultrasonic vibratory apparatus and the resistance is reported in term cavitation rate. Methods alternative to mass loss-time measurements to quantify erosion damage represent evaluation of surface roughness parameters which provide more detailed information in addition to erosion loss [4, 5]. Different types of cast iron are subject to cavitation due to the presence of graphite and relatively weak metal matrix. A significant number of studies have been carried out on the grey and austempered ductile iron, but only few on nodular cast iron with ferrite matrix may be found [6]. A small number of studies have been performed on the effect of microstructure with a wide variety of ferrite/pearlite ratios on cavitation resistance behavior of ductile cast iron [7]. In this paper, a detailed study of unalloyed ductile cast iron was subjected to intensive cavitation in water, by the application of ultrasonic equipment. The frequency of vibration and the peak-to-peak displacement amplitude of the horn were 20±0.5 kHz and 50 μm, respectively, with separation of 0.5 mm between the specimens and the horn tip. The liquid test was done in water at 25±0.5 °C. The microstructure of ductile iron consisted of spheroidal graphite in a predominantly ferrite matrix with 10% pearlite. The morphology of graphite was fully spherical with average graphite volume fraction of 10.9%, nodule size of 25 to 30 μm and nodule count of 150 to 200 per mm^2. The cavitation damage was assessed by a common mass loss technique, as well as metallographic examination of eroded surfaces by means of scanning electron microscope (SEM) JEOL JSM 6460LV, operated at 20kV. The SEM micrographs were taken after 30; 60, 120 and 240 minutes of cavitation process, while light microscope (LM) examinations were done before and after cavitation, to find eventual metal matrix modifications as a result of cavitation shock waves. At the beginning of cavitation testing the erosion and separation of graphite nodules from ferrite matrix occurs, Figure 1. With increase of testing time cavitation caused the separation of graphite nodules from ferrite matrix leaving pits, Figure 2. It was shown, that the portion remaining after the nodules removal has the form of pits with notchs which have high stress concentration and represent favorable locations for cavitation erosion. In the initial periods of cavitation, ferrite matrix was slightly attacked. With increase of cavitation time, ferrite matrix also becomes subjected to attack and undulations are formed on grain boundaries and slip bands. Increase of undulations appears with longer time of testing. It was found that with increasing time of testing the attacked area of the specimen became larger with more pits, micropits and surface deformation, Figure 3. Ductile deformation can also spread to the matrix away from the pits that formed as a result of the removal of graphite nodules. The ductile removal of the material in the matrix by coalescence of these pits with formation of deep craters was observed in Figure 4. In the last stage, after 240 min of cavitation testing, numerous craters and grooves with intense plastic deformation can be observed on the damaged surface, Figure 5. The SEM results were correlated to the results obtained by mass loss analysis, performing a linear dependence between mass loss and cavitation duration. It can be concluded that cavitation erosion of ductile cast iron begins by removal of graphite nodules and afterwards by ductile removal of material in the ferrite matrix. The cavitation rate of ductile cast iron was 1.85 higher compared with that of carbon steel with similar hardness, since graphite nodule removal produces high stress concentration in cast iron.

1. S. Hattori, H. Mori, T. Okada and J. Fluid, Engineering Transactions ASME 120 (1998) p.179.
2. T. Okada and S. Hattori, Proceedings of the International Symposium on Aerospace and Fluid Science, Sendai, Japan, (1993), p. 347.
3. K. Steller, Proceedings of the 6th International Conference on Erosion by Liquid and Solid Impact, Cambridge, UK, (1983), p. 121.
4. A. Karimi, J.L. Martin, International Metallurgical Reviews 31 (1986), p. 1-26.
5. K.Y. Chiu, F.T. Cheng, H.C. Man, Ultrasonic 43 (2005) p. 713-716.
6. K.F. Alabeedia, J.H. Abbouda, K.Y. Benyounisb, Wear 266 (2009), p. 925.
7. M. Dojcinovic, O. Eric, D. Rajnovic, S. Balos, L. Sidjanin, Metallurgical and Materials Engineering 18 (2012), p. 165
8. The authors gratefully acknowledge research funding from the Ministry of Education, Science and Technological Development of the Republic of Serbia under grant number TR34015.

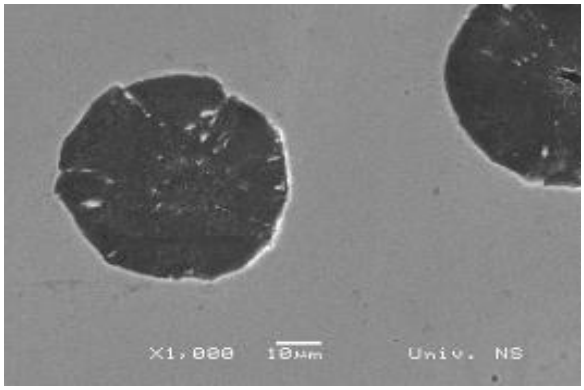

Figure 1. Erosion of graphite nodules

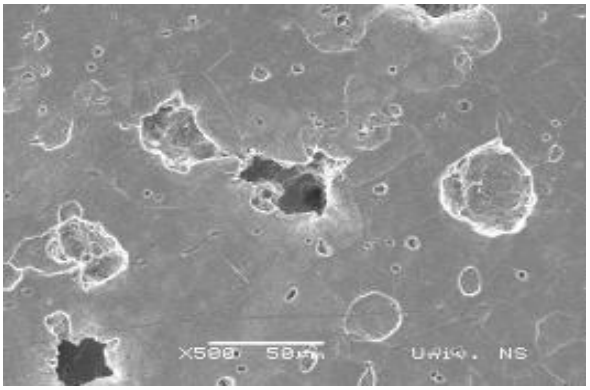

Figure 2. Pits produced by graphite nodule removal 30 min cavitation time

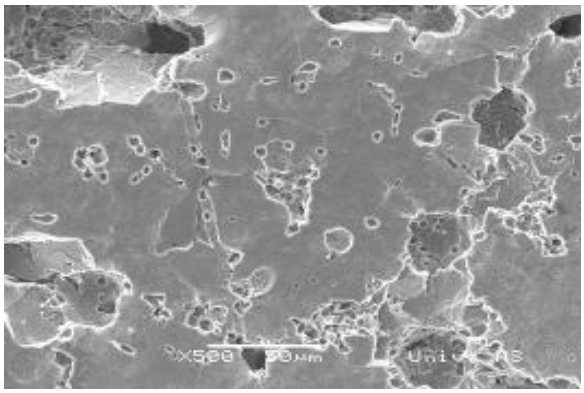

Figure 3. Formation of microcracks by coalescence of pits, 60 min cavitation time

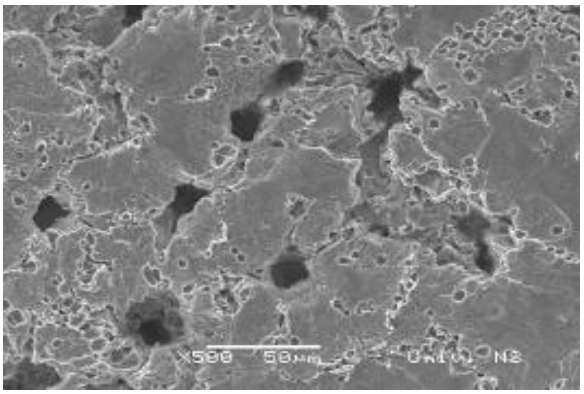

Figure 4. Groves and microvoids forming along the phase boundaries, 120 min cavitation time

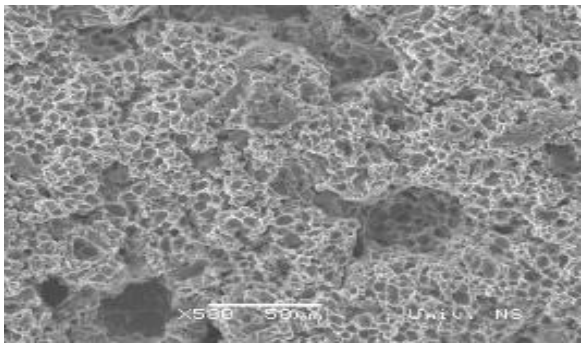

Figure 5. The eroded surface 240 min cavitation time

Alloys and Intermetallics

MS.6.P174
Microstructural SEM characterization, mechanical properties and corrosion rate evaluation of heat treated Ti-6Al-4V

A. S. Khalil[1], R. A. Abdel-Rehim[2]

[1]Mining and Metallurgy Department, Tabbin Institute for Metallurgical Studies (TIMS), Helwan, POB 109, Cairo, Egypt
[2]Casting and Foundry Department, Central Metallurgical Research and Development Institute (CMRDI), Helwan, POB 87, Cairo, Egypt

askhalil2004@yahoo.com
Keywords: Ti-6Al-4V Alloy, Heat Treatment, Scanning Electron Microscope, Mechanical Properties, Corrosion Rates

Ti–6Al–4V alloy has excellent combination of properties such as low density, high specific strength, high fatigue life, creep resistance, corrosion resistance and high biocompatibility. The alloy has been considered as one of preferential engineering materials in aeronautic, medical implants, automotive and marine industries and is considered the workhorse of titanium industry as it accounts for about 50 % of total titanium world usages [1,2].

The alloy contains 6 wt% aluminum for the close-packed (hcp) α phase stabilization and 4 wt% vanadium for the body centred cubic (bcc) β phase stabilization. These two phases coexist were the β phase distributes along the boundaries of α phase [2].

In this work, we used scanning electron microscope (FEI Inspect-S50) observations in combination with several experimental methods to assess the effects of heat treatment on the microstructure, the mechanical and electrochemical properties of commercial cast Ti-6Al-4V. The alloy chemical composition (in wt %) is: 5.9% Al, 3.65% V, 0.2% Fe, 0.2% O, 0.1% C and Ti-balance.

Samples for heat treatment were cut in the form of ~1.5 cm side cubes. The samples were solution treated in the $\alpha+\beta$ range in an inert argon atmosphere at 975 ^{o}C and held isothermally for 15 minutes followed by water quenching. The samples then aged for 6 hours duration at two different temperatures of 480 ^{o}C and 595 ^{o}C followed by water quenching. Samples for SEM observations were prepared by standard metallographic techniques which consist of polishing and etching.

In “Figure 1a.” the microstructure of the as-received sample shows the fully lamellar structure were alternating laths of α and β phases coexist in a “basket-weave” pattern. In “Figure 1b.” the acicular martensitic morphology for the quenched sample is shown, here the β phase appears to be transformed to the acicular $\alpha^{\backslash}$ supersaturated (hcp) martensite phase by the rapid cooling from 975 ^{o}C which is below the transus β temperature. The needle-like structures $\alpha^{\backslash}$ exists along the primary α phase [2]. The aging treatment, leads to the decomposition of these $\alpha^{\backslash}$ needles into fine α and β phases especially along the grain boundaries as shown in “Figure 1c.” and “Figure 1d.” for both the aging temperatures [3]. However, for the higher aging temperature (595 ^{o}C) finer α and β phases were formed accompanied by larger fraction of α phase regrowth. The microstructures were further illustrated in close-up SEM micrographs in “Figure 2b.” and in “Figure 2c.” for both aged samples in comparison with the initial martensitic structure of the quenched sample depicted in “Figure 2a.”.

In “Table 1.” a summary of the experimental results of mechanical (Vickers hardness at 30 kg load and wear resistance for 0.3 bar load and 275 rpm for 30 minutes) were presented. In addition, the corrosion rate evaluation for immersion in simulated body fluid condition was presented (using open circuit potential-time measurements and potentiodynamic polarization technique) [4].

The large increase in hardness of ~1.5 times for the quenched sample (martensitic structure) is expected. Increase of hardness values (strengthening) is also expected following aging treatment.

Aging also leads to noticeable increase in wear rates compared to that of the as-received and quenched samples. However, aging at higher temperature (595 ^{o}C) gives a lower wear rate value relative to aging at the lower temperature (480 ^{o}C). On the contrary, the corrosion rate values suggest that lamellar α and β phases microstructure favors much lower corrosion rate values compared to the very large increase for martensitic structure (water quenched sample) and the finer $\alpha+\beta$ phases (aged samples). This might be due to the large increase in interphase boundaries volume fraction formed as a result of finer observed microstructures in both quenched and aged samples and which might acts as dissolution locations enhancing the corrosion rates [4].

1. R. Boyer, Mater. Sci. and Eng. A213 (1998), p. 103.
2. E. Morita *et al,* Materials Transactions 46 (2005), p. 1681
3. G. Welsch in “Materials Properties Handbook: Titanium Alloys”, ed. G. Welsch, (ASM-Ohio) (1994), p. 1501
4. M. Atapour *et al,* Corrosion 66 (2010), p. 1

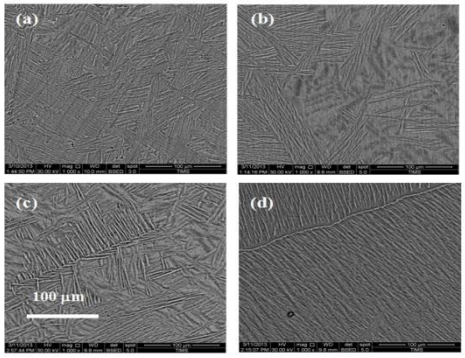

Figure 1. Backscattered electron images (magnification X1000) depicting the microstructure of (a) the as received sample, (b) water quenched, (c) aged for 6 hours at 480 C and in (d) aged for 6 hours at 595 C.

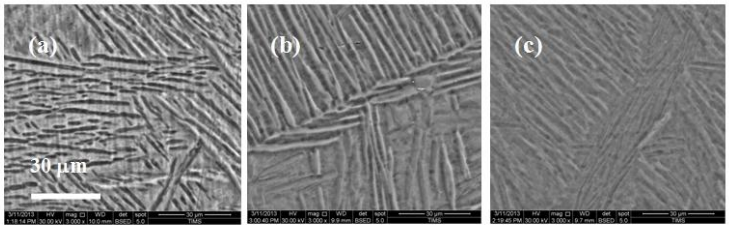

Figure 2. Backscattered electron images (magnification X3000) illustrating the acicular martensitic structure of thequenched sample and the finer $\alpha+\beta$ structure for the samples aged at 480 ^{O}C and 595 ^{O}C.

	As-Received	Water Quenched	Aged at 480 ^{O}C	Aged at 595 ^{O}C
Vickers Hardness (HV30)	390	564	569	468
Wear Resistance (Weight loss %)	1.68 %	1.62 %	3.24 %	2.77 %
Corrosion Rate (mm/year)	1.25×10^{-3}	78.90×10^{-3}	60.10×10^{-3}	82.53×10^{-3}

Table 1. A summary of the Vickers hardness, Wear resistance and corrosion rate for the different heat treatment conditions.

Alloys and Intermetallics

MS.6.P175
Characterization of the morphology and chemical composition of Fd_xPd_{1-x} nanorods by advanced FEGSEM and low-voltage EDS analyses

Z. Samardžija[1,2], K. Žužek Rožman[1], D. Pečko[1], S. Kobe[1]

[1]Jožef Stefan Institute, Ljubljana, Slovenia
[2]Center of Excellence NAMASTE, Ljubljana, Slovenia

zoran.samardzija@ijs.si
Keywords: Fe-Pd nanorods, FEGSEM, EDS

Fe-Pd alloys have many potential applications due to their unique chemical and magnetic properties, which can be tailored by changing their composition. While the equiatomic composition is interesting due to its high magnetocrystalline anisotropy, the $Fe_{70}Pd_{30}$ has the potential to be used as a magnetic shape memory alloy, which is based on phase transformation from disordered austenite (fcc) to ordered martensite (fct) phase [1,2]. However, disordered Fe_xPd_{1-x} has a narrow fct-range ($x \approx 0.68–0.70$), and therefore an accurate compositional analysis is of vital importance. In this work we have applied advanced, high-resolution, field-emission-gun, scanning electron microscopy (FEGSEM) and elemental analyses using energy-dispersive X-ray spectroscopy (EDS) to study the morphology and the composition of the Fe-Pd nanorods that were prepared via the template-assisted electrodeposition method using an Al_2O_3 membrane with a 200-nm pore diameter. A JEOL JSM-7600F FEGSEM equipped with an Oxford INCA Energy 350 System and an EDS-SDD X-max-20 silicon drift detector were used for overall analyses. Our main aim in this work was to achieve a consistent submicrometer-scale characterization of the Fe-Pd nanorods utilizing modern, high-performance, SEM/EDS analytical equipment.

SEM micrographs of the FePd nanorods were recorded using various beam-voltages from 5 kV to 15 kV and beam currents between 0.3–0.8 nA with microscope column conditions being carefully optimized for high-resolution imaging. Particularly useful was the backscattered electron (BSE) imaging in compositional contrast mode, which revealed major compositional changes along the rods, as shown Figure 1. The short, “brighter”, initial part of the rods was found to be a Pd-Pt rich region near the edge of the Pt-deposited membrane, which ends with a distinct border towards the grey, regular part of the Fe-Pd deposited alloy. High-resolution top-view image of the morphology of the Fe-Pd nanorods after dissolving the Al_2O_3 membrane is shown in Figure 2 revealing that the nanorods end with uniform, flat surface.

Quantitative compositional analyses were carried out using the low-voltage EDS approach by analysing the Fe-L□ and Pd-L□ low-energy spectral lines. The comparison of the EDS spectra acquired at three accelerating voltages 8, 6.5 and 5 kV from analytical point #4 (see Figure 1) is shown in Figure 3. The Al and O signals that originate from the Al_2O_3 membrane increase with voltage due to the larger X-ray excitation volume at higher voltages. However, in this case the true stoichiometry of the Fe-Pd nanorod and the corresponding Fe/Pd atomic ratios can be determined by normalization of the Fe and Pd concentrations. The atomic Fe/Pd ratios obtained from the quantitative EDS analyses at 10 discrete points along a Fe-Pd nanorod (shown in Figure 1) are given in Figure 4 and reveal consistent results for all the applied voltages. The advantage of low-voltage EDS is the high spatial analytical resolution due to the reduced, submicrometer-sized, X-ray excitation volume at low beam energies. This allowed us to measure the composition and/or compositional variations along the Fe-Pd nanorods on a submicrometer scale with achieved lateral analytical resolution of ≈ 0.2 □m, which is comparable to the diameter of the nanorods. In selected sample quantitative EDS analysis clearly showed that considerable Fe and Pd concentration gradient along the nanorods is present. In conclusion we found that a high-resolution FEGSEM imaging combined with low-voltage EDS analyses are very appropriate tools for reliable analyses of the morphology and chemical composition of the electrodeposited Fe-Pd nanorods [3].

1. X.L. Fei *et al*, Solid State Communications 141 (2007) p. 27.
2. N. Tasaltin *et al*, Journal of Alloys and Compounds 509 (2011) p. 4701.
3. The authors acknowledge the support of this work from Slovenian Research Agency (ARRS) within project J2-4237.

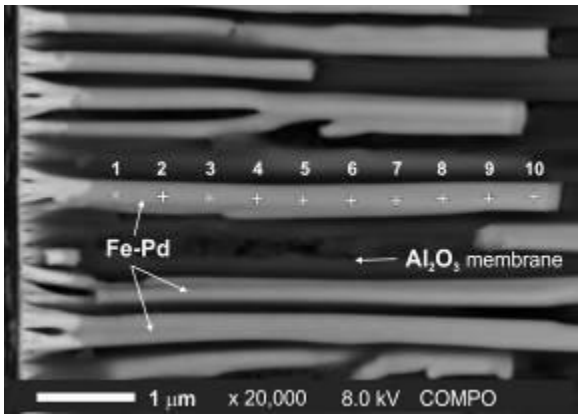

Figure 1. FEGSEM BSE micrograph of the Fe-Pd nanorods in Al_2O_3 membrane. Marked points 1-10 show the positions of point-beam EDS analyses along the nanorod.

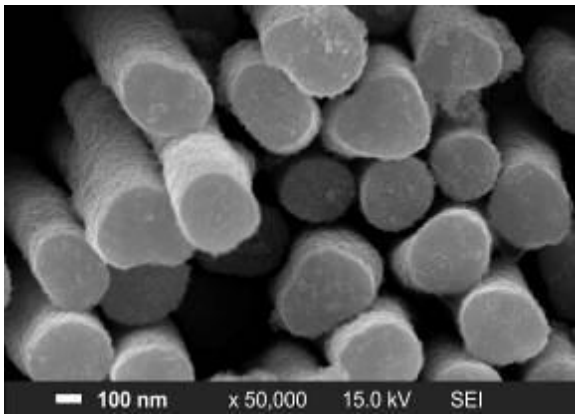

Figure 2. FEGSEM secondary electron micrograph of the Fe-Pd nanorods after dissolving the Al_2O_3 membrane

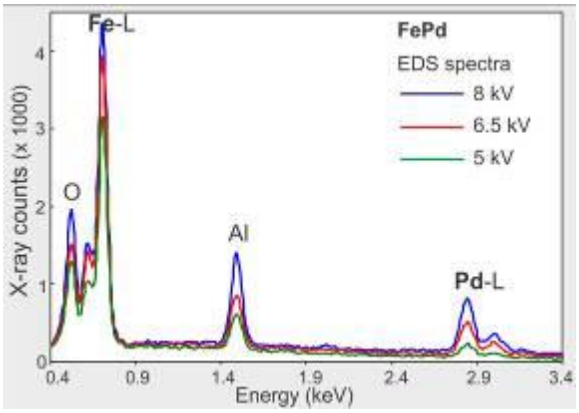

Figure 3. Comparison of low-voltage EDS spectra acquired at 8, 6.5 and 5 kV from the point 4, marked in Figure 1.

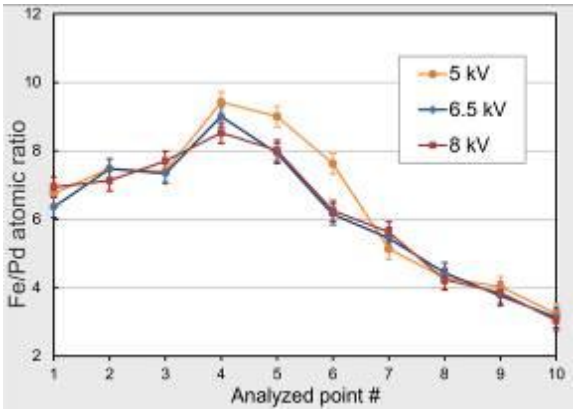

Figure 4. Variation of the atomic Fe/Pd ratios between the points 1-10 on the nanorod shown in Figure 1, calculated from the results of quantitative EDS analyses.

Alloys and Intermetallics

MS.6.P176
High resolution STEM analysis of Sr and Yb in Al - 5wt.% Si alloys

M. Albu[1], J. Li[2], G. Kothleitner[3], P. Schumacher[2], F. Hofer[3]

[1]Center for Electron Microscopy Graz, Graz, Austria
[2]University of Leoben, Chair of Casting Research, Leoben, Austria
[3]Graz University of Technology, Institute of Electron Microscopy and Nanotechnology, Graz, Austria

mihaela.albu@felmi-zfe.at
Keywords: Al-Si alloy, Trace elements, HRSTEM HAADF

Elements such as Sr and Yb may produce multiple twinning within the eutectic Si phase in Al-Si based alloys, thus improving their mechanical properties. Atomic resolution high angular annular dark field imaging (HAADF) and X-ray analysis in a monochromated and probe aberration corrected scanning transmission electron microscope FEI Titan^{3TM} G2 60-300 (S/TEM) were used to localize and analyse the influence of those elements on the modifications of eutectic Si.

Different high purity Al-5wt.% Si alloys with low concentrations of Sr (100 - 200 ppm), Fe (50 ppm) and Yb (0.63 wt.%) were produced by arc melting and subsequent melt spinning. TEM samples were prepared by using a Gatan Precision Ion Polishing System at a constant temperature of about -10 °C. The microscope has been operated at 300 kV, X-ray spectrometry being available through the ChemiSTEM^{TM} technology. The high resolution images in STEM mode were recorded with a beam diameter of 0.1 nm and a current of 0.039 nA. In order to observe the Si twinning, the particles were tilted to the principal twinning orientation of Si (<110>). Since the sample preparation still presented some surface imperfections (amorphous layer), the images were average background subtracted. Elemental quantification of the EDX spectra was performed by using the Zeta factor method [1].

We found that some Sr atoms segregate along the growing surfaces of Si twinning (see Figure 1) whereas other atoms were trapped at the re-entrant corners forming small clusters. Moreover, the Sr-rich clusters, after reaching a certain dimension (> 10 atoms), change the twinning direction with 70 degrees from one $\{111\}_{Si}$ to another one inducing the multiple twinning. Those findings provide the experimental support to the well-accepted impurity-induced twinning [2] and the twin plane re-entrant edge growth mechanisms [3, 4].

Ytterbium, despite its perfect suitable radius according to IIT growth mechanism, does not significantly produced Si twinning, although few Yb atomic chains were found to segregate along one $\{111\}_{Si}$ direction (see Figure 2). Furthermore, no Yb-rich clusters could be allocated within the eutectic Si in this sample.

1. Watanabe M, Williams DB., Journal of Microscopy 221 (2006), 89-109.
2. Timpel M., Wanderka N., Schlesiger R., Yamamoto T., Lazarev N., Isheim D., Schmitz G., Matsumura S., Banhart J., Acta Mater. 60 (2012), 3920-3928.
3. Nogita K., Yasuda H., Yoshida K., Uesugi K., Takeuchi A., Suzuki Y., Dahle AK., Scripta Mater. 55 (2006), 787-790.
4. Nogita K., Yasuda H., Yoshiya M, McDonald SD., Uesugi K., Takeuchi A., Suzuki Y. J., Alloys Compd. 489 (2010), 415-420.
5. The financial support of STEM investigations have been supported by the FFG ASTEM COIN project.

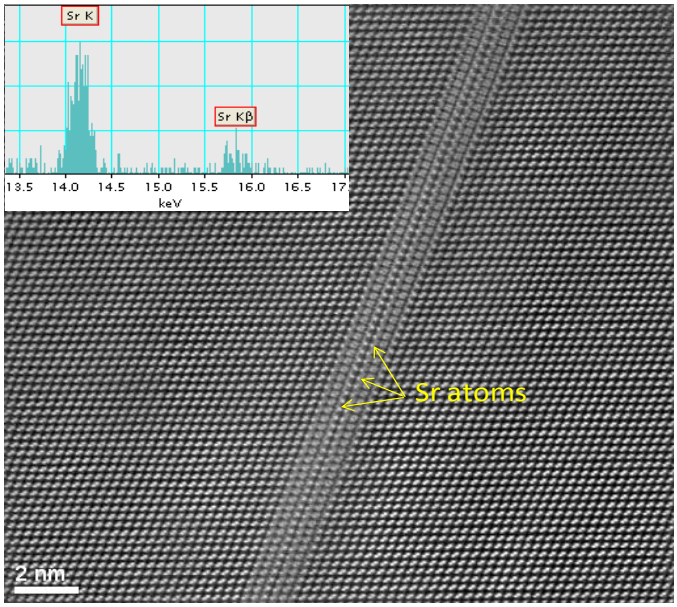

Figure 1. Eutectic Si particle having Sr atoms along the twin and the X-ray spectrum cumulated from a couple of the indicated atoms (elemental quantification indicates 0.66 wt% of Sr).

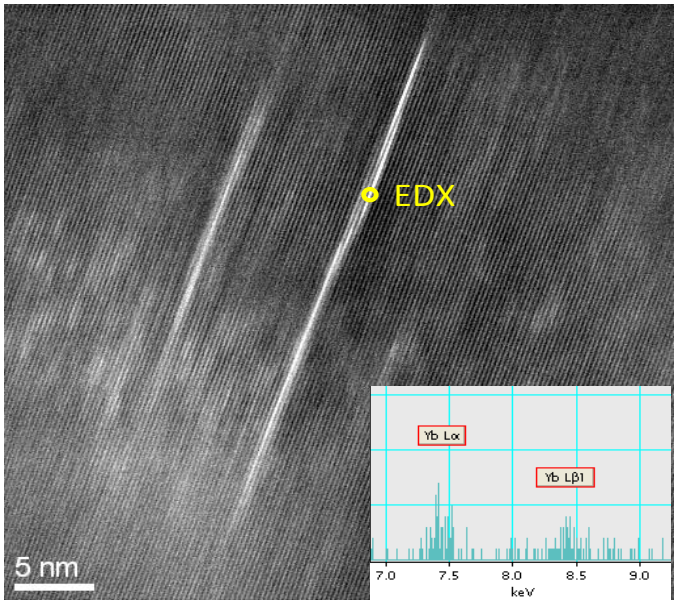

Figure 2. Ytterbium atomic chains present into eutectic Si particle and an X-ray spectrum from the marked region

Alloys and Intermetallics

MS.6.P177
Differences in intermetallic phase growth in thermally aged alloyed gold bond interconnections on aluminium

B. Maerz[1], A. Graff[1], R. Klengel[1], M. Petzold[1]

[1]Fraunhofer Institute for Mechanics of Materials IWM, Halle (Saale), Germany

Benjamin.maerz@iwmh.fraunhofer.de
Keywords: intermetallic phases, STEM-EDS, EBSD

In microelectronics in many cases microchips are connected to their periphery by wire bond contacts. Common material combinations are gold wires, which are bonded on an aluminium metallization. In this case thermosonic wire bonding is used as the welding technique.

Elevated temperature during device operation causes accelerated interdiffusion of Au and Al at the bonded interface which leads to the formation of up to five intermetallic phases. Especially phases rich of gold ($AlAu_4$, Al_3Au_8) are relatively brittle and prone to chemical corrosion and oxidation processes due to the intrusion of impurities e.g. from the package. Additionally, mechanical shocks degrade the interconnection that may finally lead to a ball lift-off and failure of the whole device. To slow down the growth of vulnerable phases, wire manufacturers successfully add alloying elements to their gold wires. Although this has been applied for several years, the responsible mechanisms behind improved performance have not yet been explained in detail.

In the literature the formation of a diffusion barrier exhibiting a higher content of the alloying elements is commonly stated [1,2,3]. The present work aims at clarifying whether this is a matter of precipitation due to supersaturation or if solid-solutions are formed. Furthermore, the growth of ternary phases must not be disregarded. For this purpose, thermally aged ball bond contacts made of three different gold wire types are investigated. In comparison to a 4N Au reference wire (Wire A) a high reliability Au wire alloyed with ~1% Pd (Wire B) and an ultimate reliability wire alloyed with ~1% Pt and Cu (Wire C) are investigated.

Basically, STEM-EDS mappings of the reaction zone visualize the local distribution of the alloying elements. Electron backscatter diffraction (EBSD) was conducted to gain a general understanding of the different intermetallic phase growth processes with each wire type. For the EDS investigations a FEI Titan G3, equipped with a Super-X EDS detector system was used. TEM samples were prepared using an insitu lift-out technique within a Ga^+ FIB [4]. For EBSD measurements a ZEISS Supra 55VP equipped with a DIGIVIEW III detector was applied.

Figure 1 shows EBSD grain structure maps of the bond interface. Samples were thermally aged at 150°C for 500h. The different intermetallic Au-Al phases are colour coded. It can be seen, that with Wire A the intermetallic phase growth is already completed. Almost only the gold rich $AlAu_4$ is present. The EBSD map of Wire B shows a similar result with slightly more of Al_3Au_8, which is located between the gold ball and the $AlAu_4$ phase and at the border. Nevertheless, the intermetallic phase growth with Wire B is nearly completed. Compared to the previous results, using Wire C the intermetallic phase area contains much more of the Al_3Au_8 phase and a smaller amount of $AlAu_4$ located in contact to the gold ball. $AlAu_2$ is located at the outer rim. This means that until aging for 500h the intermetallic growth is not complete. Besides, there are incorrectly assigned grains below the gold ball. These gave rise for further TEM/STEM investigations.

Element maps of Wire B generated by STEM-EDS show distinct grains which are found to belong to a ternary phase with composition $Al_3Au_5Pd_2$ (Figure 2). Similar investigations of a Wire C sample show a thin layer containing grains with increased Cu content near the gold ball (Figure 3). Within this layer precipitates of Pt are visible at the grain boundaries.

1. Shin et al., Electronic Components and Technology Conference (ECTC), 2010, 329-335
2. Kim et al., Microelectronics Reliability, 2011, 51, 2250-2256
3. Gam et al., J. Electronic Materials, 2006, 35, 2048-2055
4. Altmann et al., Microscopy Microanalysis, 2011, 17 (Suppl 2), 626-627
5. We kindly acknowledge the Federal County of Saxony-Anhalt for supporting the research project „Application of high resolution TEM for characterization of multi-material systems“ (project number 6060161202)

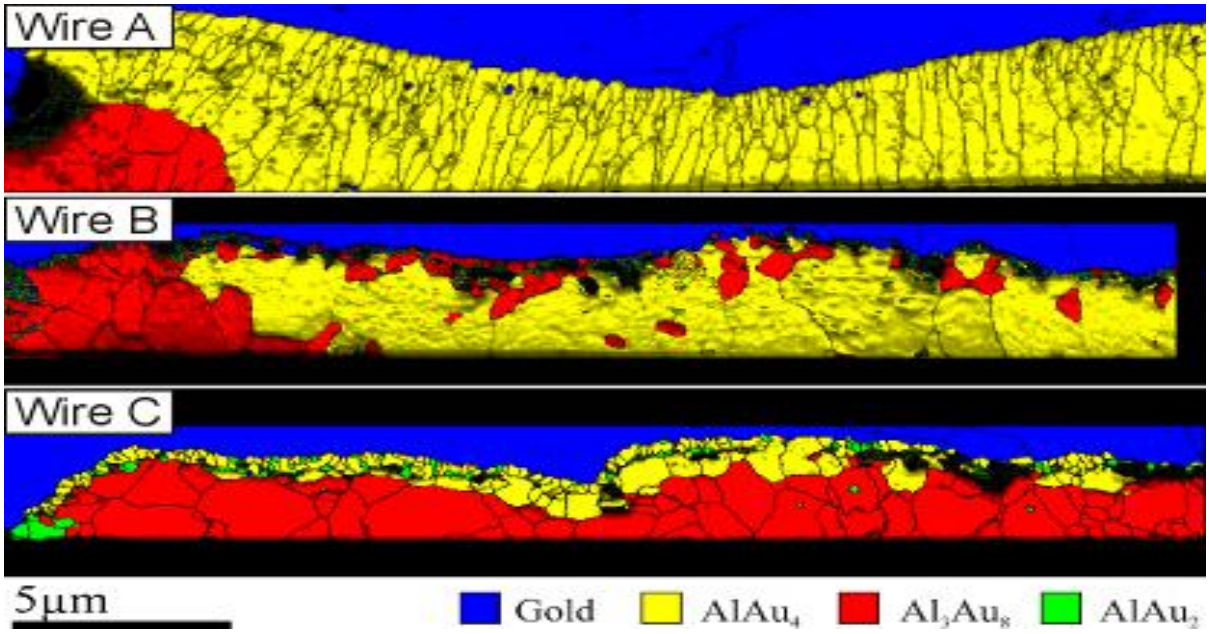

Figure 1. EBSD grain structure maps showing local phase distribution of the three wires after 500h of annealing at 150°C

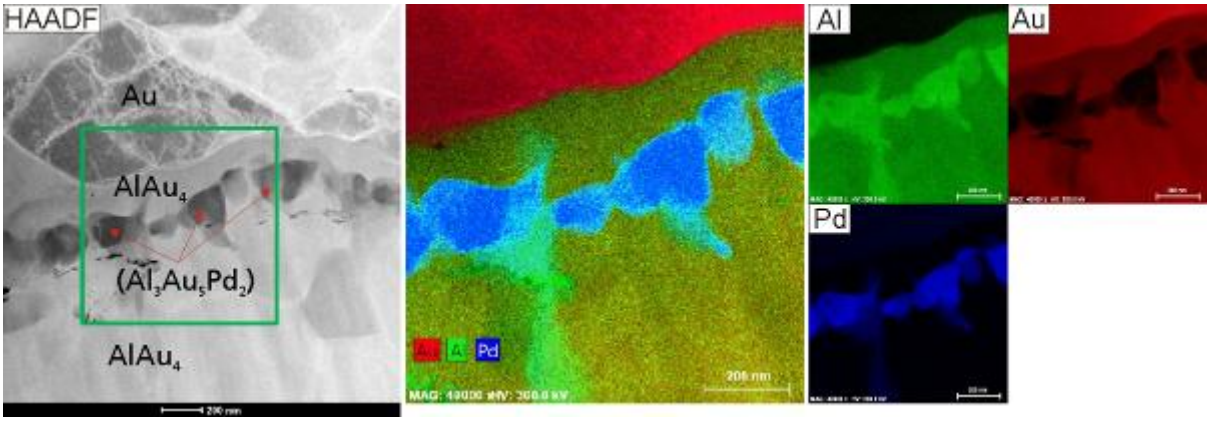

Figure 2. STEM-EDS investigation of a Wire B bond contact after annealing for 500h at 150°C

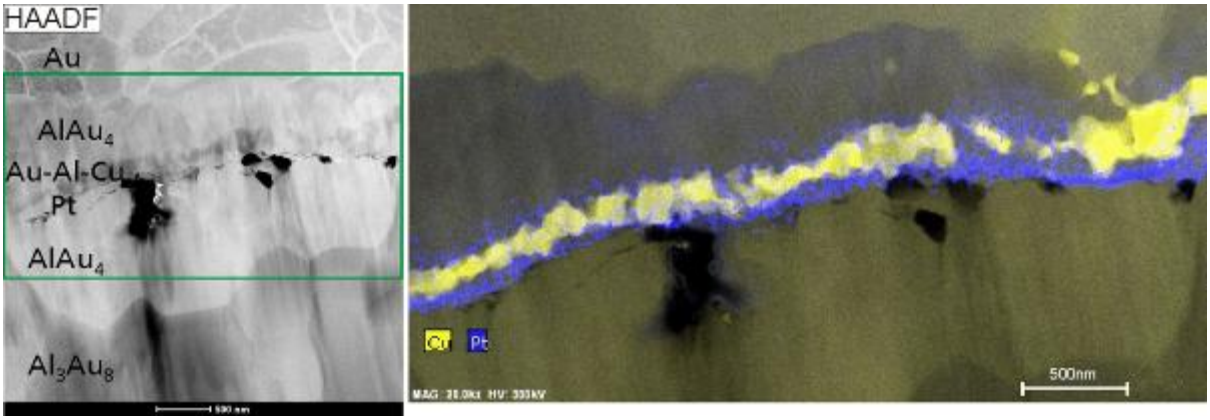

Figure 3. STEM-EDS investigation of a Wire C bond contact after annealing for 500h at 150°C

Alloys and Intermetallics

MS.6.P178
Evolution of ω_o-phase in a TiAl-Nb-Mo alloy: microstructural characterization and mechanical properties

B. Rashkova[1], M. Schloffer[1], T. Schöberl[2], Z. Zhang[2], S. Mayer[1], H. Clemens[1]

[1]Montanuniversität Leoben, Physical Metallurgy and Materials Testing, Leoben, Austria
[2]Austrian Academy of Sciences, Erich Schmid Institute of Materials Science, Leoben, Austria

boryana.rashkova@unileoben.ac.at
Keywords: titanium aluminides, Omega-phase, TEM, mechanical properties

Third generation TiAl-Nb-Mo alloys are multi-phase γ-TiAl-based alloys, where the microstructure is determined by the manufacturing process as well as subsequent heat treatments. It has been established that the formation of ω_o ($B8_2$)-phase takes place in β_o (B2)-phase during heat treatments [1,2]. In this work we studied the evolution of ω_o-phase and its mechanical properties during long term heat treatments and creep experiments in a nearly lamellar microstructure. The investigated TiAl-alloy was centrifugal cast, hot-isostatically pressed, forged and had an analyzed composition of Ti-43.6Al-4.06Nb-1.01Mo-0.09B (in at.%). Subsequently, the alloy was subjected to a multi-step heat treatment (HT) to adjust a nearly lamellar microstructure with globular γ- and β_o-grains, which are arranged on the grain boundaries of the α_2/γ-colonies. The last heat treatment step was performed at 850°C for 6h followed by furnace cooling. Creep experiments were carried out for 310h at 750°C with 150 MPa, whereby the sample reached an elongation of 1.8%. The microstructure was studied by transmission electron microscopy (TEM). Conventional TEM was carried out using a Philips CM 12 operating at 120 kV. High resolution TEM (HRTEM) studies were performed using a JEOL 2100F operating at 200 kV equipped with an image-side spherical aberration corrector (CEOS). The chemical composition of the phases was determined by energy dispersive X-ray (EDX) microanalysis with an INCA system (Oxford Instruments, UK). All specimens for TEM investigation were cut, ground, polished and electrolytically thinned to electron transparency using an electrolyte A3 from Struers. The mechanical properties were determined by nano-hardness indentation utilizing a Hysitron Triboscope, an add-on device mounted on the scanner head of a commercial, large stage scanning probe microscope (SPM) Veeco Dimension 3100. Hardness and elastic modulus were calculated from the unloading curve using the standard Oliver-Pharr method [3]. During the HT, ω_o-phase and γ-platelets (γ_p) precipitates in the β_o-phase (Fig. 1a). The evaluation of the diffraction pattern taken from $\beta_o(\omega_o)$ area (insert in Fig.1a) substantiates an ordered ω_o-phase and the following orientation relationship: $\langle 111\rangle_{\beta o}\{110\}_{\beta o}$ // $[0001]\omega_o$ $\{11\ 0\}\omega_o$. Detailed HRTEM studies (Fig. 1b) reveal that the ω_o-phase coherently precipitates with grain size mostly of 5 to 100 nm in diameter in the β_o-matrix. After the creep test, globular ω_o-grains with diameter between 50 and 200 nm inside the β_o-phase can be clearly seen (Fig. 2a). The phase fraction of the ω_o-phase increases. Quantitative analyse of 8 vol.% $\beta_o(\omega_o)$-phase reveals a ratio of 57 % ω_o-phase and 43 % β_o-phase. Many neighbouring particles in the β_o-grain possess similar contrast indicating a well-defined orientation relationship within the matrix, which was proven by evaluation of the diffraction pattern. Fig. 2b shows a Cs-corrected HRTEM image of one, dislocation free, segment of the atomically abrupt and coherent β_o/ω_o interface along the $\langle 111\rangle\beta_o$ and $[0001]\omega_o$ zone axes. The analysis of the Fourier transformed image shows that the {11 0} and { 010} lattice planes from the ω_o-phase are parallel to the {1 0} and {11 } planes from the β_o-matrix. Fig. 3 presents EDX line scans of a region with ω_o-grains in the β_o-matrix. The intensity of Mo reveals an inverse trend at the transition to the β_o/ω_o-interface. In the ω_o-grains the Mo content decreases whereas in the β_o-phase it increases (Fig. 3b). The formation of the ω_o-phase seems to depend on the local Mo content. To characterize the mechanical properties of β_o-phase containing ω_o-precipitates nano-hardness indentation was performed after different HT. After the last HT step the hardness of $\beta_o(\omega_o)$-phase is 11.3 GPa. After the growth of the ω_o-phase to spherical grains with medium size of 100 nm the hardness decreases to 9.8 GPa. However, this value is well above the hardness of ω-free β_o-phase (8 GPa) and those of the existing globular α_2- and γ-phases. Thus, the formation of the ω_o-phase increases the hardness of β_o-phase due to precipitation hardening.

1. A. Stark, A. Bartels, H. Clemens and F-P. Schimansky, Adv. Eng. Mat., 10 (2008), p.929.
2. W. Wallgram, T. Schmolzer, L. Cha, G. Das, V. Güther, H. Clemens, Int. J. Mat. Res., 100 (2009), p.1021
3. W.C. Oliver and G.M. Pharr, J. Mat. Res. 7 (1992), p.1564.

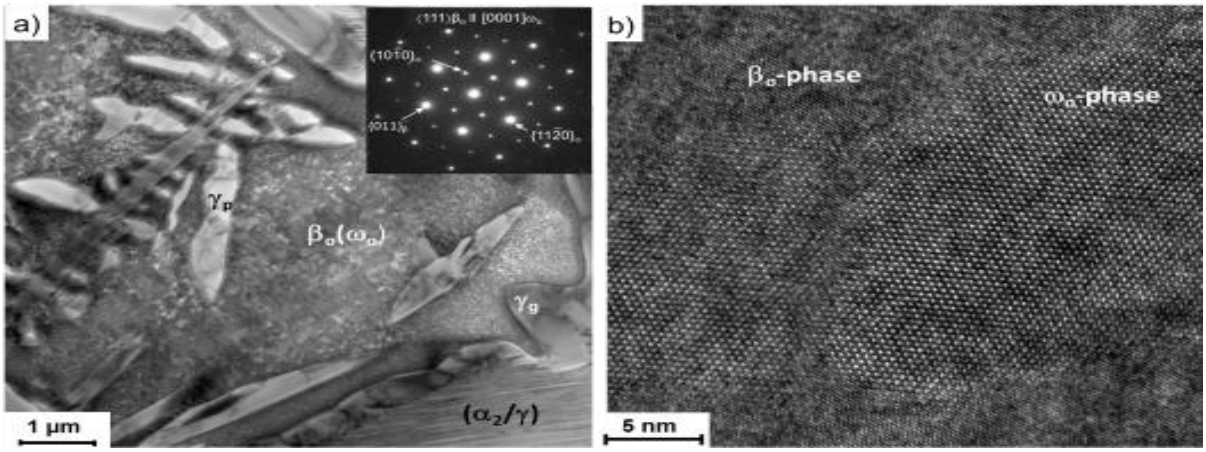

Figure 1. Microstructure and distribution of the constituent phases after HT. a) TEM BF image of β_o-phase containing ω_o-precipitates, surrounded by γ_g-grains and (α_2/γ)-colonies. The substructure inside the β_o-phase arose from the presence of fine ω_o-domains interrupted by γ_p-platelets b) HRTEM image showing the ω_o-precipitates within the β_o-phase.

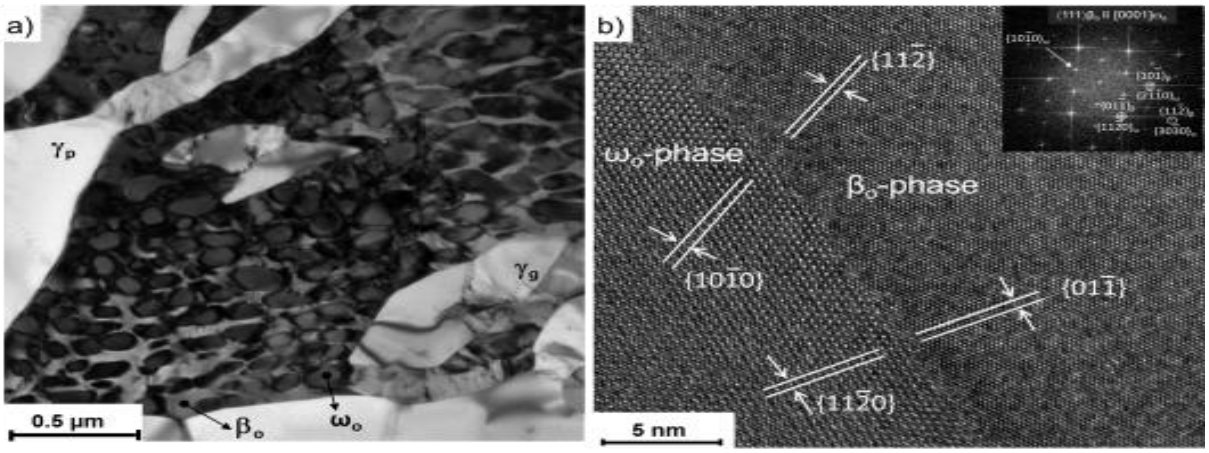

Figure 2. Microstructure after the creep test. a) TEM BF image shows ω_o-grains with a globular shape uniformly distributed in the β_o-phase, surrounded by γ_p- and γ_g-grains. b) a Cs-corrected HRTEM image of one, dislocations free, segment of the coherent β_o/ω_o interface along the $\langle 111\rangle\beta_o$ and $[0001]\omega_o$ zone axes.

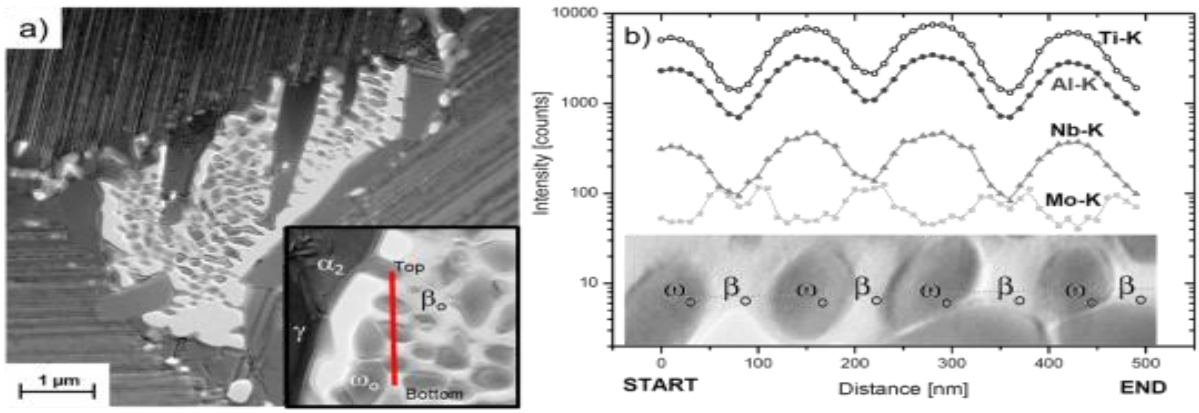

Figure 3. a) TEM BF image of a β_o-grain with ω_o-particles and γ_p-grains. The inset shows the position of the EDX-line scan. b) EDX line scans of region with alternating ω_o-grains in the β_o-matrix. The intensity of the Mo content increases at the transition to β_o-phase and shows an inverse trend to that in the ω_o-phase.

Alloys and Intermetallics

MS.6.P179
Direct metal laser sintering of a biocompatible Co-Cr-Mo alloy

E. Girardin[1], G. Barucca[2], E. Santecchia[2], P. Mengucci[2], T. Moskalewicz[3], A. Gatto[4], E. Bassoli[4], L. Denti[4], L. Iuliano[5]

[1]Università Politecnica delle Marche, DISCO, Ancona, Italy
[2]University Politecnica delle Marche, SIMAU, Ancona, Italy
[3]AGH University of Science and Technology, Faculty of Metals Engineering and Industrial Computer Science, Krakòw, Poland
[4]University of Modena e Reggio Emilia, DIEF, Modena, Italy
[5]University Politecnico di Torino, DSPEA, Torino, Italy

e.girardin@univpm.it
Keywords: biocompatible Co-Cr-Mo alloy, direct laser sintering, transmission electron microscopy (TEM), X-ray diffractometry (XRD)

The Co-Cr-Mo alloy, a Ni-free material, is extensively used for biomedical applications such as dental implants and orthopaedic prostheses due to its excellent corrosion resistance, wear resistance and biocompatibility [1]. Direct Metal Laser Sintering (DMLS) is an additive layer manufacturing technique based on laser radiation to sinter powdered metals into solid object. In the field of dental restorations, metal-ceramic fixed partial dentures (FPDs) can be produced by DMLS with a strong reduction of manual operation and accordingly higher repeatability and good savings in money and delivery times [2]. This work aims to correlate the microstructure of the samples obtained by DLMS to their mechanical properties in order to optimise the production parameters and to understand the phenomena occurring during the production process. Specimens were prepared by direct metal laser sintering using a Yb (ytterbium) fiber laser system (EOSINT-M270). A Co-Cr-Mo alloy powder having the following nominal composition in wt%, Co 59.5, Cr 31.5, Mo 5.0, Si 2.0, Mn 1.0, other 1.0, was used as basic material. Samples were characterized by X-ray diffraction (XRD), scanning electron microscopy (SEM), transmission electron microscopy (TEM) and hardness measurements. The average Rockwell C hardness (HRC) value for the samples is 47, a very high value for this kind of alloy. XRD analysis evidenced the coexistence of a face-centered cubic (fcc), γ, and a hexagonal close-packed (hcp), ε, Co-Cr-Mo phase. Broad peaks attributable to metal carbides $M_{23}C_6$ (M=Co, Cr, Mo) are also visible. The ε phase is stable from room temperature to 970 °C while the γ phase is stable above 970 °C, the γ→ε transformation being a martensitic one. Carbon addition in Co-Cr-Mo alloys improves mechanical properties, stabilizes the γ phase and forms $M_{23}C_6$ carbides that act as preferential sites for fatigue crack propagation when precipitate along grain boundaries [3]. Figure 1. shows a typical SEM image of an etched surface of the sample sectioned parallel to the laser beam direction. The lines separating the different weld pools produced by the laser scan on each layer are well visible in this image. Increasing the magnification, it is possible to observe, inside a single pool, the presence of domains formed of columns all oriented in the same direction. Adjacent domains show different orientation of the columnar structure. The microstructure characterization of the samples performed by TEM reveals the presence of small precipitates both isolated and organized in rows, Figure 2.. EDX analysis indicates very similar composition for both families of precipitates, while large differences are evident for the Mo concentration between precipitates and matrix. In order to better understand the nature of the columnar structure visible in the SEM images, further TEM observations are necessary to integrate these preliminary results.

1. J.A. Disegi, R.L. Kennedy, R. Pilliar, ASTM International, 1999.
2. I. Gibson, L.K. Cheung, S.P. Chow, W.L. Cheung, S.L. Beh, M. Savalani, S.H. Lee, Rapid Prototyping Journal, 12 (2006), 53-58.
3. A.J. Saldivar Garcia, A. Mani Medrano, A. Salinas Rodriguez, Scripta Materialia, 40 (1999), 717-722.

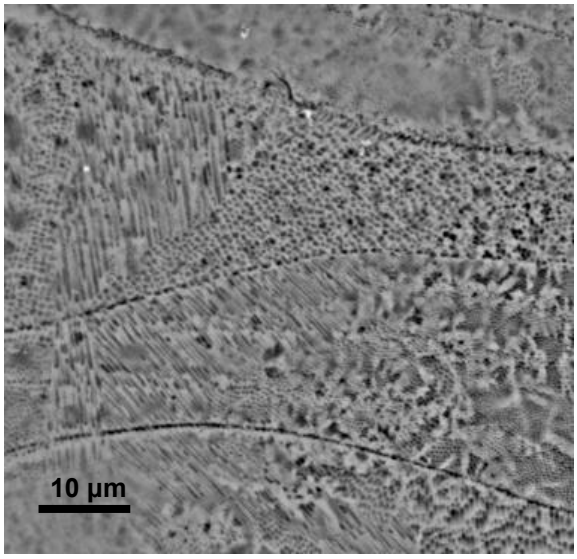

Figure 1. SEM image of an etched surface.

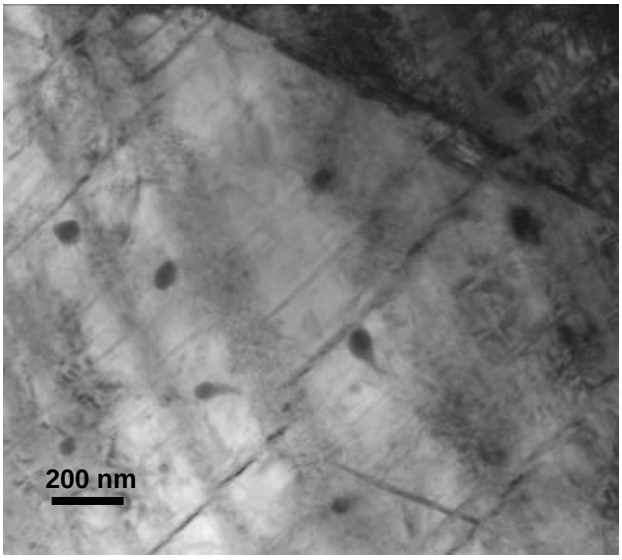

Figure 2. TEM bright field image. Precipitates are visible.

Alloys and Intermetallics

MS.6.P180
Cu and Zn atomic columns of precipitates in Al-Mg-Si alloys investigated by aberration-corrected scanning transmission electron microscopy

T. Saito[1], W. Lefebvre[2], C. Marioara[3], S. Andersen[3], R. Holmestad[4]

[1]Norwegian University of Science and Technology, Trondheim, Norway
[2]Université de Rouen, Rouen, France
[3]SINTEF Materials and Chemistry, Trondheim, Norway
[4]Norwegian University of Science and Technology, Trondehim, Norway

randi.holmestad@ntnu.no
Keywords: Al-Mg-Si alloys, precipitates, aberration-corrected scanning electron microscopy

Al-Mg-Si alloys are important structural materials characterized by formation of high number density of nano-sized precipitates. Strength of the alloys is achieved by precipitates which prevent dislocation movement. There are several types of metastable precipitates in the alloy, depending on their structure. β" precipitates are the most important for strength evolution, since they are fully coherent to the aluminium matrix [1, 2]. All metastable precipitates are structurally connected via a hexagonal network of Si atomic columns projected in the precipitate needle growth direction [1, 3]. Effects of different alloying elements on the Al-Mg-Si alloys are of key interest to understand the precipitation, e.g. the change in structure of the precipitates and the consequence for mechanical properties. In this study, the effects of Cu or Zn additions on precipitate structures in the Al-Mg-Si alloy system are investigated by aberration-corrected scanning transmission electron microscopy (STEM). High angle annular dark field STEM (HAADF-STEM) enables us to achieve atomic number contrast intensity, in particular it is possible to distinguish Cu and Zn atomic columns from Al, Mg and Si columns in the precipitates.

Two Al-Mg-Si alloys were studied; one added 0.1 wt% Cu and the other added 1 wt% Zn. The alloys were solution heat treated, subsequently kept at room temperature and isothermally heat treated ~190°C. Based on the hardness curves, the peak hardness conditions from the isothermal heat treatment were used for further studies. STEM specimens were prepared by electropolishing. The electrolyte consisted of 1/3 HNO_3 in methanol, and the solution was kept at a temperature between -20°C and -35°C. All specimens were gently ion milled and plasma cleaned before HAADF-STEM imaging in order to reduce the effect of contamination. A probe corrected JEOL ARM200F was used to acquire the HAADF-STEM images, operating at 200 kV.

Low Cu additions to the Al-Mg-Si alloys made the β" precipitate partially disordered in the same precipitate needle [4], as shown in Figure 1. The disordered part of the precipitates still contains the Si hexagonal atomic columns. It is suggested that the Cu atomic columns need a particular coordination surrounded by Mg and Si atoms which is not present in the perfect β" precipitates. However, perfect β" precipitates were also observed. Here Cu atoms partially segregated at the interface of the β" precipitates. Furthermore, the position of these Cu atoms were replaced at Si positions in the interface of the β" precipitates, see Figure 2. Additions of Zn to the Al-Mg-Si alloys lead to formation of Zn atomic columns in the β" precipitates as well as disordered precipitates, although Zn atoms were likely to be segregated along grain boundaries. These observations suggest that additions of Cu or Zn to the Al-Mg-Si alloys affect the structure of the precipitate and make particular atomic columns with their own atomic environments in the precipitates. In other words, Cu or Zn is incorporated when forming the precipitate.

1. We are grateful to Drs. F.J.H. Ehlers and R. Bjørge, Norwegian University of Science and Technology, for helpful comments and further discussions. This research is supported by Hydro Aluminum and the Research Council of Norway through the bilateral KMB project: 193619 “The Norwegian-Japanese Al-Mg-Si Alloy Precipitation Project”.
1. S.J. Andersen, H.W. Zandbergen, J. Jansen, C. Træholt, U. Tundal and O. Reiso, Acta Mater. 46, (1998), 3283.
2. H.S. Hasting, A.G. Frøseth, S.J. Andersen, R. Vissers, J.C. Walmsley, C.D. Marioara, F. Danoix, W. Lefebvre and R. Holmestad, J. Appl. Phys. 106, (2009), 123527.
3. H.W. Zandbergen, S.J. Andersen and J. Jansen, Science 277, (1997), 1221.
4. T. Saito, S. Muraishi, C.D. Marioara, S.J. Andersen, J. Røyset, R. Holmestad, Metal. Mater. Trans. A, Accepted.

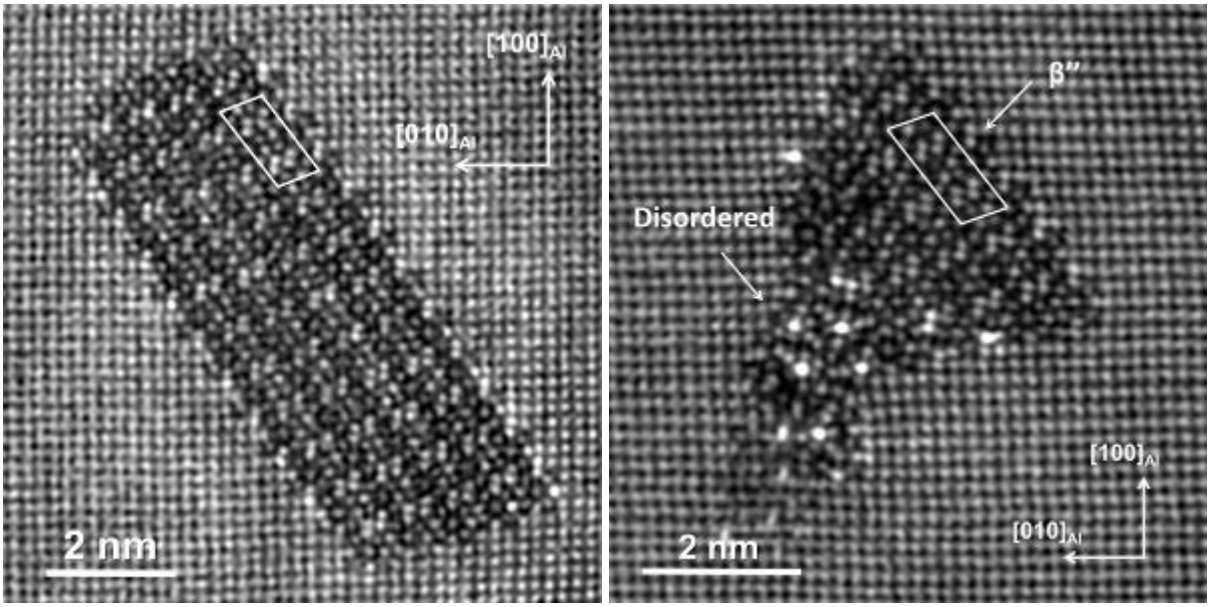

Figure 1. HAADF-STEM images from <100>Al direction for (left) Cu-containing β” precipitate and (right) Cu-containing β”/disordered precipitates. In these images, periodicity shorter than 1.5Å are filtered out with a circular band pass mask.

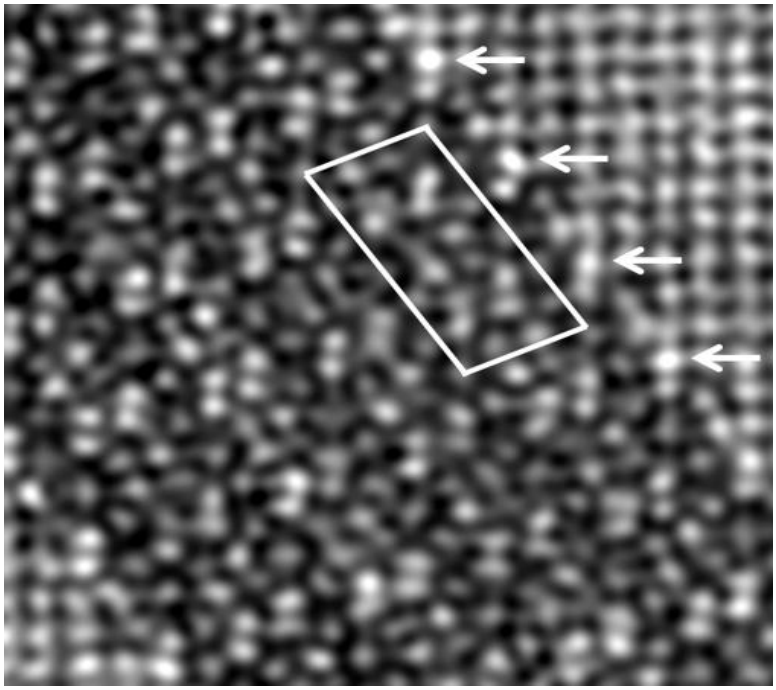

Figure 2. Enlarged part of the left image in Figure 1. Arrows indicate possible replacements of Cu atoms at Si positions in the interface of the β” precipitate, which was determined due to the atomic number contrast. The β” unit cell is drawn in the figure.

Alloys and Intermetallics

MS.6.P181
Microstructure evolution in annealed $Co_{38}Ni_{33}Al_{29}$ shape memory alloy

J. Kopecek[1], V. Kopecký[1], J. Lu[2], H. Shi[2], R. Espinoza[2], P. Sedlák[3], H. Seiner[3], M. Landa[3], D. Schryvers[2], O. Heczko[1]

[1]Institute of Physics ASCR, Dept. of Functional Materials, Praha, Czech Republic
[2]EMAT, University of Antwerp , Antwerp, Czech Republic
[3]Institute of Thermomechanics ASCR, Praha, Czech Republic

kopecek@fzu.cz

Alloys in the Co-Ni-Al system and even their shape memory properties have been studied for decades as the cobalt-based alloys were supposed to have higher transformation stresses and wider intervals of superelasticity than other shape memory alloys (SMA). As these alloys are ferromagnetic the magnetic shape memory effect could be expected like in Ni-Mn-Ga and similar alloys. Nevertheless, the published data are controversial as alloy preparation and its thermomechanical treatment are complicated and the state of the material is very sensitive to slight changes in thermomechanical history [1]. Additionally, the two-phase structure in the high-temperature austenitic state is an exception within the SMA. It contains a B2 ordered (Co,Ni)Al matrix and A1 fcc solid solution particles. The A1 (interdendritic) particles remain untransformed, whereas the B2 matrix transforms martensitically into the $L1_0$ martensite [2]. Only non-modulated $L1_0$ martensite was observed in Co-Ni-Al based alloys.

Using the Bridgman method, a set of unidirectional solidified / single crystalline samples was prepared. The samples were investigated using different microscopic methods including LOM, SEM+FIB (including EDS and EBSD), TEM, SPM (as AFM and MFM) and other methods as ultrasound wave propagation and mechanical testing. This wide set of used methods gives a complex view on a rather uncommon behaviour of these ferromagnetic SMA.

It was found that martensite observed at room or even higher temperature is not the thermodynamically stable one, but rather stress induced. The equilibrium martensitic transformation is observed close to 200 K by both in-situ neutron scattering and magnetic susceptibility measurements. The stress induced martensite existing above its equilibrium temperature has the same structure as the equilibrium one. Its appearance is given by pronounced premartensitic phenomena, which can be observed in a wide temperature region. This region shall be connected with the region of superelastic behaviour, which was observed.

There exists a large difference between “as grown” and “annealed and quenched” samples. While the first group shows simple elastic behaviour, the second exhibits significant superelasticity with strong orientation dependence. The explanation must be connected with established high temperature equilibrium during annealing and the processes of its relaxation after quenching. The set of various precipitates was already observed in quenched samples: In addition to the major constituents (B2-type ordered matrix and A1 fcc particles), fcc cobalt solid solution precipitates ranging from 5 to 25 nm were observed in material grown with pulling rate 28 $mm \cdot h^{-1}$ and annealed at 1548 K/4 h [3]. The microstructure of an annealed (1548 K/4 h, pulling rate 38 $mm \cdot h^{-1}$) alloy was investigated by TEM and rod-like precipitates of hcp-Co 10–60 nm long were observed in the austenite phase. The orientation relationship between the precipitates and the B2 matrix was found to be the Burgers orientation relation. The martensite crystal structure is tetragonal $L1_0$ with a (1–11) twinning plane [4]. Many micron-sized non-twinned, single and triple $\{111\}_{B2}$ twinned precipitates with partial $L1_2$ ordering were observed in the austenite matrix, besides the interdendritic A1 phase in material grown with pulling rate 104 $mm \cdot h^{-1}$ and annealed 1373 K/72 h [5]. The orientation relationship between precipitates and matrix in such sample was determined to be the Kurdjumov-Sachs orientation relationship. STEM-EDX analysis indicates that twinned and non-twinned precipitates are Co-rich and Al- and Ni-deficient with respect to the matrix and with a lower Co/Al ratio for the latter, a difference possibly related with the site of precipitation with respect to the eutectic regions. A 3D morphology investigation of precipitates with FIB/SEM slice-and-view imaging revealed that the single $\{111\}_{B2}$ twinned precipitates have a plate-like shape with flat {111} faces while the non-twinned precipitates have a lath-like shape and can be curved.

Besides the precipitation in the matrix the annealing causes dissolving of interdendritic particles. Such process enriches the matrix with cobalt atoms and leads to concentration gradients on the particles' borders.

In the sample, grown with a pulling rate of 104 mm·h^{-1} and annealed at 1623K/1h, the matrix shows large martensite regions while interdendritic precipitates have a complicated structure with enclosed B2 austenite areas. Also, a precipitate-austenite-martensite sandwich structure with residual austenite of several hundred nanometres wide is formed due to the depletion of Co and enrichment of Al in the chemical gradient zone and the strong martensitic start temperature dependency of the element concentrations. The austenite $[100]_a$ direction is found to be parallel to the martensite $[110]_m$ direction in this case, confirming the origin of the sandwiched area as retained austenite, Fig. 1. The mentioned processes in microstructure and ordering of $Co_{38}Ni_{33}Al_{29}$ alloy will be discussed and related to elastic properties evolution.

1. J. Kopeček, V. Kopecký, M. Landa, O. Heczko, Mat. Sci. Forum, 738-739 (2013), 416
2. J. Kopeček, F. Yokaichiya, F. Laufek, M. Jarošová, K. Jurek, J. Drahokoupil, S. Sedláková-Ignácová, P. Molnár, O. Heczko, Acta Physica Polonica A, 122 (2012), 475
3. B. Bártová, D. Schryvers, Z.Q. Yang, S. Ignácová, P. Šittner, Scripta Mater., 57 2008, 37
4. B. Bártová, N. Wiese, D. Schryvers, J.N. Chapman, S. Ignácová, Acta Mater., 56 2008, 4470
5. J.B. Lu, H. Shi, S. Sedláková-Ignacova, R. Espinoza, J. Kopeček, P. Šittner, B. Bártová, D. Schryvers, J. Alloys Comp., (2013), accepted, DOI:10.1016/j.jallcom.2013.03.228

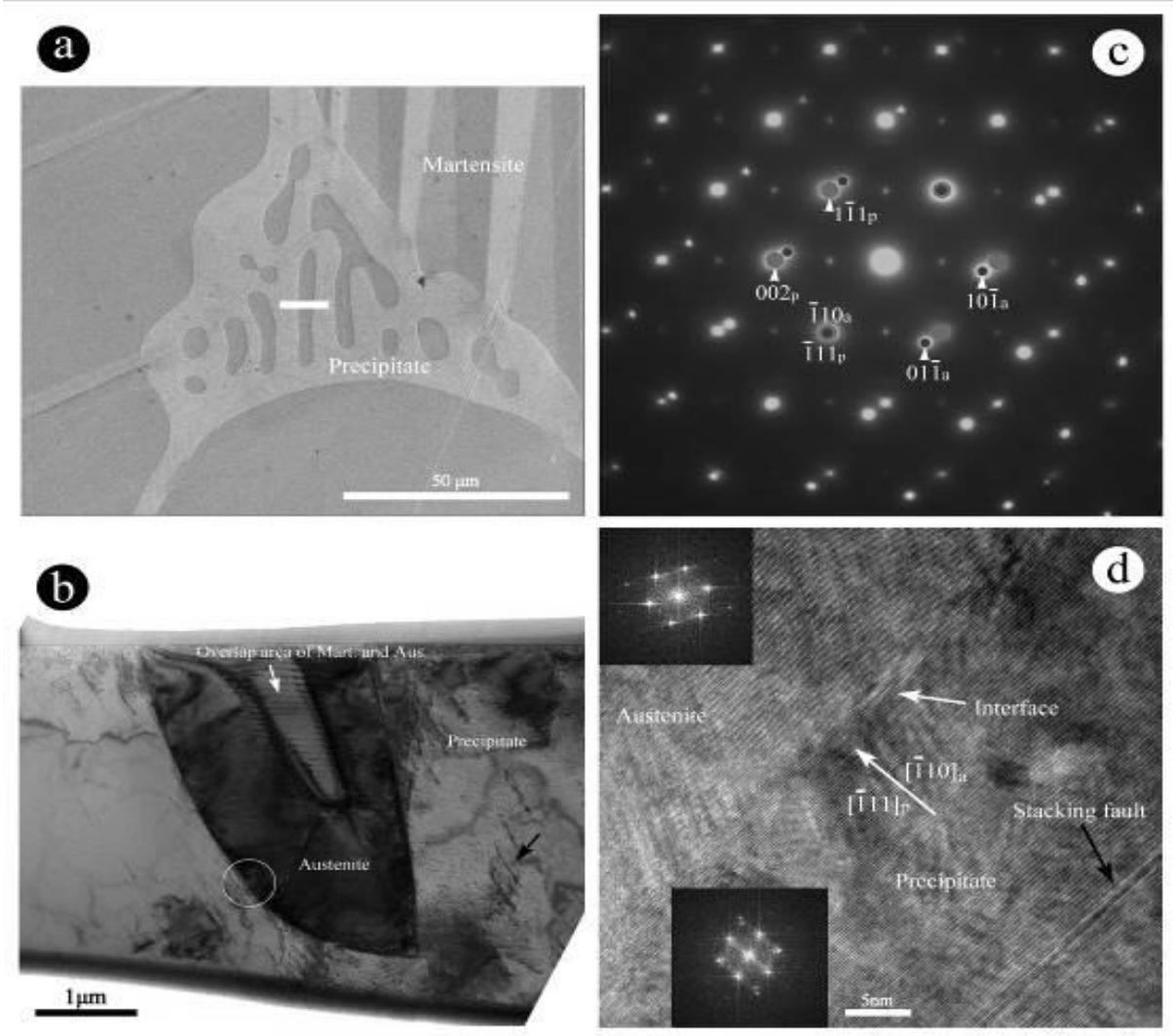

Figure 1. (a) SEM image sample grown with a pulling rate of 104 mm·h^{-1} and annealed at 1623K/1h, which shows the interdendritic morphology of a precipitate (white bar indicates the position where the TEM lamella was prepared by FIB), (b) BF TEM image of the FIB lamella, (c) Electron diffraction pattern taken from the area indicated by the white circle in (b) ($[111]_a$ / $[110]_p$), (d) HRTEM image of the interface of the precipitate and austenite corresponding to (c) including some FFT patterns.

Alloys and Intermetallics

MS.6.P182
Wear behavior of new generation powder metallurgical cold work tool steels

S. Polat[1], Ů Atapek[1], E. Türedi[1], S. Gümüş[1], M. Yaman[1]

[1]Kocaeli University, Metallurgical & Materials Engineering, Kocaeli, Turkey

sydpolat@gmail.com
Keywords: Powder metallurgy, tool steels, microstructure, wear, characterization.

Cold work tool steels are alloy steels having chromium, vanadium, tungsten which are known as strong carbide former elements. Their mechanical properties are directly affected by manufacturing technique, alloying content, heat treatment and final microstructure. The steels produced by powder metallurgical (PM) methods have more superior mechanical properties due to their fine and homogenous matrices than the ones produced by conventional casting and then deformed. Today, PM cold work tool steels are used in several industrial applications and the investigation of their wear behavior under service conditions is one of the popular subjects [1-15].

In this study, the wear behavior of Vanadis 4 (1.50 C, 0.40 Mn, 1.00 Si, 8.00 Cr, 1.50 Mo, 4.00 V, wt-%) and Vanadis 10 (2.90 C, 0.50 Mn, 0.50 Si, 8.00 Cr, 1.50 Mo, 9.80 V, wt-%), known as new generation PM cold work tool steels, was investigated under dry sliding conditions. Vanadis 4 and Vanadis 10 grade steels were solution annealed at 1050 °C and 1100°C for 20 minutes, respectively. After cooling in air, the steels were tempered at 525 °C for 250 minutes. The specimens taken from heat treated steels were ground using grinding papers of 120, 320, 600 and 1000 mesh in turn, and polished with diamond paste of 3 µm in size. The polished surfaces were then etched chemically with 3% Nital (3 ml HNO_3 + 97 ml ethanol) solution to obtain phase contrast in the structure. In order to determine the tribological characteristics, the steels were tested using "ball-on-disc" type tribometer. In the wear test, load, total distance and rotating speed were selected as 25 N, 250 m and 100 rpm, respectively. The results were evaluated using the friction coefficient-distance diagram and loss in weight. All worn surfaces were examined by light microscope (LM) and scanning electron microscope (SEM). The wear characteristics of PM steels were discussed as a function of the microstructural features.

It was concluded that (i) the steels had tempered martensitic matrices (Figure 1a and b), (ii) their matrices included precipitates as carbides (Figure 2 and b), Vanadis 10 grade had higher hardness (67 HRC) due to higher carbon and vanadium content than that of Vanadis 4 grade (63 HRC), (iii) Vanadis 10 grade had a lower friction coefficient (Figure 3), (iv) both grades exhibited abrasive-adhesive tracks on their worn surfaces (Figure 4)

1. M. Rosso, D. Ugues, M. A. Grande, Journal of Achievement in Materials and Manufacturing Engineering, 18 (2006), pp. 175-178.
2. S. Huth, N. Krasokha, W. Theisen, Wear, 267 (2009), pp. 449-457.
3. S. Kheirandish, H. Saghafian, J. Hedjazi, M. Momeni, Journal of Iron and Steel Research International, 17 (2010), pp. 40-45, 52.
4. K. S. Kumar, A. Lawley, M. J. Koczak, Metallurgical Transactions A, 22(1991), pp. 2747-2759.
5. F. K. Arslan, I. Altinsoy, A. Hatman, M. Ipek, S. Zeytin, C. Bindal, Vacuum, 86 (2011), pp. 370-373.
6. F. Yan, Z. Xu, H. Shi, J. Fan, Materials Characterization, 59 (2008), pp. 592-597.
7. F. Yan, H. Shi, J. Fan, Z. Xu, Materials Characterization, 59 (2008),pp. 883-889.
8. F. Yan, H. Shi, B. Jin, J. Fan, Z. Xu, Materials Characterization, 59 (2008),pp. 1007-1014.
9. P. Bílek, J. Sobotová, P. Jurči, Materials and Technology, 45 (2011), pp. 489-493.
10. P. Jurči, Materials and Technology, 45 (2011), pp. 383-394.
11. P. Jurči, F. Hnilica, J. Suchánek, P. Stolař, Materials and Technology, 38 (2004), pp. 13-17.
12. M. Pleterski, T. Muhič, D. Klobčar, L. Kosec, Metalurgija, 51 (2012), pp. 13-16.
13. A. R. Mashreghi, S. M. Y. Soleimani, S. Saberifar, Materials & Design, 46 (2013), pp. 532-538.
14. K. Kubota, T. Ohba, S. Morito, Wear, 271 (2011), pp. 2884-2889.
15. L. Bourithis, G. D. Papadimitriou, J. Sideris, Tribology International, 39 (2006), pp. 479-489.

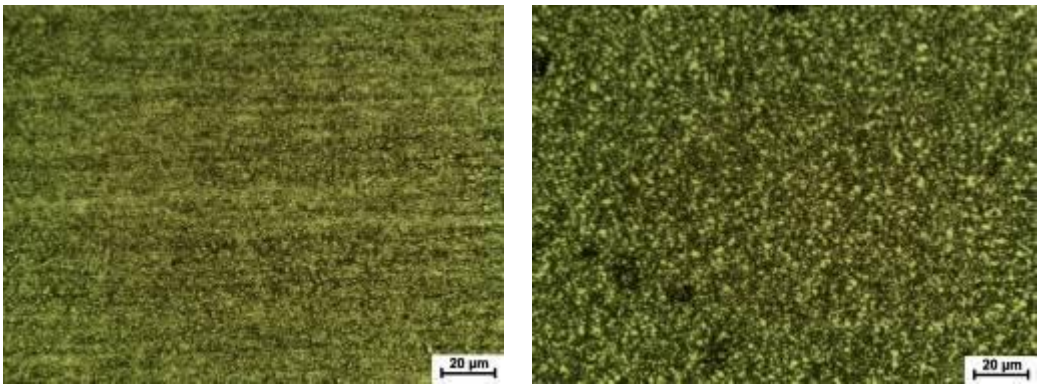

(a) (b)

Figure 1. LM micrographs showing the microstructures of heat treated MP cold work tool steels having tempered martensitic matrix; (a) Vanadis 4 and (b) Vanadis 10 grade.

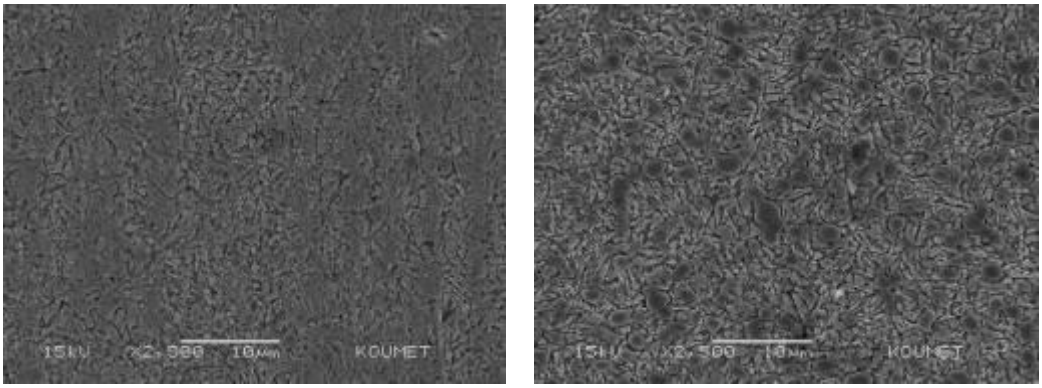

(a) (b)

Figure 2. SEM micrographs showing the microstructures of Vanadis 4 (a), Vanadis 10 grade (b).

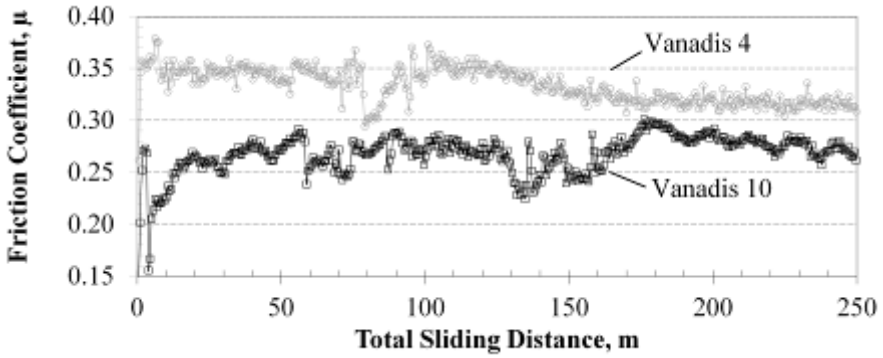

Figure 3. The relationship between friction coefficient and distance for Vanadis 4 and Vanadis 10 grade steels.

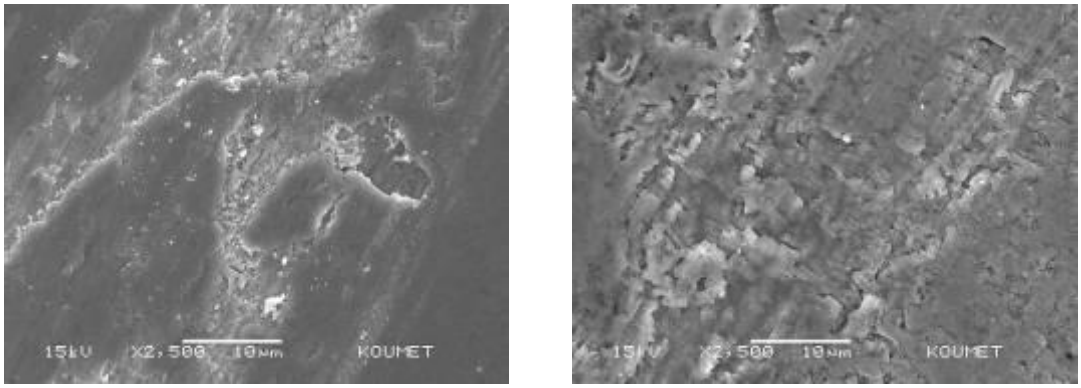

(a) (b)

Figure 4. SEM micrographs showing the abrasive-adhesive tracks on the worn surfaces of Vanadis 4 (a), Vanadis 10 grade (b)

Alloys and Intermetallics

MS.6.P183
Stress corrosion cracking in AA5083 mold material used for curing rubber compounds

A. Alkan[1], S. Gümüş[1], Ů Atapek[1], Ů Polat[1]

[1]Kocaeli University, Metallurgical & Materials Engineering, Kocaeli, Turkey

aalkanstem@yahoo.com
Keywords: AA5083 alloy, rubber curing, intergranular stress corrosion cracking, failure.

Aluminum and its alloys can fail by cracking along grain boundaries when simultaneously exposed to specific environments and stresses of sufficient magnitude. AA5083 material is a non-heat treatable wrought aluminium alloy and it is strengthened by elements in solid solution and dislocation structures introduced by mechanical deformation. After service for extended period of time at ambient temperature or elevated temperature, alloying elements may segregate to grain boundaries, leading to several different types of precipitates. If these grain boundary precipitates are anodic to the alloy matrix, they can serve as the path for intergranular stress corrosion cracking. The segregation of magnesium at grain boundaries leads to the formation of anodic intermetallic Al_3Mg_2 which is known as β-phase, and this β-phase has been proven to be the major cause of stress corrosion cracking in AA5083 material [1-10].

In this study, the failure analysis of AA5083 mold material, used for curing rubber compounds, was carried out. The problem revealed itself as the formation of bubbles, 4-6 mm in diameter, on the mold surface during curing process and caused quality problems in the final product (Figure 1a). In the first stage of the analysis, elemental distribution maps were taken by energy dispersive x-ray spectrometer (EDS) from the interior part of a bubble (Figure 1b) and accumulation of both Mg and also Cl was observed (Figure 1c, Table 1). In the second stage, two samples 10-25 mm in width were taken out from the mold material. The first sample was very close to outer part of the mold and had no contact with the rubber compound. The second sample was taken from the inner part of the mold, 5 mm in depth from the surface. The samples were embedded in resin and polished surfaces were examined using scanning electron microscope (SEM) and EDS.

It was concluded that (i) the contamination by Cl ions was due to the cutting oil used to open vent holes during mold cleaning, (ii) the outer part of mold material had finer α-Al grains whereas the inner part in contact with the compound had coarse grains due to the thermal effect of curing process (Figure 2a and b), (iii) β-phase (Al_3Mg_2) formed at the grain boundaries after a sufficient exposure to temperatures above 50 °C (Figure 2c), (iv) the grain boundaries had Mg-rich phase showing anodic behavior, while the grains had Al-rich phase showing cathodic behavior, (v) the cracks initiated and propagated through the grain boundaries as stress corrosion cracking which resulted in the separation of grains and the accumulation of gases appeared as bubbles due to thermo-mechanical aging and effects of corrosive medium.

1. M. O. Speidel, Metallurgical Transactions A, 6 (1975), pp. 631-651.
2. S. K. DeWeese, S. T. Ningileri, S. K. Das, J. A. S. Green, The Journal of The Minerals, Metals & Materials Society, 60 (2008), pp. 50-57.
3. G. L. Makar, J. Kruger, K. Sieradzki, Corrosion Science, 34 (1993), pp. 1311-1323, 1325-1342.
4. A. Zielinski, Materials Science, 34 (1998), pp. 469-475.
5. M. Bobby-Kannan, V. S. Raja, R. Raman, A. K. Mukhopadhyay, Corrosion, 59 (2003), pp. 881-889.
6. Q. Li, J. Zhao, P. Zhang, Journal of Wuhan University of Technology-Mater. Sci Ed., 27 (2012), pp. 648-651.
7. J. Gao, D.J. Quesnel. Metallurgical and Materials Transactions A, 42 (2011) pp. 356-364.
8. J.L. Searles, P.I. Gouma, R.G. Buchheit, Metallurgical and Materials Transactions A, 32 (2001), pp. 2859-2867.
9. R.H. Jones, J.S. Vetrano, C.F. Windisch, *Corrosion*, 60 (2004), pp. 1144-1154.
10. R.H. Jones, D.R. Baer, M.J. Danielson, J.S. Vetrano, Metallurgical and Materials Transactions A, 32 (2001), pp. 1699-1711.

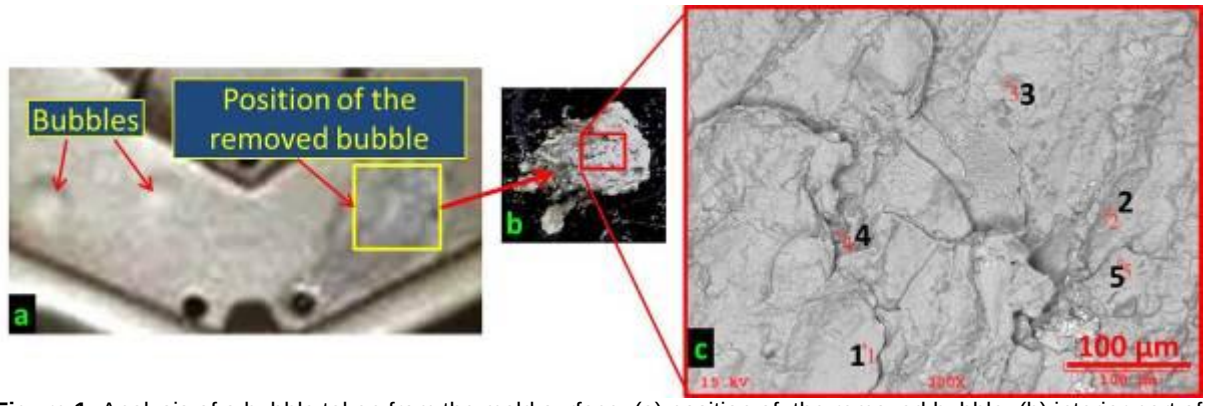

Figure 1. Analysis of a bubble taken from the mold surface; (a) position of the removed bubble, (b) interior part of the removed bubble; c) points where the spot analyses were carried out.

Spot	Element (count-%)										
	C	O	Mg	Al	Si	P	S	Cl	Ti	Mn	Fe
1	0.171	6.882	4.576	86.910	0.101	-	-	0.608	0.266	0.451	0.035
2	0.123	17.685	7.121	72.026	0.040	0.163	0.015	2.120	0.101	0.489	0.117
3	0.0037	25.904	11.761	60.129	0.040	0.255	-	1.362	0.064	0.344	0.104
4	0.028	42.319	26.048	29.842	0.237	-	0.010	1.182	0.053	0.245	0.037
5	0.618	9.557	4.318	84.391	0.028	0.223	0.019	0.493	0.052	0.257	0.042

Table 1. EDS results of the spots shown in Figure 1c.

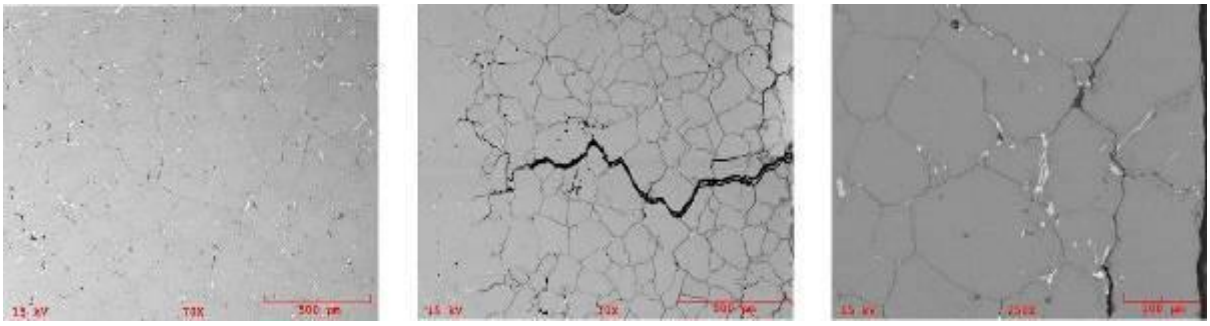

(a) (b) (c)

Figure 2. The variation of α-Al grain size in the outer (a) and inner part of mold material (b), Mg-rich phases visible in light contrast at the grain boundaries (c).

Alloys and Intermetallics

MS.6.P184
Characterization of closely crystallographically related phases in γ-TiAl alloys by HEXRD and TEM imaging

H. Gabrisch[1], S. Mayer[2], F. Pyczak[1], M. Rackel[1], U. Lorenz[1], N. Schell[1], A. Schreyer[1], A. Stark[1]

[1]Helmholtz-Zentrum Geesthacht, Geesthacht, Germany
[2]Montanuniversitaet , Leoben, Austria

heike.gabrisch@hzg.de
Keywords: gamma-md, orthorhombic distortion, B19 phase

TiAl alloys find applications in aero engines where a combination of excellent high temperature strength, sufficient room temperature ductility, and low density is required. In comparison to titanium alloys and to Ni-base alloys TiAl alloys offer high specific strength but suffer from low ductility. Therefore one goal of ongoing research is to increase the alloy's ductility.

In 2006 a γ TiAl alloy was developed that possesses improved ductility and a tensile strength above 1 GPa at room temperature [1]. The alloy is characterized by Nb additions and a processing route that leads to the coexistence of the closely crystallographically related phases □$_2$, □$_o$ and B19 within lamellar and pearlitic colonies. The presence of the meta-stable orthorhombic B19 phase leads to a modulation of the microstructure on the nano-scale that is thought to improve the mechanical properties. Subsequently much effort was directed towards the development of TiAl alloys with modulated, B19 containing microstructures and improved mechanical properties. At the same time the study of the formation and the stability of the B19 phase became an independent topic.

The close crystallographic relationship between the co-existing □$_2$/ □$_o$/B19 phases complicates the identification of the alloy's constituents. Suitable methods to distinguish between the phases involved are high-energy X-ray diffraction (HEXRD), single crystal electron diffraction and high resolution imaging in the TEM. It has been demonstrated by in-situ heating HEXRD that the B19 phase forms from the hexagonal □$_2$ phase by small atomic displacements in the close packed □$_2$ (0001) plane [2, 3]. The goal of the current work is to identify the □$_2$ and B19 phases by TEM and to characterize their spatial distribution within the alloy's microstructure. From the analysis of the diffraction data it is clear that differences between the two phases are most easily observed looking onto the □$_2$ (0001) plane.

A comparison of the Ti_3Al-□$_2$ and TiAl-B19 unit cells reveals a higher fraction of Al atoms in the orthorhombic unit cell, transpositions between Ti and Al sites and small atomic displacements (≤ 0.01 nm) compared to the parent □$_2$ phase. The displacements are not easily detected by electron diffraction or high resolution imaging, whereas the different symmetries of the two phases can be used to distinguish between them. An illustration of the site occupancy in the □$_2$ [0001] projection (parallel to B19 [100]) is given in figure 1 where the six-fold symmetry of the □$_2$ unit cell (figure 1a) is compared to the two-fold symmetry of B19 (figure 1b). Using the resulting differences in the corresponding diffraction patterns (figure 1c, d) dark field imaging can be applied to allocate the two phases within the microstructure. An example is given in figure 2, where dark field images taken with a common reflection of the □$_2$ and B19 phase (figure 2.a) and taken with a unique reflection of the □$_2$ phase are shown (figure 2.b). Imaging with the sum of B19 and □$_2$ reflections in figure 2a shows that the microstructure consists of rectangular blocks of about 50-100 nm edge length. In between these blocks, channels with a high amount of strain contrast are observed. For comparison the dark field image in figure 2.b illustrates that these blocks are made up of alternating regions of □$_2$ (bright) and B19 phase (dark).

In microstructures with lamellar (□$_2$+□ colonies it is oftentimes not possible to obtain an un-obscured view onto the □$_2$ (0001) plane because the lamellar structure is formed by □ {111} planes that are aligned parallel to the (0001) □$_2$ planes (Blackburn relationship [4]). In this configuration the □$_2$/□ interface is easily observed but not the □$_2$ (0001) plane perpendicular to it. This necessitates the search for zone axis directions where dark field imaging or contrast criteria in high resolution imaging allow to differentiate between the two phases (□$_2$ and B19). Simulations show that the □$_2$ [11-20] zone axis direction that is often used to illustrate the Blackburn orientation relationship is not well suited for two reasons: i. the diffraction patterns are identical; ii. the simulated high resolution images of B19 and □$_2$ show identical contrast behavior for ternary alloys with Nb [3]. An alternative option is to use the □$_2$ [10-10] direction parallel to B19 [031]. An example is given in figure 3 where lattice images of the □$_2$ (figure 3a) and B19 (figure 3b) phase are compared.

1. F. Appel, M. Oehring, and J.D.H. Paul, Advanced Engineering Materials 8 371-376 (2006).
2. T. Schmoelzer, et al., Advanced Engineering Materials (2012).
3. H. Gabrisch, et al., MRS Proceedings (2012 MRS Fall Meeting).
4. M.J. Blackburn, Science, Technology, and Application of Titanium 633-643 (1970).

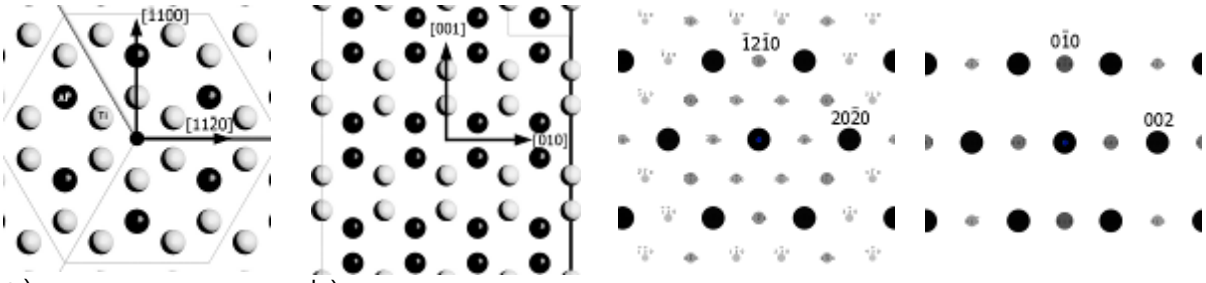

a.) b.) c.) d.)

Figure 1: Unit cells of α_2 (a.) and B19 (b.) seen along the α_2 [0001] direction parallel to B19 [100] (black = Al atoms). Simulated diffraction patterns of α_2 (c.) and B19 (d.) seen along the α_2 [0001] direction parallel to B19 [100].

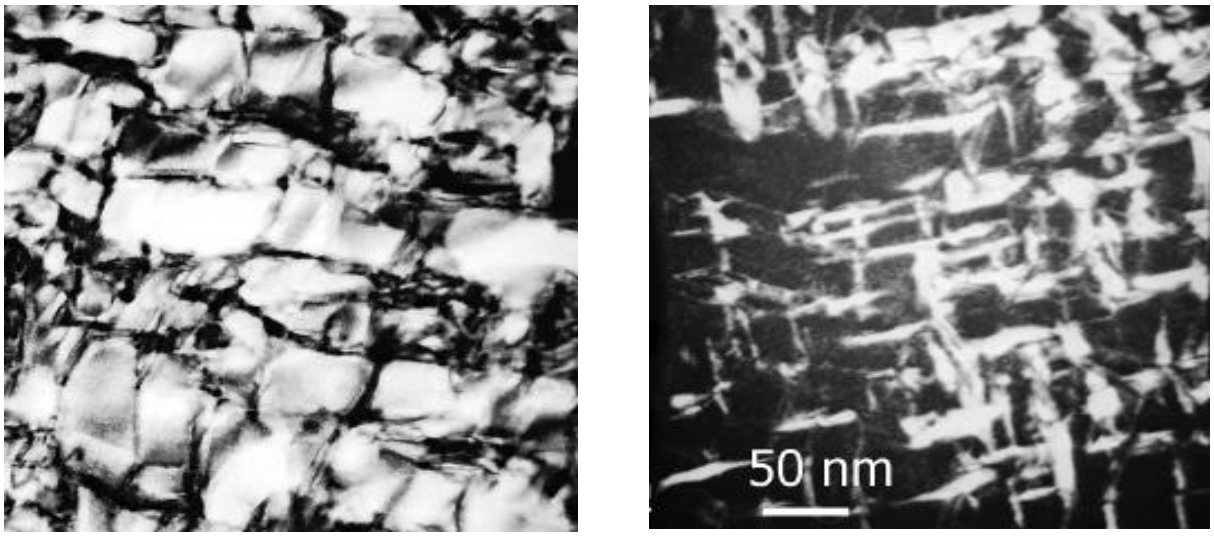

a.) b.)

Figure 2. Dark field images in the α_2 [0001] zone axis. (a.) using α_2 $\vec{g} = (\bar{1}2\bar{1}0)$ // B19 $(0\bar{1}0)$. (b.) using α_2 $\vec{g} = (11\bar{2}0)$

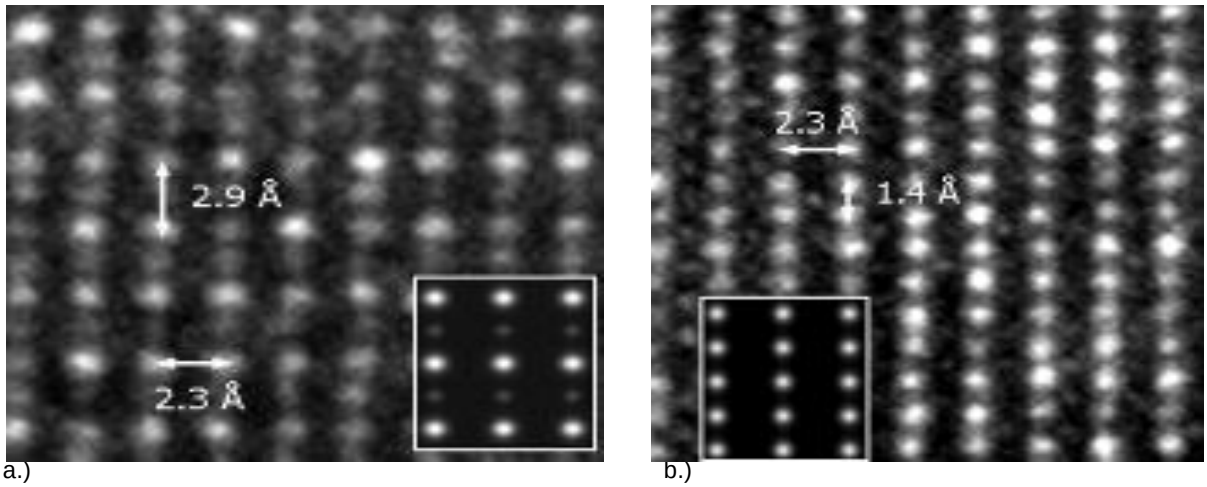

a.) b.)

Figure 3. High resolution images taken from TiAl3Mo. (a.) lattice of α_2 phase, inset shows corresponding simulated Bloch image. (b.) lattice of γ phase shown together with simulated Bloch image (inset). The two images were taken in the same specimen illustrating the gradual change between lattice structures.

Alloys and Intermetallics

MS.6.P185
TEM study of Co_3Ti made amorphous by high pressure torsion

C. Gammer[1,2], D. Geist[1], H. P. Karnthaler[1] and C. Rentenberger[1]

[1]Faculty of Physics, Physics of Nanostructured Materials, University of Vienna, Boltzmanngasse 5, 1090 Wien, Austria.
[2]National Center for Electron Microscopy, LBNL, Berkeley, California 94720, USA.

christoph.gammer@univie.ac.at, cgammer@lbl.gov
Keywords: solid state amorphization, nanocrystallization, deformation induced crystallisation

Amorphous structures can be achieved by a solid state transformation of the crystalline structure using severe plastic deformation. This has been successfully carried out by applying high-pressure torsion (HPT) deformation in the case of $L1_2$ ordered Zr_3Al [1].

In the present work the structural changes caused by HPT deformation of bulk intermetallic Co_3Ti is studied on multiple length scales using a combination of scanning (SEM) and transmission electron microscopy (TEM) methods, including high-resolution TEM (HRTEM). Co-23at.%Ti samples were alloyed from high purity elements and deformed by HPT to different degrees of deformation under a pressure of 4 GPa. TEM foils were prepared from different areas of the HPT-discs using electropolishing.

The SEM investigations of the cross-section of the HPT samples using back-scattered electrons reveal that the material deforms very inhomogeneously and shows a tendency to amorphization localized in the form of bands. With increasing deformation the volume fraction of the amorphous phase increases.

Figure 1a shows a TEM bright-field image from a region corresponding to a low deformation. A high density of stacking faults on {111} planes is observed. The selected area (SA) diffraction pattern (Figure 1b) shows streaking of the fundamental reflections along two different <111> directions but not of the superlattice reflections, thus revealing that the observed faults are stacking faults. During the deformation of $L1_2$ ordered intermetallic compounds superlattice glide dislocations are formed. The glide dislocations can reduce their energy by dissociation; which can be achieved in two different ways: (i) the dissociation into unit dislocations bounding an antiphase boundary fault, as observed in Ni_3Al and Cu_3Au or (ii) the dissociation into super-Shockley partials bounding a superlattice intrinsic stacking fault, as observed in Zr_3Al and in the present work on Co_3Ti. In a recent paper we demonstrate that a dissociation by scheme (ii) does not lead to chemical disorder but facilitates amorphization [2]. This is in good accordance with the present results. In Co_3Ti no disordering is observed but amorphization occurs at large deformations.

Figure 2a shows a TEM bright-field image of a sample deformed to a nominal shear strain of 100,000% having an amorphous structure containing a large number of crystallites (5 to 20 nm in size). The morphology of the crystals is mainly round with some faceting. The SA diffraction pattern contains diffraction spots in addition to the amorphous rings caused by crystallites embedded in the amorphous material. The analysis of the diffraction rings indicates that crystallites containing Laves phases (cubic Co_2Ti and double hexagonal $Co_{2.1}Ti_{0.9}$) occur, not encountered in the initial material. Therefore, it is concluded that the crystallites are formed during severe plastic deformation. To analyse the crystallites in more detail HRTEM images (cf. Fig. 2b and Fig. 3) were taken. Fig. 2b shows a nanocrystal with the hcp structure similar to that of pure Co. In contrast, Fig. 3 reveals that several nanocrystals have a Laves phase structure with a heavily faulted stacking sequence.

1. D. Geist, C. Rentenberger, H. P. Karnthaler. Acta Mater. 59 (2011) 4578.
2. D. Geist, C. Gammer, C. Mangler, C. Rentenberger, H.P. Karnthaler. Phil. Mag. 90 (2010) 4635.
3. The authors acknowledge support by the Austrian Science Fund (FWF):[J3397,P22440] and the National Center for Electron Microscopy, Lawrence Berkeley Lab, which is supported by the U.S. Department of Energy under Contract # DE-AC02-05CH11231.

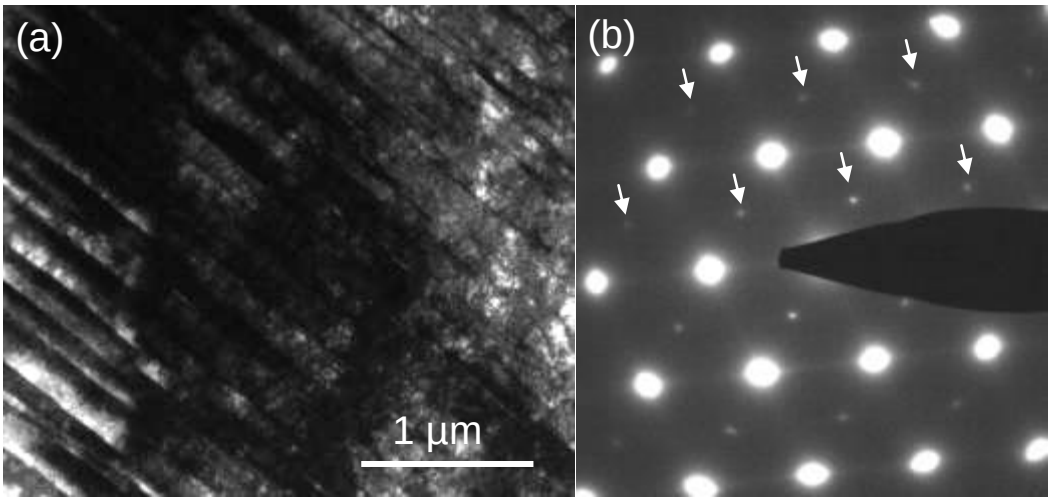

Figure 1. Co_3Ti deformed by high pressure torsion; initial stage of deformation. (a) TEM bright-field image showing a high density of stacking faults. (b) The corresponding diffraction shows both fundamental and superlattice spots (some of them marked by arrows) as the material is still ordered. The high density of stacking faults leads to streaking in the fundamental reflections.

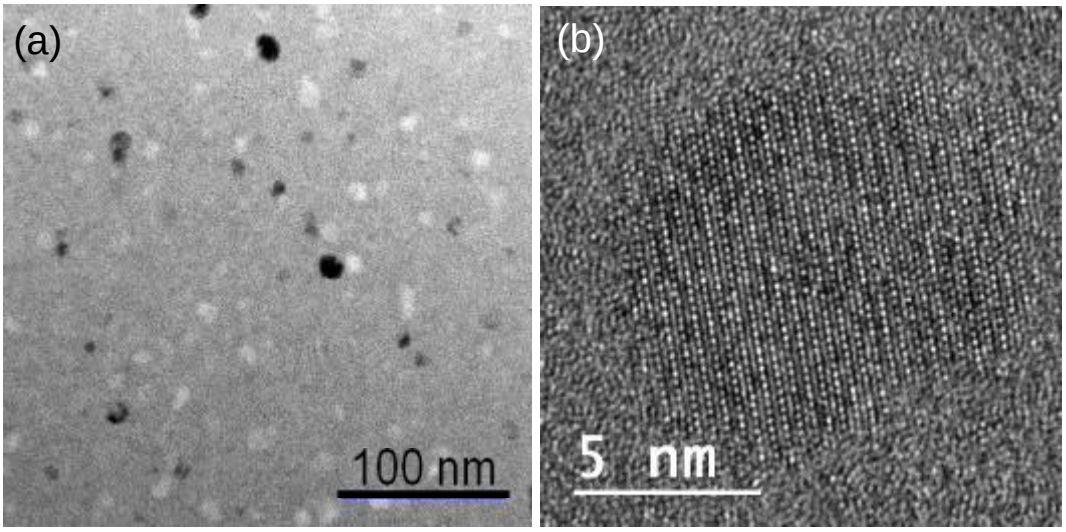

Figure 2. Co_3Ti deformed by high pressure torsion. (a) TEM bright-field image showing amorphous material containing a large number of nanocrystals. (b) HRTEM of a nanocrystal with hcp structure.

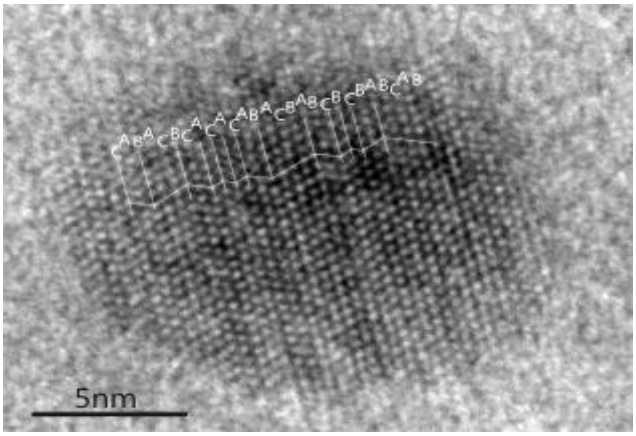

Figure 3. Co_3Ti deformed by high pressure torsion. HRTEM image showing a nanocrystal embedded in the amorphous matrix (cf. Figure 2a). A closer inspection of the HRTEM image reveals that the nanocrystal shows a highly faulted structure, comprising an alternation of the cubic and hexagonal Laves phase. The cubic Laves phase (Co_2Ti) has the stacking sequence ABCABC and the double hexagonal Laves phase ($Co_{2.1}Ti_{0.9}$) the stacking sequence ABACABAC. The stacking sequence of the nanocrystal is indicated in the figure.

Alloys and Intermetallics

MS.6.P186
Softening processes in accumulative roll-bonding processed twin-roll cast aluminium sheets studied by light and transmission electron microscopy.

M. Poková[1], M. Cieslar[1]

[1]Charles University in Prague, Faculty of Mathematics and Physics, Prague 2, Czech Republic

Miroslav.Cieslar@mff.cuni.cz
Keywords: ARB, AA8006, recrystallization

Mechanical properties of metallic materials are very sensitive to the grain size. A reduction of the mean grain size increases the yield stress and the tensile strengths according to the Hall-Petch relationship. Severe plastic deformation (SPD) is frequently used for the grain refinement of metals and alloys [1]. The basic principle of the SPD process consists in inducing the extremely high plastic strain into the material resulting in a substantial grain refinement and improved strengths. Accumulative roll-bonding (ARB) is one of the most popular SPD techniques which does not require any special equipment [2]. The homogeneity and final thermal stability of the grain structure in aluminium alloys depends on the processing temperature, number of ARB cycles but also on the grain size of the initial material and the size and distribution of coarse primary particles which are generally present in the ingot cast and cold-rolled sheets. Therefore the thermal stability and homogeneity is improved in materials with fine particles and small grain size which is typical for continuously twin-roll cast (TRC) aluminium alloys. A commercial TRC AA8006 type alloy (0.40 Mn, 0.16 Si, 1.51 Fe in wt.%) was used in the study. Supplied 2 mm thick sheets were homogenized for 18 h at 610°C and then annealed at 450°C for 30 min in order to obtain fine-grained and fully recrystallized material (F0). Specimens with three (specimen F3) and five ARB cycles were prepared. Vickers microhardness measurements were carried out on the recrystallized material F0 and ARB processed specimens F3 and F5 annealed at different temperatures (Figure 1). In the initial state, the hardness of the F3 and F5 specimens is higher than the one observed in the F0 sheet. Above 100°C the microhardness increases in both deformed materials. The maximum of the microhardness is reached at 160°C. On the other hand the microhardness of the F0 specimen, which is fully recrystallized, remains constant within the experimental error during the whole annealing cycle. Between 160°C and 300°C, F3 and F5 hardness drops until the value similar to the F0 final hardness was reached. The examples of initial structures and the evolution of microstructure during annealing are given in Figures 2, 3 and 4. The microstructure of the F0 material was not modified by the thermal treatment because this specimen was already annealed at high temperature which results in the formation of uniform recrystallized structure with stable phase composition. The significant increase of microhardness which takes place in the ARB processed materials is in accordance with the LOM and TEM results due to the microstructure refinement occurring during ARB process. The F3 and the F5 specimens contain very small and elongated subgrains, nevertheless the higher number of ARB cycles, does not visibly increase the microhardness. Huang et al. [3] have shown that in heavily deformed aluminium materials like the materials after the ARB process the partial recovery of the dislocation substructure which is coupled with the dislocation density decrease and changes in the low subgrain boundary fraction may result in a surprising increase of the strength of the material. Such behaviour was observed also in material F5 and F3 where the microhardness increases until a maximal value at 160°C. A subgrain growth which is observed around 160°C is a concurrent process which finally prevails above the strengthening of the material and the microhardness starts to decrease again at higher annealing temperatures. Between 160°C and 200°C the microhardness decreases slightly then rapidly drops between 200°C and 300°C. The TEM observations show that the beginning of the softening can be explained by the subgrains coarsening and by the first creation of nuclei in the vicinity of coarse particles. Between 300°C and 440°C the microhardness varies only modestly because the microstructure is almost fully recrystallized at 300°C and only a recrystallization finalization and a moderate coarsening of grains occur at higher annealing temperatures. The TEM observations also reveal the presence of larger grains close to the coarse particles and smaller grains in other places during the recrystallization. This effect is caused by the creation of deformed zones with a high stored energy in the vicinity of the particles during the ARB process. This process is known as a particle-

stimulated nucleation which often results in the so called continuous recrystallization and abnormal grain growth [4].

1. R. Z. Valiev, A. V. Korznikov, and R. R. Mulyukov, Mater. Sci. Eng. A168 (1993), p.141.
2. Y. Saito, H. Utsunomiya, N. Tsuji, T. Sakai, Acta Mater. 47 (1999) p.579.
3. X. Huang, N. Tsuji, N. Hansen, Y. Minamino, Mater. Sci. Eng., A 340 (2003) p.265
4. H. Jazaeri, F.J. Humphreys, Acta Mater. 52 (2004) p.3251.

5. A financial support of the Czech Scientific Foundation under the project 107-12-0921 is gratefully acknowledged.

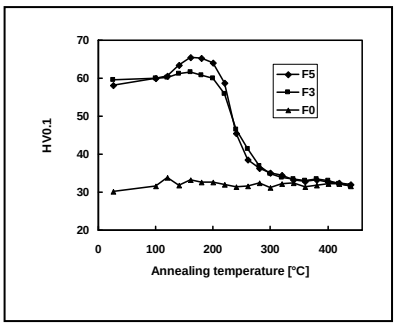

Figure 1. Evolution of microhardness in material after 0, 3 and 5 ARB passes.

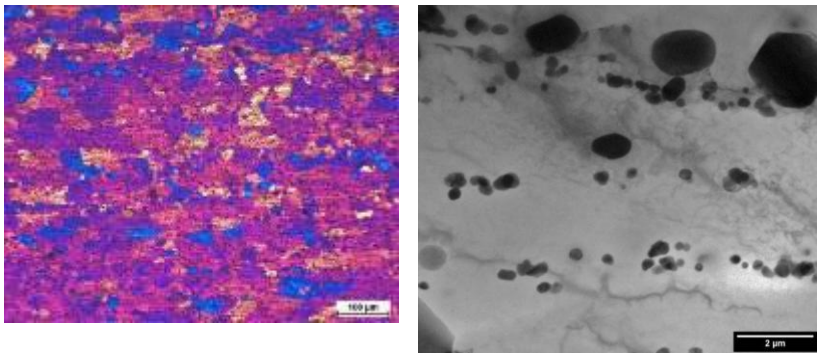

Figure 2. The microstructure of the F0 specimen (LOM left and TEM right).

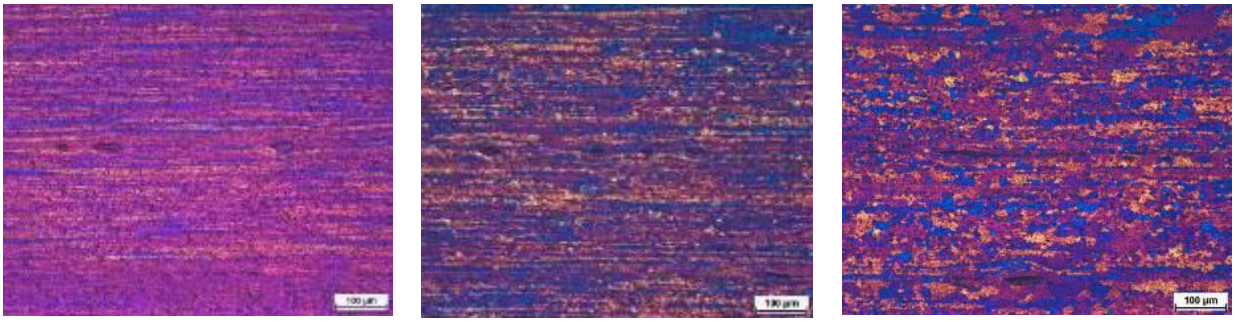

Figure 3. LOM of F3 material in the initial (left) state and after annealing up to 280 (middle) and 440°C (right).

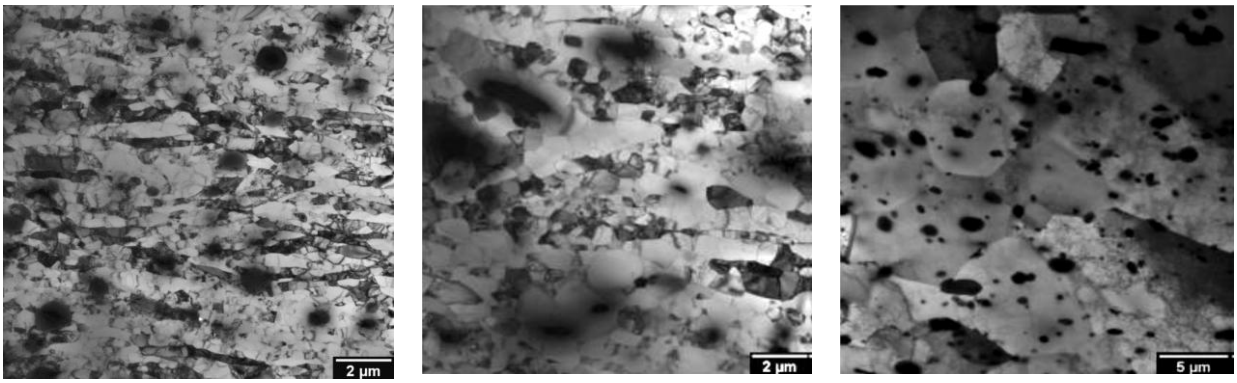

Figure 4. TEM of F3 material in the initial (left) state and after annealing up to 260 (middle) and 440°C (right).

Alloys and Intermetallics

MS.6.P187
Characterization of Ag-TiO_2 and Au-TiO_2 nanoparticles by means of transmission electron microscopy

D. Jenko[1], R. Rudolf[2,3], B. Friedrich[4], S. Stopić[4], I. Anžel[3], M. Jenko[1]

[1]Institute of Metals and Technology, Department of Physics and Chemistry of Materials, Ljubljana, Slovenia
[2]Zlatarna Celje d.d., Celje, Slovenia
[3]University of Maribor, Faculty of Mechanical Engineering, Maribor, Slovenia
[4]RWTH Aachen University, IME Process Metallurgy and Metal Recycling, Aachen, Germany

darja.jenko@imt.si
Keywords: nanoparticles, characterization, TEM

Silver (Ag) and gold (Au) nanoparticles (NPs) typically have dimensions ranging from 1 nm to 100 nm. These dimensions are similar to cellular objects and because of their high stability, biological compatibility, controllable morphology and size dispersion, and easy surface functionalization, Ag and AuNPs are of high interest. Both NPs have many potential applications in electrochemistry and medicine, as well as for the production of nanodevices.

There are many different methods for synthesis of Ag and AuNPs. We report on the synthesis by means of ultrasonic spray pyrolysis (USP), which is a simple aerosol synthetic technique [1]. USP enables synthesis of Ag and AuNPs of various sizes and shapes, including nanoparticles contaminated with metals from alloys [2, 3].

A chemically dissolved pure Ag ($HAgCl_4$) or Au ($HAuCl_4$) and ortotitanate ($Ti(OC_4H_9)_4$) were used as a precursor for the synthesis of Ag- and Au-TiO_2 NPs by means of USP, using an ultrasonic atomizer. A water solution of $HAgCl_4$ or $HAuCl_4$ and $Ti(OC_4H_9)_4$ was used for an aerosol production. The solution was then passed over to the ultrasonic atomizer at 2.5 MHz. The aerosol produced was transported by hydrogen gas into a hot reactor, where the aerosol droplets underwent drying, droplet shrinkage, solution precipitation, thermolysis, and sintering to form nanoparticles. Thermal decomposition of the resulting solution was performed at 300 °C. NPs were collected in a reactor tube and in a bottle with water.

The study focused on the transmission electron microscopy (TEM) analysis of Ag-TiO_2 (Ag/Ti-NPs) and Au-TiO_2 (Au/Ti-NPs) nanoparticles synthesized by means of USP: their size, shape, and morphology, which are associated with the key parameters of growth.

The average size of Ag/Ti-NPs ranged from around 20 nm to 80 nm (Figure 1). AgNPs were present in a matrix of TiO_2, so called 'micelle' (mixture of AgNPs and TiO_2). Micelles were spherical and varied in size between 150 nm to 300 nm. The NPs were or spherical, hexagonal or polygonal form.

The Au/Ti-NPs contained 'micelles', the mixture of AuNPs and TiO_2, as well (Figure 2). Micelles were present as bigger and smaller agglomerates and their average size was between 50 nm to 700 nm. On their surfaces, individual AuNPs were present (attached), with their size of around 7 nm to 50 nm in spherical, hexagonal or polygonal form. Some bigger nanoparticles of around 100 nm were also present. Most of the particles were around 10 nm in size. The lattice fringes were nicely observed using high-resolution TEM (HRTEM), and the growth of individual particles in the contact surfaces as well.

1. T. T. Kodas and M. J. Hampden-Smith in "Aerosol Processing of Materials", (Wiley-VCH, New York) (1999) p.680.
2. R. Dittrich, S. Stopic and B. Friedrich, Proceedings of EMC 2011 (2011), p. 1-11.
3. R. Rudolf, B. Friedrich, S. Stopic, I. Anzel, S. Tomic and M. Colic, J. Biomater. Appl. 26 (2012), p. 595-611.
4. The authors gratefully acknowledge funding from the EUREKA Programme E!4953 GoNano, Military Medical Academy, Belgrade, Project VMA/07-10/B.18 and Slovenian Research Agency, Project L2-4212 (C) 'Production technology of Au nano-particles'.

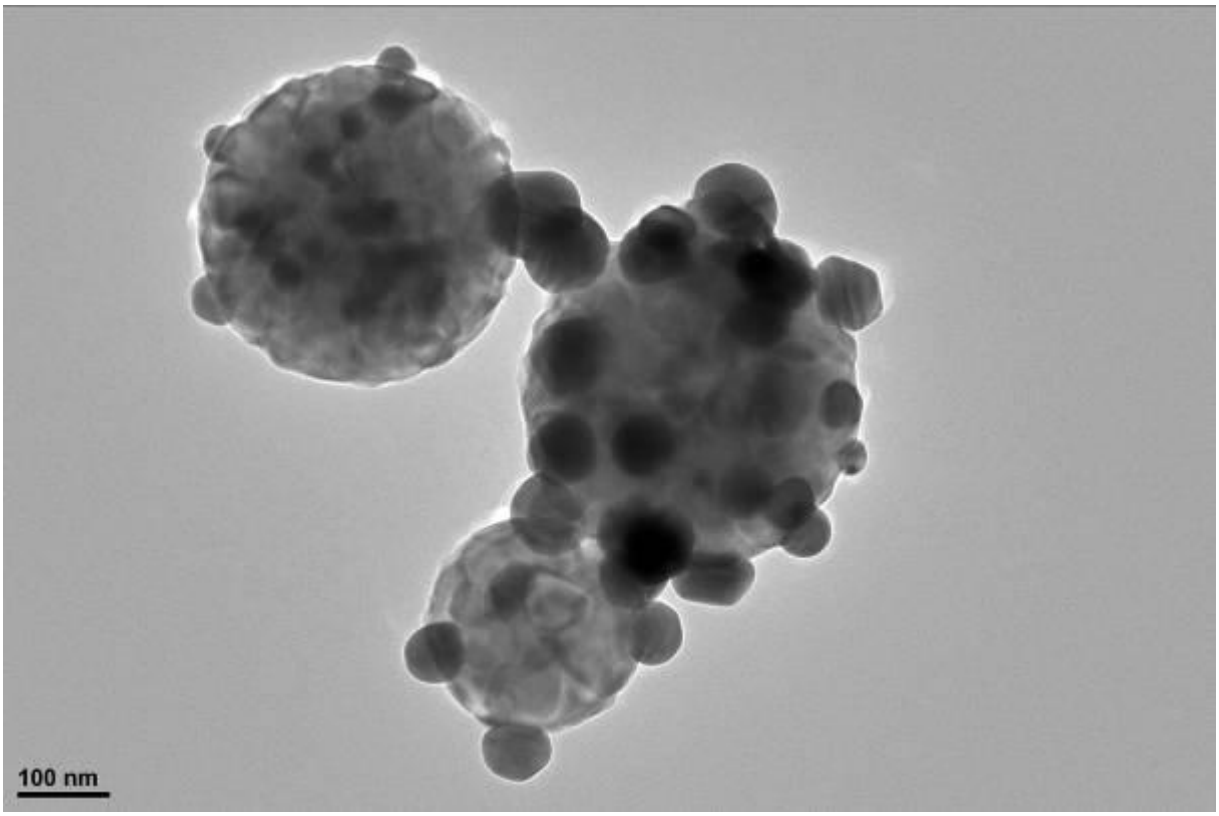

Figure 1. TEM image of Ag-TiO_2 nanoparticles.

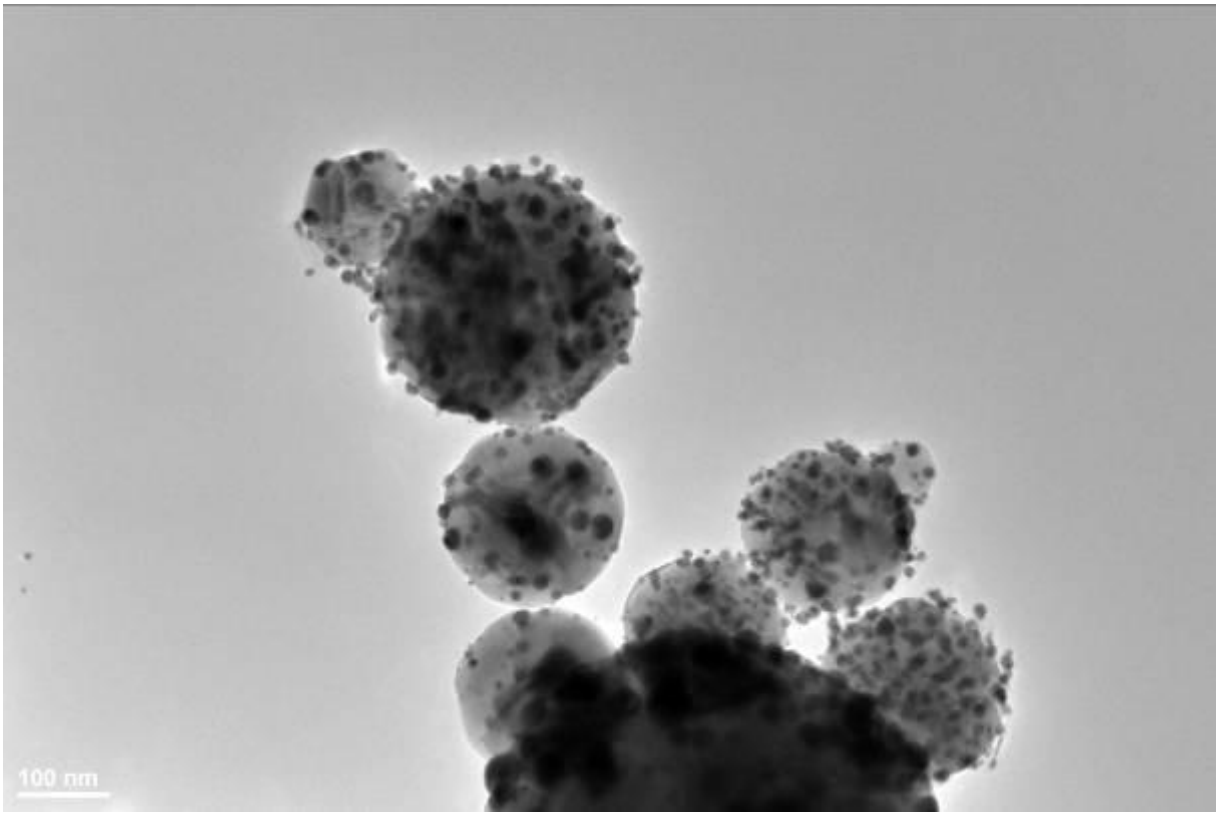

Figure 2. TEM image of Au-TiO_2 nanoparticles.

Alloys and Intermetallics

MS.6.P188
High-resolution transmission electron microscopy is one of the most important tools for visualizing the morphology and extracting crystallographic information. Al - C - N - O systems in the nanocrystalline state obtained by electric explosion of aluminum wire were studied by X-ray analysis and HRTEM.

I. Luzhkova[1], A.N. Ermakov[1], A.V. Bagazeev[2], A.M. Murzakaev[2], I.G. Grigorov[1], Y.G. Zainulin[1]

[1] ISSC of RAS, Laboratory of Structural and phase analysis, Ekaterinburg, Russian Federation
[2]Institute of Electrophysics of URAS, Ekaterinburg, Russian Federation

key703@yandex.ru

High-resolution transmission electron microscopy (HRTEM) is one of the most important tools for visualizing the morphology and extracting crystallographic information, as well as for local chemical analysis of industrial heterogeneous nanopowders. Al - C - N - O systems in the nanocrystalline state obtained by electric explosion of aluminum wire [1] with diameter 0.44 mm in a nitrogen atmosphere with butane passing were studied by X-ray analysis (Shimadzu XRD - 7000, Japan) and high-resolution transmission electron microscopy (JEOL JSM - 2100, Japan).

The studies performed revealed that in terms of X-ray analysis the electroexplosive powders are heterogeneous mixtures containing: aluminum metal and aluminum nitride (AlN, sp. gr.: P63mmc), carbonitrides (Al7C3N3, sp. gr.: P63mmc; Al6C3N2, sp. gr. R3m; Al5C3N, sp. gr.: P63mc; Al7C3N3, sp. gr.: Cmc21), oxycarbonitrides (Al4CN3O, sp. gr.: Cmc21), and aluminum oxide in the form of a surface film. The morphology of the electroexplosive powders was examined by high-resolution transmission electron microscopy. The nanoparticles have a spherical to complicate faceted shape and a prone to agglomeration. Particular attention should be paid to the nanopowder particles in the form of whiskers having highly visible faceting confirmed by Fourier analysis of the images. The phase composition of the nanopowders was additionally confirmed by HRTEM.

1. Bagazeev A.V., Kotov Y.A., Medvedev A.I. Characteristics of ZrO2 Nanopowders Produced by Electrical Explosion of Wire // Nanotechnologies in Russia, 2010, Vol. 5, Nos. 9–10, p. 656–664.

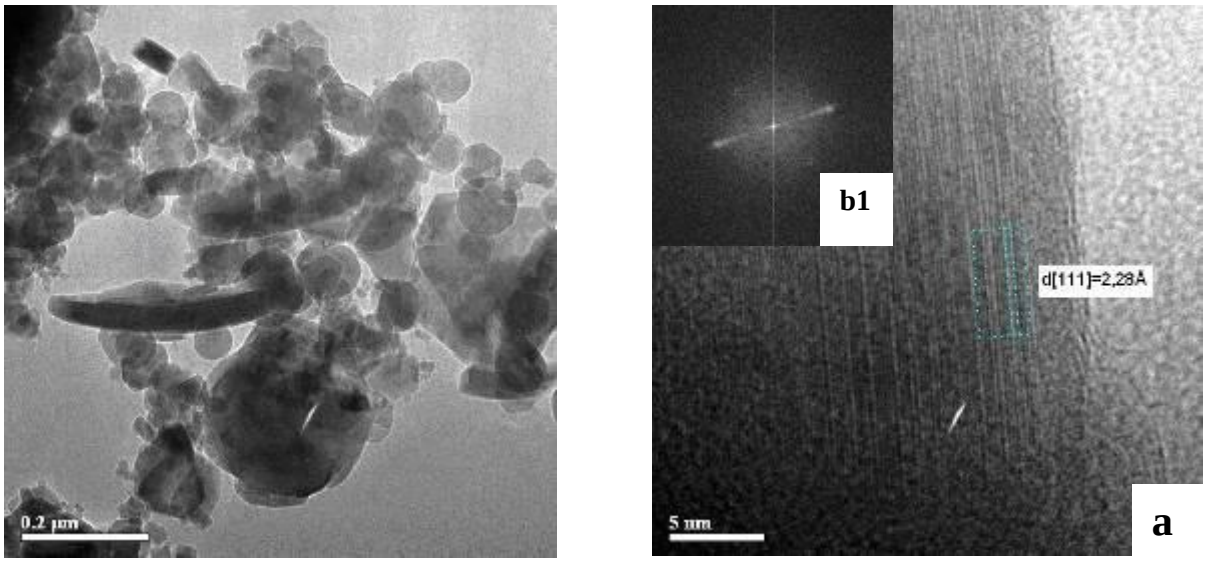

Figure 1. HRTEM image of aluminum carbonitride nanoparticles: **a** general view of electroexplosive powder; **b** a nanoparticle in the form of a whisker with interplanar distance 2,28 Å corresponding to [111] AlN plane (sp. gr. *Fm3m*); **b1** Fast Fourier Transform (FFT) of whisker.

Alloys and Intermetallics

MS.6.P189
Influence of thermal treatment on the structure of copper at ECA-pressing

A. Naizabekov[1], S. Lezhnev[1], I. Volokitina[1]

[1]Karaganda state industrial university, Temirtau, Kazakhstan

kgiu@mail.ru

The process of equal channel angular pressing (ECA -pressing) is one of the ways of metal forming (MF), under which the material undergoes intensive plastic deformation [1]. Unlike traditional methods of metal forming the main goal of this treatment is the accumulation of deformation in the material without changing its shape. The scheme of simple shear provides the ability of repeated deformation by changing the direction of action tangential stress due to which in the whole workpiece volume is uniform structure refinement [2]. Despite all its advantages, the process of ECA-pressing still is not implemented on an industrial scale, and its research is purely laboratory character. In addition, each installation for the process of metal forming itself is unique. This researches are engaged and the department "Metal Forming" of Karaganda State Industrial University. During these studies, scientists of the University has developed a number new technologies which allow produce long-ferrous and non-ferrous metals and alloys with sub ultrafine-grain structure, such as a combined process of "rolling-pressing" [3] and a combined process of "pressing-drawing" [4]. The same way scientists of the University carried out studies on the effect of the preliminary and subsequent thermal treatment on the structure that is formed in metals and alloys at ECA -pressing. This work is performed within the state budget funded theme "Getting high-quality materials by a combination of thermal treatment and intensive plastic deformation" by the program "grant research funding for 2012-2014", is devoted to the influence of intensive plastic deformation (IPD), implemented in pressing copper workpieces in equal-channel step die, and the effect of pre- and post-thermal treatment on microstructure evolution of copper and its strengthening. The material of the study was a technical copper of grade M1 (99.90% Cu). Before ECA-pressing samples were subjected to preliminary heat treatment: annealing, hardening and normalization by the standard mode. Samples of square section 15x15x70 mm were subjected ECA-pressing in the die with an angle of junction channels 125° on the route Bc with tilting the workpiece by 90° around the longitudinal axis [5].

Three types of experiments were carried out in three different modes:

- Mode 1 - pressing temperature 25 °C, 6 cycles;

- Mode 2 - pressing temperature 90 °C, 6 cycles;

- Mode 3 - pressing temperature 180 °C, 6 cycles.

As the number of passes in ECA-pressing resource of plasticity is lost and further deformation, and the use of the metal in the industry is not possible because its destruction occurs. In order to increase resource of plasticity the metal should be subjected to heat treatment. As is known, the heating above temperature the onset of recrystallization leads to a strong grain growth and to a sharp fall of the strength of copper, so it is necessary to determine the temperature of the onset of recrystallization. Calculated the approximate temperature of the onset of recrystallization on accepted formulas [6] a laboratory experiment was conducted. Samples after ECAP were cut into thin plates with thickness of 5 mm and were heated at temperatures in the range 100 - 270^{0}C with duration of exposure 1 hour. Cooling of the samples is in water. Microstructure of copper after 6 cycles of ECA-pressing at different temperatures is presented in Figure 1. Microstructure of copper samples subjected ECA-pressing, change under the simultaneous influence of two factors: the preliminary heat treatment and increasing the pressing temperature. Minimum average grain size obtained during pressing of alloy M1 is 0.6 microns. This grain size is obtained after hardening at 700^{0}C and ECAP at room temperature and 6 cycles of deformation. The use of preliminary hardening allows getting more fine-grained structure and for the alloy M1 also reducing hardness by 15%, which helps to reduce the pressing force on the first pass, with 620 to 510 MPa. The use of combined thermomechanical treatment on a "hardening at 700^{0}C -ECAP low tempering at 200^{0}C" for the alloy M1 allows to improve the characteristics of copper

and increases the resistance emergence and spread of cracks.

1. Segal V.M. Processes of structure formation of metals. - Minsk: Science and Technology, 1994. -232 p.
2. Valiev R.Z. Nanostructured materials produced of intense plastic deformation. - Moscow: Logos, 2000. – 272 p.
3. The patent № 23802 МКИ3 B21 J 5/00. Device for continuous pressing of metal. Nayzabekov A.B., Lezhnev S.N., Panin E.A.., 2006.
4. Nayzabekov A.B., Lezhnev S.N., Volokitin A.V. Research of influence of the new combined process of deformation "pressing-drawing" on the evolution of the microstructure of steel wire. / XIII International scientific conference «New technologies and achievements in metallurgy and material engineering». Czestochowa, Poland, 2012. - p. 433-437.
5. Nano-and microcrystalline materials obtained by intensive plastic deformation. The training materials for the training program. / Chuvildeev V.N., Pirozhnikova O.E., Gryaznov M.Yu. etc. / / - Nizhny Novgorod. 2006.
6. Lopatin Yu.G. The evolution of the grain structure during deformation and annealing of microcrystalline materials obtained by equal channel angular pressing. The Dissertation for the degree of the candidate of physical and mathematical sciences. Moscow. 2010.

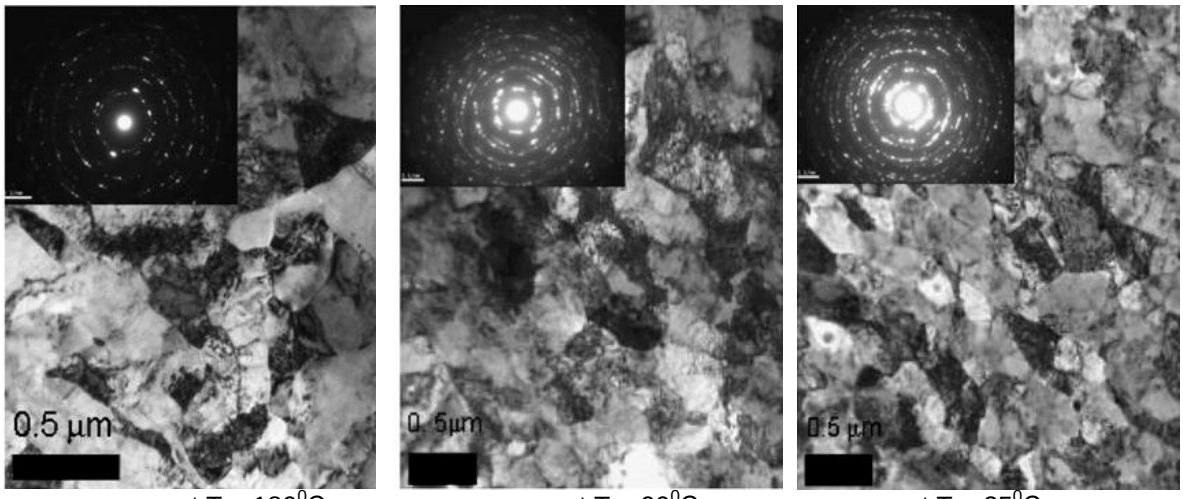

a – at T = 180^0C; в - at T = 90^0C; c - at T = 25^0C;

Figure 1. Microstructure of copper after 6 cycles of ECA –pressing.

Low Dimensional Materials and Catalysts

MS.7.190
Carbon nanocontainers and nanoreactors

A. N. Khlobystov[1]

[1]School of Chemistry, University of Nottingham, University Park, Nottingham NG7 2RD, United Kingdom

Andrei.Khlobystov@nottingham.ac.uk
Keywords: carbon nanotubes, nanoreactors, catalysis

Carbon, being a light element with half-full outer electronic shell, is capable of forming atomically thin, yet mechanically robust structures, such as graphene and single-walled nanotubes (SWNT). In our research, we utilise these nanostructures as containers/substrates for individual molecules and atoms. Because of the low atomic number of carbon (Z = 6), SWNT and graphene are particularly suitable for high resolution transmission electron microscopy (HRTEM) analysis as their contrast is sufficiently low to "see though" them and to visualise individual molecules with atomic resolution. Furthermore, SWNT and graphene are very efficient heat and electric conductors, while the chemical reactivity of graphene surface and the interior of carbon nanotubes is extremely low, which protect the structural and the chemical integrity of the molecules during HRTEM studies.

Over the past few years we have discovered, described and formulated fundamental rules governing packing [1], orientation [2,3], and van der Waals interactions [4] of molecules in nanotubes using low voltage HRTEM methodology. More recently, in collaboration with Prof. Ute Kaiser's group at the University of Ulm, we have extended this methodology to aberration corrected HRTEM (AC-HRTEM). This approach has been fruitful for unravelling complex chemical transformations in real-time and direct-space, such as formation of metal clusters [5], structural transformations in nanotube sidewalls [6], spontaneous self-assembly of graphene nanoribbons [7], and transformation of graphene to fullerene [8]. The latter study is particularly significant as it solves a long-standing mystery of the fullerene formation mechanism.

1. A.N. Khlobystov, D.A. Britz, A. Ardavan, G.A.D. Briggs, Phys. Rev. Lett. 92 (2004) art N^{o} 245507.
2. A.N. Khlobystov, K. Porfyrakis, M. Kanai, D.A. Britz, A. Ardavan, T.J.S. Dennis, G.A.D. Briggs, Angew. Chem. Int. Ed, 43 (2004) 1386-1389.
3. A.N. Khlobystov, R. Scipioni, S.G. Lyapin, A. Ardavan, R.J. Nicholas, D.G. Pettifor, G.A.D. Briggs, Applied Physics Letters 84 (2004) 792-794.
4. M. Ashino, D. Obergfell, M. Haluska, S. Yang, A. N. Khlobystov, S. Roth, R. Weisendanger, Nature Nanotech. 3 (2008) 337-341.
5. A. Chuvilin, A.N. Khlobystov, D. Obergfell, M. Haluska, S. Yang, S. Roth, U. Kaiser, Angew. Chem. Int. Ed. 49 (2010) 193-196.
6. T.W. Chamberlain, J.C. Meyer, Jannik J. Biskupek, J. Leschner, A. Santana, N.A. Besley, E. Bichoutskaia, U. Kaiser, A.N. Khlobystov, Nature Chem. 3 (2011) 732-737.
7. A. Chuvilin, E. Bichoutskaia, M.C. Gimenez-Lopez, T.W. Chamberlain, G.A. Rance, N. Kuganathan, J. Biskupek, U. Kaiser, A.N. Khlobystov, Nature Mater. 10 (2011) 687-692.
8. A. Chuvilin, U. Kaiser, E. Bichoutskaia, N.A. Besley, A.N. Khlobystov, Nature Chem. 2 (2010) 450-453.

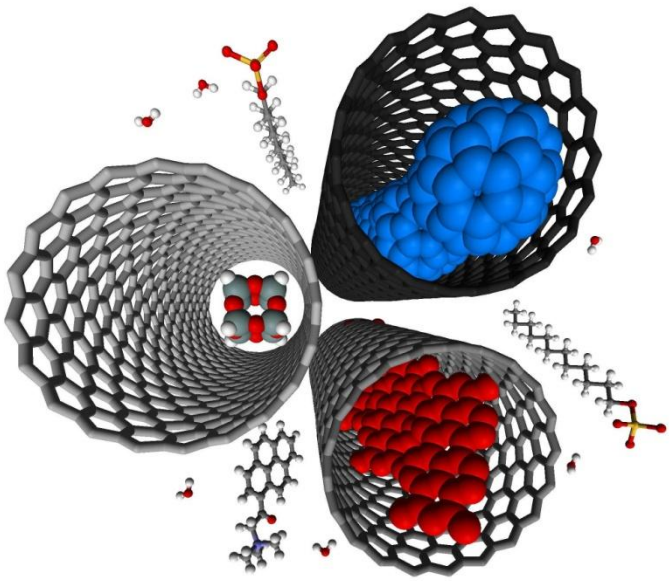

Figure 1. Carbon nanotube serves as a nanoscale bridge between the world of molecules and the macroscopic world.

Low Dimensional Materials and Catalysts

MS.7.191
Material characterization of N-doped graphene with Pt atoms and clusters for fuel cell application using a transmission electron microscope

S. Stambula[1], N. Gauquelin[1], M. Bugnet[1], S. Gorantla[2], S. Turner[3], S. Sun[4], X. Sun[5], G. Botton[1]

[1]McMaster University, Material Science and Engineering, Hamilton, Canada
[2]Leibniz Institute for Solid State and Materials Research, Institute for Complex Materials Department of Micro & Nanostructures, Dresden, Canada
[3]University of Antwerp, EMAT, Antwerpen, Canada
[4]Institut National de la Recherche Scientifique, Energy Materials Telecommunications Research Centre, Varennes, Canada
[5]University of Western Ontario, Department of Materials and Mechanical Engineering, London, Canada

stambusm@mcmaster.ca
Keywords: TEM, PEM fuel cell, Pt atoms and clusters

Fuel depletion and environmental degradation has led to the need for a new fuel source with the preference for a clean emission. The power supply of the proton exchange membrane (PEM) fuel cell makes it ideal for the replacement of the internal combustion engine. Current PEM fuel cells utilize electrodes composed of carbon black with Pt catalysts, as Pt most efficiently facilitates the oxygen reduction reaction (ORR) [1]. Unfortunately Pt adds a large cost of the fuel cell, thus impeding economic mass production. In effort to decrease the cost while maintaining the catalytic efficiency, the surface area to volume ratio of the Pt is decreased through the formation of nanoparticles or Pt clusters.

Recently, graphene has been examined as a possible substitution for the electrode support in the PEM fuel cell due to its enhanced electrical conductivity, mechanical robustness, and large surface area [2,3]. The intrinsic sp^2 bonding of the C lattice in graphene also provides a chemically inert surface, which is undesirable for Pt adsorption. Defects can be induced in the graphene lattice through functionalization, where the use of N atoms have the additional benefits of acting as active ORR sites, and increasing the Pt-C binding energy which can facilitate adsorption and decrease the Pt nanoparticle size [4,5]. However, the specific effect of each N-dopant is still controversial in the scientific literature. The size of the Pt clusters can be further decreased through the use of atomic layer deposition, as ultrasmall nanoparticles (<1 nm) are produced [6]. It is expected that the combination of ALD and increased binding energy from the N-doped graphene should produce Pt clusters.

To fully understand and design the most efficient fuel cell the material must be characterized at the atomic level to determine the size and size distribution of Pt, the predominant N-dopant type (amino, pyridinic, pyrrolic, graphitic) within the electrode, and the presence of the graphene lattice to maintain the electrical conductivity. Through the use of an aberration-corrected transmission electron microscope (TEM), sub-angström resolution imaging is possible. Various imaging and spectroscopy techniques can be utilized to fully determine the material structural and chemical characteristics. Specifically, high resolution TEM (HRTEM) under negative C_s imaging conditions can be utilized to observe the graphene lattice and observe defects, while high angle annular dark field (HAADF) scanning transmission electron microscopy (STEM) is ideal for imaging heavy atoms on light atomic substrates as it is sensitive to Z-contrast. Through the use of HRTEM and HAADF the graphene structure, and the size and size distribution of Pt can be determined, respectively. Further, electron energy loss spectroscopy (EELS) can be utilized to examine local chemical composition and binding within a material from a small spatially resolved area (~1 nm) [7]. This proves useful in the determination of the specific N-dopants in the graphene lattice.

The N-doped graphene is highly folded and multilayered, however upon the examination with high magnification (Figure 1. (a)) the graphene hexagonal lattice is visible, while the computed diffractogram illustrates the characteristic hexagonal pattern. Further, through the use of HAADF it is evident that the Pt forms atoms and clusters on the N-doped graphene surface (Figure 1. (b)), where an increase in ALD cycles increases the Pt density but does not increase the size. Image processing clearly demonstrates that the Pt sits predominately at edge locations with few atoms sitting on the N-doped graphene surface (green arrows). Lastly, the EEL spectra further indicate that the graphene lattice is maintained after N-doping as the strong π* and σ* peaks are present in the C-K edge. Each

possible N-dopant (P1-P4 in the N-K edge) is present in the graphene lattice, however the specific distributions across sheets are inhomogeneous (Figure 2.).

The preservation of the graphene lattice will permit the high electrical conductivity of the support material, while the incorporation of the N-dopants creates defect sites thus allowing Pt to strongly bind. It is illustrated that Pt clusters and atoms form due to the use of ALD in combination with N-doping. An increase in ORR and decrease in cost is expected for this electrode support, as many active sites are available through N-doping and the extremely large surface area to volume ratio of the Pt.

1. H.A. Gasteiger, S.S. Kocha, B. Sompalli, F.T. Wagner, *Appl. Catal. B: Environ. 56 (*2005), p.9–35.
2. A.K. Geim, K.S. Novoselov, *Nat. Mater.* 6 (2007), p.183–191.
3. C. Lee, X. Wei, J.W. Kysar, J. Hone, *Science* 321 (2008), p.385–388.
4. D. Wei, Y. Liu, Y. Wang, H. Zhang, L. Huang, G. Yu, *Nano Lett.* 9 (2009), p.1752–1758.
5. T. Holme, Y. Zhou, R. Pasquarelli, R O'Hayre, *Phys Chem Chem Phys*, 12, (2010), 9461.
6. W-C. Hsueh, C-C. Wang, C. Liu, C-C. Kei, T-P. Perng, *Nanotechnology*, 23 (2012),p. 405603.
7. G.A. Botton, in *Science of Microscopy*, P.Hawkes, J.C.H. Spence, Eds. (Springer, New York, 2007).

8. This work is supported by NSERC and Ballard Power Systems Incorporated via a strategic grant to the University of Western Ontario and McMaster University. The electron microscopy presented here was completed at the Canadian Centre for Electron Microscopy, a facility supported by NSERC and McMaster University.

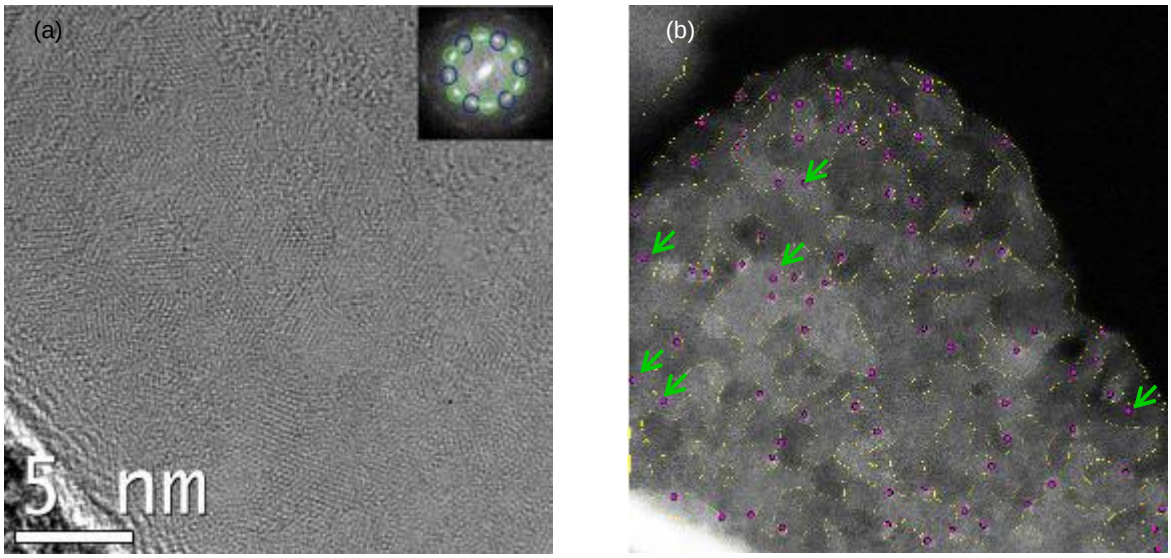

Figure 1. N-doped graphene with 50 ALD cycles of Pt using (a) HRTEM and (b) HAADF. Inset in (a) is the computed diffractogram illustrating the characteristic hexagonal pattern of graphene.

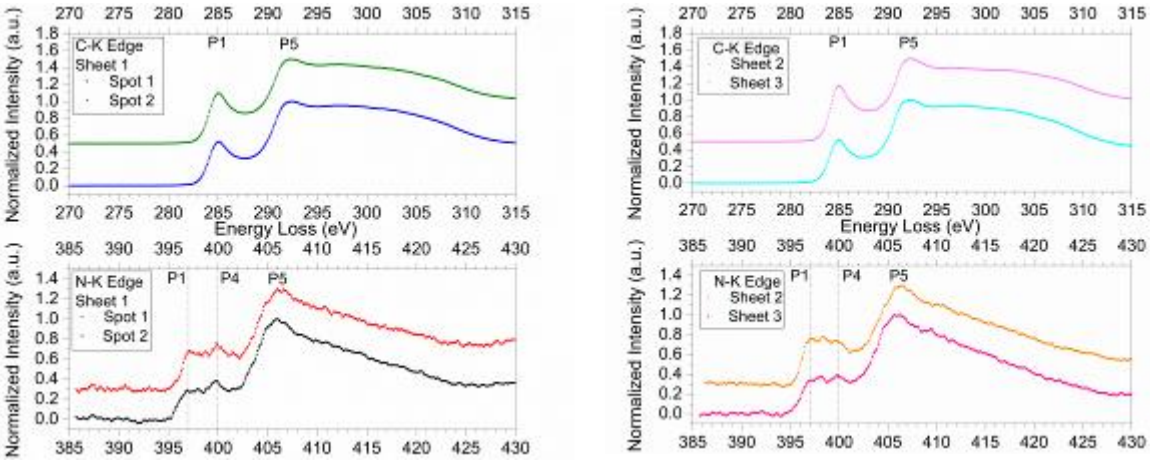

Figure 2. EEL spectra of N-doped graphene with 50 ALD Pt cycles of the C-K and N-K edge from various sheets within the graphene lattice.

Low Dimensional Materials and Catalysts

MS.7.192
Stabilities of Pd nanoparticles supported on carbon nanotubes studied by TEM

D. Su[1], B. Zhang[1]
[1]Institute of Metal Research, Chinese Academy of Science, Catalysis and Materials Science, Shenyang, China

dangsheng@fhi-berlin.mpg.de
Keywords: catalysis, Pd nanoparticles, stability, functionality, TEM

Supported metal nanoparticles are one of the widely used catalysts in many chemical processes. Apart from metal oxides, carbon nanotubes (CNTs) have been found to be a useful support in heterogeneous catalysis. CNTs have the proper pore size, moderate high specific surface area and good mechanical and chemical stability, high thermal and electrical conductivity. However, CNTs are hydrophobic and inert in nature, and they must be functionalized to anchor metal nanoparticles. The interaction between the metal nanoparticles and CNTs becomes thus important since it determines not only the charge transfer between them, but also the stability of the metal nanoparticles at high temperature [1]. In this work, we study the stability of Pd nanoparticles on oxygen- and nitrogen-functionalized CNTs (oCNT and nCNTs) using in-situ electron microscopy and spectroscopy techniques.

Concentrated nitric acid (70%) was used to get oxygen-functionalized CNTs. Nitrogen-functionalization was carried out at 600°C by introducing NH_3 into a furnace containing oCNTs for 2 hours. Pd/oCNTs and Pd/nCNTs were prepared using palladium nitrate in diluted distilled water. The as-prepared oCNTs, nCNTs, fresh Pd/oCNTs, Pd/nCNTs are placed on TEM grids using an ethanol solution containing the samples. A FEI Tecnai G2 F20 and a Philips CM200 FEG TEM operating at 200 kV were used to conduct structural investigation. A Gatan single tilt-heating holder was used for in-situ heating experiment between 330 °Cto 600 °C. The surface properties of the samples were studied by using an ESCALAB 250 set-up with Al *K*α radiation.

XPS analysis revealed that oCNTs contain as much as 14% oxygen, and nCNTs as much as 4% nitrogen, both in form of functional groups. The as prepared Pd nanoparticles on oCNTs and nCNTs have similar size of about 1.6 nm in average. Figure 1 shows the ripening process of Pd nanoparticles on nCNTs together with the histograms of particle size distribution (PDS) at room temperature and upon heating at 330°C, and 600 °C, respectively. The image and PDS clearly show the evidence that the size of Pd nanoparticles increased significantly with increasing temperature. The distribution of Pd is uniform at room temperature and 300 °C, whereas Pd particles grow up and the distribution is no more uniform at 600 °C. This change is more clearly evidenced in STEM image of Figure 1d. The mean particle size of Pd on nCNTs heated at 600 °C is estimated to be about 6.5 nm. The similar ripening process of Pd nanoparticles is also observed on oCNTs, but the mean particles size of Pd on oCNTs when heated at 600 °C is estimated to be 3 nm. This indicates a more strong interaction between Pd and oCNTs than that between Pd and nCNTs. This difference is assigned to the different role of oxygen-functional groups and nitrogen-functional groups as the anchoring sites for the Pd nanoparticles [2].

In summary, we found that the stability of Pd nanoparticles supported on CNTs depends strongly on the surface properties of CNTs. Functionalization of CNTs with oxygen- and nitrogen-functional groups allows an uniform loading of Pd particles. However, carbon oxygen single-bonds on the CNTs surface have a stronger interaction with Pd nanoparticles than that of nitrogen-containing functional groups. The Pd nanoparticles supported on oxygen-functionalized CNTs are more stable than when they are supported on nitrogen-functionalized CNTs. Our works shows that TEM with in-situ technique is an useful tool for the study of the metal support interactions in catalysis.

1. D.S.Su and G.Centi, Chemical Review, submitted
2. B. Zhang, L. Shao, W. Zhang, X. Pan, D. S. Su, to be published.
3. We kindly acknowledge the financial support provide by the IMR SYNL-T.S. Ké Research Fellowship. The National Natural Science Foundation of China (No. 21203215) and the China Postdoctoral Science Foundation (2012M520652).

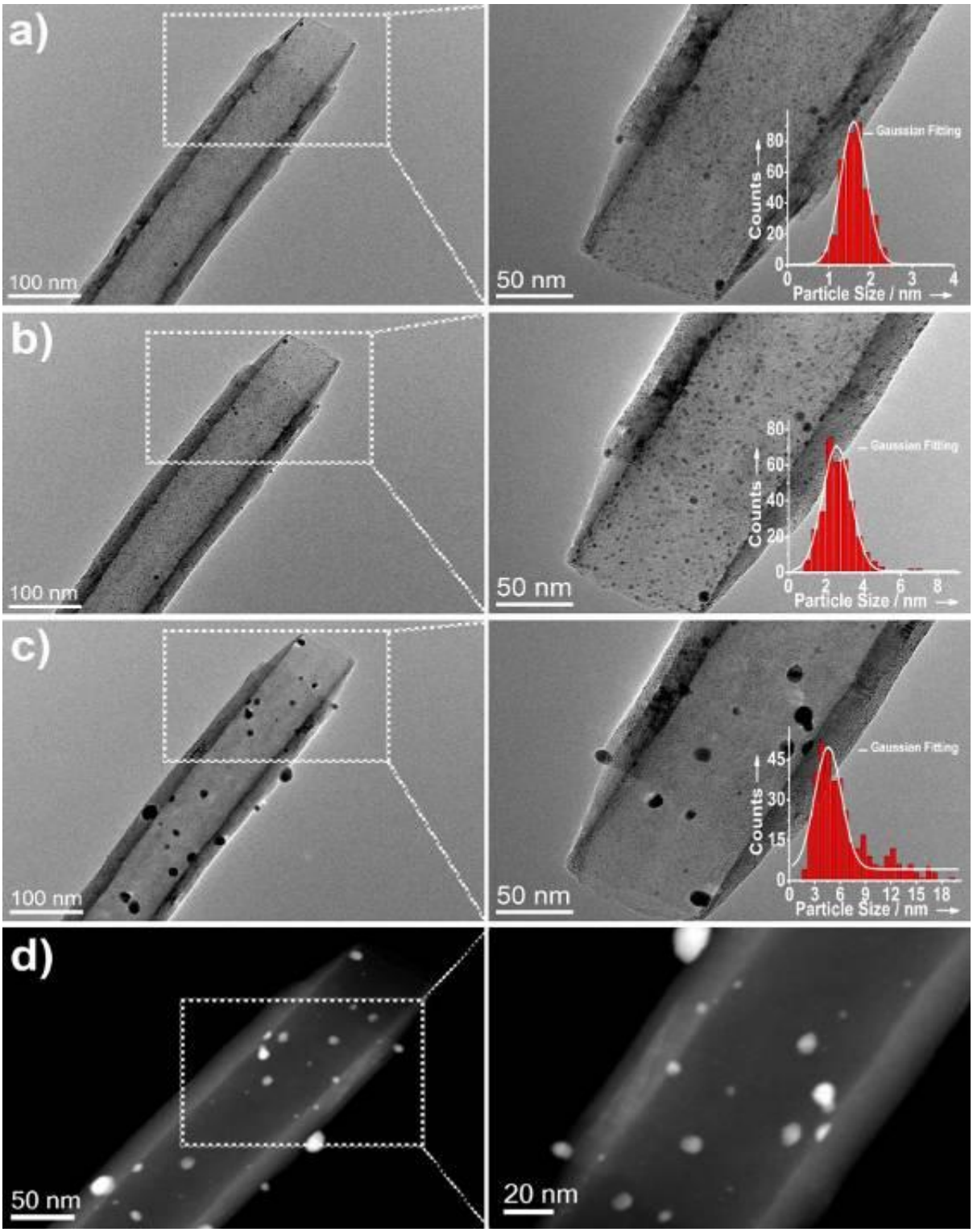

Figure 1. TEM images of Pd supported on N doped OCNT that was heated at 22 °C (a), 330 °C (b) and 600 °C (c) by heating holder in TEM, and STEM images of Pd@N-OCNT sample after heating (d). The right part is a local enlargement of the highlighted areas in the left counterpart for each illustration. The insets are the corresponding histograms of PSD.

Low Dimensional Materials and Catalysts

MS.7.193
Electron microscopy study of one-dimensional functional materials synthesized by a nonaqueous route

I. Djerdj[1]

[1]Rudjer Boskovic Institute, Zagreb, Croatia

igor.djerdj@irb.hr
Keywords: anisotropic nanoparticles, electron hopping, solvothermal synthesis

Anisotropic nanoparticles such as nanofibers, nanotubes, nanorods, and nanowires are of not only scientific but also technological interest. The anisotropy inherent in these nanomaterials provides unique properties which are expected to be critical to the function and integration of nanoscale devices. Among the different families of functional materials, metal oxides play an outstanding role due to their redox activity. The possibility to change the oxidation state and the stoichiometry provides unique opportunities to tailor the chemical and physical properties. The rapidly growing number of publications in the field of metal oxide synthesis by wet chemical routes suggests that the so-called nonaqueous (or nonhydrolytic) processes are particularly successful for the size- and shape-controlled preparation of colloidal inorganic nanoparticles [1,2]. In this talk, I will present two studied anisotropical low-dimensional systems synthesized by nonaqueous route, whose structural features were elucidated by the usage of electron microscopy. First presented study [3] involves the preparation of lanthanum hydroxide and manganese oxide nanoparticles, based on a nonaqueous sol–gel process involving the reaction of $La(OiPr)_3$ and $KMnO_4$ with organic solvents such as benzyl alcohol, 2-butanone and a 1:1 vol. mixture thereof. The lanthanum manganese oxide system is highly complex and surprising results with respect to product composition and morphology were obtained. In dependence of the reaction parameters, the $La(OH)_3$ nanoparticles undergo a shape transformation from short nanorods with an average aspect ratio of 2.1(Figure 1) to micron-sized nanofibers (average aspect ratio is more than 59.5). Although not directly involved, $KMnO_4$ plays a crucial role in determining the particle morphology of $La(OH)_3$. The reason lies in the fact that $KMnO_4$ is able to oxidize the benzyl alcohol to benzoic acid, which presumably induces the anisotropic particle growth in [0 0 1] direction upon preferential coordination to the ±(1 0 0), ± (0 1 0) and ± (−110) crystal facets. By adjusting the molar $La(OiPr)_3$-to-$KMnO_4$ ratio as well as by using the appropriate solvent mixture it is possible to tailor the morphology, phase purity and microstructure of the $La(OH)_3$ nanoparticles.

The second part of the presentation shows a nonaqueous liquid-phase route involving the reaction of vanadium oxychloride with benzyl alcohol leading to the formation of single-crystalline and semiconducting $VO_{1.52}(OH)_{0.77}$ nanorods with an ellipsoidal morphology, up to 500 nm in length and typically about 100 nm in diameter (Figure 2) [4]. Composition, structure, and morphology were thoroughly analyzed by neutron and synchrotron powder X-ray diffraction as well as by different electron microscopy techniques (SEM, (HR)TEM, EDX, and SAED). The data obtained point to a hollandite-type structure which, unlike other vanadates, contains oxide ions in the channels along the *c*-axis, with hydrogen atoms attached to the edge-sharing oxygen atoms, forming OH groups. According to structural probes and magnetic measurements (1.94 μB/V), the formal valence of vanadium is +3.81 (V^{4+}/V^{3+} atomic ratio ≈ 4). The temperature-dependent DC electrical conductivity exhibits Arrhenius-type behavior with a band gap of 0.64 eV. The semiconducting behavior is interpreted in terms of electron hopping between vanadium cations of different valence states (small polaron model). *Ab initio* density-functional calculations with a local spin density approximation including orbital potential (LSDA + *U* with an effective *U* value of 4 eV) have been employed to extract the electronic structure. These calculations propose, on the one hand, that the electronic conductivity is based on electron hopping between neighboring V^{3+} and V^{4+} sites, and, on the other hand, that the oxide ions in the channels act as electron donors, increasing the fraction of V^{3+} cations, and thus leading to self-doping. Experimental and simulated electron energy-loss spectroscopy data confirm both the presence of V^{4+} and the validity of the density-of-states calculation. Temperature-dependent magnetic susceptibility measurements indicate strongly frustrated antiferromagnetic interactions between the vanadium ions. A model involving the charge order of the V^{3+} sites is proposed to account for the observed formation of the magnetic moment below 25 K.

1. I. Djerdj, D. Arčon, Z. Jagličić, and M. Niederberger, J. Solid State Chem. 181 (2008), 1571-1581.
2. I. Djerdj, G. Garnweitner, D. Arčon, M. Pregelj, Z. Jagličić, and M. Niederberger, J. Mater. Chem. 18 (2008), 5208-5217.
3. I. Djerdj, G. Garnweitner, D.S. Su, and M. Niederberger, J. Solid State Chem. 180 (2007), 2154-2165.
4. I. Djerdj, D. Sheptyakov, F. Gozzo, D. Arčon, R. Nesper, and M. Niederberger, J. Am. Chem. Soc. 130 (2008), 11364-11375.

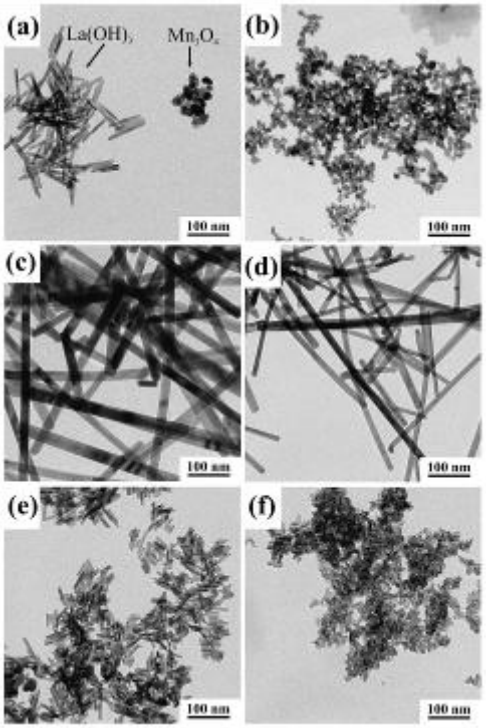

Figure 1. Representative TEM images of the nanoparticles synthesized under various conditions. (a) BA (1:1), (b) BUT (1:1), (c) BA+BUT (1:1), (d) BA+BUT (1:0.5), (e) BA+BUT (1:0.25), (f) BA+BUT (1:0). BA=benzyl alcohol, BUT=2-butanone.

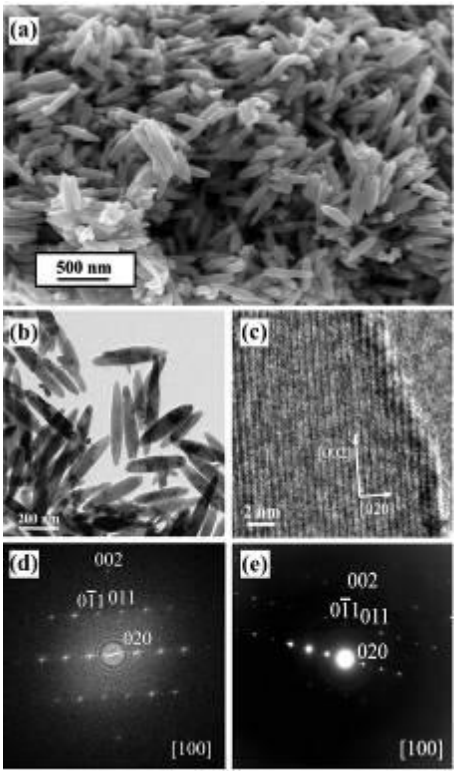

Figure 2. (a) SEM and (b) TEM overview images of $VO_{1.52}(OH)_{0.77}$ nanorods. (c) HRTEM image of a part of a nanorod. (d) Corresponding power spectrum of 2(c). (e) Corresponding SAED pattern taken from the part of the nanorod depicted in 2(c).

Low Dimensional Materials and Catalysts

MS.7.194
Active sites and aging properties of metal catalyst particles

E. Olsson[1], T. Pingel[1]

[1]Chalmers University of Technology, Department of Applied Physics, Gothenburg, Sweden

eva.olsson@chalmers.se

The toxic gases NO and NO_2 (NO_x) form during combustion in vehicles equipped with diesel or lean-burn gasoline engines. These engines have better fuel economy and are therefore preferred considering that the consumption of fossil fuels needs to be reduced due to economical and environmental aspects. However, existing standard three-way catalysts cannot reduce the NO_x species that are formed. They are harmful and are, for example, responsible for acid rain, forming ground-level ozone (which in turn is the major constituent of smog) and are also increasing the risk of respiratory allergies. Methods are developed to remove the NO_x species by exhaust gas after-treatment [1,2]. Also there are efforts to replace gasoline and diesel fuels with natural gas to reduce the net CO_2 emission. The typical levels of unburned methane in the exhausts from engines fuelled by natural gas must be lowered to comply with the emission legislations. Methods for efficient oxidation of methane at low temperature are therefore being developed [3]. During use, the efficiency of the catalysts is degraded where the mechanism responsible for the degradation can be either of thermal or chemical nature. Crucial aspects of the performance of the catalysts are the active sites and also ageing properties. The characteristics and number density of the active sites depend the size and morphology of the catalyst particles which in turn are affected by interface between the noble metal particles and the oxide supports, see Figure 1. This work addresses the effect of the interface between noble metal particles and oxide supports on the efficiency of the catalysts and on the ageing properties, see Figure 2, in different gas compositions. The activity, ageing and dispersion measurements are carried out in bench reactors. The mechanisms of degradation and the structure of the particles and interfaces are studied using electron microscopy and in particular high resolution transmission electron microscopy (TEM) and scanning TEM (STEM). High angle annular dark field (HAADF) STEM imaging using a probe corrected Titan TEM instrument provides *Z*-contrast information revealing the distribution of the noble metals on the oxide support with atomic resolution. Complementary information is extracted using monochromated electron energy loss spectroscopy (EELS) in the Titan TEM and x-ray diffractometry (including measurements at the European Synchrotron Radiation Facility).

1. H. Kannisto, K. Arve, T. Pingel, A. Hellman, H. Härelind, K. Eränen, E. Olsson, M. Skoglundh and D.Y. Murzin, Catal. Sci. Technol. 3 (2013), p. 644.
2. X. Auvray, T. Pingel, E. Olsson and L. Olsson, Appl. Catal. B: Environm. 129 (2013), p. 517.
3. D. Bounechada, S. Fouladvand, L. Kylhammar, T. Pingel, E. Olsson, M. Skoglundh, J. Gustafson, E. Lundgren, M. Di Michiel, M.A. Newton and P.-A. Carlsson, Phys. Chem. Chem. Phys. DOI:10.1039/C3CP44289F.

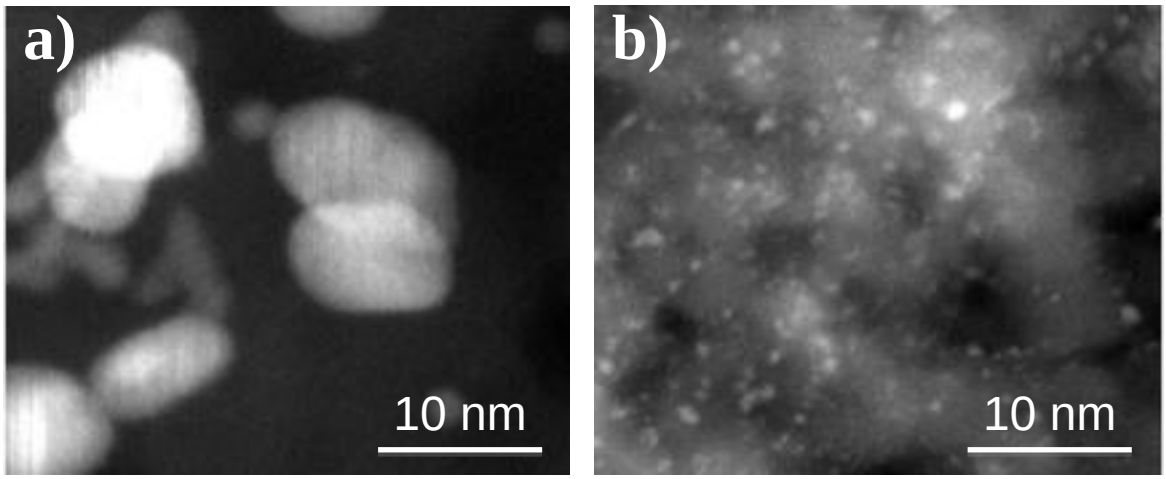

Figure 1. STEM HAADF images showing Pt particles on a) SiO_2 support and b) Al_2O_3 support. The samples were fabricated using identical parameters and the difference in Pt particle size is due to the difference in interaction at the interface between the particles and support.

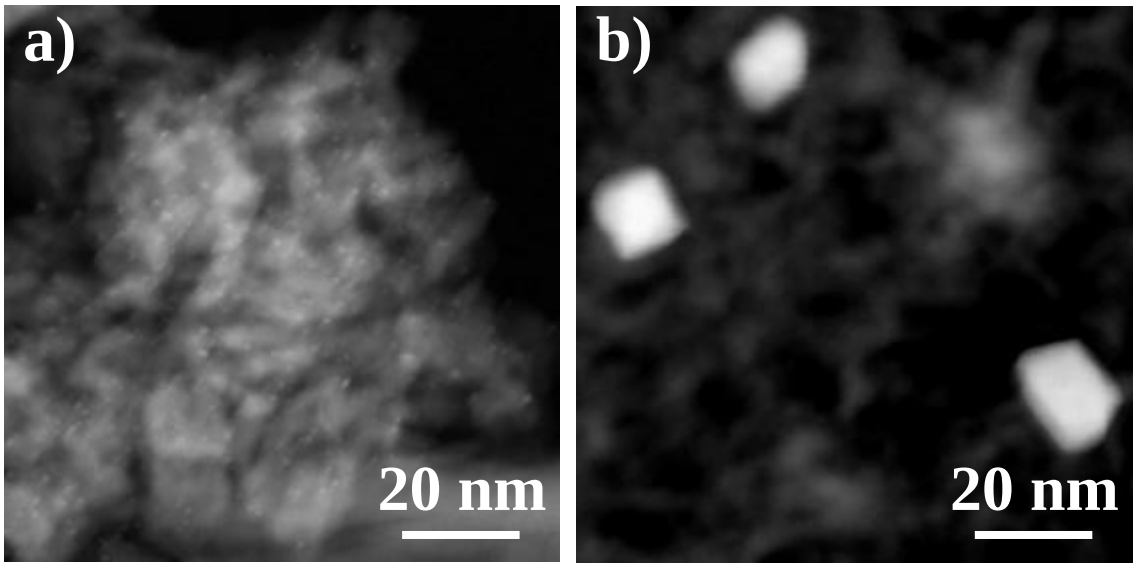

Figure 2. STEM HAADF images showing Pt particles on Al_2O_3 support before and after aging in a gas mixture of O_2 and SO_2 at an elevated temperature. a) As received sample. b) Aged in 10% O_2 and 30 ppm SO_2 at 900 °C for 2h.

Low Dimensional Materials and Catalysts

MS.7.195
Synthesis and structural properties of SiC nanowires encapsulated in carbon nanotubes

A. Bonatto Minella[1,2], D. Pohl[1], R. Erni[3], M.H. Rümmeli[1], C. Täschner[1], L. Schultz[1,2], B. Rellinghaus[1]

[1]IFW Dresden, Dresden, Germany
[2]TU Dresden, Institute of Physics, Dresden, Germany
[3]Empa, Dübendorf, Switzerland

a.kiessling@ifw-dresden.de

Carbon nanotubes (CNT) have attracted great attention since their discovery in 1991 by Iijima [1]. Their good thermal as well as electrical conductivity and high mechanical strength make them promising materials for applications such as field emission devices, tips for AFM or field effect transistors [2].

Silicon carbide, in particular as nanowires, has emerged as an interesting material for semiconductor industry due to its wide band gap [3]. One possibility to produce such carbide nanowires is using CNT as templates [4,5]. For that the CNT is converted into a SiC nanowire in a reactive SiO atmosphere. In order to produce novel functional electronic devices on the nanometer scale, several groups have been working on the combination of CNT and SiC nanowires, for instance, in form of SiC-SiO_2-C/CNT coaxial nanocables [6,7]. By high-temperature annealing these can then be transformed into SiC-CNT junctions. CNT filled with pure SiC nanowires were reported by Kokai *et al.* [8] by means of laser ablation using Si-C targets.

In this study, we present CNT filled with pure SiC nanowires that were grown via plasma-enhanced chemical vapour deposition (PE-CVD) from $Fe_{20}Ni_{80}$ ("permalloy") nanoparticles on Si/SiO_2 substrates. Characterization of the as-grown CNT was performed by means of aberration-corrected high resolution transmission electron microscopy (HRTEM) on a FEI TITAN^3 80-300 microscope operating at 80kV in order to reduce knock-on damages. Electron energy loss spectroscopy (EELS) was employed to confirm the filling being SiC without impurities of Fe or Ni. Measurements of the band gap by means of EELS were conducted utilizing a monochromized electron beam.

Figure 1 shows a CNT filled with crystalline SiC. The figure evidences that the interface between the SiC and the concentric graphene layers of the CNT is characterized by a bending of the graphene layers towards the SiC core. This leads to the assumption that both, the CNT growth as well as the formation of the SiC nanowire occur simultaneously. However, further TEM studies are necessary in order to better understand the nature of this interface.

For the measurement of the SiC band gap the surrounding CNT needed to be removed due to the carbon plasmon peak appearing in the low loss spectrum range. This would have impeded an unambiguous detection of electronic excitations across the band gap in the low loss region of the EEL spectrum. Figure 2 shows the low loss EEL spectrum of the SiC (dotted line). The solid line represents the spectrum after the subtraction of the zero loss peak. For determining the direct band gap the upper region of the spectrum was fitted by a function of the type $(E-E_g)^{0,5}$ (red line) [9]. From this fit the value for the direct bandgap E_g was therefore estimated to be 5.2 eV. This result will be compared with previously reported data in the literature.

1. S. Iijima, Nature 354 (1991), p. 56.
2. R.H. Baughman, A.A. Zakhidov and W.A. de Heer, Science 297 (2002), p.787.
3. G. Attolini in “Nanowires”, ed. P. Prete, (Intech, Vukovar / Croatia) (2010), p. 1.
4. H.J. Dai, E.W. Wong, Y.Z. Lu, S.S. Fan and C.M. Lieber, Nature 375 (1995), p. 769.
5. D. Zhou and S. Seraphin, Chemical Physics Letters 222 (1994), p. 233.
6. Y. Li, Y. Bando and D. Golberg, Advanced Materials 16 (2004), p. 93.
7. Y. Zhang, K.Suenaga, C. Colliex and S. Iijima, Science 281 (1998), p. 973.
8. F. Kokai, K. Uchiyama, H. Chigusa, E. Noguchi, Y. Kameda and A. Koshio, International Symposium on high power Laser Ablation 1278 (2010), p. 215.
9. B. Rafferty and L.M. Brown, Physical Review B 58 (1998), 10326.

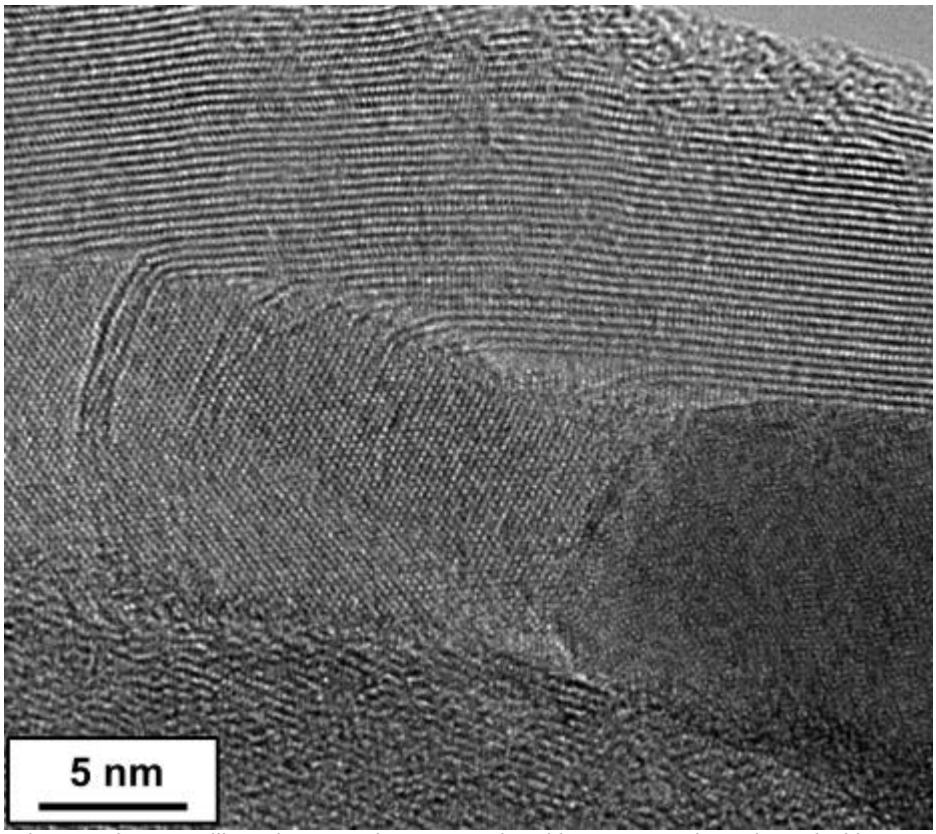

Figure 1. TEM image of a crystalline SiC nanowire encapsulated in a CNT and terminated with a permalloy catalyst particle. A pronounced bending of the graphene layers towards the SiC is visible.

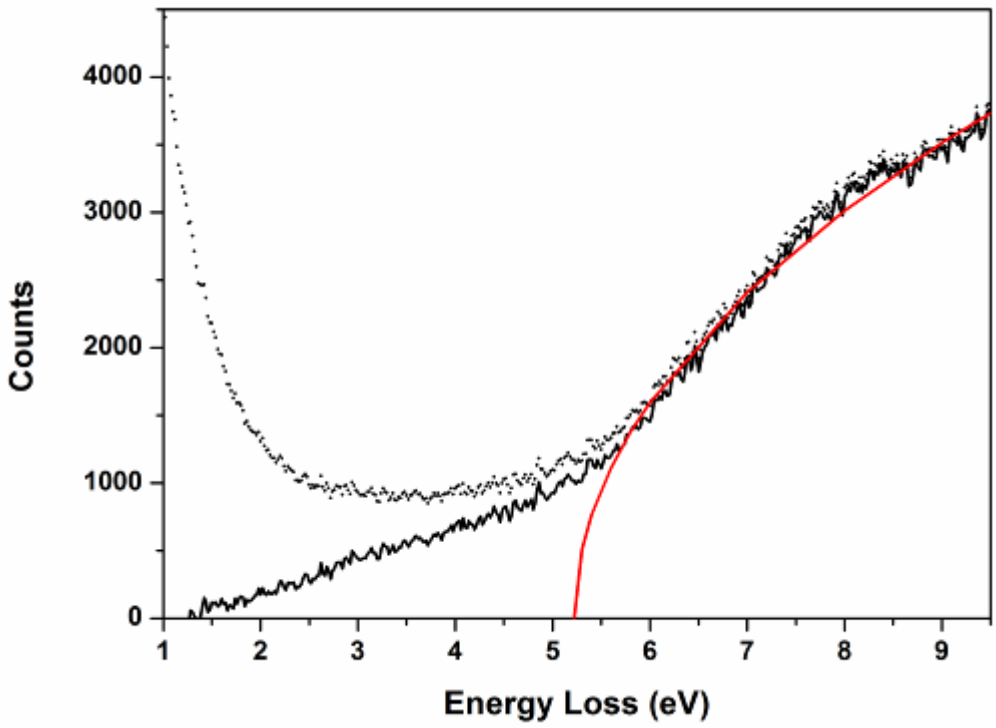

Figure 2. The dotted line represents the VEEL spectrum of the SiC nanowire (after removal of the graphene layers). The solid line results after the subtraction of the zero loss peak. The upper region of the spectrum is then fitted by the square root function $(E-E_g)^{0.5}$. This leads to a value for the indirect bandgap of 5,2 eV.

Low Dimensional Materials and Catalysts

MS.7.P196
HAADF-STEM characterization of supported uranium oxide catalysts

F. Krumeich[1], A. Amrute[2], C. Mondelli[2], J. Pérez-Ramírez[2]

[1]ETH Zurich, Laboratory of Inorganic Chemistry, Zurich, Switzerland
[2]ETH Zurich, Institute for Chemical and Bioengineering, Zurich, Switzerland

krumeich@inorg.chem.ethz.ch
Keywords: Z contrast, depleted uranium, catalysis

The oxidation of HCl to Cl_2 (so-called Deacon reaction) is an important route to recycle chlorine from HCl that is obtained in huge quantities as by-product in the production of polyurethanes and polycarbonates. In industry, materials containing RuO_2 as the active phase are utilized to catalyse this reaction [1]. Although these heterogeneous catalysts are stable and highly active at relatively low temperature, the high and fluctuating market price of Ru has triggered the search for cost-effective alternatives [2]. Promising candidates are uranium compounds that have been successfully probed as heterogeneous and homogeneous catalysts in many redox reactions of industrial relevance [3]. Furthermore, depleted uranium, which is only weakly radioactive, is available as a waste product arising during the production of enriched uranium for nuclear fuels. Therefore, uranium oxide-based catalysts have been investigated in the gas-phase oxidation of HCl to Cl_2 by combining ambient pressure catalytic tests with a comprehensive structural and textural characterization [4].

Experiments with bulk uranium oxides revealed their extraordinary stability against chlorination and thus their suitability as stable catalytically active phase for HCl oxidation. While □-U_3O_8 maintains its oxidation state, UO_2 and □-UO_3 tend to transform into □-U_3O_8 under reaction conditions [4]. The deposition of 10 wt.% uranium on different carriers by dry impregnation resulted in an improved catalytic activity with zirconia being the superior support.

To visualize the U dispersion on the ZrO_2 support, HAADF-STEM (Z-contrast) imaging was applied. This method allows one to recognize the UO_x as bright patches on the grey ZrO_2 support (Z_U = 92 *vs.* Z_{Zr} = 40). The investigations were performed on an aberration-corrected, dedicated STEM microscope (Hitachi HD-2700CS; cold-field emitter; V_{acc} = 200 kV; CEOS corrector) [5,6]. Typical HAADF-STEM images reveal that the uranium oxide is finely dispersed in the starting material (Figure 1). Two types of uranium oxide dispersions are evidenced, namely, (i) a film-like nanostructure, mostly a monolayer, visualized as a bright rim at the edge of many ZrO_2 crystallites (Figure 1a) and (ii) atomically dispersed uranium oxide identified by the presence of separated bright spots (*i.e.* single U atoms or small UO_x clusters) on some ZrO_2 crystallites (*e.g.* in Figure 1b).

Remarkably, the activity of the U_3O_8/ZrO_2 catalyst increased under reaction conditions until a stable performance is reached after *ca.* 85 h. In this activated catalyst, the reflections specific for □-U_3O_8 disappear in the XRD patterns although the uranium content remains unaltered according to ICP-OES metal analysis [4]. These results suggest that the observed catalyst activation is related to an *in situ* redispersion and a gradual transformation of the original □-U_3O_8 phase into a tinier atomically-dispersed form. This structural change is evident in the HAADF-STEM images of the catalyst after reaction (Figure 2). Even after a reaction time of 5 hours only, the bright rims of UO_x at the edge of the ZrO_2 crystallites have become broader and less dense. On the surface of the ZrO_2, many bright dots are recognizable (*e.g.* in Figure 2b) hinting at an atomically fine UO_x distribution.

The unique robustness of ZrO_2-supported uranium oxide under the harsh reaction conditions and the stable Cl_2 production for more than 100 h on stream clearly demonstrates its potential as suitable catalyst for high-temperature HCl oxidation. The understanding gained by the HAADF-STEM analysis of the catalyst structure before and after reaction demonstrates the suitability of this technique to unravel the catalysts' key features that are responsible for its superior performance and the observed activation phenomenon [7].

1. J. Pérez-Ramírez *et al.*, Energy Environ. Sci. 4 (2011) p. 4786.
2. A. P. Amrute *et al.*, J. Catal. 286 (2012) p. 287.
3. .A. R. Fox *et al.*, Nature, 455 (2008) p. 341. 4A. P. Amrute *et al.*, Chem. Science, 2013, 4, 2209.
4. H. Inada *et al.*, J. Electron Microsc. 58 (2009) p. 111.
5. F. Krumeich *et al.*, J. Phys. Chem C 115 (2011) p. 1080.[7] Electron microscopy investigations were performed at the electron microscopy center of ETH Zurich (EMEZ).

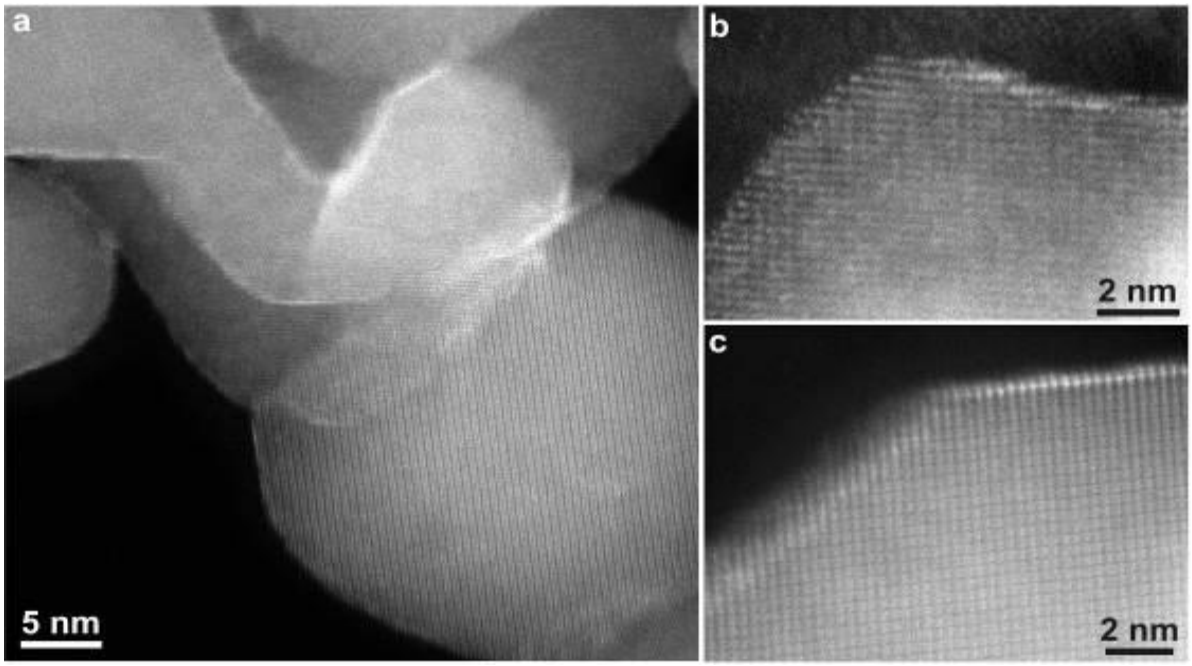

Figure 1. HAADF-STEM images of the fresh U_3O_8/ZrO_2 catalyst.
Figure 2. HAADF-STEM images of the U_3O_8/ZrO_2 catalyst after 5h (a.b) and 100 h (c,d) reaction time.

Low Dimensional Materials and Catalysts

MS.7.P197
Systematic characterization of dynamics of transition metals inside SWNT by in-situ aberration-corrected HRTEM at low acceleration voltages between 20 and 80 kV

T. Zoberbier[1], J. Biskupek[1], U. Kaiser[1], T. Chamberlain[2], A. Khlobystov[2]

[1]Universität Ulm, Electron Microscopy of Materials Science, Ulm, Germany
[2]University of Nottingham, School of Chemistry, Nottingham, United Kingdom

thilo.zoberbier@uni-ulm.de

Single-walled carbon nanotubes (SWNTs) attract great attention for their aptitude as nano-test tubes and have proven to be an ideal confinement for atomically resolved imaging of dynamics and interactions of sub-nanometer sized molecules. Apart from a matrix free stabilization of molecules, SWNT offer protection against undesired beam damage resulting from ionization or chemical etching under a highly energetic electron beam. Moreover SWNT provide a unique environment for the investigation of carbon-based reactions at the atomic scale. This unique combination make it a precious test-system for the study of interaction mechanisms between the specimen and the energetic electron-beam by nature omnipresent in transmission electron microscopy (TEM) observations.

In this study we present in-situ irradiation experiments of sub-nanometer sized *d*-element metal-nanoclusters enclosed in SWNTs by means of low voltage aberration-corrected high-resolution transmission electron microscopy (AC-HRTEM).[2,3] The transition metals are varied systematically along Groups as well as Periods of the Periodic Table of Elements in order to characterize their properties and track their interactions with the electron beam and the carbon special environment. In these experiments the particular technique of HRTEM combines imaging tool and irradiation source in one integral experiment while further benefiting from the SWNTs low and regular contrast combined with minimized susceptibility to head-on collisions of the electrons with the carbon atoms nuclei (knock-on damage) while operating with electron energies less or equal 80 keV.[4] In our experiments we pursue the methodology of varying both, the metal type and the electron acceleration voltage (between 20 kV, 40 kV and 80 kV). Thus we are able to separate the influence of the electron beam from that of the specimen which is a necessary condition for the detailed and atomically resolved study of sample or irradiation induced structural SWNT-modifications. Finally it is our aim to explicitly describe the interaction mechanisms between carbon and the different under the influence of the electron beam. While irradiating, in order to answer the demand of comparability, time series of interactions are recorded until reaching the same total electron dose of 10^{10} e^-/nm^2. Experiments are conducted using a Cs-corrected FEI Titan 80-300 operated at 80 kV and a monochromated/Cs-corrected SALVE (Sub-Ångstrøm Low-Voltage Electron Microscopy) Zeiss LIBRA prototype microscope operated at 20, 40 and 80 kV.

1. T. Zoberbier, U. Kaiser, A.N. Khlobystov, J. Am. Chem. Soc. (2012)
2. A. Chuvilin, S. Roth, U. Kaiser, Angew. Chem. Int., (2010)
3. U. Kaiser, A. N. Khlobystov, G. Benner, UM (2011)
4. J. Meyer, F. Eder, U. Kaiser, Phys. Rev. Lett. 108 (2012)

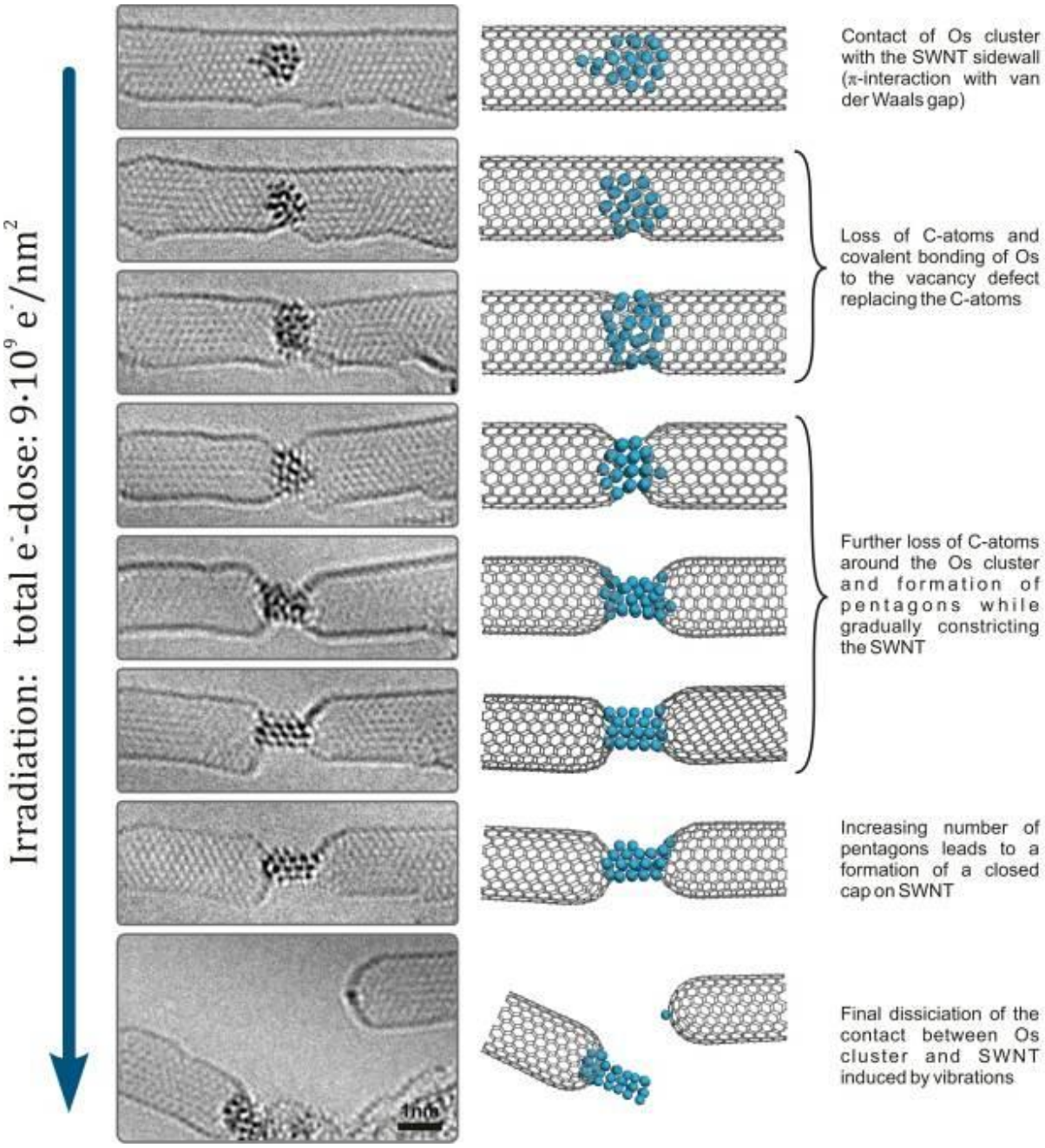

Figure 1. The time-series shows the stages of the interaction between an Os nanocluster and SWNT inner sidewall induced by the electron-beam imaged by AC-HRTEM at 80 keV. On the right column are the corresponding structural diagrams.

Low Dimensional Materials and Catalysts

MS.7.P198
Investigations of Sn-doped ZnO nanowires with multiple inversion domain boundaries

G. Schaan[1], S.-M. Hühne[1], H. Schmid[1,2], W. Mader[1]

[1]Universität Bonn, Institut für Anorganische Chemie, Bonn, Germany
[2]INM - Leibniz-Institut für Neue Materialien, Saarbrücken, Germany

One-dimensional nanostructures such as nanowires (NWs) have been synthesized from a wide variety of chemical elements and compounds. Zinc oxide is a direct n-type semiconductor with a band gap of 3.44 eV and an exciton binding energy of 60 meV, making it an interesting material for many applications. Due to its low price and excellent availability, it is envisaged as a promising alternative to materials like GaN and ITO (indium tin oxide).[1] Additions of other main group or transition metal oxides can alter its optical, electrical or magnetic properties. ZnO NWs doped with Sn are a useful material for photoanodes in dye-sensitized solar cells.[2]

Compounds of the general sum formula $ABO_3(ZnO)_m$ (A = In, Fe, $Sn^{IV}_{1/2}Zn_{1/2}$, $Sb^{V}_{1/3}Zn_{2/3}$...; B = In, Fe, Ga...; *m* = integer) exhibit layered structures composed of wurtzite-type ZnO slabs separated by single layers of edge-sharing AO_6 octahedra. These layers act as inversion domain boundaries (IDBs) for the adjacent ZnO domains. Inside each domain, a second inversion occurs at IDBs consisting of pyramidal or tetrahedral sites occupied by B cations.[3] In the case of Sn-doped ZnO, half of both octahedral and pyramidal or tetrahedral sites are expected to contain Sn. The latter has not been reported yet for bulk materials in the system $ZnO\text{-}SnO_2$.

In our work, Sn-doped ZnO NWs were synthesized by thermal evaporation and deposition following a unique growth mechanism involving Au nanoparticles as seeds.[4] A mixture of ZnO, Sn and graphite powders acts as the source for Zn and SnO vapours. These are transported to a substrate (fused silica coated with Au nanoparticles) using purified Ar enriched with O_2 as carrier gas. The NWs measure tens of µm in length and ca. 100 nm in diameter on average. According to EDXS measurements, the relative Sn content of the NWs reaches up to 2.1 at.-% of the cations.

TEM investigations reveal that the NWs indeed exhibit layered structures featuring both basal and pyramidal IDBs perpendicular to the growth direction of the NW (Figure 1). The mean distance between basal IDBs in the shown portion is 22.78 nm. This directly correlates with the relative Sn content and corresponds well with the EDXS measurements. In electron diffraction patterns of zone axes and , the nonperiodic structure gives rise to rows of diffuse reflections in the direction. TEM bright-field images were recorded using an FEI CM300 FEG-UT microscope.

Spatially resolved compositional analysis was performed in an advanced analytical TEM/STEM system (JEOL JEM-ARM 200CF equipped with cold FEG, probe Cs-corrector, X-ray and electron spectrometer (GATAN GIF Quantum ER) attachments). Spectroscopic imaging by X-ray (SIX) reveals that Sn selectively occupies both basal and pyramidal IDBs (Figure 2). The arrangement of the cations inside the IDBs and the adjacent ZnO domains in ZnO NWs as observed in high-resolution HAADF-STEM images is identical to that of well-known compounds such as $InGaO_3(ZnO)_m$ (Figure 3). Thus, we assume that Sn statistically occupies half of the octahedral as well as the pyramidal sites, the other half being occupied by Zn. Occupation of pyramidal or tetrahedral sites by Sn ions is unknown so far in bulk oxides, however, appears possible in nanostructures due to shorter diffusion paths.

1. D. P. Norton *et al.*, Mater. Today 6 (2004), p. 34.
2. Y. Zhang, N. Ye., J. Power Sources 195 (2010), p. 5806.
3. N. Kimizuka *et al.*, J. Solid State Chem. 116 (1995), p. 170.
4. H. Simon, T. Krekeler, G. Schaan, W. Mader, Cryst. Growth Des. 13 (2013), p. 572.
5. We thank E. Arzt for continuous support through INM.

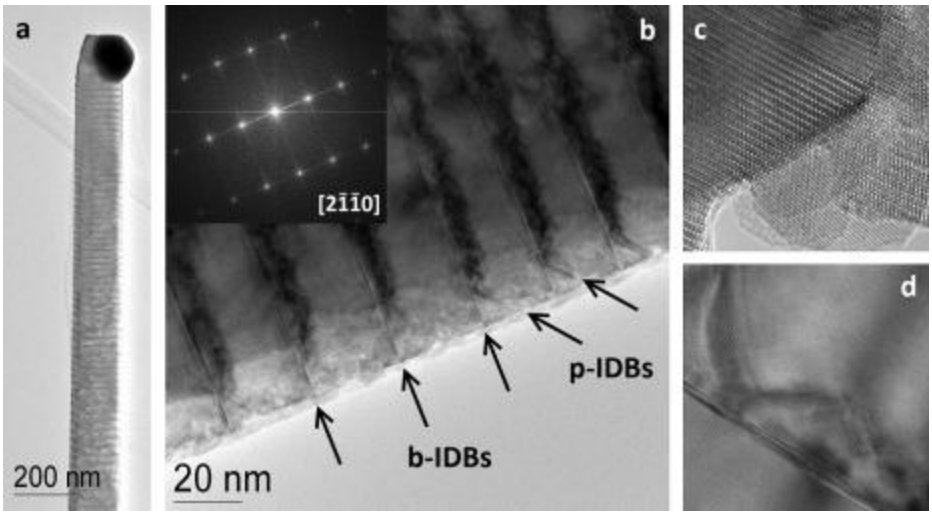

Figure 1. TEM bright-field images of a ZnO NW (a, b) featuring basal (c) and pyramidal (d) IDBs.

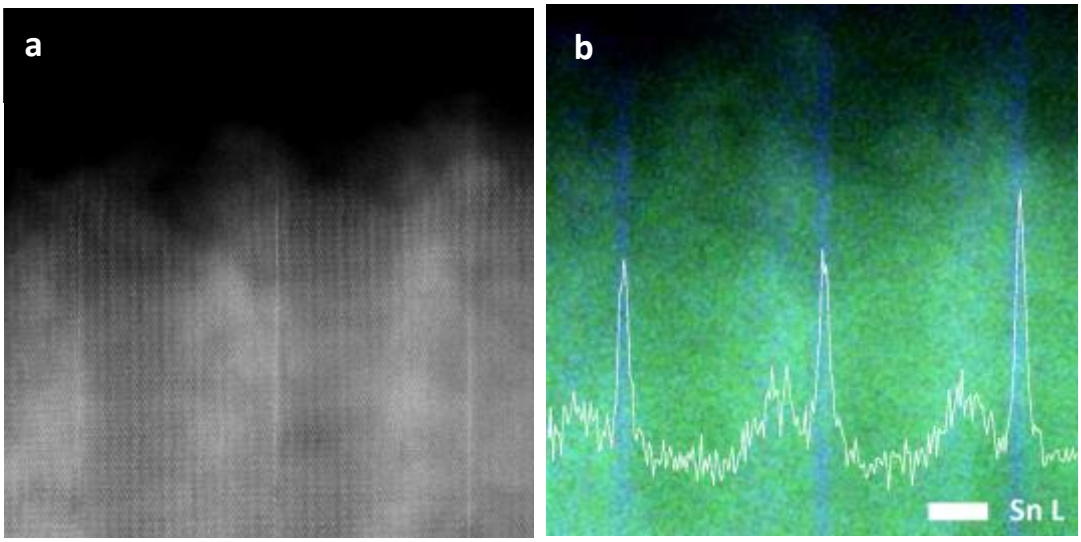

Figure 2. HAADF imaging (a) and element mapping (Sn/Zn overlay) by EDS-SIX spectroscopic imaging (b) shows that Sn selectively occupies both basal and pyramidal IDBs.

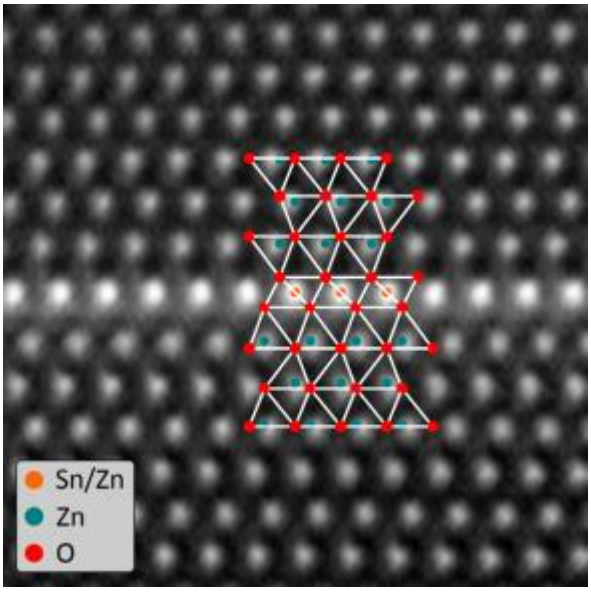

Figure 3. High-resolution HAADF-STEM image of the b-IDB in Sn-ZnO reveals that the stacking sequence of cations is identical to that in compounds with the sum formula $A^{III}B^{III}O_3(ZnO)_m$.

Low Dimensional Materials and Catalysts

MS.7.P199
Exploring optimum parameters for off-axis holograms at 80 kV with C_s-corrected Titan 80-300

D. Geiger[1], J. Biskupek[1], U. Kaiser[1]

[1]Uni Ulm, Ulm, Germany

dorin.geiger@uni-ulm.de
Keywords: Graphene, C_s-corrected TEM, low voltage, off-axis electron holography

Studying 2D structures like graphene [1] has become in the last years of major scientific interest because of their specific mechanical and electrical properties. A large number of applications e.g. as sensor, in nanoelectronics, hydrogen storage or lithium-ion batteries etc. require deep knowledge of their properties at atomic level. One of the most important investigation technique applied in this field represents the high resolution transmission electron microscopy (HRTEM) at 80 kV (or lower) (figure 1).

In order to reconstruct the object exit wave, off-axis electron holography [2] is one of the most appropriate methods. Using C_s-corrected transmission electron microscopes [3], significant progress was achieved in the last decade, especially in decreasing the phase detection limit and enhancing the spatial resolution [4]. Higher hologram contrast is required to reduce the quantum noise [2]. This can be realized by adjusting the TEM illumination to obtain increased beam coherence. For the Titan microscopes, the illumination system consists mainly of the Schottky field emission gun and three condenser lenses, C1, C2 and C3 followed by the minicondenser. To achieve the necessary interference fringe contrast, the electron beam has to be adjusted to a high elliptical spot. This is only possible by switching off the second condenser lens C2, among others because of the performance of the condenser stigmator.

By taking the C1 – C3 condenser lens setting, the coherent elliptical illumination could be optimized but the coherent dose rate remains under conventional extraction voltages too low. Because our instrument is not equipped with a high brightness gun, we analysed other possible electron gun emission settings to achieve better performances. A large range of gun extraction voltages were investigated to find an optimum. Special gun settings, allowing better energy dispersion for improved EELS measurements at 80kV, were already applied at the Titan instrument in Ulm [5]. At lower extraction voltages (down to 1.7 kV), the energy spread of the emitted electron beam should be significantly lower [6]. Consequently, an additional gain in contrast could be achieved at higher spatial frequencies of interest.

In parallel, different gun lens excitations were tested as well, trying to reduce further the quantum noise. This makes it possible to use non prohibitive exposure times per single hologram. Certain minimal exposure times are necessary, even if we process hologram series to increase the total exposure time, and on this way to improve the signal to noise ratio. This happens among others because of the object drift, which is, at least for the current stages, unavoidable at atomic resolution, and should be numerically corrected a posteriori by using single reconstructed holograms. If these are too noisy, the drift compensation programs cannot work reliably.

The effectively achieved performance could be analysed in figure 2 and 3, where the dependence of the hologram contrast on the fringe spacing and on the biprism voltage is shown. Although the hologram contrast is really competitive, the necessary high minimum exposure time per hologram of about 5 to 8 seconds requires a very high stability of the TEM stage, which is difficult to achieve. The resultant stability of all other subsystems of the Titan microscope (excepting the stage) is remarkable, allowing good fringe contrast (~15%) of empty holograms with fringe spacing of ~0.036nm at ~1.3Mx magnification even for exposure times of 20 seconds or more.

1. A. K. Geim and K. S. Novoselov, Nature Materials **6** (2007), p.183.
2. H. Lichte, Ultramicroscopy 20 (1986), p. 293.
3. M. Haider et al., Ultramicroscopy **75** (1998) p. 53.
4. D. Geiger et al., Microsc. Microanal. **14** (2008), p. 68.
5. J.C. Meyer et al., Nano Letters 9/7 (2009), p. 2683.
6. J. Biskupek et al., Ultramicroscopy 116 (2012), p. 1.

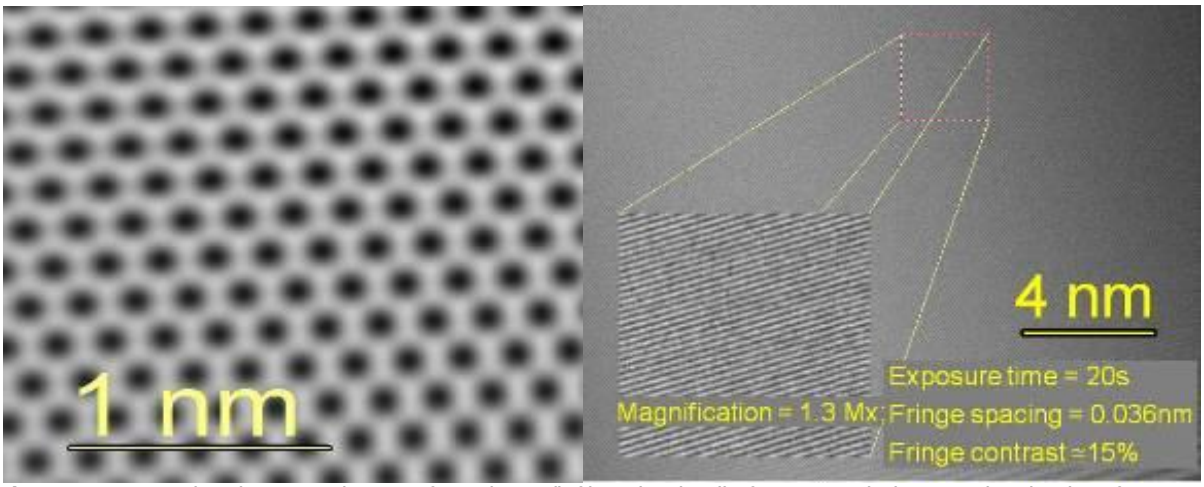

Figure 1. Conventional HRTEM image of graphene (left) and a detail of an empty hologram showing interference fringes of 15% contrast (right) taken at 80kV with the Cs-corrected Titan 80-300 in Ulm.

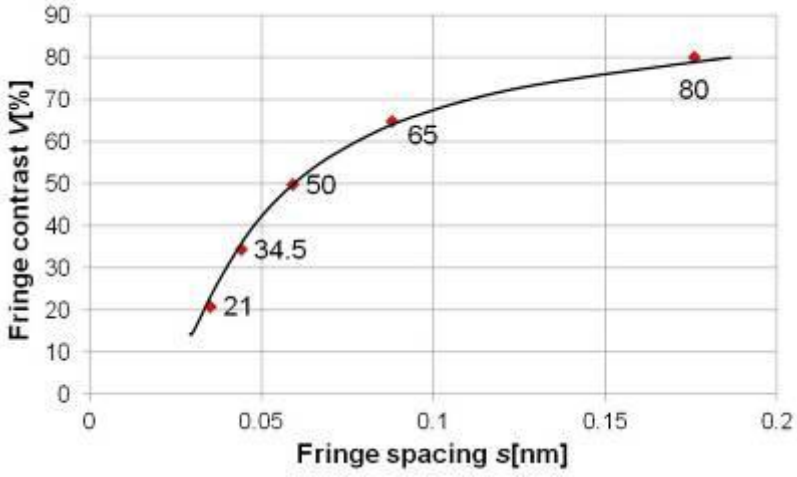

Figure 2. Fringe contrast as function of fringe spacing for Cs-corrected Titan 80-300 in Ulm (accelerating voltage 80kV, exposure time 4s, magnification 1.3 Mx).

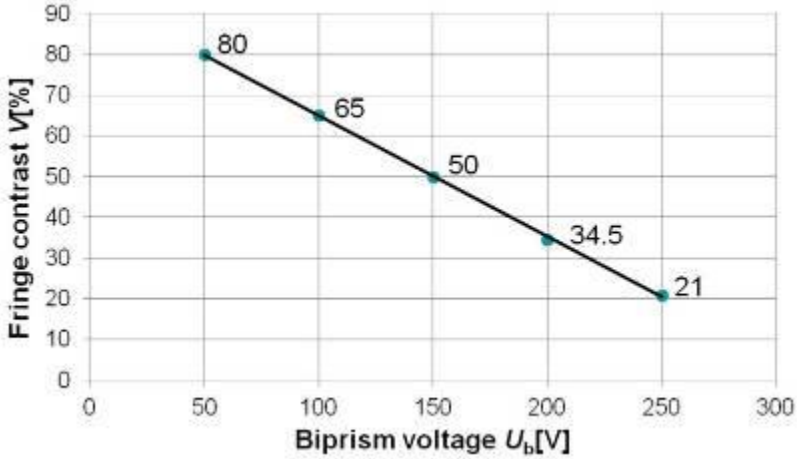

Figure 3. Linear fringe contrast dependence on the biprism voltage for Cs-corrected Titan 80-300 in Ulm (accelerating voltage 80kV, exposure time 4s, magnification 1.3 Mx).

Low Dimensional Materials and Catalysts

MS.7.P200
TEM investigation of FeGa alloy nanowires electrochemically deposited within nanoporous templates

C. Damm[1], A. Funk[1], D. Iselt[1], H. Schlörb[1], L. Schultz[1], B. Rellinghaus[1], T. Sturm[1], A. Pöhl[1]

[1]IFW Dresden, Institute for Metallic Materials , Dresden, Germany

c.damm@ifw-dresden.de
Keywords: TEM, nanowires, electrodeposition, FIB

Fe_{100-x} Ga_x (x = 20±5 at %), a low cost non rare-earth alloy with large magnetostriction ($_{max}$ = 400 ppm) and high mechanical strength is a promising material for miniaturized sensor and actuator applications. An economically priced method to produce low dimensional structures such as nanowires is the electrochemical deposition within nanoporous templates. The electrochemical co-deposition of Fe and Ga, however, is particularly challenging due to the low standard potentials of the involved metals and gallium's high tendency to hydrolyze and form insoluble oxidic species. Recently, enormous progress has been made in understanding the alloy deposition mechanism [1] and minimizing the oxygen content in Fe-Ga films by applying an alternating potential mode [2]. Moreover, the fabrication of Fe-Ga nanowires from a modified electrolyte was successfully demonstrated [3]. The objective of the present study is to investigate the local structure of the Fe-Ga nanowires in detail. The influence of the deposition technique on composition distribution, structure and microstructure is examined.

For preparation of nanowires a highly ordered hexagonally arranged nanopore array as the Anodized Aluminium Oxide (AAO) template for the following deposition process is generated. The freestanding membranes, an Au layer of 30nm thickness as the first electrical contact and a further Cu layer for mechanical stability of the template represent the working electrode [4]. Electrodeposition is performed in a three electrode arrangement and controlled by a HEKA PG 310 potentiostat/ galvanostat. A Pt foil is used as the counter electrode and a Saturated Calomel Electrode (SCE, E = 241 mV) as the reference electrode. The electrolyte contains 0.03 M $FeSO_4 \cdot 7H_2O$, 0.06 M $Ga_2(SO_4)_3 \cdot 18H_2O$, 0.5 M boric acid, 0.04 M ascorbic acid and 0.15 M sodium citrate as the complexing agent [3]. The pH value of the electrolyte is adjusted to 3 using sodium hydroxide.

Nanowires were electrodeposited by two different techniques, the potential pulse technique (A) [3] and the more simple, less time consuming potentiostatic mode (B). In mode (A) a deposition potential E_1 = -1.5 V_{SCE} is applied for t_1 = 10 s followed by a relaxation step E_2 = -0.9 V_{SCE} for t_2 = 10 s. These two steps are repeated 500 times, ending up with a total deposition time of 5000 s and a total process time of 10000 s. The length of the wires is 6.3± 0,2 µm. This approach is expected to create more homogeneous deposits through compensation of concentration gradients, interruption of hydrogen evolution and, therefore, easier escape of the smaller gas bubbles from the narrow nanopores.

Mode B is rarely used for alloy nanowire deposition due to numerous disadvantages:. Slow mass transport along the narrow nanopores can result in a significant composition gradient along the nanowire. The required low deposition potential leads to undesired bubble formation due to strong hydrogen evolution. Continued growth of these gas bubbles can block the pores and partially or even fully interrupt further nanowire growth. Simultaneous pH increase may cause the formation and incorporation of undesired hydroxides. However, complexing the metal ions with citrate is expected to significantly reduce the hydroxide formation and also seems to improve nanowire growth. Here, a constant potential of E = -1.48 V_{SCE} is applied for the overall deposition time of t = 5000 s. The length of the wires is measured to 6.1± 0,3 µm.

In order to investigate structure and microstructure transmission electron microscopy (TEM/ TECNAI T20, 200kV, LaB_6 filament) was performed. TEM samples of the FeGa nanowires embedded in aluminum oxide membrane were prepared to transparency by focused ion beam technique (FIB/ Helios Nano Lab 600 i). The sample was cut from the substrate side with an energy of 30kV to the beginning and 2kV during the finishing.

Figure 17 compares the cross sections of a) pulsed and b) non-pulsed nanowires. In both samples the nanowires appear continuous and smooth. Only few small defects are observed along the nanowire length following the surface morphology of the inner pore walls (marked with arrows in Figure 1b). The microstructure seems nanocrystalline. In some of the crystals the angle between lattice planes and the direction of the incident beam comply the Bragg`s condition exactly. In the imaging this crystals appear darker in contrast. In crystals with another incident beam conditions the contrast of the crystals come out brighter. The same effect can occur within a single stressed grain. Consequently different contrast can be

observed inside this grain. That is given in the pulsed or non- pulsed wires which exhibit strong stress. An accurate determination of the crystal size is not possible. The nanowires fabricated by pulsed deposition show a uniform stress pattern (marked with arrows in Figure 1a). These features might be attributed to the pulsed method as they are not at all observed for the potentiostatically deposited nanowires.

The diffraction ring patterns presented in the insets in Figures 1a) and b) indicate a multitude of nano crystals that can be attributed to α-Fe_3Ga with a preferred {110} orientation. In case of the pulsed wires lots of strong discrete reflexes along the diffraction pattern rings were found. This hints for a larger crystal size in the pulsed wires compared to the non-pulsed wires. Both diffraction patterns give no indications for the presence of the undesired GaOOH phase. Fast Fourier transformation (FFT) filtered high resolution TEM images suggest isolated small regions consisting of GaOOH shown on a pulsed wire in Figure 18.

EDX measurements along both types of wires indicate no gradient in chemical composition. The average composition of the non-pulsed wires amounts 68±3 at % Fe and 32±3 at % Ga. The pulsed wires were measured to 78±3 at % Fe and 22±3 at % Ga. This correlates much better with the desired composition of $Fe_{80}Ga_{20}$.

In summary, our TEM investigations reveal only minor differences in structure and microstructure of differently prepared FeGa nanowires. The pulse deposited nanowires exhibit slightly larger crystals and more pronounced stress patterns. Unexpectedly, potentiostatic deposition yields similar nanowire quality.

1. D. Iselt, K. Tschulik, S. Oswald, D. Pohl, L. Schultz, H. Schlörb, J. Electrochem. Soc. **159** H633 (2012)
2. D. Iselt, U. Gaitzsch, S. Oswald, S. Fähler, L. Schultz, H. Schlörb, Electrochim. Acta **56** 5178 (2011).
3. D. Iselt, A. Funk, L. Schultz, H. Schlörb, ECS Electrochem. Lett. **2**(3) D 13 (2013)
4. V. Haehnel, S. Fähler, P. Schaaf, M. Miglierini, C. Mickel, L. Schultz, H. Schlörb, Acta Mater. **58** 2330 (2010).

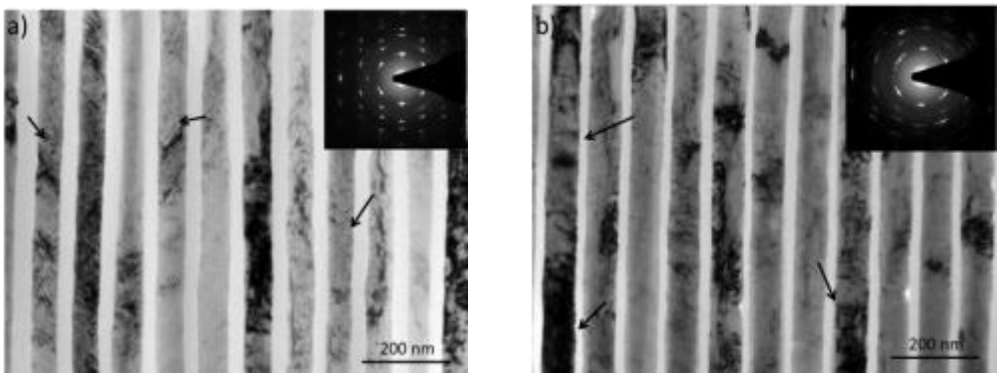

Figure 17. TEM bright field images and corresponding SAD of cross sections of a) pulsed wires (arrows point on the uniform stress pattern) and b) non- pulsed wires (arrows point on defects following the surface morphology of the inner pore walls).

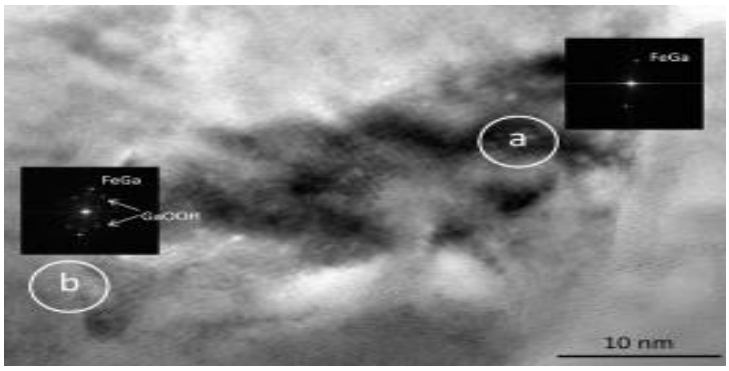

Figure 18. HRTEM image of the cross section of a pulsed wire and FFT: a) main reflexes FeGa and b) main reflexes FeGa and side reflexes GaOOH.

Low Dimensional Materials and Catalysts

MS.7.P201
Application of energy low loss backscattered electrons in material characterization and analysis

X. Liu[1]

[1]Carl Zeiss Microscopy GmbH, Oberkochen, Germany

xiong.liu@zeiss.com
Keywords: backscattered electrons, energy filtering, band-gaps, nanostructure

With the continuous size and structure shrinkage in semiconductor and electronic devices, the final performance and properties of the materials are dominated by the surface and interface layers. This requires scanning electron microscope (SEM) as a most conventional technical method in material characterization and analysis not only to be able to visualize and image such nanostructures with the secondary electron imaging under a low energy beam but also to analyze the tiny compositional differences like doping contrast, oxidation states of elements, small phases of hybrids or function group in polymers etc., which are not available via the classical backscattered electron imaging or other Energy-dispersive X-ray spectroscopy methods. Although the classical backscattered electron (BSE) imaging are from the multiple inelastic scattering process which could provide density related contrast like channeling contrast at high energy beam, the backscattering coefficient shows non-linear behavior and get very complicated [1].

In the classical backscattering process (Rutherford scattering), the backscattered electrons are mainly from the scattering of the high energy primary electrons with the nucleus charge or inner electron shells of the material. In such a case the contrast or brightness of the BSE imaging scale with material density, atomic number (Z). However the scattering between the primary beam with the outer electron shells of the materials at low impact energy (below 3 kV) region is not any more negligible which even becomes more dominant where the surface plasma resonance and ionization loss could happen and contribute to in the total contrast mechanism [2].

The unique design of the Gemini® lens integrated with a beam booster in the beam path not only maintains the brightness of the downward primary electron beam at low energies but also has a dispersion function for the generated reverse electron signals backward into the column. It means that the secondary electrons and backscattered electrons with a small energy and angle differences could be amplified and separated by the Gemini® lens in real time and space without converting the signals or by applying any additional stage bias. The separated backscattered electrons could be further filtered with an energy filtering grid and projected back into the corresponding detector. Backscattered electrons with a specific energy low loss could be picked out for imaging by setting an appropriate threshold potential to the filtering grid. After the grid filter the multiple inelastic scattered electrons could be cut away and the signal is consisted of the so-called energy low loss backscattered electrons which reveals some characteristic resonance of the materials.

Herein, a few typical materials have been investigated with the energy low loss backscattered imaging and the corresponding results will be presented and discussed. We found the Ce nanoclusters and Ce ions catalyst highly dispersed inside the mesoporous silica as could be easily characterized. As the first report, the different phases separation of ZnO_xS_{1-x} thin film on insulating Al_2O_3 substrate due to the different of band gap could be revealed at a certain low beam energy which is agreed with the results from the UV-Vis spectroscopy where there different phases give corresponding adsorption peaks at individual wavelength or energy.

1. L. Reimer, Scanning electron microscopy, 2nd edition. Springer-Verlag, 1998, Berlin Heidelberg New York.
2. H. Jaksch, Contrast mechanisms of low loss backscattered electrons in field emission SEM, EMAS conference, May 2011, France

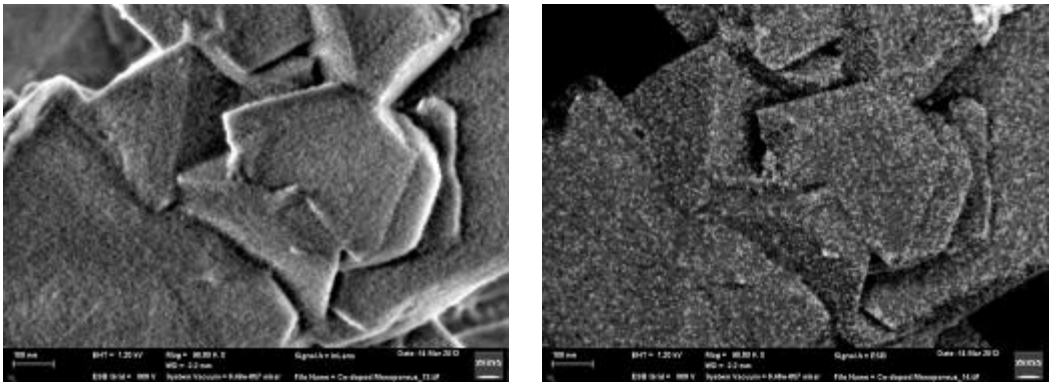

Figure 1. The SE1 image (left) and corresponding LL-BSE image (right) of the Ce incorporated into mesoporous silica as catalyst where the Ce ions and nanoclusters give high brightness.

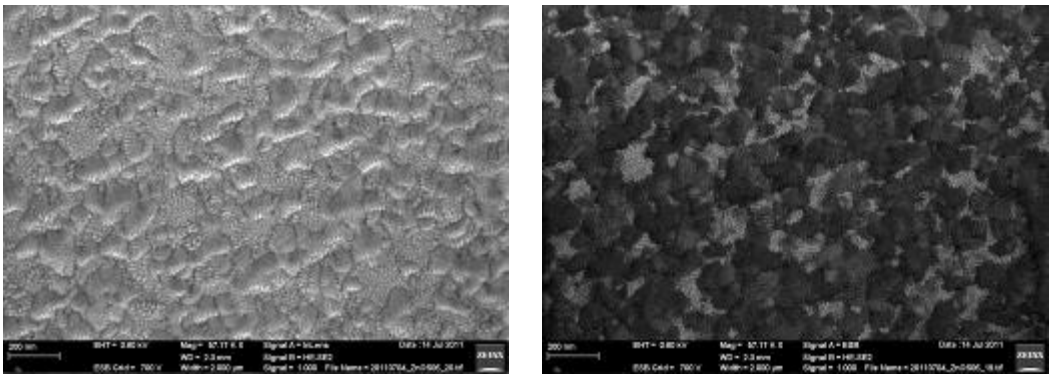

Figure 2. The SE1 image (left) and corresponding LL-BSE image (right) of the ZnS_xO_{1-x} thin film on Al_2O_3 substrate where the LL-BSE image is from the low loss BSEs with an energy between 700 eV and 800 eV.

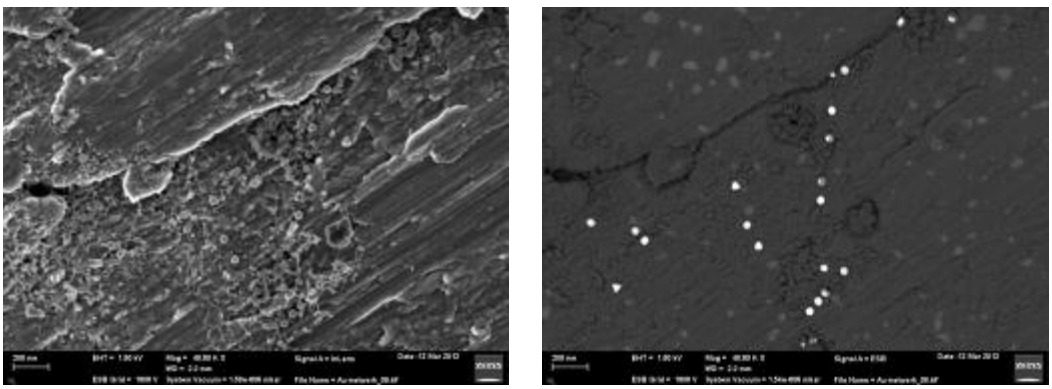

Figure 3. The SE1 image (left) and corresponding LL-BSE image (right) of Au nanoparticles stabilized with organic ligands and networks.

Low Dimensional Materials and Catalysts

MS.7.P202
Structure of composite mesoporous silica particles synthesized by low-toxic route

A. Sitnikova[1], D. Kirilenko[1,2], D. Kurdyukov[1], E. Trofimova[1], V. Golubev[1]

[1]Ioffe Institute, St-Petersburg, Russian Federation
[2]EMAT, Universiteit Antwerpen, Antwerp, Russian Federation

sitnikova@mail.ioffe.ru
Keywords: mesoporous silica particles, micelles aggregation

Mesoporous silica is known for its wide range of potential applications. Submicrometer spherical particles can be used as a building material for photonic crystals or, at the same time, as biological markers or carriers for drug-delivery. Large surface area and chemical stability of the material open way for a large set of functionalizations for various purposes.

Here we present a TEM study of highly monodispersed spherical mesoporous silica particles obtained by a novel low-toxic synthesis route [1]. Mesoporous structure of the particles is inherited from porous building blocks – micelles – formed at first steps of the synthesis process. Synthesis conditions were tuned so that the micelles are not likely to exceed 10 nm in size, which provides homogeneity in size distribution of the submicrometer spherical particles, which are further formed by micelles aggregation. The micelle is a hexagonal stack of hollow rods (ca. 2 nm in diameter) with silica walls as was proved by TEM investigation of the material at early growth stages (Figure 1.).

Thus, the spherical particle is built of many of these blocks – micelles – randomly twisted against each other. However, it does not hamper penetrability of the material and it can be soaked by various species, e.g. fluorescent compounds [2]. The particles can easily loss the compound, by which they are soaked, if they are immersed back to the medium dissolving it that can be used for prolonged drug action. Desoaking time depends on the particles size and synthesis conditions and can be tuned from 6h to 400h.

At the same time, a protective shell can be grown around the particle in order to prevent desoaking. The shell is grown by another chemical route which does not lead to formation of mesoporous structure, so that the shell is impermeable for liquids. We performed a combined HAADF-STEM and EDX study of Gd-enriched composite particles, which are supposed to be used for radiotherapy, and found highly uniform distribution of Gd in a particle interior and Gd-free shell protecting from undesirable losses of acting specie (Figure 2).

Thus, the structure of mesoporous silica obtained by a novel synthesis route has been studied by TEM. The material is built of tiny blocks – micelles – which are hexagonal stacks of hollow rods. Random arrangement of micelles does not hamper penetrability of the particles by liquids. Moreover, it also causes appearance of large pores, which increases load capacity of the particle, that, in turn, is important for applications. Composite particles with nonporous protective silica shell can be obtained in order to prevent loss of acting compound.

1. E.Yu. Trofimova, D.A. Kurdyukov et al., Nanotechnology 24 (2013), 155601.
2. E.Yu. Trofimova, S.A. Grudinkin et al., Physics of the Solid State 54 (2012), p. 1298.

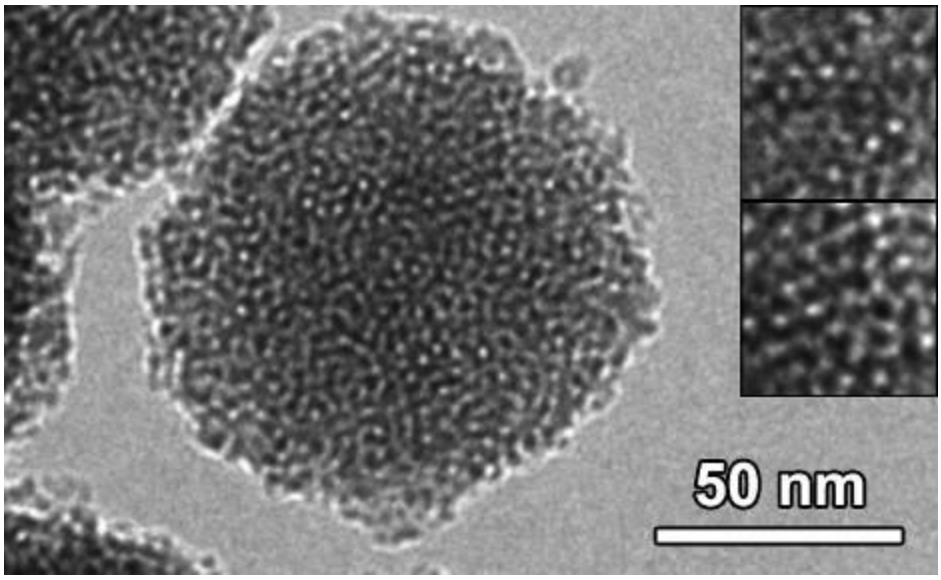

Figure 1. A mesoporous silica particle at an early stage of the synthesis showing its partially arranged structure.

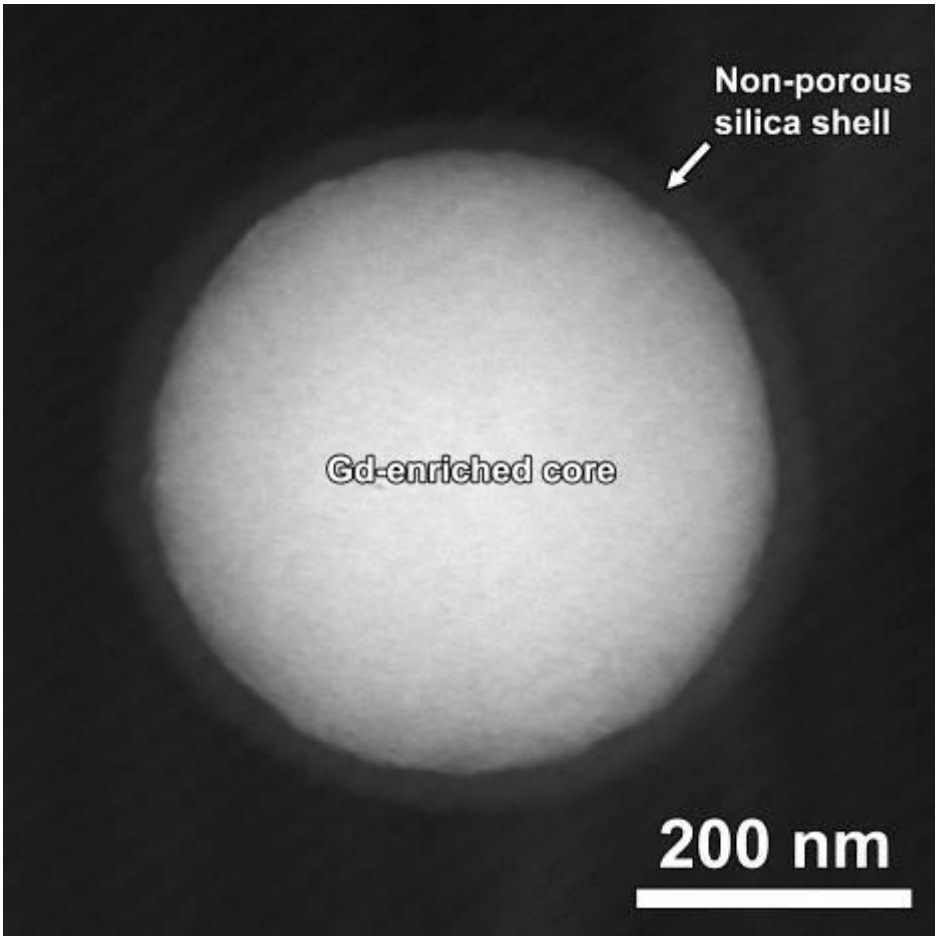

Figure 2. A mesoporous silica particle filled with Gd and covered by protective impermeable shell.

Low Dimensional Materials and Catalysts

MS.7.P203
Growth and characterization of metallic nanowires: Cu, Fe and Cu/Fe

W. Huang[1], G. Richter[2], O. Kraft[1]

[1]Karlsruhe Institute of Technology, Institute for Applied Materials, Eggenstein-Leopoldshafen, Germany
[2]2. Max Planck Institute for Intelligent Systems, Stuttgart, Germany

huang@is.mpg.de
Keywords: metallic nanowires, PVD, growth mechanism

The one-dimensional nanostructures such as wires, rods, tubes have attracted increasing research efforts as a result of their fascinating properties superior to their bulk counterparts. Referring to the Cu nanowires, they are expected to play an important role as interconnects units in electronic devices with nanoscale dimensions due to the low resistivity (≈1.68×10−8Ω•m). With the addition of Fe, the nanowires can form compound magnets, while the magnetic properties related to the structural ordering of Fe.

A novel method has been developed in our group for fabricating the freestanding metallic nanowires, involving only the physical vapor deposition (PVD) [1]. Both FCC (Cu) and BCC (Fe) nanowires have been successfully produced via this method. The morphology of the Cu wires grown on the Si substrate is demonstrated in Figure 1. The dimensions of the wires range from 50 to 400 nm in diameter and 1 to 200 μm in length, which give the aspect ratio up to 1000:1. The characterizations indicate that the FCC Cu whiskers grow along the crystallographic direction of <011> while the BCC Fe whiskers grow parallel to <001>.

For the purpose of understanding the growth mechanism of the whiskers, bimetallic nanowires are synthesized by alternating the depositing materials. The subsequent electron microscopic investigations show two phases on the nanowire. A Cu-rich and a Fe-rich phase as depicted in the figure 2. This proves a root growth fashion. Chemical analysis, such as EDX and EELS are carried out to determine the chemical distribution in the two different phases.

The Si substrates are sensitive to the deposition temperature. At temperature lower than 650°C, interdiffusion of Cu and Si happens in both wires and the substrate, which gives result of the formation of Cu_xSi_y alloys. To avoid the interdiffusion, barrier layers (W) and other substrates (W, MgO, Al_2O_3, Nitride Si) are applied. It turns out that the wires can be obtained on different substrates with the aids of amorphous C layer, while the C layer provides preferred nucleation sites for the wire growth.

The electrical and magnetic properties are tested for Cu and Cu/Fe wires separately. Both 726ft he tests indicate the promising potential 726ft he726 applications 726ft he wires.

1. G. Richter, K. Hillerich, D. Gianola, *et al*. *Nano Letters,* 2009*, 9*, 3048-3052.

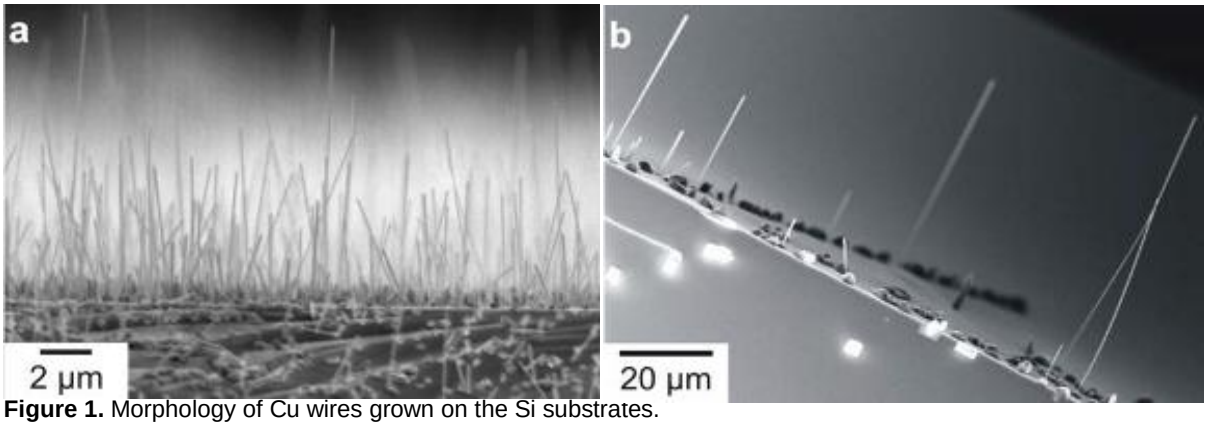

Figure 1. Morphology of Cu wires grown on the Si substrates.

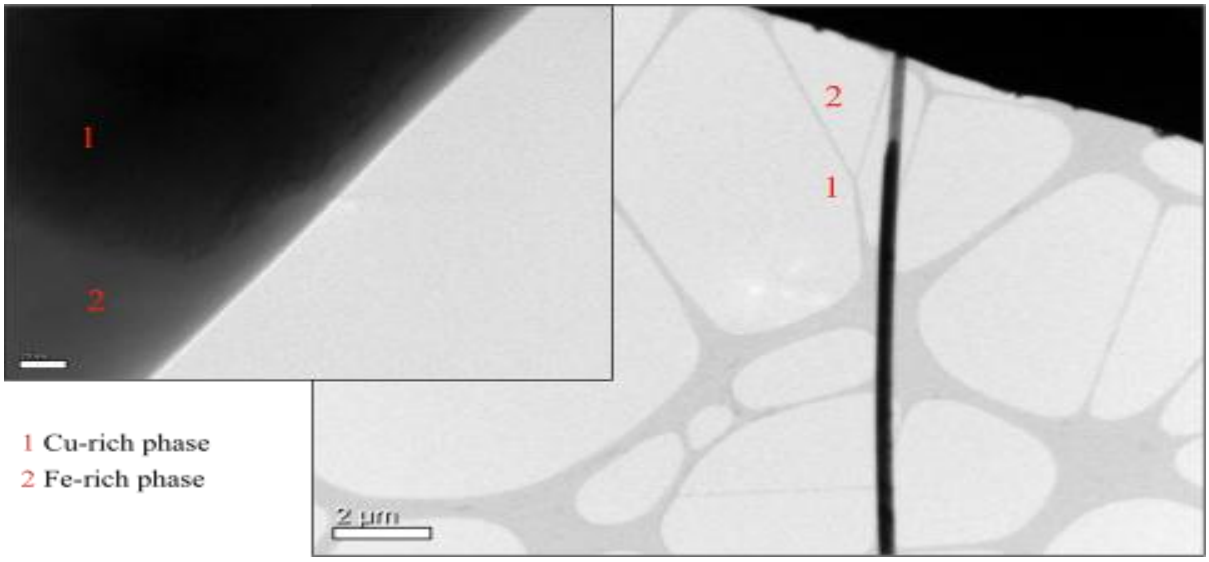

Figure 2. Indication of the 2 different phases on the Cu/Fe wires.

Low Dimensional Materials and Catalysts

MS.7.P204
Internal architecture in coffin-shaped ZSM-5 zeolite crystals unraveled by FIB-assisted TEM

J. Lu[1], D. Schryvers[1], M. Roeffaers[2], E. Bartholomeeusen[2], B. Sels[2]

[1]University of Antwerp, Physics, Antwerp, Belgium
[2]Catholic University of Leuven, Bio-engineering, Leuven, Belgium

nick.schryvers@ua.ac.be
Keywords: internal architecture, intergrowth, zeolite, FIB, TEM

Zeolites play an important role in acid-base heterogeneous catalysis. Zeolite ZSM-5 crystals possessing the MFI (mordenite framework inverted)-type micro-porous structure have drawn much attention because of their industrial applications as a leading shape selective catalyst in the synthesis of dimethylbenzene. The MFI-type structure is based on an orthorhombic crystal lattice with Pnma space group and lattice parameters a=2.0108nm, b=1.9918nm and c=1.3392nm. This structure contains straight channels (5.6×5.3 $Å^2$) along the crystallographic b-axis that are interconnected with sinusoidal channels (5.5×5.1 $Å^2$) along the a-axis. These channels control the transport of reagents and products and induce shape selectivity. In order to get a complete picture of the catalytic properties and structure-function relationship of this crystal, it is crucial to obtain fundamental knowledge on their microstructure and internal architecture [1-4]. In the present study, an approach combining optical microscopy, FIB and TEM which provides site-specific direct observation of crystallographic orientations and microstructure features in bulk samples is employed to investigate the intergrowth and internal architecture in coffin-shaped ZSM-5 crystals in which hourglass-like contrast was observed by optical microscopy. Figure a shows an optical transmission microscopy image of a crystal revealing the hourglass-like contrast inside. Figure b shows a SEM image of the same crystal observed by SEM. The white bars indicate the positions where three FIB lamellae were prepared. Figure c shows a low magnification composite STEM image of lamella A, the top of the image corresponding with the top surface of the coffin as seen in Figure b. In between the double dashed lines are the interfaces between different intergrowth components. Figure d shows a bright field image from the white square enclosed central part of lamella A. The inset shows a selected area diffraction pattern form the middle component, indicating a horizontal b-axis. Figure e shows a diffraction pattern from the white circle enclosed interface area in Figure d now revealing two variants and indicating the interface is a 90°rotational boundary. Figure f shows a low magnification STEM image of lamella B while Figure g shows a low magnification STEM of lamella C. A higher magnification STEM image of the white rectangle is shown on the left side of Figure g. The interfaces between different intergrowth components in Figures f and g are indicated by single dashed lines. The arrows indicating the [010] orientations of each component in Figures c, f and g were obtained from the corresponding diffraction patterns. Figure h shows a schematic of the internal architecture of the crystal for the so-called 2 component model which was proposed in [4,5] and which matches to a large extend the present observations. Indeed, in this model, besides the main central component, the crystal contains two pyramid-like components, one on each side and which are rotated by 90°along the common c-axis (the long axis of the coffin shape). In the coffin investigated in the present study, the interfaces between the components are less straight than in the model and show local zigzag features. According to the image in Figure c the pyramid-like intergrowth components in the middle of the crystal do not seem to touch, but the FIB cross-section could be slightly off center.

1. L Karwacki *et al.*, Nat. Mater. 8 (2009) 959.
2. MBJ Roeffaers *et al.*, J Am. Chem Soc. 130 (2008) 13516.
3. MBJ Roeffaers *et al.*, J. Am. Chem. Soc. 130 (2008) 5763.
4. MBJ Roeffaers *et al.*, Ang. Chem. 46 (2007) 1706.
5. GD Price, *et al*., J. Am. Chem. Soc. 104 (1982) 5971.
6. The authors thank the FWO for financial support

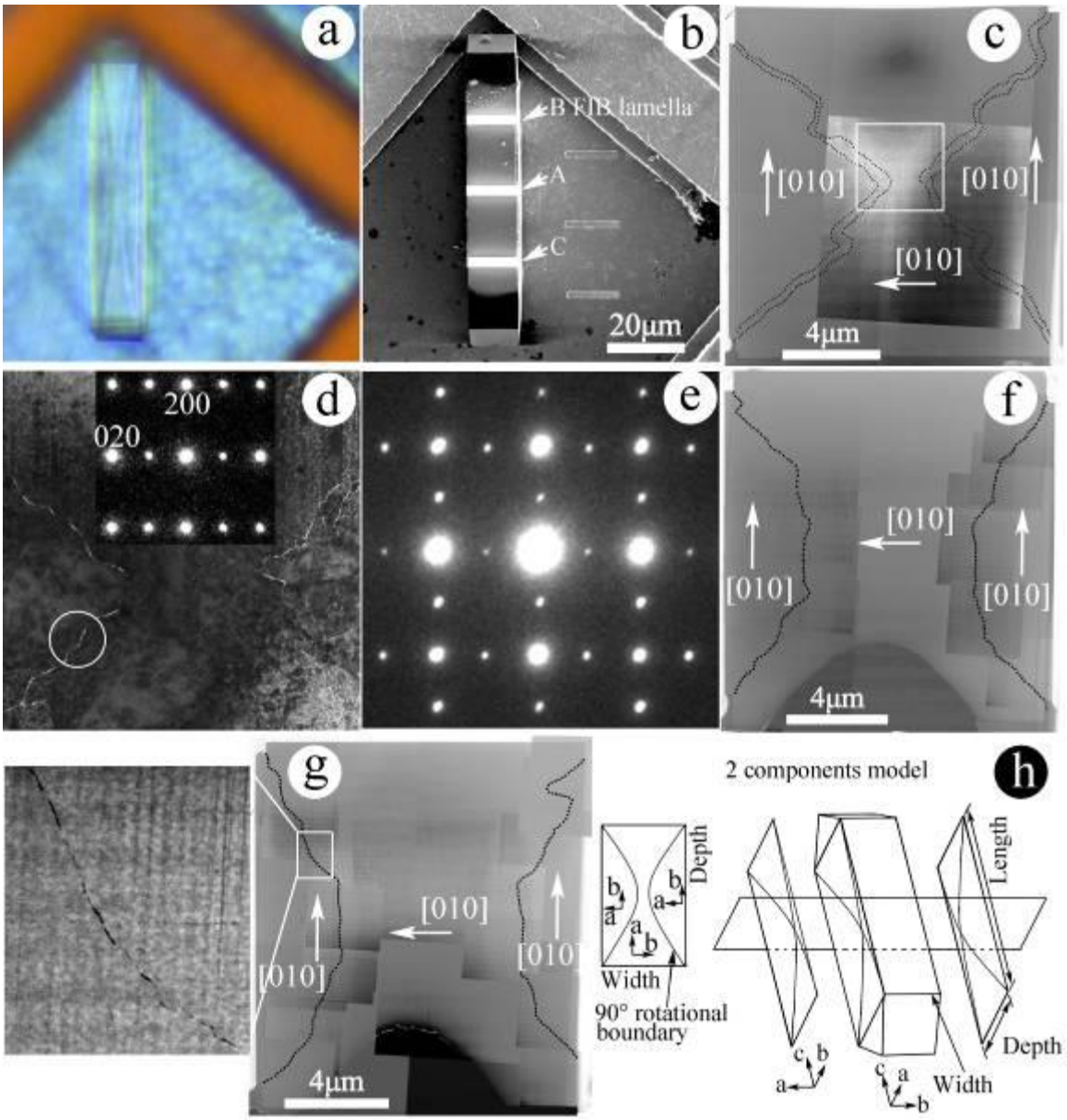

Figure (a) optical microscopy image of a ZSM-5 crystal, (b) SEM image of the same crystal in (a), (c) low magnification STEM image of lamella A, (d) bright field image of white rectangle enclosed area in (c), (e) diffraction pattern from the white circle enclosed interface in (d), (f) low magnification STEM image of lamella B, (g) low magnification STEM image of lamella C, (h) proposed 2 component model of internal architecture of the crystal.

Low Dimensional Materials and Catalysts

MS.7.P205
Towards controllable growth of SiGe single and double quantum dot nanostructures

Y. Ma[1], S.F. Huang[1], C. Zeng[2], T. Zhou[1], Z. Zhong[1], Y.L. Fan[1], X.J. Yang[1], J.S. Xia[2], Z.M. Jiang[1]

[1]Fudan University, Physics, Shanghai, China
[2]Huazhong University of Science and Technology, School of Optoelectronic Science and Engineering, Wuhan, China

biglan001@gmail.com
Keywords: MBE, single quantum dot, double quantum dot

Fabrication of semiconductor single and double quantum dot (QD) nanostructures is of utmost importance due to their promising applications in the study of advanced cavity quantum electrodynamics [1], quantum optics [2] and solid-state spin qubits [3]. For those applications, one of the greatest challenges is the precise control of positions of the QDs. For applications based on single QDs (SQDs), fabrication of QDs with low areal density and at controllable sites is highly desirable. For the applications of double QDs (DQDs), a scalable self-assembled DQD system with precise control of dot spatial position, dot size and interdot spacing (the distance between the apexes of two dots in a DQD) is in demand. Morever, for a DQD system, by controlling the interdot spacing between two QDs, one can systematically study the coupling and coherence of electronic states in the two QDs that are strictly necessary for the creation of future functional units in quantum computing.

In this paper, we focused on the controllable growth of SiGe SQD and DQD nanostructures on nanhole-patterned Si substrates via molecular beam epitaxy (MBE). An ultra-low areal density down to $1x10^7$ cm^{-2} was achieved for both SQDs and DQDs with the corresponding periodicity as large as 3 μm. The SiGe DQD occupation in the nanoholes showed critical dependence on the Ge deposition amount. We also demonstrated that the interdot spacing between the two dots in a DQD could well be adjusted by varying the nanohole elongation ratio.

Figures 1(a) and (b) show the nanoholes with precisely controlled sizes and shape fabricated on the Si (001) surfaces via electron beam lithography (EBL) and reactive ion etching (RIE). The nanoholes are elongated along Si <110> with different length-width ratios (*r*).By optimizing the growth parameters, SQDs and DQDs were both realized on nanohole-patterned substrates with a periodicity down to 3 μm, as shown in figures 1 (c) and (d), respectively. Figures 2(a)-(d) show the three-dimensional (3D) morphology evolution of a DQD unit-cell at different Ge deposition amounts, 2.4, 3.0, 3.6 and 4.4 ML respectively. The AFM linescans crossing the DQD structures along Si <110> in figures 2(a)-(d) were shown in figure 2(e). It was found that only in a narrow Ge amount 'window' the DQD was formed. Neither too little or overdose Ge amount resulted in the formation of DQDs. Figures 3(a)-(c) show AFM images of a SiGe DQD grown on nanohole patterns with different elongation ratios of *r*. Figure 3(d) clearly shows that the interdot spacing monotonically increases with increasing *r*.

For nanoholes with a certain elongation ratio (e.g. *r*=3), whether a SQD or DQD formed at the nanoholes was found to be pre-determined by the Si buffer layer growth temperature, which was explained by different surface chemical potential distributions in the nanoholes after the buffer layer growth at different temperatures. Figures 4(a)-(c) show the surface morphologies of the nanoholes after growth of Si buffer layer at different temperatures. Figures 4(d)-(f) show the corresponding AFM images of the SiGe DQDs, which were grown by deposition 3.6 ML Ge at 450-550℃. It is found that low buffer layer growth temperature benefits the DQD formation. Figures 4(g)-(i) show the calculated surface chemical potential distributions for the nanoholes as shown in figures 4(a)-(c), respectively. The calculated results confirm that the SiGe QDs nucleate and grown at the sites of surface chemical potential minimum. Two minimum sites appear in the nanohole (figure 4(g)) for which the Si buffer layer is grown at the low temperature of 350℃ (figure 4(a)), which assures the growth of a DQD in a single nanohole.

1. V. Baumann, et al., Appl. Phys. Lett. 100, (2012), 091109.
2. Z. L. Yuan, et al., Science 295, (2002), 102.
3. B. M. Maune, et al., Nature 481, (2012), 344.

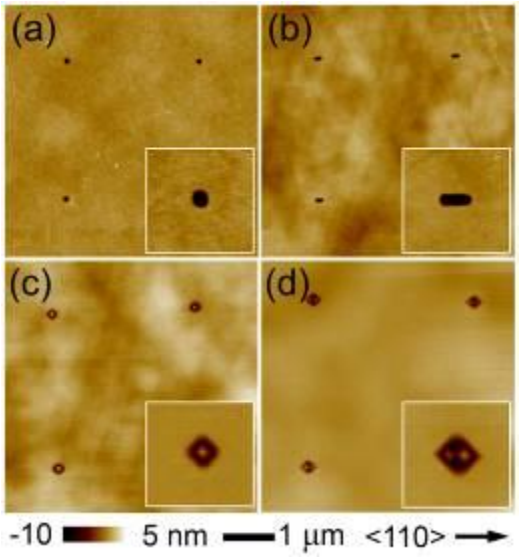

Figure 1. AFM micrographs of the nanohole pattern with a periodicity of 3 μm and different ratios of *r*. (a) *r*=1 and (b) *r*=3. Surface morphologies of the SiGe SQD (c) and DQD (b) grown on (a) and (b), respectively. Insets show enlarged AFM images of a single nanostructure.

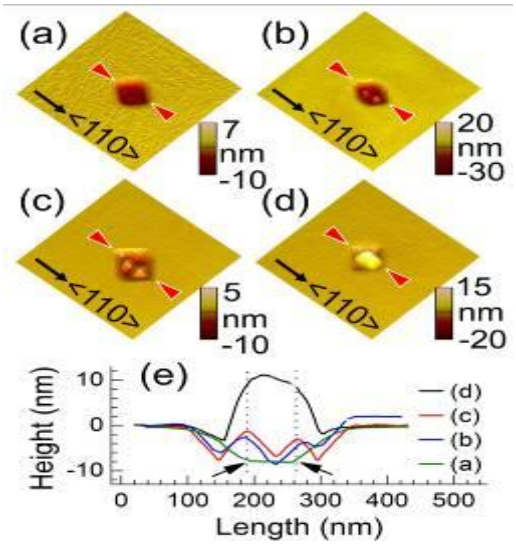

Figure 2. 3D AFM images of SiGe DQDs during the deposition of Ge (a) 2.4 ML, (b) 3.0 ML, (c) 3.6 ML and (d) 4.4 ML for nanoholes with r=3. The images are 800 x 800 nm2 in size. (e) The height profiles of the DQDs in corresponding evolution stages. The arrows and dash lines indicate the nucleation positions of the DQDs.

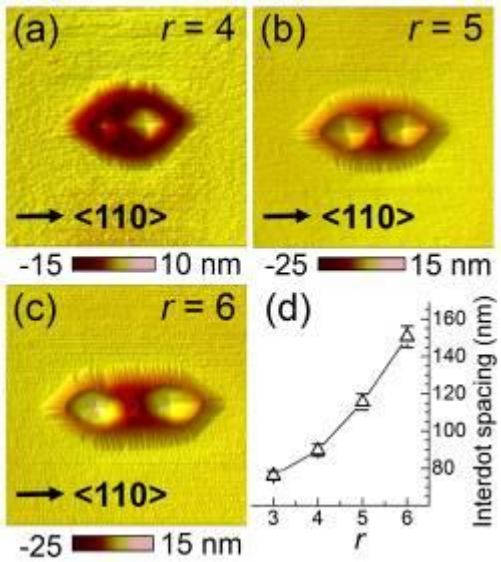

Figure 3. AFM micrographs of a single SiGe DQD unit-cell grown on nanohole patterns with different nanohole elongation ratios, (a) *r*=4, (b) *r*=5, (c) *r*=6. (d) The interdot spacing as a function of the elongation ratio. The images are 500 nm x500 nm in size.

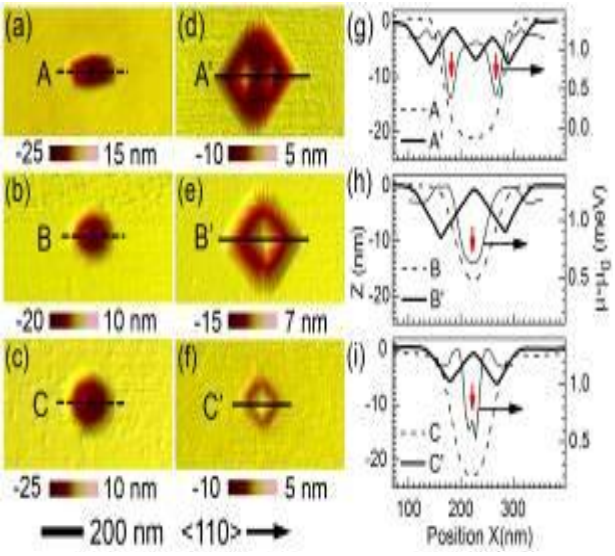

Figure 4. AFM micrographs of the nanoholes (*r*=3) after growth of a 45-nm-thick Si buffer layer at different temperatures, (a) 350℃, (b) 400-450℃, (c) 450℃, and the corresponding DQD growth results (d)-(f). (g)-(i) show the corresponding height profiles along the lines indicated in the AFM micrographs, along with the calculated surface chemical potential distributions in the nanoholes after the buffer layer growth.

Low Dimensional Materials and Catalysts

MS.7.P206
Growth, microstructures and optical properties of coupled three-dimensional Ge quantum dot crystals

Y. Ma[1], Z. Zhong[1], T. Zhou[1], X. Yang[1], Z. Jiang[1]

[1]Fudan University, State Key Laboratory of Surface Physics and Department of Physics, Shanghai, China

biglan001@gmail.com
Keywords: SiGe, quantum dot crystals, coupled, MBE, AFM, Photoluminescence

High density and three-dimensionally (3D) ordered quantum dot (QD) arrays have been referred to as quantum dot crystals (QDCs) [1]. The strong coupling among densely ordered QDs in QDCs may provide a path for the engineering of band structure and functionalities. Various physical phenomena, including electrostatic interactions [2], localized states splitting and associated quasimolecular states [3] have been studied in coupled GeSi QD systems. Generally, in 3D artificial QDCs, the QDs play a role similar to that of atoms in real crystals. The band offsets at the interfaces between the QD and the matrix in the QDC also play a role analogous to the periodic potential in real crystals. When QDs are 3D ordered, uniform and in close proximity to one another, significant carrier wave function overlap occurs. Thus, the discrete energy levels of a single QD will split into extended states and emerge as 3D minibands. Considering the compatibility with the sophisticated Si integration technology, there is a substantial motivation to investigate both the fundamental properties and the device applications of miniband formation in GeSi QDC.

In this paper, high density and 3D ordered GeSi QDCs are realized by multilayer growth of QDs on pit-patterned silicon on insulator (SOI) (001) substrates via nanosphere lithography. The QDs are arranged laterally in a hexagonal lattice with a periodicity of 100 nm. The vertical period of the QDCs is ~7 nm. A systematic investigation of the photoluminescence (PL) spectra of this QDC is performed. Both non-phonon (NP) recombination and transverse-optical (TO) phonon replica of excitons in the QDC are observed. The nearly nonshifted PL peaks and the decrease of the full width at half maximum (FWHM) of the TO peak with increasing excitation power are examined. These characteristics are explained in terms of miniband formation due to the strong coupling of closely adjacent dots and the emergence of quasioptical phonon modes due to periodic scatters in the QDC, respectively. Such unique features of QDCs can improve the optical properties, the carrier transportation, and the thermoelectricity, which may have promising applications in optoelectronic and thermoelectric devices.

1. D. Grützmacher, et al., Nano. Lett. 7, 3150 (2007).
2. M. Manoharan, et al., Appl. Phys. Lett. 92, 092110 (2008).
3. C. B. Li, et al., Electron. Lett. 46, 940 (2010).

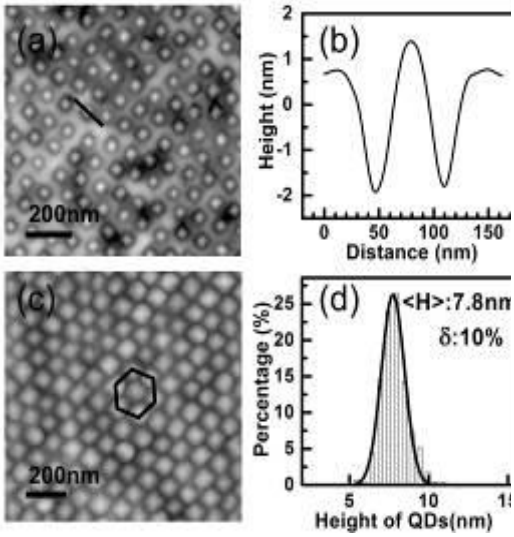

Figure 1. (a) AFM image of the ordered pyramid shaped QDs in the first layer of the QDC (bottommost layer of QDs). (b) Height profile along the line shown in (a). (c) AFM image of

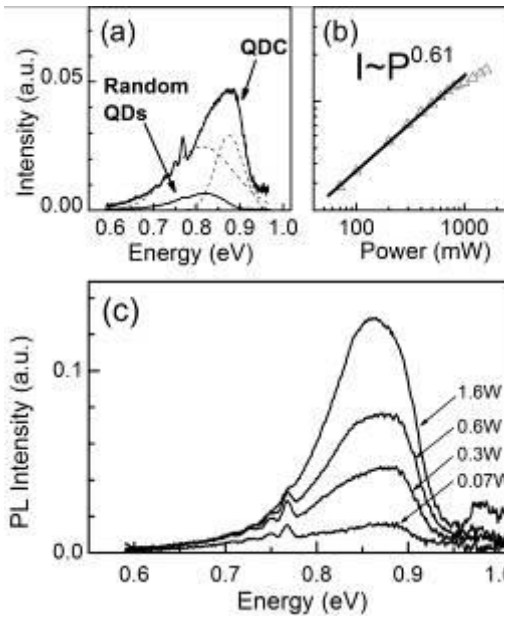

Figure 3. (a) PL spectra of the capped fifteen-layer ordered and random QDs sample at 16 K, under excitation power of 0.3 W. The decomposed NP and TO PL peaks are indicated by dash-lines. (b) Integrated PL intensity of QDs as a function of excitation power. (c) PL spectrum of the fifteen-layer ordered QDs sample as a function of excitation power at 16 K.

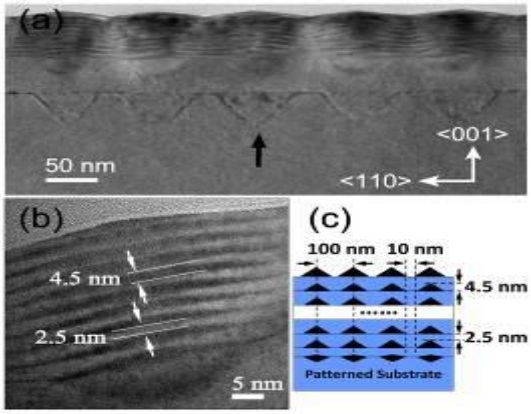

Figure 2. (a) Cross-sectional TEM image of a ten-layer GeSi QDC. The short black arrow indicates a nanopit on the substrates. (b) HRTEM image of a QD column. (c) Schematic side view illustration of the QDC structure.

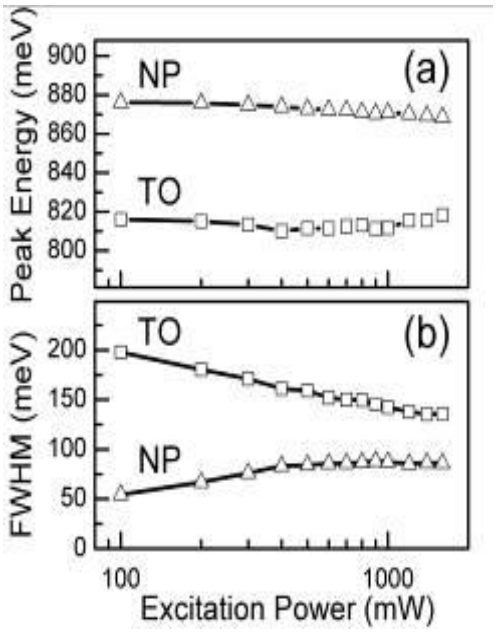

Figure 4. (a) The peak energy, (b) the FWHM of the NP and the TO peaks of QDs as a function of excitation power.

Low Dimensional Materials and Catalysts

MS.7.P207
Coupling effects of Ge/Si quantum dots studied by conductive atomic force microscopy and Kelvin probe force microscopy

F. Ye[1], Y. Zhang[1], Y. Lv[1], X. Yang[1]

[1]Fudan University, State Key Laboratory of Surface Physics Department, Shanghai, China

09110190004@fudan.edu.cn
Keywords: Coupling effects, GeSi quantum dots, Conductive atomic force microscopy, Kelvin force microscopy,

Coupling effects of semiconductor quantum dots have been received intensive attentions for both basic physical understanding and possible applications in electronic devices.[1] Therefore, it is essentially important to understand their electrical properties, especially at nanoscale.

The coupling effects of self-assembled GeSi quantum dots (QDs) are investigated by conductive atomic force microscopy (CAFM) and Kelvin probe force microscopy (KPFM) on single-layer (SL) and bilayer (BL) GeSi QDs with different dot densities at room temperature. By comparing their average currents, it is found that the BL and high-density QDs are more conductive than the SL and low-density QDs with similar sizes. On the other hand, the average current of the BL QDs increases much faster with the bias voltage than that of the SL QDs does, indicating the existence of both lateral and vertical coupling effects[1].

To fully reveal the physical nature GeSi QDs' electrical properties, I-V curves are measured on two kinds of QDs (small pyramid QDs and dome-shaped ones). We observed stair-like I-V curves both on BL and high density QDs except low density SL QDs. Our results suggest that the QD's electrical properties can be greatly regulated by the coupling effects and voltages, which are valuable for potential applications.

After conductance measurements, KPFM allow us to investigate the composition and electronic state of the local structures. We found that contact potential difference (CPD) is lower on GeSi QDs than wetting layer, and CPD value difference between QDs and wetting layer is larger on BL and high-density QDs. Our KPFM results suggest a lower Schottky barrier for BL and high-density QDs because their electronic state have been changed by their coupling.

1. Lijuan Wang, Armando Rastelli,and Oliver G. Schmidt, Adv. Mater. 21(2009), 2601–2618
2. Yifei Zhang, Fengfeng Ye, and Xinju Yang, Nanoscale Res Lett. 7 (2012), 278.

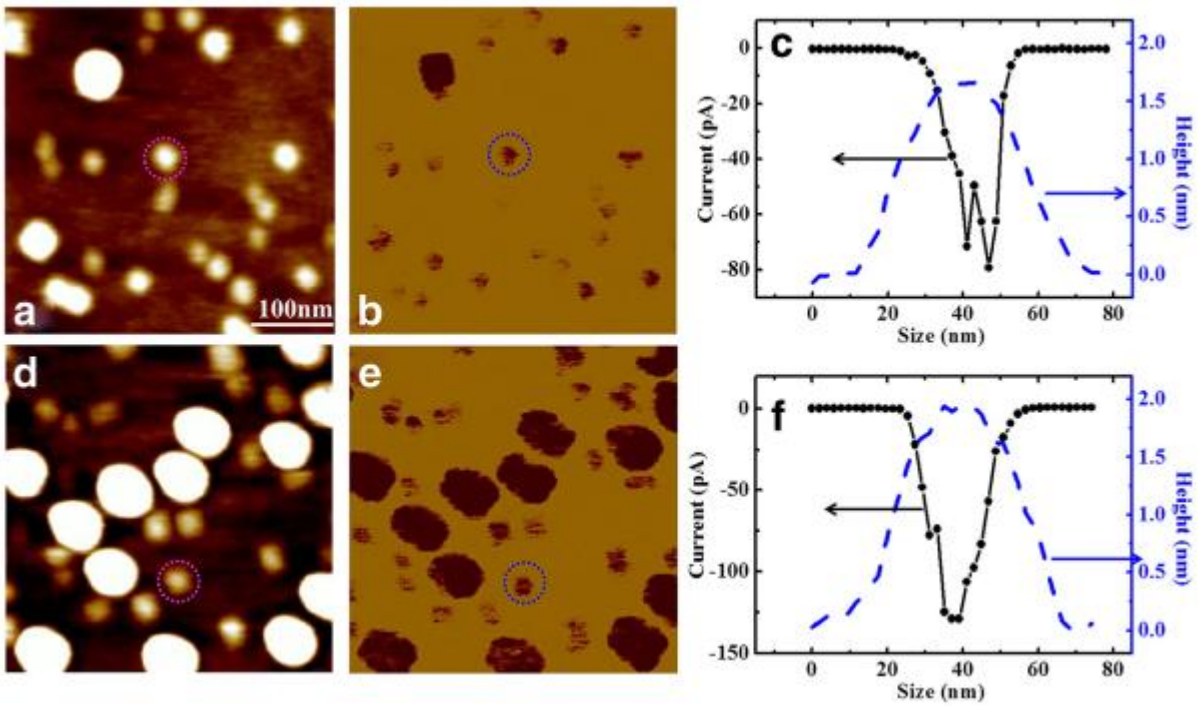

Figure 1. Topography and current images of low-density QDs with height and current profiles of small QDs. Topography and current images of SL QDs (a, b) and BL QDs (d, e) with low dot densities. The height and current profiles of the marked small QDs of sample A and sample B are plotted in (c) and (f), respectively. It shows that the two marked QDs have similar sizes, but the current of the BL QD is about two times larger than that of the SL QD.

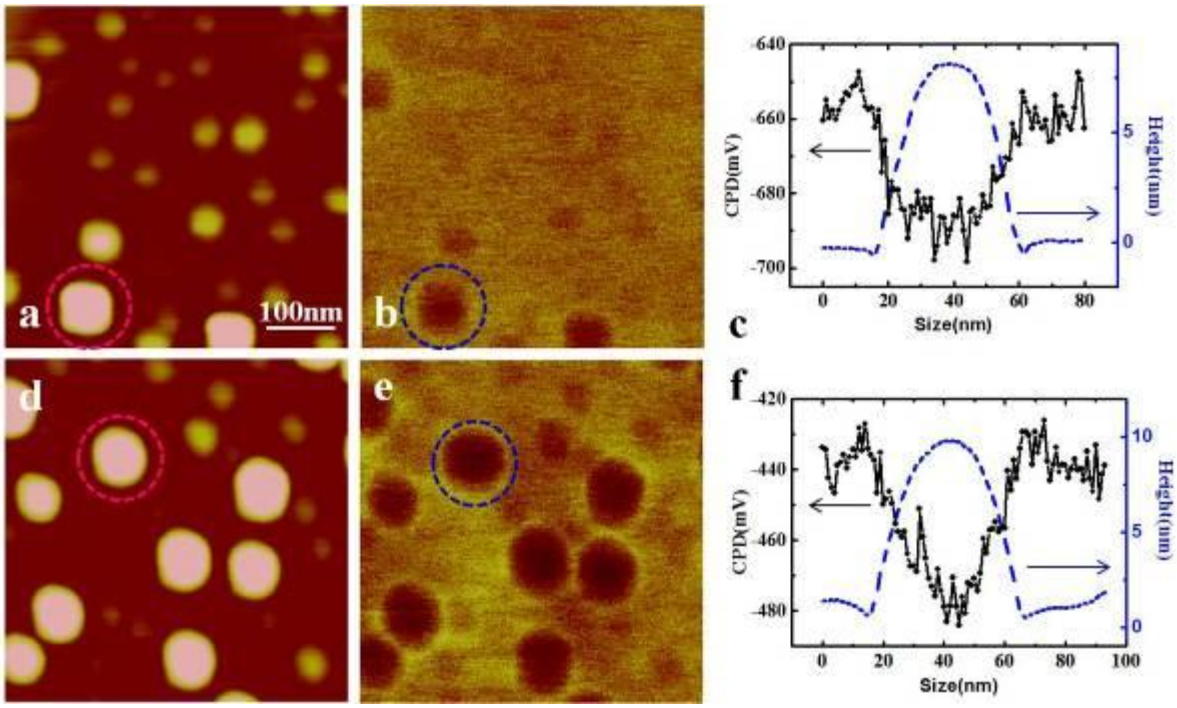

Figure 2. Topography and CPD images of low-density QDs with height and CPD profiles of large QDs. Topography and CPD images of SL QDs (a, b) and BL QDs (d, e) with low dot densities. The height and current profiles of the marked small QDs of sample A and sample B are plotted in (c) and (f), respectively.

Low Dimensional Materials and Catalysts

MS.7.P208
Interaction between electronic and mechanical degrees of freedom in graphene: probing by electron diffraction

D. Kirilenko[1,2]

[1]Ioffe Institute, St-Petersburg, Russian Federation
[2]EMAT, Universiteit Antwerpen, Antwerp, Netherlands

Demid.Kirilenko@mail.ioffe.ru
Keywords: graphene, corrugation, flexural phonons

Graphene can be considered as a specific form of matter – an electronic membrane [1,2,3]. So that the structure of a graphene sheet is formed in a strong interaction with charge carriers, which are easily generated in gapless graphene. It is well known that free-standing graphene undergoes severe corrugation [4]. The main reason for this is flexural phonons or, in other word, out-of-plane thermal oscillation which amplitude reaches several interatomic distances even at room temperature. The corrugation can also be induce by ad-atoms on graphene surface. Independently on its nature deformation of the crystal structure causes local shift of energy levels and, because of zero gap, considerable changes in charge carriers density distribution [5]. The strong coupling of the electronic behaviour with surface morphology makes graphene a sophisticated material to study.

Theory of the corrugation induced by thermal oscillations is quite non-trivial because of strongly anharmonical dynamics of flexural phonons [6]. Various models are presented in literature which differ significantly concerning the short wave-vectors range of the flexural phonon spectrum. Taking into account strain-induced charge carriers density inhomogeneities enormously complicates the task. For example, the effect suggests a specific thermal dependence of the graphene electronic properties; however, the problem is still unresolved [7].

In order to get some experimental knowledge on the issue of charge carriers-corrugation interaction we urged electron diffraction, which has shown itself as a useful tool for assessment of the corrugation of suspended graphene sheets [8]. A dynamic corrugation induce by flexural phonons can not be seen by direct imaging or low-speed scanning used by probe microscopies. At the same time, electron diffraction provides information about rapidly changing corrugation because of small time of the fast electron interaction with the specimen. Using electron diffraction one gets square of the corrugation spectrum averaged over the time of exposure, which can be extracted from diffraction tilt series. The feature of the diffraction imaging in transmission electron microscopes (TEM) is the high spatial coherency of the electron beam, which reaches 50nm in case microscopes equipped with field-emission electron gun. It allows to reach wave-vectors as small as $10^{-2}Å^{-1}$ in our measurements of the corrugation spectrum. From the right side the range is limited by low amplitude of the spectrum, which decrease as q^{-4} at this range, and can be estimated as 0.5 $Å^{-1}$.

. Interaction of the electron beam, used for obtaining of diffraction patterns, induces generation of electron-hole pairs in graphene, thus, increasing charge carriers density, which might have impact on corrugation state. One can vary charge carriers density by changing intensity of the beam. Measuring corrugation spectrum at different beam intensities provides an experimental evidence of the influence of the graphene electronic state on its structure. We have found shift of the harmonic-anharmonic border in flexural phonon spectrum with increasing beam current density, which designates the influence of increased charge carriers density. Change in small wave-vector range of the spectrum were found to be more prominent, since average electron wave-vector lays in this range.

It is very important to exclude possible effect of temperature change on our measurements, since electron beam also causes a Joule-heating of the specimen. In order to do this, we performed measurements of the corrugation spectrum under constant heating at temperatures up to 200ºC and found some change slight change in long wave-vector range of the spectrum. Our estimations of the sheet temperature increase due to effect of the incident electron beam show, that taking into account the superior thermal conductivity of graphene it is unlikely to be higher than several centigrade. So that the effect of the specimen temperature change in our experiments with varying beam currant density might not cause serious errors.

Thus, influence of the charge carriers density on corrugation of suspended graphene can be measured and degree of the specific electron-phonon coupling estimated.

1. E.-A. Kim and A. H. Castro Neto, Europhysics Letters 84 (2008), 57007.
2. D. Gazit, Phys. Rev. B 80 (2009), 161406(R).
3. P. San-Jose, J. Gonzalez and F. Guinea, Phys. Rev. Lett. 106 (2011), 045502.
4. J.C. Meyer, A.K. Geim et al., Nature 446 (2007), p. 60.
5. M. Gibertini, A. Tomadin et al., Phys. Rev. B 85 (2012), 201405(R)
6. A. Fasolino, J.H. Los and M.I. Katsnelson, Nature Materials 6 (2007), p. 858.
7. S. Das Sarma, S. Adam et al., Rev. Mod. Phys. 83 (2011), p. 407.
8. D.A. Kirilenko, A.T. Dideykin and G. Van Tendeloo, Phys. Rev. B. 84 (2011), 235417.

Low Dimensional Materials and Catalysts

MS.7.P209
Morphology of a thermally processed (1:1) AuPd alloy heterogeneous catalyst

E. Teixeira Neto[1], D.O.A. dos Santos[1], A.A. Teixeira Neto[2]

[1]Institute of Chemistry/University of Sao Paulo, Fundamental Chemistry, Sao Paulo, Brazil
[2]Universidade Federal do ABC, Centro de Ciências Naturais e Humanas, Santo André, Brazil

erico@iq.usp.br
Keywords: bimetallic catalyst, morphological development, XEDS-spectrum imaging.

The enhancement in catalytic activity that results from the addition of a metal co-catalyst to a monometallic catalyst has been an important subject of discussion within the catalysis community. The bimetallic system AuPd has been intensively investigated and employed as catalyst for many important applications such as CO oxidation, hydrogen peroxide synthesis and formic acid decomposition for hydrogen generation. It has been recognized that the control of the distribution of metallic domains within individual bimetallic particles plays a critical role in achieving target properties. [1]

Bimetallic nanoparticles may have different metallic domain distributions like homogeneous alloys, core-shell and twinned particles. Planned morphologies may be obtained by heat processing the catalyst material in controlled atmospheres. Due to the very small size and spatial dispersion of these metal particles, direct evidence of the kind of Au/Pd interaction is difficult to be obtained from common physical characterization methods. Transmission electron microscopy (TEM) is a powerful technique for the investigation of this kind of system, providing resolution enough to differentiate the individual nanoparticles. The instrument can be operated in the scanning-TEM (STEM) mode for the acquisition of X-ray energy dispersive (XED) spectrum images (SI). Elemental maps may be obtained from the XEDS-SI data cubes, providing spatially resolved compositional information on the system. [2]

In this work we show results on the determination of the morphological characteristics of an alloyed (1:1) AuPd/C (10% m/m) catalyst. This material was prepared by suspending the carbon support in a colloidal suspension of (1:1) AuPd nanoparticles and subsequently drying the mixture in a rotatory evaporator. The catalyst material was thermally processed in N_2 atmosphere at 400°C for 1 h. X-ray diffraction (XRD) data was acquired from this material and the characteristic peaks of an AuPd alloy were obtained. The images and spectroscopic information shown here are representative of a detailed investigation of this system.Figure 1 shows a bright field (BF-STEM) image of a region of the AuPd catalyst material. Individual particles appear as dark spots in the image, supported on a light gray carbon support. In the elemental maps of the area marked by a black square in BF, the good correspondence observed in the distribution of bright of both Au and Pd maps is an evidence of the compositional uniformity of the material. Figure 2 shows BF and HAADF images of a catalyst region. In Fig. 2-BF, small particles (smaller than 10 nm) are shown in Areas 1 and 2 along with a part of a large dark particle to the left of the image. In Fig. 2-HAADF, the small particle in Area 2 appear brighter than the particles in Area 1 and very small bright spots (very small particles) are visible on the support surface. These very small bright particles are not observed in Fig. 2-BF. Elemental maps of Area 1 show that the Pd Lα counts measured are distributed throughout the support and are concentrated at the particles. Any Au Lα count was measured in this Area and the Au map show the distribution of the background XEDS counts. The elemental maps of Area 2 show the few measured Au counts concentrated at the particle position and the Pd distributed both at the particle and dispersed throughout the support. These observations show an effect of the thermal treatment on the AuPd alloyed particles that was not determined by XRD. We have evidence of an exudation of Pd from the alloy, possibly in the form of PdO_x clusters, that are homogeneously distributed on the carbon support. This description of the metallic distribution represents a new morphological understanding of this system and will provide new arguments to the understanding of this catalyst performance.

1.. Y. Huang, X. Zhou, M. Yin, C. Liu and W. Xing, Chemistry of Materials 22 (2010), p. 5122.
2.. A.A.Herzing, A.F. Carley, J.K. Edwards, G.J. Hutchings and C.J. Kiely, Chemistry of Materials 20 (2008), p. 1492.
3.. Acknowledgements Fapesp and LME-LNNano-CNPEM (JEOL JEM 2100F).

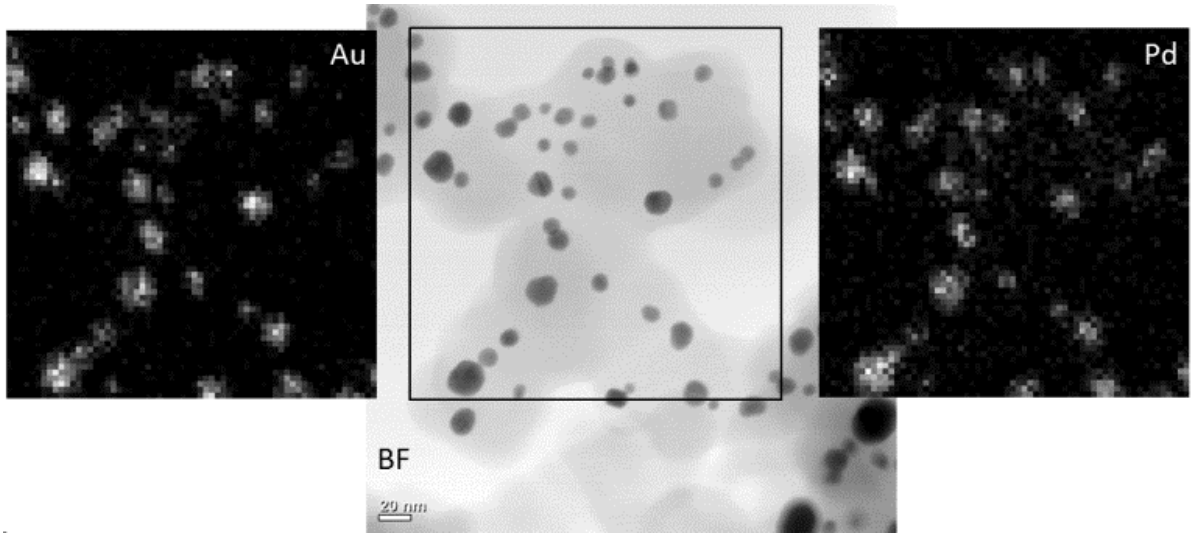

Figure 1. BF-STEM image of alloyed AuPd (1:1) catalyst particles deposited on a carbon support and XEDS elemental maps of the marked area. The observed correspondence in the Au and Pd elemental maps is an evidence of the catalyst compositional homogeneity. Scale bar corresponds to 20 nm.

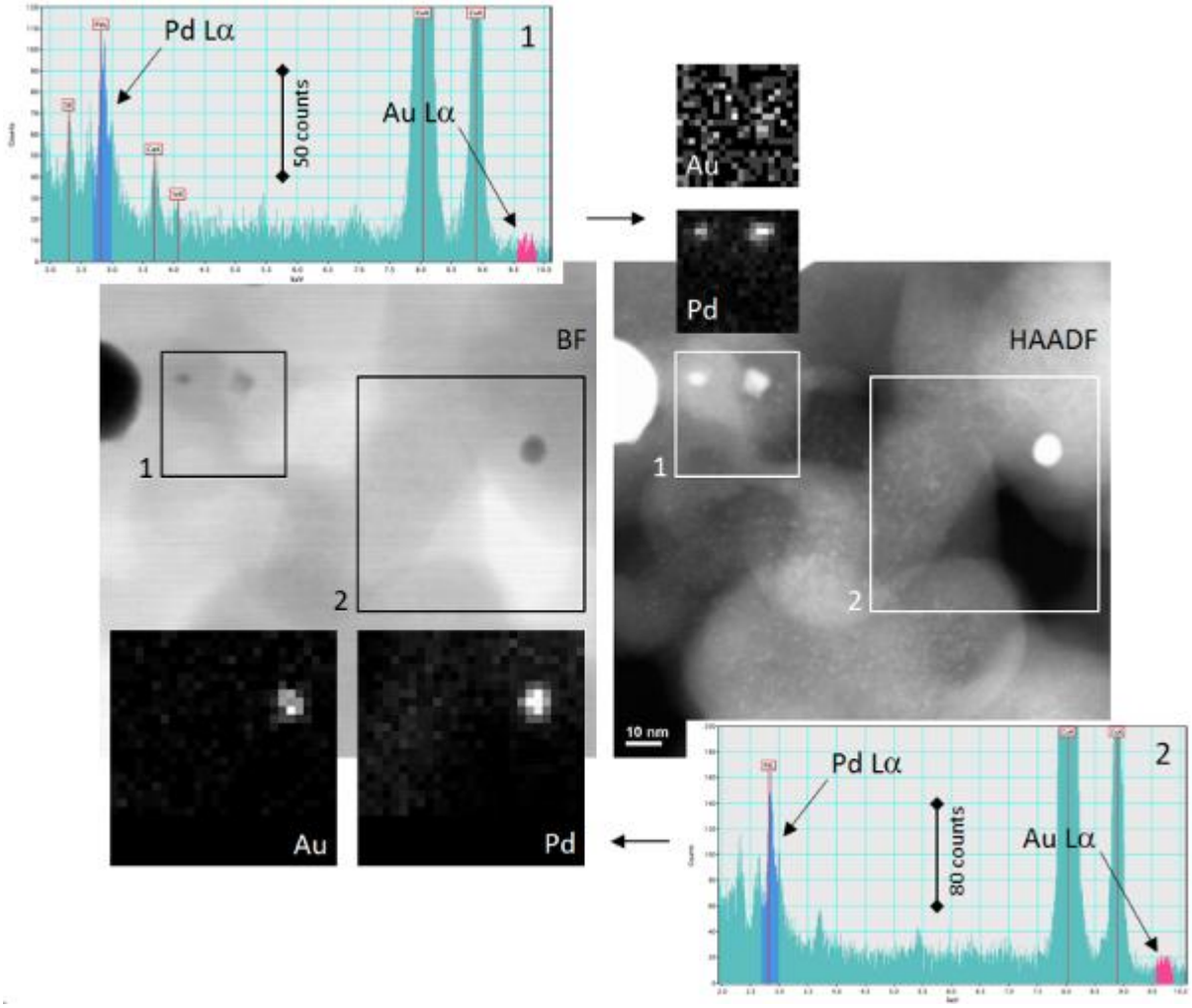

Figure 2. BF and HAADF images of a AuPd (1:1) catalyst region and XEDS elemental maps of the indicated areas. The two irregularly shaped particles in Area 1 appear bright in the HAADF image; any Au was measured in Area 1 and Pd is concentrated at the positions of the particles. The small rounded particle in Area 2 appears very bright in the HAADF image, along with very small bright spots distributed on the support surface. The corresponding elemental maps show the few measured Au counts concentrated at the particle position and the Pd distributed both at the particle and dispersed on the support. Scale bar corresponds to 10 nm.

Low Dimensional Materials and Catalysts

MS.7.P210
In-situ chlorine etching of nanowires by focused electron beam - a direct-modification approach for tailoring nanowire properties

H.D. Wanzenboeck[1], J. Mika[1], I. Bassem[1], M. Shawrav[1], A. Lugstein[1], E. Bertagnolli[1]

[1]Vienna University of Technology, Inst. f. Solid State Electronics, Vienna, Austria

Heinz.Wanzenboeck@tuwien.ac.at
Keywords: electron beam, chlorine, etching

Scanning electron microscopy is not only a high-resolution imaging technique for nanocharacterisation of materials, but the focused beam of electrons can also be used for inducing chemical reactions in the nanometer-regime. For focused electron beam induced processing (FEBIP) precursor gas is introduced into the vacuum chamber and the electrons interact with precursors adsorbed on the sample surface. It has already been demonstrated, that metalorganic precursors lead to deposition of materials including noble metals such as Pt or Au as well as magnetic metals such as Fe or Co [1,2]. Also the deposition of carbon, tungsten and even of dielectrics such as silicon oxide have been demonstrated.

We have recently introduced a controlled etching process (Fig. 1) that is sustained by the irradiating electron beam. With the semiconductors Si and Ge we have not observed spontaneous etching, while material could be etched in the areas exposed to the electron beam. A clean vacuum chamber is a prerequisite for this process [3] and has been achieved with an in-situ ozone cleaning procedure of the chamber.

In this work we report on the controlled etching of Si-nanowires and of Ge-nanowires. Nanowires themselves are smart nanomaterials with very promising characteristics and may be used for nanoelectronic devices, innovative sensor concepts and for photovoltaics applications. Focused electron beam induced etching (FEBIE) offers a further alternative to modify these nanomaterials in-situ in a SEM. With dynamic experiments in the SEM we have investigated the chemical reactions on the nanoscale. The material modification with regard to, its composition and its electrical has been investigated.

Typically properties of nanowires are defined during synthesis. The custom-designed tailoring of electrical properties of nanowires is essential for the development of new devices. Semiconductor nanowires are already low-dimensional materials but with FEBIE we have managed to modify the shape of nanowires by selectively thinning the nanowires diameter in preselected sections (Fig. 2). FEBIE is a versatile approach for trimming of Si-nanowires as the low-energy electrons inflict no significant crystallographic damage and cause no contamination of the silicon nanowire. This in-situ preparation allows to keep specimens as close as possible to their native state.

With chlorine as etch gas even without geometrical thinning of nanowires the short-term irradiation was observed to result in a change of electrical properties towards a diode-like characteristics. The effect of electron exposure under the presence of molecular chlorine was investigated. Additional to structural studies also an electrical characterisation of contacted Si-nanowires and a TEM nanostructure analysis was performed.

FEBIE has been established as a novel approach that allows for tailoring of material properties by controlled in-situ modification of nano-scaled materials. Potential future applications of FEBIE to design and to develop of new nonmaterial for sensor applications and for photonics applications will be discussed.

1. W.F. van Dorp, C.W.Hagen, A critical literature review of focused electron beam induced deposition , J. Appl. Phys. 104 (8), 081301
2. I. Utke, P. Hoffmann, J. Melngailis, "Gas-assisted focused electron beam and ion beam processing and fabrication" JVSTB 26(4), 1197-1276 (2009)
3. P. Roediger, H.D. Wanzenboeck, G. Hochleitner, G.; E. Bertagnolli, W. Buehler, "Focused electron beam induced etching of silicon by chlorine gas: Negative effects of residual gas contamination on the etching process", J. Appl. Phys. 108(12), 124316 (2010)
4. A. Lugstein, M. Steinmair, C. Henkel, E. Bertagnolli, Scalable Approach for Vertical Device Integration of Epitaxial Nanowires, Nanoletters 9(5), 1830-1834 (2009)

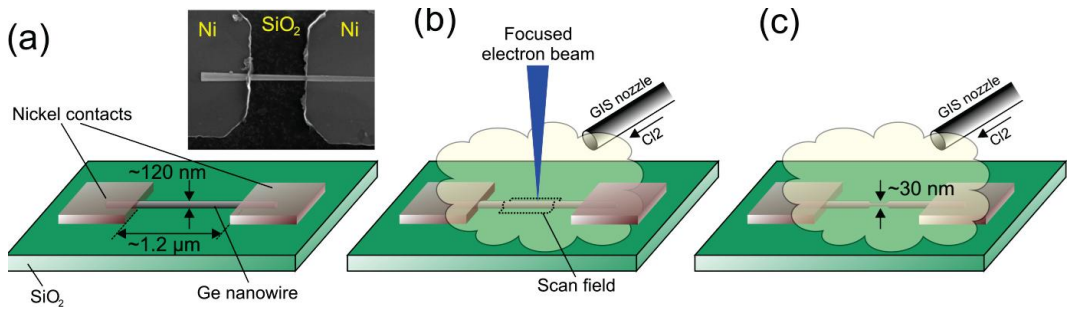

Figure 1. Panorama Schematic process of chlorine-based etching of Si-nanowire with an electron beam

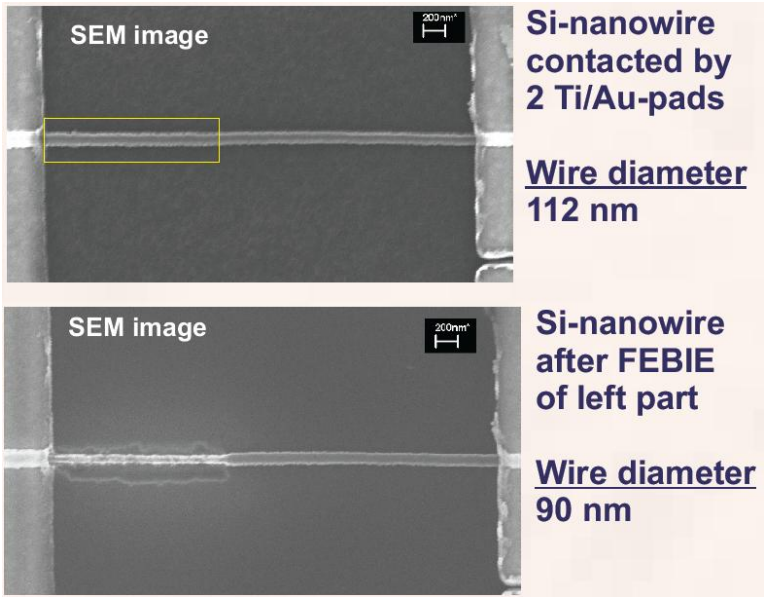

Figure 2. Top view SEM image of a Si-nanowire before and after FEBIE process. Etching by chlorine only occurred in the region scanned with the electron beam.

Low Dimensional Materials and Catalysts

MS.7.P211
Electron holography probing interlayer charge redistributions in folded graphene membranes

L. Ortolani[1], C. Degli Esposti Boschi[1], G.P. Veronese[1], R. Rizzoli[1], J. Simoni[2], R. Mazzaro[1,3], V. Morandi[1]

[1]CNR IMM-Bologna, Bologna, Italy
[2]Trinity College, Dublin, Ireland
[3]University of Bologna, Chemistry, Bologna, Italy

ortolani@bo.imm.cnr.it
Keywords: graphene, holography, DFT

Graphene is a fascinating new material [1], and its peculiar properties hold promises for a great technological impact [2]. Around the Fermi energy, the band structure of graphene presents six conical points where the energy dispersion is perfectly linear in the momentum. For this reason, low energy excitations in graphene exhibit a charge conjugation between electrons and holes, and those carriers can be described as a 2D gas of effective massless Dirac fermions [3]. Unfortunately, upon stacking to form a Few-Graphenes-Crystal (FGC), the weak interlayer interaction could induce small valence charge redistribution in the crystal lattice, suppressing the linear dispersion in the band-structure [4].

In this contribution, we will show that the combination of electron holography and HREM based 3D reconstruction [5] can open interesting capabilities to a combined structural-electrical characterization of graphene membranes based on Transmission Electron Microscopy (TEM) interferometric techniques. More in detail, we will show that, in this framework, electron holography can be used to investigate the effects of the weak charge redistributions occurring upon interaction between stacked graphene layers

Figure 1-A shows the reconstructed phase map of an individual monolayer graphene folded over itself, as experimentally reconstructed following [5] and sketched in the cartoon of Fig. 1-B.: close to the border, where the two layers are curved, the two graphene membranes are stacked at a larger distance that in the internal part of the flake. Figure 2-A) reports an HREM image of a region close to previous one, showing large atomically clean areas and nanometric graphene islands on the surface, while the FFT, reported in the inset, shows the two stacked layers. Phase profile of Fig. 1-B, shows small charge redistribution, in correspondence to the regions where the two layers are separated and decoupled. Therefore, the larger distance between the folded graphene membrane is capable to induce a measurable phase change of 0.01-0.02 rad.

Electronic density and internal potential energy experienced by an electron can be computed using *ab-initio* approaches based on Density Functional Theory with high accuracy on single and multiple graphene layers, provided that the van der Waals bonding is suitably modelled according to recent studies in the literature (see [6] for a recent account). The computed phase-shift values reported in Fig. 2-B, show that for an interlayer distance larger than 0.5 nm the graphene layers start to decouple, resulting in a fully decoupled system for a distance of about 1 nm. Moreover, the computed values are in very good agreement with the ones measured by electron holography. Both these results strongly confirm the experimental results reported above, and at the same time show the capabilities of electron holography in measuring weak charge redistributions within stacked graphene systems, strengthening the perspectives of the application of the technique, as well as of the computational approach, to more complicated and interesting systems, like curved and functionalized graphene layers.

1. K. Novoselov et al., Science, 306 (2004) p. 666.
2. A.K. Geim et al., Nat. Mater, 6, (2007) p. 183.
3. A.H.C. Neto et al., Rev. Mod. Phys., 81, (2009) p. 109.
4. S. Latil et al., Phys. Rev. Lett., 97, (2006) p. 036803.
5. L. Ortolani et al., Nano Lett. **12**, (2012) p. 5207.
6. T. Bjorkman et al., Phys. Rev. Lett. 108, (2012) p. 235502.
7. We kindly acknowledge partial financial support from the project "*FlexSolar*" within the framework of the Italian "*Industry 2015*" program, and transnational access program within the European Project *ESTEEM* (Reference 026019).

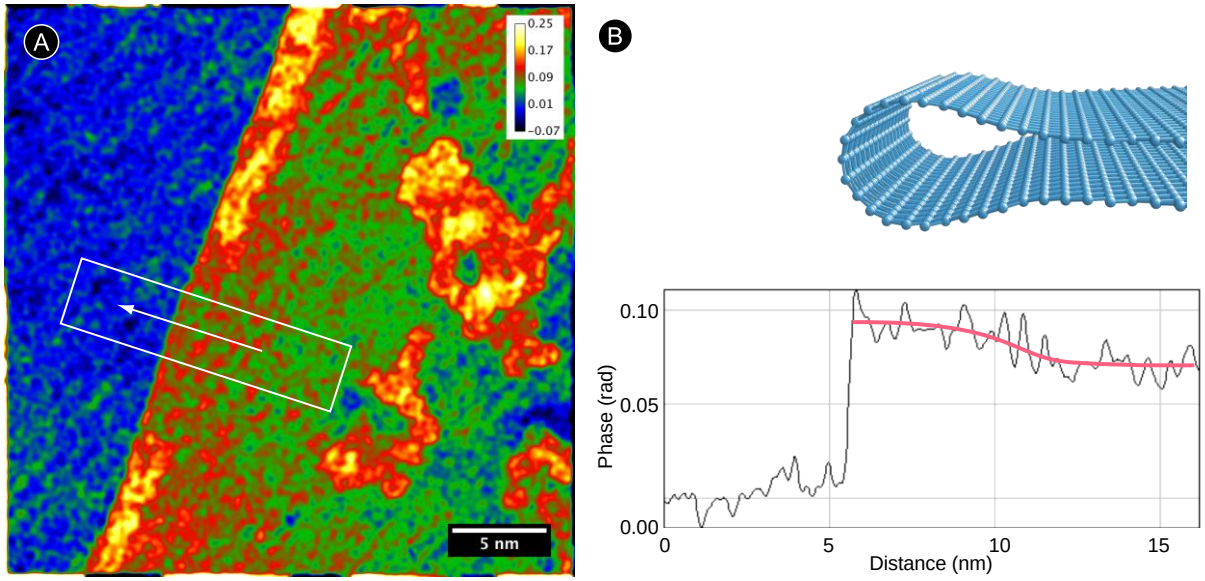

Figure 1. Holographic investigation of folded monolayer graphene. A) Reconstructed phase map obtained at 100kV of the folded border of a monolayer graphene crystal. B) Phase profile acquired over the region indicated by the white rectangle in A. Red line is guide for the eyes, highlighting the phase increasing from the internal to the curved region. A cartoon of the folded layer, as reconstructed following [5], is shown above the profile.

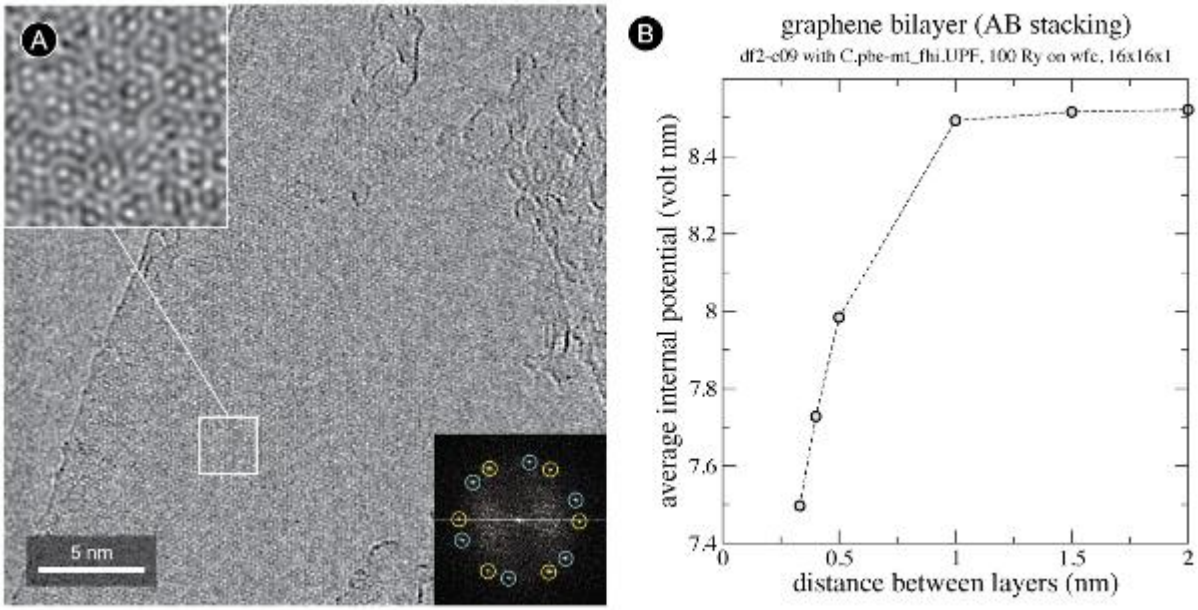

Figure 2. A) HREM image of a region close to where the hologram was acquired, showing large atomically clean areas and nanometric graphene islands on the surface. (inset) FFT of the image, showing reflections from the two stacked layers. B) Plot of the expected projected potential, resulting from DFT calculations, for two stacked graphene layers as a function of the interlayer distance.

Thin Films and Coatings

LBP.MS.P01
Orientation contrast imaging and crystallographic orientation mapping using transmission Kikuchi diffraction in the SEM

K. Kunze[1], A. Sologubenko[2], H. Ma[2], R. Spolenak[2]

[1]ETH Zurich, Electron Microscopy (EMEZ), Zürich, Switzerland
[2]ETH Zurich, Laboratory of Nanometallurgy, Zürich, Switzerland

kunze@emez.ethz.ch

Crystallographic orientation mapping is usually facilitated by rapid indexing of electron backscatter diffraction (EBSD) patterns, also referred to as orientation imaging microscopy [1]. A suitably positioned semiconductor diode (forescatter electron detector) allows recording orientation contrast images with high angular sensitivity at the same SEM conditions. The spatial resolution of both complementary techniques is restricted by considerable scattering of the primary electron beam (with energy typically between 10 and 30 keV) at shallow incidence (around 20°) to the surface of bulk sample material. This measurement geometry results in an anisotropic interaction volume and subsequent resolution of about 20nm by 50nm [2].

Recently, a setup has been introduced for crystal orientation mapping on thin electron transparent sample materials by recording transmission Kikuchi diffraction (TKD) patterns using the conventional EBSD hardware and software [3,4]. Benefits of this approach result from a horizontal sample position, i.e. perpendicular to the incidence beam. The isotropic interaction volume in the thin sample foil enables to resolve grain boundaries at 10 nm mapping step distance. Here we present a setup by commercial components of a SEM (FEI Quanta200F), a STEM sample holder (FEI) enabling a working distance of 5 mm, and an EBSD detector (Ametek-EDAX Hikari) with FSD diode attached (Figure1). We will discuss applications of TKD crystal orientation mapping on nanocrystalline metallic materials produced by severe plastic deformation or by sputter deposition, respectively. The example shows a TKD mapping on nanocrystalline Titanium, with a map size of 10 □m x 10 □m at 10 nm steps. Only reliably indexed orientations (after some moderate data cleaning) are displayed in the colour-coded map (Figure 2), were the dominating bluish colours indicate strong crystal preferred orientations. The microstructure consists of highly deformed grains with sub-micron sizes. All original data (without any postprocessing) are included in the mapping of TKD pattern sharpness (Figure 4). Grey level (qualitative) contrast arises not only from large angle grain boundaries, but also from higher dislocation densities. Holes in the thin foil are decorated by a narrow corona of poor diffraction patterns due to the extremely thin foil thickness (e.g. at the lower right corner). The complementary Besides of crystal orientation mapping, orientation contrast imaging is facilitated by recording high angle dark field STEM images using a FSD diode, available with the EBSD detection system. The orientation contrast image corresponding to the map of Figures 2 and 4 is provided in Figure 3. A vast of detailed contrast is visible, which is only party matching the contrast from the pattern contrast map. TEM studies of the intragranular defect morphology of nanocrystalline Titanium confirm a very high sensitivity of the TKD mapping to the subgrain structure and evidence the potential of TKD as a tool for the study of crystallographic relationships of nano-sized features. The complementary benefits of orientation mapping and orientation contrast imaging will be discussed.

1. B.L. Adams, S.I. Wright, K.Kunze, Metallurgical Transactions 24A (1993), 819-831
2. S. Zaefferer, Ultramicroscopy 107 (2007), 254-266
3. R.R. Keller, R.H. Geiss, Journal of Microscopy 245 (2012), 245-251
4. P. Trimby, , Ultramicroscopy 120 (2012), 16-24

Figure 1. Setup for TKD in a SEM (FEI Quanta200F) using a STEM sample holder (FEI) and EBSD detector (Ametek-EDAX) with FSD diode.

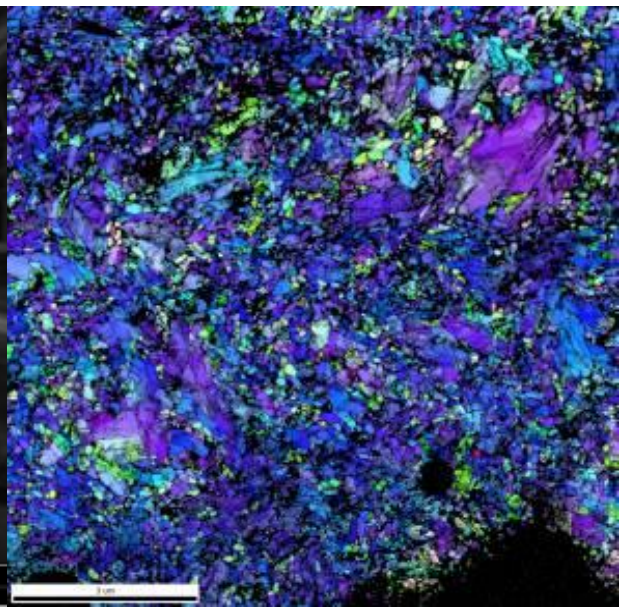

Figure 2. Crystal orientation mapping by TKD on Titanium (10um x 10um at 10nm steps). Colours indicate crystal axes along the sample normal direction according to IPF colouring scheme, grey levels mark pattern sharpness. No reliable indexing was obtained on patterns from black areas.

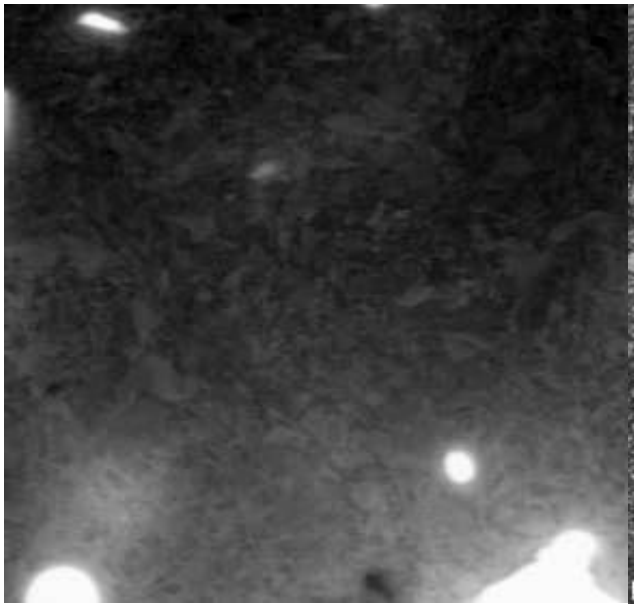

Figure 3. Crystal orientation contrast image detected by FSD diode attached to EBSD detector.

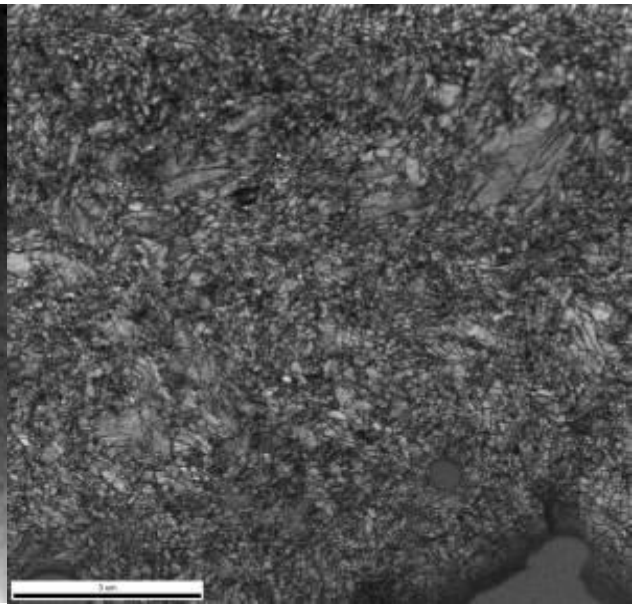

Figure 4. Crystal orientation mapping by TKD on Titanium (10um x 10um at 10nm steps). Grey levels mark pattern sharpnes.

Low Dimensional Materials and Catalysts

LBP.MS.P02
Growth and characterization of metallic nanowires: Cu, Fe and Cu/Fe

W. Huang[1], G. Richter[2], O. Kraft[1]

[1]Karlsruhe Institute of Technology, Institute for Applied Materials, Eggenstein-Leopoldshafen, Germany
[2]2. Max Planck Institute for Intelligent Systems, Stuttgart, Germany

huang@is.mpg.de
Keywords: metallic nanowires, PVD, growth mechanism

The one-dimensional nanostructures such as wires, rods, tubes have attracted increasing research efforts as a result of their fascinating properties superior to their bulk counterparts. Referring to the Cu nanowires, they are expected to play an important role as interconnects units in electronic devices with nanoscale dimensions due to the low resistivity (≈1.68×10−8Ω•m). With the addition of Fe, the nanowires can form compound magnets, while the magnetic properties related to the structural ordering of Fe.

A novel method has been developed in our group for fabricating the freestanding metallic nanowires, involving only the physical vapor deposition (PVD) [1]. Both FCC (Cu) and BCC (Fe) nanowires have been successfully produced via this method. The morphology of the Cu wires grown on the Si substrate is demonstrated in Figure 1. The dimensions of the wires range from 50 to 400 nm in diameter and 1 to 200 μm in length, which give the aspect ratio up to 1000:1. The characterizations indicate that the FCC Cu whiskers grow along the crystallographic direction of <011> while the BCC Fe whiskers grow parallel to <001>.

For the purpose of understanding the growth mechanism of the whiskers, bimetallic nanowires are synthesized by alternating the depositing materials. The subsequent electron microscopic investigations show two phases on the nanowire. A Cu-rich and a Fe-rich phase as depicted in the figure 2. This proves a root growth fashion. Chemical analysis, such as EDX and EELS are carried out to determine the chemical distribution in the two different phases.

The Si substrates are sensitive to the deposition temperature. At temperature lower than 650°C, interdiffusion of Cu and Si happens in both wires and the substrate, which gives result of the formation of Cu_xSi_y alloys. To avoid the interdiffusion, barrier layers (W) and other substrates (W, MgO, Al_2O_3, Nitride Si) are applied. It turns out that the wires can be obtained on different substrates with the aids of amorphous C layer, while the C layer provides preferred nucleation sites for the wire growth.

The electrical and magnetic properties are tested for Cu and Cu/Fe wires separately. Both ft he tests indicate the promising potential ft he applications ft he wires.

1. G. Richter, K. Hillerich, D. Gianola, *et al*. *Nano Letters,* 2009*, 9*, 3048-3052.

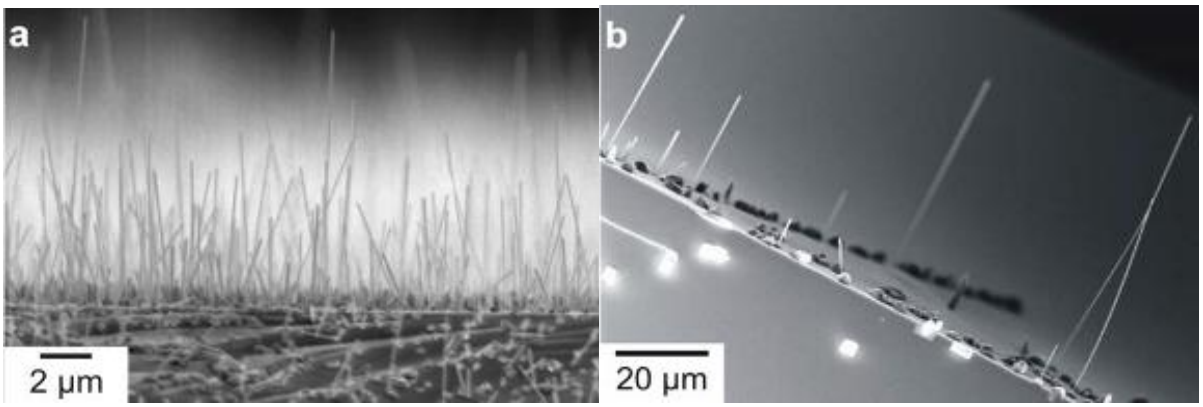

Figure 1. Morphology of Cu wires grown on the Si substrates.

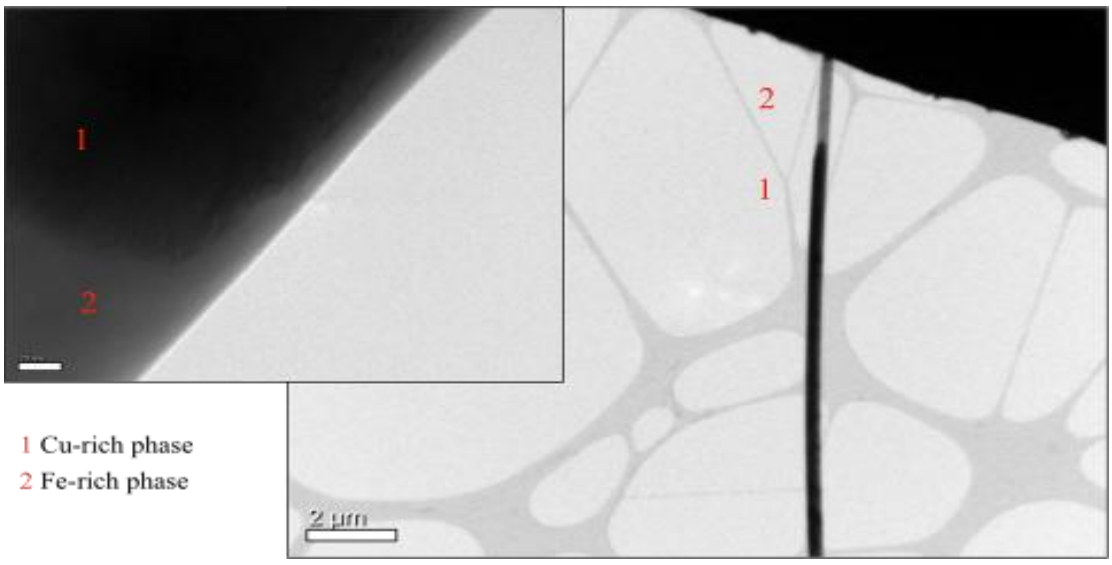

Figure 2. Indication of the 2 different phases on the Cu/Fe wires.

Thin Films and Coatings

LBP.MS.P03
Laser surface melting of 6.5 wt% yttria partially stabilized zirconia

M. Al-Tameemi[1,2]

[1]Univ. of Technology, Production Engineering and Metallurgy, Baghdad, Iraq
[2]University, Production Engineering , Baghdad, Iraq

alimohammed1957@yahoo.com

Results are reported on the effect of laser sealing of plasma sprayed yttria partially stabilized zirconia. Improvements in the topography of the plasma sprayed layers were obtained at specific energy between 1 and 2 J/mm^2. Results have been obtained showing the possibility of using laser beam to seal the porosity of low yttria partially stabilized zirconia to produce low or free porosity and fine cell structure ceramic. X-ray step-scanning analyses showed that the plasma sprayed and sealed coatings consisted mainly of t' phase without any amount of monoclinic phase (m phase) or cubic phase (c phase).

Low Dimensional Materials and Catalysts

LBP.MS.P04
A STEM-HAADF study of the distribution of vanadium atoms in the Mo-V-Te-O M1 phase

T. Epicier[1], M. Aouine[2], T.T. Nguyen[2], P. Bayle-Guillemaud[3], J.-M.M. Millet[2]

[1]INSA-CNRS, MATEIS, umr CNRS 5510, Vulleurbanne, France
[2]Université Claude Bernard, Lyon I, IRCELYON, umr 5256 CNRS, Villeurbanne, France
[3]CEA-Grenoble, Institut Nanosciences et Cryogénie – UJF / SP2M, Laboratoire d'Études des Matériaux par Microscopie Avancée (LEMMA), Grenoble, France

thierry.epicier@insa-lyon.fr
Keywords: molybdates catalysts, M1 phase, STEM-HAADF

Multicomponent molybdates based catalysts are among the most promising catalysts for light alkanes oxidation or ammoxidation. The active phase of these catalysts, called *M1,* is a solid solution with the total formula $(AO)_{2-2x}(A_2O)_{2x}M_{20}O_{56}$ with A=Te or Sb, M=Mo,V and eventually Nb, and $0<x<1$.

The structure is built up from corner sharing octahedral forming channels where Sb or Te cations are located (see figure 1a). The respective occupation level of the octahedra sites by Mo, V and Nb can vary with the composition of the phase or the preparation method [1]. If these occupation levels do not alter the crystal structure, they have a significant impact on the activity and selectivity of the catalyst. X-ray diffraction using the Rietveld method is the main technique used to determine these occupation levels but it appeared difficult to ascertain several conclusions reached. For example the site S5 was proposed to be partially occupied by vanadium in one study and not in another [2,3]. Discrepancies also exist on the occupation or not of the heptagonal channels of the structure by Te or Sb cations.

In this work high-resolution high-angle annular dark-field technique (HAADF STEM) was employed to characterize the *M1* phase, with the aim of quantifying the occupancy of sites mentioned previously.

The technique has already been used on these phases to investigate the location of Ta when it was substituted to Nb in the structure, or to characterize the Sb containing *M1* phases [4, 5]. The *M1* phase studied here contained tellurium and no niobium. It was prepared with a new method using a keplerate $\{Mo_{132}$-Te$\}$ ammonium salt precursor dissolved with vanadyl sulfate in an aqueous solution, and submitted to a hydrothermal treatment at 175°C for 24h [6]. The solid was filtered, washed with water and dried with ether. Samples for TEM observation were cut using an ultramicrotome.

According to the physics of incoherent electron scattering as collected in HAADF imaging, the intensity of atomic columns resolved in the experimental micrographs is expected to be directly linked to the nature of atoms present in these columns:

$I_{HAADF} = \square Z^{\square}_i$

where Z_i is the atomic number of chemical specie i, and $\square$ an exponent varying between 1.6 and 2 [7].

From this relationship, integrating the intensities of dots imaging atomic columns, after a background subtraction, gives the basis of a quantitative analysis of the chemical content of each column. This can be done using a parametric model [8] or directly from the images, with a normalization procedure performed on columns of known composition (if any). We apply a similar strategy to see whether the occupancy of V-containing sites can be quantified. Experiments were conducted on a 300 kV TITAN-FEI, probe C_s-corrected microscope, installed at Minatec, CEA, Grenoble. Figure 1 illustrates briefly the results. Fig. 1 b-c) refer to a sample, the composition of which was analyzed by EDX and further determined according to our quantitative analysis of HAADF intensities: both chemical compositions (regarding cations) are in very good agreement, i.e. $Mo_{0.80}V_{0.16}Te_{0.04}$ for EDX and $Mo_{0.81}V_{0.16}Te_{0.03}$ for HAADF. This method will be explored in order to understand the discrepancies encountered in the literature on site occupancies [9].

1. M. Baca, JMM. Millet, *Appl Catal A: General*, 279, (2005), 67.
2. P. DeSanto Jr, D.J. Buttrey, R.K. Grasselli, C.G. Lugmair, A.F. Volpe Jr, B.H. Toby, T. Vogt, *Z. Crystallogr.*, 219, (2004), 152.
3. H. Murayama, D. Vitry, W. Ueda, G. Fuchs, M. Anne, J.L. Dubois, *Appl Catal A: General*, 318, (2007), 137.
4. J. Yu, J. Woo, A. Borisevich, Y. Xu, V.V. Guliants, *Catalysis Communications* 29 (2012), 68.
5. M. Sadakane, K. Yamagata, K. Kodato, K. Endo, K. Toriumi, Y. Ozawa, T. Ozeki, T. Nagai, Y. Matsui, N. Sakaguchi, W.D. Pyrz, D.J. Buttrey, D.A. Blom, T. Vogt, W. Ueda, *Angew. Chem. Int. Ed.*, 48 (2009) 1.
6. R. Canioni, C. Marchal-Roch, N. Leclerc-Laronze, M. Haouas, F. Tautelle, APS. Etcheberry, S. Loridant, JMM. Millet, E. Cadot, *Chem Comm.*, 47, (2011), 6413.

7. E.J. Kirkland, R.F. Loane, J. Silcox, *Ultramicroscopy*, 23, (1987), 77.
8. S. VanAert, J.Verbeeck, R.Erni, S.Bals, M.Luysberg, D.VanDyck, G.VanTendeloo, *Ultramicroscopy*, 109, (2009), 1236.
9. Thanks are due to the French METSA network (www.metsa.cnrs.fr) for partial financial support.

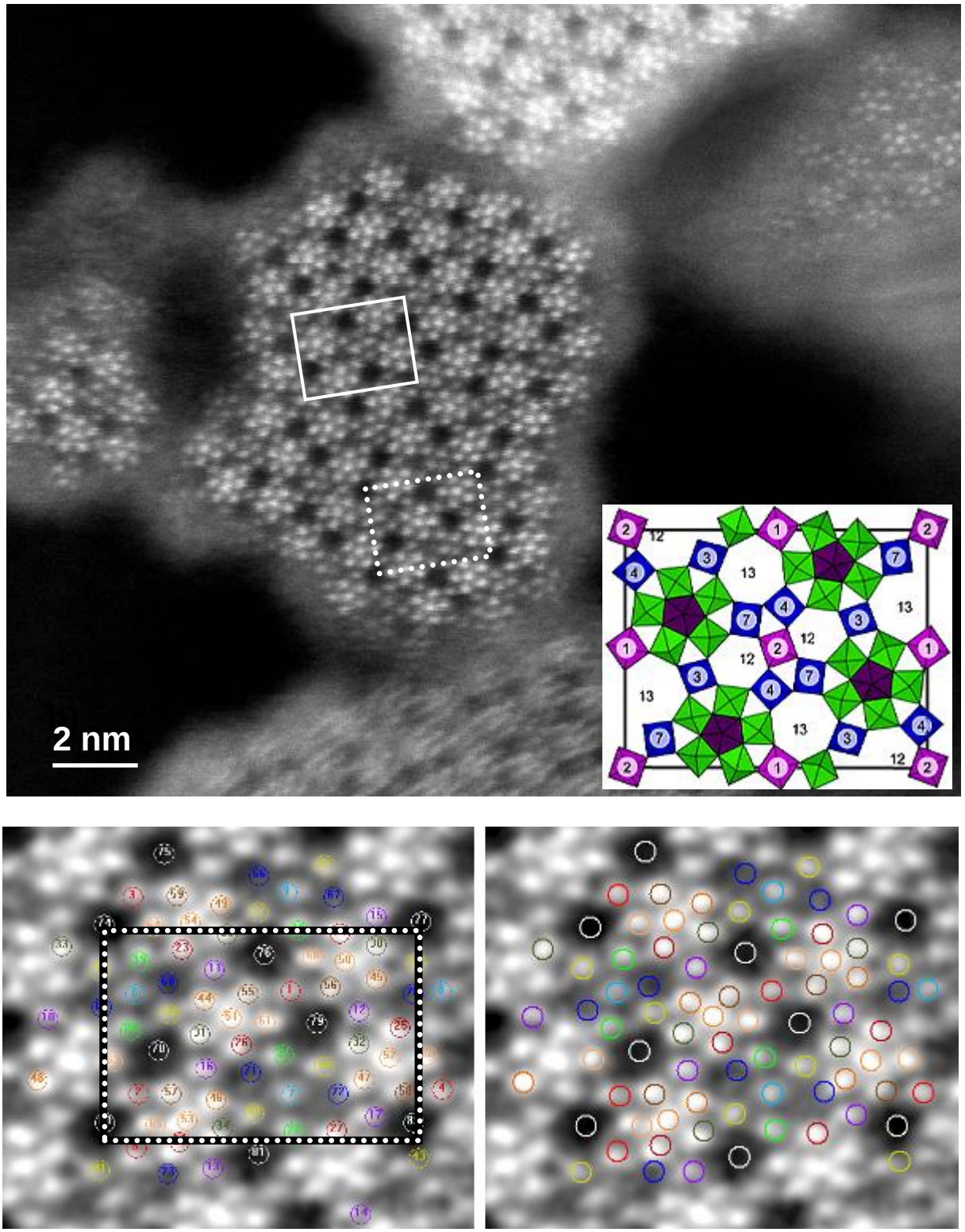

Figure 1. STEM-HAADF imaging of the Mo-V-Te-O *M1* phase. a) Low mag image showing a crystallite close to the [001] orientation; the unit cell is shown in insert (space group Pba2, with a = 2.112 nm, b = 2.659 nm [3] as underlined in the micrograph; the dotted frame refers to fig. b)). b) Detail (from another crystal) showing the starting ideal atomic positions from the crystallographic model (columns of interest for the statistical analysis of intensities are numbered). c) Refined positions (after running a 'peak search' routine) used for intensity integration, leading to the quantitative chemical analysis reported in the text.

Ceramics, Oxides, Geomaterials

LBP.MS.P05
In-situ TEM investigation on lead-free $(Bi_{1/2}Na_{1/2})TiO_3$-$xSrTiO_3$

M. Scherrer[1], L.A. Schmitt[1], M. Acosta[1], W. Jo[1], J. Rödel[1], H.-J. Kleebe[1]

[1]TU Darmstadt - Geomaterial Science, Darmstadt, Germany

$(Bi_{1/2}Na_{1/2})TiO_3$ (BNT)-based ceramics are promising candidates for actuator applications. Prospective and environment-friendly applicability of lead-free materials coupled with strong piezoelectric properties caused a progressive research in the last decades. Common drawbacks of BNT such as large coercive fields (~7 kV/mm) [1] are counteracted by the formation of solid solutions. This work focuses on the ergodic relaxor (1-x)BNT-$xSrTiO_3$ (BNT-xST) which is characterized by relatively high strains at reduced fields (~ 0.2% at 4 kV/mm) and the requirement of low poling fields (~ 3kV/mm).

Previous bulk studies covering the full compositional range of BNT-xST [1, 2] evidenced a maximum in strain at x = 0.25. As an incipient piezoceramic it attains enhanced piezoelectric properties (increased piezoelectric coefficient d_{33} and electromechanical coupling factor k_{33}) only upon electrical loading. The electric-field induced phase transition (EFPT) is rationalized to occur in a gradual manner at a fixed temperature. Sample compositions were selected to a) coincide the possible MPB (x = 0.25) and b) diverge from the latter (x = 0.1). However, an adequate correlation of temperature and electric-field dependent microstructure evolution with corresponding bulk analyses still has to be provided.

In this respect microstructure characterization was systematically carried out by conventional TEM including bright field (BF) and dark field (DF) imaging, high-resolution TEM (HR-TEM) and selected area electron diffraction (SAED) followed up by a set of challenging In-situ transmission electron microscopy (in-situ TEM) experiments.

The addition of ST to the base BNT composition leads to a decrease in depolarization (T_d) and Curie temperature (T_c) of the relaxor. Substituting the pseudo-divalent $(Bi,Na)^{2+}$ by the smaller sized cation Sr^{2+} on the A-site of the general ABX_3 perovskite cell destabilizes the ferroelectric order of BNT. This observation is manifested in the prevalent core-shell structures as depicted in BF fig. 1a and 2a and rationalized consistently by energy-dispersive X-Ray analysis (EDX) and scanning transmission electron microscopy (STEM) techniques which indicate a clear Sr-depletion in the domain-contrasted core regions. For the corresponding DF images in fig. 2b and 2c the outlined superstructure reflection ½{ooe} and ½{ooo} (o and e resemble odd and even hkl indices, respectively) in fig. 1b were utilized. These reflections are either induced by in-phase (here: $a^0a^0c^+$) or anti-phase (here: $a^-a^-a^-$) octahedral tilting as given in Howard and Stoke's notation [3] or alternatively by antiparallel cation displacement. Subsequent processing of the obtained SAED patterns allowed for a direct identification of non-cubic lattice distortion in terms of rhombohedral R3c and tetragonal P4/mbm phase coexistence within single grains.

In-situ TEM efforts were undertaken to further improve our understanding of the rhombohedral-tetragonal phase transition (T_{r-t}) within the ferroelectrically-active state under applied electric field. Based on interesting bulk measurement results indicating a change in strain mechanism from an extrinsic to an intrinsic contribution at approximately 80°C-100°C, the ceramic was additionally examined in the temperature range from room temperature to 150°C in an in-situ heating experiment.

1. W. Krauss, D. Schütz, F. A. Mautner, A. Feteira and K. Reichmann, J. Eur. Ceram. Soc. 30 (2010), p. 1827-1832.
2. Y. Hiruma, Y. Imai, Y. Watanabe, H. Nagata and T. Takenaka, Appl. Phys. Lett. 92 (2008), p. 1-3.
3. C. J. Howard and H. T. Stokes, Acta Cryst. B54 (1998), p. 782.

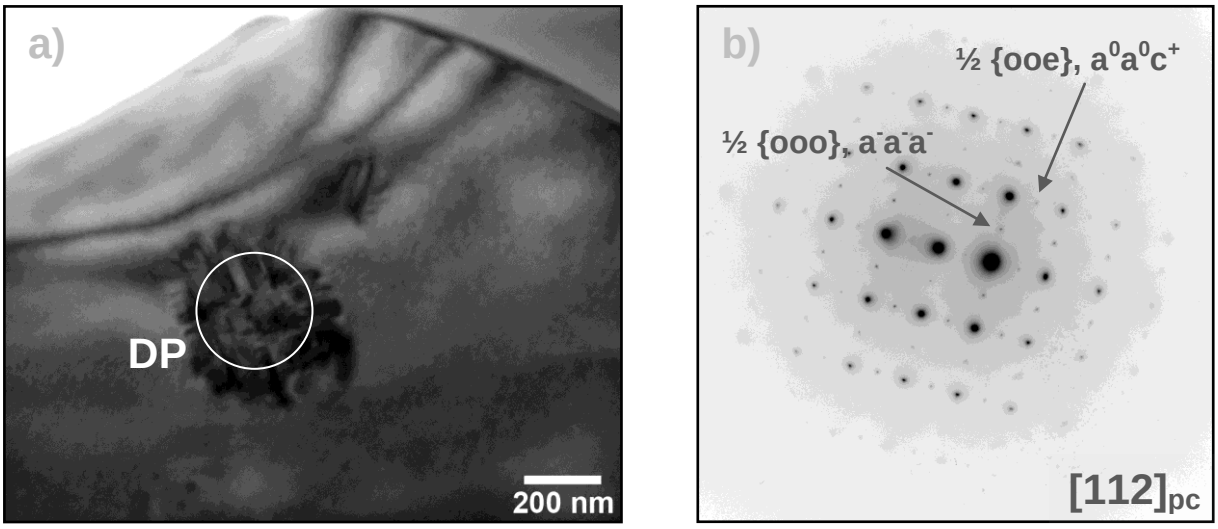

Figure 1.a) overview bright-field image of the core-shell observed in BNT-25ST. Fig. 1b) corresponding SAED pattern of the investigated grain aligned along $[112]_{pc}$ axis is shown.

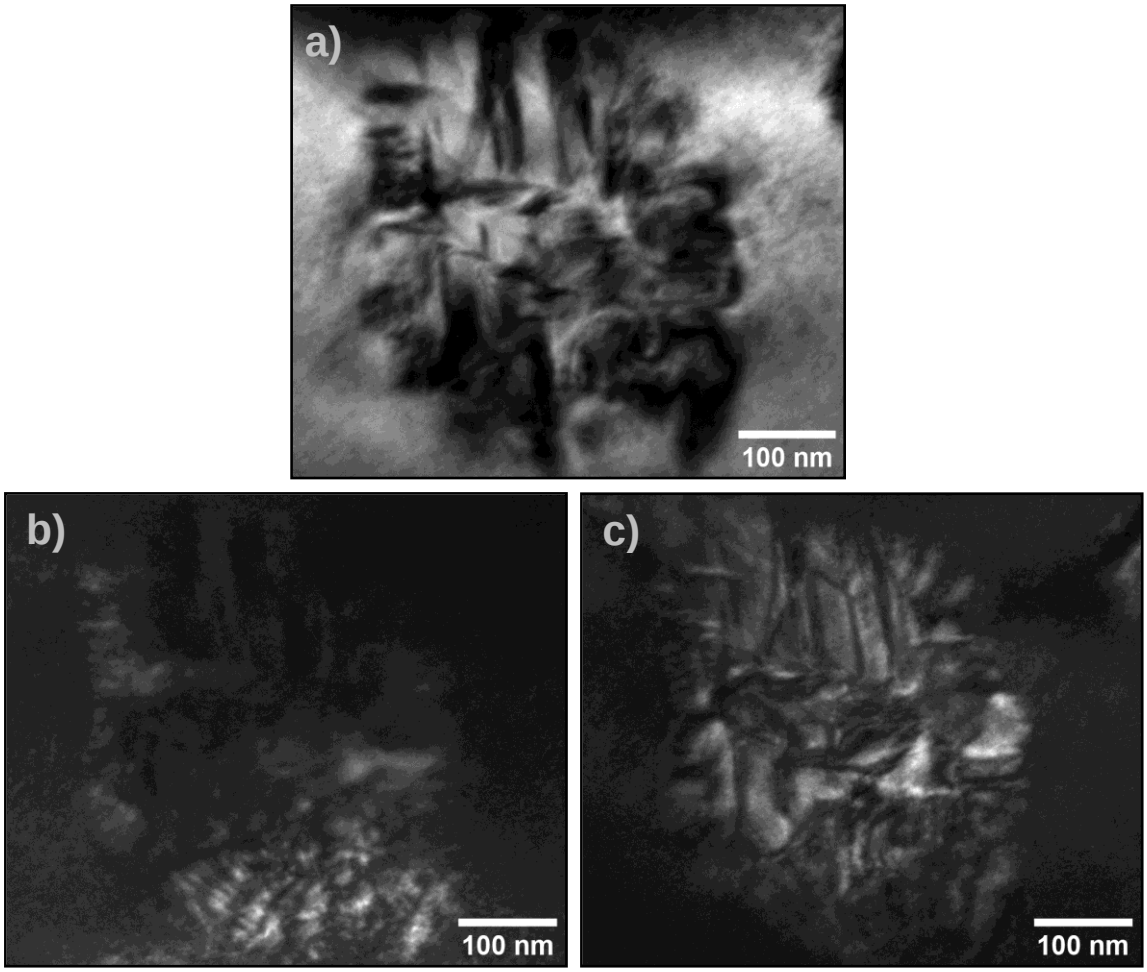

Figure 2.a.) magnified micrograph of a strongly contrasted core region in BF mode. Fig. 2b) & fig. 2c) dedicated DF images employing the above indicated superstructure reflections ½ {ooo} and ½ {ooe}, as outlined in Fig. 1b.

Materials for Energy Technology

LBP.MS.P06
Microstructure analysis of HCM12 and HCM12A steels after 100000h exposition

K. Rodak[1], A.Hernas[1]

[1]Silesian University of Technology, Department of materials Science, katowice, Poland

kinga.rodak@polsl.pl
Keywords: microstructure, STEM, 12% chromium steels, long-time exposure

The two martensitic chromium steels HCM12 and HCM12A after 100 000h exposition at 550^{o}C of steam have been studied regarding microstructural changes using Scanning Transmission Electron Microscope (STEM).

These high-strength 12%Cr heat resistant steels have been developed for the boiler and turbine of an ultra-supercritical power plant, at a temperature higher than 550^{o}C.

The composition of HCM12 steel was follows: 0.1C-12Cr-1W-1Mo-0.25V-0.2Nb. While composition of HCM12A steel was: 0.1C-12Cr-2W-0.5Mo-0.25V-0.1Nb- Cu1.Tungsten, as the main alloying element, induces precipitation of intermetalic Laves phase during long –term exposure. Fe_2W is thermally more stable than Fe_2Mo [1,2]. It is also suggest that the addition of W retards recovery of martensitic lath structure [3].

In the as-received condition the microstructure of this kind of steel consist of tempered lath martensite with high dislocation densities, precipitated particles of relatively coarse $M_{23}C_6$ and fine MX in HCM12A and additionally islands of δ- ferrite about 30% surrounded by areas of tempered martensite in HCM12 steel. Mentioned steels were analysed in initial state and after exposure at 30 000h and 70 000h by authors of this article and the results of investigations are presented elsewhere [4,5].

Figure 1 shows a comparison of the microstructure in HCM12 and HCM12A after 100 000h. The HCM12 steel undergo a recovery and recrystallisation of the matrix. The recrystallisation starts by growth of dislocation free crystals at the former grain, martensite boundaries and especially at the ferrire grains. In HCM12A steel the recovery and recrystallization advances more slowly, for this reason the grains/subgrains in HCM12A steel are much finer than in HCM12. The reason for this behaviour is the precipitation of particles which retard the movement of the dislocation. The larger number of precipitates in HCM12A steel suppresses more effectively the recovery of grain/subgrain structure.

It has been found that the phases presented in the serviced conditions are $M_{23}C_6$, Laves phase and fine MX particles observed inside grain/subgrain. STEM-EDS analysis showed that the $M_{23}C_6$ were enriched in Cr, Fe, Mn, Mo, and W. Whereas Laves phase was enriched in W and Mo to have the general composition of the $(Fe,Cr)_2(Mo,W)$ (Figures. 2-4). Within the Laves precipitation, the stacking faults could be observed as a characteristic streaks on the electron diffraction pattern (Figure 2b). MX dispersed particles was enriched in V.

The Laves phase particles are located between an $M_{23}C_6$ moreover are situated in contact with the $M_{23}C_6$ precipitates (Figures. 2a and 3). Very often the agglomeration of Laves phase have been observed (Figure 2b). The observations performed in several microareas confirmed chromium concentration in the interior of Laves phase precipitation (Figure 2b). This is probably the effect precipitation of this phase on $M_{23}C_6$ carbides. Generally the coarsening intensity of precipitates is much larger in HCM12 than in HCM12A.

1. T. Fujita, J. Iron Steel Inst. Jpn. 76 (1990), p.1053
2. F. Abe, Mater. Sci. and Eng. A319-321 (2001), p. 770
3. J. Sawada et. all, Mater. Sci. and Eng. A267 (1999), p. 19
4. A. Hernas et. all, Journ. of. Achiev. in Mater. and Manuf. Engin. 17 (2006), p.69
5. A. Hernas et. all, Materials for Advanced Power Engineering 2006, Proceedings of the 8th Liege Conference, Part III, J. Lecomte-Beckers, M. Carton, F. Schubert and P.J. Ennis (Editors), p.1357
6. Acknowledgements: This research was supported by National Centre for Research and Development (Strategic Research Project SP/E/1/67484/10)

a.) b)

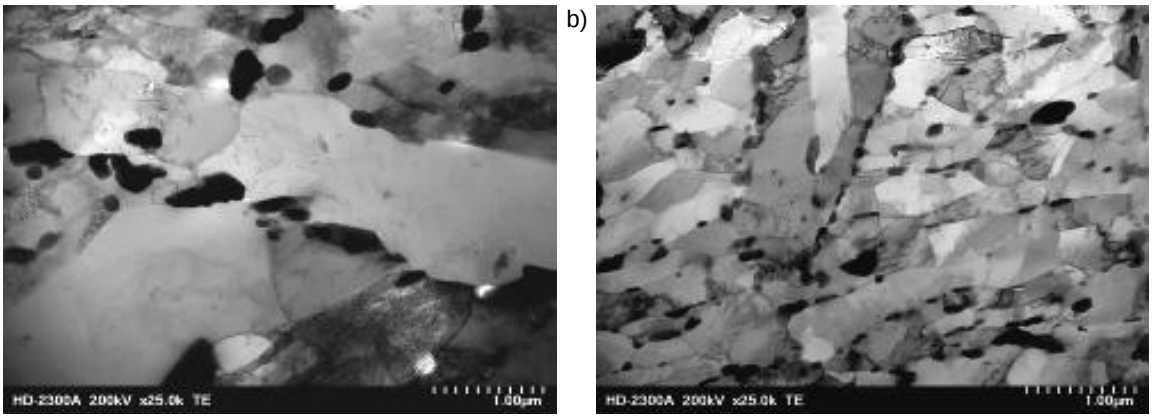

Figure 1. Microstructure of steels after 100 000h exposure a) HCM12 and b) HCM12A.

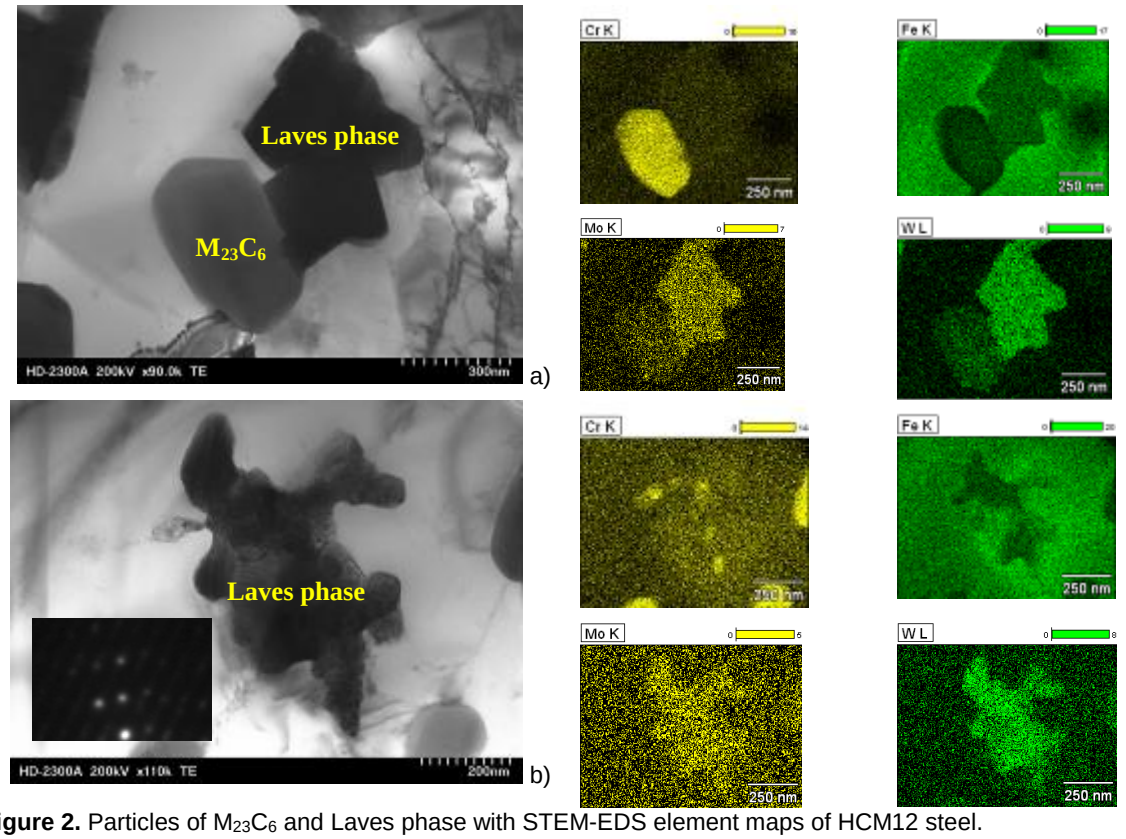

a)

b)

Figure 2. Particles of $M_{23}C_6$ and Laves phase with STEM-EDS element maps of HCM12 steel.

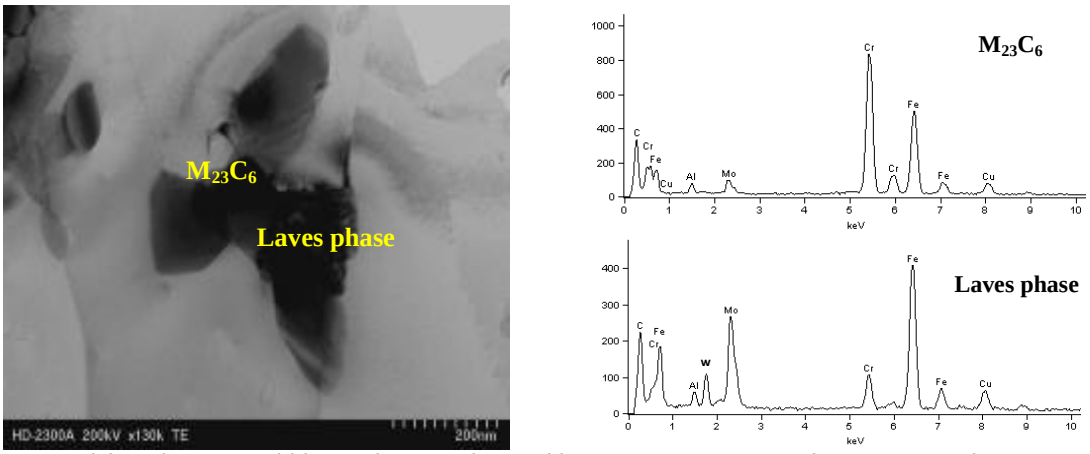

Figure 3. Particles of $M_{23}C_6$ carbides and Laves phase with STEM-EDS spectra of HCM12A steel.

Functional Materials

LBP.MS.P07
The structure of Fe_3Al intermetallic phase-base alloy after hot plastic deformation

M. Jabłońska[1], I. Bednarczyk[1]

[1]Silesian University of Technologe, Materials Science, Gliwice, Poland

iwona.bednarczyk@polsl.pl
Keywords: FeAl28 alloys, intermetallic, hot rolling, substructure, dislocation structure

Over the last ten years Department of Materials Science at Silesian University of Technology has conducted research in order to know the structural phenomena which occur during hot plastic treatment aimed at elaboration of heat and plastic treatment technology of selected alloys based on intermetallic phases from the Al-Fe system. Those alloys are classified as a group of high-temperature creep-resisting materials of advantageous physicochemical and mechanical properties at an elevated and high temperatures [1]. Their properties, such as: low density, high melting temperature, high strength and good oxidizing resistance together with good crack resistance, create wide prospects for their industrial applications, for components of machines working at a high temperature and corrosive environment. The major problem restricting their universal application is their low plasticity and their brittle cracking susceptibility. Consequently, the research of intermetallic phase based alloys focuses on their plasticity is required [2-3].

One of the factors responsible for the unfavourable technological properties of Al-Fe alloys is a tendency to coarsely crystalline primary structure. The results indicate that grain refinement by thermo-mechanical processing has positive effect on the improvement in both strength and durability of these alloys. Therefore, the important issue is the evaluation of the behaviour of the material during plastic working. It should be noted that a significant influence on the properties of Al-Fe alloys by thermo-mechanical processing is the presence long-range ordering and the strengthening by thermal vacancy [4-5].

The aim of the paper is a microstructure analysis of alloys from the Al-Fe system after hot rolling tests, conducted by using a scanning transmission electron microscopy STEM and scanning electron microscope equipped with EBSD detector. Hot rolling was carried out at Technical University of Ostrava, Faculty of Metallurgy and Material Engineering, Institute of Modelling and Control of Forming Processes. The samples were heated to a temperature of 1200˚C. The EBSD and STEM techniques have been applied in order to determine the influence of chemical composition and deformation parameters on structural changes. The microstructure analysis has included parameters such us: grain/sub-grain size, area fraction of grains/sub-grains, misorientation angles, grains/sub-grains shape aspect ratio and dislocations structure **(Figure 1).** The research structure techniques in scanning-transmission electron microscopy revealed numerous FeAl28 alloy phase separations of secondary nucleating sites favoured energetically, which are the boundary of grain/subgrain and dislocation structure. These changes in the structure of the test results have been confirmed by EBSD, which revealed the presence of grains/subgrains misorientation angle boundaries above 15°

1. Stoloff N.S**.:** Iron aluminides: present status and future, Materials Science and Engineering, A 258, 1998, pp. 1-14.
2. Pike L.M.C., Liu. T.: The effect of vacancies on the environmental yield strength dependence of boron-free and boron-doped Fe-40Al, Intermetallics 8, 2000, pp. 1413-1416.
3. Baligidad R.G., Radhakrishna A.: Effect of hot rolling and heat treatment on structure and properties of high carbon Fe-Al alloys, Materiale Science and Engineering, A308, 2001, pp. 136-142.
4. Jabłońska M., Bernstock E., Jasik A,: Microstructure and mechanical properties of intermetallics on the base of Fe-Al alloy obtained by casting, Archives of Materials Science and Engineering, Vol 28, 2007, pp. 625-628.
5. Yamaguchi H., Ito K.: *High-temperature structural intermetallics*, Acta Materialia, 48, 2000, pp. 307-322.

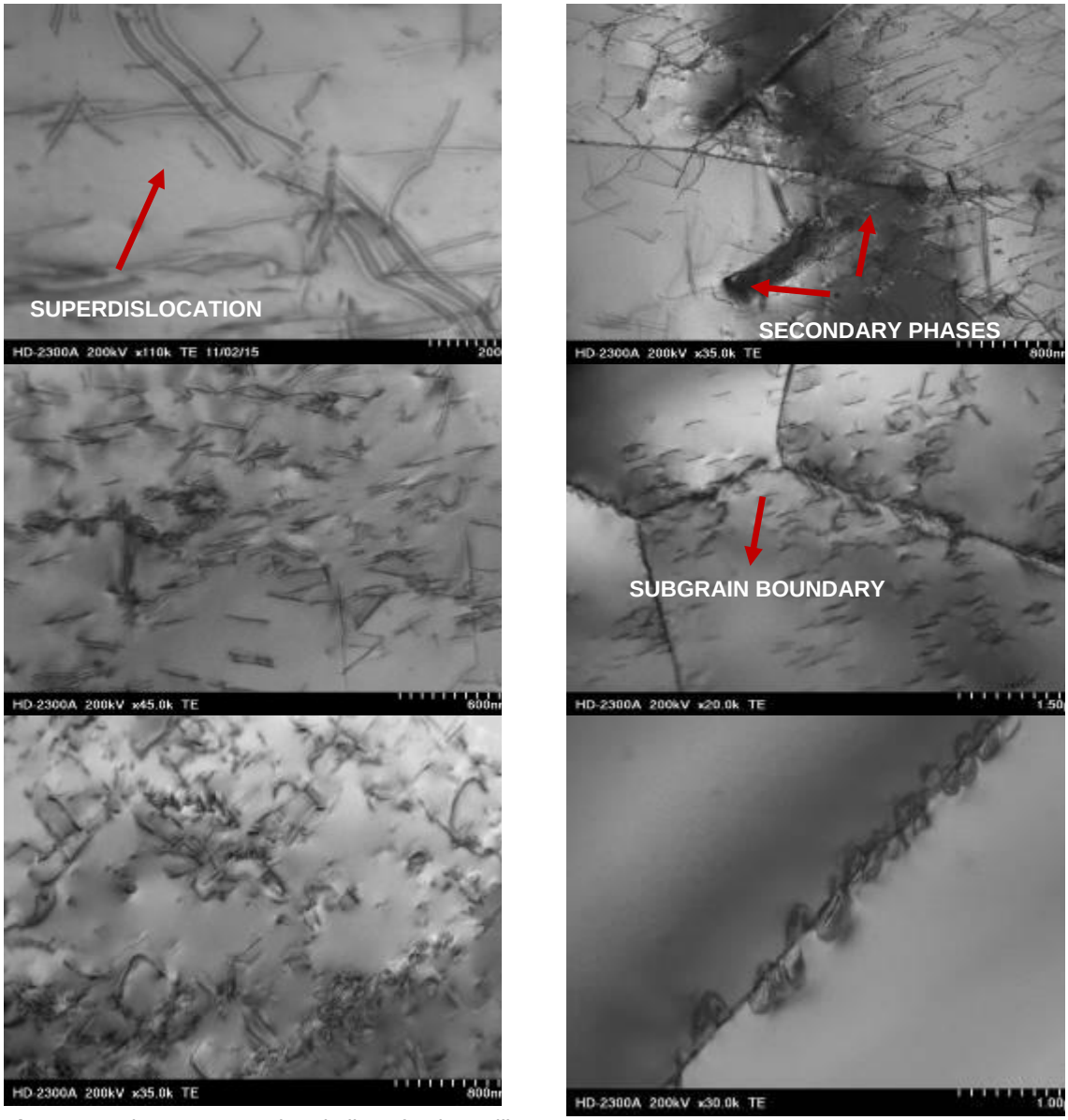

Figure 1. Substructure FeAl28Al alloy after hot rolling

$D_{śr(xy)}$=697μm

a)

b)

Grain boundaries			Fraction
	Angle		
	Min	Max	
	8˚	15˚	0,001
	15˚	180˚	0,085

Figure 2. a) EBSD microstructure map for FeAl28, b) microstructure map of missorientation angles between subgrains/grains

Figure 2b). An average grain diameter/subgrain is $D_{śr(xy)}$=697μm **(Figure 2a).**

Materials for Energy Technology

LBP.MS.P08
Structure and phase composition ofT91-ODS steel

D. Litvinov[1], L. Strassberger[1], J. Aktaa[1]

[1]Karlsruhe Institute of Technology, Eggenstein-Leopoldshafen, Germany

litvinov@kit.edu
Keywords: steel, ODS, carbide

Transmission electron microscopy (TEM) was applied to study the oxide dispersion strengthened (ODS) ferritic–martensitic steel T91 (9 wt.% Cr, 1 wt.% Mo) produced by mechanical alloying techniques. The microstructure was analyzed using Tecnai 20 FEG microscope. High angle annular dark field (HAADF) scanning TEM (STEM) with energy-dispersive X-ray (EDX) spectroscopy for the determination of the composition, conventional TEM with selected area diffraction (SAD) and high resolution TEM (HRTEM) with fast Fourier transformation (FFT) analysis for the crystallographic investigations were applied.

Figure 1a shows an overview HAADF STEM image of the investigated steel. The microstructure consists of mainly four regions. The first region shows ferrite grains with nearly no defects. Region two exhibits ferrite grains with a high defect density due to formerly martensite. In the third region there are small precipitates with a dark or bright contrast (up to 50 nm in diameter). Region 4 shows larger and non regular shaped particles with a bright contrast at the grain boundaries. EDX investigation of the particles 1-5 with different contrast in the HAADF STEM image (Figure 1b) is concluded in Table 1. The EDX analysis shows that large particle 5 consist of Y_2O_3. Taking into account the thickness of the TEM specimens and the depth (or background) of the EDX measurements, the smaller particles 1-4 also contain partly yttrium oxide. However, the measured higher C and lower Fe and Cr fractions of the dark particles 1 and 3 in compare with the bright particles 2 and 4 indicates the different composition in or around the particles. The high amount of C in all particles is due to contaminations during EDX measurements, but it is not clear why the Fe and Cr concentrations are changed in the areas of the dark and bright particles. Generally, the brightness of HAADF STEM images increases with atomic number of the elements and thickness of the TEM specimen. Therefore, "pure" Y_2O_3 particles should have a dark contrast inside the Fe-matrix. If the particle lies on the steel surface, the local increasing thickness leads to the brighter contrast. A similar bright contrast, caused by an increasing thickness of the TEM specimen, is observed on the carbides (4 in Figure 1a) which are etched very slowly in comparison with the α-Fe-matrix during TEM preparation by electropolishing, which we used.

The HRTEM image in Figure 2a shows an Y_2O_3 particle with *bcc* structure and a lattice parameter of ~ 1.06 nm close to [113]-zone axis as shown by the obtained FFT - diffractogram (cf. insert Figure 2a). SAD analysis of conventional TEM (here not shown) and the HRTEM images with diffractograms show generally the coherence relationship between the ODS particles and the matrix: <100> Y_2O_3 II <110> □-Fe.

HRTEM image in Figure 2b shows an interface between carbide $M_{23}C_6$ where M is metal and □-Fe matrix with the corresponded diffractograms. $M_{23}C_6$ has *fcc* structure with a lattice parameter of ~ 1.07 nm and is close to [111]-zone axis. The relation between the carbide and the matrix is: <112> $M_{23}C_6$ II <110> □-Fe. The EDX analysis of the carbide regions shows the existence of two kinds of the structures with a different Cr/Fe relation: 1) Cr > Fe (2 Cr : 1 Fe) and 2) Cr < Fe. Both types of carbides contain Mo (up to 4 %). Note, that the variation of the Cr/Fe concentration or the presence of Mo almost do not change lattice parameter of $M_{23}C_6$. Taking into account the thickness of the TEM specimens and the depth (or background) of the EDX measurements and according to literature data, the first type of carbides may be $Cr_{21}Mo_2C_6$. The HRTEM images reveal the existence of {111} stacking faults in the large carbide inclusions (bottom part of carbide in Figure 2b).

The EDX study combining with the diffraction analysis of other inclusions in the investigated steel shows the presents of MX phases with *fcc* (rock salt) structure and lattice parameter of ~ 0.44 nm. where M is metal and X is C,O or N.

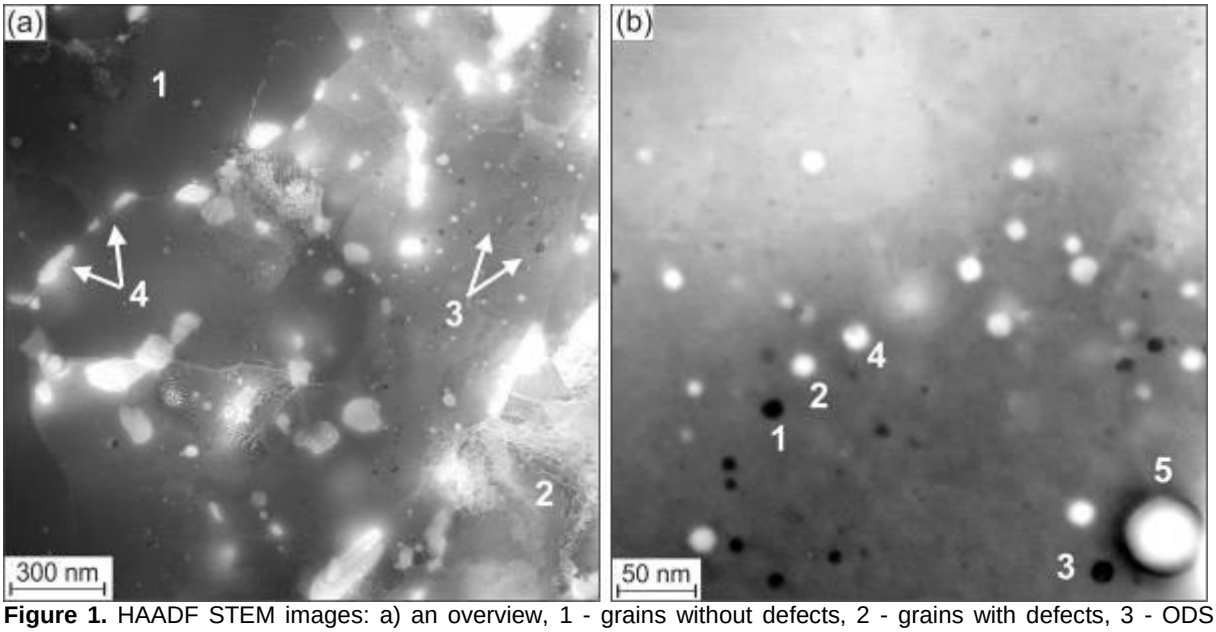

Figure 1. HAADF STEM images: a) an overview, 1 - grains without defects, 2 - grains with defects, 3 - ODS particles, 4 -carbides, b) image with ODS particles 1-5, taken for EDX measurements (see Table 1).

Region \ at. %	C	O	Cr	Fe	Y
1	73.46	19.40	0.42	2.05	4.64
2	42.20	24.77	2.86	25.31	4.84
3	81.82	11.12	0.08	1.14	5.82
4	47.56	22.48	2.51	18.10	9.32
5	11.09	61.92	0	0.93	26.03

Table 1. Results of EDX measurements of regions 1-5 from Figure 1b.

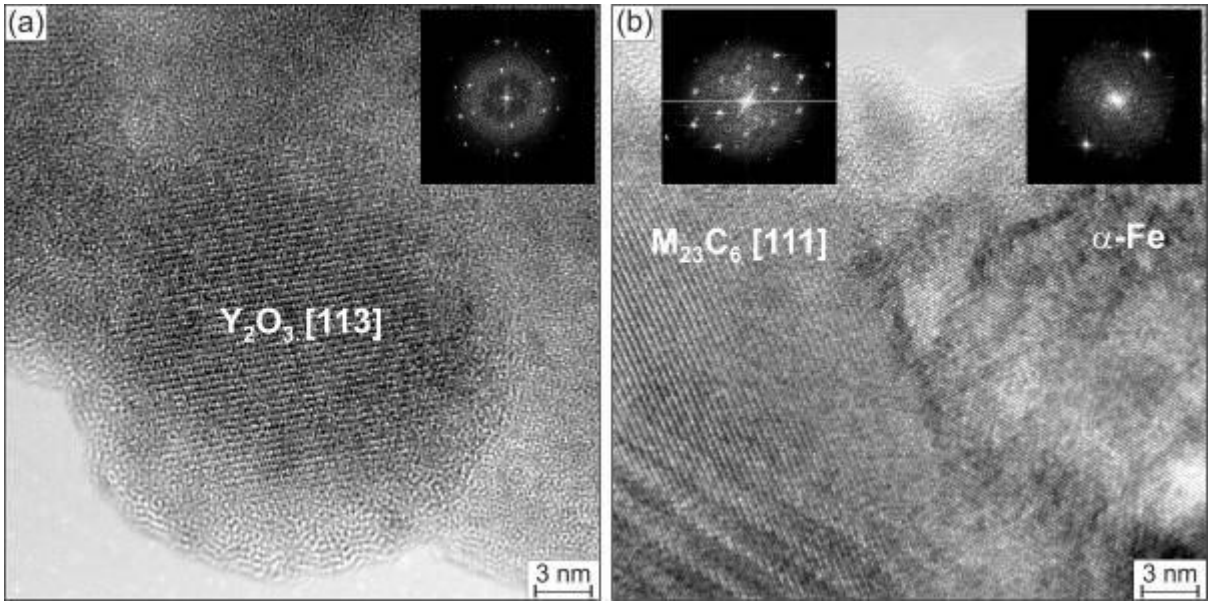

Figure 2. HRTEM images with corresponded diffractograms: a) ODS particle, b) interface between carbide and matrix.

Functional Materials

LBP.MS.P09
TEM-investigations of calcium-manganese-oxides applied for water oxidation - from amorphous state to crystalline structure

C. Göbel[1], E. Baktash[1], I. Zaharieva[2], H. Dau[2], A. Thomas[1]

[1]TU Berlin, Chemistry, Berlin, Germany
[2]FU Berlin, Physics, Berlin, Germany

Photosynthetic water oxidation is efficiently catalysed by a protein µ-oxido Mn_4Ca-cluster in nature [1]. This cluster consists of earth abundant, non-toxic elements and serves as a paragon for the development of synthetic calcium-manganese-oxide catalysts. In our work, the inorganic phase was synthesized in presence of an organic porogen (cyanamide), which afterwards was removed leaving behind more or less defined pores in the inorganic matrix. The microscopic structure of a serie of such oxides annealed at different temperatures was characterized by transmission electron microscopy (TEM) in order to correlate crystallinity, structure on nanometer- and atomic level and surface area with catalytic activity.

(HR)TEM images and corresponding SAED pattern (Figure 1) demonstrate crystallinity (short-range order change to long-range order) combined with particle growing by increasing the calcination temperatures of the investigated calcium-manganese-oxides. Oxides, synthesized at 300°C (Figure 1a), are completely amorphous and show a rather intimate mixture between calcium-manganese-oxides and the carbon nitride precursor (Figure 1a). EDX analysis exhibits the existence of C, N, Ca and Mn. The catalytic activity of these samples is low. By annealing the oxides at 400°C, the organic phase disappear forming gaseous decomposition products and nearly pure calcium-manganese-oxides of a foam-like structure remain (Figure 1b). Nitrogen could not be observed in the EDX spectra. SAED images reveal diffuse diffraction rings with calculated d-values that belong to $Ca_2Mn_3O_8$ and $CaMn_2O_4$. That indicates the presence of disordered layered structures of edge-sharing MnO_6 octahedra with crystallites on the nanometer scale. The resulting oxides show high activity as catalysts for water oxidation. When the calcium-manganese-oxides are heated up to 550°C, the porous structure becomes denser and the pore size decreases. That may be due to the reduced amorphicity and water loss of the material resulting in structural contraction. At 700° and 1000°C, the foam- or porous structure completely disappears and instead larger crystalline particles with consequently lower specific surface areas and porosities are observed (Figure 1c). Electron diffraction experiments of different areas of that samples exhibit only the characteristic reflections of $CaMn_2O_4$ (marokite). The smaller specific surface area of the marokite crystallites yields to a decrease of the catalytic efficiency of that solid material.

Layered manganese-oxides with incorporated Ca^{2+} ions have the highest activity in catalytic water oxidation [2, 3]. In the case of the investigated calcium-manganese-oxides the high catalytic activity (sample calcined by 400°C) is due on the very small crystallites (< 5 nm) with strong structural disorder (amorphicity) at the atomic level, resulting in the high number of defect sites. The disordering providing an especially high number of both protonatable (and potentially reactive) µ2-O(H) bridges and terminal water coordination sites.

1 H. Dau, I. Zaharieva and M. Haumann, Curr. Opin. Chem. Biol. (2012), 16, 3.
2- M. Wiechen, I. Zaharieva, H. Dau, P. Kurz, Chem. Sci. (2012), 3, 2330.
3. I. Zaharieva, P. Chernev, M. Risch, K. Klingan, M. Kohlhoff, A. Fischer and H. Dau, Energy Environ. Sci. (2012), 5, 7081.
4. The authors express their gratitude to the Department of Electron Microscopy (ZELMI), TU Berlin for their support with microscopic techniques.

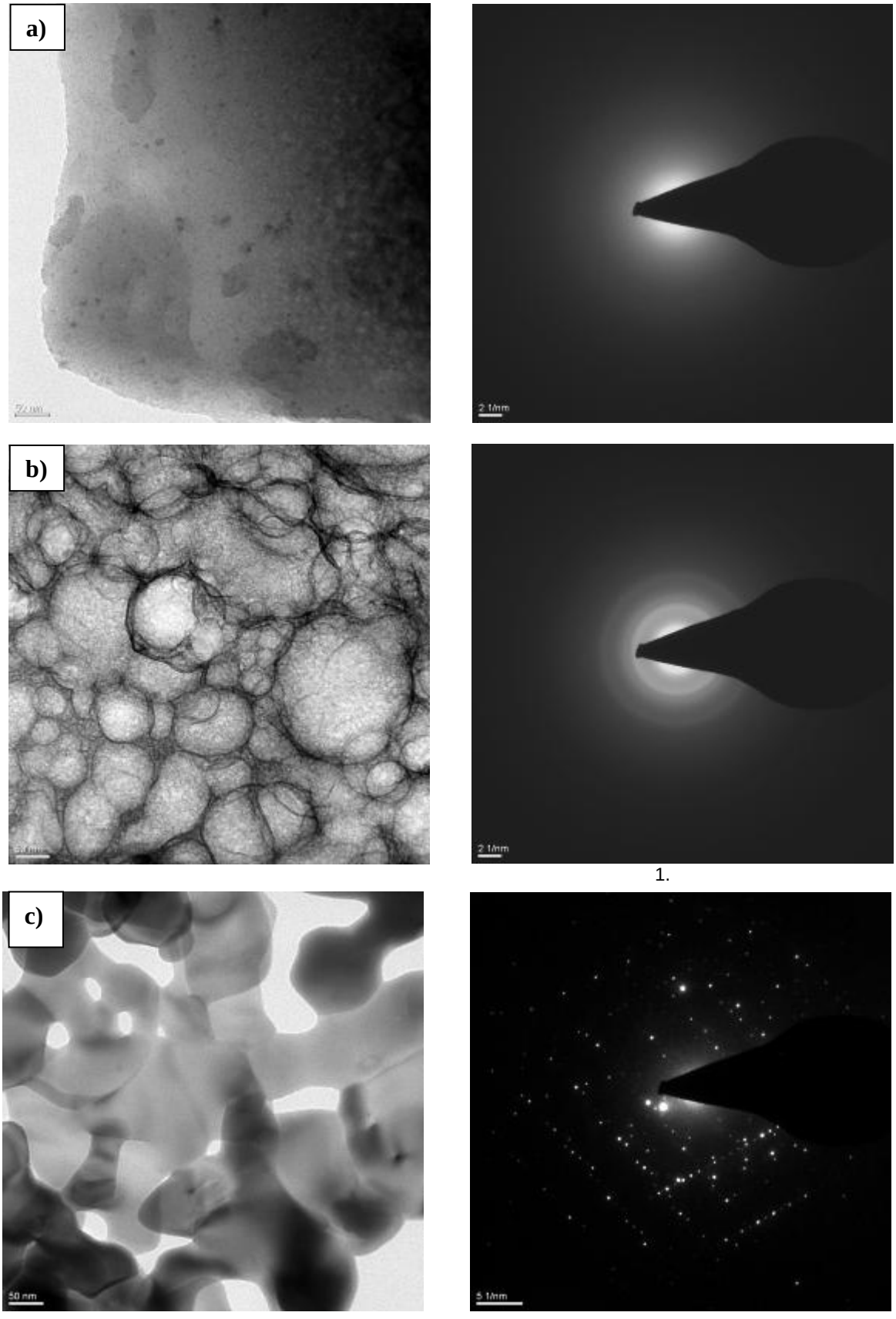

Figure 1. Bright field TEM images of calcium-manganese-oxides annealed by different temperatures and corresponding SAED pattern. **a)** 300°C, **b)** 400°C, **c)** 1000°C.

Thin Films and Coatings

LBP.MS.P10
Characterisation of MBE grown type-II superlattices with electron microscopy

Y.E. Suyolcu[1], B. Aslan[2], U. Serincan[2], S. Turan[3]

[1]Anadolu University, Nanotechnology, Eskisehir, Turkey
[2]Anadolu University, Physics, Eskisehir, Turkey
[3]Anadolu University, Materials Science and Engineering, Eskisehir, Turkey

yesuyolcu@anadolu.edu.tr
Keywords: MBE, type-II superlattice, SEM, TEM

The uses of infrared photodetectors in different areas are increasing rapidly. In recent infrared photodetector technologies, group III-V compounds have been widely used [1]. Especially, type-II InAs/GaSb superlattice (SL) structures have been proposed and heavily studied as an alternative candidate for the third generation systems [2]. It is important to study the individual InAs and GaSb layers and their interfaces of the order of 1-2 monolayers by using transmission electron microscopy (TEM) techniques since the defects in the crystal, layer thicknesses, and intermixing at the interfaces are crucial for the device performance. The most appropriate TEM techniques to investigate the layer thicknesses and to examine the packing of atoms at the interfaces are high resolution transmission electron microscopy (HRTEM) and scanning transmission electron microscopy (STEM) techniques.

Epitaxial growth of high quality electronic and optoelectronic devices require the use of high quality substrates with low defect and etch pit densities as well as the growth of atomically smooth, ideally defect-free buffer layers. The surface quality of the GaSb layer is especially critical in the detector performance; because, any roughness in the InAs/GaSb superlattices leads to inferior lateral transport and in-homogeneity of the band gap [3]. Therefore, the effect of the growth parameters such as growth temperature, V/III beam flux ratio and cooling steps for a high quality material growth was studied and the surfaces have been investigated by the SEM.

In electron microscopy the reliability of the analyses are directly related to the samples and also to the sample preparation procedures. Successful electron microscopy with all of the possible techniques depends on the quality of the specimens' examined. Preparation of TEM samples can be identified as an art more than a science. The necessity of the samples being electron transparent makes the sample preparation procedures challenging. The samples for TEM analyses are prepared in many different ways depending on the production types and/or application areas.

In this study, due to the soft and very brittle characteristics of the aforementioned structures, it was first aimed to prepare very thin (<100 nm) damage free samples for TEM analyses. After a cross-sectional TEM sample preparation recipe was improved, the TEM-BF, HRTEM and STEM techniques were used to investigate the structural properties of the MBE grown type-II SL structures. The microstructures of the SL structures were examined by the TEM-BF imaging technique after the SLs were grown. Then the layer thicknesses obtained via STEM investigations. Finally, the interfaces were examined with HRTEM technique to show the abruptness of the layers and the packing of atoms. In the SEM and TEM analyses, Zeiss Supra 50VP and JEOL™ JEM-2100F were used respectively.

1. Rogalski, A., Opto-Electron. Rev., 14**,** (2006), p. 98-84.
2. Razeghi, M., Nguyen, B.M., Hoffman, D., Huang, E.K., Delaunay, P.Y., Proc. of SPIE, 7298 (2009), p. 72981T-13-72981T-1,
3. Razeghi, M., Mohseni, H., Tahraoui, A., Wojkowski, J., Brown, G.J., Mitchel, W.C., Park, Y.S., Appl. Phys. Lett., 77 (2000), p. 1572-1574.
4. Authors would like to thank Bulent Arikan for providing MBE grown superlattice structures. This work was supported in part by TUBITAK under the Grant No. 111T335 and by Anadolu University under the project BAP-1205F083.

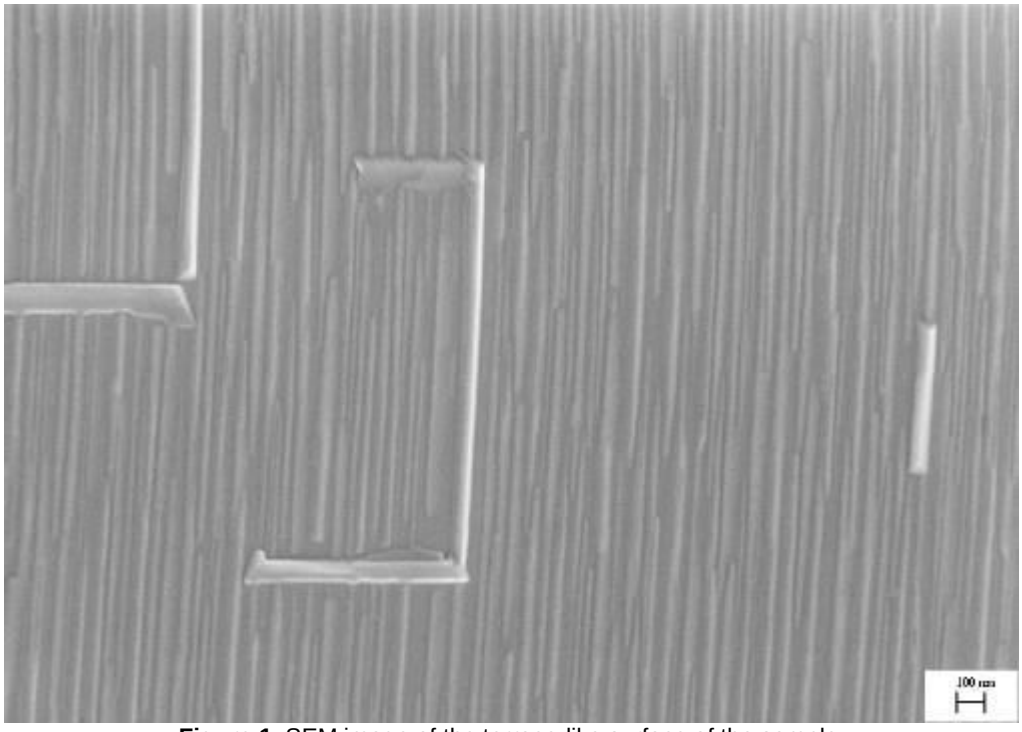

Figure 1. SEM image of the terrace-like surface of the sample.

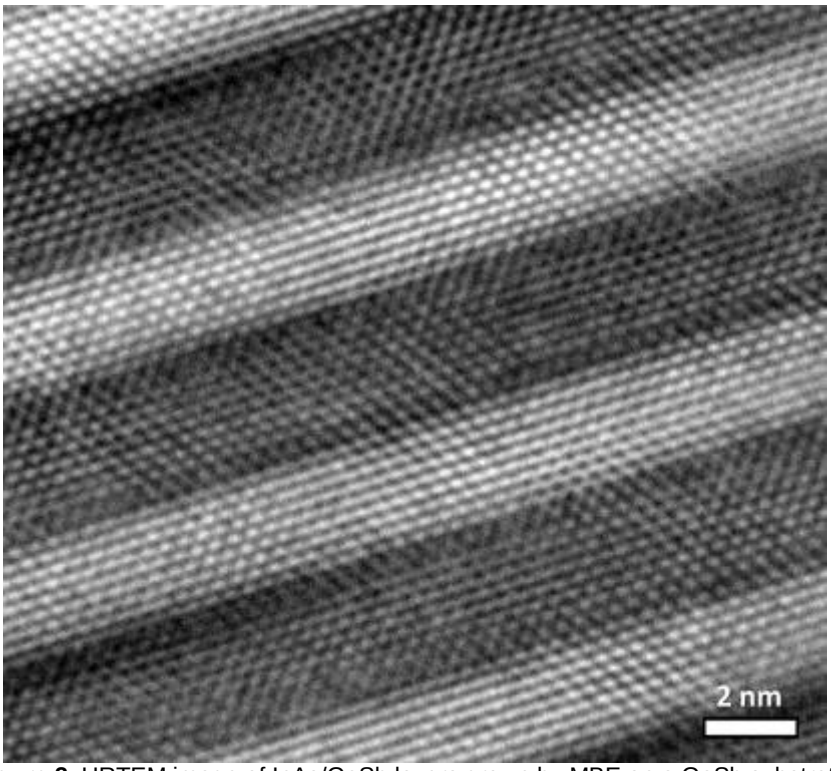

Figure 2. HRTEM image of InAs/GaSb layers grown by MBE on a GaSb substrate.

Alloys and Intermetallics

LBP.MS.P11
Bridging effect during stainless steels fracture

F.A. Emhmmed[1]

[1]Al Zaytona University, Materials , Tripoli, Libyan Arab Jamabiriya

libyatat@yahoo.co.uk
Keywords: Stainless steels, Fracture toughness, 475°C , Brittle fracture , CTOD, DCPD.

Duplex stainless steels specimens were heat treated at 475°C for different times and pulled to failure. Fracture toughness testing was performed according to BS 7448, using a clip gauge to monitor specimen displacement. In addition, the direct current potential drop (DCPD) technique was used to monitor the crack propagation. The Crack Tip Open Displacement (CTOD) was evaluated. Computational data, Shear model, were fit to the experimental ones. Discrepancy was observed between the experimental data and the computational ones. The model was able to expect the crack tip open displacement (CTOD), experimental data , only within a certain range of the material hardness i.e. microstructure . In addition, the direct current potential drop technique was more sensitive to detect the crack propagation process than that observed for the clip gauge. The fracture mode was found to be dominated by transfers brittle fracture in ferrite phase. The crack avoided the ductile regions within the tested microstructure. Ligaments , 1-2mm in size, observed at the wake of the crack path and some identified grains exerted a bridging effect on the crack tip leading to an increase in the applied stress required to propagate the crack . Discontinuous cracking was observed specially just before the arrested crack tip. Twinning was observed in the vicinity of the cracks . It was shown that unfractured austenite grains bridged the crack plane. The bridging zone was typically several mm in length. Metallographic examination confirmed that the cracking propagates transgranularly in ferrite phase . Intergranular cracking mode was not observed .The austenite phase was rarely cracked and generally acted as a crack bridge or crack arrestor . Scanning electron microscopy and transmission electron microscopy (TEM) have confirmed brittle fracture in ferrite phase and ductile tearing off in austenite phase as cracking behavior.

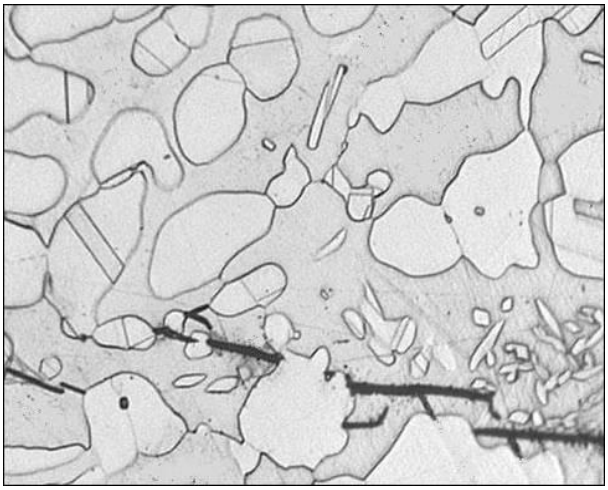

Figure 1.

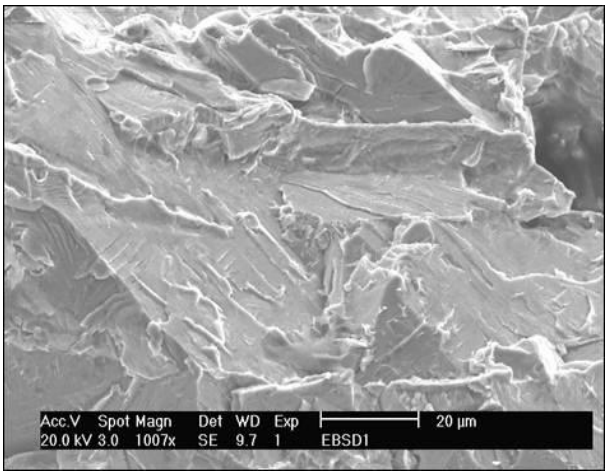

Figure 2.

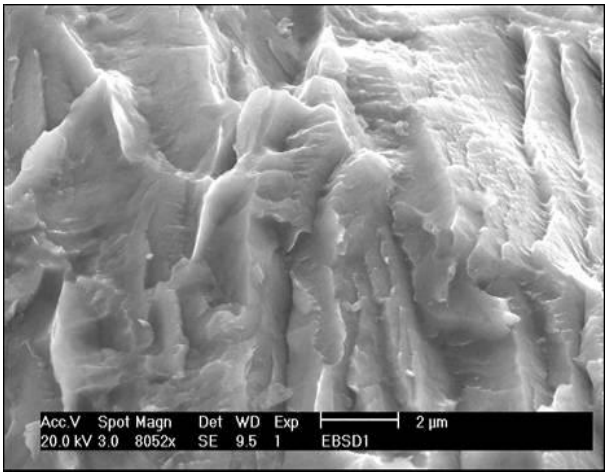

Figure 3.

Soft Matter, Polymers, Composites

LBP.MS.P12
HRTEM imaging of inorganic/organic interfaces

K. Holm[1], S. Stephan[1], H. Ines[1]

[1]Humboldt-Universität zu Berlin, Institut für Physik, AG TEM, Berlin, Germany

holm.kirmse@physik.hu.-berlin.de
Keywords: hybrid inorganic/organic interfaces, HRTEM, image analysis

The interfacial structure of hybrid inorganic/organic systems (HIOS) strongly influences their resulting physical properties. The inorganic component comprises, e.g., semiconducting materials for optoelectronic applications. In our case an extended single crystalline (0001) oriented ZnO substrate was selected. On the organic side there are conjugated molecules exhibiting a delocalised π system making the electrons available for charge transport. Para-sexiphenyl (6P) was selected for our HIOS model system. The arrangement of the molecules on the semiconductor surface is subject of vivid fundamental research. From atomic force microscopy performed after deposition of the 6P layer some information is gained on its morphology including lateral size and height of islands formed at the semiconductor surface [1]. But the evolvement of the deposition of multilayer 6P cannot be recognized by a top-view analysis after growth. Here either in-situ measurements by gracing incidence X-ray scattering [2] or – and this is the focus of this work – cross-sectional transmission electron microscopy (TEM) imaging can give valuable information. For gaining electron transparent cross-sectional specimen special care has to be taken with respect to the striking different materials properties of both components of HIOS. An appropriate route for cross sectional TEM preparation by room temperature ultramicrotomy was described elsewhere [3]. This route was applied here and resulted in a TEM specimen thickness of about 100 nm. TEM investigations were performed utilizing a TEM/STEM JEOL JEM2200FS operated at 200 kV. The 2200FS is equipped with an in-column energy filter utilized here for increasing the image contrast by inserting a slit of a width of 10 eV. Thus only elastically scattered electrons contribute to imaging.

Figure 1 shows two high-resolution TEM (HRTEM) images of the same HIOS interface area recorded for Scherzer focus (a) and for a defocus of about -1000 nm (b). The dark spots atop 6P of about 10 nm in diameter originate from ZnO nanoparticles deposited after 6P growth. The large defocus was chosen in order to enhance the phase contrast of 6P. The effect is clearly seen comparing the line scans extracted across the interface between ZnO substrate and 6P (see Fig. 1c). The dotted line corresponds to Scherzer defocus and the solid line corresponds to a defocus of -1000 nm. In order to analyze the periodicity of the 6P lattice planes the position of the HRTEM intensity maxima were identified and the inter-planar distances were extracted. The distances given in Fig. 1c are taken from the profile of the image defocused by -1000 nm. The position of the first lattice plane can hardly be seen since the fringe contrast due to Fresnel diffraction at the interface is superimposed. But comparing the two profiles, a first 6P lattice plane can be recognized at a distance of about 1.0 nm from the HIOS interface. The inter-planar distance increases to 2.4 nm within the next two monolayers.

In order to optimize the defocus condition for identifying all the 6P lattice planes several defocus series were acquired with non-linear focus change ranging between 0 nm and -2000 nm (cf. Fig. 2). 6P lattice plane positions were identified for the full set of images by an own software routine from intensity line scans taken across the HIOS interface and laterally averaged within the area marked in Fig. 2a. The results are given in Fig. 2b (see open symbols). For the entire focus series the position of the individual lattice plane remains almost constant. Against that, the position d of the Fresnel fringe changes with defocus Δf. In a first approximation this behavior can be described by $d = \sqrt{(\Delta f * \lambda)}$; λ-wavelength (see solid line in Fig. 2b). Consequently, for a certain focus range the fringe superimposes to the first 6P lattice plane hampering their identification. But with increasing defocus the fringe shifts and the first 6P lattice plane can be located as shown in Fig. 1c. The defocus scale was adjusted to zero focus by extrapolating the function of Fresnel fringe position to zero value.

The data extracted from defocus series of HRTEM images prove that the alignment of 6P molecules undergoes a modification from almost lying parallel to the ZnO surface to standing almost upright which corresponds to the monoclinic bulk structure of 6P. Thus from HRTEM measurements valuable information is gained for understanding the structure of the HIOS interface.

1. S. Blumstengel, H. Glowatzki, S. Sadofev, N. Koch, S. Kowarik, J.P. Rabe, F. Henneberger, Phys. Chem. Chem. Phys. **12** (2010) 11642.
2. C. Weber, C. Frank, S. Bommel, T. Rukat, W. Leitenberger, P. Schäfer, F. Schreiber, S. Kowarik, J. Chem. Phys. **136** (2012) 204709.
3. H. Kirmse, E. Oehlschlegel, F. Polzer, S. Blumstengel, M. Sparenberg, F. Henneberger, Microscopy of Semiconducting Materials 2013, in print.
4. The authors are thankful to F. Henneberger, S. Blumstengel, and M. Sparenberg for provision of sample. Financial support by the DFG within the SFB 951 HIOS is gratefully acknowledged.

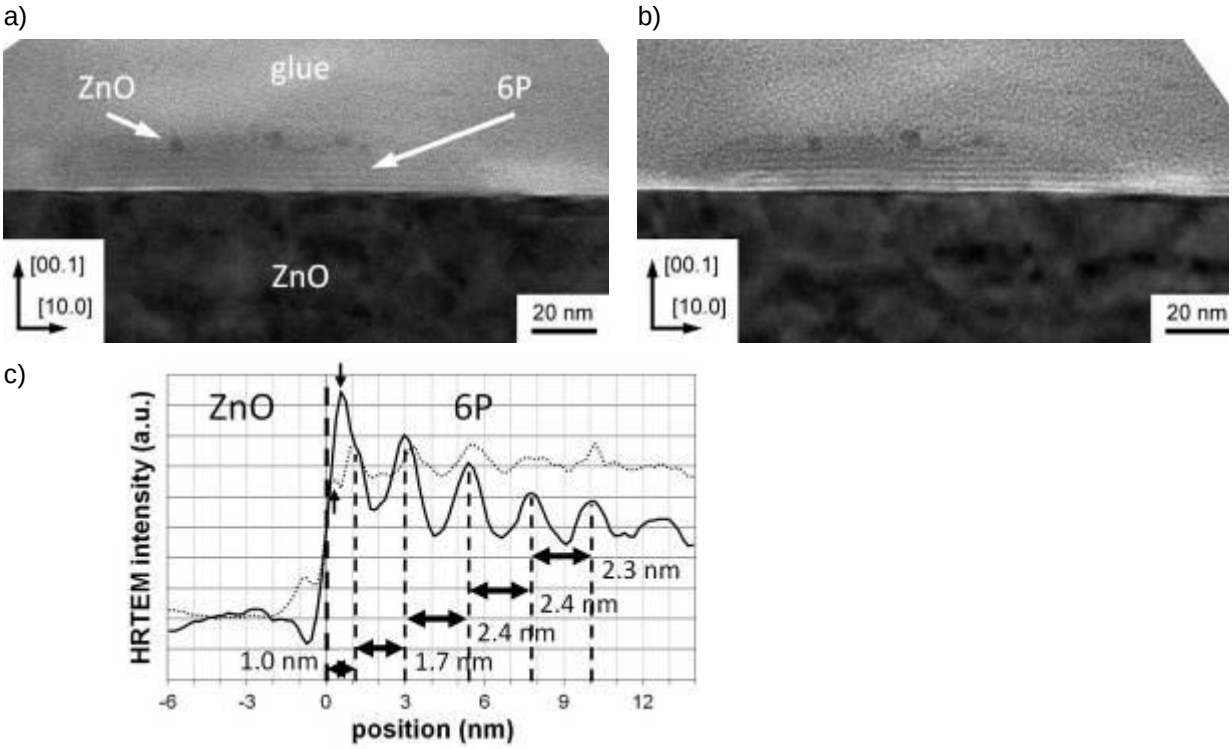

Figure 1. HIOS interface analysis by HRTEM imaging using only elastically scattered electrons: a) Scherzer defocus image showing weak phase contrast, b) enhanced phase contrast at a defocus of -1000 nm, c) HRTEM intensity profiles taken from scans across the HIOS interface (bold dashed line). Dotted line: Scherzer defocus image, solid line: out-of-focus image. The distances between the identified lattice planes are measured between maximum positions of the HRTEM intensity. The first maximum of both profiles (marked by vertical arrow) is due to diffraction at the interface. It shifts with defocus

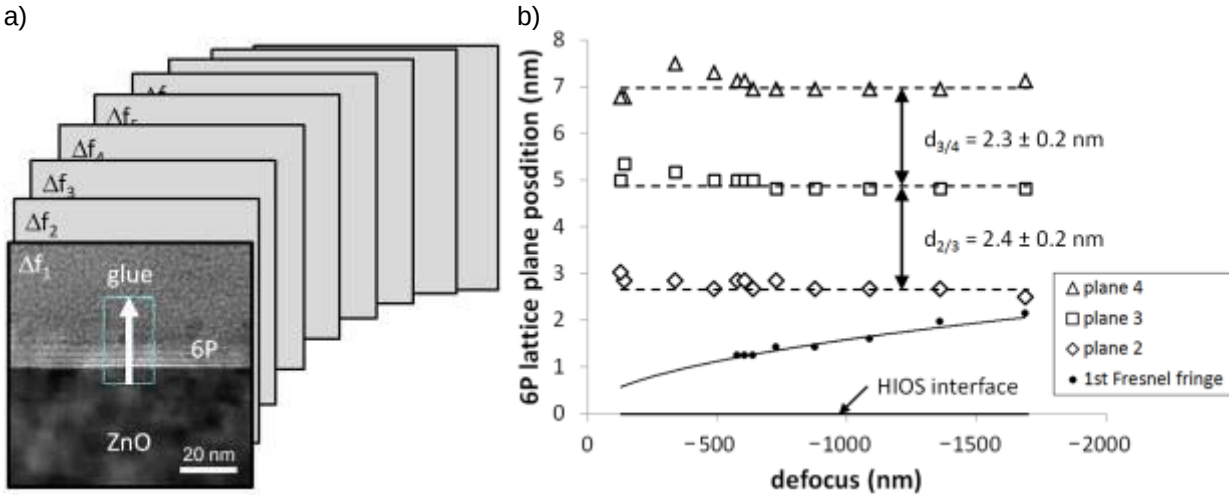

Figure 2. Distance of lattice planes from the HIOS interface for a series of defocused images: a) sketch of defocus series with indicated line scan position, b) distance of 6P lattice planes from the HIOS interface depending on defocus. The dots correspond to the detected position of the 1st Fresnel fringe due to diffraction at the HIOS interface. The solid line corresponds to the calculated position if the first Fresnel fringe.

Alloys and Intermetallics

LBP.MS.P13
EBSD study on the evolution of microstructure in pure copper after processing by high-pressure torsion

K. Al-Fadhalah[1], A. Almazrouee[2], S. Alhajeri[2], T. Langdon[3,4]

[1]Kuwait University, Mechanical Engineering, Safat, Kuwait
[2]College of Technological Studies, PAAET, Manufacturing Engineering, Kuwait City, Kuwait
[3]University of Southampton, Materials Research Group, Faculty of Engineering and the Environment, Southampton, UK, United States
[4]University of Southern California, Departments of Aerospace & Mechanical Engineering and Materials Science, Los Angeles, CA, USA, United States

khaled.alfadhalah@ku.edu.kw

The evolution of microstructure in high purity copper subjected to high-pressure torsion (HPT) has been examined by Electron backscattered diffraction (EBSD). Copper disks were processed in HPT for 1/4, 1/2, 1, 5, and 10 turns under a pressure of 6.0 GPa. Results indicate the formation of Σ3 twin boundaries by recrystallization before complete microstructural refinement. A gradual increase in the homogeneity of the microstructure occurred with increasing numbers of turns, reaching stabilized ultra-fine grain structure at 5 turns with minimum grain size of 150 nm. In addition, microhardness measurements indicate softening by recrystallization at early stages of HPT straining; further straining at large number of turns results in hardness homogeneity with maximum hardness of 157 Hv.

Introduction

The production of bulk ultra-fine grained materials has been possible by applying a severe plastic deformation process such as high-pressure torsion (HPT) [1]. In such method, a disk is subjected to a compressive pressure of several GPa and concurrent torsional straining that occurs by rotation of the lower anvil while the upper anvil is kept fixed (Fig.1). The process causes large shear strain without any significant changes in the disk dimensions, resulting in grain refinement in the microstructure with an average grain size in the submicron level (0.1-1 μm). This provides an excellent combination of strength and ductility in metals and alloys [1]. The aim of this work is three fold. First, to investigate the evolution of microstructure by EBSD for high purity copper subjected to HPT. Second, to provide some insight into the recrystallization process observed at the early stages of HPT straining. Finally, to correlate microstructural refinement by HPT to the evolution of microhardness with increasing number of turns.

Experimental Procedure

High purity copper rods were annealed for 1 hr at 400 °C and later cut into disks with diameter of 10 mm and thickness of 0.8 mm. The disks were HPT processed for number of turns *N* = 1/4, 1/2, 1, 5, 10. Compressive pressure of 6 GPa was applied and each disk was strained in torsion at rotational speed of 1 rpm. The microstructure was examined by Electron Back Scattered Diffraction (EBSD) technique equipped in Scanning Electron Microscope (SEM). Vickers microhardness was made under a load of 200 gf and dwell time of 15 sec.

Results

Figure 2 presents EBSD maps of grain boundary reconstruction, illustrating evolution of microstructure at three radial positions (center, mid-radius and near-edge) with increasing *N*. In the early straining stage (*N* = 1/4 turn), grain refinement and concurrent recrystallization occurred at the near-edge position, producing large fraction of Σ3 twin boundaries. Recrystallization shifted toward the center of the disk upon further straining. Full grain refinement was first observed in the near-edge position for *N* = 1 turn. More homogeneous and stable grain structure was achieved at 5 and 10 turns. At this level of high strain, the grain size reaches a minimum of about 150 nm. Moreover, the microhardness results in Fig.3 suggest the occurrence of recrystallization at initial stages of HPT as observed by the drop in the hardness values near the edge. Such drop shifts toward the disk center with increasing number of turns. At *N* = 5 turns and higher, more homogeneity in microhardness is achieved.

Conclusion

- Recrystallization occurs initially at early stages of HPT straining, followed by homogeneous grain refinement at higher strains.
- Drop of microhardness at near-edge indicates softening by recrystallization; further straining results in hardness homogeneity.

1. The authors would like to acknowledge Kuwait University funding project (GE 01/07) and PAAET project (TS-12-03).
2. Zhilyaev and Langdon, *Prog. Mat. Sci*., 2008, 53, 893.
3. Xu, Horita, and Langdon, Acta Mater., 2008, 56, 5168.

.

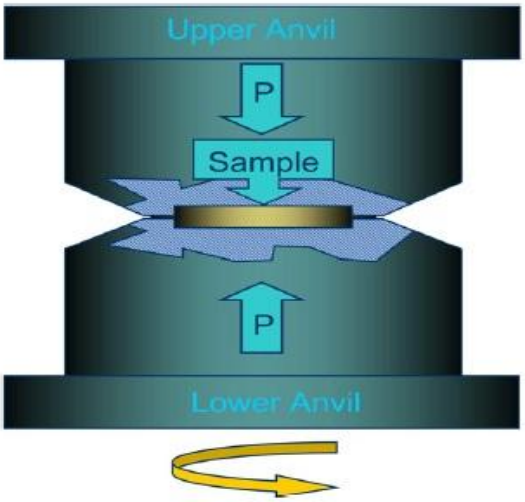

Figure 1. Schematic illustration of HPT processing [2].

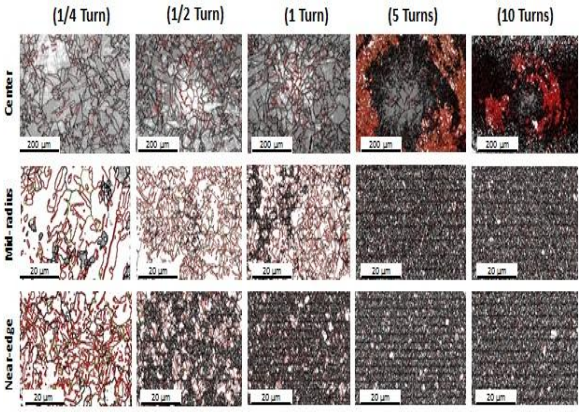

Figure 2. Grain boundary reconstruction from EBSD maps for samples processed at *N* = 1/4, 1/2, 1, 5, and 10 turns. Grey lines denote LABs, black lines denote random HABs, and red lines represent Σ3 boundaries.

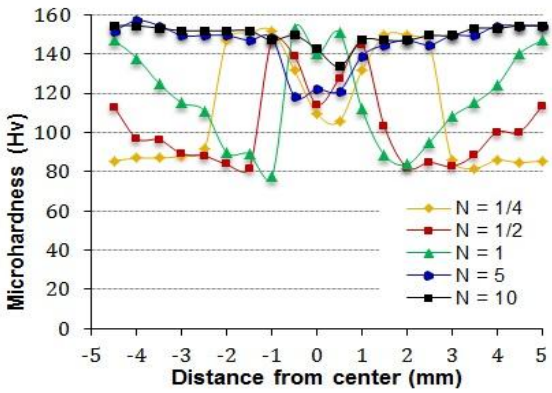

Figure3. Microhardness plots of HPT copper samples processed at *N* = 1/4, 1/2, 1, 5, and 10 turns

Thin Films and Coatings

LBP.MS.P14
In situ transmission electron microscopy study on solid-state dewetting of Au thin films

F. Niekiel[1], S.M. Kraschewski[1], B. Butz[1], E. Spiecker[1]

[1]Center for Nanoanalysis and Electron Microscopy, Universität Erlangen-Nürnberg, Department of Materials Science and Engineerging, Erlangen, Germany

florian.niekiel@ww.stud.uni-erlangen.de

Solid-state dewetting describes the instability of thin films to transform into an energetically favorable set of droplets or particles well below the melting temperature of the bulk material. The effect of solid-state dewetting becomes more severe as the film thickness decreases and thus plays an important role in the rising focus on nanotechnology [1]. There are two different perceptions of solid-state dewetting in the field of applications:

On the one hand metallic and semiconducting thin films are the key building block of modern electronics, magnetics and optics applications, whose lifetime can be drastically decreased by solid-state dewetting as a failure mechanism. Exposure to raised temperature cannot only occur in the final application but as well during the production process, making the usage of thin films a challenge. One example is the increase in sheet resistance of a NiSi thin film contact on Si due to solid-state dewetting at temperatures above 700°C [2].

On the other hand controlled solid-state dewetting of thin films can be employed to produce regular arrays of functional nanoparticles on large area substrates via a simple deposition process followed by appropriate annealing. Recent advances allow to control the order, shape and spacing of the produced nanoparticles with possible applications in the field of plasmonics [3] or as templates for the growth of other nanostructures [4].

In this work we report on the use of advanced *in situ* transmission electron microscopy (TEM) techniques to study the fundamental physics underlying the phenomenon of solid-state dewetting. Au thin films on a silicon nitride substrate (fabricated via sputtering) are heated in the transmission electron microscope using a DENSsolutions sample heating system. The samples are imaged using annular dark field scanning transmission electron microscopy (ADF-STEM) *in situ* while undergoing heat treatments at constant temperatures in the range of 200°C to 500°C.

Figure 1. shows ADF-STEM images of the as deposited Au thin film (left) and after annealing for 50 min at 300°C in the electron microscope (right). The phenomenon of solid-state dewetting is clearly visible leading to a set of separated islands of sizes between 30 and 150 nm. It has to be noted that the initial Au film was not continuous but already showed elongated voids due to the production process. This has been exploited to directly study the process of void growth without having to consider void nucleation which is the first step in solid-state dewetting [1]. The in situ experiments have been evaluated calculating difference images, as shown in figure 2., to follow the material transport. Thresholding of the images has been used to extract information such as area coverage and perimeter length to evaluate the edge velocity, a key quantity in models for solid-state dewetting. The temperature dependence of the edge velocity has been employed to estimate the activation energy giving a quantity in the range for surface self-diffusion of Au.

1. C.V. Thompson, Annual Review of Materials Research 42 (2012), pp. 399-434
2. D. Deduytsche, C. Detavernier, R.L. Van Meirhaeghe, C. Lavoie, Journal of Applied Physics 98 (2005), 033526
3. S. Yang, B. Cao, L. Kong, Z. Wang, Journal of Materials Chemistry 21 (2011), pp. 14031-14035
4. W.K. Choi, T.H. Liew, H.G. Chew, F. Zheng, C.V. Thompson, Y. Wang, M.H. Hong, X.D. Wang, L. Li, J. Yun, Small 4 (2008), pp. 330-333
5. The authors thank DENSsolutions company for providing the heating holder for this study.

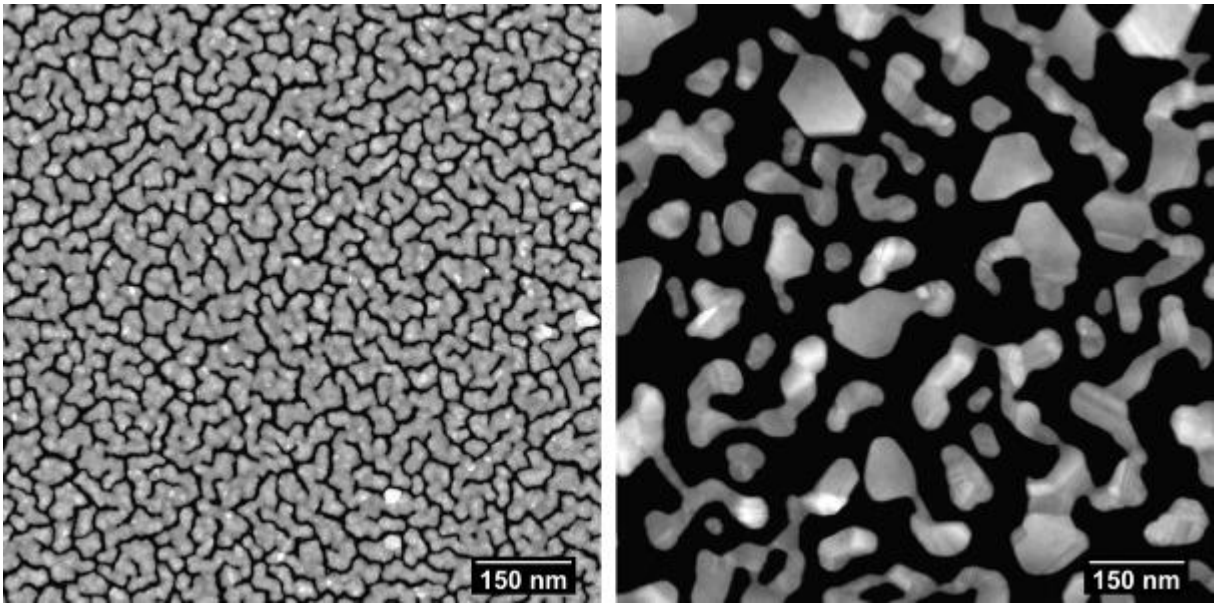

Figure 1. ADF-STEM image of (left) as deposited discontinuous Au thin film on silicon nitride membrane, (right) after annealing at 300°C for 50 min in the TEM.

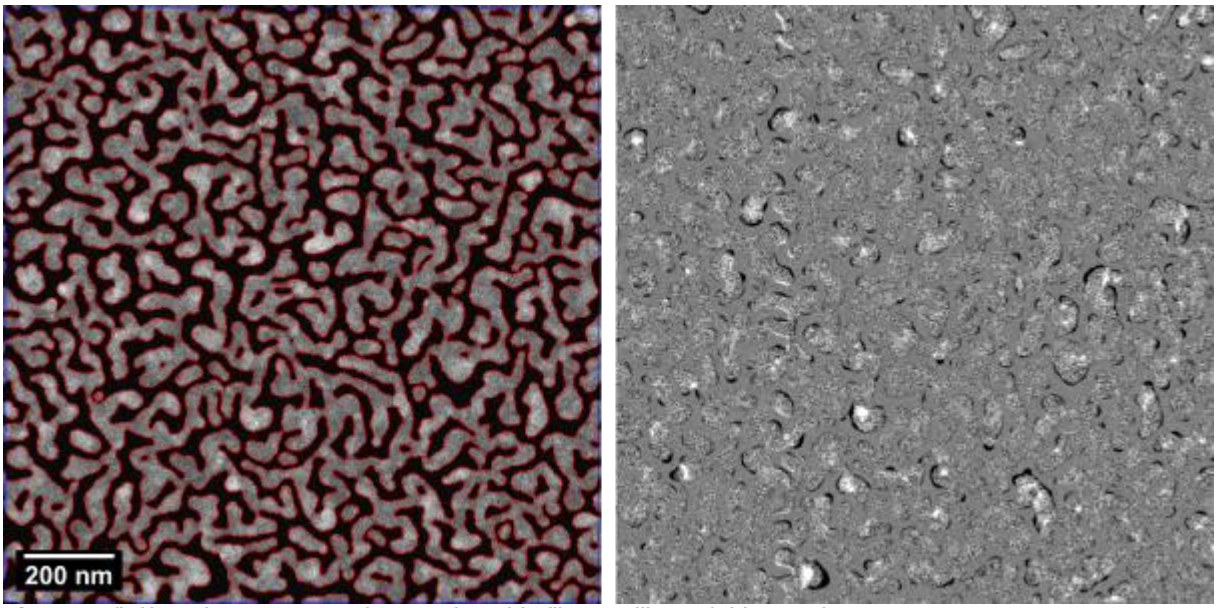

Figure 2. (left) In situ ADF-STEM image of Au thin film on silicon nitride membrane at t = 18 s at 300°C, frametime 2 s, detected perimeter used for velocity determination is overlaid in red, (right) differential image showing contrast changes from t = 16 s to t = 18 s, black corresponds to an decrease in contrast, white to an increase.

Alloys and Intermetallics

LBP.MS.P15
TEM analysis of localized, planar deformation events which govern creep of single crystalline CoNi-superalloys with γ/γ´-microstructures

Y. Eggeler[1], J. Müller[1], M.S. Titus[2], A. Suzuki[3], T.M. Pollock[2], E. Spiecker[1]

[1]Universität Erlangen-Nürnberg, Center for Nanoanalysis and Electron Microscopy (CENEM), Department for Material Science, Erlangen, Germany
[2]University of California Santa Barbara, Department for Material Sience, Santa Barbara, United States
[3]GE Global Research Center, One Research Circle, Niskayuna, NY 12309, United States

yolita.eggeler@ww.stud.uni-erlangen.de
Keywords: CoNi-Superalloys, Anti phase boundaries, Conventional Transmission Electron Microscopy,

In the present study we use transmission electron microscopy (TEM) to study the effect of creep on the microstructures of novel Co-based single crystal superalloys with γ (fcc) - γ´ ($L1_2$) microstructures [1]. The alloys investigated contain 30-39 at.% Ni [2], which was added to the Co-Al-W ternary system to expand the γ-γ´ phase field and to increase the γ'-solvus temperature [3]. Tensile creep experiments were performed along [001] at stresses of about 300 MPa, at 900°C to small strains (0.5 - 2%).

While crept Ni-base superalloys often exhibit superdislocation in the γ´-phase consisting of two closely dissociated superpartial dislocations connected by an antiphase boundary (APB) [4], the CoNi-alloys show large APBs produced by shearing of single superpartial dislocations. Different two beam conditions were performed using fundamental reflections and superlattice reflections for fault characterization by applying the invisibility criterion. In TEM samples with foil normal parallel to the tensile axis dislocations of type a/2 [011] and a/2 [01-1] are visible which cut the γ´ phase and create APBs (figure 1). Samples with foil normal perpendicular to the tensile axis reveal the presence of macroscopic planar faults extending over several precipitates on octahedral planes (see figure 2). Using higher magnifications one can observe, that these planar defects consist of APBs attached to stacking faults (SFs). By comparing bright-field (BF) micrographs showing only weak residual APB contrast with central dark-field (CDF) images taken with superlattice reflections, which provide good APB contrast, one can clearly locate the APBs, as demonstrated by figure 2 where for one precipitate the APBs are marked with continuous black arrows on both sides of the SF marked with a long dotted black arrow. Partial dislocations define the APB/SF-contact lines. A thicker part of a [110] oriented sample exhibit dislocation loops surrounding an inclined SF with a weak residual APB contrast (not shown). Based on the results mentioned above a first deformation mechanism is proposed where a single dislocation is cutting the γ'-precipitate. However, to further characterize the cutting process samples with [111] foil normal orientation will be prepared and analyzed by e. g. STEM and LACBED. Scanning transmission electron microscopy (STEM) permits analysis of extended TEM foil regions.

The present study contributes to a better understanding of these cutting events, which have not been frequently observed before and is discussed with reference to previous work published in the literature.

1. J. Sato et al," Science (2006), vol.312, p. 90
2. M. S. Titus et al, Scripta Materialia (2012), vol.66, p. 574
3. K. Shinagawa et al, Materials Transactions (2008), vol.49, p. 1474
4. A. Kostka et al, Journal of Materials Science (2007), vol.42, p. 3951
5. The authors gratefully acknowledge GE, NSF, and the DFG priority program SFB-TR 103 for financal support.

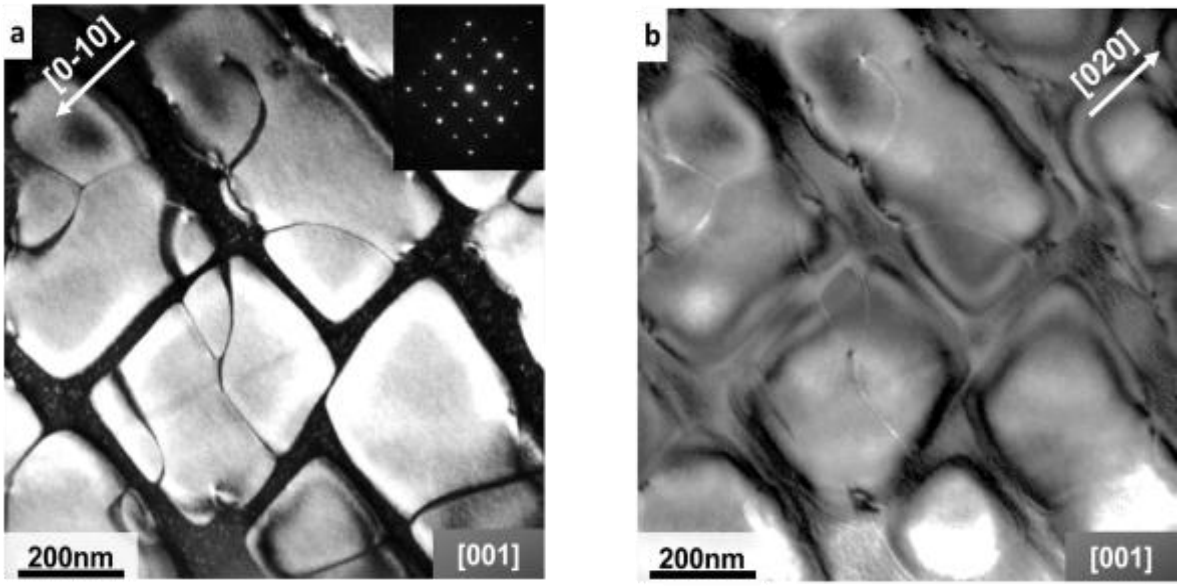

Figure 1. TEM micrographs of CoNi-A crept 0.5% under an applied stress of 310 MPa at 900°C (stress axis out of plane). a) Centered dark field image in two beam condition using superlattice reflection g=(0-10) presenting good APB contrast. b) Bright field image in two beam condition using fundamental reflection g=(020) showing dislocation contrast and weak residual APB contrast. Both micrographs were taken near Zone axis [001].

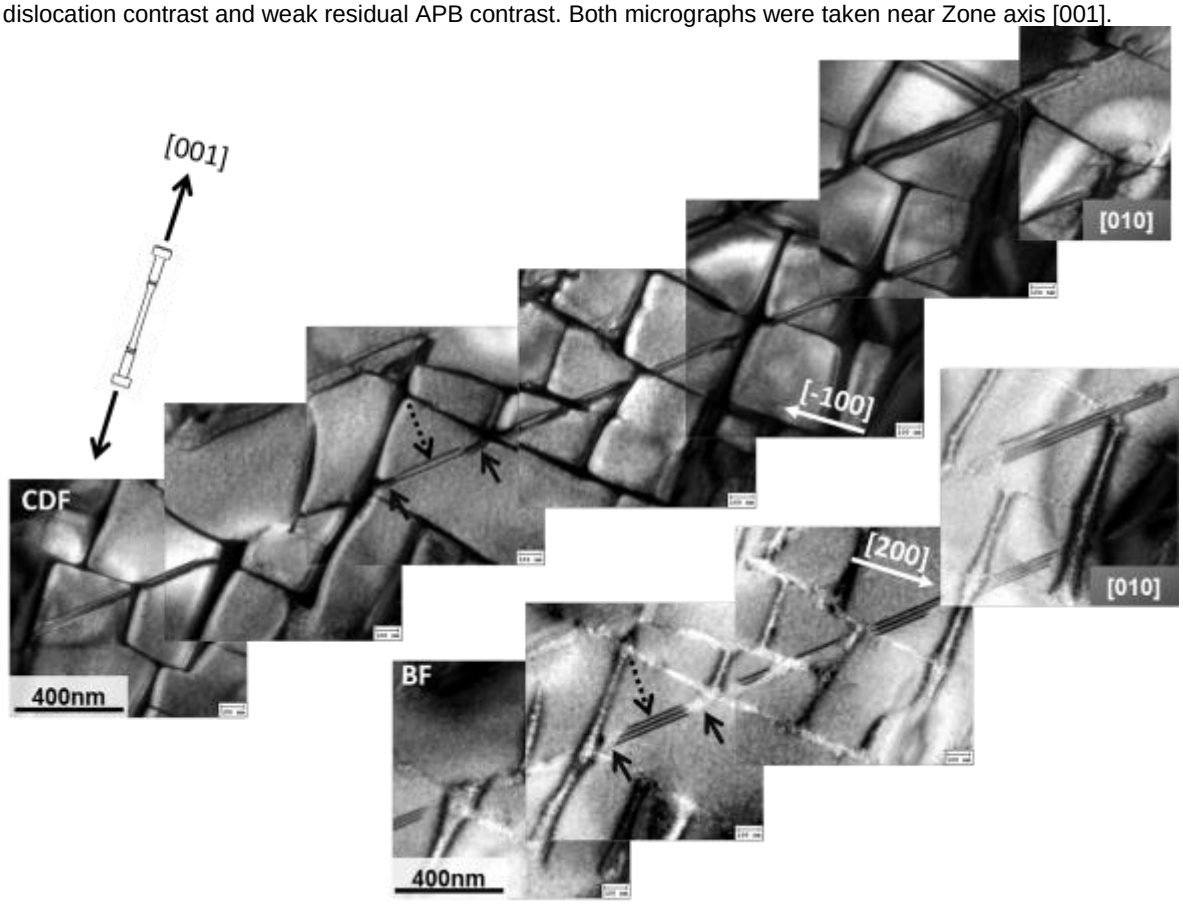

Figure 2. Montage of TEM micrographs shows macroscopic planar faults extended over several precipitates. The upper row of monatage was taken with [-100] superlattice reflection in CDF mode. The lower row of montages shows the corresponding BF contrast taken with the fundamental reflection g=(200). The long dotted arrow marks marks the SF contrast and the two continuous black arrows mark where the APBs are located for the same precipitate in CDF and BF mode. The tensile axis lies in the plane of the micrographs and is schematically drawn in the top left corner. Both modes were taken close to the [010] Zone axis.

Functional Materials

LBP.MS.P16
Investigating dislocation activity in Nb_2AlC layered carbide using In situ TEM nanomechanical testing

Y. Kabiri[1], J. Müller[1], M. Mackovic[1], E. Spiecker[1]

[1]Center for Nanoanalysis and Electron Microscopy, Erlangen, Germany

yoones.kabiri@studium.uni-erlangen.de
Keywords: Nb_2AlC, Dislocation, In situ TEM

MAX phase layered crystals have attracted much interest in scientific community because of their damage tolerance (up to ~25% dissipation energy) and high oxidation resistance (up to 1300°C), making them a promising material system for high temperature applications.

In these layered materials - unlike many crystals - dislocation activity is believed to be partially reversible and is only limited to easy slip systems along basal planes. In the past, fully reversible, rate independent and closed hysteresis loops are observed in cyclic stress-strain curves which are attributed to formation and annihilation of incipient kink bands (IKBs) and dislocation walls [1].

To date, the precise mechanism of dislocation wall and IKBs nucleation is not known and no decent investigation has been carried out to understand their dynamics using In situ TEM. It is believed that by controlling the parameters which influence these dynamics, it is possible to control the mechanical properties dramatically.

In this study, a wedge shaped thin foil of polycrystalline Nb_2AlC was prepared by special mechanical grinding and ion milling procedure. The edge of the sample was cut using Focused Ion Beam (FIB) to reduce bending of thin parts during In situ nanoindentation. Convergent beam electron diffraction (CBED) technique was used to find the suitable crystal orientation and nanomechanical testing was performed using the Hysitron® Picoindenter set up with a cube-corner indenter inside a Phillips CM30 TEM. Indentations were carried out using displacement-time mode and the corresponding force-displacement curve was collected.

Figure 1(a-e) depicts some typical dislocations inside the undeformed Nb_2AlC specimen. Tilting into two beam conditions around <0001> zone axis together with contrast analysis revealed that the dislocations lie in basal plane with 1/3<11-20> type burgers vectors. This is in agreement with previous results published by Farber et al. for another family of MAX phases (Ti_3SiC_2) [2].

Figure 2 shows one in situ TEM nanoindentation experiment for grain oriented near to <0001> direction relative to the electron beam. The blue curve in Figure 2(a) is the displacement-time and the red curve is the corresponding load-displacement function. Before the indentation, the area was pre-characterized to prove that it is dislocation free (Figure 2(b)). It can be clearly seen that basal plane dislocations nucleate and move during the loading in a same slip system without cross-slip or entanglement, confirming that these dislocations are mobile at room temperature as previously proposed by Farber et al. [2]. Lost data points in displacement-time curve during unloading as well as negative values in force-displacement curve are related to adhesion between the tip and the specimen. Discontinuities in force-displacement curve pointed by an arrow in Figure 2(a) are attributed to dislocations formation. Similar behaviour is reported by Molina-Aldareguia et al. [3] for kink band formation during Ex situ indentation on Ti_3SiC_2. Ex situ diffraction contrast analysis was carried out to further characterize the dislocations. As illustrated in Figure 2(d and e), tilting into different two beam conditions revealed that the lines are dislocations with identical burgers vector as invisibility criterion suggests.

1. M.W. Barsoum, T. Zhen, S.R. Kalidini, M. Radovic, A. Murugaiah, Nat. Mater. 2 (2003), p. 107.
2. L. Farber, M.W. Barsoum, A. Zavaliangos, T. El-Raghy, J. Am. Ceram. 81 (1998), p. 1677.
3. J. M. Molina-Aldareguia, J. Emmerlich, J-P. Palmquist, U. Jansson, L. Hultman, Scripta. Mater. 49 (2003), p. 155
4. The authors would like to acknowledge the research training group 1229 for financial support. Assistances of Christel Dieker and Hana Stara during FIB preparation are also appreciated.

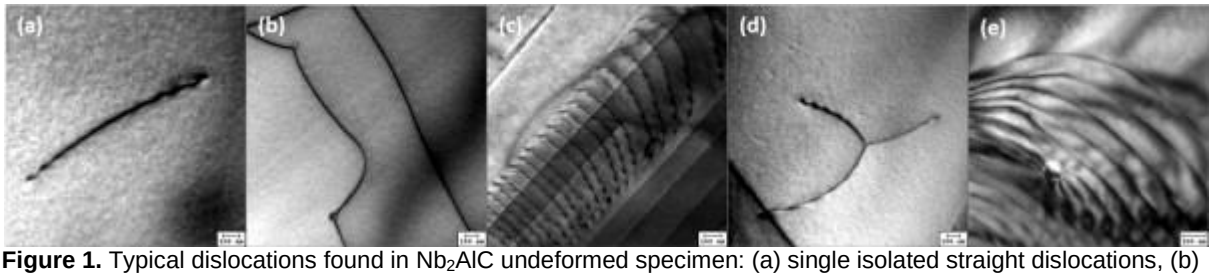

Figure 1. Typical dislocations found in Nb_2AlC undeformed specimen: (a) single isolated straight dislocations, (b) curved dislocations, (c) dislocation walls and arrays, (d) dislocation knots and (e) curved parallel dislocations

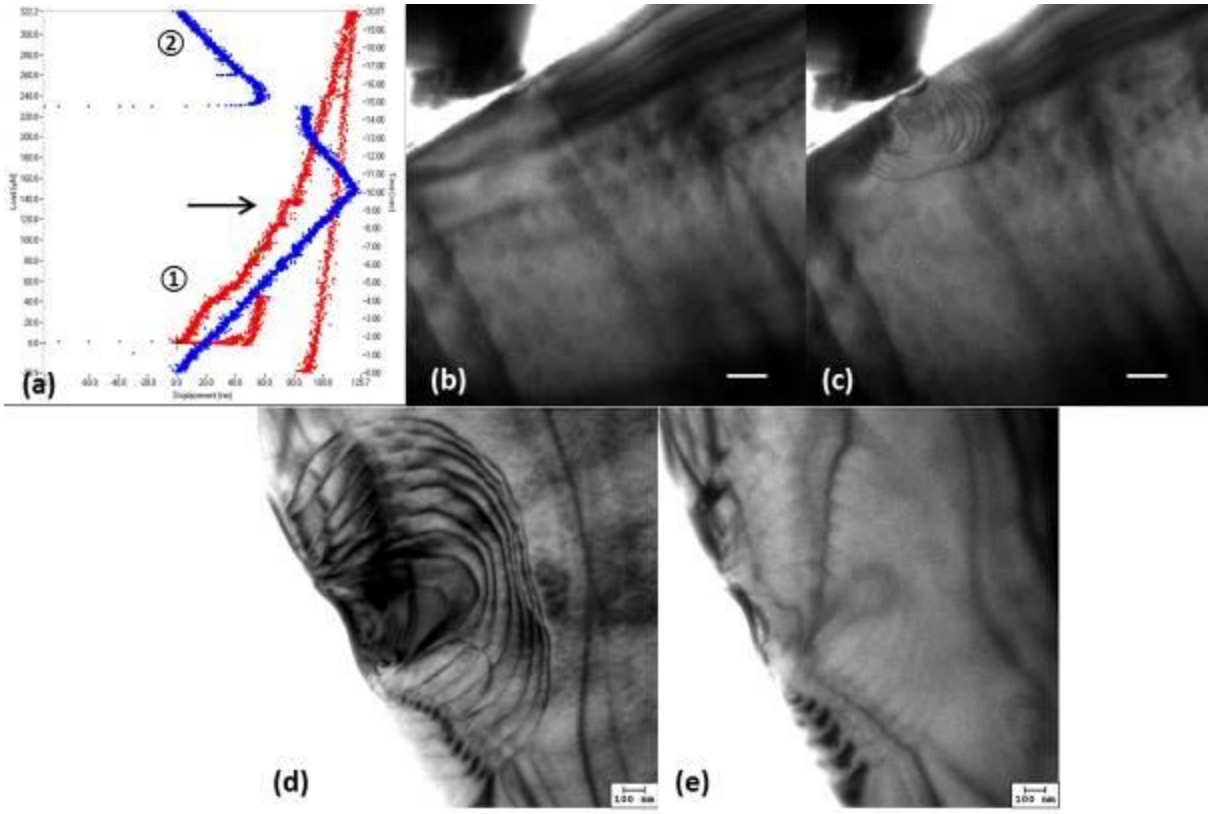

Figure 2. In situ TEM indentation near <0001> direction. (a) load-displacement (red) and displacement-time (blue), (b) start of indentation snapshot corresponding to position indicated with number 1 in (a), (c) end of indentation snapshot corresponding to position indicated with number 2 in (a), (d-e) Ex situ investigation of the same area with higher magnification and imaged with g=[11-20] in (d) and g=[2-1-10] in (e). Dislocations are visible in (d) and invisible in (e), meaning the same type burgers vector. The scale bars in figure (b) and (c) are 500 nm.

Materials for Energy Technology

LBP.MS.P17
Impact of Nickel on the accelerated degradation of Y_2O_3-stabilized Zirconia (YSZ) electrolytes

M. Stark[1], B. Butz[1], N.H. Menzler[2], S. Michel[3], H. Störmer[4], A. Utz[5], E. Ivers-Tiffée[5], D. Gerthsen[4]
E. Spiecker[1]

[1]Friedrich-Alexander-University Erlangen-Nuremberg, Center for Nanoanalysis and Electron Microscopy (CENEM), Erlangen, Germany
[2]Forschungszentrum Jülich GmbH, Institute of Energy and Climate Research (IEK-1), Jülich, Germany
[3]University Erlangen-Nuremberg, Chair of Metals Science and Technology (WTM), Erlangen, Germany
[4]Karlsruhe Institute of Technology, Laboratory for Electron Microscopy (LEM), Karlsruhe, Germany
[5]Karlsruhe Institute of Technology, Institute of Materials for Electrical Engineering (IWE), Karlsruhe, Germany

martin.stark@ww.stud.uni-erlangen.de
Keywords: EELS, oxidation state analysis

O^{2-}-conducting 8.5 mol% Y_2O_3-doped ZrO_2 (8YSZ) has been widely used as electrolyte for solid oxide fuel cells (SOFCs). It is furthermore applied in porous Ni/8YSZ ceramic-metallic (cermet) composite anodes to enhance the penetration depth of O^{2-} into the anode. Nickel is the standard anodic metal material due to its superior catalytic properties. The decomposition of pure 8YSZ is one important reason for the significant degradation of its ohmic resistance at high operating temperatures (~40% in 2500h at 950°C, [1]). This spinodal decomposition comprises both the microstructural coarsening of the tetragonal t''-YSZ phase as well as the chemical decomposition of the material [2]. It leads to Y-depleted regions (~10nm) in a Y-enriched matrix (Figure 1a, b) [1, 2]. In the presence of Nickel the decomposition of the 8YSZ is (under reducing atmosphere) accelerated by a factor of 50 [3] (Figure 1d). We assume that, when switching from oxidizing to reducing atmosphere, the dissolved Nickel ions capture electrons and change to the metallic state. The strain field, which would arise in the vicinity of the dissolved Ni species (radii: 0.69 Å Ni^{2+}, 1.25 Å Ni^0), is expected to strongly enhance the mobilities of Y- and Zr-ions of the host lattice. Moreover, the rapid diffusion of Ni-ions into 8YSZ (more than 100 µm at 1450 °C for 5 h) was observed in a recent study [3]. Owing to the rapid diffusion mentioned above, the drastic impact on the performance of the 8YSZ has to be expected if both materials, Ni and 8YSZ, are heat treated at high temperatures in oxidizing atmosphere. This applies to most state-of-the-art SOFCs, where the porous Ni/8YSZ anode (cell support) and the 8YSZ electrolyte (subsequently deposited) are co-sintered around 1400 °C. This is necessary to form a suitable network of NiO and 8YSZ within the anode (before reduction) as well as to generate a gas-tight electrolyte thin film. Consequently, one has to expect the electrolyte to be saturated by Ni.

Our aim is to investigate the oxidation state of the Ni species, dissolved in the 8YSZ, as well as the impact of the surrounding atmosphere thereon (by in situ switching the atmosphere) in order to understand the strong influence on the degradation mechanism at the atomic scale. Therefore, we apply complementary ex situ as well as in situ techniques to two types of samples: i) real anode half-cells with 10 µm thick electrolyte (cross-section shown in Figure 2a), and ii) thick-film 8YSZ electrolytes (200 µm thick), onto which NiO is deposited as thin film. To both types of samples, sintering at a high temperature (e.g., 1400 °C, 5 h) as well as various heat treatments under reducing conditions are applied. Preliminary WDXS (wave-length dispersive X-ray spectroscopy) measurements already revealed (Figure 2b) that Nickel is present to a reasonable concentration of about 1.5at% (solubility of Ni in 8YSZ) in the 8YSZ thin-film electrolyte of state-of-the-art SOFCs after co-sintering the half-cells (Figure 2a). This is in accordance with our prediction. Oxidation-state analyses by ex situ EELS utilizing the $L_{2,3}$-ionization edge allow for the site-specific characterization of the valance state of the dissolved Ni before and after the various heat treatments . However, the disadvantage of EELS is that we don't have the capability to study the change of the oxidation state in situ in our transmission electron microscope. Therefore, we plan to apply complementary in situ techniques like NEXAFS (near-edge X-ray absorption spectroscopy) and ESR (electron spin resonance) to similar samples to unveil the underlying atomistic process leading to the enhancement of ionic motion.

1. B. Butz, P. Kruse, H. Störmer, D. Gerthsen, A. Müller, A. Weber, E. Ivers-Tiffée, SSI 177 [4] (2006) 3275
2. B. Butz, R. Schneider, D. Gerthsen, M. Schowalter, A. Rosenauer, Acta Mater. 57 [18] (2009) 5840
3. B. Butz, A. Lefarth, H. Störmer, A. Utz, E. Ivers-Tiffée, D. Gerthsen, SSI 214 (2012) 37
4. J.E. Wertz, J.R. Bolton, Electron Spin Resonance, Chapman and Hall, 1986
5. The Authors thank the German Research Foundation (DFG) for financial support via the Cluster of Excellence EXC315 “Engineering of Advanced Materials”.

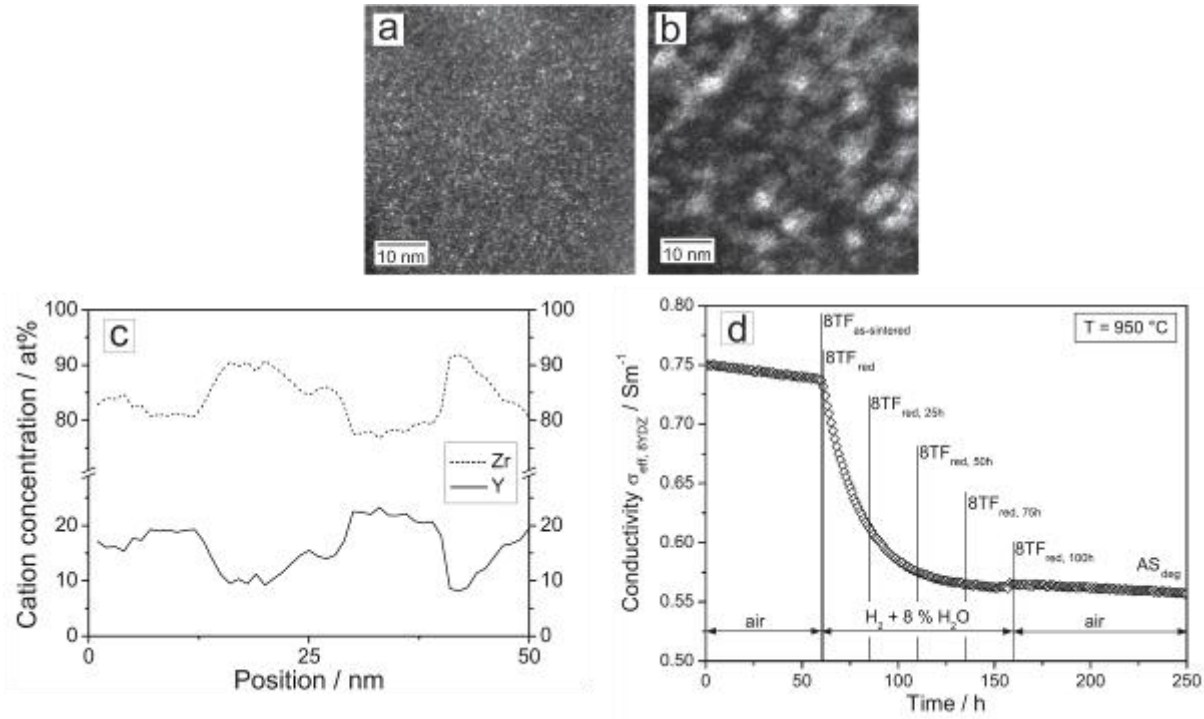

Figure 1. TEM dark-field images of a) as-sintered and b) degraded 8YSZ [3] depicting the redistribution of t’’-YSZ precipitates (indication for on-going decomposition). c) EDXS line scan across several Y-depleted regions (indicated by higher contrast in b)). d) Accelerated degradation of DC conductivity of a Ni-containing 8YSZ sample. After about 70 h the atmosphere was switched to reducing conditions and held for 100 h. In this short period under reducing atmosphere the conductivity decreased of about 25%.

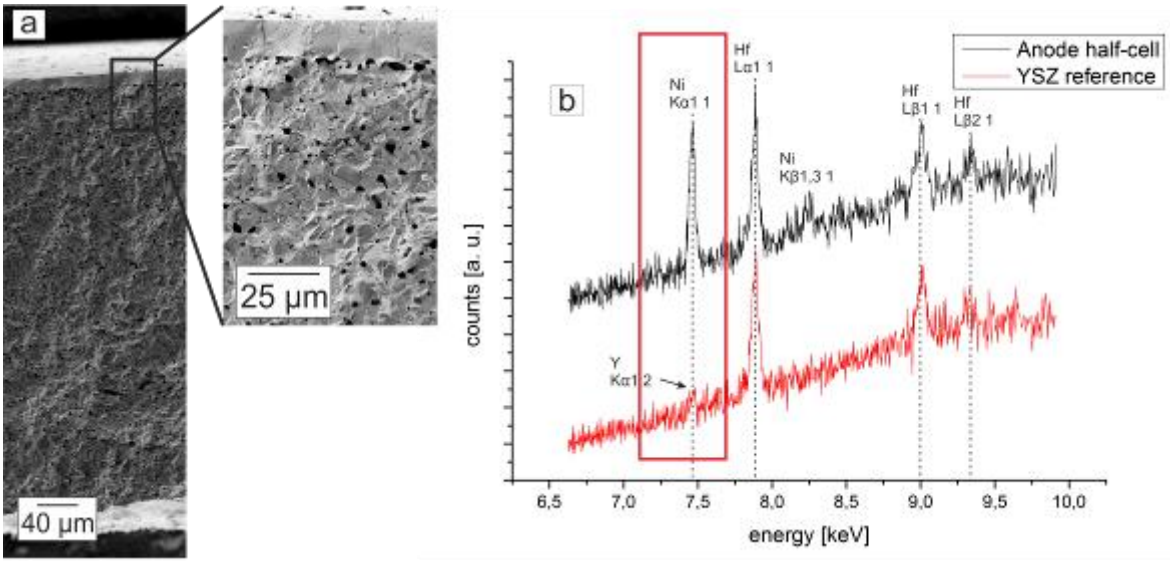

Figure 2. a) Cross-sectional SEM images of a state-of-the-art anode-based half-cell showing the dense 8YSZ layer on top of the porous (not yet reduced) anode. b) WDX spectra of the layer shown in a) and of a pure 8YSZ reference clearly indicating that Ni is already present in the 8YSZ electrolyte after the co-sintering of the anode half-cell. The Ni concentration amounts to about 1.5 at%.

Author Index

Author Index

Author Index

Author Index

Author Index

Author Index

L

Author Index

Author Index

Author Index

Author Index

Author Index

Author Index

Author Index